

NASA Technical Memorandum 4300

Reports of Planetary Geology and Geophysics Program—1990

JUNE 1991

(NASA-TM-4300) REPORTS OF PLANETARY GEOLOGY AND GEOPHYSICS PROGRAM, 1990

992-10728

--F--U--

992-10959

Includes

1991 0024935

The NASA logo, consisting of the word "NASA" in a bold, italicized, sans-serif font.

NASA Technical Memorandum 4300

Reports of Planetary Geology
and Geophysics Program—1990

*NASA Office of Space Science and Applications
Washington, D.C.*



National Aeronautics and
Space Administration

Office of Management

Scientific and Technical
Information Program

1991

Foreword

This is a compilation of abstracts of reports from Principal Investigators of NASA's Office of Space Science and Applications, Solar System Exploration Division, Planetary Geology and Geophysics Program.

The purpose of this publication is to document in summary form research work conducted in this program over the past year (1990). Each report reflects significant accomplishments within the area of the author's funded grant or contract.

No attempt has been made to introduce editorial or stylistic uniformity; on the contrary, the style of each report is that of the Principal Investigator and may best portray his research.

Joseph Boyce
Discipline Scientist
Planetary Geoscience Programs

CONTENTS

Foreword.....	iii
CHAPTER 1 - INTERIOR PROCESSES-EXPERIMENTAL AND THEORETICAL	
Processes of Deep Terrestrial Mantles and Cores.....	3
R. Jeanloz	
Implications of Convection in the Moon and the Terrestrial Planets.....	5
D.L. Turcotte	
Dynamic Models for Ridge Belt Formation on Venus.....	7
M. Simons, S.C. Solomon and B.H. Hager	
An Assessment of the Crustal Remelting Hypothesis for Volcanism in the Freyja Montes Deformation Zone.....	10
N. Namiki and S.C. Solomon	
Martian Seismicity.....	13
R.J. Phillips and R.E. Grimm	
Thermal Models for Icy Satellites.....	15
R.H. Brown	
Flow and Fracture of Ice and Ice Mixtures.....	17
W.B. Durham and S.H. Kirby	
The Effect of Volume Phase Changes, Mass Transport, Sunlight Penetration, and Densification on the Thermal Regime of Icy Regoliths.....	20
F.P. Fanale, J.R. Salvail, D.L. Matson, and R.H. Brown	
The Role of Nonuniform Internal Heating in Triton's Energy Budget.....	22
R.L. Kirk and R.H. Brown	
Physical Properties of Cryovolcanic Brines: Applications to the Evolution of Ganymede.....	25
J.S. Kargel	
The Magnesium Sulfate-Water System at Pressures to 4 Kilobars.....	27
D.L. Hogenboom, J.S. Kargel, J.P. Ganasan, and J.S. Lewis	
Properties of Planetary Fluids at High Pressures and Temperatures.....	29
W.J. Nellis, N.C. Holmes, and A.C. Mitchell	

Fluid Dynamics of Multiphase Flow in Volcanic Environments on the Earth, Io, and Other Planets.....	32
S.W. Kieffer	

CHAPTER 2 - STRUCTURE AND TECTONICS

Tectonic Evolution of Lavinia Planitia, Venus.....	35
S.W. Squyres, S.L. Frank, G.E. McGill, and S.C. Solomon	
Morphology and Evolution of Coronae and Ovoids on Venus.....	37
S.W. Squyres, D.L. Bindshadler, D.M. Janes, G. Schubert, V.L. Sharpton, and E.R. Stofan	
Hot-Spot Tectonics of Eistla Regio, Venus: Results From Magellan Images and Pioneer Venus Gravity.....	39
R.E. Grimm and R.J. Phillips	
Gravitational Spreading of Danu, Freyja and Maxwell Montes, Venus.....	41
S.E. Smrekar and S.C. Solomon	
Interpretation of the Northern Boundary of Ishtar Terra from Magellan Images and Altimetry.....	44
S. Mueller, R.E. Grimm, and R.J. Phillips	
Horizontal Stress in Planetary Lithospheres from Vertical Processes.....	46
W.B. Banerdt	
Geology, Structure, and Statistics of Multi-Ring Basins on Mars.....	49
R.A. Schultz and H.V. Frey	
Modelled and Measured Strain in Mascon Basins on the Moon.....	51
M.P. Golombek and B.J. Franklin	
Strain Accommodation Beneath Structures on Mars.....	54
M.P. Golombek, K.L. Tanaka, and W.B. Banerdt	
Early Tectonic Evolution of Mars - Crustal Dichotomy to Valles Marineris.....	57
H.V. Frey and R.A. Schultz	
The Formation of Antipodal-Impact Terrains on Mars....	59
D.A. Williams and R. Greeley	
Global Relationships Between Volcanic Vents and Fractures Radial to Large Impact Basins on Mars.....	61
B.D. Schneid and R. Greeley	

Volcanic Vents and Fractures Radial to Impact Basins..	61
B.D. Schneid and R. Greeley	
Tectonic Setting of Martian Volcanoes and Deep-Seated Intrusives.....	63
D.H. Scott and J.M. Dohm	
Timing and Formation of Wrinkle Ridges in the Tyrrhena Patera Region of Mars.....	65
T.K. Porter, D.A. Crown, and R. Greeley	
Compressive Strain in Lunae Planum-Shortening Across Wrinkle Ridges.....	67
J.B. Plescia	
Late Noachian Development of the Coprates Rise, Mars..	70
K.L. Tanaka and R.A. Schultz	
Interactions of Tectonic, Igneous, and Hydraulic Processes in the North Tharsis Region of Mars.....	73
P.A. Davis, K.L. Tanaka, M.P. Golombek and J. Plescia	
Valles Marineris Tectonism: Questions and Suggestions	75
B.K. Lucchitta, M.G. Chapman, and N.K. Isbell	
Extension and Strain in Northern Tharsis.....	77
J.B. Plescia	
Valles Marineris, Mars: Are Pit Chains Formed by Erosion and Troughs by Tectonism?.....	80
B.K. Lucchitta, R.A. Balser, and L.M. Bertolini	
Martian Seismicity Through Time from Surface Faulting.	82
M. Golombek, K. Tanaka, W. Banerdt, and D. Tralli	
A 40 th Degree and Order Gravitational Field Model for Mars.....	85
M.T. Zuber, D.E. Smith, F.J. Lerch, R.S. Nerem, G.B. Patel, and S.K. Fricke	
SO ₂ -Rich Equatorial Basins and Epeirogeny of Io.....	87
A.S. McEwen	
Structural Geology and Geological History of the Perrine and Nun Sulci Quadrangles (Jg-2 and Jg-5), Ganymede.....	90
G.E. McGill, and S.W. Squyres	
Tectonic Deformation on Icy Satellites: A Model of Compensating Horsts.....	93
R. Pappalardo and R. Greeley	

Mimas: Tectonic Structure and Geologic History.....	95
S.K. Croft	
Tethys Geology and Tectonics Revisited.....	98
S.K. Croft	
Iapetus: Tectonic Structure and Geologic History.....	101
S.K. Croft	
The Strength of Miranda's Lithosphere.....	104
R. Pappalardo and R. Greeley	

CHAPTER 3 - SURFACE PROCESSES AND GEOMORPHOLOGY

Ancient Oceans and Martian Paleohydrology.....	109
V.R. Baker, V.C. Gulick, J.S. Kargel, G. Komatsu, and V.S. Kale	
Evolution of the Martian Hydrosphere.....	111
V. Baker	
A Martian Global Groundwater Model.....	114
A.D. Howard	
Role of Groundwater in Formation of Martian Channels..	117
A.D. Howard	
Role of Artesian Groundwater in Forming Martian Permafrost Features.....	120
A.D. Howard	
Glacial and Marine Chronology of Mars.....	123
R.G. Strom, J.S. Kargel, N. Johnson, and C. Knight	
Chronology of Glaciation in the Hellas Region of Mars.	125
N. Johnson, J.S. Kargel, R.G. Strom, and C. Knight	
Glacial Geology of the Hellas Region on Mars.....	127
J.S. Kargel, R.G. Strom, and N. Johnson	
Terrestrial Glacial Eskers: Analogs for Martian Sinuous Ridges.....	129
J.S. Kargel, and R.G. Strom	
Paleolakes and Lacustrine Basins on Mars.....	131
D.H. Scott, J.W. Rice, Jr., and J.M. Dohm	
Stratigraphy of the Layered Terrain in Valles Marineris, Mars.....	133
G. Komatsu and R.G. Strom	

Hydrologic Activity During Late Noachian and Early Hesperian Downwarping of Borealis Basin, Mars.....	135
K.L. Tanaka	
Channeling Episodes of Kasei Valles, Mars, and the Nature of Ridged Plains Materials.....	138
M.G. Chapman and K.L. Tanaka	
Flood Routing of the Maja Outflow Across Xanthe Terra.	140
R.A. De Hon	
Ancient Fluvial Processes in the Equatorial Highlands of Mars.....	143
R.A. Craddock, and T.A. Maxwell	
Geologic History and Channeling Episodes of the Chryse Planitia Region of Mars.....	146
S.L. Rotto and K.L. Tanaka	
Evolution of the Water Regime of Phobos.....	149
F.P. Fanale and J.R. Salvail	
Phobos: Surface and Solid Body Properties from Digital Shape Data.....	150
P.C. Thomas	
Gradational Evolution of Young, Simple Impact Craters on the Earth.....	152
J.A. Grant and P.H. Schultz	
Styles of Crater Gradation in Southern Ismenius Lacus, Mars.....	154
J.A. Grant and P.H. Schultz	
The Gradational History of Southern Ismenius Lacus....	156
J.A. Grant and P.H. Schultz	
Soil Crusts on Mars.....	158
H.J. Moore	
Surface-Material Maps of Viking Landing Sites on Mars.	160
H.J. Moore and J.M. Keller	
Magma Generation on Mars: Estimated Volumes Through Time.....	163
R. Greeley and B. Schneid	
Crystallization During Emplacement of Lava Flows.....	165
J. Crisp	
Physical Properties of Lava Flows on the Southwest Flank of Tyrrhena Patera, Mars.....	167
D.A. Crown, T.K. Porter, and R. Greeley	

Rheological Analyses of Lava Flows on Mars.....	170
H.J. Moore and P.A. Davis	
Factors Controlling Lava Dome Morphology.....	172
J. Fink, N. Bridges, and R. Griffiths	
New Studies of Martian Volcanoes.....	174
P.J. Mouginis-Mark, M.S. Robinson, and S.H. Zisk	
The Probable Continuum Between Emplacement of Plutons and Mare Volcanism in Lunar Crustal Evolution.....	177
C.M. Pieters	
Lunar Western Limb Pyroclastic Deposits.....	179
C.R. Coombs and B.R. Hawke	
Lunar and Hawaiian Lava Tubes: Analogs and Uses Based on Terrestrial Field Data.....	181
C.R. Coombs and B.R. Hawke	
On Using a Pyroclastic Deposit as A Manned Lunar Base Site.....	183
C.R. Coombs, D.S. McKay, B.R. Hawke, and G. Heiken	

CHAPTER 4 - LITHOSPHERE/ATMOSPHERE RELATIONS

Water on Mars: Clue to Accretional History.....	187
M.H. Carr	
Variable Features in the Valles Marineris Region on Mars.....	191
P.E. Geissler and R.B. Singer	
The Potential Scale of Aeolian Structures on Venus....	194
J.R. Marshall and R. Greeley	
Relationships Between Topographic Roughness and Aeolian Processes.....	195
R. Greeley, N. Lancaster, L. Gaddis, K.R. Rasmussen, B.R. White, R.S. Saunders, S. Wall, A. Dobrovolskis, and J.D. Iversen	
Use of Radar to Assess Aeolian Processes.....	198
R. Greeley, N. Lancaster, L. Gaddis, D. Blumberg, A. Dobrovolskis, R.S. Saunders, S. Wall, J. Iversen, B. White, and K. Rasmussen	
Free Convection in the Martian Atmosphere.....	199
G.D. Clow and R.M. Haberle	

Characteristics of the Martian Atmospheric Surface Layer.....	201
G.D. Clow and R.M. Haberle	
Heat Flow vs. Atmospheric Greenhouse on Early Mars....	203
F.P. Fanale and S.E. Postawko	
New Models for the Origin of Valles Marineris Closed Depressions.....	206
J.R. Spencer and F.P. Fanale	
Degradation of Fe-Mg Silicates in Hot CO ₂ Atmospheres: Applications to Venus.....	207
D.W. Straub and R.G. Burns	
Theoretical Studies of Volatile Processes in the Outer Solar System.....	210
J.I. Lunine	

CHAPTER 5 - SPECTROSCOPY AND REMOTE SENSING

Lunar Maria and Related Deposits: Preliminary Galileo Imaging Results.....	215
R. Greeley, et al.	
Crustal Heterogeneity of the Moon Viewed from the Galileo SSI Camera: Lunar Sample Calibrations and Compositional Implications.....	218
C.M. Pieters, et al.	
Remote Sensing and Geologic Studies of the Orientale Basin Region.....	220
B.R. Hawke, P.G. Lucey, G.J. Taylor, J.F. Bell, C.A. Peterson, D. Blewett, K. Horton, and P. Spudis	
Remote Sensing and Geologic Studies of the Terrain Northwest of Humorum Basin.....	223
B.R. Hawke, C.A. Peterson, P.G. Lucey, G.J. Taylor, J.F. Bell, D. Blewett, B. Campbell, C.R. Coombs, and P.D. Spudis	
Analyses of the Lunar Surface with Advanced Remote Sensors: Expectations for the 1990's.....	226
C.M. Pieters	
Infrared Reflectance Spectra (4-12 um) of Lunar Samples.....	227
D.B. Nash	
Remote Sensing of the Martian Surface.....	229
B.M. Jakosky, B.G. Henderson, C.E. Randall, M.J. Alexander, and T.M. McCollom	

Mineralogy of the Martian Surface from Mariner 6/7 Infrared Spectrometer Data.....	231
T.Z. Martin	
Composition of Syrtis Major Volcanic Plateau.....	234
J.F. Mustard, S. Erard, J-P Bibring, Y. Langevin, J.W. Head, and C.M. Pieters	
The Perplexing Continuum Slope of Mars: Effects of Thin Ferric Coatings and Viewing Geometry.....	236
E.M. Fischer, C.M. Pieters, and S.F. Pratt	
Oxidation of Basaltic Tephra: Influence on Reflectance in the 1um Region.....	238
W.H. Farrand and R.B. Singer	
Spectroscopic Analyses of Fe and Water in Clays. A Martian Surface Weathering Study.....	240
J.L. Bishop, C.M. Pieters, J.O. Edwards, L.M. Coyne, and S. Chang	
Water Detection at the Moon, Mars and Comets with a Combined Neutron-Gamma Ray Instrument.....	242
A.E. Metzger and E.L. Haines	
Spectral Evidence for Carbonates on Mars: Hydrous Carbonates.....	244
W.M. Calvin and T.V.V. King	
Optical Properties of CO ₂ Ice and CO ₂ Snow from Ultraviolet to Infrared: Application to Frost Deposits and Clouds on Mars.....	246
G.B. Hansen, S.G. Warren, and C.B. Leovy	
Disk-Resolved Spectral Reflectance Properties of Phobos from 0.3-3.2 um: Preliminary Integrated Results from Phobos 2.....	249
S.L. Murchie, S. Erard, Y. Langevin, D.T. Britt, J-P Bibring, J.F. Mustard, J.W. Head and C.M. Pieters	
Evidence for Ammonium-Bearing Minerals on Ceres.....	251
T.V.V. King, R.N. Clark, W.M. Calvin, D.M. Sherman, G.A. Swayze, and R.H. Brown	
Reflectance Spectra of Fe ²⁺ -Mg ²⁺ Disordered Pyroxenes: Implications to Remote-Sensed Spectra of Planetary Surfaces.....	253
R.G. Burns, J.R. Besancon, and S.F. Pratt	
Pre-Terrestrial Oxidation Products in Carbonaceous Meteorites Identified by Mossbauer Spectroscopy.....	256
R.G. Burns and D.S. Fisher	

Does Lafayette = Nakhla? Not Necessarily So, Based on 4.2K Mossbauer Spectra of All of the SNC Meteorites...	259
R.G. Burns	
Infrared (2.08-14 um) Spectra of Powdered Stony Meteorites.....	262
J.W. Salisbury, D.M. D'Aria, and E. Jarosewich	
Darkening in Gas-Rich Ordinary Chondrites: Spectral Modelling and Implications for the Regoliths of Ordinary Chondrite Parent Bodies.....	265
D.T. Britt and C.M. Pieters	
The Bidirectional Reflectance Spectra of Five Gas-Rich Ordinary Chondrites.....	267
D.T. Britt and C.M. Pieters	
Reflectance Spectra of Some Fractions of Migei and Murchison CM Chondrites in the Range of 0.3-2.6 um....	269
L.V. Moroz and C.M. Pieters	
An Infrared Reflectance Study of Low Albedo Surface Constituents.....	271
L.A. Lebofsky	
Effects of Grain Size and Shape in Modeling Reflectance Spectra of Mineral Mixtures.....	274
T. Hiroi and C.M. Pieters	
Light Scattering by Lunar-Like Particle Size Distributions.....	276
J.D. Goguen	
Character of the Opposition Effect and Negative Polarization.....	279
C.M. Pieters, Y.G. Shkuratov, and D.G. Stankevich	
Laboratory Photometric Measurement of Particulate Soils Out to Very Large Phase Angles.....	280
P. Helfenstein, U.A. Bonne, S. Stolovy and J. Veverka	
The Photometric Roughness of Mimas.....	283
A. Verbiscer and J. Veverka	
Anomalous Scattering of Light on Triton.....	285
P. Helfenstein, P. Lee, D. McCarthy, and J. Veverka	
Disk Resolved Studies of the Optical Properties and Physical Nature of the Surfaces of the Outer Planet Satellites.....	288
B.J. Buratti, J.A. Mosher, and T.V. Johnson	

Europa's Phase Curve: Implications for Surface Structure.....	291
D. Domingue, B. Hapke, W. Lockwood and D. Thompson	
Charged-Particle Induced Alterations of Surfaces in the Outer Solar System.....	292
R.E. Johnson	
New Spectral Observations of Callisto and Leading/Trailing Hemisphere Distinctions.....	294
W.M. Calvin, R.N. Clark, and T.V.V. King	
Mojave Remote Sensing Field Experiment.....	296
R.E. Arvidson, S.B. Petroy, J.J. Plaut, M. Shepard, D. Evans, T. Farr, R. Greeley, L. Gaddis, and N. Lancaster	
Surface Scattering Properties Estimated from Modeling Airborne Multiple Emission Angle Reflectance Data.....	298
E.A. Guinness, R.E. Arvidson, J.R. Irons, and D.J. Harding	
Mapping Compositional and Particle Size Variations Across Silver Lake Playa - Relevance to Analyses of Mars TIR Data.....	301
S.B. Petroy, R.E. Arvidson, and A.B. Kahle	
Application of Hapke Photometric Model to Three Geologic Surfaces Using Parabola Bidirectional Reflection Data.....	304
M.K. Shepard, R.E. Arvidson, and D.W. Deering	
The Geologic Remote Sensing Field Experiment (GRSFE)..	306
M.A. Dale-Bannister, R.E. Arvidson, E.E. Guinness, S.H. Slavney and T.C. Stein	
High Resolution Lunar Radar Studies-Preliminary Results.....	308
N.J.S. Stacy and D.B. Campbell	
Models of the Diffuse Radar Backscatter from Mars.....	310
A.W. England and R.T. Austin	
Remote Sensing Observations of Kelso Dunes, California	313
R. Greeley, N. Lancaster, L. Gaddis, and E.C.I. Paisley	
Possible Martian Brines: Radar Observations and Models.....	314
A.P. Zent, F.P. Fanale, and L.E. Roth	

Preliminary Comparison of 3.5-CM and 12.6-CM Wavelength Continuous Wave Observations of Mars.....	315
H.J. Moore, T.C. O'Brien, R.F. Jurgens, M.A. Slade, and T.W. Thompson	
Surface Properties of Galilean Satellites from Bistatic Radar Experiments.....	317
R.A. Simpson and G.L. Tyler	
Radar Backscattering by the Icy Galilean Satellites and the Radar Glory Effect.....	320
E.M. Gurrola and V.R. Eshleman	
Regoliths of Icy Satellites: The Coherent Backscatter Model.....	323
B. Hapke and D. Blewett	
Coherent Backscatter and the Radar Characteristics of Outer Planet Satellites.....	325
B. Hapke	
Doppler-Radar Imaging of Spherical Planetary Surfaces.	326
R.S. Hudson and S.J. Ostro	

CHAPTER 6 - IMPACT STUDIES

Impact Craters on Venus.....	329
G.G. Schaber	
Quantitative Analysis of Terrain Units Mapped in the Northern Quarter of Venus from Venera 15/16 Data.....	332
G.G. Schaber	
Venus Impact Craters: Implications for Atmospheric and Resurfacing Processes from Magellan Observations..	334
R.J. Phillips	
Breakup of Meteoroids in the Venusian Atmosphere and Its Effects on Crater Formation.....	336
R.R. Herrick and R.J. Phillips	
Atmospheric Effects on Oblique Impacts.....	338
P.H. Schultz	
Styles of Ejecta Emplacement under Atmospheric Conditions.....	340
P.H. Schultz	
Impact Decapitation from Laboratory to Basin Scales...	342
P.H. Schultz and D.E. Gault	
Laboratory Simulation of Cratering on Small Bodies....	344
R.M. Schmidt	

Possible Misinterpretation of Lunar Cratering Record in Voyager Team Analyses of Outer Planet Satellites...	347
W.K. Hartmann	
Hydrocode Predictions of Collisional Outcomes: Effects of Target Size.....	350
E.V. Ryan, E. Asphaug, and H.J. Melosh	
Energy Coupling in Catastrophic Collisions.....	352
K.A. Holsapple and K.Y. Choe	
Continuum Modeling of Catastrophic Collisions.....	354
E. Ryan, E. Asphaug, and H.J. Melosh	
Core Formation by Giant Impacts.....	355
W.B. Tonks and H.J. Melosh	
Large Impacts and Climatic Catastrophes on the Early Earth.....	357
H.J. Melosh	
Impacts and the Early Environment and Evolution of the Terrestrial Planets.....	359
H.J. Melosh and A.M. Vickery	
Vapor Plumes: A Neglected Aspect of Impact Cratering.	360
H.J. Melosh	
Jetting and the Origin of Tektites.....	361
A.M. Vickery	
Melt Droplet Formation in Energetic Impacts.....	362
A.M. Vickery and H.J. Melosh	
Production of Impact Melt in Craters on Venus, Earth, and the Moon.....	364
A.M. Vickery and H.J. Melosh	
Impacts and Atmospheric Erosion on the Early Earth....	366
A.M. Vickery	
Characteristics of Ejecta and Alluvial Deposits at Meteor Crater, Arizona and Odessa Craters, Texas: Results from Ground Penetrating Radar.....	368
J.A. Grant and P.H. Schultz	
Depth/Diameter Relationships of Fresh Craters Within Hesperia Planum, Mars.....	370
P.J. Mouginis-Mark and J.N. Hayashi	
The Scaling of Secondary Craters.....	373
S.K. Croft	

Chemical Fractionation of Siderophile Elements in Impactites from Australian Meteorite Craters.....	375
M. Attrep, Jr., C.J. Orth, L.R. Quintana, C.S. Shoemaker, E.M. Shoemaker and S.R. Taylor	
Igneous Intrusion Models for Floor Fracturing in Lunar Craters.....	377
R.W. Wichman and P.H. Schultz	
Magnetic Effects of Large-Scale Impacts on Airless Planetary Bodies.....	379
L.L. Hood and Z. Huang	
The Spatial Distribution and Time Evolution of Impact- Generated Magnetic Fields.....	382
D.A. Crawford and P.H. Schultz	
Gravity Survey of the Mt. Toondina Impact Structure, South Australia.....	384
J. Plescia, E.M. Shoemaker, and C. Shoemaker	
 CHAPTER 7 - ASTEROIDS AND COMETS	
Asteroid Flux and Impact Cratering Rate on Venus.....	389
E.M. Shoemaker, R.F. Wolfe, and C.S. Shoemaker	
Meteorite Spectroscopy and Characterization of Asteroid Surface Materials.....	391
M.J. Gaffey	
Will Galileo Resolve the S-Asteroid Controversy?.....	394
J.F. Bell	
Mapping the Stability Field of Jupiter Trojans.....	397
H.F. Levison, E.M. Shoemaker and R.F. Wolfe	
Understanding Asteroid Collisional History Through Experimental and Numerical Studies.....	399
D.R. Davis, E.V. Ryan and S.J. Weidenschilling	
Asteroid Families.....	403
J.G. Williams	
Origin and Evolution of the Zodiacal Dust Cloud.....	405
S.F. Dermott, D. Durda, R.S. Gomes, B. Gustafson, S. Jayaraman, Y-L Xu, and P.D. Nicholson	
Photometry of the Comet 2060 Chiron.....	407
B.J. Buratti, R.L. Marcialis, and R.S. Dunbar	
A New Activity Index for Comets.....	409
F.L. Whipple	

The Angular Momentum of the Oort Cloud.....	411
P.R. Weissman	
Water/Rock Interactions in Experimentally Simulated "Dirty Snowball" and "Dirty Iceball" Cometary Nuclei..	412
J.L. Gooding and J.H. Allton	
Thermal Modeling of Comet Kopff: Implications for the CRAF Mission.....	415
P. Weissman and C. Clause	
The Influence of CO Ice on the Activity and Near- Surface Differentiation of Comet Nuclei.....	416
F.P. Fanale and J.R. Salvail	

CHAPTER 8 - SOLAR SYSTEM DYNAMICS

Formation of the Protosolar Nebula.....	419
W.M. Tscharnuter and A.P. Boss	
Fragmentation in Stellar Collapse.....	420
E.M. Myhill and W.M. Kaula	
Spectral and Isophotal Appearance of 3D Protostellar Models.....	422
A.P. Boss and H.W. Yorke	
Aerodynamic and Gasdynamic Effects in Cosmogony.....	424
S.J. Weidenschilling	
Particle-gas Dynamics in the Protoplanetary Nebula....	427
J.N. Cuzzi, J.M. Champney, and A.R. Dobrovolskis	
Bending Waves and Orbital Inclinations.....	430
W.R. Ward	
Accretion and Evolution of Solar System Bodies.....	433
S.J. Weidenschilling and D.R. Davis	
Long-Term Evolution of a Planetesimal Swarm in the Vicinity of a Protoplanet.....	436
D.M. Kary and J.J. Lissauer	
A Reexamination of Early Numerical Simulations of Planetary Accretion.....	438
R.A. Kolvoord and R. Greenberg	
Collision Probabilities in the Presence of Nebular Gas Drag.....	441
D.M. Kary and J.J. Lissauer	
Growth of Planets from Planetesimals.....	443
J.J. Lissauer and G.R. Stewart	

Tidal Disruption of Inviscid Protoplanets.....	444
A.P. Boss, A.G.W. Cameron and W. Benz	
A Geometrical Model for Shepherding.....	446
J.J. Lissauer	
Dynamics of Low Velocity Collisions of Ice Particle, Coated with Frost.....	447
F. Bridges, D. Lin, L. Boone, and D. Darknell	
Planetary Ring Studies.....	449
J.N. Cuzzi, A.R. Dobrovolskis, L. Dones, R.H. Durisen, L. Horn, and M.R. Showalter	
Research Performed in 1990 under NASA Grant-310: Physical Processes in Planetary Rings.....	452
J.A. Burns	

CHAPTER 9 - MARS GEOLOGIC MAPPING

Preliminary Geologic Mapping of Arsia Mons, Mars.....	457
J.R. Zimbelman	
Preliminary Geologic Mapping of Central Chryse Planitia, Mars.....	459
R.A. Craddock, L.S. Crumpler, and J.C. Aubele	
Geologic Mapping of Northern Lunae Planum, Mars.....	462
R.A. Craddock and T.A. Maxwell	
Mars Geologic Mapping: Dao, Harmakhis, and Reull Valles Region.....	465
K.H. Price	
Evolution of the East Rim of the Hellas Basin, Mars...	468
D.A. Crown, K.H. Price, and R. Greeley	
Geologic Mapping of MTM Quads 40292 and 40297: In the Utopian Lowlands North of the Nilosyrtis Mensae, Mars.	471
S.H. Williams and J.R. Zimbelman	
Stratigraphy of the Perrine and Nun Sulci Quadrangles (Jg-2 and Jg-5), Ganymede.....	474
G.E. McGill and S.W. Squyres	
Are Noachian-Age Ridged Plains (Nplr) Actually Early Hesperian in Age?.....	477
H.V. Frey, C.E. Doudnikoff, and A.M. Mongeon	
Mars Geologic Mapping Program: Review and Highlights.	479
D.H. Scott	

CHAPTER 10 - PLANETARY CARTOGRAPHY AND PROGRAM SUPPORT

Venus Mapping.....	483
R.M. Batson, H.F. Morgan, and R. Sucharski	
Triangulation Using Synthetic Aperture Radar Images...	489
S.S.C. Wu and A.E. Howington-Kraus	
Naming the Newly Found Landforms on Venus.....	490
R.M. Batson and J.F. Russell	
The Control Network of Mercury: April 1991.....	492
M.E. Davies and P.G. Rogers	
A Unified Lunar Control Network: April 1991.....	494
M.E. Davies	
The Control Network of Mars: April 1991.....	497
M.E. Davies and P.G. Rogers	
Publication of Topographic Atlas and Control Network of Mars.....	499
S.S.C. Wu, J.S. Billideau, and B.A. Spare	
Color-Coded Global Topographic Maps of Mars.....	503
S.S.C. Wu, A.E. Howington-Kraus, and K. Albin	
Mars Elevation Distribution.....	506
S.S.C. Wu, A.E. Howington-Kraus, and K. Albin	
Completion of Compilation of the 1:2,000,000-Scale Topographic Map Series of Mars.....	508
S.S.C. Wu, R. Jordan, P.A. Garcia, and K.K. Albin	
Mars High-Resolution Mapping.....	509
R.M. Batson, P.K. Thomas	
A New Edition of the Mars 1:5,000,000 Map Series.....	510
R.M. Batson, A.S. McEwen, and S.S.C. Wu	
Planetary Atlases.....	511
R.M. Batson, J.L. Inge, and H.F. Morgan	
CD-ROM Publication of the Mars Digital Cartographic Data Base.....	512
R.M. Batson, E.M. Eliason, L.A. Soderblom, K. Edwards, and S.S.C. Wu	
Digital Cartography of Io.....	514
A. McEwen, B. Duck, and K. Edwards	
Digital Solar System Geology.....	515
R.M. Batson, R.C. Kozak, and N.K. Isbell	

A New Catalog of Planetary Maps.....	516
R.M. Batson and J.L. Inge	
Image Retrieval and Processing System Version 2.0 Development Work.....	517
S. Slavney and E.A. Guinness	
CHAPTER 11 - LATE ABSTRACTS.....	521
AUTHOR INDEX.....	587

CHAPTER 1

**INTERIOR PROCESSES-EXPERIMENTAL AND
THEORETICAL**

PROCESSES OF DEEP TERRESTRIAL MANTLES AND CORES.

Raymond Jeanloz, Department of Geology and Geophysics, University of California, Berkeley, CA, 94720.

Ultrahigh-pressure experiments are currently focused on revealing processes occurring deep inside planets. This is in addition to the traditional emphasis on the constitution of planetary interiors, such as the identification of the high-pressure perovskite phase of $(\text{Mg,Fe})\text{SiO}_3$ as the predominant mineral inside the Earth, and probably Venus.

For example, experiments demonstrate that the mechanism of geochemical differentiation, separation of partial melt, differs fundamentally in the lower mantles of Earth and Venus than at near-surface conditions. This is because silicate melts tend to stagnate or even sink deep in the mantle, rather than rising buoyantly. The change in differentiation mechanism is caused by structural transformations of the melt, analogous to the structural transitions of crystals induced by pressure. A statistical mechanically based model of melt structure reproduces the experimentally observed shape of the high-pressure melting curve for the Mg-silicate perovskite phase, thus supporting the concept of melt densification deep inside planets.

In addition to structural transformations, changes in chemical bonding caused by pressure can also be significant for planetary interiors. In particular, experiments indicate that high-pressure bonding changes cause liquid iron to react vigorously with the silicates of the deep mantle inside Earth and Venus. The core-mantle boundary is thus inferred to be the most chemically active region of these planets. In contrast, pressures may be too low to induce the same phenomena in the mantle of Mars. The heterogeneous products of reaction between mantle and core are inferred to form the seismological D'' region, and possibly to influence the geomagnetic field of the Earth. Thus, the cores of large terrestrial planets evolve geochemically through contamination by (alloying with) the mantle over geological time.

Measurements of AC and DC electrical conductivity can be obtained at ultrahigh pressures and temperatures, to > 80 GPa and > 3000 K simultaneously, using the laser-heated diamond cell. Quantitative agreement with conductivity values and activation energies obtained by resistance heating or by shock-wave techniques attest to the reliability of the data. Contamination of the sample, including reaction with the leads, can be avoided. Oxygen fugacity is controlled (though not predetermined) in the experiments, but the available results suggest that it alone does not determine ion valences at high pressures.

Anhydrous lower-mantle assemblages (perovskite \pm oxide phases) exhibit an electrical conductivity that depends strongly on Fe content: relatively low values, $\leq 10^{-3}$ S/m at lower-mantle pressures and temperatures, are obtained for typical upper-mantle compositions (Mg value ~ 0.9), whereas the conductivity of iron-enriched assemblages (Mg value ~ 0.8) is comparable to that inferred for the outer portions of the Earth's lower mantle, $\sim 10^0$ - 10^1 S/m. Assemblages with ~ 4 wt.% H_2O also exhibit conductivities of $\sim 10^{-1}$ - 10^0 S/m.

Contrary to traditional assumptions, temperature affects the conductivity of lower-mantle assemblages relatively little: we obtain activation energies of ~ 0.1 - 0.4 eV. The conduction of the Fe-rich and Fe-poor samples is interpreted in terms of extrinsic electronic mobility and electron hopping, respectively. Similarly, pressure has only a small effect on conductivity, and we find no evidence for dominant ionic conduction either in the crystalline or molten samples at lower-mantle pressures. Instead, composition and valence states primarily seem to control the electrical conductivity at lower mantle conditions.

The Earth's deep-focus seismicity can be explained by the recycling of water into the mantle. Specifically, high-pressure experiments using the diamond cell show that hydrous minerals such as serpentine, talc and pyrophyllite generate acoustic emissions upon compression to pressures exceeding ~ 10 - 20 GPa, when temperatures are maintained below ~ 1000 K. In contrast, anhydrous assemblages involving olivine, pyroxene or their high-

pressure phases have not been found to produce acoustic emissions at elevated pressures. Hydrous minerals are present in the uppermost mantle of oceanic lithosphere due to infiltration by and reaction with seawater prior to subduction, and temperatures are expected to be sufficiently low to prevent dehydration and to produce the seismic events within the coldest portions of downgoing slabs. In addition, subduction-zone seismicity at depths ≤ 150 -200 km can in part be explained by dehydration at temperatures > 900 K.

Once present at depths greater than 200-300 km, water can be stably maintained within the crystalline phases of the mantle. Experiments with the laser-heated diamond cell, for example, demonstrate that 4 wt.% water reacts to form a stable assemblage of $(\text{Mg,Fe})\text{SiO}_3$ perovskite and Liu's phase D at pressures of ~ 20 -60 GPa. Thus, up to 10 - 10^2 times the water content of the oceans and atmosphere can be present in the deep mantle, implying that the interior may be the predominant reservoir of hydrogen for the Earth.

Implications of Convection in the Moon and the Terrestrial Planets
Donald L. Turcotte, Department of Geological Sciences, Cornell University,
Ithaca, NY 14853-1504

During the past year a principal effort has been to determine the thermal and chemical evolution of the moon and the terrestrial planets. The calculations give secular variations of the internal temperatures, Rayleigh numbers, viscosities, crustal thicknesses, lithospheric thicknesses, rates of volcanism, Urey numbers, and planetary radii. The principal effect studied during this period was the role of crustal recycling on evolution. Without crustal recycling the volcanism associated with crust formation extracts the heat producing elements from the interior of the planetary body on a relatively short time scale. Secular cooling may cause some further volcanism but convection slows as the interior cools and volcanism ceases.

Crustal creation without recycling appears to explain the observed evolution of the moon and Mars. The unresolved question primarily concern Venus. Low rates of crustal recycling imply a thick crust on Venus. We have also determined the thickness of the lithosphere on Venus for various models for the concentration of radioactive elements in the crust. A relatively thick lithosphere is obtained if a substantial fraction of the radiogenic isotopes are in the crust and these have a near-surface enrichment factor of at least two.

Our paper "Implications of crustal fractionation for planetary evolution" by D.L. Turcotte and Jie Huang remains a major effort. It has evolved into a comprehensive review of the thermal and chemical evolution of the moon and the terrestrial planets. During this period the section on Mars was expanded and brought up to date. A major effort was made to correlate the stratigraphic record of surface volcanism with the predictions. During this period our studies on the evolution of Mars were presented at the 21st Lunar and Planetary Science Conference, March 12-16, 1990. The extended abstract of this meeting was published (Turcotte and Huang, 1990). The work has also been incorporated into the review article "Origin and thermal evolution" (Schubert et al., 1991).

With the new results obtained from Venus by the Magellan Mission our efforts were concentrated on this planet. We carried out a series of studies:

- 1.) We examined alternative models for the thermal structure of the lithosphere of Venus. We considered variations in the thickness of the the crust on Venus, variations in the planetary concentrations of the heat-producing isotopes, variations in the fraction of isotopes concentrated into the crust, and we considered various models for the vertical fractionation of the isotopes within the crust. We found that the important effect was the concentration of heat-producing elements in the crust.
- 2.) We studied the statistical distribution of the locations of the coronae on Venus. We found that the distribution was fractal and had a strong resemblance to the statistical distribution of hotspots on earth.
- 3.) We examined models for the patterns of faulting around the coronae on Venus. These models considered the lithosphere on Venus to be a thin elastic shell and considered alternative models for loading the shell, including both static and dynamic force balances. Models were obtained that were in agreement with observations.

- 4.) We considered a series of viscous models for the development and relaxation of elevation anomalies on Venus.
- 5.) We studied rates of solidification of volcanic flows on Venus. Both radiative and convective heat transfer were considered.

DYNAMIC MODELS FOR RIDGE BELT FORMATION ON VENUS.

Mark Simons, Sean C. Solomon, and Bradford H. Hager, Department of Earth, Atmospheric, and Planetary Sciences, Massachusetts Institute of Technology, Cambridge, MA 02139.

Introduction. Deformation in a number of lowland plains regions on Venus is concentrated into distinct linear zones or belts^{1, 2}. High-resolution images and altimetry of such deformation belts have recently been obtained by the Magellan spacecraft for Lavinia Planitia, a broad quasi-circular lowland in the southern hemisphere. These data reveal that the belts are 50-200 km wide, several hundred kilometers long, spaced several hundred kilometers apart, and are generally elevated by several hundred meters above the surrounding plains. They are characterized morphologically by sets of closely spaced ridges and grooves that tend to parallel the trend of the belt and to be concentrated in the most elevated terrain³⁻⁵. The belts are interpreted as products of lithospheric shortening and crustal thickening. The lithospheric shortening expressed by the ridge belts has been postulated to be the result of convective downwelling beneath the lowland planitia^{6, 7}. In this paper we test this hypothesis quantitatively; specifically, we develop dynamical models for the interaction of mantle convection with the crust and we compare the models to the characteristics of the ridge belts in Lavinia Planitia.

On Earth, large scale surface-deformation is confined to the plate boundaries. This behavior is ascribable to the presence of a relatively strong plate overlying a low viscosity asthenosphere. However, on Venus, the elevated surface temperature leads to a weak lithosphere. Furthermore, the high correlation of long wavelength topography and gravity, as well as the large apparent depths of compensation, indicate that Venus does not have an asthenosphere⁷⁻¹⁰. Thus, models of tectonic deformation on Venus must account for convectively induced stresses. Because of the very low erosion rates on Venus¹², any large-scale tectonic expression of underlying convection may be preserved for considerably longer times than on Earth. Indeed, different tectonic areas of Venus may each be an expression of distinct stages in the evolution of convective upwellings and downwellings^{6, 12}.

Approach. On the basis of analytical models of convection-induced crustal flow^{13, 14}, the crust may be regarded as having two responses to convective downwelling. The first is a "flexural" response, during which the surface and crust-mantle boundary can be thought of as deforming "in phase." Following this, the crust responds by thickening, which continues until isostatic and dynamic equilibrium is established, at which point the surface boundary and the crust mantle boundary are anticorrelated. In our models, we examine the transition from the relatively instantaneous initial "flexural" response to the beginning of crustal thickening. The models use a marker chain/marker particle version of the 2-D Cartesian finite element program ConMan¹⁵, a procedure which allows us to follow the deformation of both crust and mantle. Unlike analytical models, we can employ both material- and temperature-dependent viscosities. In addition to the crust-mantle boundary and surface deformation, we also calculate the thermal gradient and the stress field in the lithosphere.

Models. A series of models have been developed to address several objectives. The most important of these are the relationship of mantle downwelling to the formation of zones of concentrated crustal thickening and the factors controlling the spacing and dimensions of deformation belts (e.g., vertical structure, initial lateral heterogeneity). The sensitivity of the crustal deformation pattern to regional thermal gradient and mean crustal thickness is also being investigated.

An example illustrates our approach. Our finite element mesh is a 70 by 70 element rectangle, where each element is 5 km high and 10 km wide. This mesh is 700 km wide and 350 km in vertical dimension. We impose free-slip boundary conditions on the top and side walls, with no flow through these walls. We apply a no-slip condition on the bottom boundary, while vertical flow through this boundary is unconstrained. In effect, this last boundary condition gives us a virtual 700 km by 700 km box. The surface topography is calculated from the vertical stresses on the top wall of the box. The crust-mantle boundary is simply the marker chain location at any given time.

We use an initial temperature field selected to explore the transient response of the crust to the initiation of mantle upwelling and downwelling. Top and bottom temperatures are fixed at 500°C and 1250°C, respectively. Initially, we impose a linear temperature gradient across the lithosphere and set the rest of the mantle to be isothermal. To initiate a plume at one corner of the bottom boundary, we fix the temperature there to be higher than that of the ambient mantle.

We have investigated several models with a constant viscosity mantle overlain by a constant viscosity crust. In these models we use crustal thicknesses of 15 or 25 km and ratios of crustal viscosity to mantle viscosity of 1 or 10. For all the models, the surface and crust-mantle boundaries initially deform "in phase," as in earlier analytical models^{13, 14}. At later stages of deformation, the crust thins over the area of upwelling and thickens over the region of downwelling. During the thickening phase, necking instabilities produce ridge-like features spaced hundreds of kilometers apart and hundreds of meters high (Figure 1). The characteristic widths of the instabilities are consistent with previous analytical results¹⁶, and the positions of the instabilities are time-dependent. If the instabilities depend on crustal thickness (or, more strictly, the density and viscosity structure), then the time-dependence may be explained by interference from different wavelengths being excited by the variation in crustal thickness with position and time. The models also indicate that an increase in initial crustal viscosity and a decrease in initial crustal thickness both favor instability growth. This behavior probably results from the interaction of horizontal extensional and compressional stresses with the shear stresses at the base of the crust.

Conclusions. These models support the hypothesis that convective stresses can produce the broad topographic depression of lowlands on Venus and can lead to the formation of ridge belts on either side of the topographic low. Future models will include temperature-dependent rheology, alternative flow geometries, and the transient effects of cessation of upwelling or other changes in flow patterns.

References: ¹V.L. Barsukov et al. (1986) *JGR*, **91**, D378-D398. ²D.B. Campbell et al. (1991). *Science*, **251**, 180-183. ³S.C. Solomon et al. (1991). *Science*, **252**, in press. ⁴S.W. Squyres et al. (1991). *LPSC*, **22**, 1309-1310. ⁵S.L. Frank and S.W. Squyres (1991). *LPSC*, **22**, 407-408. ⁶M.T. Zuber (1990). *GRL*, **17**, 1369-1372. ⁷R.J. Phillips et al. (1991). *Science*, in press. ⁸W.L. Sjogren et al. (1983). *JGR*, **88**, 1119-1128. ⁹B.G. Bills et al. (1987). *JGR*, **92**, 10,335-10,351. ¹⁰S.E. S.E. Smrekar and R.J. Phillips (1991). *EPSL*, in press. ¹¹R.E. Arvidson et al. (1990). *GRL*, **17**, 1385-1388. ¹²R.J. Phillips (1990). *JGR*, **95**, 1301-1316. ¹³D.L. Bindschadler and E.M. Parmentier (1990). *JGR*, **95**, 21,329-21,344. ¹⁴H. Schmeling and G. Marquart (1990). *GRL*, **17**, 2417-2420. ¹⁵S.D. King et al. (1990). *PEPI*, **59**, 195-207. ¹⁶M.T. Zuber (1987). *JGR*, **92**, E541-E551.

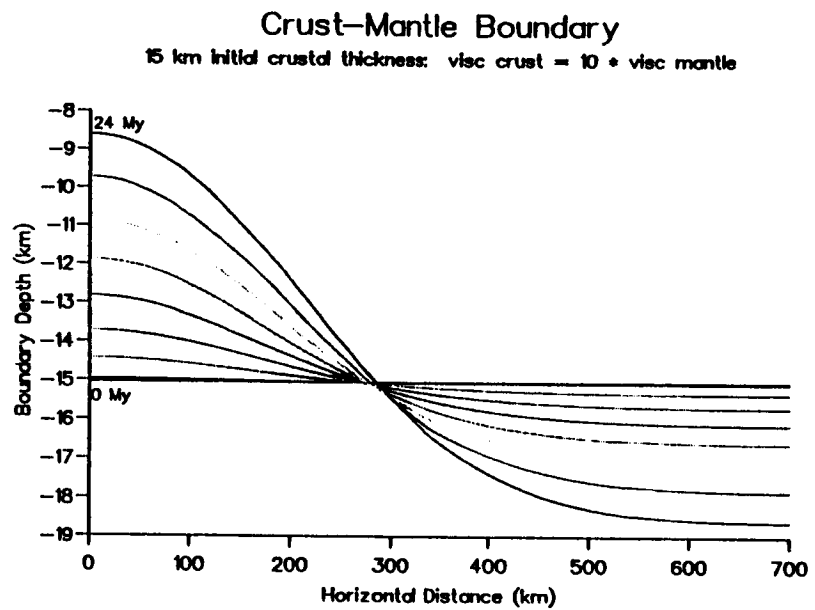
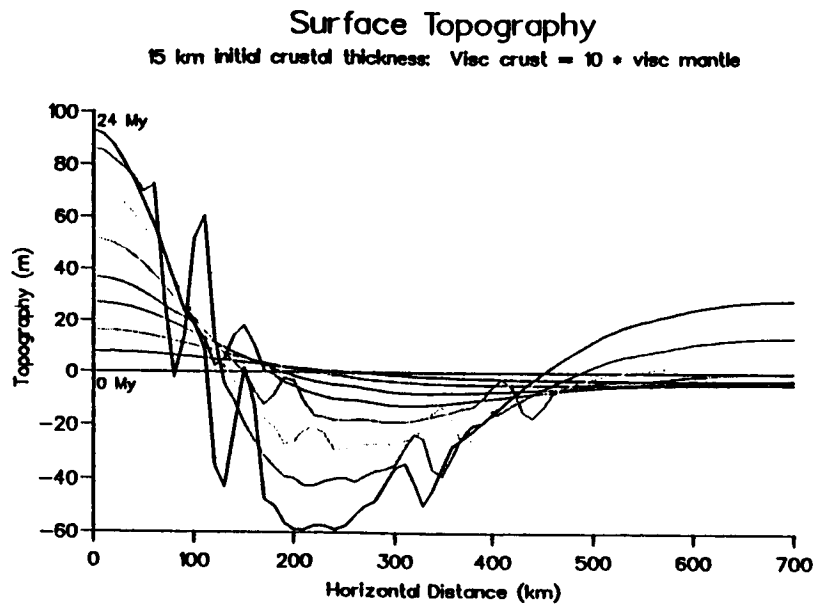


Figure 1. Deformation of the surface and crust-mantle boundary with time. The crust is initially 15 km thick and 10 times more viscous than the mantle.

AN ASSESSMENT OF THE CRUSTAL REMELTING HYPOTHESIS FOR VOLCANISM IN THE FREYJA MONTES DEFORMATION ZONE.

Noriyuki Namiki and Sean C. Solomon, Department of Earth, Atmospheric, and Planetary Sciences, Massachusetts Institute of Technology, Cambridge, MA 02139.

Introduction. The linear mountain belts of Ishtar Terra on Venus are notable for their topographic relief and slope and for the intensity of surface deformation^{1,2}. The mountains surround the highland plain Lakshmi Planum, the site of two major paterae and numerous other volcanic features and deposits^{3,4}, and evidence is widespread for volcanism within the mountains and in terrain immediately outward of the mountain belt units^{2,4}. While the mountains are generally regarded as products of large-scale compression of the crust and lithosphere^{2,5}, whether western Ishtar Terra is a site of mantle upwelling and consequent hot spot volcanism⁶⁻⁸ or of mantle downwelling and consequent convergence of lithospheric blocks^{9,10} is currently a matter of debate. If the upwelling model holds, then volcanism in Lakshmi Planum and presumably within the mountains and adjacent terrain is likely a result of pressure-release partial melting in the upwelling mantle⁶⁻⁸. If the downwelling model is appropriate for western Ishtar Terra, then partial melting in the underlying mantle is less likely, and the volcanism may require remelting of thickened crust^{9,10}. While these two hypotheses for magmatism can be distinguished on the basis of the chemistry of the melts¹¹, chemical data are presently lacking for the Ishtar region.

The competing hypotheses for magmatism in western Ishtar Terra can also be tested with thermal models, given a kinematic or dynamic model for the evolution of the region. In this paper we assess the crustal remelting hypothesis, utilizing the kinematic scenario of Head¹² for the evolution of Freyja Montes. In that scenario Freyja Montes formed by a sequence of large-scale underthrusts of the lithosphere of the North Polar Plains beneath Ishtar Terra, with successive blocks of underthrust crust sutured in imbricate fashion onto the thickened crust of Lakshmi Planum and the mantle portion of underthrusting lithosphere episodically detached¹². The time scales and several important length scales for this process are not presently derivable from geological observations but may be treated as free parameters in numerical models.

Thermal Model. The adopted kinematics of convergence, crustal underthrusting, detachment of the mantle portion of the lithosphere, crustal imbrication, and corresponding crustal thickening are depicted in Fig. 1. The time-dependent temperature field for this kinematic model is obtained by solving a finite-difference approximation to the two dimensional heat equation^{13,14}. The base of the thermal lithosphere is assumed to be defined by a homologous temperature, that is, a fixed fraction s of the mantle solidus temperature, and the asthenosphere is assumed to be well mixed and isothermal. The initial condition (i.e., prior to convergence and underthrusting) is taken to be a laterally uniform structure in thermal equilibrium. The ranges in key but poorly constrained parameters in the model are summarized in Table 1.

Numerical Results. Remelting of the crust can take place in two different ways. One is by direct contact of the crust with hot asthenosphere; the other is by heat generation in a thickened crust. If the melting temperature of crustal material at the pressure corresponding to the normal base of the crust is lower than the asthenospheric temperature, then crust melts from the time of detachment of the subcrustal portion of the lithosphere. Melting continues until a new segment of underthrust lithosphere shuts off the imbricated blocks from the asthenosphere and allows them to cool. The second mechanism for crustal melting is heating of a thickened lower crust by radioactive heat generation. Melting of this

type is strongly dependent on the asthenospheric temperature, the crustal abundance A_c of radioactive heat sources and the maximum depth h_D of underthrust crust. As A_c increases, the minimum value of h_D required for melting decreases. If h_D is larger than the lithosphere thickness, then the lower parts of imbricated blocks are surrounded by asthenosphere. The imbricated blocks are then heated efficiently, and more melt is produced.

An approximate estimate of magma production rate may be made by converting, at each time step and for each partially molten zone in the model, the temperature in excess of the melting temperature into heat of fusion. The variations in estimated melt volume per time step (about 2 My) for three representative models are shown in Figure 2. (In model 1, 2, 3: $h_c = 20, 20, 29$ km; $q_s = 35, 50, 65$ mW/m²; $s = 0.90, 0.91, 0.96$; $A_c = 20, 25, 50 \times 10^{-11}$ W/kg; $h_D = 40, 100, 100$ km; for all models: $v = 5$ mm/yr, dip angle of thrust = 15°.)

Discussion. The numerical experiments thus show that volcanic activity associated with the formation of the Freyja Montes deformation zone can be explained by crustal melting, due either to direct contact of crustal material with the hot asthenosphere or to heat generation in a thickened crustal layer. Time variations in rate of magma generation show different patterns for the two different mechanisms of melting. If crustal melting is due principally to direct heating by the asthenosphere, magma generation can show sudden increases and more gradual decreases (Fig. 2) controlled by the timing of lithospheric delamination events. Alternatively, if melting is due principally to crustal thickening, then the magma generation rate generally grows monotonically with time (Fig. 2). Such temporally distinct magmatic behavior may ultimately be distinguishable by analysis of Magellan imaging data.

References. ¹V.L. Barsukov et al. (1986). *JGR*, **91**, D378-D398. ²S.C. Solomon et al. (1991). *Science*, **252**, in press. ³K.M. Roberts and J.W. Head (1990). *EMP*, **50/51**, 193-249. ⁴J.W. Head et al. (1991). *Science*, **252**, in press. ⁵L.S. Crumpler et al. (1986). *Geology*, **14**, 1031-1034. ⁶A.A. Pronin (1986). *Geotectonics*, **20**, 271-281. ⁷A.T. Basilevsky (1986). *Geotectonics*, **20**, 282-288. ⁸R. E. Grimm and R. J. Phillips (1990). *GRL*, **17**, 1349-1352. ⁹K.M. Roberts and J.W. Head (1990). *GRL*, **17**, 1341-1344. ¹⁰D.L. Bindshadler and E.M. Parmentier (1990). *JGR*, **95**, 21,329-21,344. ¹¹P.C. Hess and J.W. Head (1990). *EMP*, **50/51**, 57-80. ¹²J.W. Head (1990). *Geology*, **18**, 99-102. ¹³P. Bird et al. (1975). *JGR*, **80**, 4405-4416. ¹⁴M.N. Toksöz and P. Bird (1977). *Tectonophysics*, **41**, 181-193. ¹⁵D. McKenzie and M.J. Bickle (1988). *J. Petrol.*, **29**, 625-679.

Table 1. Ranges in Assumed Parameters for Thermal Models

Parameter		Range
Crustal Thickness	h_c	5-100 km
Surface Heat Flow	q_s	25-75 mW/m ²
Homologous Temperature	s	0.85-0.96
Crustal Radioactive Heat Production	A_c	$0-70 \times 10^{-11}$ W/kg
Convergence Rate	v	1-100 mm/yr
Crustal Solidus	-	$1373 + 6.0 \times 10^{-8} P [\text{Pa}] \text{ K}$
Mantle Solidus	-	$P [\text{GPa}] = (T - T_0) / a + b \times \exp(c(T - T_0))$ *
Maximum Depth of Underthrust Crust	h_D	40-100 km

*) $a = 136$, $b = 4.968 \times 10^{-4}$, $c = 1.2 \times 10^{-2}$, $T_0 = 1373$ °K [Ref. 15].

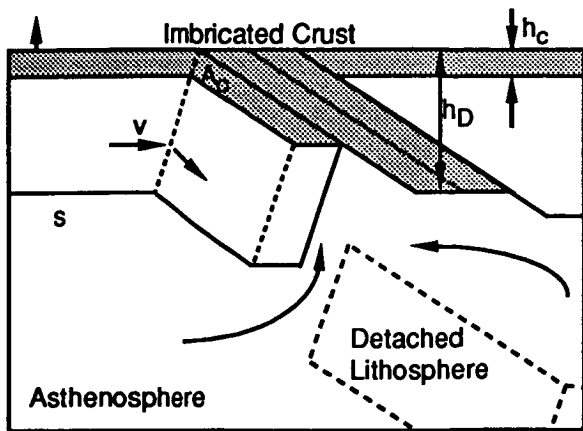


Fig. 1. Assumed kinematics of underthrusting and parameters in the thermal models.

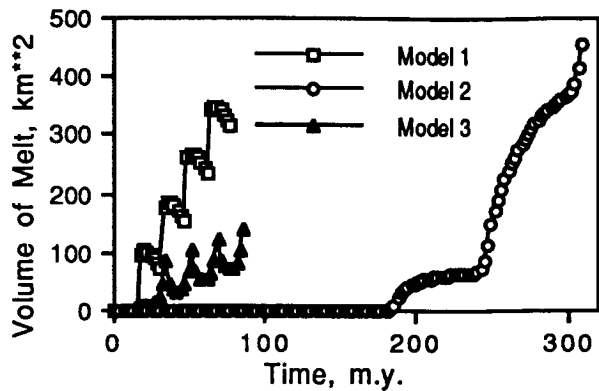


Fig. 2. Melt volume versus model time step. Remelting of the crust occurs by (1) direct contact with the asthenosphere, (2) basal melting of thickened crust, or (3) both.

MARTIAN SEISMICITY

Roger J. Phillips and Robert E. Grimm, Department of Geological Sciences, Southern Methodist University, Dallas, Texas 75275

Introduction. The design and ultimate success of network seismology experiments on Mars depends on the present level of martian seismicity. Volcanic and tectonic landforms observed from imaging experiments show that Mars must have been a seismically active planet in the past and there is no reason to discount the notion that Mars is seismically active today but at a lower level of activity. Here we explore models for present-day seismicity.

Method. The frequency of occurrence, N_f , of marsquakes as a function of surface wave magnitude, M_s , is given by the relationship

$$dN_f/dM_s = A_f \exp(-BM_s) \quad (1)$$

where the B-value adopted is 2.07 [1]. The maximum rate of shear strain over a time interval t can be related to the sum of the seismic moments, ΣM_0 , through [2]

$$d\epsilon_{\max}/dt = \Sigma M_0/\mu Vt \quad (2)$$

where V is the seismogenic volume and μ is the shear modulus (here taken at 7×10^{10} Pa). The sum of the seismic moments can be expressed as

$$\Sigma M_0 = \int_{-\infty}^{M_s(\text{Max})} M_0(M_s) [dN_f/dM_s] dM_s \quad (3)$$

where N_f is the rate of occurrence of marsquakes (a function of M_s) and $M_s(\text{Max})$ is the magnitude of the largest marsquake, which we guess by comparison to the Earth and Moon. We use a relationship between seismic moment and shear wave magnitude for intraplate earthquakes in the terrestrial oceanic lithosphere [3] (these events are probably thermoelastic in origin):

$$M_0(M_s) = 4.68 \times 10^{11} \exp(2.58M_s) \quad (4)$$

where the units are N-m. Substituting (1), (2), and (4) into (3) yields in units of (yr-magnitude)⁻¹

$$A_f = 2.40 \times 10^6 [(d\epsilon_{\max}/dt)V] \exp[-0.509M_s(\text{Max})] \quad (5)$$

Substitution of (5) into (1) and integrating over the interval (M_s , $M_s + \Delta M_s$) yields the rate of occurrence of marsquakes in that interval as a function of $M_s(\text{Max})$, strain rate, and seismogenic volume. We proceed to estimate strain rates and the attendant seismogenic volumes for various processes operating in the martian environment.

Sources of Global Seismicity. Sources of martian seismicity include thermoelastic cooling, regional loading of the surface including Tharsis and the polar caps, changes in the principal moments of inertia, obliquity changes, daily and annual solar tides, and atmospheric coupling. Seismicity is estimated for the first three mechanisms.

We performed a simple parameterized convection calculation [4], which shows that the mantle of Mars has cooled about 3° C and the lithosphere has cooled about 10° C (and thickened) in the last 10⁸ years. In the oceanic lithosphere, earthquakes occur as deep as the 800° C isotherm [5]. In the martian thermal model this corresponds to a depth of about 150 km,

which defines the seismogenic thickness, Z_L . The cooling rate in the lithosphere can be related to strain rate through the coefficient of thermal expansion, α . If $Z_L \ll R_0$, the martian radius, then

$$d\epsilon_{\max}/dt \approx \alpha(dT/dt)Z_L/R_0 \quad (6)$$

Using $M_s(\text{Max}) = 6$, strain rate as calculated from equation (6) ($= 6 \times 10^{-21} \text{ s}^{-1}$), and a spherical shell of thickness Z_L for seismogenic volume yields the frequency distribution for marsquakes shown in the figure below. From this distribution we see that thermoelastic cooling of the lithosphere would be expected to yield 17 events greater than magnitude 4 in a decade. This result is probably a lower bound in that much higher cooling rates without a proportional decrease in seismogenic volume might be expected in the Tharsis region. Whether such events are detected in a network depends, *inter alia*, on the seismic attenuation and scattering properties of the martian interior [6].

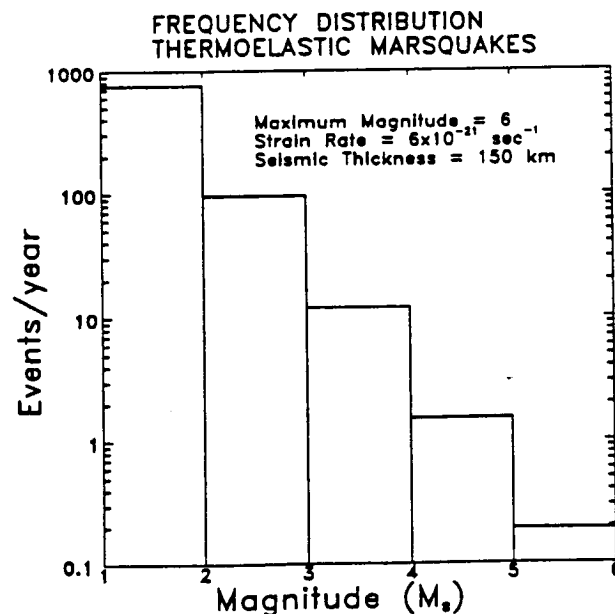
If the Tharsis load is supported in part by thermal buoyancy associated with a magmatic source region, then loss of buoyancy due to cooling leads to a strain rate:

$$d\epsilon/dt \approx -\rho\alpha(dT/dt)g_0h/E \quad (7)$$

where g_0 is planetary gravity, h is the vertical dimension of the cooling region, and E is Young's modulus. Using $h = 200 \text{ km}$ and the same cooling rate as above leads to $d\epsilon/dt = -1 \times 10^{-21}$ with $E = 2 \times 10^{11} \text{ Pa}$. Combined with a smaller seismogenic volume, this process appears to be less important than thermoelastic cooling. The cooling and contraction of Tharsis will also change the difference in the principal moments of inertia, but the accompanying strain rate is also small relative to thermoelastic effects *per se*.

Conclusions. Depending on the sensitivity and geometry of a seismic network and the attenuation and scattering properties of the interior, it appears that a reasonable number of martian seismic events would be detected over the period of a decade. The thermoelastic cooling mechanism as estimated is surely a lower bound, and a more refined estimate would take into account specifically the regional cooling of Tharsis and lead to a higher frequency of seismic events. This analysis should be repeated using the moment-magnitude relationship for body waves, and other mechanisms, as listed above, should also be evaluated.

References. [1] F.D. Stacey, *Physics of the Earth*, 113 (John Wiley, New York, 1977); [2] S.R. Bratt, E.A. Bergman, and S.C. Solomon, *J. Geophys. Res.*, **90**, 10249 (1985); [3] E.A. Bergman, *Tectonophysics*, **132**, 1 (1986); [4] R.J. Phillips and M.C. Malin, in *Venus*, 159-214 (University of Arizona Press, Tucson, 1983); [5] D.A. Wiens and S. Stein, *J. Geophys. Res.*, **90**, 6455 (1983); [6] N.R. Goins and A.R. Lazarewicz, *Geophys. Res. Lett.*, **6**, 368 (1979).



Thermal Models for Icy Satellites

Robert H. Brown
Jet Propulsion Lab/Caltech

We have completed the first major stage of this project: to constrain our solid-state greenhouse models for water ice surfaces using thermal eclipse data. As a result we have determined that at depths of 3 cm or more Europa can have about a 30 K temperature enhancement over the diurnal-mean surface temperature of about 97 K at the equator. We have also determined that the unusual shape of Europa's thermal flux curves during eclipses can be explained by the solid-state greenhouse effect.

Since we completed the work on Europa, we have applied the solid-state greenhouse models to the problem of the origin and energy sources of Triton's geyser-like plumes. There are two classes of models that can provide the required driving energy for Triton's plumes: the classical greenhouse and a variation called the "super" greenhouse. The classical greenhouse model for Triton's plumes consists of absorption of solar radiation in thick layers of relatively clear solid nitrogen on Triton's surface. Calculations show that in a 100-meter-deep layer the subsurface temperature can reach the melting point of nitrogen (63 K) within 15 meters of the surface during the present extreme summer in Triton's southern mid-latitudes. The overpressure at this point is sufficient that liquid and gas could easily vent through existing fractures in the solid overlayer. The second model called the super greenhouse consists of a layer of solid nitrogen a few meters deep overlying a dark absorbing layer. This layer absorbs solar radiation after it propagates largely unattenuated through the overlying nitrogen layer, producing a large temperature gradient. The gradient is enhanced by the remarkably low thermal conductivity of solid nitrogen and the resulting difference in equilibrium vapor pressure between the top and bottom of the nitrogen layer is enough to cause explosive shedding of the layer if it is more than 4 meters thick. More likely, though, the gases would be vented more gradually through pre-existing fissures and fractures in the ice overlayer. All these results are detailed in the paper by Brown et al. (1990).

Our next major piece of progress was the recognition that Triton's internal heatflow is probably a major contributor to its global energy balance. Internal heatflow from radioactive decay in Triton's interior along with absorbed thermal energy from Neptune total 5 to 20% of the insolation absorbed by Triton, thus comprising a significant fraction of Triton's surface energy balance. These additional energy inputs can raise Triton's surface temperature between -0.5 and 1.5 K above that possible with absorbed sunlight alone, resulting in about a factor of -1.5 to 2.5 increase in Triton's basal atmospheric pressure. If Triton's internal heatflow is concentrated in some areas, as is likely, local effects such as enhanced sublimation with subsequent modification of albedo could be quite large. Furthermore, indications of recent global albedo change on Triton suggest that Triton's surface temperature and pressure may not now be in steady state, further suggesting that atmospheric pressure on Triton was as much as 10 times higher in the recent past. A paper detailing this work was submitted to *Science* and it is scheduled to appear in the March 18, 1991 issue.

Our long-term objective is to understand and produce accurate models of the solid-state greenhouse effect on icy satellites and, in so doing, to contribute to the understanding of the thermal histories of icy satellites and their geological

evolution. We intend also to investigate the surface and near-surface temperature profiles predicted for icy satellites in order to gain a better understanding of the evolution and present state of icy-satellite regoliths.

Work this coming year will be to produce a model of the internal heat flux and temperature on Triton coupled with the surface volatile distribution. Initial calculations show that layers of nitrogen ice that are several tens of meters to kilometers thick can have a substantial effect on the internal heat distribution by virtue of the factor 50-200 difference in the thermal conductivity of water ice and nitrogen ice. This in turn will have consequences for the surface volatile distribution and local sublimation rates, and thus may help explain some puzzling features of Triton's seasonal volatile transport and distribution.

A second area of investigation will be to measure the absorption coefficient of solid nitrogen over the wavelength range 0.4-25 μm and over the temperature range 10-60 K in the JPL Extraterrestrial Ice Facility. As a result we hope to determine plausible propagation scale lengths for E-M radiation in nitrogen ice. The results will be used to further refine our solid-state greenhouse models for Triton's plumes as well as provide fundamental constraints on the average size of nitrogen crystals on Triton.

FLOW AND FRACTURE OF ICE AND ICE MIXTURES

W. B. Durham, UCLLNL, Livermore, CA 94550; and S. H. Kirby, USGS, Menlo Park, CA 94025;

Frozen volatiles make up an important volume fraction of the low-density moons of the outer solar system. Understanding the tectonic history of the surfaces of these moons, as well as the evolution of their interiors, requires knowledge of the mechanical strength of these icy materials under the appropriate planetary conditions (temperature, hydrostatic pressure, strain rate). We are conducting ongoing laboratory research to measure mechanical properties of several different ices under conditions that faithfully reproduce conditions both at the moons' surfaces (generally low temperature, to about 100 K, and low pressures) and in the deep interiors (warmer temperatures, pressures to thousands of atmospheres). We report here recent progress in two different phases of our work: rheology of ices in the $\text{NH}_3\text{-H}_2\text{O}$ system at temperatures and strain rates lower than we have ever before explored, with application to the ammonia-rich moons of Saturn and Uranus; and the water ice I \rightarrow II phase transformation, which not only applies directly to process deep in the interiors of Ganymede and Callisto, but holds implications for deep terrestrial earthquakes as well.

Rheology of $\text{NH}_3\text{-H}_2\text{O}$ Ices to $T=130$ K. The NH_3 proportion of condensed volatiles on icy moons, taken as a bulk average, may be as high as 0.15 of the H_2O mass fraction (1). Natural refinement, especially through extraction of partial melts, can increase this fraction to that of the pure ammonia dihydrate ($\text{NH}_3\cdot 2\text{H}_2\text{O}$) composition, about 0.29. We have carried out in the laboratory mechanical tests on samples of ammonia-water mixtures in the compositional range 0 to 29 wt. % NH_3 , at temperatures from above the peritectic melting temperature (176 K) to as low as 130 K, at confining pressures of 50 and 100 MPa, and at strain rates from 3.5×10^{-4} to $3.5 \times 10^{-7} \text{ s}^{-1}$ (Fig. 1). Our ability to deform at strain rates of $3.5 \times 10^{-7} \text{ s}^{-1}$, and thus induce ductile flow at $T < 145$ K without brittle failure, is the result of a recent hardware change that improved our low strain rate limit by an order of magnitude.

The new results (Fig. 1a) confirm an effect suggested by the trend of earlier results (Fig. 1b): even though ammonia dihydrate melts at 176 K, its strength is more temperature-sensitive than that of water ice, so that below about 135 K it is slightly stronger than water ice. Not surprisingly, mixtures of water ice and ammonia dihydrate are also stronger than water ice at these temperatures. This behavior has important implications for icy moons in cooler parts of the solar system. Near-surface ductility seen on the smaller moons of Saturn and Uranus will be more difficult to rationalize on the basis of ammonia-water. On the other hand, the range of viscosities that can be reached with relatively small (40 K) temperature changes in $\text{NH}_3\text{-H}_2\text{O}$ mixtures may prove to be a convenience in explaining complex features on Triton.

Ice I \rightarrow II and Deep Earthquakes. Our work on the inelastic deformation behavior of H_2O ices has provided the first systematic exploration of the fracture and plastic flow under planetary conditions (pressures up to 0.6 GPa and temperatures from 77 to 256 K (2)). In the course of carrying out this experimental program, we discovered an unusual form of faulting that has relevance for deep (360-690 km) earthquakes faulting on Earth and that may imply similar deep faulting on Ganymede and other large icy bodies in the solar system. The faulting instability in ice has several unusual properties: faulting strength does not increase with increasing pressure, a transition to ductile behavior does not occur with increasing confining pressure, and faults form in the maximum shear stress orientation (45°) to compression. These events are restricted to low temperatures and elevated pressures. Close thermodynamic parallels exist between the ice transformation and those that occur in the ferromagnesian phases (olivine and the spinel structures) of the earth's upper mantle, and the transformation kinetics in both transformations are slow. Thus the faulting instability can occur in the ice II stability field where ice I persists metastably at low temperatures and elevated pressures, and the cold thermal structure of the descending lithospheric slab in some subduction zones may be favorable for the faulting instability to develop in metastable olivine, as explained below.

There are two distinct manifestations of the transformation under nonhydrostatic stress (Fig. 2). The first, which we call *transformational faulting*, is the unusual faulting we described above. X-ray diffraction reveals small amounts of ice II in such faulted samples, and we have suggested (4) that the large volumetric strain and exothermic character of the ice I \rightarrow II transformation are the destabilizing factors that cause the faulting. The second manifestation is a *bulk transformation* that occurs at warmer temperatures (above about 175 K) where ice II nucleates at a few points in our 30-cm³-volume sample and grows in a slow and controlled manner.

Green and colleagues (5,6) have confirmed our hypothesis in observing transformational faulting in olivine-spinel transformations in Mg_2GeO_4 and in silicate olivine and have also identified a possible mechanism by which transformational faults may be nucleated by the interactions of microinclusions of the spinel phase. We recently have followed up on our earlier work on transformational faulting in ice (7), refining the faulting strength data, confirming the fault nucleation hypothesis of Green, and pointing out the importance of earlier work by Goto et al. (8) that the volume changes involved in phase transformations in subducting lithosphere can also give rise to large regional deviatoric stresses that can stimulate transformational faulting.

We think deep earthquakes occur because the reconstructive phase transition olivine \rightarrow spinel is kinetically retarded for millions of years and hundreds of kilometers depth as a slab of cool lithosphere descends into the mantle. When the transformation finally does occur, and we suggest it occurs progressively from

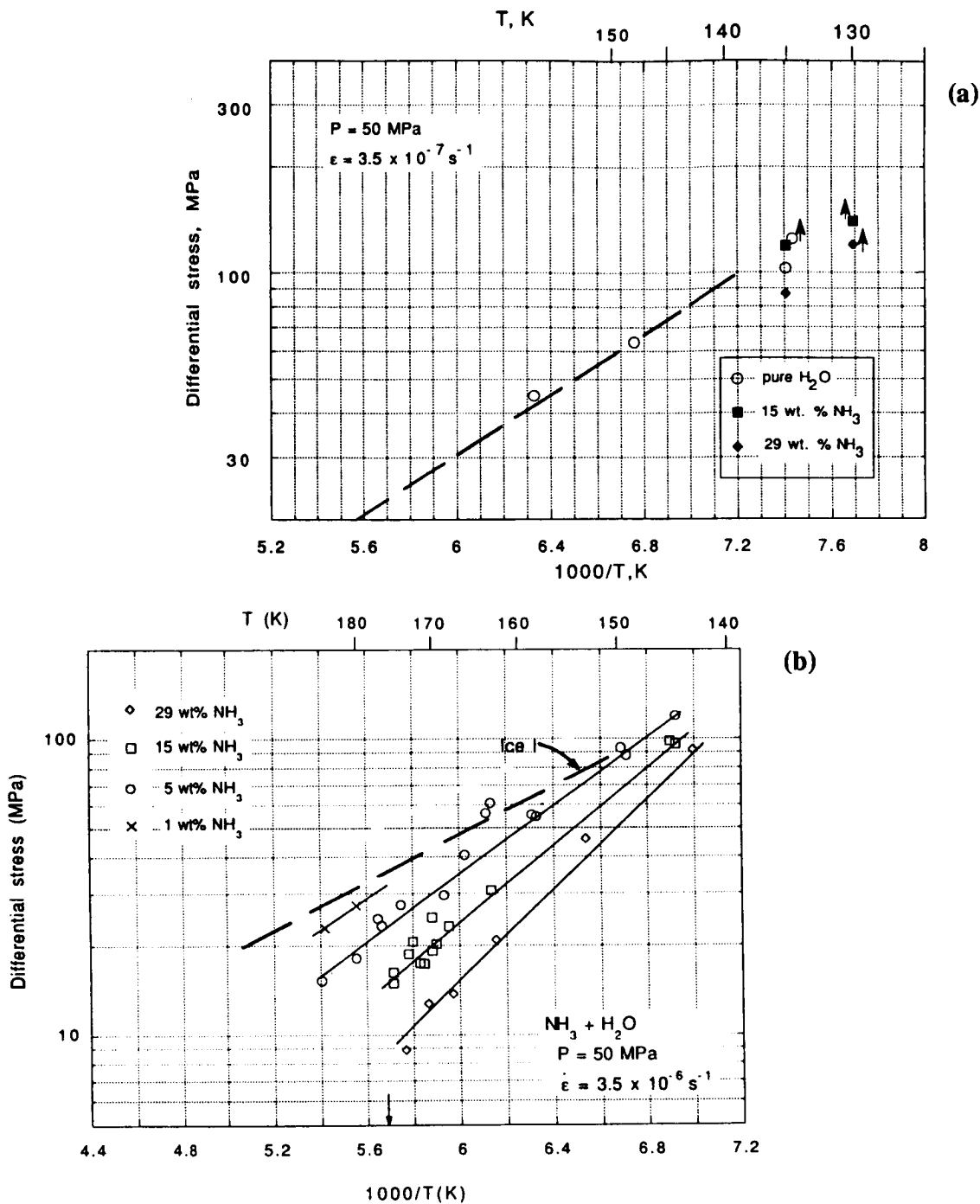


Figure 1. Flow of ices in the $\text{NH}_3\text{-H}_2\text{O}$ system in the compositional range from pure H_2O to ammonia dihydrate (29 wt. % NH_3). (a) Latest results at an imposed strain rate of $3.5 \times 10^{-7} \text{ s}^{-1}$. (b) Earlier results at $3.5 \times 10^{-6} \text{ s}^{-1}$. The figures are offset so that the temperature axes align. Dashed lines in both figures are the latest flow laws for ice I from *Durham et al.* ["The Rheology of Ice I: The Effect of Particulate impurities and Initial Grain Size," manuscript in preparation]. Up arrows in (a) indicate where brittle failure occurred before steady-state ductile flow. The arrow on the horizontal axis in (b) marks the 176 K peritectic melting temperature above which partial melting occurs and mechanical strength drops dramatically. Trends of the higher strain rate measurements (b) suggested that the strength of ammonia dihydrate (diamonds) was approaching that of pure water, but experiments were not feasible at $T < 143 \text{ K}$ because stresses exceed the breaking strength of ice. With the ability to deform at lower rates we are able to measure ductile strength almost to 130 K. Strength of water ice and ammonia dihydrate clearly are comparable at 130 K, but the results are confused by an unexpected shear instability in the ammonia samples and by unusual strain-dependent effects in water ice (the two open circles near 135 K are clearly distinct).

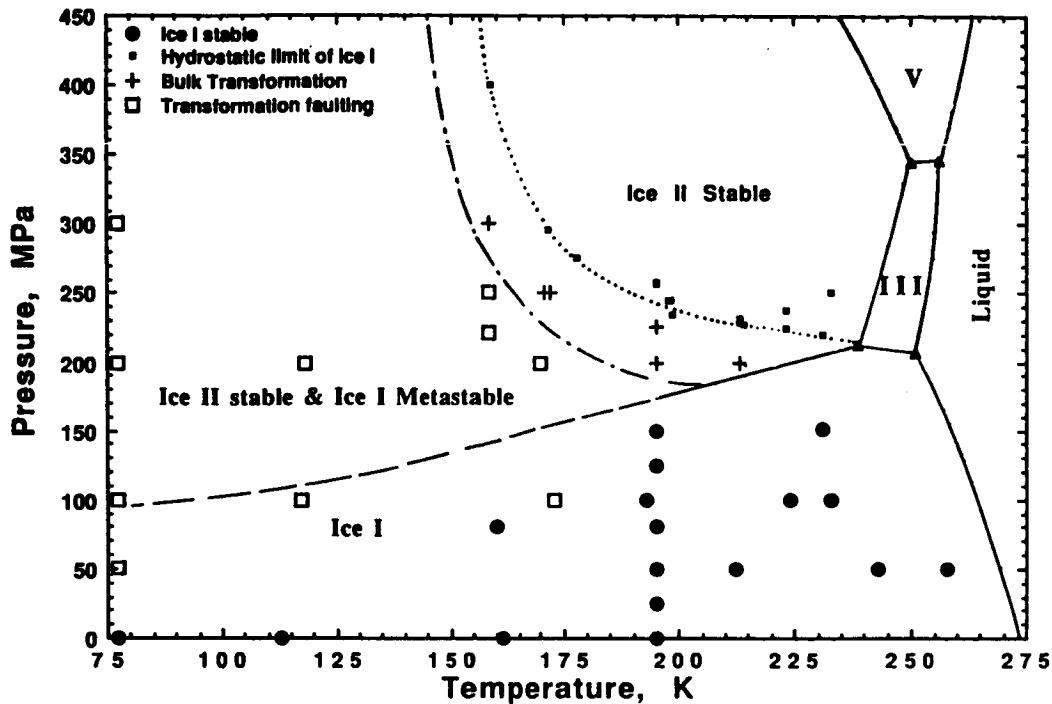


Figure 2. Phase diagram for ice and hydrostatic conditions of the experiments. When ice I is pressurized into the ice II stability field, it does not transform to ice II at the equilibrium boundary. Under hydrostatic conditions (solid boxes), the overpressurization required to cause the transformation to initiate increases sharply as temperature decreases (dotted line). The bulk transformation pressure can be lowered if a differential stress is superimposed on the hydrostatic pressure (crosses). The differential stress required for bulk transformation at any temperature is simply the difference between the actual pressure (crosses) and the hydrostatic limit (dotted line); in other words, the criterion for transformation is a maximum normal stress. At lower temperatures and pressures there seems to be a limit on the maximum differential stress that can be applied, illustrated by the open boxes. Above a shear stress that is weakly temperature sensitive (not shown: about 85 MPa at 77 K, descending to 53 MPa at 170 K) samples fail by macroscopic faulting. The process involves transformation of small amounts of ice I to ice II; hence it is termed transformational faulting, and may be an analog for deep earthquakes in the earth. Such faulting may occur at depths of 40 - 200 km on the large icy moons.

the outer boundaries of the slab inwards as the slab slowly heats up, the negative volume change of the transformation leaves the remaining wedge-shaped core of olivine in a state of slab-parallel compression (8). Stresses eventually rise to the point where transformational faulting, the process we observe in ice in the laboratory, occurs within the olivine wedge, and a deep earthquake is registered seismically.

This unified hypothesis of deep terrestrial earthquakes has implications for deep moonquakes on large, tectonically active icy bodies such as an early Ganymede. A key requirement is that conditions of metastability be present for polymorphic transformations that are strongly exothermic and involve large volume changes (e.g., ice I→II). Earth-style plate tectonics evidently did not occur on Ganymede, but planetary-scale endogenic processes (mostly tensile) certainly did, and some of them could have driven blocks of ice I below its equilibrium boundary. Some downward motion of crust is implied by the extensive resurfacing of Ganymede, for instance by blocks of silicate-laden ice I that have foundered or descended in graben formations. These conditions might also be met during cooling at constant depth and pressure.

References

- (1) Prinn and Fegley (1981) *Astrophys. J.* 249, 308-317. (2) Durham et al. (1983) *J. Geophys. Res.*, 88, B377. (3) Durham et al. (1988) *J. Geophys. Res.*, 93, 10191. (4) Kirby (1987) *J. Geophys. Res.* 92, 789. (5) Green and Burnley (1989) *Nature*, 341, 733. (6) Green et al. (1990) *Nature*, 348, 720. (7) Kirby et al. (1991) *Science*, in press. (8) Goto et al. (1987) *J. Geophys. Res.* 92, 13811.

THE EFFECT OF VOLUME PHASE CHANGES, MASS TRANSPORT, SUNLIGHT PENETRATION, AND DENSIFICATION ON THE THERMAL REGIME OF ICY REGOLITHS.

F.P. Fanale, J.R. Salvail (Planetary Geosciences Div., School of Ocean & Earth Sciences & Technology, Univ. of Hawaii, Honolulu, HI), D.L. Matson, and R.H. Brown (Jet Propulsion Lab., Calif. Instit. Technology, Pasadena, CA)

A thermal model has been developed which quantitatively accounts for the effects of sublimation, condensation, and convection throughout a volume of a porous ice crust subjected to solar insolation. The effect of penetration of insolation into ice that is translucent to visible radiation but opaque to infrared radiation is also included. The governing energy differential equation, which also satisfies conservation of mass and accounts for the possibility of free molecular or continuum flow, is solved for various conditions defined by a reasonable range of thermal conductivities, sunlight absorption coefficients, and pore sizes. Quasi-steady-state temperatures, H₂O mass fluxes, and rates of change of mass density for the ice are computed as functions of depth and time of day. We find that, when the effects of latent heat and mass transport are included in the model, the increase in the near surface temperature (the boundary condition for crustal heat flow) brought about by the "solid-state greenhouse" is greatly diminished. If the lowest thermal conductivities reported for the surface of Europa (~100 erg/cm sec K) are assumed to apply to the upper crust as well, the melting point could be approached at very shallow depth. However, this is precluded except as a transient and shallow phenomenon which could not affect deep crustal temperatures because densification would raise the thermal conductivity to ≥ 1000 erg/cm sec K in the underlying material in a geologically negligible period of time. If thermal conductivities ≥ 1000 erg/cm sec K are assumed, then the greenhouse effect raises near-surface temperatures ≤ 35 K, but the densification is slow enough that deep crustal temperatures would be augmented, allowing for melting at a depth of 7 - 19 km, depending on

assumptions concerning tidal dissipation. Thus, when the effects of latent heat, mass transport, and densification are all taken into account, the existence of a significant solid-state greenhouse effect can be shown to be compatible both with morphological evidence for significant crustal strength and with evidence for decoupling of the icy shell from the lithosphere.

THE ROLE OF NONUNIFORM INTERNAL HEATING IN TRITON'S ENERGY BUDGET; R. L. KIRK* AND R. H. BROWN†, *U.S. Geological Survey, Flagstaff, AZ 86001, †Jet Propulsion Laboratory, Pasadena, CA 91109

Introduction Triton's large heliocentric distance and high albedo, combined with its unusually large silicate mass fraction, make internal heating more important in its energy budget than in that of any other icy satellite. Brown *et al.* [1] have recently estimated that the average radiogenic heat flux F_0 (which is probably between 3.3 and 6.6 mW m⁻² depending on core size and composition) may equal 5% to 20% of the average absorbed insolation. On a global scale, this additional energy input appreciably increases the thermal emissivity required to be consistent with the observed surface temperature [2]. Brown *et al.* [1] also speculated that spatial variations of the internal heat flux may change the local sublimation-deposition balance enough to lead to observable modifications of the distribution of volatiles on Triton's surface. In this abstract we attempt to estimate the magnitude of internal heat-flux variations due to the insulating effect of the polar caps, to mantle convection, and to cryovolcanism; we evaluate the importance of these variations in modifying the volatile distribution.

Thermal Structure Our model of the thermal and convective structure of Triton's shallow interior, required for the calculations presented below, is as follows. We assume Triton is fully differentiated. We use the parameterized convection model applied by Kirk and Stevenson [3] to Ganymede, but we specify the heat flux (3.3 or 6.6 mW m⁻² [1]) and solve for the temperature at the base of the ice layer, rather than the reverse. Our calculation includes the strong temperature dependence of the thermal conductivity of ice [4]. We find that the temperature at the base of the thermal lithosphere is between 170 and 200 K, depending on the estimate of ice viscosity used. The corresponding depth is roughly 300 or 150 km, depending on the heat flux. The total thickness of the ice layer is probably close to 350 km, with the result that the layer is stable against convection for $F_0 = 3.3$ mW m⁻² and a melting-point viscosity $\eta_m \geq 2 \times 10^{14}$ Pa s.

Insulating Polar Caps The thermal conductivity of solid N₂ [5] is several hundred times less than that of H₂O ice [4] at the surface temperature of Triton; a polar cap of modest thickness may therefore be able to significantly modify the latitudinal distribution of heat flow. We have constructed a simple analytic model to test this effect, assuming linear conduction in a spherical shell, constant temperature on the inner boundary (the top of the convecting zone), and a mixed boundary condition on the outside representing the effects of the insulating cap. For simplicity, we chose a cap thickness varying as sin²(latitude), making solution for the temperature field as a sum of Legendre polynomials relatively straightforward. We find that for a N₂ layer 1 km deep at the poles, the equatorial heat flux is enhanced by 20% and 35% for the lower and upper limits on heat flux, respectively (Fig. 1). The corresponding flux decreases at the pole are roughly twice as large, leading to equator-to-pole flux ratios of 2:1 and 4:1 in the two cases. The temperature beneath the cap is elevated by roughly 9 K at the pole.

Effect on Frost Stability Models of the current energy balance on Triton (excluding internal heat but including latitudinal variation of albedo) predict the deposition of frost northward of 15° latitude [6]; the time-dependent model of Spencer [7] predicts that seasonal frost deposits currently extend even farther south. Can we account for the absence of obvious bright frost deposits in Triton's northern hemisphere by including the concentration of internal heat toward the equator in the energy balance? The answer would appear to be no. We have performed a stability analysis similar to that of Stansberry *et al.* [6], comparing the diurnally averaged insolation absorbed by a patch with albedo $A_{local} = 0.6$, appropriate to the northern hemisphere, with the global average absorption for $A = 0.8$. Adding the spatially varying internal heat flux calculated above for $F_0 = 6.6$ mW m⁻² shifts the current latitude of equilibrium by only 0.5°. The shifts for $A = 0.9$ [1] or $F_0 = 3.3$ mW m⁻² are even smaller. For $A_{local} = A$ (*cf.* [7]), the northward shift is larger, but still less than 2.5°.

Somewhat less can be said with certainty about the effect of internal heat on the long-term stability of the polar caps. The seasonally averaged insolation varies much less

strongly with latitude than the current diurnally averaged insolation, and proportionately larger shifts of the latitude of stability would therefore be expected. Unfortunately, the redistributed internal heat flux for our model cap shape passes through its global mean value almost precisely at the latitude of where seasonally averaged sublimation and deposition balance on a global frost layer. This coincidence, which limits the calculated latitude shift to less than 0.1° , would not occur if more general cap shapes were used in the heatflow model or if an unfrosted equatorial zone were excluded from the energy budget. In any event, the internal heat flux at the center of the polar caps is always reduced relative to that at their edges and beyond. This redistribution of heat would thus act to hasten—perhaps significantly—the retreat of the permanent caps toward the poles predicted as a consequence of the gradient in insolation [7].

Mantle Convection We turn now to processes capable of producing more localized enhancements of heat flux and thus perhaps able to modify the pattern of frost deposition. One candidate is mantle convection: upward heat flux at the top of the mantle is concentrated over zones of upwelling. We can estimate the extent to which variations in the flux will be attenuated across the lithosphere by a conductive model with fixed temperature on the outside of a spherical shell and with flux varying as a spherical harmonic on the interior. The attenuation factor is approximately $\frac{1}{2}(R_m/R)^{-(l+2)}$, where R and R_m are the radii of the planet and the top of the mantle, respectively, and l is the degree of the spherical harmonic. The lowest degree, hence least attenuated, spherical harmonic component of the mantle heat flux will have l equal to the number of convective-cell pairs that fit around the circumference of the planet (for roll convection; for equant convection cells, l will be roughly twice as large, leading to much greater attenuation). Using the results of the parameterized convection calculation above, we have, for $F_0 = 6.6 \text{ mW m}^{-2}$, $R_m/R \simeq 0.89$, $l \simeq 15$, and an attenuation factor of roughly 4. The attenuated flux is sufficient to shift the latitude of frost equilibrium by $\pm 2^\circ$ if the amplitude of the flux variation at the mantle is equal to the mean flux. These results are extremely sensitive to the magnitude of F_0 ; decreasing it to 3.3 mW m^{-2} both decreases R_m/R and increases l , resulting in attenuation factors of 10^3 – 10^4 .

Cryovolcanism The evidence in Voyager images for multiple styles of cryovolcanic eruption on Triton [8] raises the prospect that heat released by cryomagmas may locally contribute to the sublimation of surface frosts. Unlike the mechanisms discussed above, migration of “hot” material toward or to the surface could result in heat fluxes that exceed the global average by a large factor. On the other hand, this enhancement would be transient and hence might not be observed at a given time. We discuss the possible effects of two very different types of cryovolcanic activity.

Fitting the results of viscous spreading models [9] to the measured dimensions of the linear ridges common in Triton’s cantaloupe terrain (and extending into the south polar cap) indicates that the erupted material could be subsolidus N_2 or CH_4 or, more plausibly, ammonia-water slush or glass. Independently of the assumed composition, a conduit width on the order of 400 m may be inferred from the flow models and the thickness of the ridges. We have therefore modeled the thermal effect of a dike of this width and initial temperature equal to the NH_3 - H_2O eutectic value of 173 K, intruded into a half-space at 38 K. In this linear-conduction model we have used the conductivity of H_2O ice at 38 K; the results are only moderately sensitive to this assumption. We find that the vertical heat flux is enhanced by 3.3 mW m^{-2} or more in a zone extending some 17 km on either side of the dike. We speculate that the narrow swath apparently cleared through the polar cap by a linear ridge at latitude 10° – 15° S, longitude 345° – 0° may result in part from heating by the surface flow and its conduit. (The widening of the cleared area to the northeast conceivably results from the sensitivity of the cap to very small energy inputs near its edge as defined by insolation, although other effects such as topographic slopes may be involved). The critical problem with this suggestion is the low probability of observing a ridge soon enough after its eruption that the heatflow is still enhanced. In our model, the peak heat flux is reached at the edges of the 34-km-wide zone defined above 7×10^4 years after emplacement of the dike. No impact craters superimposed on the ridges were detected by Voyager, but a crater-density age on the order of a few hundred million years has been estimated for the Tritonian maria [8,10].

If the tens of linear ridges observed were erupted over a similar time span, the probability of observing one within 10^5 years of its formation is only of the order of 1%. This difficulty might be overcome if openings in the permanent polar cap, once created, are able to persist because of the lower albedo of the exposed substrate. Additional, numerical modeling would in any case be of interest to determine how the result of our idealized model is modified by heat released from the surface flow, which is comparable in width to the zone defined above, and how sensitive the retreating polar-cap edge is to small energy inputs.

We have also considered the effects of warm-ice diapirism on the surface heat flux. We have *not* attempted to construct a consistent model of the chemistry of the diapirs and the buoyancy forces driving them; this is in fact problematic because of the similar densities of ammonia-water liquids and their coexisting solid phases [11]. Instead, we have modeled the ascent of diapirs with a "generic" buoyancy $\Delta\rho/\rho = 0.1$ and a temperature of 173 K, which is both the $\text{NH}_3\text{-H}_2\text{O}$ eutectic temperature and the approximate temperature at the base of the lithosphere. Our results are very weakly dependent on the choice of these parameters. Because of the high ice viscosities and steep viscosity gradient in Triton's cold lithosphere, diapiric ascent proceeds not by Stokes-like flow, but by "thermal lubrication flow" [12], using its own heat to soften a thin layer of the ice around it. We have adapted the diapiric-ascent model of Kirk and Stevenson [3], incorporating this physics to Tritonian conditions. The model does not account for cooling of the diapir, so we stop the ascent after one thermal-diffusion time based on diapir radius. We find that the diapir typically ascends 1.0–1.5 of its radii before stopping (Fig. 2). Using a one-dimensional conduction model to calculate the enhanced heatflow above the center of the diapir, we find that a diapir with a radius of 70 km is required to double the ambient heat flux if $F_0 = 6.6 \text{ mW m}^{-2}$, while a 100-km-radius diapir is needed to double our smaller heat flux. The corresponding thermal-diffusion times are 50 and 100 million years. Observation of the thermally active phase is thus much more probable than was the case for the linear ridges. We suggest that the three diffuse, roughly circular, low-albedo features at latitude 5° S , longitudes $25^\circ\text{--}50^\circ$ on Triton [8] may be the result of modification of the surface frost by diapiric activity. The features are roughly 50 km in radius, and at least two of them are clearly associated with mare-type cryovolcanism.

References Cited [1] Brown, R. H., *et al.*, submitted to *Science*. [2] Tyler, G. L., *et al.* (1989) *Science*, **246**, 1454–1458; Broadfoot, *et al.* (1989) *Science*, **246**, 1459–1465. [3] Kirk, R. L., and D. J. Stevenson (1987) *Icarus*, [4] Hobbs, P. V. (1974) *Ice Physics*, Clarendon Press, 357–361. [5] Scott, T. A. (1976) *Phys. Rep.*, **27**, 85–157. [6] Stansberry, J. A., *et al.* (1990) *Geophys. Res. Lett.*, **17**, 1773–1776. [7] Spencer, J. R. (1990) *Geophys. Res. Lett.*, **17**, 1769–1772. [8] Smith, *et al.* (1989), *Science*, **246**, 1422–1449. [9] Kirk, R. L. (1990), *Lunar Planet. Sci.*, **XXI**, 631–632. [10] Strom, R. G., *et al.* (1990) *Science*, **250**, 437–439. [11] Croft, S. K., *et al.* (1988) *Icarus*, **73**, 279–293. [12] Morris, S. (1982) *J. Fluid Mech.*, **124**, 1–26.

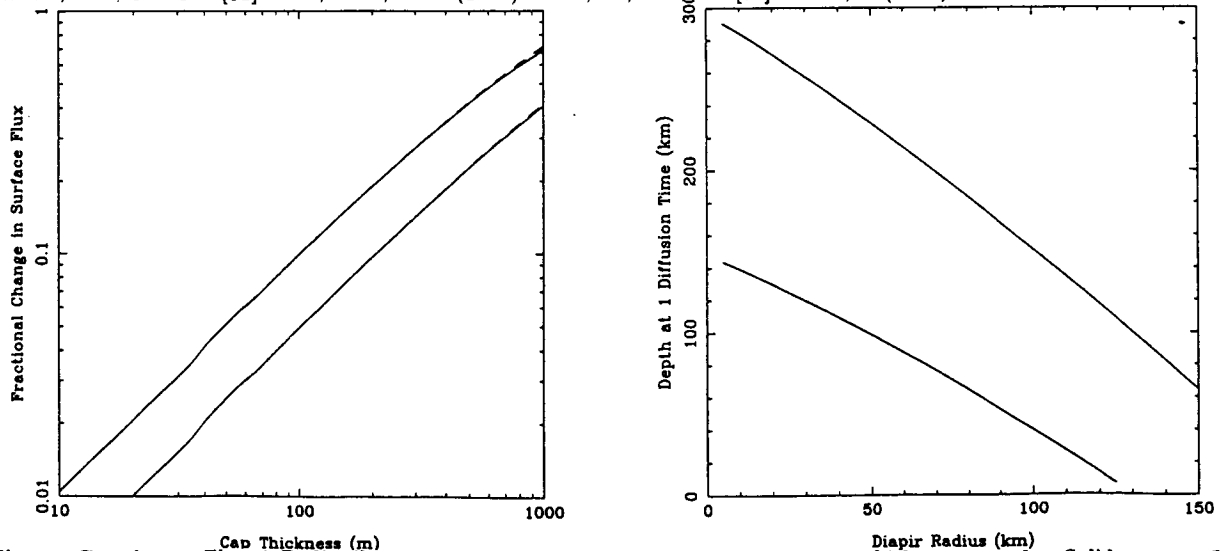


Figure Captions Fig. 1 Redistribution of internal heat flux as a function of cap thickness at pole. Solid curves: flux decrease at pole (relative to mean flux); dashed curves: twice flux increase at equator. Upper and lower curve sets correspond to maximum and minimum internal fluxes considered. Fig. 2 Minimum depth of ascent of 173 K Tritonian diapir as a function of radius. Upper and lower curves correspond to minimum and maximum internal fluxes considered.

PHYSICAL PROPERTIES OF CRYOVOLCANIC BRINES: APPLICATIONS TO THE EVOLUTION OF GANYMEDE; J.S. Kargel, Lunar and Planetary Laboratory, University of Arizona, Tucson, AZ 85721

Introduction. Carbonaceous chondrites contain abundant veins of water-soluble salts, including carbonates and hydrated sulfates of Mg, Ca, Na, Ni, and Fe. These constitute over one-fourth of the mass of the meteorite Orgueil. Magnesium sulfate is the most abundant salt, constituting nearly half the mass of all salt components combined (anhydrous), and 73% of the highly water-soluble salts [1]. The common assumption that icy satellites and asteroids contain rock compositionally similar to carbonaceous chondrites suggests that salts may be important in the cryogenic evolution of icy satellites and asteroids. Ordinary chondrites, an alternative rock component of icy satellites, lack abundant salts, although their anhydrous silicate assemblages are unstable with respect to water and would react to produce salts upon initial melting of ice. In any case salts would ultimately be involved in any melting and differentiation processes.

Here, I review some basic physicochemical properties of likely cryovolcanic brines and consider how the existence of soluble salts in Ganymede might affect its structure and evolution. Ganymede is selected for applications since it is very likely composed of relatively "simple" mixtures of water ice and rock (thus, ammonia may not be important in its evolution), because Ganymede displays photogeologic evidence consistent with brine volcanism, and since the Galileo mission will soon allow observational tests of the concepts presented here. These models are based on data appropriate to low pressures, and thus are not strictly valid for Ganymede, but should suffice to illustrate the importance of salts in icy satellite evolution, and the necessity of exploring the properties of salt-water systems at high pressures. Initial results of high-pressure experiments in the magnesium sulfate-water system are presented in another abstract [2].

Physicochemical properties of brines. The dominance of MgSO_4 in chondrite salts is a sufficient basis (but not the sole objective rationale) for concentrating attention on the magnesium sulfate-water system in this brief report. This system has a eutectic near 17% MgSO_4 (by mass) and -3.9°C [2]. The eutectic liquid coexists with water ice and $\text{MgSO}_4 \cdot 12\text{H}_2\text{O}$. The addition of other major salt components somewhat complicates matters, but MgSO_4 remains the most important solute in chondrite-equilibrated brines under most circumstances.

Figures 1 and 2 show the density and viscosity, respectively, of the MgSO_4 - H_2O eutectic liquid in the context of data for other volcanically important liquids and solids; for consistency and simplicity, these data all represent the crystal-free state at the liquidus. Real lavas commonly are erupted with ten percent or more crystals, which would have a small effect on lava density but a large effect on viscosity. Thus, Figure 2 qualitatively indicates the relative differences in the lava viscosities, and quantitatively provides minimum viscosity estimates at eruption. The MgSO_4 - H_2O eutectic is about six times more viscous than pure water. However, as shown in Figure 3, even the gravity-scaled rheology of magnesium sulfate eutectic would be "runnier" on Ganymede than the least viscous silicate lavas on Earth (komatiite). Thus, aqueous brines on Ganymede would produce sub-meter flow thicknesses except where ponded. This is at least consistent with the lack of observed flow edges in Voyager images (but image resolutions would require flow thicknesses of 50 meters or more to be resolved, thus allowing substances substantially more viscous than magnesium sulfate-water).

Models of a sulfate-rich Ganymede. Consider as a special case Ganymede Model #1 whose rocky component very closely resembles C1 chondrites, and the ice fraction is solely water ice. Like C1 chondrites, Model #1 has 38% of its S in the form of magnesium sulfate. It is trivial to calculate the total quantity of ice, salt, and rock ("rock" now refers to involatile minerals minus highly soluble salt), based on the specific gravity of Ganymede (1.93), of pressure-averaged ice (1.25), and of carbonaceous chondrite rock (2.6), and the chondritic abundance of S (6%). In this special case the $\text{H}_2\text{O}:\text{MgSO}_4$ ratio is equal to the eutectic composition (17 wt.% MgSO_4). Complete melting and melt extraction of the ice-salt eutectic fraction would leave the rocky interior barren of both ice and sulfate and would produce a crust about 600 km thick composed of about equal weight fractions of ice and $\text{MgSO}_4 \cdot 12\text{H}_2\text{O}$. Since the eutectic liquid is denser than the frozen ice-salt eutectic mixture, early brine volcanism would have given way to later intrusive activity. If differentiation was early enough the eutectic-composition crust could become heavily cratered during later stages of heavy bombardment.

Consider in Model #2 a Ganymede where the fraction of oxidized S is greater than 38%. Complete melting and melt extraction of the eutectic fraction would leave residual amounts of sulfate in the rocky core. Residual sulfate would melt incongruently in a series of stages (consult Fig. 1 of [2]). Each liquid would be denser than the eutectic-composition crust and would be unable to contribute to late-stage volcanism. On the other hand, in Model #3 the fraction of oxidized S is less than 38%, and excess water ice would exist in the rocky core after eutectic melting; melting of water ice in the core would produce more-or-less pure liquid water, which is substantially less dense than the frozen eutectic crust, and may result in late-stage water volcanism.

Conclusions. Observations indicate late-stage (post-heavy bombardment and post-tectonic) volcanism on Ganymede; on this basis Model #3 is preferred. The highly fluid character of Ganymedian volcanism is consistent with extrusions of either water or salt-water brines. Callisto, however, may have had more than 38%

of its S as sulfate, offering an explanation for the absence of late-stage volcanism there. The occurrence of abundant elemental S on Io suggests that the jovian system may exhibit a radial increase in oxidation, possibly related to mixing between the jovian and solar nebulae, or related to chemical processing in the deep, warmest portions of the jovian nebula. In any case, if magnesium sulfate is an important constituent of certain icy satellites it certainly would have been important in their geological evolution. The occurrence of sulfates in the observable surfaces of these satellites might be detected by Galileo. However, the harsh radiation environment in the jovian system may have caused the decomposition of sulfates and the production of refractory substances such as MgO.

References. [1] Fredriksson, K. and J.F. Kerridge, 1988, *Meteoritics* 23, 35-44. [2] Hogenboom, D.L., J.S. Kargel, J.P. Ganasan, and J.S. Lewis, 1991, (ABSTRACT), this volume.

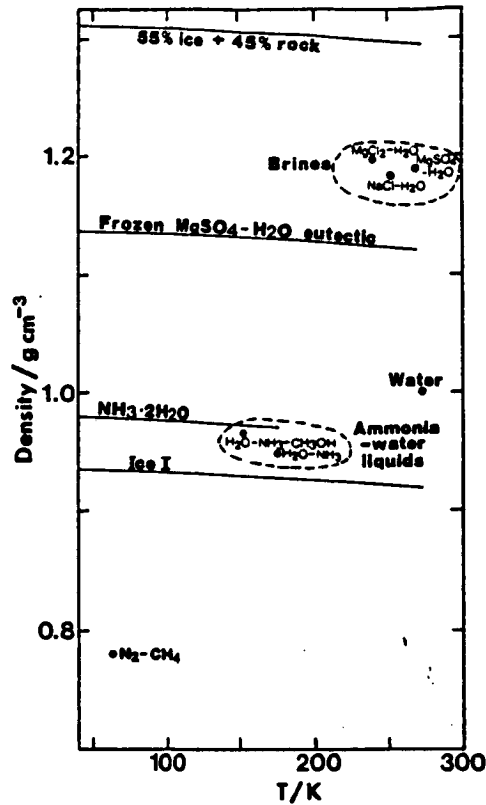


Figure 1.

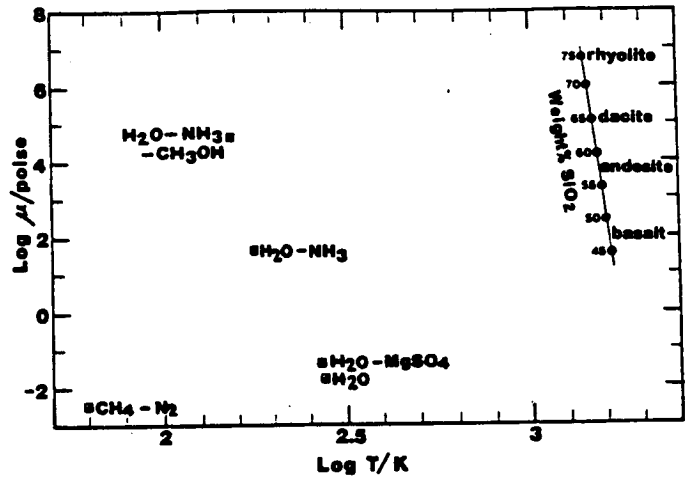


Figure 2.

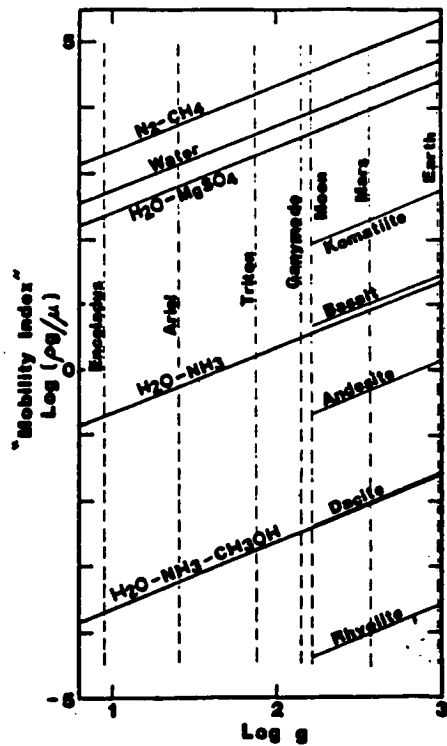


Figure 3.

THE MAGNESIUM SULFATE-WATER SYSTEM AT PRESSURES TO 4 KILOBARS; D.L. Hogenboom¹, J.S. Kargel², J.P. Ganasan¹, and J.S. Lewis²; 1: Dept. of Physics, Lafayette College, Easton, PA 18042; 2: Dept. Planetary Sciences, Univ. Arizona, Tucson, AZ 85721

Introduction. Hydrated magnesium sulfate constitutes up to one-sixth of the mass of carbonaceous chondrites, and probably is important in many icy asteroids and icy satellites. It occurs naturally in meteorites mostly as epsomite (the heptahydrate). MgSO_4 , considered anhydrously, comprises nearly three-fourths of the highly soluble fraction of C1 chondrites [1]. Thus, MgSO_4 is probably an important solute in cryovolcanic brines erupted on certain icy objects in the outer solar system [2]. While the physicochemical properties of the water-magnesium sulfate system are well known at low pressures, planetological applications of these data are hindered by a dearth of useful published data at elevated pressures [but see 3]. Accordingly, we recently explored solid-liquid phase equilibria in this chemical system at pressures extending to about four kilobars.

Experimental. Except for improved insulation of the pressure vessel which reduced the rate of cooling and warming of the sample, the apparatus used was the same as described previously [4]. The 2.6 ml sample in the pressure vessel was pressurized by additional sample through small bore tubing extending from the cold bath to the pressure system. Mercury separated the sample from the pump fluid. Changes in sample volume produced corresponding changes in transducer voltage as a magnet floating on the mercury changed position.

Results. Figure 1 illustrates phase equilibria in the MgSO_4 - H_2O system at 1 atm. A eutectic occurs near 17% MgSO_4 (by mass) where ice and magnesium sulfate dodecahydrate ($\text{MgSO}_4 \cdot 12\text{H}_2\text{O}$) melt or freeze together at -3.9°C under equilibrium conditions. Table I gives approximate low-pressure densities of relevant phases and phase assemblages [5]. Polynomial fits were determined giving the density of 17 and 15.3 wt.% MgSO_4 solution as functions of temperature, T (in $^\circ\text{C}$) at constant pressure, and pressure, P (in bars) at constant temperature. At approximately 50 bars, the lowest pressure investigated, the density of the 17% liquid is given (in g cm^{-3}) by the equation:

$$\rho = 1.19046 - (0.253577 \times 10^{-3} T) - (0.542964 \times 10^{-5} T^2) \quad (1)$$

Equation (1) is valid between $+5^\circ\text{C}$ and -15°C , and has a maximum deviation of $0.00006 \text{ g cm}^{-3}$ over this range (we do not claim such good accuracy, which is on the order of 0.001 g cm^{-3}). The density of this 17% solution at 30°C is given as a function of pressure by:

$$\rho = 1.17863 + (0.334949 \times 10^{-4} P) - (0.167615 \times 10^{-6} P^2) \quad (2)$$

Equation (2) is valid between 0 and 4000 bars, with a maximum deviation of $0.00082 \text{ g cm}^{-3}$. The density of 15.3% solution, at about 50 bars, is given by equation (3), valid from 24°C to -16°C .

$$\rho = 1.16985 - (0.250479 \times 10^{-3} T) - (0.253886 \times 10^{-5} T^2) \quad (3)$$

The maximum deviation of data from equation (3) is $0.00009 \text{ g cm}^{-3}$.

The density of 15.3% solution at 30°C is given by equation (4), valid from 0 to 3950 bars.

$$\rho = 1.15756 + (0.339366 \times 10^{-4} P) - (0.179658 \times 10^{-6} P^2) \quad (4)$$

The maximum deviation from equation (4) is 0.0007 bars.

These data are consistent with published data [6,7] suitably extrapolated.

Figure 2 is a 2 kilobar run for 15.3 wt.% MgSO_4 . The y-axis gives the measured voltage. The change in voltage is proportional to change in sample volume. The sample supercooled about 12K before crystallizing. The solution froze to a less dense assemblage (apparently ice I + $\text{MgSO}_4 \cdot 12\text{H}_2\text{O}$) as seen by the increase in voltage (volume). The solid sample then locked up, thus preventing a volume change as indicated by the constant voltage as the sample cooled. Freezing was also accompanied by a 2 K temperature rise of the sample and bomb as heat was released during crystallization. The sample must have overpressurized during lock-up. The slow release of overpressurization is indicated as the sample slowly warmed through the subsolidus region and gradually expanded. At about 248.5 K the sample melted completely at the stable eutectic. The eutectic point was closely bracketed by two reversals, as shown by the thermal loops. The direct descent of the eutectic melting trajectory to the liquid cooling/warming curve indicates the absence of a liquidus solid phase above the eutectic temperature, further indicating that at 2000 bars the eutectic shifts to about 15.3% MgSO_4 . This inference is supported by runs at 2000 bars and 17% MgSO_4 where excess magnesium sulfate melts on the liquidus above the eutectic temperature.

Figure 3 gives results for a run at 3460 bars, 17% MgSO_4 . Crystallization was preceded by 18 K of supercooling; at this pressure the sample formed a denser assemblage of ice II + $\text{MgSO}_4 \cdot 12\text{H}_2\text{O}$; the sample, as usual, locked after freezing. A temperature loop during the eutectic transition, requiring 4 hours to complete, bracketed the eutectic temperature at 3460 bars between 248.0 and 249.5 K, and confirmed that a dense solid liquidus phase (magnesium sulfate hydrate) melted at temperatures above the eutectic. Therefore, the eutectic composition at 3460 bars is still on the water-rich side of 17% MgSO_4 .

The eutectic pressure-melting curve is shown in Figure 4. As expected for systems lacking significant solid solution, composition does not affect the eutectic temperature as long as the same solid assemblage is involved. The eutectic temperature at 50 bars, the lowest pressure we investigated, is consistent with the eutectic at 1-atm shown in Figure 1. The data below 2060 bars form a single smooth curve, strongly indicating no solid-state phase changes in $\text{MgSO}_4 \cdot 12\text{H}_2\text{O}$ (and water ice) between pressures of 1 atm and 2060 bars. The melting curve has a slope break above 2060 bars, consistent with the ice I - ice II transition near this pressure. Another slope break is required near 3500 bars, consistent with the ice II - ice V transition. The relative magnitude of the volume changes at the eutectic melting transition are consistent with these various assemblages.

The data do not conclusively indicate whether or not $\text{MgSO}_4 \cdot 12\text{H}_2\text{O}$ undergoes a solid-state phase change at pressures between 2 and 4 kilobars. Figure 4 implicitly assumes no such transition. A discrepant datum (with respect to Fig. 4) was obtained at 3 kilobars, where the melting transition occurred about 3.5 K higher than expected based on replicated data near 2 and 3.5 kilobars. This result is not understood since all the runs, including that at 3 kilobars, appeared to be good ones. Perhaps the pressure interval between 2 and 3.5 kilobars is more complex than assumed, conceivably involving a phase change in solid magnesium sulfate hydrate.

Conclusions. The system $H_2O-MgSO_4$ in the region of the eutectic exhibits qualitatively constant behavior between pressures of 1 atm and 2 kilobars. The eutectic melting curve closely follows that for water ice, with a freezing point depression of about 4 K at 1 atm decreasing to around 3.3 K at 2 kilobars. The eutectic shifts from 17% $MgSO_4$ at 1 atm to about 15.3% $MgSO_4$ at 2 kilobars. Above 2 kilobars the eutectic melting curve again tends to follow that of ice, including changes in slope at pressures consistent with ice transitions, although the freezing point depression relative to the pure ice melting curve increases to 6 K at 4 kilobars.

References. 1. Fredriksson, K. and J.F. Kerridge, 1988, *Meteoritics* 23, 35-44. 2. Kargel, J.S., 1991, (ABSTRACT) this volume. 3. Livshits, L.D., et al., *Russ. Jour. Inorg. Chem.*, 8, 676-678. 4. Hogenboom, D.L., and J.S. Kargel, 1990, (ABSTRACT) *Lun. Planet. Sci. XXI*, 522-523. 5. Kargel, J.S., 1990, *Cryomagmatism in the Outer Solar System*, Ph.D. dissertation, Univ. of Arizona, Tucson, 309 pp. 6. Chen, C.T.A. et al., 1980, *J. Chem. Eng. Data* 25, 307-310. 7. *CRC Handbook of Chemistry and Physics*.

TABLE I. Densities in $MgSO_4-H_2O$ system

Phase(s)	Density ($g\ cm^{-3}$) @ 1 atm, 269 K
Water	1.000
Ice	0.917
$MgSO_4 \cdot 12H_2O$	1.47 + -0.06
Eutectic liquid	1.19
Frozen eutectic	1.12 + -0.02

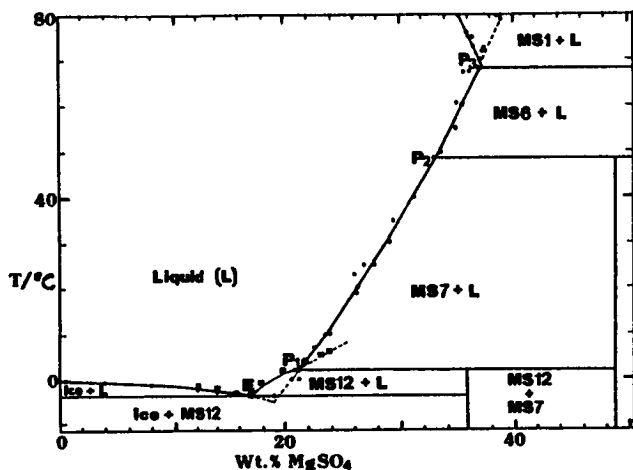


Figure 1. System $H_2O-MgSO_4$ at 1-atm.

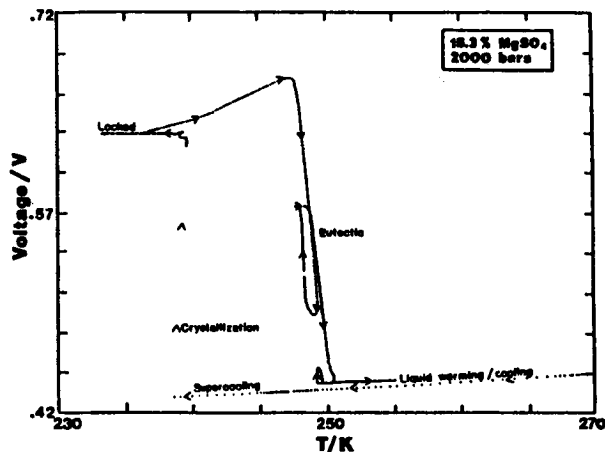


Figure 2. Run at 2000 bars for 15.3 wt.% $MgSO_4$.

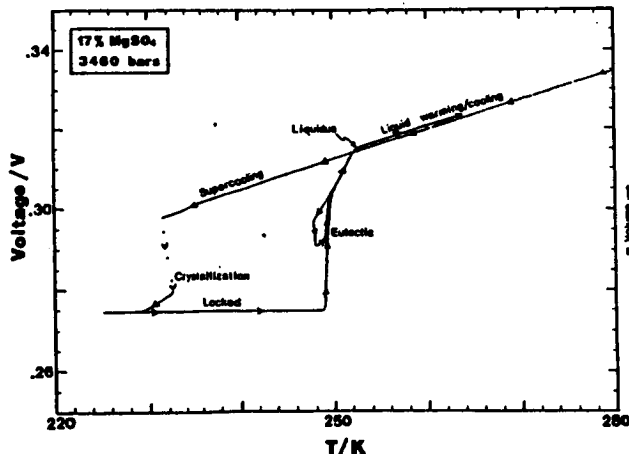


Figure 3. Run at 3460 bars for 17 wt.% $MgSO_4$.

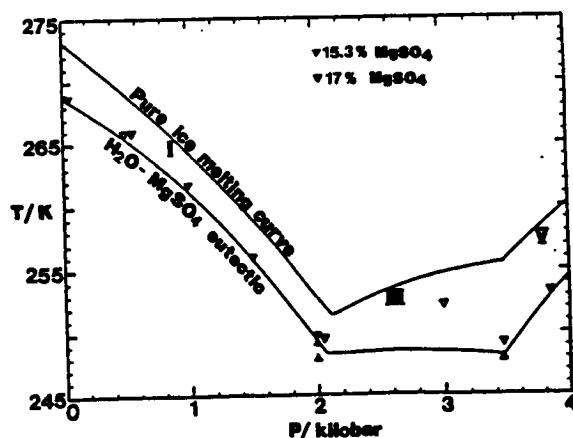


Figure 4. Melting curve for ice and $H_2O-MgSO_4$ eutectic.

Properties of Planetary Fluids at High Pressures and Temperatures.

W. J. Nellis, N. C. Holmes, and A. C. Mitchell, Lawrence Livermore National Laboratory, University of California, Livermore CA.

Observational data obtained by the Voyager space probes to the giant planets Jupiter, Saturn, Uranus, and Neptune have provided valuable information, which is used to refine our picture of the nature of the interiors of these planets. Major results from the Voyager missions include observations of substantial magnetic fields and improved models of internal density distributions. Our goal is to obtain equation-of-state (EOS) and electrical conductivity data for planetary gases (H_2 and He) and the "ices" (H_2O , CH_4 , and NH_3 , and their mixtures), which are considered to be the major constituents of the giant planets. These data are needed to test theoretical databases used to construct models of the chemical composition of planetary interiors, models which are consistent with observables such as mass, diameter, gravitational moments, rotation rate and magnetic field. The 100 GPa (1 Mbar) pressures and several 1000 K temperatures in the giant planets can be achieved in the laboratory by the shock compression of liquid specimens.

Jupiter and Saturn are thought to be composed primarily of hydrogen and helium.¹ Figure 1 shows their calculated planetary isentropes.² Figure 1 also illustrates the relevance of laboratory shock-compression experiments to the giant planets. The single-shock compression curve or Hugoniot of liquid hydrogen intersects the planetary isentropes near 20 GPa and 3000 to 4000 K. Even higher pressures and densities in the laboratory are achieved by reflecting a first shock in liquid hydrogen off a metal anvil, thereby causing a second shock wave. The second-shock states, or the double-shock Hugoniot in Fig. 1, achieve states close to the planetary isentropes at still higher pressures and temperatures.

Uranus and Neptune are thought to consist of an outer layer primarily of hydrogen and helium and an inner layer rich in the planetary "ices." Density distributions have been calculated for Uranus^{1,3,4} from the gravitational movements derived from the observed precessions of its elliptical rings, and from its mass, radius, and rotational rate. Some models show a dense "rocky" core, although the sensitivity of the external gravitational field is weak to the relatively small mass at such great depth. The H_2 -rich envelope is at radii greater than about $0.75 R_U$, where R_U is the outer radius of Uranus. The region at radii less than about $0.75 R_U$ is the ice-rich region. The magnetic fields of these planets are produced by dynamos generated by the convection of high-temperature

conducting fluids in the outer ~30% of the planetary radii.⁵ Pressures extend up toward the 100 GPa range and several 1000 K in these regions.

We measured previously single- and double-shock EOS data for "synthetic Uranus," an H-rich liquid with an H:O composition ratio of 3.5:1 and abundance ratios close to cosmological for O:C(7:4) and O:N(7:1).⁶ It is a solution of water, ammonia, and isopropanol (C₃H₈O) with mole fractions of 0.71, 0.14, and 0.15, respectively. Our four double-shock points are in the range 98 - 220 GPa. The maximum density achieved is 3 g/cm³, which probes a depth of about 0.5 R_J. The region for radii >0.5 R_J is the region probed most sensitively by gravitational moments. Our double-shock EOS points are in good agreement with the planetary isentrope.¹ This agreement suggests that the outer core of Uranus might be composed primarily of the ices. However, chemical compositions cannot be derived uniquely from laboratory data alone. In the last year we performed a double-shock temperature measurement of synthetic Uranus of 4000 K at about 100 GPa. This measurement is important because theoretical temperatures of "ice" are relatively uncertain.

We recently measured four electrical conductivity data points of shocked liquid hydrogen. These data are important for understanding the magnetic fields of all the giant planets. In particular, a scaling relationship for the conductivity is needed at relevant densities and temperatures for dynamo or kinematic calculations of planetary magnetic fields. These data also provide a measure of the narrowing of the electronic bandgap of molecular H₂ with density as it approaches metallization, a subject of fundamental scientific interest. Our experiments are in the ranges 10-20 GPa, 3000-5000 K, and volumes near 8 cm³/mol. Although our conductivity experiments are not yet complete, preliminary analysis indicates that the electrical conductivity σ scales as

$$\sigma = \sigma_0 \exp(-E_g/kT), \quad (1)$$

where E_g is the bandgap and T is shock temperature. We used calculated values of shock temperatures.⁷ Our preliminary bandgap is in agreement with recent theoretical predictions^{8,9} at the molar volume of our experiments. The gap we observe is substantially higher than previous theoretical predictions.¹⁰ The pre-exponential factor σ_0 is also substantially larger than predicted.⁵

Our measurement of the bandgap of hydrogen is the first direct one at high pressures, to our knowledge. This measurement is made possible

by shock heating, which thermally activates electronic charge carriers and induces electrical conductivity. Because of the large bandgap compared to thermal energy, negligible internal energy is absorbed in electronic excitation and the equation of state of molecular hydrogen is unaffected by electronic excitation at the conditions of the experiments.

Acknowledgements: This work was performed under the auspices of the U.S. DoE under Contract No. W-7405-ENG-48 with support from NASA grant W16.180.

References: ¹W. B. Hubbard and M. S. Marley (1989). *Icarus* **78**, 102-118. ²M. Ross (1982). *High Pressure in Research and Industry*, 721-727. ³D. J. Stevenson (1987). *Am. Astron. Soc.* **19**, 851. ⁴M. Podolak and R. T. Reynolds (1987). *Icarus* **70**, 31-36. ⁵R. L. Kirk and D. J. Stevenson (1987). *Astrophys. J.* **316**, 836-846. ⁶W. J. Nellis et al (1988). *Science* **240**, 779-781. ⁷M. Ross et al. (1983). *J. Chem. Phys.* **79**, 1487-1494. ⁸A. Garcia et al. (1990). *Europhys.Lett.* **13**, 355-360. ⁹H. Chacham and S. G. Louie (1991). *Phys. Rev. Lett.* **66**, 64-67. ¹⁰C. Friedli and N. W. Ashcroft (1977). *Phys. Rev.* **16B**, 662-672.

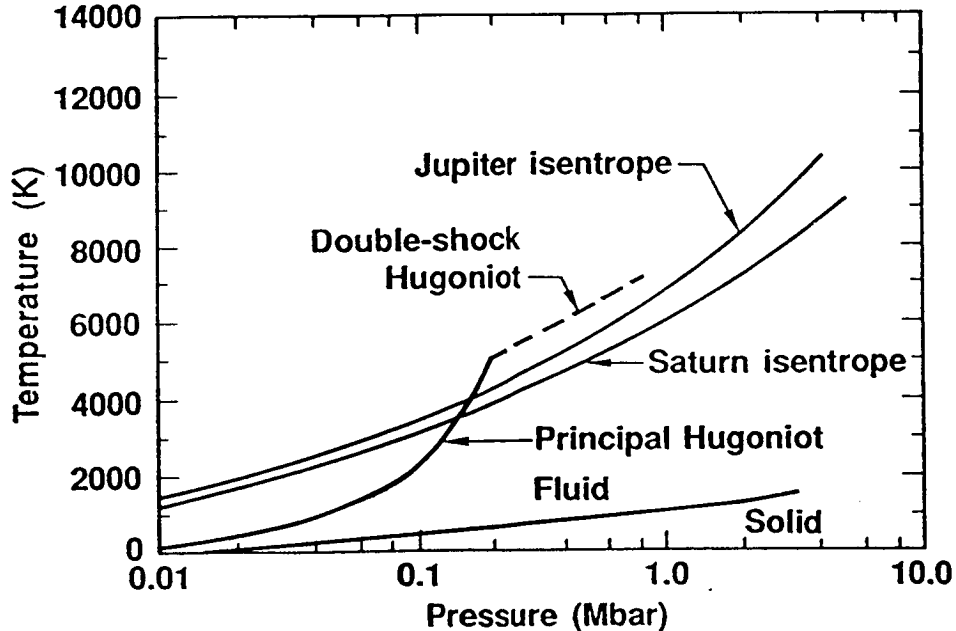


Figure 1. Isentropes of Jupiter and Saturn compared with the Hugoniot and double-shock Hugoniot of H_2 , plotted as temperature versus pressure (after Ref. 2; 1Mbar=100 GPa) .

N92-10740

FLUID DYNAMICS OF MULTIPHASE FLOW IN VOLCANIC ENVIRONMENTS ON THE EARTH, IO, AND OTHER PLANETS

Susan Werner Kieffer, Department of Geology, Arizona State University, Tempe, AZ 85287-1404

During this year, we have been compiling data on H_2O , CO_2 , S, and SO_2 and analyzing it by various techniques to prepare phase diagrams relevant to conditions on the Earth, Io, Mars, and other planets. At the same time, I have been developing a collaboration with Greg Valentine and Ken Wohletz at Los Alamos National Laboratory using their Cray models for volcanic eruptions. We are trying to develop the equations-of-state of the compounds listed above to be compatible with the Cray code so that they can be called as subroutines for the volcanic models. This is a major project, as the current code uses only the equation-of-state for a perfect gas, and requires that the atmosphere be the same composition as the volcanic gas. The analysis of the thermodynamic data is time-consuming, and has been complicated by Kieffer's move to ASU and changes from a VAX/VMS system to Macintosh's, Crays using CTSS (the original LANL language), Crays using Unicos (at ASU), and Sun work stations. It is anticipated that the work will be finished and distributed in 1991.

CHAPTER 2

STRUCTURE AND TECTONICS

TECTONIC EVOLUTION OF LAVINIA PLANITIA, VENUS. Steven W. Squyres, Cornell University, Sharon L. Frank, Brown University, George E. McGill, University of Massachusetts, Sean C. Solomon, Massachusetts Institute of Technology

High-resolution radar images from the Magellan spacecraft have revealed the first details of the morphology of the Lavinia Planitia region of Venus. Lavinia is a broad lowland over 2000 km across, centered at about 45° S latitude, 345° E longitude. The geology of Lavinia is discussed in detail in another abstract in this volume [1]. In this abstract, we discuss the tectonic evolution of Lavinia, and its possible relationship to processes operating in the planet's interior. Our discussion is restricted to the area observed in Magellan image mosaic C1-MIDR.45S350, which covers the region from 37.3 to 52.6° S latitude and from about 340 to 0° E longitude.

One of the most interesting characteristics of Lavinia is that the entire region possesses a regional tectonic framework of striking regularity. This framework is exhibited by a variety of the region's structural features, but is shown most clearly by the small ridges and grooves that are common on the volcanic plains separating the major belts of deformation. Across most of Lavinia, intersecting patterns of small sinuous ridges and long narrow grooves are common. The ridges are interpreted as compressional features, and the grooves as extensional. In nearly all cases where they occur together, the ridges lie orthogonal to the grooves, indicating a lithospheric stress pattern in which the most compressive stress was perpendicular to the axes of the ridges, and the least compressive stress was parallel to them. Considering the thin lithosphere that is expected on Venus, the regularity of this regional tectonic framework across such broad areas is remarkable. In the western part of the region, the inferred orientation of the most compressive stress is NW-SE to WNW-ESE. In the central and northeastern portions, it transitions gradually to E-W, and in the east-central portion to ENE-WSW. Only in the southeastern portion of the region is the inferred stress pattern significantly less regular. The origin of the stresses responsible for this regional pattern is not known, but similar patterns are seen on the plains in a number of other regions of the planet [2].

Lavinia Planitia is also transected by a complex pattern of belts of intense tectonic deformation [1,2], known as ridge belts. They are broad, curvilinear features that can exceed 100 km in width and 1000 km in length. Topographically, they consistently lie higher than the plains that bound them, with typical elevations above the plains of several hundred meters. This clear topographic expression suggests that the belts are the consequence of crustal shortening and thickening across the belt.

Despite the gross topographic similarity of all of the ridge belts in Lavinia, they exhibit two rather distinct styles of near-surface deformation [2]. Both are described in more detail in [1]. One type is composed of sets of broad, arch-like ridges rising above the surrounding plains. They are typically sinuous, and they tend to bifurcate and merge along strike, producing a complex anastomosing pattern. Both their morphology and their orientation parallel to the axes of the belts within which they lie lead us to conclude that they are folds. Some of the ridges are asymmetric and/or possess narrow, rugged, sinuous secondary ridges along their crests, giving an appearance very similar to that of lunar mare or "wrinkle" ridges. These characteristics may indicate that formation of some of the ridges also involves thrust faulting.

In the other type of belt, on the other hand, obvious fold-like ridges are rare to absent in the radar images. Instead, the dominant structural features observed are linear to arcuate faults and fractures, some paired closely to form narrow graben. In some such belts, a larger scale of fault spacing is also evident. Faults in these belts are concentrated into bands of intense deformation that are separated by bands of little or no apparent deformation. The typical spacing between individual deformed bands is 20-30 km, consistent with deformation of the entire thickness of a strong upper crustal layer [3]. Detailed correlation of radar images with Magellan altimetry shows that, within such belts, the areas of most intense fracturing are also the areas that are most elevated. This characteristic, the morphology of the faulting, and the small widths of the observed graben lead us to conclude that much of the deformation in the ridge belts of this sort involves flexure and extensional failure of a thin, brittle surface layer across the crests of uplifts that are caused by crustal shortening and thickening.

Both types of ridge belts show evidence for small amounts of shear distributed across the belts [2]. In the ones dominated by faulting, this is most clearly shown by instances where graben bend sharply to produce rhombohedrally-shaped downdropped blocks. In the ones dominated by

folding, the best evidence for distributed shear comes from deflection of older tectonic lineaments as they cross the belts.

Formation of all the belts was not contemporaneous. Lava sheets on the plains serve as stratigraphic markers in Lavinia, and lavas are present that partially or largely bury old belts and that are in turn deformed by the formation of later ones. Belt formation apparently took place over a significant period, with volcanism occurring intermittently throughout that period.

If both types of belts are the consequence of crustal shortening, why are there two such distinct styles of near-surface deformation? The answer appears to be related to the orientation of each belt with respect to Lavinia's regional tectonic framework. With very few exceptions, the belts that lie perpendicular to the regional axis of lithospheric compression are dominated by folding, and those that lie perpendicular to the regional extensional axis are dominated by faulting. Even more telling are the characteristics of belts that change substantially in orientation along their length. In these belts, where the belt axis changes from perpendicular to the most compressive lithospheric stress direction to parallel to it, there is a clear change in the structural character of the belt from domination by folds to domination by faults.

Despite the regularity of the regional tectonic framework across the Lavinia region, the belts within it display a full range of orientations, apparently unrelated to this framework. It is only the character of the near-surface deformation in the belts that appears to be influenced by the framework, not the orientations of the belts themselves. The process responsible for ridge belt formation seems, then, to be largely independent of whatever produced the regional stress pattern. Similar behavior is seen in many coronae on Venus, where fracturing in a corona's annulus is strongly influenced by a regional lithospheric stress pattern that appears to be independent of the process responsible for the corona's formation [4].

What is responsible for the crustal shortening and thickening involved in ridge belt formation, and for the concentration of this thickening into curvilinear belts? Several possibilities exist. It has been suggested that deformation with characteristic spacings of 10-30 km on Venus is a result of compressional instability in a strong, near-surface crustal layer, and that deformation spaced hundreds of km apart may reflect a similar instability in a strong layer in the upper mantle [3]. In this case, the ridge belts themselves may reflect deformation controlled by the strength properties of the upper mantle, while the observed faulting and folding in each belt would reflect the response of the upper crust. The independence of belt orientations from the regional tectonic framework would be attributed to a mechanical decoupling of the strong upper crust from the strong upper mantle. A possible difficulty with this hypothesis is that the spacings and orientations of Lavinia's belts are far from regular. Another possibility is that relatively small-scale mantle convection cells exert an influence on belt formation. Sheet-like convective downwellings may be common in the venusian mantle, and one would expect belt-shaped crustal thickening and uplift to take place above a linear convergence of flow. In this case, individual belts might have formed by crustal thickening above such downwellings, with the upper crust deforming in response to both the thickening and the regional stress pattern. Activity in the downwellings for which evidence is preserved is unlikely to have been concurrent, consistent with the inferred spread in belt ages. Again, the orientation of the belts would be independent of the regional tectonic framework. The difficulty with this hypothesis is that most mantle convection models for Venus predict that the scale of convection cells should be substantially larger than several hundred km. However, our emerging understanding of coronae on Venus suggests that convective upwellings with dimensions far smaller than those predicted by the same models are very common [5]. In fact, the convective scales inferred to be involved in corona formation are effectively the same as those that would be required for ridge belts.

There are other regions on Venus where ridge belts are common. As the Magellan mapping mission continues, examination of these regions should shed further light on the process of ridge belt formation and on its relationship to processes in Venus' interior. Expanded coverage will also allow mapping on a global scale of the as-yet poorly understood regional tectonic framework seen in areas like Lavinia.

References

- [1] Frank, S.L., *et al.*, *LPSC XXII*, 407 (1991). [2] Solomon, S.C., *et al.*, *Science*, in press. [3] Zuber, M.T., *J. Geophys. Res.* **92**, E541 (1987). [4] Squyres, S.W., *et al.*, this volume. [5] Stofan, E.R., *et al.*, *LPSC XXII*, 1335 (1991).

MORPHOLOGY AND EVOLUTION OF CORONAE AND OVOIDS ON VENUS. Steven W. Squyres, Cornell University, Duane L. Bindschadler, UCLA, Daniel M. Janes, Cornell University, Gerald Schubert, UCLA, Virgil L. Sharpton, Lunar and Planetary Institute, Ellen R. Stofan, Jet Propulsion Laboratory

Coronae and ovoids on Venus were first identified in Venera 15/16 data [1]. They are distinctive and apparently unique to the planet, and may be important indicators of processes operating in the venusian mantle. Magellan images have provided the first high-resolution views of corona and ovoid morphology. In this abstract, we describe the general geologic character of coronae and ovoids, and draw some inferences about their geologic evolution. In two related abstracts in this volume we discuss models of corona and ovoid formation [2], and attempt to relate the characteristics of the features to mantle processes [3].

For consistency with previous work, the following working definitions are adopted here for coronae and ovoids. Coronae are circular to elongate features surrounded by an annulus of deformational features, with a relatively raised or indistinct topographic signature and, commonly, a peripheral trough or "moat". Ovoids are circular to elongate features other than coronae with either positive or negative topographic signatures, associated with tectonic deformation and volcanism. Coronae are thus rather specifically-defined features, whereas ovoids encompass a wider range of morphology. Typical diameters of both classes of features are a few hundred km.

Magellan altimetry data have provided considerable new information on the gross topographic character of coronae. (The reader should be warned that our sample of these features to date is both geographically incomplete and biased toward features with clear topographic signatures.) The outermost topographic feature of many coronae is the moat: a broad trough that partially or completely encircles the corona. Typical moat widths are 50-100 km, and typical depths are a few hundred m. Incomplete, discontinuous moats are more common than complete ones in the coronae observed to date. Interior to the moat is an annular ridge, again typically 50-100 km wide, but generally with greater relief than is shown by the moat. Discontinuous annuli are also observed, but they are less common than discontinuous moats in our sample. There is wide variability in the elevation of corona interiors. Some rise a kilometer or more above the level of the surrounding plains, while others actually lie a few hundred meters lower than the plains. Most coronae are quasi-circular, but a few have been found that are markedly elongate or irregular in shape. A few instances of overlapping coronae have also been observed.

Corona moats are usually sites of deposition of young lavas. Where the source of these lavas can be identified, it is commonly not in the moat itself, but in the corona interior. Many corona interiors are sites of substantial extrusion of very fluid lavas, and in some cases these lavas spill over the annulus or through gaps in it, and pool in the low-lying moats. In the few instances where moats do not appear to be flooded, they still are generally characterized by less intense faulting and fracturing than much of the rest of the corona, particularly the annulus.

Corona annuli are sites of intense tectonic deformation. The most common manifestations of this deformation are radar-bright fractures and grooves. Most of the grooves are very narrow, and appear to be graben. The overall appearance is one of extensional failure of a thin brittle surface layer that has been stretched across a topographic rise. Most corona annuli display a set of concentric fractures, concentrated on the crest and/or flanks of the annular ridge. Some also display a second set of fractures that is related to a regional tectonic framework that appears to be independent of the corona itself. Some regions of Venus exhibit such a framework, with a clear preferred orientation for extensional fracturing that is consistent over large areas [4,5]. In such regions, corona annuli can exhibit fracturing that is aligned with this regional trend, independent of the local orientation of the trend with respect to the annulus.

Corona interiors commonly are sites of substantial volcanic activity [6]. Evidence for this activity takes a variety of forms, including small calderas and other collapse features, lava channels, and small volcanic cones and domes. Most significant, however, is voluminous flooding of the corona interior by low-viscosity lavas. In many coronae this flooding has obscured any evidence of former tectonic features that might have been present. In a few instances, however, remnants of older materials still protrude through the central lavas; some of these surfaces still display older tectonic features. In most such instances, the older fracturing is radial. Fracturing subsequent to flooding is also observed, and commonly aligns with a regional tectonic framework if one is present.

A variety of other circular volcanotectonic features is observed on Venus. We refer to these collectively as ovoids, although their histories and even origins may not all be similar. Of the ovoids

observed by Magellan to date, there are two primary topographic types. One is a simple dome. Several of these have been found, with heights above the surrounding plains that can exceed 1 km. The domes are broad and gently sloping, with no annular ridge and at most a very subdued partial moat. Examples include Pandora* (42.5° S lat, 6° E lon) and Baltis* (9° N lat, 348.5° E lon). The other type is a simple, nearly circular topographic depression, with no discernable bounding ridge. Examples include Damkina* (7° S lat, 13° E lon) and Amaterasu* (8.5° N lat, 12° E lon). Typical depths of these are 500 m, with relatively steep walls and flat floors.

The tectonic features associated with these two types of ovoids are as different as is their topography. The domical ovoids are characterized in most cases by a well-developed radial fracture pattern. Again, this fracturing is clearly extensional, with well-developed grabens commonly visible. Some concentric fracturing may also be observed, though it is generally less well-developed than is the radial fracturing. The ovoids that are depressions, on the other hand, are characterized primarily by concentric extensional fractures. These fractures are found both on the lip and the wall of the depression, but are less common on the floor. As is the case for coronae, fracturing of all sorts in ovoids can be enhanced where it is aligned with a preferred direction for extensional failure in the surrounding terrain.

Based on the coronae and ovoids that have been observed so far, it is possible to draw some inferences about the sequence of events involved in their formation. In the broad sense, this sequence is similar to that inferred from pre-Magellan data [7,8]. We believe that it is an important observation that dome-shaped ovoids have pronounced radial fracturing, and that some coronae also show evidence for intense radial fracturing in their interiors, now largely buried under younger lavas. In addition, coronae and domical ovoids have similar shapes, similar sizes, and commonly occur in close geographic association [2]. These observations lead us to infer a genetic relationship between the two; we believe a domical ovoid to be the first stage in formation of a corona. During this stage, the lithosphere is uplifted and intensively fractured in a dominantly radial pattern. We believe that the domical ovoids we observe are coronae either actively in the process of forming or whose formation was somehow arrested in this early stage.

Several events follow the initial central uplift phase as a corona continues its development. One clearly is volcanism. Looking at the coronae observed to date as an ensemble, there does not seem to be distinct epoch of volcanism during development of most coronae. Instead, volcanism seems to occur intermittently, and in some cases voluminously, throughout much of a corona's history. At one extreme, some domical ovoids are already partially buried by volcanics originating within the dome. At the other, many coronae that have completely lost their central uplift have young, unfractured lavas ponded in their lowest-lying areas.

Following the initial uplift and occurring concurrently with the volcanism, the topographic history of a corona seems to be characterized by subsidence of the central dome, uplift of the annulus, and subsidence of the moat. As these motions take place the lithosphere undergoes flexure and failure, sometimes influenced both by the flexure itself and by an independent regional structural framework. Through careful study of crosscutting relationships, it may be possible for us to discern a relative timing of these uplift and subsidence events, but initial examination indicates that determining the sequence, if there indeed is one, will not be straightforward.

We are uncertain of the relationship of the ovoids that are pure depressions to coronae. It may be that they are another possible endpoint of corona evolution, but we cannot exclude the possibility that they are a different genetic class of features entirely, more akin to calderas.

Coronae and ovoids are known to be present over much of the rest of Venus, and we anticipate finding many more of them as the Magellan mapping mission continues. With the complete diversity of corona and ovoid forms determined, we hope to understand more fully the genetic sequence of these features, and to relate this sequence to processes operating in the venusian interior.

References

- [1] Barsukov, V.L., *et al.*, *J. Geophys. Res.* **91**, D378, 1986. [2] Bindschadler, D.L., *et al.*, *LPSC XXII*, 105, 1991. [3] Stofan, E.R., *et al.*, *LPSC XXII*, 1335, 1991. [4] Solomon, S.C., *et al.*, *Science*, in press. [5] Squyres, S.W., *et al.*, this volume. [6] Head, J.W., *et al.*, *Science*, in press. [7] Pronin, A.A., and Stofan, E.R., *Icarus* **87**, 452, 1990. [8] Stofan, E.R., and Head, J.W., *Icarus* **83**, 216, 1990.

*All names for features used in this abstract are provisional, and have not yet been approved by the IAU.

HOT-SPOT TECTONICS OF EISTLA REGIO, VENUS: RESULTS FROM
MAGELLAN IMAGES AND PIONEER VENUS GRAVITY

Robert E. Grimm and Roger J. Phillips, Dept. of Geological Sciences, Southern Methodist University, Dallas, TX 75275.

Introduction. Eistla Regio is a broad, low, discontinuous topographic rise striking roughly EW at low northern latitudes of Venus. Some 2000x7000 km in dimension, it is the third largest rise in planform on Venus after Aphrodite Terra and Beta-Phoebe Regiones. These rises are the key physiographic elements in a hot-spot model of global tectonics [1] including transient plume behavior [2]. Since Eistla Regio is the first such rise viewed by Magellan and the latitude is very favorable for Pioneer Venus gravity studies, we attempt to test some of the predictions of a time-dependent hot-spot model here. We define western Eistla Regio as the rise including Gula and Sif Mons and central Eistla Regio as that including Sappho Patera. Superior conjunction prevented Magellan from returning data on eastern Eistla Regio (Pavlova) during the first mapping cycle.

Regional Tectonic Patterns. The largest tectonic feature viewed by Magellan in western Eistla Regio is a 700-km long anastomosing set of radar-bright lineaments extending SE from Gula Mons. The strike of individual elements varies from NW to N; indeed, some strike N and are arrayed en echelon to the NW. This region appears to be a rift zone, as many of the lineaments are troughs and most lie within a larger linear depression flanked by local highs. This depression can be traced 400 km further along the saddle joining western and central Eistla, where it joins with N- and NW-striking troughs. The rift zone is truncated by flows on the lower flank of Gula Mons; after a short switch to a northeasterly strike along the volcano's summit, graben-like lineaments continue northwesterly from Gula Mons. Two parasitic domes (coronae?) along this trend further suggest that it is a locus of extension, mantle upwelling, and partial melting. Regional tectonic fabrics are less evident at Sif Mons, but again a NW-trending band of troughs, often en echelon, extends from the NW for several hundred km although the pronounced topographic trough is absent. NW-striking lineaments also appear to the SE of Sappho Patera, but their regional importance is yet unresolved due to the small imaged area available. In summary, the regional tectonic fabric of central and western Eistla Regio is dominated by NW-striking rift zones, approximately centered on the axis of the rise, which both cut and are buried by volcanic edifices.

Impact Crater Density. Within the 3.4×10^6 km² of western Eistla Regio above the mean planetary radius, Magellan images show 5 probable impact craters (Class 1), 2 possible impact structures (Class 2), and 2 additional circular features of unknown origin (Class 3). The areal density of impact craters for this region is then $1.5/10^6$ km² for Class 1 alone and $2.1/10^6$ km² for Classes 1 and 2 together. The latter value is consistent with the mean density of $1.9 \pm 0.2/10^6$ km² for Classes 1 and 2 over the first 15% of the planet surveyed by Magellan. The surface age of western Eistla Regio does not appear to be significantly different from the mean age of the surface as a whole. Two of the nine potential impact craters on the rise actually lie on the volcanic constructs, approximately the expected number for the area of these edifices. One, a doublet of 5-km diameter structures at 20N, 350E, is doubtful, but the other, a crater 20 km in diameter at 20N, 355E (provisional name De Lalande) is a strong impact candidate. Since there are not enough craters for reliable statistics within the region, impact crater density alone cannot distinguish between the alternative hypotheses: (1) the edifices are younger than the rise, or (2) the rise and the edifices are contemporaneous. By contrast, no impact craters are visible in a 5×10^6 km² area around Sappho Patera; since it is highly unlikely that this would occur by chance, central Eistla Regio is distinctly younger than the planetary mean.

Gravity. A linearized inversion procedure [3] was used to produce a map of vertical gravity at 300-km altitude from Pioneer Venus line-of-sight accelerations over the area 10S-40N, 30W-30E. The apparent depth of isostatic compensation (ADC), derived from the correlation between gravity and topography, is 190 ± 30 km over the entire region. However, significant variations are present within this area: the ADC is 200 ± 20 km at western Eistla (15-30N, 15W-5E), but falls to 110 ± 20 km over central Eistla (5-20N, 10-25E). The ADC of central Eistla Regio is only slightly larger than those of western Aphrodite Terra, whereas the ADC of western Eistla Regio is more comparable to those of Atla and Bell Regiones.

Discussion. The presence of NW-oriented rift zones all along the topographic axis of west-central Eistla Regio indicates some crustal stretching in a NE-SW direction, either due to active mantle uplift or passive extension perpendicular to the principal axis of the rise. The crater-free surface of central Eistla Regio is consistent with the terminal stages of transient plume ascent [2], wherein the lithosphere is penetrated by a plume head and massive flood volcanism occurs [4]. Intermediate (~ 100 km) ADCs are associated with this stage. Larger ADCs such as those of western Eistla Regio are held to be associated with deep plumes that have uplifted the surface, perhaps with some advance volcanism, but without widespread resurfacing. These conditions would be satisfied if Sif and Gula Mons are younger than the rise as a whole (hypothesis 1). If, however, the volcanic edifices are as old as the rise (hypothesis 2), then the mantle plume must be long-lived rather than transient, although not much volcanism has been produced in recent geologic time. In this latter scenario, central Eistla is experiencing the effects of extensive partial melting in a transient plume head while western Eistla has entered a steady-state (plume tail) phase [6]. These same considerations should apply to Beta Regio, which has an impact crater density similar to western Eistla Regio [5], a large ADC, and contemporaneous linear rift zones and volcanic edifices.

Conclusion. The western and central portions of Eistla Regio, while part of the same broad topographic rise and tectonic framework, have distinctly different surface ages and gravity signatures. The western rise, including Gula and Sif Mons, is the expression of deep-seated uplift with volcanism limited to the individual large shields. The eastern portion, including Sappho Patera, has been widely resurfaced more recently by shallower thermal anomalies in the mantle.

References. [1] R.J. Phillips and M.C. Malin, in *Venus*, (eds. D.M. Hunten et al.), Univ. Ariz., 159, 1983; [2] Herrick and Phillips, *GRL*, 17, 2129, 1990; [3] Grimm and Phillips, *JGR*, in press, 1991; [4] R. White and D. McKenzie, *JGR*, 94, 7685, 1989; [5] D.B. Campbell et al., *Science*, 246, 373, 1989; [6] M.A. Richards et al., *Science*, 246, 103, 1989.

GRAVITATIONAL SPREADING OF DANU, FREYJA AND MAXWELL MONTES, VENUS.

Suzanne E. Smrekar and Sean C. Solomon, Department of Earth, Atmospheric, and Planetary Sciences, Massachusetts Institute of Technology, Cambridge, MA 02139.

Introduction. The potential energy of elevated terrain tends to drive the collapse of the topography. This process of gravitational spreading is likely to be more important on Venus than on Earth because the higher surface temperature weakens the crust¹. The highest topography on Venus occurs in Ishtar Terra. The high plateau of Lakshmi Planum has an average elevation of 3 km above mean planetary radius, and is surrounded by mountain belts. Freyja, Danu, and Maxwell Montes rise, on average, an additional 3, 0.5, and 5 km above the plateau, respectively. Recent high-resolution Magellan radar images of this area, east of ~330°E, reveal widespread evidence for gravity spreading². This paper describes observational evidence for gravity spreading and discusses the implications in terms of simple mechanical models.

On Earth, gravitational potential energy is known to drive extensional normal faulting near the crest of high topography, where the vertical stress is greater than the horizontal stress, and thrust faulting on the flanks, where the horizontal normal stress exceeds the vertical normal stress^{3, 4}. Strike-slip faulting occurs when additional regional stresses interact with gravitational stresses. Gravity can also be an important force for reducing topographic slope through the formation of detachments⁵, which result in normal faulting at the surface⁶.

Models. Several simple models predict that gravity spreading should be an important process on Venus. Most of the potential energy of crustally compensated mountains is a result of the mantle pushing on the root⁴. However, given an apparent depth of compensation of 130 km at Ishtar Terra⁷, Airy isostasy is unlikely to be the dominant compensation mechanism. An estimate of the deviatoric stress resulting from the topographic relief alone, without a crustal root, is simply $\rho gh/2$, where ρ is density, g is gravitational acceleration, and h is height¹. Using $\rho = 3000 \text{ kg/m}^3$, $g = 8.87 \text{ m/s}^2$, this equation gives 13 MPa/km of relief. For average elevations of 3.5, 6, and 8 km for Danu, Freyja, and Maxwell Montes, this gives respectively 50, 80, and 100 MPa. If some component of crustal compensation is present, actual stresses due to gravitational potential will be greater. Whatever the degree of crustal compensation, it is clear that gravity produces considerable tectonic stress in these mountain ranges.

The formation of ductile detachments is predicted for surface slopes such as those found in these mountains. Smrekar and Phillips⁵ developed a model for detachment in a viscous layer inclined at an angle, using a diabase flow law for the crust. As the model is highly dependent on temperature, both higher thermal gradients and thicker crustal layers, which are hotter at the base, produce greater rates of deformation. The rate of deformation also increases with surface slope. Even for a modest surface slope of 1°, a diabase crust 20 km thick with a thermal gradient of 15 K/km will flow at a rate of 10 mm/year. Locally, surface slopes in the mountains are much greater. The western flank of Maxwell Montes has a slope of ~30°; a slope of ~20° is found along Vesta Rupes. For a slope of 30°, a deformation rate of 10 mm/year is expected for a thermal gradient of 5 K/km, given a crustal thickness of only 10 km. These results predict that detachments are very likely in the mountains.

Observations. Danu Montes has the least relief of the mountain ranges. The highest topography in Danu Montes is centered near 59°N, 336°E. A large graben-like structure (10 x 50 km) occurs parallel to the crest in this region, suggesting that extension occurred along

preexisting weaknesses resulting from the formation of the range. The southwestern end of this graben is cross-cut by faults with the same NE-SW trend that is defined by the folds and thrusts that make up the mountains. The implication is that the extension occurred while regional compressional stresses were still active. Several long (~100 km) normal faults strike approximately parallel to the trend of Vesta Rupes. It is possible that these faults are the surface expressions of thrust faults, as the toes of thrust faults are frequently cut by normal faults. Although conclusive evidence in the form of the vergence of these faults is impossible to obtain, faults paralleling topographic strike are expected on the flanks of extending mountains. Numerous narrow (~1 km) graben, with lengths of tens of kilometers and a spacing of 0.5-2 km, parallel the large NW-SE trending faults, providing further evidence of extension. These narrow, closely spaced faults may represent the surface expression of deformation above a detachment.

Freyja Montes appears to have undergone intense deformation, as evidenced by high roughness and complex tectonic patterns. The north slope of Freyja Montes between 330°E and 335°E is cut by numerous graben with widths of 1-3 km and spacings of 3-10 km. These graben trend NW-SE to N-S; however their truncation at long lineations and their curved patterns suggest that they have been shortened and probably sheared. As at Danu Montes, we interpret these small-scale graben to indicate detachment at depth, and the deformation of the graben to mean that extension occurred while regional compression was still active.

NW-SE trending graben are also found on the southern front of Freyja Montes, but are less numerous and larger, up to 5 km across, and more widely spaced. This set continues tens of kilometers onto the plains of Lakshmi Planum, where the spacing is ~5 km and the width is ~1 km. A large (~100 x 150 km) dome-like structure occurs on the eastern flank of Freyja Montes, which in addition to displaying the same NW-SE trending graben set, is dissected by a N-S to NE-SW graben set with an irregular spacing of 1-10 km and widths of 1-2 km. This set appears to be older than the NW-SE set. We interpret these graben sets as normal faulting above a detachment. On the eastern side of the dome, the blocks that form where the two graben sets intersect are absent, possibly because they spread downslope. Compressional features farther downslope support this interpretation. A similar pattern occurs on the SW flank of the dome, also suggesting that material has moved downslope. This feature may be analogous to terrestrial metamorphic core complexes.

Maxwell Montes contain the highest topography and steepest regional slopes observed to date on Venus. Several pairs of long, nearly linear faults occur between Cleopatra crater and the crest of Maxwell Montes. These features are 10-20 km wide and ~100 km long. The slight undulations in these faults may indicate that they were originally straight normal faults that have been subsequently deformed. Alternatively, they may be compressional ridges that happen to be paired. Given the remarkably steep slopes (up to 30°) found on the western front of Maxwell Montes, the observed lineations are most easily interpreted as thrust faults. These features are consistent with gravitational spreading but do not provide conclusive evidence.

Two additional, perpendicular sets of graben occur on the southern slope of Maxwell Montes. One set is perpendicular to topographic strike and has a spacing of 5-10 km and widths of 2-5 km. The other set is parallel to topographic strike and curves with the border of the southern flank of Maxwell Montes, giving the two sets a radial and concentric pattern. The concentric graben have widths of ~5 km and a spacing of ~5 km. This set of graben is cut by the radial set. Similar, narrow graben sets also occur on the northern flank of Maxwell Montes. The set perpendicular to topographic strike also appears to be the youngest in this

region. Although the graben set which is parallel to topographic strike might be interpreted as faulting above a detachment, the perpendicular set is difficult to explain.

Discussion. One difficulty in using remote observations to infer interior properties is that the observed features may not have formed in response to stresses which are still active. However, the observation that gravity spreading has apparently occurred in some areas but not others suggests there is a difference between regions that have very high surface slope but do not appear to have not spread, and those which have already spread. The implication is that the thermal gradients are relatively low in the high-slope regions that lack evidence for spreading. Among possible explanations are that regions that have spread simply had higher heat flow, or that regions of steep slopes which have not spread may represent stacks of recently emplaced and relatively cold thrust sheets that have not reached thermal equilibrium. We favor the latter interpretation for the western slope of Maxwell Montes. There is evidence for volcanism at Danu Montes, favoring high heat flux, but not in the vicinity of the graben sets at Freyja and Maxwell Montes. A further implication is that these mountains probably do not have large crustal roots as they would then have to be able to resist a much greater amount of gravitationally induced stress.

References. ¹J. Weertman (1979). *Phys. Earth Planet. Inter.*, **19**, 197-207. ²S.C. Solomon et al. (1991). *Science*, **252**, in press. ³B.C. Burchfiel and L.H. Royden (1985). *Geology*, **13**, 679-682. ⁴P. Molnar and H. Lyon-Caen (1988). *Geol. Soc. Am., Spec. Paper* **218**, 179-207. ⁵S.E. Smrekar and R.J. Phillips (1988). *Geophys. Res. Lett.*, **15**, 693-696. ⁶B.C. Burchfiel et al. (1989). *Geology*, **17**, 748-752. ⁷R.E. Grimm and R.J. Phillips (1990). *Geophys. Res. Lett.*, **17**, 1349-1352.

INTERPRETATION OF THE NORTHERN BOUNDARY OF ISHTAR TERRA
FROM MAGELLAN IMAGES AND ALTIMETRY

S. Mueller, R.E. Grimm, and R.J. Phillips, Dept. of Geological Sciences, Southern Methodist University, Dallas, TX 75275.

Introduction. Part of the controversy on the origin of western Ishtar Terra concerns the nature of Uorsar Rupes, the northern boundary of Ishtar Terra. In the hypothesis of lithospheric convergence and underthrusting [1], Uorsar Rupes is held to be the main boundary thrust fault at the toe of an accretionary wedge. A topographic rise parallel to the scarp was interpreted as a flexural bulge similar to those of terrestrial subduction zones, and quantitative models of this feature seemed broadly consistent with the expected lithospheric structure of Venus [2]. In the alternative mantle-upwelling hypothesis for western Ishtar Terra [3], the outer margins of the highland are thought to be collapsing [4], and Uorsar Rupes has been interpreted as a normal fault [5]. Here we interpret Magellan images and altimetry for this region and reassess the hypothesis that a flexural signature can be distinguished.

Geologic Description. Uorsar Rupes rises over 2 km within the width of a single footprint of the Magellan altimeter (~ 20 km). The scarp is generally radar-dark and dissected by fine crenulations. At the foot of the scarp there is a group of narrow ridges (srg, Fig. 1). The top of the scarp is a complexly deformed radar-bright unit, previously termed "ridge-and-dome" [1] (rd). A sharp break in this unit occurs at 337E and is suggestive of right-lateral offset. The scarp itself takes a more gentle bend just east of here and an S-shaped ridge separates the scarp crest from an isolated rd unit at lower elevation; the planform strongly suggests that this block has detached from the scarp. The belt of basal ridges widens in the vicinity of 345E and some show broad asymmetric arches and a tight crenulation on one side, very similar to mare ridges. Plains adjacent to the basal ridge group are generally dark and featureless (pd), although a bright embayed unit (pb) grows in prominence toward the east and mottled plains (pm) also appear. The dark plains are very low to the west (the "foredeep") and the northern boundary of this basin (the "outer rise") is marked on its inner slope at 78.5-79N by a unit of intermediate radar backscatter showing east-west lineations (rlg). This unit continues even where the rise is no longer evident to the east (Fig. 2). Numerous dissected and embayed units occur throughout the study area, usually as radar-bright blocks of narrowly spaced grooves (gt). The units at 79N, 335E are abruptly truncated to the south by dark plains along an E-W line; this boundary corresponds to a drop of 300 m along orbit 520. To the north of the rise crest, the topography slopes down linearly and the number and size of western gt units decreases.

Altimetric Interpretation. We consider three models for the topography north of Uorsar Rupes: (1) the entire trend represents an "outer rise complex," (2) one component is flexural, but superimposed upon a more dominant trend (thermal, compositional, or structural), and (3) there is no geophysically significant flexure. In (1), topographic variations between 84 N and the boundary scarp imply a forebulge amplitude > 0.5 km and an outer rise wavelength of at least 500 km. Although the trench depth in orbit 510 is only about 500 m (small by terrestrial standards), the forebulge amplitude is comparable to maximum values observed on Earth and the wavelength significantly exceeds any terrestrial analog [6,7]. Therefore if a flexural response to loading at the scarp is apparent in the data it must be partially obscured as in (2). Following projection of the profiles normal to the scarp, we attempt to remove non-flexural trends by subtracting a least-squares line from the entire profile fit only to that portion between 400 and 800 km from the scarp (Fig. 3). Orbits 550 and 560 lack even a trench, whereas orbits 500 and 520 show abrupt variations. Orbit 510 so processed exhibits a distinct, gentle topographic high adjacent to the trench and so represents the best profile upon which to attempt flexural modelling. Fig. 4 shows a series of elastic flexural profiles superimposed on orbit 510; these solutions assume zero bending moment at the trench [2,7], zero in-plane force, and a range of elastic plate thicknesses from 5 to 25 km. Clearly the scale of topographic

variations far exceeds flexural behavior. Calculations for non-zero in-plane forces yield similar results.

Discussion. Although we find no evidence for flexure in Magellan altimetry, this conclusion does not rule out the possibility that lithospheric underthrusting is occurring: flexure could be masked by the topographic signatures of a variety of geologic units or else extensive faulting may not allow integral plate behavior. The scarp ridge group could be the compressional deformation where subduction is imminent and the rise lineament group, which bears some resemblance to ridge belts, may represent a new locus of crustal shortening.

Alternatively, the altimetry and images may also be interpreted under the hypothesis that the northern boundary of Ishtar Terra is undergoing extensive normal faulting, disruption, and gradual burial. The detached rd unit at 77N,340E may be the most immediate manifestation of this process: Uorsar Rupes is the present boundary fault of Ishtar Terra, analogous to the western boundary of the Sierra Nevada. The adjacent ridges are simply the local result of edifice stresses due to the sharp relief. An earlier boundary may be recorded in the rise lineament group, where the intervening basin has down-dropped and pre-existing structures (eastern gt units) buried by plains. The scarp at 79N,333E is most likely a steep normal fault, and the western gt units are being gradually buried as the topography slopes gently down to the north.

Conclusion. Magellan images of the northern boundary of Ishtar Terra show evidence of crustal shortening adjacent to Uorsar Rupes, but extension and burial dominate northwards. Altimetric profiles display the same long-wavelength trends visible in Venera data [2], but no clear evidence of lithospheric flexure. We favor a model of regional extension and burial, but regional compression cannot be ruled out.

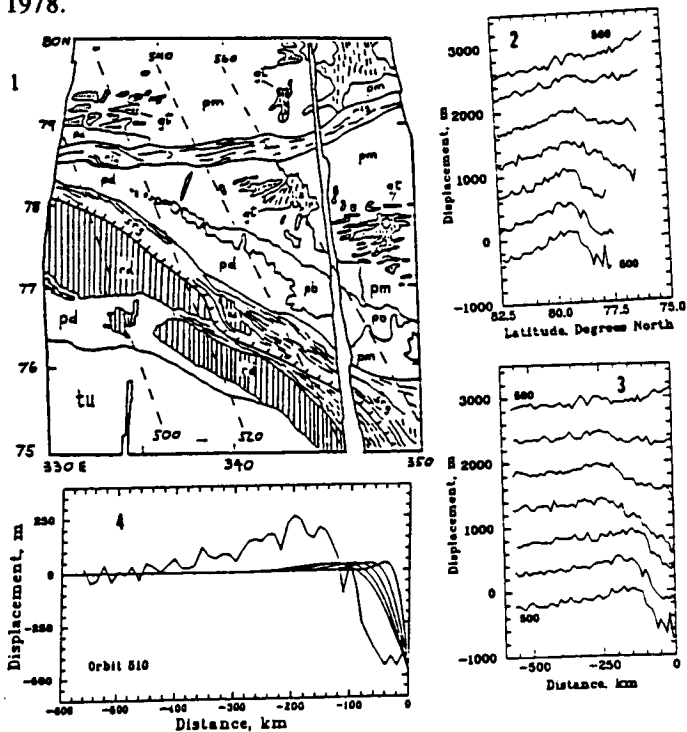
References. [1] J.W. Head, *Geology*, 18, 99, 1990; [2] S.C. Solomon and J.W. Head, *GRL*, 17, 1393, 1990; [3] A.A. Pronin, *Geotectonics*, 20, 271, 1986; [4] A.T. Basilevsky, *Geotectonics*, 20, 282, 1986; [5] A.M. Nikishin, *EMP*, in press, 1991. [6] D.L. Turcotte and G. Schubert, *Geodynamics*, J. Wiley & Sons, 1982. [7] D.C. McAdoo et. al., *GJRS*, 54, 11, 1978.

Fig. 1. Geologic sketch map of Uorsar Rupes (hachured) and surroundings; units described in text except tu, undivided tessera. Altimetry ground tracks shown as dashed lines.

Fig. 2. Altimetric profiles, ending at Uorsar Rupes. Orbit 500 referenced to mean planetary radius, others offset by 500 m each for clarity.

Fig. 3. Altimetric profiles processed by projecting normal to scarp and removing linear trend.

Fig. 4. Elastic flexural profiles superimposed on processed version of orbit 510, plate thicknesses 5-25 km.



HORIZONTAL STRESS IN PLANETARY LITHOSPHERES FROM VERTICAL PROCESSES

W. B. Banerdt, Jet Propulsion Laboratory, California Institute of Technology, Pasadena, CA 91109

Introduction. Understanding the state of stress in a lithosphere is of fundamental importance for planetary geophysics. It is intimately linked to the processes which form and modify tectonic features on the surface and reflects the behavior of the planet's interior, providing a valuable constraint for the difficult problem of determining interior structure and processes. On the Earth, most of the stress in the lithosphere can be related to lateral tectonics associated with plate dynamics; however, the tectonics on many extra-terrestrial bodies (such as the Moon, Mars, and most of the outer-planet satellites) appears to be primarily vertical in nature, and the horizontal stresses induced by vertical motions and loads are expected to dominate the deformation of their lithospheres [e.g., 1-5]. We are concerned here only with changes in the state of stress induced by processes such as sedimentary and volcanic deposition, erosional denudation, and changes in the thermal gradient that induce uplift or subsidence. This analysis is important both for evaluating stresses for specific regions in which the vertical stress history can be estimated, as well as for applying the proper loading conditions to global stress models. It is also of interest for providing a reference state of stress for interpreting stress measurements in the crust of the Earth (e.g., [6]). Most of the previous work on this subject has been directed toward the latter problem.

All references to "lithosphere" in this abstract should be understood to refer to the elastic lithosphere, that layer which deforms elastically or brittlely when subjected to stresses on geological time scales.

Boundary Conditions. A great deal of confusion exists in the literature about the effects of vertical changes in the lithosphere on its horizontal state of stress (σ_h). Much of this confusion can be traced to an uncertainty in the type of lateral boundary condition applied to the lithospheric column. Generally, a lateral constraint condition has been assumed [e.g., 7-9] in which the horizontal displacement is assumed to vanish due to the "resistance" of the surrounding rock. In that case changes in the vertical stress results in an additional horizontal stress due to a combination of (a) lateral stress accommodation ("Poisson stress"), (b) isostatic subsidence or uplift on a sphere, and (c) thermal re-equilibration, resulting in a horizontal stress given by [9]

$$\sigma_h = \rho_c g \Delta h \frac{1}{1-\nu} \left(\nu + \frac{E}{\rho_m g R} + \frac{\alpha E}{\rho_c g} \frac{dT}{dz} \right) \quad (1)$$

where ν is Poisson's ratio, Δh is the thickness of crustal material of density ρ_c added, g is the acceleration of gravity, ρ_m is the density of the material beneath the crust, E is Young's modulus, R is the radius of the planet, α is the linear coefficient of thermal expansion, and dT/dz is the thermal gradient.

McGarr [10] pointed out fundamental logical inconsistencies in the lateral constraint assumption, and argued on both theoretical and observational grounds that this situation is "thoroughly improbable". In its place, he advocated a fixed stress boundary condition, in which the state of stress in the region outside the area involved in the vertical changes is unaffected. No quantitative justification for this assumption was presented by McGarr [10], but its intuitive appeal can be confirmed in the following way: Consider the lithosphere to be an elastic plate overlying an inviscid substrate. Let the edges be fixed at a distance X from the region undergoing vertical deformation (i.e., lateral constraint at a distance). If the vertical processes result in a horizontal displacement Δx at one end of the

plate, the resulting strain in the plate will be $\Delta x/X$ and the change in the horizontal stress will be proportional to that strain. It is obvious that if X is sufficiently large, then the change in stress outside the loaded region will essentially vanish for any induced finite horizontal displacement.

In order to calculate stresses in the loaded region, McGarr [10] required that horizontal forces balance and solved for the resulting stresses. This is analogous to a horizontal version of an isostatic calculation [11]. He further assumed that: (a) changes in the overburden thickness are equivalent to changes in the elastic lithosphere thickness; (b) changes in the temperature of the lithosphere affect the lithosphere thickness through thermal expansion alone; and (c) thermal erosion and underplating of the lithosphere can be modelled as thickness changes alone, independent of other thermal effects. His result can be written:

$$\sigma_h = \rho_c g \Delta h \left\{ -\frac{H}{2\Delta h} \left(\frac{\Delta h}{H + \Delta h} + \frac{\alpha \Delta T}{1 + \alpha \Delta T} \right) + \frac{\rho_c}{\rho_m} \left[\frac{H + \frac{\Delta h}{2}}{H + \Delta h} - \frac{2H}{\Delta h} \frac{\alpha \Delta T (1 + 2\alpha \Delta T)}{(1 + \alpha \Delta T)(1 + 3\alpha \Delta T)^2} \right] \right\} \quad (2)$$

where H is the thickness of the lithosphere and $\Delta T = \Delta h \, dT/dz$ is the average temperature change of the lithosphere.

Typical boundary conditions for a real lithosphere almost certainly lie between the two end members outlined above, and are more likely nearer the fixed stress case. Thus these two end members can be used to place bounds on the magnitude of deviatoric stresses induced in the lithosphere by vertical processes. However, the published expressions for both situations [9,10] are incorrect, due to mistaken assumptions in their derivations. In this investigation I have derived the horizontal stress relations for addition or removal of overburden after correcting these errors.

Constant Stress Boundary Condition. The assumptions (a)–(c) given above for the constant stress condition are inconsistent with current understanding of the relationship between temperature and the structure of the lithosphere [e.g., 12]. For a given geologic material, the effective thickness of the elastic lithosphere is determined by the depth to a critical isotherm, which is in turn a function only of the thermal gradient. The addition or removal of overburden will not result in any change to the total lithosphere thickness once thermal re-equilibration has occurred. However, the lithosphere is, in general, composed of two major layers: a crustal layer and an elastic mantle layer, both of which overlie ductile mantle. Changes (e.g., erosion, deposition) near the surface involve material with the density of crustal rocks whereas the compensating changes at the base of the lithosphere (due to vertical migration of the critical isotherm) involve the mantle, which has a higher density. Thus the integrated vertical stress will decrease and the buoyancy of the column will increase. (Note that if the base of the elastic lithosphere is within the crust, there is no net change in the the mechanical state after addition or removal of material at the surface.)

With these modifications to the lithospheric model, the derivation of the horizontal stress can be carried out using horizontal force balance methods, giving

$$\sigma_h = -\rho_c g \Delta h \left(1 - \frac{\rho_c}{\rho_m} \right) \frac{H_c + \frac{\rho_c}{\rho_m} H_m - \frac{1}{2} \Delta h \left(\frac{\rho_m}{\rho_c} - 1 \right)}{H_c + H_m} \quad (3)$$

where H_c and H_m are the thicknesses of the crust and mantle portions of the lithosphere, respectively. Using nominal estimates for material parameters ($\alpha = 10^{-5}/K^\circ$, $dT/dz = 20^\circ/km$, $\rho_c = 2.6 \text{ Mg/m}^3$, $\rho_m = 3.3 \text{ Mg/m}^3$, $H = 30 \text{ km}$, $H_c = H_m = 15$, $\Delta h = 5 \text{ km}$), I find that the deviatoric horizontal stress is about -0.2 times the overburden stress ($\sigma_v = \rho_c g \Delta h$), whereas that predicted by equation (2) is about $+0.3 \sigma_v$. Thus there is about a 50% correction in the stress difference ($\sigma_h - \sigma_v$).

Horizontal Constraint Boundary Condition. An implicit assumption in previous derivations of the horizontal stress for this case is that the three contributions to the stress are independent, and can be computed separately and added together (see, e.g., Haxby and Turcotte [9]). Such is not the case, however. For example, the horizontal expansion induced by vertical compression acts to help support the lithosphere in a spherical geometry ("arch support"); this reduces the vertical displacement and hence the compression due to subsidence on a sphere (which depends only on the displacement).

I have derived an expression for the horizontal stress in a thick spherical lithosphere (after Love [13]):

$$\sigma_h = (3\lambda + 2\mu) A + \frac{2\mu}{r^3} B \quad (4)$$

where

$$A = \frac{-\rho_c g \Delta h}{3\lambda + 2\mu} \left[1 - \left(\frac{R-H}{R} \right)^3 \frac{1-\omega'}{1+\omega} \right]^{-1}$$

$$B = \frac{\rho_c g \Delta h R^3}{4\mu} \left[1 - \left(\frac{R-H}{R} \right)^3 \frac{1+\omega}{1-\omega'} \right]^{-1}$$

and where λ and μ are Lamé's constants, $\omega = \rho_m g (R-H)/4\mu$ is a stress parameter and $\omega' = \omega \cdot 4\mu/(3\lambda + 2\mu)$.

The new result agrees with equation (1) in the limiting cases $\omega \gg 1$ (Poisson stress dominates) and $\omega \ll 1$ (displacement stress dominates). But for values of the elastic parameters and ω appropriate for the Earth (e.g., using the previous parameter values and $\lambda = \mu = 5 \times 10^{10}$ Pa), the horizontal stress from equation (1) (omitting the thermal term) is $+0.5 \sigma_v$, whereas the corrected stress from equation (4) is about $+1.2 \sigma_v$. Thus the stress difference is of the opposite sign and about 40% larger in magnitude.

Thermal expansion effects for the lateral constraint case, along with expressions appropriate to thermal uplift or subsidence, are the subject of future work. It will then be possible to re-evaluate a large number of problems involving horizontal stress effects from vertical tectonics on planetary lithospheres.

References: [1] Solomon and Head, Vertical movement in mare basins: Relation to mare emplacement, basin tectonics, and lunar thermal history, *JGR* **84**, 1667, 1979; [2] Banerdt et al., Thick shell tectonics on one-plate planets: Applications to Mars, *JGR* **87**, 9723, 1982; [3] Banerdt et al., Stress and Tectonics on Mars, *Mars*, ed. Kieffer et al., in press, 1990; [4] Banerdt, Support of long wavelength loads on Venus and implications for internal structure, *JGR* **91**, 403, 1986; [5] Sleep and Phillips, Gravity and lithospheric stress on the terrestrial planets with reference to the Tharsis region of Mars, *JGR* **90**, 4469, 1985; [6] McGarr and Gay, State of stress in the earth's crust, *Ann. Rev. Earth Planet. Sci.* **6**, 405, 1978; [7] Price, *Fault and Joint Development in Brittle and Semi-Brittle Rock*, 1966; [8] Voigt and St. Pierre, Stress history and rock stress, *Adv. Rock Mech., Proc. 3rd Cong. Int. Soc. Rock Mech., IIA*, 580, 1974; [9] Haxby and Turcotte, Stresses induced by the addition or removal of overburden and associated thermal effects, *Geology* **4**, 181, 1976; [10] McGarr, On the state of lithospheric stress in the absence of applied tectonic forces, *JGR* **93**, 13609, 1988; [11] Artyushkov, Stresses in the lithosphere caused by crustal thickness inhomogeneities, *JGR* **78**, 7675, 1973; [12] Brace and Kohlstedt, Limits on lithospheric stress imposed by laboratory experiments, *JGR* **85**, 6248, 1980; [13] Love, *A Treatise on the Mathematical Theory of Elasticity*, p.142, 1927.

GEOLOGY, STRUCTURE, AND STATISTICS OF MULTI-RING BASINS ON MARS. *Richard A. Schultz and Herbert V. Frey, NASA Goddard Space Flight Center, Greenbelt, MD 20771.*

Multi-ring basins define the fundamental tectonic framework upon which subsequent geologic and geophysical processes of many planets and satellites are superimposed. For example, most volcanic and tectonic activity on the Moon was localized by pre-existing impact basins [1]. Control of volcanism, tectonics, erosion, and perhaps even volatile dynamics on Mars by multi-ring basins can be discerned in many areas [2] even though endogenic processes were quite vigorous over the planet's history. On the other hand, the family of impacting objects that produced these basins is probably related to planetary accretion [3], and size-frequency characteristics of impactor populations can be estimated given an accurate inventory of impact craters and basins [4]. Thus the record of multi-ring basins on Mars provides a fundamental link between the planet's accretion and its later development.

We have compiled and evaluated available data on martian multi-ring basins [5] using the new 1:15 million scale geologic maps of Mars [6] and revised global topography [7] as base maps. Published center coordinates and ring diameters of martian basins were plotted by computer and superimposed onto the base maps. In many cases we had to adjust basin centers or ring diameters or both to achieve a better fit to the revised maps. We also found that additional basins can explain subcircular topographic lows as well as map patterns of old Noachian materials, volcanic plains units, and channels in the Tharsis region [8].

Smaller impact basins on Mars such as Ladon ($D = 975$ km) are comparable dimensionally, morphologically, and structurally to Orientale ($D = 930$ km) on the Moon. In contrast, Orientale-type morphology can be recognized only for martian basins smaller than Argyre ($D = 1850$ km). Larger basins such as Isidis, Argyre, and Hellas typically show a rugged, blocky annulus with concentric grabens surrounding a central depression. Still larger structures show either multiple rings reminiscent of Valhalla on Callisto (Chryse) or persistent depressions surrounded by poorly expressed concentric structure (Elysium [9], Utopia [10]). Basin relief relative to diameter becomes progressively shallower with increasing basin diameter. Thus, the morphology and structure of martian multi-ring basins changes significantly as basins increase in size.

The formation of concentric ring structure and post-impact viscous relaxation of basin topography can differ for spherical, rather than planar, targets [11,12]. Diameters of martian multi-ring basins can be significant fractions of Mars' radius. For example, ratios of basin diameter to planetary radius are: Elysium, 1.46; Utopia, 1.39; Chryse, 1.06; Hellas, 0.68; Argyre, 0.55; and Ladon, 0.29. The value for Argyre is comparable to that of Orientale normalized by lunar radius, 0.53, or Caloris on Mercury, 0.53. Because Argyre, Orientale, and Caloris have similar normalized diameters but different morphologies, planetary curvature by itself probably did not control the morphology of these moderate sized basins. Structures larger than Chryse may have been influenced by spherical target geometry.

R-plots of basin diameters (Fig. 1) show that the martian multi-ring basin population dovetails into the smaller crater population [13] near 500 km diameter. The relative abundance of basins >1000 km in diameter is comparable on Mars and the Moon, perhaps suggesting an inner solar system source for the larger impactors [e.g., [4]]. R-plots and weighted least squares fit to cumulative frequency data (Fig. 2) both indicate that basins follow a shallow production function. Basins 500 to 1500 km in diameter show the characteristic Orientale morphology and a best-fit slope of $D^{-0.75}$. Basins larger than Argyre define a $D^{-1.7}$ slope. The slope change may in part reflect the size-frequency population of the largest impactors. Formation of large multi-ring basins on early Mars may be more analogous mechanically to impacts on icy satellites (e.g., [14,11]) than to late forming lunar basins. Thus, Orientale morphology may not scale linearly to the largest diameters on Mars.

MULTI-RING BASINS OF MARS
Schultz, R.A. and Frey, H.V.

REFERENCES: [1] Solomon & Head (1980) *Rev. Geophys.*, 18, 107-141. [2] Schultz, Schultz, & Rogers (1982) *JGR*, 87, 9803-9820. [3] Wetherill (1977) *Proc. Lunar Sci. Conf.*, 8th, 1-16; Wetherill (1981) in *Multi-ring Basins, Proc. Lunar Planet. Sci. 12A*, 1-18. [4] Strom (1987) *Icarus*, 70, 517-535. [5] R. Schultz & Frey (1989) *JGR*, submitted. [6] Scott & Tanaka (1986) *USGS Map I-1802-A*; Greeley & Guest (1987) *USGS Map I-1802-B*; Tanaka & Scott (1987) *USGS Map I-1802-C*. [7] Wu et al. (1986) PGPI-1985, NASA TM-88383, 614-617. [8] Frey & Schultz (1989) 4th Mars Conf., 106-107. [9] P. Schultz (1984) *Lunar Planet. Sci.*, XV, 728-729. [10] McGill (1989) *JGR*, 94, 2753-2759. [11] Melosh (1982) *JGR*, 87, 1880-1890. [12] Thomas & Squyres (1988) *JGR*, 93, 14,919-14,932. [13] Barlow (1988) *Icarus*, 75, 285-305. [14] McKinnon & Melosh (1980) *Icarus*, 44, 454-471.

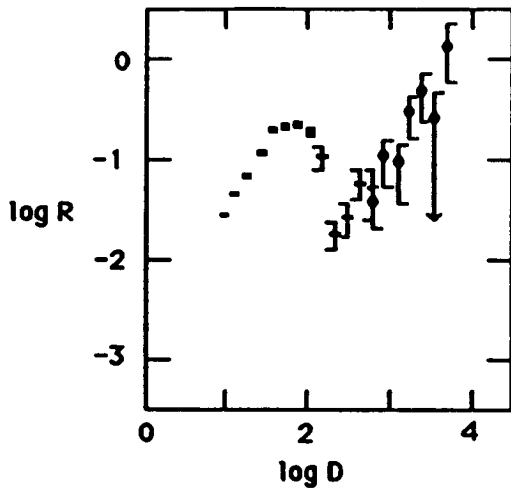


Fig. 1. *Relative frequency (R-plot) diagrams of martian craters and basins. Data for basins < 500 km in diameter from Barlow [1988].*

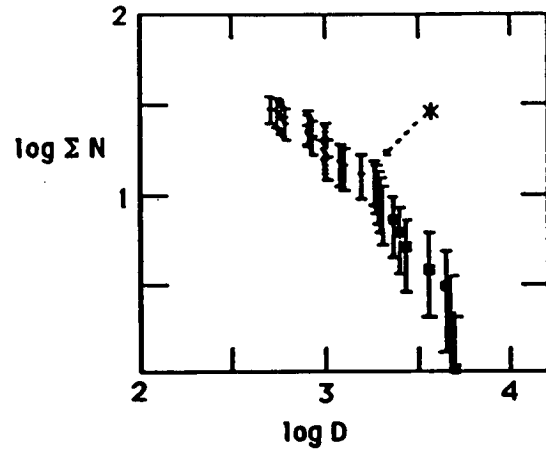


Fig. 2. *Cumulative frequency distribution of martian multi-ring basins > 500 km in diameter (unbinned data). Data normalized by surface area of Mars. Basins > 2300 km in diameter shown by dots; Argyre shown by *.*

MODELLED AND MEASURED STRAIN IN MASCON BASINS ON THE MOON
M. P. Golombek and B. J. Franklin, Jet Propulsion Laboratory, Caltech, Pasadena, CA 91109

The close association of wrinkle ridges and grabens with mascon basins on the Moon has suggested that the responsible compression and extension resulted from basin subsidence and peripheral flexing of the lithosphere. The distribution of grabens and wrinkle ridges associated with mascon basins has been further used along with elastic plate bending models to constrain the thickness of the lithosphere at the time of their formation (1). Kinematic models for basin subsidence have also been developed and compared with strains inferred from grabens and wrinkle ridges (2, 3). Note that kinematic models may be preferable to dynamic models because the strain associated with tectonic features can be compared directly with model predictions and because fewer assumptions are required for their calculation, such as perfect elasticity and specific values of the elastic moduli. In addition, if the results from kinematic models compare favorably with the strain estimated across tectonic features on the Moon, then a global strain (or stress) field, proposed by a number of workers, may not be necessary. In this abstract, the strain inferred for wrinkle ridges and grabens has been compared to that calculated from a simple kinematic subsidence model for mascon basins on the Moon.

The kinematic model used is conservative [model 1 described in (3)]. Briefly, the model assumes an initial basin that is a couple of kilometers deep (2.5 km) at its center, tapering toward the edges (approximated by a segment of a sphere with a larger radius of curvature than the original lunar surface). The basin center is assumed to subside 1-2 km from loading of the lithosphere, which is 25-150 km thick (1), with all points moving towards the center of the Moon. The radial strain due to shortening of the arc (membrane) and that due to unbending are calculated for the interior of the basin. Hoop strains are calculated from the corresponding decrease in circumference of interior small circles around the basin center. Radial extensional bending strains at the edge of the basin are calculated from the flexure of the lithosphere over the width of the graben zone (typically about 50 km) due to subsidence of the basin. Because most wrinkle ridges and grabens associated with mascon basins are concentric, the total radial compressional strain across a basin (edge to edge) and the peripheral radial extensional bending strain are the quantities most easily compared with model calculations.

Determining the extension across grabens on the Moon is straightforward. The bounding faults dip about 60° (4), so the extension on each fault is a simple function of the depth of the graben floor [see (4) for method]. Calculations are based on specific measurements already made (where

topographic data exist) or by an estimate based on the apparent depth of a graben (where topographic data does not exist).

Determining the shortening across wrinkle ridges is less well constrained. A number of different methods have been used to obtain the compressional strain, and most methods suggest between a fraction of a percent to a few percent (2, 5, 6, 7). For this application, the method of Golombek et al. (7) is used, which is based on topographic profiles across wrinkle ridges and the presence of an elevation offset, assumed due to motion on a thrust fault at depth. Wherever adequate topographic data exist, we calculate the shortening directly by unfolding the ridge profile and by slip on a 25° dipping thrust fault to produce the observed elevation offset. Because many basins do not have adequate topographic coverage, a general relationship is used between the hill width (the part of the ridge most easily identified on most images) and shortening, based on a set of 31 lunar ridges with detailed topographic data (7) and shortening estimates that suggest wider ridges have more shortening than smaller ridges. This relationship equates shortening with the hill width times 0.016 plus 122 m; it is derived from linear regression analysis and has a correlation coefficient of 0.66. Because this relationship includes uncertainties from a variety of sources and the correlation coefficient is not optimal, we choose the most sensitive parameter that affects the relationship (the fault dip) and vary it by 10° from the nominal 25°. Tests in basins where detailed topographic data do exist (Serenitatis and Crisium) show that this method adequately bounds the measured shortening.

For each basin, a number of transects were drawn to maximize the observed strain. Shortening within the basin and extension peripheral to the basin were measured using the above methods. For each basin we calculated the total radial shortening across the basin and the total peripheral radial extension for lithosphere thicknesses most appropriate for the basin (1). Reported below are the maximum measured and calculated shortenings and extensions across the eight mascon basins on the Moon. Models assume 2 km of subsidence and a lithosphere thickness of 50 km for peripheral flexure, unless otherwise noted. Symbols are: r =radius of basin, not including zone of peripheral grabens (50 km wide unless otherwise noted); sh =maximum shortening across basin (range in model results are for different lithosphere thicknesses, range in measured results are for 15-35° fault dips); ex =maximum extension across periphery; T =lithosphere thickness from (1).

For Humor (r=200 km) model results indicate $sh=1212-2210$ m for $T=50-100$ km and $ex=505$ m; measured $sh=1005-2185$ m and $ex=475$ m. For Serenitatis (r=275 km), model results indicate $sh=1076-1800$ m for $T=50-125$ km and $ex=366$ m; measured $sh=815-1760$ m and $ex=330$ m. For Smythii (r=175 km, no graben zone) model results are $sh=1874-2446$ m for $T=75-100$ km; measured

sh=365-790 m. For Crisium ($r=225$ km, no graben zone) model results are sh=1590-2920 m for $T=75-150$ km; measured sh=1040-2540 m. For Grimaldi ($r=75$ km, initial depth 1 km and 1 km subsidence) model results are sh=670-1338 m for $T=25-50$ km and ex=335 m for $T=25$ km; measured sh=340-730 m and ex=200 m. For Orientale ($r=150$ km, 100 km graben zone) model results are sh=1172-1440 m for $T=40-50$ km and ex=537 m for $T=40$ km; measured sh=400-900 m and ex=300 m. For Nectaris ($r=160$ km, 150 km graben zone) model results are sh=2002-2628 m for $T=75-100$ km and ex=944 m; measured sh=390-850 m and ex=205 m. For Imbrium ($r=540$ km) model results indicate sh=1148-1864 m for $T=50-150$ km and ex=278 m for $T=75$ km; measured sh=1090-2410 m and ex=250 m.

Results of a conservative and fairly simple kinematic model of mascon basin subsidence indicate modest radial shortening of 0.6-3 km across the basins and extension of 0.2-1 km along the basin margins. Estimates of the cumulative shortening across wrinkle ridges (0.3-2.5 km) and the cumulative extension across grabens (0-0.5 km) in transects across the basins are very similar to subsidence model calculations. In all cases the models can account for the cumulative measured extension and compression. These results argue that the superposition of global strains to account for the strain accommodated by the wrinkle ridges and grabens in mascon basins is not required. There are, however, many wrinkle ridges and a few grabens that do not appear directly related to mascon basin subsidence on the Moon, and it is possible that these features formed from a global strain. To quantify this possibility, the length of all non-mascon grabens and mare wrinkle ridges were summed, an average extension (3, 4) applied to the grabens and an average shortening applied to the wrinkle ridges (7) to calculate a change in lunar surface area. If all of this surface area change is due to a radius change, the total increase in radius needed to account for the non-mascon grabens is trivial (<5 m); the total decrease in radius needed to account for the non-mascon wrinkle ridges is <80 m. It seems reasonable that many if not all of these features are due to non-mascon related processes such as local cooling and contraction, minor settling or subsidence, so that no change in lunar radius is necessary.

References:

- (1) Solomon, S., and Head, J., 1979, *J. Geophys. Res.* 87, 1667-1682. 1980, *Rev. Geophys. Space Phys.* 18, p. 107-141.
- (2) Bryan, W., 1973, *Proc. 4th Lunar Sci. Conf.*, 93-106.
- (3) Golombek, M., and McGill, G., 1983, *J. Geophys. Res.*, 88, 3563-3578.
- (4) Golombek, M., 1979, *J. Geophys. Res.* 84, 4657-4666.
- (5) Muehlberger, W., 1974, *Proc. 5th Lunar Sci. Conf.*, 101-110.
- (6) Watters, T., 1988, *J. Geophys. Res.* 93, 10,236-10,254.
- (7) Golombek, M., Plescia, J., and Franklin, B., 1991, *Proc. 21st Lunar Planet. Sci. Conf.*

STRAIN ACCOMMODATION BENEATH STRUCTURES ON MARS

M. P. Golombek¹, K. L. Tanaka², and W. B. Banerdt¹, ¹Jet Propulsion Laboratory, Caltech, Pasadena, CA 91109, ²U. S. Geological Survey, Flagstaff, AZ 86001.

A recent review of tectonic features present on Mars (1 and references therein) shows that most of their subsurface structures can be extended, with confidence, only a few kilometers deep (exceptions are rifts, in which bounding normal faults penetrate the entire brittle lithosphere, with ductile flow at deeper levels). Nevertheless, a variety of estimates of elastic lithosphere thickness and application of accepted failure criteria under likely conditions on Mars suggest a brittle lithosphere that is many tens of kilometers thick. This raises the question of how the strain (extension or shortening) accommodated by grabens and wrinkle ridges within the upper few kilometers is being accommodated at deeper levels in the lithosphere. In this abstract, we first briefly review the non-rift tectonic features present on Mars, their likely subsurface structures, and present some inferences and implications for behavior of the deeper lithosphere.

Simple grabens are the most common type of extensional tectonic feature on Mars. Most of these structures are bounded by two inward dipping normal faults that have had the same amount of slip (equal scarp heights). Their simple geometry at the surface (untilted - flat floors and shoulders at equal elevations) argues for a simple subsurface structure, with both faults terminating at their point of mutual intersection (2). Observations of faults bounding grabens in canyon walls on Mars indicate an average dip of about 60° (3), indicating that faults bounding simple grabens on Mars only penetrate the upper few kilometers of the lithosphere (about the width of the structure, 1-5 km). As a result, it is not obvious how the extensional strain taken up by slip on the graben bounding faults in the upper few kilometers is accommodated at deeper levels in the brittle lithosphere.

Some extension of rocks beneath the graben-faulted layer may be accommodated by elastic expansion without fracturing. For example, where narrow simple grabens are spaced 100 km apart, each having about 100 m of extension (4), the total extensional strain is about 10^{-3} . Laboratory measurements of Young's modulus, based on the propagation of elastic waves in homogeneous samples, for likely basement materials on Mars (e.g., basalt) are 4×10^4 to 10^5 MPa (5). In addition, seismic velocities from basement rocks at Apollo 17 indicate a Young's modulus of about 10^4 MPa (6 and references cited therein). As a result, rock beneath the grabens will experience a tensional stress of 10 MPa, which is well below the strength of likely basement rocks on Mars at a few kilometers depth, even if the rocks are prefractured with no tensile strength (7). For elastic expansion to occur a detachment must separate the faulted and unfaulted rocks so that the extension accommodated by the grabens is distributed over the entire underlying basement. If basement rocks on Mars have some tensile strength as is likely in current models (7), elastic expansion of basement rocks without failure is possible beneath simple grabens on Mars that are spaced more than about 25 km apart and where faulted rocks are detached from underlying rocks. For many regions on Mars where grabens are spaced closer than about 25 km, the basement is likely to fail under the extensional strain as described below.

The simple subsurface geometry of grabens only allows vertical tension cracks or dikes beneath them. If one of the two shear faults did extend to a deeper level more slip would be expected on the deeper, master fault than the antithetic fault, which would result in an asymmetric or tilted structure, which is not observed. As a result, dikes or tension cracks could underlie grabens. Accepted failure criteria applied to Mars indicate that the formation of tension cracks can occur to substantial depths beneath graben bounding normal faults (7), particularly when driven by fluid (water or magma) pressure in the forming crack. Their individual widths on Mars could be up to 200 m, about twice that on the earth (8) and multiple intrusions are possible. The total width of the dikes would likely equal the extension in the overlying graben. Terrestrial analogs show that dike intrusion at depth is linked to graben formation at the surface in Iceland and Afar (9). In these areas, grabens are a few kilometers wide and are underlain by dikes that extend kilometers in depth and tens of kilometers laterally (scales comparable to martian examples), and did not erupt on the surface. In addition, dikes are known to feed fissure eruptions on the earth, so their common association with grabens and volcanic regions on Mars (such as Tharsis) supports the model linking dike intrusion at depth with graben formation near the surface. The common association of grabens with pit chains on Mars (e.g., 7) also supports underlying dikes or mechanically similar hydrofractures (fluid driven tension cracks) to provide the space at depth for the inferred subsurface drainage of material; pit chains have also been observed in grabens in Iceland and above fissures in Hawaii. In this subsurface structural model, the dike does not have to intrude directly beneath graben, but could be offset, provided that a subsurface detachment allows horizontal slip between the dike and graben. The maximum depth that underlying dikes or hydrofractures could extend is limited by the driving pressure of the fluid and so, mechanically could extend to tens of kilometers depth. Hydrofractures could extend to a depth where the fracture toughness exceeded the extensional strain, below which the lithosphere expanded elastically. Dikes could link with subsurface magma chambers or zone of melt production (upper mantle?) and thus accommodate the extension throughout the brittle crust beneath the grabens.

Wrinkle ridges are morphologically complex linear topographic highs. Most recent work has suggested two compressional kinematic models involving folding and faulting. The thick-skinned model suggests that faults beneath wrinkle ridges extend through the entire lithosphere (10). If wrinkle ridges do involve thrust faulting of most of the lithosphere, then there is no problem reconciling the compressional strain accommodated by the wrinkle ridges in the upper few kilometers of the crust with that in the rest of the lithosphere. If, however, wrinkle ridge formation involves only a thin surface layer (faulting and folding extends only a few kilometers deep), in the thin-skinned model (11), then some explanation must be provided for how the compression in the ridges is accommodated deeper in the lithosphere. The compressional strain across lunar and martian wrinkle ridges and lunar basins has been estimated at 10^{-2} to 10^{-3} (10, 11, 12). For the values of Young's modulus discussed earlier, this strain indicates a stress of tens to hundreds of MPa, which exceeds the compressional strength of low cohesion materials. Low cohesion, dry rocks on Mars are stable to failure for stress differences under compression of 35 MPa per kilometer of depth. As a result, wrinkle ridges could be expected to involve faulting down to

10 km depth if they accommodate compressional strain of order 10^{-2} . In this model, thrust faults propagate to a depth below which the imposed compressional strain was less than the elastic strength of the lithosphere.

Possible differences in strength of surface units on Mars could augment this effect and control certain aspects of wrinkle ridge formation. The strength of brecciated highland rocks is controlled by the frictional resistance to sliding on preexisting fractures, with no cohesive strength. As a result, lower stresses would be required to produce faulting in breccia than if the rock had cohesive strength. This might lead to small thrusts in highlands breccia that initiated at the surface and propagated into the shallow subsurface. In contrast, volcanic flows could possess substantial cohesive strength (30-50 MPa; 5), thereby requiring much greater differential stresses to initiate faulting in surface rocks. These higher stress levels could lead to initiation of faults at greater depths, perhaps at a mechanical discontinuity between the base of the strong volcanics and the weak underlying breccia (e.g., 6). Faults would propagate down in the ejecta until the greater strength of the volcanics was exceeded. In this scenario, faults would propagate deeper than if the entire shallow crust had the same strength as the volcanics. Thus faulting beneath wrinkle ridges in cohesive volcanic flows could involve more of the lithosphere, leading to each ridge accommodating greater shortening on fewer structures resulting in the wide spacing observed between large ridges on the ridged plains. This model is capable of explaining the observation on Lunae Planum (13) in which large, widely spaced ridges with great shortening are found in the thicker plains to the west than the smaller, more closely spaced ridges with less shortening found in the thinner plains to the east.

References:

- (1) Banerdt, Golombek & Tanaka 1991 Stress on Mars, UA Chapter Mars.
- (2) Golombek & McGill 1983 JGR 88, 3563.
- (3) Davis & Golombek 1990 JGR 90, 14231.
- (4) Tanaka & Davis 1988 JGR 93, 14893.
- (5) Hand. Phys. Const. GSA Mem 97, 1966.
- (6) Golombek 1985 JGR 90, 3065.
- (7) Tanaka & Golombek 1989 19th PLPSC, 383.
- (8) Wilson and Parfitt 1990 LPSC XXI, 1345.
- (9) Rubin & Pollard 1988 Geology 16, 143.
- (10) Golombek et al. 1989 LP Sci Con XXI, 421.
- (11) Watters 1988 JGR 89, 10236.
- (12) Bryan 1973 4th PLSC, 93.
- (13) Plescia 1991 LP Sci Con XXII, 1075.

EARLY TECTONIC EVOLUTION OF MARS - CRUSTAL DICHOTOMY TO VALLES MARINERIS; H. V. Frey and R. A. Schultz, Geodynamics Branch, Goddard Space Flight Center, Greenbelt MD 20771

In this study we addressed several fundamental problems in the early impact, tectonic and volcanic evolution of the martian lithosphere: (a) origin and evolution of the fundamental crustal dichotomy, including development of the highland/lowland transition zone; (b) growth and evolution of the Valles Marineris; and (c) nature and role of major resurfacing events in early martian history. Below we briefly summarize our results in these areas.

(a) Origin and Evolution of the Martian Crustal Dichotomy

Both internal and external processes have been invoked to explain this fundamental characteristic of the martian lithosphere. We suggest that major, basin-forming impacts have played a prominent role in the origin and development of the crustal dichotomy (1,2,3). Our study revealed little direct support for the single giant impact hypothesis (4), but did suggest a number of new, previously unrecognized large impact basins (5). Independent evidence for the Daedalia, Utopia and Elysium Basins has been presented by others (6,7,8). Most of the largest recognized basins are in the northern or western hemispheres; we believe that the overlap of these basins is responsible for the lower topography and prolonged volcanism which characterizes the northern lowland plains, and perhaps also for the growth of major volcano-tectonic complexes such as Elysium and Tharsis (3,9). A speculative model for the evolution of the northern lowlands in the Utopia-Elysium region was developed within this context (9,10). More work needs to be done to refine the inventory of major impact basins for Mars and to relate these basins to the earliest crustal development of the planet. We have found evidence in the cumulative frequency curves as well as in the morphology of the basins for a significant change in properties at Argyre-sized basins ($D \sim 1850$ km) and at Chryse size basins ($D \sim 3600$ km) (5). These changes may be related to lithospheric structure at the time of basin formation or to fundamental differences in the impacting population.

(b) Growth and Evolution of the Valles Marineris

Valles Marineris is a complex system of ancient grabens that were modified by erosion and deposition. Our detailed studies addressed several fundamental issues on trough origin and growth. Relative orientations of Coprates Chasma and wrinkle ridges and grabens located on the adjacent southern plateau suggest that the ridges and grabens grew under multiple stress states and probably predate Coprates Chasma itself (11). New structural mapping of the region (12,13) details the discontinuous distribution and interrelationships of wrinkle ridges, grabens and pit-crater chains around the troughs. Although the trough system is often assumed to have nucleated as small pit-craters, pit-crater chains appear to be distinct structures, not trough precursors (14). Unambiguous evidence for strike-slip faulting was found in Early Hesperian ridged plains materials to the south in Coprates (15,16,17). Detailed mapping of the echelon set of plateau grabens located on Ophir Planum and the adjacent Coprates trough bounding faults is unravelling the sequence of faulting in central Valles Marineris. The curving geometries of grabens in Ophir and trough faults near Melas Chasma indicate that the local stress state was spatially variable, but probably regionally uniform, during early trough growth (18). Our work reveals unexpected complexities in the growth and tectonic development of the Valles Marineris region.

(c) Major Resurfacing Events in Martian History

Resurfacing has been a major process during most of martian history, but detailing the characteristics of major events has been difficult. We have adapted the Neukum and Hiller technique (19) for larger crater diameters in order to study older terrains and the resurfacing which has modified them. We showed that a major resurfacing event within and around the highland/lowland transition zone occurred at the time of ridged plains emplacement in Lunae Planum and elsewhere (20). Similar study of the Tempe Terra region in western Mars shows

that comparable resurfacing at about the same time occurred there (21) as well as in Xanthe Terra, Lunae Planum and Coprates (22,23). It appears that there was a major, perhaps planet-wide resurfacing on Mars corresponding to the eruption of Lunae Planum Age (LPA) ridged plains. We also find evidence for an older resurfacing event which can be related to intercrater plains development (cratered plateau material) recognized in geologic studies (24). In the Tempe region a common-age resurfacing event younger than LPA affecting the cratered terrain and adjacent plains-forming lowland units appears to correlate with the Vastitas Borealis Formation (21,24). We have also extracted information on the thickness of materials associated with different resurfacing events from the cumulative frequency curves. Thicknesses associated with the major LPA resurfacing vary greatly depending on location: in the Lunae Planum, Tempe and Coprates ridged plains 350-600 m is common (21,23,25) but in the adjacent cratered terrain in Xanthe Terra, Tempe Terra and elsewhere the corresponding value is less than 100 m. These results can provide an independent stratigraphy based on major resurfacing events correlated at many places around Mars, which can both date the resurfacing events and also locate the depth to older, now buried surfaces.

In a related study (26) we find evidence that what have been mapped as Noachian age ridged plains in Memnonia and Argyre may be Early Hesperian in age. These plains are sufficiently thin that a large number of medium-sized craters show through from an older surface below. This may mean that the eruption of ridged plains was more temporally confined than previously thought, which would have important implications for the thermal history of Mars.

References: (1)Frey, H. and R. A. Schultz, GRL 15, 229-232, 1988. (2)Frey, H. and R. A. Schultz, MEVTV Workshop on Early Tectonic and Volcanic Evolution of Mars, LPI Report 89-04, p35-37, 1989. (3)Frey, H. and R. A. Schultz, 4th Internat. Conf. on Mars, 106-107, 1989. (4)Wilhelms, D. E. and S. W. Squyres, Nature 309, 138-140, 1984. (5)Schultz, R. A. and H. V. Frey, JGR submitted, 1989. (6)Craddock, R. A., R. Greeley and P. R. Christensen, JGR in press, 1990. (7)McGill, G. E., JGR 94, 2753-2759, 1989. (8)Schultz, P. H., LPS XV, 728-729, 1984. (9)Frey, H. and R. A. Schultz, LPS XX, 315-316, 1989. (10)Frey, H. and R. A. Schultz, JGR submitted, 1989. (11)Schultz, R. A. and H. V. Frey, EOS Trans. Am Geophys. Un. 69, 389-390, 1988. (12)Schultz, R. A. and H. V. Frey, 4th Internat. Conf. on Mars, 183-184, 1989. (13)Schultz, R. A. and H. V. Frey, LPS XX, 974-975, 1989. (14)Schultz, R. A., MEVTV Workshop Tectonic Features on Mars, 12-22, 1989. (15)Schultz, R. A., MEVTV Workshop Tectonic Features on Mars, 23-25, 1989. (16)Schultz, R. A., Nature 341, 424-426, 1989. (17)Schultz, R. A., LPS XXI(this volume), 1990. (18)Schultz, R. A., LPS XXI(this volume), 1990. (19)Neukum, G. and K. Hiller, JGR 86, 3097-3121, 1981. (20)Frey, H. V., A. M. Semeniuk, J. A. Semeniuk and S. Tokarcik, Proceed. LPSC 18th, 679-699, 1988. (21)Frey, H. V. and T. D. Grant, JGR submitted, 1989. (22)Grant, T. D. and H. V. Frey, EOS Trans. Am. Geophys. Un. 68, 1342, 1987. (23)Frey, H. V. and T. D. Grant, LPS XX, 313-314, 1989. (24)Tanaka, K. L. Proceed. LPSC 17th, JGR 91, E139-E158, 1986. (25)Frey, H. V., J. A. Semeniuk and T. D. Grant, MEVTV Workshop on Early Tectonic and Volcanic Evolution of Mars, LPI Report 89-04, p38-40, 1989. (26)Frey, H. V., C. E. Doudnikoff and A. M. Mongeon, LPS XXI(this volume), 1990.

THE FORMATION OF ANTIPODAL-IMPACT TERRAINS ON MARS;
D. A. Williams and R. Greeley, Department of Geology, Arizona State University,
Tempe, Arizona 85287

The regions antipodal to Mars' three largest impact basins, Hellas, Isidis, and Argyre, were assessed for evidence of impact-induced seismically-disrupted terrains. Photogeology and preliminary computer modeling using the Simplified Arbitrary Lagrangian-Eulerian computer program (Watts et al., 1989) [1] suggest such terrains could have been formed by the Hellas and Isidis impacts. Maximum antipodal pressures are 1.1×10^9 Pascals for Hellas, 5.2×10^8 Pascals for Isidis, and 1.5×10^8 Pascals for Argyre.

Previously, the only assessment of potential surface disruptions on Mars antipodal to large impacts was by Peterson (1978) [2]. He described the terrain at the antipodes of Hellas, Isidis, and Argyre impact basins, and suggested that focusing of seismic shocks from the Hellas impact might have produced the volcanic conduit at Alba Patera through which magma could reach the surface. He also suggested that older fractures in Noctis Labyrinthus may have been generated or modified by the Isidis impact.

Our results give credence to Peterson's assertions. For Hellas, the computer model clearly suggests that antipodal pressures were probably strong enough to have fractured the crust and disrupted the surface, and may account for aspects of volcanism at Alba Patera. Alba Patera has long been recognized as unusual (or perhaps unique) in the solar system (Carr et al., 1977a) [3]. It is a "central vent" volcano containing a caldera complex about 100 km across and has flows that can be traced radially more than 1000 km, making it the largest such volcano seen anywhere. The long flows indicate high rates of effusion (Greeley and Spudis, 1981) [4] which ordinarily are associated with flood eruptions from fissures. For example, long flows seen on the Moon are inferred to have been derived from fissures associated with basin-related fractures (Schaber, 1973) [5]. In contrast, the Alba Patera flows appear as narrow sheets and tube-fed flows erupted from vents of limited extent. This would suggest that the magma supply and conduit system is centrally-located and different from that of the Moon. Moreover, the low flank slopes of Alba Patera may indicate a different style of volcanism than that of the other Tharsis volcanoes on Mars, all of which are high-standing edifices.

We suggest that the Hellas impact produced sufficient focused energy at its antipode to produce deep fractures in the Martian crust centered below the current caldera for Alba Patera. With the generation and evolution of magma in the Tharsis area, the fracture system provided a ready conduit for early-stage eruptions of Martian lavas derived from deep in the crust/upper mantle, perhaps of komatiitic composition (Burns and Fisher, 1989) [6]. These fluid lavas were erupted at high rates from the central zone of the antipodal fractures and spread to great distance to form the basal lavas of Alba Patera. This occurred in the Hesperian, long after Hellas disrupted the antipodal interior. The change in morphology.

FORMATION ANTIPODAL TERRAINS--MARS: Williams, D.A. and Greeley, R.

to tube-fed flows at Alba Patera for the later deposits suggests lower rates of effusion of a sporadic character (Greeley and Spudis, 1981) [4], which may reflect lower rates of magma production, more constrained conduits, more "evolved" magmas, or some combination of these factors.

The computer model gives antipodal pressures for the Isidis impact very close to those produced by the Imbrium impact on the Moon and by the Caloris impact on Mercury, suggesting that disrupted terrains should have been produced. Although none are seen, Peterson (1978) [2] suggested that some of the fractures of the Noctis Labyrinthus system may have been generated or influenced by the Isidis impact. Some of the fractures in the Noctis Labyrinthus system are radial to or concentric about the Isidis antipode. Carr (1974) [7] suggested this topographically high region might be due to crustal upwarping caused by mantle convection in Tharsis. The load from Tharsis volcanics may have reactivated certain aligned older fractures, previously emplaced by Isidis antipodal activity (Peterson, 1978) [2]. Thus, Noctis Labyrinthus may be a younger feature that owes its location at least partly to the antipodal effects of a major impact. The lack of visible features at the Argyre antipode suggests that either the low antipodal pressures were insufficient to disrupt the terrain, or such terrain was produced but has since been obliterated.

References: [1] Watts, A.W., R. Greeley, and H.J. Melosh, 1989, *Lunar and Planetary Science XX*, pp. 1183-84.; [2] Peterson, J., 1978, *Lunar and Planetary Science IX*, pp. 885-6.; [3] Carr, M.H., K.R. Blasius, R. Greeley, J.E. Guest, and H. Masursky, *J. Geophys. Res.*, **82**, pp. 3985-4015, 1977a.; [4] Greeley, R. and P.D. Spudis, *Reviews of Geophysics & Space Physics*, **19**, #1, pp. 13-41, Feb., 1981.; [5] Schaber, G.G., *Proc. 4th Lunar Sci. Conf.*, pp. 73-92, 1973.; [6] Burns, R.G. and D.S. Fisher, *LPI Tech. Report 89-04*, pp. 20-22, LPI, Houston, Texas, 1989.; [7] Carr, M.H., *J. Geophys. Res.*, **79**, # 26, pp. 3943-3949, 1974.

GLOBAL RELATIONSHIPS BETWEEN VOLCANIC VENTS AND FRACTURES RADIAL TO LARGE IMPACT BASINS ON MARS.

Byron D. Schneid and Ronald Greeley, Department of Geology, Arizona State University, Tempe, AZ 85287.

The relation of volcanic vents on Mars to impact basins has been studied previously (1,2,3,4,5,6). It has been asserted that the concentric fractures around impact basins extend into the crust and might localize some features, including volcanoes (e.g. 4). In this study, we assess the possibility of radial fractures inferred to be associated with impact basins as an additional control on the location of volcanoes on Mars. Geologic mapping at 1:2 million scale enabled 250 central vents and fissure vents to be identified. Patterns of vent distribution (fig. 1) superimposed on a globe show that most are located on three distinct circles. The first is a great circle which passes through Arsia Mons, Pavonus Mons, Ascreaus Mons, and Tempe Fossae, along Protonilus Mensae (an area of fractured terrain), through Syrtis Major, Hadriaca Patera, and a series of fissure vents southwest of Tharsis. A similar great circle trends SW to NE from the Hellas basin, through Hadriaca Patera, Tyrhenna Patera, Elysium, Alba Patera (which is approximately antipodal to the Hellas basin), southern Tempe Fossae, the eastern Valles Marineris chaotic region, and the Amphitrites Patera vents on the southwest rim of the Hellas basin. The third series of vents is on a small circle ~4800 km in diameter centered at ~104°W, 2°N. This site is near the center of the Tharsis gravity anomaly (7) and the loci of associated tensile stresses (8). Most fissure vents not located on the Tharsis trend of volcanics are on this small circle, as are Alba Patera and other central vents.

There are two more possible great circles which may be superimposed onto the martian globe. The first can be traced along the escarpment dividing the northern lowlands from the southern highlands, across Isidis Planitia (the site of a possible impact basin at ~273°W, 13°N), fractured terrain in Solus Planum (a possible fissure vent source area), and through Juventae Chasma. This circle may reflect the role of inferred radial fractures in modifying the surface without associated volcanism. The second possible great circle passes through the Hellas impact basin, some large unnamed central vent volcanoes (at ~205°W, 48°S), Apollonaris Patera, the escarpment north of Alba Patera and the Tempe Fossae region, and into Acidalia Planitia. Acidalia Planitia is also along the trend of the Tharsis chain of volcanoes and may indicate an impact site centered near 30°W, 60°N.

VOLCANIC VENTS AND FRACTURES RADIAL TO IMPACT BASINS

Schneid, B.D. and Greeley, R.

Although concentric fractures of smaller impact basins may influence local vent sites, the global setting appears to be governed by radial fractures associated with major impact basins. This is supported by the association of one or perhaps two great circles with the Hellas impact basin, and possible great circles associated with the Isidis basin and Acidalia Planitia. The distribution also suggests that larger impacts produce larger fractures and can, therefore, accommodate more volcanic vents. Isidis, Argyre, Procellarum, and Hellas basins in that order, have an increasing number of vents inferred to be associated with them.

REFERENCES: (1) Albin, E.F. and Greeley, R., Proc. LPSC XVII, pp. 7-8, 1986. (2) Albin, E., Masters Thesis, Arizona State University Press, 1986. (3) Craddock, R.A., Greeley, R., and Christensen, P.R., Journal of Geophysical Research, in press. (4) Schultz, P.H., Schultz, R.A., and Rogers, J., Journal of Geophysical Research, 82, B12, pp.9803-9820, 1982. (5) Schultz, P.H., Proc. LPSC XV, pp.728-729, 1984. (6) Wichman, R. and Schultz, P.H., NASA TM-89810, pp.474-475, 1987. (7) Phillips, R.J. and Lambeck, K., Reviews of Geophysical Space Research, 18, pp. 27-76, 1980. (8) Phillips, R.J. and Ivens, E.R., Physics of Earth and Planetary Interiors, 19, pp. 107-148, 1979.

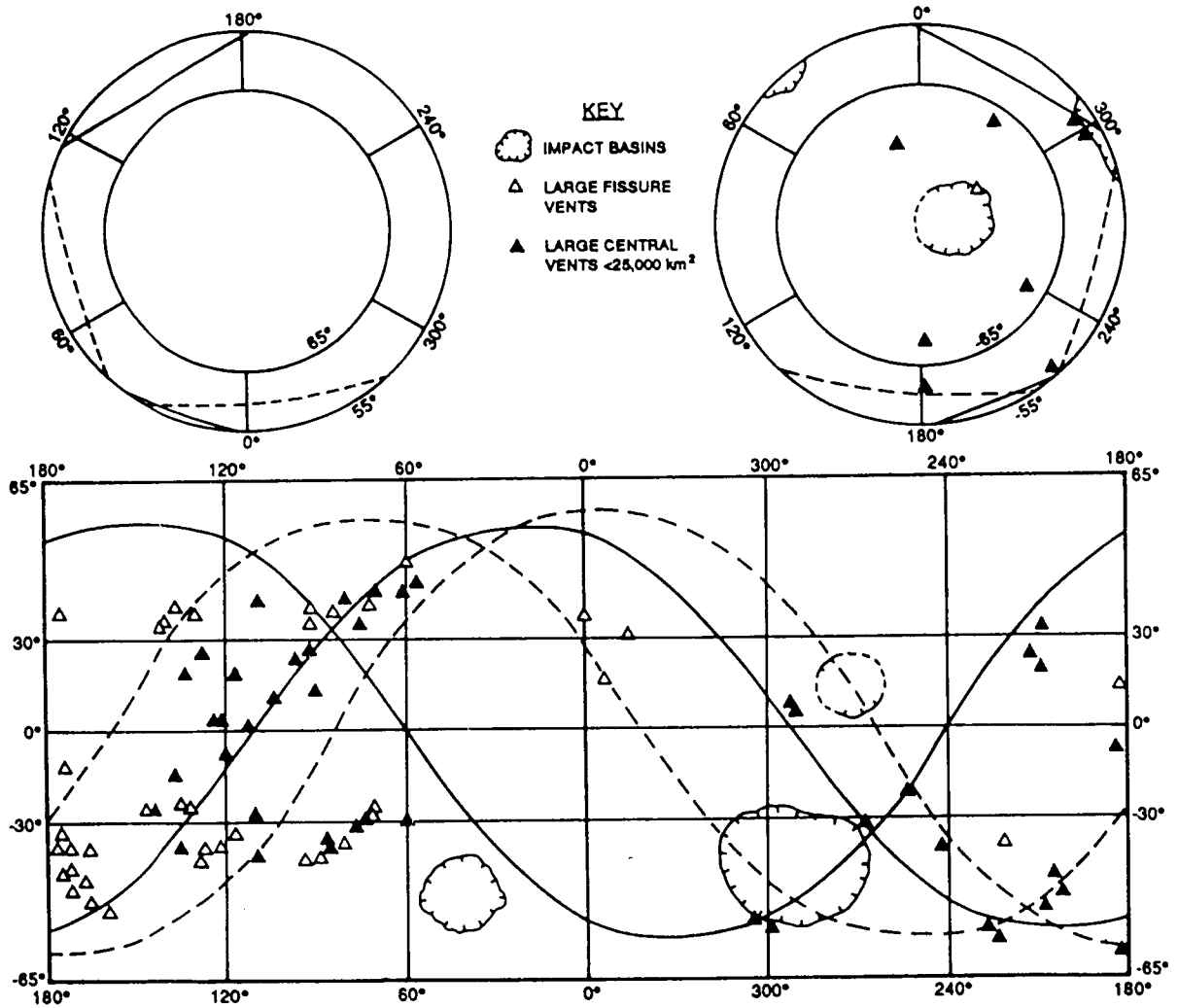


Diagram illustrating mercator projection of great circles and selected volcanic vents on Mars.

TECTONIC SETTING OF MARTIAN VOLCANOES AND DEEP-SEATED INTRUSIVES
D.H. Scott and J.M. Dohm, U.S. Geological Survey, Flagstaff, AZ 86001

More than 50 volcanoes have been mapped on Mars [1,2,3], and recent geologic studies [4] indicate structural evidence of deep-seated intrusive bodies (Fig. 1). Most volcanoes in the Tharsis region are volcanotectonic features: they have been associated with large-scale tectonic and volcanic processes. They occur along complex systems of faults and grabens having a dominant northeast-southwest trend closely coincident with a great circle [5], which extends along 90° of arc from Tempe Patera to probable volcanic mountains near lat 40° S., long 150°. Olympus Mons, Alba Patera, and a small volcano between them are aligned nearly parallel to the Tharsis axial trend; the boundary of the Martian crustal dichotomy is largely covered by young lava flows in this region but appears to lie within the corridor between these two trends. Clusters of relatively small volcanoes occur around the south end of the Tharsis rise, particularly in the Thaumasia area where ancient rocks are transected by networks of intersecting faults.

Deep-seated intrusive bodies are also concentrated in the Tharsis region and are recognized mostly where faults have been deflected around their cores. The intrusives have no observable topographic expression or associated lava flows except for Tempe Patera [6], a relatively small volcano that appears to be the surface expression of a much broader and older intrusive body. Three large, circular, rimless structures clustered in the southwestern part of the Tharsis region (Fig. 1) do not resemble impact craters and may be volcanotectonic depressions [7].

The Elysium Mons-Amphitrites Patera volcanic alignment is subparallel to that of Tharsis but is longer, extending through about 120° of arc; it transects the dichotomy boundary and is radial to the Hellas basin. Unlike the Tharsis trend, however, it is not associated with recognizable fault or graben systems. No evidence of intrusive bodies has been found along this trend or in the entire eastern region of Mars. Several volcanoes occur in the south polar region [3] but here, too, no major fault trends or intrusives are present. Many small volcanoes and pyroclastic cones occur in the northern lowland plains, but even medium-size (~50-km-diameter) volcanotectonic structures are not discernible; if they exist, lava flows of Late Hesperian and Amazonian age have probably obscured all evidence of their presence.

Volcanoes in the Tharsis region have the widest age range (Early Noachian-Late Amazonian) of all volcanoes on Mars, as determined by the size-frequency distribution of their craters having diameters of 2, 5, and 16 km. Volcanotectonic intrusive centers in the Tempe area are Middle Noachian to Late Hesperian, as indicated by faults of these ages that have been partly deflected around their centers. Volcanoes in the eastern hemisphere are Hesperian to Early Amazonian.

References

- [1] Scott D.H. and Tanaka K.L. (1986) U.S. Geol. Misc. Inv. Ser. Map I-1802A.
 [2] Greeley R. and Guest J.E. (1987) U.S. Geol. Survey Misc. Inv. Ser. Map I-1802B. [3] Tanaka K.L. and Scott D.H. (1987) U.S. Geol. Survey. Misc. Inv. Ser. Map I-1802C. [4] Scott D.H. and Dohm J.M. (in press) Lunar and Planet. Sci. Conf. 20. [5] Wise D.U., Golombek M.P., and McGill, G.E. (1979) Icarus, 38, p. 456-472. [6] Plescia J.B. and Saunders R.S. (1979) Proc. Lunar Planet. Sci. Conf. 10, p. 2841-2859. [7] Scott D.H. (1982) Jour. Geophys. Res., 87, p. 9839-9851.

TIMING AND FORMATION OF WRINKLE RIDGES IN THE TYRRHENA PATERA REGION OF MARS

Tracy K. Porter, David A. Crown and Ronald Greeley, Department of Geology, Arizona State University, Tempe, Arizona 85287

Wrinkle ridges are distinctive linear to curvilinear arches topped by crenulated ridges and have been identified on the Moon, Mercury and Mars. Lunar wrinkle ridges, located mainly within the maria, may have volcanic [1] or tectonic [2] origins, or a combination of the two [3]. Ridges in the Yakima member of the Columbia River basalts are considered terrestrial analogs to wrinkle ridges; the Yakima ridges are thrust faults draped on the surface by layered basalt flows [4]. On the Earth and the Moon, wrinkle ridges are found within volcanic materials; because of this association, the presence of wrinkle ridges on other planetary surfaces has been used as a criterion for identifying volcanic plains [5].

Watters and Chadwick [6] observed an orthogonal network of wrinkle ridges in Hesperia Planum (20°S, 250°W), with ridges trending NW-SE and NE-SW. These ridges are attributed to "two superimposed episodes of buckling", suggesting two distinct compressional regimes. Recently, due to the presence of lava flow lobes and leveed channels, Greeley and Crown [7] identified an area within Hesperia Planum as a flank flow unit associated with Tyrrhena Patera. Hesperia Planum surrounds Tyrrhena Patera and embays the eroded shield of the volcano to the north and east.

The Tyrrhena Patera flank flow unit extends ~1000 km from the summit caldera to the southwest [7,8]. More than 55 wrinkle ridges have been identified on this flank flow unit. As in Hesperia Planum, there are two dominant ridge trends: NW-SE (roughly concentric to Hellas) and NE-SW (roughly radial to Hellas) [6,9]. Those trending NE-SW are aligned with a major ridge system SE of the flow unit and with the general trend of the flow unit.

The relationships between the lava flows and wrinkle ridges within the flank flow unit allow relative ages to be determined. Wrinkle ridges are classified as "post-flow" if flow lobes appear to arch over the rises undeformed, with no evidence of flow ponding on the upstream side of the ridge, or of flows breaching the rises (Figure 1). Ridges that appear to be contemporary with or older than the flow unit have also been identified. These "flow-associated" ridges appear to be topographic barriers to flows in some instances. Several flow lobes, when traced to their source, can be followed upstream until they intersect a ridge (Figure 2). These flows appear to emanate from wrinkle ridges - although the ~90 - 230 m/pixel resolution does not allow the precise relationship to be determined. The younger, post-flow ridges trend NW-SE, whereas the older, flow-associated ridges trend NE-SW (Figure 3). This pattern appears to be consistent across Hesperia Planum. Analysis of the highest resolution images available for Hesperia Planum (~90 m/pixel) reveals many instances of NW-SE trending ridges cross-cutting NE-SW trending ridges. Where a NW-SE trending ridge intersects a NE-SW trending ridge, a NW-SE trending scarp is seen on the surface of the NE-SW trending ridge, suggesting that the NW-SE ridge formed the superposed scarp by compression. Therefore, it appears that the NW-SE trending ridges are younger than the NE-SW trending ridges. The Tyrrhena Patera flank flow unit has 121 craters greater than 5 km in diameter (normalized to 10^6 km^2), suggesting that the unit was emplaced during the Upper Hesperian [10]. According to Tanaka's [10] model 2, this corresponds to 3.55 - 3.7 b.y. ago, thus placing maximum and minimum ages on the NE-SW trending and NW-SE trending ridges, respectively.

Wrinkle ridges within Hesperia Planum and the Tyrrhena Patera flank flow unit that trend NW-SE appear younger than the flank flow unit; ridges trending NE-SW appear older than, or contemporaneous with, the flank flow unit. If both ridge sets formed by tectonic processes, the age relationships suggest that the local stress regime shifted by 90° after the emplacement of the Tyrrhena Patera flank flow unit. The orientation of the post-flow ridges (orthogonal to the flank flow unit and concentric to the Hellas Basin) and the presence of ridge-related scarps suggest a non-volcanic, compressional origin for these ridges. However, the presence of flow lobes apparently emanating from NE-SW oriented ridges suggest that these ridges may have a volcanic origin: they may represent feeder dikes or localizations of near-surface lateral lava transport. This is supported by alignment of the flank flow unit, individual flow lobes and lava channels

RIDGES OF TYRRHENA PATERA: Porter, T.K. *et al.*

with the flow-associated ridges. Thus, within the Tyrrhena Patera flank flow unit, it is likely that the older ridges have a volcanic component, whereas the younger ridges appear to be of tectonic origin.

References: [1] Strom, R.G., 1972, in *The Moon*, S. Runcorn and H. Urey, eds., 187-215. [2] Tija, H.D., 1970, *Bull. Geol. Soc. Am.* **81**, 3095-3100. [3] Colten, G.W., Howard, K. A. and Moore, H.J., 1972, *App. 16 Prelim. Sci. Rep.*, NASA SP-315, 29.9-29.33. [4] Bentley, R.D., 1977, *Geologic Excursions in the Pacific Northwest*, 339-389. [5] Potter, D.B., 1976, *USGS Map I-941*. [6] Watters, T.R. and Chadwick D.J., 1989, *LPI Technical Report 89-06*, 68-70. [7] Greeley, R. and Crown, D.A., 1990, *JGR* **90**, 7133-7149. [8] Crown, D.A., Porter, T.K. and Greeley, R., 1991, this issue. [9] Crown, D.A. and Greeley, R., 1990, *Lun. Planet. Sci. Conf. XXI*, 250-251. [10] Tanaka, S., 1986, *Proc. Lun. Planet. Sci. Conf. 17th*, E139-E158.

COMPRESSIVE STRAIN IN LUNAE PLANUM-SHORTENING ACROSS WRINKLE RIDGES; J. B. Plescia, Jet Propulsion Laboratory, California Institute of Technology, Pasadena, CA, 91109

Wrinkle ridges have long been considered to be structural or structurally-controlled features. Most [e.g., 1,2,3,4,5], but not all [6] recent studies have converged on a model in which wrinkle ridges are structural features formed under compressive stress; the deformation being accommodated by faulting and folding. However, the fault dip and the relative importance of folding and faulting remain controversial [c.f., 2,3]. Given that wrinkle ridges are compressive tectonic features, an analysis of the associated shortening and strain provides important quantitative information about local and regional deformation.

Lunae Planum is dominated by north-south trending ridges extending from Kasei Valles in the north to Valles Marineris in the south. This region was selected for detailed because of the well-developed ridges, the relatively simple geologic setting, and the lack of interference from other structures. Lunae Planum is Hesperian-age "ridged plains material" [7] that thicken westward from an eastern contact with Noachian-age highly modified heavily cratered terrain.

To quantify the morphometric character, a photoclinometric study was undertaken for ridges on Lunae Planum using the technique of [8]. Phase-dependent photometric coefficients for the clear and minus-blue filters are presented by [9], the coefficient for the red filter is from [10]. Profiles are typically about 20 km in length and include all of the ridge visible in the image and extending onto the plains on either side; however, profiles could not be extended to adjacent ridges because of albedo variations. Clearly, this is a limitation in the data set, but one which is unavoidable. Comparisons between stereogrammetric topography and shadow determined relief indicate that, under carefully controlled conditions, photoclinometric results are within 10-15% of the relief determined by the other methods. Accuracy of this level is sufficient to estimate the morphometry of ridges. When used in the context of a specific model of formation and internal structure, the morphometric data can be used to assess the amount of compression accommodated by faulting and folding and thus the local and regional strains.

More than 25 ridges were examined between longitudes 57° and 80°, latitudes 5° to 25°N. For each ridge, several (1-15) profiles were obtained along its length. Ridge width, total relief, and elevation offset were measured for each ridge. Width is defined as the distance across the ridge for which relief relative to the surrounding plains is observed. Total relief is defined as the relief from the lowest plains unit to the summit of the ridge. Elevation offset is the difference in elevation of plains on one side of the ridge relative to that on the opposite side [2,11,12,13]. For ridges measured on Lunae Planum, widths ranged from 1.5 to 14 km (mean of 5 km), total relief varied from 16 to 370 m (mean of 127 m), and elevation offsets were 0 to 225 m (mean of 55 m).

Using the model of [1,2] for the internal structure of a wrinkle ridge--anticlinal deformation of the surface above a low-angle thrust fault; the fault presumably breaking the surface--the morphometric data can be used to estimate the shortening due to folding and faulting. Shortening due to faulting is proportional to fault dip and the elevation offset. Shortening due to folding is the difference between integrated surface length across the ridge and the horizontal point to point straight-line distance across the ridge. The dip of the proposed thrust fault is unobserved, but it has been estimated to be about 25° (see [2] and references therein for a complete explanation).

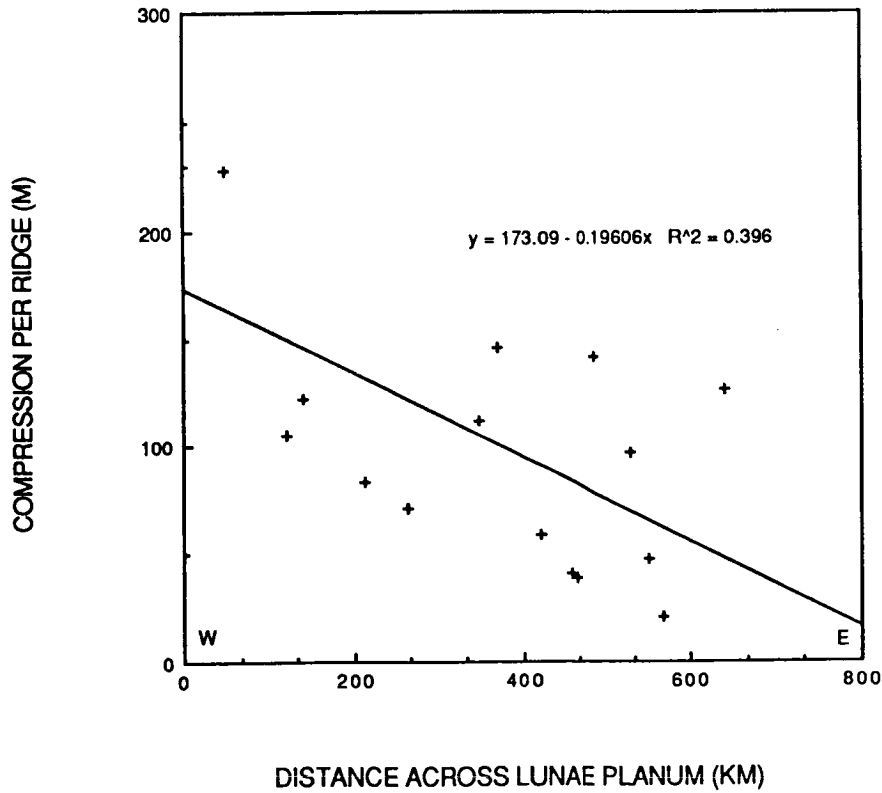
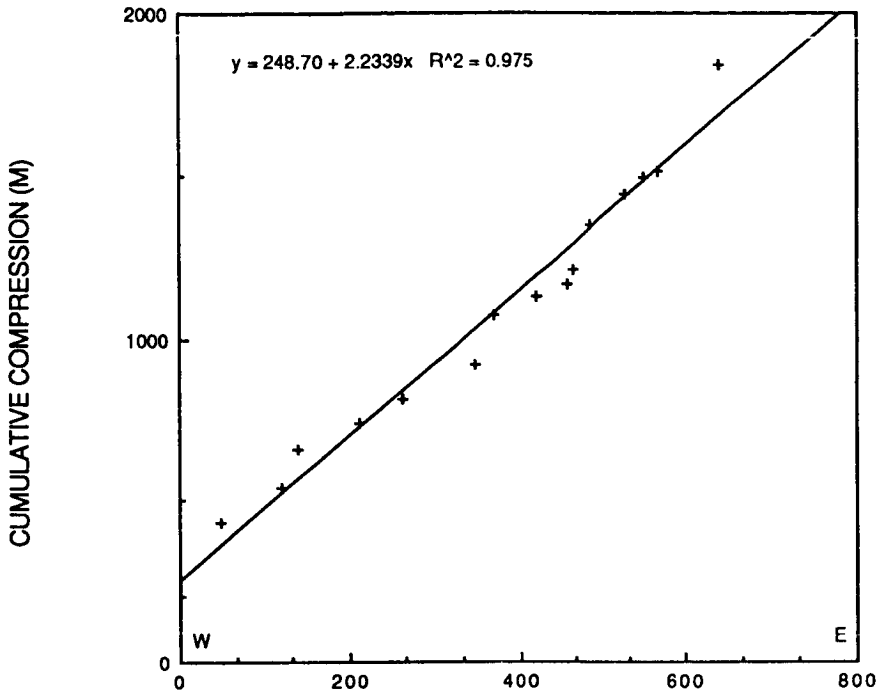
Using these relations, the total shortening due to faulting across the ridges that were measured varied from 0 m (no offset) to about 480 m; the mean value of shortening is 117 m. Shortening due to folding is 1 to 75 m with a mean value of 10 m. The ratio of shortening due to faulting to that due to folding is about 12, similar to values derived for lunar wrinkle ridges [2]. Using this same data set, the net compression and strain across Lunae Planum at 20°N was examined. Seventeen ridges are crossed by this profile which extends from 72° to 59° longitude. The values for each ridge represent the average of all measurements along that ridge. The profile has a total length of 641 km (measured from the westernmost to the easternmost ridge). Total shortening amounts to 1840 m (faulting shortening is 1712 m; folding shortening is 128 m); average shortening per ridge is 108 m. This corresponds to a net compressive strain along the profile length of 0.29% (faulting strain is 0.27%; folding strain is 0.02%). These values are similar in magnitude to shortening strain estimated from kinematic models of lunar mare basins (e.g., Humorum) of 0.16-0.31% [14].

Ridges are not uniformly spaced in longitude across Lunae Planum. Ridges are typically smaller, less well developed, and more numerous east of longitude 65° than to the west. Eleven ridges occur east of 65°W compared with six to the west. Total shortening west of 65° amounts to 924 m (average ridge shortening is 132 m); east of 65° it is 916 m (average ridge shortening is 92 m). Clearly, the net shortening is the same in the two areas, but individual ridges to the west accommodate greater amounts of shortening than those in the east. The relative and absolute magnitudes of faulting and folding shortening are similar in the two regions. The compressive strain in the west is 0.26% and 0.31% to the east, essentially indistinguishable. These data indicate that the net shortening and the net strain, at least within Lunae Planum, is relatively uniform with distance from Tharsis.

References: [1] Plescia, J. B., and M. P. Golombek, *Geol. Soc. Amer. Bull.*, 97, 1289-1299, 1986. [2] Golombek, M. P., J. B. Plescia, and B. J. Franklin, *Proc. 21st Lunar Planet. Sci. Conf.*, in press, 1990. [3] Sharpton, V. L., and J. W. Head, *Proc. 18th Lunar Planet. Sci. Conf.*, 307-317, 1988. [4] Watters, T., *J. Geophys. Res.*, 89, 10236-10254, 1988. [5] Watters, T., MEVTV Workshop: Early Tectonic and Volcanic Evolution of Mars, pp. 63-65, Lunar and Planet. Sci., Houston, TX, 1988. [6] Scott, D., MEVTV Workshop Tectonic Features on Mars, LPI Tech. Rept. 89-06, pp. 52-54, Houston, TX., 1989. [7] Scott, D. and K. L. Tanaka, *U. S. Geological Survey Misc. Inv. Series Map I-1082-A*, 1986. [8] Davis, P. A., and L. A. Soderblom, *J. Geophys. Res.*, 89, 9449-9457, 1984. [9] Tanaka, K. L., and P. A. Davis, *J. Geophys. Res.*, 93, 14893-14917, 1988. [10] Thorpe, T., *Icarus*, 20, 482-489, 1973. [11] Maxwell, T. A., F. El Baz, and S. H. Ward, *Geol. Soc. Amer. Bull.*, 86, 1273-1278, 1975. [12] Lucchitta, B. K., *Proc. 7th Lunar Sci. Conf.*, 2761-2782, 1976. [13] Plescia, J. B., *Abstracts 21st Lunar Planetary Science Conference*, 967-968, 1990. [14] Golombek, M. P., and G. McGill, *J. Geophys. Res.*, 88, 3563-3578, 1983. [15] Tanaka, K. L., *Proc. 17th Lunar Planet. Sci. Conf., Part I, J. Geophys. Res.*, 91, E139-E158, 1986.

Figure Captions: Upper panel shows the cumulative compression across Lunae Planum. Individual crosses represent the compression for each ridge. A least squares line has been fit to the data. Lower panel shows the amount of compression (faulting and folding) for each ridge along the profile. A least squares line has been fit to the data.

LUNAE PLANUM 20N



LATE NOACHIAN DEVELOPMENT OF THE COPRATES RISE, MARS

Kenneth L. Tanaka, U.S. Geological Survey, Flagstaff, Ariz.,
and **Richard A. Schultz**, Mackay School of Mines, Univ. of
Nevada, Reno, Nev.

The Coprates rise forms a 900-km-long, north- to northeast-trending ridge south of Coprates Chasma between long 56° and 60°. Radar [1] and stereophotogrammetric [2] data indicate that the rise is 2-4 km above a neighboring trough to the east. The break in slope between the rise and this trough is well defined topographically and in Viking images. In turn, the trough is bordered to the east at long 52° by a much gentler rise (relief <1 km). West of the Coprates rise, the terrain dips about 0.2° to roughly long 75°. The rise and flanking highs were previously interpreted to be tilted fault blocks formed by either Tharsis tectonism or an ancient impact [1, 3]. We report here results of a preliminary geologic investigation that documents Late Noachian growth of the Coprates rise as an asymmetric fold. More comprehensive work will lead to a mechanical analysis of the kinematic development of the rise.

Four west-northwest-trending "rift" zones (intensely faulted arches) spaced 150 to 200 km apart on higher parts of the rise are characterized by closely spaced normal faults and graben-and-horst structures (Nectaris Fossae) that are aligned with the rift zones. Locally, fault scarps bound rift valleys about 20 km across. Embayment by Upper Noachian materials and advanced surface and impact-crater degradation (see prominent 85-km-diameter, pre-Late Noachian crater {A} in Fig. 1) suggest that the rift zones are Early to Middle Noachian in age [4]. Two large massifs (not shown) about 50 km across in the northern rift zones appear channeled and faulted; the northern massif has a large, rimmed summit crater. These massifs may be ancient volcanoes [4]. Irregular massifs {B, C} also formed along the southern rift zones.

Interrift areas of the northern part of the Coprates rise are covered by a complex of flat-lying plains and gently sloping materials whose surfaces are locally marked by channels, degraded craters, lava flows, and north-trending wrinkle ridges and fault scarps. Ridged plains material embays and buries these materials and structures on both sides of the rise. Crater densities (where $N(5)$ is the number of craters having rim diameters larger than 5 km per 10^6 km²) for the ridged plains material ($N(5) \sim 200$) indicate an age coincident with the Noachian/Hesperian boundary, whereas the interrift materials (which reflect the age of deformation) have a Late Noachian crater age ($N(5) \sim 300$) [5].

South of lat 26° S., strata were upturned on both sides of the rise during the Late Noachian (prior to deposition of ridged plains material). On the northwest side, a patch of dissected crater-fill material {D} has been tilted toward the

northwest and is embayed by a bed of ridged plains material {E}. That bed is overlain by one or two more beds {F}, seen in places on either side of the western part of the rift zone {G}. The apparent tilting indicates at least local, modest (hundreds of meters?) uplift of the Coprates rise and possibly some growth or uplift of the southern rift zone relative to the western plateau.

The sequence of upturned strata on the southeast side of the rise is much more clearly seen. We have identified as many as four or five layers in this sequence. These layers form prominent hogbacks having well-defined dip slopes {H}; a lava-flow origin is consistent with the layers' apparent resistance to erosion and association with the southern rift zone. Several sets of grooves, perhaps formed by erosion of joints, cut the strata. The grooves connect with sinuous channels {I} at their upper ends, indicating the runoff of ground water after uplift; lower channel reaches have been buried by ridged plains material {J}. The upslope edge of the lowermost upturned layer forms a prominent (probably more than 100 m high), linear scarp {K} that may be the result of normal faulting. Another upturned bed {L} is exposed south of the massif at {C}. Following the apparent normal faulting and warping south of that massif, strata {M} were emplaced across the southwest end of the Coprates rise (some embay the upturned bed at {L}) and were later folded, faulted, and dissected. The deep sculpturing of the strata suggests that they are easily erodible (pyroclastic?) rocks. These deposits (and channels that cut them) apparently issued from the rift zone {G}.

We conclude that the Coprates rise formed during the Late Noachian by 2-4 km of asymmetric uplift (steeper on its east flank). The timing is inconsistent with an origin by an early impact, but it coincides in time with early Tharsis-centered radial faulting at Syria Planum (about 2,500 km west of the rise) [6]. The deformational history may be consistent with thrust faulting or buckling of the lithosphere. Tectonism was accompanied by volcanism, and such activity probably caused runoff of ground water.

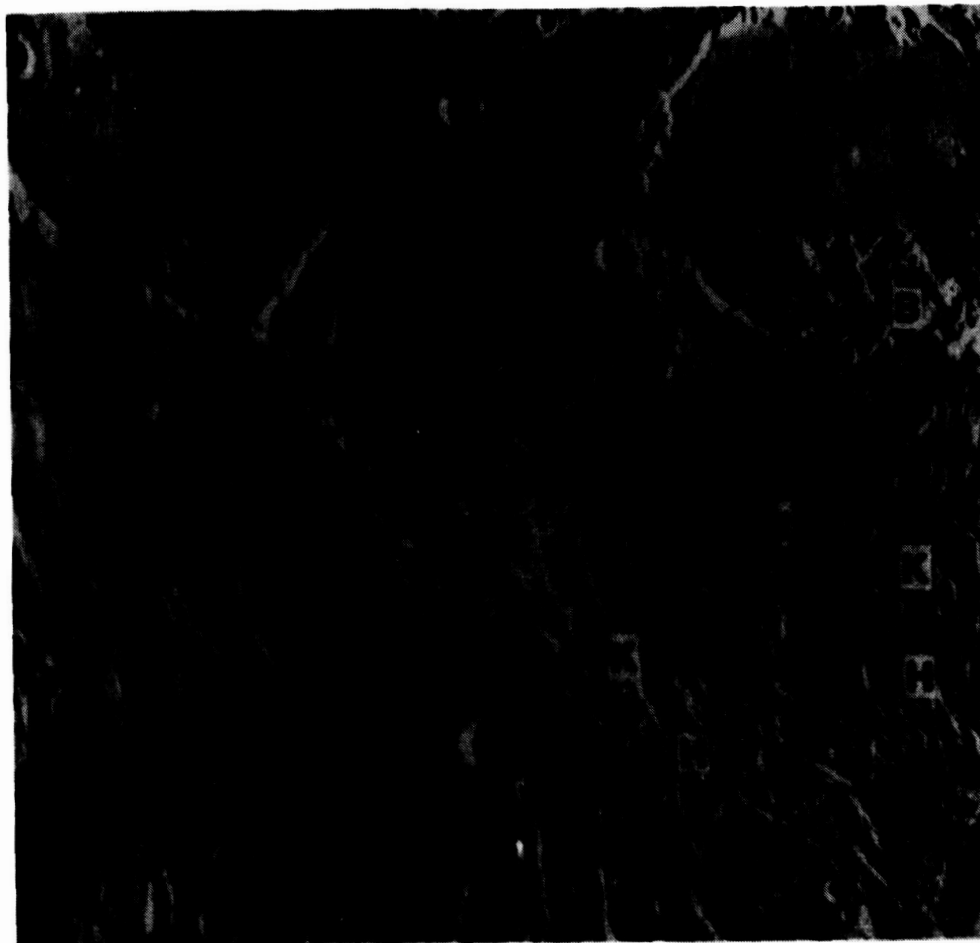


Figure 1. Part of southern Coprates rise. Letters identify features discussed in text. [Viking Orbiter image 610A42]

References Cited

- [1] Plescia, J.B., Roth, L.E., and Saunders, R.S. (1980) **NASA TM 81776**, 68-70. [2] U.S. Geological Survey (1989) **USGS Map I-2030**. [3] Craddock, R.A., Greeley, R., and Christensen, P.R. (1990) **JGR**, **95**, 10,729-10,741. [4] Scott, D.H. and Tanaka, K.L. (1986) **USGS Map I-1802-A**. [5] Tanaka, K.L. (1986) **JGR**, **91**, E139-E158. [6] Tanaka, K.L. and Davis, P.A. (1988) **JGR**, **93**, 14,893-14,917.

ORIGINAL PAGE IS
OF POOR QUALITY

INTERACTIONS OF TECTONIC, IGNEOUS, AND HYDRAULIC PROCESSES IN THE NORTH THARSIS REGION OF MARS

P.A. Davis¹, K.L. Tanaka¹, M.P. Golombek², and J. Plescia²: ¹U.S. Geological Survey, Flagstaff, Ariz. 86001; ²Jet Propulsion Laboratory, Pasadena, Calif. 91109.

Recent work on the north Tharsis region of Mars (lat 15° to 50° N., long. 80° to 120°) has revealed a complex geologic history involving volcanism, tectonism, flooding, and mass wasting [1-8]. Our detailed photogeologic analysis of this region found (1) many previously unreported volcanic vents, volcanoclastic flows, irregular cracks, and minor pit chains; (2) additional evidence that volcanotectonic processes dominated this region throughout Martian geologic time, and (3) the local involvement of these processes with surface or near-surface water. Also, we have obtained photoclinometric profiles within the region of troughs, simple grabens, and pit chains, as well as average spacings of pits along pit chains. We have used these data, together with techniques described in [9-11], to estimate depths of crustal mechanical discontinuities that may have controlled the development of these features. In turn, such discontinuities may be controlled by stratigraphy, presence of water or ice, or chemical cementation.

The trough depths indicate base levels of erosion at 0.4 km and 1.5 km. The shallower depth, obtained on the Tempe Terra plateau, is close to the thickness range of the Tempe Terra Formation in this region [12]. The 1.5-km trough depths, obtained within the Tempe Terra and Alba Patera regions, are close to the average depth found for a widespread discontinuity within the megaregolith in the equatorial region south of the current study area [10]. This discontinuity may have involved ice, water, or chemical cementation.

The faulted-layer depths estimated from 172 graben measurements have a large range (0.6 km to 7.2 km), similar to graben depths found in the equatorial region (0.4 km to 5.0 km [10]). The pit spacings have a narrower range between 0.8 km and 2.8 km. The frequencies of both faulted-layer depths and pit spacings show concentrations at 1.4 and 2.0 km, which is in marked contrast to the unimodal (at 1.0 km) distribution obtained within the adjacent equatorial region [10]. There is no obvious spatial correlation among faulted-layer depth and elevation, latitude, or pit spacing in the north Tharsis region. However, the average faulted-layer depth (within a 100-km radius) does increase logarithmically from 1.0 km near the base of Alba Patera to 3.5 km near its summit caldera, but the higher average values have a large standard deviation. Despite this apparent relation, the faulted-layer depths within 500 km of the Alba Patera summit cover the entire range of reported values and have a random distribution.

The concentrations of faulted-layer depths and pit spacings at 1.4 km and 2.0 km and of trough depths at 1.5 km, and the random areal distribution of these data, indicate at least two widespread mechanical discontinuities (at about 1.4 km and 2.0 km) within the north Tharsis region. Because these measurements were obtained on a variety of geologic units of Noachian to Amazonian age, the discontinuities are probably independent of local geology and geologic time. The model presented by [13] predicts the base of the proposed ice layer to be 1.5 km to 2 km between lat 30° and 45° N. Our photogeologic analysis in this region has found evidence for the existence of ground water or ice throughout recorded geologic time. This evidence includes etched, channeled, and smooth units of Noachian age, lahars and channeled pyroclastic(?) deposits of Hesperian age, and shallow fracture-controlled

troughs in Tempe Terra and a braided channel system (Olympica Fossae) of Amazonian age that originates from an enlarged crack of Ceraunius Fossae. The water that produced these features may have been entrapped and possibly frozen in the megaregolith, and it may have been released by magma heating with fractures acting as conduits. Small volcanic shields formed along fractures at about the same time as the formation of the channels and troughs.

The depth to consolidated basement around Alba Patera may be 5-7 km, if we assume a 3-4 km total accumulation of Amazonian volcanic material (based on elevation) and a 2-3 km average depth to basement in surrounding regions [10]. Thus, the greater depths (5-7 km) indicated by graben measurements may correspond to the megaregolith-basement interface.

The drainage of pit chains in this region may have been facilitated by the opening of tension cracks or dikes beneath particular grabens. This hypothesis is supported by the simple geometry of the grabens; the formation of similar structures on Earth; photogeologic evidence of lava flows emanating from grabens, fractures, and fissures; and mechanical models and failure criteria relating the extension in the grabens to opening of the subsurface cracks [14]. Collapse of the overlying poorly consolidated material into the widened tension cracks would have been facilitated by hydraulic relaxation and subsidence of the magma. Magma eruption near the pit chains may have been inhibited by the frozen ground. Secondary subsurface erosion caused by turbulent flow of ground water along cracks may have induced further collapse in places. At Tempe Terra, scalloped troughs indicate coalescence of pits, perhaps due to mass wasting of icy slope material.

Calculations using measured pit volumes and pit chain lengths and a reasonable estimate of tension crack width (25-90 m), based on the extension across faults bounding grabens, indicate that cracks 1-3 km deep can provide the space for the material evacuated from the pits. Cracks of these dimensions are reasonable on the basis of similarity in scale to terrestrial analogs and simple failure criteria applied to Mars [14].

References: [1] Mouginis-Mark *et al.*, 1988, Bull. Volcanol. 50, 361; [2] Gulick and Baker, 1990, J. Geophys. Res. 95, 14,325; [3] Mouginis-Mark, 1990, Icarus 84, 362; [4] Scott and Dohm, 1990, Proc. 20th Lunar Planet. Sci. Conf., 503; [5] Tanaka, 1990, Proc. 20th Lunar Planet. Sci. Conf., 515; [6] Wise, 1979, U.S. Geol. Surv. Misc. Invest. Ser. Map I-1154; [7] Witbeck and Underwood, 1984, U.S. Geol. Surv. Misc. Invest. Ser. Map I-1614; [8] Scott and Tanaka, 1986, U.S. Geol. Surv. Misc. Invest. Ser. Map I-1802-A; [9] Golombek, 1979, J. Geophys. Res. 84, 4657; [10] Davis and Golombek, 1990, J. Geophys. Res. 95, 14,321; [11] Horstman and Melosh, 1989, J. Geophys. Res. 94, 12,433; [12] Frey and Grant, J. Geophys. Res., 95, 14,249; [13] Rossbacher and Judson, 1981, Icarus 45, 39; [14] Tanaka and Golombek, 1989, Proc. 19th Lunar Planet. Sci. Conf., 383.

VALLES MARINERIS TECTONISM: QUESTIONS AND SUGGESTIONS

Baerbel K. Lucchitta, Mary G. Chapman, and Nancy K. Isbell, U.S. Geological Survey, Flagstaff, Arizona 86001

Much has been learned about the Valles Marineris, and stratigraphic relations inside the troughs have been reasonably well established. However, many questions remain, especially questions pertaining to tectonism and origin.

What is the age of the troughs?

The central Valles Marineris troughs disrupted lavas of Lunae and Syria Plana of Early Hesperian age [1]. Accordingly, they may be as old as Early Hesperian. The Noctis Labyrinthus troughs, which disrupted Upper Hesperian or Amazonian lavas [2], may be of Early Amazonian age. An analysis of shallow grabens that parallel the Valles Marineris and of wrinkle ridges that trend perpendicular to them suggests that wrinkle ridges developed first, grabens second [3,4], and the Valles Marineris either at the same time as the grabens or last [5,6], all perhaps in Early Hesperian time.

Interior layered deposits were emplaced on top of chaotic materials in the eastern and northern troughs that merge with outflow channels of middle to Late Hesperian age. Therefore these troughs are at least as old as the channels, but the deposits are younger.

Geologic relations suggest that some troughs may be split lengthwise into older segments filled by interior layered deposits and younger segments that are devoid of interior layered deposits and locally expose former plateau materials on their floors [7]. Hebes Chasma and the southern parts of Ophir, eastern Candor, and Melas Chasmata appear to be older, as are the peripheral troughs that merge with outflow channels. The northern parts of Ophir and eastern Candor Chasmata are younger, as may be the entire length of the Ius and Tithonium, central Melas, and Coprates Chasmata system [8]. Overall, the opening of the troughs seems to have had several episodes, extending in time from Early Hesperian to Amazonian.

What is the evidence for tectonic origin?

Blasius et al. [9] advocated a tectonic origin for the troughs, because they lie on the flanks of the Tharsis rise and are radial to its center, are paralleled by grabens, and are bounded by fault scarps having triangular facets on truncated spurs. Yet, an erosional origin remained attractive because of an apparent morphologic continuum between pit chains of probable erosional origin and large troughs. A recent morphometric study comparing the width-to-depth relations of all the depressions in the area [10] showed that a continuum between pit chains and large troughs does not exist, suggesting that the large troughs probably formed through deep-seated coherent failure. However, our work in progress shows that erosional back wasting from fault scarps on the major troughs may have played a significant role. Thirty-two percent of the area of the troughs is attributable to such erosion. We are currently using a digital terrain model of the troughs to calculate the volumes of the materials removed from the walls.

How do the Valles Marineris relate to the Tharsis rise?

Geophysical models indicate that isostatic adjustment of the Tharsis rise would have caused circumferential tensile stresses in the western part of the Valles Marineris, whereas external loading (flexing the elastic lithosphere downward) would have caused such stresses in the eastern chasmata [11-15]. Thus, these stress models require two distinct events. The different ages of the troughs as outlined above do not agree with an age difference between western and eastern troughs. Perhaps local structural inhomogeneities perturbed the regional stress system.

The Valles Marineris are paralleled by shallow, east-trending grabens that are part of graben systems radial to Tharsis. However, the sector north of the Valles Marineris is almost devoid of such grabens. It appears that the Tharsis stresses at Valles Marineris were released by a few major, deep faults rather than by distributed shear.

The structural relief of the Valles Marineris, which is 8-10 km throughout the central troughs, decreases uniformly eastward to 3-5 km in Coprates Chasma. This decrease would indicate less strain toward the outer periphery of the Tharsis rise, but the stress models do not predict this decrease. The discrepancy is not yet explained.

The amount of strain on the Valles Marineris also depends on the attitude of fault planes. Carr [16] postulated near-vertical planes, whereas Golombek and Davis [17] found planes with dips near 60°. We are currently studying fault-plane attitudes by mapping fault traces on stereophotogrammetric models across areas of high relief.

What additional factors may have influenced the origin of the Valles Marineris?

Carr [16] mentioned that the location of the troughs may be related to subterranean aquifers. The 4-km contour on the plateau adjacent to the Valles Marineris coincides approximately with the appearance of chaotic materials in the eastern (Capri, Eos, and Gangis) and northern (Juventae) chasmata that merge with channels. This observation suggests that an aquifer is intersected near the 4-km-elevation horizon. Perhaps subterranean water, transported from the Tharsis center toward the outflow channels along the Valles Marineris, may have increased the pore pressures and lowered the strength of the crust, permitting failure to occur more readily.

The Valles Marineris lie along the crest of a regional, elongated topographic bulge extending eastward from Tharsis. Wise et al. [18] suggested that the troughs represent a "key-stone" collapse of the crest of this bulge, formed by the extension accompanying arching. Alternatively, the elongated bulge may have formed from isostatic rebound after trough formation. Another explanation for both arching and rifting is aborted plate tectonism [19]. However, most terrestrial rifts have many parallel faults in an echelon patterns that taper out along strike, and the rifted beds are tilted. By contrast, the Valles Marineris faults are more widely spaced, trough ends are blunt, fault planes appear to be steep, and tilted beds are relatively few. Perhaps the difference is due to a thicker or more homogeneous crust on Mars than commonly occurs in rift zones on Earth [19].

- References: [1] Scott, D.H., and Tanaka, K.L. 1986. U.S. Geol. Surv. Misc. Inv. Ser. Map I-1802-A, scale 1:15,000,000. [2] Tanaka, K.L., and Davis, P.A. 1988. *J. Geophys. Res.* 93, 14893-14917. [3] Watters, T.R., and Maxwell, T.A. 1983. *Icarus* 56, 278-298. [4] Watters, T.R., and Maxwell, T.A. 1986. *J. Geophys. Res.* 91, B8113-B8125. [5] Schultz, R.A. 1989. *Lunar and Planetary Science XX*, 974-975. [6] Schultz, R.A. 1989. MEVTV Workshop on Tectonic Features on Mars (Washington, D.C., April 20-21, 1989), 21-22. [7] Lucchitta, B.K., and Bertolini, L.M. 1989. *Lunar and Planetary Science XX Conference*, 590-591. [8] Schultz, R.A. *Lunar and Planetary Science XXII*, in press. [9] Blasius, K.R., Cutts, J.A., Guest, J.E., and Masursky, Harold. 1977. *J. Geophys. Res.* 82, 4067-4091. [10] Lucchitta, B.K., Balser, R.A., and Bertolini, L.M. 1990. *Lunar and Planetary Science XXI*, 722-723. [11] Banerdt, W.B., Phillips, R.J., Sleep, N.H., and Saunders, P.S. 1982. *J. Geophys. Res.* 87, 9723-9733. [12] Willemann, R.J., and Turcotte, D.L. 1982. *J. Geophys. Res.* 87, 9793-9801. [13] Sleep, N.H., and Phillips, R.J. 1985. *J. Geophys. Res.* 90, 4469-4489. [14] Phillips, R.J., Sleep, N.H., and Banerdt, W.G. 1990. *J. Geophys. Res.* 95, 5089-5100. [15] Banerdt, W.B., Golombek, M.P., and Tanaka, K.L. In *Mars*, Kieffer, H.H., Jakosky, B.M., Snyder, C.W., and Matthews, M.S., eds., University of Arizona Press, in press. [16] Carr, M.H. 1981. *The Surface of Mars*. 232 pp. [17] Davis, P.A. and Golombek, M.P. 1990. *J. Geophys. Res.* 95, 14231-14248. [18] Wise, D.U., Golombek, M.P., and McGill, G.E. 1979. *Icarus*, 38, 456-472. [19] Frey, H. 1979. *Icarus*, 32, 142-155.

EXTENSION AND STRAIN IN NORTHERN THARSIS; J. B. Plescia, Jet Propulsion Laboratory, California Institute of Technology, Pasadena, CA, 91109

The northern areas of Tharsis, south of Alba Patera, are remarkable in that they are dominated by extensive, generally north-trending graben. Some graben are small isolated features whereas others are complex overlapping features in which individual fault pairs are impossible to separate. This pattern indicates an east-west extensional stress regime, consistent with stress models for Tharsis [1].

To estimate the regional east-west extension and strain, graben along a profile at 35°N latitude, between longitudes 135° and 93° were studied. This profile (about 1800 km long) was chosen because the graben have a northerly trend, the structures are relatively simple, the profile is anchored to ancient Noachian age crust, and high resolution images are available. The western end of the profile begins at Acheron Fossae (long. 135°W) and ends in the east at the southwestern part of Tempe Fossae (long. 93°W). Plains units cut by the graben include Hesperian- and Amazonian-age members of the Alba Patera and Ceraunius Fossae Formations [2,3,4]. The ages of the faults have been studied [4]; all are Stage III faults--early Amazonian (700-1800 my) in age.

Study of graben morphometry allows an estimation of the extension and strain. Martian graben are almost certainly similar in nature to terrestrial graben--i.e., brittle extension of the crust along normal faults dipping at about 60° toward the center of the graben [5,6]. For each graben the width and depth were measured. Using this data and assuming a 60° fault dip, the extension and the thickness of the faulted layer (the depth at which the graben-bounding faults intersect) were calculated. Depth measurements were obtained by use of shadow measurements and photogrammetry [7]. Shadow measurements were derived using the solar incidence angle at the location of the measurement (obtained from SEDR data) and counting shadowed pixels. The length of the shadow could be overestimated by a maximum of 2 pixels, though 1 pixel is probably a better limit. Typical incidence angles were 70° and typical pixel scales were 75 m/pixel, resulting in an uncertainty of 25 m in the estimated depth. For those graben that did not have shadows, photogrammetric profiles were used to estimate depths. Corrections for atmospheric haze were determined for each frame from true shadows elsewhere in the scene. Photogrammetric depths have an uncertainty of about 10-15% [8].

Observed wall slopes were considerably less than the 60° fault dip assumed. The difference between the observed and expected slopes indicate that either the walls have been subjected to scarp erosion or the controlling faults have a low dip. Scarp retreat would be expected in any geologic environment and is observed for terrestrial, lunar, and martian graben; whether the faults are shallower than expected is unknown, but estimates for normal faults elsewhere on Mars [6] suggest that they have steep dips near 60°. If however, the faults do dip at a more shallow angle, then the amount of extension across the graben would be greater than that estimated here (about a factor of 5 for a 20° dipping fault).

Data were collected within 2°-3° latitude of 35°N and averaged for each graben. Average measured graben widths ranged from 979 to 8661 m with a mean value of 3652 m; graben depths ranged from 10 to 636 m with a mean value of 117 m. The corresponding extension ranged from 11 to 734 m with a mean value of 135 m. Total cumulative extension along the profile amounts to 8062 m and would correspond to a regional strain of 0.0045 (0.45%). This value is a minimum because data was not obtained for a few small graben and a 60° fault dip was assumed; the addition from the other grabens is negligible; but shallower fault dips would produce a corresponding

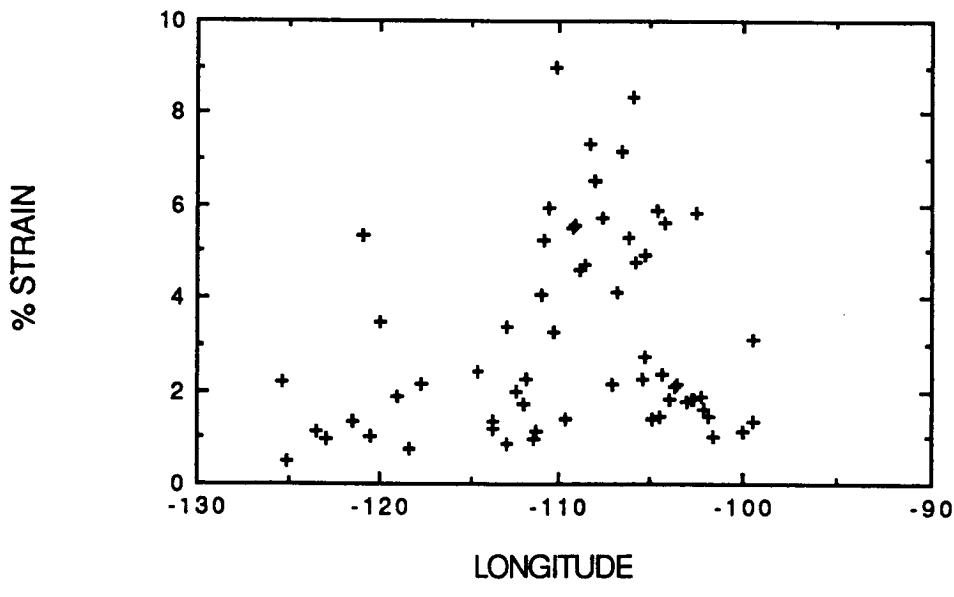
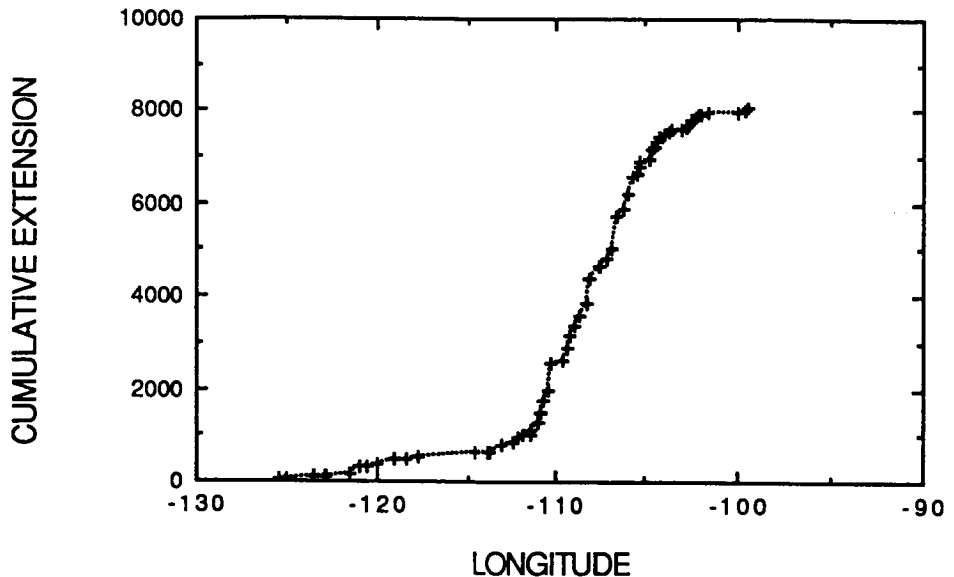
increase in the extension. The thickness of the faulted layer varies across the region, ranging from about 848 to 7500 m. The morphometry of the graben are not uniform along the profile. Graben along the eastern and western ends of the profile (west of 115° and east of 100°) are narrow (<3000 m), shallow (<150 m) and with small extension (<100 m). Between 115° and 100° (maximum at about 109°) the graben are much larger; widths up to 8000 m, depths in excess of 500 m, and extensions in excess of 500 m occur in a narrow band. Within this central zone, strains (as calculated from the individual graben extension and the preextension graben width) range from 2 to 9%, compared with 2% or less to the east and west. The thickness of the faulted layer is also at a maximum near longitude 110°, about 3-7 km whereas to the east and west it is much shallower at about 2 km.

Extension, strain, and morphology all vary across the profile with the extremes occurring in the center near longitude 110°. This region has clearly experienced considerably greater deformation than adjacent areas and could reflect either a variation in the stress field or the response of the material. This area lies directly north of the intensely fractured Ceraunius Fossae area--a locally high area extensively cut by north-trending graben (Stage II faulting; 3-3.5 by [4]). The geology would suggest that many of the young faults examined here are a reactivation of older structures now buried by the volcanic plains.

Morphometric data for graben at 35°N between longitudes 135° and 93° indicate post early Amazonian cumulative east-west extension of about 8062 m corresponding to a regionally averaged extensional strain of 0.45%. Extension and strain are at concentrated near longitude 110°W where local strains in excess of 5% are observed. All of the extension is oriented in an east west direction.

References: [1] Banerdt, W. B., Golombek, M. P., and Tanaka, K. L., 1990, Stress and tectonics on Mars, *Mars*, University of Arizona Press. [2] Scott, D. A., Tanaka, K. L., and Schaber, G. G., 1981, U. S. Geological Survey Map I-1278. [3] Scott, D. A., Tanaka, K. L., and Schaber, G. G., 1981, U. S. Geological Survey Map I-1276. [4] Tanaka, K. L., 1990, Proc. 20th Lunar Planet. Sci. Conf., 515-523. [5] Golombek, M. P., 1979, *J. Geophys. Res.*, 84, 4657-4666. [6] Davis, P. A., and Golombek, M. P., 1989, *J. Geophys. Res.*, 92, 14231-14248. [7] Davis, P. A., and L. A. Soderblom, *J. Geophys. Res.*, 89, 9449-9457, 1984. [8] Tanaka, K. L., and P. A. Davis, *J. Geophys. Res.*, 93, 14893-14917, 1988.

Figure Captions: Upper panel shows the cumulative extension across the profile. Crosses represent values for individual graben. Extension is expressed in an east-west direction having been corrected for the strike of the graben. Lower panel shows the amount of extensional strain across individual graben as a function of longitude.



VALLES MARINERIS, MARS: ARE PIT CHAINS FORMED BY EROSION AND TROUGHS BY TECTONISM?; B.K. Lucchitta, R.A. Balser, and L.M. Bertolini, U.S. Geological Survey, Flagstaff, AZ 86001.

The origin of the Valles Marineris remains controversial. Erosional [1], tectonic [2], and hybrid processes [3] have been proposed. Erosional processes appeared attractive because a morphologic continuum was thought to exist from pit chains of probable erosional origin to larger troughs. Schultz [4], however, refuted the existence of this continuum. To clarify these contradictions, we compared the widths and depths of pit chains and troughs and found that the features do not form a continuum. Rather, results are consistent with the hypothesis that pit chains formed by surficial collapse and troughs by deeper seated and coherent failure.

We classified by inspection all pit chains and linear depressions in the Valles Marineris region into six morphologic categories: (1) pit chains (linear arrays of small pits), (2) floored chains (arrays of pit chains having flat or hummocky floors), (3) scalloped troughs (wider linear depressions with scalloped wall segments), (4) narrow troughs (depressions of intermediate width with straight wall segments), (5) wide troughs (broad, linear depressions), and (6) chaotic troughs (more irregular depressions displaying some channel morphologies). We drew topographic profiles across the classified depressions at each degree of longitude between long 45° and 90°, on the basis of 1:2,000,000-scale topographic maps of MC 18 NW [5] and 18 NE and SE (work in progress). For each profiled depression, we determined the erosional width between plateau margins, the depth from the surrounding plateau level to the deepest part, and the geologic unit (modified from Witbeck et al. [6]) exposed at the deepest point.

Depths and widths are shown in Figs. 1 and 2. Fig. 1 shows measurements of all troughs. Fig. 2 is the same but with omissions of three types: (1) chaotic troughs, which are genetically linked to outflow channels; (2) troughs east of long 61°, which are transitional to chaotic troughs; and (3) troughs whose maximum depth is not likely to reflect the approximate structural depth because of thick fill from landslides or interior deposits.

Results of the study, as deduced from the figures, are as follows:

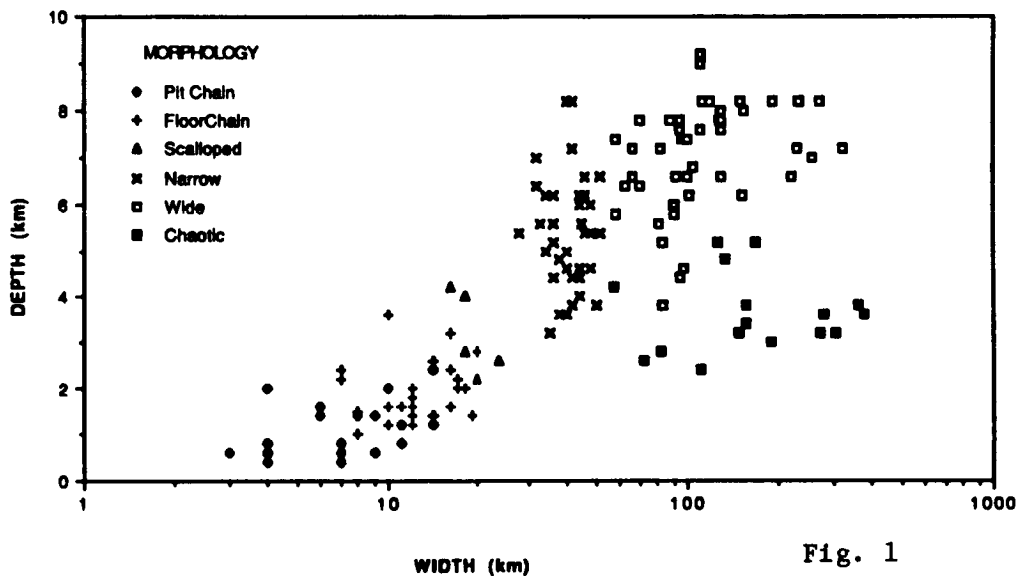
1. Pit chains, floored chains, and scalloped troughs lie along a continuously ascending trend that suggests a common origin. Surficial erosional collapse into linear subsurface voids or tension cracks [3] is compatible with this observation. The limiting depths of about 4 km may be due to a discontinuity at that depth or to restricted size of the underlying voids.
2. Narrow and wide troughs form a continuum that suggests their formation by similar processes. The straight scarps bordering these troughs suggest control by faulting rather than surficial collapse.
3. A gap in data occurs at widths of 20-35 km, separating pit chains, floored chains, and scalloped troughs from narrow and wide troughs. Only two transitional points are located within this gap. The gap suggests an abrupt change in physical conditions or processes. Apparently, deep-seated, more coherent failure was activated for troughs wider than about 35 km.

4. Most troughs bottom out at 8-9 km regardless of width, perhaps implying a controlling discontinuity or limit in the amount of extension.

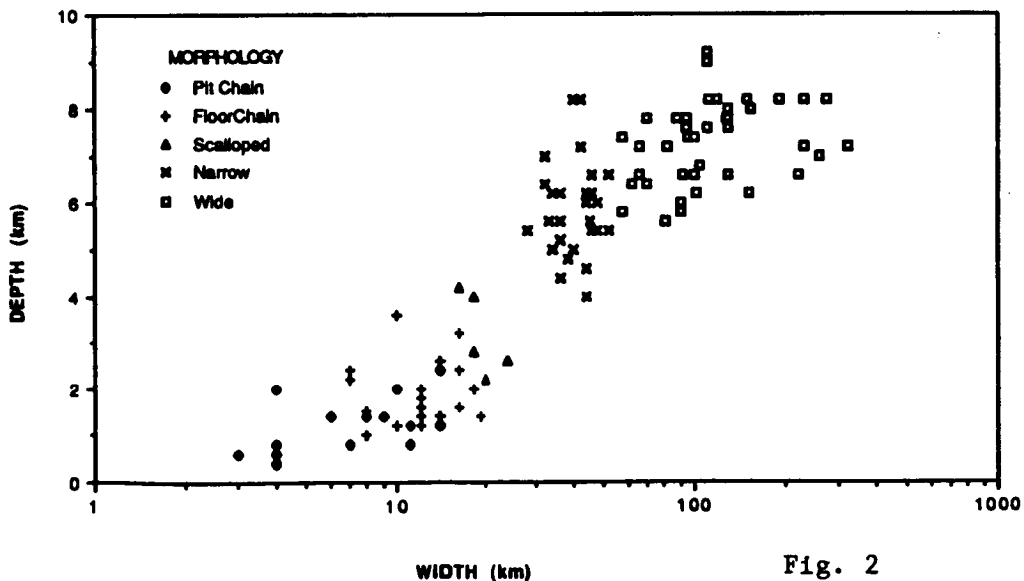
REFERENCES

[1] McCauley, J.F., M.H. Carr, J.A. Cutts, W.K. Hartmann, Harold Masursky, D.J. Milton, R.P. Sharp, and D.E. Wilhelms (1972) Icarus 17, 289-327.
 [2] Blasius, K.R., J.A. Cutts, J.E. Guest, and Harold Masursky (1977) Jour. Geophys. Res. 87, 9723-9733; [3] Tanaka, K.L. and M.P. Golombek (1989) Proc. 19th Lunar and Planet. Sci. Conf., 383-396; [4] Schultz, R.A. (1989) MEVTV Workshop on Tectonic Features on Mars, 21-22; [5] U.S. Geological Survey (1986) U.S. Geol. Surv. Misc. Inv. Map I-1712; [6] Witbeck, N.E., K.L. Tanaka, and D.H. Scott (in press) U.S. Geol. Surv. Misc. Inv. Ser. Map I-2010.

DEPTH VS. WIDTH OF VALLES MARINERIS TROUGHS



**DEPTH VS. WIDTH OF VALLES MARINERIS TROUGHS
FOR LONGITUDES > 61 DEGREES**



MARTIAN SEISMICITY THROUGH TIME FROM SURFACE FAULTING

M. Golombek¹, K. Tanaka², W. Banerdt¹, and D. Tralli¹, ¹Jet Propulsion Laboratory, Caltech, Pasadena, CA 91109, ²U. S. Geological Survey, Flagstaff, AZ 86001.

An objective of future Mars missions involves emplacing a seismic network on Mars to determine the internal structure of the planet. An argument based on the relative geologic histories of the terrestrial planets suggests that Mars should be seismically more active than the Moon, but less active than the Earth (e.g., 1). Although the Viking 2 seismometer failed to detect a marsquake, the poor sensitivity of the instrument (on the lander) does not preclude Mars from being a seismically active planet (2). In addition, calculations (1) indicate that stresses induced by cooling of the martian lithosphere through time should give rise to marsquakes that exceed the occurrence of high-frequency teleseisms on the Moon (28 events in 5 years) thought to be similar to tectonic earthquakes (3). The seismic moment M_0 , is defined as, $M_0 = \mu SA$, for slip (S) over a fault of area A , and rigidity μ . Therefore measuring the slip across a fault of known or estimated area allows a determination of the seismic moment, which can be related to the magnitude of an equivalent earthquake, assuming an appropriate moment-magnitude relationship. In this abstract, we estimate the seismicity expected on Mars through time from slip on faults visible on the planet's surface. These estimates of martian seismicity must be considered a lower limit as only structures produced by shear faulting visible at the surface today are included (i.e., no provision is made for buried structures or non-shear structures); in addition, the estimate does not include seismic events that do not produce surface displacement (e.g., activity associated with hidden faults, deep lithospheric processes or volcanism) or events produced by tidal triggering or meteorite impacts. Calibration of these estimates suggests that Mars may be many times more seismically active than the Moon.

Tectonic features on Mars are preferentially found around the Tharsis region, which covers the entire western hemisphere of Mars. Tharsis faults formed mainly during two tectonic periods (4, 5), one during Late Noachian/Early Hesperian and the other during Late Hesperian/Early Amazonian. A recent review of martian structures (6) defines a number of tectonic features that formed by shear faulting. The most common tectonic feature is the simple graben, which is bounded by two inward dipping normal faults with dips of about 60° (7). The widths of the structures and geometrical considerations indicate that on average the bounding faults extend down dip about 2.5 km, and have experienced 150 m of slip (8). We have estimated the faulting on narrow grabens from a data set (9) that includes the locations and lengths of all visible grabens (about 7000), about half of which formed during each of the two tectonic periods. Larger grabens and rifts that involve more of the lithosphere (proportional to their width) also are found on Mars, principally

in Valles Marineris, Thaumasia, Tempe Terra, and Alba. Faults bounding the Thaumasia graben, which formed during the Late Hesperian/Early Amazonian period and canyons in Valles Marineris, which formed during both periods are likely to extend through the entire brittle lithosphere, which is about 40 km thick (6); slip was estimated from the observed topographic relief (4-8 km for Valles Marineris; 1.5 km for the Thaumasia graben). Grabens at Alba and Tempe Terra are narrower, probably involving the upper 5-10 km of the lithosphere. Grabens at Alba formed mostly during the Early Amazonian and have experienced 0.2-0.5 km of slip. Tempe Terra rifts are about 0.5 km deep and formed in the Late Noachian. Lengths of the faults were measured directly from surface maps.

Abundant compressional wrinkle ridges around Tharsis formed during the Early Hesperian. Interpretations of the subsurface structure of ridges include folds above reverse faults that extend a couple of kilometers deep (10). We applied a recent model (11) that infers subsurface thrust faults dipping about 30° that extend 5 km down dip with about 150 m of slip to the lengths of about 2000 ridges around Tharsis (9). In addition, we measured the length and average width (inferred depth) of Middle and Late Amazonian grabens, to derive fault areas and slips for these two youngest time periods. Caldera collapse also was included in the measurements of Late Amazonian activity, because a detailed seismologic study (12) on Earth shows that it occurs by an equivalent shear process, producing fairly large earthquakes. We measured the length of circular caldera faults on the tops of Olympus, Ascraeus, Pavonis and Arsia Mons, assumed the faults extend 10 km deep (13) and estimated slip from present relief (14). We assumed a μ of 10^{11} dyne/cm², based on likely properties of the outer layers of Mars (4), to calculate the total accumulated moment for each of the 4 time periods discussed above.

The total moment in each time period was divided by its duration, based on two crater/absolute age time scales (e.g., 15) to produce a plot of seismic moment release per year (M_0 /yr) through time. M_0 /yr was greatest during Late Noachian/Early Hesperian period of Tharsis deformation at $1.5-3.7 \times 10^{23}$ dyne-cm/yr, decreasing to $1 \times 10^{23}-5.1 \times 10^{22}$ dyne-cm/yr during the Late Hesperian/Early Amazonian Tharsis deformation period, and to $1.7 \times 10^{22}-4.7 \times 10^{21}$ dyne-cm/yr during the Middle and Late Amazonian periods. M_0 /yr during the first two periods is dominated by that contributed from Valles Marineris faults, which have large slip, depth and length. The decrease in M_0 /yr appears to follow an exponential decay toward the present, which argues that Mars is nearly as seismically active today as it has been for the entire Late Amazonian. The best estimate for the present, inferred for the Late Amazonian, or the past 250 m.y. is 1.3×10^{22} dyne-cm/yr. Assuming a moment-frequency distribution (16) similar to oceanic intraplate earthquakes allows determination of the number of marsquakes of a given moment per year. Results suggest hundreds of marsquakes of moment 10^{16} dyne-cm per year, about 1 marsquake of moment 10^{20} dyne-cm per year, and thousands of years between marsquakes of moment 10^{26} dyne-cm.

On the Earth, seismic activity is distributed over a range of earthquake magnitudes, described by the empirical relation $\log N = a - bm$, where N is the number of earthquakes larger than magnitude (m). The slope of the curve b is 0.9 for intraplate oceanic earthquakes (16). If we assume the largest marsquake is equivalent to a magnitude 6 earthquake, based on the largest shallow moonquake (17), the largest intraplate oceanic earthquake (18), and the smallest teleseismic marsquake likely to have been detected by Viking 2 (2), and we assume $b = 0.9$, we can calculate a distribution of marsquakes per year from M_0/yr , assuming a moment-magnitude relationship of the form $\log M_0 = A + Bm$ ($B=2.35$; $A=11.71$ [body-wave] for intraplate oceanic earthquakes; 18). The most likely present seismic moment release rate of 1.3×10^{22} dyne-cm/yr results in recurrence intervals of 435, 55, 7, and 1 yrs for equivalent body-wave magnitude 5-6, 4-5, 3-4, and 2-3 earthquakes on Mars, respectively. (A number of factors argue that an equivalent magnitude 4 earthquake on Mars would be similar in detectability to a magnitude 5 earthquake on the Earth [1].) Whereas, 7 years might be considered a long time to wait for an equivalent body-wave magnitude 3-4 earthquake on Mars, it must be remembered that these estimates are likely minima. For example on Earth, substantially more earthquakes occur without surface breaks than those that do produce faulting at the surface. If there are 100 earthquakes of a given magnitude without surface breakage for each earthquake with surface breakage, then these estimates predict about 2, 15, and 115 equivalent body-wave magnitude 4-5, 3-4, and 2-3 per year, respectively, on Mars at present. By way of calibration, we extrapolated the total moment release on the Moon at present from all observed grabens, which formed from 3.8-3.6 b.y. and mare wrinkle ridges, which formed from 3.6-3.0 b.y.; results predict a rate of moment release about 1000 times below that observed (10^{22} dyne-cm/yr [17, 20]). If our estimates for Mars are similarly low, then Mars could have of order 100 marsquakes of equivalent 3-6 Earth magnitude per year (about 2 per year of magnitude 5-6), which presents a promising prospect for future missions to Mars. These calculations predict a present day moment release for Mars of about 10^{25} dyne-cm/yr, which agrees with theoretical lithospheric cooling calculations for Mars (1, 19) and is midway between the total moment release (20) for the Moon (10^{22} dyne-cm/yr) and the Earth (10^{29} dyne-cm/yr) as would be expected.

References: (1) Solomon, Phillips, Okal et al. 1991 Mars Seis Net Wkshp Rpt. (2) Anderson et al. 1977 JGR 82, 4524, Goins & Lazarewicz 1979 GRL 6, 368. (3) Nakamura et al. 1979 PLPSC 10th 2299, Nakamura 1980 PLPSC 11th 1847. (4) Tanaka, Golombek & Banerdt 1991 sub JGR. (5) Scott and Dohm 1990 PLPSC 20th, 487. (6) Banerdt, Golombek & Tanaka 1991 "Stress and Tectonics on Mars", UA, Mars. (7) Davis & Golombek 1990 JGR 95, 14231. (8) Tanaka & Davis 1988 JGR 93, 14893. (9) Watters & Maxwell 1983 Icarus 56, 278. (10) Plescia & Golombek 1986 GSA Bull 79, 1289, Watters 1988 JGR 93, 10236. (11) Golombek et al. 1991 PLPSC 21st. (12) Filson et al. 1973 JGR 78, 8591. (13) Zuber & Mouginiis-Mark 1990 NASA TM 4210, 389, Thomas et al. 1990 JGR 95, 14345. (14) Mouginiis-Mark 1981 PLPSC 12th 1431, Pike 1978 PLPSC 9th 3239. (15) Tanaka 1986 PLPSC 17th E139. (16) Bergman & Solomon 1980 JGR 85, 5389 and pers. com. 1991. (17) Oberst 1987 JGR 92, 1397. (18) Bergman 1986 Tectonophys 132, 1. (19) Phillips & Grimm 1991 LPSci XXII 1061. (20) Goins et al. 1981 JGR 86, 378.

A 40TH DEGREE AND ORDER GRAVITATIONAL FIELD MODEL FOR MARS

M.T. Zuber¹, D.E. Smith¹, F.J. Lerch¹, R.S. Nerem¹, G.B. Patel², and S.K. Fricke³, ¹Laboratory for Terrestrial Physics, NASA/Goddard Space Flight Center, Greenbelt, MD 20771; ²ST Systems Corporation, Lanham, MD 20706; ³RMS Technologies, Inc., Lanham, MD 20706.

Understanding of the origin and evolution of major physiographic features on Mars, such as the hemispheric dichotomy and Tharsis rise, will require improved resolution of that planet's gravitational and topographic fields. The highest resolution gravity model for Mars published to date [1] was derived from Doppler tracking data from the Mariner 9 and Viking 1 and 2 spacecraft, and is of 18th degree and order. That field has a maximum spatial resolution of approximately 600 km, which is comparable to that of the best current topographic model [2]. The resolution of previous gravity models was limited not by data density, but rather by the computational resources available at the time. Because this restriction is no longer a limitation, we have re-analyzed the Viking and Mariner datasets and have derived a gravitational field complete to 40th degree and order with a corresponding maximum spatial resolution of 300 km where the data permit.

Derivation of the field was based on analysis of 235 orbital arcs consisting of 1200 days of S-band Doppler tracking data from the Mariner 9 and Viking 1 and 2 spacecraft, collected by the Deep Space Network from 1971-1978. The data were processed using the GEODYN/SOLVE orbit determination programs. These programs, which have previously been used in the determination of a series of standard Earth gravitational models (the 'GEM' models [cf. 3]), have recently been adapted for analysis of planetary tracking data [4].

The Martian gravitational potential at spacecraft altitude was represented in spherical harmonic form [5]

$$V_M(\vec{r}) = \frac{GM_M}{r} \sum_{l=0}^N \sum_{m=0}^l \left(\frac{r_M}{r} \right)^l P_m(\sin\phi) [C_{lm} \cos m\lambda + S_{lm} \sin m\lambda] \quad (1)$$

where \vec{r} is the position vector of the spacecraft in areocentric coordinates, r is the radial distance from the center of mass of Mars to the spacecraft, ϕ and λ are the areocentric latitude and longitude of the spacecraft, r_M is the mean radius of the reference ellipsoid of Mars, G is the gravitational constant, M_M is the mass of Mars, P_{lm} are the normalized associated Legendre functions of degree l and order m , C_{lm} and S_{lm} are the normalized spherical harmonic coefficients which were estimated from the tracking observations to define the gravitational model, and N is the maximum degree representing the size (or resolution) of the field. The gravitational force due to Mars which acts on the spacecraft corresponds to the gradient of the potential, V_M . In our analysis, the origin of the field was taken to be the center of mass of Mars, which required that $C_{00}=1$ and $S_{00}=C_{10}=C_{11}=S_{11}=0$.

To determine the field, orbits were computed for each arc by estimating from the tracking data the initial position and velocity of the spacecraft, along with the atmospheric drag, solar radiation pressure, and Doppler tracking biases. After the arc solutions were iterated to convergence, information equations were created for each arc by evaluating the partial derivatives of the observations with respect to the arc parameters and gravity coefficients along each arc. The gravitational model was then found by adding together the information equations for each arc and solving the resulting linear system. The dominant error sources in the model are the uncertainties in the spacecraft orbits, which are affected by the tracking coverage as well as the assumed models of atmospheric drag and solar radiation pressure, and perturbations caused by spacecraft angular momentum desaturations. Details of the treatment of these parameters are discussed in [4]. As in previous analyses [e.g. 1], we imposed *a priori* constraints on the model based upon Kaula's Rule [5] rescaled to Mars, which causes poorly observed (usually high degree and order) coefficients to tend toward zero, but has little effect on coefficients that are well sensed by the tracking data [3,6].

Error analyses based on the observation data demonstrate that the new field is characterized by

a significantly better rms orbital accuracy ($=0.212 \text{ cm s}^{-1}$) than previous models ([1]= 0.535 cm s^{-1}). In addition, the field shows a greater resolution of identifiable geological structures. Free air gravity anomalies calculated from the most recent iteration of the model, MGM-515, are plotted in Figure 1. As for previous models, the gravity anomalies correlate well with principal features of Martian topography, indicating either that topography is only partially compensated, or that deep-seated mantle processes are responsible for both the topography and gravity [7]. For the current model, gravity anomalies associated with essentially all major features, including volcanic shields, impact basins and the Valles Marineris, show considerably higher magnitudes than in previous models. A higher dynamic range of power (2100 m vs. 1950 m for [1]) is also observed in the geoid representation of the field. Figure 1 also shows a possible trend along the hemispheric dichotomy of Mars in the longitude range $120^\circ < \lambda < 240^\circ$. Free air anomalies across the dichotomy boundary would be inconsistent with a simple model of isostatic compensation due to a change in crustal thickness across the boundary, such as suggested by [8]. However, detailed modeling of individual arcs which cross the boundary in areas spatially removed from the influence of Tharsis and Elysium will be required to more accurately resolve the nature of the gravity signature of this feature.

References: [1] Balmino, G., B. Moynot, and N. Valès, *J. Geophys. Res.*, 87, 9735-9746, 1982. [2] Bills, B.G., and A.J. Ferrari, *J. Geophys. Res.*, 83, 3497-3508, 1978. [3] Marsh, J.G., et al., *J. Geophys. Res.*, 93, 6169-6125, 1988. [4] Smith, D.E., F.J. Lerch, J.C. Chan, D.S. Chinn, H.B. Iz, A. Mallama, and G.B. Patel, *J. Geophys. Res.*, 95, 14115-14167, 1990. [5] Kaula, W.M., *Theory of Satellite Geodesy*, 124 pp., Blaisdell, Waltham, 1966. [6] Lerch, F.J., et al., *NASA TM 100713*, 1988. [7] Phillips, R.J., and K. Lambeck, *Rev. Geophys.*, 18, 27-76, 1980. [8] Phillips, R.J., *EOS Trans. Am. Geophys. Un.*, 16, 389, 1988.

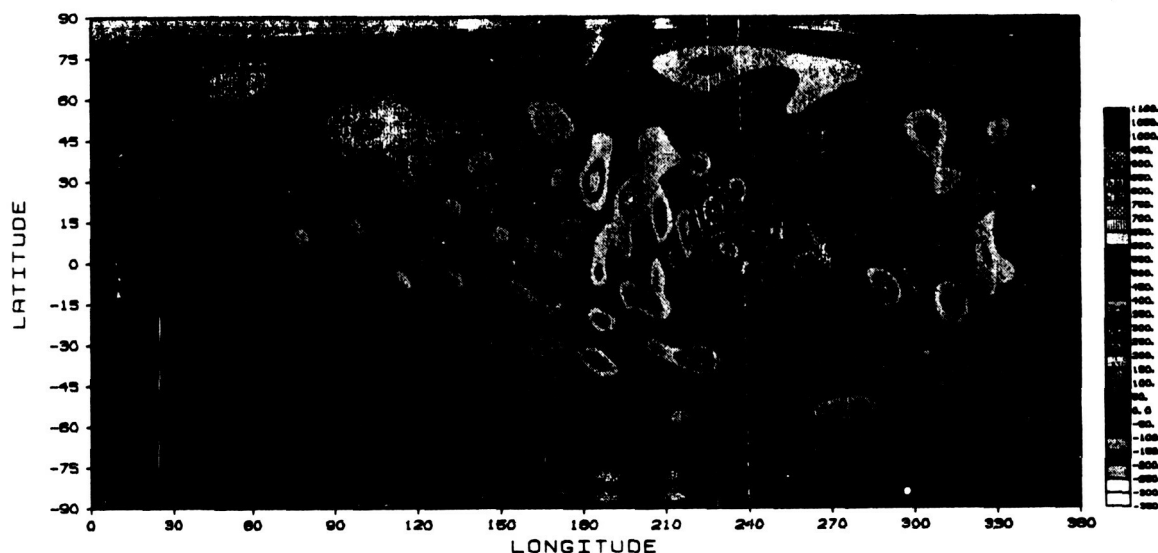


Figure 1. Free air gravity anomalies computed from Mars Gravity Model (MGM) 515 to 40×40 . The contour interval is 50 mgals.

ORIGINAL PAGE IS
OF POOR QUALITY

SO₂-RICH EQUATORIAL BASINS AND EPEIROGENY OF IO

Alfred S. McEwen, U.S. Geological Survey, Flagstaff, AZ 86001

OBSERVATIONS

Comparison of Io's large-scale topography (Gaskell et al., 1988) with an SO₂-abundance map (McEwen et al., 1988) shows that SO₂ is concentrated in equatorial topographic basins. In these basins, about 30% of the surface is covered by SO₂ at all elevations above the mean triaxial figure, and SO₂ coverage increases with decreasing elevation to as much as 56% at elevations below -1.5 km. The correlation is not good from long 240° to 360° where bright areas are covered by red, Pele-type plume fallout, and in the polar regions where the topography is poorly known. The histogram of SO₂ abundance binned by elevation appears bimodal, with a secondary concentration of SO₂ at high elevations, but it is not certain that this is significant.

Additional observations suggest that the basins have relatively little higher frequency topographic relief. The Loki basin was covered by Voyager high-resolution (1 km) images; the U.S. Geological Survey map (1987) shows this region to be devoid of large mountains or other rugged topographic features. Tectonic features and aligned volcanoes are concentric to the Loki basin (Schaber et al., 1989). In addition, limb images indicate that the Colchis Regio basin has little relief at scales greater than about 4 km (McEwen et al., 1989).

The distributions of active plumes and hotspots show no obvious correlation with the topography. However, the large Pele-type plumes (Pele, Surt, and Aten) all erupted from regions higher than the mean figure, and five of the eight Prometheus-type plumes erupted from regions below the mean figure. Pele-type eruptions are more energetic and are associated with high-temperature (600 K) hotspots, whereas Prometheus-type plumes are long lived and require large volatile (SO₂) reservoirs (McEwen and Soderblom, 1983). The hotspot distribution shows no clear pattern in relation to the topography, but one cannot rule out their concentration near the margins of basins and swells, similar to the pattern of recent volcanism and enhanced heat flow around the margins of the Colorado Plateau (e.g., Keller et al., 1979). However, possible plateau margins are difficult to locate in the Io topographic dataset because of the sparse and irregular datapoint distribution.

MODELS OF HEAT FLOW AND UPLIFT

The pattern of alternating basins and swells in Io's equatorial region (Gaskell et al., 1988) is similar to the pattern expected if tidal heating in a thin asthenosphere controls the elevation (Segatz et al., 1988). A key question concerning the SO₂/topography relation is whether heat flow increases or decreases with elevation. Gaskell et al. (1988) proposed that broad uplifts are due to increased heat flow and lithospheric thinning, as has been documented and modeled for broad uplifts on Earth, both

oceanic and continental (Crough and Thompson, 1976; Morgan, 1983; many others). Gaskell et al. applied a simple lithospheric thinning model (from Morgan and Phillips, 1983) to Io and showed that epeirogenic movements of ± 1 km could be explained. This model includes only a lithosphere and asthenosphere, with no differentiated crust. Inclusion of a crust has little effect on uplift unless thinning progresses into the crust (Morgan, 1983).

Ross et al. (1990) interpreted literally this model simplification (with no crust) and rejected it because of evidence that Io should be differentiated, and because this model did not seem consistent with the polar topography (even though the polar topographic data are poorly constrained). They proposed that the basins correspond to areas of higher heat flow, but they did not explain how increased heat flow could lead to lower elevations. Their model (Fig. 6 cartoon) shows a thick "differentiated lithosphere" (i.e., crust with no thermal lithosphere) under topographic highs with a large embayment into the underlying asthenosphere, and a thin lithosphere in topographic lows with an embayment of asthenosphere into the lithosphere. Why would there be a thicker crust over areas of lower asthenospheric heat production? The opposite relation is expected, because the increased magmatic differentiation should thicken the crust over areas of higher asthenospheric heat production. Furthermore, magma production and rise is expected to result in warming and thinning of the lithosphere (or crust), resulting in epeirogenic uplift. If Io's long-wavelength topographic pattern is related to asthenospheric tidal dissipation, then the cause-and-effect relation must be that the pattern of tidal heat production determines the topography. The model of Ross et al. suggests that any correspondence between topography and asthenospheric heat flow is coincidental, thus negating their conclusions about asthenospheric versus mantle tidal heating rates.

WHY IS THE SO₂ CONCENTRATED IN BASINS?

Cold trapping probably concentrates SO₂ frost in optically thick patches (cf. McEwen et al., 1988). There must be some initial mechanism to produce brighter (and colder) surfaces before cold trapping is effective. To preferentially concentrate SO₂ in the basins, either the cold traps are preferentially initiated in the basins or frost deposits are preferentially removed from the highlands (or both).

The behavior of sulfur flows suggests one possible mechanism for initiating cold traps in basins. Sulfur lava flows may cover extensive lowland areas on Io (e.g., the basin west of Pele; see Schaber et al., 1989). As sulfur flows cool and age in near-vacuum conditions they become bright white (Nash, 1987), thus initiating cold traps for atmospheric/volcanic SO₂.

Alternatively (or additionally), SO₂ may be concentrated in basins because the frost deposits are removed or buried more frequently in the highland regions. Io's SO₂ is probably delivered to the surface via volcanic outgassing, so we might expect to see

greater concentrations of SO₂ near volcanically active areas. However, the increased heat flow associated with active volcanism might also serve to volatilize and remove surface SO₂, or the SO₂ could be buried by other volcanic deposits. The result could be that we see SO₂ everywhere, but it is patchy and transient in the more volcanically active, topographically elevated regions, whereas cold traps in the basins are long lived so the SO₂ becomes optically thick and extensive. Perhaps the secondary SO₂ concentration at high elevations is due to volcanic outgassing.

REFERENCES

- Crough, S. T., and Thompson, G. A., 1976, Numerical and approximate solutions for lithospheric thickening and thinning. *Earth Plan. Sci. Lett.* 31, 397-402.
- Gaskell, R. W., Synnott, S. P., McEwen, A. S., and Schaber, G. G., 1988, Large-scale topography of Io: Implications for internal structure and heat transfer. *J. Geophys. Res.* 15, 581-584.
- Keller, G. R., Braile, L. W., and Morgan, P., 1979, Crustal structure, geophysical models, and contemporary tectonism of the Colorado Plateau. *Tectonophysics* 61, 131-147.
- McEwen, A. S., Johnson, T. V., Matson, D. L., and Soderblom, L. A., 1988, The global distribution, abundance, and stability of SO₂ on Io. *Icarus* 75, 450-478.
- McEwen, A. S., Lunine, J. I., and Carr, M. H., 1989, Dynamic geophysics of Io. *In* Belton, M. J. S., West, R. A., and Rahe, J., eds., *Time-Variable Phenomena in the Jovian System*, NASA SP-494, 11-46.
- McEwen, A. S., and Soderblom, L. A., 1983, Two classes of volcanic plumes on Io. *Icarus* 55, 191-217.
- Morgan, P., 1983, Constraints on rift thermal processes from heat flow and uplift. *Tectonophysics* 94, 277-298.
- Morgan, P., and Phillips, R. J., 1983, Hot spot heat transfer: Its application to Venus and implications to Venus and Earth. *J. Geophys. Res.* 88, 8305-8317.
- Nash, D. B., 1987, Sulfur in vacuum: Sublimation effects on frozen melts, and applications to Io's surface and torus. *Icarus* 72, 1-34.
- Ross, M. N., Schubert, G., Spohn, T., and Gaskell, R. W., 1990, Internal structure of Io and the global distribution of its topography. *Icarus* 85, 309-325.
- Schaber, G. G., Scott, D. H., and Greeley, R., 1989, Geologic map of the Ruwa Patera quadrangle of Io (Ji2). USGS Misc. Inv. Ser. Map I-1980, scale 1:5,000,000.
- Segatz, M., Spohn, T., Ross, M., and Schubert, G., 1988, Tidal dissipation, surface heat flow, and figure of viscoelastic models of Io. *Icarus* 75, 187-206.
- U.S. Geological Survey, 1987, Shaded relief map of Io. USGS Misc. Inv. Ser. Map I-1713, scale 1:15,000,000.

N92-10762 !

STRUCTURAL GEOLOGY AND GEOLOGICAL HISTORY OF THE PERRINE AND NUN SULCI QUADRANGLES (Jg-2 AND Jg-5), GANYMEDE.

George E. McGill, Department of Geology and Geography, University of Massachusetts, Amherst, MA, and Steven W. Squyres, Center for Radiophysics and Space Research, Cornell University, Ithaca, NY.

Structural Geology: Grooves are the dominant structural features on Ganymede. While single grooves are found in many areas, it is somewhat more common to find them grouped together in groove sets -- groupings of grooves with common structural trends. Grooves in sets are often nearly parallel, but fan-shaped sets are also observed. Groove spacing can vary substantially from one groove set to another, but within a given set tends to be more nearly constant. Sets may intersect with one another in complex crosscutting relationships, and the central region of Jg-5 is one of the most complicated on Ganymede in this regard. Where one groove set crosscuts another, no trace of the cut groove set is generally observed within the crosscutting set. There are a few exceptions to this rule, however, as at 40°N, 314°W. The boundaries of groove sets are often marked by particularly long and deep grooves, and the boundary between light and dark terrain is commonly marked by a single groove, or by a groove set that lies in the light terrain and parallels the boundary.

It is generally believed that the grooves on Ganymede are extensional features (Smith et al., 1979a, b; Squyres, 1980; Parmentier et al., 1982). Their underlying geologic nature cannot be determined from Voyager images, however. It appears likely that they are grabens, but the images are insufficient to rule out the possibility that they are modified extension fractures or some kind of ductile necking features. The interpretation of grooves (and groove sets) as extensional features leads to interesting possible interpretations of some structural relationships. One common relationship among grooves occurs where a groove set terminates abruptly against a single groove or groove set that runs transverse to it. In such cases, it is probably not correct to infer that the terminated groove set predates the feature cutting it. Instead, extensional deformation in the truncated groove set most likely postdates the truncating feature, with the truncating feature acting as an older margin. This interpretation is similar to that generally inferred for truncating relationships among sets of rock joints on the earth.

There is some direct but limited evidence for structural shear in the map region, seen where groove sets appear to be offset by several tens of km along narrow shear zones. Compelling evidence for compression is limited, although the feature at 40°N, 314°W cited above appears to possess parallel ridges rather than grooves, and could be compressional.

Geological History: The oldest materials within the Nun Sulci and Perrine quadrangles occur within the cratered dark materials (dc) unit (McGill and Squyres, 1991), as is generally the case for all of Ganymede. This is the most widespread of the dark units mapped in these two quadrangles. Crater densities within cratered dark materials are consistent with an age on the order of several billions of years (Smith et al., 1979a), and thus cratered dark terrain probably represents crust that has survived from the end of the primordial intense bombardment phase of solar-system history. The second most widespread dark unit is grooved dark materials (dg). Within the Nun Sulci and Perrine quadrangles it is not clear if any of the grooves that define this unit are older than light materials. Many grooves clearly pass from grooved light materials into

grooved dark materials, and there are no unequivocal truncation relationships suggesting that the grooves in the dark terrains are older than similar-appearing grooves in abutting grooved light materials. Consequently, it is possible that grooved dark materials were originally the same as cratered dark materials. The present difference in appearance and the apparently smaller density of superposed craters would thus be due to structural modification at the time of global groove formation.

After formation and cratering of the old crust now represented by the dark materials this crust was fractured and dismembered, with widespread emplacement of light materials between or on top of the surviving crustal fragments. The process of emplacement is inferred to be extrusion of relatively ice-rich magmas. The resulting light materials were subsequently extensively faulted, resulting in the intricate pattern of grooves which characterizes much of the light terrain in these quadrangles. Complex cross-cutting and truncation relationships indicate that faulting and groove formation occurred over a protracted time period, and that it almost certainly overlapped in time with the extrusion of ice-rich magmas. Furthermore, in some places clear truncation relationships indicate that smooth light materials are younger than the grooves in adjacent grooved light and dark terrains, indicating that ice volcanism continued after local cessation of groove formation.

Impact structures were forming throughout the history recorded by the light and dark materials. Basins and degraded large craters (C_1) are superposed on cratered dark materials but not on grooved dark materials or on light materials. As discussed above, they may once have existed on grooved dark materials and subsequently been rendered unrecognizable on the available images by younger grooving. It is not likely that C_1 craters and basins ever existed on any of the light units. Well preserved craters without bright ejecta (C_2) are the most abundant class of craters. Some of these are clearly older than light materials, but most are probably younger than all light units except possibly smooth light materials. Bright ray craters (C_3) appear to be younger than all light and dark units.

Two palimpsests occur in the Nun Sulci quadrangle. One of these ($356^{\circ}\text{W } 29^{\circ}\text{N}$) is very ancient, and probably is the oldest impact structure in this area. The second palimpsest ($335^{\circ}\text{W } 30^{\circ}\text{N}$) is something of an anomaly because it is superposed on light materials and is thus much younger than most palimpsests found on Ganymede (Thomas and Squyres, 1990). The change from the formation of palimpsests to the formation of lunar-like multi-ringed basins probably reflected a change in the rheology of Ganymede's crust and lithosphere (Passey and Shoemaker, 1982). If so, the existence of a relatively young palimpsest on light terrain implies two periods of rheology transition; an early one for crust with low-albedo surfaces, and a much later one for crust with high-albedo surfaces.

This brief geological history is almost certainly greatly oversimplified as a result of the poor resolution and unfavorable viewing geometry of most the images covering this area. Textural features that are just at the resolution limit of the best images suggest that a much more complex and more interesting history can be inferred when better images are returned by some future mission.

References Cited:

McGill, G.E. and S.W. Squyres, 1991, Stratigraphy of the Perrine and Nun Sulci quadrangles (Jg-2 and Jg-5), Ganymede, *This Volume*.

Passey, Q.R., and Shoemaker, E.M., 1982, Craters and basins on Ganymede and Callisto: morphological indicators of crustal evolution, in Morrison, D., ed., *Satellites of Jupiter*: Tucson, University of Arizona Press, p. 379-434.

Parmentier, E.M., Squyres, S.W., Head, J.W., and Allison, M.L., 1982, The tectonics of Ganymede: *Nature*, vol. 295, p. 290-293.

Smith, B.A., and the Voyager Imaging Team, 1979a, The Jupiter system through the eyes of Voyager 1: *Science*, vol. 204, p. 951-972.

Smith, B.A., and the Voyager Imaging Team, 1979b, The Galilean satellites and Jupiter: *Science*, vol. 206, p. 927-950.

Squyres, S.W., 1980, Volume changes in Ganymede and Callisto and the origin of grooved terrain: *Geophysical Research Letters*, vol. 7, p. 593-596.

Thomas, P.J., and Squyres, S.W., 1990, Formation of crater palimpsests on Ganymede: *Jour. Geophys. Res.*, 95, 19,161-19,174.

TECTONIC DEFORMATION ON ICY SATELLITES: A MODEL OF COMPENSATING HORSTS;

Robert Pappalardo and Ronald Greeley, Department of Geology, Arizona State University, Tempe, Arizona 85287

Voyager images demonstrate that the icy satellites have been shaped by a variety of magmatic and tectonic processes, of which ridge and trough terrain is a manifestation. This terrain is observed on Ganymede, Enceladus, Miranda, and Ariel, and many models have been proposed to explain its origin. A likely model is horst-and-graben style normal faulting, in which horizontal extension results in a series of downdropped grabens and relatively uplifted horsts. The apparent negative elevation of ridges and troughs relative to surrounding terrain has been used to argue such an extensional-tectonic origin for ridge and trough terrain on Ganymede [1] and Enceladus [2]. A ridge or ridge set which stands above a presumed original base level, on the other hand, might be suspect of having a magmatic or compressional origin.

It has been demonstrated that rotation of "domino-style" normal faulting, which involves rotation of fault blocks about a fulcrum, can allow ridges to stand slightly above the original base level [3], and this relative uplift may be amplified by isostatic uplift [4]. Isostatic compensation of an individual graben underlain by a ductile layer is commonly manifest as upraised rift flanks, as predicted theoretically [5,6] and manifest in laboratory experiments of horst-and-graben normal faulting [7].

Compensation might also be accomplished through uplift of adjacent horsts [6,8]. Although in nature compensation is likely partitioned between uplift of horsts and internal deformation of blocks, we examine the case of a series of horsts and grabens underlain by a ductile material in which compensation of graben downdrop is accomplished exclusively through horst uplift. This allows geometrical estimation of the absolute amounts of graben downdrop and horst uplift relative to the original (pre-faulting) base level.

Figure 1 illustrates the downdrop by an amount h_1 of a series of identical trapezoidal grabens, displacing a volume proportional to this downdrop and the length L_1 of each graben's base. Ductile material flows beneath the two adjacent horsts causing their uplift, and each horst is forced upward by material displaced by its two neighboring grabens. Equating the volume displaced by a graben to that causing horst uplift, as for the case of a single horst and graben pair [6],

$$L_1 h_1 + \frac{h_1^2}{\tan \delta} = L_2 h_2 + \frac{h_2^2}{\tan \delta} \quad (1)$$

where L_2 is the base length and h_2 the vertical uplift of each horst, and δ is the dip of each graben's downward-converging bounding faults, assumed to remain constant with depth. Friction on the faults is taken to be negligible. The base length of each graben is related to its observable surface width T_w as

$$L_1 = T_w - \frac{2t}{\tan \delta} \quad (2a)$$

and horst base length is related to surface width R_w as

$$L_2 = R_w + \frac{2t}{\tan \delta} \quad (2b)$$

where t is the original (unfaulted) thickness of the brittle layer. The assumed geometry of the fault blocks constrains the layer's thickness to $t \leq 0.5 T_w \tan \delta$. The relation

$$h_1 + h_2 = d \quad (3)$$

links displacements h_1 and h_2 to the observed final elevation difference d between two neighboring blocks. Equations (1), (2), and (3) combine to give

$$h_1 = d \frac{R_w \tan \delta + 2t + d}{(R_w + T_w) \tan \delta + 2d} \quad (4)$$

and h_2 can be obtained from equation (3). In this way the absolute vertical displacement of horst and graben blocks relative to an original base level can be related to model parameters.

Figures 2a and 2b illustrate the effects of brittle layer thickness t and fault dip ($\delta = 40-90^\circ$) on the total vertical displacement of horsts and grabens. Figure 2a shows a "grooved" case ($R_w > T_w$), which could

pertain to areas of "grooved terrain" on Ganymede ($R_w = 8$ km; $T_w = 4$ km); Figure 2b is for a "ridged" case ($R_w < T_w$) and may pertain to Elsinore Corona, Miranda ($R_w = 4$ km; $T_w = 8$ km). In both examples, d is taken to be 0.4 km. Relative horst uplift increases with increased fault dip, decreased t , and a greater difference $T_w - R_w$.

As illustrated by Figure 2b, if horsts are more narrow than their intervening grabens, there exists a critical layer thickness

$$t_{crit} = 0.25(T_w - R_w) \tan \delta \quad (5)$$

at which $h_2 = h_1 = d/2$. If $t < t_{crit}$, then a greater portion of the total observed elevation difference d is due to horst uplift above the original base level rather than to graben downdrop. In the example of Figure 2b, for $\delta = 50^\circ$, $t_{crit} = 1.2$ km. The thinner the brittle plate relative to t_{crit} , the greater the difference between ridge uplift and trough downdrop.

The compensating horsts model demonstrates that horsts may stand above the level of surrounding unfaulted terrain if isostatic compensation is accomplished through (or significantly partitioned into) horst uplift. Indeed, the magnitude of horst uplift may exceed that of graben downdrop if horst width is less than graben width. This should be considered when evaluating ridge-and-trough-forming processes on icy satellites and elsewhere.

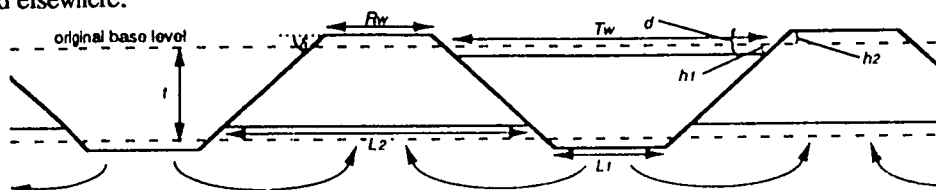
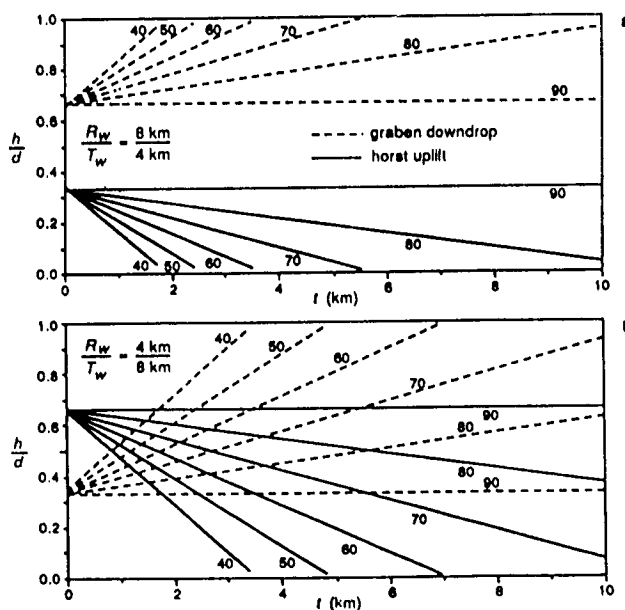


Figure 1.



- [1] Shoemaker, E.M. et al., in *Satellites of Jupiter*, p. 435, 1982. [2] Squyres, S.W. et al., *Icarus*, 53, 319, 1983. [3] Leeder, M.R. and R.L. Gawthorpe, in *Continental Extensional Tectonics*, p. 139, 1987; Barr, D., *J. Struct. Geol.*, 9, 491, 1987. [4] Jackson, J.A. and D. McKenzie, *J. Struct. Geol.*, 5, 471, 1983. [5] Heiskanen, W.A. and F.A. Vening Meinesz, *The Earth and its Gravity Field*, 1958. [6] Bott, M.H.P., *Tectonophys.*, 36, 77, 1976. [7] McGill, G.E. and A.W. Stromquist, *JGR*, 84, 1979; Vendeville, B. et al., in *Continental Extensional Tectonics*, p. 95, 1987. [8] Lonsdale, P., *Mar. Geophys. Res.*, 3, 251, 1977.

Mimas: Tectonic Structure and Geologic History.

Steven K. Croft. Lunar & Planetary Laboratory, University of Arizona, AZ 85721.

Introduction. Mimas, the innermost of the major saturnian satellites, occupies an important place in comparative studies of icy satellites. It is the smallest icy satellite (mean radius = 199 km) known to have an essentially spherical shape (Thomas et al., 1986). Smaller icy objects like Hyperion and Puck are generally irregular in shape, while larger ones like Miranda and Enceladus are spherical. Only Proteus, a newly discovered satellite of Neptune (1989N1, see Smith et al., 1989), is slightly larger than Mimas and yet has a significantly non-spherical shape. Thus Mimas is near the diameter where the combination of increasing surface gravity and internal heating begin to have a significant effect on global structure. The nature and extent of endogenic surface features provide important constraints on the interior structure and history of this transitional body.

The major landforms on Mimas are impact craters. Mimas has one of the most heavily cratered surfaces in the Solar System (Plescia & Boyce, 1982; Strom, 1987; Lissauer et al., 1988). The most prominent single feature on Mimas is Herschel, an unrelaxed complex crater 130 kilometers in diameter. Relative to the radius of the satellites, Herschel is one of the largest craters in the solar system. The craters themselves are unremarkable, with morphologies and dimensions comparable to craters on other icy satellites (Schenk, 1989).

The only other recognized landforms on Mimas are tectonic grooves and lineaments. These structures were briefly described by Smith et al. (1981). Groove locations were mapped by Schenk (1985, 1989) in a search for directional trends that could related to recognizable stress sources, but without analysis of groove structures or superposition relationships. Mimas' tectonic structures are re-mapped here (Figure 1) in more detail than previously as part of a general study of tectonic features on icy satellites.

Description. Mimas' tectonic features have been divided into three major classes on the basis of width, morphology and relative age. Subclasses are defined on the basis of orientation.

Class 1: Fresh Chasmata. Only two features are included in this class, Ossa and Pelion Chasmata. Although they are not the largest tectonic features, they are the most prominent. These chasmata are V-shaped troughs typically 10 km wide, 2 - 3 km deep, and in segments 100 to 150 km long. The depths are based on photoclinometric profiles (Schenk, 1989), limb profiles (Dermott & Thomas, 1988), and stereo comparison with nearby fresh craters. The chasmata form a single system oriented roughly east-west between 20° and 30° south latitude. A circle fit to the chasmata segments by least-squares has a center at 57.5° N, 258° W and an angular diameter of 172°, very nearly a great circle. These features formed relatively late in Mimas' geologic history: they are superposed by several fresh craters, but cut through older, more degraded craters.

Class 2: lineaments. This class comprises a large number of long, narrow features. Lineament widths range from near the limit of resolution (1-2 km on the best images) to about 4 km. Lineament segments range in length from a few tens to several hundreds of kilometers. Vertical topographies are estimated to be on the order of hundreds of meters. Lineaments exhibit a variety of morphologies: a) scarps or ridges, good examples are located tangent to the crater Gawain in FDS #s 34938.18, 34940.34; b) graben-like grooves, good examples between the crater Arthur and Pelion chasma and just south of the craters Uther and Igraine; and c) and at least one chain of pits running north-south between 30° and 60° south near 350° west.

Most of the lineaments are members of curvilinear sets of parallel structures with fairly constant spacings and distinct orientations. Five sets are defined in Table 1, labeled by nearby features for convenience. There are also a few individual lineaments which cross the labeled sets at significant angles: one centered near 40° S, 340° W crossing set 1 at an angle near 60°, another near 40° S, 290° W crossing set 2 at near 60° (both seen in FDS #34944.21), and a poorly defined feature near 30° N, 195° W crossing set 4 at nearly right angles (best seen in FDS #34938.18). The first two individual lineaments cross Pangea Chasma and are roughly parallel to each other. There are a number of other possible lineament segments between these two lineaments visible in FDS #34944.21 that appear to follow the same directional trend. These features may comprise another lineament set ("Trans-Pangea"), but if so, they are very poorly defined. Sets 1 & 3 are topographically prominent compared to sets 2 & 4, probably in part because sets 2 & 4 are imaged at significantly higher sun angles than sets 1 & 3. Set 5 is also topographically prominent, but less well characterized because of the significantly lower resolutions (4-6 km/pixel) at which it was imaged. Most of the lineament sets may be parts of a single global system: extrapolation of the gently curving trend of set 2 connects smoothly onto the trends of set 3; set 1 trends change smoothly in a counter-clockwise sense from W to E, becoming close to the trends of set 3 near the common boundary of both sets; certainly the trends of both sets 1 & 3 become nearly parallel in the south polar area and connect directly onto the trends of set 5. It must be noted that though the trends may be concordant between sets, lineaments directly connecting the sets, particularly over the south pole area, have not been found, perhaps due to the limited imagery.

Superposition relations indicate that most of the lineaments formed relatively late in Mimas' geologic history. Like the fresh chasmata, the lineaments in the sets cross some impact craters and are cut by others. Straight sections of the rims of some fresh craters (e.g., SW rim of Igraine) also indicate the establishment of the structural pattern before the formation of many of the fresh craters. Set 5 crosses Herschel, indicating structural activity after Herschel's formation. Superposition relations between the lineament sets and the fresh chasmata are uncertain. Ossa Chasma cuts across the trends of several lineaments in set 2. No continuation of lineament structure can be seen across Ossa's floor (see FDS #34940.34) and a lineament may form a "T"-type termination (see Golombek & Allison, 1981) at Ossa's eastern end, suggesting a later formation for the chasma. However, the resolution of available images is too poor to be sure. The "trans-Pangea" and the other individual lineament are heavily degraded and are very difficult to trace at times, suggesting that they are substantially older than the lineament sets.

Class 3: Degraded Chasmata. The largest tectonic features on Mimas are the degraded chasmata and scarps. This group of features includes the other named chasmata (Oeta, Avalon, Tintagil, Pangea, and Camelot), and a few large, apparently unpaired scarps. These scarps, previously undocumented, occur between the craters Herschel and Morgan, and define three large horst-like blocks centered near: 1) 15° S, 150° W (seen in FDS #34933.50, 34936.23, and 34938.18 on the terminator), 2) 40° N, 157° W (FDS #34933.50 and 34936.23), and 3) 15° N, 182° W (FDS #34936.23 and 34938.18). The eastern sides of the blocks parallel the Avalon and Oeta chasmata, whereas the western sides of the latter two blocks are more north-south. The chasmata are typically 15-20 km wide and a few kilometers deep. Most of the degraded chasmata appear to form a single globe-girdling set of features reminiscent of the Ithaca Chasma system of chasmata on Tethys: Avalon, Oeta, Tintagil, and Pangea chasmata all fall within a few degrees of a great circle with a pole near 30° S, 67° W, and define about 212° of its circumference. Camelot Chasma and its branch past Iseult crater angle about 30° counter-clockwise away from the "great circle" system, thus bearing about the same relation to it as the Polar-Odysseus Tangent chasmata on Tethys bear to the Ithaca system (Croft, 1991).

As implied by the class designation, all of these features are heavily degraded by superposed impact craters. Their heavily cratered state indicates that they are older than most of the lineaments, and the "trans-Pangea" group lineaments cross Pangea Chasma. Two lines of evidence suggest that these chasmata predate Herschel. First, the scarps and chasmata appear more heavily cratered than Herschel, and many of the superposing craters are muted in appearance, suggesting that they are overlain by Herschel ejecta (Schenk,

1989). Second, Oeta Chasma is directly superposed by Herschel. Pangea and Camelot Chasmata cannot be directly related to Herschel stratigraphically. If Pangea Chasma is part of the same system as Avalon, etc., then it may have formed at the same time (prior to Herschel). However, just as the Ithaca system has segments of different ages, Pangea may not have formed at the same time as Avalon/Tintagil. Camelot is placed in the same group because of its heavily cratered appearance.

Other Features. A search was made for other geologic features that might not be due to impact or tectonic processes. None were noted except a horseshoe-shaped dark patch about 50 km wide and 70 km long near 20° S, 357° W visible in the last and highest resolution sequence of images of Mimas (FDS #34944.17 ff). The patch is about 20% darker than its surroundings, but does not stand out on the color ratio map of Buratti et al. (1990). The patch does not appear to be due to partial shadowing; although part of it lies in a shallow trough, it also extends over the rolling cratered terrain; further, the patch makes a continuous 180° turn without an obvious break or change in apparent albedo, difficult to achieve by topographic alone. The edges of the patch are moderately sharp. The patch appears to be dark material draped over the topography of the heavily cratered surface with no apparent thickness. The arms of the horseshoe extend along lines parallel to nearby Pangea Chasmata. No similar feature was seen elsewhere on Mimas.

Discussion. The range in preservation states of Mimas' tectonic features, and superposition relations between them and the craters indicate that tectonic activity continued over a period of time comparable to that required to form the suite of visible craters. The degraded chasmata formed first, followed by the Herschel impact, and then the lineaments and the fresh chasmata. If this order is correct, it implies that most of the tectonic strain was generated before the Herschel impact.

The number and locations of tectonic features found here largely agree with those mapped by Schenk (1989). He proposed that the grooves may be related to the formation of Herschel, but that groove orientations may also permit a tidal origin as well. Schenk grouped all of the mapped features together in his stress trajectory analyses. However, as noted here, the tectonic features can be divided into classes with different morphologies, orientations and formation times, suggesting that more than one stress source may need to be invoked to account for them.

The axis of the fresh chasmata system is approximately radial to the crater Herschel: a great circle fit to the segments is tangent to Herschel's NNW rim. Schenk (1989) suggested that this geometry indicated that these chasmata may be due to fracturing by the Herschel impact, perhaps analogous to the grooves on Phobos around the crater Stickney (Thomas, 1979). This is certainly possible as there are some similarities. However, the chasmata are in the hemisphere antipodal to Herschel and no fresh chasmata occur closer than about 90° from the crater, whereas the most prominent grooves on Phobos cluster on Stickney's rim. The lineaments that do cross Herschel appear not to be related to fresh chasmata system.

Lineament set trends can be fit into at least two possible global frameworks. First, sets 1, 2, 3, and 5 can be interpreted as parts of a roughly concentric set of lineaments centered near 20° N, 190° W. The "center" is poorly determined due to the broad width of the sets and the lack of images that could constrain the extent and trends of the assumed system into the northern hemisphere. Such a concentric system could be related to cyclic tidal deformation resulting from high orbital eccentricity (Helfenstein & Parmentier, 1980), but relative to a different long axis than the current one. Set 4 does not seem to fit this putative global concentric pattern, as its trends are at roughly right angles to its eastern neighbor, set 5. Thus set 4 and the individual lineaments would need to have been formed by a different set of stresses than sets 1, 2, 3, and 5. Second, all of the lineament sets may be parts of a global set of conjugate fractures running around Mimas' equator. If the "trans-Pangea" set is real, the cross pattern between them and set 1 would be an example of a conjugate set. Such a system could be due to tidal despinning superposed on global expansion (Melosh, 1977). However, no circumpolar normal faults also predicted by the despinning model are apparent. Further, lineament cross-patterns are not apparent in the other images, only single trends. Finally, the broadly curved traces of the lineaments and the change in trends within and between sets (e.g., set 1) do not appear to follow a simple conjugate fracture pattern.

The origin of the degraded chasmata system might be attributed to the formation of Herschel analogous to Odysseus and Ithaca on Tethys. However, in this case, the pole of the great circle is a crater radius outside Herschel's rim, and the chasmata are apparently older than the crater, indicating that the degraded chasmata are unrelated to the giant impact. The origin of the system is unclear. It may be related to internal convection patterns.

Based on morphology, the tectonic features on Mimas are all interpreted as extensional in origin. No compressional features appear to be present. The areal extension represented by the classes of tectonic features can be estimated using the method of Golombek (1982), in which the new area (A) for each scarp is related to the length (L), depth (d), and assumed angle of dip (Θ) for the underlying faults by: $A = Ld/\tan(\Theta)$. Adopting $\Theta = 60^\circ$ and noting that features like the chasmata have 2 scarps (twice the area of a single scarp) yields the following areal increases from the cumulative measured lengths of the three tectonic groups: 1) fresh chasmata (adopted $d = 3$ km) - 0.4%, 2) lineaments ($d = 0.3$ km) - 0.2%, and 3) degraded chasmata ($d = 2$ km) - 1.2%. Given the obvious uncertainty in the adopted depths, these estimates are probably only good to within a factor of 2. However, these results: 1) indicate the relative tectonic importance of the different classes of features, 2) are similar to the expansion estimates obtained for the uranian satellites (Croft & Soderblom, 1990). Neither the inferred areal expansion nor the implied failure stresses (10-20 bars) can be obtained from traditional thermal models for Mimas (e.g., Ellsworth & Schubert, 1983). However, preliminary calculations indicate that both the expansion and necessary stress levels can be reached for Mimas if a deep, low conductivity regolith is assumed.

The question of cryovolcanic activity on Mimas is unresolved. Plescia & Boyce (1982) resurfacing in the south polar area on the basis of a local paucity of large craters. Lissauer et al. (1988), however, suggest that the lack of large craters in the area is consistent with random statistical variations, and thus does not constitute evidence for resurfacing. There are no apparent extrusive features on Mimas, unless the dark albedo spot is one. The characteristics of the patch may be accounted for by low-energy extrusion or expulsion along pre-existing fractures, somewhat like the swirls on Dione and Rhea. Its orientation along trends parallel to nearby chasmata is consistent with this model. However, the feature also resembles dark deposits around impact craters on other icy satellites unrelated to extrusive processes.

References

- Croft, S.K. (1991) Tethys' geology and tectonics revisited. This volume.
Dermott, S.F. and P.C. Thomas (1988) The shape and internal structure of Mimas. *Icarus* 73: 25-65.
Golombek, M.P. (1982) Constraints on the expansion of Ganymede and the thickness of the lithosphere. *Proc. Lunar Planet. Sci. Conf. 13th, J. Geophys. Res.* 87(Supp.): A77-A83.
Golombek, M.P. and M.L. Allison (1981) Sequential development of grooved terrain and polygons on Ganymede. *Geophys. Res. Lett.* 8: 1139-1142.
Helfenstein, P. and E.M. Parmentier (1980) Fractures on Europa: possible response of an ice crust to tidal deformation. *Proc. Lunar Planet. Sci. Conf. 11th*, p. 1987-1998.
Lissauer, J.J., S.W. Squyres, and W.K. Hartmann (1988) Bombardment history of the Saturn system. *J. Geophys. Res.* 93: 13,776-13,804.

Plescia, J.B. and J.M. Boyce (1982) Crater densities and geological histories of Rhea, Dione, Mimas, and Tethys. *Nature* 295: 285-290.

Strom, R.G. (1987) The Solar System cratering record: Voyager 2 results at Uranus and implications for the origin of impacting objects. *Icarus* 70: 517-535.

Schenk, P.M. (1985) Mimas grooves and catastrophic breakup revisited. *Bull. Amer. Astron. Soc.* 17: 738-739.

Schenk, P.M. (1989) Mimas grooves, the Herschel impact, and tidal stresses. *Lunar Planet. Sci.* XX, p. 960-961, Lunar & Planetary Inst.

Smith, B.A. and the Voyager Imaging Team (1981) Encounter with Saturn: Voyager 1 imaging science results. *Science* 212: 163-191.

Smith, B.A. and the Voyager Imaging Team (1989) Voyager 2 at Neptune: imaging science results. *Science* 246: 1422-1449.

Suyres, S.W. and S.K. Croft (1986) The tectonics of icy satellites. In *Satellites*, J.A. Burns and M.S. Matthews, editors, pp. 293-341, Univ. of Arizona Press.

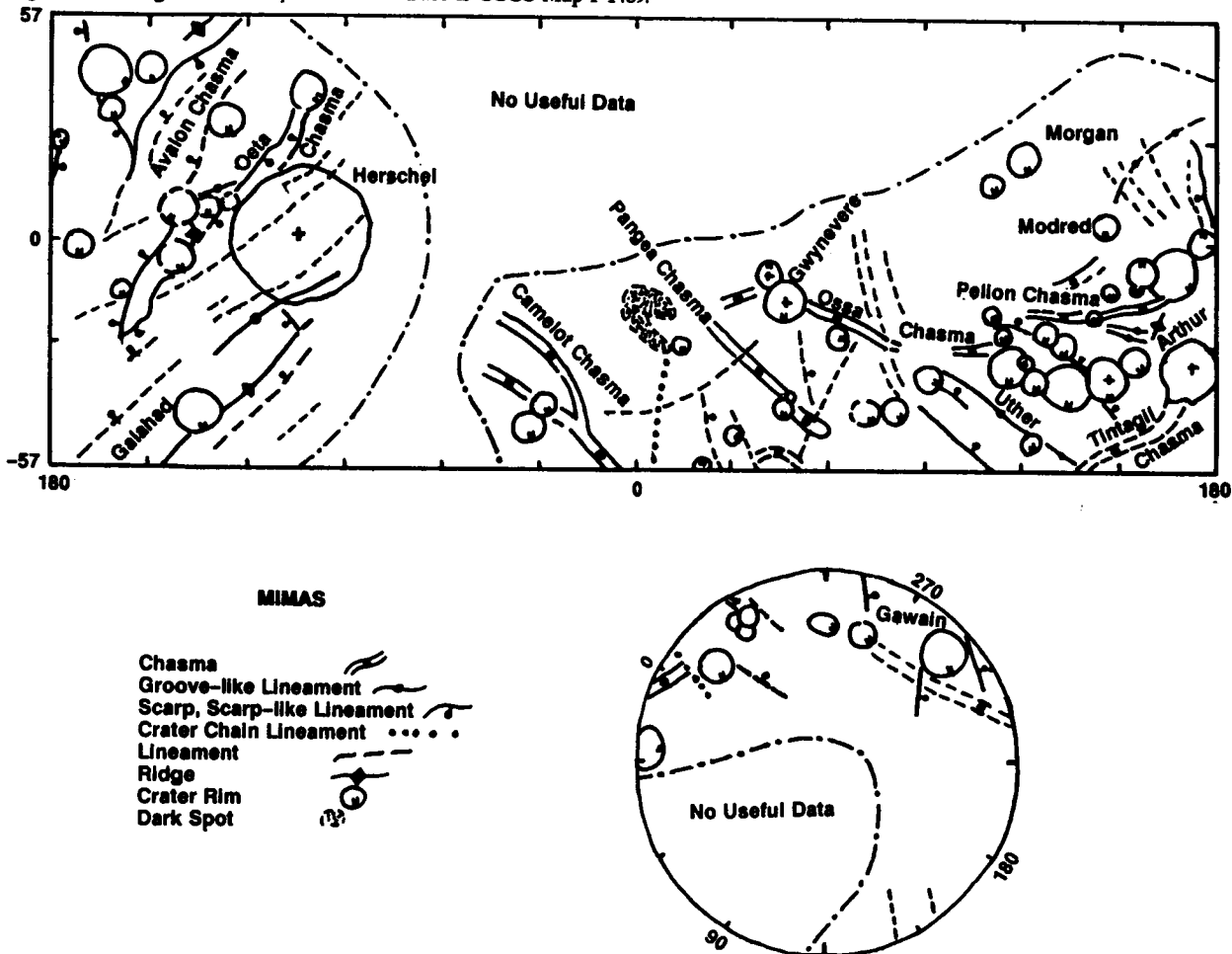
Thomas, P. (1979) Surface features of Phobos and Deimos. *Icarus* 40: 223-243.

Thomas, P., J. Veverka, and S. Dermott (1986) Small Satellites. In *Satellites*, J.A. Burns and M.S. Matthews, editors, pp. 802-835, Univ. of Arizona Press.

Table 1. Lineament Set Parameters

Set Designation	Center	Spacing	Direction Trends	Best Image
1. Pangea-South Pole	55° S, 340° W	15-20 km	N-S to 20° west of north	34944.21
2. Trans-Ossa	20° S, 280° W	6-10 km	10° to 30° west of north	34940.34
3. Uther-Gawain	55° S, 250° W	≈20 km	NW-SE	34938.18
4. Morgan-Modred	20° N, 200° W	≈10 km	30° west of north	34938.18
5. Herschel-Galahad	30° S, 130° W	15-30 km	NE-SW	34932.04, 20

Figure 1. Geologic sketch map of Mimas. Base is USGS Map I 1489.



Tethys Geology and Tectonics Revisited. Steven K. Croft, Lunar & Planetary Laboratory, University of Arizona, Tucson, AZ, 85721.

Tethys, a medium-sized icy satellite of Saturn, was imaged by both the Voyager 1 and 2 spacecraft at sufficiently high resolution to allow some geologic analysis (Smith et al, 1982). One fairly complete (Moore & Ahern, 1983) and several brief descriptions of Tethys' geology (e.g., Smith et al., 1982; Soderblom & Johnson, 1982; Moore & Ahern, 1982; McKinnon & Benner, 1989) have been given. This report gives the partial results of a new analysis of Tethys' geology done as part of a comparative tectonic and cryovolcanic study of the saturnian satellites.

Geologic Description. A new geologic sketch map of Tethys' north polar area is shown in Figure 1. This map is based on a sequence of images (FDS #43980.27, 5.41, 95.58, and 44003.57) transformed to a polar stereographic projection at the same scale. The images present the same area under different illuminations, each of which brings out different features. A new global map is in progress. Tethys' surface has been divided into two primary geologic units (Moore & Ahern, 1982;1983): a heavily cratered unit which covers most of the surface (and most of Fig. 1), and a less heavily cratered plains unit which covers about 20% of the surface, an edge of which appears at lower right in Fig. 1. Individual geologic features are classified as impact craters or tectonic structures.

Tectonics. Ithaca Chasma: The most prominent tectonic feature on Tethys is the globe-girdling Ithaca Chasma, which is 60 to 100 km wide, 3-4 km deep, and can be traced through at least 270° of a rough great circle (Smith et al, 1982; Moore & Ahern, 1983). The nature of the chasma changes along its length, and is described here in 5 sections. Section 1: South Pole to about 20° S; here the chasma consists of two branches trending roughly N-S and parallel to each other for at least 100 km of their lengths. Each branch appears to be a simple, graben-like trough 30-40 km wide. The west branch, seen at moderate resolution (5 km/px) on the terminator in FDS #34937.06, is heavily cratered and about 3 km deep. The east branch, the southern extension of the main chasma, is seen in FDS #34926.18. Resolution is poor (11 km/px), but the east branch has relatively straight (i.e., unbroken by large craters) bounding scarps and reasonable definition compared to the west branch, which is nearly invisible in FDS #34926.18, suggesting that the east branch is not as heavily cratered as the west branch. Section 2: between 20° S and 5° N; here the chasma is a single branch about 40 km wide which makes a 40° turn and joins another short branch chasma to form a very broad scarp-bounded trough about 100 km wide with prominent upraised rims. The bounding scarps appear fresh and unbroken by craters along the chasma's entire length in the low-resolution image FDS #34926.18, an impression confirmed for the portion seen in the high resolution (2 km/px) image FDS #44003.57. Indeed, the scarps and floor of the chasma have virtually no visible superposed craters in this section. The lack of observed craters is not entirely due to the high sun angle because craters appear in abundance on the cratered terrain on either side of the chasma right up to the rim. The floor of the chasma is seen in the high-resolution section to have several subdued scarps/ridges paralleling the prominent bounding scarps, possibly the northward extension of the two branch chasmata at the south end of the wide section. Section 3: between 5° N and Telemachus (about 55° N); this section is entirely on the high-resolution image FDS #44003.57 and extends onto the map in Fig. 1. Topographically, the chasma consists here of at least three parallel shallow troughs continuing along the same trend as the broad portion of section 2. These troughs are not visible in 03.57, but are prominent in FDS #43995.58 where the scarp faces are nearly perpendicular to the solar direction. The prominent features in this section in 03.57 are a bundle of parallel grooves about 5 km wide and 12 km apart trending about 20° counter-clockwise of the main chasma. This section is more heavily cratered than section 2, but less heavily cratered than the surrounding terrain. Section 4: between Telemachus and Eurycleia; this section is nearly indiscernible in high-resolution in 03.57, but stands out sharply in 95.58. Here the branches combine into a single trough 60 km wide north of Telemachus which splits again into two 30 km wide branches near Eurycleia. The rims appear slightly raised along portions of the chasma. The crater density on this section of chasma is indistinguishable from the surrounding cratered terrain. Section 5: south of Eurycleia past the west rim of Odysseus; here the branches of the chasma become progressively shallower and less sharply defined towards the south (stereo pair: FDS #43985.41, 88.57), dwindling into isolated linear massifs in the section closest to Odysseus, and becoming lost south of the equator in the available images (e.g., FDS #43980.27). This section appears heavily degraded and is superposed by several 50-100 km diameter craters.

Other Tectonic Features. Odysseus Tangent Chasma: A prominent chasma 60-80 km wide and at least 800 km long (90° arc), visible in 80.27, is tangent to the rim of Odysseus, trending about 10° east of north. The chasma intersects a ridge-bounded trough radial to Odysseus (see Fig. 1 and below) and is then lost in the zone around the North Pole that is shadowed in all of the extant images. However, extrapolation of the trend over the pole connects almost directly into the trend of the grooves just south of Telemachus (Fig. 1). Continuation of the same trend farther south passes close to the short branch in section 2 of Ithaca Chasma. Two other poorly defined troughs, each 35-40 km wide and at least 300 km long, are visible in 80.27. One is a linear feature parallel to the Odysseus Tangent feature, and the other defines a broad curve along the equator sub-radial to Odysseus. The features intersect near 10° N, 190° W. Another prominent trough about 35 km wide and 120 km long runs N-S of the crater Penelope (85.41 & 88.57). It is radial to the crater, but it appears more degraded than Penelope, suggesting that it is a pre-existing tectonic structure. Lineaments: a set of lineaments running NE-SW are visible in FDS #34937.06 and 10 north and south of the crater Circe. The lineaments appear to be graben-like troughs about 10 km wide. The lineaments cut degraded appearing craters (keeping in mind the 5 km/px resolution) and are cut by fresh appearing craters up to about 30 km in diameter. A number of graben-like lineaments trending NE-SW also cross Odysseus from the south, cutting both the rim and floor.

All of the tectonic features on Tethys appear extensional. The analysis of the global areal expansion inferred from the observed tectonic features is not yet complete. Preliminary estimates have been made, however. Assuming the features are simple grabens, the method of Golombek (1982) yields estimated minimum global areal expansion for Ithaca Chasma alone of 0.25% (assuming an average depth of 3 km). Noting the branching of the chasma (usually two parallel branches) doubles the estimate to about 0.5%. The total area of Ithaca Chasma is about 6% of Tethys' surface, but, recognizing resolution limitations, the morphology is similar to graben-like chasmata on other icy satellites, and not to a giant extension crack, thus the total area of the system does not represent the areal expansion. The Odysseus Tangent system is comparable in extent to the Ithaca system, increasing the estimated expansion to about 1%. The lineaments are numerous, but shallow, indicating little net expansion, leaving the global estimate near 1%, which is similar to the estimated expansions on several other icy satellites (Croft & Soderblom, 1990; Croft, 1991a).

Craters. The largest and most prominent crater on Tethys is Odysseus, visible at upper left in Fig. 1. The crater consists of a primary rim with some evidence of terracing and a central complex of concentric ridges and massifs. RMS fits yield a diameter of 441+14 km for the rim and 169+9 for the central complex. Limb profiles and photoclinometry (Schenk, 1989) show a crater about 8 km deep. The central complex is uplifted 2-3 km and has a narrow central depression. Chapman & McKinnon (1986) suggested the crater may be an incipient pit crater; alternatively, Odysseus may be a peak ring basin.

Ejecta facies have not been previously recognized for Odysseus. However, several features noted in the current study may indicate Odysseus ejecta. 1) A number of crater chains are mapped in Fig. 1. Most of these correspond to chains mapped by Moore & Ahern (1983). They also mapped a number of chains to the east of Odysseus, most of which have been confirmed in this study. As may be seen in Fig. 1 (and in Moore & Ahern's Fig. 6), nearly all of the long axes of the chains are radial to Odysseus, suggestive of secondary crater chains. The diameters (15-25 km) and ranges from Odysseus' center (600-700) of the largest chain craters correspond

to the scaled sizes and ranges of secondaries on other planets in the solar system (Croft, 1991b), supporting their interpretation as Odysseus secondaries. 2) The overall density of craters 40-50 km in diameter mapped in Fig. 1 decreases sharply within about 500 km of Odysseus' center. Large (50-100 km) craters within 500 km of Odysseus also appear significantly degraded compared to craters farther away. It is recognized that the resolution of the images used to make Fig. 1 changes from 8 km/px near Odysseus' rim to 5 km/px near Elpenor crater, however, craters >40 km in diameter are large enough that they should be visible even at the poorer resolution if they were present. Thus their absence near Odysseus appears real. The lower crater density and greater degradation of craters near Odysseus may be explained by the presence of a continuous ejecta blanket. The approximate radial extent of the putative blanket, 500 km, again corresponds to the expected scaled size (Croft, 1991b). 3) A number of ridges are mapped in the center and lower right of Fig. 1, most of which are radial to Odysseus. The pair of parallel ridges over the North Pole bound a deep trough that extends at least to Ithaca Chasma. The smaller ridges SE of Telemachus parallel the crater chains. The morphology, location, and orientation of these features are reminiscent, respectively, of radial gouges and ray-like ejecta deposits seen around large impact basins such as Orientale on the Moon.

Two other large degraded craters not previously documented were found in this study: a 260 km crater centered near 43° S, 7° W (FDS #34926.18), and a 190 km crater centered near 50° N, 20° W (FDS 343995.58 & 44003.57), mapped in Fig. 1. The morphometry of smaller craters on Tethys was discussed by Schenk (1989).

Discussion. Most of the discussions of Tethys' geology (e.g., Smith et al., 1982; Soderblom & Johnson, 1982; Moore & Ahern, 1983; McKinnon & Benner, 1989) have been dominated by analyses of the two most prominent features: Odysseus and Ithaca Chasma. The location of Odysseus near the center of the great circle of Ithaca Chasma led early to the suggestion that Ithaca was genetically related to the Odysseus impact (Smith et al, 1982). Suggested mechanisms included impact induced seismic fracturing (Moore & Ahern, 1983) and viscous stresses generated in mantle flow due to isostatic rebound of Odysseus' interior (McKinnon, 1985; McKinnon & Benner, 1989). Non-Odysseus related suggestions, such as expansion due to internal freezing (Soderblom & Johnson, 1982), did not provide a ready mechanism for localization of tectonic strain into a single, apparently unique, global system.

One question relevant to the relationship of Odysseus to Ithaca that can be considered geologically is: what is the stratigraphic relation between Odysseus and Ithaca? Several features suggest that portions of Ithaca Chasma predated the Odysseus impact. 1) There appear to be significantly more 30+ km diameter craters superposed on at least section 5 of Ithaca and elsewhere on the heavily cratered terrain (Fig. 1 and Moore & Ahern, 1982) than in and around Odysseus, suggesting that this part of Ithaca existed before Odysseus. 2) Several of the crater chains in Fig. 1 cross Ithaca, and a few appear to breach the bounding scarps. If the chains are Odysseus secondaries, then Odysseus formed later than the chasma. 3) The trace of Ithaca Chasma is most poorly defined closest to Odysseus, and virtually disappears for a short distance east of Eurycleia. This may be due to obscuration by Odysseus ejecta: in this location, the chasma is near the apparent edge of Odysseus' continuous ejecta, and mounds of material (Fig. 1) that may be ejecta come very close to, and may cross the chasma. On the other hand, the large trough radial to Odysseus is cut by the north scarp of Section 4 of Ithaca, though there is a breach in the south scarp that may be a continuation of the trough. If the trough is a radial gouge, then the chasma scarp came later than the impact. However, reactivation of older fractures is common in extensional tectonic environments, and activity may renew scarps on one side of a chasma and not on the other (e.g., the 340' Chasma on Miranda, see Croft & Soderblom, 1990). It is important to note that, based on the variation in crater density in the various sections of Ithaca, the chasma did not form all at once: section 2 appears younger than nearly any other feature on the satellite, whereas sections 4 & 5 appear as old as the average cratered terrain. Thus reactivation may have occurred in section 4.

Unfortunately, poor resolution prevents any of the above observations from being unambiguous, but the current evidence favors formation of parts of Ithaca before Odysseus. If true, then there is no genetic relation between the two features. Theoretical relaxation calculations for Odysseus in progress (Bus & Melosh, 1990, private communication) explicitly including a lithosphere are as yet unable to produce a stress field capable of generating an Ithaca Chasma, contradicting earlier models which did not include a lithosphere. In this context, it is worth noting that there is a non-negligible chance that the location of Odysseus near a pole of Ithaca is purely fortuitous. Calculations assuming a purely random impact locations indicate a 15% chance of the center of Odysseus being within 28° of the great circle pole. However, the pole is only about 24° from Tethys' apex of motion. If the Odysseus projectile originated external to the system, then its probability of landing near the apex of motion, and hence near the great circle pole, is several times higher than the random probability, making it likely that the location of the crater near the pole is only fortuitous. While a genetic relation between Odysseus and Ithaca is certainly not ruled out, there is enough evidence that they may not be related to search for other possible mechanisms for Ithaca's origin.

A second relevant question is: is Ithaca Chasma unique, thus requiring a unique explanation? Two features of Ithaca have been cited (Smith et al., 1982; Moore & Ahern, 1983; McKinnon & Benner, 1989) as unusual (unique?): first, the chasma traces 3/4 of a great circle, and second, most of the apparent tectonic strain on Tethys is concentrated in a narrow lane rather than more evenly distributed around the globe. Recent work has turned up other tectonic systems with similar attributes. As noted above, there is apparently a second great circle system on Tethys, the system tangent to Odysseus, that can be traced through at least 200°. The system may extend farther, but the rest of the putative circuit is in the unimaged portions of the satellite. This system is tilted 20° to 30° to the Ithaca system, predates it, and represents a tectonic strain similar to Ithaca's. There is no crater comparable to Odysseus near its poles. Another pair of great circle systems has been identified on Mimas (Croft, 1991a). Herschel, the giant impact on Mimas, is substantially farther from the poles of those systems than Odysseus is from Ithaca Chasma's pole. A relative concentration of strain is seen in the chasmata systems of Oberon and Titania, although these are not great circle systems. Therefore, Ithaca Chasma may not be unique.

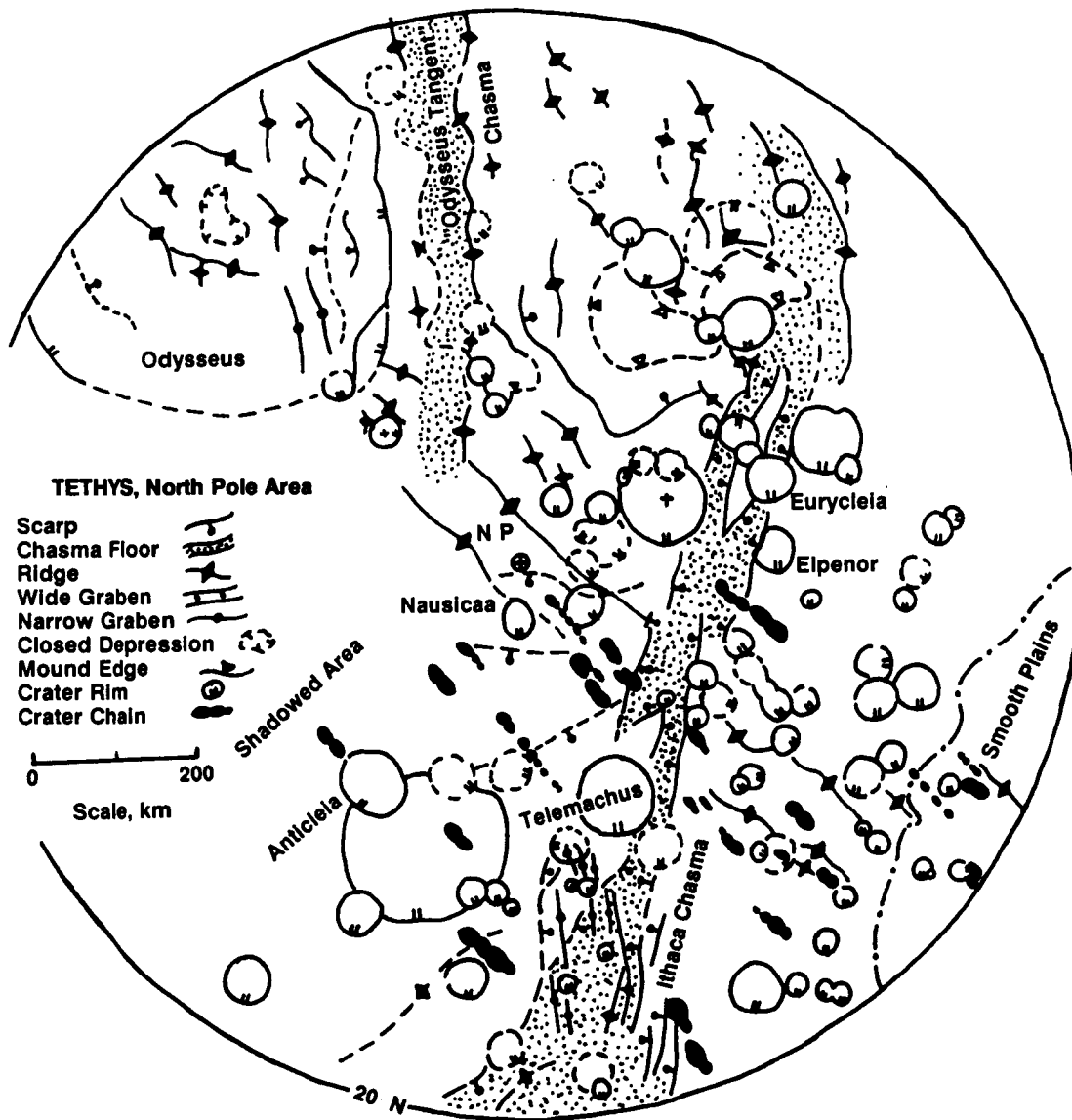
There is evidence for some cryovolcanism on Tethys. The plains unit centered in the trailing hemisphere is probably due to flooding by melted material (Smith et al., 1982; Moore & Ahern, 1983). The edges of the unit are diffuse and lack raised edges, indicating material of relatively low viscosity. Crater statistics (Strom, private communication) show a paucity of craters in the 20-40 km diameter range, but preservation of larger craters. This indicates a regional thickness of the melt sheet of at least several hundred meters, enough to overtop the rims of the vanished craters. Long sections of Ithaca chasma have upraised rims. In analogy with terrestrial rifts, this suggests the possibility of low density intrusions under the axis of the chasma. However, there are no recognizable deposits on the floors of Ithaca comparable to the plains materials. The western margin of the plains unit do not reach Ithaca at any point, indicating that the source vents for the plains are not in these sections of Ithaca Chasma. Poor resolution at the eastern border of the plains prevents definitive determination of the relationship there.

References

- Chapman, C.R. and W.B. McKinnon (1986) Cratering of planetary satellites. In *Satellites*, J.A. Burns and M.S. Matthews, editors, pp. 492-580. Univ. of Arizona Press.
- Croft, S.K. (1991a) Mimas: tectonic structure and geologic history. This volume.
- Croft, S.K. (1991b) Scaling of impact crater ejecta features on the terrestrial planets and the icy satellites. *Icarus*, submitted.

McKinnon, W.B. (1985) Origin of Ithaca Chasma. *Bull. Am. Astron. Soc.* 17: 922.
 McKinnon, W.B. and L.A.M. Benner (1989) Origin of Ithaca Chasma, Tethys, II: the importance of the lithosphere. In *Lunar Planet. Sci. XX*, p. 679-680.
 Moore, J.M. and J.L. Ahern (1982) Tectonic and geological history of Tethys. In *Lunar Planet. Sci. XIII*, p. 539-539.
 Moore, J.M. and J.L. Ahern (1983) The geology of Tethys. *Proc. Lunar Planet. Sci. conf. 13th, part 2*, In, *J. Geophys. Res., Suppl.* 88: A577-A584.
 Schenk, P.M. (1989) Crater formation and modification on the icy satellites of Uranus and Saturn: depth/diameter and central peak occurrence. *J. Geophys. Res.* 94: 3813-3832.
 Smith, B.A. and the Voyager Imaging Team (1982) A new look at the Saturn System: the Voyager 2 images. *Science* 215: 504-537.
 Soderblom, L.A. and T.V. Johnson (1982) The moons of Saturn. *Sci. Am.* 246(#1): 100-116.

Figure 1. Geologic sketch map of north polar area of Tethys. Polar stereographic projection.



Iapetus: Tectonic structure and geologic history.

Steven K. Croft, Lunar & Planetary Laboratory, University of Arizona, Tucson, AZ, 85721.

Introduction. Many papers have been written about the surface of Iapetus, but most of these have discussed either the nature of the strongly contrasting light and dark materials (e.g., Smith et al., 1982; Morrison et al., 1986; Bell et al., 1985) or the cratering record (e.g., Plescia & Boyce, 1985; Lissauer et al., 1988). Little has been said about other geologic features on Iapetus, such as tectonic structures, which would provide constraints on Iapetus' thermal history. Most references (Smith et al., 1982; Ellsworth & Schubert, 1983; Consoimagno, 1985; Squyres & Croft, 1986) have suggested that there is no conclusive evidence for any tectonic activity on Iapetus, even when thermal history studies indicate that there should be. The one exception is Murchie (1990), who noted the apparent existence of scarps in the north polar area of Iapetus. The minimal geologic analysis of Iapetus is probably due to the poor resolution (≈ 8 km/pixel) of even the best Voyager images. However, in a new study of Iapetus' surface involving the use of stereo pairs, an extensive tectonic network has been recognized. A few new observations concerning the craters and dark material were also made. Thus the geology and geologic history of Iapetus can be more fully outlined than before.

The tectonic network is shown along with prominent craters and part of the dark material in the geologic/tectonic sketch map in Figure 1. The base for the sketch map is FDS 43907.08, which shows the region around the north pole and anti-saturn facing hemisphere down to the equator. Features on the geologic/tectonic sketch map are based on examination of Voyager 2 images FDS 43885.45 (resolution: 12 km/px), 43894.20 (10 km/px), 43907.08 (9 km/px), and 43913.35 (8 km/px). These images were chosen because they represent the highest resolution images available, and because they allow viewing the surface in stereo, a great aid in recognizing geologic structures. Stereo discernment for the image pairs is: low for 85.45 and 94.20, good near the image centers for 94.20 and 07.08, and good globally for 07.08 and 13.35. The topography of crater rims and scarps are quite apparent and recognizable in the different image pairs. The heights and slopes of various features given below are based on comparison with the depths of craters 50 to 100 km in diameter, which are assumed to have the same depths (3-4 km) as craters of similar diameter on Rhea and Titania (see Schenk, 1989).

Tectonic Features. The primary tectonic landforms on Iapetus are individual scarps. The features mapped as scarps are typically on the order of 1-3 kilometers high, and 300 to 500 km long. The apparent scarp widths are ≈ 10 -20 km, indicating nominal slopes of 5° to 10° . Several short segments a few tens of km long occur, as well as at least one, the OCO (Oliver-Charlemagne-Ogier) scarp, which is over 1000 km long. Some of the scarps appear to pair together to form chasmata, of which three fairly well-defined ones (Chasmata A, B, and C) are labeled on Figure 1. The chasmata are about 60-75 km wide and several kilometers deep. The crests of several of the scarps (e.g., the N bounding scarp of Chasma A and OCO scarp) appear to be raised somewhat (\leq kilometer) above the terrain on the higher side of the scarp. A few features are mapped as ridges: n. Hamon and the parallel feature to the NW. These ridges may be simply scarps with raised crests. Certainly, n. Hamon is an asymmetric structure with a bright eastern slope ≈ 50 km wide and a western slope ≈ 10 km wide. Several lineaments are mapped near the north pole, the crater Ogier, and along the equator near the crater Baligant. These marginally resolved linear features are probably also scarps: they follow directional trends characteristic of the prominent scarps (see below), and one in particular, n. Baligant along the equator, extends into the region containing deposits of dark material and joins the remarkably linear northern boundary of the otherwise irregularly-shaped dark deposit centered near 5° N, 225° W. The sharp, linear boundary suggests a topographic discontinuity like a scarp almost regardless of the assumed origin of the dark material. The lineament n. Marsilion may be a ridge along the light-dark material boundary.

The scarps may be placed into groups with distinct directional trends. The polar group trends parallel to the 180° Meridian through crater Marsilion right over the pole into the terminator. This group includes the majority of the mapped scarps and Chasmata A and C. The second "group" contains only the OCO scarp trending about 45° counter-clockwise from the polar group. The third group trends at roughly right angles to the polar group and consists of the BB (Baligant-Besgun) scarp and Chasma B near crater Besgun. The BB scarp appears to be a southward extension of the northern Chasma B scarp. The ridges near crater Hamon may fall into this group, but they are arcuate in plan rather than straight, and may only coincidentally parallel the BB scarp in the map area. Other trends may exist: the extant images of the map area are unfortunately all illuminated from about the same direction, and different lighting conditions could highlight different structural features. However, no other trends were seen despite the stereo analysis.

The scarp groups appear to have formed over an extended period. The BB scarp group is cut by all of the others and appears very degraded: its trace is completely lost in a few spots. The ridges are also very degraded and are cut by the OCO scarp. Thus the BB scarp group is oldest, and the OCO scarp is next. The polar group of scarps is the youngest, cutting across scarps of the other groups. These scarps also appear morphologically less degraded morphologically than the others. Even so, the polar scarp group is geologically old since its members are superposed by nearly all of the craters visible on the surface.

Two elevated plateau-like blocks are marked by hatched patterns near the craters Oliver and Besgun. The sides of the blocks are formed by members of different scarp groups.

Crater Morphology. As far as can be discerned given the poor resolution, the morphologies of fresh craters on Iapetus are similar to crater morphologies on the other icy satellites (cf. Schenk, 1989; Croft & Soderblom, 1990): larger craters have relatively shallow, flat floors and central peaks typical of complex craters, while smaller craters appear to have the relatively deeper, bowl-shaped interiors of simple craters. The central peaks (many marked with crosses on the map) are usually solitary conical massifs typical of central peaks on other icy satellites. In particular, Marsilion (≈ 230 km in diameter) has a massive, conical central peak similar to that of Dido or Aeneas on Dione. Marsilion's central peak is located off-center, its only unusual feature. The smallest craters with discernable central peaks are 40-50 km in diameter, somewhat larger than the simple-complex morphology transition seen on similar-sized icy satellites (Schenk, 1989). However, since the smallest observed central peaks are about a pixel pair across, the difference is probably due to poor resolution and not a real difference. The consistency of crater morphologies between satellites and the consistent correlation of complex crater depths with simple-complex transition diameters provide the basis for the crater depths assumed above.

Dark Material. As has been noted before (e.g., Smith et al., 1982; Bell et al., 1985), the dark material forms a broad oval deposit, Cassini Regio, centered in the leading hemisphere. The oval has irregular borders. Numerous detached and semi-detached patches of dark material are found along the boundaries of the oval, with complex clusters extending off of the east and west ends. The planform of most of these patches are subcircular, leading Smith et al. (1982) to suggest that the patches were deposits on the floors of craters. The large, 300 km diameter ring at the east end of the oval is particularly reminiscent of annular flooding in a large central peak crater. In contrast, Bell et al. (1985) suggested that the dark patches were instead located on slopes facing the leading apex of motion rather than in depressions on crater floors. The location of the dark material on apex-facing slopes would be more consistent with an orbital origin of the dark material (Bell et al.'s hypothesis) than locations in sheltered depressions, which would be more consistent with an internal flooding origin. The only contribution to that discussion here is the observation that at least a few of the dark patches occur on the bottoms of craters whose rims are topographically perceptible in stereo, notably crater A and a smaller crater to the south. The dark materials in Baligant, its two neighbors to the NW, and Hamon also appear to be on the crater floors, but topographic discernibility decreases rapidly toward the limb, where these craters lie. The material in Hamon may extend up the apex-facing crater rimwall. The

large dark patches south of Baligant again appear to lie in large depressions while the light patches appear to form high-standing massifs, but unfortunately, topographic discernibility is low. Similarly, two bright spots on the limb of 07.08 appear to extend above the limb defined by the darker material, but a numerical limb analysis will be needed to test this. Finally, if the lineament n. Baligant is indeed a scarp, then the straight border it forms to the dark material strongly suggests topographic confinement of the dark material. Thus the observations made in this study tend to confirm the location of dark material in low spots, suggesting either an internal origin for (part of?) the dark material, or an active process driving orbitally-derived dark material on slopes downward into depressions.

Comparisons and Interpretations. Titania and Oberon are two icy satellites very similar in size to Iapetus. To first order, similar heat flows and thermal histories might be expected for all three bodies, thus it is of interest to compare their surface features. The scarp/chasma network on Iapetus is similar in planform and topography with the chasma networks observed on Titania and Oberon (Croft & Soderblom, 1990). Dimensionally, the mean major chasma widths are 50-60 km on Titania and 70-80 km on Oberon, compared with 60-75 on Iapetus; chasmata on all three satellites are typically several hundred kilometers long. Features comparable to the smaller, graben-like structures seen on Titania and Oberon would be below the limits of resolution on Iapetus. Chasma morphology is similar on all three satellites, apparently including raised crests on some chasma-bounding scarps. Unpaired scarps are found on all three satellites, but they appear to be more common on Iapetus than on Titania or Oberon.

The morphology of the scarps and chasmata on Iapetus imply formation by extensional tectonic stresses. The areal extension represented by the classes of tectonic features can be estimated using the method of Golombek (1982), in which the new area (A) for each scarp is related to the length (L), depth (d), and assumed angle of dip (Θ) for the underlying faults by: $A = Ld/\tan(\Theta)$. Adopting $\Theta = 60^\circ$ and noting that chasmata have 2 scarps yields the following areal increases from the cumulative measured lengths of the tectonic groups: 1) prominent scarps (adopted $d = 2$ km): 0.26%, 2) smaller scarps ($d = 2$ km): 0.20%, 3) lineaments ($d = 0.3$ km): 0.03%, and 4) ridges (interpreted as asymmetric scarps with $d = 2$ km): 0.10%. The cumulative areal increase is 0.59%. This is somewhat smaller than the 1-1.5% seen for the uranian satellites, but is probably due to poor resolution and the heavily degraded state of most of the tectonic features.

The scarps extend across the entire mapped area, indicating at least regional, and probably global, sources for the stresses. The predominance of extensional morphologies indicates an overriding tensional stress, probably thermal expansion. Several possible sources of secondary stress are capable of modifying the overall tensional field to produce the observed directional patterns. Tidal despinning (Melosh, 1977) may account for the trends of the older scarps, like the BB and OCO scarps, but does not obviously account for the younger polar band. That band, which extends from the Saturn-facing hemisphere over the pole to the anti-Saturn hemisphere, follows the trend predicted for orbital recession (Melosh, 1980). Unfortunately, the maximum increase in semi-major axis for Iapetus' orbit due to tidal evolution allowed by the minimum dissipation factor, Q, for Saturn determined by Goldreich & Soter (1966) is only about one part in 10^7 , corresponding to a maximum tidal stress of order 10^{-7} bars. This level of stress is completely negligible compared to the ≈ 70 bars estimated from friction-dominated strength (Golombek & Banerdt, 1986) required to generate Iapetus' chasmata. Another possible source of stress is interior convection (e.g., Zebib et al., 1983). A single axisymmetric cell with fluid rising at one pole (in this case, under the north pole) of the convection pattern and falling at the other could produce the correct stress field. Another possibility is a 2-cell, axisymmetric convection pattern with fluid rising along the equator of flow and falling in at the poles of flow, where the equator of flow is oriented along the 180° meridian through the North Pole. This latter type of flow provides the best means of producing the consistent directional trends of the polar band.

The raised crests of several of the scarps on Iapetus may indicate the existence of cryovolcanic plutons at depth (Croft, 1991) in a largely undifferentiated interior. The large plateau-like blocks appear structurally to be horsts. Plateau-like features appearing in the limb profile of Titania (Thomas, 1988) may be similar structures.

The large ridges near the crater Hamon are sufficiently different in morphology and trend from the other scarps to suggest the possibility of a different origin. The arcuate pattern of n. Hamon and its counterpart to the west, and the asymmetry of the ridge profile - steep on the inside of the curve and broad on the outside - are both consistent with an origin as rim elements of a large, heavily degraded impact crater. If so, the inferred crater would be about 1000 km in diameter and centered near $30N, 300W$. The western rim would pass near craters Othon and Turpin seen in the Voyager 1 images, but unfortunately the resolution is too poor in these images (≈ 50 km/line pair) to show either a degraded rim structure or a remnant depression on the limb that might confirm the postulated crater. If the crater is real, it is large compared to the satellite ($\approx 1.4x$ Iapetus' radius), and substantially larger than the next largest impact structures: Marsilion and the inferred crater associated with the 300 km diameter dark ring seen in Voyager 1 images near $5N, 325W$.

The chronology of geologic activity on Iapetus differs somewhat from that observed on Oberon and Titania: all of Iapetus' scarps predate most of the craters; Oberon has geologically old chasmata like Iapetus, but it also has a set of chasmata that largely post-date the large craters; Titania's chasmata almost entirely post-date the large craters. Thus, Iapetus' tectonic activity preceded the last stage of heavy cratering. There is also evidence of extensive (global) resurfacing on Titania and Oberon, but, unless one counts the dark material, there is no positive evidence for endogenic resurfacing on Iapetus.

The geologic history of Iapetus may now be outlined as follows: 1. Accretion to final size, saturated cratered surface (time scale $10^4 - 10^5$ yr based on Safronov, 1972). 2. Continued heavy bombardment of surface, formation of n. Hamon structure, possibly by impact. 3. Global expansion due to internal heating generates older scarps (time 10^6 yr). 4. Continued expansion generates polar band of scarps, possibly after onset of interior convection (few times 10^8 yr). 5. Heavy bombardment, which has continued through events 3 and 4, tapers off. 6. Dark material is emplaced, either by extrusion of internal carbon-bearing melts or by modification of surface materials by orbital debris.

References

- Bell, J.F., D.P. Cruikshank and M.J. Gaffey (1985) The composition and origin of the Iapetus dark material. *Icarus* 61: 192-207.
- Consolmagno, G.J. (1985) Resurfacing Saturn's satellites: models of partial differentiation and expansion. *Icarus* 64: 401-413.
- Croft, S.K. (1991) Miranda's geology: a cryovolcanic/tectonic interpretation. *Icarus*, submitted.
- Ellsworth, K. and G. Schubert (1983) Saturn's icy satellites: thermal and structural models. *Icarus* 54: 490-510.
- Goldreich, P. and S. Soter (1966) Q in the Solar System. *Icarus* 5: 375-389.
- Golombek, M.P. (1982) Constraints on the expansion of Ganymede and the thickness of the lithosphere. *Proc. Lunar Planet. Sci. Conf.* 13th, *J. Geophys. Res.* 87(Supp.): A77-A83.
- Golombek, M.P. and W.B. Banerdt (1986) Early thermal profiles and lithospheric strength of Ganymede from extensional tectonic features. *Icarus* 68: 252-265.
- Lissauer, J.J., S.W. Squyres and W.K. Hartmann (1988) Bombardment history of the Saturn System. *J. Geophys. Res.* 93: 13776-13804.
- Melosh, H.J. (1977) Global tectonics of a despun planet. *Icarus* 31: 221-243.
- Melosh, H.J. (1980) Tectonic patterns on a tidally distorted planet. *Icarus* 43: 334-337.

Morrison, D., T. Owen and L.A. Soderblom (1986) The satellites of Saturn. In *Satellites*, J.A. Burns and M.S. Matthews, editors, pp. 764-801, Univ. of Arizona Press.

Murchie, S. (1990) The tectonics of icy satellites. *Adv. Space Res.* 10:173-182.

Plescia, J.B. and J.M. Boyce (1985) Impact cratering history of the Saturnian satellites. *J. Geophys. Res.* 90: 2029-2037.

Safronov, V.S. (1972) *Evolution of the protoplanetary cloud and formation of the Earth and planets*. Israel Prog. for Scientific Translations, Jerusalem, 206 pp.

Schenk, P.M. (1989) Crater formation and modification on the icy satellites of Uranus and Saturn: depth/diameter and central peak occurrence. *J. Geophys. Res.* 94: 3813-3832.

Smith, B.A. and the Voyager Imaging Team (1982) A new look at the Saturn System: the Voyager 2 images. *Science* 215: 504-537.

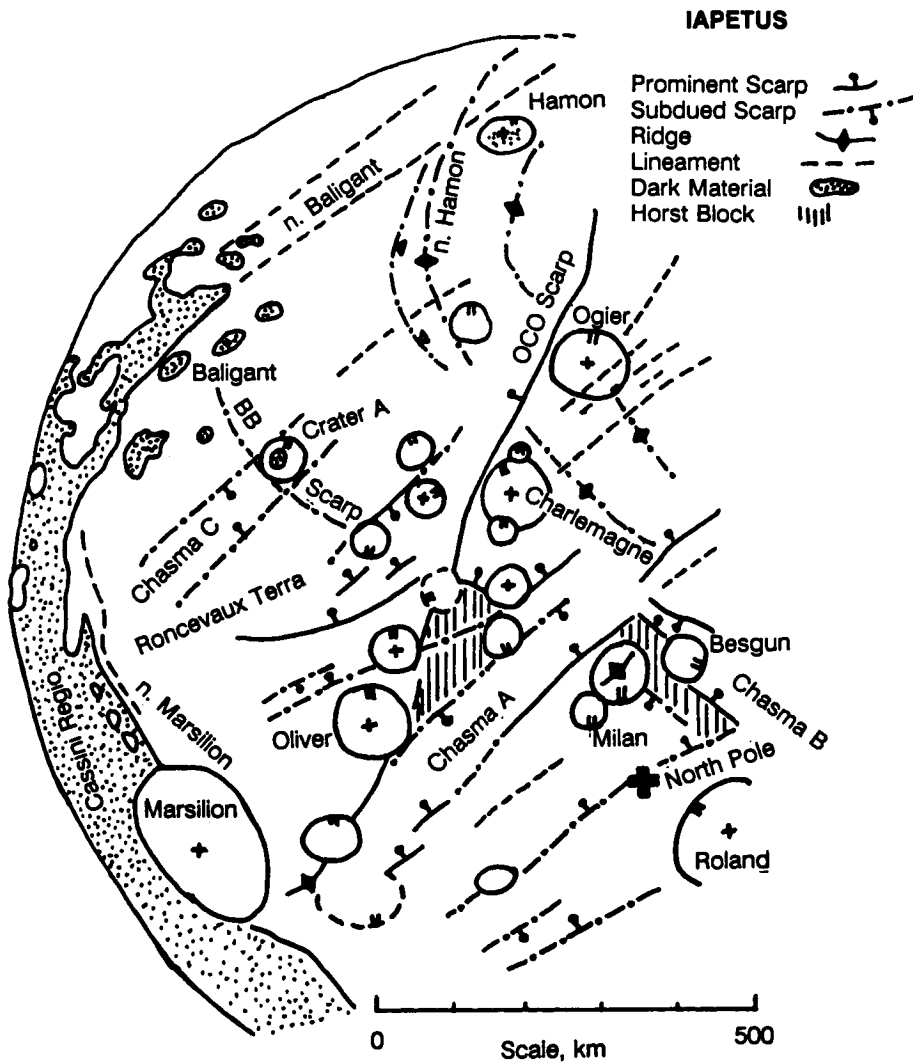
Squyres, S.W. and S.K. Croft (1986) The tectonics of icy satellites. In *Satellites*, J.A. Burns and M.S. Matthews, editors, pp. 293-341, Univ. of Arizona Press.

Thomas, P.C. (1988) Radii, shapes, and topography of the satellites of Uranus from limb coordinates. *Icarus* 73: 427-441.

Wetherill, G.W. (1989) The formation of the Solar System: consensus, alternatives, and missing factors. In *The formation and evolution of planetary systems*, H.A. Weaver and L. Danly, editors, p. 1-30, Cambridge Univ. Press.

Zebib, A., G. Schubert, J.L. Dein and R.C. Paliwal (1983) Character and stability of axisymmetric thermal convection in spheres and spherical shells. *Geophys. Astrophys. Fluid Dynamics* 23: 1-42.

Figure 1. Geologic sketch map of the North Pole area of Iapetus.



THE STRENGTH OF MIRANDA'S LITHOSPHERE;

Robert Pappalardo and Ronald Greeley, Department of Geology, Arizona State University, Tempe, Arizona 85287

In attempting to understand the endogenic processes which have shaped the surface of an icy satellite, it is desirable to quantify the failure strength of the satellite's lithosphere. In a crust that is fractured on a large scale, frictional sliding along pre-existing fractures occurs in response to lower differential stresses than required to initiate fracture of pristine rock, thus governing failure of a brittle lithosphere. Failure is predicted along favorably-oriented fracture planes; if fractures of all orientations are assumed to be present in the crust (as is expected of a heavily cratered lithosphere), frictional failure relations are directly applicable. The Coulomb criterion predicts that the shear stress σ_τ and normal stress σ_n components on a fracture plane at failure are related as $\sigma_\tau = \mu\sigma_n + S_0$ where S_0 is the cohesion and μ is the coefficient of friction. At moderate to high pressures, the frictional sliding strength of most materials is found to be $\sigma_\tau = 0.85\sigma_n$ [1]. This strength is largely independent of rock type and strength, strain rate, and temperature.

The frictional failure curve for ice, however, deviates from this law [2]. At low temperatures ($77 \leq T \leq 115$ K) and moderate pressures ($\sigma_n < 200$ bar), ice frictional failure can be described by $\sigma_\tau = 0.55\sigma_n + 10$ bar, independent of temperature or sliding rate. The frictional failure curve for real surfaces probably does not have a cohesion intercept, but may instead have vertical tangency to the shear stress axis, conceptually intercepting the origin [3]. Constraining the frictional failure line for ice to pass through the origin, $\sigma_\tau = 0.69\sigma_n$ is obtained [2].

At low confining pressures ($\sigma_3 \lesssim 30$ bar), frictional sliding of a variety of rock types is strongly dependent on the surface roughness of the pre-existing fractures [1, 3]. Such low stresses are applicable in considering frictional failure of low gravity satellites such as Miranda. The frictional strength of ice has been tested down to $\sigma_3 = 3$ bar [2], but the effect of surface roughness has not been directly evaluated.

Near the horizontal surface of a planet, lithospheric stresses may be resolved into three principal stress directions, one of which is vertical and the other two are horizontal. In a lithosphere of average density ρ subject to gravitational acceleration g , the vertical principal stress can be equated (in the absence of pore pressure) to the lithostatic pressure ρgz at some depth z . In the case of horizontal compression, the maximum compressional stress σ_1 is horizontal and the minimum compressional (maximum tensional) stress σ_3 is vertical; in the case of horizontal extension, the opposite is true. With one principal stress thus known, the other necessary to induce failure may be determined by

$$\frac{\sigma_1}{\sigma_3} = 2\mu \left[\sqrt{\mu^2 + 1} + \mu \right] + 1$$

for some value of friction and negligible cohesion [4].

The maximum horizontal stress that may be supported in a lithosphere may be represented as the difference $\sigma_H - \sigma_V$ between the horizontal and vertical principal stresses [5], with compression being considered positive. Frictional failure stress is plotted a function of depth in Figure 1 for a crustal density of 1000 kg m^{-3} , gravity $= 0.09 \text{ m s}^{-2}$, and friction values $\mu = 0.5$ and 0.7 , chosen as bounds to the ice frictional failure data.

As illustrated by Figure 1, frictional failure strength of the brittle lithosphere increases with depth as lithostatic pressure increases for both compression (σ_3 vertical, positive stress) and extension (σ_1 vertical, negative stress) until the brittle-ductile transition depth is reached. Below this depth, lithospheric strength is controlled by creep of the ductile crust and decreases with depth. Behavior of the ductile lithosphere is dependent upon composition, temperature, and strain rate. Plotted on Figure 1 are curves that represent the ductile strength of cold ice based on the data of [6]. A strain rate of 10^{-16} s^{-1} and a surface temperature of 60 K are chosen, and the labeled curves represent thermal gradients of 2, 5, 10, and 20 K km^{-1} .

The plot shows that the maximum strength of Miranda's lithosphere (that at the brittle-ductile transition) is small. Failure in compression (reverse faulting) is induced by $\lesssim 50$ bar of horizontal stress, a stress close to that which may cause folding of an ice crust [7], indicating that both deformation styles might be active in a compressional regime. Less than 20 bar could cause failure in extension (normal faulting), a stress which could be supplied by satellite expansion of $\lesssim 0.05\%$ [8].

If troughs in Miranda's Elsinore Corona are graben whose faults intersected near the brittle-ductile depth transition at the time of their formation, a transition depth of ~ 5 to 10 km is implied [9]. This necessitates a paleo-thermal gradient ~ 10 to 20 K km^{-1} . A steeper thermal gradient (and/or a lesser strain rate) is suggested if narrow troughs (~ 1 km wide) in Elsinore and Inverness Coronae are graben that formed in a similar fashion. A lower thermal gradient earlier in Miranda's history may have facilitated formation of broader troughs, which appear to be more ancient [10].

Comparing the results of Figure 1 to those for Ganymede [2], it is apparent that lower satellite gravity results in much lower frictional strength and in a somewhat deeper brittle lithosphere. Lower surface temperature significantly lowers the depth to ductile ice behavior for a given lithospheric stress, thermal gradient, and strain rate. The results here can be directly applied to Enceladus, which has a gravity and a surface temperature similar to those of Miranda. Enceladus displays subparallel troughs ~ 4 km wide that may be graben which formed in a brittle lithosphere ~ 3 km deep. For a water ice lithosphere, low stress but high paleo-thermal gradient ($>20 \text{ K km}^{-1}$) is indicated. Such a high gradient is likewise necessary to account for the shapes of some craters on Enceladus if a water ice lithosphere is assumed [11].

The results of Figure 1 are somewhat suspect because of poor constraints on the creep of ice at very low temperatures. In addition, the lithospheres of Miranda and Enceladus are probably not composed of pure water ice: Miranda possesses a dark contaminant, and both lithospheres may be composed of a mixture of water and other ices, which could allow ductile behavior at lower temperatures and more gentle thermal gradients. In addition, the possible effect of fracture roughness needs to be evaluated, as this might cause the friction coefficient μ to vary by more than an order of magnitude, greatly affecting the slope of the frictional strength line.

The low frictional strength of low-gravity satellites permits relatively minor lithospheric stress to result in surface deformation; therefore, only small horizontal stresses are necessary to account for observed endogenic deformation on Miranda and Enceladus. The low surface temperature of these satellites necessitates steep thermal gradients to produce shallow ductile behavior of a water ice lithosphere.

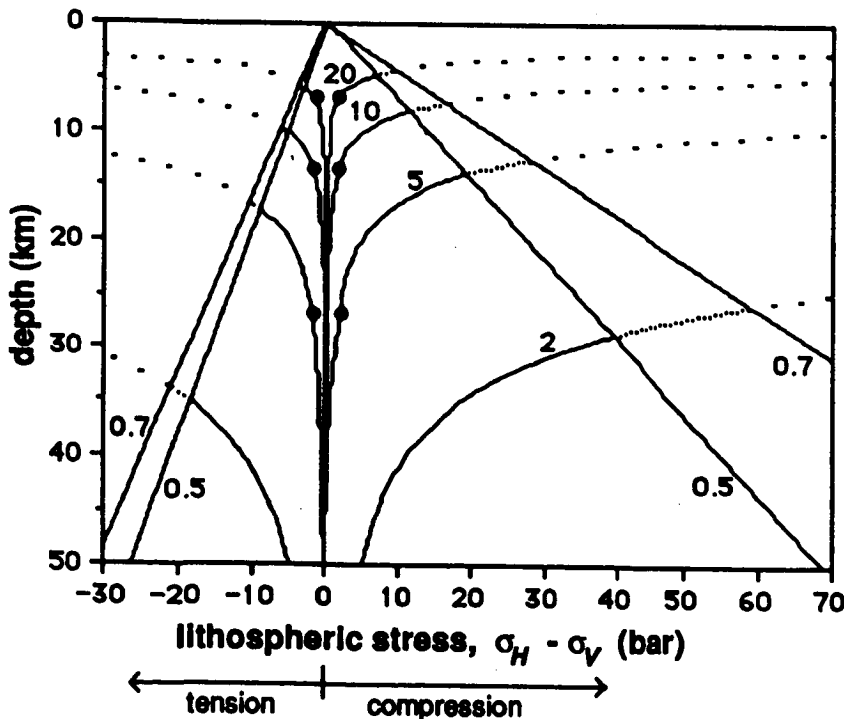


Figure 1. Maximum horizontal stress which can be supported in an ice lithosphere for Miranda (or Enceladus). Strength of the brittle lithosphere is controlled by frictional failure and is bracketed by straight lines for $\mu = 0.5$ and 0.7 for gravity $g \approx 0.09 \text{ m s}^{-2}$. Ductile strength curves for cold ice are for a strain rate of 10^{-16} s^{-1} , a surface temperature of 60 K , and thermal gradients as indicated. Dots indicate depths at which $T = 195 \text{ K}$ is

STRENGTH OF MIRANDA'S LITHOSPHERE: R. Pappalardo and R. Greeley

attained, below which the low-temperature ice flow law parameters used here are no longer strictly valid [6]. Compressional stress is taken to be positive.

- [1]Byerlee, J.D., *Pure Appl. Geophys.*, 116, 615, 1978. [2]Beeman, M. *et al.*, *JGR*, 93, 7625, 1988. [3]Barton, N., *Int. J. Rock Mech. Min. Sci. Geomech. Abstr.*, 13, 255, 1976. [4]Jaeger, J.C. and N.G.W. Cook, *Fundamentals of Rock Mechanics*, 1979. [5]Brace, W.F. and D.L. Kohlstedt, *JGR*, 85, 6248, 1980. [6]Kirby, S.H. *et al.*, *J. Physique*, 48, suppl., 227, 1987; Durham, W.B. *et al.*, *JGR*, 88, B377, 1983. [7]Pappalardo, R. and R. Greeley, *in prep.* [8]Consolmagno, G.J., *Icarus*, 64, 401, 1985. [9]Pappalardo, R. and R. Greeley, *BAAS*, 22, 1057, 1990. [10]Croft, S.K., submitted to *Icarus*. [11]Passey, Q.R., *Icarus*, 53, 105, 1983.

CHAPTER 3

SURFACE PROCESSES AND GEOMORPHOLOGY

ANCIENT OCEANS AND MARTIAN PALEOHYDROLOGY. V.R. Baker, R.G. Strom, V.C. Gulick, J.S. Kargel, G. Komatsu, and V.S. Kale, Lunar and Planetary Laboratory, University of Arizona, Tucson, AZ 85721.

The concept of the hydrological cycle is one of the great achievements in the understanding of nature. Intellectual history's premier hydrologist, Leonardo da Vinci, seems to have held two simultaneous views of the cycle: (a) an external process in which evaporation from ponded areas leads to precipitation and runoff from the land (the prevailing terrestrial view), and (b) an internal process in which subsurface pressures from within the Earth force water upward, as in blood pumped through a human body. After 500 years, a very similar paradox applies to our modern view of the long-term planetary hydrological cycle on Mars. Numerous morphological features, notably the valley network systems of the heavily cratered terrains (1,2,3), imply formation by dynamical cycling of water. The sapping process responsible for most valley networks (4) requires a persistent flow of ground water that can only occur with long-term hydraulic head differentials to drive the flow in subsurface aquifers (5,6). Either endogenetic or exogenetic hydrological cycling is necessary to explain these relationships.

Endogenetic hypotheses for valley genesis on Mars maintain the necessary prolonged ground-water flows by hydrothermal circulation associated with impact cratering (7) or with volcanism (8,9,10). However, we note that the extensive volcanogenetic hydrological systems necessary to explain widespread valleys are consistent with a continuum of processes up to the megascale of Tharsis and Elysium. This observation, plus the discovery of evidence for extensive inundation of the northern plains of Mars (11,12,13,14) and the discovery of evidence for extensive glaciation in the southern hemisphere (15), led to our proposal of episodic ocean formation and related hydroclimatological change throughout Martian history (16,17). Our model was found consistent with a range of otherwise enigmatic observations, including the formation of Amazonian valley networks (5,18) and the formation of layered deposits in Valles Marineris through repeated lake filling and breaching (19). Our continuing work reveals even more detailed consistency with this conceptual scheme, including the extensive glaciation of the Hellas region (20) in Middle Amazonian time (21), further documentation of the glacial landforms used to establish southern hemisphere glaciation (22), and a coincidence of ages (within resolution capabilities) of principal elements in the late-stage global hydrological system (23).

We find it remarkable that the various Amazonian phenomena that we describe exist in temporal and spatial associations that imply a common genetic cause. Alternative hypotheses can be offered for many of the individual glacial, oceanic, fluvial, periglacial, and permafrost landforms that we have associated with a global hydrological system. If these apply, how fortuitous that the resulting landforms have been positioned to also be consistent with regional glaciation, ocean formation, and associated climatological change.

The best preserved evidence of ocean formation and related glaciation occurs late in Martian history. The ephemeral Amazonian sea in the Elysium basin, described by Chapman et al. (24), is probably a vestige of this late epoch. The associated phenomena are concentrated volcanic activity at Tharsis and Elysium, plus phases of outburst flooding. Our model of outburst through the Valles Marineris (16) is consistent with morphology there (25), but the precise volcanogenetic mechanism requires further formulation. Nevertheless, we note that the clear association of the Mangala Vallis outflow system with a local source at Memnonia Fossae (26) implies a similar connection to a Tharsis volcanogenetic source. The concentration on Mars near Tharsis of 90% of flood discharges indicated by outflow channel sizes is another fortuitous circumstance if the indicated genetic connection is denied as an "outrageous hypothesis."

Pre-Amazonian episodes of ocean formation and warm-wet climate are also indicated. Ocean development may have been more extensive, but associated landforms are degraded and not easily related to ocean size. Theoretical scenarios for ocean formation (27) and warm-wet climatic

conditions (28) are most convincingly argued for earliest Martian history, when direct landform evidence is lacking. The best evidence for these model scenarios is indirect, in the temporal sequence of valley network development (29), presumably in response to the prevailing climatic conditions. However, endogenetic mechanisms of cycling water (hydrothermal systems) complicate this relationship (30).

Modeling of small-scale volcanogenetic hydrothermal systems for typical Mars conditions (30) shows adequate discharges achieved for valley network development. Scaling upward to the immense hydrothermal system that would have to be associated with large-scale Tharsis volcanism exceeds any terrestrial experience by orders of magnitude. The cataclysmic initiation of outflow centered upon Tharsis is so remarkable as to compel a genetic association. Alternatives may be found to our hypothesis of massive volcanism triggering the water outflows (16), but these must also explain the numerous attendant phenomena that are manifested in the Martian landscape. Any alternative scheme must provide for global hydrological cycling, achieving, as in Leonardo's paradox, an overall consistency and economy of explanation.

References. 1. Pieri, D.C. (1980), *Science*, **210**, 895-897. 2. Carr, M.H., and Clow, G.D. (1981), *Icarus*, **48**, 91-117. 3. Baker, V.R. (1982), *The Channels of Mars*, Univ. Texas Press. 4. Baker, V.R., Kochel, R.C., Laity, J.E., and Howard, A.D. (1991) in *Groundwater Geomorphology* (eds. C.G. Higgins and D.R. Coates), Geol. Soc. Am. Spec. Pap. 252, 235-266. 5. Gulick, V.C., and Baker, V.R. (1990), *J. Geophys. Res.*, **95**, 14325-14344. 6. Howard, A.D. (1990), *NASA Tech. Memo.* **4210**, 342-344. 7. Brakenridge, G.R., Newsom, H.E., and Baker, V.R. (1985), *Geology*, **13**, 859-862. 8. Gulick, V.C., Marley, M.S., and Baker, V.R. (1988), *Lunar and Planet. Sci. XIX*, 441-442. 9. Wilhelms, D.E., and Baldwin, R.J. (1989), *Proc. Lunar and Planet. Sci. Conf.*, **19**, 355-365. 10. Brakenridge, G.R. (1990), *J. Geophys. Res.*, **95**, 17289-17308. 11. Jons, H.P. (1985), *Lunar and Planet. Sci. XVII*, 404-405. 12. Lucchitta, B.K., Ferguson, H.M., and Summers, C.A. (1985), *NASA Tech. Memo.* **88383**, 450-453. 13. Lucchitta, B.K., Ferguson, H.M., and Summers, C. (1986), *J. Geophys. Res.*, **91**, E166-E174. 14. Parker, T.J., Saunders, R.S., and Scheeberger, D.M. (1989), *Icarus*, **82**, 111-145. 15. Kargel, J.S., and Strom, R.G. (1990), *Lunar and Planet. Sci. XXI*, 597-598. 16. Baker, V.R., Strom, R.G., Croft, S.K., Gulick, V.C., Kargel, J.S., and Komatsu, G. (1990), *Lunar and Planet. Sci. XXI*, 40-41. 17. Baker, V.R. (1990), *NASA Tech. Memo.* **4210**, 339-341. 18. Gulick, V.C., and Baker, V.R. (1989), *Nature*, **341**, 514-516. 19. Komatsu, G., and Strom, R.G. (1990), *Lunar and Planet. Sci. XXI*, 651-652. 20. Kargel, J.S., and Strom, R.G. (1991), Glacial Geology of the Hellas Region of Mars, *Lunar and Planet. Sci. XXII* (this volume). 21. Johnson, N., Kargel, J.S., Strom, R.G., and Knight, C. (1991), Chronology of Glaciation in the Hellas Region of Mars, *Lunar and Planet. Sci. XXII* (this volume). 22. Kargel, J.S., and Strom, R.G. (1991), Terrestrial Glacial Eskers: Analogs for Martian Sinuous Ridges, *Lunar and Planet. Sci. XXII* (this volume). 23. Strom, R.G., Kargel, J.S., Johnson, N., and Knight, C. (1991), Glacial and Marine Chronology on Mars, *Lunar and Planet. Sci. XXII* (this volume). 24. Chapman, M.G., Scott, D.H., and Tanaka, K.L. (1990), *Lunar and Planet. Sci. XXI*, 180-181. 25. Komatsu, G., and Strom, R.G. (1991), Stratigraphy of the Layered Terrain in Valles Marineris, Mars, *Lunar and Planet. Sci. XXII* (this volume). 26. Tanaka, K.L., and Chapman, M.G. (1990), *J. Geophys. Res.*, **95**, 14315-14323. 27. Schaefer, M.W. (1990), *J. Geophys. Res.*, **95**, 14291-14300. 28. Pollack, J.B., Kasting, J.F., Richardson, S.M., and Poliakov, K. (1987), *Icarus*, **71**, 203-224. 29. Gulick, V.C., and Baker, V.R. (1990), *Lunar and Planet. Sci. XXI*, 443-444. 30. Gulick, V.C., Marley, M.S., and Baker, V.R. (1991), Numerical Modeling of Hydrothermal Systems on Martian Volcanoes: Preliminary Results, *Lunar and Planet. Sci. XXII* (this volume).

EVOLUTION OF THE MARTIAN HYDROSPHERE. V. Baker, Department of Geosciences and Department of Planetary Sciences, University of Arizona, Tucson, AZ 85721.

The concept of the hydrological cycle is one of the great achievements in the understanding of nature. Intellectual history's premier hydrologist, Leonardo da Vinci, seems to have held two simultaneous views of the cycle: (a) an external process in which evaporation from ponded areas leads to precipitation and runoff from the land (the prevailing terrestrial view), and (b) an internal process in which subsurface pressures from within the Earth force water upward, as in blood pumped through a human body. After 500 years, a very similar paradox applies to our modern view of the long-term planetary hydrological cycle on Mars. Numerous morphological features, notably the valley network systems of the heavily cratered terrains (1,2,3), imply formation by dynamical cycling of water. The sapping process responsible for most valley networks (4) requires a persistent flow of ground water that can only occur with long-term hydraulic head differentials to drive the flow in subsurface aquifers (5,6). Either endogenetic or exogenetic hydrological cycling is necessary to explain these relationships.

Endogenetic hypotheses for valley genesis on Mars maintain the necessary prolonged ground-water flows by hydrothermal circulation associated with impact cratering (7) or with volcanism (8,9,10). Moreover, the extensive volcanogenetic hydrological systems necessary to explain widespread valleys are consistent with a continuum of processes up to the megascale of Tharsis and Elysium. This observation, plus the discovery of evidence for extensive inundation of the northern plains of Mars (11,12,13,14) and the discovery of evidence for extensive glaciation in the southern hemisphere (15), led to a proposal of episodic ocean formation and related hydroclimatic change throughout Martian history (16,17). The model is consistent with a range of otherwise enigmatic observations, including the formation of Amazonian valley networks (5,18) and the formation of layered deposits in Valles Marineris through repeated lake filling and breaching (19). Continuing work reveals even more detailed consistency with this conceptual scheme, including the extensive glaciation of the Hellas region (20) in Middle Amazonian time (21), further documentation of the glacial landforms used to establish southern hemisphere glaciation (22), and a coincidence of ages (within resolution capabilities) of principal elements in the late-stage global hydrological system (23).

Ocean formation on Mars was episodic. The best evidence for the process is for the latest episodes. Coincident cataclysmic flood discharges to the northern plains, probably triggered by Tharsis volcanism (16), would lead to immense consequences. Potential volumes of ponded water are summarized in Table 1. Regrettably, these figures are highly approximate because of large errors (as great as ± 1.5 km) in the existing topographic data set. At various contour levels the modern northern plains geometry permits water bodies up to oceanic proportions, 4.0×10^7 km² in area, holding up to 6.6×10^7 km³ water with an average depth of as much as 1.6 km. Much smaller pondings are possible within the basin, but long-term deformation of the planetary surface precludes meaningful analysis of the inadequate topographic data. Nevertheless, it is interesting that the maximum water volume that might reside in Oceanus Borealis at its theoretical maximum extent is equivalent to a planetwide water layer 450 meters thick. This figure is consistent with other estimates of the Martian water inventory.

The outflow channels have a complex history of multiple flooding events over a prolonged period of planetary history. We hypothesize episodic outbursts of simultaneous discharge triggered by the planetary-scale volcanism. The consequences of such episodes are summarized in Table 2. At total combined discharge rates consistent with the indicated outflow channel dimensions, the various sizes of Oceanus Borealis determined in Table 1 would be achieved in time periods of days to a few years. The potential source zone of Martian upland terrain that could hydraulically provide this water transfer would have to be saturated with water and ice to some thickness. The volumes indicated for various sizes of Oceanus Borealis require saturated thick-

nesses averaging between 0.5 and 6.6 km over the source region, depending upon the assumed porosity. The elevated region of Tharsis, underlain by porous lava flows, would probably provide unusually thick source regions from which to derive outflow discharges.

The massive transfers of water through the outflow channels, from subsurface storage to Oceanus Borealis, would generate profound changes in climate. The cataclysmic outpouring of subsurface water would rapidly release dissolved CO₂ and evaporated water vapor to the atmosphere. Additional massive amounts of these two greenhouse gases would be generated by inundation of the polar carbon dioxide cap and by evaporation of water and sublimation of ice in the newly formed Oceanus Borealis. As Martian temperatures rose during the resulting transient H₂O-CO₂ greenhouse conditions, additional global change could occur by melting ground ice in the permafrost of the heavily cratered uplands and possibly by releasing adsorbed CO₂ from the previously cold regolith. Modulated by periodic changes of orbital eccentricity and obliquity, the planet would experience a period of maritime climate with exogenetic hydrological cycling from ocean to atmosphere to land by precipitation. Colder regions, such as the south polar latitudes, would receive snow, resulting in the glacial responses described above.

Carbon dioxide is a critical greenhouse gas for driving the modification of Martian climate. Table 3 lists the sources of carbon dioxide that could be associated with massive, cataclysmic water transfers late in Martian history. Although we have not done the indicated radiative transfer calculations, it is clear that much less atmospheric carbon dioxide is needed to produce warm, wet conditions late in Mars history because of solar luminosity values close to those of today. Even at the greatly reduced solar luminosity of earliest Mars history, Pollack and others (24) calculate that on the order of 1 bar atmospheric pressure is required to bring the Martian surface temperature to the melting point of water ice. Potential sources of CO₂ are sufficient (Table 3), and feedback mechanisms involving the atmospheric effects of associated massive amounts of water vapor will add to the surface warming.

It is remarkable that theoretical possibilities and observed Martian surface phenomena are in such accord. The various Amazonian oceanic, volcanic, and glacial phenomena exist in temporal and spatial associations that imply a common genetic cause. Alternative hypotheses can be offered for many of the individual glacial, oceanic, fluvial, periglacial, and permafrost landforms that are ascribed to a global hydrological system. If these apply, how fortuitous that the resulting landforms have been positioned to also be consistent with regional glaciation, ocean formation, and associated climatological change. Alternatives may be found to the hypothesis of massive volcanism triggering the water outflows (16), but these must also explain the numerous attendant phenomena that are manifested in the Martian landscape. Any alternative scheme must provide for global hydrological cycling, achieving, as in Leonardo's paradox, an overall consistency and economy of explanation.

Acknowledgments: This research was supported by the NASA Planetary Geology and Geophysics Program, Grant NAGW-285.

References: 1. Pieri, D.C. (1980), *Science*, **210**, 895-897. 2. Carr, M.H., and Clow, G.D. (1981), *Icarus*, **48**, 91-117. 3. Baker, V.R. (1982), *The Channels of Mars*, Univ. Texas Press. 4. Baker, V.R., Kochel, R.C., Laity, J.E., and Howard, A.D. (1991) in *Groundwater Geomorphology* (eds. C.G. Higgins and D.R. Coates), Geol. Soc. Am. Spec. Pap. 252, 235-266. 5. Gulick, V.C., and Baker, V.R. (1990), *J. Geophys. Res.*, **95**, 14325-14344. 6. Howard, A.D. (1990), *NASA Tech. Memo.* **4210**, 342-344. 7. Brakenridge, G.R., Newsom, H.E., and Baker, V.R. (1985), *Geology*, **13**, 859-862. 8. Gulick, V.C., Marley, M.S., and Baker, V.R. (1988), *Lunar and Planet. Sci.* **XIX**, 441-442. 9. Wilhelms, D.E., and Baldwin, R.J. (1989), *Proc. Lunar and Planet. Sci. Conf.*, **19**, 355-365. 10. Brakenridge, G.R. (1990), *J. Geophys. Res.*, **95**, 17289-17308. 11. Jons, H.P. (1985), *Lunar and Planet. Sci.* **XVII**, 404-405.

12. Lucchitta, B.K., Ferguson, H.M., and Summers, C.A. (1985), *NASA Tech. Memo.* 88383, 450-453. 13. Lucchitta, B.K., Ferguson, H.M., and Summers, C. (1986), *J. Geophys. Res.*, **91**, E166-E174. 14. Parker, T.J., Saunders, R.S., and Scheeberger, D.M. (1989), *Icarus*, **82**, 111-145. 15. Kargel, J.S., and Strom, R.G. (1990), *Lunar and Planet. Sci.* **XXI**, 597-598. 16. Baker, V.R., Strom, R.G., Croft, S.K., Gulick, V.C., Kargel, J.S., and Komatsu, G. (1990), *Lunar and Planet. Sci.* **XXI**, 40-41. 17. Baker, V.R. (1990), *NASA Tech. Memo.* 4210, 339-341. 18. Gulick, V.C., and Baker, V.R. (1989), *Nature*, **341**, 514-516. 19. Komatsu, G., and Strom, R.G. (1990), *Lunar and Planet. Sci.* **XXI**, 651-652. 20. Kargel, J.S., and Strom, R.G. (1991), Glacial Geology of the Hellas Region of Mars, *Lunar and Planet. Sci.* **XXII**. 21. Johnson, N., Kargel, J.S., Strom, R.G., and Knight, C. (1991), Chronology of Glaciation in the Hellas Region of Mars, *Lunar and Planet. Sci.* **XXII**. 22. Kargel, J.S., and Strom, R.G. (1991), Terrestrial Glacial Eskers: Analogs for Martian Sinuous Ridges, *Lunar and Planet. Sci.* **XXII**. 23. Strom, R.G., Kargel, J.S., Johnson, N., and Knight, C. (1991), Glacial and Marine Chronology on Mars, *Lunar and Planet. Sci.* **XXII**. 24. Pollack, J.B., Kasting, J.F., Richardson, S.M., and Poliakoff, K. (1987), *Icarus*, **71**, 203-224.

Table 1: Hypsometry of Oceanus Borealis

Contour km	Volume 10 ⁷ km ³	Area 10 ⁷ km ³	Average Depth km	Equivalent Water Layer m
0	6.6	4.0	1.6	450
-1.0	3.2	2.0	1.1	220
-2.0	1.0	1.4	0.7	70

Table 2: Filling Rates for Oceanus Borealis

	Contours (m)		
	0	-1.0	-2.0
Filling Rates			
10 ⁹ m ³ s ⁻¹	2 yr	1 yr	15 wk
10 ¹⁰ m ³ s ⁻¹	11 wk	5 wk	10 days
Source Zone Thickness at			
25% Porosity	2.6 km	1.3 km	0.4 km
10% Porosity	6.6 km	3.2 km	1.0 km

Table 3: Sources of Carbon Dioxide

A. North Polar Cap	20 mb
B. Massive Volcanism	100 mb
C. Sequestered in Previous Cycle	
1. Adsorbed in Regolith	
a. Ocean Basin	~200 mb
b. Land	~600 mb
2. Ground Water (Confined)	~1000 mb
3. CO ₂ Clathrate	~1000 mb

A MARTIAN GLOBAL GROUNDWATER MODEL

Alan D. Howard, Department of Environmental Sciences, University of Virginia, Charlottesville, VA 22903

A global groundwater flow model has been constructed for Mars to investigate hydrologic response under a variety of scenarios, improving and extending earlier simple cross-sectional models [1]. The model is capable of treating both steady-state and transient flow as well as permeability that is anisotropic in the horizontal dimensions. A single near-surface confining layer may be included (representing in these simulations a coherent permafrost layer). Furthermore, in unconfined flow locations of complete saturation and seepage are determined. The flow model assumes that groundwater gradients are sufficiently low that Dupuit conditions are satisfied and the flow component perpendicular to the ground surface is negligible. In spherical coordinates the governing equation is:

$$\frac{\partial}{\partial \lambda} \left\{ h_e \left[\frac{K_{\lambda}}{\cos \Phi} \frac{\partial h}{\partial \lambda} + K_{\lambda \Phi} \frac{\partial h}{\partial \Phi} \right] \right\} + \frac{\partial}{\partial \Phi} \left\{ h_e \cos \Phi \left[\frac{K_{\lambda \Phi}}{\cos \Phi} \frac{\partial h}{\partial \lambda} + K_{\Phi} \frac{\partial h}{\partial \Phi} \right] \right\} \\ = R^2 \cos \Phi \left[S \frac{\partial h}{\partial t} - Q \right],$$

where λ is longitude, Φ is latitude, h is the local hydraulic head, R is the planetary radius (assumed constant), S is the specific storativity (confined portions of the aquifer) or specific yield (unconfined areas), Q is distributed vertical recharge, K_{λ} , K_{Φ} , and $K_{\lambda \Phi}$ are the three components of the symmetric hydraulic conductivity tensor, and h_e is an *effective* aquifer thickness which, in the case of an aquifer with K that does not change vertically (termed the *uniform* case) is equal to $(h_u - h_l)$, where h_u and h_l are the elevations of the top and base of the aquifer, respectively. In confined situations h_e equals $(h_c - h_l)$, where h_c is the base of the confining layer. In some simulations K was assumed to decrease exponentially with depth from the surface at elevation h_s (the *exponential* case), giving an effective thickness of

$$h_e = \frac{1}{\alpha} e^{-\alpha(h_s - h_u)}$$

where α is a decay constant (in these simulations the aquifer is assumed to be unbounded at depth). In these simulations storativity was assumed also to decrease exponentially with depth with the same decay constant. In unconfined regions h_u equals the water table elevation, but in confined circumstances h_u is the base of the confining layer, h_c .

Surface elevations were taken from the new 1:15M Mars topographic map. Two sets of elevations were recorded for each grid-point location, the first (the *nominal* set) being the local elevation, which, however, was adjusted upwards to the level of the surrounding uplands if the gridpoint occurred within a crater or in an erosional channel. However, locations in craters large enough to encompass more than one grid points (e.g., Hellas and Argyre) were represented by the local elevation. The second set of elevations (the *fluvial* set) was taken in the same manner as the nominal set except that the elevation was adjusted downwards to the elevation of the bottom of any nearby erosional channel. Thus the nominal set is assumed to represent the pre-channeling landscape and the fluvial set to represent the present fluvial base level. Examination of both outflow and the larger cratered-terrain valley networks reveals that most flowed down essentially the present regional topographic gradients. The few local disparities between inferred channel flow directions and topographic maps (e.g. Nirgal, Dueteronilus, Mangala) are probably as likely to be due to uncertainties in topographic mapping as to regional tectonism. The major exception is the Tharsis volcanic construct, largely postdating the development of valley networks. However, flow directions of most outflow channels associated with the margins of Tharsis appear to be consistent with present topographic gradients, suggesting that most of the marginal updoming and normal faulting in Valles Marinaris predated the outflow channels. In addition, the direction and degree of development of

the valley networks suggests that the north-south topographic discontinuity (highlands-lowlands transition) had essentially its present configuration prior to the development of the late Noachian valley networks. Thus the present topography reasonably can be considered to be indicative of conditions during channel development.

In simulations with a finite aquifer thickness, the local base of the aquifer, h_1 , was set to a given elevation below the local fluvial elevations. In the present simulations the aquifer thickness below the fluvial elevations was assumed to be areally uniform.

The flow equations were solved using a finite difference method employing 10-degree spacing of latitude and longitude. A successive over-relaxation method (SOR) was used for steady-state solutions and a Crank-Nicholson method with iterative solution at each time step was used for transient simulations. The correctness of the solution method was checked in part by confirming mass conservation. In addition, an independent, finite element flow model was also constructed for steady-state conditions and compared to the finite difference model. The finite element model represented the planet by triangular planar elements matched at their edges and the flow equations were cast in cartesian form. The two models gave essentially identical solutions.

The initial guess for steady state flow simulations was a level water table with an elevation equal to the lowest surface elevation on the planet (the bottom of Hellas). If the base of the aquifer was above this level then the water table was set to the base of the aquifer. Steady state simulations assumed a constant recharge of the aquifer from the surface. In most cases an areally uniform recharge rate was assumed, but some simulations were conducted that assumed recharge to be a function of latitude and/or elevation:

$$Q = Q_0 [\text{Cos}\Phi] \{1 + \beta h_s\}$$

where Q_0 is a nominal recharge rate, and β is an input parameter. The bracketed latitude correction is optional. Recharge to fixed-head and confined portions of the aquifer was set to zero. The only location on the planet that was specified as fixed-head at the beginning of the iterative solution was the bottom of Hellas. Locations of saturation and, therefore, seepage were determined during the SOR iterative solution by identifying during each iteration locations where the predicted head, h , was greater than the surface elevation, h_s . Such locations were converted to fixed-head for succeeding iterations until the steady-state solution was achieved. A similar procedure was used to identify confined portions of the aquifer wherever the predicted head was greater than the bottom of the confining layer, h_c .

Transient flow simulations started from steady state conditions, and involved either of two scenarios: 1) *Draining*: The aquifer system is initially equilibrated with a specified recharge rate and then drained with no further recharge, and 2) *Filling*: The aquifer system initially has no available water (i.e., it is set to the initial conditions for the steady state iterations as described above) and the aquifer then fills towards steady state with a specified constant recharge.

Steady-state flow simulations. Steady-state flow simulations have been conducted to investigate effects of parameter variation, particularly the ratio of recharge rate, Q , to intrinsic permeability, k . Hydraulic conductivity has been assumed to be isotropic and uniform in these simulations. Another set of runs examines the effects of a confining permafrost layer extending from the poles to a variety of latitudes. Finally some simulations have been conducted to examine the effects of spatially variable recharge and anisotropic permeability.

Transient flow simulations. A two-dimensional flow model had previously been used to calculate the length of time for martian aquifers to drain following cessation of recharge [1]. These figures are updated here using the global flow model. Results from a number of simulations run with different sets of model parameters were analyzed by multiple regression to determine estimating equations for the length of time for specified percentages of filling, t_f , or draining, t_d , of the aquifer. The estimating equation for draining flows is given by

$$t_d = C_d \frac{v\eta}{kg} G^{\delta} V_r^{\gamma}$$

where C_d is a coefficient (see table below), ν is the water viscosity, η is the porosity, k is the intrinsic permeability (note that hydraulic conductivity, K equals kg/ν), g is the gravitational constant, G is the average hydraulic gradient at the start of aquifer draining, and V_r is the ratio of the available water volume (water above the lowest discharge point in Hellas) to the total water volume (including water below the lowest discharge point) at the start of aquifer draining. The exponents take the values of $\delta=-1.3$ and $\gamma=1$ for the uniform case and $\delta=-1.0$ and $\gamma=-1.4$ for the exponential case. Similarly, for the case of filling flows:

$$t_f = C_f \eta Q \left[\frac{\nu}{kg} \right]^\epsilon D^\gamma$$

where D is the depth from the surface to half-value of the permeability ($0.693/\alpha$) and the exponents take the values of $\sigma=-0.8$, $\epsilon=0.2$ and $\gamma=0$ for the uniform case and $\sigma=-0.8$, $\epsilon=0.2$ and $\gamma=1.3$ for the exponential case. The times to filling or draining can be specified in two ways: 1) the time required to drain or fill a specified percentage of the total available water volume (constants C_{dv} and C_{fv}); or 2) the time required for the total discharge of water to decrease or increase by a specified percentage (constants C_{dq} and C_{fq}). The values of the coefficients are given below:

Percent Change	Uniform Case				Exponential Case			
	C_{dv}	C_{fv}	C_{dq}	C_{fq}	C_{dv}	C_{fv}	C_{dq}	C_{fq}
10	13.59	0.545	4.33	1.94	69	0.33	29.4	8.49
25	36.9	1.45	10.3	3.58	255	0.84	90.7	1.34
50	146	3.07	31.6	5.61	1148	1.78	306.3	2.67
75	463	5.32	108.4	7.91	5115	2.96	1195	3.92
90	904	7.73	298	9.91	30019	4.17	3346	5.11

In using this table Q is expressed in cm/yr, D in km, k in darcies, g in cm/sec², ν in cm²/sec, and times, t , in 10⁶ yr.

The times for aquifer draining are generally comparable to those reported for the two-dimensional simulations [1]. For example, for the uniform permeability case with $\eta=0.2$, $k=1$, $G=0.0017$ and $V_r=0.67$ the 2-D simulations with a representative aquifer length of 3000 km indicate the time to 75% draining as 5.6×10^6 yr, and the present simulations indicate 12×10^6 yr for the uniform aquifer and 48×10^6 yr for the exponential aquifer. However, the draining times increase much more strongly with percent draining than in the case of the 2-D simulations because the length-scale increases as draining progresses and the water must flow towards more distant exit points.

Times for aquifer recharge are essentially inversely proportional to recharge rate. Furthermore, recharge generally occurs much more rapidly than draining for comparable regolith permeability. For example, recharge at a rate of 1 cm/yr will fill the regolith to 75% of its steady-state capacity in only 150,000 years (assuming $\eta=0.2$ and $k=1$) compared to tens of millions of years for a comparable percentage of draining. In addition, recharge rates are only weakly dependent upon aquifer permeability.

References:

- [1] Howard, 1990, *Rpts. Planetary Geol. Geophys. Prog.*, NASA TM 4210, 342-344.

ROLE OF GROUNDWATER IN FORMATION OF MARTIAN CHANNELS

Alan D. Howard, Department of Environmental Sciences, University of Virginia, Charlottesville, VA 22903

A global 3-D model of groundwater flow [1] has been used to investigate possible behavior of groundwater on Mars and its role in creating fluvial features. This report supplements and expands on conclusion drawn from an earlier 2-D groundwater model [2], and is organized into topical headings:

Timescales of groundwater flow: Results from the 3-D model [1] confirm the timescales for draining of near-surface aquifers inferred from the 2-D model [2]. The modeling indicates the difficulty of sudden mobilization of large quantities of groundwater to create outflow channels as suggested by Carr [3]. Aquifers with high permeability (e.g., 10^3 darcies) would tend to drain to the lowest available discharge point within 10^4 years, probably shorter than timescales for development of confining permafrost. If this water were confined by a coherent permafrost, highest artesian gradients would not be in the location of outflow channels but in the lowest basins on Mars, including those in the northern plains and especially Hellas (Fig. 1).

Because of the distributed nature of inputs, recharge of aquifers from surface infiltration from rain, snowmelt, or permafrost degradation occurs very rapidly, with timescales for equilibration with a constant recharge rate of 1 to 10 cm/yr being on the order of 10^5 to 10^4 years. Spring-fed streams and groundwater sapping processes would become active during relatively brief periods of climatic amelioration due to orbital variations, volcanic activity, or impact events or due to regional changes in geothermal heat flux due to volcanism.

"Wet" Areas on Mars and location of outflow channels: The global simulations imply which areas were likely to have been characterized by the presence of near-surface waters or groundwater efflux during past epochs. The groundwater model utilizes present topography (Fig. 1), except that most simulations conceptually fill in fluvial channels in order to examine flow conditions contributing to their formation. An accompanying abstract [1] argues that the present topography can be considered to be indicative of conditions during channel development.

Figure 2 shows areas that have steady-state water levels less than 200 meters below average land surface elevations under for areally uniform recharge and for a variety of values of the recharge to permeability ratio (Q/k). Although the assumption of surface recharge may be invalid for most or all of Mars' history, the simulations still show the likely flow patterns, relative depths, and exit locations of water introduced into regional aquifers from any source, including melting of surficial permafrost layers. Potential wet areas are primarily located in the lowest portions of the planet (Hellas and low portions of the northern lowlands) but also in moderate-depth regional depressions (e.g., Argyre). Wet areas also occur along lower portions of regional slopes, particularly in low areas intruding into highlands; such areas are generally also locations of strong groundwater discharge. Outflow channels and some larger valley networks are generally located in such areas (Fig. 1), such as Al Qahira, Ma'adim, lower Kasei, Maja, and Vedra Valles, the possible source of Kasei adjacent to Hebes Chasma, and the chaotic terrain of Margaritifer Sinus and associated outflow channels. The major exceptions are the channels emptying into Deuteronilus and Protonilus Mensae (Arequah and Huo Hsing Valles and Deuteronilus channel) which according to present topographic maps are near the crest of the upland-lowland scarp, and Mangala Valles, which is indicated to flow across a topographic nose.

Implications for Valley Networks: By contrast with the outflow channels, concentrations of valley networks (stippled in Fig. 1) generally occur on high portions of the cratered uplands and thus in areas that are relatively "dry" (Fig. 2). That is, any recharge or release of water by melting of regolith ice would tend to migrate vertically to a deep water table and then flow laterally to exit in the "wet" areas of Mars. This implies that the suggestions of a sapping origin to these channels [4,5,6,7] are unlikely unless the surface aquifer is very shallow (e.g. perched on permafrost or a duricrust) or water is released locally by melting of permafrost due to volcanic intrusions [6] or impact-generated heat [7,8]. However, the amount of surficial materials eroded during formation of the networks suggests that more volume of water was required than could be stored in the regolith at levels above the channels [2,9,10]. Thus the channels may have originated by runoff erosion (or sapping erosion from perched aquifers) during a warmer and moister Noachian climate [2,11].

The enigma of Hellas: The bottom of Hellas is the lowest location on Mars by a margin of about

2 km. It would therefore be the ultimate base level for global groundwater and regional surface flow. A variety of evidence has accumulated that the northern lowlands has served as a sink for sediment eroded from the highlands-lowlands boundary with corresponding water, mud, or ice-covered seas, and features suggestive of shorelines have been identified [12]. Valles Marineris has layered deposits that may represent subaqueous deposition [13]. The bottom of Hellas also has deposits that could be fluvial or lacustrine, and it has received drainage from two outflow channels. However, cursory inspection of images of the Hellas basin does not reveal the prominent shorelines that should have been formed if Hellas has served as the baselevel for local and planet-wide groundwater flow. A variety of explanations could be devised for the absence of lacustrine features (particularly impermeable rocks on the flanks of Hellas, rapid evaporation, obliteration of shorelines by mass-wasting or eolian erosion, etc.), including the possibility that pronounced regional groundwater flow has never occurred on Mars except under special circumstances such as by geothermal melting of permafrost.

Absence of fluvial or periglacial features on Syrtis Major: Most of the strongly sloping highland-lowland scarps exhibit either development of outflow channels or periglacial features such as fretted terrain [14]. The absence of either on the strong Syrtis Major slope is problematical, particularly because Syrtis Major is a major re-entrant of the highland-lowland scarp, which in other circumstances has generally encouraged formation of channels. One explanation might be the absence of late-Hesperian or Amazonian volcanism, which has been argued to be instrumental in melting of ground ice to form the circum-Tharsis outflow channels [3,15]. However, Syrtis Major has a very small contributing upland area, and much of the subterranean water could have been diverted to the nearby and lower Hellas (Fig. 1). In fact, the simulations show that "wet" conditions are mostly limited to Isidis Planitia (where features suggestive of a former periglacial and/or lacustrine environment abound [16]) and do not extend far up the regional slope onto Syrtis Major (Fig. 2). The presence of thick volcanic plains in Syrtis Major may also have contributed to a deep water table.

Development of chaotic terrain and associated outflow channels: A role of artesian groundwater in development of chaotic terrain and its associated outflow channels has been suggested by Carr [3]. Carr's model, involving rupture of an artesian groundwater reservoir confined by permafrost, requires very high regolith permeability, but this model has deficiencies discussed above. Chaotic terrain has also been compared to collapse features resulting from permafrost degradation or to sudden mobilization (liquefaction) of sediments with high void ratios [17]. These models require mechanisms for generation of large ice contents in the regolith. A mechanism is suggested here which combines aspects of the Carr [3] and Nummedal and Prior [17] models. The chaotic terrain lies near the base of the highland-lowland boundary in the Chryse trough (Fig. 1). This is a potentially wet area under unconfined conditions and an area of high artesian pressures if confined by permafrost, as pointed out by Carr. Although permafrost is in long-term disequilibrium in equatorial areas [18], import of water from groundwater flow would easily compensate for slow dehydration by water vapor diffusion to the surface through the regolith. Thus a coherent permafrost is likely to have formed in this area. Furthermore, segregated ice would probably have been formed during permafrost growth, and intrusions of ice sills and laccoliths may have occurred due to the artesian conditions. Thus the role of artesian groundwater may not have been a direct dewatering of a large aquifer, but more indirect through slow development of thick ice layers which might then have melted due to intrusions or enhanced geothermal heat flow. Another possibility is slow intrusion but sudden breaching of water laccoliths emplaced at the base of the permafrost. In either case the need for very high aquifer permeability is avoided.

Structurally-controlled valley networks: Some martian scarps are dissected by long, narrow, reticulate valleys that are obviously structurally controlled. The best examples occur in and around the bend of Kasei Valles at 10-33°N 70-80°W, including the Sacra Fossa and the arborescent network dissecting the floor of Kasei. The angle, ψ , included between the tapering sidewalls is a function of the ratio, R , of the scarp backwasting rate along the fracture to that of inter-fracture areas:

$$\sin \psi/2 = 1/R .$$

Measurements in Sacra Fossa suggests R values from 5 to more than 35. Recharge-fed sapping valley networks on the Colorado Plateau show much less extreme structural control, even where fracture control is best developed [19]. The very strong structural control may be due to sapping by artesian upwellings

along fractures. This area may have been characterized by artesian groundwater capped by permafrost with water derived from the Lunae Planum uplands [14]. The spacing between enlarged fractures (ca. 25 km) is probably much larger than the characteristic spacing of fractures in the plateau material, suggesting control by flow through only the widest fractures coupled with inhibition of erosion along intervening fractures due to drawdown effects of those fractures that have been enlarged. The eroded debris could either have been removed by fluvial flow (although the valley walls lack the sinuous undercutting that characterizes valleys such as Nirgal) or by ice flow, analogous to the fretted terrain.

References: [1] Howard, 1991, A martian global groundwater model [this volume]; [2] Howard, 1990, NASA TM 4210, 342-344; [3] Carr, 1979, *J. Geophys. Res.*, 84, 2995-3007; [4] Pieri, 1980, NASA TM 81979, 362 p.; [5] Baker, 1982, *The Channels of Mars*, U. Texas, Austin, 198 p.; [6] Brakenridge et al., 1985, *Geology*, 13, 859-62; [7] Brakenridge, 1990, *J. Geophys. Res.*, 17289-308; [8] Wilhems and Baldwin, 1988, *LPSC XIX*, 1270-1; [9] Howard, 1988, NASA SP 491, 1-5; [10] Goldspiel and Squyres, 1991, *Icarus*, 89, 392-410; [11] Masursky, 1973, *J. Geophys. Res.*, 78, 4009-30; McCauley et al, 1972, *Icarus* 17, 289-327; [12] Parker et al., 1989, *Icarus*, 82, 111-45; [13] Nedell et al, 1987, *Icarus*, 70, 409-41; [14] Howard, 1991, Role of artesian groundwater in forming martian permafrost features [this volume]; [15] Tanaka and Chapman, 1990, *J. Geophys. Res.*, 95, 14315-23; [16] Griffazi and Schultz, 1989, *Icarus*, 77, 358-81; [17] Nummedal and Prior, 1981, *Icarus*, 45, 77-86; [18] Fanale, 1976, *Icarus*, 28, 179-202; Clifford and Hillel, 1983, *J. Geophys. Res.*, 88, 2456-74; [19] Howard and Kochel, 1988, NASA SP 491, 6-56; [20] Pieri, 1976, *Icarus*, 27, 25-50; Carr and Clow, 1981, *Icarus*, 48, 91-117.

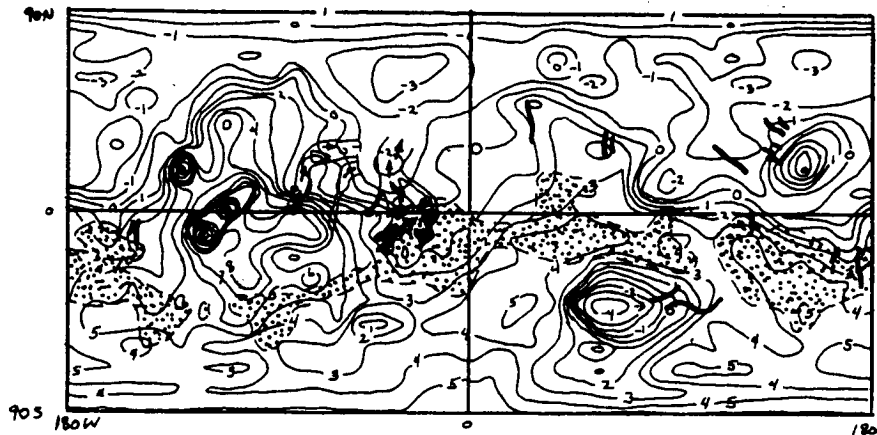


Fig. 1. Contours of generalized mars topography (kms) with areas of abundant small valley networks stippled (from [20]), major outflow channels as heavy lines or thin lines with arrows (Chryse region), and chaotic terrain (cross-ruled).

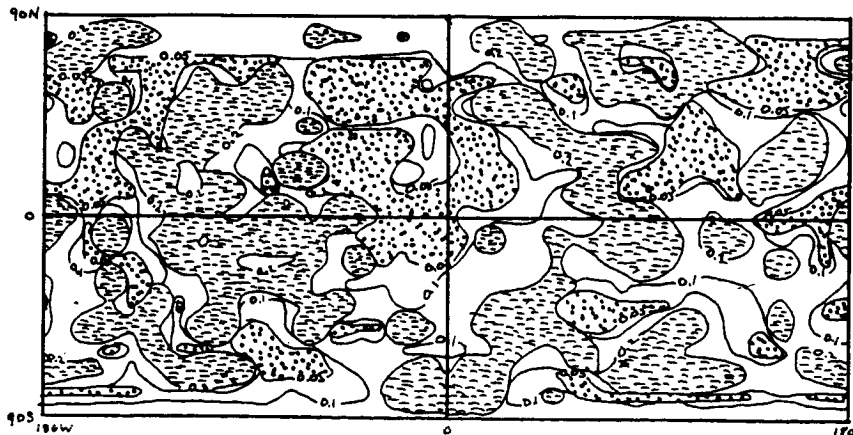


Fig. 2. Wet and dry areas of Mars. Contours show areas with groundwater at steady state within 200 m of ground surface (including saturated areas) for various values of the ratio of vertical recharge, Q (in cm/yr), to intrinsic permeability, k (in darcies). Particularly "wet" areas are stippled ($Q/k \leq 0.5$) and "dry" areas shown by dashed pattern ($Q/k \geq 0.2$ for near-saturation conditions).

ROLE OF ARTESIAN GROUNDWATER IN FORMING MARTIAN PERMAFROST FEATURES

Alan D. Howard, Department of Environmental Sciences, University of Virginia, Charlottesville, VA 22903

Various landforms possibly related to formation (growth), movement, or decay of ground ice have been identified on Mars, including fretted terrain (*ft*) and associated lobate debris aprons (*lda*) [1,2,12,13], the chaotic terrain [3], concentric crater fills (*ccf*) [2], polygonal ground [4], "softened" terrain [5], small domes that are possibly pingos [6], and curvilinear (fingerprint) features (*cu*) [4,7]. Glaciers may also have been formerly present [8]. Some of these may have involved ice derived from artesian groundwater.

Mars groundwater and the location of permafrost features: Several permafrost landforms including *ft*, *lda*, *ccf*, and, possibly, *cu* are located in narrow latitudinal belts [2,4,5] (Fig. 1). The lack of such features poleward of $\pm 60^\circ$ latitude may result from ground temperatures too low for appreciable ice flowage, and the equatorward limit at $\pm 30^\circ$ is thought to result from climatic disequilibrium of permafrost in equatorial regions. The permafrost features are widely distributed in the northern band, but occur in the southern hemisphere only in the vicinity of Hellas and Argyre (Fig. 1). Squyres [2] suggests that the restricted southern distribution may be due to regolith properties in the vicinity of major impacts. However, these permafrost features reveal a consistent topographic pattern (Fig. 1). *The fretted terrain, concentric crater fills, and lobate debris aprons (and, possibly, curvilinear features) occur along, and particularly near the base of, high-relief regional slopes.* Most are associated with the north-south highland-lowland scarp, but some occur on the lower flanks of Elysium and in the Hellas and Argyre depressions. The southern highlands lacking these features, and in the north these features are absent near the tops of volcanic constructs and rare in the center of the major basins. Their absence poleward of $\pm 60^\circ$ may be related more to the absence of strong regional slopes than to reduced ice mobility.

The *ft*, *lda*, *ccf*, and *cu* occur where groundwater may have discharged if it were unconfined [9]. Lowland areas are thus more likely to have developed permafrost with a completely saturated regolith than highlands such as the southern hemisphere cratered terrain (which is likely to have been drained of near-surface water during warmer epochs, during the early periods with higher geothermal heat or due to episodes of ground heating by volcanism or impact cratering). Even if early climates were occasionally warm enough for recharge from precipitation, water tables would have been deep in highlands [9].

In addition, the scarp-base locations of permafrost features favor artesian overpressuring. A martian global groundwater model [10] was utilized to predict where artesian overpressuring might occur (Fig. 2). In this simulation groundwater is assumed to be recharged (and discharged) in the latitude belt $\pm 20^\circ$ (groundwater could also be derived from melting of permafrost). Poleward of $\pm 20^\circ$ a coherent, impermeable permafrost was assumed to extend from the surface to a depth of 1 km at the equatorward limit and to a depth of 4 km at the poles. Figure 2 shows contours of the artesian gradient, defined as $(h - h_c)/(h_s - h_c)$, where h is the hydraulic head, h_s is the surface elevation, and h_c is the elevation of the base of the permafrost. Values greater than zero indicate artesian conditions (values less than zero are not shown). The permafrost features generally occur in areas predicted to have artesian conditions. The exceptions are portions of Deuteronilus, Protonilus, and Nilosyrus Mensae, which extend high onto the highlands-lowlands scarp. However, the distribution and magnitude of artesian gradients are highly sensitive to the assumed distribution and thickness of ground ice, the assumed locations and magnitude of recharge, uncertainties in the surface topography, and the hydrologic properties of the regolith. Minimally the artesian conditions would assure development of permafrost with ice completely filling voids. In addition, as detailed below and in [9], other effects may have occurred, including springs, supply of water to glacial flows, development of segregated ice, intrusion of ice (or water sills) and pingos, and rapid release of water derived from melting of segregated or intruded ice.

Softened terrain, possibly resulting from creep of ground ice [5], does not follow the above distributional pattern. It is more widely distributed latitudinally and occurs on a variety of topographic setting. If it is a permafrost feature (see dissent [11]) it probably does not involve artesian groundwater.

Role of artesian groundwater in formation of fretted terrain, lobate debris blankets, and concentric crater fills: The *ft*, *lda*, and *ccf* are thought to result from slow flow of debris and ice outward from steep scarps, with differences primarily resulting from variations in the topographic setting (narrow troughs, scarp margins, and crater interiors). Mechanisms that have been proposed are gelifluction [12], rock-glacier flow with ice derived from seasonal frosts incorporated in mass-wasted debris [2], and flow

of ice-rich layers beneath the uplands, which thereby erodes the scarp margin [13]. As pointed out by Squyres [2], the shape of the debris blankets suggests bulk movement rather than surficial movement of the debris, casting doubt on gelifluction. Lucchitta [13] has criticized seasonal frost trapping as being insufficient to generate a high enough ice/rock ratio to permit bulk flow. In addition, the debris blankets show very little variation with aspect, which would probably occur if deposition and ablation of seasonal frosts were involved. In turn, the mechanism of flow of ice-rich layers beneath the plateau units is also deficient. Emplacement of a high ice content beneath the plateau units must be accomplished (filling voids and development of segregated or intruded ice from artesian groundwater is one possibility). However, if ice-rich layers in the plateau material were involved in bulk flow, lowering (as the ice flowed out) and tilting (due to areal variations in ice content) of the plateau surface should occur, as well as break-up and separation into small blocks due to tensional stresses on coherent upper layers. This breakup would be accentuated by upward displacement of geothermal isotherms below plateaus (see below). Although Lucchitta [13] points out an instance of such effects along a fretted channel margin there is little evidence for downdrop, tilting, or relative movement of residual upland blocks and mesas.

A somewhat different mechanism for generation and flow of ice relies on artesian water pressures. The height of fretted terrain scarps is on the order of 1-2 km, about the same order of magnitude as the permafrost thickness. Therefore the bottom of the permafrost is displaced upwards below the scarp (Fig. 3A), and the thinnest permafrost is found near the scarp base. If the sub-permafrost aquifer were saturated and under artesian pressure, the gradient through the permafrost would be greatest near the scarp base, and this, coupled with the tendency for the saturated regolith to flow downwards and outwards could lead to a steady-state situation in which outward flow of ice and debris from the base of the scarp (aided, perhaps, by development of segregated ice and ice intrusions) would be balanced by replacement of ice by flow and freezing of groundwater (Fig. 3B). Depending upon the locus of the lower ice-water contact, greater or lesser amounts of regolith would be incorporated in the outward glacial flow (with corresponding variation in backwasting rates). This speculative scenario requires modeling of the heat budget, groundwater flow, ice movement, and regolith response to demonstrate its feasibility.

Source of glacial ice: The former presence of glaciers has been suggested based upon identification of possible moraines or ice-carved features [8]. Although groundwater as a water source for such glaciers has been suggested [8], objections have been raised. Carr [14] notes that springs in Arctic areas do not form large masses of ice, but flow for long distances before freezing. Lucchitta [8] feels that the confined form of the putative glaciers occupying portions of Mars' outflow channels is not the domical shape that might form from freezing of water reaching the surface. However, glaciers may have been fed by a mechanism similar to that suggested for the lobate debris blankets (Fig. 3B) in which groundwater does not have to reach the surface. A variety of phenomena might accompany such glaciation, including rapid headcutting of the scarps (Fig. 3B), creation of ice-dammed lakes with the potentiality of catastrophic draining, and jokulhlaups created by episodic draining of sub-ice lakes created by intrusion of groundwater.

Pingos and other pseudo-volcanic structures: Numerous small domes, some with central depressions, occur on the southern portion of the northern lowlands. The predominant explanation is that they are small volcanic domes [15], although an origin as pingos has also been suggested [6], based upon the very strong resemblance in size and form of open-system pingos to small volcanic cones [17]. An origin as either closed- or open-system is possible, with the position near the highland-lowlands boundary possibly providing the requisite artesian pressures for the latter type.

References: [1] Sharp, 1973a,b, *J. Geophys. Res.*, 78, 4063-72, 4073-83; [2] Squyres, 1978, *Icarus*, 34, 600-13; Squyres, 1979, *J. Geophys. Res.*, 84, 8087-96; [3] Carr, 1979, *J. Geophys. Res.*, 84, 2995-3007; Nummedal and Prior, 1981, *Icarus*, 45, 77-86; [4] Rossbacher and Judson, 1981, *Icarus*, 45, 39-59; [5] Squyres and Carr, 1986, *Science*, 231, 248-52; Squyres, 1989, *Icarus*, 79, 229-88; [6] Lucchitta, 1981, *Icarus*, 45, 264-303, Costard and Dollfus, 1986, *LPI Tech. Rpt. 87-02*, 211-2; [7] Parker et al., 1989, *Icarus*, 82, 111-45; [8] Lucchitta, 1982, *J. Geophys. Res.*, 87, 9951-73; [9] Howard, 1991, Role of Groundwater in Formation of Martian Channels [*This volume*]; [10] Howard, 1991, A Martian Global Groundwater Model [*This volume*]; [11] Zimbleman et al., 1988, *LPSC XIX*, 1321-2; Moore, 1990, *J. Geophys. Res.*, 95, 14279-89; [12] Carr and Schaber, 1977, *J. Geophys. Res.*, 82, 4039-54; [13] Lucchitta, 1984, *J. Geophys. Res.*, 89, B409-18; [14] Presentation at 1989 Fall AGU; [15] Frey and Jarosewich, 1982, *J. Geophys. Res.*, 87, 9867-70; [16] Muller, 1959, *Medd. om Gronland* 153(3), 127p.

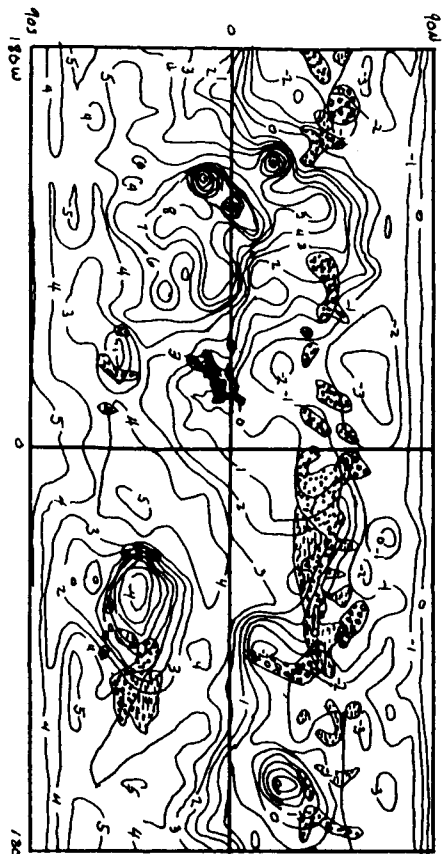


Fig. 1. Generalized Mars topography, showing location of felled terrain (heavy dots), concentric crater fills (dashes), curvilinear features (open circles), and chaotic terrain (cross-hatching). Based upon published maps [2,4,5].

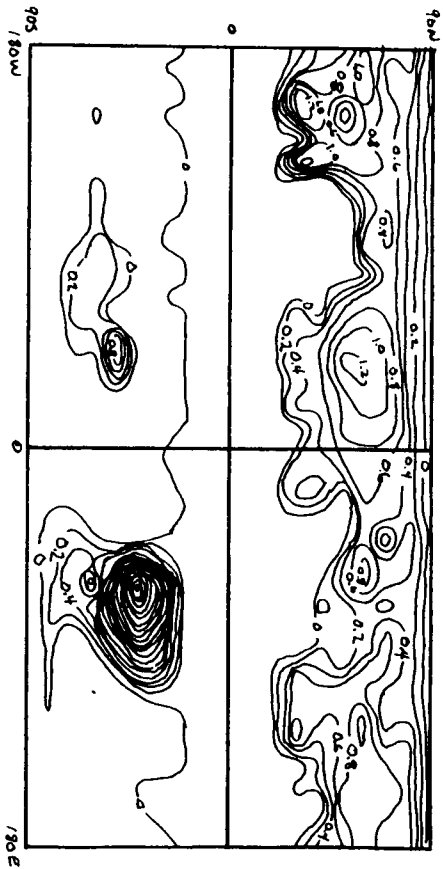


Fig. 2. Contours of steady-state artesian gradients through near-surface permafrost under conditions of complete permafrost poleward of $\pm 20^\circ$ latitude and recharge in equatorial regions.

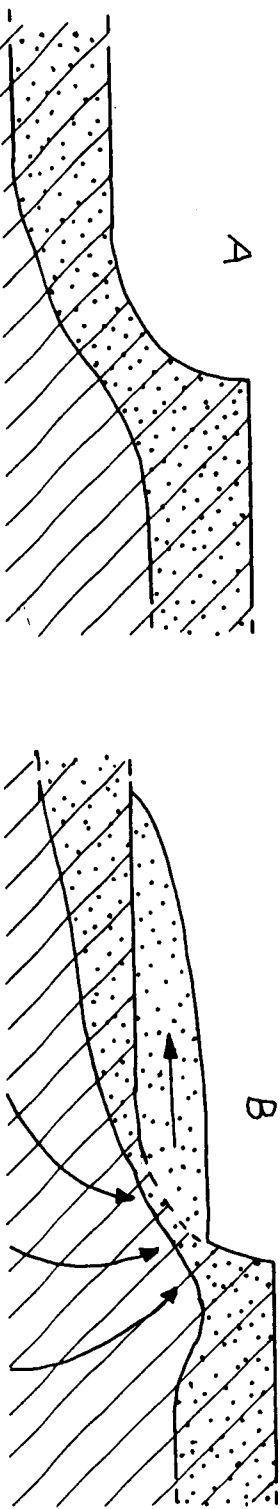


Fig. 3. (A) Distribution of permafrost beneath a scarp under conditions of no groundwater or ice flow, and (B) Distribution of ground ice, debris apron, and ice and water flow patterns under hypothesized model for origin of lobate debris apron. Dotted areas are permafrost or ice-cored debris apron, ruled areas are regolith.

GLACIAL AND MARINE CHRONOLOGY OF MARS; Robert G. Strom, Jeffrey S. Kargel, Natasha Johnson, and Christine Knight; Lunar and Planetary Laboratory, University of Arizona, Tucson AZ 85721

A hydrological model involving episodic oceans and ice sheets on Mars has been presented by Baker, *et al.* (1,2). One of the main uncertainties concerning this model is the age and correlation of these events. Even more uncertain are their absolute ages. However, based on stratigraphic and cratering evidence, the most recent occurrence of these events was relatively late in Martian history.

The cratering record on Mars can be divided into three general periods: 1) the period of late heavy bombardment, 2) a transition period at the end of late heavy bombardment, and 3) the post heavy bombardment era (3). The crater size/frequency distribution represented by the period of late heavy bombardment is characterized by a complex curve with a differential -2 slope (cumulative -1) at diameters less than about 50 km diameter, while the post heavy bombardment size distribution has a differential -3 slope (cumulative -2) over the same diameter range (Fig. 1). On the Martian time-stratigraphic scale, the period of late heavy bombardment occurred during Noachian and Early Hesperian time and came to an end during the Middle Hesperian. The post heavy bombardment era began in Late Hesperian time and extends through the Amazonian Epoch to the present day (3).

Although a Noachian ocean is suggested as a theoretical consequence of a warm, wet early Mars (4,5), as an element in the hydrological cycling responsible for the widespread Noachian valley networks, and a cause of an erosional episode near the end of late heavy bombardment (6), there is no direct evidence for such an ocean. Evidence for a more recent sporadic formation of great northern plains oceans has been presented by Parker, *et al.* (7). Since most of the northern plains are Late Hesperian (3,8) these oceans cannot be older. The outflow channels, thought to be the sources of the oceans, show multiple flow episodes and ages ranging from Late Hesperian to Late Amazonian (8). High density valleys on Alba Patera have been attributed to water runoff possibly associated with a nearby ocean (9). The age of the surface on which these superposed valleys occur is Early Amazonian indicating the valleys and ocean are younger (Early to Middle Amazonian). Chapman, *et al.* (10) present evidence that the Elysium basin was occupied by an ephemeral sea which they date as Amazonian based on stratigraphic evidence. This "sea" may have been part of the late ocean mentioned above.

There is mounting evidence that widespread episodic glaciation occurred in the southern hemisphere southward of about -40 degrees (2, 11, 12, 13). The most detailed studies are of the Argye and Hellas regions (11, 12, 13). Crater counts in the Hellas basin, presented in a companion abstract by Johnson *et al.* (13), indicate that the Hellas glaciation occurred during the Middle Amazonian. We also counted craters on the southern floor of Argyre occupied by ridges (eskers). Although there is evidence for at least two glacial epochs, the esker plains appear to be the most recent. The craters were divided into three types: 1) craters with ejecta blankets, 2) craters with no visible ejecta blankets but relatively sharp rims, and 3) no ejecta blankets and highly degraded rims. The craters with ejecta blankets are probably post glaciation and equivalent to ejecta blanket craters in Hellas. Fig. 2 is an "R" plot of the size/frequency distribution of ejecta blanket craters on the Argyre esker plains and similar craters in Hellas. Also shown for reference are the Northern Plains (Late Hesperian) and the Tharsis Volcanic Plains (Amazonian). The Hellas and Argyre curves are essentially identical within the errors, indicating similar ages of glaciation during Middle Amazonian time. The glacial features (eskers, outwash plains, etc.) recognized in Argyre, Hellas and elsewhere (11, 12, 13) require glacial melting and running water for relatively long periods of time. This in turn requires a temperate climate with summer temperatures above the melting point of ice during Middle Amazonian time. Fig. 3 summarizes the relative chronology of oceans, ice sheets and other major events in Martian history.

The absolute ages of these events is very uncertain and depends on one's assumptions about the origin of the impacting objects and the cratering rate. If the period of late heavy bombardment ended the same time on Mars and the Moon, then the Middle Hesperian is about 3.8 Gy old. However, if the objects responsible for late heavy bombardment were accretional remnants, their sweep-up time at Mars would be extended by about 1 Gy due to perturbations of the objects into the u_6 secular resonance (14). In this case the Middle Hesperian is about 2.8 Gy old. Thus, ocean and ice sheet formation on Mars must be substantially younger than 3.8 or 2.8 Gy. Depending on different models (15, 16), the Middle Amazonian could be anywhere between about 2.3 to 0.25 Gy, and therefore ice sheets and a temperate climate were present sometime during this time span. In a separate abstract (12) we estimate that the Middle Hesperian glacial epoch lasted for a period on the order of 2 million years, to an order of magnitude.

CHRONOLOGY OF MARS: Strom, *et al.*

References. 1. Baker, *et al.*, 1990, Lun. Planet. Sci. XXI, 40-41. 2. Baker, *et al.*, 1991, Nature, submitted. 3. Strom, *et al.*, 1991, Mars, Univ. Arizona Press, in press. 4. Pollack, *et al.*, 1987, Icarus, 71, 203-224. 5. Schaefer, M.W., 1990, J. Geophys. Res., 95, 14291-14300. 6. Chapman and Jones, 1977, Ann. Rev. Earth Planet. Sci., 5, 515-540. 7. Parker, *et al.*, 1989, Icarus, 82, 111-145. 8. Tanaka, K.L., 1986, Proc. Lun. Planet. Sci. Conf. 17th. J. Geophys. Res., 91, E139-E158. 9. Gulick and Baker, 1990, J. Geophys. Res., 95, 14325-14344. 10. Chapman, *et al.*, 1990, Lun. Planet. Sci. Conf. XXI, 180-181. 11. Kargel and Strom, 1990, Lun. Planet. Sci. Conf. XXI, 597-598. 12. Kargel, *et al.*, 1991, Lun. Planet. Sci. Conf. XXII, this volume. 13. Johnson, *et al.*, 1991, Lun. Planet. Sci. Conf. XXII, this volume. 14. Wetherill, G.W., 1975, Proc. Lunar Planet. Sci. Conf. 6th, Pergamon Press, 1539-1561. 15. Neukum and Wise, 1976, Science, 194, 1381-1387. 16. Hartman, *et al.*, 1981, Basaltic Volcanism on the Terrestrial Planets, Pergamon Press, New York, 1049-1127.

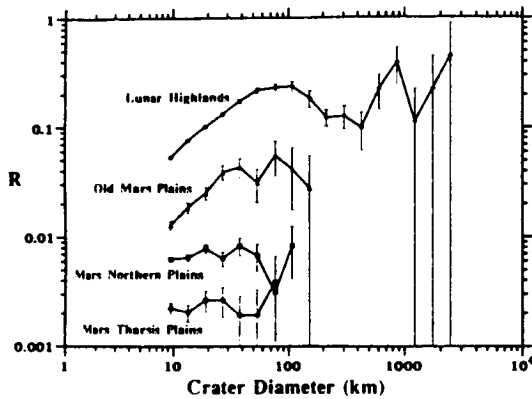


Fig. 1. "R" plot of the crater size/frequency distribution of the lunar highlands, martian old plains (Early Hesperian), Mars Northern Plains (Late Hesperian), and Mars Tharsis Plains (Amazonian).

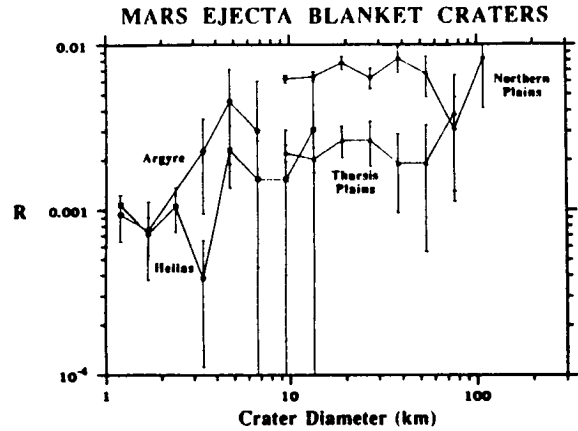


Fig. 2. "R" plot of the size/frequency distributions of post-glacial craters in Argyre and Hellas compared to the martian Northern and Tharsis Plains.

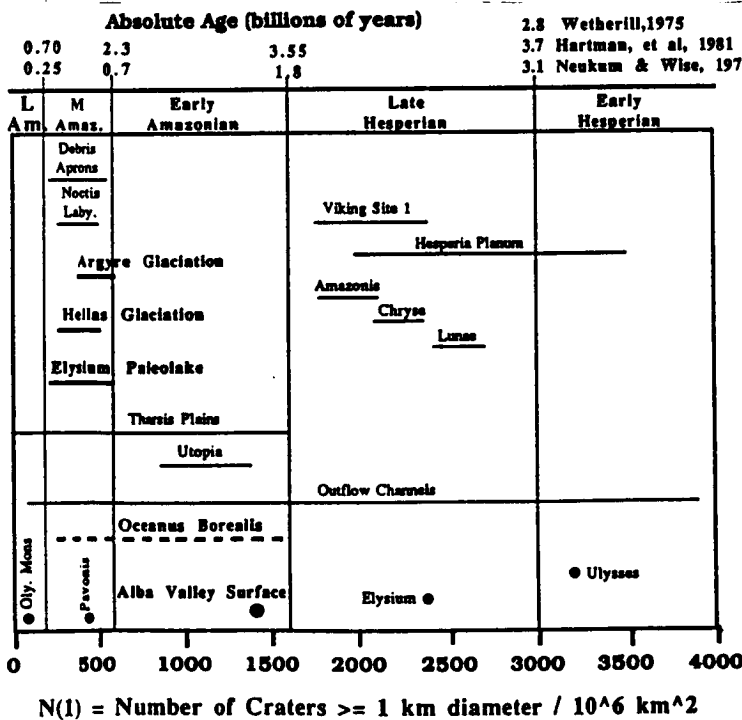


Fig. 3. Summary of the time-stratigraphic age of ice sheet and ocean formation together with several other major events in Martian history.

CHRONOLOGY OF GLACIATION IN THE HELLAS REGION OF MARS; N. Johnson, J.S. Kargel, R.G. Strom, and C. Knight, Dept. of Planetary Sciences, Univ. Arizona, Tucson, AZ

Introduction. The Hellas Impact Basin is one of the oldest features on Mars, as indicated by the high density of large impact craters in parts of the basin. The highly degraded condition of Hellas seems consistent with great antiquity. However, many of the most strikingly modified landscapes in the basin, believed to be glaciogenic [1], also appear to be geologically youthful. Stratigraphic relations suggest two episodes of glaciation. In this report we impose chronologic constraints on glaciation based on the impact cratering record. We focus on the southwestern portion of Hellas (USGS quad MC-27SE). Major terrain units are mapped in Figure 1. The lineated terrain (see also Fig. 1 of reference 1) and ridged plains form the summit and flanks of a large shield volcano, Amphitrites Patera, which was superimposed over the southwestern rim of Hellas toward the end of heavy bombardment. The ridged plains and lineated terrain are crossed by numerous wrinkle ridges. The lineated terrain is distinguished by a pervasive system of deep erosional troughs and sharp ridges thought to have been glacially sculpted by the Hellas Lobe. The heavily cratered Hellas rim shows evidence for both glacial erosion and widespread debris blanketing; most large craters on the Hellas rim are highly degraded, and some have been cut by fluvial channels probably related to deglaciation.

Chronology. Visual inspection of Viking images shows deep erosion of many impact craters in the MC27SE photomosaic, particularly in the lineated terrain. To investigate the history of cratering and crater degradation we generated crater statistics for over a thousand impact craters using 126 high-resolution images (about 100 m per line-pair). Craters were classified according to their state of preservation. Class A craters display sharp rims and crisply-preserved ejecta blankets. Class B craters have partially eroded ejecta blankets. Ejecta blankets of Class C craters are entirely absent. Rim morphology of Class B and C craters ranges from sharp to highly degraded. In the deeply eroded lineated terrain the classification seems to separate preglacial (B and C) from postglacial craters (A) in most instances. In the less deeply eroded Hellas rim (Hellas Montes) and ridged plains the classification is less reliable in this regard. Since the ridged plains and lineated terrain apparently have the same volcanic age, comparison of the cratering record of the lineated terrain and ridged plains provides valuable insights into the nature of the erosional event.

Figure 2 shows crater size-frequency distributions for crater classes (A + B + C) (combined), for the lineated terrain, ridged plains, and Hellas rim. Cumulative crater statistics are provided in Table 1. The density of craters with diameters (D) greater than 16 km on the Hellas rim is comparable to the lunar highlands. Plots for the lineated and ridged plains show much lower crater densities; data for D > 4 km indicate that these terrains share essentially the same early Hesperian volcanic age, consistent with the age of the "Hellas Plains" reported previously [2]. However, small craters (D < 4 km) with ejecta blankets are sharply depleted on the lineated terrain compared to the ridged plains. For 1 km < D < 2 km this depletion amounts to nearly a factor of two, a statistically highly significant (4 σ) difference. The simplest explanation is that the lineated terrain suffered widespread erosional removal of small craters, consistent with pervasive large-scale scouring most obvious in the lineated terrain [1].

Figure 3 and Table 1 compare class (A + B) craters in the lineated terrain and ridged plains. Figure 4 gives complementary data for class C. Figure 3 shows a greater proportion of ejecta blankets for craters of all sizes on the ridged plains compared to the lineated terrain, indicating less erosion on the ridged plains. Figure 4 shows a sympathetic relationship for craters lacking ejecta, where, at D > 2 km, the deeply eroded lineated terrain has more class C craters than the ridged plains; at D < 2 km this relationship reverses, consistent with nearly complete removal of small craters, including their rim and bowl as well as ejecta. These data document the deep and widespread glacial erosion and thorough resetting of the relative chronometer based on small craters in the lineated terrain, and less extensive erosion on the ridged plains, consistent with independent morphological observations.

The density of class A craters on the lineated terrain, 280 (+/-40) > 1 km per 10⁶ km², gives a lower limit on the relative age of glaciation, equivalent to late Middle Amazonian [3]. This age is a younger limit (probably a close limit) since the criteria to qualify for class A were rather stringent. The size-frequency distribution for class A craters is consistent with the characteristic production distribution function known for the younger crater population on Mars, suggesting that erosion of the lineated terrain occurred at a discrete point in geologic time. An upper limiting age of glaciation, 491 (+/-54) craters > 1 km per 10⁶ km², corresponding to early Middle Amazonian, is obtained by considering classes A and B together. This upper limit is unlikely since class B ejecta by definition show evidence of erosion and since Class B craters do not show a production size distribution.

Table 1 provides crater densities for class (A + B) (craters with ejecta blankets) in Argyre's esker plains. The data indicate statistically identical upper limiting relative ages of glaciation in the two regions (N₁ = 491 and 511 for Hellas lineated terrain and Argyre esker plains, respectively, for classes A + B). Global age correlations of significant Middle Amazonian events are discussed in more detail in an accompanying paper [4].

Conclusions. Glaciation in Hellas occurred during the Middle Amazonian, roughly coeval with glaciation in Argyre. We compare the maximum and minimum relative ages of glaciation with two models giving absolute age conversions [3], inferring higher and lower absolute age estimates of about 2300 and 250 million years, respectively.

References. [1] Kargel, Strom, and Johnson, 1991, ABSTRACT, this volume. [2] Strom, R.G., S.K. Croft, and N.G. Barlow, 1991, chapter in Mars book, IN PRESS, Univ. Arizona Press. [3] Tanaka, K.L., 1986, *Proc. Lun. Planet. Sci. Conf.* 17th, *J. Geophys. Res.*, 91, suppl., E139-E158. [4] Strom et al., 1991, ABSTRACT, this volume.

Table 1. Cumulative numbers, N, of craters > 1, 4, and 16 km diameter per 10⁶ km²

TERRAIN	AREA (km ²)	N ₁ (error)	N ₄ (error)	N ₁₆ (error)
Hellas Lineated Terrain				
Class A (min. glacial age)	169,000	284 (41)	18 (10)	0
Class B		207 (35)	41 (16)	0
Class C		792 (68)	284 (41)	59 (19)
Class A + B + C		1283 (87)	343 (45)	59 (19)
Class A + B (max. glacial age)		491 (54)	59 (19)	0
Hellas Ridged Plains				
Class A	249,000	394 (40)	24 (10)	4 (4)
Class B		752 (55)	145 (24)	32 (11)
Class C		611 (50)	458 (85)	32 (11)
Class A + B + C		1756 (84)	285 (34)	68 (17)
Class A + B		1145 (68)	169 (26)	36 (12)
Hellas Rim				
Class A	71,000	140 (44)	0	0
Class B		519 (85)	42 (24)	28 (20)
Class C		2034 (169)	785 (105)	210 (54)
Class A + B + C		2707 (195)	842 (109)	210 (54)
Class A + B		659 (96)	42 (24)	0
Argyre-Esker Plains				
Class A + B	43,000	511 (109)	116 (52)	0
Class A + B + C		1695 (198)	186 (66)	0

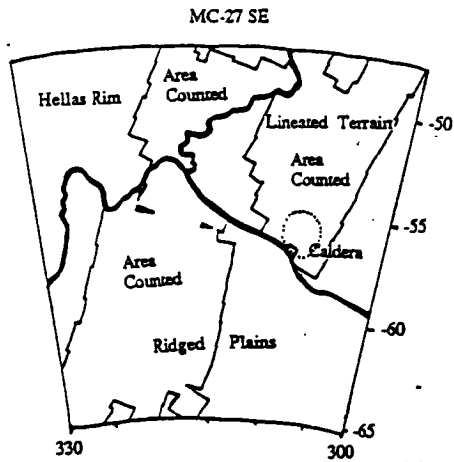


Figure 1. Terrain map of the region MC-27SE showing crater counting areas.

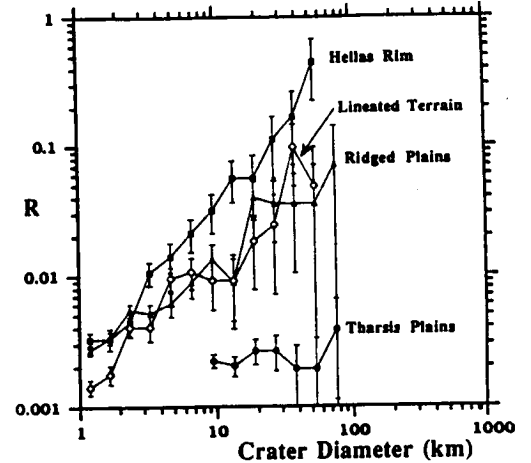


Figure 2. 'R-plot' showing crater size-frequency distribution for craters of classes A, B, and C, combined, in the lineated terrain, ridged plains, and Hellas rim.

EJECTA BLANKET CRATERS

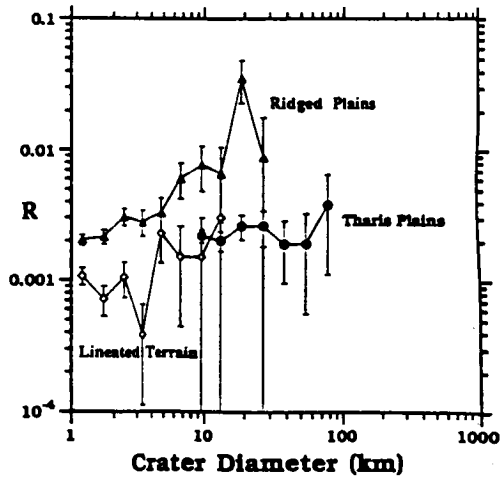


Figure 3. 'R-plot' showing crater size-frequency distribution for Classes A and B, combined (those having ejecta blankets), in lineated terrain and ridged plains.

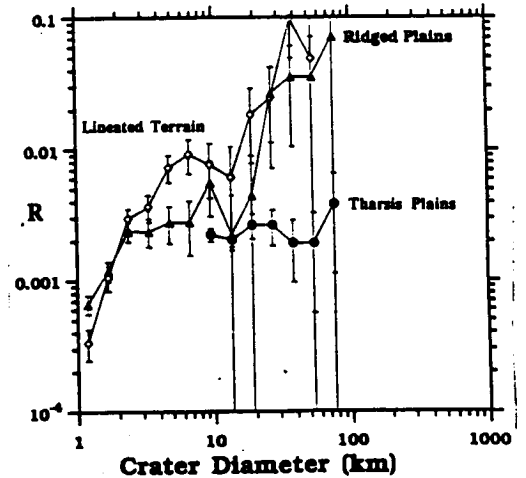


Figure 4. 'R-plot' showing crater size-frequency distribution for Class C craters alone (those lacking ejecta blankets) in the lineated terrain and ridged plains.

GLACIAL GEOLOGY OF THE HELLAS REGION ON MARS; Jeffrey S. Kargel, Robert G. Strom, and Natasha Johnson; Lunar and Planetary Laboratory, Univ. of Arizona, Tucson 85721

Introduction. We recently presented a glacial geologic interpretation for Argyre [1], which we now extend to Hellas. This glacial event is believed to constitute an important link in a global cryohydric epoch of Middle Amazonian age [2, 3]. At glacial maximum, ice apparently extended far beyond the regions of Argyre and Hellas, and formed what we term the Austral Ice Sheet, an agglomeration of several ice domes and lobes including the Hellas Lobe.

Regional landform associations. The Hellas Lobe originated on the summit and slopes of the giant shield volcano Amphitrites Patera, and dominated northward inflow into the Hellas impact basin (Figs. 1 and 2). The Hellas-facing side of Amphitrites Patera is dominated by a ridge-and-trough structure, indicating pervasive scouring perhaps similar to that of glaciated lineated terrains in Canada [4]; thus, we term this region the lineated terrain. The erosive agent appears to have been an aerially extensive, high-standing medium such as ice. It efficiently erased most craters smaller than 2 km, apparently at essentially a discrete point in geologic time [5]. The erosive agent flowed around several of the largest craters, preserving their rims while severely degrading or completely removing their ejecta blankets, and producing deep upslope and lateral fluting. Orientations of lineations are strongly correlated with large-scale topography, thus confirming an essentially down-slope movement of the erosional medium. Subsidiary fluvial erosion, probably by glacial meltwater, also occurred.

The lineated terrain passes northward into a complex region on the floor of Hellas including an area of streamlined ridges and equant hills interpreted as a drumlinoid terrain; the orientations of drumlinoid features are consistent with northward flow of ice from the lineated terrain. Long, sinuous ridges, believed to be eskers [6], are also present but uncommon. Drumlinoid terrain grades northward into a region interpreted as hummocky ground moraine formed by glacial till deposition and massive ice disintegration. Hummocky deposits form thick blankets of material terminating northward along transverse cusped ridges and escarpments, consistent with our interpretation that these are moraines of southward derivation. The cusped ridges spaced across the floor of Hellas mark terminal and recessional margins of the former Hellas Lobe. At glacial maximum ice apparently flowed to and terminated near the deepest part of the basin. Other ridges in the northern part of Hellas resemble lunar-type wrinkle ridges and have not been mapped.

Smooth channel-fed plains, interpreted as proglacial lake deposits, are widespread on the floor of Hellas, especially in the east-northeastern sector. Large channels entering the area from highlands to the east become subdued and strongly anastomosing, apparently indicating transition to a depositional regime as the channels entered the lake area. Escarpments in the glaciolacustrine plains area may have been wave-cut, and thus possibly indicate former lake levels. Moraine-like ridges in the vicinity of the glaciolacustrine plains area are often flat-topped, also consistent with erosional planation by wave activity.

Volume of the Hellas Lobe. The Hellas Lobe extended nearly 1500 km from Amphitrites Patera to its northern terminus and covered an area of approximately 1.5×10^9 km². We constructed a simple model of the ice profile based on Bingham rheology and a combined parabolic and inclined plane solution incorporating isostatic adjustments. The model thickness of ice on the slopes of Amphitrites Patera ranges from 450 to 900 m, consistent with the heights of ridges and the flowage of ice around large craters. On the basin floor the parabolic solution indicates ice thicknesses ranging to nearly 4000 meters. The integrated volume of the Hellas Lobe model is 4.7×10^9 km³. If the Hellas Lobe was typical of the entire Austral Ice Sheet, and if this ice sheet covered around 12% of the planet's surface (2/3 of the area lying between the South Pole and 40° S. Lat.), then the total ice volume would be 5.5×10^7 km³, equivalent to a global layer of water 340 meters thick. This estimate is of the same order as the water budget of Mars calculated on independent grounds [e.g., 7, and other references in 2].

Depth of erosion. The vertical scale of troughs and ridges in the lineated terrain suggests erosion to a depth of order 500 m in the most strongly affected localities. We base an independent estimate on crater statistics. In a separate abstract [5] we show that the lineated terrain exhibits a great deficiency of craters in the 1-2-km size class, and a smaller deficiency between 2-4 km, a feature attributed to glacial erosion. The average ratio $d:D$ (depth : Diameter) for fresh, simple craters on Mars is 1:6, indicating $d = 170$ and 670 m for fresh craters having $D = 1$ and 4 km, respectively. A crater would probably be obscured if erosion occurred to a depth of 0.6d. Thus, the cratering record indicates that the lineated terrain has suffered widespread erosion to a depth of 100 m and locally to 400 m (based on removal of most 1-km and some 4-km preglacial craters). We take 200 m as a rough average erosional depth.

Chronology of glaciation. Statistics for fresh craters indicate a Middle Amazonian age of glaciation in Hellas. The Middle Amazonian also saw extensive cryohydric activity elsewhere on Mars. The Argyre region apparently also was glaciated during the Middle Amazonian, and lobate debris aprons (rock glaciers?) were widely deposited in the Northern Hemisphere [3], collectively indicating a global humid epoch of glacial-periglacial conditions within this period. Earlier indications that fluvial erosion on Alba Patera may have been synchronous with glaciation now seem more doubtful since this fluvial event may have occurred in the later part of the Early Amazonian or earliest Middle Amazonian, before the glacial event [8]. The absolute chronology is more problematic. However, in an accompanying abstract we estimate that Middle Amazonian glaciation in Hellas probably occurred not earlier than 2300 million years ago and not later than 250 million years ago. We cannot exclude the possibility that older episodes of glaciation may also have occurred in this area.

We estimate the duration of glacial erosion in the lineated terrain by considering the average rate of glacial erosion on Earth. Laurentide glaciation eroded an average of about 150 meters of rock from affected areas over the

past 3 million years [9]. Approximately half of this period represents glacial epochs and half is interglacial. Thus, the average rate of Laurentide glacial erosion calculated for the glacial epochs is about 0.010 cm y^{-1} . At this rate 200 m of erosion in the lineated terrain would require 2×10^8 years of glaciation. Of course martian glacial erosion rates may not have been similar to terrestrial rates. Amphitrites Patera, being a shield volcano, would likely be composed of highly fractured volcanic rock, thus enhancing the efficiency of plucking and favoring high erosional rates and short durations; warm-based glaciers, as we believe the Hellas Lobe was, would also favor high erosional rates. On the other hand, the lower surface gravity on Mars would decrease shear stresses and erosional rates relative to the Earth (this factor, however, is partially offset by a thickening of the martian ice sheet relative to terrestrial ice sheets also due to the g factor). Thus, two million years is an order-of-magnitude estimate of the duration of Middle Amazonian glaciation in the Hellas region.

Alternative mechanisms. We acknowledge that morphologies discussed here can be explained nonglacially. For example, winds may have scoured the lineated terrain. Dust storm activity apparently cycles a meter or so of dust between hemispheres on the relatively short precessional timescale, resulting in dramatic atmospheric effects but very little actual erosion of rock, as testified by the preservation of many blocks at the Viking landing sites on terrains which must be on the order of a billion years old [10]. It seems unlikely that hundreds of meters of erosion of apparently basaltic lava in the lineated terrain could have occurred. Anyway, aeolian processes would not likely produce down-slope orientations of lineations in the lineated terrain; the magnitude of the negative thermal anomaly associated with Hellas is less than half that of the positive Tharsis anomaly where no orographically-associated aeolian erosion is observed; at Hellas the maximum vertical component of mechanically- and thermally-forced orographic winds is on the order of only a few cm sec^{-1} [11]. Furthermore, other processes would be required to explain young fluvial systems on the lineated terrain and other glacial-appearing morphologies in the Hellas region. The regional associations and ordered sequences of landforms, their relationships to large-scale topography, and the age of this event relative to other proposed glacial/periglacial events on Mars, are all well explained by glaciation. Alternative hypotheses will have to compete with the economy of the glacial hypothesis in explaining these important aspects as well as the morphologies of individual landforms.

Conclusions. 1) Hellas was apparently heavily glaciated. 2) Glaciation was young by martian standards (Middle Amazonian), and ancient by terrestrial standards. 3) Glaciation occurred during the same period that other areas on Mars were experiencing glaciation and periglacial activity. 4) Glaciation occurred as a geologically brief epoch of intense geomorphic activity in an era characterized by long periods of relative inactivity.

References. 1. Kargel, J.S. and Strom, 1990, *Lun. Planet. Sci.* XXI, 597-598. 2. Baker et al., 1990, *Nature*. 3. Strom et al., 1991, *Lun. Planet. Sci.* XXII (ABSTRACT), this volume. 4. Smith, H.T.U., 1948, *Amer. J. Sci.* 246, 503-514. 5. Johnson et al., 1991, *Lun. Planet. Sci.* XXII (ABSTRACT), this volume. 6. Kargel et al., 1991, *Lun. Planet. Sci.* XXII (ABSTRACT), this volume. 7. Carr, M.H., 1987, *Nature* 326, 30-34. 8. Gulick, V.C. and V.R. Baker, 1990, (ABSTRACT) *Lun. Planet. Sci.* XXI, 443-4, and private comm. 9. Bell, M. and E.P. Laine, 1985, *Quat. Res.* 23, 154-174. 10. Arvidson, R., E. Guinness, and S. Lee, 1979, *Nature* 278, 533-535. 11. Webster, P.J., 1977, *Icarus* 30, 626-649.

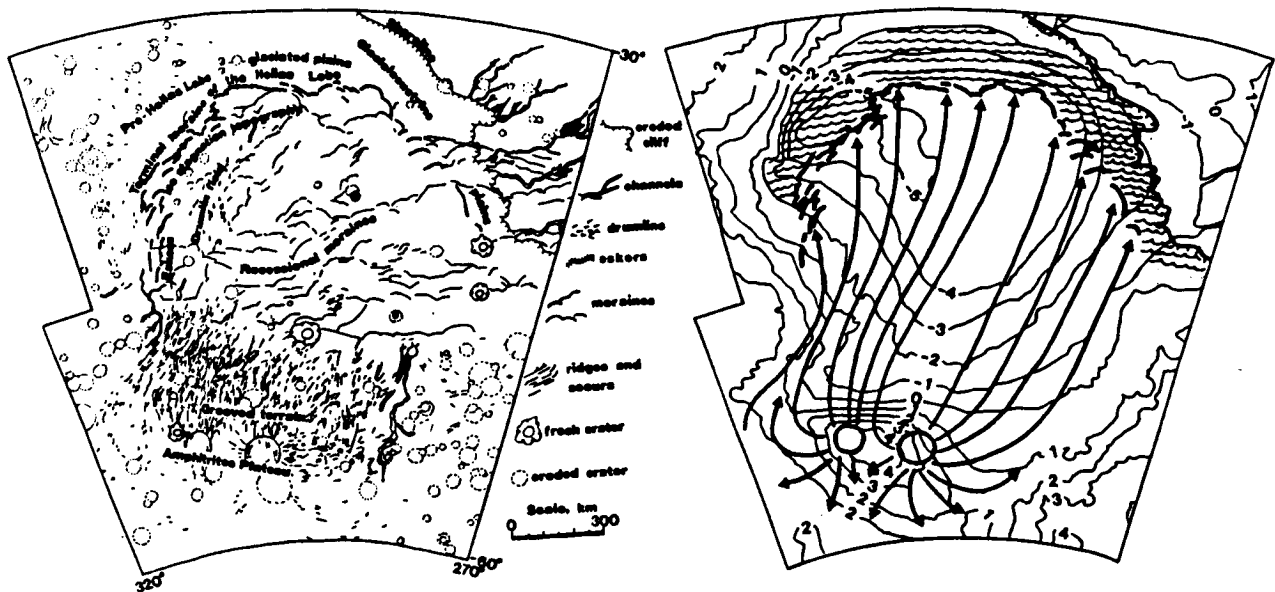


Figure 1. Distribution of selected glacial features in Hellas.

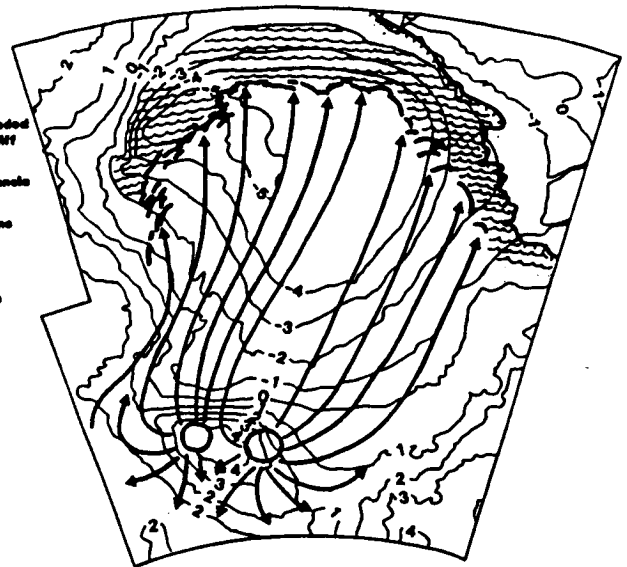


Figure 2. Schematic ice flow lines and former distribution of glacial ice and a proglacial lake in Hellas.

TERRESTRIAL GLACIAL ESKERS: ANALOGS FOR MARTIAN SINUOUS RIDGES; J.S. Kargel and R.G. Strom, Lunar and Planetary Laboratory, Univ. Arizona, Tucson, AZ 85721

Introduction. Last year we introduced a glacial model for the Argyre region [1], a concept which we now extend [2], and which we recently integrated with a Global Hydrologic Model incorporating many other aspects of martian geology [3]. The original insight for the glacial interpretation came from an unusual system of sinuous ridges in Argyre (Figs. 1,2). Similar ridges occur in many areas of Mars, mostly at middle to high latitudes (Figure 3). Very few geologic mechanisms can form such ridge systems, inasmuch as they have distinctly fluvial planimetric structures, yet are ridges, not valleys or channels. Proposed origins as sand dunes, wrinkle ridges, lava flows, dikes, clastic dikes, or beach ridges [4-7] have no observational support in our view, since they are unsatisfactory in explaining ridge morphologies, planimetric structure, scale, and regional landform assemblages. Despite wide agreement that the martian ridges strongly resemble glacial eskers, this hypothesis has been presented with great equivocation due to a perceived lack of other glacial landforms [5,8]. Quite to the contrary, we have shown that the martian ridges actually do occur in logical ordered sequences with many other types of characteristically glacial-appearing landforms [1,2]. Here, we further support the esker hypothesis in isolation from considerations of regional landform assemblages.

The esker model. Glacial meltwater streams flowing on the surfaces of stagnant glaciers or in subglacial tunnels collect coarse sediment on their beds, as most streams do, but leave these deposits as elevated ridges, termed *eskers*, after the ice ablates (Figs. 4,5). Eskers are among the most abundant, widespread, and most clearly diagnostic features indicating Pleistocene glaciation [9]. Terrestrial eskers occur on almost as wide a range of scales as normal streams, from several m to over 400 km long, from a few cm to 200 m high, and from 25 cm to 6 km wide [9,10]. Landsat images show hundreds of eskers 300-1200 m wide extending in well-integrated systems across much of Canada [11,12].

Terrestrial eskers sometimes occur as lone, sinuous ridges, in alignments of disconnected bead-like hills, or in complex systems (Figure 6). Common dendritic and anastomosing planimetric structures of complex esker systems [9,11,13] may reflect normal meltwater drainage, or can be inherited from preglacial fluvial valleys on the glacier bed. Dendritic distributary patterns are also known [14]. These patterns can be modified by ice shear, producing *en echelon* patterns. Rectilinear and orthorhombic esker systems can be generated by drainage through glacial crevasses. Eskers can be deposited across subglacial topographic divides and may cross-cut other eskers. Eskers commonly grade longitudinally into or occur on the floors of subglacially-eroded fluvial valleys ("tunnel valleys") formed during catastrophic bursts of subglacially stored meltwater [14]. Terrestrial eskers can be sharp-crested, rounded, flat-topped, or double-ridged, and commonly have axial depressions (kettles) on their crests [9]. Axial depressions and double-ridged structures are collapse features formed when ice cores melt.

Terrestrial eskers are composed mostly of sand and gravel, but also boulders and clay, sometimes all in one vertical section. Sediments are usually well-sorted as they are in most other fluvial deposits (Fig. 4), and both normal and reverse grading are common, indicating large variations in water discharge. Fig. 4 shows a large faceted boulder embedded in otherwise well-sorted esker sediments; the boulder apparently fell in from the roof or wall of the ice tunnel in which the esker was deposited. Slumping and other minor mass wasting commonly occurs as ice tunnel walls melt and withdraw their support. Planar subhorizontal bedding and cross-stratification are common in eskers; the scale of these layerings ranges from centimeters to tens of meters.

Martian eskers. Every aspect of terrestrial eskers and esker systems is matched by analogs on Mars. Martian esker systems are up to 800 km long; individual ridges are typically 100-200 km long, 600-2400 m wide, and on the order of 40-160 m high. They occur as lone, sinuous ridges; in cross-cutting and *en echelon* sets; in anastomosing, dendritic, rectilinear, and distributary-type systems; they occur in associations with tunnel valleys, braided outwash, and many other glacial landforms; and, martian eskers include sharp-crested, flat-topped, rounded, and double-ridged varieties, and display internal bedding.

Conclusions. Martian sinuous ridges are similar in every respect to terrestrial eskers: scale, morphology, planimetric pattern, and associations with other probable glaciogenic landforms. In sum, we find the esker hypothesis well supported. Eskers are glaciofluvial structures, and owe their existence to large-scale melting of stagnant temperate glaciers. Thus, eskers are indicators of an ameliorating climatic regime after a protracted episode of cold, humid conditions. We infer from the apparent existence of eskers on Mars that large areas of that planet were formerly heavily glaciated; that Mars underwent climatic variations similar to those of the Pleistocene on Earth; and that the martian atmosphere was formerly moist, dense, and warm.

References. 1. J.S. Kargel and R.G. Strom, 1990, *Lun. Planet. Sci.* **XXI**, 597-598. 2. Other abstracts, these volumes, by Kargel *et al.*, Johnson *et al.*, Strom *et al.*, and Baker *et al.* 3. V.R. Baker, R.G. Strom, V.C. Gulick, J.S. Kargel, G. Komatsu, and V.S. Kale, 1991, submitted to *Nature*. 4. M.H. Carr *et al.*, 1980, *Viking Orbiter Views of Mars*, NASA SP-441, p. 122; and M.H. Carr in *The Geology of the Terrestrial Planets*, NASA SP-469, p. 232. 5. S.W. Ruff and R. Greeley, *Lun. Planet. Sci.* **XXI**, 1047-1048. 6. K.L. Tanaka and D.H. Scott, 1987, USGS Map I-1802-C. 7. T. Parker, 21st Lun. Planet. Sci. Conf., personal communication. 8. A. Howard, 1981, *Repts. Planet. Geol. Prog.* - 1981, NASA TM 84211, 286-287. 9. R.J. Price, 1973, *Glacial and Fluvio-glacial Landforms*, Hafner Publ. Co., New York, 242 pp. 10. H. Lee, 1965, *Geol. Surv. Canada Pap.* 65-14, 1-17. 11. glacial map of Canada. 12. G.S. Boulton and C.D. Clark, 1990, *Nature* **346**, 813-817. 13. R.L. Shreve, 1985, *Quat. Res.* **23**, 27-37. 14. H.E. Wright, 1973, *Geol. Soc. Amer. Mem.* **136**, 251-276.



Figure 1. Portion of martian Argyre Basin showing features supportive of glaciation, including anastomosing system of esker, glaciolacustrine plains, and associated cirques, aretes, rock glaciers, and other glacial/periglacial landforms. Scene width about 300 km, illumination from top right.



Figure 2. Close-up of esker ridge system in Argyre. Scene width about 50 km, illumination from top.

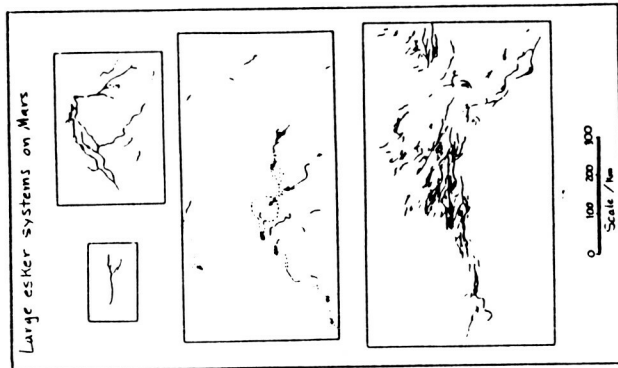


Figure 3. Planimetric patterns of esker systems on Mars.



Figure 4. Glaciofluvial sediments in an esker in Minnesota. Keys for scale.



Figure 5. Esker emanating from subglacial meltwater channel at the front of the Woodsworth Glacier (upper right, very dirty) in Alaska and terminating in an outwash fan (lower left). Note also striated till and kettles.

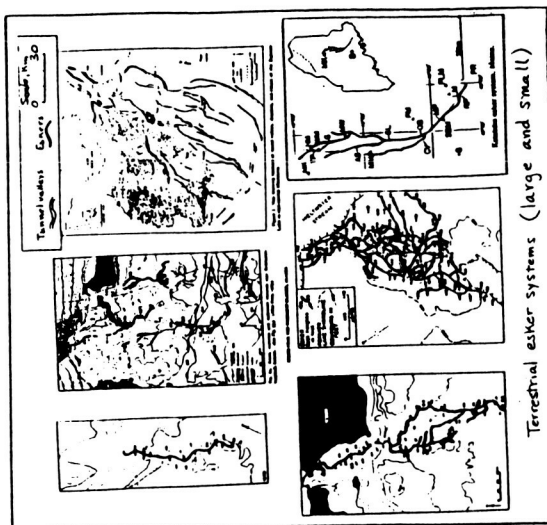


Figure 6. Planimetric patterns of terrestrial esker systems.

PALEOLAKES AND LACUSTRINE BASINS ON MARS. David H. Scott, James W. Rice, Jr., and James M. Dohm, U.S. Geological Survey, Flagstaff, Arizona 86001

The problems of how warm and wet Mars once was and when climate transitions may have occurred are not well understood. Mars may have had an early environment similar to Earth's that was conducive to the emergence of life. In addition, increasing geologic evidence indicates that water, upon which terrestrial life depends, has been present on Mars throughout its history (1-8). This evidence does not detract from the possibility that life may have originated on early Mars, but rather it suggests that life could have developed over longer periods of time in longer lasting, more clement local environments than previously envisioned. Indications of past or present life most likely would be found in areas where liquid water existed in sufficient quantities to provide for the needs of biological systems. We suggest that such environments may have been provided by paleolakes—located mostly in the northern lowlands and probably ice covered. Such lakes probably would have had diverse origins. Glacial lakes may have occupied ice-eroded hollows or formed in valleys obstructed by moraines or ice barriers. Depressions in which larger lakes accumulated probably originated by processes other than glacial action, such as crustal warping or impact. Unlike the case on Earth, the Martian record of the origin and evolution of possible life may not have been erased by extensive deformation of the surface. Thus the basins that may have contained the paleolakes are potential sites for future biological, geological, and climatological investigations.

Our initial work combining geologic information acquired earlier (1,2,8) with a study of new topographic maps of Mars (9) has identified at least 15 large basins that exceed 100,000 km² in area and 1000 m in depth (Fig. 1). For comparison, in Pleistocene time, Lake Bonneville in Utah had a maximum areal extent of about 50,000 km² (10). Elysium is the only basin on Mars where we have found direct evidence, both geologic and topographic, of former water levels and spillways or other outlets (8). Spillway elevations indicate that Elysium was probably filled to a depth of about 1500 m during a recent period in Martian history. The Chryse and Aurorae basins are known to have contained substantial volumes of water during the Hesperian Period (1,3), and eight other basins show evidence of interior drainage.

Many of the postulated paleolakes shown in Figure 1 may once have been connected by waterways, as suggested by the occurrence of small channels identified in places on Viking images and by topographic data (9). For example, if water extended above the -1000-m contour line enclosing the Elysium basin, it may have drained east and northeast into the Amazonis basin as well as westward into the Utopia, Isidis, and Cebrenia basins. In Amazonis, small channels and landforms that appear to have been modified by water flow are visible on Viking images. Crater densities are very low (1,11), indicating an Amazonian age for the floor deposits of the paleolake that may have existed here.

If water extended above the -2000-m contour enclosing the Amazonis basin, it may well have drained across a narrow saddle centered near lat 40°N., long 155° (9) into the Diacria basin (Fig. 1). Small channels near the saddle area, as well as those mapped (1) farther north, lead directly into Diacria. The Diacria basin, in turn, may have been connected with both the Chryse and Acidalia basins by a waterway extending around the north margin of the Alba Patera lava flows, which are now covered by low-lying plains of the Arcadia Formation (1,2). The Acidalia basin also probably received runoff from the profuse channels in Deuteronilus Mensae near lat 45°N., long 340° (3,4).

The waterways noted above that may have connected the Isidis, Utopia, and Cebrenia basins are suggested by topographic contours (9) and by channels observed on Viking images during our studies. The large impact basins Hellas and Argyre have inflow channels along their margins; they may have been important water reservoirs and may contain extensive areas of sedimentary deposits (1,3). Basins 12-15 (Fig. 1) show no evidence of interior drainage and are considered the least likely sites for ancient lakes.

References: (1) Scott, D.H., and Tanaka, K.L., 1986, U.S. Geol. Survey Misc. Inv. Series Map I-1802-A. (2) Tanaka, K.L., and Scott, D.H., 1987, U.S. Geol. Survey Misc. Inv. Series Map I-1802-C. (3) Greeley, Ronald, and Guest, J.E., 1987, U.S. Geol. Survey Misc. Inv. Series Map I-1802-B. (4) Parker, T.J., Schneeberger, D.M., Pieri, D.C., and Saunders, R.S., 1986, NASA TM 8910, 319-321. (5) Squyres, S.W., 1989, *Icarus*, v. 79, 229-288. (6) Gulick, V.G., and Baker, V.R., 1989, *Nature*, v. 341, 514-516. (7) Baker, V.R., Strom, R.G., Croft, S.K., Gulick, V.G., Kargel, J.S., and Komatsu, G., 1990, *Lunar and Planet. Sci. Conf. 21, Proc.*, 40-41. (8) Scott, D.H., and Chapman, M.G., in press, *Lunar and Planet. Sci. Conf. 21, Proc.* (9) U.S. Geol. Survey, 1989, Misc. Inv. Series Map I-2020. (10) Curry, D.R., 1990, *Paleogeography, Paleoclimatology, Paleocology*, v. 76, 189-214. (11) Tanaka, K.L., Isbell, N.K., Scott, D.H., Greeley, Ronald, and Guest, J.E., 1988, *Lunar and Planet. Sci. Conf. 18, Proc.*, 665-678.

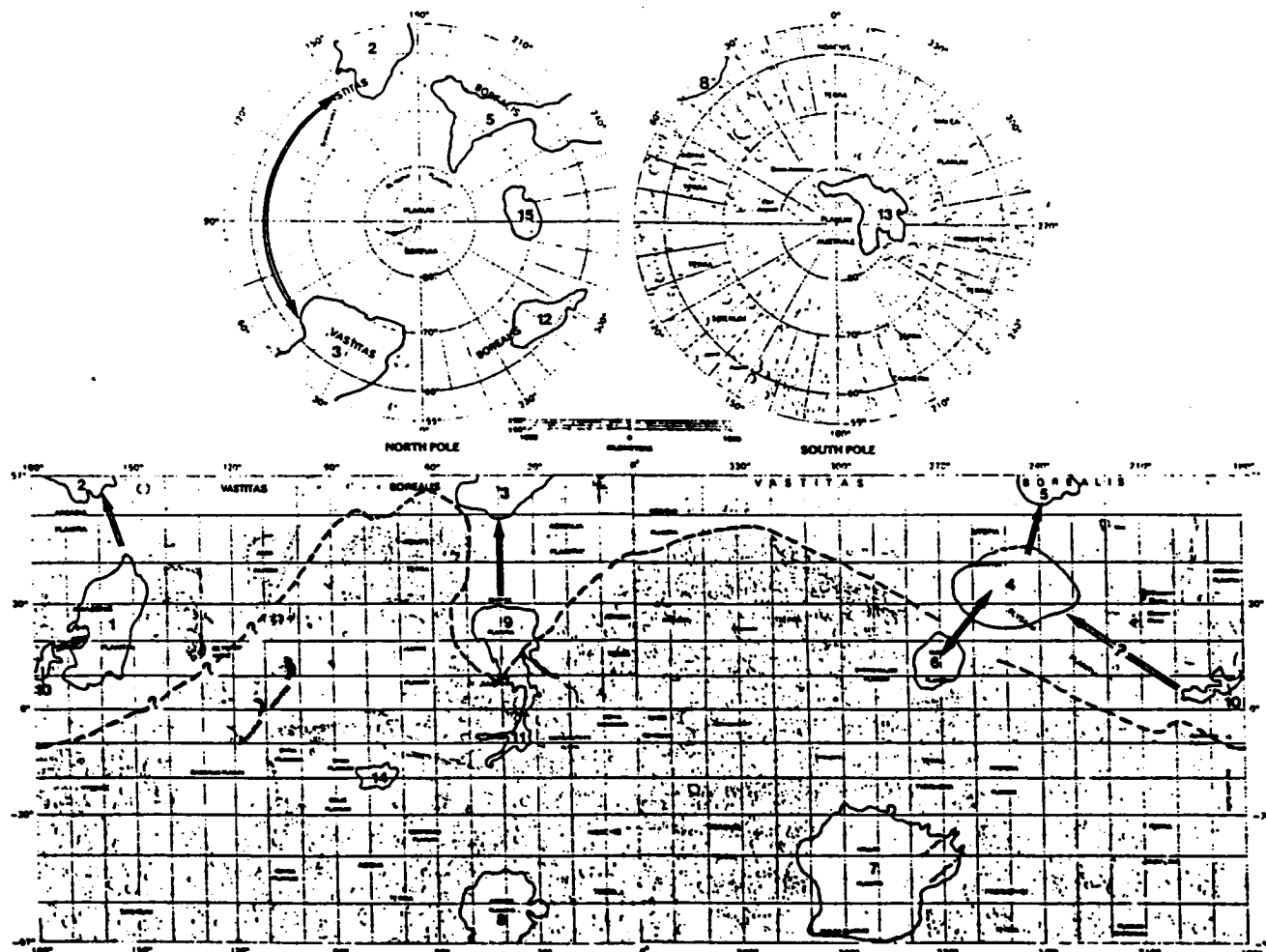


Figure 1. Index map of Mars showing location of basins exceeding 100,000 km² in area. Arrows indicate possible waterways between basins. Highland-lowland boundary dashed. (1) Amazonis, (2) Diacria, (3) Acidalia, (4) Utopia, (5) Cebrenia, (6) Isidis, (7) Hellas, (8) Argyre, (9) Chryse, (10) Elysium, (11) Aurorae, (12) Isenius, (13) Prometheus, (14) Sinai, (15) Pyramus.

Stratigraphy of the layered terrain in Valles Marineris, Mars

G. Komatsu and R.G. Strom. Lunar and Planetary Laboratory, University of Arizona, Tucson, AZ 85721.

The layered terrain in Valles Marineris provides information about its origin and the geologic history of this canyon system. Whether the terrain is sedimentary material deposited in a dry or lacustrine environment, or volcanic material related to the tectonics of the canyon is still controversial. However, recent studies of Gangis Layered Terrain [1] suggests a cyclic sequence of deposition and erosion under episodic lacustrine conditions.

We extended our stratigraphic studies to four other occurrences of layered terrains in Valles Marineris in an attempt to correlate and distinguish between depositional environments.

1) Juvantae Chasma: Juvantae Chasma contains two major layered deposits. One shows alternating thin conformable light and dark layers. The other similar deposit overlies chaotic terrain (figure 1), suggesting deposition after chaotic terrain formation. The thickness of the layers in both deposits is similar.

2) Hebes Chasma: Hebes Layered Terrain is a single deposit up to 5 km thick and described in detail by S. Croft (personal communication). The upper portion of this terrain (estimated to be a few hundred meters thick) consists of alternating dark and light layers which seem to form a less resistant cap-rock unconformably overlying a more massive unit. The lower unit exhibits very prominent fluting which dissects deeply in some parts of the cliff. In the eastern end of the layered terrain, the cap-rock has been eroded away exposing the top of the massive unit which has been severely fluted (figure 2). This suggests that these two major units have very different physical properties. Furthermore, the canyon wall material exhibits an even different erosional style indicating it has still different mechanical properties.

3) Ophir and Candor Chasmata: There are four main layered terrains (A,B,C,D) in these two connected chasmata. The lower sections of layered terrain B, C and D are composed of massive weakly-layered units which often, but not always, develop prominent fluting on their slopes. The fluting tends to be continuous from the top to the bottom of these units. C and D in Candor Chasma show very fine layers on the slopes of the non-fluted areas. In limited areas of the massive weakly-layered units of A and B in Candor, and C in Ophir Chasma, fine layers have been accentuated by the erosion. In the massive weakly-layered units (A,B and D), there is at least one relatively thick low albedo layer (figure 3). Terrain B, C and D's uppermost layers have a different erosional style than the lower massive weakly-layered units. These top layers seem to have a steeper slope, and in many cases, a fine horizontal layered structure.

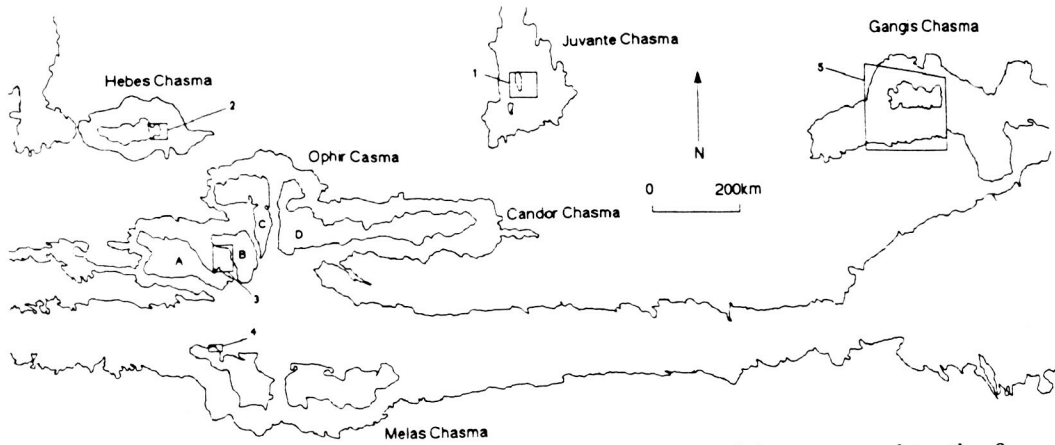
4) Melas Chasma: There are two major layered terrains located in the southern part of this Chasma (figure 4). They are both highly dissected by erosional processes and exhibit both accentuated fine and dark layers.

5) Gangis Layered Terrain's structure is composed of three major layers [2] (figure 5). The upper two layers have steep slopes, many sublayers, and overlie unconformably a massive, fluted unit. Probable dikes and domes have intruded and been exposed in this terrain.

Although there are broad similarities among the layered terrains, no two deposits are exactly alike. This suggests that there was no synchronized regional depositional processes to form all the layered deposits. However, the similar erosional style of the lower massive weakly bedded unit in Hebes, Gangis and Ophir-Candor suggests it may have been deposited under similar circumstances. There is a fairly good correlation of layered units within individual chasma (Juvantae, Melas and Ophir-Candor Chasmata). This suggests that each layered terrain formed under a similar depositional environment. Nedall et al. [1] suggested a possible correlation of layers between terrains B and D in Ophir-Candor Chasmata. Layered terrains in Ophir-Candor Chasmata are separated, but they all have a similar lower weakly bedded unit (A, B, C, D), often with dark layers (A, B, D), and an upper thinner layered unit (B, C, D). All four terrains have similar maximum thicknesses (5000-6000m). Hence, the layered terrains in Ophir and Candor chasmata (A, B, C, D) may have been connected and deposited in a similar environment. If they were connected, they were breached and eroded, probably by fluvial processes and later modification by eolian action. Catastrophic outflow of ponded water from the closed canyon as suggested by Lucchitta and Ferguson [3] might be responsible for this erosion. Two layered terrains in Melas Chasma are severely eroded, and some layers of both terrains are about same thickness suggesting a similar depositional environment. Two major layered terrains in Juvantae Chasma also may have formed under similar circumstances suggested by similar thickness of the layers in both terrains. The layered terrain in each chasma seems to have had a separate stratigraphic history and somewhat different depositional environments in which water played a major role.

REFERENCES

- [1]Nedall et al. (1987). *Icarus*, 70, 409-441. [2]Komatsu, G. and Strom, R.G. (1990). *Lunar and Planet. Sci.* 21, 651-652 [3]Lucchitta, B.K. and Ferguson, H.M. (1983). *Proc. Lunar and Planet. Sci.* 13, A553-A568.



Location map of the layered terrains in Valles Marineris. 1, 2, 3, 4, and 5 correspond to the figures. See text for A, B, C and D.

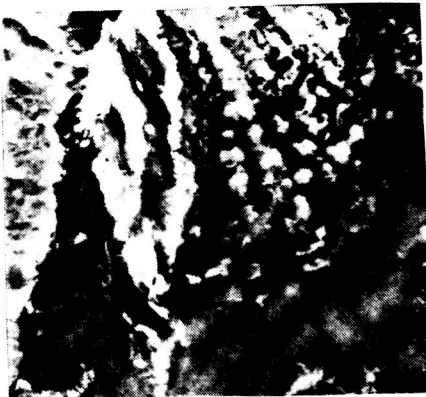


Figure 1.



Figure 2.



Figure 4.



Figure 5.



Figure 3.

**HYDROLOGIC ACTIVITY DURING LATE NOACHIAN AND EARLY HESPERIAN
DOWNWARDING OF BOREALIS BASIN, MARS**
Kenneth L. Tanaka, U.S. Geological Survey, Flagstaff, Ariz.
86001

Introduction. Pronounced global volcanism as well as fracturing and erosion along the highland-lowland boundary (HLB) during the Late Noachian (LN) and Early Hesperian (EH) [e.g., 1, 2] led McGill and Dimitriou [3] to conclude that the Borealis basin formed tectonically during this period. This scenario provides a basis for interpretation of the initiation and mode of formation of erosional and collapse features along the HLB. The interpretation, in turn, is integral to hypotheses regarding the development of ancient lakes (or an ocean) and their impact on the climate history of Mars.

Hydrologic features. These features are considered to include all structures and terrains that I interpret to have formed or been modified by fluvial erosion or piping (erosion and removal of subsurface debris by fluid flow). They include sapping, runoff, outflow, and fretted channels [4]; fracture-controlled but widened troughs; warped, chaotic, fretted, knobby, and pitted terrains; and floor-fractured craters. The examples discussed below may be LN or EH in age as determined by previous work [5] or by stratigraphic relations seen on maps [6, 7]; they are concentrated in highland rocks along and near the HLB and account for its degraded appearance. These temporal and physiographic relations suggest that the basic mechanism for the origin of the hydrologic features was the drainage of ground water from highland regions toward Borealis as the basin lowered. The instigation of ground-water outbreaks and associated channeling by vertical tectonic movement elsewhere on Mars has been proposed for eastern Tharsis/Valles Marineris and the circum-Chryse channels [8, 9] and western Tharsis and Mangala Valles [10].

Runoff channels include Al-Qahira, Ma'adim, Nanedi, Nirgal, Parana, and Samara Valles [4]; the latter three fed the Ladon-Ares Valles outflow-channel system that debouches into Chryse Planitia. Other outflow channels include Mawrth Vallis and an unnamed channel that originates near lat 36° N., long 350°; these channels terminate in Acidalia Planitia. The unnamed outflow channel issues from a discontinuous chain of large craters that extend south for more than 600 km. Some of these and other nearby craters have fractured floors, suggesting that liquefaction and drainage took place in the crater-floor material. The impacted crustal rocks were probably highly permeable [9], facilitating high ground-water discharges from them.

Fretted channels and troughs have irregular morphology; some are discontinuous and appear to have formed by collapse. Previous workers [e.g., 4, 11] proposed a ground-water sapping origin for these features. Because lowering of the Borealis

basin was contemporaneous with high surface discharges, as noted above, I suggest that ground-water sapping discharges may also have been high and sufficiently vigorous to induce piping. Piping may have been largely responsible for the fretted channels and the fracture-controlled troughs along the HLB that include Huo Hsing, Auqakuh, and Mamers Valles [4]; Ismeniae (south of Deuteronilus Mensae) and Mareotis Fossae; and Aeolis and Nylosyrtis Mensae. Also, warped and chaotic terrains at Cydonia Mensae (along the HLB) are thought to result from removal of subsurface material and catastrophic collapse, because Late Hesperian outflow channels south of Chryse Planitia head in such terrains. Subsurface channels may have emerged in lower parts of the HLB scarp, where chaotic and knobby terrains and dispersed mesas occur; these areas obviously underwent more extensive erosion. However, these suggestions are speculative, because the early geomorphologic record in the lowland plains north of the HLB was largely erased by sedimentation and reworking during the Late Hesperian. The degree of erosion in some of these areas indicates that considerable water discharge was involved, although wind or sublimation of ground ice later augmented the erosion.

Why, though, was piping apparently the dominant degradational process only in the high-latitude (lat 30°-50° N.) areas of fretted terrain, whereas runoff channels were dominant in lower latitude regions? This latitude relation suggests that ground ice may have provided an impermeable barrier to upward ground-water flow [8, 9] at high latitudes. In a permeable material, a hydraulic gradient (induced, say, by tectonism) should simply result in ground-water flow and, wherever the water table intersects the surface, in effluence and runoff. However, where permeable material is capped by impermeable material, tectonic tilting may result in high pore-water pressure and eventual liquefaction of the permeable material. This condition may lead to catastrophic debris flows, as has been proposed for the development of the circum-Chryse chaotic terrain and channels [9, 12].

Implications for paleolakes and climate history. Ground-water runoff from highland rocks near the HLB may have produced large, temporary paleolakes or even a vast (though shallow) ocean in the Borealis basin. (If so, the period when they were formed would have been the earliest lacustrine period on Mars.) Such bodies of water could have led to voluminous carbonate formation at the expense of atmospheric CO₂ [13], resulting in a thinner atmosphere and a cooler climate than before. If these conditions indeed occurred, they may have had some geologic implications. First, precipitation that may have occurred through much of the Noachian Period could have ceased, resulting in no further valley-network formation. Alternatively or in addition, valley-network formation by hydrothermal means may have shut

down with the cessation of widespread highland igneous activity during the EH [14]. Second, equatorial regions may have been frozen at the end of the EH. This change is consistent with the following channel history deduced for the equatorial region: (1) during the Noachian and Early Hesperian, shallow runoff, sapping, and outflow channels formed from discharge of near-surface ground water (and perhaps from runoff of precipitation); and (2) during and following the Late Hesperian, deep outflow channels (including the circum-Chryse and Elysium channels and Mangala Valles) were carved by processes presumably instigated by high pore-water pressure buildup at depth (probably a kilometer or more) beneath frozen rock; sites of outbreak include fractures and chaotic terrain.

References

- [1] Greeley, R. (1987) *Science*, **236**, 1653-1654.
- [2] Maxwell, T.A. and McGill, G.E. (1988) *PLPSC 18th*, 701-711.
- [3] McGill, G.E. and Dimitriou, A.M. (1990) *JGR*, **95**, 12,595-12,605.
- [4] Baker, V.R. (1982) *The Channels of Mars*, ch. 3.
- [5] Tanaka, K.L. (1986) *JGR*, **91**, E139-E158.
- [6] Scott, D.H. and Tanaka, K.L. (1986) *USGS Map I-1802-A*.
- [7] Greeley, R. and Guest, J.E. (1987) *USGS Map I-1802-B*.
- [8] Carr, M.H. (1979) *JGR*, **84**, 2995-3007.
- [9] MacKinnon, D.J. and Tanaka, K.L. (1989) *JGR*, **94**, 17, 359-17,370.
- [10] Tanaka, K.L. and Chapman, M.G. (1990) *JGR*, **95**, 14,315-14,323.
- [11] Milton, D.J. (1973) *JGR*, **78**, 4037-4047.
- [12] Nummedal, D. and Prior, D.B. (1981) *Icarus*, **45**, 77-86.
- [13] Kahn, R. (1985) *Icarus*, **62**, 175-190.
- [14] Wilhelms, D.E. and Baldwin, R.J. (1989) *PLPSC 19th*, 355-365.

CHANNELING EPISODES OF KASEI VALLES, MARS, AND THE NATURE OF RIDGED PLAINS MATERIAL

Mary G. Chapman and Kenneth L. Tanaka, U.S. Geological Survey, Flagstaff, Ariz. 86001

Our geologic mapping compiled at 1:500,000 scale of the northern Kasei Valles area of Mars (MTMs 25062 and 25067) indicates (1) at least three periods of Kasei Valles channeling, (2) the development of Sacra Fossae (linear depressions on Tempe Terra and Lunae Planum) in relation to Kasei channeling episodes, and (3) the nature of ridged plains material dissected by Kasei Valles on northern Lunae Planum. (The three channeling periods consist of two flood events and a later, sapping-related event.) These findings suggest hydrologic conditions and processes that formed Kasei Valles and associated features and terrains.

Two periods of flooding in the Kasei Valles region are indicated by different erosional levels [1,2,3]. The lower level (the Kasei floor) is more than 1 km lower than channel-dissected surfaces of Sacra Mensa (a mesa separated from Lunae Planum by the narrow south branch of Kasei), of Labeatis Mensa (west of the map area at lat 25.5° N., long 74.5°), and of northern Lunae Planum (whose erosional features are best seen at lat 21.7° N., long 72°) [2]. Streamlined features on the higher, Lunae Planum level lie at an angle to the north and south Kasei channels and are cut by them [1,2]. These streamlined features trend east and may be related to a large, east-trending, streamlined island at lat 18° N., long 78.5° (west of the map area). The island lies on the channel floor but does not align with the presumed water source of most recent flooding (Echus Chasma [4]); thus, the source region of the earlier flood may be west of northern Kasei Valles [5] and now buried beneath younger lava flows of Tharsis Montes [6].

The streamlined features on Sacra Mensa are cut by the Sacra Fossae; some of these depressions end as hanging valleys above the Kasei floor, a result of downcutting during the second period of outflow-channel development (lat 26.95° N., long 66.1°). Also, two Sacra Fossae depressions were apparently utilized and enlarged by younger flooding, which carved the narrow north and south Kasei branch channels that wind around the large mesa of Sacra Mensa [7]. Therefore, we interpret the Sacra Fossae to have developed during and between the two periods of Kasei flooding, which augments evidence cited above of cross-cutting streamlined features that support the same conclusion. Other Sacra Fossae depressions are enlarged and enclosed, indicating collapse into voids that may have developed through hydrofracturing and subsurface erosion by turbulent flow of ground water (lat 25.4° N., long 64.4°). Along the east edge of Sacra Mensa and the north edge of Lunae Planum, several fossae form large valleys having the same base level as Kasei Valles (best seen at lat 24.8° N., long 64°); the valleys apparently formed by sapping along joints and scarp retreat [8]. One large fossa at lat 24° N., long 66.5° on Sacra Mensa is thought to be the site of a catastrophic outbreak of ground water [9], because eroded and chaotic terrain borders the depression downslope. On the broad floors of Kasei Valles, narrow, rectilinear to sinuous channels document erosion by the third and final period of channel activity. The erosional features probably result from ground-water sapping of channel-floor material,

perhaps immediately following the second period of flooding. Also, some discharge from plateau material is indicated by a channeled fan, which originated from a Sacra Fossa depression on the mesa and spills onto the Kasei channel floor at lat 26.9° N., long 67.1°.

Our mapping has also provided some insight into the nature of plains material on Lunae Planum marked by wrinkle ridges and rare lobate scarps; the morphology and occurrence of such ridged plains material has led to its interpretation as lava-flow material [10, 11]. It appears to be layered in several places along the walls of the plateau, both in the map area and farther east [12]; alternating layers have contrasting albedo. The surface layer and some lower layers appear resistant, because they form cap rock on streamlined islands on Sacra Mensa and on parts of the Kasei floor (e.g., at lat 27° N., long 70°). In places on Sacra Mensa where this resistant layer was eroded away by early flooding on the Lunae Planum level, an underlying, apparently friable layer was degraded into rough and knobby material (lat 26° N., long 65°). Many areas showing evidence of sapping indicate that the ridged plains material included relatively porous and permeable aquifers. Remnant ground ice within layers of the ridged plains material is suggested by moats surrounding Labeatis Mensa (west of the map area). The moats may have formed when lavas embayed ice-rich debris blankets that have since sublimated away [2, 13]. In addition, several impact craters on the plateau are associated with landslides; heat generated by impact may have melted ice, lubricating the slides.

In conclusion, an early period of flooding, whose source is perhaps buried beneath lava flows of Tharsis Montes, may have eroded streamlined features in northern Lunae Planum. Later floods originating from Echus Chasma carved the Kasei floor and formed the mesas adjacent to the plateau. The Sacra Fossae formed after the initial flooding and during the second flooding by sapping, outbreak, scarp retreat, and collapse along joints and fractures in ridged plains material. Later sapping discharge may have produced narrow, sinuous channels in the Kasei floor; discharge from fossae eroded some young fan deposits. Some layers of the ridged plains material were sufficiently porous and permeable to support sapping and outbreaks of ground water; hydraulic pressures may have reached levels capable of generating hydrofractures.

References

- [1] Lucchitta, B.K. (1982) *JGR*, **87**, 9951-9973.
- [2] Chapman, M.G. and Scott, D.H. (1989) *Proc. LPSC 19th*, 367-375.
- [3] Scott, D.H. and Dohm, J.M. (1990) *LPSC XXI*, 1115-1116.
- [4] Robinson, M.S. and Tanaka, K.L. (1990) *Geology*, **18**, 902-905.
- [5] Jöns, H.-P. (1988) *Die Geowissenschaften*, **6**, 173-181.
- [6] Scott, D.H. and Tanaka, K.L. (1986) *USGS Map I-1802-A*.
- [7] Carr, M.H. (1974) *Icarus*, **22**, 1-23.
- [8] Tanaka, K.L. and Golombek, M.P. (1989) *Proc. LPSC 19th*, 383-396.
- [9] Tanaka, K.L. and MacKinnon, D.J. (1989) *Fourth Int. Conf. Mars, Abs.*, 200-201.
- [10] Scott, D.H. and Carr, M.H. (1978) *USGS Map I-1083*.
- [11] Greeley, R. and Spudis, P.D. (1981) *Rev. Geophys. Space Phys.*, **19**, 13-41.
- [12] D.H. Scott, person. commun., 1990.
- [13] Lucchitta, B.K. and Chapman, M.G. (1989) *LPI Tech. Rept. 89-04*, 51-53.

FLOOD ROUTING OF THE MAJA OUTFLOW ACROSS XANTHE TERRA:

R. A. De Hon, Department of Geosciences, Northeast Louisiana University, Monroe, LA 71209.

The object of this study is to trace a single flood crest through the Maja outflow system and to evaluate the effects of topography on ponding and multiple channel routing. Maja Valles provides a good model because it has a single source and a well-defined channel system. The 1500 km long Maja Valles originates in Juventae Chasma. The outflow system stretches 1100 km northward along the Lunae Planum--Xanthe Terra boundary, then eastward across the Xanthe Terra highlands. It descends to Chryse Planitia where it extends northeastward toward the middle of the basin.

The Lunae Planum Outflow Complex (1) includes the Maja Valles canyon section and related valleys (Vedra, Maumee, and Bahram Valles) that transect Xanthe Terra. The Maja flood traveled the first two-thirds of its distance as a semi-confined sheetflood. At the northern end, it ponded on the Lunae Planum surface until the waters rose to spill over the Xanthe Terra revetment onto the lower Chryse Planitia surface. The flow first crossed the highland terrain as sheetflood flow, but broken by irregularities in the rugged highland surface, it incised a complex series of anastomosing channels (Fig.1). Early formed channels were abandoned as hanging valleys as a few main channels captured most of the drainage (2). Flow from the trans-Xanthe channels ponded on the western edge of Chryse Planitia behind the wrinkle ridge system (3,4). As the impounded water crested the ridges, the flood continued downslope toward the center of the basin where it lost volume by infiltration and evaporation.

During much of its brief history, the Maja outflow is marked by a single flood crest. However, multiple flood crests formed as the flow across Xanthe Terra separated into multiple anastomosing channels, then recombined in the downstream reaches. Modeling the flood surge across Xanthe Terra provides insight into the erosional and depositional history of the flood in the lower portions of the channels (Fig. 2).

The distance across the highland is 75 km along the most direct route and ranges up to 150 km along channel routes of greatest diversion. Maumee Valles consists of 118 possible flow routes and a total of 795 km of channel segments with approximately 400 cubic km of channel storage. Vedra consists of 40 possible routes with 250 cubic km of channel storage. The "South" drainage (informal name for valley headed in the crater Dixie) consists of 6 segments and 65 cubic km of channel storage. Maja Valles (canyon section across Xanthe) was established after the other valleys, but it eventually captured the remaining drainage from Lunae Planum.

As in any flow across a rugged surface, ponding occurred in local basins. The chief impoundments, providing more than 500 cu km of temporary storage, were in the lowland basin near the Lunae Planum--Xanthe Terra boundary, the crater Bahn, the crater Dixie, an unnamed crater at the lower end of the "South" drainage, and a lowland trough at near the mouth of Maja canyon. At these impoundments, the flood crests were delayed from 3 to 6 hours as the crater or basin filled to capacity. Then, one or more new flood crests formed as flood waters spilled through breaches in the downstream side of impeding basins.

FLOOD ROUTING ACROSS XANTHE TERRA De Hon, R. A.

In the Maja canyon section, the flow onto Chryse Planitia was impeded by a highland ridge. Initially, the flow ponded in a trough on the highland side of the ridge and was diverted to the south through a 65 km relief channel. However, the flood waters eventually topped the confining ridge and cut the present gorge to allow direct drainage onto the Chryse surface.

Release of water from the lake on Lunae Planum has been modeled using weir and spillway formulas to calculate discharge as the lake drained. Within the range of reasonable limits, approximately one-half of water stored in the lake would have been drained in 1.5 to 5 days. Because the head drops during draining, discharge rates fall. From 65 to 225 days are required to drain all water from the lake.

If the Lunae Planum impoundment received a prolonged influx from the ultimate source region in Juventae Chasma, then the length of time for discharge into the trans-Xanthe channels is extended. Also, if only the main channels carried water after the initial release at high discharge rates, the duration of flow in the channels is prolonged. The flow through the channels lasted for many months.

Modeled times for the initial flood crest to transverse the Xanthe highland region range from 3 to 15 hours depending on flood routing and retardation within impoundments in the valley systems. Hydrographs of the flow at the termini of the chief valleys provide a graphic view of the surges as they reached the end of the valley systems. The initial flood crest was reduced to multiple surges along a prolonged flow at the terminus. Anastomosing flow was primarily responsible for reducing the initial flood crest into a prolonged flow with a series of minor ebb and flows. Ponding and release was responsible for the greatest retardations and the separation of major flood crests at the termini of the canyons.

Thus, flood routing through multiple channels and retardation in local impoundments are responsible for breakup of the initial flood crest and the formation of multiple flood crests. Recombined flow near the mouths of these canyons results in an extended flow regime and multiple flood surges. As a result of ponding along the flood course, depositional sites are localized and renewed erosion downstream (from ponded sites) results in sediment source areas not greatly removed from depositional sites. Some sites, especially at the mouths of the trans-Xanthe canyons, experienced a complex history of deposition and erosion in response to the ebb and flow of multiple flood crests imposed by flood routing and multiple ponding. The flow history after the initial flood surge is measured in months rather than hours or days.

References:

1. De Hon R.A. (1987) Lunar Planet. Sci. XVIII, 227-228.
2. Greeley R. et al. (1977) J. Geophys. Res. 82, 4093-4109.
3. Thelig E. and R. Greeley (1979) J. Geophys. Res. 84, 7961-7984.
4. Baker V.R. and R.C. Kochel (1979) J. Geophys. Res. 84, 7994-8010.

FLOOD ROUTING ACROSS XANTHE TERRA
De Hon, R. A.

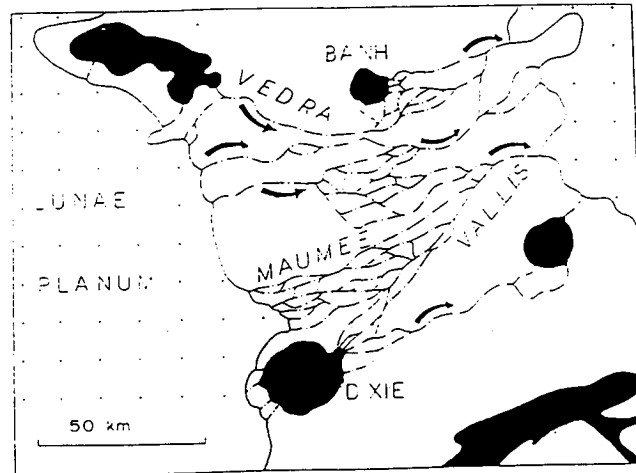


FIGURE 1. Subparallel and anastomosing channels across Xanthe Terra.

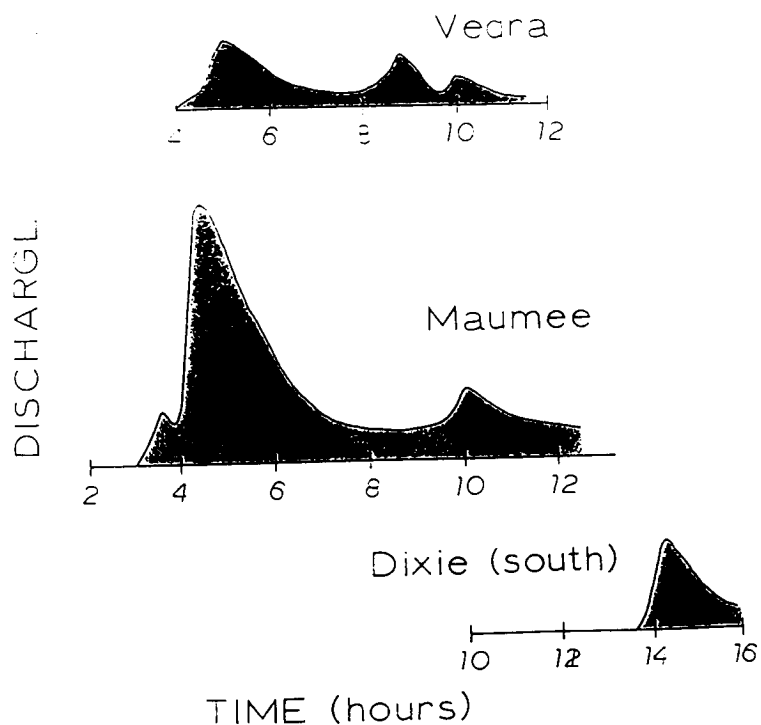


FIGURE 2. Model hydrographs for discharge at the mouths of the trans-Xanthe valleys. From a single flood surge at the head of the valleys, multiple channel routing and intra-valley basin storage produces multiple flood crests at the mouths.

ANCIENT FLUVIAL PROCESSES IN THE EQUATORIAL HIGHLANDS OF MARS

Robert A. Craddock and Ted A. Maxwell; Center for Earth and Planetary Studies, National Air and Space Museum, Smithsonian Institution, Washington, D.C. 20560.

Martian highland craters typically lack ejecta deposits, have no noticeable rim, and are flat-floored. In addition, crater size-frequency distribution curves show that highland craters have depleted populations <20-km-diameter. A variety of processes have been suggested to explain these observations including deposition of aeolian [e.g., 1] or volcanic [2] materials up to the crater rim crests, thermal creep [3], terrain softening [4], and mass-wasting [5]. However, none of these processes adequately explains both the crater morphology and population distributions.

Deposition of aeolian or volcanic materials up to the crater rim crest could produce a flat-floored, rimless crater at a given diameter; however, smaller diameter craters would become buried, and the larger diameter craters would still have obvious rims. Thermal creep requires a narrow range of climatic conditions not currently present on Mars [3], and which would have been highly dependent upon latitude if present in the past. Terrain softening occurs only at higher martian latitudes and current models [4] do not explain the size range of flat-floored, rimless crater morphology. Mass-wasting suggests that flat-floored, rimless craters should not only occur everywhere on Mars but also on planets such as the Moon or Mercury, and this is not the case. Mass-wasting should also be an ongoing process, but crater populations suggest that the modification process ceased at -3.3 Ga [early Hesperian; 6,7,8].

In order to explain both the martian highland crater morphology and population distributions, we have proposed a fluvial process capable of removing the loose crater rim material [8]. The resulting effect is to decrease the crater diameter, thereby causing the population curves to bend over. The eroded material is redistributed, burying or partially burying smaller diameter craters before complete erosion. This material may also be deposited into local topographic lows, creating the depositional basins observed recently in a variety of highland regions [9]. A fluvial process explains both sets of observations: crater morphology and crater population distribution curves.

As previously reported [10], we have expanded our study to include the entire equatorial highland region of Mars. Based on the published 1:15M geologic maps of Mars, we are limiting our study to two materials: the Noachian cratered plateau unit (Npl₁) and the Noachian dissected plateau unit (Npl_d). Although it is apparent that other Noachian materials in the highlands contain flat-floored, rimless craters, the interpretations of these materials include resurfacing by processes we feel are separable from a global, more extensive process. Using published 1:15M topographic maps of Mars, these materials were binned by elevation.

Preliminary results indicate that the resurfacing process ceased in Npl₁ materials before Npl_d materials. This suggests, perhaps, that ancient valley networks represent the waning stage or a change in the

nature of the process [10]. It also indicates that the resurfacing process occur over a long period of time (i.e., from the middle Noachian to the early Hesperian). This agrees with observations by Arvidson [6] and Gurnis [7] that highland resurfacing occurred through the end of late heavy bombardment.

A preliminary observation is the apparent relation between timing of resurfacing and elevation. Typically at higher elevations the resurfacing process ceased at an earlier time than at lower elevations (Fig. 1). This supports fluvial resurfacing over volcanic or mass-wasting processes, both of which would be independent upon elevation. It also permits some speculation as to the history of the fluvial activity. If the fluvial resurfacing were the result of an endogenic process such as seepage of ground water due to melting, then with time the aquifer should become depleted (Fig. 2a). The result is a gradual lowering of the water table with volatiles migrating to lower elevations. If the fluvial resurfacing were the result of an exogenic process such as rainfall, resurfacing becomes dependent upon the rate of atmospheric degassing. Initially rainfall occurs over the entire surface, but as the atmosphere becomes thinner, cloud condensation, and thus rainfall, occurs at progressively lower elevations (Fig. 2b). In either scenario, the effect is to isolate higher elevations from the resurfacing process with time.

Absolute ages of martian periods determined by Hartmann *et al.* [11] and Neukum and Wise [12] from modelled crater fluxes suggests that resurfacing occurred over a ~400 million year or ~600 million year period, respectively (middle Noachian to early Hesperian). Previously we estimated the amount of material eroded from fluvial resurfacing in the Amenthes and Tyrrhena regions to be between 751,000 to 2,580,000 $\text{km}^3/10^6 \text{ km}^2$ based upon Mars global production crater curves [13] and a modelled production curve [8]. This suggests denudation rates of between 0.001 to 0.006 mm/yr. These rates occur in places such as northern Canada or Siberia on Earth [14], but are typically very low by terrestrial standards. Further study will refine these values and enhance the preliminary observations presented here.

Previous work has been presented in the Journal of Geophysical Research, vol. 95, no. B9, pgs. 14,265-14,278, 1990. Supported by NASA Grant NAGW-129.

References. [1] Wilhelms, D.E. and R.J. Baldwin, Proc. Lunar Planet. Sci. Conf., 19th, 355-365, 1989. [2] Cruikshank, D.P. *et al.*, Moon, 7, 440-452, 1973. [3] Sharp, R.P., Icarus, 8, 472-480, 1968. [4] Squyres, S.W., Icarus, 79, 229-288, 1989. [5] Grant, J.A. and P.H. Schultz, Lunar Planet. Sci., XXII, 487-488, 1991. [6] Arvidson, R.E., Icarus, 22, 264-271, 1974. [7] Gurnis, M., Icarus, 48, 62-75, 1981. [8] Craddock, R.A. and T.A. Maxwell, J. Geophys. Res., 95, 14,265-14,278, 1990. [9] Goldspiel, J.M. and S.W. Squyres, Icarus, 89, 392-410, 1991. [10] Craddock, R.A. and T.A. Maxwell, Lunar Planet. Sci., XXI, 236-237, 1990. [11] Hartmann, W.K. *et al.*, In Basaltic Volcanism on the Terrestrial Planets, Chap. 8, pp. 1049-1127, Pergamon, New York, 1981. [12] Neukum, G. and D.U. Wise, Science, 194, 1381-1387, 1976. [13] Neukum, G. and K. Hiller, J. Geophys. Res., 86, 3097-3121, 1981. [14] Rice, R.J., Fundamentals of Geomorphology, 387 pp., Longman, New York, 1977.

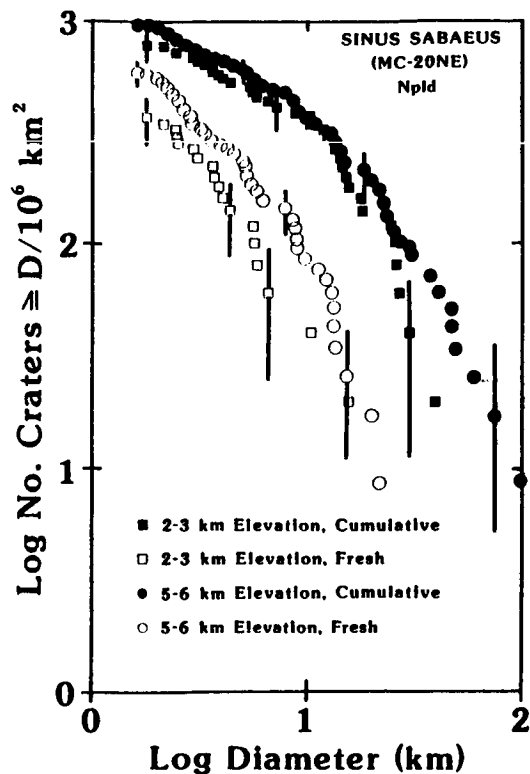
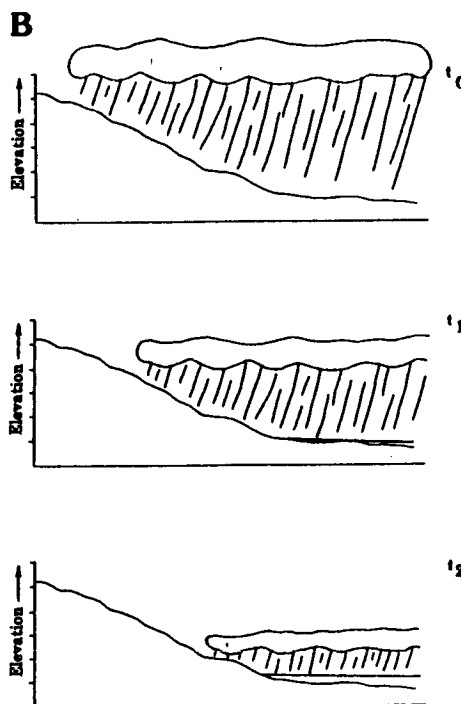
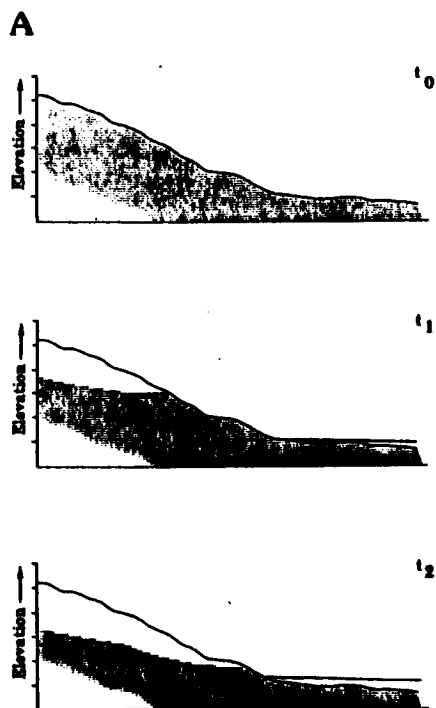


Figure 1 (left). Crater size-frequency distribution curve of Npld materials in Sinus Sabaeus. The curves illustrate relation between timing of resurfacing event and elevation. Fresh crater curves suggest that at lower elevations (2-3 km) the resurfacing ceased earlier ($N[5] = \sim 130$) than at higher elevations (5-6 km; $N[5] = \sim 240$).

Figure 2 (below). (A) Elevation-dependent fluvial resurfacing involving an endogenic process. Progressively later episodes of ground water seepage lower the water table, isolating higher elevations from resurfacing effects. (B) Exogenic process involving rainfall. With atmospheric degassing, cloud condensation occurs at progressively lower elevations.



GEOLOGIC HISTORY AND CHANNELING EPISODES OF THE CHRYSE PLANITIA REGION OF MARS

Susan L. Rotto and Kenneth L. Tanaka, U.S. Geol. Survey, Flagstaff, Ariz.

Introduction. Our investigation of the Chryse Planitia region of Mars is based on geologic mapping on a 1:5,000,000-scale shaded relief map base [1]. The map area includes Chryse and southern Acidalia Planitiae; the circum-Chryse channels and chaotic terrains; Xanthe, southern Tempe, and western Arabia Terrae; Lunae Planum; and northeastern Valles Marineris. The aim of the study is twofold: (1) to obtain relative ages of the outflow channels by performing and compiling detailed stratigraphic analyses, and (2) to correlate channeling episodes with causative mechanisms (such as volcanism and tectonism) and resulting effects (such as climate change). Preliminary mapping has been completed. It incorporates previous, broad-based work [2-4] and ongoing, high-resolution (1:500,000-scale) mapping by colleagues [e.g., 5]. The following geologic history, based on this mapping, includes the documentation of a previously unproposed channeling episode in the region as well as our presently favored hypotheses concerning the nature and origin of the channeling events.

(1) **Early to Middle Noachian.** Chryse and Aram basins, other large impact features, and heavily cratered terrain were formed during this period, when bombardment was intense. Ancient crater material makes up much of the highland plateaus and probably underlies most other areas covered by younger materials.

(2) **Late Noachian to Early Hesperian.** This period is marked by the development of several runoff and outflow channels and by degradation of older lowland materials. We propose that these events are correlative and demonstrate a common episode of activity. Runoff channels that include Nandedi and Bahram Valles cut the southwest exposed rim of Chryse basin, as well as the rim's buried trace. Other runoff channels southeast of the map area (including Nirgal, Parana, and Samara Valles) fed the Ladon-Ares outflow system (only the northern section is in the map area). This system is made up of discontinuous outflow channels (Uzboi, Ladon, and Ares Valles and an unnamed channel southeast of Margaritifer Chaos) linked by chaotic terrain (Margaritifer and Iani Chaos) and basin deposits (Ladon and Holden [6]). In Arabia Terra, the outflow channel Mawrth Vallis originates north of crater Trouvelot and near other large craters and winds down into southeastern Acidalia Planitia. Intercrater plains formed near many of the channels and thus may consist in part of flood-plain deposits. Below the mouths of the runoff and outflow channels, possible flood-plain deposits are buried by younger material. However, extensive fields of relatively small knobs of degraded Noachian materials are embayed by younger plains material in southern Acidalia Planitia. In places these fields grade into mesas and fractured highland materials. Many of the knobs form rings--the remnants of impact-crater rims. Thus the channels and knobs of this period appear to be the result of ground-water outbreak, sapping, and runoff from highland rocks onto lowland plains.

We suggest that tectonic movements and heat from intrusions generated the hydraulic gradients necessary to produce such hydrologic activity. North of Acidalia Planitia, Borealis basin lowered [7], while igneous activity and local uplift occurred at Syria Planum [8] and the Coprates rise [9]. (It is uncertain whether Valles Marineris was active at this time [10].) During the Early Hesperian, wrinkle ridges formed on possible lava and flood plains of that age that cover Lunae Planum and much of Chryse Planitia and Arabia Terra [2].

(3) **Late Hesperian.** The majority of outflow-channel systems in the map area formed during the Late Hesperian. They originate from large areas of chaotic and warped terrains, some of which connect with or occur in eastern canyons of Valles Marineris. The channels locally cut deeply into highland rocks and make shallower cuts in higher areas of Chryse Planitia.

Some of these channel systems, such as Kasei Valles, show evidence for two or more episodes of erosion [11]. In lower Ares Valles (northwest of lat 11° N., long 27°), a resistant flow material (that we interpret to be lava) covered the earlier channel floor and was in turn eroded by flooding during this episode. In eastern Chryse Planitia (around lat 22° N., long 36°), a lobate deposit (probably more lava) was carved by flows from Ares, Tiu, and Simud Valles. Within deeper outflow channels (carved into highland rocks), lobate fields of knobs may be deposits of late-stage debris flows [12]. In Chryse and Acidalia Planitiae, neither clearly defined deposits nor paleoshorelines are recognized [13], and thus the mode and location of deposition of eroded materials and the fate of the released water are uncertain. However, wrinkle ridges in northern Chryse Planitia are subdued, perhaps due to embayment by sediments.

Most of the channel systems appear to consist of single channels originating from one or more areas of chaotic terrain. Shalbatana Vallis, however, is made of a series of channels that document progressive outbreak upslope. The youngest event was the largest and produced a narrow, deep canyon that originates from large depressions and chaotic terrain (in an impact crater) south of lat 1° N. (at 3,000-m elevation [14]). At lat 8° N. (0-m elevation), this canyon cuts a narrow but shallower canyon that in turn connects with a lower (and older), small area of chaotic terrain (at lat 12° N., -1,000-m elevation) from which extends a broad and shallow channel.

Chaotic and warped terrains are thought to form by liquefaction and removal of wet, subsurface material and collapse of near-surface, impermeable (ice-cemented?) material [15-17], which may lead to generation of debris flows. Retrogressive slope failure occurs in submarine environments on Earth as a consequence of evolving slope-stability conditions; Shalbatana Vallis also may have developed in a retrogressive sequence. Hydraulic conditions and quaking that could have led to such activity may have been produced by later episodes of Tharsis and Valles Marineris tectonism. In lower Kasei Valles, chaotic and fractured terrains associated with enlarged fractures suggest that outbreaks there may have occurred by hydrofracturing [18].

(4) Amazonian. The extent of channel activity during the Amazonian is as yet uncertain, pending further study. Landslides, however, occurred along high scarps in Valles Marineris and in some outflow channels, initiated by impacts and perhaps by seismic shaking as faulting continued at Valles Marineris. More wrinkle ridges formed in western Chryse Planitia and lower Kasei Valles [11], probably as a result of compression due to extensive erosion [19]. Extensive fields of lava flows were erupted from the Tharsis Montes region during this period; some of the flows buried upper reaches of Kasei Valles [3].

Conclusions. The geologic history of the Chryse region suggests that two major periods of tectonic activity resulted in two episodes of channeling in the highlands surrounding Chryse Planitia. The first channel episode was related to distant activity at the Syria and Coprates rises and downwarping of Borealis basin; erosion was shallow and relatively moderate, resulting in shallow channels, thin flood-plain deposits, and knobby lowland terrain. The second episode was primarily influenced by uplift and rifting at Valles Marineris and perhaps by Tharsis volcanotectonic activity. The formation of deep channels and chaotic terrains suggests liquefaction and transport of large volumes of wet debris.

References

- [1] U.S. Geological Survey (1982) USGS Map I-1448.
- [2] Greeley, R. et al. (1977) JGR, 82, 4093-4109.
- [3] Scott, D.H. and Tanaka, K.L. (1986) USGS Map I-1802-A.
- [4] Tanaka, K.L. (1986) JGR, 91, E139-E158.

- [5] Chapman, M.G. and Scott, D.H. (in press) USGS Map I-2107.
- [6] Schultz, R.A. and Frey, H.V. (1990) JGR, 95, 14,175-14,189.
- [7] McGill, G.E. and Dimitriou, A.M. (1990) JGR, 95, 12,595-12,605.
- [8] Tanaka, K.L. and Davis, P.A. (1988) JGR, 93, 14,893-14,917.
- [9] Tanaka, K.L. and Schultz, R.A. (this volume).
- [10] Witbeck, N.E. et al. (in press) USGS Map I-2010.
- [11] Chapman, M.G. and Scott, D.H. (1989) Proc. LPSC 19th, 367-375.
- [12] Tanaka, K.L. (1988) LPSC XIX, 1175-1176.
- [13] Scott, D.H. (1990, pers. commun.).
- [14] U.S. Geological Survey (1989) USGS Map I-2030.
- [15] Nummedal, D. and Prior, D.B. (1981) Icarus, 45, 77-86.
- [16] MacKinnon, D.J. and Tanaka, K.L. (1989) JGR, 94, 17,359-17,370.
- [17] Tanaka, K.L. (this volume).
- [18] Chapman, M.G. and Tanaka, K.L. (this volume).
- [19] Turcotte, D.L. and Schubert, G. (1982) **Geodynamics: Applic. Continuum Phys. Geol. Prob.**, New York: John Wiley and Sons, Inc., p. 108.

EVOLUTION OF THE WATER REGIME OF PHOBOS.

F.P. Fanale and J.R. Salvail (Planetary Geosciences Div., School of Ocean & Earth Sciences & Technology, Univ. of Hawaii, Honolulu, HI)

An improved model of the evolution of the water regime of Phobos has been developed. The central feature of the model is a time-dependent solar insolation that is influenced both by the increasing solar power output over geologic time and by the obliquity and eccentricity cycles of Mars and Phobos which vary over time scales of 10^5 to 10^6 years. A one-dimensional model is used to calculate temperatures, water fluxes, and ice depths over geologic time. Results are obtained at various latitudes for two assumed cases of porosity and pore size and for three putative values of the mass fraction water initially allocated to Phobos. Results are obtained for one model that assumes that water ice is driven toward the surface by the internal thermal gradient near the poles. Results for the (more likely) surface-concentrated model indicate that ice may be found from 270 to 740 m at the equator and from 20 to 60 m at 80° latitude, depending on porosity and pore size, and subject to limits implied by assumptions of the initial mass fraction of free ice. A two-dimensional model is used to compute temperatures, heat and vapor fluxes, and ice removal/deposition rates for a two-dimensional grid over one obliquity cycle assuming that ice is distributed uniformly throughout Phobos. The heat and vapor fluxes and the ice removal/deposition rates are integrated over time to obtain the water loss at the surface, the lateral heat and vapor transport toward the poles, and the change in ice concentration at interior points. The results show that a relatively large amount of vapor is produced within 1 km of the surface, mostly at lower latitudes. Some of the vapor is transported to the surface where it is lost, and the remainder is transported to greater depths, where it is condensed at much lower rates over a much larger volume. For the large pore size/ porosity case, we estimate that the current H_2O loss rate is ~ 3 g/sec. The possible effects of the radiative contributions from Mars, the shadowing by Mars, and the use of an ellipsoidal shape for Phobos are also explored.

PHOBOS: SURFACE AND SOLID BODY PROPERTIES FROM DIGITAL SHAPE DATA

P. C. Thomas, Center for Radiophysics and Space Research, Cornell University, Ithaca, NY

The combination of irregular shape and significant tidal forces makes much of the scientific investigation of Phobos's surface conditions and solid body properties dependent on techniques more specialized than those used on ellipsoidal objects. Stereogrammetric and limb coordinate data have been used (from Viking and Phobos 2 images) to derive a digital shape model of Phobos at 2° grid spacing. Uncertainties in grid positions are mostly under 75 m, but some areas with only low resolution imaging have uncertainties of 300 m. One view is given in Fig. 1.

The effective gravitational topography has been calculated using the potential energy equations (1), and an average gravitational acceleration to derive a "pseudo topography." The points that are gravitationally low have the lowest potential energy and should accumulate debris if it is able to move over the surface of the satellite. The gravitational topography was calculated for several different orbital radii to test the effects of orbital evolution on slopes on Phobos.

There are several, often non-intuitive aspects to the gravitational topography on Phobos:

1. Points with the greatest radii are in fact gravitationally the lowest areas on Phobos at present. At greater orbital radii this tendency is much less pronounced, and regional slopes are much reduced or even reversed. Further orbital evolution toward Mars exaggerates the topography.

2. The magnitude of surface gravity does not correlate simply with body radius; as the satellite evolves inward the relation become progressively less direct. At 5.0 Mars radii, surface gravity ranges from 0.49 to 0.57 cm/s²; at present it ranges from 0.35 to 0.57 cm/s².

Some of the consequences of the data are:

1. Equatorial areas at 270° and 90° longitude are the highest regions of the satellite; the area near 270° has several characteristics that suggest less regolith is present there, and the regions at 0° and 180° longitude have some features suggesting deep regolith. Thus it would appear that a significant fraction of regolith volume has been generated or subject to redistribution since tidal effects became important (since the orbit was at about 1.5 times the present distance; no absolute time scale is possible.)

2. The asymmetry of crater Stickney may suggest formation or modification in a strong tidal regime because the western part of the crater is subject to significant slumping to the center while the eastern side apparently is not. Fill inside some craters near Stickney confirms the general slope in this vicinity.

3. The shape gives a uniform density moment of inertia parameter (B-A/C) of 0.125; which would imply a forced libration of 1.02° (2); This is within the error bars of the determination of libration (3). If the libration measurement is interpreted without error bars, the moment of inertia values imply a modest central condensation of Phobos, consistent with some extra porosity in the outer few hundred meters. However, the uncertainties admit a uniform density model.

REFERENCES: (1) Dobrovolskis, A., and J. Burns (1980), *Icarus* 42, 422-441. (2) Peale, S. J. (1977), in *Planetary Satellites*, pp. 87-112. (3) Duxbury, T. C. and J. D. Callahan (1989), *Icarus* 77, 275-286.

ACKNOWLEDGMENT: This work was supported by NASA Grant NAGW-111.

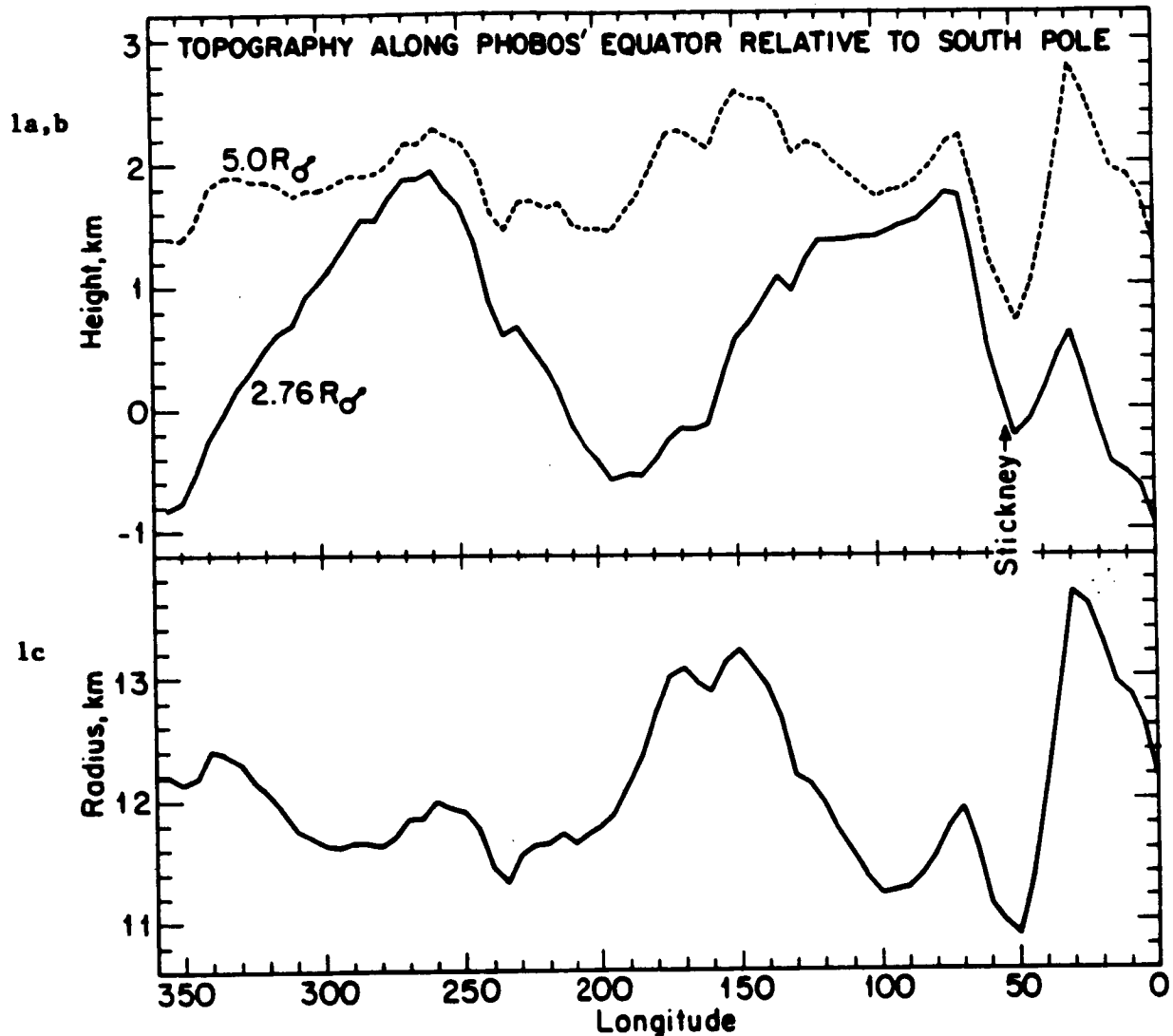


Figure 1a,b. Effect of orbital evolution on effective topography on Phobos. Height is relative to the south pole and is calculated from the potential energy at the surface and an average acceleration of 0.49 cm/s^2 , and is shown for locations along the equator of Phobos. Note that the topography at 5.0 Mars radii although reduced along the equator is on average nearly 2 km above the south pole. The effects of tides and rotation start to dominate at the present orbital radius (2.76 Mars radii), to give high points at leading and trailing sides, and low points on the Mars and anti-Mars points.

1 c. Radii corresponding to points in a,b; note the asymmetry and near anti-correlation with topography for 2.76 Mars radii in 1b.

Gradational Evolution of Young, Simple Impact Craters on the Earth; J.A. Grant and P.H. Schultz, Brown University, Providence, RI 02912.

Introduction: Impact craters on the Earth occur in a variety of geologic and climatologic settings. As random, non-volcanic, instantaneously created landforms, consideration of their preserved gradational morphologies provides an unique opportunity to assess the number and intensity of erosional processes acting since the time of their formation. The present study examines the age and preserved morphology associated with three simple impact craters in varying stages of preservation in order to develop a gradational evolutionary sequence. All three are unglaciated and formed into nearly flat-lying target rocks: A) the 1.2 km diameter, 50,000 year-old Meteor Crater in Arizona (35.3°N, 111.2°W); B) the 1.8 km diameter, 62,000 year-old Lonar Crater in India 20.0°N, 76.5°E); and C) the 1.75 km diameter, 0.5-3.0 million year-old Talemzane Crater in Algeria (33.3°N, 4.0°E). It is concluded that backwasting and downwasting of the raised-rim by fluvial and mass-wasting processes dominates erosion of these craters.

Discussion: The present morphology around all three craters demonstrates that fluvial processes dominate erosion over-all; however, it is recognized that other processes predominate in some geologic settings (e.g. eolian at Wabar Craters, Saudi Arabia). Lithology is considered to impart mainly second order controls on gradational morphology at these impact sites despite differences in target rock types. General similarity between erosional styles developed on limestone/dolostone and sandstone ejecta types at Meteor Crater (1,2) supports this contention. Conclusions are based on the results of field work (Meteor Crater), analysis of air photos (all three), and Landsat TM images (Meteor Crater). The following first-order gradational evolutionary sequence is proposed (Fig. 1).

Subsequent to impact, the steep interior walls and rim-crest undergo rapid erosion by mass-wasting, fluvial, and lesser eolian activity. These processes combine to create a smoothed, undulating, but largely unincised rim-crest supported by an interior wall backwasted to expose more coherent bedrock along upper sections. Lower portions of the interior wall are buried by talus (debris chutes and aprons) and alluvium (Meteor Crater). As the upper walls become stabilized, fluvial activity incises the now largely inactive debris chutes and erodes bounding talus deposits (Meteor Crater). During this stage, the slope of the interior wall is reduced, but remains fairly high (Fig. 1). Fluvial and eolian processes dominate early modification of the crater exterior at rates in near-rim areas ($<0.25R$) that are 10-20X higher than those on more distal ejecta. Fluvial activity outside the crater creates small incised gullies on the upper and mid flank that transport material to lower flank alluvial fans and more distal diffuse-drainage (Meteor Crater). Drainage densities on interior and exterior walls are high at this early stage (Fig. 1); however, the small scale of exterior drainage precludes accurate mapping both in air photos and Landsat images, whereas apparently high densities on interior walls primarily reflect drainage control by relict debris chutes.

At intermediate stages (Fig. 1), crater walls continue to backwaste and rim-crest elevations decrease, thereby leading to increased amounts of crater fill (3, Lonar). Reduced average slopes on the interior wall indicate mass-wasting processes are still active, but are becoming less important relative to fluvial processes. A paucity of exposed talus and ejecta along interior walls (Lonar) supports this statement. Erosion of rim-crest ejecta down to uplifted bedrock leads to fairly uniform elevation and lower erosion rates. Drainage densities (determined from air photos) decrease in the crater interior as largely relict debris chutes and talus are destroyed; however, remaining systems are larger and extend up to the rim, thereby resulting in a "notched" appearance (Fig. 1). Erosion of the ejecta surrounding the crater continues by fluvial and lesser eolian activity causing enlargement of radial gullies and (presumably) continued deposition in larger alluvial fans. The scale of most drainages implies detectability at TM resolution (30 m/pixel).

At more advanced stages (Fig. 1), the crater rim becomes wholly breached by some interior drainages resulting in capture of some exterior near-rim systems. The resultant increase in drainage area causes additional flow into, and deposition on the crater floor leading to burial of relict mass-

wasting deposits (4). The rim-crest continues to be lowered and narrowed through downwasting, backwasting of the interior wall, and lesser erosion of the lower gradient exterior flank. A decrease in raised-rim width from early (Meteor Crater) to late (Talemezane) of $\sim 0.1\text{--}0.15R$ accounts for $\sim 10\%$ crater enlargement. The continued paucity of exposed talus on the lower interior wall coupled with decreasing average wall slope (5) highlight the lessening importance over-all of mass-wasting activity. Interior/near-rim drainage density during late stage erosion (from air photo) is high as new systems evolve/are captured on the exterior mid and upper flank (Fig. 1). Exterior drainage capture by interior systems results in reduced exterior stream power and density on the crater flanks. The large scale of interior drainages implies easy detection in Landsat TM imagery; however, the reduced scale of exterior systems suggests they may go undetected. As fluvial processes decrease on the crater exterior due to loss of high gradient tributaries, the relative importance of eolian processes may increase.

Summary: From these three craters a first-order gradational evolutionary sequence can be proposed. As crater rims are reduced by backwasting and downwasting through fluvial and mass-wasting processes, craters are enlarged by $\sim 10\%$. Enlargement of drainages inside the crater eventually forms rim breaches, thereby capturing headward portions of exterior drainages. At the same time, the relative importance of gradational processes may reverse on the ejecta: eolian activity may supersede fluvial incisement and fan formation at late stages of modification. Despite actual high drainage densities on the crater exterior during early stages of gradation, the subtle scale of these systems results in low density estimates from air photos and satellite images. Because signatures developed on surfaces around all three craters appear to be mostly gradient dependent they may not be unique to simple crater morphologies. Similar signatures may develop on portions of complex craters as well; however, important differences may also occur. As progressively larger craters are formed, the probability of interrupting pre-crater drainages increases. Hence, crater modification by regional fluvial activity may become more important. Deposition by pre-crater drainages on the distal ejecta at Meteor Crater supports this statement.

References: (1) Grant, J.A. and Schultz, P.H., 1990: p. 433-434, in *Lunar and Planet. Sci. XXI* (abstracts), Lunar and Planetary Institute, Houston, Texas. (2) Grant, J.A., 1990: Ph.D. Dissertation: *Geology*, Brown University, Providence, Rhode Island, 401p. (3) Fredriksson, K., Dube, A., Milton, D.J. and Balasundaram, M.S., 1973: *Science*, v. 180, p. 862-864. (4) Lambert, P., McHone, J.F., Jr., Dietz, R.S. and Houfani, M., 1980: *Meteoritics*, v. 15, p. 157-179. (5) Karpoff, R., 1963: *Meteoritics*, v. 1, p. 31-38.

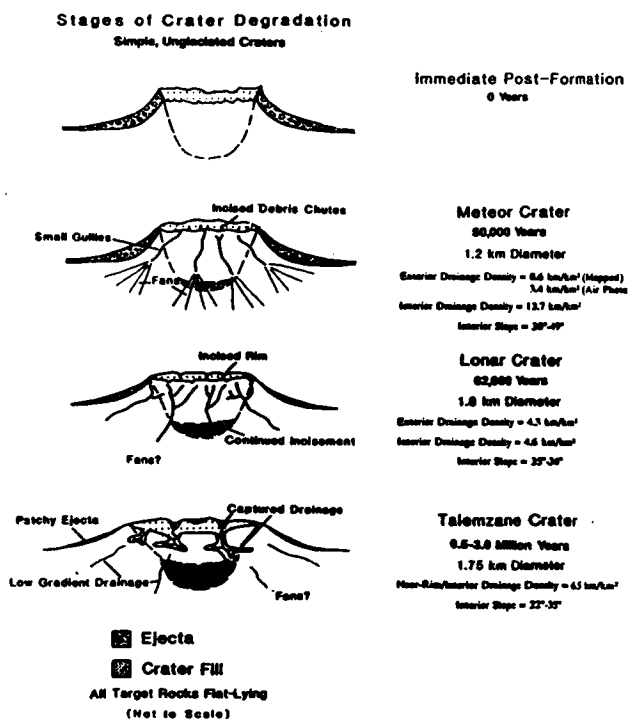


Figure 1. Hypothesized stages of crater degradation. Profiles are exaggerated for illustration. With increasing erosion: A) the rim-crest outline changes from rough and irregular to more undulating (Meteor Crater) to notched (Lonar) to incised (Talemezane); B) rim-crest elevations are reduced as the crater is rapidly widened (Meteor Crater) until underlying bedrock is exposed (Lonar) whereupon slower rates prevail as the rim-crest diameter and elevation continue to slowly increase and decrease, respectively (Talemezane). A well-defined raised-rim is present at all stages; however, breaches form in the rim during advanced fluvial dissection of the interior, resulting in drainage capture of outer flank systems and increased flow into the crater (Talemezane). Initially steep wall slopes (Meteor Crater) decrease (Lonar and Talemezane) as the importance of mass-wasting decreases relative to fluvial activity. The evolution of drainage reflects this change in styles as initially high drainage densities first decrease as debris chutes and aprons on the interior wall are destroyed (Meteor Crater to Loner) then increase again as the systems begin to breach the raised-rim (Lonar to Talemezane). All drainage densities are derived from air-photos except as noted.

Styles of Crater Gradation in Southern Ismenius Lacus, Mars; J.A. Grant and P.H. Schultz, Brown University, Providence, RI 02912.

Introduction: Preserved morphology around selected impact craters together with results from study of longterm gradational evolution (1) are used to assess processes responsible for crater modification in southern Ismenius Lacus (30°-35°N, 325°-360°W). Results are compared with the gradational styles of selected terrestrial craters (2). Although most craters in the region display complex primary morphologies, some first order comparisons with the gradational styles around simple terrestrial craters may be valid (2). Nearly complete high resolution coverage (Revs 199S-212S, -40-50 m/pixel) provides a basis for studying morphologic features at scales comparable to those observed in Landsat TM images of terrestrial craters (2). In addition, 816 craters >1-2 km in diameter within the study area were classified (Table 1) as degraded (rimless/mostly rimless, buried) pristine (most primary features present), and superpristine (unmodified at available resolution). Nearly 2/3 of the degraded craters are rimless/mostly rimless (Table 1). The average slope on the interior walls of both degraded and pristine craters is 27°-30° (Table 2), close to the angle of repose for material dominated by silt and sand-sized grains (3). The maintenance of these gradients into advanced degraded morphologies implies an abundance of fine-grained material in the country rocks.

This statement is consistent with the low regional thermal inertia (4). Epochs of accelerated gradation affected southern Ismenius Lacus from early until mid/late Noachian and during the Hesperian (1). Widespread remnants of an air-fall deposit emplaced/modified during the second epoch are preserved in eastern sections of the region; however, more sustained erosion farther west left only isolated remnants (1). We conclude the relative importance of gradational processes differs around the terrestrial and martian craters considered here: martian rimless morphologies are produced by mass-wasting, eolian deposition/erosion, and limited fluvial incisement resulting in downwasting and significant backwasting of crater walls.

Discussion: Clues to the origin of degraded crater morphologies in the study area are found in the regional geologic history. Emplacement of air-fall deposits during the second gradational epoch smoothed crater topography, especially in eastern sections where buried morphologies are more common. However, uniform deposition on a cratered surface should preserve a raised-rim around larger craters (5,6). Thus, mantling alone can not conceal raised-rims. Subsequent erosion of air-fall deposits would proceed most rapidly on exposed crater walls and rim-crests. These exposed topographic highs would in turn act as a windbreak, thereby slowing deflation on surrounding lower gradient surfaces. Hence, air-fall deposition/partial removal could produce a rimless/mostly rimless morphology. The absence of air-fall deposits around some rimless/mostly rimless craters in the region requires additional rim removal mechanisms.

Some partially rimless craters display walls modified by catastrophic mass-wasting through failure of large wall sections (e.g. 32.7°N, 359.9°W). Because material derived from wall failure is not easily identified as landslide and debris flow deposits inside these craters, the mass-wasting deposits must be either reworked across the crater floor or removed. Low drainage densities observed on associated crater walls implies an analogy with the fluvial redistribution of material that occurs in terrestrial craters is unrealistic (7). If the target rocks are comprised largely of reworked ejecta and buried lenses of volatile-rich material with abundant fine-grained sediment (1,7), eolian redistribution of landslide and debris flow deposits could modify their appearance. Redistribution would proceed most rapidly during gradational epochs when atmospheric density may have been higher and carrying capacity was enhanced. In addition, air-fall deposition and subsequent erosion/redistribution further mask mass-wasting deposits.

Maintenance of constant slope angles throughout increasing degradation implies that a less catastrophic means of mass-wasting may contribute to raised-rim removal also. As the debris forming the crater walls is partially redistributed across the crater by eolian activity the resultant oversteepening would cause minor slumping, backwasting and restoration of the angle of repose. Dessica-

tion of possible water/ice-rich lenses exposed in crater walls (1,7) would also reduce wall strength, thereby inducing slumping.

In addition to craters where the surrounding ejecta has been modified by air-fall deposition/erosion, some retain ejecta only in near-rim areas. The greater thickness of near-rim ejecta around these craters may have trapped sufficient impact heat to cause partial welding of the fragments and/or may be composed of more competent lithologies, thereby enhancing preservation. Low drainage density and a paucity of recognizable fluvial depositional features analogous to those observed around Meteor Crater (7) suggests that fluvial processes play a secondary role to eolian activity in erosion of the distal ejecta. Ejecta sedimentology at Meteor Crater implies martian ejecta and regolith has moderate to high hydraulic conductivity (7); therefore, the role by fluvial processes in over-all erosion of Martian craters may be limited in the absence of high magnitude precipitation events or widespread catastrophic groundwater release.

Gradational Evolution: As craters are formed in southern Ismenius Lacus they excavate material possessing abundant fine-grained material (sand and silt) and possibly containing lenses of water/ice (1,7). Shock preconditioned walls slump during the late stages of crater formation to -27° - 30° (Table 2). Reduced fluvial activity on the low gradient ejecta surfaces relative to the Earth causes eolian processes to become relatively more important during subsequent gradation. In some areas air-fall deposition simply buries ejecta while in others the distal ejecta is entirely stripped away. Surface lag deposits analogous to those observed at Meteor Crater (7) undoubtedly slow deflation. Gradation at least since Hesperian times occurs largely through mass-wasting and eolian processes rather than fluvial activity. Both catastrophic and slow, sustained backwasting of the interior wall and lowering of the rim-crest results in rim removal from up to 50% of the degraded craters. In many cases rim removal occurs without complete erosion of the continuous ejecta. Crater floor deposits created by mass-wasting are redistributed by eolian activity and/or are buried by later air-fall deposition. In contrast, gradation of selected simple terrestrial craters is dominated by slow, steady downwasting and backwasting of the rim by both fluvial and mass-wasting erosion (2,7). Comparison of degraded martian craters with pristine craters in the surrounding terrain and degraded craters on the Earth suggests destruction of the raised-rim by backwasting in Ismenius Lacus accounts for crater enlargement of -10 - 15% . Air-fall deposition/erosion during late gradation also created rimless morphologies in $\sim 15\%$ of the craters (Table 1).

References: (1) Grant, J.A. and Schultz, P.H., 1991: in Lunar and Planet. Sci. XXII (this volume), Lunar and Planetary Institute, Houston, Texas. (2) Grant, J.A. and Schultz, P.H., 1991: in Lunar and Planet. Sci. XXII (this volume), Lunar and Planetary Institute, Houston, Texas. (3) Lambe, T.W. and Whitman, R.V., *Soil Mechanics, SI Version*: New York, N.Y., John Wiley and Sons, 553p. (4) Zimbelman, J.R., 1986: *Advances in Planetary Geology*, NASA Tech. Memo. 88784, p. 271-572. (5) Zimbelman, J. and Greeley, R., 1981: p. 1233-1235, in Lunar and Planet. Sci. XII (abstracts), Lunar and Planetary Institute, Houston, Texas. (6) Craddock, R.A. and Maxwell, T.A., 1990: *Jour Geophys. Research*, v. 95, p. 14,265-14,278. (7) Grant, J. A., 1990: Ph.D. Dissertation: Geology, Brown University, Providence, Rhode Island, 401p.

Table 1 - Crater Classification in Southern Ismenius Lacus

General Classification	Number	% Total
Total Craters	816	100
Degraded	330	40
Pristine	417	51
Super Pristine	69	9
Degraded Craters		
Rimless - Mostly Rimless	104	32
Rimless - Mostly Rimless w/ Ejecta	50	15
Rimless - Mostly Rimless Buried	27	8
Rimless - Mostly Rimless Buried w/Ejecta	25	8
Partly Rimless w/Ejecta	20	6
Partly Rimless Buried w/Ejecta	11	3
Complete Rim	35	10
Other (Inverted, Ghost Craters)	5	2
Undifferentiated	53	16
Pristine Craters		
Pristine	361	87
Pristine Valley-Modified	56	13

Table 2 - Crater Wall Slopes in Southern Ismenius Lacus

	Measured Average	Range
Degraded Craters		
Rimless - Mostly Rimless	28°	17°-40°
Rimless - Mostly Rimless w/ Ejecta	29°	20°-36°
Rimless - Mostly Rimless Buried w/Ejecta	27°	—
Pristine Craters		
Pristine	27°	24°-35°
Pristine Valley-Modified	30°	25°-28°

The Gradational History of Southern Ismenius Lacus; J.A. Grant and P.H. Schultz, Brown University, Providence, RI 02912.

Introduction: The gradational evolution of a heavily cratered region in southern Ismenius Lacus (30°-35°N, 325°-360°W) is assessed through detailed analysis of both surface morphology and crater statistics. The region occurs within a broad area of low thermal inertia (2) and is dominated in central sections by the 110 km diameter crater Cerulli which interrupts the up to 5 km wide Mamers Valles. Primary reasons for selection of southern Ismenius Lacus for study include: A) broad, nearly complete coverage by high resolution Viking images (40-50 m/pixel); B) the abundance of fairly pristine, young craters whose interior walls and continuous ejecta are incised by relatively high drainage densities; and C) large portions of the region are partially/mostly buried by material resembling unconformable air-fall deposits found elsewhere on Mars (1). Results provide further constraints on the timing/intensity of climate-controlled gradation on Mars.

Gradational History: Techniques/assumptions employed in compilation/interpretation of all statistics are discussed in an earlier publication (1). Relative ages are expressed as the log number of craters >5 km as determined by comparison of statistics with the standard crater function for Mars (3). Crater statistics of all superposed craters reveal an oldest recognizable surface with an age intermediate between the Hellas and Isidis Basins (Fig. 1). Following formation of this basement surface, a period of accelerated gradation affected the area as evidenced by: A) departure from the expected production slope in the statistics for crater diameters less than 22 km; B) an abundance of degraded, rimless craters; and C) formation of Mamers Valles. Activity during this early epoch saw the emplacement of a thick basal unit of reworked material possibly containing lenses of volatile-rich material and produced many rimless/mostly rimless crater morphologies. Drainage density along Mamers Valles, whose size typifies similar aged systems, is 0.015-0.020 km/km². Statistics of pristine craters from west and central sections and all craters less than 16 km in diameter from the east yield an N5 age of 2.6; therefore, the end of gradation associated with this first epoch correlates with mid to late Noachian highlands intercrater plains formation (4,5).

The formation of crater Cerulli marked the next major event in the area at an N5 age of 2.5 as determined by crater densities on ejecta surrounding the crater (Fig. 1). Drainage densities in and around Cerulli are at least 0.12 km/km² and 0.13 km/km², respectively; however, occurrence of inverted relief and/or buried segments along some valleys suggests actual densities are slightly higher.

Activity during a second later gradational epoch is constrained by statistics of nearly pristine craters from eastern portions of the study area, small diameter craters superposing crater Cerulli ejecta, and superpristine craters from the western section of the region. These statistics imply that the duration and intensity of activity during the second epoch varied from west to east: gradation ended in the east by an N5 age of -2.1-2.0, but persisted in central and western sections until N5 ages of -1.8 and 1.5, respectively (Fig. 1). Abundant relict morphology across the region indicates an extensive air-fall deposit was emplaced and modified during the second gradational epoch: A) isolated remnants of layered deposits in and around some craters throughout the study area; B) occurrence of remnants over a broad range of both regional and local relief; C) the subdued primary morphology around many impact craters (especially in the east) that suggests many remain buried; D) the fine-grained nature of near-surface material implied by low regional thermal inertia; E) examples of inverted topographic valleys (including the interior of Cerulli); F) pedestal craters superposing the thick basal unit; G) occurrence of valley networks lacking identifiable source regions and interpreted as superposed drainage; and H) valley networks incised into deposits that have steep fronted depositional features implying emplacement occurred in craters partially filled by some material. The greater abundance of partially/completely mantled craters in eastern sections coupled with the earlier ending of gradation there during the second epoch reflects the preservation of a relatively continuous layer of air-fall deposits. In contrast, the more sustained gradation in central and western areas along with the more isolated nature of deposit remnants indicates more complete removal. Superposed drainage in

the air-fall deposits indicates at least a locally volatile-rich nature during emplacement/modification. Based on the scale of drainages interpreted as superposed, the buried appearance of many craters in eastern sections, and the thickness of deposit remnants, an original deposit thickness of up to several hundred meters is estimated. The density of small valleys (100–150 m wide) preserved in surfaces formed during the second epoch of activity are locally as high as 0.36 km/km², but are up to 0.85 km/km² on some crater walls; however, densities in most parts of the study area are much lower if any valleys are present at all. Cessation of gradation following the second epoch of accelerated geomorphic activity in east and central areas correlates with ridged plains emplacement 500–700 km to the east (6) and the end of accelerated Hesperian gradation elsewhere on Mars (1,7–9). The end of gradation farther west coincided with peak outflow channel formation (10). Emplacement and modification of the air-fall deposit marked the end of significant gradation in the region; however, deposition and subsequent reworking of relatively thin deposits (11) at scales too small to be recognized in this study may have continued into recent martian history.

Summary: Two epochs of accelerated gradation affected the geomorphic evolution of southern Ismenius Lacus (Fig. 1). These periods of enhanced gradational activity were likely related to periods of more clement climate induced by release of either recycled exogenic or juvenile endogenic (12) atmospheric volatiles (1). Variations in the intensity and duration of gradation during the second epoch are indicated by the variability in the timing of cessation and degree of air-fall deposit removal across the study area. Over-all intensity of gradation decreased through successive epochs based on: A) the decreasing diameter at which cumulative statistics from the respective surfaces cease to follow the expected production function; and B) the decrease in size/increase in density of preserved valley networks incised into surfaces of differing age (Fig. 1). A comparable decrease in valley density with time has been noted in the Isidis region (13).

References: (1) Grant, J. A. and Schultz, P. H., 1990: *Icarus*, v. 84, 166–195. (2) Zimbelman, J.R., 1986: *Advances in Planetary Geology*, NASA Tech. Memo. 88784, p. 271–572. (3) Neukum, G. and Hiller K., 1981: *Jour. Geophys. Research*, v. 86, p. 3097–3121. (4) Greeley, R. and Guest, J.E.: USGS Map I-1802-B. (5) Craddock, R.A. and Maxwell, T.A., 1990: p. 236–237, in *Lunar and Planet. Sci. XXI* (abstracts), Lunar and Planetary Institute, Houston, Texas. (6) Dimitriou, A.M., 1990: p. 293–294, in *Lunar and Planet. Sci. XXI* (abstracts), Lunar and Planetary Institute, Houston, Texas. (7) Grizzaffi, P. and Schultz, P.H., 1989: *Icarus*, v. 77, p. 358–381. (8) Schultz, P.H. and Lutz, A.B., 1988: *Icarus*, v. 73, p. 91–141. (9) Grant, J. A., 1987: *Advances in Planetary Geology*, NASA Tech. Memo. 89871, p. 1–268. (10) Masursky, H., Boyce, J.M., Dial, A.L., Schaber, G.G. and Strobell, M.E., 1977: *Jour. Geophys. Research*, v. 82, p. 4016–4038. (11) Christensen, P.R., 1986: *Jour. Geophys. Research*, v. 91, p. 3533–3545. (12) Greeley, R., 1987: *Science*, v. 236, p. 1653–1654. (13) Schultz, P.H. and Britt, D., 1986: p. 775–776, in *Lunar and Planet. Sci. XVII* (abstracts), Lunar and Planetary Institute, Houston, Texas.

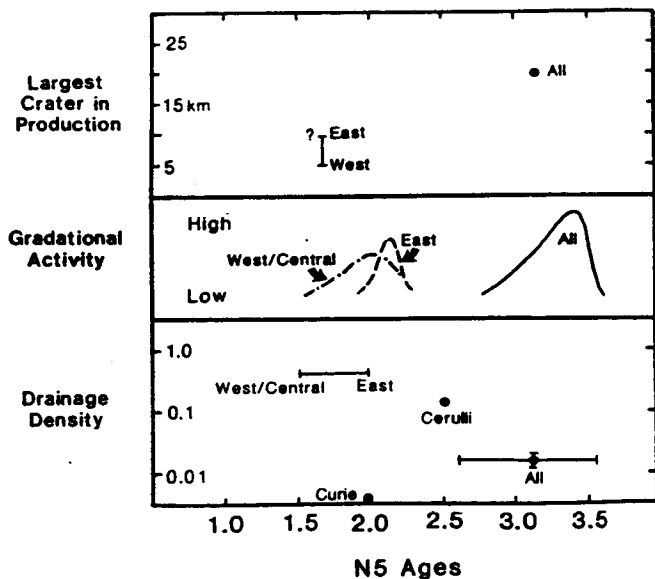


Figure 1. Summary of geologic processes in southern Ismenius Lacus. Gradational activity in the region occurred during an early period of intense, widespread activity (N5 age 3.6–2.6) that ended about the time of initial activity at Tyrrhena Patera and is widely recognized on the planet. This first epoch led to formation of a thick (>0.5 km) basal unit in the region. A second period of accelerated gradation occurred concurrent with increased activity northwest of Isidis, in the vicinity of crater Millochau, the Electris region, Sinus Meridiani, Margaritifer Sinus, the interior of Isidis basin, and elsewhere (1,7–9). This later period was shorter lived in eastern sections (N5 age 2.1–1.9) than farther to the west (N5 age 1.5). Nearby crater Curie (100 km in diameter) formed at an N5 age of 2.0. Drainage size/density decrease/increase in scale with decreasing age with the exception of Curie which shows no incisement. Based on this observation and the diameter at which crater statistics from modified surfaces cease to display a production population of craters, it is concluded that the intensity of gradation in the study area decreased with time.

SOIL CRUSTS ON MARS; H.J. Moore, U.S. Geological Survey, Menlo Park, CA, 94025.

Three distinct soillike materials sampled by the Viking landers (VL) on Mars are (in order of increasing strength): (1) drift, (2) crusty to cloddy, and (3) blocky [1]. Relative strengths of these materials are manifested by footpad penetrations during landing (VL 1), depths of deep holes, motor-currents during sampling, sampler backhoe penetrations, comminutor motor-currents, impact pits, trench tailings, and successful acquisitions of the coarse fraction (only blocky material). Cementation by S and Cl compounds [2] probably contributes to the relative strengths. This is shown in Fig. 1 where the weight percent of $\text{SO}_3 + \text{Cl}$ of each material is plotted against their relative strengths. A similar result is obtained using SO_3 alone, but not Cl which is deficient in VL 2 samples. Although analytical uncertainties are large, VL 2 samples of surface crusts appear to have more $\text{SO}_3 + \text{Cl}$ (samples U-1,5; about 8.8%) than those from depth (U-6,7; about 8.1%).

Morphological evidence for crustification of the soillike materials parallels their $\text{SO}_3 + \text{Cl}$ contents. Undisturbed drift material is fractured showing that it has cohesion and deformation of the surfaces at the tips of shallow sample trenches produces relatively smooth bulges of the surface with some evidence for a thin, weak crust; but the tailings of the trenches are composed chiefly of lumpy masses and fines. Undisturbed crusty to cloddy material is fractured into tile-like prismatic units and deformation of the surface at the tips of shallow sample trenches commonly include thin tile-like units of crust and/or thicker prisms of soillike material; tailings of trenches commonly include a chaotic array of thin slabs of crust and fines. Undisturbed blocky material, which is usually covered by a thin layer of fines and clodlets, is also fractured into prismatic units and deformation at the tips of shallow trenches include thick tabular clods which are best illustrated by the reddish tabular clods on the XRFS funnel at the end of the mission [1].

Processes involved in the formation of the crusts are not understood, but they appear to occur at the surface-atmosphere interface and crust development may be a function of time. The processes are near-surface ones because "waterline" ledges of crust were present on rocks displaced by the samplers [1,3]. Process appear to be a function of time because the weakly-developed to almost non-existent crusts of the younger drift material (superposed on blocky material) contrast with the well-developed crusts of the older blocky material. There may also be a latitudinal effects because the Cl contents at Lander 1 are larger than those at Lander 2.

The role of crusts in martian eolian processes is not fully appreciated. Crusts form structural units with variable mechanical stabilities that affect the eolian erodibility of

SOIL CRUSTS ON MARS; H.J. Moore

the soillike materials [4]. The responses of the soillike materials to erosion by engine exhausts during landings [1,5,6] and the Dust Storm of Sol 1742 [7] are more akin to those of arable soils on Earth [4] than sand. As on Earth, soillike materials exposed to the wind are more prevalent than sands.

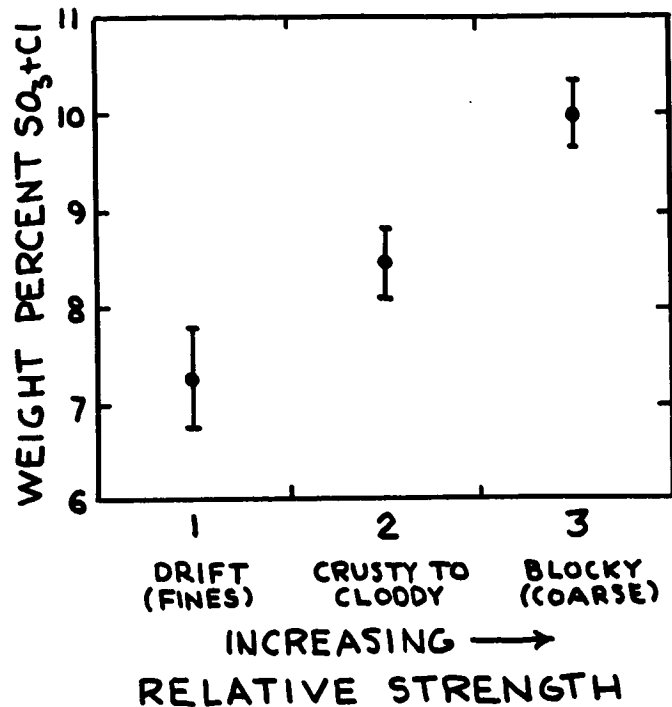


Figure 1. Comparison between weight percent SO₃ + Cl in drift, crusty to cloddy, and blocky (coarse fraction) materials and their relative strengths. Sample numbers of Clark [2] are: drift (C-1,6,7,8), crusty to cloddy (U-1,2,4,5,6,7), and blocky (C-2,5,13). One sample of fines (C-8; 6.6%) has been included with drift material, but this does not significantly alter the relations. A VL 1 bulk sample (C-9; 8%) is excluded because it appears to include drift and blocky materials.

REFERENCES

- [1] Moore, H.J., et al., 1987, U.S.G.S. Prof. Paper 1389, 222p.
- [2] Clark, B.C., 1982, J.G.R., v. 87, p. 10,059-10,067.
- [3] Moore, H.J., et al., 1978, U.S.G.S. Prof. Paper 1081, 21p.
- [4] Chepil, W.S., 1945, Soil Sci., v.52, p. 305-320.
- [5] Hutton, R.E., et al., 1980, The Moon and Planets, v. 23, p. 293-305.
- [6] Moore, H.J., et al., 1979, J.G.R., v. 84, p. 8365-8377.
- [7] Moore H.J., 1985, J.G.R., v. 90, p. D163-D174.

N92-10787

SURFACE-MATERIAL MAPS OF VIKING LANDING SITES ON MARS; H.J. Moore, U.S. Geological Survey, Menlo Park, CA, 94025; J.M. Keller, Stanford University, Stanford, CA, 94309.

We have mapped the surface materials at the Viking landing sites [1] to gain a better understanding of the materials and rock populations at the sites and to provide information for the future exploration. The maps extend to 9 m in front of each lander and are about 15 m wide -- an area comparable to the area of a pixel in high resolution Viking Orbiter images.

The maps are divided into near and far fields (Fig. 1). Data for the near fields are from: 1/10-scale maps [2], unpublished maps, and lander images. Data for the far fields are from: 1/20-scale contour maps [3], contoured lander camera mosaics [3], and lander images. Rocks were located on these maps using stereometric measurements and the contour maps.

Map units are: (1) fine, (2) soillike, and (3) rock materials. Coordinates, length (L), width (W), and height (H) for each rock are recorded in a file for computational purposes. For many rocks, L or W was estimated. Size-frequency and area-covered distributions of rocks (Fig. 2) are derived from the file according to the surrounding map unit, field, and size. All rocks mapped within fine material and all rocks >0.25 m in the two fields are included in the distributions, but rocks <0.25 m in the soillike areas of the far fields are assumed to have the same distribution as rocks <0.25 m in the soillike areas of the near fields.

The forms of our size-frequency distributions of rocks are similar to previous ones [2,4]. Frequencies of rocks >0.18 m are larger at Lander 2 than Lander 1, but the reverse is true for smaller rocks. Fractions of area covered by the larger rocks in logarithmic size-bins are irregular and yield no simple relations for extrapolations to larger sizes of rocks, but the areas covered by small rocks diminish rapidly with decreasing size (Fig. 2). Our fractions of area covered by centimeter-size and larger objects and rocks are about 0.12 at Lander 1 and about 0.16 at Lander 2. Outcrops of rock cover an additional 4.5% of the area at the Lander 1 site. These fractions of area are comparable to those estimated for the sites from Viking Orbiter thermal data for rock abundances with unspecified size-frequency distributions, but assumed to be equivalent to rock surfaces about 0.10 to 0.15 m across [5].

We suggest that the following equation [6] for the fraction of area covered by rocks larger than 0.10 m could be used for preliminary design and planning studies because mathematical descriptions of martian rock populations are unknown and the possibilities are large [7]:

$$A = C * D^{-0.66},$$

where A is the fraction of area covered by rocks with diameters larger than D (in meters) and C varies with location on Mars.

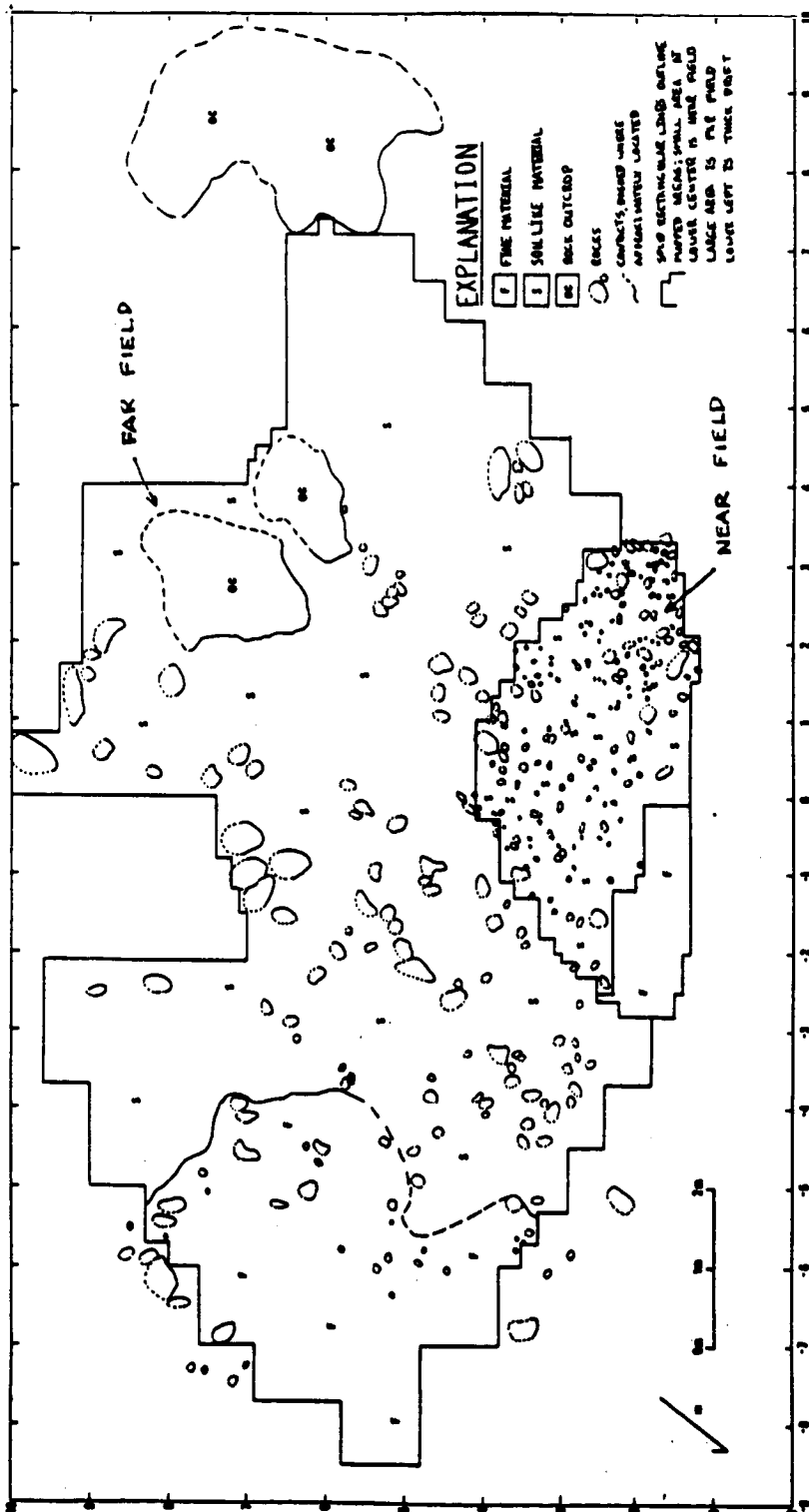


Figure 1 . Surface-material map at the Viking 1 site. Mapped area is divided into a near field (A) and a far field (B). The population of rocks <0.25 m within the soillike areas of the far field are assumed to be the same as those for soillike areas in the near field. Coordinates are in meters from center of Lander 1 (0,0). (Map prepared by John M. Keller).

SURFACE-MATERIAL MAPS, MARS: Moore, H.J. and Keller, J.M.

For various locations, we also suggest that C can be adjusted to give values of A that match those of rock abundance maps [5b]. In reality, the exponent on D varies. For ejecta from craters in rock, the exponent on D can vary with the size interval considered and distance from the crater; values may range from -3, or so, to even positive ones. Values of C for craters also vary and may be near zero for alluvium. For the Moon, a nominal value for the exponent on D is -0.5.

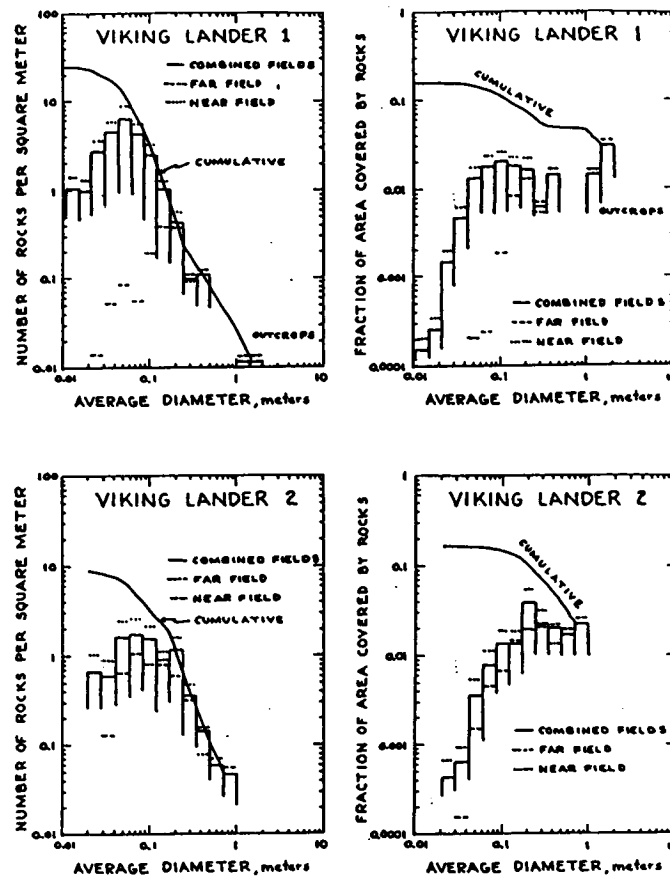


Figure 2. Size-frequency distribution and fraction of area covered for rocks at the Viking 1 and 2 landing sites.

REFERENCES

- [1] Moore, H.J. and Keller, J.M., 1990, NASA TM 4210, p. 533-535. [2] Moore, H.J., et al., 1987, U.S.Geol. Survey Prof. Paper 1389, 222p. [3] Liebes, S. Jr., 1982, NASA CR 3568, 290p. [4] Binder, A., et al., 1977, J.G.R., v. 82, p. 4439-4451. [5] Christensen, P.R., (a) 1982, J.G.R., v. 87, p. 4439-4451; (b) 1986, Icarus, v. 68, p. 217-238. [6] Moore H.J. and Jakosky, B.M., 1989, Icarus, v. 81, p. 164-184. [7] Malin, M.C., 1989, NASA TM 4130, p. 363-365.

MAGMA GENERATION ON MARS: ESTIMATED VOLUMES THROUGH TIME

R. Greeley and B. Schneid, Department of Geology, Arizona State University, Tempe, AZ 85287-1404

Images of volcanoes and lava flows (1), chemical analyses by the Viking landers (2), and studies of the SNC meteorites (3) show that volcanism has played an important role in the evolution of Mars. Photogeologic mapping (4-8) suggests that half of Mars' surface is covered with volcanic materials. A previous estimate for the volume of volcanic materials (9) assumed a uniform thickness of 1 km for plains and plateau units, and did not consider plutonic materials. Here we present results from new mapping, including estimates of volcanic deposit thicknesses based on partly buried and buried impact craters using the technique of DeHon (10), infer the volumes of possible associated plutonic rocks, and derive the volumes of magmas on Mars, generated in its post-crustal formation history. We also consider the amount of juvenile water that might have exsolved from the magma through time.

1:2,000,000 photomosaics served as the bases for mapping volcanic materials, following the conventions from the 1:15 M photogeologic maps of Mars (5-6). Our higher resolution mapping enabled better distinction of volcanic materials and ages. We estimate the total exposed volcanic materials to be $66.98 \times 10^6 \text{ km}^3$, or about 46.5% of the martian surface. Not included are possible igneous rocks of the "original" crust, for which no diagnostic volcanic signatures are visible. Thus, Early Noachian materials are excluded and this is a conservative estimate. The outline of each volcanic area was digitized into a computer data base and "tagged" as to geologic age. The method of DeHon (10) was used to derive thicknesses of volcanic plains units. Thicknesses were entered into the digital data base and contoured to derive total volumes of exposed units by age. The volumes for volcanic deposits having significant relief, such as the shield volcanoes, were derived from paleostratigraphic (11) and topographic maps. The method outlined above accounts for only the materials exposed on the surface. The total areal extent, including buried surfaces, for each geological epoch followed the estimates of Tanaka et al. (8, Table 4), assuming that the ratio of volcanic to non-volcanic buried materials is the same as the ratio of exposed materials, to derive the total volume of volcanic materials by age (Table 1).

Table 1. Estimated Volumes of Volcanic and Plutonic Materials on Mars, and Inferred Associated Water Released, Expressed as a Layer on the Planet

Epoch	Age ζ 10 ⁹ yr	Volcanic 10 ⁶ km ³	Plutonic 10 ⁶ km ³	Total Magma 10 ⁶ km ³	H ₂ O, m
L. Amazonian	0.1	2.06	1.44	3.50	.81
M. Amazonian	0.5	9.73	13.29	23.01	5.32
E. Amazonian	1.3	16.72	36.39	53.29	12.31
L. Hesperian	2.5	18.52	74.25	92.86	21.46
E. Hesperian	3.3	17.45	106.33	123.79	28.60
L. Noachian	3.6	9.36	58.93	68.29	15.78
M. Noachian	4.0	1.77	17.71	19.48	4.50
E. Noachian	4.6	—	—	—	—
Totals		75.6	308.34	384.22	88.78

ζ Approximate age at start of epoch

We next consider the total magma produced on Mars through time. Crisp (12) surveyed the ratios of intrusive and extrusive rocks on Earth and found a range of ratios of ~ 5:1 for oceanic localities to 10:1 for continental localities. We used a ratio of 10:1 for martian ages of Late Hesperian and older on the assumption that the early crust of Mars consisted of megaregolith which might be comparable to terrestrial continental crust. We used a ratio of 5:1 for Middle Amazonian and younger materials on the assumption that the Tharsis province and younger volcanic areas might have crusts somewhat similar to oceanic areas on Earth. A ratio of 8:1 was used for Early Amazonian as an intermediate value. Based on these assumptions, the total magma produced on Mars is estimated at $\sim 384 \times 10^6$ km³ with peak production in the Early Hesperian epoch. If the Middle Noachian is taken as the time when the surface record is first preserved, and it is assumed that ~ 4.0 ae is the start of this epoch, then the rate of magma production on Mars is less than 0.1 km³/year, substantially less than the 26 to 34 km³/year estimated for Earth over the last 180×10^6 years (12). If we assume that juvenile water was released in association with martian magmas, and if we take a value of 1% by weight for exsolved juvenile water, then the total volume of water outgassed from the magma would form a layer of water 88.8 m deep on Mars.

1. Carr M. et al., 1977. *J. Geophys. Res.* 82, 3985-4015.
2. Clark B. et al., 1977. *J. Geophys. Res.*, 82, 4577-94.
3. McSween, H. 1985, *Geology* 12, 3-6.
4. Greeley, R. and P.D. Spudis, 1981. *Rev. Geophys. Space Physics*, 19, 13-41.
5. Scott, D.H. and K. L. Tanaka, 1986. *U.S. Geol. Sur. Misc. Invest. Ser.* I-1802A.
6. Greeley, R. and J. E. Guert, 1987. *U.S. Geol. Sur. Misc. Invest. Ser.* I-1802B.
7. Tanaka, K.L. and D. H. Scott 1987. *U.S. Geol. Sur. Misc. Invest. Ser.* I-1802C.
8. Tanaka et al., 1988. *Proc. LPSC 18*, 665-678.
9. Greeley, R. *Science*, 236, 1653-4.
10. DeHon, R. A., 1974, *Proc. LSC 5*. 53-69.
11. Scott, D. H., and K. L. Tanaka, 1981, *Icarus*, 45 304.
12. Crisp, J. A., 1984. *J. Volc. Geotherm Res.*, 20, 177-211.

CRYSTALLIZATION DURING EMPLACEMENT OF LAVA FLOWS

J. Crisp, Jet Propulsion Laboratory, California Institute of Technology, Pasadena, CA

Thermal models of lava flows provide a way of estimating emplacement durations and eruption rates of planetary lava flows, which can help constrain magma ascent, rheology and composition. Most of the models that have been developed consider only the effects of cooling by radiation. However, heating due to crystallization can be a large component of the overall heat budget of a flow¹.

Little is known about the amount of crystallization and latent heating during flow advance. We have these examples and constraints: {1} The Yakima flood basalt experienced almost no crystallization during flow advance². {2} The 1947-48 Hekla flows were erupted undercooled (1000°C), which did not allow the inner core to crystallize during flow advance.³ Shearing action in the crust, margins, and flow front triggered crystallization and raised the temperature to 1150°C in these outer zones³. {3} An upper bound for the maximum amount of crystals in any flow is about 50-60%, based on studies of Marsh⁴, which indicate that at higher crystal contents, the bulk viscosity does not allow a flow to move. {4} Half-way downstream (11 km), the Mauna Loa 1984 1A flow had 15% more crystals than at the vent. For typical Hawaiian and Etna lava flows, the amount of crystallization during advance is probably between 15 and 50%. A more in-depth discussion of example {4} is given below.

Crystal size distribution (CSD) measurements were made to quantify and study the effects of crystallization in the well-documented 1984 Mauna Loa flow. Plots of frequency versus crystal size reveal two crystal populations (Fig. 1). The smaller crystals (microlites) nucleated and grew during emplacement, whereas the larger ones nucleated in the rift zone before eruption. The theory of CSD analysis has been developed for the study of crystallization rates in rocks^{5,6}. A sample CSD plot for microlites in quenched-dip samples of the Mauna Loa flow is shown in Figure 2. For most igneous rocks, this type of plot is linear with a slope equal to $-1/\tau G$ and an intercept (crystal size = 0) of J/G , where τ is the time for crystal growth (time spent travelling in channel), G is growth rate, and J is nucleation rate^{5,6}. Crystal growth and nucleation rates for the microlites in the Mauna Loa flow were found to be $10^9 - 10^7 \text{ cm s}^{-1}$ and $10^4 - 10^5 \text{ cm}^{-3} \text{ s}^{-1}$.

The volume fraction Φ of crystals expected at time (t) can be approximated as a function of growth (G) and nucleation rate (J) and nucleation time (t'), by the formula⁷:

$$\Phi = 1 - \exp \left[\frac{-4\pi}{3} \int_{t'-0}^{t-t} J \left(\int_{t'}^t G dt \right)^3 dt' \right] \quad (1)$$

Assuming that the values of J and G calculated for microlites during the first 11 km of travel remained constant throughout flow advance, equation (1) would predict that the Mauna Loa flow would have solidified several kilometers short of its 26 km extent (based on measured flow velocities⁸). Thus, the rate of microlite crystallization must have decreased downstream, most likely as a result of increased undercooling. If this can be determined for other flows, then equation (1) should be evaluated by integrating appropriate estimates of G and J as functions of time and/or temperature. Note that Φ is a key parameter required in thermal models of lava flows.

For 15% crystallization during the first 11 km travel on April 6, 1984, the latent heat effect in the Mauna Loa flow was about 0.016 J per gram of magma per second ($\tau \approx 1$

hour). Assuming a maximum crystallinity of 50% during flow advance⁴, latent heating during the last 16 km of travel would have been less than $10^{-3} \text{ J g}^{-1} \text{ s}^{-1}$ ($\tau > 1.5$ days). Integrated over time, the latent heating (J g^{-1}) for this lower 16 km stretch could have equalled that of the first 11 km.

These crystallinity measurements provide us with a rough guide to the amount of crystallization and latent heating likely in other flows, as a function of emplacement duration. Using the nucleation and growth rates for the microlites in the Mauna Loa flow and integrating over emplacement duration, crystallization is estimated to have contributed a 2-75° increase in temperature for the Puu Oo flows and 20-50° for the Etna flows listed in Crisp and Baloga¹ (the *net* effect of radiation, convection, conduction, and latent heating was a temperature decrease¹). It would be preferable to have actual measurements of crystallization in these flows, but without this, we must use the rates for the Mauna Loa flow to make estimates for other flows.

Thermal models used to estimate eruption rates of planetary lava flows should include latent heating. Measurements of crystallization during flow advance are needed because they provide the only independent way to validate theoretical cooling models, by constraining temperatures and latent heating. For flows on Mars, we must assume that the amount of crystallization is similar to that in terrestrial flows and place minimum and maximum bounds on the latent heat effect. Unfortunately, as examples {1}-{4} show, there can be anywhere from 0 to 60% crystallization during flow advance. To improve our constraints for martian flows, we need to search for correlations in terrestrial flows between flow morphology and the amount of crystallization during emplacement.

REFERENCES: ¹Crisp and Baloga (1991) *Lunar Planet. Sci. Conf. XXII* 257-258. ²Shaw and Swanson (1970). *Proc. 2nd Columbia River Basalts Symp.*, 271-299. ³Einarsson et al. (1949) *The eruption of Hekla 1947-1948*. Visindafelg Islendinga, Reykjavik, Iceland. ⁴Marsh (1981) *Contrib. Mineral. Petrol.*, 78:85-98. ⁵Marsh (1988) *Contrib. Mineral. Petrol.*, 99:277-291. ⁶Cashman and Marsh (1988) *Contrib. Mineral. Petrol.*, 99:292-305. ⁷Kirkpatrick (1981) *Rev. in Mineral.*, 8:321-398. ⁸Lipman and Banks (1987) *USGS Prof. Paper* 1350:1527-1567.

Figure 1. Number of crystals per μm^2 , as a function of size, for a sample of the 1984 Mauna Loa flow

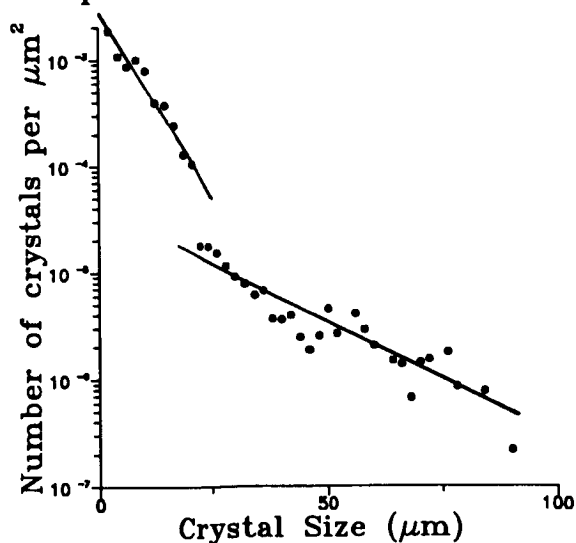
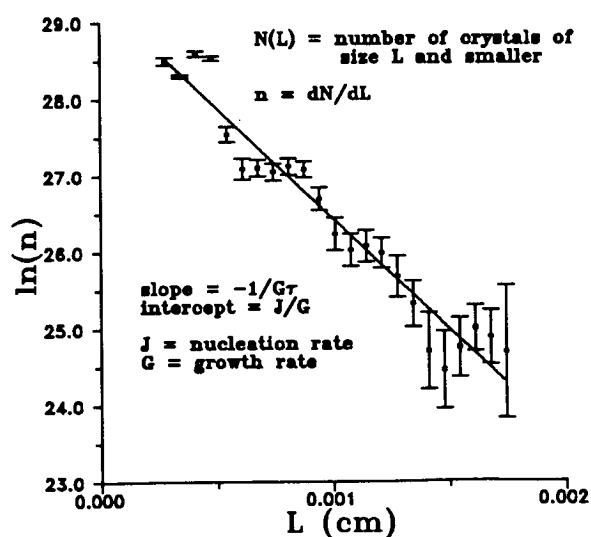


Figure 2. Plagioclase microlite size distribution plot for the Mauna Loa 1984 flow



PHYSICAL PROPERTIES OF LAVA FLOWS ON THE SOUTHWEST FLANK OF TYRRHENA PATERA, MARS

David A. Crown, Tracy K. Porter, and Ronald Greeley, Department of Geology, Arizona State University, Tempe, Arizona 85287

Tyrrhena Patera (22°S, 253.5°W), a large, low-relief volcano located in the ancient southern highlands of Mars, is one of four highland paterae thought to be structurally associated with the Hellas basin [1-3]. The highland paterae are Hesperian in age [4] and among the oldest central vent volcanoes on Mars. The morphology and distribution of units in the eroded shield of Tyrrhena Patera are consistent with the emplacement of pyroclastic flows [5]. A large flank flow unit extending from Tyrrhena Patera to the SW contains well-defined lava flow lobes and leveed channels (Figure 1) [5-6]. This flank flow unit is the first definitive evidence of effusive volcanic activity associated with the highland paterae and may include the best preserved lava flows observed in the southern hemisphere of Mars.

A large volcano-tectonic channel, similar in morphology to lunar sinuous rilles, connects the flank flow unit to the summit caldera of Tyrrhena Patera, which is interpreted to be filled with late-stage lavas [5]. The flank flow unit extends ~1000 km from the summit toward the Hellas basin. The flow unit averages ~185 km in width (max. = ~275 km) and embays the older, eroded shield units. Numerous wrinkle ridges are contained within the unit and exhibit NW-SE (Hellas-concentric) and NE-SW (Hellas-radial) trends [6]. The NW-SE trending ridges post-date flow emplacement and the NE-SW ridges are contemporaneous with or older than the flows [7].

The flank flow unit is characterized by a series of SW-trending flow lobes, with average widths of ~2-15 km and lengths of ~10-120 km (Table 1). Most are single lobate flows with sinuous, lobate scarps defining their margins. Some individual lobes feed other lobes near their termini. In several locations, a complex of flows is evident with one or two large lobes and several smaller lobes branching from the same region. Many flows can be traced upstream to NE-SW trending wrinkle ridges; some appear to emanate from ridges or to have sources adjacent to ridges, implying that the ridges serve as feeder dikes or delineate fractures along which magma rose to the surface.

On the flanks of Tyrrhena Patera, the volcano-tectonic channel changes in character from a linear depression to a leveed, channelized flow. Discontinuous segments of this channelized flow can be observed at distances as great as 650 km from Tyrrhena's summit, where a ~1.3 km wide channel extends from a partially collapsed segment. Other regions of partial collapse also suggest that this feature was at one time a continuous conduit for lava, analogous to a terrestrial lava tube. Segments of this channelized flow have been covered by later lava flows within the flank flow unit, and flows emanating from individual segments indicate that it also partially buried itself.

This extensive channelized flow and the large lava flows of the flank flow unit, which are morphologically different from flows in the Tharsis region, can be used to constrain the differences in volcanic style between the younger northern plains and the ancient, cratered highlands. Standard rheologic models have been used to estimate effusion rates [8], yield strengths [9], and viscosities [10], assuming the mapped flows were emplaced as single lobes (Table 1). Because accurate flow thicknesses are not available, calculations for idealized 10- and 100-m thick flows are shown. The regional slope of 0.25° is assumed for the calculations [5]. Inferred viscosities of ~10⁴ Pa s for 10-m thick flows are significantly less than estimates for lavas in the Tharsis region (including Olympus Mons) [11-13], whereas viscosities of 100-m thick flows (~10⁸ Pa s) are comparable to estimates for Tharsis flows. Yield strength estimates for Tyrrhena flows (~10² Pa for 10-m thick and ~10⁴ Pa for 100-m thick flows) are also less than estimates for Tharsis and Alba Patera flows [12-14]. Effusion rate estimates for Tyrrhena flows (~10³ m³/sec for 10-m thick and ~10² m³/sec for 100-m thick flows) fall at the minimum end of the range previously determined for Tharsis and Alba Patera lavas [12-15]. If the Tyrrhena flows are 10's of meters thick, the calculations indicate a general trend to higher viscosities and yield strengths from Tyrrhena Patera to Alba Patera to the

TYRRHENA PATERA LAVA FLOWS: Crown, D.A. et al.

Tharsis volcanoes, which suggests a temporal evolution of the nature of martian magmas. In the future, thickness estimates and further applications of physical models for flow emplacement will better constrain these trends.

References: [1] Peterson, J.E., 1978, *Proc. Lunar Planet. Sci. Conf.*, 9th, 3411-3432. [2] Schultz, P.H., 1984, *Lunar Planet. Sci. Conf.*, XV, 728-729. [3] Wichman, R.W., and P.H. Schultz, 1989, *J. Geophys. Res.*, 94, 17333-17357. [4] Greeley, R., and J.E. Guest, 1987, *U.S. Geol. Surv. Misc. Invest. Ser. Map I-1802B*. [5] Greeley, R., and D.A. Crown, 1990, *J. Geophys. Res.*, 95, 7133-7149. [6] Crown, D.A., and R. Greeley, 1990, *Lunar Planet. Sci. Conf.*, XXI, 250-251. [7] Porter, T.K., D.A. Crown, and R. Greeley, 1991, this issue. [8] Hulme, G., and G. Fielder, 1977, *Phil. Trans. R. Soc. Lond. A.*, 285, 227-234. [9] Moore, H.J., et al., 1978, *Proc. Lunar Planet. Sci. Conf.*, 9th, 3351-3378. [10] Nichols, R.L., 1939, *J. Geol.*, 47, 290-302. [11] Fink, J.H., 1980, *Lunar Planet. Sci. Conf.*, XI, 285-287. [12] Hulme, G., 1974, *Geophys. J. R. Astron. Soc.*, 39, 361-383. [13] Zimbelman, J.R., 1985, *Proc. Lunar Planet. Sci. Conf.*, 16th, D157-D162. [14] Cattermole, P.J., 1987, *Proc. Lunar Planet. Sci. Conf.*, 17th, E553-E560. [15] Baloga, S.M., and D.C. Pieri, 1985, *NASA TM-87563*, 245-247.

Table 1. Rheologic and Eruptive Properties of Tyrrhena Patera Lava Flows

Flow	Length (km)	Average Width (km)	Effusion Rate (m ³ /sec) d = 10 m	Effusion Rate (m ³ /sec) d = 100 m	Yield Strength Pa d = 10 m	Yield Strength Pa d = 100 m	Viscosity Pa S d = 10 m	Viscosity Pa S d = 100 m
1	69.4	10.1	1.3E+04	1.3E+03	1.0E+02	1.0E+04	1.2E+04	1.2E+08
2	90.5	10.5	1.7E+04	1.7E+03	9.6E+01	9.6E+03	8.9E+03	8.9E+07
3	74.5	9.0	1.2E+04	1.2E+03	1.1E+02	1.1E+04	1.1E+04	1.1E+08
4	32.3	11.1	6.4E+03	6.4E+02	9.0E+01	9.0E+03	2.5E+04	2.5E+08
5	34.2	6.0	3.7E+03	3.7E+02	1.7E+02	1.7E+04	2.4E+04	2.4E+08
6	43.7	14.4	1.1E+04	1.1E+03	7.0E+01	7.0E+03	1.9E+04	1.9E+08
7	22.0	8.0	3.2E+03	3.2E+02	1.3E+02	1.3E+04	3.7E+04	3.7E+08
8		7.3			1.4E+02	1.4E+04		
9		5.5			1.8E+02	1.8E+04		
10		8.8			1.1E+02	1.1E+04		
11	32.6	4.5	2.6E+03	2.6E+02	2.2E+02	2.2E+04	2.5E+04	2.5E+08
12	25.9	5.9	2.7E+03	2.7E+02	1.7E+02	1.7E+04	3.1E+04	3.1E+08
13	117.4	11.9	2.5E+04	2.5E+03	8.4E+01	8.4E+03	6.9E+03	6.9E+07
14	100.5	7.0	1.3E+04	1.3E+03	1.4E+02	1.4E+04	8.1E+03	8.1E+07
15	13.1	2.1	5.0E+02	5.0E+01	4.7E+02	4.7E+04	6.2E+04	6.2E+08
16	93.4	8.7	1.5E+04	1.5E+03	1.2E+02	1.2E+04	8.7E+03	8.7E+07
17	22.7	2.8	1.2E+03	1.2E+02	3.5E+02	3.5E+04	3.6E+04	3.6E+08
18	21.1	3.3	1.3E+03	1.3E+02	3.0E+02	3.0E+04	3.8E+04	3.8E+08
19	51.3	7.2	6.7E+03	6.7E+02	1.4E+02	1.4E+04	1.6E+04	1.6E+08
20	38.1	4.7	3.2E+03	3.2E+02	2.1E+02	2.1E+04	2.1E+04	2.1E+08
21	55.4	6.0	6.0E+03	6.0E+02	1.7E+02	1.7E+04	1.5E+04	1.5E+08
22	23.2	5.4	2.3E+03	2.3E+02	1.9E+02	1.9E+04	3.5E+04	3.5E+08
23	652.1	2.5	3.0E+04	3.0E+03	4.0E+02	4.0E+04	1.2E+03	1.2E+07

Effusion Rate: $Q = (G_z \kappa x) (w/d)$

Yield Strength: $\tau_0 = \rho g d^2 w$

Viscosity: $\eta = \rho g d^2 \sin \alpha / 3u$

x = flow length

w = average flow width

d = flow thickness

κ = thermal diffusivity = $6 \times 10^{-7} \text{ m}^2/\text{sec}$

G_z = Graetz number = 300 (when flow stops)

g = gravitational acceleration = $3.71 \text{ m}^2/\text{sec}$

ρ = density = 2700 kg/m^3

α = slope = 0.25°

u = flow velocity = Q/wd

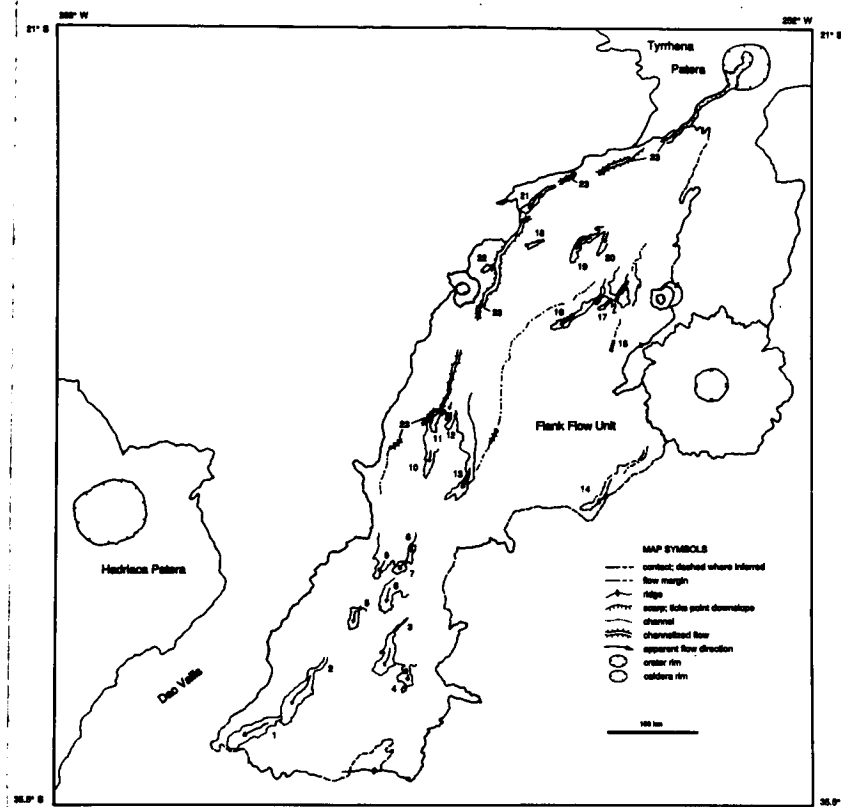


Figure 1. Simplified sketch map of the southwest flank flow unit of Tyrrhena Patera showing the distribution of lava flow lobes. The boundaries of Hadriaca Patera and the Tyrrhena Patera basal shield unit [5] are also indicated. Numbers are keyed to Table 1. Flows were mapped from images with ~90 - 230 m/pixel resolution.

RHEOLOGICAL ANALYSES OF LAVA FLOWS ON MARS; H.J. Moore, U.S. Geological Survey, Menlo Park, CA, 94025 and P.A. Davis, U.S. Geological Survey, Flagstaff, AZ, 86004.

We have obtained some 183 profiles of lava flows on Mars using photoclinometry [1]. These photoclinometric profiles were leveled by adjusting them until the levee crests or bases had the same elevations (depending on the situation). Here, we report some of the results of our analyses of twenty-seven flows on the flanks of Alba Patera (3 flows), near the summit of Ascraeus Mons (6 flows), the flanks of Arsia Mons (3 flows), and the flanks of Olympus Mons (15 flows).

In our rheological analyses, we use a wide-flow model [2], Hulme's model [3], and model 1 of Baloga and Crisp [4]. Effusion rates are estimated by using an unmixed-cooling model [5] that is calibrated by using Hawaiian flows [6] and a Graetz-number model [4,7]. Our Graetz-number effusion rates vary from about 0.4 to 1.2 times those of the unmixed-cooling model; a mixed-cooling model [5] yields effusion rates that are 20 times larger than the unmixed-cooling model.

The models have been applied to terrestrial flows that range from basalts to rhyolites (Fig. 1A) [6].

Despite the use of different models by different workers [8,9,10,11], the results are similar in that the range of values are quite large, especially for the Bingham viscosities (Fig. 1B). Our average yield strengths for each flow range from about 1 to 20 kPa and average Bingham viscosities for each flow range from about 0.02 to 8 MPa*s. Our results are compared with those of others [9,10,11] in Table 1.

Although estimates using our empirical procedures are subject to many uncertainties, the results in Figures 1A and 1B suggest to us that the flows examined to date are not felsic or ultramafic; rather, they probably range from basalts to basaltic andesites. The same general conclusion is reached when the same model set is applied separately to the data sets. Thus, the suggestion that flows on Olympus Mons [8], and elsewhere [6,9,10], may be more silicic than Hawaiian basalts is supported by our results. These suggestions are testable with suitable measurements of silica contents of the flows.

Table 1. Comparison between our yields strengths and Bingham viscosities and those listed under reference (in parentheses) for three martian volcanoes.

Volcano	Yield Strength (kPa)	Bingham Viscosity (Pa*s)	Reference
Ascraeus Mons	5-9 (10-40)	0.05-6 (1-100)	[9]
Olympus Mons	1-20 (2-40)	0.02-8 (0.7-20)	[10]
Alba Patera	2-6 (8-28)	0.09-0.9 (0.1-2)	[11]

LAVA FLOWS ON MARS; H.J. Moore and P.A. Davis

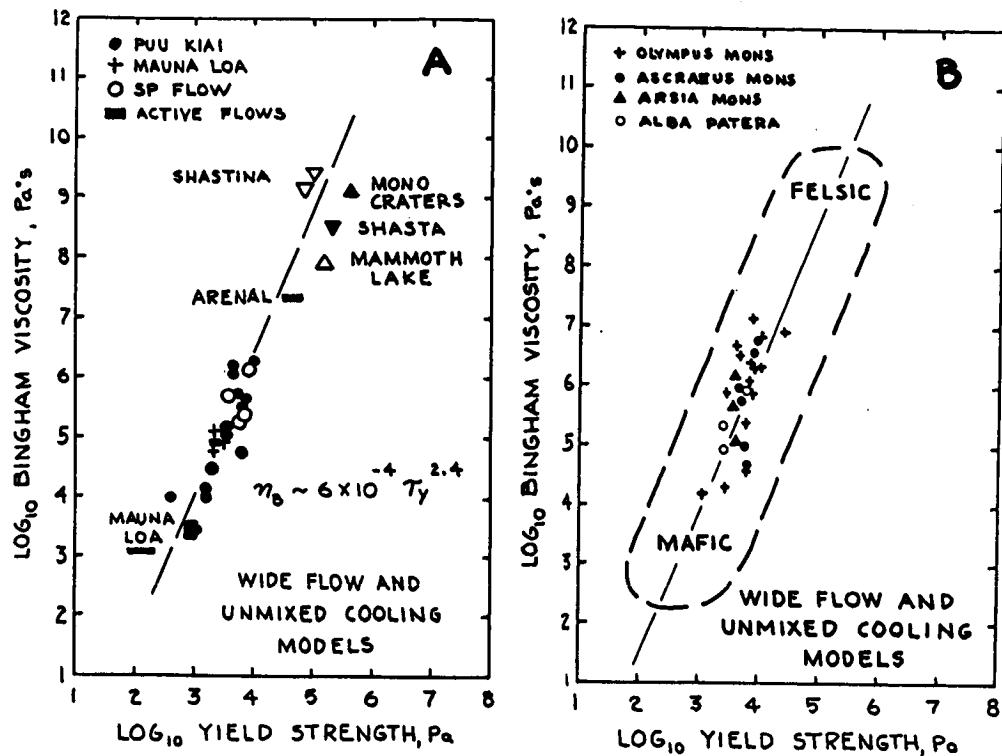


Figure 1. Bingham viscosity versus yield strength. A. Terrestrial flows with compositions that range from basalt to rhyolite [6]. B. Average values for martian flows and composition fields from A.

REFERENCES

- [1] Davis, P.A., et al., 1984, *J. Geophys. Res.*, v. 89, p. 9449-9457. [2] Moore, H.J., et al., 1975, *Proc. 6th LSC.*, p. 101-118. [3] Hulme, G., 1974, *Geophys. J. Roy. Astron. Soc.*, v. 39, p. 361-383. [4] Baloga, S.M. and Crisp, J., 1988, unpubl. rept., 35 p. [5] Pieri, D.C., et al., 1986, *J. Volc. Geotherm. Res.*, v. 30, p. 29-45. [6] Moore, H.J., et al., 1989, *Repts. Planet. Geol. Geophys. Prgm.-1988*, NASA TM 4130, p. 387-389. [7] Hulme, G., et al., 1977, *Phil. Trans. Roy. Soc., Lond.*, ser. A, v. 285, p. 227-234. [8] Hulme, G., 1976, *Icarus*, v. 28, p. 207-213. [9] Zimbelman, J.R., 1985, *J. Geophys. Res.*, v. 90, Suppl. D, p. D157-D162. [10] Zimbelman, J.R. and Fink, J.H., 1989, *Lunar and Planet. Sc. XX*, p. 1241-1242. [11] Cattermole, P., 1987, *J. Geophys. Res.*, v. 92, p. E553-E560.

FACTORS CONTROLLING LAVA DOME MORPHOLOGY

Jonathan Fink and Nathan Bridges, Geology Department, Arizona State University, Tempe, AZ 85287 and Ross Griffiths, Research School of Earth Sciences, Australian National University, Canberra 2601, Australia.

Among the many spectacular venusian features revealed by Magellan, the large circular domes around Alpha Regio have generated some of the greatest interest. Early reports have suggested that, based on their shapes, such constructs may be made of high silica lavas. In order to evaluate the validity of such inferences and to better understand the factors controlling lava dome shapes, we have conducted theoretical analyses and a series of laboratory simulations designed to evaluate the role of various factors on dome aspect ratio.

The most widely used method of estimating the rheology of extra-terrestrial lava flows has been to relate the height (h) of marginal levees to their yield strength (τ_0): $\tau_0 = \rho g h \sin \theta$, where ρ = lava density, g = gravity and θ = underlying or surface slope^{1,2}. A recently published model³ has shown that the height (H) and radius (R) of sub-circular lava domes similarly can be related to the yield strength of the lava: $\tau_0 = 0.32 H^2 \rho g / R$. Both of these models were derived by balancing the gravitational stresses driving a flow forward with the yield strength holding it back, and both assume that the yield strength is a material constant of the magma, independent of its temperature. Inspection of the second of these equations shows that for a given dome diameter, height will scale as the inverse of the square root of gravity. Thus, for lava of a given yield strength, domes on the moon will tend to be about 2.5 times taller than those on earth.

Attempts to uniquely relate the yield strengths of lavas (estimated using the above equations) to composition have been largely unsuccessful^{1,2}. We suggest that it is the thickness of a lava flow's cooled carapace, rather than chemical composition, that determines the *effective* yield strength. This solidified crust that forms at the flow surface and cascades off the front to create a talus pile provides the resistance to advance commonly attributed to the lava yield strength. Thus the more rapidly crust forms, the greater the resistance to buoyant stresses, and the sooner a flow will come to rest. For a fixed eruptive volume, more rapid crust growth will lead to shorter, thicker flows and domes. Similarly, decreased gravitational stresses (as on smaller planets) will also lead to relatively stubby extrusions.

Intuitively one might assume that planetary surface temperature would play a major role in determining how rapidly a flow cools and thus what morphology will result. However, calculated cooling rates for lavas experiencing a combination of convection and radiation for likely surface conditions on all of the terrestrial planets reveal that the time scale for the flow surface to begin to solidify will be negligible relative to total emplacement times for all but the smallest extrusions. As a consequence, variations in surface temperature should not lead to significantly different dome shapes as long as the temperature does not approach the magmatic solidus.

While ambient temperature may not strongly influence the shape of domes, the *rate of extrusion* does play an important role. For a given eruptive volume, a higher extrusion rate will allow lava to flow further before surface solidification is able to stop its advance. Slower extrusion rates will result in shorter, steeper domes. Cooling is even more effective if the erupted volume comes out in a series of pulses separated by repose intervals, rather than as a single episode. The larger the number of eruptive pulses and the longer the intervening repose periods, the more effective cooling will be and the thicker the resulting extrusion. Observations of natural domes support this idea.

To begin to quantify this relationship we have conducted two sets of four experiments each in which polyethylene glycol wax was injected into a tank of cold sucrose solution. In each series, total erupted volume, repose interval, and wax properties were held constant, but the number of eruptive episodes was either 1, 2, 4, or 8. Figure 1 illustrates the results for these two series. In both cases, the aspect ratio of the dome (height/diameter= H/D) scaled linearly with the number of eruptive pulses. We are currently conducting additional experiments to evaluate how the length of the repose period affects aspect ratio. Another set of completed experiments showed that whether new magma is added to the surface (exogenous growth) or interior (endogenous growth) of a dome depends on the length of the repose period, confirming a conclusion obtained from topographic measurements of the Mount St. Helens dome⁵.

Our results thus suggest that variations in lava dome morphology on different planets will depend much more critically on local gravity and the style of eruption than on the magma composition, ambient temperature, or the relative roles of convective and radiative cooling. Eruption style in turn reflects differences in tectonic conditions and the ability of magma to exsolve volatiles. Observed crude correlations between silica content and calculated yield strengths for terrestrial lava flows and domes^{1,2} probably are due to differences in extrusion rate and volatile solubility, rather than intrinsic rheological properties. Thus, even after taking the known effect of gravity into account, observed differences in gross dome morphology on different planets cannot by themselves be directly related to composition. Additional information such as the distribution of surface textures and structures, or spectroscopic data will be needed to conclusively establish dome compositions.

REFERENCES

- (1) Moore H. J., Arthur D. W. and Schaber, G.G. (1978) Yield strengths of flows on the Earth, Mars and Moon. *Proc Lun. Planet.Sci. Conf.* 9: 3351-3378.
- (2) Hulme G. (1974) The interpretation of lava flow morphology. *Geophys. J. Roy. Astr. Soc.* 39: 361-383.
- (3) Blake S. (1990) Viscoplastic models of lava domes. *IAVCEI Proc. in Volcanology* 2: 88-126.
- (4) Fink J. H. and Griffiths R. W. (1990) Radial spreading of viscous-gravity currents with solidifying crusts. *Journal of Fluid Mechanics* 221: 485-509.
- (5) Fink J.H., Malin M.C. and Anderson S.W. (1990) Intrusive and extrusive growth of the Mount St. Helens lava dome. *Nature* 348: 435-437.

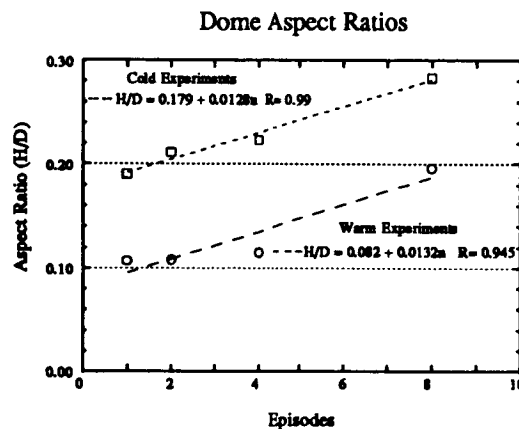


FIGURE 1. Aspect ratio as a function of number of eruptive episodes for two series of wax experiments.

NEW STUDIES OF MARTIAN VOLCANOES

Mouginis-Mark, P. J., M. S. Robinson and S. H. Zisk Planetary Geosciences Divn., Department Geology & Geophysics, SOEST, Univ. Hawaii Honolulu, HI 96822.

To investigate the morphology, topography and evolution of volcanic constructs on Mars, we have been studying the volcanoes Olympus Mons, Tyrrhena Patera, and Apollinaris Patera. These studies have relied upon the analysis of digital Viking Orbiter images to measure the depth and slopes of the summit area of Olympus Mons (1), new Earth-based radar measurements for the analysis of the slopes of Tyrrhena Patera (2), and the color characteristics of the flanks of Apollinaris Patera (3).

OLYMPUS MONS

In order to constrain the sequence of collapse events and subsequent tectonic deformation of the summit caldera of Olympus Mons, we have made a series of height and slope measurements for the summit of the volcano using digital Viking Orbiter images. The highest resolution images (~12 m/pixel) show that the circumferential graben and circumferential ridges within the caldera parallel the contours derived by Wu et al. (4), and that the circumferential ridges in the main crater (Crater #1; ref. 5) are located at a slight break in slope on the eastern part of the caldera floor. The linear ridges that are common on the floors of the younger craters (Craters 4 and 5; ref. 5) are absent from the topographically higher parts of the caldera floor (i.e., areas that exceed an elevation of 23.8 km). With respect to the rim of the caldera, there are azimuthal variations in slope stability, which we interpret to be an indication either of variations in rock strength or areas of localized stress. On the northwest and southeast rims, block faulting has taken place on walls that are less than 1,000 m high, while the southern rim of Crater 6 (ref. 5) is over 3,000 m high and yet the wall rocks show no signs of incipient failure.

In earlier studies (5, 6) we identified both compressional and extensional features on the floor of the Olympus Mons caldera. Our recent topographic measurements show that compressional features include broad (1 - 3 km wide) ridges that are morphologically similar to wrinkle ridges on the Moon and narrower (< 1 km width) linear ridges that are approximately circumferential to the perimeter of Crater 1. A topographic profile across one of the larger wrinkle ridges on the floor of Crater #5 shows that it is > 300 m high on its eastern side and 2 km wide. Typical planar dimensions for the wrinkle ridges on the floor of Craters 1 and 5 are 0.8 - 1.4 km width and 3 - 15 km in length. Maximum dimensions for the largest ridge are 1.8 km width and 23.0 km length.

An extensive series of graben around the perimeter of Crater 1 are the primary extensional features found within the caldera, although additional narrow fractures can be seen both on the caldera floor and upon the rim. We are confident that these features are indeed graben because of their symmetrical geometry (two bounding faults), flat floors, and approximately constant width. Shadow length measurements (from frame 473S28) show that the larger of these graben are ~420 - 450 m wide, may extend for more than 25 km in length, and ~180 - 200 m deep. The smaller fractures are typically 100 m in width, < 5 km in length, and are too shallow for us to confidently determine their depths at an image resolution of ~15 m/pixel.

Within Craters 4 and 5 there are numerous narrow sinuous ridges. These sinuous ridges are typically < 100 m wide, < 5 km in length, and are sufficiently low that their heights cannot be measured from their shadow lengths (i.e., they are probably <~20 m high). Sinuous ridges appear to be superimposed upon the wrinkle ridges, and often traverse the crater floor, a wrinkle ridge, and back to the crater floor without changing their orientation. The small size and their superimposition upon the broader wrinkle ridges suggests to us that these narrow sinuous ridges are older features than the wrinkle ridges, because otherwise their orientations and locations would have been constrained by the wrinkle ridges. We interpret the wrinkle ridges to be the products of compression during the subsidence of the entire caldera floor, and the narrow

sinuous ridges to be constructional features produced when an individual segment of the caldera floor was forming, perhaps analogous to pressure ridges that form on the surface of terrestrial lava lakes (7). Several irregular collapse pits and sinuous troughs can also be found on the floor of Crater 5, and these features may also have formed during the solidification of the surface of a lava lake by localized draining of the near-surface magma (we have observed comparable features on the surface of the September 1982 Kilauea lava flow, Hawaii, where drain-back into the vent followed the termination of activity, and left several irregular-shaped pits at the surface).

TYRRHENA PATERA

Tyrrhena Patera (21.5°S, 253.2°W) is one of several heavily dissected volcanoes in the southern highlands of Mars (8). Recent geologic mapping (9) has confirmed that it is a broad volcano possibly composed of four or five principal units, the oldest and most extensive of which are thought to be ash units on the basis of their morphology and erosional characteristics. Tyrrhena Patera represents the earliest central vent volcanism identified on Mars and may reflect a transition from flood-style eruptions which dominated early Martian history.

Because the currently favored models for the formation of the flank units on Tyrrhena Patera involve the emplacement of gravity-driven pyroclastic flows (9), we have taken advantage of the 1988 Mars Opposition to collect new Earth-based radar topographic data for Tyrrhena Patera in order to help refine our knowledge of the volcano's height and slope characteristics. Between August 30th - November 13th 1988, one of us (SHZ) collaborated with the JPL Radar Group and collected seven new topographic profiles between 20.0° - 25.1°S using the Goldstone, CA, radar system (2). Data were collected at X-band (3 cm) and S-band (12 cm), and were obtained at latitudes 20.0°, 20.2°, 20.7°, 21.7°, 21.9°, 22.3°, 22.4° and 25.1°S. These radar profiles augment the topographic information obtained by Downs et al. (10) in 1971 and 1973, which were located at 17.26°, 18.19°, 18.33°, 19.82° and 20.40°S.

The radar data show that the maximum height of Tyrrhena Patera to be 4.71 km above the 6.1 mb datum at 21.9°S (2). Slopes for the upper flanks of the volcano are ~1.18° for ~40 km east of the summit, and 0.64° for ~60 km west of the summit. The eastern basal plain surrounding the volcano is ~400 m lower in altitude than the plain surrounding the western side of the volcano: ~3,100 m above datum compared to 3,500 m above datum. The maximum height variation as one ascends the volcano is 1.5 km along a profile at 21.9°S between 250 - 254°W. This gives an average flank slope of 0.43° over a distance of 220 km. To the west of the summit, the change in elevation is 1.05 km over 220 km (average slope 0.30°) between 254 - 258°W. The volcano has an inferred height-to-basal diameter ratio of ~0.003.

North and south of the volcano, the ridged plains materials of Hesperia Planum are almost flat at a mean elevation of ~3,250 m to the north (at 18.19°S) and 2,900 m to the south (at 25.1°S). This means that the north-south gradient from the volcano summit to the north is 0.42°, and 0.60° from the summit to the south. These values can be compared directly to two slope estimates of Greeley and Crown (ref. 9; their slope "C", which they estimate to be 0.21° and we measure to be 0.42°, and their slope "D", which was estimated to be 0.37° and we measure as 0.60°). We can also approximate the measurement of slope "F" (ref. 9), which was estimated to be 0.19° and is indicated by the radar data to be 0.21°. The steepest slope measured is 3.03° for a 13 km segment of the northern flanks. These radar-derived slopes compare to the 0.09° - 0.37° slopes estimated for Tyrrhena Patera over distances varying from 304 - 634 km (9), and our photoclinometric measurements of $3.6^\circ \pm 0.5^\circ$ for the maximum slope (11).

APOLLINARIS PATERA

In addition to the topographic studies of Martian volcanoes, we have also started detailed analysis of the color data for certain volcanoes, which we hope will yield further information regarding their surface properties. For instance, our preliminary analysis of 3 color and 5 monochrome images of Apollinaris Patera (3), shows that the northern summit of the volcano

has very unusual surface deposits, in the form of temporally-variable high albedo deposits. The spectral behavior of the Apollinaris spot is quite unusual, in that the spot is seen over a long period of time (9/16/76 - 7/7/80), but is variable over a short time period (seen 2/16/78, not seen 3/14/78, seen 3/18/78), and is not correlated with season (Ls). Calibrated Viking Orbiter color data permit a plot of red vs. violet DN values to be constructed (3), and this information indicates that the spot becomes darker at a slower rate than the adjacent terrains for increasingly larger phase angles. Most intriguing is the color shift relative to the rest of the area; the violet radiance of the spot relative to the volcanics changes such that the spot has a lower radiance than the surrounding volcanics at lower phase and a higher radiance at higher phase. We have conducted preliminary investigations of the possible physical character of this albedo feature on the rim of Apollinaris, and consider that an origin either due to unusual composition or photometry is possible (3). Clouds and/or meteorology may also be possible, but the longevity and consistent shape when observed makes this idea less favorable. More significantly, the spot is relatively red, whereas the clouds and fog are blue relative to the rest of the Martian surface. Part of our current effort is designed to further investigate both the temporal variability of this Apollinaris Patera deposit, and to consider the possible role that viewing geometry may have played in the origin of this time-variable feature. We hope that in subsequent years, where appropriate color data exist, we will search for comparable features elsewhere on the planet.

FUTURE WORK

Our future studies of Martian volcanoes will place emphasis on the geologic evolution of the volcanoes based upon the combination of photoclinometrically derived topography and analysis of the Viking Orbiter images. For example, from our limited analysis to date (2), there does not appear to be a correlation between the degree of dissection of the flanks of the Tyrhena Patera and the local slopes. This is somewhat surprising, if either of the two most plausible models for their formation (the channels were carved either by pyroclastic flows (9) or by sapping processes (12)) are valid, because we would expect erosion to have been greatest on the steepest slopes. One of our objectives for the study will therefore be to combine the radar-derived slope information with our photoclinometric profiles to better understand the erosional processes that have shaped the Martian highland patera. We hope to be able to assess whether the larger valleys formed on steeper slopes or whether they were the result of unusually large volume eruptions. Photoclinometry and parallax measurements will, in fact, be the only methods by which topographic information can be derived for some of the other small Martian volcanoes that possess channelized flanks (such as Hecates Tholus, Hadriaca Patera, and Ceraunius Tholus) because these volcanoes lie poleward of the radar ground tracks.

This research was supported by NASA Planetary Geology & Geophysics Grant NAGW-437.

REFERENCES

- 1) Mouginis-Mark, P.J. and M. S. Robinson (1991). Evolution of the Olympus Mons Caldera, Mars. Submitted to Bull. Volc.
- 2) Zisk, S. H. et al. (1991). Lunar Planet. Sci. XXII, 1555 - 1556.
- 3) Robinson, M. S. et al. (1991). Lunar Planet. Sci. XXII, 1127 - 1128.
- 4) Wu, S.S.C. et al. (1984). Nature, 309, 432 - 435.
- 5) Mouginis-Mark, P. J. et al. (1990). Lunar Planet. Sci. XXI, 815 - 816.
- 6) Mouginis-Mark, P. J. et al. (1991). "The Physical Volcanology of Mars", In: MARS, Univ. Arizona Press, in press.
- 7) Peck, D. L. and W. T. Kinoshita (1976) U.S. Geol. Survey Prof. Paper 935-A.
- 8) Greeley R. and Spudis, P. D. (1981). Rev. Geophys., 19, 13 - 41.
- 9) Greeley R. and Crown, D. A. (1990). J. Geophys. Res., 95, 7133 - 7149.
- 10) Downs, G. S. et al. (1975), Icarus, 26, 273 - 312.
- 11) Robinson, M. S. (1990). Lunar Planet. Sci. XXI, 1027 - 1028.
- 12) Gulick, V. C. and V. R. Baker (1990). J. Geophys. Res. 95, 14,325 - 14,344.

THE PROBABLE CONTINUUM BETWEEN EMPLACEMENT OF PLUTONS AND MARE VOLCANISM IN LUNAR CRUSTAL EVOLUTION Carl M. Pieters, Brown University, Providence RI 02912

Facts and generally accepted information

- Ages of basaltic surface units sampled by the Apollo and Luna missions have been measured directly in the laboratory and range from around 3.2 to 3.9 Ga [1]. Crater degradation analyses indicate ages of unsampled basalt units can extend to about 2.0 Ga [2]. Superposition arguments for the Lichtenberg region suggest limited deposits with even younger ages [3].
- A great diversity of mare basalt types exist within the lunar sample collections [4]. Remote sensing studies show that only about 1/3 of basalts that exist as extensive surface units on the nearside have been directly sampled [5].
- "Pristine" samples of the original lunar crust that somehow escaped the brecciation transformation suffered by most highland materials continue to be identified [e.g. 6]. These pristine samples form two distinct suites with different chemical trends [7]: the ferroan anorthosites (hypothesized to be remnants from a magma ocean scale differentiation) and the Mg-rich suite (hypothesized to represent intrusions or plutons emplaced within the plagioclase-rich crust). Although compositional trends observed for the two suites of pristine materials are similar to those observed for materials found at the Stillwater, a classic layered mafic intrusion, these two lunar suites are not believed to be directly related based on other geochemical and isotopic properties [7, 8].
- As components of the original lunar crust, the pristine lunar samples are naturally old, clustering near 4.3 Ga, but with the oldest almost 4.5 Ga. There is no clear age relation between the Ferroan and the Mg-rich suites, although it is assumed the Mg-rich suite must be later [1, 7].

Additional new information.

- Fragments of mare basalts have been found in the sample collection with ages as old as 4.2 Ga [9]. The existence of ancient volcanism partially covered by subsequent lighter deposits has been argued on the basis of orbital chemistry, albedo, and reflectance spectroscopy [3, 10].
- A variety of surface compositions ranging from what is almost certain to be anorthosite to compositions consistent with several Mg-suite/KREEP rock types have been identified for areally extensive highland regions overflowed by the Apollo gamma ray experiment [11]. This variety is particularly important information about the farside highland crust, which is presumed to be thicker than the nearside and to contain only minor amounts of mare-like volcanism.
- A diversity of rock types reminiscent of layered mafic plutons have been identified at higher spatial resolution using large nearside craters as probes to the interior [12]. The classic example is at Copernicus, where the dunite-troctolite central mountains range about factor of three in olivine abundance [13]. Additional examples of deep-seated rock types distinct from the noritic anorthosite breccias that apparently dominate the nearside highland megaregolith [12] include the clinopyroxene-rich gabbro pervasive at Tycho [14, 12], the clinopyroxene-rich gabbro and troctolite mixtures at Aristarchus [12], and the variety of gabbros overlying crystalline norite at Bullialdus [16]. The age of these large craters is Eratosthenian or Copernican [17].

Hypothesis

Any one of these additional fragments of information can be viewed as unusual or simply interesting, but taken together they suggest there is no gap in magmatic evolution of the Moon. Only the form varies with time and random events as the crust evolves. The scale and variety of highland materials observed with remote observations is inconsistent with a compositionally homogeneous crust to 25 - 60 km depth. The association of frequent

"unusual" compositions at 5-10 km depth for nearside crustal areas excavated by late large impact events suggests extensive plutonism occurred in the nearside highland crust roughly contemporaneous with the mare basalts. Although our current data about the Moon are seriously incomplete and we are in desperate need of regional and global information, the following scenario appears to be consistent with these data and the leading hypothesis of formation of the Moon and is worthy of discussion and testing:

Ga b. p.	Event(s)
4.6 - 4.5	Proto-Earth forms, differentiates, and meets other large proto-planetary body in disruptive event creating a large mass of material in near-earth orbit.
4.5 - 4.45	Moon accretes and forms refractory An-rich crust [and mantle and core (?)]. Concentration of KREEP-rich zones must occur during the later stages.
<-->	Continued heavy bombardment
4.4 -->	Initiation of internal magmatism. Several (Mg-suite) plutons must have formed and cooled by 4.3.
4.3 - 3.8	Basin forming period (with rigid crust). These events mixed and delivered much of the highland material eventually to be sampled. They also fractured the crust to depths providing easier conduits for low density melts.
3.9 - 3.2	Major outflow of mare basalts on the nearside Plutonic activity continued within the highland crust.
3.2 - 2.0	Continued basaltic volcanism until conduits closed. Plutonic activity within crust paralleled mare volcanism.
2.0 - present	Random local activity (degassing, minor melt, etc.)

Conclusion

Although the volume of mare basalts is estimated to be only 0.1% of the lunar total [1], this value should not be taken to represent the amount of partial melt produced within the lunar interior nor should the mare basalts be viewed to represent the only products of internal heating. The actual amount of magmatic activity is certain to be substantially larger, but cannot be estimated without a global assessment of lunar highland heterogeneity and the character, scale, and abundance of lunar plutons.

References:

- [1] S. R. Taylor (1982) *Planetary Science: A Lunar Perspective*, pp. 481.
- [2] J. M. Boyce et al. (1974), *Proc. Lunar and Planet. Sci. Conf. 5th*, pp. 11-23.
- [3] P. H. Schultz and P. Spudis (1983), *Nature*, 302, 233-236.
- [4] J. J. Papike et al. (1976), *Rev. Geophys. Space Physics*, Vol. 14, No. 4, pp. 475-540.
- [5] C.M. Pieters (1978), *Proc. Lunar and Planet. Sci. Conf. 9th*, pp. 2825-2849.
- [6] J. W. Shervais (1988), *Moon in Transition*, pp. 82-91.
- [7] P. H. Warren (1985), *An. Revs. Earth Planet. Sci.*, 13, 201-240.
- [8] L.D. Raedeke and I.S. McCallum (1980), *Proc Conf. Lunar Highland Crust*, pp. 133-153.
- [9] L.A. Taylor, L.E. Nyquist, and J.C. Laul (1983), *Earth Planet. Sci. Lett.* 66, pp. 33-47.
- [10] B.R. Hawke and J.F. Bell (1981), *Proc. Lunar and Planet. Sci. Conf. 12B*, pp. 655-678.
- [11] P.A. Davis and P.D. Spudis (1985), *Proc. Lunar and Planet. Sci. Conf. 16, J. Geophys. Res.*, D61-D74.
- [12] C.M. Pieters (1986), *Revs. Geophys.*, Vol 24, No. 3. pp. 577-578.
- [13] C. M. Pieters (1990), *Lunar and Planetary Science XXI*, pp. 962-963.
- [14] B. R. Hawke et al. (1986), *Lunar and Planetary Science XVII*, pp. 999-1000.
- [15] P. Lucey et al. (1986), *Proc. Lunar Planet. Sci. Conf 16th, J. Geophys. Res.*, D344-D354.
- [16] C.M. Pieters (1989) *Lunar and Planetary Science XX*, pp. 848-849.;
----- (1990) *Remote Geochemical Analysis*, LPI and Cambridge Univ. Press, in press.
- [17] D.E. Wilhelms (1987) *The Geologic History of the Moon*, USGS-PP #1348, pp. 302.

LUNAR WESTERN LIMB PYROCLASTIC DEPOSITS

C.R. Coombs, SN15, NASA, Johnson Space Center, Houston, TX 77058; B.R. Hawke, Planetary Geosciences Division, SOEST, Univ. of Hawaii, 2525 Correa Road, Honolulu, HI, 96822.

Introduction

It has become increasingly evident that lunar pyroclastic volcanism played an important role in the formation and resurfacing of many areas on the Moon. On-going analysis of lunar Orbiter and Apollo photographs continues to locate and identify pyroclastic deposits and suggests that they just may be more ubiquitous than once thought. Located near mare/highland boundaries, many of these deposits formed contemporaneously with effusive mare volcanism. The mantling deposits formed as products of fire-fountaining.^(e.g., 1,2,3) Probable source vents for these deposits include irregular depressions at the head of associated sinuous rilles and/or along irregular fractures in the floors of ancient craters.⁴ Here, we provide a brief synopsis of the nature of the dark mantling deposits and briefly discuss several newly identified deposits on the western limb.

Lunar Dark Mantle Deposits

Based on recently acquired geologic and remote sensing data two genetically distinct types of pyroclastic deposits are known: regional and localized. Both the regional dark mantling deposits (RDMD) and localized dark mantling deposits (LDMD) are widely distributed across the lunar nearside (Figs. 1 and 2). The larger RDMD are typically located in lunar highland areas adjacent to many of the major lunar maria, while the smaller LDMD are often found on the floors of pre-Imbrian and Imbrian craters.

While all of the RDMD are basaltic in nature, returned sample and telescopic remote sensing data indicate that several of the RDMD contain a significant amount of Fe²⁺-bearing glass. Volcanic green, orange and black glass spherules returned by the Apollo 15 and 17 missions are believed to be relatively unfractionated samples of the deep lunar interior. These glasses are thought to have originated from a depth of approximately 300 km or greater.¹ Volatile-rich coatings on the surfaces of these spherules strongly suggest the existence of a gaseous phase in their eruptive history. It has been suggested that the RDMD eruptions are analogous to terrestrial strombolian-type eruption activity and, as such, are likely to disperse and sort the pyroclasts over thousands of 1000's km²⁽⁵⁾. In these deposits the coarser material is concentrated in a zone peripheral to the vent while the finer debris is scattered over much greater distances.

Localized dark mantling deposits (LDMD) are generally associated with small (<3 km) endogenic dark halo craters. The endogenic source craters for the LDMD may be distinguished from the other exogenic or impact craters in that they lack obvious crater rays and are generally non-circular in shape.⁵ An eruption mechanism similar to terrestrial vulcanian eruptions is suggested to be the origin for these deposits.⁵ For these types of eruptions on the Moon, the maximum dispersion range of pyroclasts larger than 1 cm is about 4 km, while the smaller clasts may be ejected up to tens of kms. Magma source depths for these deposits are thought to be relatively deep also although material from different levels along the conduit walls is often entrained in the body of magma erupted.

Recent analyses of near-infrared and infrared reflectance data^{6,7} of various LDMD has shown that although they may be genetically and morphologically similar, they are spectrally, and thus compositionally, distinct. Three types or classes of LDMD have been identified thus far based on the depth, center and overall shape of the ~1 μm band. Group 1 contains highland-type material with minor amounts of olivine and/or volcanic glass. Group 2 spectra resemble mature mare basalts and Group 3 have olivine and pyroxene as the dominant mafic constituents.

Analyses of western limb photographs and newly collected telescopic spectral reflectance data indicate that many of the pyroclastic deposits on the western limb fall into the LDMD categories. Twenty-three pyroclastic mantling deposits have been studied thus far (Fig. 3), some of which are newly identified. These include: Aestatis (68.4W, 15.0S, 320 km²), Autumni (82.2W, 9.5S, 330 km²), Cavalerius 66.9W, 5.1N, 880km²), 4 at Crüger (66.7W, 16.7S, 50-760 km²), a probable coalesced deposit at Grimaldi (68.3W, 5.2S, 1200 km²), Grimaldi F

**Lunar and Hawaiian Lava Tubes:
Analogues and Uses Based on Terrestrial Field Data**

Cassandra R. Coombs, SN15, NASA Johnson Space Center, Houston, TX 77058. *B.Ray Hawke*, Planetary Geosciences Division, School of Ocean and Earth Science and Technology, University of Hawaii, Honolulu, HI 96822.

Introduction

Lava tubes and sinuous channels are prevalent in many volcanic settings on Earth and have also been identified on the Moon. Thermal erosion may have played an important role in the final formation of some of these features. Downcutting due to thermal erosion is fairly common on Earth and has been documented during the formation of some active flows on the island of Hawaii and modelled for several sinuous rilles/lava tubes on the Moon. Previously, Coombs *et al.* (1987, 1990)^{1,2} discussed the nature and origin of several sinuous rilles and possible lava tubes in the north-central region of the Moon and compared them to similar features in Hawaii. Hörz (1985)³ and Coombs and Hawke (1988)⁴ have suggested that intact lava tubes would be useful in establishing a future lunar base. While most workers agree that these features hold promise for future lunar base expansion, there is sufficient uncertainty surrounding them to warrant further study before committing them to use at the first lunar base site. Thus, in order to understand better the processes that formed these features and their overall character, data was recently collected from more than 400 lava tubes from many different lava flows on three islands in Hawaii. The lava tubes studied were of varying ages from minutes to hundreds of years old and are at various stages of degradation. This paper presents the analysis of the data collected for a large number of Hawaiian lava tubes on the islands of Oahu, Molokai, and Hawaii and extrapolates the results to lunar conditions.

About Lava Tubes

A lava tube may form when the uppermost portion of an active stream of basaltic lava forms a continuous crust. More specifically, depending on the rheology of the lava and the rate of flow, a lava tube may form by one of several methods: (1) An open channel may form a crust that extends from the sides to meet in the middle and eventually thicken and form a roof. (2) Crustal slabs riding along the tops of more vigorous flows may break apart, raft down the channel, and eventually get hung up and refit themselves together to form a cohesive roof. (3) Lava sloshing, overflow and spattering may form levees which may eventually grow upward and inward to form a roof. Or, (4) Lava tubes may form as advancing pahoehoe lava toes leave voids behind (e.g., 2,4,5,6). Thermal erosion may increase the depth and sinuosity of the lava channels and tubes. Once formed, lava tubes may remain intact for years. Terrestrial field evidence as well as calculations by Oberbeck *et al.* (1969)⁷ support the theory that many of these lunar features are evacuated and have remained intact during the millions of years of meteoritic bombardment and seismic shaking to which they have been subjected since their formation.⁴ Several large prehistoric and historic lava tubes on Hawaii have maintained their structural integrity despite their great age and location in a region with a high frequency of earthquakes.

Under lunar environmental conditions (lack of atmosphere, lower gravity field), the basaltic eruptions that formed the lunar lava tubes would have been somewhat different than on Earth and would have produced features an order of magnitude greater. Pyroclastic deposits associated with some lunar basaltic eruptions extend as far as several hundred kilometers away from the source vent. Likewise, lunar lava tubes, where present, reach sizes of 100's of meters to kilometers wide by 100's of meters deep and 10's of kilometers long.^{1,2,4} Because of these large dimensions and the likelihood that they may be open, the lunar lava tubes should be considered when planning future lunar settlements.

Field Data

In an effort to characterize these features, more than 400 lava tubes were studied in the field. Over 200 were studied in the vicinity of Kilauea in the Volcanoes National Park, 100 within a military bombing range along the north flank of Mauna Loa, and 100 from several localities on the islands of Hawaii, Oahu, and Molokai. Measurements were taken of

their horizontal width (H), vertical height (V), depth from surface, roof thickness, floor thickness and, where determineable, the length, sinuosity, and number of flows making up the tube. Figure 1 shows the variation in measurements among all the tubes analyzed. A simple regression was performed on the data to illustrate the non-uniform relationship between the vertical and horizontal components measured for each tube. This correlates with what was seen in the field; that is, no lava tubes were perfectly spherical in cross-section. Rather, the majority of the lava tubes were wider than they were tall, thus the less than one to one relationship.

Also, where possible, a measure of the degree of thermal erosion was estimated. Three lava tubes were identified that exhibited definite evidence for thermal erosion. These were located on Oahu, Molokai, and Hawaii. The prime example of thermal erosion is Whittington lava tube on the south shore of Hawaii. This lava tube formed in successive stages and cut its way down through preexisting lava layers that contain tree molds.

A comparison of these measured terrestrial lava tubes with their lunar counterparts suggests that they are very similar, despite the order of magnitude size difference. Earlier modelling of a lunar lava conduit systems^(c.g., 1,2) suggests that thermal erosion may have played a role in their formation. Extrapolating the recently collected field data to lunar conditions suggests that we should find a similar trend in the lava tubes found on the Moon. That is, they will vary in vertical and horizontal dimension, with the horizontal being the larger of the two. Also, roof thickness, floor thickness and number of flows making up the tube will also be highly variable as reflected in the data collected for the Hawaiian lava tubes.

Conclusion

Lava tubes did form on the Earth and Moon, many of which are still intact. These features are relatively stable over time, as illustrated by the rigidity of the Hawaiian prehistoric lava tubes as well as the historic tubes located in the bombing range near Mauna Loa. These natural structures should be considered for use in planning for the expansion and advanced stages of the future manned lunar base.

References (1) Coombs, C.R., B.R. Hawke, L. Wilson, (1987) *PLPSC 18th*, 339-353. (2) Coombs, C.R., B.R. Hawke, L. Wilson (1990) *PLPSC 20th*, 195-206. (3) Hörz F. (1985) *Lunar Bases and Space Activities of the 21st Century*, W.W. Mendell, ed., 405-412. (4) Coombs, C.R. and B.R. Hawke (1988) Submitted to *Lunar Bases II*, 26pp. (5) Cruikshank D.P. and C.A. Wood (1972) *The Moon*, 3, 412-447. (6) Wentworth C.K. and G.A. MacDonald (1953) *Geol. Surv. Bull.* 994, 98 pp. (7) Oberbeck, V.R., W.L. Quaide, and R. Greeley (1969) *Modern Geology*, 1, 75-80.

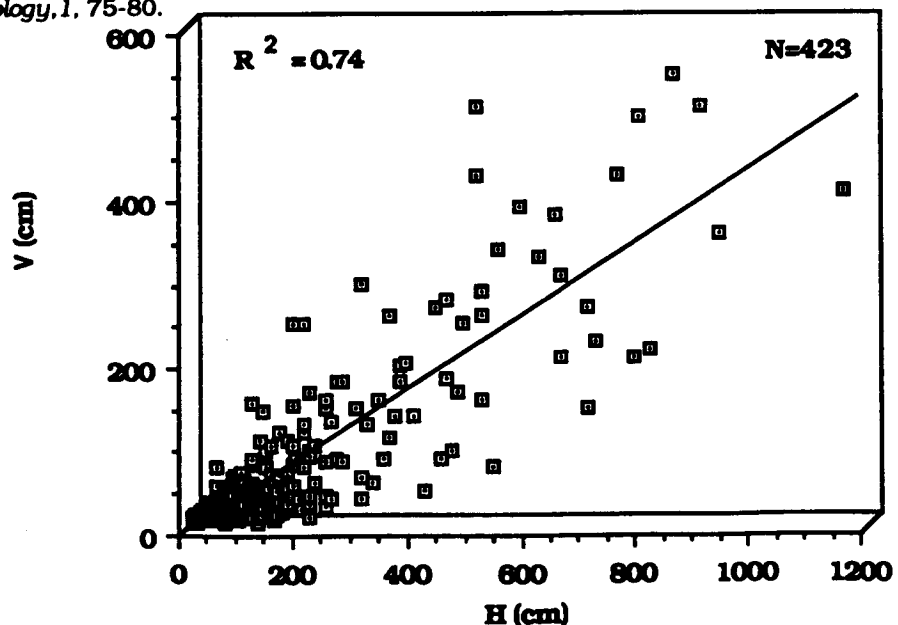


Figure 1: Vertical height (V) vs horizontal width(H) lava tube data from Oahu, Molokai, and Hawaii.

On Using a Pyroclastic Deposit as A Manned Lunar Base Site

Cassandra R. Coombs¹, David S. McKay¹, B. Ray Hawke², and Grant Heiken³

¹Code SN, NASA Johnson Space Center, Houston, TX 77058, ²School of Ocean and Earth Science and Technology, Univ. of Hawaii, Honolulu, HI 96822, ³MS D462, Los Alamos National Laboratory, Los Alamos, NM 87545

The potential of lunar regions mantled by pyroclastic deposits for resource utilization has recently been summarized by Hawke et al. (1990). We agree that such areas have high resource potential and suggest that they have high scientific potential as well. On the Apollo 17 mission, orange glass beads and their crystallized black equivalents were found in high concentration at Shorty Crater. These beads were interpreted by various authors as impact melt ejecta from large impacts which had penetrated to more mafic material at depth, vapor condensates, splash droplets from impacts into lava lakes, or pyroclastic rocks. A pyroclastic origin is now commonly accepted. It is also commonly accepted that the dark mantle geologic units are made from similar pyroclastic materials.

The explosive eruptions that formed the lunar dark mantling deposits have been likened to some types of terrestrial volcanic activity. The largest, or regional, lunar pyroclastic deposits most likely formed in a manner similar to terrestrial strombolian fire-fountaining, while the smaller, localized, deposits most likely formed by vulcanian-type explosions. The strombolian eruptions consist of a series of discrete time transient explosions separated by periods of less than 0.1s to hours. The fire-fountains form when jets of disrupting magma are released. The jets are driven by excessive volatile gas pressure escaping from the rising and expanding bubbles within the magma. The vulcanian-type eruptions, on the other hand, occur when gas and pressure build up beneath a cap rock in the magma conduit. Explosive decompression occurs as the cap rock is broken away and the magma and gas expand upward and outward. Material from these eruptions is deposited 100's - 1000's km away from the source with the coarser fragments falling closer to the vent and the finer particles at the fringes. A detailed study of the deposits of such eruptions at or near a base would reveal much about the early volcanic history of the moon and the volatile component of lunar magmas.

Hawke et al. (1990) suggest that ilmenite found in Apollo 17 -type pyroclastic glass may provide feedstock for the hydrogen-reduction-of-ilmenite process for producing lunar oxygen. They also suggest that the ilmenite may help retain solar wind hydrogen and helium which can be extracted for use at a lunar outpost or even transported back to earth for fusion fuel in the case of helium-3. Therefore, they suggest that ilmenite-rich material may be the best candidate. Here we propose a somewhat different approach. We propose that the pyroclastic glass can be reduced directly to produce oxygen and one or more metals. Sulfur would be another important byproduct of this processing. This process would eliminate the need for having specific minerals such as ilmenite or for doing any mineral concentration. The bulk pyroclastic would provide the feedstock. Some recent experiments performed at Johnson Space Center suggest that an iron-rich composition would be the most suitable for this direct feedstock reduction and that the titanium content may not be important.

In addition to providing feedstock for oxygen extraction, the lunar pyroclastic deposits would be extremely useful in constructing and supporting the lunar base. Unlike typical maria and highland areas, the unconsolidated nature, chemical makeup and block-free surfaces of the pyroclastic deposits would provide a source of uniform, relatively unconsolidated, block-free material which could be easily mined and used for a variety of lunar base needs including radiation protection, construction material, and feedstock for various extraction and processing operations as suggested by Hawke et al. (1990).

Hawke, B.R., C.R. Coombs, B. Clark (1990) Ilmenite-rich pyroclastic deposits: An ideal lunar resource. Proc. 20th Lunar and Planet. Sci. Conf., 249-258.

CHAPTER 4

LITHOSPHERE/ATMOSPHERE RELATIONS

Water on Mars: clue to accretional history. Carr, M. H., U. S. Geological Survey, Menlo Park, CA

Geological evidence for large amounts of water at the martian surface appears to be in conflict with geochemical evidence from SNC meteorites that suggests that Mars the Mars mantle is dry and should have lost almost all of its initially large inventory of water during accretion. Several possibilities are suggested here as to how the apparently conflicting data from two sources may be reconciled.

The effects of water and ice on the martian surface have been recognized since the early nineteen seventies¹⁻³. Features ascribed to the action of water and ice include valley networks, large floods, debris flows, softened terrain at high latitudes, various types of patterned ground, and several characteristics of impact craters. While the evidence for water and ice action is clear, quantifying the amount of water from the geologic evidence has proven more difficult. The polar layered terrain, ice caps, and weathered debris could contain as much as 20 m averaged over the whole planet, but most of the outgassed water is probably hidden from view as ground-ice or groundwater. Carr⁴ attempted to estimate the amount of water outgassed from the amount of erosion performed by large floods. He estimated that at least the equivalent of 45 m planet-wide of water had flowed down the large flood channels around the Chryse basin. Most of this water may still remain as ice deposits at the ends of these channels. The presence of flood channels elsewhere, and the almost ubiquitous presence of valley networks in the old cratered terrain suggests that groundwater was not restricted to the Chryse region. More probably, floods were more common in Chryse because the conditions required for massive release of water were more commonly met there. Extrapolating from Chryse to the entire planet, Carr suggested that at least 500 m of water had outgassed. This may be a conservative estimate, since all the groundwater in the Chryse region is unlikely to have been brought to the surface. However, the estimate could be in error if the water that participated in the floods was recycled.

In contrast, the geochemical evidence suggests that Mars is very dry. Estimates of the outgassed water inventory from ¹⁵N, ³⁶Ar and D/H in the atmosphere range from 3-130 m, with the lower values being preferred. These estimates have been critically reviewed elsewhere⁶, and are suspect because of the possible loss of atmospheric gases through hydrodynamic escape and impact erosion, and because of the rapid evolution of D/H in the atmosphere, as a result of limited exchange of water with the surface. The SNC meteorites, which are widely assumed to represent martian rock ejected into free space by impact of large bodies are extremely dry. Shergotty, for example contains only 180 ppm H₂O⁷ as compared with an average of 2100 ppm in terrestrial ocean ridge basalts. From this value Dreibus and Wanke⁸ estimated that the mantle contained 36 ppm water. They also estimated water in the martian mantle from Cl in SNC meteorites. By comparing the relative solubilities of Cl and H₂O in silicate melts, and assuming that no water was left on the martian

surface at the end of accretion, they estimated that the Mars mantle contained 36 ppm H₂O, fortuitously the same value they had derived from direct measurements of water in the meteorites. Thus the geochemical evidence suggests that the Mars mantle is dry relative to the Earth's.

A dry martian mantle is consistent with other geochemical reasoning. The Earth and Mars are both thought to have accreted from two different components: component A, a highly reduced, volatile poor, metal-bearing component, similar in composition to enstatite chondrites, and component B an oxidized, volatile rich component similar to carbonaceous chondrites⁹. During accretion, most of the water in the volatile rich component would have reacted with metallic iron in the volatile poor component to form FeO and H₂ which would have escaped. On Earth, chemical disequilibrium between the upper mantle and core suggests that part of the volatile rich component was added late, after the core formed. The SNC meteorites suggest that Mars had a higher proportion of the volatile rich component, but the Mars mantle, in contrast to the Earth's, is in equilibrium with the core. There is no evidence of the volatile rich veneer. Most of its water should, therefore, have been lost by reaction with metallic iron. Thus the low estimates of water in the Mars mantle are consistent with geochemical models for how the planet accreted.

The apparently conflicting evidence of a wet surface with a dry mantle may be reconciled in various ways. The Mars mantle may be dry, in part, because of the lack of plate tectonics. It is not known to what extent the water in the Earth's mantle has been derived from the surface. Jambon and Zimmerman¹⁰, suggest that there are two sources of mantle water, subducted crust, and juvenile mantle sources, which they estimate contain 200-300 ppm. Thus, although their estimates of the water content of juvenile mantle sources is still higher than the estimates for the martian mantle, part of the contrast between the mantles of Earth and Mars is probably due to plate tectonics.

Mars, like the Earth, may have acquired a late volatile rich veneer, but the mantle contains no evidence of this veneer because the volatile-rich near-surface materials have not been folded into the mantle by plate subduction. If one percent of Mars accumulated late, after core formation, then the equivalent of 2.7 km of water would have been added. Because of the lack of plate tectonics, this could still remain close to the surface and not have affected the chemistry of SNC meteorites, with magma sources deep within the planet. Thus Mars would have been left with a volatile rich crust and a dry mantle, in chemical equilibrium with the core.

The accretional history of the two planets may have contributed to their contrasting water distributions. Modelling of accretion by Matsui and Abe¹¹ suggest that as the Earth accreted water started to accumulate at the surface by impact degassing by the time the planet had reached about one fifth of its present radius. Ultimately, a steam atmosphere

formed, thereby insulating the surface. Surface temperatures rose, the surface melted, and water in the atmosphere was able to dissolve in the surface melts and become distributed through the mantle. As the accretion rate tapered off, the surface cooled and the water condensed to form the oceans. However, much of the water in the steam atmosphere was lost by hydrodynamic escape and by impact erosion of the atmosphere. For Mars, the models give very different results. Impact degassing begins at roughly two fifths the present radius, but for plausible accretion rates, a steam atmosphere never develops. The degassed water remains condensed on the surface, and the surface never melts, so water does not dissolve into surface melts and become distributed through the mantle. On Mars, because a steam atmosphere never develops, loss of water by hydrodynamic escape and impact erosion of the atmosphere should have been suppressed. At the end of accretion Mars could have had a dry mantle but a water-rich surface.

These considerations indicate that there are several plausible explanations for the apparent conflict between the geochemical evidence of little water on Mars and geologic evidence of abundant water. The contrast is a reflection of the contrasting accretional histories of the two planets and their contrasting tectonics. One possible conclusion is that Mars has a primitive volatile-rich crust that has been partly overplated with young, dry, mantle-derived volcanics of which we have samples in the SNC meteorites.

REFERENCES: 1. Sharp (1973). *J. Geophys. Res.*, 78, 4222-4230. 2. Baker and Milton (1974). *Icarus*, 23, 27-41. 3. Masursky (1973). *J. Geophys. Res.*, 78, 4037-4047. 4. Carr (1986). *Icarus*, 68, 187-216. 5. Carr (1987). *Nature*, 326, 30-35. 6. Carr (1990). *Icarus*, 87, 210-227. 7. Fallick et al (1983). *LPSC XIV* 183-184. 8. Dreibus and Wanke (1987). *Icarus*, 71, 225-240. 9. Ringwood (1979). *Origin of the Earth and Moon*. 10. Jambon and Zimmerman (1990). *Earth and Planet. Sci. Lett.*, 28, 323-331. 11. Matsui and Abe (1987). *Earth, Moon and Planets*, 39, 207-214.

Carr, M. H. (1990) The effects of floods, volcanism and polar processes on D/H in the martian atmosphere. LPSC XXI, 168-169.

Carr, M. H. (1990) D/H on Mars; The effects of floods, volcanism, impacts, and polar processes. Icarus, 87:210-227

Carr, M. H., (1990) Mars: in The New Solar System (J.K. Beatty, B O'Leary and A. Chakin, eds). Sky Publishing Corp., Cambridge

Variable Features in the Valles Marineris Region of Mars

Paul E. Geissler and Robert B. Singer, Planetary Image Research Laboratory,
Department of Planetary Sciences, University of Arizona, Tucson 85721.

Transient phenomena on Mars have long been recognized in Mariner [1-5] and Viking [6,7] images as well as in decades of Earth-based telescopic observations [e.g., 8]. These events are of interest because of the information they present on currently active meteorological and geological processes. Changes in surface albedo patterns and atmospheric conditions can also affect the analysis and interpretation of image data based on spectral or morphological properties of geologic units on the surface.

Sources of secular variability include the occurrence of condensate clouds, fog, frost and haze, and the deposition or erosion of surficial materials by eolian processes. Albedo pattern changes caused by the transportation of dust and sand raise a number of important geological issues. First, are the albedo variations caused by deposition or by erosion? The darkening of a specific region might be caused by either deposition of dark sands or by the removal of a previously deposited bright dust layer, for example. Second, are the processes driving these changes cyclic or episodic in nature? This is particularly relevant since a cyclic deposition mechanism is believed to be responsible for the formation of layered sedimentary deposits found in the equatorial canyons and at the poles of Mars. Finally, where are the sources and sinks of the materials being transported?

In the course of examining low resolution apoapsis images as part of a program of spectrophotometric mapping of the Valles Marineris and environs, we have noticed a number of transient phenomena which occurred during the Viking mission. Early morning images often show the canyons filled with fog which partially or completely obscures the underlying topography (e.g., VO image 620A63). Surface frost deposits in the region have been interpreted by Neukum [9], but reliable criteria for their identification in spacecraft images have yet to be established. Condensate clouds are best recognized from their appearance in multispectral composites (e.g. images 583A34, 38, and 40) or their often distinctive wave morphology in monochrome images (as in 762A88).

Localized dust cloud activity in the region to the west and south of Echus Chasma was described by Martin and James [10]. Marked changes in surface albedo have also been noted in this area; transient bright streaks, perhaps genetically related to the dust clouds [10], were interpreted as depositional in origin [11]. Figure 1 shows the Echus Chasma region at 4 different times during the Viking mission from 1976 to 1980, each acquired while Mars was near aphelion ($L_S = 36^\circ$ to 102°). These images show the evolution of a distinctly linear bright streak to the southwest of Echus, and are consistent with the interpretation [10] of eolian deflation of a bright dust deposit.

A much larger scale albedo change occurred on the plains to the south of Eos Chasma. Figure 2 compares two image mosaics constructed from data obtained by Viking Orbiter 1 during orbits 544 (top, December 1977) and 1334 (bottom, February 1980). Each mosaic covers an area of about 1500 km by 700 km. An area of some 300000 km² was affected by the change, most of which occurred between January and April 1978 ($L_S = 40^\circ - 70^\circ$, just before aphelion). On the basis of the limited Mariner 9 and Viking data available, the change is believed to be episodic in nature. Mariner 9 A-camera images (e.g. 05596748) show the region to appear in 1972 much as it did in 1977, prior to the change. Viking continued to observe the area for another full Martian year after the event, but the plains south of Eos remained dark.

The mechanism responsible for this albedo pattern change is currently under investigation. Generation and subsequent transportation and deposition of dark sands has been interpreted in the Valles [12], however the removal of a bright dust layer is more consistent with the rapid time period of the change (about 2 months) and with preliminary multispectral mapping results which suggest that the dark streak south of Eos and Coprates Chasmata is spectrally distinguishable from the dark saltating materials found elsewhere in the canyon system. If a layer of bright dust was removed to affect the albedo change,

questions concerning how such micron-sized particles are mobilized by winds during a normally quiescent season (southern hemisphere Autumn) should be addressed.

This research is supported under NASA Planetary Geology grant NAGW 1059.



Figure 1: Variable features near Echus Chasma. Changes in albedo patterns (arrows) and dust/condensate cloud activity (C) discussed by Martin and James [10]. Images acquired by Viking Orbiter 1 during revolutions (1) 40, July 1976; (2) 583, January 1978; (3) 701, May 1978; (4) 1334, February 1980.

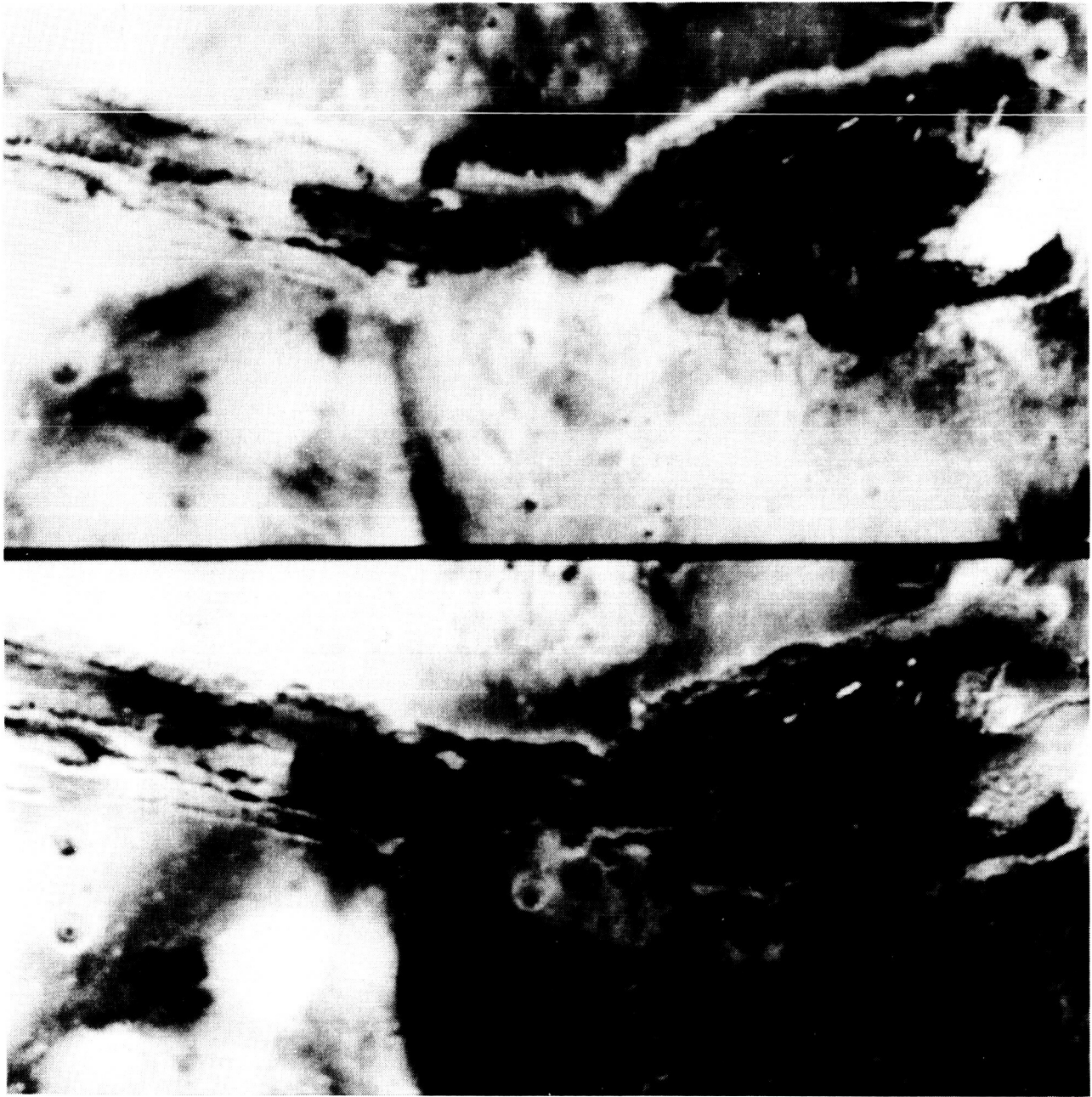


Figure 2: A large scale albedo change on the plains south of Eos Chasma. Each image mosaic covers approximately 1500 km by 700 km. Top: VO 1 orbit 544, December 1977. The dark spot near the north rim of Coprates Chasma is the shadow of Phobos. Bottom: VO 1 orbit 1334, February 1980. The area affected by the change is close to 300,000 km².

References: [1] Sagan, C., J. Veverka, P. Fox, R. Dubisch, J. Lederberg, E. Levinthal, L. Quam, R. Tucker, J. Pollack, B. Smith, *Icarus* 17, 346-372, 1972. [2] Sagan, C., J. Veverka, P. Fox, R. Dubisch, R. French, P. Gierasch, L. Quam, J. Lederberg, E. Levinthal, R. Tucker, R. Eross, J. Pollack, *J.G.R.* 78, 4163-4196, 1973. [3] Veverka, J., C. Sagan, L. Quam, R. Tucker, R. Eross, *Icarus* 21, 317-368, 1974. [4] Sagan, C., J. Veverka, R. Steinbacher, L. Quam, R. Tucker, R. Eross, *Icarus* 22, 24-47, 1974. [5] Veverka, J. *Icarus* 25, 595-601, 1975. [6] Veverka, J., P. Thomas, R. Greeley, *J.G.R.* 82, 4167-4187, 1977. [7] Thomas, P. and J. Veverka, *J.G.R.* 84, 8131-8146, 1979. [8] de Mottoni y Palacios, G., *Icarus* 25, 296-332, 1975. [9] Neukum, G., ESA SP-185, 117-120, 1982. [10] Martin, L. and P. James, *Icarus* 77, 35-58, 1989. [11] Thomas, P., J. Veverka, S. Lee, A. Bloom, *Icarus* 45, 124-153, 1981. [12] Geissler, P., R. Singer and B. Lucchitta, *J.G.R.* 95, 14399-14414, 1990.

The Potential Scale of Aeolian Structures on Venus

J.R. Marshall and R. Greeley (Department of Geology, Arizona State University, Tempe, AZ 85287-1404)

Simulations of the Venusian aeolian environment with the Venus Wind Tunnel have shown that microdunes are formed during the entrainment of sand-size material. These structures are several tens of centimeters long (2-3 cm high) and combine the morphological and behavioral characteristics of both full-scale terrestrial dunes and current ripples formed in subaqueous environments. Their similarity to both reflects the fact that the Venusian atmosphere has a density intermediate between air and water. Although the development of microdunes in the wind tunnel experiments was limited by tunnel dimensions, it is possible to make some predictions about their potential size on Venus, and the potential size of related aeolian structures.

Microdunes are fluid-formed structures (as are dunes and current ripples) and as such have no theoretical upper limit to their size from a fluid-dynamics standpoint. Limitations to size observed in subaqueous structures are set by, for example, water depth; limitations to the size of dunes is set by, for example, sand supply. It is therefore reasonable to suppose that microdunes on Venus could evolve into much larger features than those observed in experiments. In addition, we note that current ripples (which are closely related to microdunes) are often found in association with giant ripples that have dimensions similar to aeolian dunes. Thus, it may also be reasonable to assume that analogous large-scale structures occur on Venus. Both (terrestrial) aeolian and subaqueous environments generate structures in excess of one hundred meters in wavelength. Such dimensions may therefore be applicable to Venusian bedforms. Analysis of Magellan data may resolve this issue.

RELATIONSHIPS BETWEEN TOPOGRAPHIC ROUGHNESS AND AEOLIAN PROCESSES

R. Greeley, N. Lancaster, L. Gaddis (Department of Geology, Arizona State University), K.R. Rasmussen (Institute of Geology, Aarhus University), B.R. White (Department of Mechanical Engineering, University of California at Davis), R.S. Saunders, S. Wall (Jet Propulsion Laboratory), A. Dobrovolskis (NASA-Ames Research Center), and J.D. Iversen (Department of Aerospace Engineering, Iowa State University).

The interaction between winds and desert surfaces has important implications for sediment transport on Earth, Mars and Venus, and for understanding the relationships between radar backscatter and aerodynamic roughness as part of the NASA Shuttle Imaging Radar (SIR-C) Mission [1,2]. We report here results from measurements of boundary layer wind profiles and surface roughness at sites in Death Valley and discuss their implications. The sites included a flat to undulating gravel and sand reg, alluvial fans, and a playa.

Table 1. Estimates of average particle size composition of Death Valley Sites.

Site	Mean Particle Size Composition (% of surface covered)				
	Clay/silt	Sand	Gravel	Cobbles	Boulders
Stovepipe Wells Flats	1.3	42.5	45.0	11.5	
Kit Fox Fan		63.0	20.0	11.0	6.0
Golden Canyon Fan	25.0	23.0	28.3	17.0	6.7
Trail Canyon Fan			65.0	20.0	15.0
Confidence Mill Playa	100.0				

Boundary layer wind profiles were measured using cup anemometers at heights of 0.75, 1.25, 2.07, 3.44, 5.72, and 9.5 m, temperature sensors at 1.3 and 9.6 m, and wind vanes at 9.7 m and 1.5 m. More than 200 wind profiles were measured at each site. Data were sorted by direction and stability characteristics after calculation of the bulk Richardson number (Ri). Following corrections for atmospheric stability, z_0 and u^* were estimated using least-squares methods. Aerodynamic roughness (Table 2) increases from the smoothest Confidence Mill Playa, to the roughest site, Golden Canyon Fan. Differences in z_0 for different wind directions suggest that local conditions may affect aerodynamic roughness.

Table 2: Arithmetic mean values of aerodynamic roughness (z_0)

Site	Wind Direction	N-NE	SE-S	W-NW	NW-NNW
Stovepipe Wells			0.00026		0.00055
Kit Fox					
	Mast 1	0.00107	0.00237		
	Mast 2	0.00085	0.00078		
Golden Canyon					
	Mast 1	0.00356	0.00360		0.00537
	Mast 2	0.00110	0.00245		0.00113
Trail Canyon		0.00190	0.00182	0.00012	
Confidence Mill		0.00063	0.00018		

Micro-topographic measurements were made using a template and a laser-photo device. After the linear trend in the data due to overall surface slope was removed, the RMS height and correlation length were calculated from the unfiltered data (Table 3). Comparisons show that the RMS height derived from the

laser data is ~ an order of magnitude less than that of the template data, suggesting that it is measuring particle roughness. Roughness (RMS height) increases in the same sense as that suggested by visual inspection of the surface. Both the template and site characterization data suggest that Golden Canyon Fan was the roughest site studied. Kit Fox Fan and Trail Canyon Fan differ only slightly from each other. The E-W roughness is less in all cases than the N-S values, probably as a result of the E-W orientation of the bar and swale topography at an oblique angle, a further index of the surface roughness is the geometric mean of the N-S and E-W RMS heights.

Table 3: RMS height (m) derived from template and laser profiles

	N-S	E-W	Mean
Stovepipe Wells			
Laser			0.0056
Kit Fox Fan			
Template	0.0615	0.0328	0.0420
Laser			0.0097
Golden Canyon Fan			
Template	0.0772	0.0394	0.0571
Laser			0.0150
Trail Canyon Fan			
Template	0.0660	0.0256	0.0364
Laser			0.0076
Confidence Mill			
Laser			0.0066

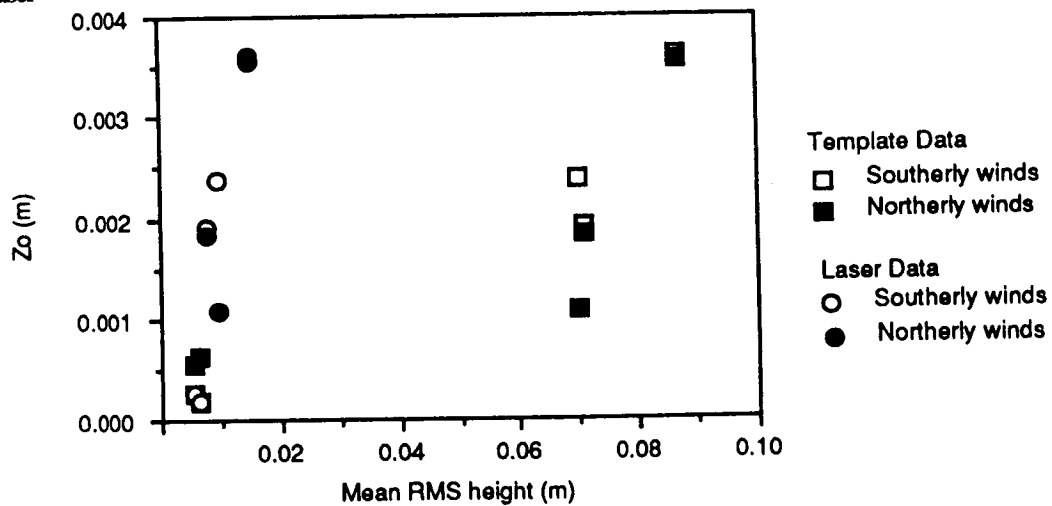


Figure 1: Relationships between geometric mean of RMS height for template transects and laser profiles and aerodynamic roughness estimates.

The aerodynamic roughness of a surface is a function of its microtopographic and particle roughness characteristics. At the alluvial fan sites studied, particle roughness is superimposed on the microtopography of the bars and swales developed on the fan surface. There is a good relationship between unfiltered RMS height and aerodynamic roughness, suggesting that the RMS height of the surface is a good index of its overall roughness. However, as the wind crosses the surface at an oblique angle to the terrain profiles, the geometric mean of the RMS height for both laser profiles gives better "3-D" characterization of the surface, which correlates well with aerodynamic roughness estimates (Fig.1). Data for the laser profiles

**RELATIONSHIPS BETWEEN TOPOGRAPHIC ROUGHNESS AND AEOLIAN PROCESSES,
R. Greeley, et al.**

at each site provide a measure of particle roughness. There is a similarly good correlation between mean RMS height for each site and aerodynamic roughness estimates.

REFERENCES CITED

1. Greeley, R. and Iversen, J.D.: Measurements of wind friction speeds over lava surfaces and assessment of sediment transport. *Geophys. Res. Letters* 14, 925-928 (1987).
2. Greeley, R., Lancaster, N., Sullivan, R.J., Saunders, R.S., Theilig, E., Wall, S., Dobrovolskis, A., White, B.R., and Iversen, J.D.: A relationship between radar backscatter and aerodynamic roughness: preliminary results. *Geophys. Res. Letters* 15, 565-568 (1988).

N92-10802

Use of Radar to Assess Aeolian Processes

R Greeley, N Lancaster, L Gaddis, D Blumberg and A Dobrovolskis
(Department of Geology, Arizona State University, Tempe, Arizona
85287-1404; 602-965-7045)

R S Saunders and S Wall (Jet Propulsion Laboratory, Pasadena,
California 91109; 818-393-0877)

J Iversen (Iowa State University, Ames, IO 50010)

B White (University of California Davis, Davis, California 55419)

K Rasmussen (Aarhus University, Aarhus, Denmark)

The interaction between wind and desert surfaces has important implications for sediment transport on Earth, Mars and Venus, and for understanding the relationship between radar backscatter and aerodynamic roughness. We report here results from measurements of atmospheric boundary-layer profiles, assessment of radar backscatter at P, L, and C wavelengths, and surface roughness in Death Valley, the Mojave Desert, and Lunar Lake, NV, and discuss the implications for aeolian process. The sites include playas, gravel and sand regs, alluvial fans, and lava flows. Boundary-layer wind profiles were measured using anemometers at heights of 0.75, 1.25, 2.07, 3.44, 5.72, and 9.5 m; temperature sensors at heights of 1.3 and 9.6 m; and wind vanes at 9.7 m and 1.5 m. Microtopographic measurements were made using a "template" and a laser-photo device to obtain the RMS height. RMS height derived from laser data is ~10 times less than that of template data, suggesting that it is measuring particle roughness. Results show that L-band radar ($\lambda \approx 24$ cm) correlates best with aerodynamic roughness in comparison to C-band ($\lambda \approx 5.6$ cm) and P-band ($\lambda \approx 68$ cm). Because L- and P-bands are most sensitive to topographic roughness of ~24 to 70 cm, this suggests that this is the scale of topographic roughness governing or strongly influencing aerodynamic roughness of the sites analyzed.

This study demonstrates that radar backscatter coefficients obtained from airborne and perhaps orbiting instruments could permit the derivation of aerodynamic roughness values for large areas. Such values, when combined with wind frequency data, could enable assessment of aeolian processes on a regional scale. Future work will include additional field studies and development of models to explain the correlations among aerodynamic roughness, radar backscatter, and surface topography.

Free Convection in the Martian Atmosphere

G.D. Clow (U.S. Geological Survey, MS 946, Menlo Park, CA 94025) and R.M. Haberle (NASA/ Ames Research Center, Moffett Field, CA 94035)

We investigate the "free convective" regime for the martian atmospheric boundary layer (ABL). This state occurs when the mean windspeed at the top of the ABL drops below some critical value U_c and positive buoyant forces are present. Such forces can arise either from vertical temperature or water vapor gradients across the atmospheric surface layer. During free convection, buoyant forces drive narrow plumes that ascend to the inversion height with a return circulation consisting of broad slower-moving downdraughts. Horizontal pressure, temperature, windspeed, and water vapor fluctuations resulting from this circulation pattern can be quite large adjacent to the ground (within the surface layer). These local turbulent fluctuations cause non-zero mean surface stresses, sensible heat fluxes, and latent heat fluxes, even when the mean regional windspeed is zero. Although motions above the surface layer are insensitive to the nature of the surface, the sensible and latent heat fluxes are primarily controlled by processes within the interfacial sublayer immediately adjacent to the ground during free convection. Thus the distinction between aerodynamically smooth and rough airflow within the interfacial sublayer is more important than for the more typical situation where the mean regional windspeed is greater than U_c . Buoyant forces associated with water vapor gradients are particularly large on Mars at low pressures ($P < 30$ mb) and high temperatures ($T > 250$ K) when the surface's relative humidity is 100%, enhancing the likelihood of free convection under these conditions. On this basis, Ingersol [1] postulated the evaporative heat losses from an icy surface on Mars at 273 K and current pressures would exceed the available net radiative flux at the surface, thus prohibiting ice from melting at low atmospheric pressures.

Recently, Schumann [2] has developed equations describing the horizontal fluctuations and mean vertical gradients occurring during free convection. However, his model is limited to the case where free convection is driven solely by thermal buoyancy and the surface is aerodynamically rough. Within these restrictions, model results compare very well with those of a detailed large-eddy simulation (LES) which in turn generally agree with available atmospheric observations [3]. Despite large horizontal wind velocities associated with the updraughts, the LES demonstrates that the time-derivatives for horizontal motion in the surface layer are small, validating the use of Monin-Obukhov theory in the model.

We have generalized Schumann's model to include convection driven by water vapor gradients and to include the effects of circulation above both aerodynamically smooth and rough surfaces. Applying the model to Mars, we find that nearly all the resistance to sensible and latent heat transfer in the ABL occurs within the thin interfacial sublayer at the surface. Free convection is found to readily occur at low pressures and high temperatures when surface ice is present. At 7 mb, the ABL should freely convect whenever the mean windspeed at the top of the surface layer drops below about 2.5 m s^{-1} and surface temperatures exceed 250 K. Mean horizontal fluctuations within the surface layer are found to be as high as 3 m s^{-1} for windspeed, 0.5 K for temperature, and $10^{-4} \text{ kg m}^{-3}$ for water vapor density. Airflow over surfaces similar to the Antarctic Polar Plateau (surface roughness length $z_0 \approx 0.03 \text{ cm}$) is found to be aerodynamically smooth on Mars during free convection for all pressures between 6 and 1000 mb while surfaces with $z_0 \approx 1 \text{ cm}$ are aerodynamically rough over this pressure range.

Free convective latent-heat fluxes are of particular interest because they establish the *minimum* evaporative heat losses that will occur for an icy surface at a given temperature. Fig.1 shows the predicted latent heat fluxes during free convection for the limiting case where the ABL is isothermal and the surface temperature is 273 K. For a surface resembling average terrestrial polar snows (curve A), our predicted fluxes are a factor of 4 smaller than those given by Eq.(1) Ingersol [1], making it proportionally easier to melt ice on Mars. Fig.2 shows the albedo required for the net radiative flux at the surface to just balance the predicted latent heat losses at 273 K at the time of maximum incoming solar radiation. The lowest albedo that can be achieved for martian ice surfaces is about 0.2 [4]. Hence, atmospheric pressures need to be at least 100 mb at the poles and about 6 mb at the equator before ice can melt under the best of conditions.

References: [1] Ingersol, A.P. (1970) *Science*, 168, 972-973; [2] Schumann, U. (1988) *Boundary-Layer Meteorol.*, 44, 311-326; [3] Schmidt, H. and U. Schumann (1989) *J.Fluid Mech.*, 200, 511-562; [4] Clow, G.D. (1987) *Icarus*, 72, 95-127.

Figure 1: Predicted minimum evaporative heat losses from an icy surface at 273° K. Two surface roughness values are considered. Shown for comparison are the free convection predictions of Ingersol [1], (dashed line).

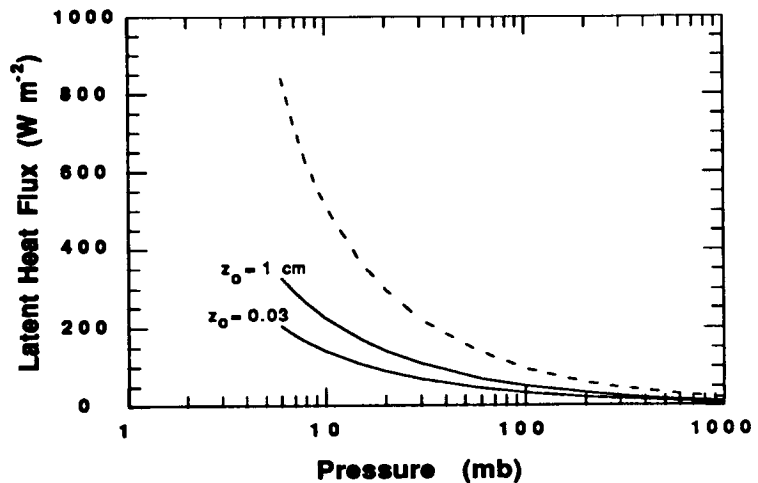
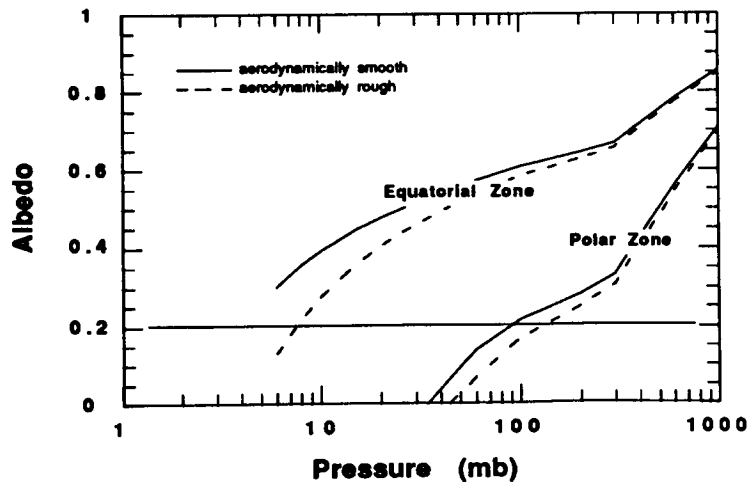


Figure 2: Highest albedos for which ice can melt under optimal conditions, assuming all the available net radiation is used to balance evaporative heat losses.



Characteristics of the Martian Atmospheric Surface Layer

G.D. Clow (U.S. Geological Survey, MS 946, Menlo Park, CA 94025) and R.M. Haberle (NASA/Ames Research Center, Moffett Field, CA 94035)

We extend elements of various terrestrial boundary layer models to Mars in order to estimate sensible heat, latent heat, and momentum fluxes within the martian atmospheric surface ("constant flux") layer. The atmospheric surface layer consists of an interfacial sublayer (#1) immediately adjacent to the ground and an overlying fully turbulent surface sublayer (#2) where wind-shear production of turbulence dominates buoyancy production. Within the interfacial sublayer, sensible and latent heat are transported by non-steady molecular diffusion into small-scale eddies which intermittently burst through this zone. Both the thickness of the interfacial sublayer and the characteristics of the turbulent eddies penetrating through it, depend on whether airflow is aerodynamically smooth or aerodynamically rough, as determined by the Roughness Reynold's number. Within the overlying surface sublayer (#2), similarity theory can be used to express the mean vertical windspeed, temperature, and water vapor profiles in terms of a single parameter, the Monin-Obukhov stability parameter.

To estimate the molecular viscosity and thermal conductivity of a $\text{CO}_2\text{-H}_2\text{O}$ gas mixture under martian conditions, parameterizations were developed using data from the TPRC Data Series [1] and the first-order Chapman-Cowling expressions; the required collision integrals were approximated using the Lenard-Jones (12,6) potential. Parameterizations for specific heat and binary diffusivity were also determined. The Prandtl and Schmidt numbers derived from these thermophysical properties are found to range 0.78 - 1.0 and 0.47 - 0.70, respectively, for Mars. Brutsaert's model for sensible and latent heat transport within the interfacial sublayer for both aerodynamically smooth and rough airflow has been experimentally tested under similar conditions [2], validating its application to martian conditions. For the surface sublayer (#2), we modify the definition of the Monin-Obukhov length to properly account for the buoyancy forces arising from water vapor gradients in the martian atmospheric boundary layer. This length scale is then utilized with similarity-theory turbulent-flux profiles with the same form as those used by Businger *et al.* [3] and others.

We find that under most martian conditions, the interfacial and surface sublayers offer roughly comparable resistance to sensible heat and water vapor transport and are thus both important in determining the associated fluxes. Airflow over surfaces similar to terrestrial polar snow (surface roughness length $z_0 \approx 0.03$ cm) is generally found to be aerodynamically smooth at low martian pressures ($P < 30$ mb) but aerodynamically rough at high pressures ($P > 300$ mb); airflow at the Viking Lander sites is aerodynamically transitional under current martian conditions. For aerodynamically smooth airflow, the thickness of the interfacial sublayer is found to be up to 100 times thicker for Mars than is typical for the Earth. At low pressures ($P < 30$ mb) and high temperatures ($T > 250$ K), buoyancy forces due to water vapor gradients can become so high on Mars that the surface sublayer (#2) essentially disappears (the Monin-Obukhov length becomes comparable to the thickness of the interfacial sublayer). At this point, the atmospheric boundary layer transitions to the "free convection" regime [4]. Free convection sensible and latent heat fluxes are smaller than those for the case when the surface sublayer (#2) is present. As expected, friction velocities u_* and the sensible and latent heat fluxes are found to be extremely sensitive to the Monin-Obukhov stability parameter for stable atmospheric conditions and mildly sensitive for unstable conditions.

The ability to predict heat losses across an interfacial boundary layer and to predict the shapes of the windspeed and temperature profiles in the atmospheric surface layer, should prove useful for estimating heat losses from engineering structures deployed on the martian surface and for improving our understanding of water vapor transfer rates from icy surfaces (such as the poles) to the atmosphere.

References: [1] Touloukian, Y.S. (1972) *Thermophysical Properties of Matter: The TPRC Data Series*, vol. 3,6,11; [2] Brutsaert, W. (1975) *Water Resour. Res.*, **11**, 543-550; [3] Businger *et al.* (1971) *J. Atmos. Sci.*, **28**, 181-189; [4] Clow, G.D. and R.M. Haberle (1990) *Lunar and Planet. Sci. XXI*, 210-211.

HEAT FLOW vs. ATMOSPHERIC GREENHOUSE on EARLY MARS

F.P. Fanale and S.E. Postawko (Planetary Geosciences Div., School of Ocean & Earth Science & Technology, Univ. of Hawaii, Honolulu, HI)

Long term climate change on Mars is suggested by an apparent difference in the erosional style exhibited by the ancient cratered terrain as opposed to terrain of later origin. In particular, the morphology and distribution of valley networks on Mars clearly indicates a difference in erosional style ~3.8 billion years ago versus mid-to-late martian history. Liquid water was certainly involved in network formation, although sapping processes rather than rainfall seem indicated. Two major factors could have contributed toward making early conditions more favorable to formation of valley networks:

First, it has been argued (1) that higher internal regolith temperatures, associated with a much higher heat flow 3.8 AE, would cause groundwater to be closer to the surface than at present. Higher heat flows are expected early in Mars' history primarily because of dissipation of the original heat of formation, although a higher rate of production of radiogenic heat is also a factor.

Second, if enough CO₂ is in the atmosphere, surface temperatures could be raised, due to an increased atmospheric greenhouse effect, to near the freezing point of water despite a weak early sun - at least at the equator and for the most favorable part of the orbital and axial cycle. Current greenhouse models indicate that CO₂ surface pressures of between about 0.75 and 5 bars are needed to raise the surface temperature on early Mars to the freezing point of water. Only slightly lower pressures characterize greenhouse warmings that are 10 to 20° K cooler.

In fact, the effectiveness of both these mechanisms is dependent on a high early heat flow: In the case of the atmospheric greenhouse, this is because the atmospheric mean residence time (M.R.T.) of CO₂ in the presence of fluvial activity is believed to be much shorter than the span of time over which network formation occurred. Thus, the atmospheric P_{CO₂} would have been dependent almost exclusively on the recycling time for regolith carbonate rather than the instantaneous supply of juvenile CO₂. Both of these parameters can be quantitatively related to the heat flow. The depth to the water table, ΔZ_{273} , also depends on internal regolith temperatures. For a given regolith conductivity, k , the temperature at any depth is determined by the heat flow, which determines the gradient, $\partial T/\partial Z$, and the surface temperature, T_s .

We have derived a quantitative relationship between the effectiveness of an atmospheric greenhouse and internal heat flow in producing the morphological differences between early and later martian terrains. Our derivation is based on relationships previously derived by other researchers (2). Thus, while the validity of our derivation is dependent on the validity of these previously derived relationships, no new assumptions or mathematical relationships are necessary - merely algebraic manipulation of relationships already in the literature.

Our reasoning may be stated as follows: The CO₂ mean residence time in the martian atmosphere, although not well known, is almost certainly much shorter than the total time span over which early climate differences are thought to have been sustained. Therefore recycling of previously degassed CO₂ quickly becomes more important than ongoing supply of juvenile CO₂. If so, then the atmospheric CO₂ pressure - and therefore the surface temperature - may be approximated mathematically as a function of the total degassed CO₂ in the atmosphere plus buried material and the ratio of the atmospheric and regolith mean residence times. The latter ratio can also be quantitatively expressed as a function of heat flow. Hence, it follows that the surface temperature may be expressed (given assumptions as to regolith conductivity) as a function of heat flow and the total amount of "available" CO₂. However, the depth to the water table - again assuming the same regolith conductivity - can simultaneously be expressed as a function of heat flow and the surface temperature (the boundary condition). Therefore, for any given values of total available CO₂ and regolith conductivity, there exist coupled independent equations which relate heat flow, surface temperature and the depth to the water table. This means that we can now derive simultaneous values of surface temperature and the depth to the water table for any value of the heat flow. We utilize the derived relationship for two purposes: 1) To evaluate the relative importance of the atmospheric greenhouse effect and the internal regolith thermal gradient in producing morphological changes for any value of the heat flow and 2) to assess the absolute importance of each for values of the heat flow which are thought to be reasonable on independent geophysical grounds.

Figure 1 illustrates that for a given amount of total available CO₂, regolith conductivity and atmospheric M.R.T., the relative roles of internal heat flow and atmospheric greenhouse are inextricably interlocked. Figs. 1a and 1b are for a case of a cool early sun, favorable orbital situation, and an equatorial site (after ref. 2). The mean residence time of atmospheric CO₂, and regolith conductivity are the same in both figures. The figures show surface temperature (T_s) as a function of depth to the water table (z). The numbers in parentheses indicate heat flow in mW m⁻².

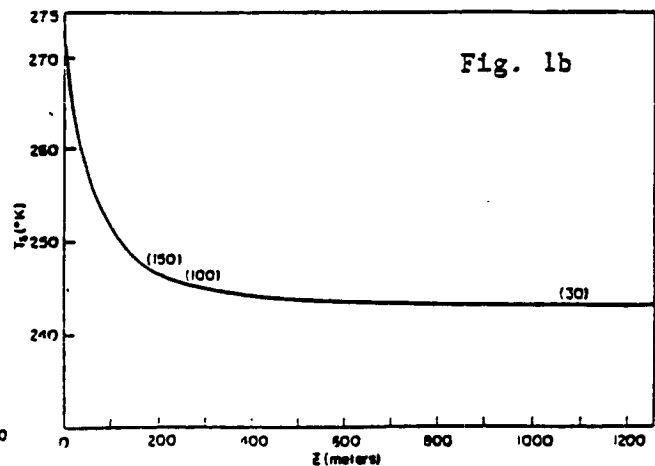
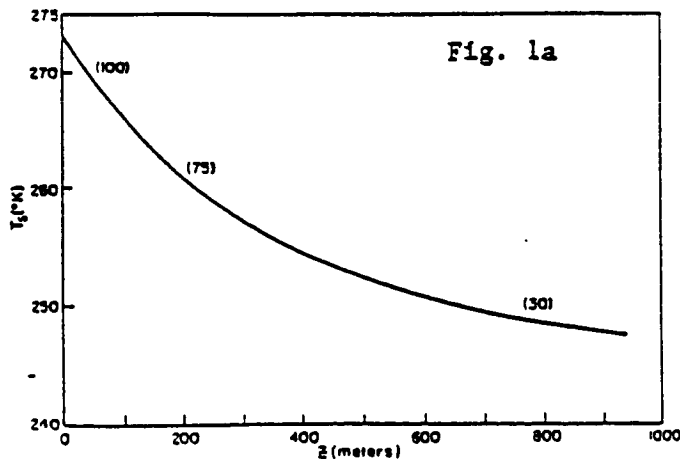
In Figure 1a, total CO₂ = 3.5 bars. Note that the internal heat flow predicted by (1) for ~3.8 AE ago, that is ~150 mW m⁻², is more than sufficient to recycle enough CO₂ to keep surface temperature at the freezing point because we have assumed so much total CO₂. In this case, the surface greenhouse effect plays a dominant role. However, if one considers that a water table depth of < 350 m is sufficient to permit widespread sapping, it is clear that the internal thermal gradient also plays a major role in widening the latitudes and time bands in which sapping would be prevalent. Thus this case is not very different either in assumptions or result from those discussed by (2).

In Figure 1b total CO₂ is only one bar. This case is important because in many plausible versions of the early Mars volatile inventory it is entirely possible that the total available CO₂ at 3.8 AE might have been only a bar, or even less. In this case we find that the atmospheric greenhouse effect plays almost no role because the low total CO₂ abundance requires incredibly fast recycling in order to keep any significant abundance in the atmosphere. Thus for plausible values of earlier heat flow, the surface temperature changes by only a few degrees. On the other hand, the early heat flow produces an enormous direct effect on the depth to the 273K isotherm despite the near constancy of surface temperature; at $Q = 30 \text{ mW m}^{-2}$ the depth is over a km, but at $Q = 100 \text{ mW m}^{-2}$ it is less than 300 m and near the critical depth suggested by (1).

All these calculations are sensitive to the values chosen for the (unknown) regolith conductivity, the CO₂ atmospheric mean residence time, and especially total CO₂ inventory assumed. Thus it is important to explore the sensitivity of the conclusions to the values chosen. Although our exploration of the parametric space has been limited, the qualitative characteristics of the system are apparent.

We find that if the total available CO₂ has always been ~4 bars or more, then the atmospheric greenhouse effect can easily account for the change in erosional style, and the primary role of the heat flow is to raise ground water temperatures. This result is in keeping with the earlier results of (2). On the other hand, if the total CO₂ were only ~1 bar, the atmospheric greenhouse effect does not raise the surface temperature by more than a few degrees, but for plausible values of regolith conductivity the change in internal gradient accompanying higher early heat flow can still easily decrease the water table depth by a large factor, from well over a kilometer to less than 350 m, enabling network formation at 3.8 AE.

REFERENCES: (1) Squyres, 1989. Fourth International Conf. on Mars, Tucson, AZ. (2) Pollack et al., 1987. *Icarus* 71, 203-224. (3) Schubert et al., 1979. *Icarus* 38, 192-211.



NEW MODELS FOR THE ORIGIN OF VALLES MARINERIS CLOSED DEPRESSIONS

J.R. Spencer and F.P. Fanale (Planetary Geosciences Div., School of Ocean & Earth Sciences & Technology, Univ. of Hawaii, Honolulu, HI)

Current models for the formation of the abundant large closed depressions of Valles Marineris have serious shortcomings. Purely tectonic mechanisms are inconsistent with the morphology of many depressions, and removal of large quantities of ground ice from the canyon walls is inconsistent with the observed strength of the walls. Accordingly, we offer some alternatives. One possibility involves decay of ice-rich bodies occupying partially sediment-choked ancient graben that predated the overlying cratered and ridged plains. Other possibilities involve the removal of massive equatorial carbonate deposits storing much of the planet's CO₂ inventory, generated during greenhouse conditions on early Mars. Solution by carbonic acid derived from the atmosphere (analogous to terrestrial karst) requires extensive recycling of the available water supply. Solution by various groundwater acids, possibly derived from the Tharsis magmas, requires less water, especially if only the smaller closed depressions are due to carbonate decay. Alternatively, volume loss due to decarbonation of carbonate during early high heat flow or a later Tharsis-related heat pulse can produce extensive collapse, especially if the carbonates have high silica content.

**DEGRADATION OF Fe-Mg SILICATES IN HOT CO₂
ATMOSPHERES: APPLICATIONS TO VENUS**

D'Arcy W. Straub and Roger G. Burns

Department of Earth, Atmospheric and Planetary Sciences, Massachusetts Institute of
Technology, Cambridge, MA 02139.

Introduction. When basaltic magma extrudes onto the surface of a terrestrial planet, the crystallizing ferromagnesian silicates may interact with the atmosphere as the minerals cool down causing changes of oxidation state and mineralogy of iron. On Earth during the Archean and continually on the surfaces of Mars and Venus, hot olivine and pyroxenes in basalt lava flows were exposed to CO₂-dominated atmospheres, causing Fe²⁺ ions to be vulnerable to weathering reactions. Under present-day conditions on the Venusian surface, chemical weathering is occurring on lowlands [1,2] at temperatures of ~450-475 °C and pressures of ~90-100 bars in an atmosphere of ~97 vol. % CO₂. Under these conditions, degradation of primary igneous minerals is predicted from equilibrium thermodynamic calculations [e.g.,3-6]. However, comparatively few experimental measurements have been made to verify chemical weathering reactions of minerals in hot CO₂-dominated atmospheres [1]. Preliminary experiments of powdered igneous rocks heated in CO₂ produced darkening [7] tentatively attributed to the oxidation of iron-bearing minerals in the rocks to magnetite, which was predicted to be the stable form of iron on the Venusian surface [1,2,8]. However, hematite was suggested to be present in darkened basaltic surfaces of Venus, based on correlations of multispectral images of the Venera 9 landing site and high temperature laboratory reflectance spectra of basaltic materials [9]. Such conflicting information lead to measurements described here of olivine and pyroxenes heated in CO₂ atmospheres, extending recent investigations of products of aerial oxidation of Fe²⁺-bearing olivines [10] and pyroxenes [11] heated in Earth's atmosphere.

Experimental Details. Minerals heated in CO₂ included olivine (Fa₄₉), orthopyroxene (Fs₂₉), augite (Wo₄₇Fs₁₀En₄₆), Mn-hedenbergite (Wo₅₀Fs₄₀Mn₁₀), stoichiometric magnetite (Fe²⁺Fe³⁺₂O₄), and crystalline hematite (Fe₂O₃). Powdered samples (particle diameters < 45 microns) were heated at 790 °C (olivine) or 800 °C (pyroxenes, oxides) for 1-28 days in a muffle furnace under continuously flowing CO₂ (containing 30 ppm O₂) at slow (0.25 ml/sec) or fast (3.0 ml/sec) flow-rates. The Mössbauer spectra of the products from the CO₂-degradation experiments were measured at room temperature, 77K and 4.2K to identify structural Fe²⁺ and Fe³⁺ ions in the minerals and nanophase ferric oxides formed by oxidation. Comparisons were made with the spectral profiles of the oxidized minerals obtained from high temperature aerial oxidation measurements described previously [10,11].

Results. Magnetite and Hematite. In one-day experiments at 800 °C, hematite remained unchanged when heated in CO₂. The magnetite became non-stoichiometric and was partially converted to hematite.

Olivine. In a 6-day experiment performed in CO₂ at 790 °C by Bruce Fegley, almost 80% of the Fe²⁺ in olivine was oxidized to hematite. The oxidation product yielded a magnetic hyperfine spectrum at 295K indicative of "crystalline" hematite instead of superparamagnetic (nanophase) Fe₂O₃ which was encountered previously in aerially oxidized [11] and the CO₂-degraded pyroxenes described below.

Orthopyroxene. The ferric iron initially present in the unheated orthopyroxene (~7.5% Fe³⁺) increased rapidly to ~18.5% after heating in CO₂ for 7 days and levelled off at ~22.5% after 4 weeks. The 295K and 77K Mössbauer spectra showed negligible amounts of magnetically-ordered Fe₂O₃. However, by 4.2K a hematite sextet had appeared accounting for some of the ferric iron. Thus, some nanophase hematite with particle sizes ≤4 nm [12,13] had been formed by oxidation of Fe²⁺ in orthopyroxene, in contrast to earlier aerial oxidation experiments

in which almost 50% of the ferrous iron was oxidized to nanophase hematite in runs performed at similar temperatures and time periods [11].

Pigeonite. After heating pigeonite in CO₂, the hematite sextet was prominent in the 295K Mössbauer spectrum together with Fe²⁺ and Fe³⁺ doublets, indicating that ferrous iron in this pyroxene is particularly vulnerable to oxidation.

Augite. In the unheated pyroxene, ~26% of the iron occurs initially as structural Fe³⁺ ions. After heating in CO₂ for 7 days, ferric iron increased to 42% and levelled off at ~50% after 4 weeks. No ferric oxide sextet appeared in the 4.2K Mössbauer spectrum of the oxidized augite.

Hedenbergite. The 4.3% ferric iron initially present in the hedenbergite increased to ~33.3% after heating in CO₂ for 2 weeks. A magnetic sextet attributable to hematite appeared in the 4.2K Mössbauer spectrum together with a poorly defined ferric sextet attributed to structural Fe³⁺ ions. Similar results were obtained previously for hedenbergites heated in Earth's atmosphere [11].

Discussion. The experiments demonstrate that oxidation of ferromagnesian silicates and magnetite occurs when these minerals are heated at 800 °C in 1 atmosphere of CO₂, under which conditions hematite is thermodynamically stable [14]. The 30 ppm oxygen impurity in the CO₂ presumably facilitates the oxidation of some of the ferrous iron initially present in the crystal structures of the minerals. The Mössbauer spectral measurements reveal, however, that only in CO₂-degraded olivine and pigeonite is hematite formed as a magnetically-ordered phase at ambient temperatures. In orthopyroxene, some of the ferric iron produced by oxidation is present as nanophase hematite which, because it remains superparamagnetic until 4.2K, must exist as particles ≤ 4 nm in diameter. In the calcic pyroxenes, however, much of the oxidized ferrous iron may still remain as structural Fe³⁺ in the host silicates. Some ferric iron may also be present as unit-cell sized Fe₂O₃ inclusions in the pyroxenes, or be segregated along cleavage planes, or be coating mineral grains. In these states of aggregation, the Fe₂O₃ is unidentifiable by X-ray diffraction and in low temperature Mössbauer spectra.

Applications to Venus. The temperatures used in the CO₂-degradation experiments are considerably higher than those encountered on the present-day surface of Venus. However, the lower partial pressure of CO₂ used in the experiments and the inherent impurity of oxygen may be compensatory, by analogy with reactions involving SO₂-CO₂ gas mixtures [15]. Although equilibrium calculations predict an oxygen mole fraction of ~10⁻²⁴ in the near-surface troposphere of Venus [2,8], published results obtained from the Venera 13 and 14 space missions [17] show the presence of ~18 ppm O₂. Therefore, the 30 ppm O₂ present in the 1 atmosphere CO₂-degradation experiments described here may, in fact, be *less* oxidizing than conditions existing in the high pressure atmosphere on Venus. Certainly, the positive identification of hematite, and not magnetite, as the oxidation product of olivine, pigeonite, hedenbergite and, perhaps, orthopyroxene after being heated in CO₂ correlates with observations from multispectral imaging [9] indicating that Venus has a highly oxidized surface [2].

The presence of hematite on Venus is also consistent with the normative mineralogy calculated from analyses of surface rocks at the Vega 2 landing site [18]. The *in situ* XRF analysis reported the iron as 7.7 ± 1.1 wt. % FeO [18]. Assuming that all of the iron is in the ferrous state, CIPW norm calculations [19] yield 26% orthopyroxene, 10% olivine, 3% calcic clinopyroxene and zero percent hematite or magnetite [20]. If, however, the assumption is made that there are equi-molecular proportions of FeO and Fe₂O₃ in the XRF analysis, the computed normative mineralogy corresponds to 31% orthopyroxene, 3% calcic clinopyroxene, 5% hematite, 1% magnetite and zero percent olivine. This mineral assemblage is consistent with the experimental evidence that heated olivines are most vulnerable to oxidation in CO₂-dominated and terrestrial atmospheres, supporting observations [2,9] that the surface of Venus is oxidized.

Acknowledgments. We thank B. Fegley for assistance at the initiation of the project. Research is supported by NASA grant NAGW-2037.

References. [1] J.L.Gooding, ch.9 in *The Solar System Observations and Interpretations* (M.G.Kivelson, ed.; Prentice-Hall), p.208 (1986); [2] V.P.Volkov *et al.*, ch.4 in *Chemistry & Physics of Terrestrial Planets* (S.K.Saxena, ed.; Springer), p.136 (1986); [3] I.L.Khodakovsky *et al.*, *Icarus*, **39**, 352 (1979); [4] V.L.Barsukov *et al.*, *JGR*, **87**, A3 (1982); [5] S.Nozette & J.S.Lewis, *Science*, **216**, 183 (1982); [6] J.S.Lewis & R.G.Prinn, ch.4.2 in *Planets and Their Atmospheres* (Academic Press, 1984); [7] J.L.Gooding, *NASA Tech. Memos* **84211**, 460 (1981) & **85127**, 327 (1982); [8] J.S.Lewis & F.A.Kreimendahl, *Icarus*, **42**, 330 (1980); [9] C.M.Pieters *et al.*, *Science*, **234**, 1379 (1986); [10] K.S.Bartels & R.G.Burns, *LPS*, **XX**, 44 (1989); [11] D.W.Straub & R.G.Burns, *LPS*, **XXI**, 1216 (1990); [12] W.Kundig *et al.*, *Phys. Rev.*, **142**, 327 (1966); [13] R.V.Morris *et al.*, *JGR*, **94**, 2760 (1989); [14] D.Lindsley, *Rev. Min.*, **3**, L-63 (1976); [15] B.Fegley & R.G.Prinn, *Nature*, **337**, 55 (1989); [16] V.L.Barsukov *et al.*, *LPS*, **XVII**, 28 (1986); [17] N.E.Andreeva *et al.*, *LPS*, **XIV**, 7 (1983); [18] Yu.A.Surkov *et al.*, *JGR*, **91**, E215 (1986); [19] M.G.Best, *Igneous and Metamorphic Petrology* (W.H.Freeman) p.616 (1982); [20] R.Wilt, unpub. MIT term paper (1987).

Theoretical Studies of Volatile Processes in the Outer Solar System

Jonathan I. Lunine, Lunar and Planetary Laboratory, University of Arizona, Tucson.

Triton Surface-Atmosphere Interactions

In collaboration with Roger Yelle and Donald Hunten, a study was undertaken to understand the energy and mass couplings between the surface and atmosphere of Triton. Consideration of the role of thermal conduction, eddy mixing, condensation and radiative heating in the thermal balance of the lower atmosphere results in the conclusion that the temperature gradient is negative in the lower atmosphere but becomes positive at higher altitudes. The negative temperature gradient is caused by eddy mixing, which drives the temperature towards the dry adiabat. The positive gradient at higher altitudes is a result of the downward conduction of heat produced in the ionosphere. The low concentrations of thermally active molecules and small aerosol optical depths imply that radiative processes have a negligible effect on the thermal structure. We show that this temperature profile is reasonably consistent with the data from the Voyager radio-occultation experiment, but different from the standard interpretation of these data. Based on the height of the geyser-like plumes seen by Voyager we suggest that the convective and conductive regions of the atmosphere join at the tropopause near 10 km. Rather modest geyser action in the subliming nitrogen ice cap triggers moist convective plumes (figure 1) which must have diameters of at least 1 km and may have velocities up to 100 m/sec; they stop within about 1 km of the tropopause (1).

A model of volatile transport on Triton's surface was constructed in collaboration with J.A. Stansberry, Carolyn C. Porco and Alfred McEwen. We used Voyager imaging data to constrain the albedo variation across the surface and incorporate these in a thermal balance model involving insolation, reradiation and latent heat of sublimation of nitrogen ice. The model predicts that Triton's surface north of 15° north latitude is experiencing deposition of nitrogen frosts, as are the bright portions of the south polar cap near the equator. This result potentially explains why the south cap covers nearly the entire southern hemisphere of Triton (2)

Numerical models of the Evolution of Titan's Surface and Atmosphere

Chris McKay, James Pollack, Regis Courtin and the author completed a coupled ocean-atmosphere model of Titan. The atmospheric model is based on the Ames 1-D non-grey radiative-convective simulation, and represents a higher-fidelity atmosphere model than that used previously. The ocean model is self-consistently coupled to the atmosphere in that the partitioning of the available inventory of volatiles (i.e., N₂, CH₄, and C₂H₆) is determined by the computed temperature. We also considered a surface model in which an ocean was absent, but small methane lakes were included. The decreased solar luminosity over time is also included. Several cases for the initial volatile inventory of methane are considered (corresponding to various possible present-day relative humidities). We find that in general temperatures on the surface of Titan were 10-20K cooler than at present, and that the spectral properties of the IR gaseous absorbers in the 400-600cm⁻¹ window in the thermal infrared determine the response of the surface temperature to changing solar luminosity. We find a similitude between the climate-controlling roles of methane on Titan and water on Earth, and between molecular hy-

drogen on Titan and carbon dioxide on Earth. The former gases are strong greenhouse gases that are limited by condensation, while the latter are trace gases which play a key role in closing major infrared windows.

Rheology of Ammonia-Water Liquids

A collaboration with Jeff Kargel, Steve Croft and John Lewis has concerned experimental and theoretical study of the rheological properties of ammonia-water and ammonia-water-methanol liquids and crystal-liquid slurries. The viscosities of the liquid mixtures examined in this work are much greater than would be expected based on the assumption that the endmember models are non-interactive; in combination with molar volume and vapor pressure data this indicates that the liquid is highly structured (figure 2). With supercooling and/or partial crystallization, these liquids/slurries may attain viscosities ranging up to 10^6 poise or higher. The results were applied to the icy satellites of the outer solar system (including Triton), on which a number of regions have features which could be interpreted as volcanic in origin. While the enormous variation in morphology of flow features requires a great range in rheological properties at the time of eruption, these properties are nonetheless within the range of viscosities for likely compositions. Even some of the more viscous flows can be explained by partially-crystallized binary materials (e.g., ammonia-water), or ternary mixtures with (e.g.) methanol (3).

Chemical evolution of interstellar grains

In a collaboration with Steffi Engel and Bashar Rizk, we examined the frictional heating, sublimation and re-condensation of grains free-falling into the solar nebula from a surrounding interstellar cloud. The sublimation model includes the effect of various volatile species, and accounts for the poor radiating properties of small grains using Mie theory. The amount of water ice sublimated, and the maximum grain temperature reached, vary over a wide range-- from 90% of the grain mass and 170 K at 30 AU from the nebular center to 0% and 50 K at roughly 1000 AU. The process of grain sublimation in the nebula is analyzed from the point of view of the nebular water vapor budget. We conclude that essentially all of the water sublimated eventually recondenses, because the cold nebular gas beyond 10 AU is able to hold only a small fraction as vapor. The adiabatic expansion of the sublimating gas from the grain surface leads to cooling and recondensation of most of the gas at nebular ambient temperature. Such a process in the 30-50 AU region would lead to at least two populations of primarily-water-ice grains: (1) essentially unaltered interstellar grains which did not sublimate due to drag or accretion shock heating and (2) a component comprised of water ice co-condensed, after drag heating, with more volatile processed gases at nebula-ambient temperatures (~50 K), yielding volatile-rich amorphous phases with properties akin to the crystalline clathrate hydrates. Component (2) may be by far the most abundant in the outer solar nebula; the combination of (1) and (2) may explain the peculiar composition of comets relative to the interstellar medium and solar nebula models.

References: (1) Yelle, R.V., Lunine, J.I. and Hunten, D.M. *Icarus* 89, 347-358 (1991); (2) Stansberry, J., Lunine, J.I., Porco, C.C., McEwen, A.S. *Geophys. Res. Ltr.*, 17, 1773-1776 (1990); (3) Kargel, J.S., Croft, S.K., Lunine, J.I. and Lewis, J.S. *Icarus* 89, 93-112 (1991).

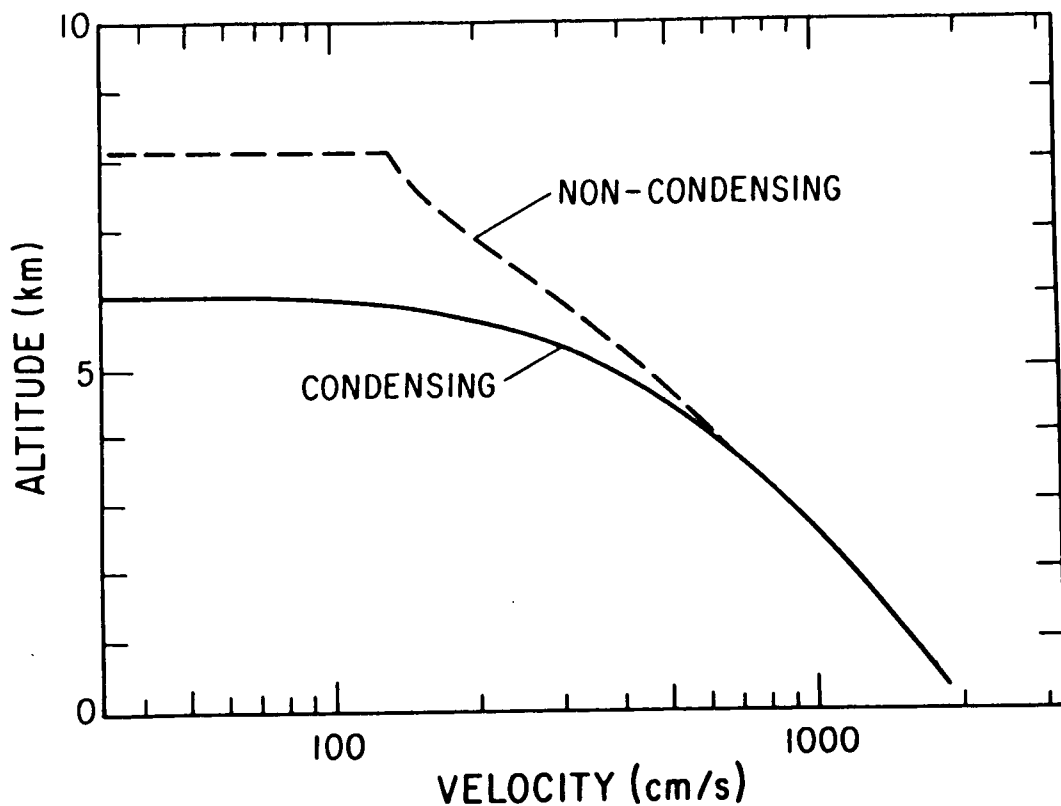


Figure 1. Upward velocity of a moist convective plume, for a surface geyser velocity of 20 meters/second. The line labeled "condensing" applies to an atmosphere which is saturated with nitrogen and has active condensation occurring; the other line applies to a slightly supersaturated atmosphere in which condensation is inhibited. From (1).

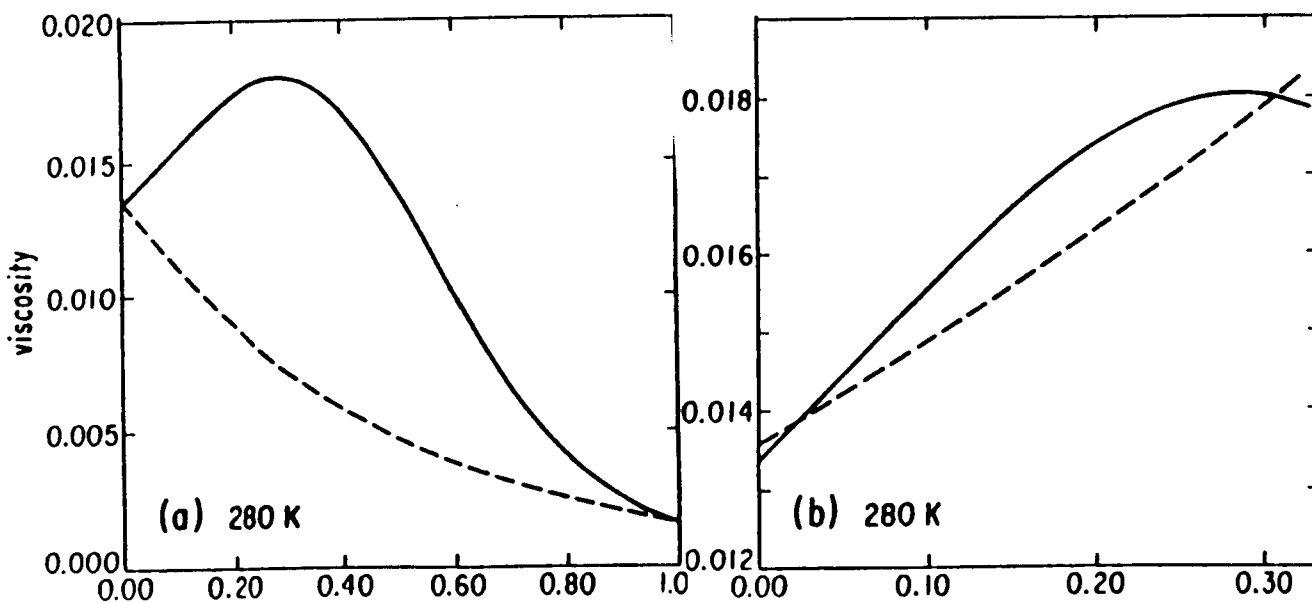


Figure 2. Viscosity (poise) versus ammonia mole fraction at 280 K is shown by the solid lines. The dashed lines are model fits assuming (left) a liquid composed of separate ammonia and water molecules and (right) a liquid in which the ammonia component is contained in ammonia-water clusters. From (3).

CHAPTER 5

SPECTROSCOPY AND REMOTE SENSING

LUNAR MARIA AND RELATED DEPOSITS: PRELIMINARY GALILEO IMAGING RESULTS

*R. Greeley*¹, *M. Belton*², *L. Bolef*¹, *M. Carr*³, *C. Chapman*⁴, *M. Davies*⁵, *L. Doose*⁶, *F. Fanale*⁷, *L. Gaddis*¹, *R. Greenberg*⁶, *J. Head*⁸, *H. Hoffman*⁹, *R. Jauman*⁹, *T. Johnson*¹⁰, *K. Klaasen*¹⁰, *R. Koloord*⁶, *A. McEwen*¹¹, *S. Murchie*⁸, *G. Neukum*⁹, *J. Oberst*⁹, *C. Pieters*⁸, *C. Pilcher*¹², *J. Plutchak*⁸, *M. Robinson*⁶, *R. Sullivan*¹, *J. Sunshine*⁸, *J. Veverka*¹³

1. Ariz St U, Tempe, AZ. 2. NAOO, Tucson, AZ. 3. USGS, Menlo Park, CA. 4. PSI, Tucson, AZ. 5. Rand, Santa Monica, CA. 6. U AZ, Tucson, AZ. 7. U Hawaii, Manoa, HI. 8. Brown U, Providence, RI. 9. DLR, Munich, Germany. 10. JPL, Pasadena, CA. 11. USGS, Flagstaff, AZ. 12. NASA, Washington, D.C. 13. Cornell U, Ithaca, NY.

During the Earth-Moon flyby the Galileo Solid State Imaging (SSI) system (1) obtained new information on lunar maria. Imaging data in 7 spectral bands (0.4 to 1.0 μm wavelength) provide color data for deposits on the western limb, including the Orientale basin (2) and part of the farside (3). General objectives were to determine the composition and stratigraphy of mare and related deposits for areas not previously seen well (or at all) in color, and to compare the results with well-studied nearside maria (4). The imaging sequence began with observations of the Apollo 12 and 14 landing sites and extended west to include Oceanus Procellarum and the Humorum basin. This sequence enabled relative calibration of Galileo data using previous earthbased multispectral observations and spectral data obtained from Apollo samples. A later imaging sequence extended around the western limb and provided new color data for mare deposits in the Orientale basin and those associated with the craters Grimaldi, Riccioli, and Schickard. The last imaging sequence covered part of the farside and included mare deposits in the Apollo basin, light plain deposits such as those in the Korolev basin, and dark mantle (pyroclastic?) materials.

Initial results from images reduced with preliminary calibrations show that Galileo spectral reflectance data are consistent with previous earthbased observations. Color visualization images were prepared from ratios of Galileo SSI filter data (violet/0.76blue, 0.76/violetred; 0.76/IRgreen) in order to assess the relative titanium (blue is relatively high Ti, red is relatively low Ti) and mafic content of maria. Galileo results are comparable to those derived from earthbased spectra for Oceanus Procellarum (7) and Humorum (8). The relative color of mare units correlates with photogeologic features and the titanium content as determined from lunar samples (5 and reviewed by 6). These areas and the general western nearside maria are highly complex and include volcanic centers of the Rümker Hills, Marius Hills, and Aristarchus Plateau (9-14). Mare units in these areas also have a wide range of titanium contents (15) and ages (16). Galileo data show the compositional complexity of western nearside maria and demonstrate that calibrated images can be used to map the color of maria on the farside and in limb areas not readily seen from Earth such as regions of the western limb. For example, small deposits of Imbrian-age lavas are seen on the western margin of Oceanus Procellarum. Galileo data suggest that these deposits consist of relatively bluer flows that were erupted early in the emplacement of lavas in the area. Also seen on the western limb are the impact structures Grimaldi, Riccioli, and Schickard. Grimaldi is a 430 km basin centered at 5° S, 68° W and contains a 230 km ring filled with mare deposits of Eratosthenian age. It is a major mascon mare (17, 18). Riccioli is a 146 km crater

LUNAR MARIA AND RELATED DEPOSITS: R. Greeley et al.

superposed on the northwestern part of the outer ring of Grimaldi; patches of mare deposits (undated) occur on the floor and in the northern half of Riccioli. Irregular depressions in the mare deposits may indicate subsidence of lava lakes (19). Galileo SSI data distinguish the mare deposits associated with Grimaldi and Riccioli.

Schickard is a 227 km basin centered at 44° S, 55° W. Unlike most lunar structures of this size, it has no apparent ring or central peak complex. It is filled with light plains material and mare deposits of Imbrian age. The light plains may represent ejecta from the Orientale basin (6). Galileo color data for Schickard maria are consistent with previous spectral reflectance measurements, showing an intermediate (violet/0.76) color. In addition, a strong mafic component is seen around Schickard and extends as a large regional patch southeast toward Schiller. This area corresponds to the zone proposed to be an older mare deposit now mantled by light plains (20, 28). It was suggested that dark halo craters excavated basaltic materials from beneath the light plains and Galileo results support this model.

Mare deposits in the Orientale basin include Mare Orientale, Lacus Veris (between the Inner and Outer Rook Mountains), and Lacus Autumni (between the Outer Rook and Cordillera Mountains), as described by (23-25). Earthbased spectral reflectance data obtained by Spudis et al. (26) suggest that Lacus Veris and Lacus Autumni are "contaminated" by material derived from the local highlands. Except for this mixing, they proposed that the mare deposits are similar in composition to nearside maria. Galileo spectral reflectance data show heterogeneities in Mare Orientale, with the eastern region being more Ti-rich than the western region.

Apollo is a 505 km basin containing a central ring 250 km across, centered at 36°S, 151°W. A partial third ring has also been described (6). Patches of maria fill parts of the Apollo basin. The superposition of Apollo on the rim of the South Polar-Aitken basin may have enhanced the eruption of mare lavas (10). Galileo SSI data distinguish the mare deposits, but await further calibration before assessment of composition. The general area within the South Pole-Aitken basin shows a strong mafic component. This signature can be attributed to iron-rich material excavated from the lower crust or upper mantle, or to the presence of a cryptomaria. The possible cryptomare deposits in both the South Polar and Schickard basins may represent very early volcanism on the Moon.

Dark mantle deposits are seen in the Aristarchus Plateau, southeast of Copernicus, and in the Orientale basin. Consistent with earthbased observations (29, 30), Galileo data show the Aristarchus deposits to be similar to Apollo 17 orange glass whereas the deposits southeast of Copernicus are similar to the Apollo 17 black glass deposits. Dark mantle deposits on the southwestern part of the Orientale basin form a ring about 200 km in diameter. Galileo data suggest that these presumed pyroclastic deposits have closer affinities with the black glasses found at the Apollo 17 site than the orange glass.

In the mid 1970s a simple two-fold model of mare basalts was developed that involved high and low titanium lavas; it was thought that low titanium lavas erupted during early lunar volcanic history from shallow magma chambers, and that high titanium lavas were erupted later from deeper sources. Subsequently, it was recognized that mare lavas have a wide range of titanium content and neither their ages nor depth of origin correlate well with titanium content. Galileo results confirm this complexity. The preliminary results presented here are given in qualitative terms relative to earthbased observations of the Oceanus Procellarum-Humorum region. Calibration efforts currently underway (3, 27) should lead to quantitative spectral reflectance data obtained from the Galileo images for extrapolation to the lunar western limb and farside.

LUNAR MARIA AND RELATED DEPOSITS: R. Greeley et al.

1. Belton, M.J.S. et al., 1991 (this vol.)
2. Head, J.W. et al., 1991 (this vol.)
3. Pieters, C.M. et al., 1991 (this vol.)
4. Fanale, F., 1990. EOS, Dec 8. 1803-1804
5. Pieters, C.M., 1978. *Proc. Lunar Planet. Sci. Conf.* 9. 2825-2849
6. Wilhelms, D.E., 1987. *U.S. Geol. Surv. Prof. Paper* 1348 302 p
7. Pieters, C.M. et al., 1980. *J. Geophys. Res.*, 85. 3913-3938
8. Pieters, C.M., et al., 1975. *Proc. Lunar Sci. Conf.* 6. 2689-2710
9. Guest, J.E., 1971. *Geo. and Phys. of the Moon*. Ch. 4. 41-53
10. Head, J.W., 1976. *Rev. Geophys. and Space Phys.* 14. 265-300
11. Head, J.W., Gifford, A., 1980. *Moon and Planets* 22. 235-258
12. Whitford-Stark, J., Head J.W., 1977. *Proc. Lunar Planet. Sci. Conf.* 8. 2705-2724
13. Whitford-Stark, J., Head J.W., 1980. *J. Geophys. Res.*, 85. 6579-6609
14. Greeley, R., Spudis, P.D., 1978. *Proc. Lunar Planet. Sci. Conf.* 9. 3333-3349
15. Papike, J.J., Vaniman, D.T., 1978. *Geophys. Res. Lett.* 5. 433-436
16. Boyce, J., 1976. *Proc. Lunar Planet. Sci. Conf.* 7. 2717-2728
17. Sjogren, W.L. et al., 1974. *The Moon*, 9. 115-128
18. Solomon, S.C., Head, J.W., 1980. *Rev. Geophys. and Space Phys.*, 18. 107-141
19. Schultz, P.H., 1976. *Moon Morphology*. U. Texas Press
20. Hawke, B.R., Bell, J.F., 1981. *Proc. Lunar Planet. Sci.* 12b. 665-678
21. Head, J.W., 1974. *The Moon* 11. 327-356
22. Moore, H.J. et al., 1974. *Proc. Lunar Sci. Conf.* 5. 71-100
23. Greeley, R., 1976. *Proc. Lunar Sci. Conf.* 7. 2747-2759
24. McCauley, J.F., 1977. *Phys. Earth Planet. Int.* 15. 220-250
25. Scott, D.H. et al., 1977. *USGS Misc. Invest. Map I-1034*
26. Spudis, P.D. et al., 1984. *J. Geophys. Res.* 89. C197-C210
27. McEwen A. et al., 1991 (this vol.)
28. Bell, J.F., Hawke, B.R., 1984. *J. Geophys. Res.* 89. 6899-6910
29. Adams, J.B. et al., 1974. *Proc. Lunar Planet. Sci.* 5. 171-186
30. Gaddis, L.R. et al., 1985. *Icarus*, 61. 461-489.

CRUSTAL HETEROGENEITY OF THE MOON VIEWED FROM THE GALILEO SSI CAMERA: LUNAR SAMPLE CALIBRATIONS AND COMPOSITIONAL IMPLICATIONS. C. M. Pieters¹, M. Belton², T. Becker³, M. Carr⁴, C. Chapmann⁵, F. Fanale⁶, E. Fischer¹, L. Gaddis^{3,7}, R. Greeley⁷, R. Greenberg⁸, H. Hoffmann⁹, J. Head¹, P. Helfenstein¹⁰, R. Jaumann⁹, T.V. Johnson¹¹, K. Klaasen¹¹, A. McEwen³, S. Murchie¹, G. Neukum⁹, J. Oberst⁹, C. Pilcher¹², J. Plutchak¹, S. Pratt¹, M. Robinson⁶, R. Sullivan⁷, J. Sunshine¹, J. Veverka¹⁰. ¹Brown Univ., ²NOAO, Tucson AZ, ³USGS/Flagstaff, ⁴USGS/Menlo Park, ⁵Planetary Sci. Inst., ⁶Univ. of HI, ⁷AZ State Univ., ⁸Univ. of AZ, ⁹DLR, Oberpfaffenhofen FRG, ¹⁰Cornell Univ., ¹¹JPL Pasadena, ¹²NASA Hq.

The Galileo fly-by of the Earth-Moon system on December 8, 1990 provided an extraordinary opportunity to test an array of sophisticated remote sensing instruments using "ground truth" information (returned samples) about the lunar surface. The synoptic view from the spacecraft also provided an exceptional scientific opportunity to assess the character of unexplored portions of the western limb and farside of the Moon. The SSI multi-spectral camera uses a CCD array detector with a series of seven filters that span the spectral range from 0.4 to 1.0 μm . Several sets of multispectral images of the Moon were obtained over a wide range of viewing and lighting conditions: from over 100° phase angle for the first images of the nearside to 20° phase when viewing the Orientale basin. The variety of mare and highland compositions discerned from these data and their calibration linked with the lunar samples are summarized here. Companion abstracts in these volumes highlight the SSI camera and Earth-Moon encounters, Orientale and South-Pole-Aitken basins, and lunar maria (1, 2, 3).

SUMMARY OF SPECTRAL CALIBRATION. Shown in Figure 1 are bidirectional reflectance spectra of mature soils and rock powders from the Apollo collection. Superimposed are five SSI effective filter bandpasses (two methane filters were not used in this analysis initially). Since the color of the Moon is known to vary with viewing geometry (4), detailed bidirectional reflectance measurements of mature lunar soils were undertaken to provide the calibration data necessary for the specific geometry encountered by Galileo and are discussed elsewhere (see 5). Because the surface calibration site preferred by astronomers was beyond the terminator (Apollo 16), secondary standards were selected on the western nearside that have been well studied using earthbased telescopes (and calibrated to Apollo 16). The chosen sites include several mare and highland areas in and around Mare Humorum and the Surveyor I site (in Flamsteed P) (6). Earth-based spectra of these standard areas were convolved with the effective Galileo filters and calibrated with the bidirectional measurements of Apollo 16 soil obtained at the appropriate geometry. Preliminary calibration procedures to the raw data included standard dark current removal and flatfield correction (initially using preflight data), "dust blemish" removal, and ghost image and scattered light removal (the latter are thought to be due to a dust cover over the aperture of SSI that could not be removed before the encounter).

The spectral properties of the lunar surface measured with SSI filters using pre-flight calibration shows systematic color deviations up to 40% when compared to the "ground truth" spectrum of the surface derived from appropriate bidirectional spectra of lunar samples. This apparent error in absolute color is presumed to be related to the dust cover and will be checked before and after the dust cover is removed later this year. Relative color can be checked independent of absolute color, but is sensitive to the accuracy of the gain and offset corrections mentioned above. Shown in Figure 2a,b is a comparison of telescopic and SSI relative reflectance spectra for four areas on the western nearside. All spectra are relative to the standard area MH0 in Mare Humorum and are scaled to unity at 0.76 μm . MH0, Flamsteed and MH203 represent a range of mare compositions, MH40 is typical highland, and MH45 is a fresh mare crater. These SSI relative reflectance spectra are in qualitative agreement with the telescopic spectra and thus confirm that the data are reliable. Precise quantitative analyses await inflight calibration and refinement of the ghost image and scattered light removal techniques.

COMPOSITIONAL PARAMETERS. The spectra in Figures 1 and 2 demonstrate the primary spectral properties of lunar materials in the spectral range covered by the SSI camera. There is a generally smoothly varying continuum from 0.4 to about 0.76 μm and an absorption band between 0.9 and 1.1 μm which is due to a variety of mafic minerals (largely, different types of pyroxenes). Highland soils are relatively red through the visible range and normally exhibit a weaker feature at 1 μm (less mafics) than the mare. The visible continuum slope of mature mare soils varies significantly and is linked to TiO₂ content (e.g. 7). For our initial science analyses we have chosen the 0.40, 0.76 and 1.0 μm filters to evaluate spatial variations across the Moon: the 0.40/0.76 μm ratio is sensitive to variations in continuum slope and the 0.76/1.0 μm ratio provides a good indication of the strength of absorption bands due to the presence of mafic minerals.

SUMMARY OF NEARSIDE COLOR. Familiar color variations on the lunar nearside (7,8) are apparent in the SSI multispectral images providing additional confidence in data quality. Most feldspathic highlands are relatively red (low 0.40/0.76 μm) with only minor mafic components (low 0.76/1.0 μm). The basaltic mare are distinguished by a stronger mafic mineral signature (higher 0.76/1.0 μm) and the great variety of high and low-Ti basalts in Oceanus Procellarum are readily recognized (through variations in 0.40/0.76 μm). Fresh craters are easily distinguished from mature soils: mare craters exhibit a much stronger mafic mineral absorption (very high 0.76/1.0 μm) and highland craters exhibit a flat continuum (very blue, or high 0.40/0.76 μm) with a variably weak mafic mineral absorption. There are several intriguing exceptions for familiar areas. For example, southwest of Humorum

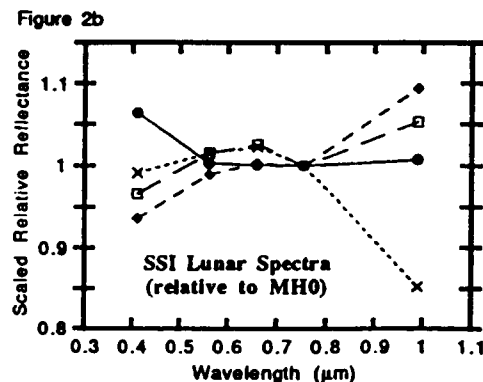
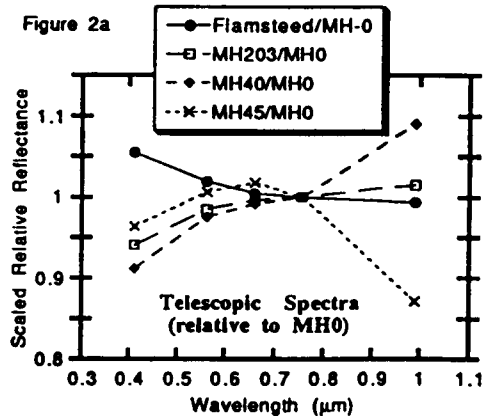
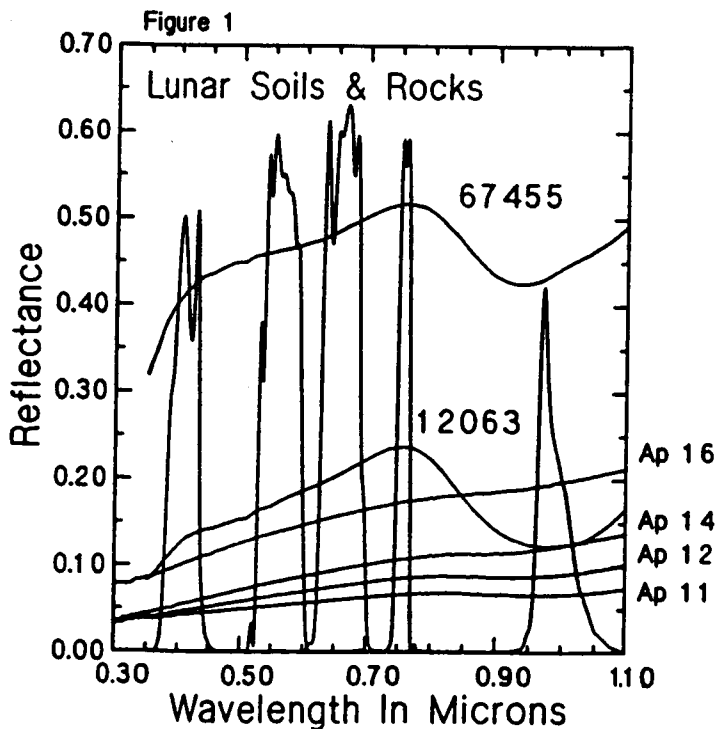
in the highlands surrounding Schickard is a large region several hundred kilometers in extent that exhibits a distinctly enhanced mafic signature (high 0.76/1.0 μm) suggestive of a regionally extensive mare component in the soils (2).

SUMMARY OF LIMB AND FARSIDE COLOR. Most distinctions between mare and highlands are also evident on the farside and the general spectral properties of broad regions of the northern highlands indicate a predominance of feldspathic soil approximately comparable to that returned by Apollo 16. The basalts of Orientale are heterogeneous, with the eastern basalts perhaps being more Ti-rich (slightly higher 0.40/0.76 μm) (see discussion in 3). Strong spectral variations are associated with immature highland surfaces, many of which are relatively blue (low mafic) highland craters and their ray systems (several of which are notably asymmetric). On a more spectrally subtle scale, the limb and farside soils appear very heterogeneous. There are distinct 0.40/0.76 μm variations of a few percent that define areally extensive units and imply variations in iron (or glass) content. One of the largest and "reddest" regions is the interior of the South Pole-Aitken basin (see discussion in 2).

Perhaps most interesting are large and small farside areas that are enriched with mafic minerals. The largest region is in the southern portion of South Pole-Aitken basin and appears to extend eastward, a tantalizing suggestion that the basin excavated compositions of the lower crust/upper mantle or cryptomare. Furthermore, while many highland craters exhibit classic feldspathic characteristics (bright blue, low mafic), several distinctive craters are also identified as mafic-rich from their enhanced 0.76/1.0 μm [Lowell, Wright, Guthlick].

OVERVIEW. The farside of the Moon has held its secrets well since initial Zond and Apollo exploration. This large area of lunar crust is dominated by heavily cratered terrain and basin deposits that represent the products of the first half billion years of crustal evolution. Continuing analysis of the returned lunar samples suggest a "magma ocean" and/or "serial magmatism" model for evolution of the primordial lunar crust (e.g. 9). Testing either hypothesis, however, requires compositional information about crustal stratigraphy and lateral heterogeneity, and resolution of this important planetary science issue is dependent on additional data. These new Galileo multispectral images indicate previously unknown local and regional compositional diversity of the farside crust. Future analyses will focus on individual features and a more detailed assessment of crustal stratigraphy and heterogeneity.

References: 1. Belton M. et al. (1991) these volumes; 2. Head J.W. et al. (1991) these volumes; 3. Greeley R. et al. (1991) these volumes; 4. Lane A.P. and Irving W.M. (1973) *Astron. J.*, 78, 267-277; 5. Pieters C. et al. these volumes; 6. Johnson T.V. et al. (1972) *Icarus*, 19, 224-229; Pieters C. et al. (1975) *PLPSC6th*, 2689-2710; Pieters C.M. et al. (1980) *JGR*, 85, 3913-3938; 7. Pieters C. (1978) *PLPSC9th*, 2825-2849; 8. McCord T.B. et al. (1976) *Icarus*, 29, 1-34; McCord T.B. et al. (1979) *Icarus*, 37, 1-28; Johnson T.V. et al. (1977) *PLPSC8th*, 1013-1028; Whitaker E.A. (1972) *The Moon*, 4, 349-355; 9. Walker D. (1983) *PLPSC14th*, B17-B25; Warren P. (1985) *An Revs. Earth Planet. Sci.*, 13, 201-240.



REMOTE SENSING AND GEOLOGIC STUDIES OF THE ORIENTALE BASIN REGION

B. R. Hawke, P. G. Lucey, G. J. Taylor, J. F. Bell, C. A. Peterson, D. Blewett, and K. Horton, Planetary Geosciences Division, School of Ocean and Earth Science and Technology, University of Hawaii, Honolulu, HI 96822.
P. D. Spudis, Lunar and Planetary Institute, Houston, TX 77058

INTRODUCTION

During its first encounter with the Earth-Moon system, in early December, 1990, the Galileo spacecraft obtained a wealth of new spectral data and imagery for portions of the Moon's western limb and farside. This information is being used to address a variety of important lunar issues. The focus of the Galileo lunar observations is the Orientale region of the Moon. Orientale is the youngest and best preserved of the giant multiringed impact basins on the Moon. It straddles the western limb; about half of it is visible from Earth. This region is geologically fascinating, and unanswered questions abound. We do not know the surface composition of the western limb area with certainty, nor do we know how the composition varies with depth. A detailed study of the region will address both problems because Orientale, like other basins, is a natural drill hole into the lunar crust. Smaller craters and basins are also present in the area, so in principle we can obtain a fairly detailed picture of crustal stratigraphy. Furthermore, we can use compositional data and inferred stratigraphy to test models of the mechanics of basin formation. Finally, we can determine the characteristics of the volcanic products that partially fill the basin and occur in other areas outside it, and also measure the extent of pre-Orientale mare volcanism.

We have been conducting a variety of spectral observations of the Orientale region. Our present efforts continue work reported previously by Spudis et al.¹ We combine both visible and near-infrared spectral observations with multispectral imaging. The purposes of this paper are 1) to present the preliminary results of this effort; 2) to address the fundamental questions outlined above; and 3) to provide a framework in which to interpret the observations made by the Galileo mission.

METHOD

Over 100 near-infrared reflectance spectra (0.6-2.5 μ m) were obtained at the 2.24-m telescope of the Mauna Kea Observatory (MKO) during a series of observing runs conducted during favorable lunar librations. In addition, two observing runs were conducted utilizing the University of Hawaii 60-cm (Air Force) telescope, and fifty spectra were obtained. Digital multispectral images of the Orientale region were obtained at one of the MKO 60-cm telescopes simultaneous with some of the spectral observations. Images were obtained in UV, visible and near-infrared wavelengths (0.375, 0.40, 0.73, 0.86, 0.90, 0.93, 0.96, and 1.00 μ m, each with 10 nm bandwidth) with a 384x576 element Thompson CCD installed in a commercial astronomical CCD camera produced by Photometrics, Inc. Observations of the Mare Serenitatis standard site were made for photometric calibrations. A rectified color composite of near-IR multispectral imaging intended to show the distribution of anorthosite and noritic material in the Orientale region was produced.

RESULTS AND DISCUSSION

We discuss the results in terms of geological location.

Oriente interior

With the exception of the Inner Rook massifs, all the highlands units inside the Orientale basin appear to be composed of either noritic anorthosite or anorthositic norite.¹ The Maunder Formation is composed of smooth plains that grade laterally outward into rough-textured material, and is thought to be composed largely of impact melt.^{2,3,4,5} Spectra obtained for portions of the Maunder Formation with mature regolith surfaces are almost identical to those taken in the vicinity of the Apollo 16 site. Spectra of fresh surfaces on the Montes Rook Formation, a hummocky unit thought to be primary basin ejecta,^{4,5} and of the massifs of the Outer Rook Mountains are similar to one another and indicate the presence of plagioclase and low-Ca pyroxene.¹ Mature surfaces on the Montes Rook Formation are similar in composition to those in the Apollo 16 area.

The Inner Rook Mountains are markedly different from other units within the Orientale basin. Our previous data¹ indicated that two of these mountains are composed of anorthosite. Our new multispectral images confirm this view: the entire eastern Inner Rook Mountains contain only minute amounts of low-Ca pyroxene. Thus, it appears that the Inner Rook ring of the Orientale basin is a mountain range composed of anorthosite. The plagioclase absorption band at 1.25 microns occurs in some spectra, but not in all, suggesting different shock histories for different parts of the Inner Rook ring.

Oriente exterior

The Hevelius Formation occurs outside the prominent Cordillera ring and probably contains large amounts of primary ejecta from Orientale. It consists of hummocky to lineated to swirl-textured deposits that extend to almost one basin-diameter (930 km) beyond the Cordillera scarp. We have taken numerous spectra of this deposit, including several radial traverses across it. The Hevelius Formation is surprisingly uniform in composition and strikingly similar to Apollo 16. It consists largely of noritic anorthosite, like much of the interior deposits in Orientale. The Hevelius Formation grades outward into smooth highlands plains deposits, some of which also appear to be similar in composition to the Apollo 16 highlands.

Crüger region

Spectral observations of the Crüger region have been reported and discussed by Hawke et al.⁶ Crüger is a 46-km diameter, mare-filled impact crater. Spectra of its west rim and of Darwin C (a 16-km crater southwest of Crüger) indicate that the highlands are composed of noritic anorthosites here also. However, the spectrum for the 8-km diameter crater Crüger G exhibits a pyroxene absorption feature minimum beyond 0.95 μm , which indicates a gabbroic anorthosite composition. Gabbroic anorthosite was also exposed by Byrgius A, a 19-km diameter impact crater south of Crüger.⁷ The area east of Crüger exhibits unusual characteristics in the multispectral imagery. Some areas mapped as highlands exhibit a mare basalt signature. This suggests that portions of this region could have been the sites of pre-Oriente mare volcanism.

Grimaldi Region

Grimaldi is a small (430 km) two-ringed impact basin. Our spectral data indicate that there might be anorthosites on its inner ring, analogous to those in the Inner Rook ring of Orientale. We have obtained one spectrum of an anorthosite from a portion of the inner ring. Other spectra for the inner ring exhibit a very shallow pyroxene absorption feature, which indicates the presence of very minor amounts of orthopyroxene. These areas may also prove to be composed of anorthosites. Other highlands deposits emplaced in the Grimaldi region as a result of the Orientale impact event appear to be composed of noritic anorthosite.

Schiller-Schickard Region

Although this region is over 1000 km from the Cordillera ring, it has been heavily affected by the Orientale impact event. This area contains numerous unusual features. These include the crater Wargentín, the Schiller-Zuccius impact basin, the large crater Schickard (D=227 km), whose floor contains mare deposits as well as a light plains unit, and a high density of dark-haloed impact craters.⁸ Bell and Hawke^{9,10} presented spectral data which demonstrated that dark-haloed impact craters excavated ancient mare basalts from beneath light plains deposits in the Schiller-Schickard region. They concluded that early (>3.8 Ga) mare deposits existed in the Schiller-Schickard region prior to the Orientale impact and that these basaltic units were covered with a thin layer of highland debris as a consequence of the formation of Orientale basin. Spectra for the light plains deposits in this region exhibit relatively strong "1 μm " bands. Either Orientale primary ejecta in the region contains more pyroxene than similar material in other areas or pyroxene-rich local material (mare basalt?) was incorporated in the light plains deposits by Orientale secondary craters.

Humorum Region

Humorum is an old multiringed basin east-southeast of Orientale. Our data indicate that anorthosites are exposed on the main ring of this basin. Spectra obtained for small craters in the highlands northwest of the basin indicate the presence of a mare basalt component, which suggests that the region experienced mare-type volcanism prior to the formation of the Orientale basin.

SUMMARY OF OBSERVATIONS

1) Anorthosites occur in the Inner Rook Mountains of Orientale, the inner ring of Grimaldi, and the main ring of Humorum. Imaging spectroscopy shows that the entire eastern Inner Rook Mountains are composed of anorthosites.

2) Orientale ejecta are strikingly like the surface materials in the region where Apollo 16 landed. This similarity indicates similar mineralogy, noritic anorthosite. Thus, Orientale ejecta is more mafic (10-20% low-Ca pyroxene) than the Inner Rook Mountains (no more than a few percent pyroxene). This situation is also true for the Nectaris, Humorum, and Gramaldi basins.

3) Isolated areas in the Orientale region show the presence of gabbroic rocks, but in general Orientale ejecta are noritic anorthosites, which contain much more low-Ca pyroxene than high-Ca pyroxene.

4) Ancient (pre-Orientale) mare volcanism apparently occurred in several areas of the western limb.

REFERENCES: 1) P. Spudis, et al. (1984) *PLPSC*, 15, C197; 2) J. Head (1974) *The Moon*, 11, 327; 3) H. Moore et al. (1974) *PLSC*, 5, 71; 4) J. McCauley (1977) *Phys. Earth Planet. Inter.*, 15, 220; 5) D. Scott et al. (1977) *USGS Map 1-1034* 6) B. Hawke et al. (1989) *PLPSC*, 19, 127; 7) C. Pieters (1986) *Rev. Geophys.*, 24, 557; 8) P. Schultz and P. Spudis (1979) *PLPSC*, 10, 2899; 9) B. Hawke and J. Bell (1981) *PLPSC*, 12, 665; 10) J. Bell and B. Hawke (1984) *JGR*, 89, 1899.

REMOTE SENSING AND GEOLOGIC STUDIES OF THE TERRAIN NORTHWEST OF HUMORUM BASIN

B. Ray Hawke, C.A. Peterson, P.G. Lucey, G.J. Taylor, J.F. Bell, D. Blewett, B. Campbell, Planetary Geosciences Division, School of Ocean and Earth Science and Technology, University of Hawaii, Honolulu, HI 96822

C.R. Coombs, Johnson Space Center, Houston, TX 77058

P.D. Spudis, Lunar and Planetary Institute, Houston, TX 77058

INTRODUCTION

A portion of the highlands terrain northwest of the Humorum basin, a large multiringed impact structure on the southwestern portion of the lunar nearside, exhibits anomalous characteristics in several remote sensing data sets. The most complete ring of the basin is 440 km in diameter and bounds Mare Humorum.¹ A rimlike scarp almost twice as large (820 km in diameter) and resembling the Cordillera ring of the Orientale basin lies outside of this mare-bounding ring.¹ Gaddis et al.² first noted the unusual nature of the highlands terrain northwest of the main ring. They pointed out that an area (45,000 km²) west of Gassendi crater exhibited relatively low depolarized 3.8-cm radar returns in the radar images presented by Zisk et al.³ This area, which is centered at 43°W, 15°S, also exhibits unusually low values in 70-cm radar images provided by T. Thompson. Gaddis et al.² noted the possibility that this area was mantled with relatively high-albedo pyroclastic debris and suggested that additional evidence bearing on the presence of pyroclastic mantling material in this area might come from near-infrared reflectance studies.

We have been conducting a variety of remote sensing studies of the terrain northwest of Humorum basin in order to determine the composition and origin of this anomalous unit as well as the composition of the highland material exposed by the Humorum impact event. The purpose of this paper is to present the preliminary results of this investigation.

METHOD

Near-infrared reflectance spectra were obtained utilizing the University of Hawaii 2.24-m telescope at the Mauna Kea Observatory. The Planetary Geoscience Division indium antimonide spectrometer was used. This instrument successively measured intensity in each of 120 wavelengths covering a 0.6-2.5 μm region by rotating a filter with a continuously

variable band pass. By using the $f/35$ oscillating secondary mirror on the 2.24-m telescope in its stationary mode, it was possible to collect spectra for relatively small areas (5-10 km) near the lunar western limb. Differential atmospheric refraction limited such high-resolution observations to periods when the Moon was near zenith.

The lunar standard area at the Apollo 16 landing site was frequently observed during the course of each evening, and these observations were used to monitor atmospheric extinction throughout each night. Extinction corrections were made using the methods described by McCord and Clark.⁴ These procedures produce spectra representing the reflectance ratio between the observed area and the Apollo 16 site. These relative spectra were converted to absolute reflectance utilizing the reflectance curve of an Apollo 16 soil sample. Analyses of pyroxene band positions and shapes as well as continuum slopes were made using Gaussian-band fitting and other techniques described by McCord et al.⁵

In addition, the 3.8-cm radar data presented by Zisk et al.³ was reprocessed and utilized in this investigation.

RESULTS AND DISCUSSION

At least a portion of the mare-bounding ring of Humorum is composed of pure anorthosite. Spectra were collected for Mersenius C (diameter=14 km) and the Gassendi E and K complex. These small impact craters expose fresh material from beneath the surface of massifs in the mare-bounding ring. The "1 μm " absorption features in these spectra are extremely shallow. Only very minor amounts of low-calcium pyroxene are present in the areas for which these spectra were obtained; an anorthosite lithology is indicated. Anorthosite also appears to have been exposed by Liebig A, a 12-km impact crater on the western portion of the mare bounding ring. A preliminary analysis of the spectra obtained for other highlands features in the Humorum region indicates the presence of noritic anorthosite. Anorthosite has now been identified on rings associated with the Orientale⁶, Nectaris⁷, Grimaldi⁸, and Humorum basins.

Lucey et al.⁹ have recently presented the results of imaging spectroscopy of the Humorum basin region. They identified a spectral unit in the highlands northwest of Humorum which appeared to represent a mixture of highlands debris with lesser amounts of mare material. This spectral unit generally correlates with the area which exhibits anomalously low 3.8-cm radar returns. We have obtained near-infrared reflectance spectra for Gassendi F and G. Both impact craters are 8 km in diameter and they excavated material from beneath the surface of the anomalous unit. Gassendi G has a partial dark halo. Analysis

of our spectral data indicates that both Gassendi G and F excavated mare basalt from beneath a surface enriched in highlands debris. An episode of mare volcanism may have emplaced basaltic units in this region after the formation of the Humorum basin. Subsequently, large impacts in the vicinity, such as those which formed Gassendi, Letronne, and Mersenius craters, emplaced a veneer of highlands debris atop the basalt flows. The mare material could have been mixed with highlands debris either by "local mixing" during ejecta emplacement or by vertical mixing due to small crater-forming impacts in the area. Other interpretations are possible, and additional work will be required to fully confirm the model outlined above.

REFERENCES

- 1) D. Wilhelms (1987) *USGS Prof. Paper 1348*.
- 2) L. Gaddis et al. (1985) *Icarus 61*, 461.
- 3) S. Zisk et al. (1974) *Moon 10*, 17.
- 4) T. McCord and R. Clark (1979) *Publ. Astron. Soc. Pac. 91*, 571.
- 5) T. McCord et al. (1981) *JGR 86*, 10883.
- 6) P. Spudis et al. (1984) *PLPSC 15*, C197.
- 7) P. Spudis et al. (1989) *PLPSC 19*, 51.
- 8) B. Hawke et al. (1991) *LPSC XXII*, 537.
- 9) P. Lucey et al. (1991) *PLPS 21*, 391.

Analyses of the Lunar Surface with Advanced Remote Sensors: Expectations for the 1990's

C. M. Pieters, Department of Geological Sciences, Brown University, Providence, RI
02912

One of the most important lessons learned from the recent Galileo fly-by of the Moon is that, in spite of the wealth of Apollo data, a small increment of new data with advanced sensors provides unexpected surprises about the Moon. The classic strategy for planetary exploration (Reconnaissance, Exploration, In-Depth Study) has been implemented more-or-less in reverse order for the Moon. The scientific finale of the Apollo program was the return of lunar samples, an event which logically falls well into "in-depth study." The character, diversity, and complexity of the lunar surface, however, was not explored in any systematic manner and the post-Apollo era was left with scant information to put the valuable samples into a global geologic context.

In the two decades since Apollo much progress has nevertheless been made in both advanced sensor technology and our recognition of how to use these tools to address fundamental science issues of the Earth-Moon system. During this interlude remote compositional analyses focused on analysis of the equatorial band of Apollo gamma-ray and X-ray data and the expanding variety of spectroscopic data obtained for the lunar nearside using earth-based telescopes. We now know, for example, that the bulk of the lunar samples are not representative of several important lithologies: KREEP is distinctly non-uniformly distributed and if it represents a rock type, it has probably not been sampled directly; a great diversity of mare basalt compositions have been detected, two-thirds of which are unsampled; several craters have excavated deeper crustal material and exposed what appears to be a suite of lunar plutons. These fragments of information underline the need for a full global assessment of the compositional and geophysical character of the Moon. Today's advanced sensor capabilities provide unprecedented opportunities for exploration that mesh well with the science requirements for a sophisticated integration of several types of remotely acquired information. Science priorities for the 1990's include (a) an evaluation of the global composition and structure of the primordial lunar crust in order to model its origin and evolution, (b) using the Moon as a natural laboratory to study the impact process and time-cumulative events at 1 AU, and, ultimately, (c) constraining the origin of the Moon and its relation to Earth.

INFRARED REFLECTANCE SPECTRA (4-12 μm) OF LUNAR SAMPLES

Douglas B. Nash, San Juan Institute, San Juan Capistrano, Ca 92675

This work addresses infrared reflectance properties of lunar samples and is part of an ongoing study to assess the potential for using mid-IR thermal emission spectroscopy (TES) to map mineral composition on the Moon's surface from orbiting spacecraft. A recent evaluation of the TES technique (Nash et al, 1991) shows that despite some earlier worker's misgivings the TES technique holds great promise for providing useful mineralogical information about the Moon's surface.

Here are presented infrared reflectance spectra of a typical set of Apollo samples to illustrate spectral character in the mid-infrared (4-12 μm) of lunar materials and how it varies between three main forms: soil, breccia, and igneous rocks. Reflectance spectra, to a close approximation, are the inverse of emission spectra; thus for a given material the spectral reflectance (R) at any given wavelength is related to emission (E) by $1 - R = E$. We therefore can use reflectance spectra of lunar samples to predict how emission spectra of material on the lunar surface will appear to spectrometers on orbiting spacecraft or earthbased telescopes.

Spectra were measured in the lab in dry air using an FTIR spectrometer with cooled HgCdTe detector measuring reflectance from 2.3 to 25 μm relative to a gold-coated sandpaper reference material (for detail of the measurement system see Nash, 1986). Shown here is only the key portion (4-12 μm) of each spectrum relating to the principal spectral emission region for sunlit lunar materials and where the most diagnostic spectral features occur (Nash et al, 1991).

Spectra of seven typical lunar samples are shown in Figure 1. The zero level of each spectrum (except the bottom one) is offset upward in 10% increments for clarity. The compositional character of each sample (data from the Lunar Sample Catalogs) is shown in Table 1.

The spectra contain subtle but diagnostic features. The most prominent one is the minimum in reflectance (maximum in emission) occurring near 8 μm . This is the Christiansen Frequency (CF) feature, and it's wavelength position is a strong indicator of composition (Conel, 1969; Salisbury and Walter, 1989), shifting to longer wavelength with increasing mafic composition. Next, weak absorption features in the 4.5 to 6.0 μm region, which are combination and overtone bands from molecular vibrations. And finally, the Reststrahlen Band (RB) region from 8.5 to 12.0 μm , where stretching vibration bands are diagnostic of composition but subdued by effects of fine particle size (Salisbury and Walter, 1989).

The spectra shown in Figure 1 illustrate several mid-IR spectral properties of lunar materials:

1. The breccias, in addition to having very high spectral contrast between 4 and 8 μm , show distinct spectral features indicating an Anorthite-rich plagioclase content. These features include the combination tone bands near 4.5, 5.6, and 6.2 μm ; the distinct CF minimum at 8.1 μm ; and the relatively flat sloping RB region from 8.5 to 12.0 μm (Nash and Salisbury, 1990).

2. The soils display medium spectral contrast between 4 and 8 μm ; the CF minimum shifts to longer wavelength with increasing soil maturity; the strength of combination tone bands near 5.2 and 6.2 μm are greater for soils with high crystalline content, lower for soils with high glass or agglutinate content.

3. Soils with high crystalline mineral content have a well-defined CF-minimum feature and combination tone bands at 5.2 μm (indicating pyroxene) and 6.2 μm (indicating plagioclase).

4. Igneous rock spectra show overall low spectral contrast, and a broad, poorly defined CF-minimum feature due to contributions from several mineral phases (plag, pyrox, oliv), but stronger reflectance in the RB region due to the absence of the effects of fine particle size.

These results suggest that in order to effectively utilize mid-IR thermal emission spectroscopy for lunar compositional mapping it is important that the origin of subtle features in spectra of soil and breccia materials be well understood, since it is these fine-particle-size forms of material that blanket most of the lunar surface, and that will dominate the character of any spectra measured from lunar orbit or beyond. Such work including laboratory measurements and theoretical modeling needs to be carried out.

IR REFLECTANCE OF LUNAR SAMPLES: Nash, D.B.

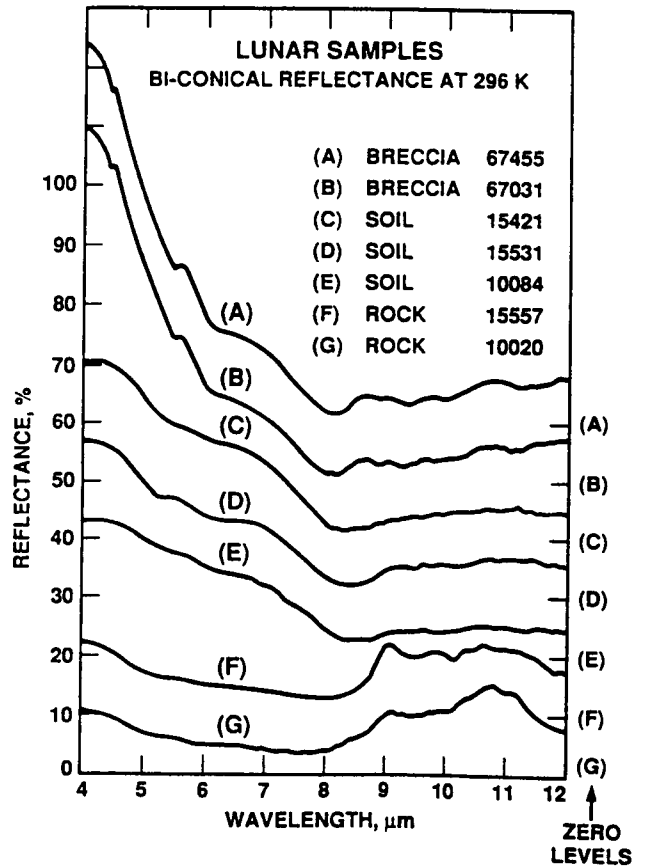
References: Conel, J. E. (1969); Infrared emissivities of silicates: Experimental results and a cloudy atmosphere model of spectral emission from condensed particulate mediums; JGR 74, 1614-1634. Nash, D.B. (1986); Mid-infrared reflectance spectra (2.3-22 μm) of sulfur, gold, KBr, MgO, and Halon; Appl. Opt. 25, 2427-2433. Nash, D.B. and J. Salisbury (1990); Infrared reflectance spectra of plagioclase feldspars; LPSC XXI, 845-846. Nash, D.B., J. Conel, P. Christensen, P. Lucey, and J. Salisbury (1991); Evaluation of thermal emission spectroscopy for compositional mapping of the Moon's surface from a polar-orbiting spacecraft; (submitted to JGR). Salisbury, J.W. and L.S. Walter (1989); Thermal infrared (2.5-13.5 μm) spectroscopic remote sensing of igneous rock types on particulate planetary surfaces; JGR 94, 9192-9202.

Acknowledgements: I thank John Salisbury and Jim Conel for helpful discussions. This is SJI contribution 8, supported by NASA Grant NAGW 1350 in the Geology and Geophysics Program.

		Plag	Pyrox	Oliv	Ilmen	spinel, troil., or crist. Fe	Agglut. Glass	lithic	notes
(A) Breccia	67455	80-90	10-20	?	?		~10?		[1]
(B) Breccia	67031	~90?	~10?	trace	-----scarce-----		trace		[2]
(C) Soil	15421	1	2				97		[3]
(D) Soil	15531	8?	30?	6?	-----?-----		A-23 G-5	35?	[4]
(E) Soil	10084	2	-----4-----		-----1-----		65	26	[5]
(F) Rock	15557	35	50	10-15	-----5-----				[6]
(G) Rock	10020	30	50	4	16				[7]

- Notes: [1] Matrix has black/grey material.
 [2] Has clasts of gabbro/norite; ferran anorthosite.
 [3] Very immature soil; green glass.
 [4] Immature soil; lithics 21%, breccia 6%, indeterminate 8%.
 [5] Mature soil; mare-basalt lithics 24%, highland lithics 2%.
 [6] Very friable, medium grained; olivine basalt.
 [7] Olivine basalt.

Figure 1. Reflectance spectra in dried air at room temperature. Rock spectra are for clean surface of solid chips, all others are for particulate material as it was returned from the Moon, placed loosely in analysis cups, and lightly compressed with glass slide to make a smooth flat surface.



REMOTE SENSING OF THE MARTIAN SURFACE. Bruce M. Jakosky, Bradley G. Henderson, Cora E. Randall, M. Joan Alexander, and Thomas M. McCollom*, Laboratory for Atmospheric and Space Physics, University of Colorado, Boulder, CO 80309-0392. * Now at Washington University in St. Louis.

The martian surface has been extensively imaged from orbiting spacecraft, revealing processes which affect the surface at spatial scales of tens of meters and larger. At smaller scales, available orbiter imaging or observations from landers are not available over a large fraction of the surface; remote-sensing observations are used to determine global surface properties and thereby infer the nature of ongoing surface processes. The various remote-sensing techniques, including radar reflection and scattering and thermal emission observations at multiple times of day, wavelengths, or viewing geometries, are sensitive to the properties of the surface at spatial scales ranging from tens of microns up to meters. The processes which are responsible for producing properties at this scale, or for producing spatial variations in these properties, include eolian erosion and deposition, physical and chemical weathering of surface materials, and solution or precipitation of materials due to the possible presence of liquid water.

As part of our ongoing research program, we have been investigating the physical properties of the martian surface as inferred from a combination of orbiting and Earth-based remote-sensing observations and in-situ observations. This approach, to synthesize a variety of different observations, each of which is sensitive to slightly different aspects of the near-surface layer, provides the most-detailed and self-consistent view of the global and regional nature of the surface.

Our results during the past year focus on the areas of (i) modelling the diurnal variation of the surface temperature of Mars incorporating the effects of atmospheric radiation, with implications for the interpretation of surface thermal inertia; (ii) modelling the thermal emission from particulate surfaces, with application to observations of the surfaces of the Earth, Moon, and Mars; (iii) modelling the reflectance spectrum of Mars in an effort to understand the role of particle size in the difference between the bright and dark regions; and (iv) determining the slope properties of different terrestrial surfaces and comparing them with planetary slopes derived from radar observations.

The correct interpretation of surface temperature measurements in terms of the thermal inertia (and, hence, particle size) of the surface depends on understanding the energy balance at the surface. We completed our initial analysis of the atmospheric radiative effects on the diurnal temperature behavior of the martian surface, with implications for the derivation of thermal inertia of the surface and the particle size of surface materials. In addition, we did preliminary analysis of the Phobos eclipse observations; although we did not construct the required detailed eclipse thermal model, we did some simple scaling analysis that should correctly predict the magnitude of the atmospheric correction which should be applied. The interpretation of these results in terms of the derived thermal inertia of the surface affects the inferences of particle size of the surface materials; our results suggest that the thermal inertias are lower than previously thought, and that the particle sizes are smaller. A paper on these results has been submitted to *Icarus*, and is now in press and should appear before summer (Haberle and Jakosky, 1991).

Previous work in thermal infrared emission was carried out as part of the Geological Remote Sensing Field Experiment (GRSFE). We measured the emission from various surfaces, of different roughnesses, at a variety of emission angles. A Monte Carlo model of

infrared emissivity from powdered materials has been constructed and applied to some of the results from the GRSFE experiment. The model traces individual photons through the emission process, and incorporates both emission from individual grains and scattering of energy between grains. The scattering process correctly includes the polarization of the radiation throughout the scattering and emission process. The model has been applied to the observed variation of emission from a sand surface as a function of emission angle, obtained as part of our GRSFE experiment, and reproduces the observations with no free parameters. Additionally, the model has been applied to observation of oblique emission from the Moon (as in the telescopic observations of Prof. Paul Lucey), the role of multiple scattering in affecting the observed infrared emission spectrum, and the possible polarization of thermal emission at different viewing angles. Preliminary results have been presented at the 1990 Fall A.G.U. Meeting in San Francisco (Henderson et al., 1990) and will be discussed in the context of other GRSFE analyses at a special session at the 1991 Spring A.G.U. Meeting in Baltimore (Jakosky et al., 1991). We hope to have a manuscript on these results prepared by the beginning of summer.

We have almost completed a modelling study of the role of particle size in determining the visible and near-infrared (VNIR) reflectance of the martian surface. The results were based on a comparison between martian bright- and dark-region spectra; the lack of any spectral features in the ratio of the two, except for a smooth variation from shorter to longer wavelengths, suggested that the bright and dark regions might differ primarily in their particle size and the resulting difference in scattering efficiency. We used Hapke's model of the reflectance of a surface, as a function of particle size and optical constants, to examine this possibility in two different ways. First, we used constant optical properties in order to understand the role of particle size in determining the VNIR continuum, rather than using the standard technique of drawing some sort of a straight-line continuum. Second, we used the optical constants of putative martian surface materials to directly determine the effects of varying the particle size of the surface. The results indicated that proper interpretation of the Mars spectral reflectance, and in particular interpretation of the differences in the spectra of bright and dark regions, required the incorporation of particle size variations in the analysis. Preliminary results were presented at the 1990 Fall A.G.U. Meeting in San Francisco (Alexander and Jakosky, 1990), and a manuscript is currently in preparation.

Finally, we examined the distribution of surface slopes of a number of terrestrial surfaces by field measurement, and compared the results to planetary radar data. Slope distributions of the measured surfaces differed considerably from the distributions assumed by accepted models of radar scattering. Rms slope values for the terrestrial surfaces ranged from 0 to 16.5 degrees, compared to a range of rms slope values of <1 to 10 degrees for planetary surfaces as inferred from radar observations. While the great majority of planetary surfaces observed by radar have rms slope estimates in the lower end of this range, nearly all of the terrestrial surfaces we measured have rms slope values greater than 5 degrees. We also used the Hagfors model of radar scattering to predict the return that would be expected from surfaces where two discrete surface types were present within the radar field of view, and found that the shapes of the predicted spectra differed from those predicted for homogeneous surfaces; additionally, the resulting best-fit rms slope was a non-linear combination of those of the pure surfaces, emphasizing the smoother surface. Together, these results suggest that current methods of determining surface roughness from radar significantly underestimate the roughness of planetary surfaces, and that the derived rms slope can only be used as a qualitative guide to actual surface properties. A manuscript by McCollom and Jakosky which details these results has been submitted for publication.

MINERALOGY OF THE MARTIAN SURFACE FROM MARINER 6/7 INFRARED SPECTROMETER DATA.

T.Z. Martin, Jet Propulsion Lab

The Mariner 6/7 Infrared Spectrometer experiment data from the 1969 Mars flyby encounters represent a valuable source of information about the IR reflection/emission spectrum of Mars in the 1.9 to 14.4 μm region. The author in 1989 archived a digital version of the raw data set through Planetary Data System; that data set has stimulated considerable interest for its potential to resolve mineralogical questions about the Martian surface and airborne dust. The author has continued study of the data set both to improve understanding of its calibration, and to pursue specific research goals.

During 1990, the wavelength calibration of the IRS data was completely redone, using information from inflight spectra of Mars taken through a polystyrene film and from the locations of Martian CO_2 bands. The response functions of the various wavelength channels of the two instruments were then rederived, using laboratory blackbody spectra.

Also during 1990, a particular approach was taken to study the IRS data in which the effects of uncertain wavelength and intensity calibration can be minimized. This involves doing ratios of spectra. These are of particular value when applied to study contrasts between various albedo domains on the Mars surface, and between spectra with differing emission angle. The latter provide a means of assessing the contribution of the atmosphere and airborne dust to the spectra.

In Fig. 1 we show two near-IR radiance spectra for very different albedo regions. In the 2-2.5 μm range, the brightness difference is obvious. Note, however, that beyond the 2.7 μm CO_2 band, the spectra do not differ. This region is dominated by the absorption of bound water in surface materials. It is apparent that the strength of this band does not correlate with the albedo. Thus, it is unlikely that light-colored dust has a different proportion of bound water than darker materials.

Fig. 2 shows a ratio of two spectra obtained at very different total solar pathlength (airmass). The two marked features indicate how atmospheric bands are accentuated. This technique is being applied to study the behavior of various spectral features. Fig. 3 contains a radiance spectrum covering the entire spectral range of the instrument, showing the transition from solar reflectance to thermal emission domains. Note the strong silicate absorption feature between 8 and 12 μm . This spectrum is made possible by recent attention to the problem of calibrating the IRS instruments.

An additional result is the first radiance spectra of the south polar CO_2 ice cap in the transition region (Fig. 4). Here, noise is evident near 6 μm . The behavior of the 15 μm band edge indicates a strong thermal inversion. The peak near 9.5 μm is likely due to emission by dust in the atmosphere over the cold cap.

REFERENCES: Martin, T.Z. (1990) Mariner 6/7 Infrared Spectrometer: Data Set Restoration. Submitted to *Icarus*.

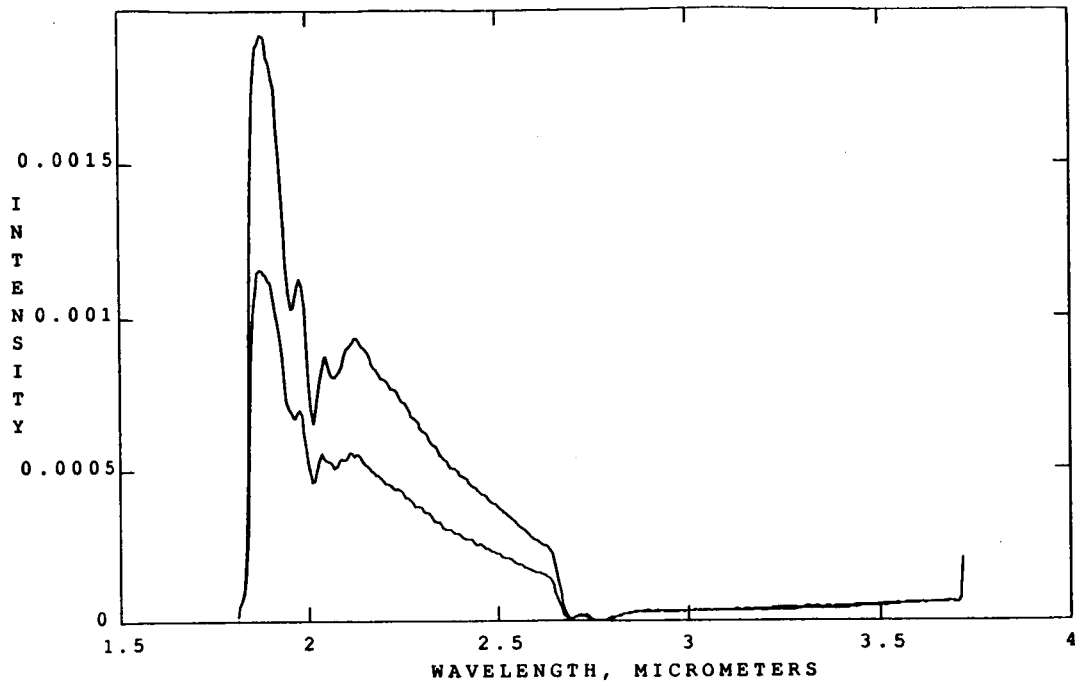


Fig. 1. Near-IR spectra with differing albedo.

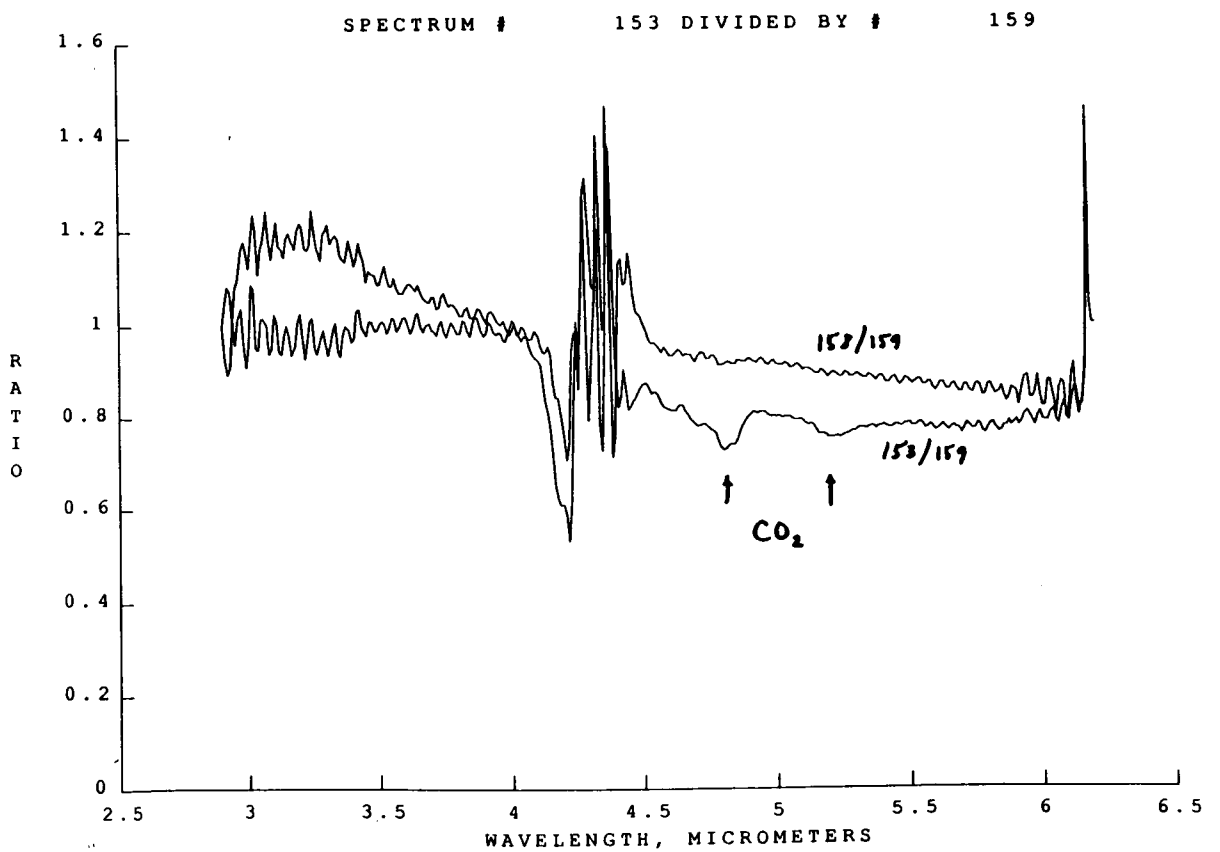


Fig. 2. Ratio spectra showing atmospheric features.

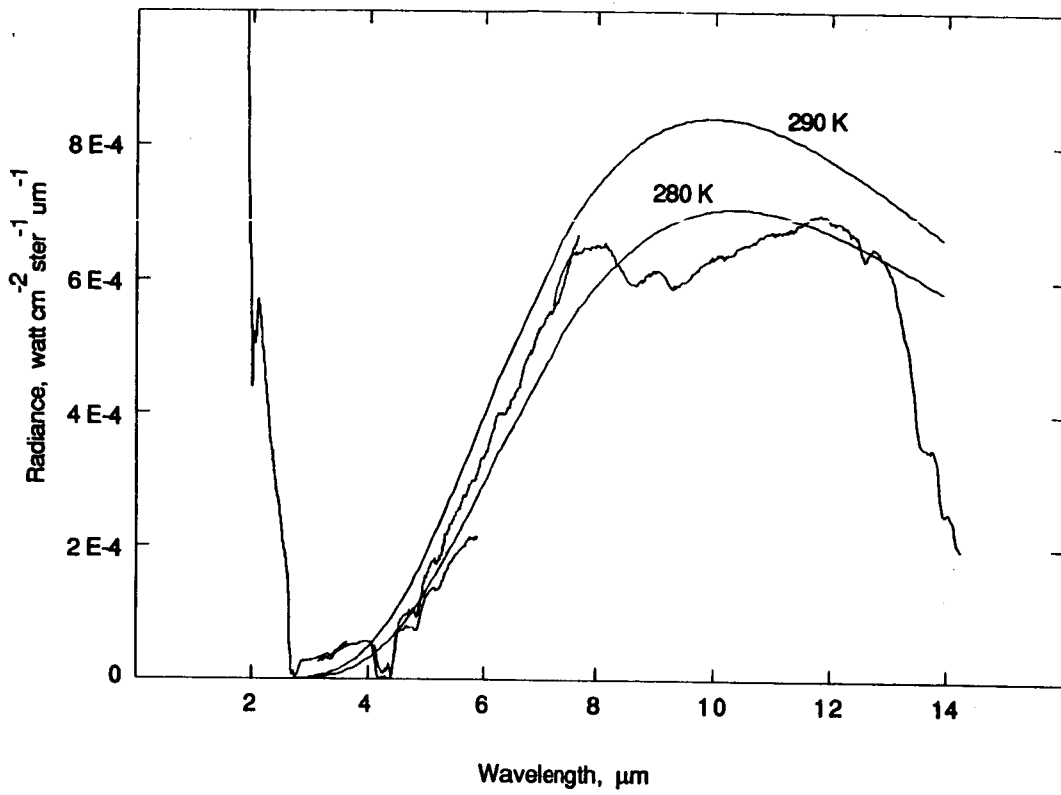


Fig. 3. Radiance spectrum - Mariner 7 #98.

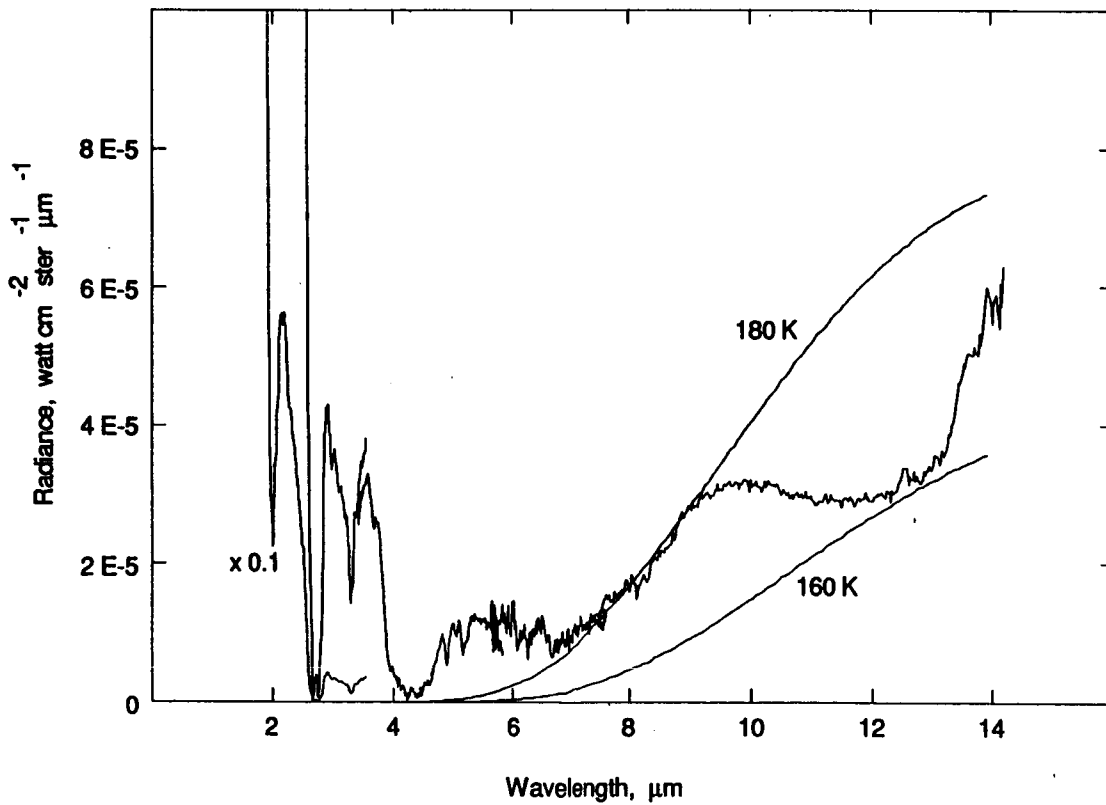


Fig. 4. Radiance spectrum of the south polar cap.

COMPOSITION OF SYRTIS MAJOR VOLCANIC PLATEAU John F. Mustard¹, S. Erard², J.-P. Bibring², Y. Langevin², J. W. Head¹, C. M. Pieters¹ (1) Dept. Geol. Sci., Box 1846, Brown University, Providence RI, 02912, (2) Institut d'Astrophysique Spatiale, Université of Paris Orsay, 91405 Orsay France

Introduction: Syrtis Major, a low relief volcanic shield centered near 295° 10°N, is an old, well preserved and exposed volcanic region on Mars (1) which formed at the end of the heavy bombardment period (2). The composition of these volcanic materials has importance for understanding the thermal and chemical history of Mars. Imaging spectrometer data of the Syrtis Major volcanic plateau are used in this analysis to identify major compositional components. These data were acquired in March 1989 by the ISM instrument onboard the Phobos-II spacecraft. Previous analyses of these data have determined that the surface is spectrally heterogeneous down to the observing limit of the instrument (3) and there exists significant compositional variation in this region (4). Band ratios sensitive to mafic mineral absorptions have been used to identify spatial associations of surface materials containing mafic minerals (4). However identification of specific mineral species, and therefore surface compositions, from the ISM data have been hindered by residual calibration difficulties. New constraints on the calibrations have significantly improved the estimates of radiometric intensities such that mineralogic and lithologic interpretations can now be made.

Data Reduction: Detailed discussions of general data reduction are presented in (4). Briefly, all well characterized instrumental, solar, and atmospheric effects are removed in a series of additive and multiplicative steps, including new corrections for the third order overlap. As part of this process an improved spectral model for Phobos, based on laboratory meteorite spectra with an additive thermal component, is used. Absolute radiometric accuracy is estimated to be 10% with the greatest uncertainty at wavelengths < 0.9 μm (3). Detailed examination of calibrated ISM data from the Isidis-Syrtis Major region indicates that there are small (1-3 %) systematic offset errors in addition to radiometric inaccuracies related to the Phobos spectral model. The offset errors are remarkably uniform and are only visible because of the extraordinary signal to noise performance ($\approx 500:1$) of the instrument (4).

To correct for these remaining calibration concerns, we use a spectral model for bright and dark regions of Mars based on the telescopic observations of (5). The ISM data for the Syrtis-Isidis window were searched to find the closest match to the spectral model in both albedo and general slope. In this calibration, the second order even channels between 0.77 and 1.51 μm are considered but we will apply this approach to the 1st order even channels between 1.6 and 3.15 μm in the future. Spectra from the matched regions are averaged and then regressed against the model spectra to determine a set of gain and offset corrections which are then applied to the entire image. Inspection of the corrected data indicates that systematic and persistent offset errors have been removed and the shape of the spectra are more consistent with the large body of telescopic data.

Results: First and second order even channel reflectance spectra between 0.77 and 2.55 μm from four broad classes of materials on Syrtis Major are shown in Figure 1. For the volcanic materials, there are three primary classes characterized by albedo, slope, and shape of the 1.0 μm band. To emphasize the latter, straight line continua have been removed from each spectral segment and replotted in Figure 2. Each spectrum shows a band minima near 0.96 μm and 2.15 μm indicative of pyroxene mineral absorptions. Comparison of these band minima with studies of pyroxene reflectance spectra suggest that the pyroxenes in the volcanics of Syrtis Major are high calcium pyroxene with a Ca/(Mg+Fe+Ca) ratio of 0.2-0.3 (6,7) and the most likely pyroxene is an augite.

Although the ISM spectra from Syrtis Major show relatively constant band minima, there are clear differences in the shape of the 1.0 μm band. Spectra for the eastern part of Syrtis Major exhibit a broadening towards shorter wavelengths probably from a ferric surface component. This area also exhibits the strongest negative spectral slopes which (8) demonstrated can be caused by thin coatings of dust or oxidized rinds on basaltic substrates. We interpret this broadening combined with large negative slopes as due to a coating of ferric bearing dust or an oxidized rind on a volcanic surface. Spatial distributions of surface materials with these spectral properties

correlate with regions of Syrtis Major with observed color on Viking orbiter color photomosaics (9) suggestive of dust or oxidized coatings. A similar distribution in spectral slope from ISM and color from Viking observed in data acquired 10 years apart tends to support that the coatings are stable, oxidized rinds rather than transient dust deposits. Spectra of Nili Patera and along the topographic axis of Syrtis Major display a broadening of the 1.0 μm band towards longer wavelengths with an inflexion near 1.15 μm . Materials common in volcanic materials with absorptions longwards of 1.0 μm include olivine, anorthite, and glass and we are currently evaluating these possibilities. The broadening towards longer wavelengths is closely related to the area of the 1.0 μm band. To illustrate spatial variations in this compositional parameter, band area calculated from the ISM data is presented in Figure 3 overlain on digital Viking Orbiter photomosaics.

The major components of the surface of Syrtis Major, which includes direct evidence for augitic pyroxene, are identified in this analysis. We are continuing the analysis to characterize additional mineral components and relationships of compositional variations to surface features.

References: (1) Schaber, G. C. (1982), *J. Geophys. Res.* 87, 9852-9866 (2) Barlow, N.G., (1988) *Icarus* 75, 285-305. (3) Bibring, J-P., *et al.*, (1989) *Nature*, 341, 591-592 (4) Erard, S. *et al.*, Spatial variations in composition of the Valles Marineris and Isidis Planitia regions of Mars derived from ISM data, (1991) (*in press*) *Proc. LPSC. 21st* (5) Singer, R. B., *et al.*, (1979) *J. Geophys. Res.* 84, 8415-8426 (6) Adams, J. B. (1974) (7) Cloutis, E. *et al* (1991) Pyroxene spectroscopy revisited: Spectral-compositional correlations and applications to geothermometry (*submitted*) *J. Geophys. Res.* (8) Singer, R. B. and T. L. Roush (1983) (abstract) in *LPSC XIV*, 708-709 (9) Soderblom L, (1991) Visible and near infrared reflectance spectra of the Martian surface (*in press*) in Mars, (Kieffer, et al, eds)

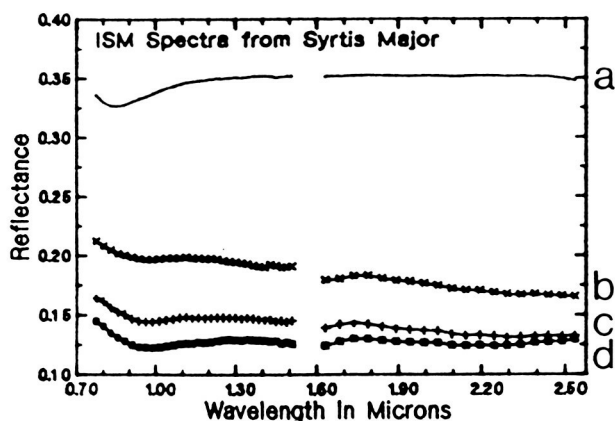


Figure 1. Spectra of major surface units in Syrtis Major. Spectra locations are shown in Figure 3. (a) Isidis (b) Syrtis East (c) Syrtis West (d) Nili Patera

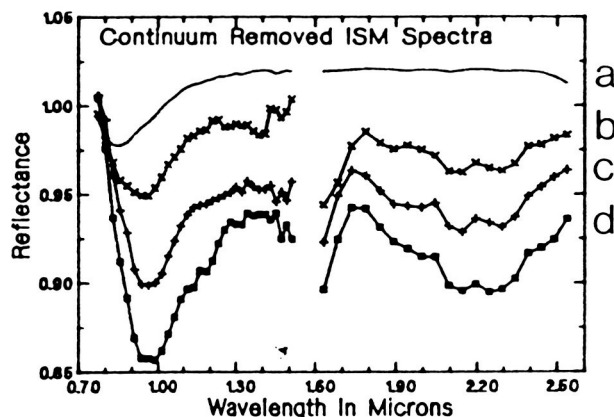


Figure 2. Same spectra as in Fig. 1 with straight line continuum removed. 0.96 and 2.15 μm band minima indicate augitic pyroxene. Broadening of 1.0 μm band in (d) suggests the presence of olivine, glass, or anorthite.



Figure 3. Area of the 1.0 μm ferrous absorption bands of Syrtis Major calculated from ISM data. A simple straight line continuum was fit to the reflectance data and the area is the sum of the difference between the continuum and the spectra. Note that the materials along the topographic axis of Syrtis Major contain the strongest absorptions and the eastern part of Syrtis Major has weaker absorptions than the western part. Data dropouts are indicated as the bright rectilinear areas.

THE PERPLEXING CONTINUUM SLOPE OF MARS: EFFECTS OF THIN FERRIC COATINGS AND VIEWING GEOMETRY; Erich M. Fischer, Carle M. Pieters and Stephen F. Pratt, Department of Geological Sciences, Brown University, Providence, RI 02912.

Introduction: One of the most interesting and perhaps most perplexing features of martian reflectance spectra is a decrease of reflectance toward long wavelengths observed for many surface terrains. This spectral feature (hereafter referred to as the continuum slope) is most commonly associated with darker martian materials and has been observed both with spot-reflectance techniques (e.g., 1) and also with the French imaging spectrometer, ISM, experiment aboard the Phobos spacecraft (2). Although atmospheric dust may contribute somewhat to the slope of some martian spectra (3), it has convincingly been shown that thin ferric coatings on dark basaltic substrates produce slopes in the laboratory similar to what is observed for Mars (4). The goal of the present study is to evaluate the effects of ferric coatings more thoroughly and determine whether differences in viewing geometry, in addition to variations of the ferric coating thickness, produce continuum slopes comparable to those observed for Mars. The experiment was designed to constrain interpretations of variations in continuum slope observed for Mars, specifically the continuum slope variations which define several spectral annuli on the flanks of Olympus Mons, observed in the ISM imaging spectrometer data. The ISM Olympus Mons data reveal that the rings, seen as alternating brighter and darker reflectance in Viking data, correspond to annuli of alternating shallower and steeper continuum slope (5).

Experimental procedure: Small slabs of identical thickness were cut from the interior portion of a large hand sample of basalt from Taos, New Mexico. The slabs were roughened with 400 grit to minimize diffraction from irregularities on the surface and then ultrasonically cleaned. Spectra were obtained of several slabs cut from different areas of the rock to ensure that the spectral properties of the hand sample were spatially constant. All spectra were obtained with the RELAB spectrometer at Brown University (6).

Hematitic material from Mauna Kea, Hawaii was crushed and wet sieved to <25 micron size and then suspended in ethanol to separate very fine grains from the bulk. The collected suspension average grain size was 2-3 microns. Different thicknesses of ferric coating were deposited on the basalt slabs by suspending different amounts of the ferric material in ethanol and then pouring the suspension into a container in which the grains settled evenly onto a slab as well as a glass slide as the ethanol evaporated. Using a binocular petrographic microscope, coating thickness was calculated by first focussing upon the surface of the coating deposited on the glass slide, then focussing upon the surface of the slide itself at the bottom of a knife-edge scribe in the coating and measuring the vertical distance between the two points of focus. After the samples were prepared, spectra were taken at several different viewing geometries (both forward and backward scattering) listed in the table below. Letters (a-i) refer to spectra presented in Figures 1 and 2 and for data obtained at those parameters.

Coating thickness (μm)	Viewing geometry (incidence, emergence, phase)				
	30,0,30	30,60,30	0,60,60	55,40,15	40,-50,90
0	a	x	x	x	x
4.3	b	x	x	x	x
6.3	c				x
11.0	d	x	x	x	x
17.3	e				
37.5	f				x
225.0	g	h	x	x	i

Results: Several factors involved in the cause of continuum slope (calculated as the change of reflectance per micron between 1.68 and 2.48 microns) are identified in this study. First, differences in thin ferric oxide coating thickness contribute to variations of continuum slope. Spectra of several different thickness samples measured at the standard RELAB viewing geometry, $i=30^\circ$ $e=0^\circ$, are shown in Figure 1 along with the spectrum of a loose powder of the ferric material. The continuum slope is thought to occur because the ferric coating is transparent at longer wavelengths (4). Therefore, with optically thin coatings, the dark underlying basalt dominates the long wavelength region of the spectrum while the bright ferric powder dominates the short wavelength region. Together, these account for the decrease in reflectance toward longer wavelengths. Note in Figure 1 that as the thickness of sample increases, the slope becomes more negative until the ferric coating starts to become optically thick at long wavelengths.

The continuum slope of a sample is also affected by several variables associated with surface texture and viewing geometry. Perhaps the most intriguing contributor to negative continuum slope appears to be differential forward scattering. In Figure 2 are shown spectra of a sample with an optically thick ferric coating (225 microns of coating thickness) measured at several different viewing geometries. Note that two of the

THE CONTINUUM SLOPE OF MARS: Fischer, E. M. et al.

spectra (h and g) both exhibit a negative continuum slope, whereas the continuum of the spectrum at a forward scattering geometry (i) is almost flat. As the coating is optically thick, transparency at long wavelengths of thin ferric coatings on a dark substrate cannot explain the continuum slope. Instead, for the thick ferric coating there appears to be an increase in forward scattering (and a decrease in backscatter radiation) at longer wavelengths. This results in a negative continuum slope when observed from backscatter geometries. Variations of continuum slope are also observed for samples with prepared differences of surface texture (packed versus loose), suggesting that surface texture, forward scattering and continuum slope are interrelated. The smooth textural nature of the ferric coatings (a crust created by liquid settling when producing the more thickly coated samples) clearly influences the continuum slope at backscattering geometries. Further analysis of the textural effects on continuum slope and the possible link to duricrust on Mars is underway.

In summary, at least three factors contributing to continuum slope can be identified in this study – ferric coating thickness, viewing geometry, and surface texture. Because the Olympus Mons spectral annuli were observed at nearly constant backscatter geometries in the ISM data, with only slight viewing variations due to the volcano's flank slopes, the difference of continuum slope between annuli probably cannot be explained by viewing geometry alone. This suggests that the variation of some fundamental surface characteristic(s), such as ferric dust/rind thickness or surface texture, is the cause of the Olympus Mons spectral annuli observed in the ISM imaging spectrometer data. Further studies currently underway include an examination of the effects on continuum slope of different particle size ferric dust, ferric rinds and coating texture. The primary objective is an in depth exploration of the geologic significance of the spectral annuli around Olympus Mons.

Acknowledgements: This material is based upon work supported under a National Science Foundation Graduate Fellowship. RELAB is supported by NASA as a multi-user facility under grant NAGW-748.

References: 1) McCord, T. B. et al. (1982) *JGR* 87, 3021; 2) Bibring, J.-P. et al. (1989) *Nature* 341, 591; 3) Erard, S. et al. (1991) *Proc. LPSC XXI*, in press; 4) Singer, R. B. and T. L. Roush (1983) *LPSC XIV*, 708; 5) Fischer, E. M. et al. (1990) *Brown/Vernadsky Micro. 11*; 6) Pieters, C. M. (1983) *JGR* 88, 9534.

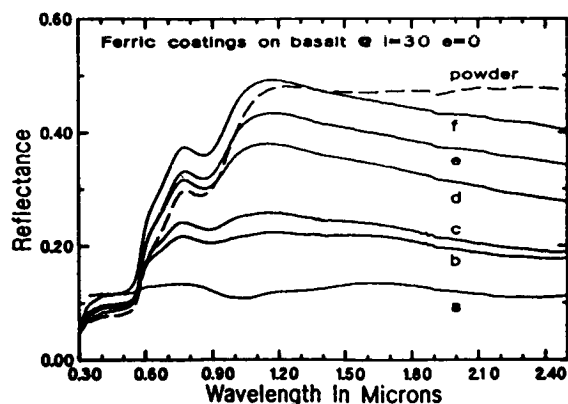


Fig. 1: Spectra of loose ferric powder and of various thicknesses of ferric coating on basalt at $i=30^\circ$ $e=0^\circ$. Letters refer to the table on the previous page.

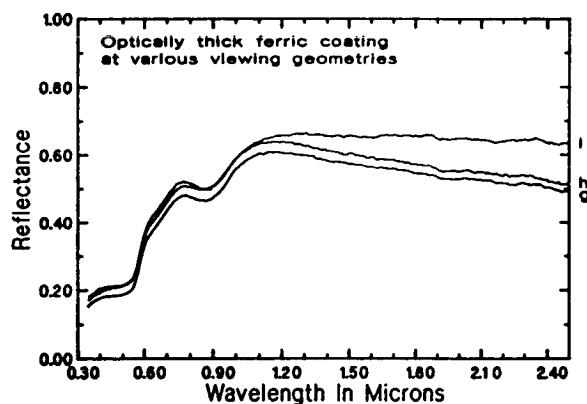


Fig. 2: Spectra of an optically thick ferric coating on basalt at various viewing geometries. Letters refer to the table on the previous page. Spectrum i is at a forward scattering geometry.

OXIDATION OF BASALTIC TEPHRAS: INFLUENCE ON REFLECTANCE IN THE 1 μ m REGION

William H. Farrand and Robert B. Singer, Planetary Image Research Laboratory, LPL, University of Arizona, Tucson, AZ 85721

Vitric basaltic glasses* are widespread on the Earth, Moon and Mars as well. On Earth, basaltic ashes resulting from Strombolian fire fountaining are prominent at such volcanic centers as Hawaii and Iceland. Basaltic tephtras can also result from hydrovolcanic activity [1]. To distinguish these tephtras from those formed in anhydrous eruptions they can be referred to as *hydroclastic* materials [2]. The dark mantling deposits of the Moon [3], presumed to be the product of Strombolian fire fountaining, are formed of basaltic glasses. Given the Moon's reduced state, these ashes never alter. However, on Mars, as on the Earth basaltic glasses are susceptible to alteration. Indeed, the alteration product of sideromelane, palagonite, is thought by many to be a major component in Martian dust [4,5]. Possible extensive deposits of unaltered basaltic ash, perhaps rich in tachylite, have also been identified in Valles Marineris on Mars [6].

Pristine basaltic hydroclasts are composed dominantly of sideromelane. Sideromelane alters via a process of hydration and oxidation to the mineraloid palagonite. In the current instance, we are concerned solely with the oxidation process. The best way to track the process of oxidation is in the transformation of iron from the ferrous to the ferric state, and an ideal tool for tracking that transformation is visible and near infrared (Vis/IR) spectrometry.

As part of an ongoing study into the products of hydrovolcanism, tuffs were examined from the Cerro Colorado and Pavant Butte tuff cones. The former resides in the northeastern corner of the Pinacate Volcanic Field in Sonora, Mexico and the latter is in the Black Rock Desert of southern Utah. Numerous samples were collected and many of these had their Vis/IR reflectance measured at Brown University's RELAB facility [7].

Figures 1a and 1b show spectra from Cerro Colorado and Pavant Butte respectively. The high reflectance spectra in each of the aforementioned figures are oxidized palagonite tuffs. The low reflectance spectra are unoxidized sideromelane tuffs. Evident in both sets of spectra are absorption features in the 1 μ m region. The low reflectance of the sideromelane tuffs presents the illusion that their "1- μ m" absorptions are weaker than the palagonite tuffs, but in fact the reverse is true.

The primary cause of the "1- μ m" feature in the sideromelane tuffs is Fe^{2+} in octahedral sites within the sideromelane producing a crystal field absorption. The 1- μ m feature is a characteristic feature of such ferrous iron bearing minerals as olivine, pyroxene and even plagioclase. Indeed, point counts of thin sections indicate that approximately 10% of the sideromelane tuffs are discrete crystals, predominantly plagioclase with lesser amounts of olivine and clinopyroxene. Certainly these phases contribute to the observed 1 μ m absorption, but are not by any means the primary cause.

The cause of the 1- μ m feature in the palagonite tuffs is less well constrained. Ferric iron phases have an absorption in the 0.86 to 0.93 μ m region caused by the ${}^6A_1 \rightarrow {}^4T_1$ [8]. For hematite this band occurs at 0.86 μ m, for goethite (α -FeOOH) at about 0.90-0.93 μ m. As can be seen in Figure 2, some of the most oxidized tuffs from Cerro Colorado have band centers at about 0.92 μ m. In thin section, the primary sideromelane in these tuffs has altered almost completely to palagonite. Thus one could be tempted to say that the ferric iron bearing phase is goethite; however, the 0.63 μ m band characteristically associated with goethite is not present. It seems likely that for most of the palagonite tuffs the 1- μ m feature is in fact a composite band formed by contributions from ferrous and ferric iron phases.

Figure 2 shows the band depth [9] of the 1- μ m feature versus band center for 21 samples from Cerro Colorado and Pavant Butte. This figure clearly displays the shift in band center from the unoxidized sideromelane tuffs to the oxidized palagonite tuffs. Less striking, but also noticeable is a decrease in band depth with increasing oxidation. Band width also tends to decrease with increasing oxidation. The shorter band center and decrease in band width are indicative of the increasing influence of ferric over ferrous iron mineralogies. However, the decrease in band depth seems to indicate that some of the ferrous iron which had been contributing to the 1- μ m band in the sideromelane tuffs is no longer contributing to the equivalent shorter wavelength band in the palagonite tuffs. This makes sense in two regards. First, unlike the absorption produced by ferrous iron, Fe^{3+} bands are spin forbidden and thus are inherently weaker than the equivalent ferrous 1- μ m band. Secondly, ferric iron mineralogies in palagonite can be "nanocrystalline"; i.e. with grain

* Clear vitric basaltic glass is known as sideromelane, devitrified glass as tachylite.

sizes less than 10 nm. In such cases the 0.86 or 0.89 μm band for hematite or goethite disappears [10]. Therefore, it seems likely that in the palagonite tuffs there is a combination of nanocrystalline ferric oxide phases contributing to the UV absorption edge but not to the 1- μm band, plus more crystalline ferric oxides which do contribute to that band as well as ferrous iron within unaltered sideromelane which is skewing the band center to longer wavelengths.

This work has obvious implications for spectroscopic observations of Mars. As was noted earlier, basaltic tephra are believed to be an important surface material on Mars. Likewise recent observations of Mars [11,12] have shown there to be absorptions in the same wavelength region being discussed here. The present work indicates that when ferrous and ferric iron phases are both present their combined spectral contribution is a single band in the vicinity of 1 μm . The center, depth and width of that feature has the potential to be used to gauge the relative proportions of ferrous and ferric iron phases. Certainly, this is an area where laboratory work examining the oxidation of artificial, or hand picked natural, glasses would prove fruitful.

REFERENCES: [1] Wohletz K.H. and Sheridan M.F. (1983) *Am.J.Sci* 283, 385-413. [2] Fisher R.V. and Schmincke H.U. (1984) *Pyroclastic Rocks*. [3] Head J.W. (1974) *PLSC* 5, 207-222. [4] Evans D.L. and Adams J.B. (1979) *PLPSC* 10, 1829-1834. [5] Singer R.B. (1982) *JGR* 87, 10159-10168. [6] Geissler P.E. et al. (1990) *JGR* 95, 14399-14413. [7] Mustard J.F. and Pieters C.M. (1989) *JGR* 94, 13619-13634. [8] Morris R.V. et al. (1985) *JGR* 90, 3126-3144. [9] Clark R.N. and Roush T.L. (1984) *JGR* 89, 6329-6340. [10] Morris R.V. and Lauer H.V. (1990) *JGR* 95, 5101-5109. [11] Bell J.F. et al. (1990) *PLPSC* 20, 479-486. [12] Singer R.B. et al. (1990) *Bull.Am.Astron.Soc.* 22, 1061.

Fig. 1: Reflectance spectra of tuffs from Cerro Colorado and Pavant Butte. In each figures, the palagonite (top) and sideromelane (bottom) tuff occurred beside each other in outcrop. Arrows indicate band center.

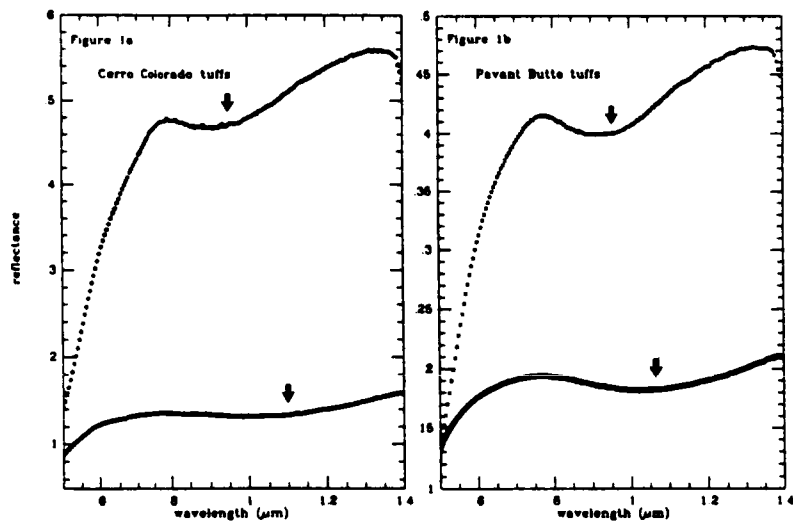
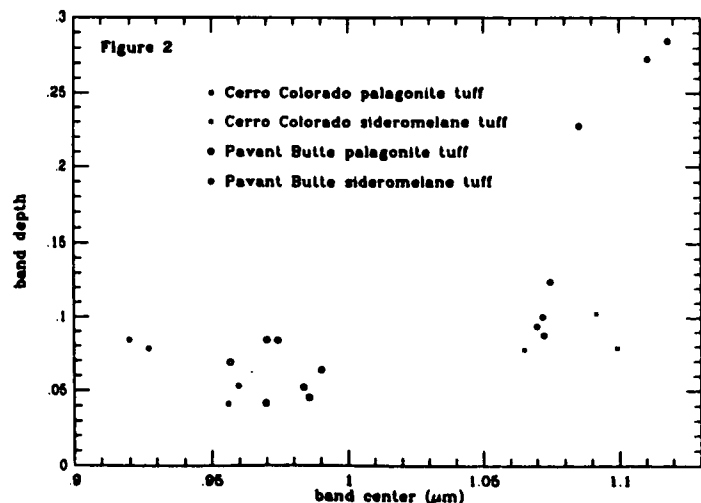


Fig. 2: Plot of band depth vs. band center. Palagonite tuffs cluster on the lower left and sideromelane tuffs on the right. The most highly oxidized tephra (shortest band centers) are from Cerro Colorado. The least oxidized tephra (longest band centers, deepest band depths) are from Pavant Butte. The 3 sideromelane tuffs in the upper right hand corner represent an earlier phase of the Pavant Butte eruption than those in the lower right.



SPECTROSCOPIC ANALYSES OF FE AND WATER IN CLAYS. A MARTIAN SURFACE WEATHERING STUDY; J. L. Bishop, C. M. Pieters and J. O. Edwards, Brown University, L. M. Coyne, San Jose St. Univ. and S. Chang, NASA-ARC, Moffett Field, CA

Martian surface morphology suggests the presence of liquid H₂O on Mars in the past.¹ Visible and NIR reflectance spectra of the Martian surface include features which correspond to the crystal field transitions of iron², as well as features supporting the presence of ice and minerals containing structural OH and surface water.³ Clays have been associated with the Martian surface through reflectance spectroscopy and the Viking chemistry and biology experiments.^{4,5} We have initiated further spectroscopic studies of surface iron and water and structural OH in clays in order to determine what remotely obtained spectra can indicate about the presence of clays on Mars based on a clearer understanding of the factors influencing the spectral features. Vibrational spectroscopy of minerals has involved in the past either the diagnostic Near-Infrared (NIR) or the fundamental Mid-IR regions. Current technology allows us to better correlate the low frequency fundamental stretching and bending vibrations of O-H bonds with the diagnostic water NIR overtone and combination bands used in mineral characterization and identification.

The spectral features in clays near 1.4, 1.9 and 2.2 μm are comprised of multiple overlapping peaks which vary as a function of octahedral cation and bond strength of structural OH and adsorbed water molecules.^{6,7,8} Therefore, understanding these vibrations in minerals requires understanding the chemical environment of water molecules and hydroxyl groups in minerals. Extensive H-bonding in water lowers the vibrational energy of the stretching and bending frequencies. Bound water induces broadening of the absorption features as the vibrational energies become widely distributed. The interlayer cations also affect these fundamental vibrations by interacting with the water molecules (e.g. forming cation-water clusters⁹) and by migrating into the hexagonal hole of the silicate layer.^{7,10} (for example) In order to more accurately understand the effect of clay composition on the shape of the 1.4, 1.9 and 2.2 μm features, we are examining a series of montmorillonite samples prepared with varying quantities of exchangeable iron and water.

SWy-1 montmorillonite was obtained from the Clay Mineral Society, Source Clays Repository as a starting material. The naturally present Ca and Na interlayer cations were then exchanged chemically with varying amounts of Fe, Ca, Na and H according to the Banin method.² Due to the swelling properties of smectite clays the interlayer regions can accommodate exchange values above the normal 100% cation exchange capacity (CEC). The clays were dried through lyophilization, ground by hand and then sieved to < 125 μm particle size. X-Ray fluorescence analysis was performed to enable us to make quantitative correlations of the composition with spectral features. Spectra were measured using the RELAB (reflectance experiment laboratory) at Brown University (0.3 - 3.6 μm) and a Nicolet 740 FTIR (the 1 - 5 μm range was measured using a PbSe detector and the 2 - 25 μm range using a TGS detector). Nicolet spectra were measured against KBr and the sample chamber can be purged with water-free air. RELAB spectra were measured using a halon standard and were obtained under ambient atmospheric humidity.

Initial spectra have been obtained with the Nicolet and the band shape and position of spectral features in the NIR and Mid-IR overlap regions correlate well (Fig.1). A spectrum of the 100% Fe-clay (Fig.1) shows the stretching (ν) and bending (δ) vibrations for structural OH and bound water¹¹: ν_{OH} (2.75 μm), ν_{w} (~3 μm), δ_{w} (~6 μm), δ_{OH} (11-12 μm) and the NIR overtone and combination water bands⁶: $2\nu_{\text{OH}}$ (1.41 μm), $\nu'_{\text{w}} + 2\delta_{\text{w}}$ (1.41 μm), $\nu_{\text{w}} + 2\delta_{\text{w}}$ (1.45 μm), $\nu'_{\text{w}} + \delta_{\text{w}}$ (1.91 μm), $\nu_{\text{w}} + \delta_{\text{w}}$ (1.97 μm), $\nu_{\text{OH}} + \delta_{\text{AlOH}}$ (2.2 μm). (ν'_{w} indicates the stretching vibration of residual interlayer water molecules and has an energy slightly less than ν_{OH}). Fig.2 shows NIR spectra of 300% Fe-exchanged montmorillonite obtained using a) Nicolet, purged, b) Nicolet, unpurged and c) RELAB. Slight increases in moisture content from a) to c) exemplify the differences in character of the water represented in the peaks and shoulders of the NIR features. For example, the growth of the 1.9 μm peak relative to the 1.4 μm peak implies that the 1.9 μm peak has more bound water

character. Fig.3 shows significant variability in the shape of ν_w (bound water stretching vibration) as a function of interlayer cation for the exchanged clays (spectra measured under purged conditions with the Nicolet FTIR): the sharper portion of the peak represents structural OH and residual water, while the broader portion near 3 μm represents molecular water with significant H-bonding. These spectra show the strong effects that interlayer cations have on the stretching vibrations of interlayer water. Shown in Fig.4 are the crystal field Fe transitions near 0.9 μm and the diagnostic NIR features of a) 100 % Fe-clay, b) 200 % Fe-clay, c) 300 % Fe-clay and d) 600 % Fe-clay (spectra measured with the RELAB spectrometer). The 1.4, 1.9 and 2.2 μm features are all suppressed in the 600 % Fe-clay relative to the others. The larger amount of Fe in this sample was verified through XRF and is shown spectroscopically by the deep Fe crystal field band. A similar reversal in band intensity in the NIR water features has been observed in other highly exchanged Fe-montmorillonite,¹² which suggests a complex Fe-water relationship in Fe-rich clays. Our initial spectra show variability in the fundamental stretching and bending vibrations of surface water as a function of surface cation. More detailed analyses will explore the effects of these cations on the NIR combination and overtone bands.

Acknowledgements: Support through the NASA Graduate Student Researchers Program at NASA-ARC, Moffett Field, is greatly appreciated by J. Bishop. RELAB is a multi-user facility supported by NASA under grant NAGW-748. The authors also wish to thank Joachim Hampel of U.C., Berkeley and Dorothy Bishop of the LLNL, Livermore, CA for the XRF analyses.

References: ¹Carr, M.H. (1979) *The Surface of Mars* (New Haven: Yale University Press). ²Singer, R.B., et al. (1979) *J.G.R.* 84: 8415-26. ³McCord, T.B., R.N. Clark and R.L. Huguenin (1978) *J.G.R.* 83:5433-41. ⁴Toulmin, P., et al. (1977) *J.G.R.* 82:4625-34. ⁵Banin, A., G. Carle, S. Chang, L. Coyne, J. Orenberg and T. Scattergood (1988) *Origins of Life* 18: 239-65. ⁶Cariati, F., L. Erre, G. Micera, P. Piu and C. Gessa (1983) *Clays Clay Miner.* 31: 447-9. ⁷Sposito, G., R. Prost and J.-P. Gaultier (1983) *Clays Clay Miner.* 31: 9-16. ⁸Coyne, L., J. Bishop, T. Scattergood, A. Banin, G. Carle and J. Orenberg (1990) in *Spectroscopic Characterization of Minerals and Their Surfaces*, ed. L.M. Coyne (Washington, D.C.: Am. Chem. Soc.). ⁹Fripiat, J. (1980) in *Advanced Chemical Methods for Soil and Clay Minerals Research*, eds. Stucki, J. W. and W. L. Banwart (Reidel Publishing Co.: Dordrecht, Holland). ¹⁰Farmer, V. C. and J. D. Russell (1971) *Trans. Faraday Soc.* 67: 2737. ¹¹Grim, R. E. and G. Kulbicki (1961) *Amer. Miner.* 46: 1329-69. ¹²Coyne, L. M., J. L. Bishop and T. Scattergood (1990) submitted to *J.G.R.*

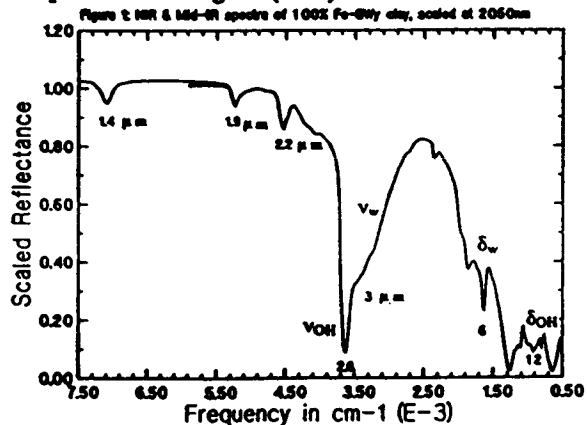


Figure 1: NIR & Mid-IR spectra of 100% Fe-SWy clay, scaled at 2000cm

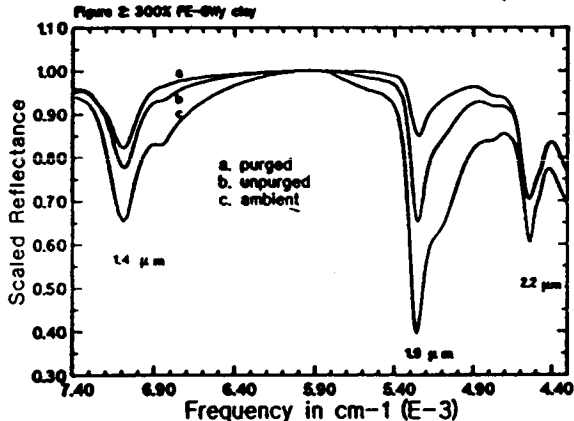


Figure 2: 300% Fe-SWy clay

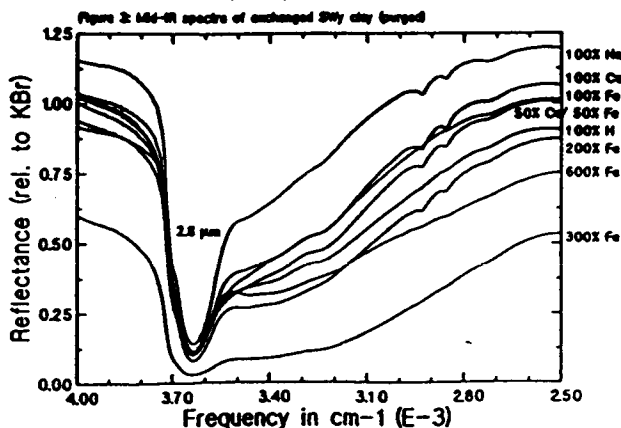


Figure 3: Mid-IR spectra of exchanged SWy clay (purged)

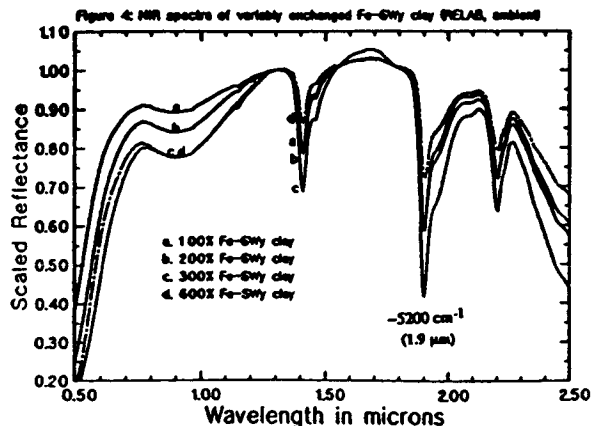


Figure 4: NIR spectra of variably exchanged Fe-SWy clay (RELAB, ambient)

WATER DETECTION AT THE MOON, MARS AND COMETS WITH A COMBINED NEUTRON-GAMMA RAY INSTRUMENT

Albert E. Metzger, Jet Propulsion Laboratory, Pasadena, CA 91109
and Eldon L. Haines, Sunrise Research Inc., Eugene, OR 97404

Measuring the fluxes of thermal and epithermal neutrons at a planetary object in conjunction with gamma-ray spectroscopic observations will provide information about the chemical composition of the surface which is less model-dependent than the gamma-ray measurements by themselves. We have devised a passive neutron detector for this purpose. The detector employs only two dissimilar layers of material added to a gamma-ray spectrometer. An outer layer containing samarium or cadmium absorbs most of the incident thermal neutrons, while an inner layer containing boron absorbs many of the epithermal neutrons. The neutron absorbers emit characteristic gamma rays which are measured by the gamma-ray spectrometer. Neutrons which are partially moderated in planetary materials and leak back into space may be detected and characterized by such a passive neutron detector, augmenting the compositional information gathered by the gamma-ray spectrometer and offering new information other instruments cannot provide. The neutron detector is particularly sensitive to small changes in the neutron flux produced by the presence of hydrogen as in water. It is thus also well suited to detecting and mapping small amounts of water which may be trapped near the lunar poles, searching for permafrost on Mars, and supplementing a gamma-ray spectrometer's measurement of elemental composition from orbit or in a comet nucleus via a penetrator.

An experimental model of this passive neutron detector was designed and built. Neutrons for the experiments were generated by a small Cf-252 source having a strength of about 30 microcuries. The Cf-252 source was centered in a five liter spherical flask filled with water to moderate the fast (≈ 2 MeV) fission neutrons. The 83 cm³ high-purity Ge detector and its mounting assembly were mounted vertically on a liquid nitrogen cryostat. Pulse-height data were recorded from each experiment for subsequent analysis of the Sm, B, H, and calibration lines. Three variables provided the basis for the set of experiments: 1) thickness of the Sm and B layers, 2) presence or absence of the ACS, and 3) position of the source relative to the PND's cylindrical axis.

Six experiments were performed to test the effects of Sm thickness, source position, and presence of the ACS. Three simulation models, based on different assumptions about the incident neutron fluxes, were applied to each set of experimental count rates. A simulation code was created to account for the perturbations to the incident neutron flux caused by the PND through absorption, scattering, and escape processes (1). The code tallies the effects of each event at each energy level and follows those neutrons which lose energy through scattering with H.

We observed that the Sm and B layers absorbed more neutrons than expected from calculations of normally incident neutrons on non-scattering media, and accounted qualitatively for these enhancements in terms of the distribution of incident angles and the scattering properties of the PND

and ACS. An analysis of the simulation model showed it to be inadequate in accounting for these factors. The model was empirically corrected with the experimental data and shown to work moderately well.

The empirically corrected model was used to derive a transfer function for the PND. The transfer function was applied to assumed thermal and epithermal neutron leakage fluxes from the Moon and from Mars, and to the subsurface flux of a comet nucleus, in order to calculate the expected gamma-ray count rates from a PND employed in missions to those three bodies. From the statistics of those count rates we derived water sensitivities from the measurement of neutron fluxes and gamma rays. The uncertainties in element concentrations, especially those of Fe, Ti, and the rare-earth elements, impact the sensitivity of the neutron measurements. The simultaneous application of the PND and GRS permits the improvement of both the neutron flux and element concentration determinations. The PND's sensitivity for determining H is 40 times better than that derived from a H gamma-ray signal in orbit at the Moon and 15 times better at Mars. For a comet probe, the PND provides no sensitivity advantage for water relative to the GRS, but is still valuable in finding the thermal and epithermal neutron fluxes for determining element concentrations.

REFERENCE: Metzger, A. E. and E. L. Haines, Reports of Planetary Geology and Geophysics Program-1987, NASA TM 4041, p. 213-5 (1988).

SPECTRAL EVIDENCE FOR CARBONATES ON MARS: HYDROUS CARBONATES W. M. Calvin, and T. V. V. King, U. S. Geological Survey, Denver

The presence of carbonates on Mars has long been argued based on the abundance of CO₂ in the atmosphere and geomorphological evidence of fluvial features. Numerous spectral searches have repeatedly failed to find evidence of carbonates (most recently by Blaney and McCord [1] and references therein). Recently Pollack *et al.* [2] report evidence of carbonate spectral features near 6.7 μm and on the shorter wavelength side of the atmospheric absorption at 7.3 μm, but assign no specific mineralogy to the features.

An extensive re-analysis of the Mariner 6 and 7 spectrometer data in the wavelength region from 2 to 6 μm (Calvin and King [3]) identified several new absorption features not noted in terrestrial observations, particularly a potential hydroxyl feature at 2.76 μm. Unfortunately this band occurs in the middle of strong atmospheric CO₂ features, but is also indicated in non-atmosphere removed spectra.

Laboratory reflectance measurements from 2.5 to 25 μm of several types of hydrous carbonates presented by Miyamoto and Kato [4] indicated that these minerals are likely candidates for the features identified by Calvin and King [3], as well as by Pollack *et al.* [2].

We have measured the spectral reflectance of 3 samples provided by M. Miyamoto (University of Tokyo) in the spectral region from 0.2 to 25 μm and find that these samples have additional spectral characteristics that make them plausible candidates for the martian surface. We have measured two samples of hydromagnesite (Mg₅(CO₃)₄(OH)₂·XH₂O) and one of artinite (Mg₂(OH)₂CO₃·3H₂O). An additional sample of artinite provided by Gene Foord (U. S. Geological Survey) was also measured.

These samples are unique in that they do not exhibit the strong absorption features typically associated with carbonates [1,4,5,6]. That is, typical carbonate bands from 2.2-2.5 μm, from 3.2-3.6 μm, and from 3.8-4.1 μm, which are usually extremely strong, are only weakly present, if at all, and are shifted in wavelength. It is not necessarily that these samples are Mg-bearing, but the fact that they contain H₂O and OH in the crystal structure that gives them their unique spectral characteristics. (Although the presence of Mg may help to bind water to the structure during formation [7].) The presence of water gives these minerals broad adsorbed water bands near 3 μm, and washes out the typical CO₃ absorption features.

Both the hydromagnesite and the artinite have absorption features near 6.7 μm. In addition the hydromagnesites have a feature that occurs from 7.1-7.2 μm, depending on the sample. The location of these features is consistent with features reported by Pollack *et al.* [2], and attributed to CO₃.

All the samples have broad adsorbed water bands, consistent with the Mariner 6 and 7 data, although this is not a unique indicator of mineralogy. In addition, the artinite sample has a hydroxyl feature at 2.76 μm that correlates extremely well with that seen in atmosphere-removed spectra of Calvin and King [3]. As stated previously, this band can not be definitively identified due to possible difficulties in removing the model atmosphere. However, when the laboratory reflectance spectra are convolved to the Mariner instrument resolution and multiplied by the atmospheric transmission, the resulting spectra are extremely similar to the Mariner spectra. The hydroxyl feature in the artinite only broadens the atmospheric band near 2.78 μm, no separate feature can be discerned.

Spectral measurements from 2.25-2.45 μm, indicated that there are additional mineralogical features in this spectral region [8]. Much of this wavelength region is confused by the signature of atmospheric CO, and the exact contribution of the atmosphere to the observed spectra does not appear to be well determined [9, 10].

HYDROUS CARBONATES ON MARS: Calvin and King

However, between 2.26 and 2.30 μm all the atmospheric models indicate that there is no atmospheric interference. Here, there is absorption feature centered on 2.28 μm [8]. This band has been associated with the mineral scapolite [8]. Our new spectral measurements indicate that this band is also well correlated with a feature in the spectrum of artinite and with a feature in hydromagnesite. The artinite has only the feature at 2.28 μm while the hydromagnesite has several features in this region. The strongest features in the hydromagnesite occur between 2.32 and 2.36 μm , depending on the sample. This latter region is obscured in the spectra of Mars due to atmospheric CO.

The only other strong features in the hydrous carbonates we have measured occur at 1.4 and 1.9 μm . Features in this region are unlikely to be observed from terrestrial observations because of atmospheric interference by water, and the Mariner spectra do not extend to short enough wavelengths. It is unknown if the PHOBOS/ISM experiment has the spectral resolution to characterize absorptions in these regions. In addition water in the martian atmosphere will also tend to obscure these bands.

The hydrous carbonates exhibit a spectral downturn in the visible, beginning about 0.5 μm , again consistent with observed Mars spectra, but not a unique indicator of mineralogy. This downturn would likely be obscured due to the presence of abundant Fe-oxides on the surface which also have strong spectral downturns in the visible.

Hydrous Mg-carbonates form terrestrially as weathering products in aqueous environments often at low temperature [11]. Artinite and hydromagnesite occur along with coalingite ($\text{Mg}_{10}\text{Fe}_2\text{CO}_3(\text{OH})_{24}\cdot 2\text{H}_2\text{O}$) in the surface weathering zone of a California serpentinite [12]. In addition, hydromagnesite and nesquehonite ($\text{Mg}(\text{HCO}_3)(\text{OH})\cdot 2\text{H}_2\text{O}$) have been identified as weathering products on Antarctic meteorites [13]. The exact formation mechanism on the meteorites is not yet well known [14], but one suggestion is that olivine weathers to nesquehonite and Fe-oxides such as goethite [12]. The stability of these minerals in the current martian environment is unknown. The current surface temperatures of Mars are compatible with the low-temperature, most hydrated phases, but the low atmospheric water abundance may lead to dehydration. Obviously more work is required to determine the stability of such minerals in the martian environment.

In summary, although many of the spectral features are not unique mineralogical indicators, much of the current spectral data is consistent with (possibly abundant) hydrous carbonates on the surface of Mars. The absorption features in the samples we have measured are quite weak compared to those of anhydrous carbonates. The weak features imply that significantly more hydrous carbonates can be incorporated onto the surface before becoming spectrally evident; however exact limits have yet to be determined. The stability of these minerals in the martian environment is not known, but their formation and occurrence in low-temperature terrestrial environments makes them appealing candidates for weathering products on Mars.

- [1]Blaney and McCord, 1989. *J. Geophys. Res.*, **94**, 10159-10166. [2]Pollack, *et al.*, 1990. *J. Geophys. Res.*, **95**, 14595-14627. [3]Calvin and King, 1990. *LPSC XXI*, 153-154, [Abstract]. [4]Miyamoto and Kato, 1990. *LPSC XXI*, 801-802, [Abstract]. [5]Hunt and Salisbury, 1971. *Mod. Geo.*, **2**, 23-30. [6]Gaffey, 1987. *J. Geophys. Res.*, **92**, 1429-1440. [7]Mackenzie *et al.*, 1983. In: *Carbonates: Mineralogy and Chemistry, Rev. Miner.*, **11**, 97-144. [8]Clark, *et al.*, 1990. *J. Geophys. Res.*, **95**, 14463-14480. [9]Encrenaz and Lellouch, 1990. *J. Geophys. Res.*, **95**, 14589-14593. [10]Rosenqvist, *et al.*, 1990. *Bull. Amer. Astron. Soc.*, **22**, 1076 [Abstract]. [11]Ming, 1981. M.S. Thesis. Colorado State University. [12]Mumpton, *et al.*, 1965. *Amer. Min.*, **50**, 1893-1913. [13]Jull, *et al.*, 1988. *Science*, **242**, 417-419. [14]Gooding, J. 1991. Personal communication.

OPTICAL PROPERTIES OF CO₂ ICE AND CO₂ SNOW FROM ULTRAVIOLET TO INFRARED: APPLICATION TO FROST DEPOSITS AND CLOUDS ON MARS

Gary B. Hansen, Geophysics Program AK-50, University of Washington, Seattle, WA 98195 U.S.A.

Stephen G. Warren and Conway B. Leovy, Department of Atmospheric Sciences AK-40,
University of Washington, Seattle, WA 98195 U.S.A.

The planet Mars has a tenuous atmosphere which is ~97% carbon dioxide. The annual variation of atmospheric pressure is about 40% of the mean value of 6 mbar, with most of the variation due to condensation in the winter hemisphere, where radiative cooling lowers the temperature of the surface and/or atmosphere to below the equilibrium condensation point. Modelling of the heat balance of the Martian poles depends on the radiative properties of the CO₂ clouds and frost which in turn depend on the refractive index and absorption coefficient of bulk CO₂ ice as well as particle size distributions and dust optical properties. These optical properties must be known throughout the visible and near infrared as well as in the thermal infrared.

Warren[1] has reviewed measurements of the optical constants of CO₂ ice, which contain a large number of gaps and uncertainties. Calvin[2], using the scattering model of Hapke[3], has shown that the spectral reflectance calculated with the Warren[1] index estimates in the near infrared do not match with the spectra of laboratory frosts or the spectra returned by Mariner 7. Indications are, however, that the absorption of CO₂ ice is very low in the visible and near ultraviolet and between the strong absorption bands in the infrared. This increases the reflectance and reduces the emissivity of a surface of small particles since photons can pass through more particles and be scattered out of the surface before being absorbed. Using the optical properties from Warren[1] and radiative transfer models [4,5], Warren et al.[6] calculated the spectral albedo and emissivity of CO₂ snow from 0.2 to 25 μ m as a function of particle size and dust or water ice contamination. The differences with our more common experience with water snow are striking, with near infrared reflectance > 90% and thermal infrared emissivity < 20% in some spectral regions and for some particle sizes (water snow is 'black' in these regions). The strength of these effects is dependent on accurate knowledge of absorption between the strong bands, which is not now available.

Previous investigators have found it difficult to grow CO₂ ice in other than thin films. This is apparently due to frost-like non-equilibrium growth or to excessive thermal stresses, which cause clouding or cracking [7]. The imaginary index of refraction has therefore been poorly measured or not measured at all where linear absorption < 10 cm⁻¹. Among the existing measurements of the absorption of CO₂ ice in the regions of low absorption are those from 0.3 μ m to 1 μ m with impure ice and those from 2.5 μ m to 25 μ m with cracked and cloudy samples [7]. However Gaizauskas[8] succeeded in growing clear crystals of several millimeters thickness to measure the absorption bands near 7 μ m. Measurements have never been made beyond 25 μ m, between 1 μ m and 2.5 μ m except for the strong bands or between the strong ultraviolet absorption < 0.15 μ m and 0.3 μ m.

We have found that it is possible to grow large clear samples of CO₂ ice at Mars-like temperatures of 150K-170K if a temperature-controlled refrigerator is connected to an isolated two-phase pure CO₂

system. In this way, the system pressure adjusts to the equilibrium value dictated by the refrigerator temperature and the ice grows at a rate consistent with the gas supply. Samples of up to 18 cm³ have been grown from ultra-high purity gas in this way. We have designed a chamber for transmission measurements whose optical path between the 13mm diameter windows is adjustable from 1.6mm to 107mm. This will allow measurements of linear absorption down to <0.01 cm⁻¹. The test chamber is thermally isolated from the lab by a large vacuum chamber and radiatively isolated from the walls of the large chamber by a low emissivity shield. The test chamber is instrumented internally with two platinum thermistors for temperature measurement. The spectral resolution will be provided from the vacuum ultraviolet to 4.8μm by a half-meter grating monochromator whose slit image is focused in the chamber center and on the following detector by mirror optics. Imprecision in the exact alignment of the test chamber on the cold finger required the construction of highly articulated mirror mounts. Sources for this part of the investigation include a UV discharge source, a tungsten-halogen lamp, a Xenon discharge lamp and an infrared glow rod. An intricate moving mirror system has been designed to provide a path around the test chamber for reference. The detectors include a photomultiplier tube for the UV, a silicon photodetector for the visible and NIR, and an indium-antimonide (InSb) detector for the IR. A few of the combinations of source-grating-filter-detector remain to be tested before measurements can begin. All the light sources are chopped and the detector outputs fed through a lock-in amplifier to reject background and minimize noise. A preliminary transmission spectrum of a thick sample of CO₂ ice in the near infrared is shown in Fig. 1.

The spectral region from 2.5μm to 50μm will be measured by a Fourier transform spectrometer. The absorption coefficient will be determined by a linear fit to the logarithm of the absorption at different optical path lengths for each wavelength. Measurements will be made at two distinct temperatures, so some estimate of the temperature variation of the coefficients can be made. It may also be possible to make sufficiently accurate measurements of the real index of refraction to help constrain the Kramers-Kronig analysis made by Warren[1].

Once the revised optical constants have been determined as a function of wavelength and temperature, they can be applied to spectral reflectance/emissivity models for CO₂ snow surfaces, both pure and contaminated with dust or water ice, using the delta-Eddington approach of Warren et al.[6] and/or the modified two-stream approach of Hapke[3]. It will be useful, also, to develop an infrared scattering-emission cloud radiance model (especially as viewed from near the limb) in order to develop a strategy for the identification of CO₂ cloud layers by the PMIRR (atmospheric infrared radiometer) instrument on Mars Observer.

Acknowledgements. We are grateful for the use of the laboratory and fabrication facilities at the Jet Propulsion Laboratory, Pasadena, CA, for this study, and the help of Vachik Garakanian, Robert Carlson and William Smythe. This work was supported by NASA under grant NAGW-1734.

REFERENCES

- [1] Warren, S.G., 1986, *Appl. Optics*, **25**, 2650. [2] Calvin, W.M., 1990, *J. Geophys. Res.*, **95**, 14743. [3] Hapke, B., 1981, *J. Geophys. Res.*, **86**, 3039. [4] Warren, S.G., and W.J.Wiscombe, 1980, *J. Atmos. Sci.*, **37**, 2734. [5] Wiscombe, W.J., and S.G.Warren, 1980, *J. Atmos. Sci.*, **37**, 2712. [6] Warren, S.G., et al., 1990, *J. Geophys. Res.*, **95**, 14717. [7] Ditteon, R., and H.H.Kieffer, 1979, *J. Geophys. Res.*, **84**, 8294. [8] Gaizauskas, 1955, PhD thesis, Univ. of Toronto, Toronto, Ontario, Canada.

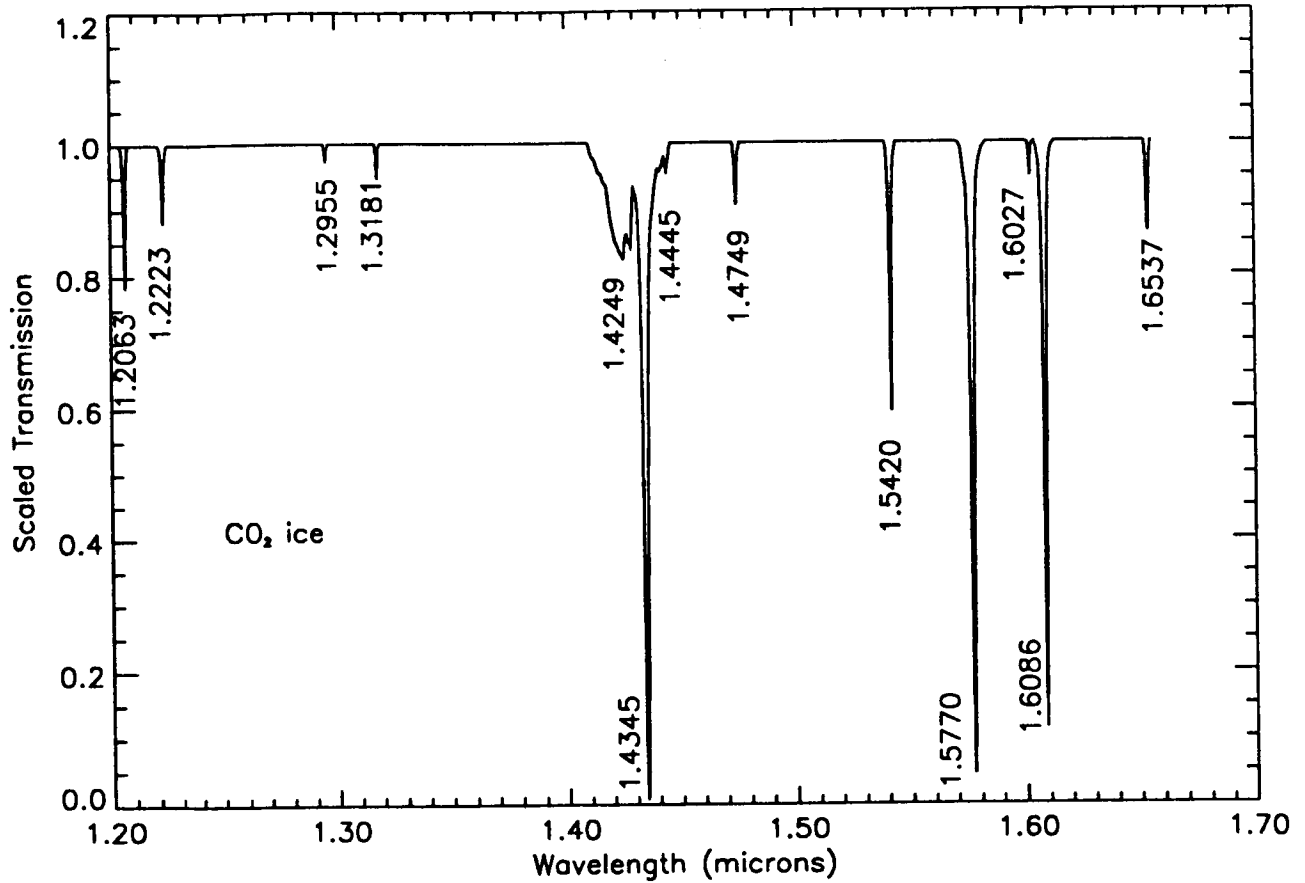


Figure 1: Preliminary absorption spectrum of a sample of CO₂ ice from 1.2 to 1.66 μm . The continuum background has been set arbitrarily to unity since its level is uncalibrated. The frequency calibration is based on the 1.4345 μm line shown in [1]. Note the unusual fine structure for a solid phase, with most lines only $\sim 2\text{nm}$ wide.

**DISK-RESOLVED SPECTRAL REFLECTANCE PROPERTIES OF PHOBOS FROM
0.3-3.2 μm : PRELIMINARY INTEGRATED RESULTS FROM PHOBOS 2.**

Scott L. Murchie¹, Stephane Erard², Yves Langevin², Daniel T. Britt¹, Jean-Pierre Bibring², John F. Mustard¹, James W. Head¹, and Carle M. Pieters¹; ¹ *Department of Geological Sciences, Brown University, Providence, RI 02912, U.S.A.*; ² *Institut d'Astrophysique Spatiale, University of Paris, Orsay, France.*

Introduction. The *Phobos 2* mission provided multispectral observations of Phobos over a large wavelength range and with relatively high spectral resolution. The VSK TV cameras obtained 0.40-0.56 μm ("visible") and 0.78-1.1 μm ("NIR") images with resolutions of 0.3-0.5 km, covering the longitude region 30°-250°W [1]. The KRFM instrument obtained ~0.9-km resolution, 8-channel 0.3-0.6 μm spectra of two groundtracks in low-latitude regions [2]. The ISM imaging spectrometer obtained 128-channel, 0.76-3.16 μm spectra of part of the trailing hemisphere with a spatial resolution of ~0.7 km [3]. In this abstract we integrate results from the three multispectral detectors, by determining the UV-visible and NIR spectral properties of color and brightness features recognized in VSK images. We present evidence that there are two fundamental spectral units within the region of overlapping coverage by the detectors, we describe the units' spectral and reflectance properties, and we discuss the implications of these results for the composition of Phobos.

Synopsis of Previous Analyses. The spectral and reflectance properties of the surface of Phobos determined previously from these experiments are summarized below. Laboratory measurements of possible meteorite analogs to Phobos provide some basis for interpretation of these observations. The analogs include hydrous CI and CM carbonaceous chondrites, anhydrous CO and CV carbonaceous chondrites, and anhydrous, optically darkened ordinary chondrites or "black chondrites." (a) Color ratio images constructed from visible/NIR VSK image pairs show that the surface is spectrally heterogeneous with a color ratio of ~0.75-1.4, and may be subdivided into "red," "reddish gray," "bluish gray," and "blue" color ratio units. The "blue" and "bluish gray" units compose the interior of the crater Stickney and a surrounding lobate deposit extending west to ~160°W, interpreted as the crater's ejecta [1,4]. (b) In low phase angle images, rims of many fresh craters west of ~160°W exhibit a brightening relative to surrounding older surfaces, but bright-rimmed craters are conspicuously absent from the region extending east from ~160°W to the crater Stickney [1]. In the laboratory, analogous brightening at low phase angles is observed in particulate carbonaceous chondrites. An analogous effect is also observed in black chondrites, but only at small particle sizes characterized by unrealistically large reflectances for Phobos [5]. (c) The "red," "reddish gray," and "bluish gray" color ratio units were sampled by the KRFM spectrometer. The "red" and "reddish gray" units have similar UV-visible spectra which are relatively flat at 0.4-0.6 μm and exhibit a falloff in reflectance below 0.4 μm , but the "bluish gray" unit has a much lesser falloff in reflectance below 0.4 μm [4]. (d) The spatial distributions of the color ratio units, their reflectance systematics, and their UV-visible spectral properties indicate that color variations originate from optical or compositional heterogeneity. The reddest and bluest materials form the interiors and flanks of craters, and are interpreted to have been excavated from a heterogeneous interior overlain by a "reddish gray" surficial layer [4]. (e) The very blue color ratio of "blue" material supports a mafic, black chondrite-like composition rather than a carbonaceous chondritic composition. UV-visible spectra of "bluish gray" material are more similar to spectra of black chondrites than carbonaceous chondrites. Spectra of "reddish gray" and "red" materials also more resemble spectra of black chondrites, but are comparable to spectra of some carbonaceous chondrites [4,6]. (f) ISM observed only the "red" and "reddish gray" color ratio units. The 3- μm absorption due to hydration is very weak or negligible [3], suggesting that Phobos's regolith is anhydrous. (g) The density of Phobos, $1.90 \pm 0.1 \text{ g/cm}^3$, is much lower than that of meteorite analogs, indicating significant internal porosity [1]. The amount of porosity would be more realistic if high-density anhydrous carbonaceous chondrite or black chondrite were diluted by lower-density CM-like carbonaceous chondrite [4,7], if this material has been dehydrated by regolith processes to account for NIR spectral properties.

Calibration. *VSK:* VSK images were calibrated initially using instrumental parameters measured on-ground and in-flight [1]. Visible/NIR color ratio images were recalibrated on the basis of a portion of Mars observed in the background of Phobos in some images, employing telescopic spectra resampled into the visible and NIR bandpasses as described by Murchie *et al.* [4]. *KRFM:* Initially published locations of the two groundtracks [2,8] have been refined by correlating along-track brightness profiles with portions of visible-band VSK images [4]. Previously published spectra [4] for the longer, more southern groundtrack (track 1) were recalibrated by dividing by a "standard" area with an "average" color ratio, and multiplying by the disk-integrated ("average") spectrum [9]. When recalibrated in this way, spectra of Mars obtained at the end of the track (beyond the satellite's limb) are consistent with telescopic spectra. Spectra from track 2 could not be recalibrated because this track lacks a suitable "standard" area, and because no spectra of Mars were acquired at either end of it [4], and so are therefore not used in the present analysis. *ISM:* These spectra have been calibrated using instrumental parameters measured on-ground and in-flight [10]. We are attempting several methods of recalibration, including (a) dividing by a "standard" area and multiplying by spectra of anhydrous meteorites whose spectral properties in VSK and KRFM bandpasses closely match those of the "standard" area, and (b) deriving revised gains and offsets for each channel using spectra of various regions on Mars.

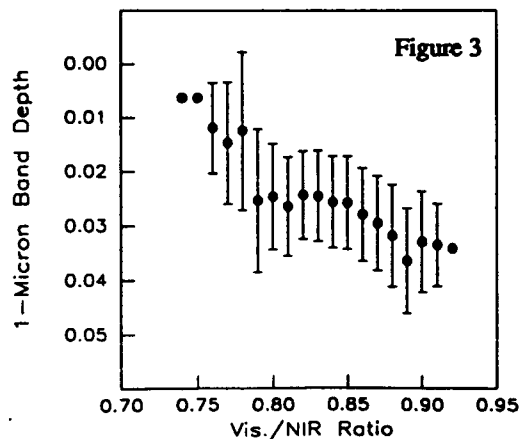
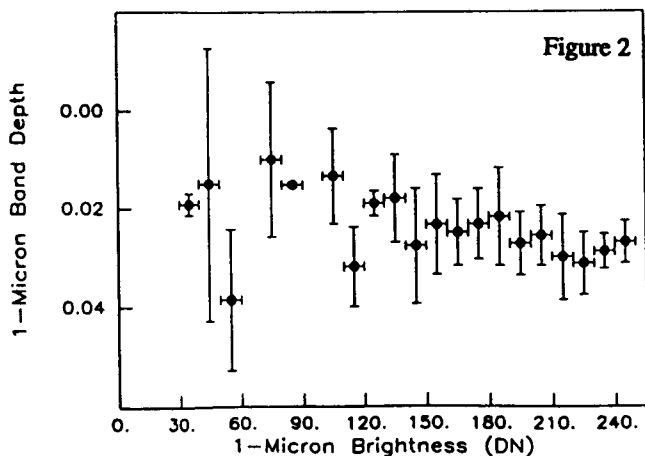
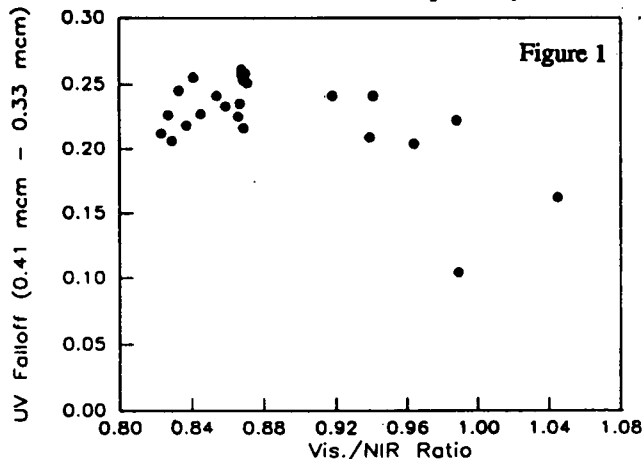
Properties of Spectral Units on Phobos. The area west of Stickney lacking bright-rimmed craters is closely correlated spatially with materials having color ratios of ≥ 1.0 ; the western outliers of this bluish material coincide with dark patches between the easternmost bright-rimmed craters, and the bright-rim craters in the distal portion of the bluish material form outliers of the redder material prevalent to the west. The magnitude of the falloff in reflectance below 0.4 μm is also related to color ratio (Figure 1). Materials with a color ratio of >1.0 exhibit a relatively flat spectrum with

only a 10-16% UV falloff; materials with a color ratio <1.0 exhibit a 20-26% falloff in reflectance, independent of color ratio within this range. These results are interpreted as revealing two basic spectral units in this region of Phobos: (a) "bluer" Stickney ejecta with a color ratio of ≥ 1.0 , a relatively flat UV-visible spectrum, and lacking bright material on rims of young craters; and (b) "redder" material with a color ratio of <1.0, a greater falloff in UV reflectance, and exhibiting pervasive bright material on rims of young craters.

Of these two basic units, ISM observed only the "redder" one. We have focused our analysis of this data set on the 1- μm and 2- μm absorptions diagnostic of mafic minerals. The depth of the 1- μm absorption, defined as the drop in reflectance at 0.91-1.09 μm relative to a continuum between 0.8 and 1.2 μm , was found to vary laterally by up to ~5%. Depth of the absorption is independent of illumination (Figure 2), but is correlated with visible/NIR color ratio (r , 0.71 ± 0.01) (Figure 3). Areas with relatively redder color ratios have the weakest absorption, and areas with relatively bluer color ratios have the deepest absorption. If the current calibration is nearly correct, then the 1- μm absorption is weak or absent in areas with the reddest color ratios (<0.8). A weak 2- μm absorption feature is also present in some of the areas with a relatively strong 1- μm absorption and relatively bluer color ratio. Spectra of a mixed population of meteorite analogs [11,12] reveal a similar relationship between color ratio and the depth of the 1- μm absorption. Carbonaceous chondrites generally have weak or negligible 1- μm absorptions; black chondrites generally have 1- μm absorptions with depths of ~2-7%, and as a class of materials have a bluer color ratio than do carbonaceous chondrites [4].

Implications for the Composition of Phobos. Tentatively, we interpret these results as follows: "Bluer" material considered to be Stickney ejecta is interpreted here as having a black chondrite-like composition, based on its UV-visible spectral properties, its very blue color ratio, and its lack of bright-rimmed craters. "Redder" material is a mix of a red component with a weak or negligible 1- μm absorption, and a gray component possibly containing olivine and (locally) pyroxene. Based on the correlation of the depth of the 1- μm absorption with color ratio, the character of the UV-visible spectrum, and the presence of bright-rimmed craters throughout the "redder" unit, we propose that its gray component is black chondrite-like in composition and that its red component is analogous to lower-density carbonaceous chondritic material such as CM chondrites. This mixed composition reconciles spectral evidence of a black chondrite-like composition in some areas with the satellite's low density, which requires a more reasonable porosity (~35%) if a porous interior has a large component of low-density carbonaceous chondritic material. The implied structure of Phobos's interior is a rubbly mixture of carbonaceous chondrite and either ordinary chondrite or some other mafic material containing a similar mineral assemblage. This association is not thought to be compatible with formation within a single parent body [13], and implies that the material composing Phobos originated from more than one asteroidal and/or planetary source.

References: [1] Avanesov et al., *Planetary and Space Science*, in press, 1990. [2] Ksanfomality et al., *Planetary and Space Science*, in press, 1990. [3] Langevin et al., *Lunar Planet. Sci. XXI*, 682-683, 1990. [4] Murchie et al., *J. Geophys. Res.*, in press, 1990. [5] Shkuratov et al., *Abstracts of Papers Submitted to the 12th Soviet-American Microsymposium*, pp. 78-79, Moscow, 1990. [6] Britt et al., *Lunar Planet. Sci. XXI*, 129-130, 1990. [7] Hartmann, *Lunar Planet. Sci. XXI*, 457-458, 1990. [8] Ksanfomality et al., *Nature*, 341, 588-591, 1989. [9] Pang et al., *Science*, 199, 64-66, 1978. [10] Erard et al., *Proc. Lunar Planet. Sci. Conf. 21*, in press, 1990. [11] Gaffey, *J. Geophys. Res.*, 81, 905-920, 1976. [12] Britt, D. and C. Pieters, unpublished spectra. [13] Dodd, R., *Meteorites: A Chemical-Petrologic Synthesis*, Camb. Univ. Press, 1981.



EVIDENCE FOR AMMONIUM-BEARING MINERALS ON CERES; T. V. V. King, R. N. Clark, W. M. Calvin, D. M. Sherman, G. A. Swayze (U.S. Geological Survey, Denver), and R. H. Brown (J.P.L., Pasadena)

Spectra of 1 Ceres has an absorption feature centered at $3.07 \mu\text{m}$ which we attribute to the presence of an NH_4 -bearing species on the surface of Ceres. This absorption feature was first reported by Lebofsky et al. (1) to be centered at $3.1 \mu\text{m}$ and was interpreted to be due to water ice. The wavelength position and width of the $3.07\text{-}\mu\text{m}$ absorption on Ceres are very similar to a NH_4 absorption in naturally occurring and synthetically produced NH_4 -bearing materials. This interpretation is based on four nights of observations from NASA's Mauna Kea IRTF using the CGAS detector and the Mars grating with a resolution of $0.013 \mu\text{m}$.

Prior to analysis, the Ceres spectra from all the observations had the thermal component removed. This was accomplished by determining the overall disk temperature and then by adjusting the wavelength independent emissivity(ϵ) and normalization constant (n) from the standard thermal model of Lebofsky et al. (2) to match the geometric albedo of Ceres reported by Feierberg et al. (3). The integrated disk temperature for Ceres used in this study is 243.7 K. The thermally-corrected spectrum of Ceres was compared to spectra from the USGS digital spectral library. After extensive research, we found that the $3.07\text{-}\mu\text{m}$ absorption feature can not be attributed to OH, H_2O , CO_3 , SO_4 , or other ions in geologically significant minerals.

The composite Ceres spectrum was compared to NH_4 -bearing mineral species including naturally occurring buddingtonite and a NH_4 -bearing illite/smectite, as well as laboratory samples including a NH_4 -substituted dioctahedral nontronite (Ng-1), a Ca/Na montmorillonite (SWy-1), a ferruginous smectite (SWa-1), and a trioctahedral saponite (SAPCa-1). The phyllosilicates used in the cation exchange process are standards of the Clay Mineral Repository (see Clark et al. (4) for additional discussion). The NH_4 -bearing saponite provides the best spectral comparison to Ceres. Comparison of the ammoniated-saponite and neat-saponite (nothing done to the clay) show that the NH_4 fundamental vibration matches the $3.07\text{-}\mu\text{m}$ feature and is stronger than the fundamental OH-absorption which occurs near $2.7 \mu\text{m}$.

The high resolution telescopic spectra indicate that the center of the NH_4 absorption on Ceres occurs at $3.07 \pm 0.02 \mu\text{m}$ vs. $3.05 \mu\text{m}$ for our laboratory samples. The width of the Ceres absorption is $0.127 \pm .08 \mu\text{m}$ vs. $0.145 \mu\text{m}$ for the laboratory sample. The depth of the $3.07\text{-}\mu\text{m}$ feature on Ceres is approximately 10%.

Lebofsky et al. (1) and Jones (5) have attributed a $3.1\text{-}\mu\text{m}$ absorption feature on Ceres to the presence of water ice. However, theoretical calculations of water ice spectrum at many grain sizes, shows that the $3.07\text{-}\mu\text{m}$ Ceres absorption is much too narrow to be caused by the presence of water ice. The spectrum of water ice at grain sizes of $1 \mu\text{m}$ indicate that the width of the feature is greater than 3.5 times the width of the $3.07\text{-}\mu\text{m}$ absorption on Ceres. Water ice at larger grain sizes would have greater widths because the absorption band is saturated.

To better understand the physio-chemical origins of the Ceres spectrum, we completed two laboratory studies in which we theoretically computed and physically mixed components that mimicked the spectrum of Ceres. We computed a spectrum using the derived optical constants of ammoniated-saponite, a black (low albedo mixture) and a gray (medium albedo) mixture. The best spectral agreement was achieved using a mixture of 7 wt. % ammoniated-saponite (grain size of $2 \mu\text{m}$), plus 52 wt. % of the black component (grain size of $5 \mu\text{m}$), and 41 wt. % of the gray material (grain size of $10 \mu\text{m}$). This produced a $3.07\text{-}\mu\text{m}$ absorption feature of 12 % versus 10 % for Ceres. The reflectance level of the calculated spectrum was less than 1 % lower than the reflectance level of the Ceres spectrum (~ 0.04 at $3.0 \mu\text{m}$). We also calculated the spectrum of a mixture which maintained the same proportions and grain sizes, but in

AMMONIUM-BEARING MINERALS ON CERES: King et al.

which water ice was substituted for ammoniated-saponite. The resulting spectrum produced an absorption feature which was dominated by a very broad water ice absorption which extended from approximately 2.85 to 3.4 μm . The water ice dominated spectrum does not in any way resemble the Ceres spectrum. The band shape, depth and width are significantly different. A recent work by Calvin and Clark (6) indicates that increasing or decreasing the grain size of the water ice component would not produce a spectrum which could be confused with the spectrum of Ceres. The laboratory computed spectrum that includes the ammoniated-saponite component is a good spectral comparison to the high-resolution data of Ceres published by Lebofsky et al. (1).

A physical mixture of ammoniated-saponite and carbon black (8 wt. %) produced a spectrum which resembles the features in 3.07- μm wavelength region of Ceres. However, the reflectance level of the laboratory mixture is too low compared to Ceres when the strength of the 3.07- μm feature is correct. This suggests that the ammoniated-laboratory mixture contains more NH_4 than Ceres. The presence of additional absorption features in this Ceres data set, which have yet to be verified, may provide additional insight to the exact mineralogical association resulting in the 3.07- μm NH_4 absorption.

(1) Lebofsky, L.A., M.A. Feierberg, A.T. Tokunaga, H.P. Larson, and J.R. Johnson, 1980, *Icarus*, **48**, 543-459. (2) Lebofsky, M.A., M.V. Sykes, E.F. Tedesco, G.J. Veeder, D.L. Matson, R.H. Brown, J.C. Gradie, M.A. Feierberg, and R.J. Rudy, 1986, *Icarus*, **68**, 239-251. (3) Feierberg, M.A., L.A. Lebofsky, and H.P. Larson, 1981, *Geochem. Cosmochem. Acta*, **45**, 971-981. (4) Clark, R.N., T.V.V. King, M. Klejwa, G.A. Swayze, and N. Vergo, 1990, *Jour. Geophys. Res.*, **95**, 12,653-12,680. (5) Jones, T.D., 1988, Ph.D Thesis, University of Arizona. (6) Calvin W.M and R.N. Clark, 1991, *Icarus*, *in press*.

**REFLECTANCE SPECTRA OF Fe^{2+} - Mg^{2+} DISORDERED
PYROXENES: IMPLICATIONS TO REMOTE-SENSED SPECTRA OF
PLANETARY SURFACES**

Roger G. Burns,¹ James R. Besancon,² and Stephen F. Pratt³

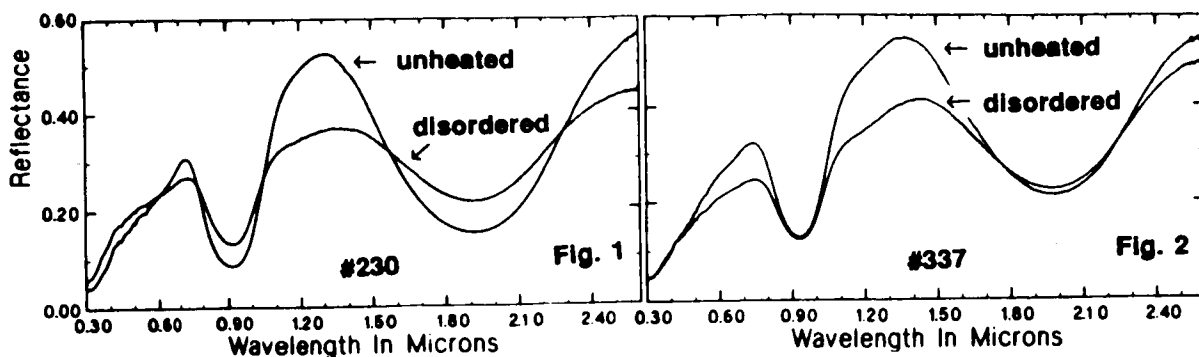
¹ MIT, Cambridge MA; ² Wellesley College, Wellesley MA; ³ Brown Univ., Providence RI.

Introduction. Pyroxenes are identified in telescopic and laboratory reflectance spectra by the broad, intense bands centered at 0.90-1.05 μm and 1.80-2.30 μm [1]. These spectral features originate from crystal field (CF) transitions in Fe^{2+} ions located in the very distorted, non-centrosymmetric M2 sites of the pyroxene crystal structure. In pigeonites and orthopyroxenes, strong enrichments of Fe^{2+} ions in the M2 sites obscure weaker CF bands at $\sim 0.9 \mu\text{m}$ and $\sim 1.20 \mu\text{m}$ produced by electronic transitions in minority proportions of Fe^{2+} ions situated in the less distorted M1 octahedral sites that are occupied mainly by Mg^{2+} ions [2]. Numerous experimental studies [e.g., 3-6] have shown that temperature-induced disordering of Fe^{2+} (M2 site) and Mg^{2+} (M1 site) cations in orthopyroxenes takes place relatively rapidly even at temperatures as low as 450-500 $^{\circ}\text{C}$ [6]. Since re-equilibration of Fe^{2+} ions between the M2 and M1 sites is expected to affect near infrared spectra [7,8], we undertook reflectance spectral measurements of a variety of orthopyroxenes after they had been heated under controlled oxygen fugacities.

Experimental Details. Orthopyroxenes used in this study comprised several specimens from granulite facies rocks, including a Tanzanian specimen, TZ ($\text{Fs}_{50}\text{En}_{47}\text{Wo}_1\text{Mn}_2$), used in previous cooling rate experiments [6]; two specimens from Western Australia [9] with similar bulk Fe but different Mn contents, #230 ($\text{Fs}_{36}\text{En}_{61}\text{Wo}_2\text{Mn}_1$) and #337 ($\text{Fs}_{38}\text{En}_{48}\text{Wo}_2\text{Mn}_{12}$); specimens #4645 ($\text{Fs}_{26}\text{En}_{74}$) and KC ($\text{Fs}_{61}\text{En}_{38}\text{Mn}_1$); and a synthetic ferrosilite (Fs_{85}). Specimens heated to 700 $^{\circ}\text{C}$ were equilibrated for several hours in CO_2/H_2 atmospheres providing oxygen fugacities close to or less than the iron-wüstite buffer. Different samples of specimen TZ were equilibrated under these conditions for time periods ranging from a few minutes to several hours. Orthopyroxene specimens heated to 500 $^{\circ}\text{C}$ were equilibrated at this temperature for three months in evacuated quartz tubes containing metallic Fe. The Fe^{2+} occupancies of the pyroxene M1 and M2 sites before and after heating, as well as the percentage of ferric iron in each orthopyroxene, were determined from computed peak areas in Mössbauer spectra measured at 77 K [6]. Visible - near infrared spectra were measured using the RELAB facility [10], and deconvoluted into component bands using a modified Gaussian model [11].

Results. Spectra of specimens #230 and #337 before and after Fe^{2+} - Mg^{2+} disordering are illustrated in Figures 1 and 2. Particularly conspicuous in these spectra are the reduction of the band depths at 0.90 μm and 1.95 μm , especially in specimen #230 (Fig. 1), and the increased absorption around 1.20 μm . Both of these effects are indicative of the removal of Fe^{2+} ions from the M2 sites into the M1 sites; they are less severe in the spectra of the manganiferous specimen #337 (Fig. 2) due to the stronger preference of Mn^{2+} ions for the M2 sites which cause higher concentrations of Fe^{2+} ions to occur initially in the M1 sites prior to re-equilibration. These trends are supported by the site occupancies determined from the Mössbauer spectra. For example, after heating the orthopyroxenes at 500 $^{\circ}\text{C}$ for 3 months, the $\text{Fe}^{2+}/(\text{Fe}^{2+}+\text{Mg}^{2+})$ ratios of the M1 sites increase from 0.09 to 0.22 (specimen #230) and from 0.16 to 0.27 (specimen #337). There are also small increases of ferric iron in the two specimens (from 2.5% Fe^{3+} and 3.1% Fe^{3+} to $\sim 4.3\%$ Fe^{3+} in both #230 and #337, respectively), which produce increased absorption around 0.66 μm in the reflectance spectra (Figs 1 and 2).

Similar trends occur in specimen TZ following Fe^{2+} - Mg^{2+} disordering at 700 $^{\circ}\text{C}$. The development of the 1.20 μm spectral feature with increasing duration of heating is illustrated in Figure 3, with equilibrium disordering being achieved in about 1 hour. In Figure 4, the reflectance spectra of unheated (Fig. 4A) and equilibrated (Fig. 4B) samples have been



Figures 1 and 2 (above). Reflectance spectra of orthopyroxenes unheated and disordered at 500 °C.

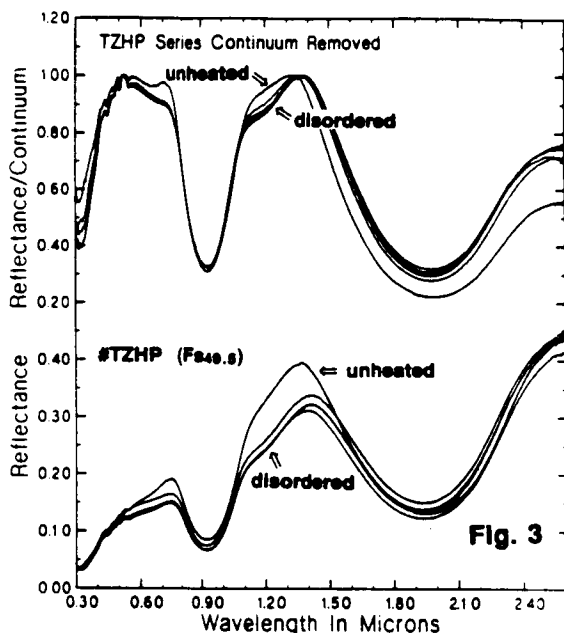
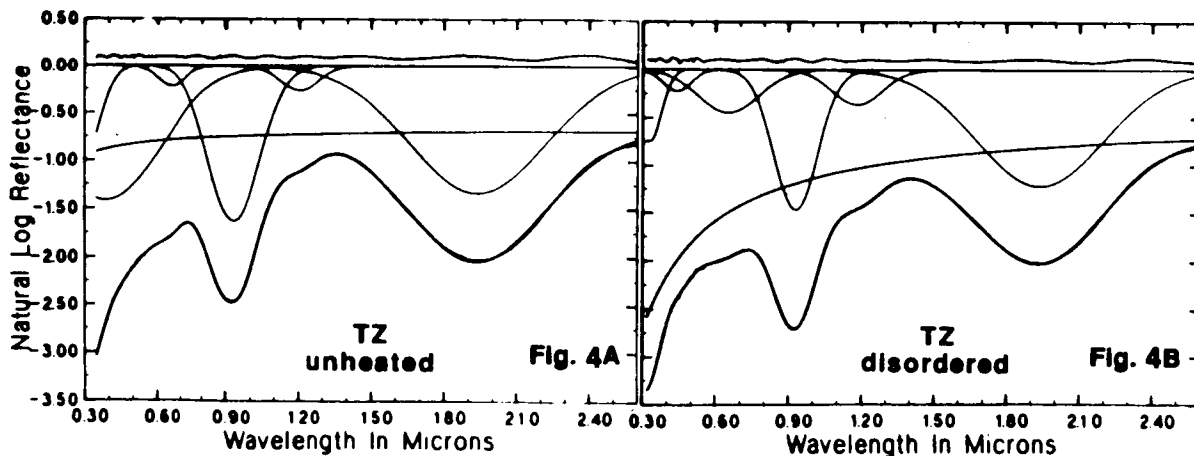


Figure 3 (left). Reflectance spectra of orthopyroxene specimen TZ before and after Mg^{2+} - Fe^{2+} disordering at 700 °C for time periods ranging from 6 minutes to 20 hours. Note the intensification of the Fe^{2+} /M1 site crystal field spectral feature at 1.20 μm .

Figure 4 (below). Deconvoluted reflectance spectra of specimen TZ before (Fig. 4A) and after (Fig. 4B) equilibrium cation disordering at 700 °C. Note the intensification of the Fe^{2+} /M1 site crystal field band at 1.20 μm and the $Fe^{2+} \rightarrow Fe^{3+}$ intervalence charge transfer band at 0.66 μm .



deconvoluted into component gaussian bands. The increased relative intensity of the band at 1.20 μm in Figure 4B correlates with the change of M1 site $Fe^{2+}/(Fe^{2+}+Mg^{2+})$ ratio from 0.15 (unheated) to 0.28 (re-equilibrated). The band at 0.66 μm in the reflectance spectra may be assigned to an intervalence charge transfer (IVCT) transition between Fe^{2+} and Fe^{3+} ions in M1 sites separated by only 3.15 Å. The higher intensity of this $Fe^{2+} \rightarrow Fe^{3+}$ IVCT band in the re-equilibrated sample (Fig. 4B) again results from increased M1 site occupancy of Fe^{2+} ions.

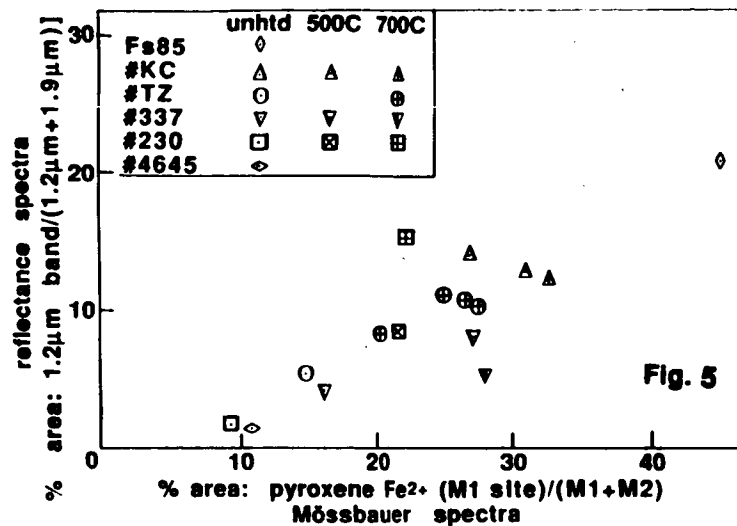


Figure 5. Correlations between peak area data obtained from deconvoluted reflection spectra and fitted Mössbauer spectra of unheated and disordered orthopyroxenes.

Correlations between the $\text{Fe}^{2+}/\text{M1}$ site occupancies determined from computed peak areas in the reflectance spectra and the Mössbauer spectra are illustrated in Figure 5 for the suite of orthopyroxenes studied. There is clearly a linear trend between Fe^{2+} (M1 site)/(M1+M2) ratios estimated from the deconvoluted reflectance spectra and the two-ferrous doublet fits of the Mössbauer spectra of the orthopyroxenes.

Applications. The reflectance spectra of Fe^{2+} - Mg^{2+} disordered orthopyroxenes illustrated in Figures 1-4 are relevant to surfaces of terrestrial planets onto which basaltic magma has been extruded. If cooling rates of basalt lava flows were fast, equilibrium iron intersite partitioning may not have been achieved so that abnormal enrichments of Fe^{2+} ions in M1 sites would occur. The two intense pyroxene $\text{Fe}^{2+}/\text{M2}$ site CF bands in the "1 micron" and "2 micron" regions would continue to dominate the reflectance spectra so that the pyroxene composition and structure-type would be readily identified in telescopic spectral profiles. However, abnormal intensification of the $\text{Fe}^{2+}/\text{M1}$ site CF band at $1.20 \mu\text{m}$ could lead to the false identification of olivine in remote-sensed spectra because in pyroxene-olivine mixtures the inflection around $1.20 \mu\text{m}$ is the only spectral feature for detecting the presence of olivine [12]. The identification of iron-bearing plagioclase feldspars, too, would be obscured by the pyroxene $\text{Fe}^{2+}/\text{M1}$ site CF band at $1.20 \mu\text{m}$. Such interference at $1.20 \mu\text{m}$ from pyroxene $\text{Fe}^{2+}/\text{M1}$ site cations would be a major problem if *in situ* reflectance spectra could be measured on the surface of Venus where ambient temperatures are as high as $475 \text{ }^\circ\text{C}$. Disordering of Fe^{2+} and Mg^{2+} ions comparable to that in the orthopyroxenes used in this spectral chemical study might be expected in low Ca pyroxenes occurring on the venusian surface.

We conclude that pyroxene $\text{Fe}^{2+}/\text{M1}$ site spectral features need to be carefully assessed in remote-sensed spectra before deductions are made about the presence of olivine on planetary surfaces.

Acknowledgments. Research supported by NASA grants NAGW-2037 (MIT) and NAGW-748 (Brown Un.).

References. [1] R.G.Burns, *Min. Mag.*, 53, 135 (1989); [2] S.Ghose, *Z. Krist.*, 122, 81 (1965); [3] D.Virgo & S.S.Hafner, *Min. Soc. Amer. Spec. Pap.*, 2, 67 (1969) & *Am. Min.*, 55, 201 (1970); [4] S.K.Saxena & S.Ghose, *Am. Min.*, 56, 532 (1971); [5] K.K.Khrstoforov *et al.*, *Dokl. Acad. Nauk. SSSR*, 214, 909 (1974); [6] J.R.Besancon, *Am. Min.*, 66, 965 (1981); [7] D.S.Goldman & G.R.Rossman, *Phys. Chem. Min.*, 4, 43 (1979); [8] G.Steffen *et al.*, *Phys. Chem. Min.*, 16, 120 (1988); [9] L.R.Davidson, *Contrib. Min. Pet.*, 19, 239 (1968); L.R.Davidson & C.I.Mathison, *Neues Jahrb. Min., Mh.*, 2, 47 (1973) [10] C.Pieters, *JGR*, 90, 12393 (1985); [11] J.M.Sunshine *et al.*, *JGR*, 95, 6955 (1990); [12] R.B.Singer, *JGR*, 86, 7967 (1981).

**PRE-TERRESTRIAL OXIDATION PRODUCTS IN CARBONACEOUS
METEORITES IDENTIFIED BY MÖSSBAUER SPECTROSCOPY**

Roger G. Burns and Duncan S. Fisher

Department of Earth, Atmospheric and Planetary Sciences, Massachusetts Institute of Technology,
Cambridge, MA 02139

Introduction. The occurrence of ferric-bearing assemblages, comprising phyllosilicates, oxide hydroxides and magnetite, in carbonaceous chondrites (hereafter abbreviated as **CC**) indicates that these meteorites underwent pre-terrestrial sub-aqueous oxidation reactions. Although several analytical studies of **CC**, have been reported [e.g.,1,2], the poor crystallinity of matrix phases makes it very difficult to estimate the modal mineralogy and proportions of Fe^{3+} and Fe^{2+} in these meteorites [2]. Early studies of Mössbauer spectra of meteorites at room temperature demonstrated that this technique may provide quantitative information on iron-bearing phases in **CC** [e.g.,3,4]. In a recent study of ureilites, for example, major proportions of metallic Fe and nanophase goethite were identified in these carbonaceous achondrites [5]. The metallic Fe occurs mostly as sub-microscopic inclusions in forsteritic rims where they have formed by carbon-induced reduction of Fe^{2+} cations in olivine grains in contact with the carbonaceous matrix [6]. The cryptocrystallinity of the metallic Fe inclusions renders the metal extremely vulnerable to oxidation so that nanophase ferric oxides (i.e. "rust") occur in all ureilites, including specimens collected as *falls*. The vulnerability of olivines in ureilites to such redox reactions suggested that other pre-terrestrial oxidation processes might be elucidated in **CC**, the olivines in which have undergone reactions producing serpentines, magnetite and poorly crystalline phases such as ferrihydrite and tochilinite [e.g.,2,7,8]. Reported here are results of a Mössbauer spectral study of a suite of **CC** demonstrating that a variety of ferrous and ferric-bearing phases may be distinguished in different classes of this meteorite-type.

Carbonaceous Chondrite Specimens. Samples of several **CC** catalogued as *falls* were obtained from the Harvard Mineralogical Museum Collection, and included: Orgueil (**C1**); Murchison, Murray, Cold Bokkeveld and Renazzo (**CM**); Allende (**CV3**); Warrenton (**CO3**); Karoonda (**C5**); and the *find* Coolidge (**C4**). Specimens acquired from the Antarctic Meteorite Collection, including some powdered (**P**) samples, comprised: ALH 83100(**P**) and MAC 88107 (**CM**); ALHA 83108 and LEW 85332 (**C3**); EET 87256(**P**) and ALHA 85002(**P**) (**C4**); EET 87860(**P**) (**C5**); and LEW 87009(**P**) (**C6**). Experimental details for measuring Mössbauer spectra of meteorites are described elsewhere [9].

Results. Room temperature Mössbauer spectra of several **CC** have been published previously [3,4,10-12]. In our investigation, systematic measurements were made of several **CC** petrologic types at both 295 K and 4.2 K. Trends observed in these spectra include:

- (1) The relatively simple 295 K spectrum of Allende (**CV3**) (Fig. 1) consists of Fe^{2+} and Fe^{3+} quadrupole doublets alone representing mainly olivine and phyllosilicates, respectively, and with $\% \text{Fe}^{3+}/\text{total Fe} = \text{approx. } 10\%$. The 4.2 K spectrum of Allende is dominated by peaks from magnetically ordered Fe^{2+} ions in olivine. No magnetic ferric phase is present in Allende.
- (2) The spectrum of Cold Bokkeveld (**CM**) at 295 K also consists of Fe^{2+} and Fe^{3+} doublets alone, but with comparable intensities (Fig. 2). In the 4.2 K spectrum of this and other **CM** meteorites, however, the Fe^{2+} doublet of ferroan serpentine remains while magnetic ordering of Fe^{3+} has occurred, indicating the presence cronstedtite [12,13] possessing a magnetic ordering temperature of ≤ 8 K [14]. The iron hydroxysulfide mineral tochilinite, which is particularly abundant in **CM CC** [2], does not magnetically order at 4.2K, by analogy with related mackinawite [15], and is recognized by peaks centered near 0.2 mm/s. The relative proportions of these secondary minerals, which formed during aqueous alteration on the meteorite parent body, differ in the Mossbauer spectra of other **CM CC** meteorites (Murchison, Murray, ALH 83100).
- (3) The 295 K spectrum of Karoonda (**C4**) contains the Fe^{2+} olivine doublet and a much weaker Fe^{3+} doublet than Allende, as well as the characteristic magnetic hyperfine spectrum of magnetite which constitutes about 15% of the iron modal mineralogy (Fig. 3). The relative intensities of paired-peaks in the magnetite spectrum are not in the ratio 1:2, however, indicating that this oxide in Karoonda and in other thermally metamorphosed **CC** is an oxidized magnetite departing from $\text{Fe}^2\text{Fe}^{3+}_2\text{O}_4$ stoichiometry. The 4.2 K spectrum of Karoonda is dominated by magnetite and magnetically-ordered Fe^{2+} in olivine. Similar 295 K and 4.2 K spectra were obtained for other **C4**, **C5** and **C6** specimens studied (i.e. ALHA 85002, EETA 87860, EET 87526, LEW 87009). Coolidge (found in 1937) contains no magnetite; instead, its 4.2K spectrum contains broadened peaks attributed to terrestrial nanophase goethite.

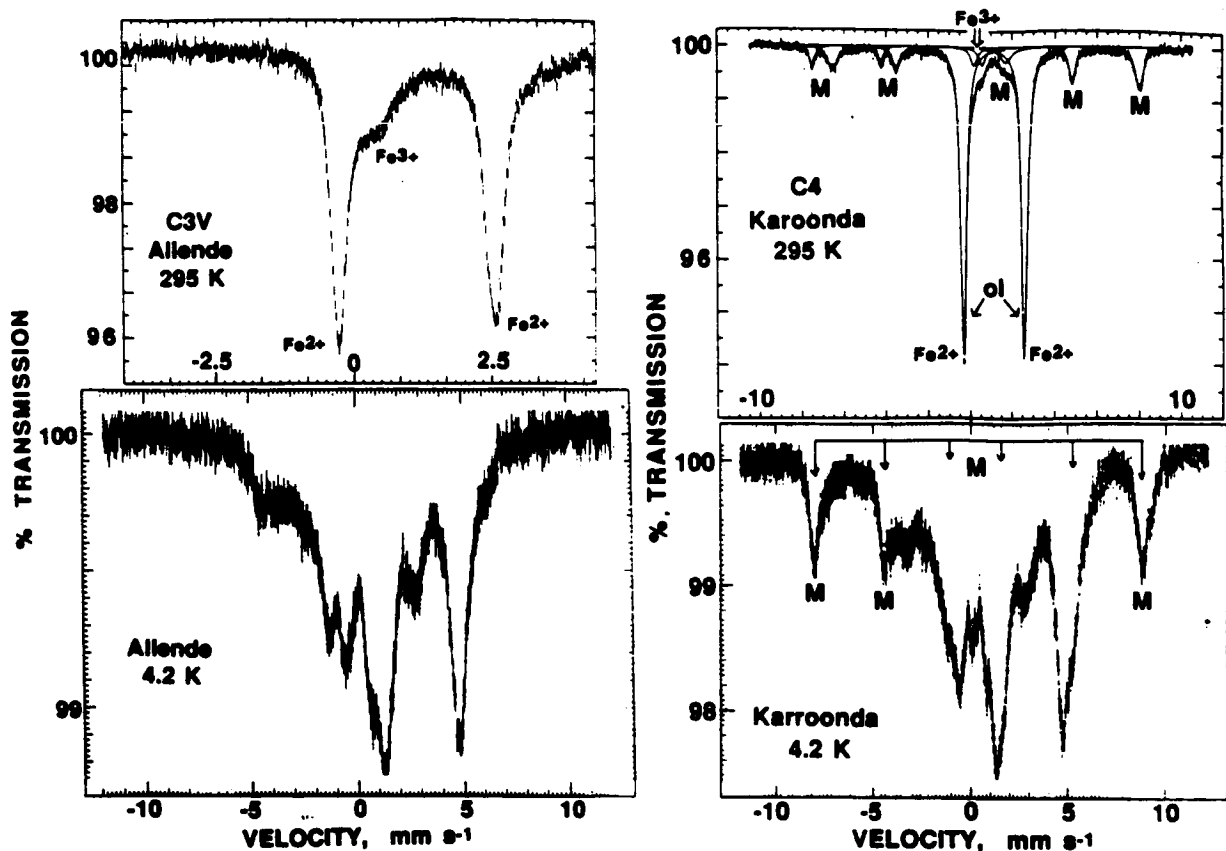


Figure 1. Mössbauer spectra of the Allende meteorite. The spectra of this carbonaceous chondrite are dominated by olivine, Fe^{2+} ions in which are magnetically ordered in the 4.2 K spectrum.

Figure 2. Mössbauer spectra of the Karroonda meteorite. Olivine (ol) and non-stoichiometric (slightly oxidized) magnetite (M) occur in this and other thermally metamorphosed carbonaceous chondrites.

(4) The spectrum of Orgueil (C1) at 295 K resembles previously published spectra of this CC [3,16], and consists of an intense Fe^{3+} doublet, a very weak Fe^{2+} doublet and the magnetic hyperfine profile of non-stoichiometric magnetite (Fig. 4). At 4.2 K, the Fe^{3+} doublet has collapsed to a sextet, the peaks of which flank and broaden the magnetite peaks. This behavior is indicative of ferrihydrite [16], recently identified [8] as the superparamagnetic phase proposed in Orgueil [17,18]. The spectra of Orgueil are thus consistent with the occurrence of magnetite, ferrihydrite, Fe^{3+} serpentine (cronstedtite) and Fe^{2+} serpentine in the matrix [8]. Similar Mossbauer spectra were obtained for other C1 meteorites (Ivuna, Tonk, Alais).

(5) The Mössbauer spectra of other CC not illustrated here revealed that Renazzo has major metallic Fe, minor magnetite, and Fe^{2+} and Fe^{3+} doublets of comparable intensities which do not order magnetically at 4.2 K. Metallic Fe but no magnetite occurs in ALHA 83108 (C3) and LEW 85332 (CO3) together with nanophase goethite, apparently formed by oxidative weathering in Antarctica, by analogy with ordinary chondrites [9]

Ureilite Mössbauer Spectra. Following previous discoveries [5] by Mössbauer spectroscopy of high modal proportions of metallic Fe and the presence of ferric oxides in all ureilites studied, as well as further examples of pigeonite Fe^{2+} exceeding olivine Fe^{2+} , additional ureilites were acquired for further spectral measurements at 4.2K to confirm these trends.

(1) Major amounts of metallic iron were determined in Goalpara, ALHA 82106, ALHA 82130, and LEW 85440. Minor amounts of Fe occur in MAC 88177 and EETA 83309, in which carbonaceous matrix is either negligible or localized in discrete areas not surrounding olivine grains.

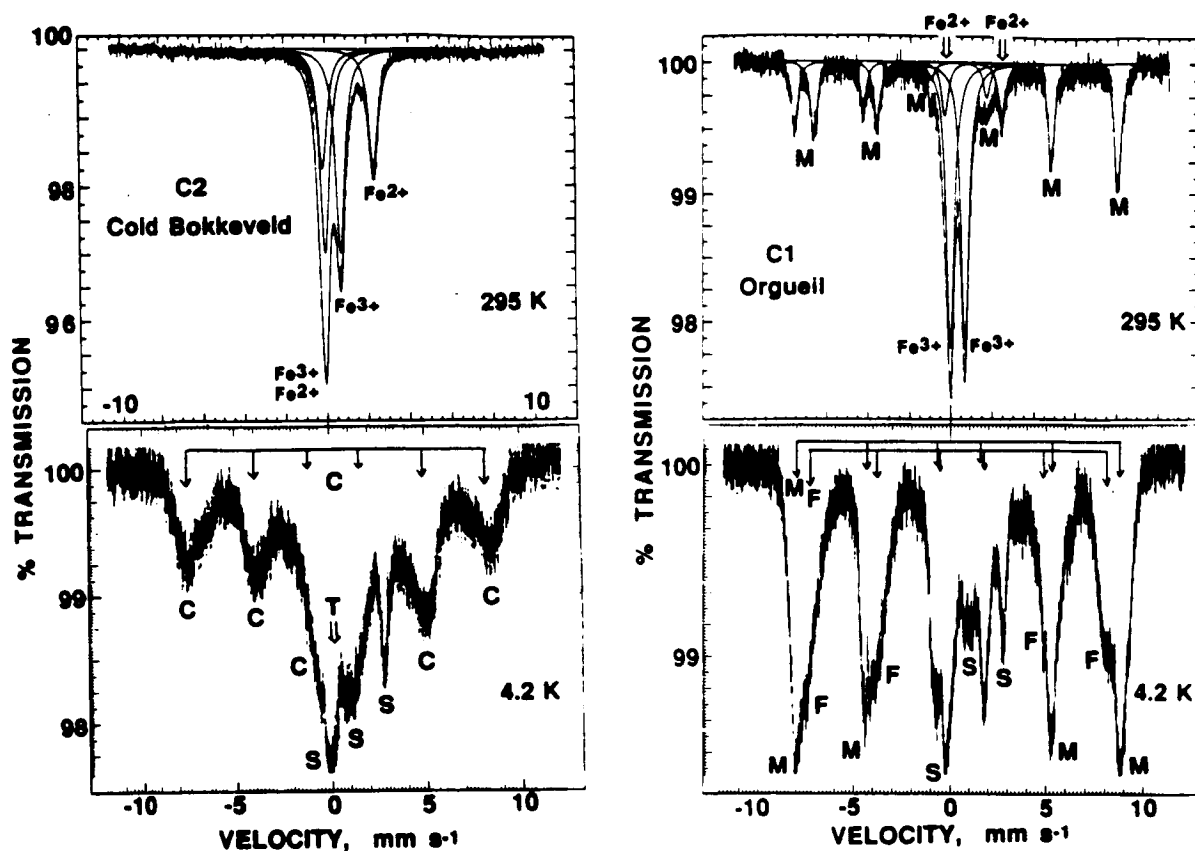


Figure 3. Mössbauer spectra of the Cold Bokkeveld meteorite. In 4.2 K spectra of this and other **CM** carbonaceous chondrites, features attributed to tochilinite (T), Fe^{2+} - Fe^{3+} serpentine (S) and magnetically ordered cronstedtite (C) may be distinguished.

Figure 4. Mössbauer spectra of the Orgueil meteorite. In this and other **CI** carbonaceous chondrites, non-stoichiometric magnetite (M) is present together with Fe^{2+} - Fe^{2+} -bearing phyllosilicates (S) and ferrihydrite (F) which becomes magnetically ordered by 4.2 K.

(2) The modal proportion of Fe^{2+} olivine exceeds Fe^{2+} pigeonite in Goalpara, EETA 83225, LEW 85440 and MAC 88177. The Fe^{2+} modal proportions are reversed in ALHA 82106 and ALHA 82130, with pyroxene > olivine. Pyroxene is a very minor constituent of EETA 83309.

(3) Each of these ureilites contains significant to high proportions of ferric oxides, including Goalpara, the freshness of which led to the speculation that it was recovered soon after an unrecorded fall. [19]. The FeOOH content is least in MAC 88177, the ureilite with negligible carbonaceous matrix.

These observations confirm the mechanism of carbon-induced reduction of Fe^{2+} in olivine in ureilites [6] and the vulnerability of the sub-microscopic metallic Fe inclusions to rusting, presumably upon exposure to Earth's atmosphere.

Acknowledgments. Research supported by NASA grant NAGW-2037.

References. [1] H.Y. McSween & S.M. Richardson, *GCA*, 41, 1145 (1977); [2] H.Y. McSween, *GCA*, 51, 2469 (1987); [3] W. Herr & B. Skerra, in *Meteorite Research* (P.M. Millman, ed.), p.106 (1968); [4] H. Roy-Poulsen *et al.*, *Phys. Scripta*, 23, 1113 (1981); [5] S.L. Martinez & R.G. Burns, *Proc. 21st LPSC*, 736 (1991); [6] J.L. Berkley *et al.*, *GCA*, 40, 1429 (1976); *ibid.*, 44, 1579 (1980); [7] M.E. Zolensky & I.D.R. Mackinnon, *Am. Min.*, 71, 1201 (1986); [8] K. Tomeoka & P.R. Buseck, *GCA*, 52, 1627 (1988); [9] T.C. Solberg & R.G. Burns, *Proc. 19th LPSC*, 313 (1989); [10] F.W. Oliver, *Planet. Space Sci.*, 26, 289 (1978); [11] F.W. Oliver *et al.*, *Meteoritics*, 19, 75 (1984); [12] W.F. Müller *et al.*, *Tsch. Min. Pet. Mitt.*, 26, 293 (1979); [13] T.E. Bunch & S. Chang, *GCA*, 44, 1543 (1980); [14] J.M.D. Coey *et al.*, *Phys. Chem. Min.*, 7, 141 (1981); [15] D.J. Vaughan & M.S. Ridout, *J. Inorg. Nucl. Chem.*, 33, 741 (1971); [16] E. Murad & U. Schwertmann, *Am. Min.*, 65, 1044 (1980); [17] M.B. Madsen *et al.*, *Nature*, 321, 501 (1986); [18] T.J. Wdowiak & D.G. Agresti, *Nature*, 311, 140 (1984); [19] J.T. Wasson *et al.*, *GCA*, 40, 1449 (1976).

**DOES LAFAYETTE = NAKHLA? NOT NECESSARILY SO, BASED ON
4.2K MOSSBAUER SPECTRA OF ALL OF THE SNC METEORITES**

Roger G. Burns

Department of Earth, Atmospheric and Planetary Sciences, Massachusetts Institute of
Technology, Cambridge, MA 02139.

Introduction. In previous Mossbauer spectral studies of many of the SNC meteorites [1,2], attention was drawn to the close similarities of spectrum profiles between Lafayette [3] and Nakhla [4], which were once suggested to be identical meteorites [5]. These observations lead to the acquisition of Governador Valadares [6] and another specimen of Nakhla [7], as well as Zagami [8] and Shergotty [8,9], for Mossbauer spectral measurements at 4.2K. Results reported here demonstrate that there are subtle differences between the three nakhlites (Nakhla, Lafayette, and Governador Valadares), as there are for three of the shergottites (Shergotty, Zagami, EETA 79001/lithologies A and B) and olivine-dominated Chassigny and ALHA 77005 [2], indicating that all eight of the SNC meteorites discovered to date fell independently to Earth.

Meteorite Samples. The British Museum (Natural History) was the source of ~100 mg chips of Nakhla, Governador Valadares and Zagami, while the Mineralogical Museum at Harvard University provided samples of Nakhla. The latter specimen enabled portions to be extracted from the fresh interior and black vitreous fusion crust of the meteorite. Samples of Shergotty (fragment A; [9]) and shergottite EETA 79001 (lithologies A and B; [10]) were also obtained. Each meteorite sample was pulverized to <45 microns, mixed with sucrose, and encapsulated in small plastic cylinders for Mossbauer spectral measurements at 4.2K and room temperature. Other experimental details are described elsewhere [1,2].

Results. Compiled in Figure 1 are the 4.2K Mossbauer spectra of suites of three of the shergottites (left panel) and the three nakhlites (right panel). The nakhlite spectra are complex due to the onset of magnetic ordering of Fe²⁺ ions in olivine [11] demonstrated previously [2,12] for olivine-rich Chassigny, Brachina, and ALHA 77005, the 4.2 K Mossbauer spectra of which are reproduced in Figure 2. Three of the olivine peaks at -4.2, +1.3 and +4.6 mm s⁻¹ are particularly sensitive to variations of composition and temperature [11], requiring that the temperature be rigidly maintained at 4.2K during spectrum acquisition. Figure 1 (right panel) shows that the 4.2K spectra of all three nakhlites resemble one another closely. Weak broad features at -7.8 and +8.7 mm s⁻¹ attributed to Fe³⁺-bearing phases are present in the spectra of all three nakhlites, including nanophase goethite + phyllosilicate assemblages comprising iddingsite [13] of preterrestrial origin [14,15]. The ferric features are particularly conspicuous in the spectrum of Lafayette and cannot be due entirely to fusion crust impurities. Overall, the spectrum profile of Lafayette more closely resembles that of Governador Valadares than Nakhla.

The shergottite spectra illustrated in Figure 1 (left panel) are dominated by absorption by Fe²⁺ ions in pyroxenes, the subtle differences of spectrum profiles reflecting differences of modal proportions of augite, low Ca pyroxenes and olivine [10,16]. The very weakly developed Fe³⁺ peaks around -7.8, -4.5 and +8.7 mm s⁻¹ in Shergotty and Zagami are attributed to ~2% titanomagnetite reported in these meteorites [8]. The 4.2K spectrum profiles of the shergottites are clearly different from those of nakhlites (Figure 1, right) and chassignites illustrated in Figure 2.

The 4.2 K Mossbauer spectra of the olivine dominated achondrites assembled in Figure 2 show that ferric oxide peaks are particularly conspicuous in Brachina (found in South Australia in 1974) which is not, however, a SNC meteorite. Similar ferric oxide peaks are barely perceptible in Chassigny (which fell in France in 1815) and in ALHA 77005.

Discussion. The small but perceptible differences of Mossbauer spectral profiles between Lafayette and Nakhla indicate that they are separate meteorites. Whereas events relating to the fall of Nakhla in 1912 are well documented [4,7], details for Lafayette prior to 1931 (when it was first recognised as a meteorite in the collection at Purdue University) are ambiguous [3,5].

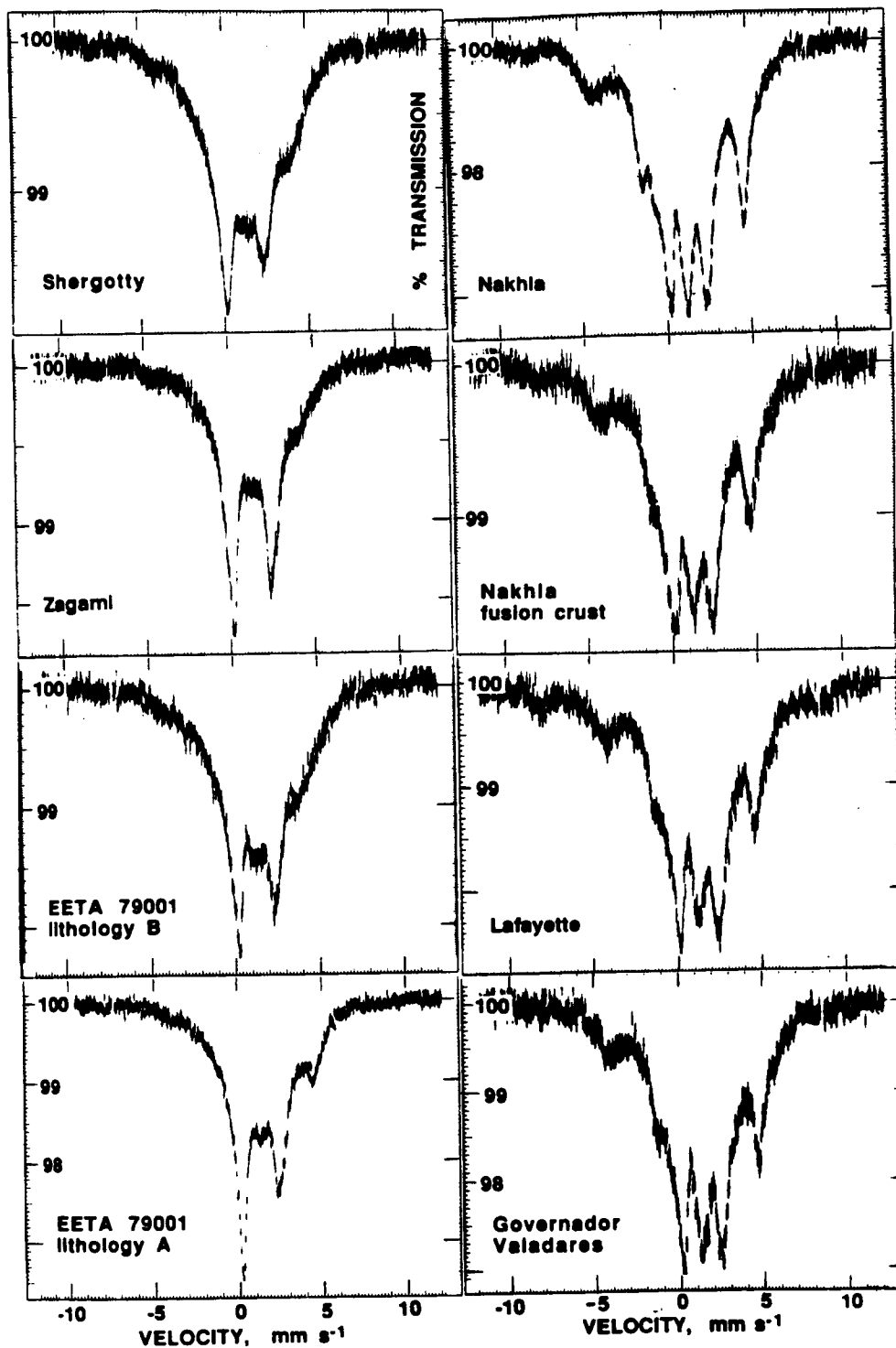


Figure 1. Mossbauer spectra of shergottites and nakhlites at 4.2 K. Left panel: shergottites; Right panel: nakhlites. Vertical dotted lines indicate the positions of the two outermost peaks of magnetic hyperfine sextets used to identify ferric oxides.

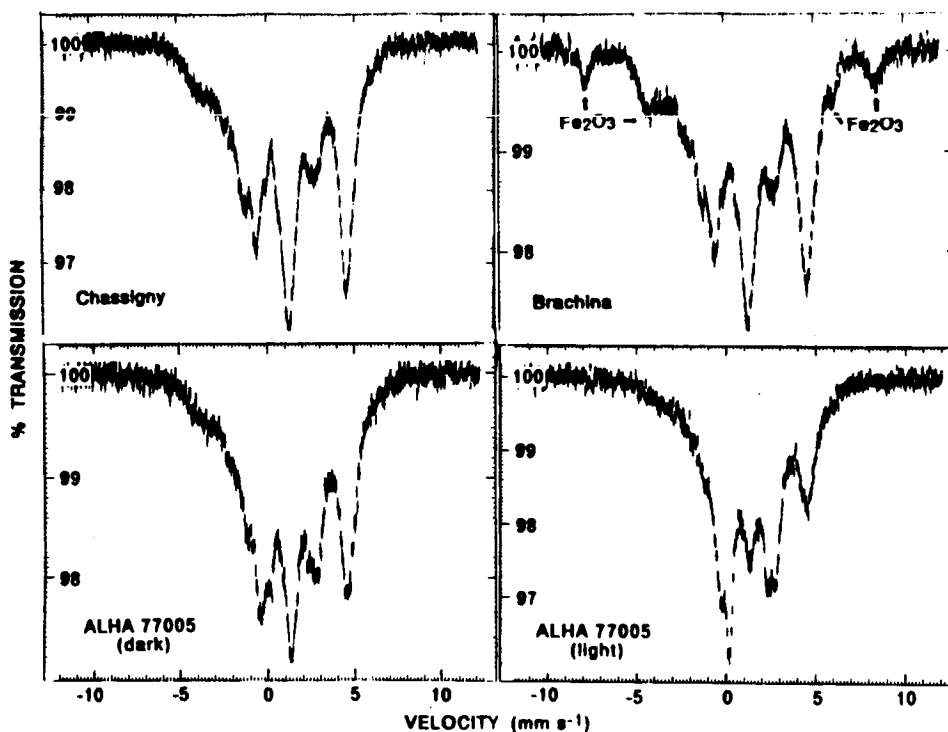


Figure 2. 4.2 K Mossbauer spectra of the olivine-dominated Brachina and SNC meteorites Chassigny and ALHA 77005

The two meteorites were once proposed to be identical [5] based on similarities of Xe isotopic data, bulk compositions, modal mineralogies, K-Ar and cosmic ray exposure ages [5,17,18] and Mossbauer spectra [2]. The discovery of the third nakhlite, Governador Valadares, with similar Mössbauer spectra and K-Ar and cosmic radiation ages to Nakhla and Lafayette [19], coupled with the fact that shergottites, themselves, also have virtually identical K-Ar and cosmic radiation ages, compositions, mineralogies [18,20] and Mossbauer spectra (Fig.1), would appear to dispell doubts that Lafayette is merely a mislabelled piece of Nakhla [18]. The three nakhlites may be genetically related, however, but their subsequent exposure histories in space and oxidative weathering on Earth have produced slight differences of Fe^{3+}/Fe^{2+} contents observed in the Mossbauer spectra. Alteration along cracks associated with shock metamorphism may be responsible for some of the FeOOH associated with iddingsite found in the three nakhlites [7,14]. However, chemical weathering on the surface of the Earth may have contributed to some of the FeOOH found in Governador Valadares. The high FeOOH content of Lafayette remains anomalous if, indeed, it was collected soon after falling to earth by the Purdue University student fishing near Lafayette [3].

Acknowledgments. Sincere thanks are due to R.Hutchinson, B.Mason, C.Francis and J.C.Laul who provided meteorite samples. Research supported by NASA grant NAGW-2037.

References. [1] T.C. Solberg & R.G. Burns, *Proc. 19th LPSC*, 313 (1989); [2] R.G. Burns & S.L. Martinez, *LPS*, XXI, 147 (1990); *Proc. 22 LPSC*, in press; [3] H.H. Nininger, *Pop. Astron.*, 43, 404 (1935); [4] G.T. Prior, *Min. Mag.*, 16, 274 (1912); [5] M.W. Rowe *et al.*, *JGR*, 71, 4679 (1966); [6] F.G. Burrigato *et al.*, *Meteoritics*, 10, 374 (1975); [7] T.E. Bunch & A.M. Reid, *ibid.*, 10, 303 & 317 (1975); [8] E.M. Stolper & H.Y. McSween, *GCA*, 43, 1475 (1979); [9] J.C. Laul, *GCA*, 50, 875 (1986); [10] H.W. McSween & E. Jarosewich, *GCA*, 47, 1501 (1983); [11] V.U.S. Rao *et al.*, *J. Appl. Phys.*, 50, 2408 (1979); [12] R.G. Burns, *LPS*, XX, 129 (1989); [13] R.A. Eggleton, *Clays Clay Min.*, 32, 1 (1984); [14] J.R. Ashworth & R. Hutchison, *Nature*, 256, 714 (1975); [15] R.G. Burns, *Nature*, 320, 55 (1986); [16] J.V. Smith *et al.*, *JGR*, 88, B229 (1983); [17] F.A. Podosek, *EPSL*, 19, 135 (1973); [18] R. Ganapathy & E. Anders, *GCA*, 33, 775 (1969); [19] D.D. Bogard & L. Husain, *GRL*, 4, 69 (1977); [20] H.Y. McSween, *Rev. Geophys.*, 23, 391 (1985).

INFRARED (2.08-14 μm) SPECTRA OF POWDERED STONY METEORITES.

J. W. Salisbury, Department of Earth and Planetary Sciences, Johns Hopkins University, Baltimore, MD 21218, D. M. D'Aria, Astronomy Program, Space Sciences Building, University of Maryland, College Park, MD 20742, and E. Jarosewich, Department of Mineral Sciences, National Museum of Natural History, Washington, DC 20560.

Infrared biconical reflectance spectra of 60 powdered meteorite samples, representing 50 different stony meteorites, have been measured as analogues of asteroidal regolith. Representative samples have also been measured in directional hemispherical reflectance to assure that Kirchhoff's Law can be used to predict relative emissivity from the reflectance spectra¹.

These spectral data confirm that the O-H fundamental absorption band near 2.9 μm is an extremely sensitive indicator of incipient alteration^{2,3}, which often has taken place in powdered meteorite samples exposed only to water vapor in the air. Such non-carbonaceous samples typically contain less than 1% water by weight.

Likewise, the C-H fundamental absorption bands near 3.4 and 3.5 μm are equally sensitive indicators of contamination with volatile hydrocarbons, which can also be adsorbed from the air. The heavy, macromolecular hydrocarbons native to chondrites do not display such bands, making detection of these bands in remote sensing of asteroids⁴ unlikely.

Despite the spectral artifacts introduced by alteration and hydrocarbon contamination, powdered stony meteorites display a wide variety of real spectral features that can be used for their identification. These include:

Residual reststrahlen bands. Ever since Lyon⁵ showed that fundamental molecular vibration bands, or reststrahlen bands, become difficult to detect in the spectra of fine particulate materials, efforts have been made to determine alternative spectral features (see below) that can be used to characterize composition in the mid-infrared region of the spectrum. However, our meteorite spectra show that, although reststrahlen bands become subtle compared to other features in the spectra of fine (<75 μm) particulate material, they do not completely disappear. Some minerals, such as olivine, have particularly persistent reststrahlen features that remain easily discernable, while other minerals contribute more subtle features, but all can be used for meteorite identification in spectra with sufficient spectral resolution and signal-to-noise to resolve them.

Absorption bands. While the strong reststrahlen bands of the major meteorite-forming minerals are dominated by surface scattering, and hence are expressed as reflectance peaks, other bands occur in the 4 to 7 μm region that have much weaker absorption coefficients. As a result, volume scattering dominates the spectral behavior in this region and these bands are expressed as troughs. Such overtone and combination tone bands have compositional significance for many particulate materials⁶, and meteorites are no exception. Both olivine and pyroxene have prominent spectral features in this region that change wavelength position with iron content of the minerals.

Christiansen feature. The reflectance minimum associated with the Christiansen frequency has been shown to be indicative of the compositions of minerals and rocks^{7,8}. Most naturally occurring mineral mixtures result in a single average Christiansen feature, but when the individual minerals have Christiansen features that are too far apart in wavelength, a complex spectral feature may result. This occurs in spectra of some kinds of carbonaceous chondrites. In such a case, changing spectral resolution may substantially affect the apparent wavelength of the Christiansen feature. Thus, laboratory and remote sensing spectral data should be compared at the same resolution.

We find that the wavelengths of the peaks or troughs of each one of the spectral features described above can be used independently to infer meteorite composition (see Figure 1), but the best results are obtained when the entire spectral curve is used, or at least the portion of it encompassed by the 8 to 14 μm atmospheric window, in a digital search library. Effects of the vacuum environment on such a spectral curve⁹ have yet to be fully assessed, but should be minimal for materials as dark as stony meteorites.

REFERENCES:

1. Nicodemus F.E. 1965. *Applied Optics* 4, 767-773.
2. Salisbury J.W., and G.R. Hunt 1974. *J. Geophys. Res.* 79, 4439-4441.
3. Miyamoto M. 1988. *Earth and Planet. Sci. Letters* 89, 398-402.
4. Cruikshank, D. P., and R. H. Brown 1987. *Science* 244, 183-184.
5. Lyon R.J.P. 1964. NASA-CR-100. Washington, D.C. 262 pp.
6. Salisbury J. W., B. Hapke, and J. W. Eastes 1987. *J. of Geophys. Res.* 92, 702-710.
7. Conel J.E. 1969. *J. Geophys. Res.* 74, 1614-1634.
8. Salisbury J.W., and L.S. Walter 1989. *J. Geophys. Res.* 94, 9192-9202.
9. Logan L.M., G.R. Hunt, J.W. Salisbury, and S.R. Balsamo 1973. *J. Geophys. Res.* 78, 4983-5003.

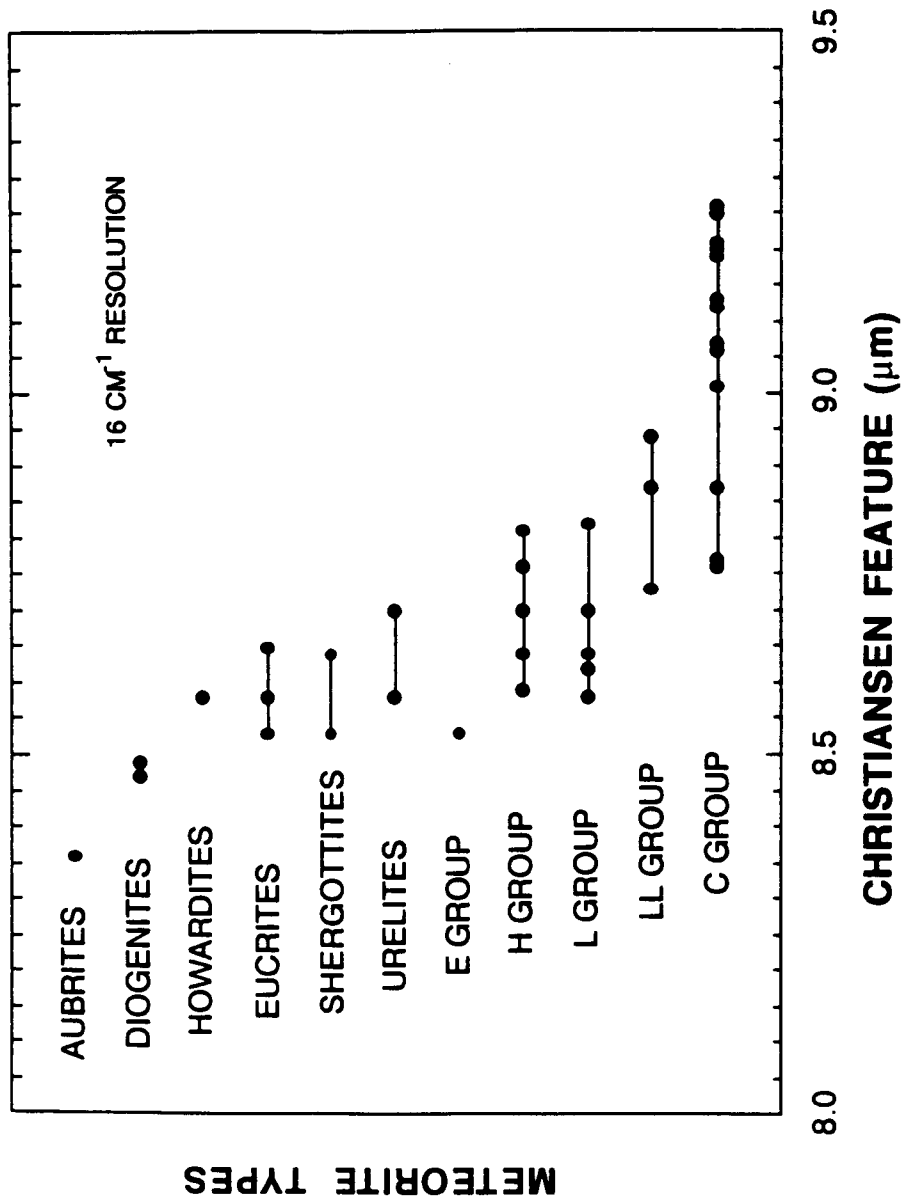


Figure 1. Wavelength of the Christiansen feature measured at 16 wavenumber resolution for all meteorite types examined.

DARKENING IN GAS-RICH ORDINARY CHONDRITES: SPECTRAL MODELLING AND IMPLICATIONS FOR THE REGOLITHS OF ORDINARY CHONDRITE PARENT BODIES. D.T. Britt and C.M. Pieters. Dept. of Geological Sciences, Brown Univ., Providence, RI 02912.

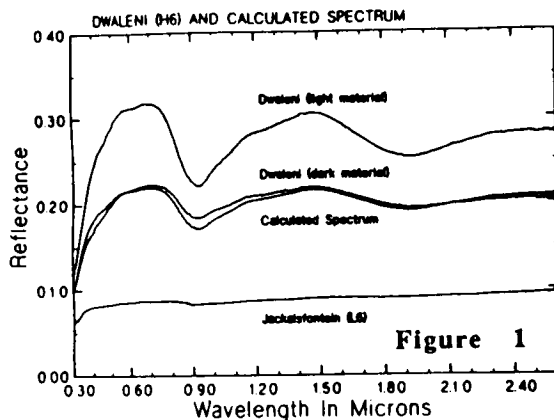
Introduction: The connection between asteroids and meteorites is based, in part, on the strong similarities between remotely sensed telescopic spectra and laboratory spectral data that have linked most of the major meteorite types with asteroid spectral types [1]. However, the major exception to this link is the failure to unequivocally identify any main asteroid belt parent bodies for the most numerous type of meteorite, the ordinary chondrites. Important clues to the identification of ordinary chondrite parent bodies may be found in the dark matrix material of gas-rich ordinary chondrites. The dark portions of gas-rich ordinary chondrites contain high levels of solar wind implanted gases and solar flare tracks strongly indicating that this material was exposed on asteroidal surfaces [2]. The implication is that the dark material represents samples of the regolith soil of ordinary chondrite parent bodies. The spectra of the dark material is altered from that of normal ordinary chondrites [3,4]. Not only is the reflectance lowered, but the diagnostic spectral absorption bands are shallowed and subdued. This would suggest that the regolith soil of ordinary chondrite parent bodies is also spectrally altered. Isolating the cause of the spectral darkening in of gas-rich chondrites may provide insight on the spectral characteristics of the regolith soil and, by implication, the spectral characteristics of the elusive ordinary chondrite parent bodies.

Spectral Mixture Modelling: The preferred way of examining the optical properties of the opaque fraction in gas-rich chondrites is to analyze the spectra of a sample of pure gas-rich dark matrix material. However such samples are extremely rare due to the intimate mixture between the dark matrix and the light clasts. The "dark" matrix of gas-rich chondrites is typically a fine grained mass of light clasts and fragments mixed with smaller amount of dark, gas-rich grains. It is simply impossible to separate grains with a particle sizes as small as a few tens of microns that are mixed on a scale of tens of microns and produce enough material for a laboratory bidirectional reflectance measurements. All the gas-rich samples used in this spectral study had a substantial fraction of light clast material mixed with the dark matrix. It is possible, however, to use an intimate mixing model based on the bidirectional reflectance theory of Hapke [5] to simulate the spectral mixing of light clast material with dark matrix material. The dark matrix material has an opaque morphology similar to that of black chondrites [6]. Photomicrographs and SEM images show that the particle size and distribution of metal and troilite is very similar to that in black chondrites. Counts show that the density of opaques and attenuation of photon path length is also well within the range seen in black chondrites [6]. If we assume that the "pure" dark matrix material has a spectrum similar to that of black chondrites, the intimate mixing technique can be used to test this assumption by examining how a mix of black chondrite and light clast spectra can replicate the spectrum of the dark area of a gas-rich chondrite. The first simulation uses the spectra of the light portion of the gas-rich chondrite Dwaleni (H6) and black chondrite Jackalsfontein (L6) as end-members. Point counts of a thin section of Dwaleni show that the dark component contains approximately 65% light clast material and about 35% dark grains. Shown in Figure 1 are the spectra of the light and dark components of Dwaleni and the simulated spectrum with a mix of 65% light component and 35% black chondrite based on the point count data. The close match between the simulated and actual dark area spectra show that there are strong spectral similarities between the "pure" dark matrix material in gas-rich chondrites and black chondrites. Shown in Figure 2 is a similar mixing experiment using the light portion of the gas-rich chondrite Fayetteville (H4-6) and the black chondrite Novosibirsk (H5-6). Once again a mix of these components in fractions corresponding to observed light/dark components replicates with great accuracy the spectrum of the dark area.

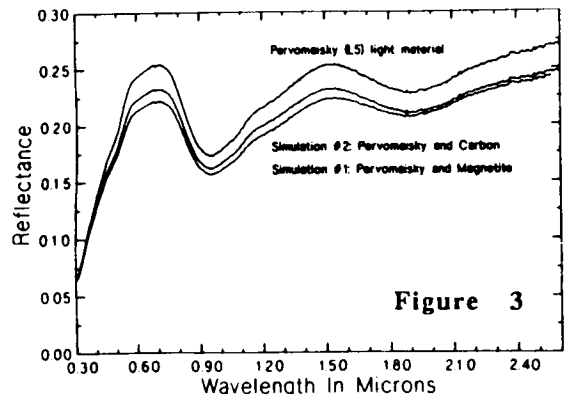
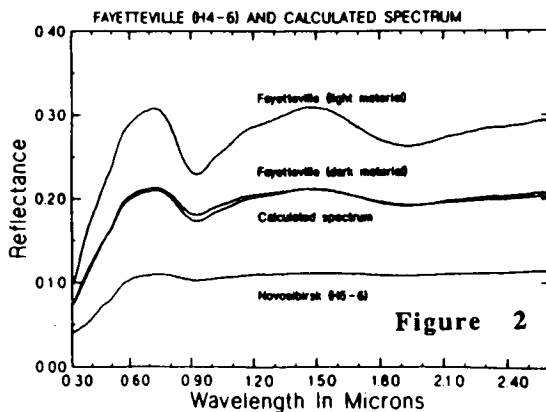
Simulations were also run to test the optical effects of the other opaque fractions in gas-rich ordinary chondrites. Two in particular, magnetite and carbon, have been suggested as optically important [7,8]. The results of these simulations are shown in Figure 3. Using the observed mass fractions and particle size distribution, both magnetite and carbon failed to produce anything close to the required optical alteration. This is not to say that chromite, magnetite,

ilmenite and carbon are not contributing to the optical darkening seen in black chondrites. Clearly all the opaques in the meteorite contribute to the overall effect. However, the relatively large particle size, limited distribution, and the very small mass fraction of these minor opaques makes their contribution minor. Metal and troilite are so much more abundant that their effects swamp the contributions of other opaque fractions.

The Cause of Darkening in Gas-rich Ordinary Chondrites: The dark fine-grained matrix of gas-rich ordinary chondrites replicates many of the physical, morphological, and spectral characteristics of the highly shocked and optically altered black chondrites. Spectral mixture modelling shows that the darkening and spectral attenuation seen in the dark matrix can be simulated with realistic mass fractions of light host material and black chondritic material. All these factors point to the conclusion that the dark matrix of gas-rich ordinary chondrites is dark due to the same processes that darkens black chondrites, shock-distributed small particle size FeNi metal and troilite. Because the darkening is not seen in any of the non-gas-rich light portions and is only seen in the gas-rich grains of the meteorite, the shock-darkening would have to occur as part of the matrix's exposure to regolith processes. Since all gas-rich grains are darkened, it follows that darkening is not only common, but pervasive in asteroidal regoliths. These results imply that the upper, optically active layer of an ordinary chondrite parent body should have the spectral characteristics of a black chondrite, which are a dark, relatively featureless spectrum with modest red slope in the infrared. These are the characteristics of spectral type C asteroids [1].



References: [1] Bell J.F. et al. (1989) *Asteroids II*, 921-945 [2] Bell J.F. and Keil K. (1988) *Proc. 18th*, 573-580 [3] Fredriksson K. and Keil K. (1963) *G & C Acta*, 27, 717-739. [4] Britt D.T. and Pieters C.M. (1991) This volume. [5] Hapke (1981) *JGR*, 86, 3039-3054. [6] Britt D.T. and Pieters C.M. (1991) In preparation. [7] Rubin et al., (1983) *Proc. 13th, JGR* 88, A741-A754. [8] Keil K. (1982) LPI tech. rept. 82-02, 65-83.



THE BIDIRECTIONAL REFLECTANCE SPECTRA OF FIVE GAS-RICH ORDINARY CHONDRITES.
D.T. Britt and C.M. Pieters, Dept. of Geological Sciences, Brown University, Providence, RI 02912.

Introduction: A major objective in asteroid science is the identification of the main asteroid belt parent bodies of ordinary chondrite meteorites. Ordinary chondrites account for 80% of observed meteorite falls, but so far no main belt parent bodies have been unequivocally identified for this meteorite type. Part of the answer to this puzzle may lie in the spectral characteristics of the ordinary chondrite parent body regoliths. The spectra of gas-rich ordinary chondrites can provide clues to reconstructing the spectra of an ordinary chondrite regolith. Gas-rich ordinary chondrites are generally characterized by a light/dark structure of light clasts, chondrules, and fragments of chondrules set in a dark, fine-grained matrix containing grains rich in solar wind implanted gases [1,2]. The dark matrix grains contain not only solar wind gases, but also dense assemblages of solar flare tracks indicating that these grains were exposed on the surface of the parent body and probably represent samples of relithified regolith soil [3,4]. If this material is regolith soil, its spectral characteristics would help clarify the spectral effects of regolith processes and provide insight into the spectra of ordinary chondrite parent bodies.

The Distribution of Light and Dark Material: While the optical characteristics of gas-rich chondrites are dominated visibly by their light/dark structure, the distribution of light and dark material makes it difficult to obtain the spectra of relatively "pure" dark material. This is due to the intimate mix of light clasts, chondrules, and fragments, and dark grains in the matrix. Although the dark matrix is fine grained, the light material is apparent in all particle sizes down to fractions as fine as the dark grains within the matrix. The light material occupies a significant fraction of the "dark" matrix area. Point counts using thin sections of Dwaleni (H6) and Leighton (H5) show that the light material accounts for approximately 67% and 49% respectively of the aerial coverage in the "dark" matrix area. Clearly, any spectrum of material from a dark area will include a significant component of light clast material.

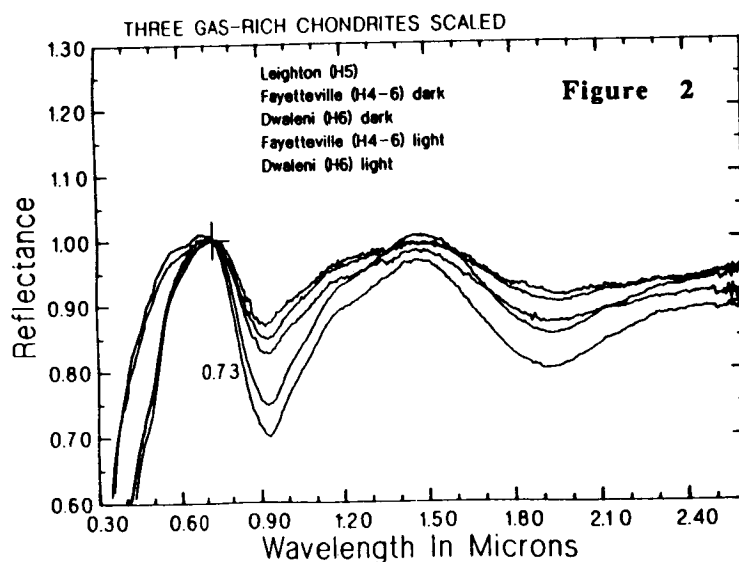
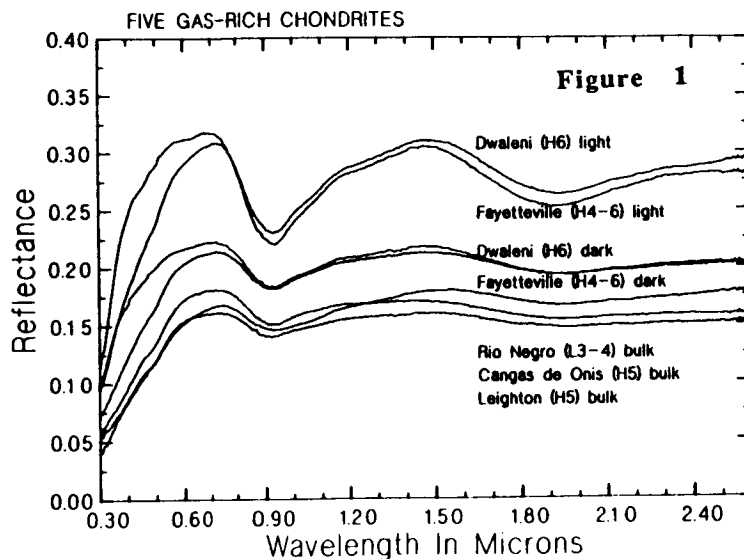
The Spectra of Gas-Rich Ordinary Chondrites: Shown in Figure 1 are the spectra of five gas-rich ordinary chondrites. The samples of Dwaleni (H6) and Fayetteville (H4-6) have relatively definite light and dark areas and the spectra of separates from these areas are shown, although it should be emphasized that the dark areas of these meteorites still have a significant fraction of light material. The spectrum of the dark area is by no means a spectrum of "pure" dark matrix.. The samples Leighton (H5), Cangas de Onis (H5) and Rio Negro (L3-4) were too intimately mixed to separate light and dark fractions and as a result, the spectra of crushed bulk samples are shown. In all cases bidirectional reflectance spectra were obtained of crushed powders at a viewing geometry of $i=30^\circ$, $e=0^\circ$, using the RELAB spectral facility.

The light fractions of both Dwaleni and Fayetteville are very bright with visible reflectances of 0.32 and 0.27 respectively. The light area spectra also show very strong, high contrast absorption bands that are excellent examples of normal ordinary chondrite spectra [5]. The dark portions of these meteorites exhibit evidence of alteration of their optical properties. In both samples the reflectance and band depth has been significantly diminished. For Dwaleni reflectance at $0.55 \mu\text{m}$ decreases from 0.32 to 0.22, a drop of over 30%. Although some reduction in apparent band depth would be expected due to the decreased reflectance, in this case the reduction is substantially out of proportion to the drop in reflectance. Shown in Figure 2 are the spectra of Dwaleni, Fayetteville and Leighton scaled to unity at $0.73 \mu\text{m}$. The depth of the $1.0 \mu\text{m}$ band is approximately 30% for the light portion of Dwaleni, while the corresponding dark material shows a band depth of 17%, a reduction of 43%. The $2.0 \mu\text{m}$ band is similarly reduced by approximately 35%. For Fayetteville the band reductions are 40% for the $1.0 \mu\text{m}$ band and 46% for the $2.0 \mu\text{m}$ band. Another feature of these spectra is the change in overall spectral slope. In the light portions of both Dwaleni and Fayetteville the spectra are slightly blue sloped, decreasing in reflectance about 11% and 9% respectively between $0.73 \mu\text{m}$ and $2.6 \mu\text{m}$. This blue slope has been reduced in the dark fractions to about 5% for both samples, a reduction of 55% and 45% respectively. This suggests that the darkening agent in the matrix not only reduces the reflectance and suppresses the absorption features, but also has a modest red slope. It should be

emphasized that these reductions in reflectance and band depth occur despite significant proportions of light material in the dark areas. The spectra of these areas are not spectra of pure dark matrix but a complex mix of clasts from the light material along with the dark gas-rich grains.

The spectra of bulk samples of Leighton, Rio Negro, and Cangas de Onis also show substantial reductions in reflectance and band depth relative to normal ordinary chondrites. As shown in Figure 2 Leighton has a 1.0 μm band depth of 12% while the range for normal ordinary chondrites is approximately 20-30%. Once again, these samples are a mix of light and dark material and the spectrum of pure dark material would be substantially darker.

Conclusions: In general, the spectra of the dark areas of gas-rich ordinary chondrites show reductions in both reflectance and band depth relative to the spectra of the light areas and the spectra of normal ordinary chondrites. The dark areas of these samples show spectral alteration despite having substantial fractions of light material intimately mixed with the dark, gas-rich grains. If the spectra of the dark gas-rich grains represent the spectral characteristics of a regolith soil on an ordinary chondrite parent body, then that surface would display a dark and strongly subdued spectrum.



Acknowledgements: The authors wish to express thanks to C.A. Francis of the Harvard University Mineralogical Museum, G.J. MacPherson of the Smithsonian Institution, R. Hutchison and V. Jones of the British Museum (Natural History), and D. Sears of the University of Arkansas for generously granting access to their respective collections and for the loan of meteorite samples. This research was supported by NASA grant NAGW-28 and by a NASA Graduate Student Research Fellowship to D.T. Britt. RELAB is supported as a NASA-multiuser facility under grant NAGW-748.

References: [1] Fredriksson K. and Keil K. (1963) *Geochim. Cosmochim. Acta*, 27, 717-739. [2] Williams C.V. et al. (1985) *Meteoritics*, 20, 331-345. [3] Keil K. (1982) LPI tech. rept. 82-02, 65-83. [4] Lal D. and Rajan R.S. (1969) *Nature*, 223, 269-271. [5] Gaffey M.J. (1976) *JGR*, 81, 905-920.

REFLECTANCE SPECTRA OF SOME FRACTIONS OF MIGEI AND MURCHISON CM CHONDRITES IN THE RANGE OF 0.3-2.6 μm

L.V.Moroz (Vernadsky Institute, USSR Academy of Sciences, Moscow 117975, USSR), C.M.Pieters (Department of Geological Sciences, Brown University, Box 1846, Providence, RI 02912, USA).

INTRODUCTION: Some spectral differences exist between type CI and CM meteorites. These differences include in particular the slope of the spectral curve in the near-IR region. The reflectance spectral curves of CI's are neutral in the 0.9-2.6 μm range, while for CM meteorites the increasing of the reflectance with wavelength in this region is typical. This phenomenon is often called as "reddening". The various slopes of the spectral curves are also typical for the reflectance spectra of C-type asteroids and the degree of the reddening increases in general with heliocentric distance (1). The reddening observed in CM chondrites is not understood. Johnson and Fanale (2) observed that as CM chondrites are more finely powdered their spectra become more reddened. In the process of meteorite crushing the chondrules are broken up. Those authors suggested that in this case the silicate components of the chondrules (mainly olivine), which have higher IR reflectivities, were able to contribute more to overall spectrum. Gaffey and McCord (3) proposed two possible physical mechanisms, which could produce such effect. But it is also possible that the presence of the organic polymers in the matrix material results in the reddening of CM spectra (4,5).

To test these two hypotheses the matrix material and the material enriched in olivines were separated from Migei and Murchison CM chondrites using binocular microscope. The spectra of these fractions were compared with the spectra of the bulk samples of Migei and Murchison. The spectra of bulk Orgueil (CI1) samples were also measured, but not discussed here. The specimens were powdered and sieved to obtain two particle size fractions (40-100 and 100-200 μm). The 40-100 μm powders were ground and sieved to <40 μm . Bidirectional reflectance spectra were measured in the range of 0.3-2.6 μm using the RELAB spectrometer (Brown University, USA).

MIGEI: The data obtained show that the spectral curves of the samples enriched in olivines are redder than those of the matrix material in the near-IR. Thus the presence of the olivine grains and chondrules appears to be responsible for the Migei reddened spectra (Fig.1a-c). The spectral curves of matrix material (40-100 and 100-200 μm) even have some negative slopes. Their slopes and albedos almost don't depend on the particle sizes, but the slopes and albedos of the fractions enriched in olivines are strongly affected by the particle sizes. This result shows that significant disparity between the grain sizes in the matrix and those of the chondrules and olivine aggregates, is responsible for the increasing of the spectral reddening with the decreasing of particle sizes. This effect is consistent with one of two mechanisms proposed by Gaffey and McCord (3).

The finest "matrix" fraction (<40 μm) is contaminated with olivines, because after grinding of 40-100 μm powder the olivine grains from the internal parts of the matrix particles reached the surface and have affected to the spectral characteristics. The spectrum is redder and albedo is higher than those of the coarser matrix fractions.

MURCHISON: The albedos of the "matrix" powders are lower than those of the fractions enriched in olivines, but the spectral curves of Murchison "matrix" and "enriched in olivines" fractions have identical slopes in the near infrared for similar particle sizes (Fig.1d-f). In addition, there is a shallow inflection near 1 μm in the "matrix" spectra, so the spectral contribution of olivine is evident. This "contamination" seems to result from the petrological peculiarities of Murchison, rather than low quality of separation.

BULK SAMPLES: The bulk samples of Migei and Murchison seem to be weathered, because they were ground to powders several years ago, while the "matrix" and "enriched in olivines" fractions are relatively fresh. The spectra of bulk samples are even more particle size dependent than those of the fractions enriched in olivines (especially for Murchison). Further studies are needed to understand these effects of the weathering.

ABSORPTION FEATURES: Only two absorption features are presented in the spectra of the most "clean" matrix powders: UV-falloff shortward of 0.5 μm and weaker feature centered at 0.74 μm (similar features are presented in CCD spectra of some low albedo asteroids(6)). Both features appear to be the charge transfer ones, related with Fe^{3+} -bearing clay minerals. Hydrosilicates in carbonaceous chondrites are in the intimate intergrowth with the opaque phases. The latter suppress other absorption bands of hydrosilicates and significantly decrease the albedo. The broad shallow feature near 1 μm due to olivine is presented in the spectra of "bulk", "enriched in olivine" and some "matrix" powders.

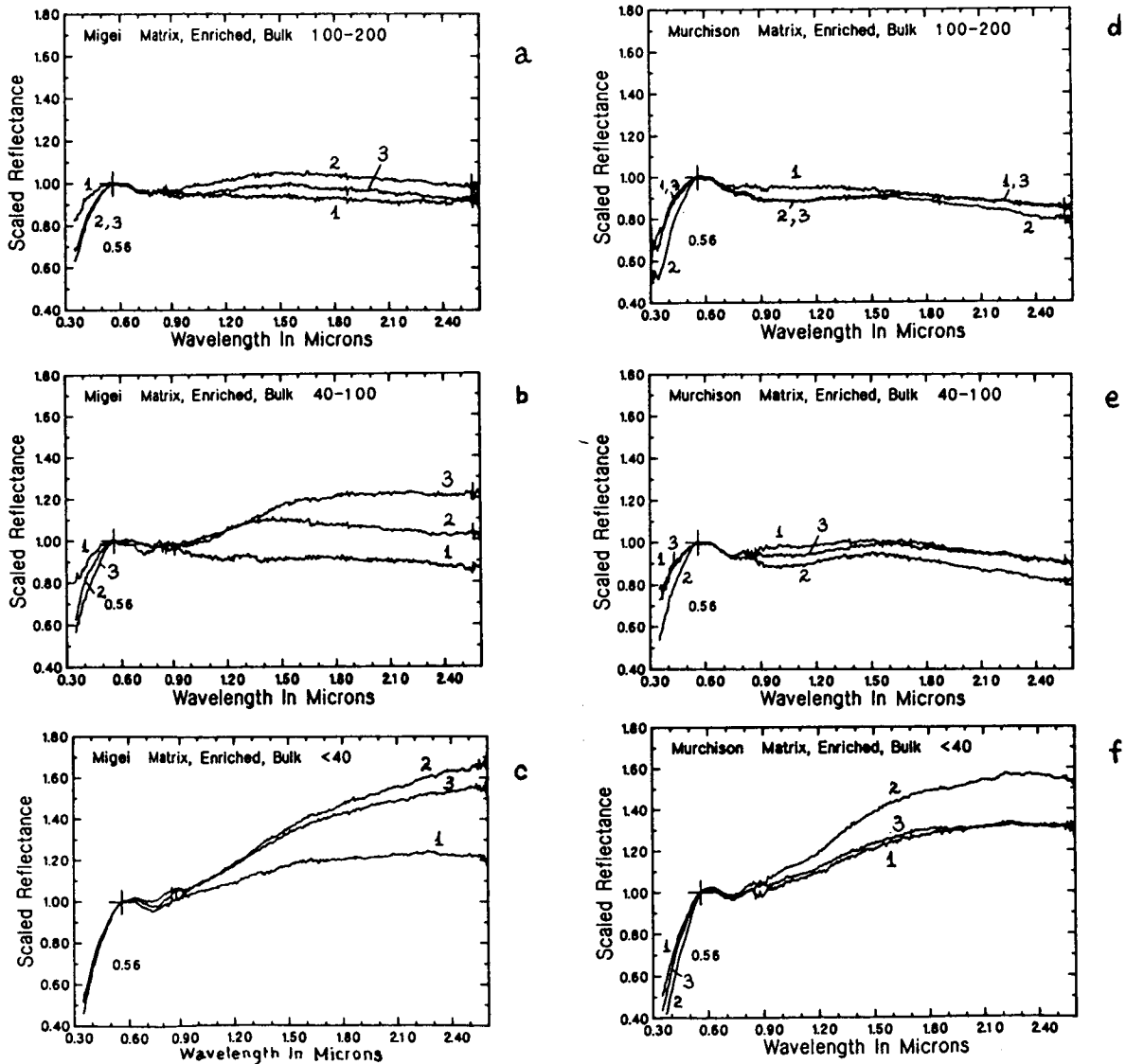
IMPLICATIONS FOR C-TYPE ASTEROIDS: The spectra of the most "clean" Migei matrix fractions indicate that the reddish slopes of CM spectral curves in the near infrared are due to the enhanced olivine feature, rather than to organic matter. We can propose that the red slope of the spectra of some C-type asteroids may indirectly

REFLECTANCE SPECTRA OF CM CHONDRITES: Moroz, L.V. and Pieters, C.M.

suggest the presence of olivine in the surface material. At the same time the red-sloped spectra of more distant D-type asteroids seem to be due to the presence of organic materials (7,8). If so then the chemical (or physical) form of this organic matter must be quite different from the organic materials which would be on the surfaces of the parent bodies of CM chondrites (most likely C-type asteroids). It is also possible that the content of organic components in CM matrix is too low to change the slope of the spectra.

REFERENCES: 1) Feierberg M.A. (1985) et al., *Icarus* 63, 183-191. 2) Johnson T.B. and Fanale F.P. (1973), *JGR*, No. 35, 8507-8518. 3) Gaffey M.J. and McCord T.B. (1979), in: *Asteroids* (T.Gehrels, Ed.), Univ. of Arizona Press, Tucson, 688-723. 4) Larson H.P. et al. (1979), *Icarus* 39, 257. 5) Gaffey M.J. (1980), *LPS XI*, 312-313. 6) Vilas F. and Gaffey M.J. (1989), *Science* 246, 790-792. 7) Gradie J. and Veveřka J. (1980), *Nature* 283, 840-842. 7) Moroz L.V. et al., this volume.

Fig.1. Bidirectional reflectance spectra of various Migei and Murchison fractions (normalized to 1 at 0.56 μ m). a) Migei (particle size 100-200 μ m); b) Migei (40-100 μ m); c) Migei (<40 μ m); d) Murchison (100-200 μ m); e) Murchison (40-100 μ m); f) Murchison (<40 μ m). 1. Matrix material. 2. Bulk material. 3. Material enriched in olivines as compared with the bulk samples.



AN INFRARED REFLECTANCE STUDY OF LOW ALBEDO
SURFACE CONSTITUENTS

Larry A. Lebofsky, Lunar and Planetary Laboratory,
University of Arizona, Tucson, Arizona, 85721

We are continuing our analysis of spectra obtained under the Planetary Astronomy Program and making laboratory spectral measurements for comparison with these telescopic observations. Our work has resulted in a chapter in the Atmospheres book (Lebofsky *et al.* 1989), in talks presented at the 1988 Asteroids II conference, 1988 and 1989 Meteoritical Society Meetings, Lunar Science Conference, American Chemical Society Meeting, the 1989 DPS, and at the 1991 Tucson Resources meeting. A chapter is now being written for the book that is coming out of the Resources meeting. Our results will also be presented at this year's Meteoritical Society and DPS meetings. Two papers have been published in *Icarus*, including a paper based on Tom Jones' dissertation. A chapter (from the ACS meeting) with M. J. Gaffey, L. Lebofsky, T. Jones, and M. Nelson has just been accepted. Finally, a paper with Bell on the analysis of groundbased Deimos spectra is in preparation.

Our most recent work has been on the analysis of the spectra of low-albedo, outer belt and Trojan asteroids (Lebofsky *et al.* 1990). We summarize the results here.

Unaltered asteroids are thought to represent the raw materials available for terrestrial planet formation and so are important to our understanding of the origin and evolution of the Solar System. Compositional variation in the asteroid belt has long been interpreted as primordial, with asteroids becoming more volatile-rich with distance from the sun. Gradie and Tedesco (1982) showed that the asteroid compositional types varied systematically with heliocentric distance and inferred that the asteroids probably formed very close to their present locations in the asteroid belt. From their inferred composition, Gradie and Tedesco also concluded that the outer belt and Trojan asteroids were probably more "primitive" than the C-class asteroids which dominate the main belt. This interpretation was consistent with the earlier laboratory study of asteroid analogs by Gradie and Veverka (1980), who concluded that the low albedo D-class asteroids were probably "ultraprimitive" in composition, *i.e.*, composed largely of hydrated silicates and organic material. However, recent observations (Jones 1988, Jones *et al.* 1990, and Lebofsky *et al.* 1989, 1990) suggest that much of the surface mineralogy seems to be due to alteration events subsequent to formation rather than primordial composition. The distribution of water is the key to understanding the volatile content of the asteroid belt and controls much of the later alteration.

Observational testing of this idea relies on the exploitation of the 3- μm absorption feature in hydrated silicates—the only diagnostic spectral band evident in the dark, volatile-rich CI and CM meteorites (Lebofsky 1978). The existence of the band has demonstrated the presence of hydrated silicates on asteroids (Lebofsky *et al.* 1981, 1989, 1990; Jones 1988; Jones *et al.* 1989). An example of this feature is shown in the spectrum of the CI meteorite Orgueil (Fig. 1). The feature is characterized by a sharp reflectance drop at 2.7 μm , due to structural OH, and by an absorption due to H₂O that decreases slowly out to about 3.5 μm .

In our present observational program we are expanding our observations to include other low-albedo classes of asteroids, asteroids that range primarily from the middle and outer asteroid belt (>2.5 AU) to the Trojan region at 5.2 AU. Our preliminary results indicate that the outer belt and Trojan asteroids do not show features diagnostic of hydrated silicates and we conclude that these asteroids have not undergone the alteration processes that we see in the C-class asteroids. However, our observations show that only half of the C asteroids show the water of hydration band and in our most recent work, we have found a main-belt D that does show the band (Fig. 3, 4). This means that we must be very careful in assuming that the classes relate directly to mineralogy and that, in reality, there appear to be major differences in mineralogy within individual classes.

Before the start of our program very little high-resolution reflectance data existed on meteorites and asteroid analogs in the $3\text{-}\mu\text{m}$ spectral region. We now have a large dataset of laboratory spectra for comparison with our telescopic spectra (Jones 1988, Jones *et al.* 1990, 1991 in preparation). With these data in hand and results from our future efforts, we hope to understand better the composition of the primitive, relatively unaltered asteroids. Coupled with studies of meteorites and new theories of Solar System formation, this picture of asteroid composition may illuminate the materials and source regions for terrestrial planet formation.

REFERENCES

- GRADIE, J. C., AND E. F. TEDESCO 1982. Compositional structure of the asteroid belt. *Science* **216**, 1404-1407.
- GRADIE, J. C., AND J. VEVERKA 1980. The composition of the Trojan asteroids. *Nature* **283**, 840-842.
- JONES, T. D. 1988. An infrared reflectance study of water in outer belt asteroids: Clues to composition and origin. PhD Dissertation, Univ. of Arizona, Tucson. 281 pp.
- JONES, T. D., L. A. LEBOFISKY, J. S. LEWIS, AND M. S. MARLEY 1990. The composition and origin of the C, P, and D asteroids: Water as a tracer of thermal evolution in the outer belt. *Icarus* **88**, 172-192.
- LEBOFSKY, L. A. 1978. Asteroid 1 Ceres: Evidence for water of hydration. *MNRAS* **182**, 17p-21p.
- LEBOFSKY, L. A., M. A. FEIERBERG, A. T. TOKUNAGA, H. P. LARSON, AND J. R. JOHNSON 1981. The 1.7- to $4.2\text{-}\mu\text{m}$ spectrum of asteroid 1 Ceres: Evidence for structural water in clay minerals. *Icarus* **48**, 453-459.
- LEBOFSKY, L. A., T. D. JONES, AND F. HERBERT 1989. Asteroid volatile inventories. In *Origin and Evolution of Planetary and Satellite Atmospheres* (S. K. Atreya, J. B. Pollack, and M. S. Matthews, Eds.), Univ. of Arizona Press, Tucson, pp 192-229.
- LEBOFSKY, L. A., T. D. JONES, P. D. OWENSBY, M. A. FEIERBERG, AND G. J. CONSOLMAGNO 1990. The nature of low albedo asteroids from $3\text{-}\mu\text{m}$ spectrophotometry. *Icarus* **83**, 16-26.

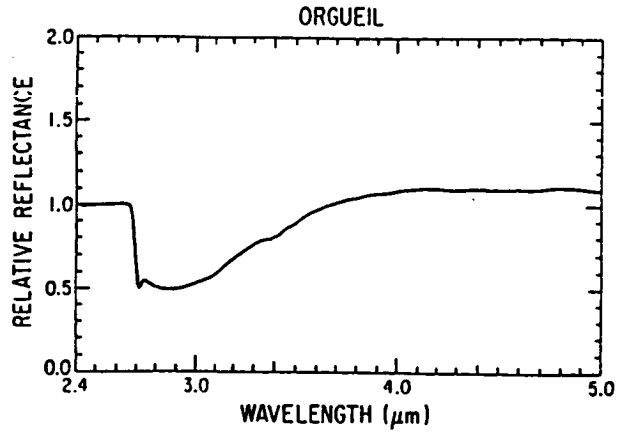


FIG. 1. A laboratory reflectance spectrum (2.4 to 5.0 μm) of the CI meteorite Orgueil. The spectrum is scaled to 1.0 at 2.5 μm (from Jones 1988).

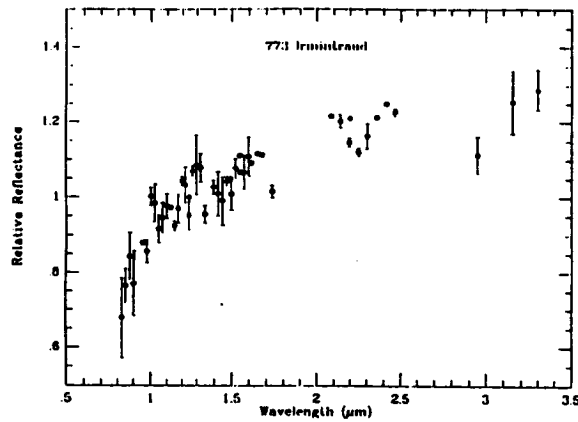


FIG. 2. Preliminary spectrum of asteroid 773 Irmintraud, a main belt D asteroid that appears to show the presence of a 3- μm water of hydration band.

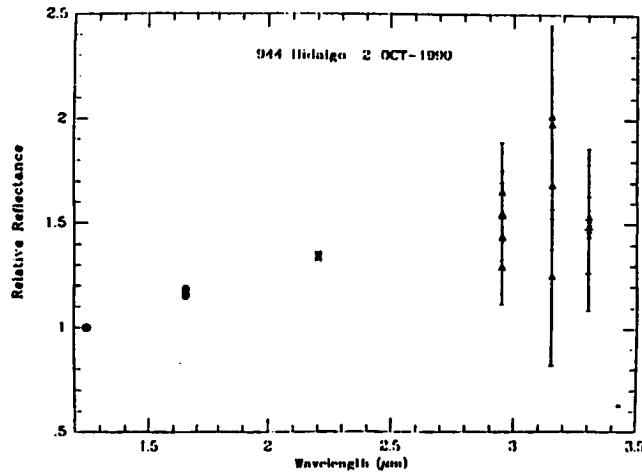


FIG. 3. Preliminary spectrum of asteroid 944 Hidalgo, an unusual D asteroid (on dynamic arguments, a possible extinct comet) that does not show the 3- μm band.

EFFECTS OF GRAIN SIZE AND SHAPE IN MODELING REFLECTANCE SPECTRA OF MINERAL MIXTURES; T. Hiroi and C. M. Pieters, Department of Geological Sciences, Brown University, Providence, RI 02912, U.S.A.

The effects of grain size and shape on reflectance spectra of mineral mixtures are investigated to improve a reflectance model called "isograin model" [1], whose prototype [2] was proposed by M. Kinoshita in 1985. The sample powder is assumed to consist of infinite number of layers, each of which has the same thickness with the grain size d .

Fig. 1 (a) shows the mixing of two components which have scattering activities s_1 and s_2 , transmitting activities t_1 and t_2 , and mixing ratios c_1 and c_2 ($c_1 + c_2 = 1$), respectively. Unit incident light from the upper layer to a grain is transmitted by t to the lower layer and scattered by s to the upper layer (ω_1 portion) and within the layer ($1 - \omega_1$ portion). An incident light x from within the layer is transmitted by t and scattered by s to the upper and lower layers (ω_2 portion, respectively) and within the layer ($1 - 2\omega_2$ portion).

If x is homogeneous within the interstices of grains of one layer, total light flux from grains to interstices should be equal to the opposite one. Then we can obtain x as:

$$x = (1 - \omega_1)s_M / [1 - t_M - (1 - 2\omega_2)s_M]$$

$$s_M = c_1s_1 + c_2s_2, t_M = c_1t_1 + c_2t_2$$

Therefore in a mixture, s and t combine linearly.

Reflectance R and transmittance T of one layer become

$$R = \omega_1s_M + \omega_2s_Mx, T = t_M + \omega_2s_Mx,$$

where R and T have no more linearity. Reflectance of the whole sample (infinite number of layers) R_∞ is

$$R_\infty = 2R / (B + \sqrt{B^2 - 4R^2}), B = 1 + R^2 - T^2$$

Here, s and t are assumed to be expressed in the same way as a flat crystal. Fig. 1 (b) shows the light scattering process of a flat isotropic crystal, whose thickness is d , absorption coefficient is α , and boundary reflectivities from outside and inside are r_E and r_I , respectively. This gives

$$t = (1 - r_E)(1 - r_I)p / (1 - r_I^2p^2), s = r_E + ptr_I, p = e^{-\alpha d}$$

By assuming isotropic light and Fresnel's law, r_E and r_I are deduced from refraction index n [3] as is shown in Fig. 2. Because it was difficult to deduce n from reflectance of powders, a function $n = 1.2286 + 0.2214/\lambda$ (λ : wavelength / μm) was adopted for all the transparent minerals here, and ω_1 and ω_2 were assumed to be 0.3 and 0.1, respectively.

Fig. 3 shows reflectance spectra of eight grain-size fractions of blue glass powder. Calculated spectra agree well with observed ones except for the smallest size fraction

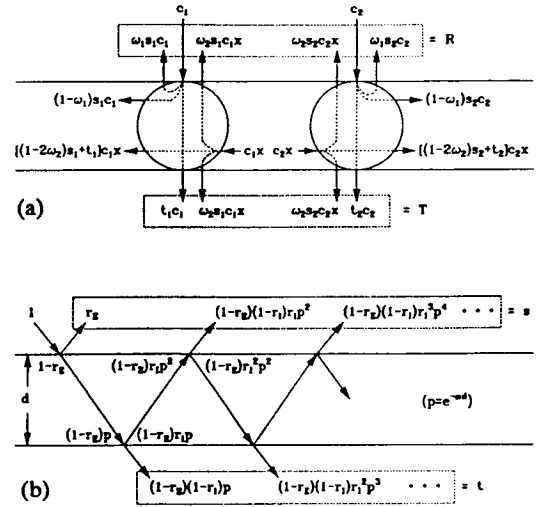


Fig. 1. Isograin model.

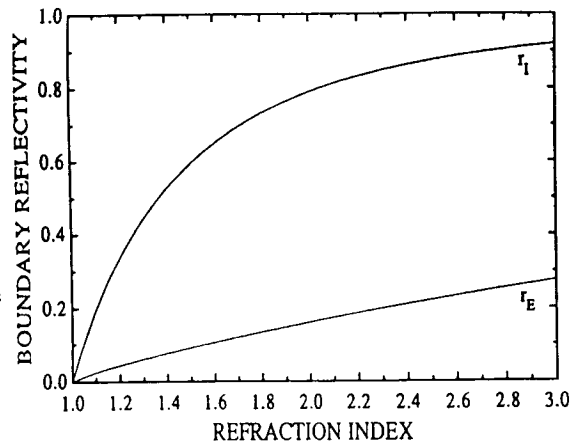


Fig. 2. Refraction index v.s. boundary reflectivities.

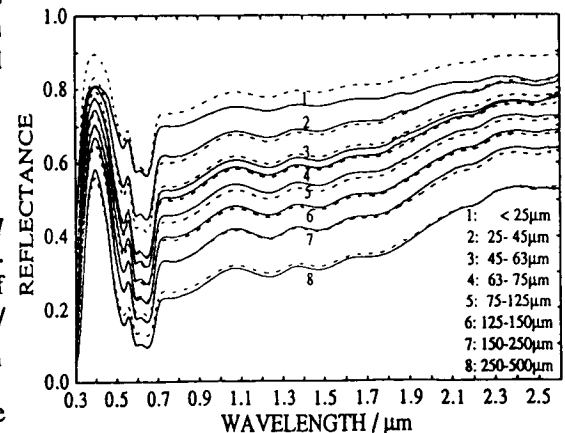


Fig. 3. Reflectance spectra of grain-size fractions of blue glass (solid: observed, broken: calculated).

(<25μm) and around the strong absorption band. We used a simple average of two mesh sizes for each grain size *d*. Glass was chosen for this test so that *n* could also be measured directly (in progress).

Fig. 4 shows the optimization of mixing ratios for quartz-alunite mixtures of the same grain sizes. Calculated spectra fit observed ones well, and errors of mixing ratios are within 3%.

Not all grains in a mixture, however, are equidimensional. In general, scattering and transmitting activities should be mixed in proportion to the total scattering area *a* of each component, which is not proportional to its total volume *v* in a mixture of different size or shape grains.

For a spherical grain, volume and scattering area of one grain are $(4\pi/3)(d/2)^3$ and $\pi(d/2)^2$, respectively. Therefore,

$$a(\text{sphere}) \propto \frac{v(\text{sphere})}{(4\pi/3)(d/2)^3} \pi(d/2)^2 = \frac{v(\text{sphere})}{(2/3)d}$$

For a thin disk-shaped grain, the effective scattering area is reduced to a half of its surface area after averaged for all the directions of incident lights. Therefore,

$$a(\text{disk}) \propto \frac{v(\text{disk})}{\pi(d/2)^2\delta} \pi(d/2)^2/2 = \frac{v(\text{disk})}{2\delta}$$

where δ indicates the thickness of the disk. By comparing the above two results,

$$a(\text{sphere}) : a(\text{disk}) = \frac{v(\text{sphere})}{d} : \frac{v(\text{disk})}{d_e}, d_e = 3\delta,$$

where *d_e* indicates effective grain size of a disk-shaped grain, which can be used for any nonspherical grains for convenience.

We provide two examples of reflectance spectra of mixtures that require this grain shape consideration.

Fig. 5 shows reflectance spectra of olivine-metal mixtures prepared by E. A. Cloutis [4] and measured at RELAB at Brown University. For opaque minerals as metals, transmitting activity *t* should be 0 and only its scattering activity *s* must be determined. Because each metal grain had a flat shape (average thickness about 10μm measured by a scattering electron microscope), an effective grain size *d_e* should be used in the mixing formula. Thus obtained *d_e* value 39μm corresponds to the disk thickness of 13μm, which agrees well with the observed one.

Fig. 6 shows reflectance spectra of calcite-chlorite mixtures also measured at RELAB. Chlorite is a member of phyllosilicates that have a perfect cleavage, and each grain has a flat shape. The optimized thickness 31μm is reasonably thin compared with its average diameter 191μm.

Acknowledgements: We thank Dr. E. A. Cloutis for his spectra and metal powder, and Nikko Exploration and Development Co., Ltd. for quartz, alunite, calcite, and chlorite powders. RELAB is a multiuser facility supported by NASA under NAGW-748. This work is partly supported by Yamada Science Foundation, Japan.

References: [1] Hiroi T. and Takeda H. (1990) *Icarus* 88, 205-227. [2] Kinoshita M. and Miyamoto M. (1990) Proc. NIPR Symp. Antarct. Meteorites 3, 230-239. [3] Hapke B. (1981) *J. Geophys. Res.* 86, 3039-3054. [4] Cloutis E. A., Gaffey M. J., Smith D. G. W., and Lambert R. St J. (1990) *J. Geophys. Res.* 95, 8323-8338.

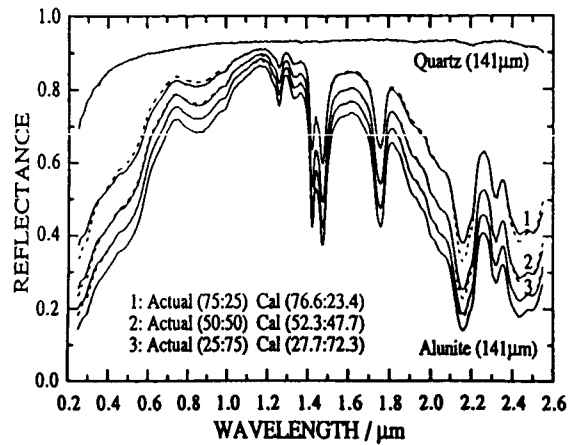


Fig. 4. Mixing ratio optimization for quartz-alunite mixtures.

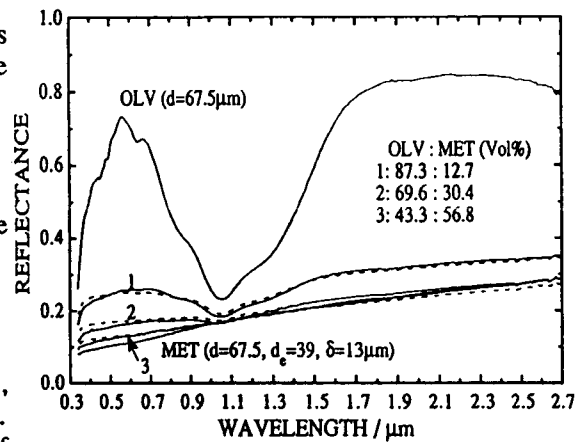


Fig. 5. Olivine-metal mixtures.

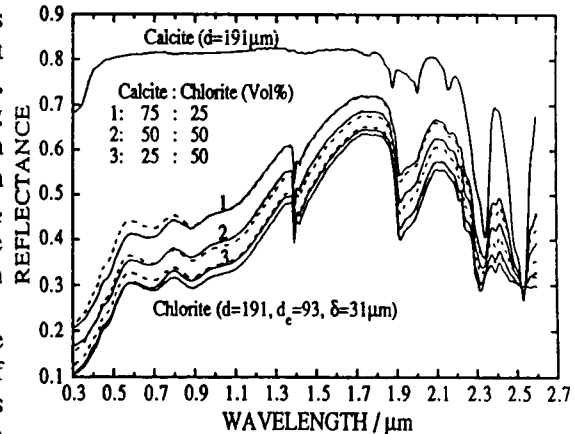


Fig. 6. Calcite-chlorite mixtures.

LIGHT SCATTERING BY LUNAR-LIKE PARTICLE SIZE DISTRIBUTIONS.

Jay D. Goguen, Jet Propulsion Lab, MS 183-501, Pasadena, CA 91109.

A fundamental input to models of light scattering from planetary regoliths (1) is the mean phase function of the regolith particles. Using the known size distribution for typical lunar soils (2), the mean phase function and mean linear polarization for a regolith volume element of spherical particles of any composition were calculated from Mie theory (3).

The 2 contour plots in fig. 1 summarize the changes in the mean phase function and linear polarization with changes in the real part of the complex index of refraction, $n - ik$, for $k = 0.01$, the visible wavelength 0.55 micrometers, and the particle size distribution of the typical mature lunar soil 72141. Fig. 2 is a similar "index-phase" surface, except with $k = 0.1$. Figs. 1 and 2 are only a small subset of the full range of parameters surveyed in this study, but they will serve to illustrate some of the important conclusions reached. The range of n and k spanned covers many compositions of interest and the region of most rapid change with k . The corresponding index-phase surface for dielectric ($k = 0$) particles is similar to fig. 1; the surface for perfectly conducting particles is similar to fig. 2.

Even though the increment in k is a factor of 10 between these plots and k traverses the range of most rapid change in the scattering properties of the particles, the shape of these index-phase surfaces changes slowly. Completed calculations also include the surfaces corresponding to $k = 0, 0.001, 0.003, 0.03, \text{ and } 1$ to provide sufficient detail for interpolation. Note that all compositions show increasing brightness near opposition that is suggestive of the backscattering behavior observed for many regoliths. The persistent region of negative linear polarization centered near $n = 1.6$ and phase angle = 20 degrees in both figures may be responsible for the "negative branch" of polarization observed for many regoliths at small phase angles. To quantitatively relate the mean phase function and linear polarization from this survey to the observable quantities of the intensity and polarization of light scattered by an optically thick regolith, multiple scattering must be calculated.

The "index-phase" surfaces from this survey are a first order description of scattering by lunar-like regoliths of spherical particles of arbitrary composition. They form a basis of functions that span a large range of parameter-space. Only small changes in the mean phase function and polarization result if they are calculated for the size distribution of the coarse and poorly sorted, immature lunar soil 71061, at the opposite end of the range of size distributions of lunar soils. Because the Mie calculations are a function of the ratio of the particle radius to the wavelength, another consequence of the integration over a broad particle size distribution is that the index-phase surfaces are only weakly dependent on wavelength. Additional calculations show that changes in wavelength by a factor of 2 across the visible spectrum also result in only small changes to the index-phase surfaces because a factor of 2 is small compared to the decades of particle radius that contribute to the scattering. The dominant effect of wavelength on the scattering occurs through large excursions of n and k with wavelength, especially in the vicinity of absorption bands.

ACKNOWLEDGEMENTS: This research was supported by the NASA Planetary Geology Program under Grant 151-01-70-56-00.

REFERENCES: (1) Hapke (1981). *J. Geophys. Res.* **86**, 3039-3054. (2) McKay *et al.* (1974). Proc. Fifth Lunar Sci. Conf., *Geochim. Cosmochim. Acta*, Suppl. 5, Vol. 1, pp. 807-906. (3) Hansen and Travis (1974). *Space Sci. Rev.* **16**, 527-610.

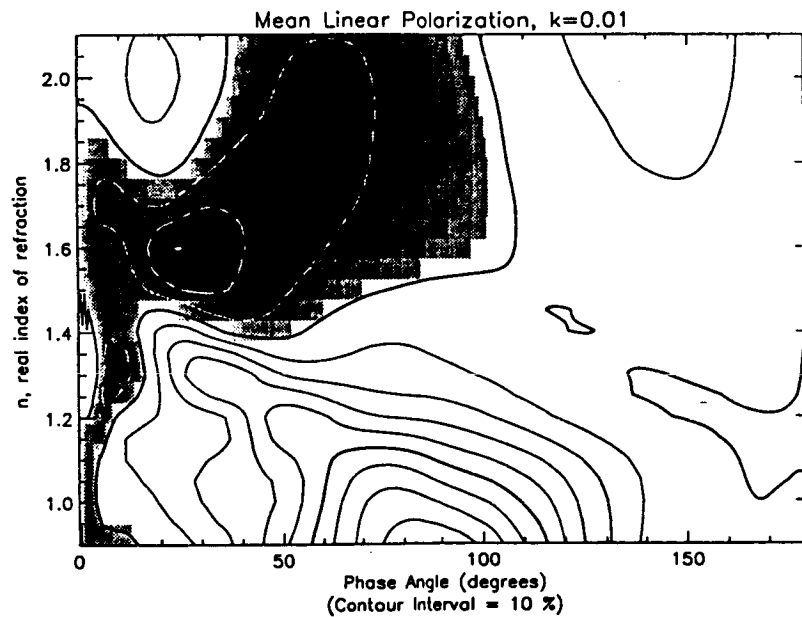
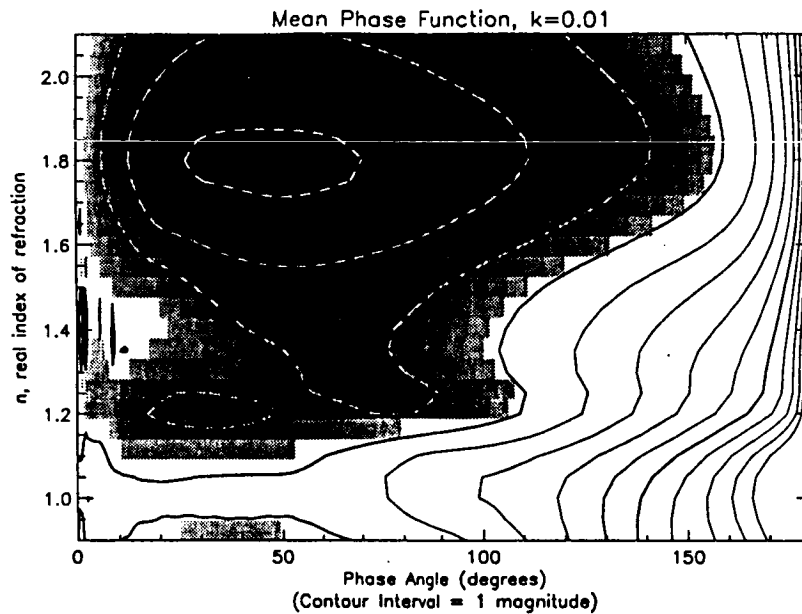


Figure 1. Contours plots of $2.5 \log \Phi$, where Φ is the mean phase function, (top) and linear polarization (bottom) for spherical particles with the size distribution of a typical mature lunar soil, 72141. The composition of the particles is indicated by the complex index of refraction, $n - 0.01 i$. In both plots, negative values are indicated by white, dashed contour lines on a shaded background. The calculations refer to a wavelength of 0.55 micrometers, but the plots are only weakly dependent on wavelength (see text).

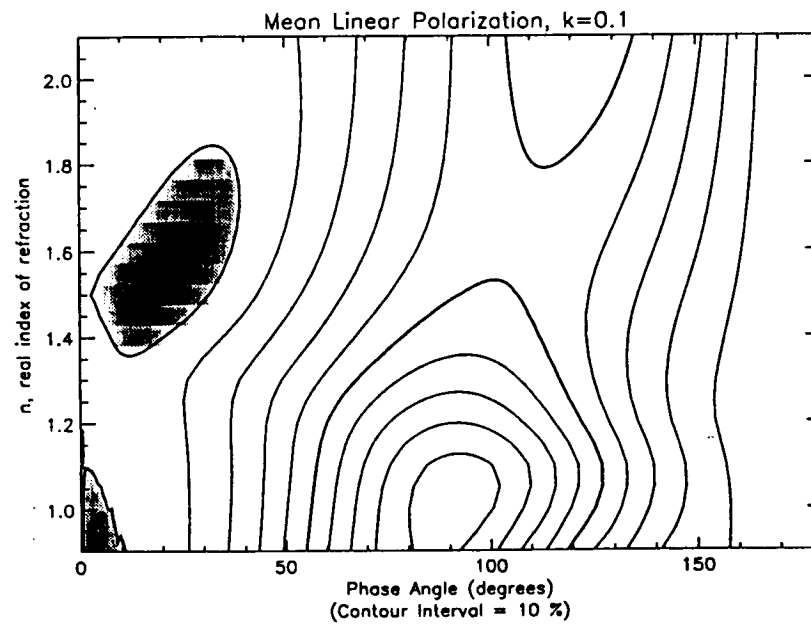
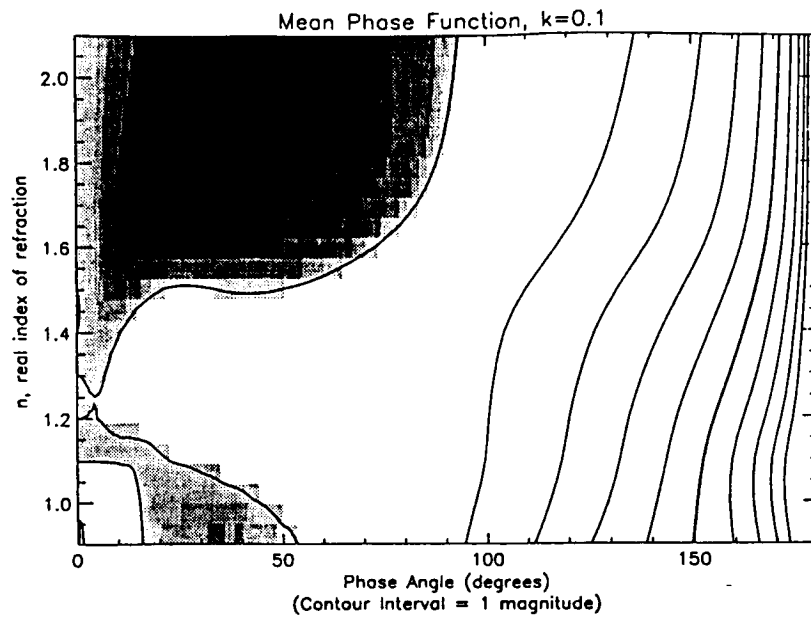


Figure 2. Same as Fig. 1, except with $k = 0.1$.

CHARACTER OF THE OPPOSITION EFFECT AND NEGATIVE POLARIZATION

C. M. Pieters (Brown Univ., Providence, RI), Yu. G. Shkuratov, and D. G. Stankevich (Kharkov St. Univ., USSR)

Photometric and polarimetric properties at small phase angles have been measured for silicates with controlled surface properties in order to distinguish properties that are associated with first surface reflection from those that are associated with multiple scattering from internal grain boundaries. These data provide insight into the causes and conditions of photometric properties observed at small phase angles for dark bodies of the solar system. Cut surfaces of obsidian and basalt were ground with a 5 μm Al oxide powder and with a 40 μm Al oxide powder to produce two comparable surface textures (called "smooth" and relatively "rough" surfaces). The obsidian was chosen to represent a silicate dielectric with no internal scattering boundaries. A fine-grained basalt was chosen to be a similar silicate but with internal grain boundaries. The reflectance and polarization properties ($15^\circ < \alpha < 90^\circ$) of these 4 relatively dark surfaces and particulate samples of the same material were measured in the RELAB and are discussed in Yon and Pieters (1988, LPSC 18, 581-592). We have extended these measurements to 3° phase angle using the precise laboratory photometer/polarimeter at the Kharkov Astronomical Observatory. The surfaces of all four specially prepared samples exhibit negative polarization at small phase angles. The obsidian characteristics, however, are quite different from those of the basalt. The increase of polarization with phase angle is completely monotonic for both samples of obsidian with the inversion angle (angle of zero polarization) being quite small, 6° for the smooth surface surface and 8° for the rougher surface. There is thus no "polarization minimum" for the obsidian samples. The value at 3° is -0.58% P for the smooth surface and -1.05% P for the rougher surface. The basalt samples, on the other hand, appear to exhibit a polarization minimum plateau and zero polarization occurs at larger angles (9° for the smooth surface and 12° for the rougher surface). Polarization minimum occurs near -0.7% P for the smooth surface and near -0.8% P for the rougher surface. For the photometric analyses, the data for all four surfaces were scaled to the albedo measured at 3° relative to halon. The obsidian samples show no opposition effect whatsoever. Brightness decreases in a distinctly linear fashion with phase angle, the smoother surface decreasing about a factor of two more rapidly. A brightness decrease for the smooth basalt is almost as linear as that observed for the obsidian. The rough basalt surface is the only one to exhibit an opposition effect.

Because the obsidian is free of internal scatterers, light reflected from both the rough and smooth obsidian samples is almost entirely single and multiple Fresnel reflections from surface facets with no body component. Surface structure alone cannot produce an opposition effect. Comparison of the obsidian and basalt results indicates that for an opposition effect to occur, surface texture must be both rough *and* contain internal scattering interfaces. Although the negative polarization observed for the obsidian samples indicates single and multiple reflections are part of negative polarization, the longer inversion angle of the multigrain basalt samples implies internal reflections must also contribute a significant negative polarization component.

**LABORATORY PHOTOMETRIC MEASUREMENT OF PARTICULATE SOILS
OUT TO VERY LARGE PHASE ANGLES**

Paul Helfenstein, Ulrich A. Bonne, Susan Stolovy, and Joseph Veverka
Center for Radiophysics and Space Research, Cornell University, Ithaca, NY 14853

Introduction: The use of photometric methods in planetary geology has advanced substantially in the past few decades, largely due to the development and continuing refinement of physically motivated radiative transfer models, such as Hapke's^{1,2,3} equation. These models seek to describe the angular reflective behavior of rough particulate surfaces in terms of surface physical properties. The properties are themselves characterized by model parameters such as average particle single scattering albedo ω_0 , the average topographic slope angle of macroscopic surface roughness, θ , parameters h and B_0 which relate the angular width and amplitude of the opposition surge, respectively, to the surface state of compaction and optical properties of particles, and parameters which describe the angular scattering properties of average particles, that is, the particle phase function, $P(\alpha)$.

Until recently, most applications of photometric theory have involved only relative comparisons of photometric parameters derived from spacecraft and telescopic observations of different planetary surfaces. However, as demands to extract more detailed physical information from photometry arise, quantitative interpretation of Hapke parameters becomes crucial. Applications such as estimating mineral abundances in multicomponent soils on the basis of spectral features rely heavily upon accurate determinations of particle single scattering albedos and phase functions. Since $P(\alpha)$ and ω_0 are closely related⁴, an inaccurate understanding of one can adversely affect our confidence in the other⁵.

Considerable study has been devoted to the phase function behavior of real particles. Most studies that examine scattering behavior out to large phase angles consider only scattering properties of dispersed particles separated by large interparticle distances. It is generally assumed that the effective phase functions of the particles remain unchanged when particles are brought into mutual contact, as in a soil or regolith. It is not presently clear how radiant energy involved in scattering processes such as diffraction (which creates a strong forward scattering lobe in $P(\alpha)$ for systems of dispersed particles) is redistributed when particles are brought into mutual contact. Recent investigations^{6,7} of very large isolated particles suggest that even relatively low-albedo particles should exhibit forward scattering components of $P(\alpha)$, however, detailed forward scattering behavior in actual particulate surfaces has been studied principally for high-albedo materials such as snow and frost⁸.

Objectives: In the present study, our objectives are to develop the laboratory methods and tools to conduct photometric observations of dark particulate samples over a large range of phase angles ($0^\circ \leq \alpha \leq 160^\circ$), and to demonstrate whether forward scattering behavior can be seen in a surface constructed of low-albedo material. We also examine the adequacy of various model formulations of $P(\alpha)$ to describe the effective scattering properties of our sample.

Experimental Approach: The Cornell Goniometer was constructed over 15 years ago to study the spectrophotometric properties of particulate samples over visible and near-infrared wavelengths (0.4-1.2 μm) at a variety of photometric geometries. We have modified the instrument to extend its usable range of incidence (i), emission (e), and phase (α) angles. A

beam splitter attachment was constructed to observe opposition surge behavior over $0^\circ \leq \alpha \leq 18^\circ$, with the device, and at overlapping phase angles ($\alpha > 4^\circ$) with the device removed. In addition, we invented a variable-geometry elliptical iris to restrict the collimated incident light beam so that it projects onto the sample as a circular disk even out to large incidence angles. This device enabled observations at simultaneously large incidence and emission angles. At emission angles greater than about 60° , the detector field of view extends beyond the illuminated portion of the sample dish. We have discovered that the appropriate correction for this geometric effect can be obtained directly by measuring the sample's reciprocity. If the reflectance behavior of a given sample is represented as $r(i, e, \alpha)$, then reciprocity principle states that $r(i, e, \alpha)/\cos(i) = r(e, i, \alpha)/\cos(e)$. To use this principle, we fix the detector at a given emission angle (for example $e=0^\circ$) and vary i from 0° - 77° . We then make the reciprocal measurement (fix $i=0^\circ$ and vary e from 0° - 77°). The correction factor, $C(e, \alpha) = (\cos(e)/\cos(i))(r(i, e, \alpha)/r(e, i, \alpha))$, is then unity for all $e < 60^\circ$, and systematically increases with increasing e elsewhere.

Results: For our sample, we have chosen a sieved 75-149 μm sized fraction of crushed augite. The normal reflectance of this material (relative to BaSO_4) is typically 10% at $\lambda=0.5 \mu\text{m}$. 460 observations of this sample were obtained in the scattering plane over $0^\circ \leq i \leq 85^\circ$, $0^\circ \leq e \leq 77^\circ$, and $0^\circ \leq \alpha \leq 162^\circ$. We can express these observations in terms of particle phase function, $P(\alpha)$, as follows⁵: For a macroscopically smooth ($\theta=0^\circ$) low albedo surface in which multiple scattering of light is not significant we isolate the product, $F(\alpha) = (1+B(\alpha))P(\alpha)$ of Hapke's opposition surge function and $P(\alpha)$ as $F(\alpha) = 4(\mu_0 + \mu) r_m(i, e, \alpha) / (\omega_0 \mu_0)$, where $\mu_0 = \cos(i)$, $\mu = \cos(e)$, and $r_m(i, e, \alpha)$ is the measured bidirectional reflectance of the sample. We eliminate the constant $4/\omega_0$ by normalizing to our observation at $F(0^\circ)$. Fig. 1a shows a plot of $F(\alpha)$ vs. α for our augite sample. The opposition surge at small phase angles can readily be distinguished from the rest of the $F(\alpha)$ curve. At $\alpha > 120^\circ$, $P(\alpha)$ clearly exhibits a strong forward scattering lobe.

Analysis: We have conducted least-squares fits of a variety of commonly-used $P(\alpha)$ models. A simple, one-term Henyey-Greenstein function, often used in planetary applications, is inadequate for describing $P(\alpha)$ at all phase angles. As Fig. 1a shows, a linear combination of two one-term Henyey-Greenstein functions appears to be the simplest model to yield good results. Our least squares fit gives particle phase function asymmetry factors of $g_1 = -0.31$ and $g_2 = +0.40$ for the forward and backward lobes, respectively, with the backward scattering component contributing 36% to $P(\alpha)$. The corresponding value of $\omega_0 = 0.20$. Opposition surge parameters $h = 0.027$ and $B_0 = 0.59$ are well-constrained by our data.

Fig. 1b illustrates how macroscopic surface roughness may reduce the detectability of forward scattering behavior in planetary regoliths. We have used our best-fit Hapke parameters to predict phase curves for hypothetical crushed augite-covered planets having varying degrees of macroscopic roughness ($0^\circ \leq \theta \leq 60^\circ$). Phase curve data for the Earth's moon is shown for comparison. As roughness is increased, the phase curves become more strongly backscattering. While we have not chosen our sample to simulate lunar regolith in any way, the augite phase curve for $\theta = 50^\circ$ is remarkably similar in shape to the lunar phase curve. Since macroscopic roughness can often be independently constrained by limb-darkening across a planetary disk, disk-resolved photometric observations should help in distinguishing the presence of forward scattering from planetary phase curves.

ACKNOWLEDGEMENTS: This research was funded by NASA Grant NSG-7606/2084.

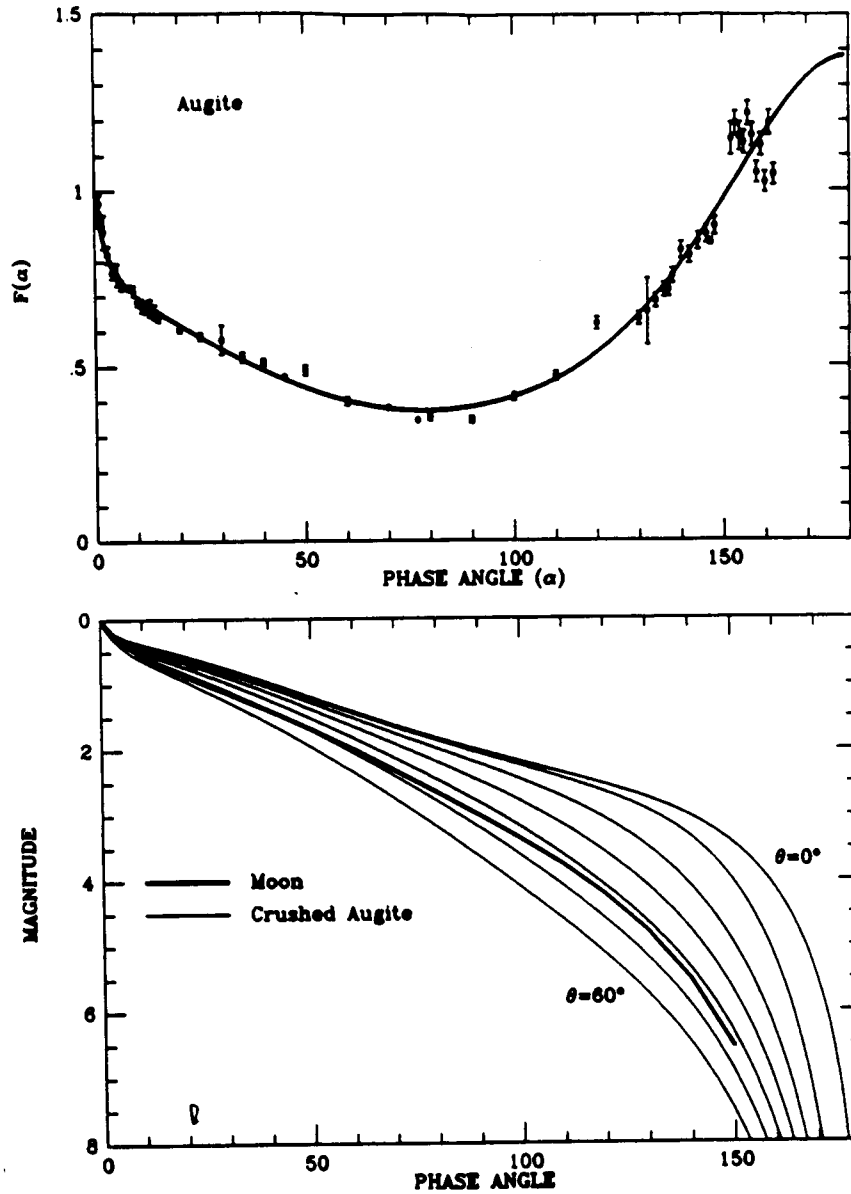


Fig.1: a) $F(\alpha)$ vs. α for crushed Augite sample. b) Predicted phase curves for hypothetical crushed-augite covered planets with different roughnesses. Lunar phase curve shown for comparison.

REFERENCES: ¹Hapke, B. (1981), *JGR* **86**, 3039-3054. ²Hapke, B. (1984). *Icarus* **59**, 41-59. ³Hapke, B. (1986). *Icarus* **67**, 264-280, ⁴Chandrasehkar, S. (1960). *Radiative Transfer*, Dover Press, NY. ⁵Helfenstein, P. and J. Veverka (1990). In *Asteroids II*, Univ. Ariz. Press, Tucson. ⁶McGuire, A. and B. Hapke (1989). *LPSC* **21**, ⁷Giese, R. et al. (1978). *Astr. Astrophys.* **65**, 265-272, ⁸Verbiscer, A. and J. Veverka (1990), *Icarus* **88**, 418-428.

THE PHOTOMETRIC ROUGHNESS OF MIMAS

A. Verbiscer and J. Veverka, Cornell University, Ithaca, NY

Voyager imaging observations of Mimas lie between 6° and 132° in phase angle and provide sufficient data with which to model such surface characteristics as large-scale roughness and directional scattering properties. Multiple scattering dominates the photometric behavior of the bright icy surface of Mimas which has been shown to be moderately backscattering (Verbiscer *et al.* 1990). We have analyzed disk-integrated and disk-resolved Voyager clear filter photometric data using a modified version of Hapke's (1986) equation which accommodates anisotropic multiple scattering.

The disk-integrated data and solar phase curve are shown in the accompanying figure. The larger error associated with the observation at 6.2° results from corrections necessary to compensate for the excessive scattered light from the planet and its broad rings. Clearly, more observations at low phase angles are needed in order to characterize completely the opposition surge of the surface of Mimas. For our fitting purposes, we assume that the opposition surge of Mimas is similar to that of Rhea. The parameters which describe Rhea's opposition surge are angular width $h = 0.06$ and amplitude $B_o = 0.75$. From the phase curve we determine the geometric albedo of Mimas $p_v = 0.70 \pm 0.05$ and phase integral $q = 0.77 \pm 0.05$. These correspond to a spherical albedo $A = p_v q = 0.54 \pm 0.1$. Since the spectrum of Mimas is fairly flat (Buratti 1984), we can approximate the Bond albedo A_B with the spherical albedo.

Using the non-linear least squares algorithm developed by Helfenstein (1986) and described by Helfenstein *et al.* (1991) we simultaneously fit both full-disk observations, corrected for rotational albedo variations, and disk resolved data to the modified Hapke's equation. The fit is described by single scattering albedo $\tilde{\omega}_o = 0.961 \pm 0.003$, macroscopic roughness parameter $\bar{\theta} = 32^\circ \pm 2^\circ$, and Henyey-Greenstein asymmetry parameter $g = -0.19 \pm 0.01$.

The photometric roughness $\bar{\theta}$ is greater than that derived in similar manners from other bright icy satellite surfaces, though comparable to the 30° determined for Mimas by Buratti (1985) who applied the Hapke theory and the $30 \pm 25^\circ$ found by McEwen (1987) who used fits to the Minnaert k parameter to determine $\bar{\theta}$.

This research was supported in part by NASA grants NGT 50482 and NSG 7156.

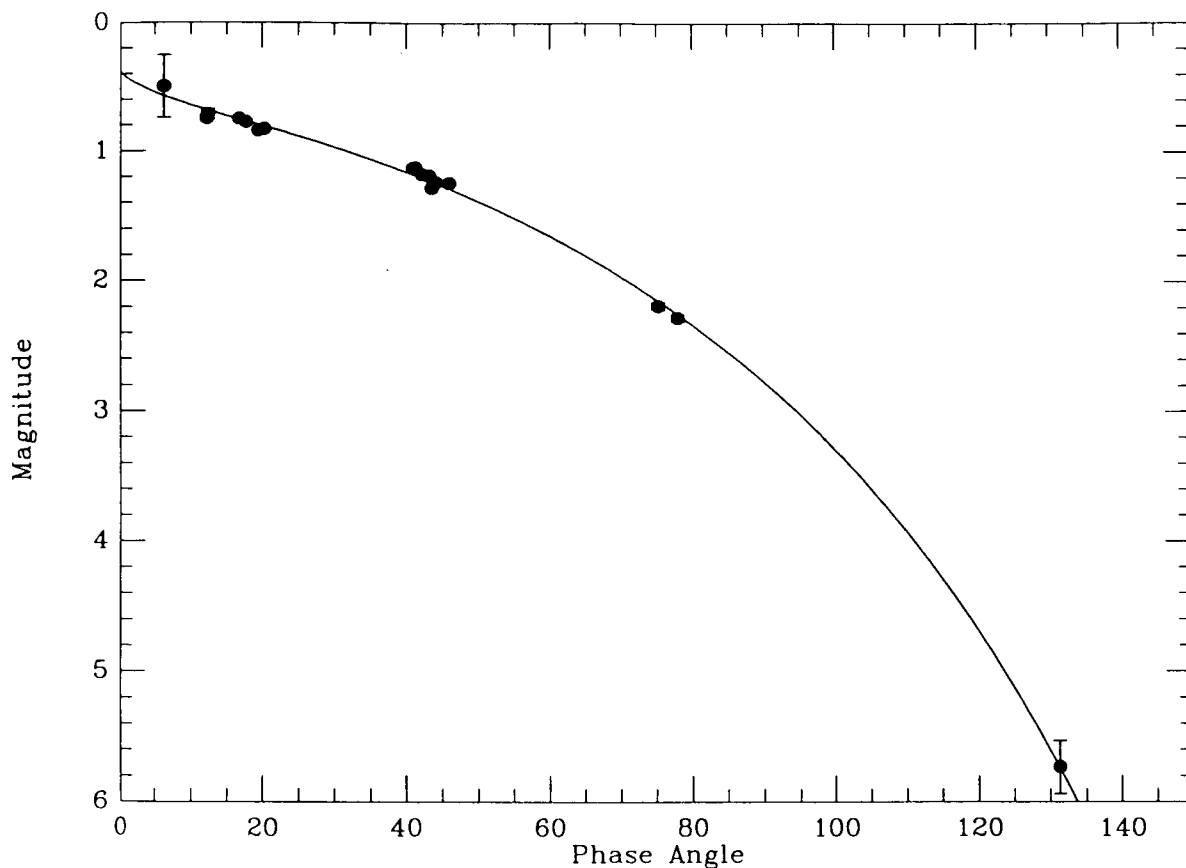
REFERENCES

- Buratti, B. J. 1984. Voyager disk resolved photometry of the Saturnian satellites. *Icarus* 59, 392-405.
- Buratti, B. J. 1985. Application of a radiative transfer model to bright icy satellites. *Icarus* 61, 208-217.
- Hapke, B. 1986. Bidirectional reflectance spectroscopy 4. The extinction coefficient and the opposition effect. *Icarus* 67, 264-280.
- Helfenstein, P. 1986. *Derivation and Analysis of Geological Constraints on the Emplacement and Evolution of Terrains on Ganymede from Applied Differential Photometry*. Ph.D. thesis, Brown University, Providence, RI.

- Helfenstein, P., J. Hillier, C. Weitz, and J. Veverka 1991. Oberon: Color photometry from Voyager and its geological implications. *Icarus*, in press.
- McEwen, A. S. 1987. Photometric functions for photoclinometry and other applications. Submitted for publication.
- Verbiscer, A., P. Helfenstein, and J. Veverka 1990. Backscattering from frost on icy satellites in the outer solar system. *Nature* 347, 162-164.

Figure Caption:

Solar phase curve of Mimas based on Voyager clear filter data. Magnitudes are normalized to $-2.5 \log p$ at 0° where p is the geometric albedo at $0.48 \mu\text{m}$. Solid line is a fit to a modified version of Hapke's 1986 equation.



ANOMALOUS SCATTERING OF LIGHT ON TRITON

Paul Helfenstein, Pascal Lee, Derek McCarthy and Joseph Veverka

Center for Radiophysics and Space Research, Cornell University, Ithaca, NY 14853

Introduction: Since Voyager II's 1989 encounter with the Neptune system, significant progress has been made toward identifying and understanding the diverse color and photometric properties of Triton's terrains. Color variations on Triton's surface were recognized early on¹, and several detailed studies have since applied color analysis as a means of classifying different terrain units^{2,3}. Recent photometric investigations of Triton have focused on average global properties of the surface^{1,2,3,4,5,6}. Preliminary whole-disk phase curves for Triton¹ revealed an unusual upturn at large phase angles ($\alpha > 140^\circ$) attributed to forward scattering from Triton's thin atmosphere. The photometric behavior of Triton's atmosphere has now been modeled^{4,5} and average photometric properties of Triton's surface expressed in terms of the parameters of the well-known Hapke^{7,8,9} photometric model for rough, particulate surfaces.

Surface-resolved variations in the photometric properties of individual terrains on Triton have not been studied in detail with the exception of an unsuccessful search for specular reflections as potential indicators of relatively smooth glazed ice patches on Triton's surface¹⁰. With the advent of an accurate photometric model for Triton's atmosphere⁶, we have begun to study detailed differences in photometric properties of individual terrains. We report here the discovery of an isolated region of anomalously forward scattering materials on the surface of Triton.

Analytical Methods: We have employed two methods to examine phase-angle dependent differences in the photometric properties of Triton's terrains. The first, which we call the photometric ratio method, is an image processing technique by which we identify the presence, photometric character, and areal extent of a terrain whose photometric behavior with phase angle contrasts that of average Triton materials. We select two images obtained in the same Voyager filter wavelength, but at significantly different phase angles. Following the approach of Lee et al.¹⁰, average global photometric parameters (for the specific Voyager wavelength) are applied to correct for broad-scale limb-to-terminator changes in brightness associated with varying incidence and emission angles. We reproject one of the "shading corrected" images to the other's viewing geometry, geometrically register common features, and then construct an image ratio. Albedo differences are eliminated (bland) in the photometric ratio images while regions that differ in photometric behavior with phase angle are accentuated in appearance.

Contrasting photometric behavior with phase angle may be caused by differences in regional macroscopic surface roughness (Hapke's θ parameter) or/and the phase functions (characterized by the asymmetry factor g of the Henyey-Greenstein particle phase function) of constituent regolith particles. In our second analytical method, we attempt to distinguish quantitatively these two possible causes by performing least-squares fits of the Hapke model to disk-resolved observations over a wide variety of incidence, emission, and phase angles.

The boundary and interior of a distinctive region in a photometric ratio image is used as a location map for restricting photometric observations to the identical area in other Voyager images obtained over a range of phase angles. Best-fits of θ and g , as well as the average particle single scattering albedo ω_0 , to these data can then be compared to average Triton parameters in order to see which properties best account for the anomaly.

Results: In the present investigation, we focus on the analysis of Voyager green-filter ($\lambda=0.56 \mu\text{m}$) images, for which the effects of atmospheric contributions are relatively minor⁶. Our photometric ratio image constructed from FDS 11394.16 ($\alpha=66.4^\circ$) and FDS 11396.11 ($\alpha=99.7^\circ$) reveals a large area of unusual scattering extending from about 10°N to 40°N in latitude and at least 60°E to 40°W in longitude (see Figure 1). At $\alpha=99.7^\circ$, this region's brightness relative to the surrounding bright frost material is greater than at $\alpha=66.4^\circ$. We've identified the region in five green-filter Voyager images covering phase angles $28^\circ, 39^\circ, 63^\circ, 67^\circ$ and 100° , and sampled its brightness in each image over a variety of incidence and emission angles. To these data we obtained Hapke parameter fits of $\omega_0=0.978\pm 0.001$, $g=-0.05\pm 0.05$, and $\theta=0^\circ\pm 22^\circ$ (compared to $\omega_0=0.995$, $g=-0.23$, $\theta=11.5^\circ$ for average Triton materials⁶). Our one-sigma error estimates show that ω_0 and g are well-constrained, but constraints on θ are poor. On the basis of present data, we can say only that the anomalous region's roughness is statistically indistinguishable from that of average Triton materials.

We have compared our photometric ratio image to Voyager green/violet color ratio images of Triton. In location, the area corresponds approximately to McEwen's² unit 1, and Thompson and Sagan's³ class III, units 16, 22, and 24, which were classified on the basis of color *and* albedo. At large phase angles the anomalous region coincides with a distinct area of comparatively large green/violet color ratios. Its green/violet ratio at $\alpha=99.7^\circ$ is 12% higher than for Frost Band materials and 6% higher than for average South Polar Cap materials. Not surprisingly, the contrast in green/violet ratios between the anomalous region and other terrains changes at different phase angles. While the anomalous region's green/violet ratio is uniformly larger than for any other visible terrain at $\alpha=99.7^\circ$, at $\alpha=28^\circ$, its green/violet ratio is typically 6% lower than for South Polar Cap materials, but 19% higher than for Frost Band materials.

Discussion: Our best-fit Hapke parameters indicate that regolith particles in the anomalous-scattering region are not only less backward scattering, but also slightly lower in single scattering albedo than average materials on Triton's surface. While it may be possible to account for such differences in terms of differences in particle size and transparency, it is also possible that the anomalous region is compositionally distinct from other terrains. It is noteworthy that, for the anomalous region, there exists a distinctively strong spatial correlation between the photometric ratios and green/violet color ratios at large phase angles, and that, relative to other terrains, the anomalous region reddens at a different rate with increasing phase angle.

We are currently analyzing additional Voyager violet and clear filter data in order to better distinguish how composition, particle-size, and particle structure may contribute to

the distinctive photometric properties of the anomalous region. We are also investigating the relationship between color and photometric ratios as a means of globally mapping the areal extent of anomalous scattering materials. Our continued work on Hapke analysis of Voyager disk-resolved observations for other terrains on Triton offers the greatest promise for characterizing the physical properties that distinguish terrains, and for ultimately relating these properties to the geological and/or climatological agents responsible for their emplacement.

Acknowledgements: This research was supported by NASA Grants NAGW 2084, NSG 7156 and the Voyager project. We thank J. Hillier for use of his Triton atmosphere photometric model.

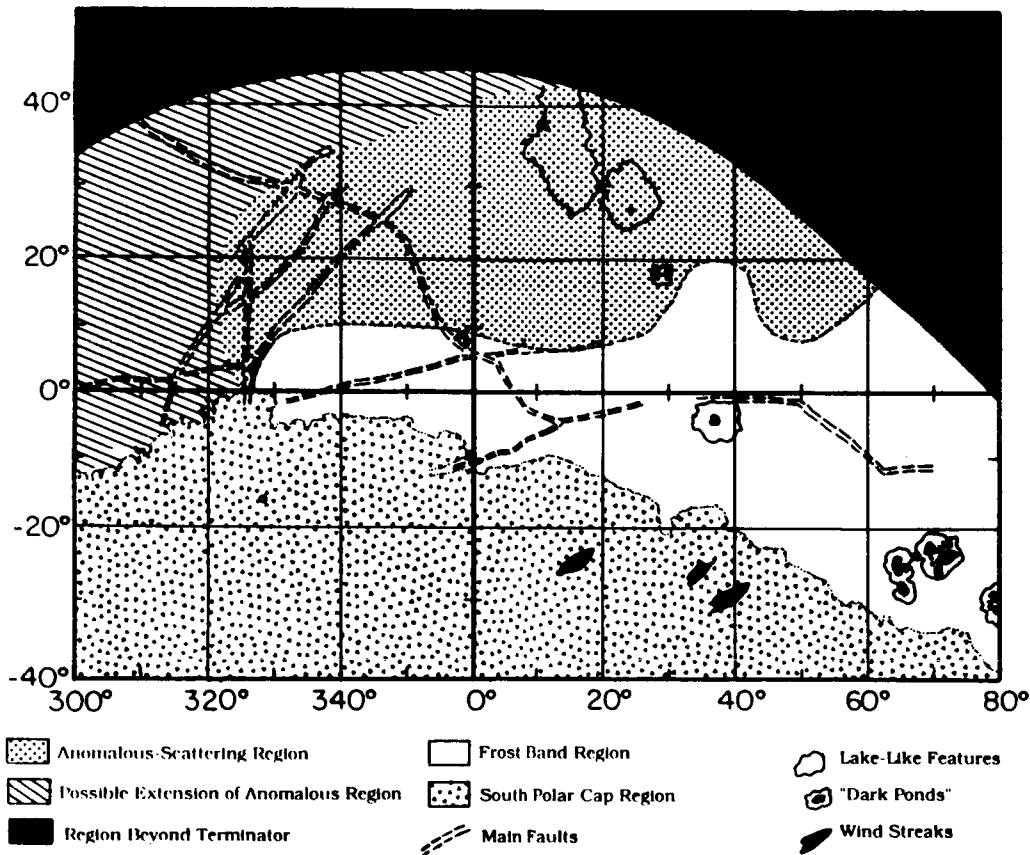


Fig. 1: Preliminary sketch map showing location and observed spatial extent of the region of anomalous light scattering.

REFERENCES: ¹Smith et al. (1989), *Science* **206**, 1422-1449. ²McEwen, A. (1990), *GRL* **17**, 1733. ³Thompson, W.R. and C. Sagan (1990), *Science* **250**, 415-418. ⁴Hillier et al.(1990), *Science* **250**, 419-421. ⁵Hillier et al.(1991a), *JGR* submitted, ⁶Hillier, J. et al.(1991b), *JGR*, submitted. ⁷Hapke, B. (1981), *JGR* **86**, 3039-3054., ⁸Hapke, B. (1984) *Icarus* **59**, 41. ⁹Hapke, B. (1986) *Icarus* **67**, 264. ¹⁰Lee, P. et al.(1991), *JGR* submitted. ¹¹Verbiscer et al. (1990), *Nature* **347**, 162-164.

DISK RESOLVED STUDIES OF THE OPTICAL PROPERTIES AND PHYSICAL NATURE OF THE SURFACES OF THE OUTER PLANET SATELLITES

B. J. Buratti, J. A. Mosher, T. V. Johnson, JPL/Caltech, Pasadena, CA 91109

The spatially resolved albedo, color, compaction state, roughness, and constituent particle sizes of the surfaces of the satellites of Jupiter, Saturn, and Uranus provide important constraints in understanding the geologic evolution and relevant exogenic processes operating in these satellite systems.

A. Saturnian System

Color and albedo maps based on Voyager images show that the optical properties of the major airless Saturnian satellites are almost totally unrelated to geologic features and terrains, except for Rhea (Buratti et al., 1990). The influence of exogenic processes, including micrometeoritic and magnetospheric bombardment and the influence of the E-ring, have been investigated. Albedo maps (Figure 1) show that the leading sides of these objects are brighter than the trailing sides, and that the extent of this bright region increases towards Saturn. These observations are in qualitative agreement with the expected effects of cometary and meteoritic bombardment (Shoemaker and Wolfe, 1982).

B. Uranian System

Color and albedo maps based on Voyager images for these satellites show good correlation with geologic features. However, we find evidence that the leading sides of the satellites are preferentially reddened, and that this effect becomes more pronounced as the distance from Uranus increases (Buratti and Mosher, 1991; see Figure 2). We attribute this observation to the accretion of low albedo, reddish meteoritic dust which originates on undiscovered retrograde (captured) satellites located outside the orbit of Oberon. The spectrum of this material is similar to that of D-type objects, including primitive asteroids, comets, Hyperion, and the dark side of Iapetus. Alternatively, the satellites could have accreted the dust during formation of the Uranian system. In this case, our measurements give a rough indication of the dust gradient in the circum-Uranian primordial cloud.

C. Jovian System

An analysis of ground-based and Voyager images of Callisto shows that the leading side of this satellite is composed of less compacted, more backscattering particles than the trailing side (Buratti, 1991). Based on laboratory goniometric measurements, we attribute the backscattering properties to a decreased particle size on the leading side (Figure 3), due to preferential micrometeoritic gardening. Previous work has shown the opposite hemispheric dichotomy for Europa, due to magnetospheric bombardment. For Ganymede, no hemispheric dichotomies exist

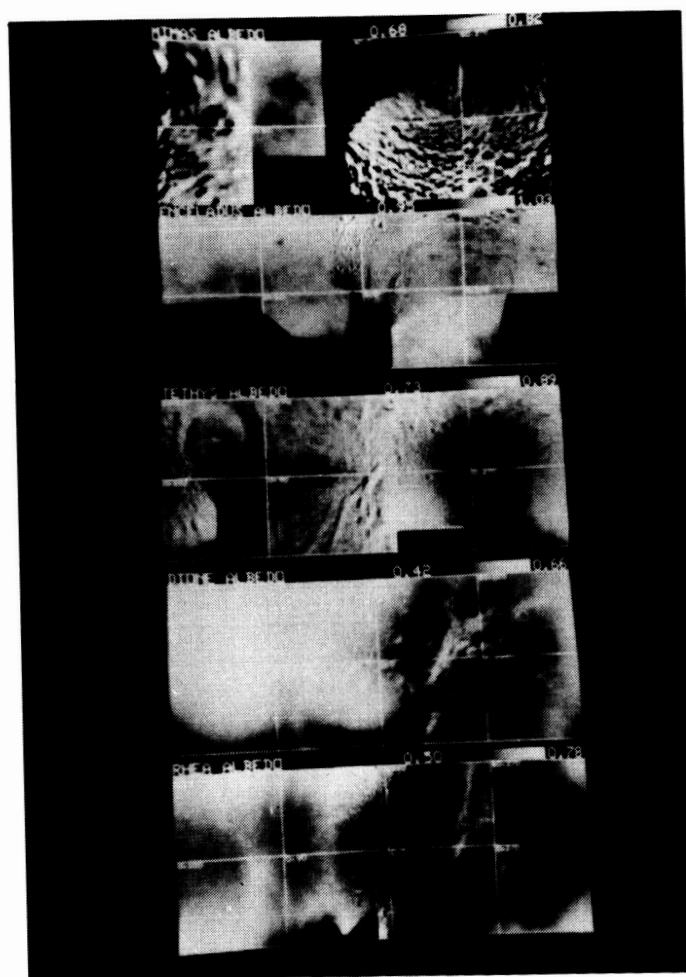
because the two effects balance.

ACKNOWLEDGEMENT. Work performed under contract to NASA/JPL.

REFERENCES

- Buratti, B. J. (1991). Icarus, accepted for publication.
Buratti, B. J., J. A. Mosher, T. V. Johnson (1990). Icarus 87, 339.
Buratti, B. J., J. A. Mosher (1991). Icarus 89, 1.
Shoemaker, E., Wolfe, R. (1982). In Satellites of Jupiter (D. Morrison, ed.) Univ. of Arizona Press, Tucson, 277.

Figure 1. Maps in Mercator coordinates of the normal reflectances in the Voyager clear filter (0.47 microns) of five Saturnian satellites. From top to bottom: Mimas, Enceladus, Tethys, Dione, and Rhea.



ORIGINAL PAGE
BLACK AND WHITE PHOTOGRAPH

Figure 2. The scans on the left show the longitudinal distribution of normal reflectance for the five major Uranian satellites. On the right, the longitudinal distribution of the ratio of the Voyager green and violet filters is shown.

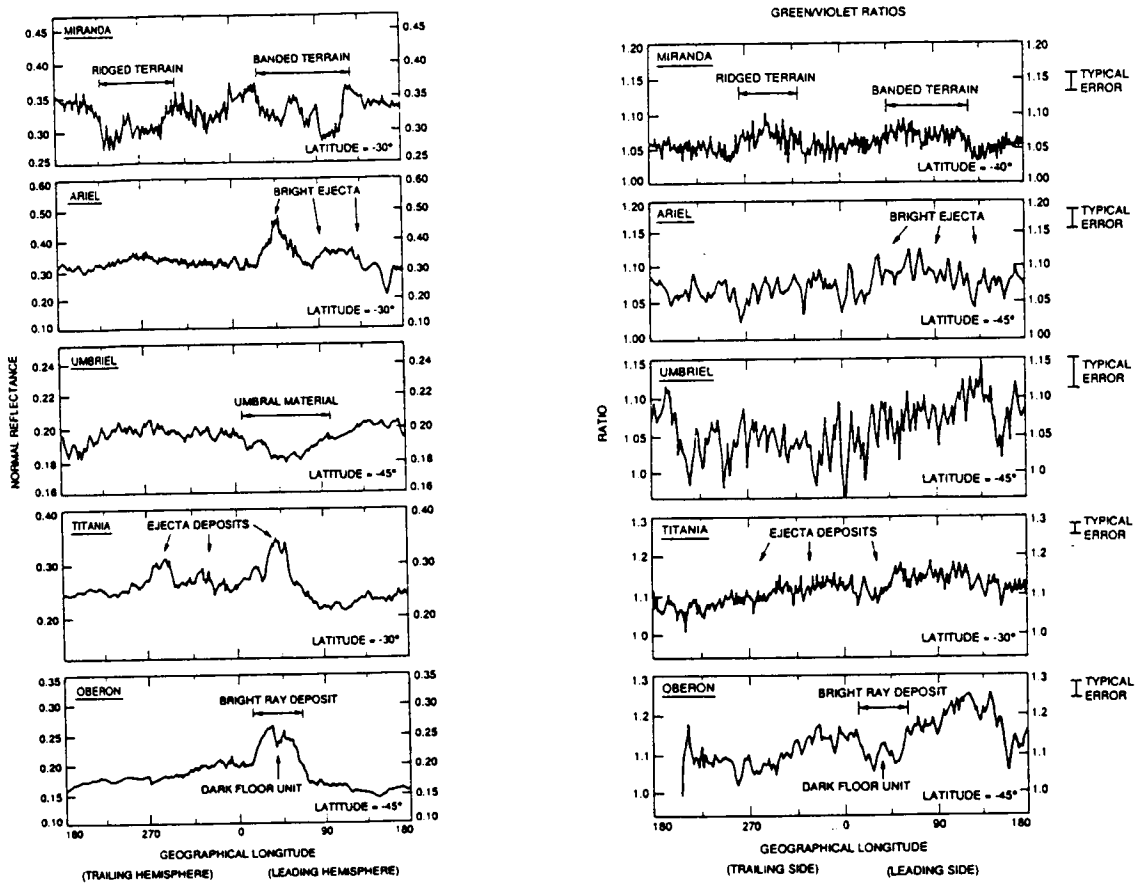
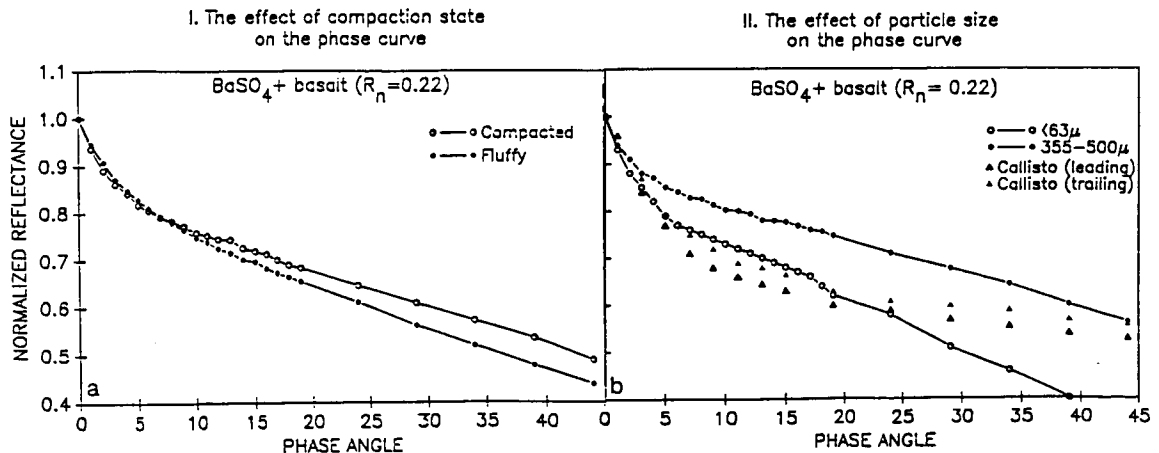


Figure 3. Laboratory measurements of the effect of compaction state and particle size on the phase curve of photometric analogues of Callisto's surface (R_n is the normal reflectance).



EUROPA'S PHASE CURVE: IMPLICATIONS FOR SURFACE STRUCTURE

D. Domingue and B. Hapke, Dept. of Geology and Planetary Science, University of Pittsburgh, Pittsburgh, PA and W. Lockwood and D. Thompson, Lowell Observatory, Flagstaff, AZ.

Ground-based photoelectric measurements taken with narrow band filters at 0.47 and 0.55 μm at small phase angles clearly show the existence of a narrow opposition peak. We have combined these data with Voyager images to obtain a range of phase angle coverage from 0.3 to 119°. The integral phase data were analyzed using Hapke's photometric model. The photometric parameters are remarkably similar for both wavelengths and hemispheres. The following values at $\lambda = 0.55 \mu\text{m}$ for the leading side are typical: single scattering albedo $w = 0.946$, opposition effect amplitude $B_0 = 0.5$, opposition effect width $h = .0016$, double-lobed Henyey-Greenstein factors $b = 0.429$, $c = 0.113$, and mean roughness angle $\bar{\theta} = 10^\circ$. The photometric roughness is smaller than on most other bodies of the solar system, and implies that the low surface relief seen at kilometer scales in the Voyager images extends down to centimeter scales. If the very narrow opposition surge is due to shadow hiding, the porosity must be large, on the order of 96%, which is much higher than that of a regolith generated by meteoritic gardening. Both the small roughness and high porosity imply that endogenic processes dominate surface formation even at centimeter scales. The single particle scattering function is more back scattering on the leading hemisphere, which contradicts the scattering properties expected on a planetary surface that is being preferentially bombarded by ions on its trailing hemisphere.

CHARGED-PARTICLE INDUCED ALTERATIONS OF SURFACES
IN THE OUTER SOLAR SYSTEM

R.E. Johnson, School of Engineering and Applied Science
University of Virginia, Charlottesville, Virginia 22903-2442

Solar system surfaces unprotected by an atmosphere can be modified by plasma bombardment. This is one aspect of planetary surface weathering. This knowledge can be used to establish the age of the surface layer and the rates for geologic processes. The list of possible irradiation effects is long and, indeed, the list is likely to be increased as the data on Uranus, Halley, and Pluto are further analyzed. In addition there is the renewed interest in the lunar surface for which plasma effects are well documented but only partially understood. In this work we make accurate assessments of surface of objects for which relevant laboratory information on irradiation effects is available or can be successfully extrapolated. Until sample return missions are possible, the limitations of observations to the outer layers of solid objects requires careful evaluation of the surface modifications which can affect interpretations of remote sensing data. Irradiation effects have been used to account for many initially uncertain observations, and often these initial guesses have been wrong. Our modelling, therefore, provides an important constraint and much of the recent work has been summarized in a monograph Energetic Charged-Particle Interaction.

In the previous we have placed strong emphasis on describing the plasma interaction with possible Io surface constituents SO_2 , sulfur, and Na_2S in order to interpret polar darkening by radiation and ejection of species into the atmosphere and torus. More recently we have calculated the plasma bombardment profiles of the surfaces of the icy Saturnian satellites to interpret reflection spectra and the effect of charged particles on the surfaces (mantles) of Pluto and of comets in the Oort cloud.

Pluto's exposure to cosmic rays results in a slow alteration of the reflectance of the methane condensed on its surface and the UV absorbed in the atmosphere can produce precipitates. We showed that, depending on the rates of the competing regolith processes and the rates for replenishment of the methane, the surface can appear bright, 'red', or 'dark'. Using laboratory data we showed that the amount of darkening occurring in one orbit is small. Therefore, transport, burial and re-exposure of organic 'sediments' must control the reflectance, and the average reflectance is established by the radiation altered species accumulated over many orbits with the observed spatial, and possibly temporal, differences in albedo due to transport. The cosmic rays although producing changes in reflectance slowly, do so inevitably. Therefore, the fact that the surface is not dark everywhere implies that it is active and the exposure rates vs. depth into the surface given in the paper on Pluto can be used to constrain turnover rates.

Comets in the Oort cloud experience similar effects. This irradiation processing occurs in competition with a number of surface alteration processes evaluated by Stern. We have corrected the many different estimates of cosmic ray dose that have led to 'primordial' mantles varying from 50 m to a few cm. These discussions are summarized in a review chapter in the Bamberg proceedings and in an article in the proceedings of the Milipitas conference on the Rosetta mission. Because a sample return is being proposed and because CRAF

was to have a penetrator the thickness of the primordial crust is important. Recently we have used experimental data to show that this crust should survive the thermal shock of the comet's entrance into the inner solar system.

Our most recent efforts has been to develop analysis for determination of satellite surface composition from local plasma measurement by Cassini and the proposed Lunar orbiter. The coupling between the ions in lunar corona with the composition of the local surface indicates unique surficial information is available from the plasma measurements. Directly sputtered species or species ejected by micrometeorites were shown to give a corona indicative of the average composition of the moon's surface. Similarly, at Saturn the plasma instrument may be the most hopeful for determining trace species in the surfaces of the icy moons.

References

Pospieszalska, M.K. and R.E. Johnson, Magnetospheric Ion Bombardment Profiles of Satellites: Europa and Dione, Icarus 78 1-13 (1989).

Johnson, R.E., Application of Laboratory Data to the Sputtering of a Planetary Regolith, Icarus 78 206-210 (1989)

Johnson, R.E., The Effect of Irradiation on the surface of Pluto, Geo. Res. Lett. 16 1233-1236, 1989.

Johnson, R.E., in Report of the Lunar Atmosphere Working Group of LExSWG (ed. A. Stern) 1990.

R.E. Johnson and E.A. Sittler, Sputter-Produced Plasma as a Measure of Satellite Surface Composition: The Cassini Mission, G.R.L 17, 1629 1990.

Strazzulla, G. and R.E. Johnson, Irradiation Effects on Comets and Cometary Debris. in Comets in the Post-Halley Era (Bamburg Proceedings) in Press, 1991.

Strazzulla, G. Barratta, R.E. Johnson and B. Donn The Primordial Comet Mantle: Irradiation Production of a Stable, Organic Crust. Icarus in press, 1991.

Johnson, R.E., Irradiation Effects in a Comet's Outer Layers, JGR in press (1991)

NEW SPECTRAL OBSERVATIONS OF CALLISTO AND LEADING/TRAILING HEMISPHERE DISTINCTIONS W. M. Calvin, R. N. Clark, and T. V. V. King, U. S. Geological Survey, Denver

In December, 1989 and January, 1990 new observations of the leading and trailing hemispheres of Callisto were made from the NASA Infrared Telescope Facility on Mauna Kea in Hawaii. Using the Cooled Grating Array Spectrometer spectral coverage was obtained from 1.89 to 2.46 μm and 2.8 to 4.2 μm for both the leading and trailing hemispheres. In addition, spectral coverage of the leading hemisphere was obtained from 1.30 to 2.55 μm and from 4.2 to 4.8 μm .

In the wavelength region from 1.9 to 2.5 μm , both Clark *et al.* [1] and Pollack *et al.* [2] noted that the trailing hemisphere spectrum was suppressed relative to the leading hemisphere near 2.2 μm . That is, the peak at 2.2 μm associated with the long wavelength edge of the 2.0 μm water ice absorption feature was not observed on the trailing hemisphere. (We believe the labels for leading and trailing hemispheres are reversed in the Pollack *et al.* paper.) However, data presented by Roush *et al.* [3], and the observational data presented here in Figure 1, indicate the spectra of the leading and trailing hemispheres are quite similar in this spectral region, with at most a slight slope change between the two. Variations in orbital phase cannot account for the difference in the data sets. A re-examination of the Clark *et al.* data indicates that errors in standard star data may have eliminated a 2.2 μm peak from the spectrum of the trailing hemisphere. It is not known if the Pollack *et al.* data are subject to the same uncertainties.

The longer wavelength coverage of the leading hemisphere allowed for a model removal of the ice signature and indicates a possible absorption feature from 1.8 to 1.9 μm , associated with hydrous mineral phases. This is consistent with the modeling study of Calvin and Clark [4], which indicated a large adsorbed water band at 3 μm in the non-ice material on the surface. Unfortunately, this feature occurs where absorption by water in the terrestrial atmosphere is quite strong, and it may in fact be a remnant atmospheric feature. In the short wavelength spectral region (Figure 1), these high resolution data show no other spectral features except those which can be assigned to water ice. The slight difference in slope between the trailing and leading hemispheres can be attributed to variations in ice grain size or grain size distribution. The shallower slope on the trailing hemisphere indicates larger ice grain sizes, consistent with the interpretation of spectra at longer wavelengths discussed below.

In the spectral region from 2.8 to 4.2 μm several distinctions between the leading and trailing hemispheres are observed (Figure 2). A broad absorption from approximately 3.1 to 3.6 μm is present on the leading hemisphere. The trailing hemisphere also exhibits a different spectral slope with respect to the leading hemisphere from approximately 3.0 to just beyond 3.1 μm . Problems with extinction corrections in the region from 3.18 to 3.33 μm yielded data that are noisy and the resulting bad data points have been deleted in Figure 2.

The broad absorption band centered over 3.4 μm on the leading hemisphere can be seen in data presented by Pollack *et al.* [2] and Roush *et al.* [3], but at a much poorer resolution and signal-to-noise ratio. This feature was not discussed in either of those papers. The high resolution data presented here indicate that this feature can be attributed to a very small amount of fine-grained water ice present on the leading hemisphere. Spectral modeling has shown that 0.5 to 1.0 wt% ice at grain sizes near

30 to 50 μm can account for the presence of this absorption feature. The depth of this feature varies from near 35% in the earliest observations to approximately 10% in the present data. This variation is evidence of preferential erosion through sublimation of the finest ice grains on the surface. Such grains are created by meteoroid bombardment and the competition between the two processes appears to be dynamic on decade-like time scales.

The spectral shape of the trailing hemisphere can be modeled reasonably well using a broad adsorbed water band with the addition of some large-grained ice. The modeling suggests that there may be additional absorption near 3.1 μm , particularly on the leading hemisphere. A model removal of the ice signature in this wavelength region shows an absorption that is very similar to that seen in the spectrum of the asteroid Ceres (Lebofsky *et al.* [5] and King *et al.* [6]). This absorption on Ceres has been interpreted as being caused by NH_4 -bearing clays [6]. Unfortunately the model ice removal in this spectral region is subject to a greater uncertainty than in other wavelength regions as both the index of refraction and the absorption coefficient are at extreme values and varying rapidly near 3.1 μm . Such uncertainty may affect the slopes of modeled spectra and thus precludes a definitive identification.

- [1] Clark, R. N., R. B. Singer, P. D. Owensby, and F. P. Fanale 1980. *Bull. Am. Astron. Soc.*, 12, 713-714. [Abstract] [2] Pollack, J. B., F. C. Witteborn, E. F. Erickson, D. W. Strecker, B. J. Baldwin, and R. T. Reynolds 1978. *Icarus*, 36, 271-303. [3] Roush, T. L., J. B. Pollack, F. C. Witteborn, J. D. Bregman, and J. P. Simpson 1990. *Icarus*, 86, 355-382. [4] Calvin, W. M., and R. N. Clark, 1991. *Icarus*, in press. [5] Lebofsky, L. A., M. A. Feierberg, A. T. Tokunaga, H. P. Larson, and J. R. Johnson 1981. *Icarus*, 48, 453-459. [6] King, T. V. V., R. N. Clark, W. M. Calvin, G. A. Swayze, and R. H. Brown 1990. *Bull. Amer. Astron. Soc.*, 22, 1123. [Abstract]

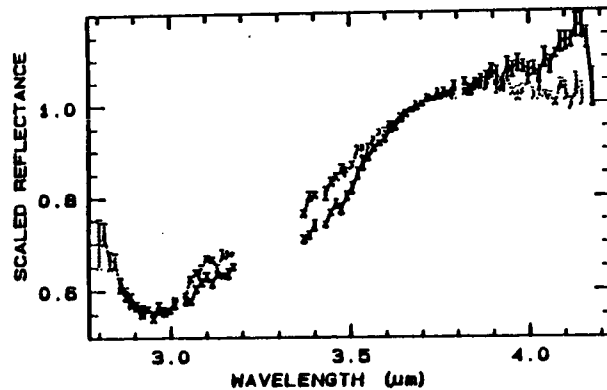
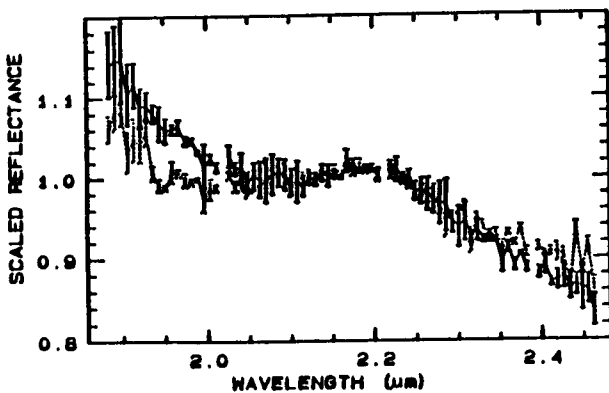


Figure 1: New observations 1.9-2.5 μm .

Figure 2: New observations 2.8-4.2 μm .

Leading hemisphere is the solid line, trailing hemisphere is the dotted line.

MOJAVE REMOTE SENSING FIELD EXPERIMENT

R. E. Arvidson, S. B. Petroy, J. J. Plaut, and M. Shepard (Department of Earth and Planetary Sciences, Washington University, St. Louis, MO 63130) D. Evans and T. Farr (Jet Propulsion Laboratory, Pasadena, CA 91109) R. Greeley, L. Gaddis, and N. Lancaster (Department of Geology and Center for Meteorite Studies, Arizona State University, Tempe, AZ 85287-1404)

The Mojave Remote Sensing Field Experiment (MFE), conducted in June, 1988, involved acquisition of Thermal Infrared Multispectral Scanner (TIMS), C, L, P band polarimetric radar (AIRSAR) data, and simultaneous field observations at the Pisgah and Cima volcanic fields, and Lavic and Silver Lake Playas, Mojave Desert, California. A Landsat thematic mapper (TM) scene acquired on April 18, 1988, is also included in the MFE archive. TM-based reflectance and TIMS-based emissivity surface spectra were extracted for selected surfaces. Radiative transfer procedures were used to model the atmosphere and surface simultaneously, with the constraint that the spectra must be consistent with field-based spectral observations. AIRSAR data were calibrated to backscatter cross section using corner reflectors deployed at target sites.

Analyses of MFE data focused on extraction of reflectance, emissivity, and cross section for lava flows of various ages and degradation states. Generally, as flows age, weathering and mass movements remove roughness (1). In addition, the surfaces are mantled by quartz, feldspar, and clay-bearing aeolian deposits and covered with a basalt-cobble desert pavement (1). MFE data analyses show that the smoothing process increases reflectances, as does the exposure of aeolian deposits. For example, average reflectance varies from 0.10 for young flows to 0.20 for a 4 Ma old flow. Emissivity minima for young flows range from 9.5 to 9.7 micrometers, consistent with fundamental vibrational absorptions due to mafic minerals. Increasing age shifts the minima to shorter wavelengths because of the exposure of felsic minerals in the aeolian deposits. Polarized and depolarized radar cross sections decrease from young to 4 Ma old flows. However, the oldest flow examined (7 Ma) shows a reversal to lower reflectances, longer wavelength emissivity minima, and an increased P band backscatter cross section. These changes are a consequence of fluvial dissection that removes the aeolian mantle and roughens the surface at length scales relevant to P band backscatter.

Results have relevance for the evolution of volcanic plains on Venus and Mars. For example, Figure 1 shows radar cross sections for various surfaces extracted from Magellan and AIRSAR data. The dark plains on Venus, located in paraboloidal ejecta deposits (2) are as smooth as Lavic Lake playa. Some relatively young flows on Gula Mons have cross sections comparable to what is found for young a'a flows at the Cima volcanic field. Finally, we are pursuing an evaluation of the color and thermal properties of lava flows of varying stratigraphic age on the Tharsis Plateau, Mars, using MFE results as a guide to help interpret flow degradation styles.

References

- (1) Wells et al., (1985) Geological Society of America Bulletin, 96, 1518-1529. (2) Arvidson et al., (1991) Science, in press. (3) Plaut, J.J. (1991) Ph.D. Thesis, Washington University, p. 351.

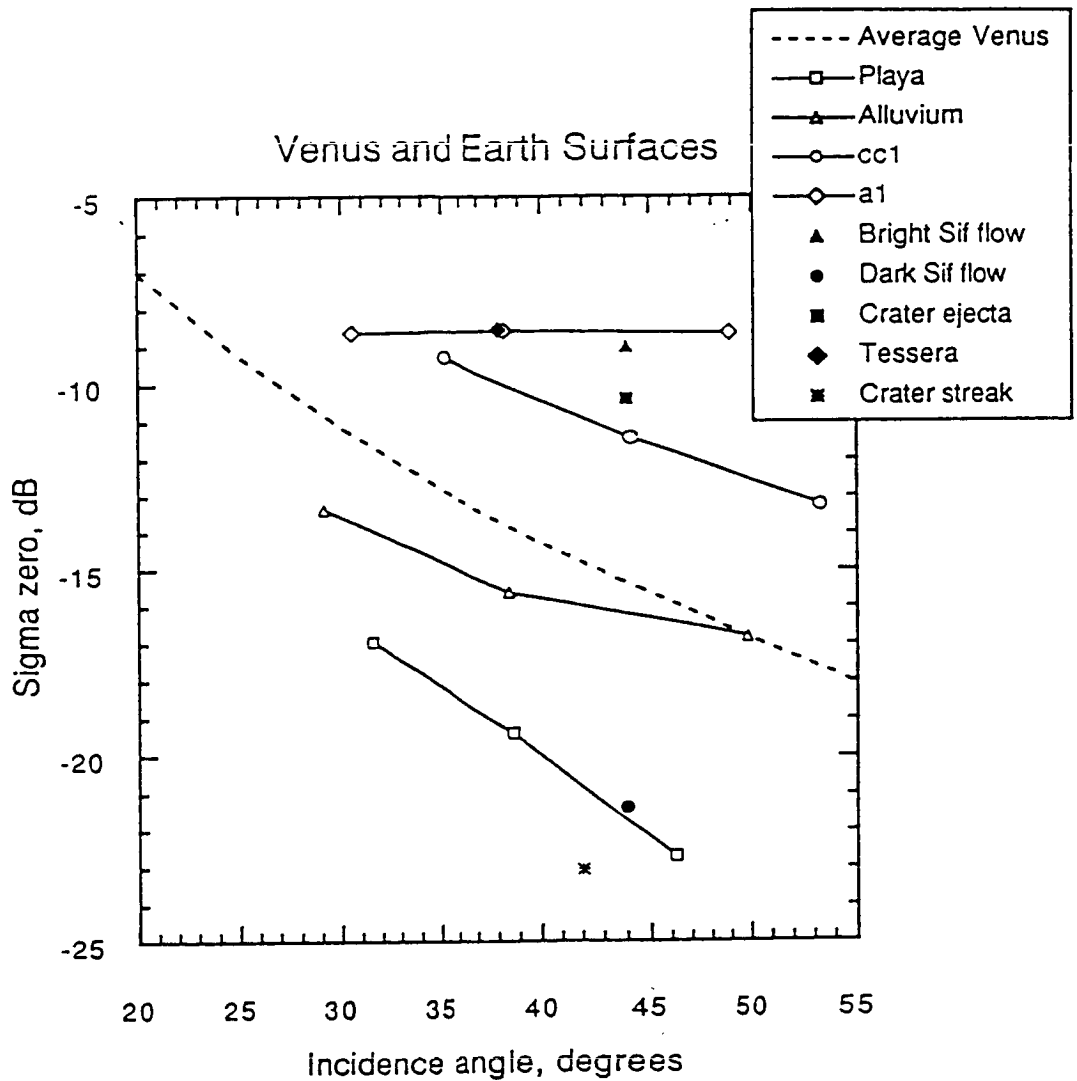


Figure 1- Radar cross section vs incidence angle for an average of Pre-Magellan results, Magellan data, and AIRSAR data for selected areas. Polarization is HH. Venus data are S-Band. AIRSAR S-Band data were simulated by a wavelength-weighted average of C and L-Band data. SIF flows are lavas. Crater streak is part of paraboloidal ejecta deposit. Figure from (3).

SURFACE SCATTERING PROPERTIES ESTIMATED FROM MODELING AIRBORNE MULTIPLE EMISSION ANGLE REFLECTANCE DATA

E. A. Guinness, R. E. Arvidson, McDonnell Center for the Space Sciences, Department of Earth and Planetary Sciences, Washington University, St. Louis, MO, 63130; and J. R. Irons, Biospheric Sciences Branch, D. J. Harding, Geophysics Branch, both at Goddard Space Flight Center, Greenbelt, MD, 20771.

Photometry has been used extensively to study the physical properties of materials exposed on the surface of planets and asteroids [e.g., 1-3]. A model that is often used in such studies is the Hapke photometric function [4]. The Hapke function has been successfully applied to laboratory bidirectional reflectance data of powdered samples [e.g., 5-6]. However, only a few studies [e.g., 7] have applied the model to terrestrial geological surfaces where the physical properties of the surface can be independently determined. In this study we apply the Hapke function to airborne bidirectional reflectance data collected over three terrestrial surfaces. The objectives of this study are (1) to test the range of natural surfaces that the Hapke model fits and (2) to evaluate model parameters in terms of known surface properties. The data used in this study are multispectral and multiple emission angle data collected during the Geologic Remote Sensing Field Experiment (GRSFE) over a mud-cracked playa, an artificially roughened playa, and a basalt cobble strewn playa at Lunar Lake Playa in Nevada. GRSFE was an experiment in which airborne remote sensing data and associated field measurements were acquired at the same time [8]. The airborne data for this study were acquired by the Advanced Solid-State Array Spectroradiometer (ASAS) instrument [9]. ASAS is a 29 spectral band (0.465 to 0.871 μm) imaging system that flies in the NASA C-130 aircraft. Seven emission angles are collected on each pass varying from 45° forward looking to 45° backward in 15° increments. Two ASAS tracks acquired during the morning of July 17, 1989 were used in this study. For the first track the aircraft flew parallel to Sun direction, which is also known as the principal plane. For the second track the aircraft flew at an azimuth of about 41° away from the principal plane. The phase angles for both tracks ranged from 20° to 97°.

Three 50x50 m sites on Lunar Lake Playa were established for modeling studies. The cobble site consisted of basalt fragments up to several tens of centimeters across sitting on silty playa sediment. The area covered by gravel and cobble size fragments ranged from 20 to 85 percent. The cobble site also contained several bushes up to 1.5 m across and 0.4 m high. The smooth playa site was a natural playa surface consisting of compacted, clay-rich sediment, 20-30 cm wide mud-cracks, a few 2-3 cm size basalt fragments, and one bush about 1 m in diameter. The rough playa site is compositionally the same as the smooth playa site. The rough playa site was artificially disturbed and roughened by driving a vehicle over the site until the playa material was churned up. The roughened surface consisted of loose powder, centimeter size clods of playa sediment, and patches of undisturbed playa. There were 6 bushes ranging from 0.4 to 1 m in diameter on the rough playa site. Radiance factors for each modeling site were computed from the 3 ASAS bands centered at 0.563, 0.649, and 0.693 μm .

Atmospheric contributions to ASAS data were evaluated by comparing ASAS data to radiances computed with the LOWTRAN-7 atmospheric scattering model and to field spectrometer reflectance measurements. LOWTRAN-7 model parameters were chosen such that the model matched optical depth values measured from the ground during the time of ASAS data collection. Optical depths ranged from about 0.06 to 0.15 over the wavelengths of the ASAS bands. The LOWTRAN model was used to predict the radiance reaching ASAS (at an altitude of 5 km above the ground) for a

bright and dark surface. The atmospheric model indicates that most of the radiance reaching ASAS is from ground reflection of direct solar irradiance. The direct component comprises 76 to 82 % of the total radiance for the dark surface and comprises 84 to 86 % of the total radiance for the bright surface. There is no significant variation in the diffuse or skylight components as a function of emission angle. Measurements of the rough playa reflectance were made with a Daedalus AA440 Spectrafax field spectrometer at the time of ASAS data acquisition. The Daedalus reflectance was corrected for atmospheric attenuation on the incoming and outgoing paths using an optical depth of 0.06. The difference between the ASAS reflectance value and the corrected Daedalus value is less than the uncertainty in the absolute calibration of ASAS. This result also implies that the diffuse illumination and skylight components are of second order importance. Thus, we used ASAS reflectance data to estimate surface scattering properties without correcting for atmospheric scattering. Caution should be used in interpreting the absolute values of surface scattering parameters because the atmosphere is not fully accounted for. The estimated surface scattering parameters can be used for comparisons between the sites and to evaluate the ability of the Hapke function to model these surfaces.

The Hapke function [4] has at least five independent parameters: single-scattering albedo, average macroscopic surface roughness, width of the opposition effect, magnitude of the opposition effect, and terms defining the single particle phase function. The Henyey-Greenstein scattering function was used to model the particle phase function. The smallest phase angle in the ASAS data set was about 20° . For most materials the opposition effect is best constrained by viewing the surface with smaller phase angles [2, 4]. We found that the model fits to the ASAS data were not significantly changed by varying the two opposition effect parameters. Therefore, we concentrated on estimating the single scattering albedo, roughness parameter, and asymmetry factor of the particle phase function. Hapke parameters were estimated by minimizing the chi-square residual between the data and the Hapke fit. For the cobble and rough playa sites, a set of Hapke parameters was found that explains the variation in reflectance data from both ASAS tracks. Hapke parameters determined for these two sites are listed in Table 1, along with estimated uncertainty in the parameters. For the smooth playa site, a single set of parameters could not be found that explains the variation in ASAS reflectance data from both tracks.

The cobble and rough playa site have systematic differences in all three Hapke parameters. The rough playa site has a larger single scattering albedo than the cobble site at all three wavelengths as would be expected from the high reflectance values from the playa. The relatively high values of single scattering albedo for the cobble site are likely to be because 15 to 80 % of the surface is covered by bright silt and clay playa sediment. The Hapke roughness parameter is larger for the cobble site than for the rough playa site. There is a correlation between the size of the roughness elements and the Hapke roughness parameter for the cobble and rough playa sites, with the roughness elements being larger on the cobble site. There is no large variation in the roughness parameter as a function of wavelength for both sites. The asymmetry factor for the cobble site indicates that the particle phase function for the cobble site is slightly forward scattering. The degree of forward scattering increases with wavelength, which is consistent with trends noted by [1]. The asymmetry factor for the rough playa site is backscattering and shows no systematic variation with wavelength. The values for the rough playa site are consistent with values derived for the Moon [1]. The ASAS data for the smooth playa could not be explained with the Hapke function for the available range in lighting and viewing geometries. No unique set of Hapke

parameters was found for the smooth playa ASAS data. Instead, several solutions with large differences in the Hapke parameters were found to produce approximately the same chi-square value. Solutions with near zero roughness, and weakly backscattering phase functions fit as well as solutions with a higher single scattering albedo, higher roughness values, and more strongly backscattering phase functions. ASAS data for the smooth playa show only a small change in reflectance with phase angle. An alternative interpretation for the smooth playa data is that the surface is similar to a Lambertian scatterer over the observed geometries with the reflectance only a function of incidence angle. The difference in reflectance between the two ASAS tracks is consistent with the change in incidence angle between the two tracks.

In summary, ASAS reflectance data for a cobble-strewn surface and an artificially rough playa surface on Lunar Lake Playa can be explained with the Hapke model. The cobble and rough playa sites are distinguishable by the single scattering albedo, which is controlled by material composition; by the roughness parameter, which appears to be controlled by the surface texture and particle size; and the asymmetry factor of the single particle phase function, which is controlled by particle size and shape. A smooth playa surface consisting of compacted, fine-grain particles has reflectance variations that are also distinct from either the cobble site or rough playa site. The smooth playa appears to behave more like a Lambertian surface that cannot be modeled with the Hapke function.

REFERENCES

- [1] Helfenstein, P., and J. Veverka, *Icarus*, 72, 342-357, 1987. [2] Domingue, D., and B. Hapke, *Icarus*, 78, 330-336, 1989. [3] Arvidson, R., et al., *J. Geophys. Res.*, 94, 1573-1587, 1989. [4] Hapke, B., *Icarus*, 67, 264-280, 1986. [5] Hapke, B., and E. Wells, *J. Geophys. Res.*, 86, 3055-3060, 1981. [6] Mustard, J., and C. Pieters, *Proc. Lunar Planet. Sci. Conf.*, 17th, Part 2, *J. Geophys. Res.*, 92, Suppl., E617-E626, 1987. [7] Pinty, B., et al., *Remote Sens. Environ.*, 27, 273-288, 1989. [8] Arvidson, R., and D. Evans, *Lunar Planet. Sci.*, XXI, 26-27, 1990. [9] Irons, J., et al., *IEEE Trans. Geosci. Remote Sensing*, 29, 66-74, 1991.

TABLE 1

Modeling Site	Wavelength (μm)	Single Scattering Albedo	Roughness Parameter (degrees)	Asymmetry Parameter	Chi-square
Cobble Site					
	0.563	0.617 0.001	28.0 1.2	0.045 0.014	0.11
	0.649	0.663 0.009	31.1 1.4	0.074 0.018	0.10
	0.693	0.761 0.008	35.2 1.3	0.184 0.020	0.24
Rough Playa Site					
	0.563	0.854 0.001	20.1 0.1	-0.171 0.001	6.93
	0.649	0.898 0.001	20.4 0.1	-0.194 0.002	2.97
	0.693	0.918 0.001	21.7 0.1	-0.162 0.002	3.89

Note that the second value in the single scattering albedo, roughness parameter, and asymmetry parameter columns is the estimated uncertainty in that parameter.

MAPPING COMPOSITIONAL AND PARTICLE SIZE VARIATIONS ACROSS SILVER LAKE PLAYA - RELEVANCE TO ANALYSES OF MARS TIR DATA

S.B. Petroy, R.E. Arvidson, McDonnell Center for the Space Sciences, Earth and Planetary Sciences Department, Washington University, St. Louis, MO., 63130; and A.B. Kahle, MS 183-501, Jet Propulsion Laboratory, 4800 Oak Grove Dr., Pasadena, CA, 91109.

The high spectral and spatial resolution thermal infrared (TIR) data to be acquired from the upcoming Mars Observer-*TES* mission will map the composition and texture of the martian sediments [1]. To prepare for these data, portions of two remote sensing field experiments (MFE-1988 and GRSFE-1989) [2,3] were conducted to test procedures for extracting surface property information from TIR data. What follows is a report of the continuing analyses of Thermal Infrared Multispectral Scanner (TIMS) data, field emission spectra, laboratory FTIR reflectance spectra, and field observations with respect to the physical characteristics (composition, emissivity, etc.) of Silver Lake playa in southern California.

In February, 1989, emission data were collected over two sites at Silver Lake with the JPL Portable Field Emission Spectrometer (PFES) [4]. The analyses of these data were reported in Petroy and Arvidson (1990) [5]. The PFES was unavailable the following field season; thus, in May, 1990, samples were collected from five sites at the north end of Silver Lake. Reflectance spectra (between 6.0 and 14.0 μm) of these samples were collected in the laboratory using the JPL FTIR spectrometer. An integrating hemisphere has been attached the spectrometer, providing a means for collecting total hemispheric reflectance measurements. The reflectance data were then converted to emissivity using Kirchoff's law ($1 - \text{reflectance} = \text{emissivity}$) [6].

Emission spectra from samples collected at three of the sites are shown in Fig. 1. These spectra represent the range of data collected from all the samples. All three spectra are dominated by the strong absorption feature centered at 9.6 μm due to the stretching vibrations of the Si-O bonds in the layered clays. XRD data have confirmed that the dominant constituent in the samples is smectite clay. The quartz absorption feature is represented by the diagnostic quartz doublet, consisting of two lobes centered at approximately 8.4 and 8.8 μm . The intensity of the absorption feature decreases from site B to site D indicating either a change in the particle size of the quartz sands from each site [7], or a variation in the amount of quartz exposed at each site.

The distribution of quartz particles sizes was measured for each sample and is approximately the same from site to site on the playa, ranging from silt size to fine-medium grained sands (0.54 μm to 250 μm). Therefore, the change in the quartz absorption feature from site B to site D probably represents a variation in the amount of quartz exposed at each site. To test this hypothesis, point counts were made over each playa tiles to determine the amount of quartz sand versus the amount of clay material exposed at the surface (referred to as the QC ratio). The FTIR spectra were then normalized by setting the emissivity values between the wavelength region 7.4 and 7.7 μm (i.e. the Christiansen frequency) to 1.0. The area beneath the curves was then

integrated between 7.4 μm and 12.0 μm (12.0 μm was selected because the emission spectra from all of the sites approached constant values of 0.96 at this wavelength).

The QC ratio calculated for each sample was then plotted against the normalized area under the curve derived from the emission spectra collected over the samples. The results of this analysis are displayed in Fig. 2. There is a linear relationship between the amount of quartz exposed at the surface of the playa tiles versus the depth of the quartz absorption feature suggesting that similar approaches can be used to extract compositional information from TES data.

References

- [1] Christensen et al., preprint, [2] Wall, S., et al., (1988) *Bull. Am. Ast. Soc.*, 20, p.809. [3] Arvidson, R.E. and D.L. Evans (1989) *GSA Abst. with Prog.*, p. A121. [4] Hoover, G. and A.B. Kahle (1987) *Phot. Eng. and Rem. Sens.*, vol. 53, p. 627-632. [5] Petroy, S.B. and R.E. Arvidson (1990) *Abst. with Prog. - 21st Lunar Plant. Sci. Conf.*, p. 952-953. [6] Nicodemus, F. (1965) *App. Opts.*, p. 767-773, [7] Conel, J.E. (1969) *J. Geophys. Res.*, 74, p. 1614-1634.

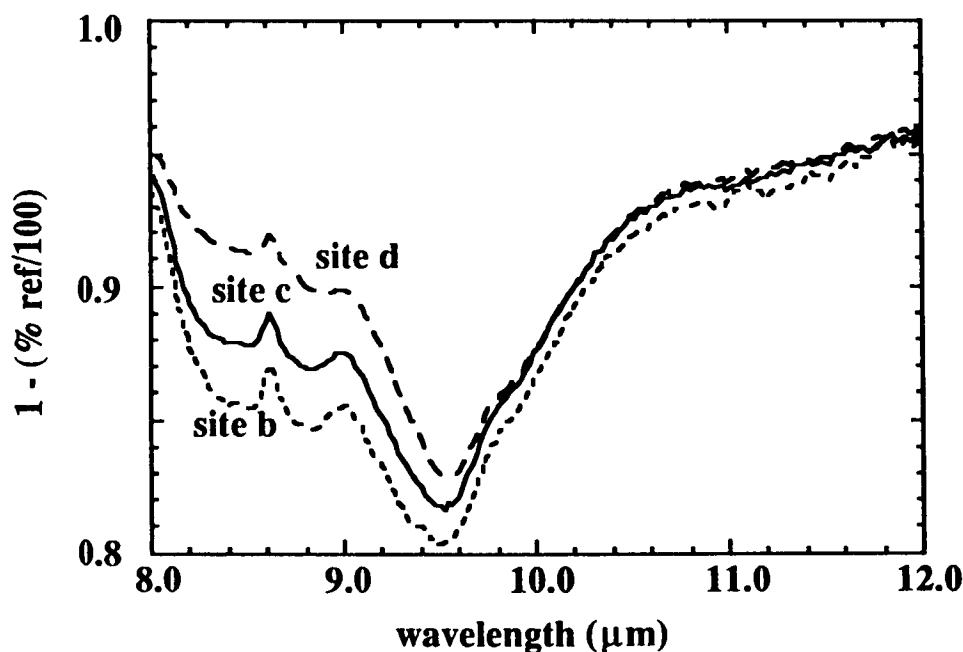


Fig. 1: FTIR reflectance spectra (converted to emission) for samples from three sites at Silver Lake playa.

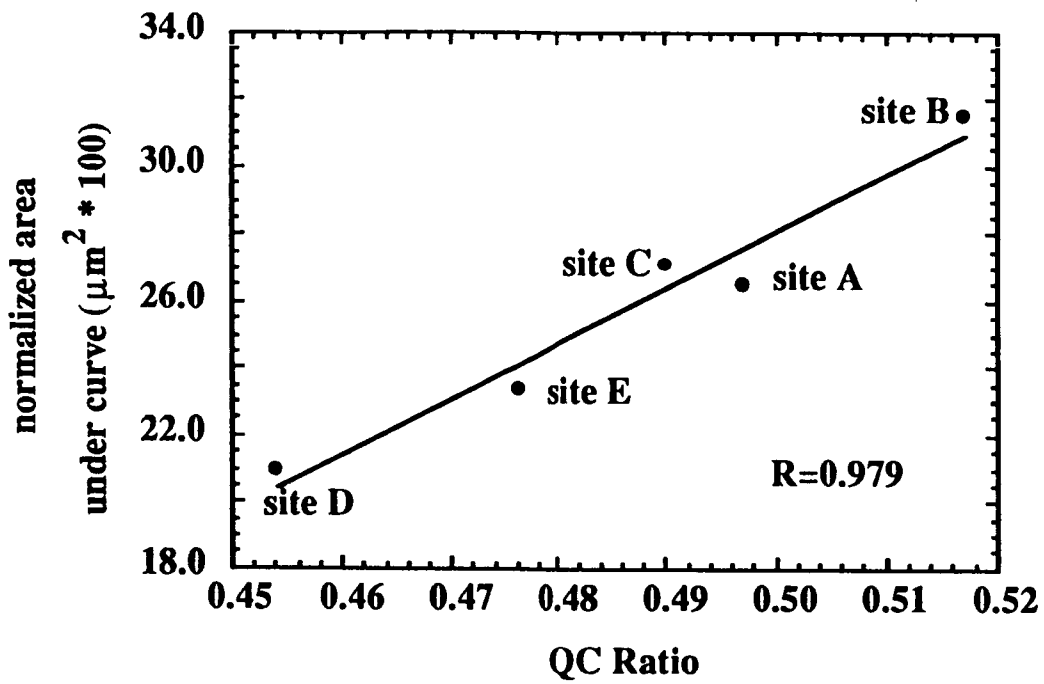


Fig. 2: Plot of QC ratio (surface distribution of quartz vs. clay) for each sample against the normalized area under the curve derived from the emission spectra collected from each sample.

APPLICATION OF HAPKE PHOTOMETRIC MODEL TO THREE GEOLOGIC SURFACES USING PARABOLA BIDIRECTIONAL REFLECTION DATA; Michael K. Shepard, Raymond E. Arvidson, McDonnell Center for the Spaces, Department of Earth and Planetary Sciences, Washington University, St. Louis, Missouri, 63130; and Donald W. Deering, Laboratory for Terrestrial Physics, Goddard Space Flight Center, Greenbelt, Maryland, 20771.

The Geologic Remote Sensing Field Experiment (GRSFE) was conducted in July and September of 1989 to collect data with both ground and airborne instrumentation [1]. A major objective of GRSFE was to collect data which could be used to test radiative transfer models for the extraction of composition and textural surface properties from remotely acquired data. This abstract reports initial results from an application of the Hapke photometric model [2,3,4] using data from PARABOLA (Portable Apparatus for Remote Acquisition of Bidirectional Observations of Land and Atmosphere) [5].

PARABOLA is a ground based radiometer with three spectral channels centered at 0.66 μm , 0.83 μm , and 1.66 μm . The radiometer is mounted on a rotating boom and measures ground radiance in a 15° instantaneous field of view from over 70 different viewing geometries in about 11 seconds. The mechanics of the instrument do not permit the same point on the ground to be measured with each look; rather, each pixel represents the radiance from a different portion of a 35m x 35m area. To insure that the data are representative of the surface, a homogeneous section of each site is selected for the instrument to measure.

PARABOLA data were acquired in the Lunar Crater Volcanic Field in Nevada [6], specifically from the region of Lunar Lake, a playa. Several modeling sites were established in this area and data from three of these sites were collected with PARABOLA. The first site consisted of a section of the Lunar Lake playa which was characterized by a clay rich, hard packed surface with decimeter size mudcracks. The second site, called the cobble site, was similar to the playa site but was strewn with basaltic cobbles and pebbles from a nearby flow. The cobbles were centimeter to tens of centimeters in size and varied in abundance from about 25% to 85% over the playa [E.Guinness, pers. comm]. The third surface consisted of a mantled basalt lava flow. This surface was the most inhomogeneous of the three and contained small amounts of visible silt and significant vegetation in the form of bushes.

Data were acquired five times during the day from the playa and cobble sites, and six times from the lava flow. The times of data acquisition were spaced to provide a wide variety of solar incidence angles for each site, typically from approximately 20° to 70°. Periodically throughout the day, a barium sulfate plate was measured by PARABOLA as a reference Lambertian scatterer. Dividing the radiance from the surface by the radiance from the reference plate and the cosine of the incidence angle gives a measure of reflectance termed the radiance factor [2].

Radiance factors from each site were inverted to extract the Hapke parameters; single scattering albedo, roughness, opposition surge amplitude and width, and particle phase function described by a Henyey-Greenstein asymmetry factor. Inversion techniques included a grid map and a grid search algorithm [7]. Initial analyses of the lava and cobble sites have only used channel 1 (0.66 μm) data. The analysis of the playa site is more complete - all three channels of data have been fit with the Hapke model. The effects of atmospheric scattering were estimated using the numerical radiative transfer model, LOWTRAN-7 [8], and found to be approximately four orders of magnitude lower than the surface reflectance, and therefore negligible.

The modeling results were mixed. The playa, although a particulate surface and the most homogeneous of the sites, could not be adequately fit with the Hapke model. At moderate incidence angles (<40°) the playa behaved as a Lambertian scatterer. At higher incidence angles (>50°), the playa displayed a strong forward scattering lobe in the solar principal plane. The presence of this lobe could not be accounted for with the Hapke model. Removal of this lobe resulted in reasonable Hapke parameters (Table 1). We hypothesize that the presence of clay and micaceous minerals in non-random orientations (i.e. layered) are responsible for this behavior and

the poor description by the Hapke model. Hapke assumes that particulates are equant and randomly oriented in his derivation and therefore an initial condition for the use of the model is not met. Reasonable solutions could not be found for the cobble site. In addition to the poor description of the underlying playa, we believe that variability in the cobble distribution and preferential shadowing of the playa by the cobbles are responsible for the model's failure. The lava flow could be modeled, but dubiously. Smaller variances in the data from the model fit were found for the lava flow but much of this is due to the darkness of the flow compared to the playa and cobble sites. Modeled roughness is low, 15°, compared with approximately 20-30° estimated from topographic profiles generated by helicopter stereophotography.

In conclusion, we have found the Hapke model to be inadequate for three relatively common geologic surfaces. The model is not at fault; rather, the complexity of most geologic surfaces is not accounted for in the initial assumptions.

	(0.66 μm)	Table I (0.83 μm)	(1.66 μm)
single scattering albedo	0.982	0.986	0.981
roughness	13.4°	13.3°	10.8°
opposition surge amplitude	3.8	4.1	4.7
opposition surge width	0.114	0.131	0.071
asymmetry factor	0.704	0.714	0.810
variance	0.00012	0.00014	0.00017

REFERENCES

- [1] Arvidson, R.E., and D.Evans (1989) GSA Abstracts with Programs, v. 21, n.6, A121.
- [2] Hapke, B. (1981) J. Geophys. Res., v. 86, 3039-3054.
- [3] Hapke, B. (1984) Icarus, v. 59, 41-59.
- [4] Hapke, B. (1986) Icarus, v. 67, 264-280.
- [5] Deering, D.W., (1988) SPIE, v. 924, 249-261.
- [6] Dohrenwend, J.C. et al. (1987) GSA Bulletin, v.99, 405-413.
- [7] Bevington, P.R. Data Reduction and Error Analysis for the Physical Sciences, McGraw-Hill, Inc, 1969.
- [8] Kneizys, F.X. et al. (1989) Users Guide to LOWTRAN-7, AFGL-TR-88-0177, Hanscom AFB.

THE GEOLOGIC REMOTE SENSING FIELD EXPERIMENT (GRSFE)

Mary A. Dale-Bannister, Raymond E. Arvidson, Edward E. Guinness, Susan H. Slavney, and Thomas C. Stein, Earth and Planetary Remote Sensing Laboratory, McDonnell Center for the Space Sciences, Washington University in St. Louis.

Approximately 40 scientists from eight universities and three NASA centers participated in the Geologic Remote Sensing Field Experiment (GRSFE), which was co-sponsored by the NASA Planetary Geology and Geophysics Program and the NASA Geology Program. The GRSFE airborne campaign included data acquisition by several airborne instruments within a period of a few months, including the Airborne Visible and Infrared Imaging Spectrometer (AVIRIS; collected September 28, 29 and October 4, 1989), Thermal Infrared Multispectral Scanner (TIMS; collected July 17 and September 27 and 29, 1989), Advanced Solid-State Array Spectroradiometer (ASAS; July 17, 1989), and Polarimetric Synthetic Aperture Radar (AIRSAR; September 13 and 14, 1989). The sites covered were Lunar Crater Volcanic Field in Nevada, and a number of sites in the Mojave Desert of California. Table I contains a summary of the data acquired.

Field measurements were done at the time of the flights and were concentrated in the Lunar Lake area. They included measurements for characterizing the atmosphere using a weather station, wind speed towers, measurements using the Portable Apparatus for Rapid Acquisition of Bidirectional Observations of the Land and Atmosphere (PARABOLA), a spectral hygrometer, and a Reagan radiometer. Visible/near-infrared measurements were made using the Single Beam Visible/Infrared Intelligent Spectroradiometer (SIRIS), and a Daedalus Spectrafax AA440 field spectrometer. Thermal spectral radiance measurements were made with the Portable Field Emission Spectrometer (PFES). Surface temperatures were measured using a Raynger Raytek II Plus and arrays buried of thermistors. To assist in the calibration of the radar data, corner reflectors were deployed. Stereo photography (from a helicopter) was acquired, and topographic profiles were constructed. Field differential Geopositional Satellite (GPS) microterrain survey techniques were also used to extract topographic profiles.

The GRSFE data will be published on a set of 9 CD-ROMs, which will be available for distribution in June 1991. The CDs will contain documentation explaining the overall Experiment, including: documentation for the instruments, the calibration of the instruments, the techniques used in the field, and any documentation available for individual readings or scenes. There will also be complete documentation on the formats of the data files.

The GRSFE data are meant to be used in a variety of investigations, including tests of multispectral radiative transfer models for scattering and emission from planetary surfaces in support of the Earth Observing System (EOS), Mars Observer and Magellan Missions. Studies will also be pursued to establish the neotectonic and paleoclimatic history of the arid southwestern United States. GRSFE data will also be used to support Mars Rover Sample Return (MRSR) simulation studies. Finally, we expect this collection of data to be a useful tool in the teaching of geological remote sensing.

References: Arvidson, Raymond E. and Diane Evans (1989) Geology Remote Sensing Field Experiment. *In GSA 1989 Abstracts With Programs*, p. A121.

TABLE I

GRSFE
DATA INVENTORY OVERVIEWNUMBER OF SCENES/READINGS
(May be more than one file per set)

INSTRUMENT	CM	DD	DG	KL	LL	LV	MH	PV	SW	TC	UB	Total
-----	--	--	--	--	--	--	--	--	--	--	--	-----
AIRSAR	-	-	-	-	5	-	2	-	1	-	3	11
ASAS	-	-	-	-	4	1	-	-	-	-	1	6
AVIRIS	2	-	2	1	-	12	-	3	-	6	2	28
TIMS	1	-	-	1	9	8	-	1	3	2	2	27
DAEDALUS	98	31	41	92	192	-	-	-	-	50	17	521
ELEV PROFILES	-	1	2	-	4	13	3	-	1	1	1	26
HYGROMETER	-	-	-	-	1	-	-	-	-	-	-	1
PARABOLA	-	-	-	-	17	-	-	-	-	-	-	17
PFES	5	-	-	4	22	-	-	-	-	-	-	31
REAGAN RAD	-	-	-	-	2	-	-	-	-	-	-	2
SIRIS	9	-	4	8	24	-	-	-	-	4	7	56
WIND EXP	-	-	-	-	2	-	-	-	-	-	-	2
WEATHER STAT	-	-	-	-	2	-	-	-	-	-	-	2
----	----	----	----	----	----	----	----	----	----	----	----	----
Total	115	32	49	106	284	34	5	4	5	63	33	730

SIZE OF DATA FILES
(Airborne in MB; Field in KB; .LBL files not included)

INSTRUMENT	CM	DD	DG	KL	LL	LV	MH	PV	SW	TC	UB	Total
-----	--	--	--	--	--	--	--	--	--	--	--	-----
AIRSAR	-	-	-	-	193	-	75	-	39	-	116	423 MB
ASAS	-	-	-	-	760	151	-	-	-	-	176	1087
AVIRIS	288	-	288	144	-	1729	-	432	-	865	288	4034
TIMS	9	-	-	19	190	148	-	25	69	51	32	543
DAEDALUS	301	95	126	283	599	-	-	-	-	154	52	1610 KB
ELEV PROFILES	-	574	1168	-	2293	7654	1804	-	451	603	512	15059
HYGROMETER	-	-	-	-	2	-	-	-	-	-	-	2
PARABOLA	-	-	-	-	604	-	-	-	-	-	-	604
PFES	154	-	-	123	676	-	-	-	-	-	-	953
REAGAN RAD	-	-	-	-	9	-	-	-	-	-	-	9
SIRIS	166	-	74	123	24	-	-	-	-	74	129	590
WIND EXP	-	-	-	-	22	-	-	-	-	-	-	22
WEATHER STAT	-	-	-	-	-	-	-	-	-	-	-	-
----	----	----	----	----	----	----	----	----	----	----	----	----
Total (MB)	298	1	288	163	1147	2036	77	457	108	907	613	6095 MB

HIGH RESOLUTION LUNAR RADAR STUDIES-PRELIMINARY RESULTS

Nicholas J.S. Stacy and Donald B. Campbell, Dept. of Astronomy, Cornell University, Ithaca, New York 14853.

High resolution 12.6cm radar data for the lunar surface were acquired over fourteen sites in June and November 1990 using the new 10MHz data taking system at the Arecibo Observatory. The raw data collected for each site covers an area approximately 100km by 400km and will be processed using delay-Doppler techniques into images of backscatter cross section with three to four independent looks. Five of the sites were observed with a spatial resolution potentially better than 50m and the other nine at mixed spatial resolutions better than 150m. All observations transmitted a circularly polarized signal and both senses of circular polarization were received containing the polarized and depolarized components of the backscatter signal. The relative power in these two polarizations provides useful information on properties of the surface, in particular surface roughness.

The effort to date has focused on the initial data analysis with new software being written to perform a full synthetic aperture focusing on the raw radar data. The resulting image data will be analyzed to: 1) study the scattering mechanisms, particularly, the polarization properties, associated with fresh impact craters, impact crater rays and volcanic flow units; 2) attempt to measure the dielectric constant and, hence, the porosity of the tenuous upper layer by mapping the ratios of the appropriately oriented linearly polarized components of the echo received from high incidence angle observations of the lunar mare; 3) investigate interferometric techniques in an attempt to derive lunar surface topography by unwrapping the interference fringes between two time delayed observations of the same site. This analysis will involve the use of complementary high resolution optical and topographic data sets to aid interpretation of surface scattering mechanisms.

The fourteen sites include the Dawes and Euler complex impact craters which were imaged at incidence angles of $\sim 30^\circ$ and $\sim 40^\circ$ respectively, the Gruithuisen domes which may be similar to the many domes on the Venus surface revealed by the Magellan spacecraft, the Hadley-Apennine and Littrow-Tarus regions near the Apollo 15 and 17 landing sites for comparison with ground truth information, the Aristarchus Plateau which has anomalously low radar backscatter at 3.8cm wavelength indicating a very smooth surface and/or regolith material with a high loss tangent [1], mare at high incidence angles for possible regolith dielectric constant measurements and Mare Orientale which is thought to be the youngest impact melt on the lunar surface and was recently imaged by the Galileo spacecraft [2]. Initial multilook images of the 17km complex impact crater Dawes are anticipated in mid spring. At the better than 50m resolution expected for the Dawes crater site we hope to analyze the radar echoes from smaller morphologic elements including the crater hummocky floor deposits, slump terraces within its walls, scalloped rim and the ejecta blanket. Of particular interest are the polarization signatures of the inner wall and ejecta which may provide a quantitative assessment of the blockiness and linear structures in these features. There is extensive supporting data for this area including Apollo metric and panoramic imaging, Earth based multispectral imaging and 1:50,000 scale (5m contour) Lunar Topo Photo maps. Quantitative assessment of the high resolution radar characteristics should provide useful insights into the local structural elements of this complex crater.

The analysis of lunar data will continue with the fresh crater Bessel, the complex crater Euler, volcanic rilles, flows and domes, mare regolith dielectric properties and interferometric analysis.

The dielectric constant of the lunar regolith at radar wavelengths is a measure of the porosity of the tenuous upper layer and is estimated from the ratio of the backscatter in the local horizontal and vertical linear polarizations. This estimate is based on the assumption that the observed backscatter is from the subsurface material only. High incidence angle observations of the lunar mare are preferred for regolith dielectric constant measurements because of the assumed low surface backscatter and good coupling of the vertical polarization to the surface when imaged near the Brewster's angle (incidence angle $\sim 60^\circ$). Interferometric analysis requires observations with a viewing geometry limited to $\sim 0.01^\circ$ and, hence, fortuitous alignment of the Earth-Moon system when visible from Arecibo Observatory.

Due to the libration of the moon some areas on the lunar surface are observable from Arecibo Observatory at incidence angles varying by as much as 10° . We will take advantage of this to try to quantitatively estimate variations in the relative quasi-specular and diffuse radar echoes with incidence angle which should aid interpretation of the scattering mechanisms. A third observing run at Arecibo Observatory is planned for late summer 1991 in which we will revisit some of the sites previously observed at the highest resolution to collect information suitable for multiple incident angle and interferometric analysis.

References:

- [1] Zisk, S., et al., *The Moon*, **17**, 59, 1977; [2] Head, J.W., et al., *PLPSC*, **22**, 547, 1991.

Models of the Diffuse Radar Backscatter from Mars

A. W. England and R. T. Austin, Department of Electrical Engineering and Computer Science, University of Michigan, Ann Arbor, Michigan 48109-2122

Earth-based, time-domain radar surveys of Mars exhibit a specular return from a sub-Earth region of Mars followed by diffuse returns from concentric rings that are centered on the sub-Earth point. A characteristic of the diffuse return is that the radar incidence angle increases from zero degrees at the sub-Earth point to nearly 90° at ring diameters that correspond to Mars' limb. An interpretation of the diffuse backscatter beyond inferences based upon the Rayleigh roughness criterion requires some assumption about the roughness statistics of the Mars surface, and requires a scattering theory that permits roughness at all scales. Our efforts during the first year of this project have focused upon the expected roughness statistics.

Several investigators have argued that natural surfaces are scaling [1, 2]. We explore that possibility through an Earth analog of a Mars volcanic region. The topographies of several debris flow units near the Mount St. Helens Volcano were measured at lateral scales of millimeters to meters in September 1990. Mount St. Helens was chosen because of its ease of access and its extremely young terrains. Our objective was to measure the surface roughness of the debris flows at scales smaller than, on the order of, and larger than the radar wavelength of common remote sensing radars. We used a laser profiling system and surveying instruments to obtain elevation data for square areas that varied in size from 10 cm to 32 m. The elevation data were converted to estimates of the power spectrum of surface roughness. The conversions were based upon standard periodogram techniques, and upon a modified spectral estimation technique that we developed.

The surfaces that we examined were located in the debris avalanche west-northwest of the volcano, along the North Fork Toutle River Valley. Most of the debris was deposited during and immediately after the eruption of Mount St. Helens on 18 May 1980. Since then, the deposits have undergone significant erosion by wind and water. A geologic description of the debris avalanche is given by Glicken [3].

Laser Profiler. A 2D laser profilometer was developed specifically for this experiment. Its main component is a surveying electronic distancemeter (EDM) which uses an infrared laser to measure distance. The EDM is mounted on an XY table that is supported 1.5 m above the ground (the minimum range of the EDM) by 4 tripods. Stepper motors are used to move the mounting platform across the table in both directions, allowing the EDM to scan a 1 m^2 surface area. The stepper motors and the EDM are controlled by a laptop computer, allowing the system to run unattended after startup. DC power is provided by two 12 V marine batteries.

Debris surfaces were spray-painted to increase reflectivity. The EDM laser has a spot diameter of $\sim 1.5 \text{ mm}$. In its most precise mode, the standard deviation of the measured surface height is 3 mm. Because each measurement requires 2–3 seconds, a typical scan of $10 \text{ cm} \times 10 \text{ cm}$ with sample interval $\Delta = 2 \text{ mm}$ (2601 points) takes ~ 1.8 hours. Since time was a limiting factor, an increase in surface area required a corresponding increase in Δ . Scans were performed at each site using at least two sampling intervals. A typical surface height grid is shown in Figure 1.

Surveying. Larger-scale topography was surveyed with a self-leveling level and stadia rod. Square grids with sides of 16 or 32 m were delineated by cables with markers at 1 m intervals. A typical survey grid is shown in Figure 2.

Surface Spectra. Estimates of roughness power spectra were developed from the elevation

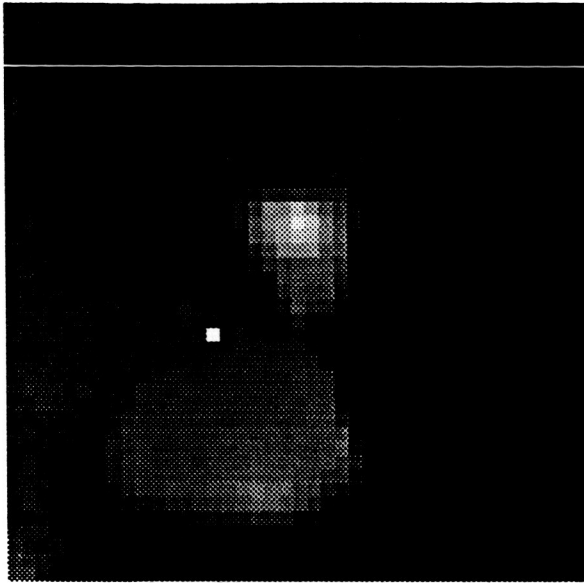


Figure 1. A profilometer grid showing surface height (dark = low). The grid measures 40 cm x 40 cm, with data points spaced 1 cm apart. Total height variation is 10.76 cm.

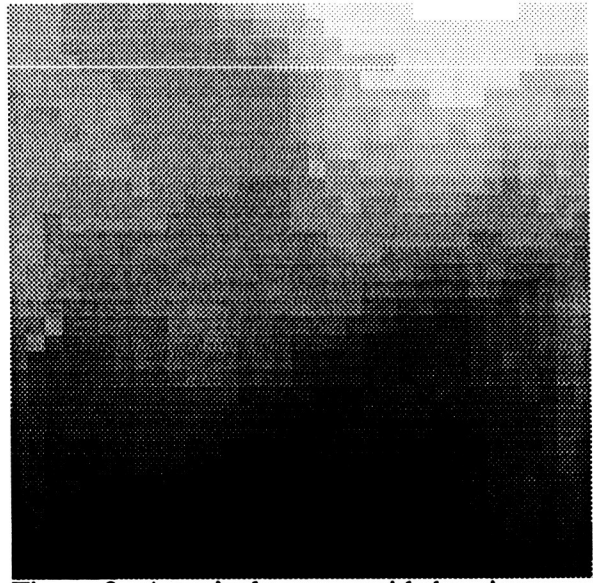


Figure 2. A typical survey grid showing surface height (dark = low). The grid measures 32 x 32 m, with data points 1 m apart. Total height variation is 8.28 m.

data, but the processing steps differed for profilometer and survey data. Profilometer data suffered from errors which prevented use of standard spectral estimation techniques. These errors were of two types: (1) incorrect height impulses due to overheating of the EDM, and (2) intermittent level shifts due to instability in the EDM. Removal of errors due to overheating involved a combination of median and quartile difference filtering, and is fully described in [4].

Level shifts of 2-7 mm often occurred after 20-30 minute periods of normal EDM operation. This caused subtle horizontal bands in the profilometer scans. Although these level shifts were small compared to variations in topography, they might corrupt spectral estimates enough to make their elimination worthwhile. We developed a procedure of spectral estimation by linear sampling in which we assume that the surface statistics are isotropic. Linear profiles (rows of the profilometer scan) then become samples of the surface. By using individual scan rows (and removing the mean surface height or dc level from each), we avoid the level shifts because the reference level is stable within most rows. Rows in which level shifts occur are discarded. Furthermore, averaging the autocorrelation estimates obtained in different rows reduces the effect of any remaining impulse errors as well as the variance inherent to a surface random process. The assumption that the surface statistics of the debris flows are isotropic is justified by observation. The debris flows showed no directional structure.

The algorithm for obtaining a spectral estimate from linear profiles is developed rigorously in [4]. We show that if the the surface height $Z(x,y)$ is a wide-sense stationary random process that is ergodic in correlation, and if the x direction is along the row of the profilometer scan, then the autocorrelation function $R_Z(r)$ ($r^2 = \delta_x^2 + \delta_y^2$) for an isotropic surface is

$$R_Z(r) = R_Z(\delta_x, 0) = \lim_{T_y \rightarrow \infty} \left[\frac{1}{2T_y} \int_{-T_y}^{T_y} dy \lim_{T_x \rightarrow \infty} \left\{ \frac{1}{2T_x} \int_{-T_x}^{T_x} dx Z(x + \delta_x, y) Z^*(x, y) \right\} \right] \quad (1)$$

We use a lag window in our spectral estimate to reduce side lobes and to assure a positive spectral estimator. The window, $W(r)$, which is analogous to the Parzen window used in 1D spectral estimation, is:

$$W(r) = \left(\frac{2}{\pi}\right) \frac{1}{2a^2} \Pi\left(\frac{r}{2a}\right)^{**2} \quad (2)$$

where $a = (N_x - 1)\Delta$, N_x is the number of samples in direction x , Δ is the sample interval, Π is the 2D rect function which is centro-symmetric, and $**2$ indicates that the function is convolved with itself in two dimensions. The spectral estimation then becomes:

$$\hat{S}_Z(k) = 2\pi \int_0^{(N_x-1)\Delta} dr r R_Z(r) W(r) J_0(kr) \quad (3)$$

where J_0 is the zero-order Bessel function. $S_Z(k)$ is therefore the Hankel transform of $R_Z(r)$. A typical plot of $S_Z(k)$ is shown in Figure 3.

SURVEY SPECTRA. Spectral estimates from the survey data were more straightforward in that a standard spectral estimator, the periodogram, was used in the estimation of the survey spectra. A typical periodogram estimator resulting from the survey data is shown in Figure 4.

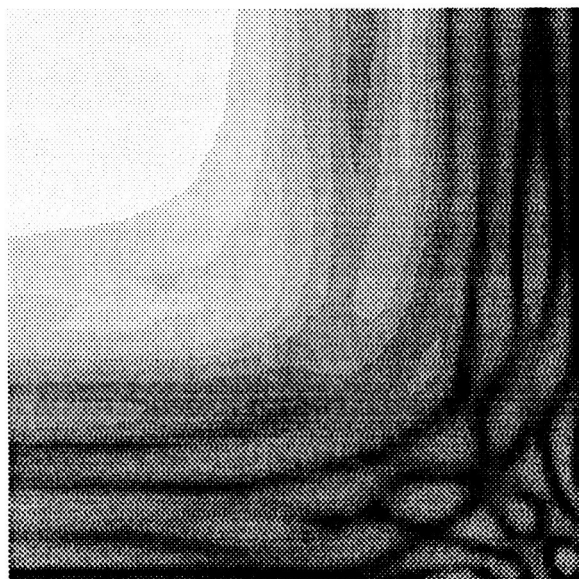
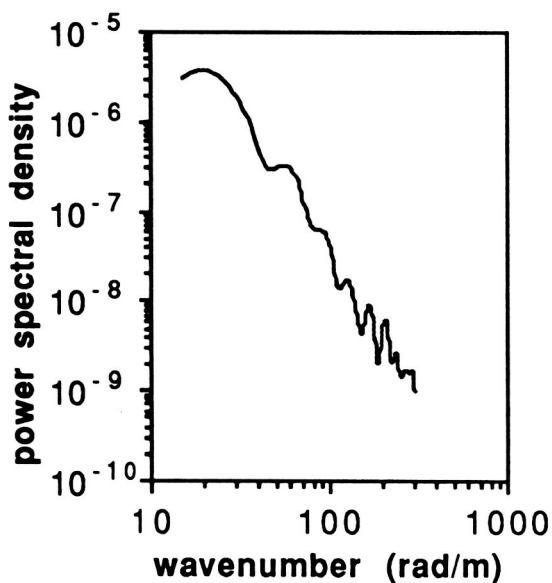


Figure 3: Surface spectral estimator $S_Z(k)$ for a typical profilometer scan.

Figure 4: Periodogram spectral estimator for a typical surface survey.

ACKNOWLEDGEMENTS: This work is supported under NASA Grant NAGW-2199 and NASA Johnson Space Center Contract NCC-9-19 for work under a SIR-C project.

REFERENCES: [1] A. W. England, *Geological Survey of Canada Paper 90-4*, 1990. [2] J. Huang and D. L. Turcotte, *Journal of Geophysical Research*, vol. 94, pp. 7491, 1989. [3] H. Glicken, *U. S. Geological Survey Professional Paper 1488*, 304 pp., 1989. [4] R. T. Austin and A. W. England, *Proceedings of IGARSS'91*, Espoo, Finland, June 3-6, 1991.

REMOTE SENSING OBSERVATIONS OF KELSO DUNES, CALIFORNIA

Greeley, R., Lancaster, N., Gaddis, L., Paisley, E.C.I., Department of Geology, Arizona State University, Tempe, AZ 85287-1404

The extensive field studies necessary to understand the development of desert sand seas are hampered by their large size and inaccessibility. Remote sensing data used in conjunction with detailed field studies and textural and mineralogical analyses of surface sediments at specific ground-control points can provide a wealth of information on dune types and activity, regional aeolian dynamics, sediment sources and thickness, and depositional history for sand seas. Herein we compare the information available from Landsat TM (VNIR), AIRSAR (microwave), and AVIRIS (high spectral resolution VNIR) using Kelso Dunes as a test case.

Landsat TM data can be used to map areas of different dune morphology and activity. A ranking of dune areas based on their brightness on TM images compares well with their activity assessed in field studies. Active dune areas are bright because they are composed of well sorted unimodal sand, whereas inactive dunes are darker as a result of admixtures of dark fine-grained particles. Areas of olivine and amphibole rich sand can also be distinguished, pointing to varying source areas for Kelso dune sand.

High resolution (~10 m) multiple wavelength (C-band: 5.6 cm, L-band: 24 cm, and P-band: 68 cm) and polarization aircraft radar data (AIRSAR) show that shorter wavelengths are best for discriminating geologic units in dune areas. P-band data provide a good representation of dune topography. C-band data are optimal for distinguishing areas of active and inactive dunes via subtle variations in surface roughness of the dune surfaces due to the growth of vegetation on the dunes.

AVIRIS provides VNIR data with a high spectral (210 10 nm spectral bands) and ground resolution that permits subtle variations in the composition and morphology of dune areas to be detected. These include areas of sands with a high magnetic content, and stabilized dunes with a high silt and clay content.

POSSIBLE MARTIAN BRINES: RADAR OBSERVATIONS AND MODELS

A.P. Zent, F.P. Fanale (Planetary Geosciences Div., School of Ocean & Earth Sciences & Technology, Univ. of Hawaii, Honolulu, HI), and L.E. Roth (Jet Propulsion Lab., Calif. Instit. Technology, Pasadena, CA)

The 1971 and 1973 Goldstone 12.6-cm radar observations of Mars are separate data sets which include reflectivity as a function of latitude, longitude, and season. It has been argued that secular reflectivity variations of Mars' surface are indicated by the data and that shallow subsurface melting is the causal mechanism most compatible with the observations; however, the melting hypothesis conflicts with accepted notions of the state and distribution of water on Mars. We have examined the data to identify temporal and spatial domains within which statistically significant changes in measured reflectivity are clustered. A few reflectivity changes may be genuine; others may be due to ephemeris errors or binning during data reduction. Brines which might satisfy the best supported reflectivity variations are out of equilibrium with the chemical megaenvironment. It is unclear whether such a brine, if emplaced in the martian regolith at a depth shallow enough to affect the radar reflectivity, could survive even a single freeze-thaw cycle. We suggest that some combination of unique scattering properties or some as yet unidentified process other than melting is responsible for any genuine reflectivity variations.

PRELIMINARY COMPARISON OF 3.5-CM AND 12.6-CM WAVELENGTH CONTINUOUS WAVE OBSERVATIONS OF MARS; H.J. Moore, U.S. Geological Survey, Menlo Park, CA, 94025 and T.C. O'Brien, R.F. Jurgens, M.A. Slade, T.W. Thompson, Calif. Inst. Tech., Jet Propulsion Laboratory, Pasadena, CA, 91109.

Radar observations of Mars at Goldstone in 1990 were conducted by transmitting pure sinusoidal signals at 3.5-cm wavelengths and receiving the Doppler-spread echoes from Mars at Earth. Radar transmissions were circularly polarized and the echoes recorded in two senses: depolarized (SC, same sense) and polarized (OC, opposite sense). Latitudes of the subradar points are between 3.5° and 11.1° S; longitude coverage is discontinuous (Fig. 1). A similar set of observations were conducted in 1986 at 12.6-cm wavelengths between latitudes 3.1° and 13.9° S [1,2].

Here, we compare and discuss the observed depolarized and polarized echo total cross-sections and their ratios for the two wavelengths. Depolarized echo total cross-sections at 3.5-cm wavelength are typically near or less than those at 12.6-cm except near 300° W where they are larger (Fig. 1A). Factors contributing to the variations and differences in cross-sections are unclear at this time. By analogy with the Moon, stronger echoes would be expected at the shorter wavelength, but this is not always the case for Mars. The relatively weaker 3.5-cm and stronger 12.6-cm echoes from 135° to 181° may be partly related to burial of diffuse scatterers by dust (particularly in the Tharsis-Elysium regions) and attenuation of the radar waves with depth; this attenuation is about 3 to 4 times greater at 3.5-cm than at 12.6-cm wavelength. On the other hand, concentrations of wavelength-size diffuse scatterers could be less for the shorter wavelength and greater for the longer one as is suggested by the rock frequency distribution at the Lander 2 site [3]. The strong echoes near 300° W are puzzling and may be related to observational uncertainties rather than Mars; large observational scatter is implied by the results between 135° and 181° W.

Polarized echo total cross-sections at 3.5-cm wavelength, like those at 12.6-cm, show large variations with longitude (Fig. 1B). The two sets of observations are more or less comparable between 25° and 80° W. Elsewhere, there are differences. Weak 3.5-cm echoes (near 0.055) near 135° - 181° W and 4.7° S suggest very weak quasi-specular echoes (near 0.035) as one might expect for the dust covered region of Tharsis [4]; the large range of cross-sections at 11° S may be partly due to observational scatter, but the surface sampled is variable and includes different terrains than those near 4.7° S. The weak echoes near 210° - 235° W are puzzling because they do not correlate with thermal inertias [5] or the 12.6-cm results. Similarly, the extremely strong echoes (>0.12) between 280° and 320° W are much stronger than the 12.6-cm echoes, a result that is difficult to explain.

MARS RADAR OBSERVATIONS: H.J. Moore et al.

Ratios of the 3.5-cm depolarized and polarized echoes (Fig. 1C) are similar to those at 12.6-cm except near 200°-232° W where they are much larger; these larger values are due to the weak depolarized echoes.

Analyses and modelling of 3.5-cm wavelength total cross-sections and echo spectra are in progress.

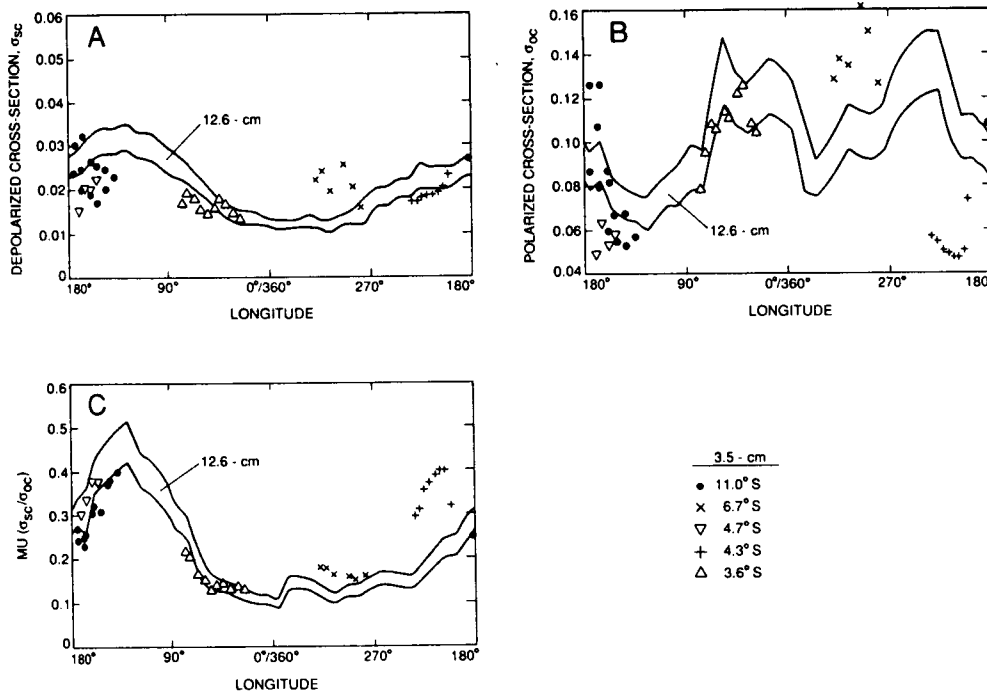


Figure 1. Comparison of Goldstone radar observations at 3.5-cm and 12.6-cm wavelengths as a function of longitude at latitudes between 3° and 14° S. A. Depolarized echo total cross-sections. B. Polarized echo total cross-sections. C. Ratio of depolarized and polarized echo total cross-sections.

REFERENCES

- [1] Thompson, T.W., 1988, LPI Tech. Report 88-05, p. 125-126.
 [2] Thompson, T.W. and Moore, H.J., 1989, Proc. 19th Lunar and Planet. Sci. Conf., p. 409-422. Moore, H.J. and Thompson, T.W., 1991, Proc. 21st Lunar and Planet. Sci. Conf., in press. [4]
 Moore, H.J. and Jakosky, B.M., 1989, Icarus, v. 81, p. 164-184. [5] Palluconi, F.D. and Kieffer, H.H., 1981, Icarus, v. 45, p. 415-426.

**SURFACE PROPERTIES OF GALILEAN SATELLITES
FROM BISTATIC RADAR EXPERIMENTS**

R.A. Simpson and G.L. Tyler

Center for Radar Astronomy, Stanford University, Stanford, CA

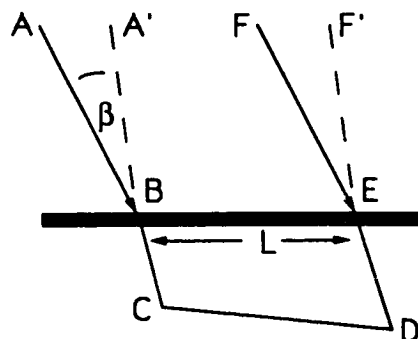
The icy moons of Jupiter were the first to show unusual radar backscatter behavior in earth-based experiments. Arecibo studies of Europa, Ganymede, and Callisto revealed strong echoes and a "reversed" sense of circular polarization (Campbell, *et al.*, 1978). In addition, no quasi-specular component has been detected to date, although that mechanism cannot be ruled out. Explanations have varied; dense hemispherical ice craters (Ostro and Pettengill, 1978), "crazed and fissured (surfaces) covered by jagged ice boulders" (Goldstein and Green, 1980), refractive scattering (Hagfors, *et al.*, 1985), mode decoupling (Eshleman, 1986a; Eshleman, 1986b; Eshleman, 1987), and bidirectional coherence (Hapke, 1990) have been proposed. No explanation has been entirely satisfactory because of the difficult constraints imposed by the existing data.

The (scalar) bidirectional coherence model (Hapke, 1990) predicts an opposition effect, or enhancement in the backscatter direction, resulting from coherent addition of backscatter from identical (but oppositely directed) ray paths (Fig. 1). The mode decoupling model yields a similar, vector result in which the observed polarization properties of the backscattered wave can also be obtained (Eshleman, 1986a; Eshleman, 1986b; Eshleman, 1987). The half-width of the enhanced backscatter lobe which results from either model, $\theta_B = \lambda/2\pi L$, may be related to a "photon diffusion length" L in the medium which can be measured by performing bistatic experiments (Hapke, 1990).

We have considered the possibilities for conducting such experiments using the Galileo spacecraft, now en route to Jupiter. Both conventional oblique-forward bistatic experiments (to determine basic electrical and physical properties of the surface material on centimeter-meter scales) and near-backscatter experiments (to sample the enhanced backscatter lobe) have been considered.

The forward scatter conditions in a conventional downlink bistatic experiment with Galileo are illustrated in Fig. 2. In this example the spacecraft approaches the earth-facing hemisphere of Europa at approximately 6.2 km/sec and passes within 152 km of the surface before continuing on (proposed Galileo tour 83-01, Europa encounter #4). The angle of incidence changes by one degree every six seconds 1-2 minutes before closest approach ($\phi=77.91^\circ$ at $t=0$; Fig. 2a). At $\lambda=3.6$ cm (X-band) intrinsic Doppler spread-

 Fig. 1: The bidirectional coherent backscatter model predicts enhancement because waves traveling along path ABCDEF and along FEDCBA add coherently at the receiver. For such enhancement in a bistatic configuration, angle β must be small enough that paths A'B'CDEF and F'EDCBA differ by no more than a small fraction of the wavelength λ . Measuring the angle β at which the enhancement has been reduced by 50% gives the photon diffusion length L in the material.



ing for the assumed rms surface slope ($\xi=5.7^\circ$) exceeds 36 kHz during the encounter, but the narrow spacecraft antenna beamwidth limits the observed spread to about 2700 Hz. The strength of the echo signal, as well as its width, is also reduced because of the narrow antenna beam. The detectability¹ is plotted in Fig. 2d for both wavelengths² available to Galileo and for both circular polarizations received on the ground, assuming right-circularly polarized (RCP) waves are transmitted (an elliptically polarized wave is actually transmitted at S-band). The detectability at the two wavelengths is similar until about 1700 seconds after closest approach, when the beam-limiting ceases to be a factor at S-band (beam limiting continues at X-band until about 7000 sec)³. Detection of the Brewster angle ($\phi_B=51.7^\circ$ for assumed dielectric constant $\epsilon=1.6$) would independently confirm estimates of surface dielectric constant derived from overall echo strength. Passage through the Brewster angle occurs, however, during one of the times when the signal is most dynamic ($t = -170$ sec).

In a near-backscatter geometry Galileo can be used to probe the anomalous backscatter lobe -- mapping its strength as a function of the bistatic angle β within a few degrees of zero. Various combinations of frequencies and receiving sites give detectabilities $0.1 < D < 0.8$ for these echoes when we assume that the spacecraft antenna (half-power half-beamwidth θ_T) underilluminates the satellite disk (radius R_p at distance d from the spacecraft), that the radar cross section for the illuminated area is $\sigma \approx \pi(d\theta_T)^2 \eta(\beta)$, and that $\eta \approx 1$ for $\beta=0$. The underillumination condition is satisfied when the spacecraft to target distance is $d \leq R_p/\theta_T$. In the Europa encounter used here, Galileo X-band sampling of the backscatter lobe is thus possible for $d \leq 3 \cdot 10^8$ m, and more than 12 hours are available prior to closest approach during which $\eta(\beta)$ can be investigated. Averaging many measurements would increase the "effective" detectability above the $0.1 < D < 0.8$ level for one second observations.

-
- Campbell, D. B., J. F. Chandler, S. J. Ostro, G. H. Pettengill and I. I. Shapiro (1978). Galilean satellites: 1976 radar results. *Icarus* **34**, 254-267.
- Eshleman, V. R. (1986a). Mode decoupling during retrorefraction as an explanation for bizarre radar echoes from icy moons. *Nature* **319**, 755-757.
- Eshleman, V. R. (1986b). Radar glory from buried craters on icy moons. *Science* **234**, 587-590.
- Eshleman, V. R. (1987). The radar-glory theory for icy moons with implications for radar mapping. *Adv. Space Sci.* **7**, 133-136.
- Goldstein, R. M. and R. R. Green (1980). Ganymede: radar surface characteristics. *Science* **207**, 179-180.
- Hagfors, T., T. Gold and M. Ierik (1985). Refraction scattering origin of the anomalous radar returns of Jupiter's satellites. *Nature* **315**, 637-640.
- Hapke, B. (1990). Coherent backscattering and the radar characteristics of the outer planet satellites. *Icarus* **88**, 407-417.
- Ostro, S. J. and G. H. Pettengill (1978). Icy craters on the Galilean satellites? *Icarus* **34**, 268-279.

¹ Detectability D is defined as the ratio of received echo power at a 70-m antenna of NASA's Deep Space Network to the receiver noise power in the bandwidth occupied by the echo signal multiplied by the square root of the bandwidth (one second measurements).

² The second wavelength is 13.1 cm (S-band)

³ For comparison, Viking bistatic echoes from Mars were highly useful at the $D \sim 20$ dB level.

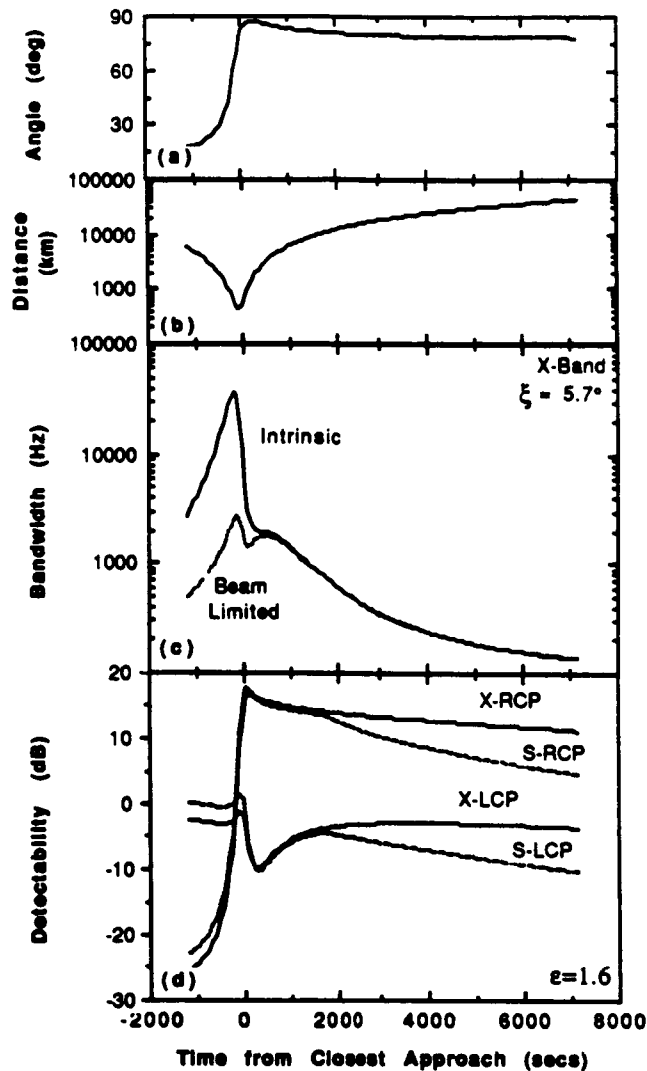


Fig. 2: Galileo bistatic geometry and performance for a hypothetical close Europa encounter (Europa encounter #4 of proposed tour 83-01). At closest approach the spacecraft is 152 km above Europa's surface, moving at 6.2 km/sec. The incidence angle (a) at closest approach is 77.91° and is increasing at $0.12^\circ/\text{sec}$. Slant range to the specular point is shown in panel (b). Doppler spreading of the intrinsic echo signal (without regard to the spacecraft antenna pattern) reaches 36 kHz (c), but the antenna beam reduces the observed echo width to about 2700 Hz. The detectability of the echo signal D is maximum shortly after closest approach (d), but less dynamic observing conditions an hour or more later may facilitate observations.

Radar echoes from the icy Galilean satellites—Europa, Ganymede, and Callisto—are unique in character, and they may be explained by a phenomenon that has been called the radar glory effect.^{1,2,3,4} We have analyzed the radar glory backscattering from buried craters as a possible model for this effect. These craters have a smaller refractive index below the crater than above as shown in Fig. 1(A). The possibility exists that the rays shown will be totally internally reflected at the crater walls, and we assume this to be true in the following. The rays which contribute to the backscattering will come from a circular annulus, when viewed before the refraction occurs at the ice-vacuum surface, in a plane orthogonal to the rays reflected from the crater (see Fig. 1(B)). For craters near the limb of the satellite some of the rays may be blocked by the crater rim, and this circular annulus will break up into two circular arcs. We assume that these glory arcs are broken up into glints of dimension H , assumed larger than the wavelength, and that the fields from a pair of glints connected by the ray shown add coherently while the fields from the various glint pairs add incoherently. The coherent addition of the fields from glint pairs arises because for the ray shown in Fig. 1(A), there is another ray that travels the exact same path, but in the opposite direction.

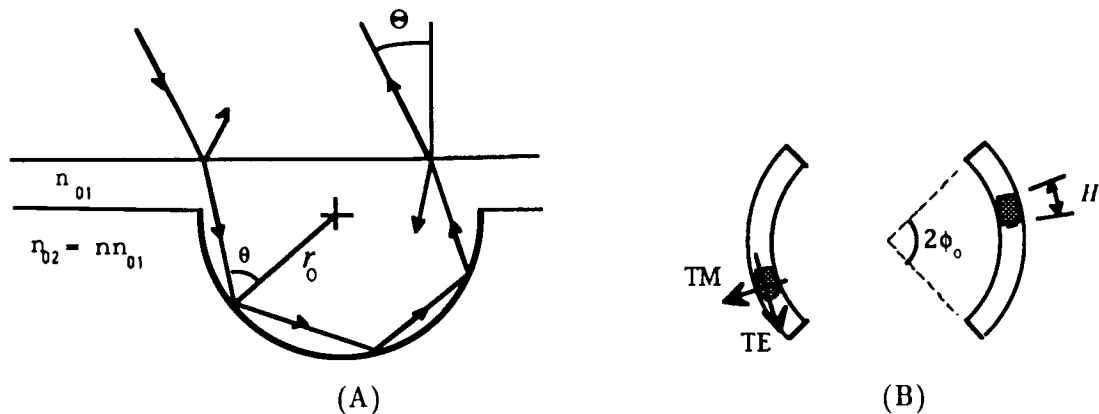


Figure 1. (A) Geometry of a buried crater and a three-bounce ($N=3$) ray. The angle Θ is between the surface normal of the satellite and the radar line of sight. For an ice-overburden, $n_{01} = 1.8$. In the model $n_{02} < n_{01}$ (i.e., $n < 1$). (B) Glory arcs of angular extent $2\phi_0$ and a pair of glints of dimension H . TE and TM electric field vectors are also shown.

Consider a crater located near the surface of the satellite at coordinates (R, Θ, Φ) , where R is the satellite radius, Θ is longitude with $\Theta = 0$ in the direction of Earth, and Φ is latitude with $\Phi = \pi/2$ in the plane defined by the spin axis of the satellite and the $\Theta = 0$ direction. The radar cross-sections for fields received in the orthogonal and same linear (OL and SL respectively) polarizations and those for fields received in the orthogonal and same circular (OC and SC respectively) polarizations are

$$\sigma_{SL}(\Theta, \Phi) = CA_L(3 - X_L) \quad , \quad \sigma_{OL}(\Theta, \Phi) = CA_L(1 + X_L) \quad (1)$$

$$\sigma_{SC}(\Theta) = 2CA_C(1 + X_C) \quad , \quad \sigma_{OC}(\Theta) = 2CA_C(1 - X_C). \quad (2)$$

The constant C is proportional to the number of glint pairs in the glory arcs, and is given by $C = \pi r_0^2 FH/\lambda$ where F is the fraction of the glory arcs filled by glints, H is defined in Fig. 1(B), and λ is the radar wavelength. The A 's and X 's are given by

$$A_L = \frac{1}{2}\hat{\sigma}_0\{[(T_1^2 + T_2^2) + (T_1^2 - T_2^2)\cos 2(\Phi - \Phi_P)][\phi_0 - (1+x)\delta] + 2T_1T_2(1+x)\delta\} \quad (3)$$

$$A_L X_L = \hat{\sigma}_0\{ 2T_1T_2x\phi_0 + [(T_1^2 - T_2^2)\cos 2(\Phi - \Phi_P) - (T_1^2 + T_2^2)\cos 4(\Phi - \Phi_P)][\phi_0 - (1+x)\delta] + 2T_1T_2[3(1+x)\delta - x\phi_0]\cos 4(\Phi - \Phi_P)\} \quad (4)$$

$$A_C = \hat{\sigma}_0\{(T_1^2 + T_2^2)\phi_0 - (T_1 - T_2)^2(1+x)\delta\} \quad (5)$$

$$A_C X_C = 2\hat{\sigma}_0 T_1 T_2 x \phi_0 \quad (6)$$

where

$$\hat{\sigma}_0 = \frac{\sin 2\theta}{N} \frac{\cos^2 \Theta}{n_{01}^2 \cos^2 \Theta'}, \quad (7)$$

$n_{01} \sin \Theta' = \sin \Theta$, Φ_P is the direction of polarization for the linear polarization case, $T_1 = 4n_{01} \cos \Theta \cos \Theta' / (\cos \Theta + n_{01} \cos \Theta')^2$ is the product of the TE Fresnel transmission coefficient for the ray entering the ice and the TE Fresnel transmission coefficient the ray exiting the ice, $T_2 = 4n_{01} \cos \Theta \cos \Theta' / (n_{01} \cos \Theta + \cos \Theta')^2$ is the same product for the TM fields, $x = \cos[2N \tan^{-1}(\cos \theta (\sin^2 \theta - n^2)^{1/2} / \sin^2 \theta)]$ is the mode decoupling factor defined in reference 1, $\delta = \phi_0/4 - \sin(4\phi_0)/16$, and $\phi_0 = \pi/2$ if no shadowing occurs or $\sin \phi_0 = \cot \theta \cot \Theta'$ when this last definition has a real solution.

The power spectra are sums of the contributions from several craters along lines of constant Doppler shift which are lines, when projected onto the plane of the sky, orthogonal to the line of sight and parallel to the spin axis. That is, the cross-sections at a specified frequency are integrals of the cross-sections in equations (1) and (2) on semi-circles on the satellite surface where $\cos \Theta \cos \Phi = \text{constant}$. In Fig. 2 we compare the computed cross-section for circular polarization with echoes obtained from Eurpoa; this spectrum is typical of the spectra obtained.

The total cross-section of each satellite is an integration of the cross-sections in equations (1) and (2) over the entire illuminated surface. These total cross-sections can be written in a form similar to those in equations (1) and (2) except that the A 's and X 's are the same for linear and circular polarizations and are complicated integrals that must be computed numerically. In Table 1 we compare a summary of the main features of the data with the model predictions. The scaling constant C for these total cross-sections is given by $C = (M\pi r_0^2/4\pi R^2)(FH/\lambda)$ where M is the total number of craters on the surface.

ACKNOWLEDGEMENTS: This research was supported by NASA grants NGL-05-020-014 and NGT-70056 and NSF grant AST 87-21880.

REFERENCES: ¹Eshleman (1986), *Science* 234, 587. ²Eshleman (1986), *Nature* 319, 755. ³Eshleman (1987), *Advances in Space Research* 7.5, 133. ⁴Gurrola and Eshleman (1990), *Advances in Space Research* 10.1, 195. ⁵Ostro (1982), chapter 8 in *Satellites of Jupiter*, edited by D. Morrison, University of Arizona Press, Tucson.

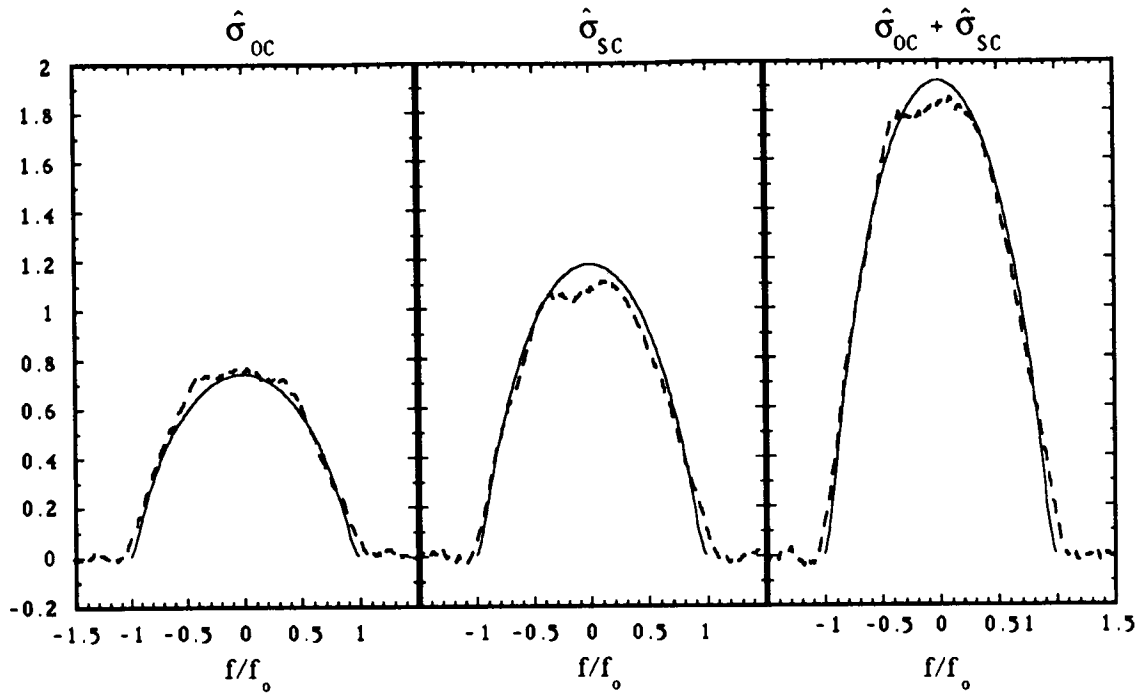


Figure 2. OC, SC, and OC+SC cross-sections obtained from Europa (dashed curves) on January 10, 1990 at the Arecibo Observatory at 12.6 cm- λ and from the model (solid curves) using $N = 3$, $n=0.7967$. The data and the model have been scaled to give a total cross-section of 2.6.

	Europa	Ganymede	Callisto	Buried craters $N = 3, n=0.7967, C = 1$
$\hat{\sigma}$	2.60	1.52	0.64	0.67
$\hat{\sigma}_{SC}/\hat{\sigma}_{OC}$	1.56	1.55	1.19	1.60
$\hat{\sigma}_{OL}/\hat{\sigma}_{SL}$	0.47	0.47	0.55	0.44
m	1.73	1.46	1.43	1.95

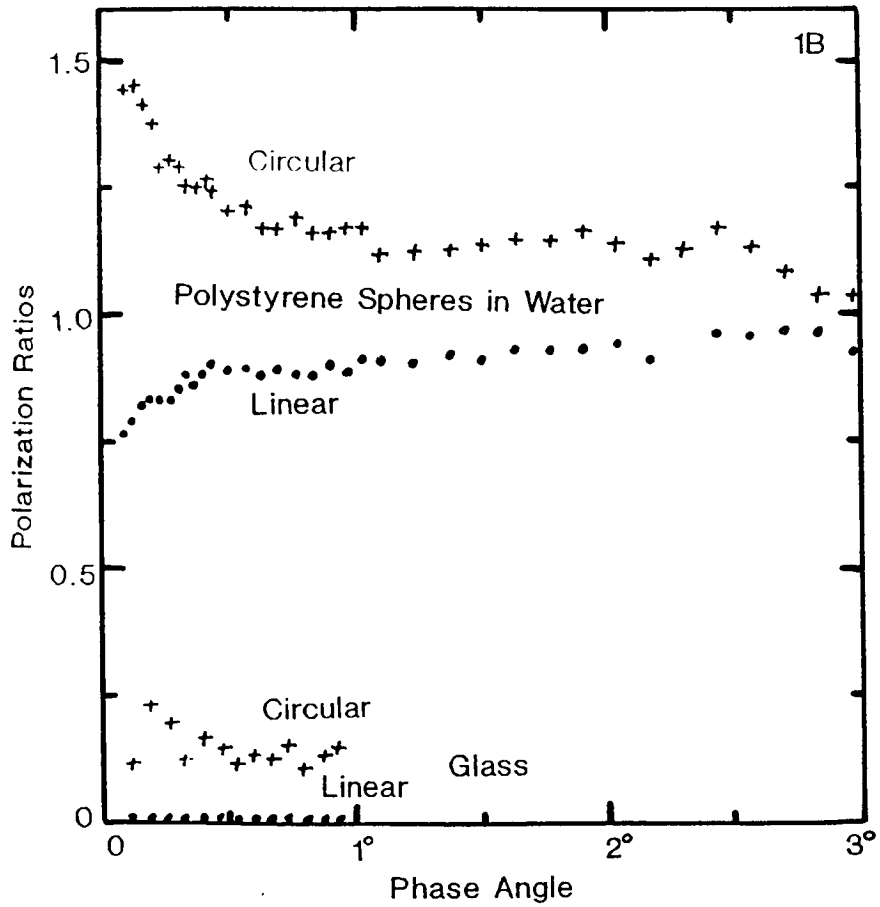
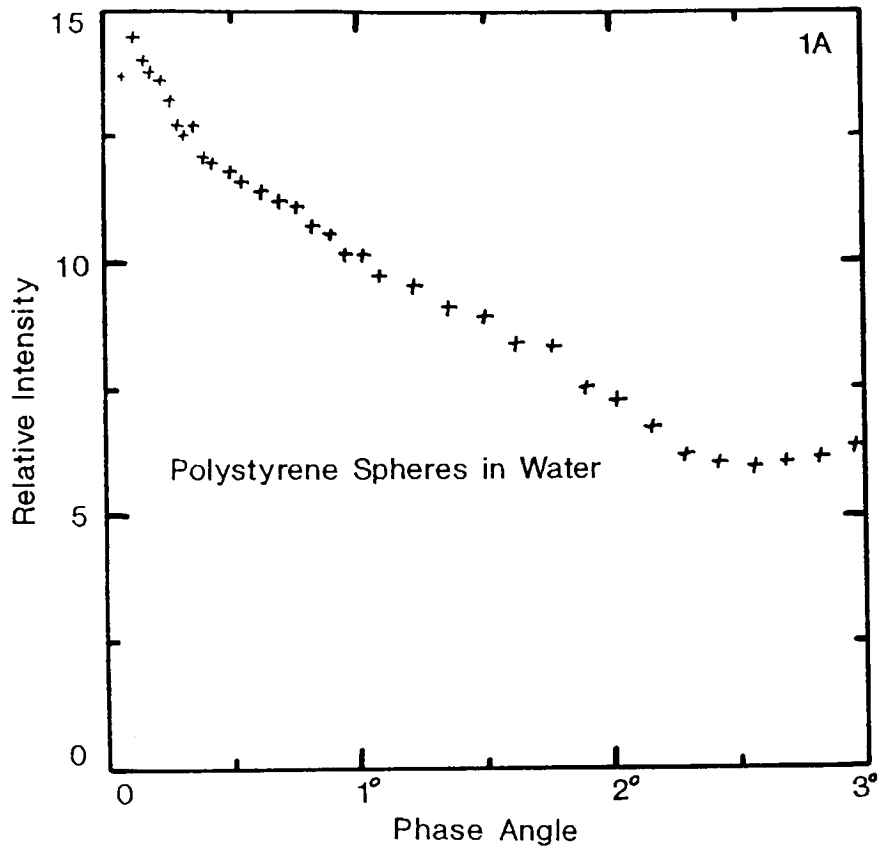
Table 1: The data for the Galilean satellites are for 12.6 cm- λ and are from Ostro⁵. $\hat{\sigma} = \hat{\sigma}_{SC} + \hat{\sigma}_{OC} = \hat{\sigma}_{SL} + \hat{\sigma}_{OL}$. These cross-sections are normalized by the geometrical area πR^2 , i.e., $\hat{\sigma} = \sigma/\pi R^2$. Here m is the exponent for a least squares fit of the power spectra to a $\cos^m \Theta$ law.

REGOLITHS OF ICY SATELLITES: THE COHERENT BACKSCATTER MODEL
B. Hapke and D. Blewett, Dept. of Geology and Planetary
Science, University of Pittsburgh, Pittsburgh, PA

The coherent backscatter model of radar scattering from icy satellites argues that most of the received power comes from radio waves that have been multiply scattered from numerous refractive index discontinuities randomly located under the surfaces of the regoliths. In a laboratory analog experiment we have measured the circular and linear polarizations in light scattered from a suspension of polystyrene spheres in water illuminated by laser

Figure 1A gives the relative intensity versus phase angle, and shows the coherent backscatter peak about 0.5° wide superimposed on a wider glory. Figure 1B shows the linear and circular polarization ratios. Outside the peak the ratios are close to one, as expected for waves whose orientations are randomized by multiple scattering. However, in the peak the linear polarization ratio drops to about 0.7 and the circular polarization ratio increases to 1.5.

These results confirm that coherent backscatter from particulate media reproduces the large intensity and unusual polarizations observed in the radar data. The model implies that the regoliths of icy satellites consist of matrices of small refractive index containing imbedded scatterers separated by distances of the order of a wavelength.



COHERENT BACKSCATTER AND THE RADAR CHARACTERISTICS OF OUTER PLANET SATELLITES

B. Hapke, Dept. of Geology and Planetary Science,
University of Pittsburgh, Pittsburgh, PA

The radar properties of Europa, Ganymede and Callisto are characterized by high reflectivities dominated by a diffuse component, and a large amount of polarization in the opposite sense of that expected if the waves were specularly reflected once. It is pointed out that these are the properties that might plausibly be expected when a collimated source illuminates a weakly absorbing, particulate medium in which wavelength-sized scatterers are separated by distances somewhat larger than the wavelength, such as a regolith consisting of voids and/or silicate rocks imbedded in an icy matrix. No specialized structures are required. Portions of the wave front that are multiply scattered within the medium and that traverse the same path in opposite directions combine coherently in the backscatter direction to produce an increased intensity. The enhancement is different for the two components of polarized reflected radiation, such that the incident sense of polarization tends to persevere more strongly than the opposite sense. This model explains the observed linear polarization ratio and may be able to account for the observed circular polarization ratio. The coherent effects are confined to a peak centered on the backscatter direction of angular half-width $\lambda/2\pi D$, where λ is the wavelength and D is the photon diffusion length in the medium. Bistatic radar observations would test this model and give information on the structures of the regoliths. The same phenomenon may play a role in radar scattering from Saturn's rings and also in the sharp opposition effects observed on outer planet satellites at optical frequencies.

DOPPLER-RADAR IMAGING OF SPHERICAL PLANETARY SURFACES

R. S. Hudson, Elec. and Computer Eng'g Dept., Washington State University

S. J. Ostro, Jet Propulsion Laboratory

A new approach to making radar reflectivity images of spherical planetary objects uses echo spectra acquired as a function of rotation phase and at an arbitrary number of subradar latitudes. The technique is tailored for depolarized or diffuse (nonspecular) polarized backscatter and works best when the limb-darkening is minimal.

In developing the doppler-imaging system, the target's reflectivity distribution is expanded in a truncated spherical harmonic series and the distribution of echo power in rotation phase and doppler frequency is obtained as a linear, analytic function of the series coefficients. To estimate the coefficients from an observed phase-doppler distribution, the inversion is cast as a least-squares problem and solved using singular value decomposition. The result is a linear imaging system whose capabilities and sensitivity to such factors as subradar latitude coverage and signal-to-noise ratio has been explored with simulations.

Doppler imaging can be applied to existing (or readily obtainable) radar data to map the diffuse component of echoes from Mars, Mercury, and Venus and to make north-south ambiguous maps of Europa, Ganymede, and Callisto. The technique can be applied to data obtainable with the upgraded Arecibo to make maps of Titan, Io, and the largest asteroids. Because of its relative simplicity in terms of data acquisition, reduction, and storage, doppler imaging may prove to be an attractive alternative to more complicated and computationally intensive techniques, especially for the weaker targets, including Ceres, Pallas, Vesta, and the spherical satellites of Jupiter and Saturn.

CHAPTER 6

IMPACT STUDIES

IMPACT CRATERS ON VENUS

G.G. Schaber, U.S. Geological Survey, Flagstaff, Arizona
86001

Compared with volcanism and tectonism, impact cratering on Venus has played an overall minor role in sculpting the present-day landscape. Venus is much less cratered than the Moon and Mars (Fig. 1) but has a crater density that is remarkably similar to that of the combined north American and European cratons¹. However, the study of Venus impact craters is vital to help place the chronology of the geologic features we see on the surface in the context of the planet's geologic evolution. In addition, the degradation of impact craters provides information on surface and interior processes, particularly alteration by tectonism and volcanism. Both the geographic distribution and the density of craters provide constraints on local, regional, and global resurfacing rates over the last few hundred million to 1 billion years².

Through orbit 1422, Magellan has mapped about 450 impact craters, with diameters ranging from 2 to 275 km, within an area of about 226 million square kilometers, or 49 percent of the planet's surface (Fig. 2). These craters and their associated deposits show surprisingly little evidence of degradation at the 75m/pixel resolution of the Magellan SAR. Remarkably few craters in the Magellan images appear to be in the process of being buried by volcanic deposits or destroyed by tectonic activity.

Based on the density of craters >25 km in diameter and the population of observed Venus-crossing asteroids³, the average surface age of Venus is estimated to be between 150 and 500 million years. One model for the resurfacing rate of Venus, based on the population and the pristine nature of the craters, suggests that Venus may have been completely resurfaced over a rather short period of time about 800 million years ago, and that it is now in a phase of considerably reduced volcanic and tectonic activity (about 15% that of Earth) that operates sporadically on a much smaller scale than formerly.^{2,4}.

The morphology of impact craters on Venus is strongly dependent on crater size, an effect attributed in part to aerodynamic breakup and dispersion of projectiles of different initial mass, density, and strength during their passage through the dense atmosphere. The distribution of morphologic types by size shows a sharp drop in number of complex craters and an increase in the number of irregular and multiple craters where the crater size exceeds about

13 km. Figure 1, however, shows that impact craters with diameters less than about 30 km have been greatly reduced in number from that expected from the slope of the size-frequency distribution of the larger craters (>30 km in diameter).

Complex craters on Venus, like those on other solid bodies in the Solar System, are characterized by terraced walls, well-developed hummocky and smooth facies of the continuous ejecta, circular rim, and flat floors commonly containing a central peak or peak ring. Irregular craters have noncircular rims, topographically complex floors, and commonly asymmetric ejecta blankets; they are interpreted to form from the nearly simultaneous impacts of multiple, tightly grouped fragments created by aerodynamic breakup of what was probably a single body prior to atmospheric entry. The Magellan images are showing that multiple craters, or "crater fields," are also abundant on Venus, as was expected. These are formed from the impacts of more widely dispersed fragments ^{2,5}. Simple (bowl-like) craters <15 km in diameter, typically observed on airless bodies like the Moon, are extremely rare on Venus, and they are in fact replaced there by irregular craters.

Lobate flow fields and radar-dark haloes commonly extend well beyond the outer ejecta of many Venusian craters. Some of the radar-dark haloes are horn shaped or parabolic and extend many hundreds of kilometers west beyond the craters. Many of these deposits often have abnormal radar reflectivity or emissivity value relative to their surroundings^{6,7}. Various hypotheses are being considered to explain these features, including that of upper atmospheric interaction with fine-grained crater ejecta. Many radar-dark haloes surrounded by radar-bright haloes are not associated with a recognizable crater but may reflect the atmosphere/surface interaction of meteoroid entry-shock fronts on the surface following the complete disintegration of the projectile.

ACKNOWLEDGMENTS: This research was supported by NASA under Contracts W-15,814 and WO-8777 to the U.S. Geological Survey.

REFERENCES: ¹Schaber et al., (1991). LPSC XXII, 1063-1064. ²Phillips et al. Science, in press. ³Shoemaker and Shoemaker. (1991). LPSC XXII, 1253-1254. ⁴Arvidson et al. (1990). Geophy. Res. Lettr. 17, 1385-1388. ⁵Melosh (1989). Oxford Univ. Press, 245 p. ⁶Tyler et al. Science, in press. ⁷Arvidson et al. Science, in press.

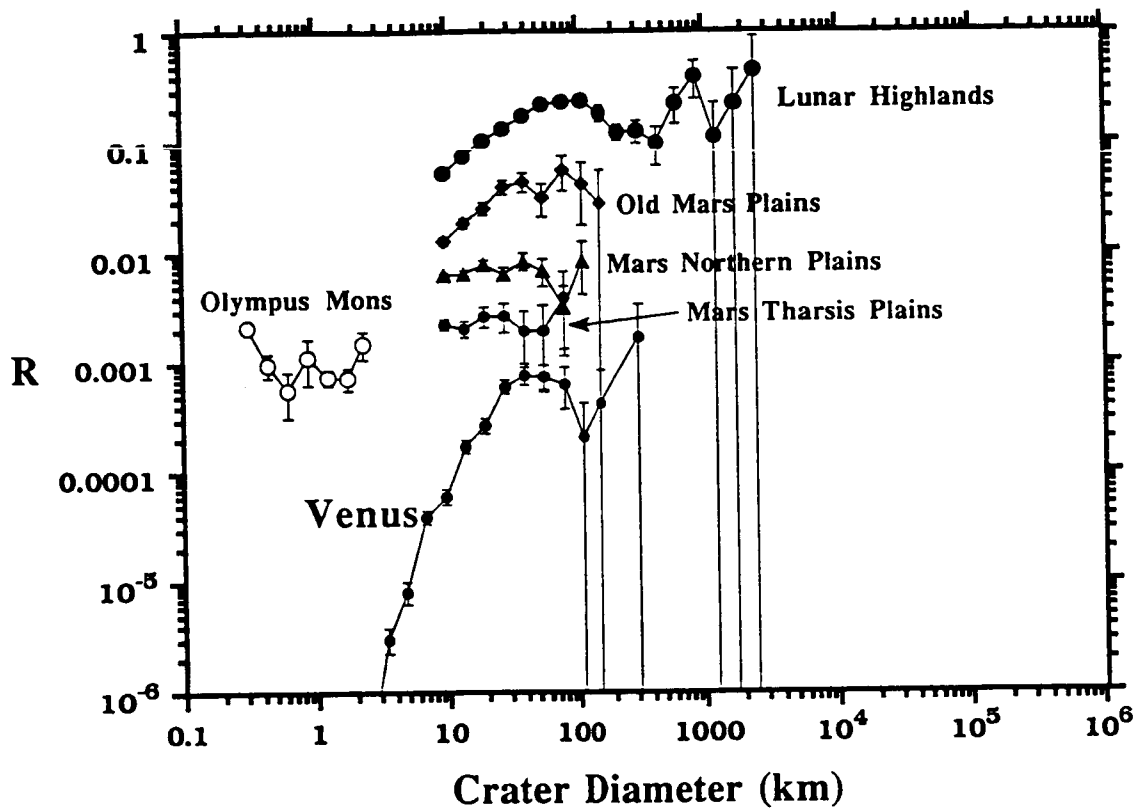


Figure 1- Relative R-plot) cumulative crater size frequency distribution curves for impact craters on Venus and selected lunar and Martian surfaces. Venus data inclusive through Magellan orbit 1422.

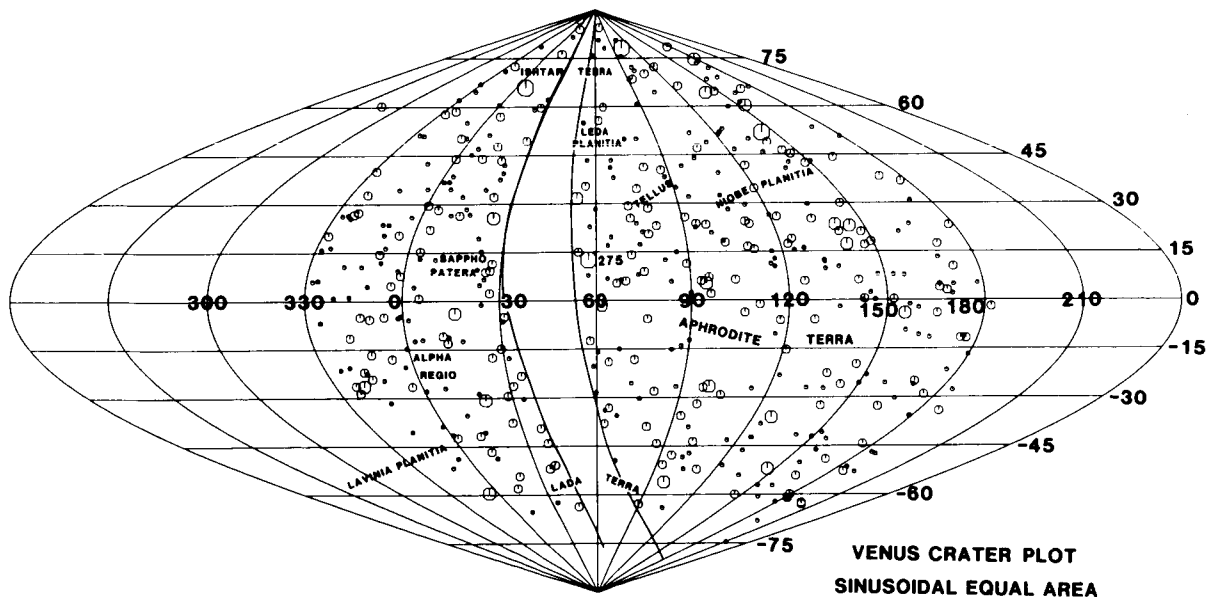


Figure 2- Sinusoidal Equal-Area map of Venus showing the distribution of 445 impact craters mapped by Magellan through orbit 1422. Range of crater diameters is shown by octagons: smallest octagons = crater diameters <15 km; 2nd smallest diameters = 15-50 km; 3rd smallest diameters 50-100 km; largest diameters >100 km.

N92-10853 4

QUANTITATIVE ANALYSIS OF TERRAIN UNITS MAPPED IN THE NORTHERN QUARTER OF VENUS FROM VENERA 15/16 DATA

G.G. Schaber, U.S. Geological Survey, Flagstaff, Arizona
86001

The contacts between 34 geologic/geomorphic terrain units in the northern quarter of Venus mapped by Schaber and Kozak^{1,2} from Venera 15/16 data were digitized and converted to a Sinusoidal Equal-Area projection. The result was then registered with a merged Pioneer Venus/Venera 15/16 altimetric database, root mean square (rms) slope values ($C\text{-power}^{-1/2}$), and radar reflectivity (ρ) values (uncorrected for diffuse scatter) derived from Pioneer Venus^{3,4}. The resulting information, described by Schaber⁵, includes comparisons among individual terrain units and terrain groups to which they are assigned in regard to percentage of map area covered, elevation, rms slopes, reflectivity, and density and latitudinal and longitudinal distribution of suspected craters >10 km in diameter. Table 1 gives 10 physical characteristics of 12 terrain groups; each terrain group consists of 1 or more of the 34 individual map units (see Schaber⁵ and Schaber and Kozak¹). The area included in this study of the northern quarter of Venus is $111.4 \times 10^6 \text{ km}^2$.

ACKNOWLEDGMENTS: This research is supported by NASA under Contract W-15,814 to the U.S. Geological Survey.

REFERENCES: ¹Schaber, G.G., and Kozak, R.C. (1990). U.S. Geol. Surv. Open-File Rept. 90-24, 1:15,000,000 scale, 2 sheets. ²Schaber, G.G., and Kozak, R.C. (1990). Repts. Planet. Geol./Geophys. Program-1989, NASA TM 4210, 6-7. ³Pettengill, G.H. and 5 others (1980). J. Geophys. Res., 85, 8261-8270. ⁴Pettengill, G.H., Gorf, P.G., and Chapman, B.D. (1988). J. Geophys. Res., 93, 14. ⁵Schaber, G.G. (1990). U.S. Geol. Surv. Open-File Rept. 90-468, 57 p.

Table 1 - PHYSICAL CHARACTERISTICS AND CRATER DATA FOR TERRAIN GROUPS
IN THE NORTHERN QUARTER OF VENUS MAPPED FROM VENERA 15/16 (AFTER SCHABER⁶)

Group	Symbol	% of map area	Area (10 ⁶ km ²)	Elevation (km)	SD in Elev. (km)	Mean rms slope (°)	SD in rms slope (°)	Mean refl.	SD in refl.	Number of impact crts.	Impact crts/10 ⁶ km ²
LP		52.58	58.57	6051.30	0.59	2.20	0.90	0.133	0.083	55	0.94
LFT		14.94	16.63	6051.36	0.82	2.14	1.15	0.144	0.089	26	1.56
T		9.64	10.72	6053.46	1.55	4.82	3.09	0.127	0.141	9	0.84
RT		9.05	10.07	6051.14	0.70	2.79	1.43	0.118	0.083	8	0.79
UP		4.79	5.33	6053.35	1.42	2.91	2.10	0.130	0.119	9	1.69
SPT		3.60	3.99	6052.50	1.26	2.22	0.95	0.135	0.080	3	0.75
DU		1.74	1.94	6052.49	1.12	3.05	1.80	0.114	0.079	2	1.94
CO		1.44	1.60	6051.88	0.62	3.33	2.32	0.134	0.106	0	0
LMB		1.17	1.30	6052.57	1.15	4.72	3.30	0.126	0.132	1	0.77
HMB		0.68	0.76	6056.57	2.28	7.45	4.19	0.275	0.227	3	3.96
HT		0.23	0.26	6052.74	0.82	3.35	1.58	0.127	0.078	0	0
CR>45 KM		0.18	0.20	6051.29	0.55	1.85	0.84	0.138	0.080	0	0

LP=LOWLAND PLAINS; LFT=LINEATED/FRACTURED PLAINS; T=TESSERA; RT=RIDGED TERRAIN
UP=UPLAND PLAINS; SPT=SHIELDS, PATERAE, THOLII; DU=DOMED UPLANDS; CO=CORONAE;
LMB=LOW MARGINAL BELTS; HMB=HIGH MARGINAL BELTS; HT=HILLY TERRAIN; CR>45 KM=IMPACT CRATERS >45 KM IN DIAMETER

VENUS IMPACT CRATERS: IMPLICATIONS FOR ATMOSPHERIC AND RESURFACING PROCESSES FROM MAGELLAN OBSERVATIONS

R.J. Phillips, Department of Geological Sciences, Southern Methodist University, Dallas, Texas 75275 and other members of the Magellan Science Team

Introduction. Observations of impact craters on Venus by Magellan yield important insights into (i) atmospheric effects on the formation of impact craters and their attendant ejecta deposits and (ii) the resurfacing history of the planet [1].

Atmospheric Processes. Most craters smaller than 15 km are classified as "irregular"; they possess irregularly shaped rims, and multiple hummocky floors. The irregular nature of these craters is interpreted to be the consequence of breakup and dispersion of incoming meteoroids by the dense atmosphere [2].

Two major ejecta facies of venusian impact craters are "hummocky ejecta" and "outer ejecta". The latter is akin to "continuous ejecta" seen on other planets, except that on Venus azimuthal sectors of ejecta are often missing, and this is attributed to the effects of oblique impact amplified by an atmospheric cushion. The distal edge of the outer ejecta of complex craters on Venus is sharp and lobate to slightly pointed, often with a petal-like appearance suggesting emplacement by flow. Schultz and Gault [3,4] have described a mechanism that may explain this observation. They showed that below a critical size, the ballistic paths of ejecta material are significantly modified by an atmosphere. In particular, small particles are decelerated and form an ejecta cloud that is deposited as turbulent ejecta and flows outward as a base surge from the crater rim.

A number of craters documented in the Magellan images possess often non-radial, "flow-like ejecta" indicative of a low viscosity material. Typically the flows extend up to two crater diameters from either beneath or within the crater's hummocky and outer ejecta deposits. The origin of the flow-like ejecta is problematical, and there is more than one form of this unit (e.g., uniformly radar bright, or bright just along the boundaries), and multiple origins are possible. Three hypotheses for the origin of flow-like ejecta are: (i) turbidity flows of very-fine-grained ejecta, (ii) flows consisting of a mixture of ejecta and magma released during the impact event, and (iii) flows of impact melt.

Approximately half of the impact craters observed with the Magellan radar are partially or wholly surrounded by areas with low radar backscatter cross sections, σ_0 ; we term these areas "dark margins". In most cases these regions are irregularly shaped and extend up to 3 or 4 crater diameters from the crater center; in a few cases the dark areas are much more extensive. The interface between this dark area and the surrounding brighter terrain occurs over a relatively short distance but, in general, it is not a sharp, well-defined boundary. The crater Stephania, for example, has dark margins that extend from about 25 km west of the crater to approximately 60 km to the east. The dark margins appear to be areas that are very smooth, with little wavelength-sized roughness to diffusely scatter the incident radar signal.

Hypotheses for the origin of dark margins include ablated meteoroid material, ejecta sorting, seismic shaking, and surface pulverization by the shock/pressure wave associated with the incoming meteoroid. Energy considerations show that the last mechanism is quite feasible [1].

Resurfacing Processes. Venera 15/16 imaging data showed that impact craters are not uniformly distributed on the surface of Venus [5,6,7], and this is evident in the Magellan data. Particularly apparent are regions that do not have any impact craters at all, for instance, the Sappho Patera region in central Eistla Regio. The hypothesis that the observed areal distribution of craters is random can readily be tested. The area around Sappho that is devoid of impact craters comprises approximately 5×10^6 km². We consider 135 (the total number of impact craters observed in the first 277 mapping orbits) Bernoulli trials for impact into the Sappho region. A "success" occurs when a crater is formed at Sappho and the probability of success for a spatially random process must be the ratio of the Sappho area to

the total area surveyed, or 1/14. The resulting probability distribution must be binomial, $b(x, 135, 1/14)$, with $\mu = 9.6$ and $\sigma = 3.0$. This meets the criterion, $\mu \geq 3\sigma$, that ensures the sampling area is large enough to have at least 1 crater [6]. In fact, the compliment of this outcome, the probability of observing *no* craters at Sappho under a random spatial distribution is 4.5×10^{-5} ($b(0, 135, 1/14)$). Thus it is highly unlikely that the "event" of no craters at Sappho can occur. However, this does not reject the hypothesis that the null occurrence of craters can belong to a random process because the Sappho area is part of a larger sampling population. If this experiment is repeated a sufficient number of times (i.e., other 5 million square kilometer areas are examined), the probability that at least one such area will be found with no craters will approach unity. The maximum number of experiments possible is 92, the surface area of the planet divided by 5×10^6 . The expected number of 5 million square kilometer areas with no craters is approximately $92 \times b(0, 135, 1/14) = .004$. Therefore, if Venus truly has a spatially random distribution of impact craters, the probability of finding a region the size of the Sappho area with no craters is essentially nil.

Those areas on Venus with few or no impact craters must have young surfaces undergoing rapid resurfacing on a geological time scale. At Sappho, volcanism is playing a major role; elsewhere, tectonic processes may also be important. A hypothesis that might explain the impact crater distribution on Venus is that cratering occurs randomly in space and time, whereas resurfacing has a spatial and temporal dependence [8]. In this case, craters are preserved in relatively pristine form in tectonically and volcanically quiescent regions. Areas of recent volcanism and tectonism have completely removed craters because resurfacing rates have been so high. This hypothesis appears to account for the seemingly contradictory observations that: (i) very few impact craters are observed to be in the process of removal by resurfacing, yet (ii) there are areas of the planet where no impact craters are observed, and thus *there must be* processes removing craters on a regional basis.

A simple, end-member model for this hypothesis is one of "regional resurfacing". This model is an end-member construction because it is binary: either craters are pristine, or they are completely removed; there are no craters in the process of removal. In a production model, for a surface of age τ , the cumulative size-frequency distribution, C_p , is given approximately by $C_p = R_p \tau D^{-\alpha}$, where R_p is the present cratering rate, D is crater diameter, and α is the power-law exponent that determines size distribution. For a regional resurfacing model, the information that can be gleaned from cumulative crater statistics is not surface age (production model) or retention age/resurfacing rate (equilibrium model), but instead the *areal resurfacing rate of the planet*. With the binary assumption, the cumulative size-frequency distribution, C_r , is given by $C_r = 0.5(R_p/f_r)D^{-\alpha}$, where f_r is the fraction of the planet resurfaced in one year. The reciprocal of f_r is T_r , the average time it takes to resurface the planet once. The portion of the cumulative size-frequency distribution curve unaffected by the atmosphere ($D \geq 25$ km) is well matched by $T_r = 0.8$ Ga. In this model there is no one unique age of the surface; surface ages span the range from 0 to 800 Ma, with Sappho, for example, representative of one of the youngest regions on the planet. We consider that this is the most realistic interpretation of the crater data, in terms of both the cumulative statistics and the appearance of individual craters.

References. [1] R.J. Phillips *et al.*, submitted to *Science* (1990); [2] G.G. Schaber *et al.*, this volume; [3] P.H. Schultz and D.E. Gault, *J. Geophys. Res.* **84**, 7669 (1979); [4] P.H. Schultz and D.E. Gault, in *Geological Implications of Impacts of Large Asteroids and Comets on the Earth*, GSA Special Paper 190, 153 (1982); [5] G.A. Burba, *Lunar and Planet. Sci.* **XX**, 123 (1989); [6] J.J. Plaut and R.E. Arvidson, *J. Geophys. Res.* **93**, 15339 (1988); [7] G.G. Schaber, *U.S. Geological Survey Open-File Report 90-468* (1990); [8] R.E. Arvidson *et al.*, *Geophys. Res. Lett.* **17**, 1385 (1990).

BREAKUP OF METEORIODS IN THE VENUSIAN ATMOSPHERE AND ITS EFFECTS ON CRATER FORMATION

R. R. Herrick and R. J. Phillips, Department of Geological Sciences, Southern Methodist University, Dallas, TX 75275

Introduction. Early results of the Magellan mission to Venus show that almost all of the observed impact craters appear to be unaffected by erosion, burial, and tectonic deformation (1). Therefore it is reasonable to assume that the observed paucity of small craters in the cumulative size-frequency distribution (SFD) relative to the simple power laws observed on airless planets is most likely due to atmospheric effects on the incoming meteoroids. Furthermore, many of the impact events appear to be formed by multiple fragments, indicating breakup of the initial meteoroid in transit through the atmosphere.

Simple models (2,3) have been used to predict a minimum crater diameter and certain features of the SFD using data from the Venera mission. However, these models did not include the effects of gravity on the meteoroid's trajectory and they did not model meteoroid breakup. Passey and Melosh (4) developed a model for travel and breakup of a meteoroid in an atmosphere, but their model was never used to estimate a SFD. Our study attempts to match the cumulative SFD and the number and size distribution of multiple-floored craters and crater fields using the Passey and Melosh model.

Procedure. Passey and Melosh give a set of five coupled first order differential equations that describe passage of a meteoroid through the atmosphere using a drag force equal to $C_d \rho_a A V^2$ where C_d is the drag coefficient, ρ_a is atmospheric density, A is cross-sectional area of the meteoroid, and V is meteoroid speed. Although ablation is included in the calculations, it has a negligible effect on the size of meteors considered here. Atmospheric density is assumed to be as in (2) and all other parameters are as in (4) unless otherwise specified. Breakup of the incoming meteoroid occurs when the pressure differential between its front and back becomes greater than the yield strength. A yield strength of 10 MPa was assumed. It was also assumed that the meteoroid breaks into four fragments 1/2, 1/4, 1/8, and 1/16 of the initial mass with the remaining mass (1/16) discarded.

To generate a SFD one must know the size, velocity, density and angular dependence of the incoming meteoroids and then have a way to convert this information into crater diameters. We assumed a size distribution proportional to $R^{-\alpha}$ (R is radius, α constant), a velocity distribution evenly spaced from 10 to 25 km/s, angular dependence proportional to $\sin \theta \cos \theta$ (θ is angle with respect to the planetary surface), and initially a meteoroid density of 3000 kg m^{-3} (corresponding to "stony" asteroids). We used a diameter scaling function based on crater gun work (5) with an adjustment factor of 2.6 to a) bring this function in line with those derived from pi-scaling (6) and explosion craters (7) and b) account for rebound and slumping of the transient crater. The initial meteoroid and its corresponding four fragments were integrated down to the surface, and a downrange distance and crater diameter were calculated for each. The final crater diameter was calculated as the greater of the following: a) the diameter D produced by an unbroken meteoroid or b) $0.5(D1 + D2) + dx$, where $D1$ and $D2$ are the diameters produced by the largest and smallest fragments that reach the surface, and dx is their separation. If dx is $>0.5D$, then the crater is assumed to be multiple floored or a crater field is formed. It was assumed that any objects that strike the surface below a critical velocity V_{cr} do not form craters.

The three parameters that were allowed to vary to match the observed SFD were C_d , V_{cr} , and α . The parameter α primarily controls the overall slope of the resulting SFD with larger

values giving steeper slopes. Increasing either C_d or V_{cr} has the general effect of increasing the minimum size crater formed.

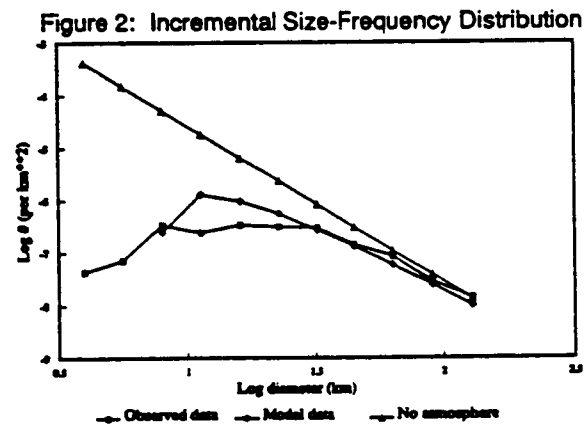
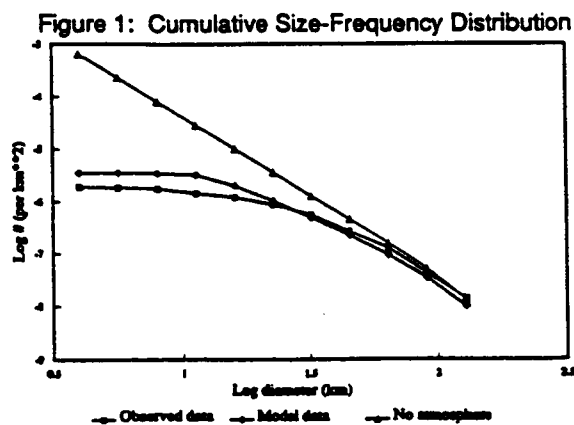
Results and Discussion. The best fit to the observed data was obtained using $C_d = 1.5$, $V_{cr} = 3$ km/s, and $\alpha = -2.5$. The cumulative and incremental ($\sqrt{2}$ binning) size-frequency distributions are shown in Figures 1 and 2 for the observed data, the modeled data, and the data modeled in the absence of an atmosphere. The model data fits the observed data reasonably well, with three main discrepancies:

1. The model could not reproduce the flatness of the incremental SFD for craters 10–30 km in diameter. This flatness produces the gentle roll-off in the observed cumulative SFD.
2. In order to match the roll-off in the cumulative SFD for large diameters, C_d and V_{cr} had to have large values; this produced no craters below ~ 6 km in diameter, as compared to the observed 3-km cutoff (1).
3. Large values of C_d and V_{cr} also prevented all but a few multiple-floored craters from forming in the model data.

The values required for C_d and V_{cr} are plausible, but seem rather high. This may indicate that either meteoroid breakup or cross-sectional area is being modeled incorrectly. At least some of the discrepancy between data and model can be alleviated by including a small percentage of iron meteoroids. Assuming that only the density is different for iron meteoroids (8000 kg m^{-3}), they will have a lower diameter cutoff and produce more multiple-floored craters. Combined with stony meteoroids, iron meteoroids will lead to a smoother roll-off in the cumulative SFD.

Future work. It is important to note that the unique shape of the size-frequency distribution, the lack of erosional effects on this distribution, the cutoff in crater diameter, and the distribution of multiple-floored craters make this problem well constrained. Further evaluation is required of the physical model and its input assumptions, and the effects of varying different parameters needs to be explored further.

References. (1) Phillips, R. J., *et al.*, 1991, *Science*, in press. (2) Ivanov, B. A., *et al.*, 1986, *JGR*, 91, D413–D430. (3) Ivanov, B. A., 1991, *EM & P*, 50, in press. (4) Passey, Q. R. and H. J. Melosh, 1980, *Icarus*, 42, 211–233. (5) Gault, D. E., 1974, *A primer in lunar geology*, NASA Ames, 137–175. (6) Holsapple, K. A. and R. M. Schmidt, 1982, *JGR*, 92, 1849–1870. (7) Nordyke, M. D., 1962, *JGR*, 67, 1965–1974.



ATMOSPHERIC EFFECTS ON OBLIQUE IMPACTS; P.H. Schultz, Brown University, Geological Sciences, Providence, RI 02912

Laboratory experiments and theoretical calculations often use vertical impact angles (90°) in order to avoid the complicating effects of asymmetry. Nevertheless, oblique impacts represent the most likely starting condition for planetary cratering (1, 2, 3). Gault and Wedekind (2) provided a classic study of the effect of impact angle on crater morphology and crater scaling. More recent studies (4, 5) have underscored the importance of impact angle on energy partitioning and the implications for projectile survival. When an atmosphere is introduced, the change in energy partitioning is dramatically revealed as kinetic energy carried away by the projectile is rapidly converted to thermal energy (3,4). Additionally, the presence of an atmosphere affects the cratering process at laboratory scales by adding atmospheric pressure to lithostatic pressure, by introducing viscous drag, and by introducing strong dynamic pressures associated with the projectile wake (6). For gravity-controlled growth, such effects are expressed by reduced cratering efficiencies, reduced crater aspect ratio (due to arrested crater growth), and increased turbulent power affecting the styles of ejecta emplacement (7). Changing both impact angle and atmospheric pressure not only allows testing previous results for vertical impacts but also reveals phenomena whose signatures would otherwise be masked in the planetary cratering record.

LABORATORY EXPERIMENTS: The laboratory studies were performed with the NASA-Ames Vertical Gun Range (AVGR), which is a national facility for investigating impact cratering processes. Impact angles at the AVGR can be increased from 0° to 90° in 15° increments while maintaining a flat target surface (see 2). The launch tube is isolated from the target chamber through the use of a thin mylar diaphragm which does not modify sufficiently large (≥ 0.1 cm) and strong (aluminum) projectiles. The large target chamber allows tracing the effects of both entry and ricochet without complex interactions created by the chamber walls. Different atmospheres (nitrogen, argon, and helium) characterized the effects of both gas density and mach number. Targets varied according to purpose: dry-ice (powder and blocks), carbonates, plasticene, and aluminum blocks were used to study early-time phenomena; compacted pumice, loose sand, low-density microspheres, and powdered dolomite emphasized aerodynamic effects on crater scaling and ejecta emplacement. Because of the complexities in atmosphere-impactor-ejecta interactions, no single combination allows direct simulation of a planetary-scale (10-100 km) event. Nevertheless, fundamental processes and observed phenomena allow formulating first-order models at such broad scales.

PHENOMENOLOGY: Five important early-time processes emerge as impact angles decrease and have implications for recognizing planetary signatures. First, the energy partitioned to the projectile at impact does not appear to be significantly changed: downrange ricochet fragments initially retain 50-80% of the original impactor kinetic energy. Nevertheless, these fragments directly and quickly couple with the atmosphere and result in rapid deceleration and intense heating downrange. Scouring of the downrange target surface and the paucity of smaller pits produced on downrange witness plates indicate that drag and turbulence effectively entrained the ricochet debris. Second, ionized vapor generated at impact (separate from the jetting process) is progressively changed with increasing atmospheric pressure (P) from an expanding hemispherical cloud moving downrange (low P) to a tight fireball pursuing ricocheted fragments (high P) at low angles (15°). Third, interactions between the impact-generated vapor cloud and the early-time impact cavity change significantly with impact angle. At high impact angles ($\geq 45^\circ$) the ionized cloud is contained and redirected uprange as a jet (3, 8). Consequently energy coupled with the surrounding atmosphere (and related blast effects) is significantly reduced soon after first contact between impactor and target. Fourth, early-time high-speed ejecta quickly establish the classic cone shape but this profile becomes increasingly asymmetric (high uprange, low downrange curtain angle) as impact angle decreases. This ejecta plume further confines the vapor cloud for higher angle impacts, thereby further decoupling the cloud from the atmosphere. Fifth, the heated atmosphere behind the projectile rapidly closes (within a projectile radius). Consequently, the projectile wake not only forms an ionized tube, but gases within this wake pursue the projectile at a comparable velocity. For higher angle impacts, the pursuing wake gases are partly confined within the ejecta

plume and are effectively decoupled from the surrounding atmosphere. For lower angle impacts, wake gases separated from the projectile pursue the ricochet debris. These five processes generally occur within the first 10% of the time required to form the crater in particulate targets. Their effects, however, are clearly expressed on the target surface beyond the continuous ejecta facies as atmospheric pressures increase.

Evolution of both the ejecta curtain and late-stage crater excavation cavity is modified by dynamic pressures within the atmosphere. At high impact angles, the ejecta curtain angle increases as aerodynamic drag effects increase (increased atmospheric density, decreased particle size or density). For oblique impacts, a similar change in ejecta curtain angle is observed. One consequence is considerable asymmetry in the ejecta patterns at unexpectedly high impact angles (60°). Although early-time asymmetries in the ejecta curtain are lost at late times under vacuum conditions, considerable azimuthal asymmetry remains in ejecta thickness. Under atmospheric conditions, this asymmetry is enhanced. Impact angles as high as 60° resulted in butterfly ejecta lobes for craters in compacted pumice and atmospheric pressures of nearly one bar. Under vacuum conditions, the butterfly pattern does not become evident until much lower angles (<10°). At high atmospheric pressures, ejecta emplacement is further modified by airflow drawn by the downrange-moving assemblage of ricocheted fragments, vapor, and wake gases.

Previous studies (2) documented that cratering efficiency (displaced target mass/projectile mass) decreases as $\sin \theta$ for particulate targets (including pumice) and $\sin^2 \theta$ for strength-dominated targets. This decrease can be understood if the vertical component of impact velocity principally controls scaling. For gravity-controlled cratering, this result can be simply expressed in terms of the dimensionless π_2 parameter as $gr/(v\sin\theta)^2$ as suggested in (9). Under vacuum conditions, cratering efficiency for pumice decreases as $\pi_2^{-\alpha}$ with $\alpha = 0.52$ (10); hence, cratering efficiency changes as $(v\sin\theta)^{1.04}$. Under atmospheric conditions cratering efficiency was significantly reduced; nevertheless, the power-law dependence on impact angle remained essentially constant with a value of 1.1 from 30° to 90°. This result indicates atmospheric pressure and drag modifies gravity-controlled crater growth even at oblique angles.

PLANETARY IMPLICATIONS: Under the dense atmospheres of Earth and Venus, impact-generated vapor and entrained projectile material from oblique impacts (<30°) should largely decouple from crater excavation, thereby affecting the surface downrange prior to ejecta emplacement. The character of this cloud in the laboratory evolved into a lobe of turbulent, ionized gas and the atmosphere constricted lateral expansion as aerodynamic drag reduced its downrange velocity. The lateral extent of this cloud scaled to the original impactor diameter will depend on $(\delta kv^2/\rho)^{1/3}$ where δ and v are the density and velocity of the projectile, respectively; with ρ representing the ambient atmospheric density and k an efficiency factor for the fraction of the impactor energy coupled to the atmosphere. The efficiency factor depends to a large degree on impact angle (given impact velocity) not only due to the role of projectile ricochet and target heating but also due to interference created by the early-time transient cavity. For a value of $k = 0.1$ and lateral growth reduced to 700 m/s, the lateral expansion on Mars would exceed 100 projectile diameters, whereas on Earth and Venus this value would reduce to about 30 and 10, respectively. Numerical models reveal that a 1 km complex of vapor/melt/debris exiting at 15° with an initial velocity one half the impactor velocity would escape the atmospheres of Mars and Earth but would be rapidly decelerated (within 300 km) on Venus. Hence, signatures of early-time phenomena associated with jetting and vaporization should be a widespread scour zone on Mars (11), a turbulent downrange fireline on Earth (4), and a turbidity flow emerging from below the later stage ejecta facies on Venus.

References: (1) Shoemaker, E. (1962). In Kopal (ed.) *Physics and Astronomy of the Moon*, Academic Press, pp. 283-351. (2) Gault, D.E. and Wedekind, J.A. (1978). *Proc. Lunar Planet. Sci. Conf. 9th*, 3843-3875. (3) Schultz, P.H. and Gault, D.E. (1982). In *Geol. Soc. Amer. Special Paper 190* (L.T. Silver and P.H. Schultz, Eds.), 153-174. (4) Schultz, P.H. and Gault, D.E. (1990). In V.L. Sharpton and P.D. Ward (Eds.) *Global Catastrophes in Earth History: An Interdisciplinary Conference on Impacts, Volcanism, and Mass Mortality*, Geological Society of America Special Paper 247 (in press). (5) Schultz, P.H. and Gault, D.E. (1990). *Lunar and Planet. Sci. XXI*, LPI, Houston, TX, 1099-1100. (6) Schultz, P.H. and Gault, D.E. (1991). "Atmospheric Effects on Cratering Efficiency," *J. Geophys. Res.* (in review). (7) Schultz, P.H. (1991). "Atmospheric Effects on the Shape of Impact Craters," *Icarus* (in review). (8) Schultz, P.H. and Gault, D.E. (1979). *J. Geophys. Res.* 84, 7669-7687. (9) Chapman, C.R. and McKinnon, W. (1988). In *Satellites*, U. Arizona Press, 492-580. (10) Schultz, P.H. and Gault, D.E. (1985). *J. Geophys. Res.* 90, 3701-3732. (11) Schultz, P.H. (1988). *Lunar and Planet. Sci. XIX*, LPI, Houston, TX, 1037-1038.

STYLES OF EJECTA EMPLACEMENT UNDER ATMOSPHERIC CONDITIONS; P.H. Schultz, Geological Sciences, Brown University, Providence, RI 02912.

Although small in scale, laboratory experiments provide essential first-order constraints on processes affecting ballistic ejecta and styles of ejecta emplacement under different atmospheric environments at planetary scales. The NASA-Ames Vertical Gun allows impacting different fine-grained particulate targets under varying atmospheric pressure and density (different gas conditions), thereby helping to isolate controlling variables. Previous reports described general phenomena associated with the dynamic interactions with implications for Mars (1, 2, 3), Earth (4), and Venus (1, 5). Further analysis now permits characterizing distinct modes of emplacement that reflect the degree of ejecta entrainment within a turbidity flow created by ejecta curtain movement through the atmosphere.

Laboratory experiments establish that target material is ballistically ejected in response to the mechanical transfer of energy/momentum from the impactor to the target regardless of an atmosphere. Nevertheless, the presence of an atmosphere can change the ejection angle as atmospheric pressures increase. Comparison of high frame rate imaging for impacts under different densities reveals that this ejection angle is at least partly controlled by the ratio of aerodynamic drag to gravitational forces. As this ejecta curtain advances, it creates a characteristic circulation within the atmosphere, and aerodynamically decelerated fine-grained ejecta (for a given atmospheric density and crater size) become entrained in this atmospheric response (1, 2, 3). With increasing atmospheric density, increasing amounts of ejecta become entrained, and the late-stage ejecta curtain becomes severely distorted in comparison with the conical curtain under vacuum conditions. Additionally, a systematic change in ejecta emplacement styles occurs with increasing atmospheric pressure (2,3). For compacted pumice targets (median grain size of 80μ), a distinctive contiguous ridge is formed on the ejecta deposits for atmospheric pressure as low as 0.1 bars. As atmospheric pressure increases, the contiguous ejecta ridge (termed a "rampart") forms at greater distances from the rim. Atmospheric pressures exceeding about 0.5 bars typically result in the formation of individual ejecta lobes exhibiting even greater run-out distances (over 10 crater radii). Still greater pressures (1 bar) result in radially scoured inner ejecta facies and a distinctive near-rim moat, with distal ejecta lobes becoming very thin and dispersed. This systematic change can be correlated with the reduction in cratering efficiency.

Underlying processes controlling this systematic change in emplacement style can be identified by observing the evolution of the ejecta curtain, by changing target materials (including layered targets and low-density particulates), by varying atmospheric density, by changing impact angle, and by comparing the ejecta run-out distances with first-order models of turbidity flows. On this basis, three distinct styles of ejecta emplacement can be characterized that reflect the response of individual ejecta particles to vortical winds created by the outward-moving ejecta curtain. Ejecta ramparts result from sudden deposition of coarser clasts sorted and suspended by these winds. Deposition occurs as the thinning ejecta curtain no longer can generate the recovery winds. This style of "wind-modified" emplacement represents minimal ejecta entrainment in the atmospheric response and is enhanced by a bimodal size distribution in the target. As aerodynamic drag and atmospheric pressure increase, the intensity and carrying capacity of the recovery wind increases. The resulting basal ejecta flow runs off and scours the inner ejecta facies, thereby producing rampart-bordered outer facies beyond the eroded continuous inner ejecta. Such "eddy-supported flows" are observed to increase in run-out distance (scaled to crater size) with increasing atmospheric pressure. By analogy with turbidity flows, this crater-scaled distance should increase as \sqrt{R} for a given atmospheric pressure and target lithology. As crater size increases, the turbulent power in the atmospheric response increases. Self-sustaining ejecta flows eventually develop as excessive turbulent power entrains more ejecta and further increases the carrying capacity. Such "auto-suspended flows" result in much greater run-out distances which no longer follow a simple \sqrt{R} scaling relation. Target composed of low-density (0.7 g/cm^3) micro-spheres (100μ) dramatically demonstrated that both ejecta ramparts beyond the inner facies and much farther auto-suspended flows can develop around the same crater.

Present conditions on Mars are ideal to test these laboratory results. Although tenuous, the present martian atmospheric circulation generates and sustains dust storms with wind velocities (10 m/s) much lower than the expected vortex velocities (>100 m/s) expected to be generated by the outward moving ejecta curtain. Moreover, the diverse geologic history has produced lithologies ranging from solid, massive basalts to easily eroded fine-grained air-fall deposits. The wide range in ejecta sizes reflecting different target lithologies far exceeds the effects of elevation and cyclic changes in atmospheric pressure. Application of the laboratory results to this planetary-scale environment and setting reveals that many of the characteristics commonly ascribed to buried water also can be accommodated by variations in target lithology, i.e., grain size (1, 2, 3). Consequently, increasing ejecta run-out with increasing crater size need not indicate excavation of larger quantities of volatiles at depth but the increased role of ejecta entrainment due to increased turbulence from recovery winds. Such conclusions do not disprove the existence of near-surface water but imply that the role of water in ejecta emplacement may have been a contributing, rather than controlling, factor in many of the ejecta emplacement styles. Consequently increased ejecta run-out with latitude could reflect the increased abundance of aeolian-sorted materials in the ejecta. Nevertheless, near-surface volatiles (including chemically bound water) released by frictional heating of impacting ejecta or entrained secondary debris should significantly enhance the autosuspension process and produce distal ejecta lobes with large run-out distances. Buried water should principally affect remobilization of inner, ballistically emplaced ejecta facies.

While fluidized facies on Mars would be composed of sand-size particles, analogous facies on Venus could contain meter-scale blocks (1), thereby more resembling a rock avalanche. On the basis of inferences drawn from experiments, craters on Venus should not be engulfed by ejecta fall-out (3) but should exhibit fluidized inner facies surrounded by thin distal channelized flows. The inner ejecta facies reflect emplacement by atmosphere-entrained debris flows collapsing from a nearly vertical ejecta wall, similar to martian craters formed in sedimentary deposits. Additionally, turbulence and flow separation will create ejecta-entrained atmospheric turbidity currents with much greater run-out distances and complex channelized forms. These late-stage ejecta deposits should superimpose signatures of early-time atmosphere-impact interactions and high temperature projectile/target phases.

References: (1) Schultz, P.H. and Gault, D.E. (1979). *J. Geophys. Res.* 84, 7669-7687. (2) Schultz, P.H. and Gault, D.E. (1984). *Lunar and Planet. Sci. XV*, LPI, Houston, TX, 732-733. (3) Schultz, P.H. (1989). In *Fourth International Conference on Mars* (abstract), U. Ariz. Press, Tucson, AZ, 181-182. (4) Schultz, P.H. and Gault, D.E. (1982). In *Geol. Soc. Amer. Special Paper 190* (L.T. Silver and P.H. Schultz, Eds.), 153-174. (5) Schultz, P.H. (1981). In *Papers Presented to an International Conference on the Environment of Venus*, p. 6.

IMPACT DECAPITATION FROM LABORATORY TO BASIN SCALES; P.H. Schultz, Geological Sciences, Brown University, Providence, RI 02912 and D.E. Gault, Murphys Center of Planetology, Murphys, CA 95247.

Although vertical hypervelocity impacts result in the annihilation (melting/vaporization) of the projectile, oblique impacts ($<15^\circ$) fundamentally change the partitioning of energy with fragments as large as 10% of the original projectile surviving (1, 2, 3). Laboratory experiments reveal that both ductile and brittle projectiles produce very similar results where limiting disruption depends on stresses (σ_θ) proportional to the vertical velocity component, i.e., $v^2 \sin^2 \theta$. The failure process occurs in two ways. First, shock pressures generated at first contact spall the top of the projectile. The resulting decapitated projectile fragments impact downrange due to the added upward velocity component. The size of the largest fragment depends on the rise time of the shock wave, which depends on both depth of penetration before the shock reaches the back surface (related to impact velocity and material properties) and a dimensionless penetration time, τ , expressed as projectile diameter ($2r$) divided by the horizontal impact velocity component ($v \cos \theta$). As previously reported (3), the impactor fragments form craters downrange that are distinct from secondaries (defined as impacting target debris); hence, they have been termed "sibling" impacts. The distance from the uprange crater rim, x , is approximately given as $2r/v \tan \theta'$ where θ' reflects the altered trajectory (from horizontal) due to the upward spall velocity component. Experiments reveal that θ' can be significantly modified by entrainment in impact-generated vapor. Specifically, vapor produced during impacts into water, plasticene, and carbonate targets disperse the sibling fragments and extend the impact distance.

The second failure mode is expressed by pits overlapping the downrange rim of the oblong primary craters formed in strength-controlled aluminum at (15°). This mode may reflect simple shear as the projectile penetrates farther into the target with time and as strain rates decrease. This layer-cake failure style is most suggestive for ductile aluminum projectiles at lower impact velocities (3 km/s) or low angles and for projectiles with low yield strengths (e.g., pure aluminum). Downrange witness plates in such cases record a vertical chain of sibling impacts with reduced lateral dispersion. Paired downrange pits to either side of the trajectory axis commonly occur for hard (2024) aluminum spheres impacting aluminum and may indicate conjugate shear sets.

For strength-controlled cratering, the resulting profile of the primary crater along the trajectory exhibits deepest penetration uprange (reflecting energy partitioned at first contact) and a distinctive shelf-like region downrange (sibling impacts by the sheared projectile) at relatively modest impact angles (15°). As impact velocity or projectile-target density ratio decreases, however, the primary crater takes on a distinctive arrowhead shape with deeper penetration downrange. Clustered impacts provide an extreme example of this morphology (4). For gravity-controlled craters, such profiles also occur, but require much lower impact angles ($<5^\circ$). Even though the profile and outline for craters in loose particulates are not dramatically changed at 15° , impacts by sibling fragments nevertheless emerge downrange from beneath the ejecta.

Failure of the projectile at laboratory impact velocities (6 km/s) is largely controlled by stresses established before the projectile has penetrated a significant distance into the target. This can be demonstrated by comparing the ricochet pattern and size distribution for an oblique (15°) impact into a thick plasticene block with an impact into a thin plasticene layer (equal to r) coating an aluminum block. The resulting siblings impacted downrange at identical distances; hence, the spall velocity was established by the plasticene, not the aluminum. Moreover, the underlying aluminum block showed only a subtle dent. Use of a thin water layer over aluminum gave the same results.

The planetary surface record exhibits numerous examples of oblique impacts with evidence for projectile failure and downrange sibling collisions. Selected examples were present previously (3) but a further survey has allowed quantifying the results. Figure 1 presents data for Mars where the downrange distance to the smaller sibling scaled to primary crater width is compared with the primary crater shape in plan. If crater width is controlled by strength scaling while crater length is controlled by the work expended during penetration, then crater length/width should be proportional to $\cot \theta$. Similarly, the downrange sibling impact distance scaled to crater width

should scale as $\cot\theta/v^{2/3}$ for $\theta' \sim \theta$. The assumption of strength control in Figure 1 on the extreme reduction in peak stress expected for extremely low-angle impacts (0.8% vertical). Oblique impacts without downrange companions could indicate ejection off the planet. The crater Hale can be linked with downrange oblique sibling craters with arrowhead shapes extending completely around the planet.

The Crisium Basin on the Moon provides a specific example that bears remarkable similarities to strength-controlled craters in the laboratory. Figure 2 shows a sketch map identifying the basin massifs, mare units, and outer scarp. In addition to its oblong shape the western end exhibits the characteristic pinched morphology, whereas the eastern end exhibits a shelf and breach in the massif ring. Both elements are consistent with an east-west impact direction. The interior ring is more circular and offset to the west, analogous to the deeper penetration uprange observed in the laboratory. The striking similarity between the laboratory impacts and Crisium raises several intriguing questions. First, could Mare Marginis indicate downrange sibling collisions? If created by simple shear and allowing for surface curvature, such a scenario would lead to a projectile 360 km in diameter with an impact angle of 25° . If, instead, the eastern shelf marks impacts by this failure mode, then the projectile approaches 120 km in diameter with an impact angle of 15° . Mare Marginis would then represent decapitated sibling impacts. Second, could Mare Angus and Mare Undarum also indicate sibling fragments created by conjugate shear failure of the middle portion of the projectile? And third, what other impactor signatures exist on the planets and can the different modes of failure (e.g., Orcus Patera vs Crisium) provide new clues about basin-scale collisional processes and scaling?

References: (1) Gault, D.E. and Wedekind, J.A. (1978). *Proc. Lunar Planet. Sci. Conf. 9th*, 3843-3875. (2) Schultz, P.H. and Gault, D.E. (1990). *Global Catastrophes in Earth History: An Interdisciplinary Conference on Impacts, Volcanism, and Mass Mortality*, Geological Society of America Special Paper 247 (in press). (3) Schultz, P.H. and Gault, D.E. (1990). *Lunar and Planetary Sci. XXI*, LPI, Houston, TX, 1101-1102. (4) Schultz, P.H. and Gault, D.E. (1985). *J. Geophys. Res.* 90, 3701-3732.

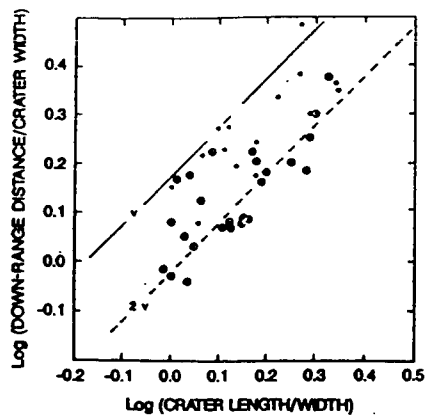


Figure 1. Distance from uprange crater rim (first contact) to downrange decapitation impact separated from crater (dots) or overlapping the crater (open circle) as a function of crater shape in plan. Lines correspond to two different relative velocities (v) predicted from strength scaling.

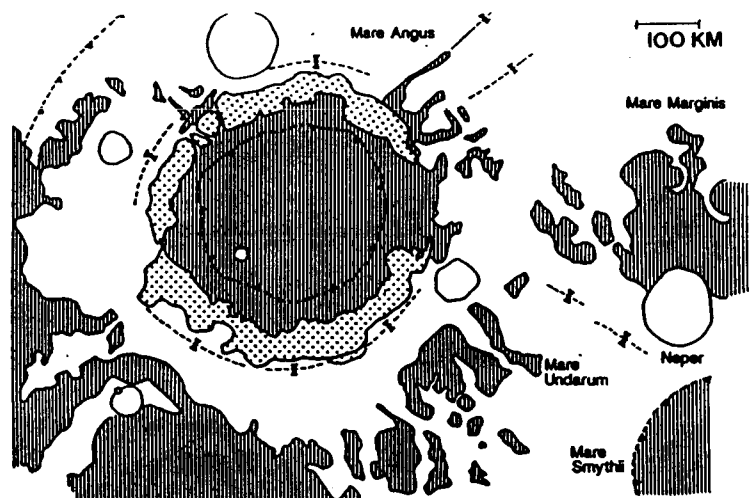


Figure 2. Terrain map of the Crisium Basin showing massifs (stipple) and mare regions. Eastern mare shelf may indicate consequence of projectile shear failure while Mare Marginis may indicate decapitation impacts.

LABORATORY SIMULATION OF CRATERING ON SMALL BODIES

Robert M. Schmidt, Boeing Co., M/S 87-60, Seattle WA 98124

A new technique using external pressure has been developed to simulate the lithostatic pressure due to self gravity of small bodies as suggested by Housen and Holsapple (1990). A 13-inch diameter cylindrical test chamber with L/D of 1 has been fabricated to accommodate firing explosive charges with gas overpressures of up to 6000 psi. The chamber has been hydrotested to 9000 psi. The method allows much larger scale factors than can be obtained with existing centrifuges and has the correct spherical geometry of self gravity. A simulant for jointed rock to be used in this fixture has been developed using weakly cemented basalt. The lowest strength variation of this material corresponding to a "rubble pile" is comprised of 50% basalt 2-mm aggregate, 20% 0.4-mm iron grit, 22% type F flyash, 2% type C flyash, and 6% water. The material bulk density is 2.6 gm/cc, the static unconfined compressive strength is 101 ± 33 psi and the static tensile strength (ASTM 496) is 17.2 ± 0.94 psi. These strengths are averages based on 22 compression tests and 8 tension tests for cure times of 7 to 42 days corresponding to specific target ages. Increasing the amount of type C, while holding the total amount of flyash constant provides compressive strength to as much as 4500 psi with a tensile strength of 1100 psi and all other properties constant. Various strength/pressure scaling theories can now be examined and tested.

Samples were cast in 15 cm diameter spherical molds and allowed to cure for at least 7 days. Two standard cylindrical specimens were also cast with each sphere to obtain the strength measurements at the time the spheres were used. An explosive charge was grouted into each sphere. Although the equivalent charge burial depth to simulate impact fragmentation has not yet been established, a depth of approximately 1 charge radius was used, as suggested by Holsapple (1980) for impact cratering. Variations in the burial depth over the range of 1 to 2 charge radii did not seem to produce significant differences. However, some calibration experiments should be performed to verify this. A single impact test was conducted (shot 876), but was of insufficient energy to produce a useful evaluation of equivalence.

Crater configurations for various confining pressures and charge sizes are shown in Fig. 1, demonstrating significant pressure strengthening due to the applied pressure. In Fig. 2, a plot of cratering efficiency versus strength parameter provides a means to determine the value of μ for the coupling parameter directly. Lastly in Fig. 3, when the applied external pressure is equated to an equivalent lithostatic pressure due to self-gravity, the corresponding plot of cratering efficiency versus gravity scaled size, π_2 is obtained. These experiments also yielded valuable data on fragmentation of small bodies in the gravity regime which is presented and discussed in the last three listed references below.

Holsapple, K. A. (1980) Equivalent depth of burst for impact cratering, *Proc. LPSC 11th*, 2379-2401.

Housen, K. R. and K. A. Holsapple (1990) Fragmentation of asteroids, *Icarus* **84**, 226-253.

Housen, K. R. *et al.* (1991) Scaling of fragmentation, *LPS XXII*, Lunar and Planetary Science XXII, pp. 593-594, Lunar and Planetary Institute, Houston, TX.

Schmidt R. M. and Housen K. R. (1991) Simulations of large scale fragmentation, *ibid.*, pp. 1185-1186.

Housen K. R. and Schmidt R. M (1991) Laboratory simulations of large scale fragmentation events, manuscript submitted to *Icarus* 2/12/91.

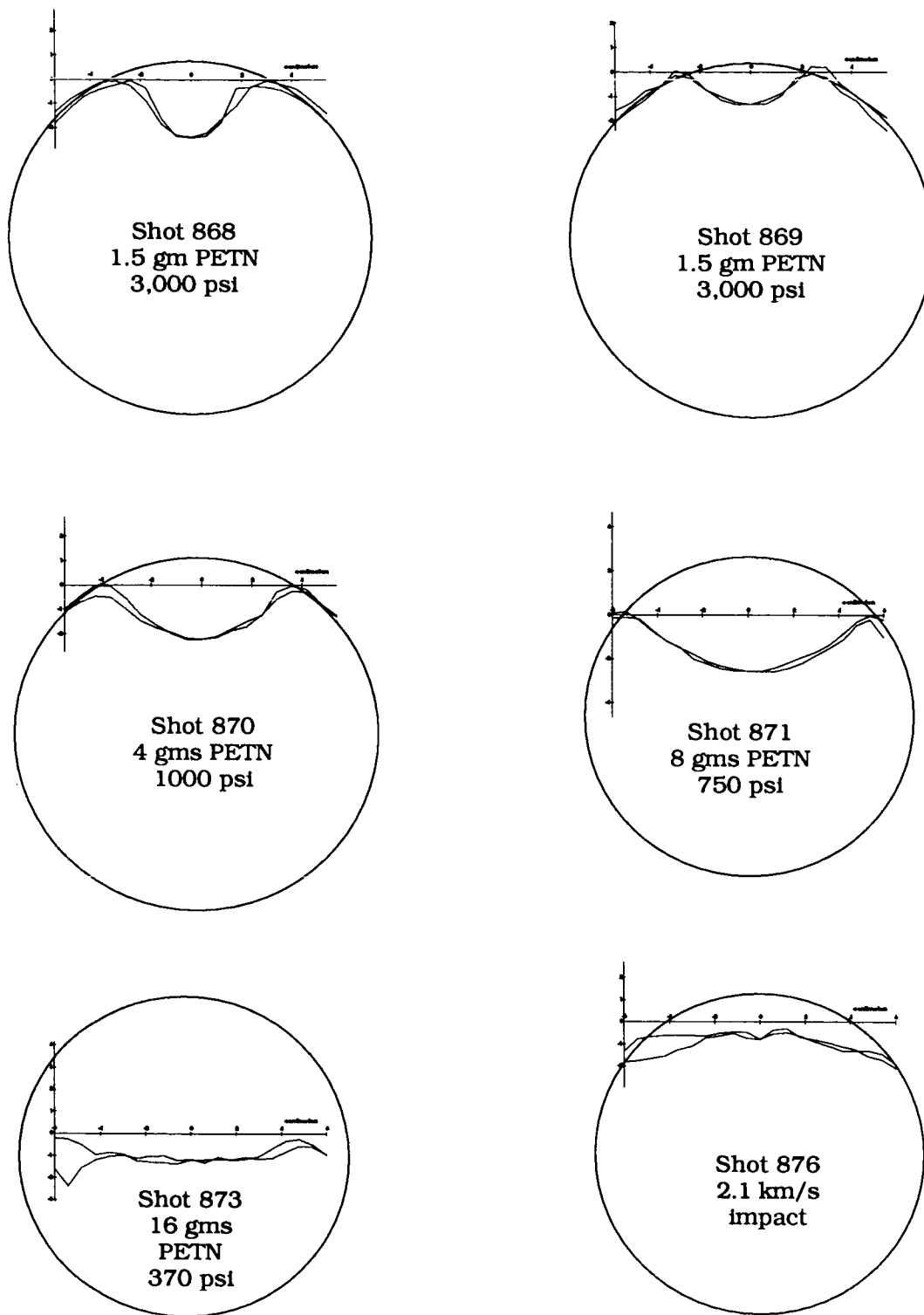


Figure 1 Typical craters formed in small bodies in a simulated self-gravity regime. Shot 873 shows a crater with diameter equal to that of the parent body having removed half the mass without disrupting the remaining largest fragment.

Figure 2. Pressure data is used to solve for μ directly giving a scaling law as follows: $\pi v = C \times \pi(t+p)^{-3\mu/2}$.

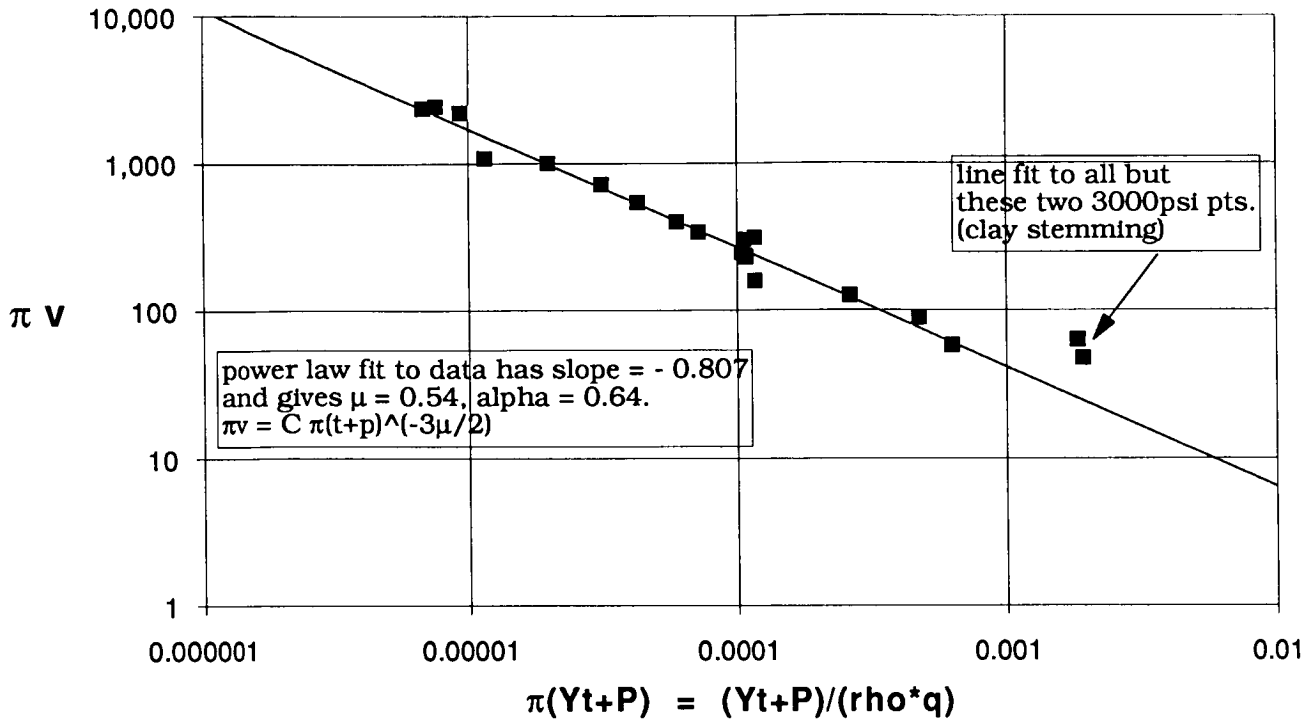
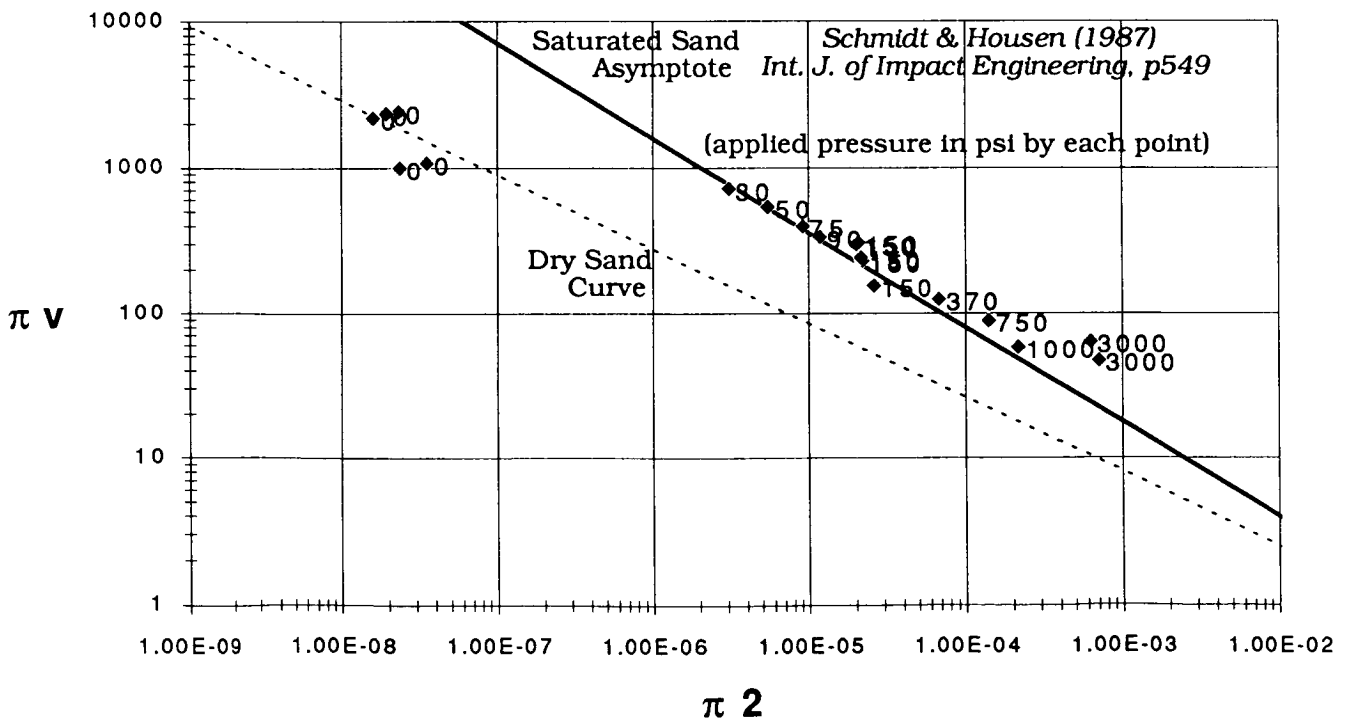


Figure 3. Cratering efficiency versus π^2 where applied external pressure is equated to "equivalent gravity" X density X crater depth.



POSSIBLE MISINTERPRETATION OF LUNAR CRATERING RECORD IN VOYAGER TEAM ANALYSES OF OUTER PLANET SATELLITES

William K. Hartmann, Planetary Science Institute, Tucson AZ 85719

While interpreting outer planetary satellites, the Voyager imaging team repeatedly referred to a lunar frontside highland calibration curve which they say represents "the most ancient, heavily cratered bodies in the solar system" (1). They assume that it is unmodified and not in steady state equilibrium, but rather records all impacts that have occurred. They assume also that it records the size distribution of an early population of impactors, called "Population I" (1), evidence for which they found on various satellites.

This paper reports new evidence that the Voyager team interpretation of this fundamental reference population is wrong, a conclusion that seriously affects the cratering histories reported for outer planet satellites.

The R-plot in Figure 1 (a plot of crater densities relative to the -1.83 index power law found by Hartmann for pure upland populations) shows the situation prior to this work. The heavy horizontal line is a fit to "pure" uplands (defined as uncontaminated by intercrater plains) on several moons and planets. The open circles and S's show data generated for the frontside lunar highlands by Hartmann and Strom, respectively. They are in reasonable agreement, and define a V-shaped curve (thin solid curve in Figure 1). (Strom's counts extended only down to diameters around 8 km; mine extend to smaller sizes, where they turn up due to secondary craters. For clarity, all error bars, based on \sqrt{n} values, have been dropped; they vary, but are typically $\pm 30\%$. The Voyager team interprets this V-shaped curve as a record of a pristine, unique population of ancient impactors, different from more recent populations.

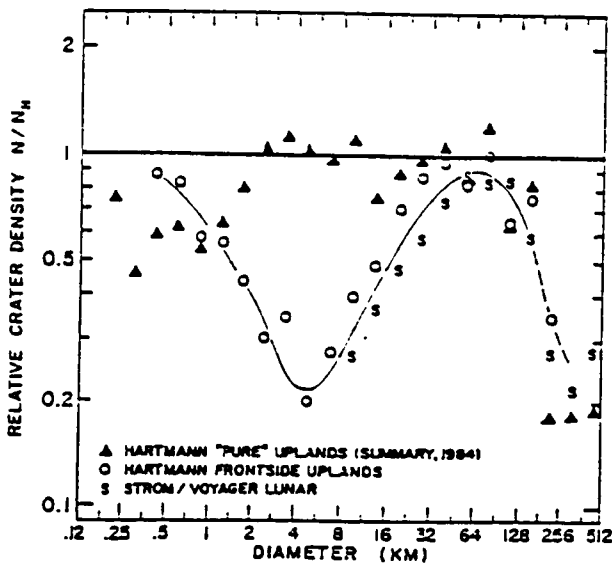


Fig. 1. Old data (through 1984). Left axis shows density relative to that found in most heavily cratered regions. See text for discussion.

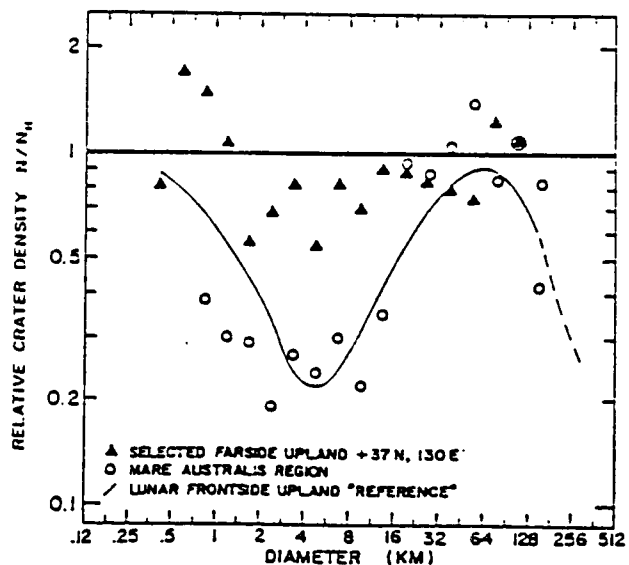


Fig. 2. New data (1990). Mare Australe flooded region matches lunar frontside uplands reference curve (solid curve). A farside test region clusters nearer the "pure" upland heavy horizontal line.

The Voyager team interpretation goes back to the work of Woronow, Strom, and Gurnis (2), who used the V-shaped lunar frontside upland curve to study Jupiter satellites. They stated that in this curve "the imprint of the size-frequency distribution of the impacting bodies may be recovered...(as) preserved in the ancient lunar uplands." Following this assumption, the Voyager team has identified as many as five different populations of impactors; an independent review (3), while questioning some points, also inclines toward "at least four and perhaps all five" populations.

Hartmann (4), however, argued that the V-shaped population is neither characteristic of pristine lunar uplands, nor a marker of a pristine population of ancient craters. Instead, he found that the upland curve in "pure" uplands on the lunar farside is flat, like that of recent mare populations, and that the V-shape comes from loss of small craters through obliteration by uplands plains. (Craters smaller than about 8 km were obliterated; the left side of the V was quickly restored by post-obliteration secondary craters -- see ref. 3 for details).

To test the two interpretations I have made new counts in the moon's Mare Australis region, and on the lunar farside. "Mare" Australis is a perfect region to test for the effects of flooding on crater populations because it marks recent partial flooding by dark flows. One can clearly see that large craters have been flooded to some depth, leaving the large crater rims visible, but destroying smaller craters. A region on the farside (Lat. 37 N, 130 E, Orbiter V-185 Medium and High Resolution) was also counted. A "nesting frames" technique was used, counting large craters on a medium-resolution view, and smaller craters in successively smaller, but representative, subregions at higher resolution).

Preliminary results are shown in Figure 2. The solid triangles, marking the relatively pure farside upland region, cluster near the heavy solid curve as before, though with more scatter (it being a smaller region with fewer statistics). This behavior should not exist in the uplands, according to the Voyager team interpretation. The thin solid curve is copied from Figure 1 for reference. The Mare Australe points cluster along it, in agreement with an association between this shape and upland flooding.

The preliminary conclusions are that flooding in the Mare Australe region has created almost the same curve that was found in the lunar frontside uplands, and that this signature involves not a primordial "Population 1" of unique impactors, but rather obliteration of small craters, and subsequent re-establishment of the secondary branch by post-mare cratering.

If these conclusions are correct, the Voyager team interpretations of outer planet satellite crater and impactor populations may be fundamentally flawed, as the turn-downs found there (the right branch of the V) may indicate not distinct impactor populations, but ancient obliteration/flooding processes.

This work is supported by the NASA Planetary Geology and Geophysics Program.

1. Smith, B. A. and 39 others. (1986) *Science*, 233, 43-64;
2. Woronow, A., R. Strom, and M. Gurnis (1982). In *Satellites of Jupiter*, D. Morrison and M. Matthews, eds. (Tucson: U. Ariz. Press);
3. Chapman, C. and W. McKinnon (1986) in *Satellites*, eds. J. Burns and M. Matthews (Tucson: Univ. of Arizona Press).
4. Hartmann, W. K. (1984) *Icarus*, 60, 56-74.

BIBLIOGRAPHY

Hartmann, W.K., and Grinspoon, D.G. (1990) Early Intense Cratering of the Earth-Moon System (abstract). Meteoritical Society Meeting, Perth, Australia.

Hartmann, W.K. (1990) Notes: Additional Evidence about an Early Intense Flux of C Asteroids and the Origin of Phobos. *Icarus* 87:236-240.

Hartmann, W.K. (1990) Phobos and the Scattering of C Asteroids at the end of Planet Formation. In *Proceedings of the Conference on Lunar and Planetary Science 21*, p. 457-458. Houston, Tex.: Lunar and Planetary Institute.

HYDROCODE PREDICTIONS OF COLLISIONAL OUTCOMES: EFFECTS OF TARGET SIZE; E.V. Ryan, Planetary Science Institute, Tucson AZ; E. Asphaug, University of Arizona, Tucson; H.J. Melosh, University of Arizona, Tucson.

Traditionally, laboratory impact experiments, designed to simulate asteroid collisions, have attempted to establish a predictive capability for collisional outcomes given a particular set of initial conditions. Thus, after specifying an impact velocity, target/projectile size, material, etc., the objective is to predict the degree of fragmentation of the target, and the size and velocity distributions of the ejected fragments. This understanding of the collisional process could then be applied to interpreting the dynamics of the asteroid belt. Unfortunately, in laboratory experiments we are restricted to using targets considerably smaller (diameters typically ~ 0.1 m) than the objects we wish to model (asteroids, diameters of the order of 1 km). It is therefore necessary to develop some methodology for extrapolating the extensive experimental results to the size regime of interest. To do this, we must isolate which initial parameters have a dominant influence on the resultant collisional outcome.

We report here on results obtained through the use of a two-dimensional hydrocode based on Los Alamos' 2-D SALE (1) and modified to include strength effects, and the Grady and Kipp (2) fragmentation equations. The hydrocode has been tested by comparing its predictions for post-impact fragment size distributions to those observed in laboratory impact experiments. The series of experiments done by Takagi *et al.* (3) using basalt targets were used for the initial comparisons. Figure 1 is an example of how well the hydrocode can replicate the experimental results given the target and projectile masses, material properties, and the projectile velocity as initial conditions.

It has been suggested in the literature (4) that target size might have a critical influence on collisional outcomes. Since we are unable to vary this parameter to any great extent experimentally, the hydrocode was used to determine what effect if any simply changing the size of the target has on the resultant fragment size distribution in an impact event. The parameters kept constant were the projectile/target mass ratio, the impact velocity, and therefore specific energy Q (projectile kinetic energy/target mass). Target size was varied from 10 cm to 10 km, restricting this study to the strength regime for large bodies (gravitational forces are minor). Figure 2 shows how the mean fragment size (normalized to the target diameter) was found to decrease with increasing target diameter. The implication is that even when the energy per unit mass available to fragment a target is being held fixed, larger and larger bodies will fragment into relatively smaller pieces. A linear fit to the variation of the normalized mean fragment size with target diameter yields a slope of -0.26 . The strain-rate exponent in this analysis is $\sim 1/4$, possibly implying a connection between strain-rate dependence and the influence of target size.

- (1) Amsden, A.A., H.M. Ruppel, and C.W. Hirt (1980), Los Alamos Scientific Report LA-8095; (2) Grady, D.E. and M.E. Kipp (1980), *Int. J. Rock Mech. Min. Sci. and Geomech. Abstr.* 17; (3) Takagi, Y., H. Mizutani, and S. Kawakami (1984), *Icarus* 59, 462-477; (4) Housen, K. and K. Holsapple (1990), *Icarus* 84, 226-253;

HYDROCODE PREDICTIONS OF COLLISIONAL OUTCOMES; Ryan, *et al.*

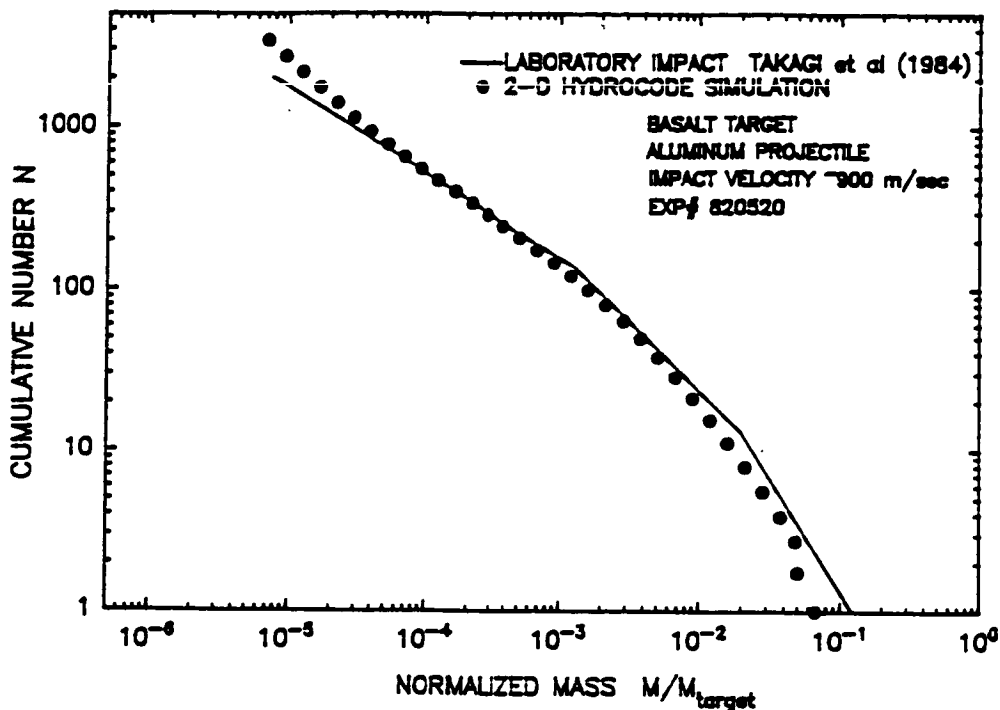


Figure 1. Fragment mass distribution obtained from hydrocode calculations compared to laboratory results of Takagi *et al.* (1984) using basalt targets.

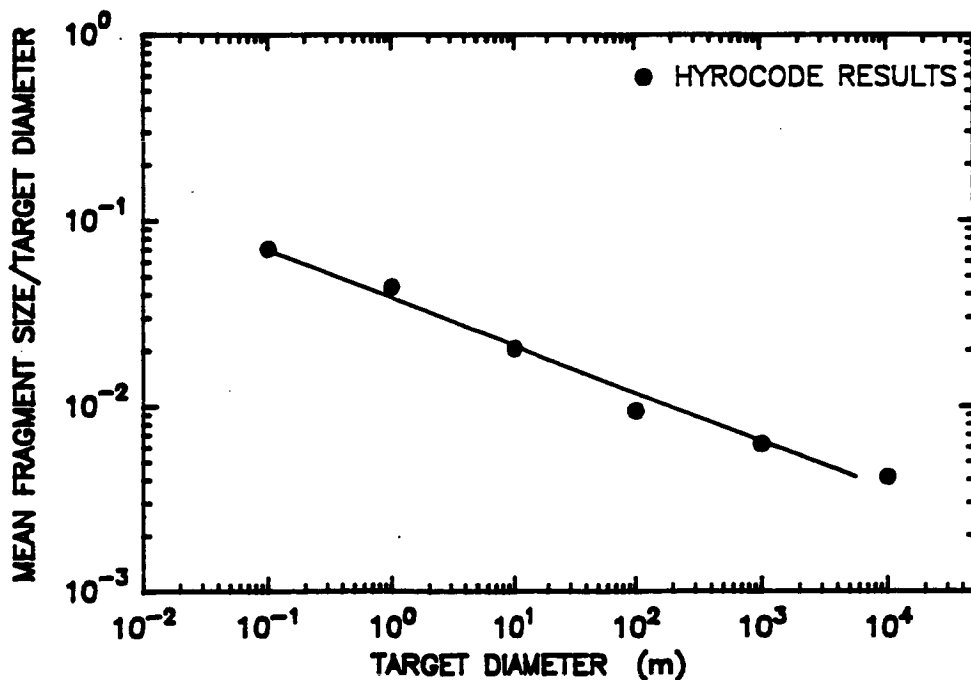


Figure 2. The variation of mean fragment size (normalized to target diameter) with target diameter. The solid line is a linear fit to the theoretical calculations, having a slope of -0.26.

N92-10862

ENERGY COUPLING IN CATASTROPHIC COLLISIONS

K.A. Holsapple and K.Y. Choe

University of Washington FS-10, Seattle, WA 98195

The prediction of events leading to the catastrophic collisions and disruption of solar system bodies is fraught with the same difficulties as are other theories of impact events; since one simply cannot perform experiments in the regime of interest. In the catastrophic collisions of asteroids, that regime involves bodies of a few tens to hundreds of kilometers in diameter, and velocities of several kilometers per second. For hundred kilometer bodies, gravitational stresses dominate material fracture strengths, but those gravitational stresses are essentially absent for laboratory experiments. Furthermore, there is reason to believe that the very nature of the material for the large bodies may be substantially different than laboratory specimens. Only numerical simulations using "hydro-codes" can in principle analyze the true problems, but they have their own major uncertainties about the correctness of the physical models and properties.

The bridges linking laboratory experiments to applications of interest are the scaling theories of catastrophic disruption. There are several possibilities for those theories, including that developed by *Holsapple and Housen* [1,2,3], that by *Mizutani and Takagi* [3], and the classical energy theory [1]. All have two fundamental features: a single choice for a measure of the magnitude of the effect of the impactor, and a measure of the resistance of the asteroid to fracture. Those two choices then totally determine the resulting scaling theory [1,2]. In the energy theory, the measure of the impactor is its kinetic energy, and the measure of the fracture resistance is a single fracture stress. In the *Holsapple and Housen* theory, the more general point-source coupling-parameter measure of the impactor (see [4]) is used, in conjunction with a rate-dependent fracture strength. That gives as a special case the classical energy approach. *Mizutani and Takagi* use a transmitted stress for the impactor measure, and a constant fracture strength. For large bodies, the measure of the resistance should include the gravitational stresses, as discussed in [1,2] and in the *Housen et al* abstract in these proceedings. In any case, the choice of any single scalar measure of the impactor infers that the impact can be modeled as a point source. That point-source assumption clearly must break down when the impactor dimensions approach those of the target body, and for very low impact velocities. The first observation is important in the collisional disruption problem since the cases of interest may include bodies of comparable size. The second observation is of particular importance since some experiments are conducted at only about a kilometer per second impact velocity. Testing the limits of those assumptions is therefore necessary to determine the limits of the scaling theories.

Here the question of the measure of the impactor and its energy coupling is investigated using numerical code calculations. The material model was that of a generic silicate rock, including high pressure melt and vapor phases, and includes material nonlinearity and dissipation via a Mie-Gruniesen model. A series of calculations with various size ratios and impact velocities will be reported. Here results are shown for an impactor with a diameter of 10 km, and a target body diameter of 100 km., with impact velocities of 1, 5 and 10 km/sec. The pressure profiles near the time the shock reaches the far antipodal point is shown in figs.1 and 2 for impact velocities of 1 and 5 km/sec.

Scaling information can be deduced from fig 3. Any point source approximation requires that all cases with variable impactor size and velocity should be indistinguishable when normalized to the correct point-source measure in the regions governed by that assumption (i.e. sufficiently far from the impact point). For an over-all measure of the solution we have chosen the kinetic energy of the target material as a function of time, ignoring that material jetting up and away from the impact site. The appropriate point-source scaling of the energy and time is as shown in the labels of that figure. The classical energy scaling requires that the exponent μ of that scaling be equal to $2/3$, while the more general coupling parameter measure allows any value between $2/3$ and $1/3$. The choice $\mu = 0.5$ was made for the plot, which gave the best results: the curves for the higher velocities superimpose after the initial short

initiation phase. Thus, the point source approximation and a coupling parameter measure does hold, with $\mu \sim 0.5$ for velocities of 5 km/sec or higher. However, the 1 km/sec case is distinctly different, and cannot be compared to the higher velocity cases with the existing scaling theories. The limits on impact velocity and impactor/target size ratio for the various scaling theories will be discussed.

References. [1] Holsapple and Housen, *Memorie Della Soc. Astron. Ital.* 57, 65-85, (1986). [2] Housen and Holsapple, *Icarus* 84, 226-253, (1990). [3] Fugiwara et al, *Asteroids II*, pp 240-265, (1989). [4] Holsapple and Schmidt, *J. Geophys. Res.* 92, 6350-6376, (1987).

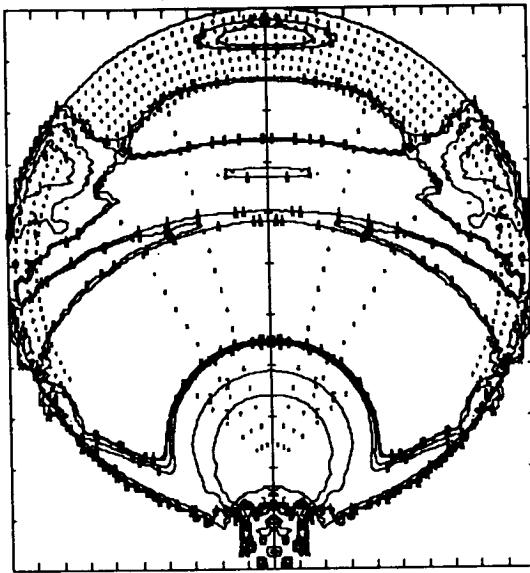


Figure 1. Pressure Contours for a 1 km/sec Impact of a 10 km into a 100 km Silicate Asteroid

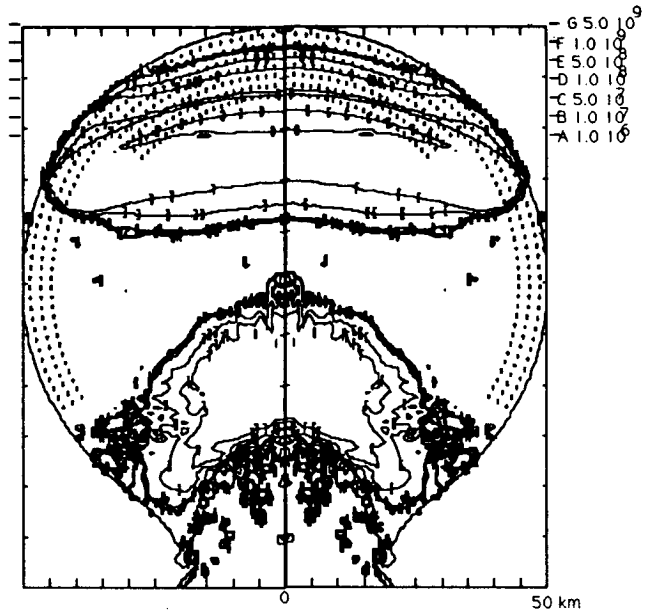


Figure 2. Pressure Contours for a 5 km/sec Impact of a 10 km into a 100 km Silicate Asteroid

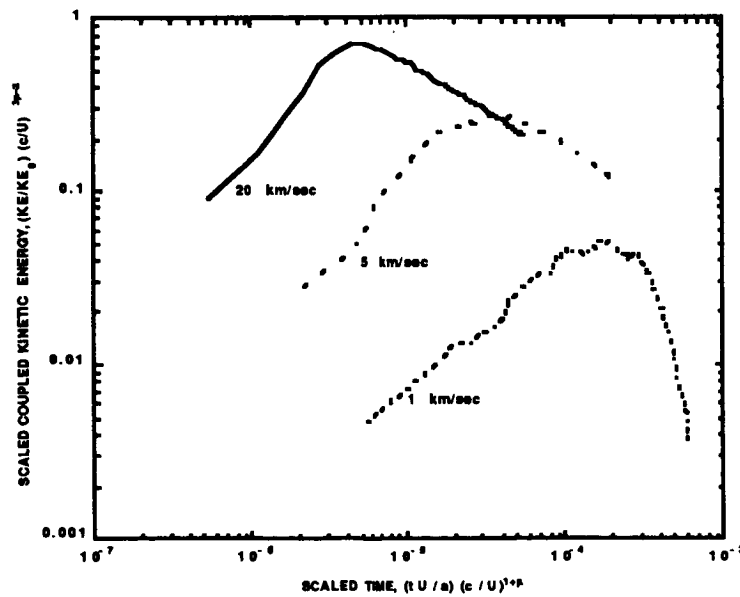


Figure 3. The Coupled Kinetic Energy For Three Impact Velocities

CONTINUUM MODELING OF CATASTROPHIC COLLISIONS

Eileen Ryan (Planetary Science Institute), Erik Asphaug (University of Arizona), and H. J. Melosh (University of Arizona)

Conventionally, the debris from active comets has been thought to give rise to the zodiacal cloud. However the Infrared Astronomical Satellite's (IRAS) discovery of interplanetary dust bands associated with asteroids suggests that asteroids are a likely source for at least some of the zodiacal dust complex. Catastrophic collisions between asteroids produce the dust which maintains and replenishes the population of the dust bands. In an effort to better understand collisions between solid bodies, we report here on the development of a continuum damage model to study an impact event, where fracture growth, fragmentation, and stress wave propagation are predicted as a function of time.

A two-dimensional hydrocode based on Los Alamos' 2-D SALE (Amsden et al., 1980) has been modified to include strength effects and Grady and Kipp's (1980) fragmentation equations for fracture resulting from tensile stress in one dimension. Output from this code includes a complete fragmentation summary for each cell of the modeled object: fragment size (mass) distributions, vector velocities of particles, peak values of pressure and tensile stress, and peak strain rates associated with fragmentation. Contour plots showing pressure and temperature at given times within the object are also produced. By invoking axial symmetry, three-dimensional events can be modeled such as zero impact parameter collisions between asteroids. The code was tested against the one-dimensional model of Melosh (1987), and the analytical solutions of Grady and Kipp (1980) for a linearly increasing tensile stress under constant strain rate. The two-dimensional routine showed no systematic deviation from the analytic solutions, and a closer correlation than the one-dimensional results.

By comparing computational results from the hydrocode with data from actual laboratory impact experiments, it will be possible to both gauge the success of and further refine the collisional model. We will then gain a better predictive capability for the degree of fragmentation and for size and velocity distributions of fragments ejected in an impact event.

For testing of the hydrocode, two convenient laboratory experiments were a basalt-basalt collision and a pyrex-basalt collision done by Hartmann (1979, unpublished) at the Ames Vertical Gun Range (AVGR). In these cases, the specifics of the projectile/target mass, density, impact velocity (both <300 m/s), etc. were easily available. The cumulative fragment mass distributions predicted by the code in each case match the experimental outcomes acceptably well, considering inherent experiment scatter. Improved correlation should be possible with minor adjustments to the Grady-Kipp fragmentation algorithm. However, additional comparisons of the model to laboratory impacts covering a variety of velocities and materials will be necessary.

REFERENCES: Amsden, A.A., H.M. Ruppel, and C.W. Hirt (1980). Los Alamos Scientific Lab Report LA-8095. Grady, D.E. and M.E. Kipp (1980). Int. J. Rock Mech. Min. Sci. and Geomech. Abstr. 17. Melosh, H.J. (1987). Int. J. Impact Engng 5, 483-492.

CORE FORMATION BY GIANT IMPACTS. W. B. Tonks and H. J. Melosh. Lunar and Planetary Laboratory, University of Arizona, Tucson, Az. 85721.

Ideas about the accretion and early evolution of the Earth and the other terrestrial planets have recently undergone a number of revolutionary changes that have made much of the older work on the subject obsolete [1]. It has become clear that giant impacts were far from rare events. In the later stages of accretion any given planetary embryo is liable to be struck several times by other bodies of up to half its own diameter. Such an impact may have the ability to trigger core formation. Traditional accretion models have had great difficulty explaining the formation of a core [2]. This is because the first material to accrete should form a cold, strong inner nucleus that is difficult for later, hotter material added above it to disrupt. This difficulty is a direct consequence of the assumption that the later material is deposited in layers much thinner than the diameter of the growing planet. If, on the other hand, one admits the importance of infrequent large events that may melt an entire hemisphere, the core formation difficulty vanishes. Millimeter-size iron blebs in the melted region will rain out due to their density difference with the silicate melt. Core formation may not require the melting of an entire hemisphere of the planet. In this paper we explore the conditions under which impact induced core formation may occur. The idea of impact induced core formation is illustrated in figure 1.

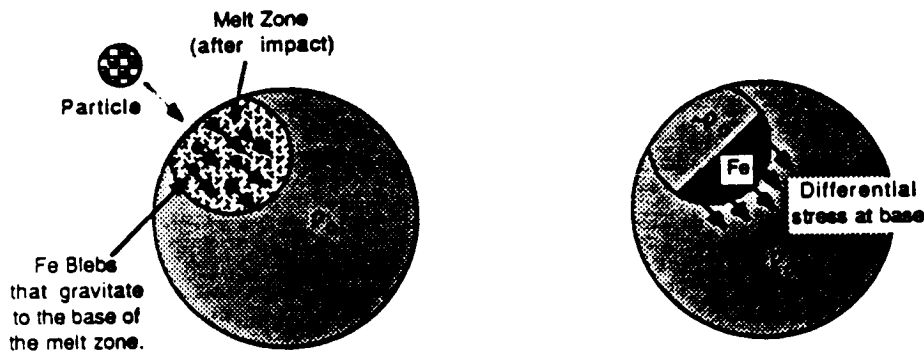


Figure 1a.

Figure 1b

Figure 1. Impact Induced Core Formation

We envisage an approximately chondritic initial assemblage composed of chondrules, millimeter sized solid iron blebs, and matrix material. A large (compared to the size of the planet) hypervelocity impact will generate a large, approximately hemispherical region of melt. The iron blebs will also melt and rain out to the base of the melt zone (Fig. 1a). Subsequent crater modification will cause the iron to be overlain by material with approximately the same density as the original material. The iron forms a large negatively buoyant region that must be supported by the strength of the material underneath. If the stress created by the iron is too large, the iron essentially breaks through the planet and flows to the center (Fig 1b). We now explore the conditions under which core formation by this mechanism might occur.

A hypervelocity impact creates a core region of high and essentially constant pressure known as the isobaric core. The shock moves outward with diminishing pressure. As the shock passes through the material, it rapidly compresses the material to a higher pressure which then decompresses adiabatically. However, irreversible $p dV$ work has been done on the material and it is hotter than before the shock passed. If the shock pressure is sufficiently high, melting occurs. The minimum shock pressures required to melt various geological materials are around 100 GPa [3]. A value of 110 GPa, corresponding to the minimum melting shock pressure in ANEOS dunite, was used in the calculations that follow.

We estimated the effects of the growth of planetesimals in an environment governed by a cumulative mass distribution of the form, $N(>m) = Cm^{-q}$, where $N(>m)$ is the number of particles with mass greater than m , C is a normalizing constant, and q is the power of the distribution. Evidence of a diameter distribution of D^{-2} exists from crater counts [3], the distribution of comet

nuclei sizes [4], and in numerical models of accretion. Because $\text{mass} \sim D^{1/3}$, $q \sim 2/3$. The actual distribution is not precisely known and might evolve over time, thus we treat it as a free parameter. We randomly generate a mass distribution over a limited mass range using the above distribution. The largest mass in the distribution is used as the bombarded planetesimal. We also input the mass of the largest planetesimal in the accretion zone of our bombarded planetesimal and the Safronov number, which determines the limits of the random velocity component. The random component is added vectorially to the escape velocity of the bombarded planetesimal. The thermal effects of the impact are estimated as follows. The radius of the isobaric core region is calculated by requiring the energy imparted to the target equals the energy (internal and particle velocity) of this region. The pressure is found using the Hugoniot equation $P = \rho_0 v_p U$, where ρ_0 is the uncompressed density of the target, v_p is the particle velocity, and U is the shock pressure. The shock pressure is modeled using the linear shock-particle velocity relationship ([3], appendix 2). We assume the material is 30% metallic iron by mass, consistent with the composition of primitive chondrites. If melting occurs, the metal melts and forms a pool at the bottom as described above. The density contrast creates a differential stress. If the average stress caused by the iron-silicate separation is greater than the yield stress, we consider the metal to have broken through the rock and a core formed. If a core did not form, another particle in the distribution is chosen. The process continues until all 1000 particles either impact, or the planetesimal is disrupted by the input of projectile kinetic energy exceeding the planetesimal's gravitational binding energy, or a core is formed. The mass of each incoming particle is added to the planetesimal's mass. Each planetesimal calculation was repeated 100 times using different random numbers to determine the probability of core formation. Figure 2 shows the results of our preliminary runs.

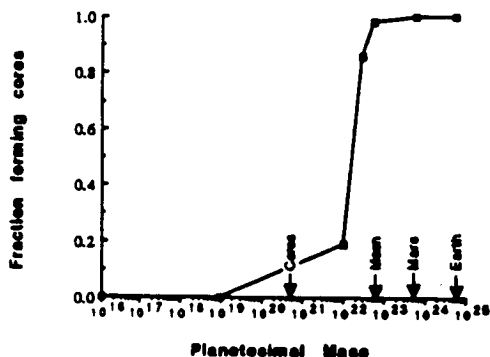


Fig. 2. Fraction of planetesimals that will form cores as a function of initial planetesimal mass. The planet grows in the calculations but does not more than double. Run condition: $q = 2/3$, Safronov number = 2.6, maximum material stress = 1 kbar, minimum melting shock pressure = 110 GPa, yield stress = 1 kbar, mass of largest planetesimal in the accretion zone = mass of planetesimal under investigation. Note the abrupt transition from planets that do not form cores under our run conditions to planets that do between 10^{21} and 10^{22} kg.

These runs show that the onset of impact induced core formation is quite sharp and occurs (by our criteria) in slightly smaller than lunar-sized planetesimals. Core formation requires relatively large high velocity particles. However, the planetesimal must be fairly massive to prevent disruption by such a particle. Bodies smaller than $\sim 10^{22}$ kg tend to be disrupted by impacts that are fast enough to induce widescale melting. Additionally, the acceleration of gravity on small objects is low; thus a small differential stress is created by the iron. It appears from this work that previously undifferentiated bodies that are lunar-sized and larger have a high probability of forming cores by large impacts. More work is needed to understand the seemingly abrupt threshold shown above and more runs are needed to check the effects of changing parameters in the calculation.

REFERENCES

- [1] Wetherill, G. W. 1990. *Ann. Rev. Earth Planet. Sci.* 18:205-256. [2] Stevenson, D. J. 1990. in *Origin of the Earth.* Eds. H. Newsom and J. Jones, New York: Oxford University Press., pp.231-250. Stevenson, D. J. 1981. *Science*, 214:611-619. [3] Melosh, H. J. 1989. *Impact Cratering, a Geological Process.* New York: Oxford University Press; Melosh, H. J. 1990. in *Origin of the Earth.* Eds. H. Newsom and J. Jones, New York: Oxford University Press., pp.69-83. [4] Delsemme, A. H. 1987. in *Symposium on the Diversity and Similarity of Comets*, pp. 19-30. ESA SP-278.

LARGE IMPACTS AND CLIMATIC CATASTROPHES ON THE EARLY EARTH; H. J. Melosh, Lunar and Planetary Laboratory, University of Arizona, Tucson, AZ 85721.

Radiometric dates of cratered lunar surfaces suggest that the cratering rate on the ancient Moon was substantially larger than the present rate before about 3.2 Gyr. A fit to this data suggests that the cumulative flux $N_{cum}(m)$ of impactors of mass m can be adequately represented by the expression $N_{cum}(m) = a[1 + B e^{-\lambda(t+4.6)}]m^{-b}$, where $a = 1.55 \times 10^{-23} \text{ kg}^b \text{ m}^{-2} \text{ sec}^{-1}$, $b = 0.47$, $B = 2300$ and $\lambda = 4.53 \text{ Gyr}^{-1}$. Since the cratering rate was higher than present on the Moon, it seems likely that it was similarly higher on the Earth. It is thus gratifying that Lowe and Byerly (1) have recently reported the occurrence of beds of spherules up to 2 m thick in 3.2 to 3.5 Gyr old Archean rocks. These spherule beds closely resemble the 3 mm thick spherule beds associated with the K/T boundary (including elevated iridium abundances), widely believed to have been deposited in association with the impact of a 10 km diameter comet or asteroid.

Until recently it was believed that the spherules at the K/T boundary were transported worldwide as windblown dust. However, it is clear from the 0.1 to 1 mm diameter reported for the bulk of these spherules that their atmospheric residence time is very short, only a few hours, leaving ballistic transport as the only viable means for their global dispersal. We have argued previously (2) that when ballistically transported spherules and other debris reenter the atmosphere approximately 1/6 of their total energy is converted to thermal radiation on the Earth's surface, whereas about 1/3 is deposited in the atmosphere itself, absorbed by water and CO_2 . In the case of the K/T impactor the energy irradiating the Earth's surface was about 10 kW/m^2 , and the adsorbed energy was capable of raising the average temperature of the lower atmosphere by about 10°C . This amount of thermal radiation is just capable of causing spontaneous ignition of the Cretaceous forests, thus explaining the soot and charcoal found in the boundary clays (3), but the temperature rise of the lower atmosphere is not sufficient to alter its overall stability (the potential temperature difference between the surface and the stratosphere is between 100° and 140° , depending on latitude(4)). On the other hand, the reentering debris would have been relatively efficient at producing NO. Using an estimated efficiency of NO production of one molecule/40eV of energy deposited, or $7 \times 10^{-9} \text{ kg}$ of NO/Joule (5), the ejecta from the K/T impact may have produced 1-3.5 kg of NO/ m^2 , or NO concentrations of 100-350 ppm. The low Ph caused by such an increase in NO has been suggested (6) as potentially responsible for major oceanic as well as terrestrial extinctions.

The spherule beds in the Archean rocks, however, suggest still greater climatic perturbations. Since thermal energy generation scales directly as the mass deposited, a 10 cm thick spherule bed, if deposited ballistically over the entire Earth, implies thermal irradiation powers of roughly 300 kW/m^2 for periods of time of about an hour (the time scale for deposition is the same for large and small events), temperature rises in the lower atmosphere approaching 300°C , and NO production approaching 1% of the total atmospheric mass (assuming that the ancient Earth's atmosphere was similar in density and structure to the present atmosphere). Surface temperatures on rocks or soil would have approached 1000 to 1700°C , the temperature of the radiating ejecta in the upper atmosphere. It seems unlikely that any life could have survived the thermal pulse on the surface, although oceanic life would have been protected by the evaporation of a few tens of cm of water. The rise in overall atmospheric temperature would have been sufficient to overturn the atmosphere, mixing the suddenly heated troposphere into the stratosphere on a time scale of a few hours. After this sudden event further climatic perturbations may be expected to have continued for some time, perhaps years. Using the equation for the impact cratering flux on the Moon given above, an impact of this magnitude should occur roughly once every 150 Myr on the Earth. The 2 m thick spherule beds imply corresponding greater, although rarer, catastrophes.

The early Earth thus appears to have been a violent and rather inhospitable place: The recent detailed study of the K/T impact has shown that the climatic perturbations of large impacts appear to be more profound than previously estimated. Although ideas similar to this have

been previously suggested (7) for very large impacts, we argue here that even the smaller events recorded by ejecta layers in Archean rocks probably played an important role in shaping the environment of the early Earth, and thus the environment in which life arose.

REFERENCES:

- (1) D. R. Lowe and G. R. Byerly, *Geology* **14**, 83-86 (1986). (2) H. J. Melosh, N. M. Schneider, K. J. Zahnle, and D. , *Nature* **343**, 251-254 (1990). (3) W. S. Wolbach, I. Gilmour, E. Anders, C. J. Orth and R. R. Brooks, *Nature* **334**, 665-669 (1988). (4) J. T. Houghton, *The Physics of Atmospheres*, Cambridge (1977). (5) H. J. Melosh, *Impact Cratering*, Oxford (1989). (6) J. S. Lewis, G. H. Watkins, H. Hartman and R. G. Prinn, *Geol. Soc. Amer. Spec. Pap.* **190**, 215-221 (1982). (7) N. H. Sleep, K. J. Zahnle, J. F. Kasting, H. J. Morowitz, *Nature* **342**, 139-142 (1989).

IMPACTS AND THE EARLY ENVIRONMENT AND EVOLUTION OF THE TERRESTRIAL PLANETS.

H. J. Melosh and A. M. Vickery (both at: Lunar and Planetary Laboratory, University of Arizona, Tucson, AZ 85721)

A revolution has recently occurred in our understanding of impact processes during accretion of the planets. Stemming partly from the giant impact scenario for the moon's origin, it is now admitted that very large impacts may have played an important role in the accretion of the terrestrial planets. The size-frequency distribution of these impacts fits the formal definition of a catastrophic process: the mass and momentum added by a rare large impact is larger than that added by all the more frequent small impacts combined. The effects of such large impacts on the thermal states of growing planets are profound: By the time a planet has reached the size of Mars, impacts with objects half its diameter are capable of melting either the entire planet or at least one hemisphere as the shock wave from the impact traverses the planet. In this scenario core formation becomes quick and inevitable: the occurrence of a major melting event on a growing planet allows metallic iron particles to separate rapidly from the silicate melt, forming a pool of iron at the bottom of the melted region. This pool may be large enough to displace even strong underlying silicate rocks and form a proto-core. Subsequent impact and melting events will add more material to the core in a batchwise manner. Vigorous convection in the melted regions (magma oceans) following major impact events results in rapid cooling times (a few thousands to tens of thousands of years) and may prevent crystal-liquid density segregation when the Rayleigh number is high enough to ensure turbulent convection.

At a later stage of planetary evolution, the smaller impacts during late heavy bombardment may have played an important role in stripping the original gaseous atmospheres of the planets and in segregating condensable substances (eg. water) from volatile ones (eg. CO₂). A large meteorite that strikes the surface of a planet possessing an atmosphere can interact with the atmosphere in three ways: During its initial passage through it, by means of high-speed ejecta thrown out from the crater, and by the expanding vapor plume that is produced when the impact velocity is high enough to vaporize either the target rocks or the meteorite itself. The most important of these interactions is with the vapor plume. The leading edge of this rapidly expanding plume of hot vapor may move many times faster than the meteorite that formed it. In sufficiently large impacts on Earth (meteorites > 300 m diameter) the plume may have enough energy to blow aside the atmosphere and vent vaporized rock directly into space. In still larger impacts (>10 km diameter) the overlying atmospheric gases may be accelerated to greater than escape velocity and atmospheric erosion may occur. Mars may have lost most of its early atmosphere this way during the era of heavy bombardment.

VAPOR PLUMES: A NEGLECTED ASPECT OF IMPACT CRATERING; H. J. Melosh, Lunar and Planetary Laboratory, University of Arizona, Tucson AZ 85721 USA.

When a meteorite or comet strikes the surface of a planet or satellite at typical interplanetary velocities of 10-40 km/sec, the projectile and a quantity of the target body vaporize and expand out of the growing crater at high speed. The crater continues to grow after the vapor plume has formed and the now-familiar series of ejecta deposits is laid down ballistically while the crater collapses into its final morphology. Although the vapor plume leaves little evidence of its existence in the crater structure or surface deposits, it has become clear that it may play a major role in a number of impact-related processes. In the past, vapor plume dynamics has been neglected for a number of reasons besides the dearth of plume-related deposits: Vapor plumes form only at velocities greater than the maximum achievable in the laboratory, and numerical computations performed by US investigators have been so narrowly focussed on the growing crater that the vapor plume is often eliminated from the computation (Soviet investigations have been more careful to include the plume, but most of this work is poorly known outside the USSR).

The vapor plume expanding away from the site of an impact, however, carries between 25% to 50% of the total impact energy. Although the plume's total mass is only a few times the mass of the projectile (and hence only a few percent of the total mass excavated), its high specific energy content means that it is the fastest and most highly shocked material in the cratering event. Estimates based on Zel'dovich and Raizer's model of vapor plume expansion indicate that the leading edge of the plume from a 25 km/sec silicate-on-silicate impact leaves the impact site at speeds up to 65 km/sec. The mean velocity of expansion can easily exceed the escape velocity of the target planet, so that the net effect of a sufficiently high-speed impact is to erode material from the planet.

There are several important consequences of this high-speed vapor plume. First, it facilitates the ejection of material from a target planet possessing a substantial atmosphere by displacing the atmosphere. Thus, tektites are probably blobs of impact melt carried above the Earth's atmosphere along with a quantity of much hotter vapor (which may itself condense later to produce microtektites). Small, high-speed fragments of solid, lightly shocked ejecta spalled from the surface can be entrained in the vapor plume and carried free of the planet, so that rare samples of each of the terrestrial planets should occasionally be ejected into interplanetary space to fall as meteorites onto the other planets. On planets with atmospheres impact-generated vapor plumes carry away part or all of the atmosphere above the plane tangent to the point of impact, resulting in a net erosion of the atmosphere. Although this effect appears to be small at the present time, during heavy bombardment it probably had a major influence on the atmospheric inventories of the terrestrial planets. Finally, the portion of the vapor plume that does not escape can have important effects on the climate of the planet. It appears that the 10 km diameter asteroid or comet that struck the Earth at the end of the Cretaceous ejected a large quantity of material in ballistic orbits that fell back into the atmosphere from above. Using the observed mass loading of about 10 kg/m^2 , this implies that about 10 kw/m^2 of thermal radiation from the reentering ejecta bathed the Earth's surface for about an hour after the impact, explaining the soot found in the boundary layer as a result of the spontaneous ignition of all of the Earth's forests at that time. Thicker layers of ejecta discovered in Archean rocks by D. Lowe indicate that even more extreme conditions may have accompanied impacts in the Earth's early history.

JETTING AND THE ORIGIN OF TEKTITES; A. M. Vickery, Lunar and Planetary Laboratory, University of Arizona, Tucson, AZ 85721

The scientific consensus is that tektites were produced by impacts on the earth, but the exact mechanism by impacts might form tektites is still unclear. The most widely cited mechanism is jetting, which results from the extremely high pressures generated at the intersection of two bodies whose surfaces converge obliquely at high speed. In this work, the theory of jetting for thin plates is extended to the case of the impact of a sphere onto a half-space. The calculations are done for the impact of a silicate sphere onto a silicate target for impact speeds of 15, 20, and 25 km/sec, spanning the range of reasonable impact speeds for asteroids. The angle of impact is varied from 0° (normal impact) to 75°. The mass jetted, the jet velocity, projectile fraction in the jet, the azimuthal distribution of the jet, and the phase of the jetted material (vapor or liquid) are calculated as functions of time. The total mass jetted and the overall mass-averages of jet velocity, etc. are also calculated. For the 75° impacts, there is a very fast, early jet (with a small jet in the back-range direction), followed by a significantly slower, but much longer lasting jet. The initial portion of the jet has an elevation angle of ~ 3° above the horizontal; the elevation angle increases with time up to a maximum of ~35°. These results agree at least qualitatively with the results of impact experiments on ice at 75° (P. H. Schultz, personal communication). Thus the use of this simple model gives results that agree in general with the available experimental data.

The initial, vapor portion of the jet is the fastest and has the highest mass flux; it is postulated that this portion of the jet can drive away atmosphere ahead of it, so that the liquid portion of the jet is ejected into a much rarified atmosphere. This overcomes one of the major problems for the theory of the terrestrial impact origin of tektites, which is how to propel molten material through the atmosphere for distances of hundreds to thousands of kilometers without the melt breaking up into a fine mist because of turbulent interactions with the air (Adams, 1965).

The results also show, however, that the jet comprises roughly half projectile material, which is strongly at odds with the observation that tektites, with one exception (Morgan, 1978), show no detectable projectile contamination. Although the jetting model used is quite simple, so that there is considerable uncertainty in the absolute projectile fraction, no reasonable variation in the assumptions will allow for a jet comprising only target material. This result seems intuitively obvious in retrospect, because jetting by definition requires the intimate interaction of impactor and target, and so the jet must contain a significant fraction of the projectile material. This leads to the firm conclusion that jetting cannot have produced tektites.

Jetting may, however, have produced the spherule beds recently found in Archean Greenstone belts in South Africa and Australia (Lowe and Byerly, 1986; Lowe et al., 1989). The largest of the South African spherule beds originally extended over an area at least 30 km by 100 km, ranges in thickness from a few centimeters to 1 m, and comprises 0.1 to 4 mm diameter spherules. The spherules were apparently deposited rapidly and simultaneously in a wide variety of sedimentary environments as a single fall layer. There is no evidence for volcanic or volcanoclastic material. The beds show extreme, though variable, Ir enrichment, and at least two of the beds are also enriched in Pd, Os, Pt, and Au in roughly chondritic proportions. The major element compositions are consistent with a mixture of underlying rock types and chondritic material.

Adams, E. (1965) *N. Jb. Miner. Mh.*, No. 9-11, 332-350.

Lowe, D. R. and G. R. Byerly (1986) *Geology* 14, 83-86.

Lowe, D. R., G. R. Byerly, F. Asaro, and F. J. Kyte (1989) *Science* 245, 959-962.

Morgan, J. W. (1978) *Proc. Lunar Planet. Sci. Conf. 9th*, 2713-2730.

MELT DROPLET FORMATION IN ENERGETIC IMPACTS; A. M. Vickery and H.J. Melosh, Lunar and Planetary Lab, The University of Arizona, Tucson, AZ 85721

It has long been known that impacts between rocky bodies at velocities exceeding about 15 km/s are capable of melting or vaporizing both the impacting object and a portion of the target (1). We have recently shown (2, 3) that geological materials initially shocked to high pressure approach the liquid-vapor phase boundary from the liquid side as they decompress, breaking up into an expanding spray of liquid droplets. We present a simple theory for estimating the sizes of these droplets as a function of impactor size and velocity. We show that these sizes are consistent with observations of microtektites and spherules found in the Cretaceous-Tertiary boundary layer, the Acraman impact structure, Archean beds in South Africa and the lunar regolith. The model may also apply to the formation of chondrules.

Although it has thus become clear that spherule formation is an important part of the impact cratering process, until now no reliable method has been found for estimating the spherules' size in a given impact event. Previous methods began with the assumption that the highest energy portion of the ejecta plume is completely vaporized (4) and that the condensates formed by homogeneous nucleation from the vapor phase. However, the studies of Montanari et al. (5) clearly indicate that the K/T spherules quenched from a liquid phase. Furthermore, our recent studies of the decompression of shocked dunite (2,3,6) and quartz using the ANEOS equation of state program (7) show that at common asteroidal impact velocities on Earth (~ 20 km/s) the shocked material follows a release path that intersects the liquid-vapor phase curve from the *liquid* side.

Shortly after an energetic impact event the impacting projectile and a roughly equal volume of the target are compressed to high pressure (8) and a density roughly twice the zero-pressure density. Highly shocked material begins in the liquid phase and expands to lower pressure and density. At this time the liquid undergoes an initial fragmentation into clumps whose diameter d_0 is determined (9) by the balance between surface tension σ and the local kinetic energy, $1/2 \rho_l v^2$, where $v = \dot{\epsilon} d_0$. This balance yields an initial clump size of $d_0 = (40\sigma / \rho_l \dot{\epsilon}^2)^{1/3}$, where ρ_l is the liquid density at the moment of fragmentation and $\dot{\epsilon}$ is the strain rate of the expanding melt. We estimate the strain rate as the ratio of the mean expansion velocity, v_{exp} , to the radius of the plume at the time of droplet formation, R_f . We assume that $R_f \approx L/2$, where L is the impactor diameter and $v_{exp} \approx v_i/2$ (10), where v_i is the impact velocity. For a 1 km diameter projectile striking at 20 km/s this yields $d_0 \approx 2$ cm, which is comfortably close to the size of tektites, supposing that some of the melt ejected from the crater escapes further fragmentation. This is more likely to occur in the lower speed, inner and slower, portion of the ejecta where most of the melt is derived from the target, consistent with the lack of siderophile element (projectile) contamination of tektites (11).

Following the initial fragmentation of the homogeneous melt, a second generation of droplet formation occurs in the more energetic part of the ejecta plume. Hydrocode computations we performed using the ANEOS parameters for dunite (3) show that vaporization begins when the mean density in the expanding melt falls to about half of its uncompressed density, or when the melt plume is about 1.6 times larger than its initial radius. The vapor mass fraction quickly reaches about 0.5, then begins to decline slowly as condensation onto existing droplets occurs. The ultimate droplet size is thus established in an environment in which both vapor and melt droplets are present. Assuming that the volume of vapor is much greater than the volume of melt, the

droplet radius r is estimated from the balance of aerodynamic forces and surface tension. Our hydrocode calculations indicate that very rapidly reach an equilibrium size when the liquid fraction is at its minimum. This size is given by $r_{eq} = \sqrt{15\sigma C_D / 4\rho_d a}$, where C_D is the drag coefficient, ρ_d is the droplet density, and a is the acceleration of gas due to pressure gradients: The steady-state differential velocity between the drops and the gas is $\Delta v = \sqrt{5\sigma / \rho_g r_{eq}}$ and the time scale for droplet formation is $t_{eq} = [(1 - \ell)\Delta v] / a$, where ρ_g is the gas density and ℓ is the liquid fraction. Using various approximations for the maximum (initial) pressure, the pressure gradient as a function of radius and time, a linear U_s - u_p EOS for quartz, and other constraints (10), we find that the minimum equilibrium droplet size for the high-energy portion of the ejecta plume is $r_{eq} \approx 0.11\sqrt{L} / v_i$ (SI units).

Assuming that the KT impact involved a ca. 10 km diameter asteroid with $v_i \approx 20$ km/sec, our model predicts $r_{eq} \approx 550 \mu\text{m}$, consistent with the observed spherule sizes in the KT boundary layer outside North America(12). The model also predicts $\Delta v \approx 1.3$ m/s, which is small compared to the mean expansion velocity of the plume, $v_{exp} \approx 10$ km/sec, and $t_{eq} \approx 0.05$ ms, which is small compared to the characteristic plume expansion time, $t_{exp} = R/v_i \approx 800$ ms. The smallest reported sizes of the late Eocene microtektites (13), microirghizites (14), and Ivory Coast microtektites (Glass, unpub. data) are consistent with the predictions of our model for reasonable combinations of L and v_i . For the Archean Greenstone Belt microspherules (15) and the Australasian microtektites (16), however, the smallest sizes are inconsistent with this model, requiring extremely high impact velocities and/or impactor sizes unreasonably small for the masses of the strewn fields. Perhaps the spherules deposited in the near vicinity of impact craters are smaller than predicted by our formulation because the melt droplets were subjected to a further stage of breakup when the expanding melt and vapor plume from the impact came in contact with the ambient air, establishing a strong decelerating dP/dr gradient. Detailed numerical computations of the interaction of the projectile plume with the surrounding atmosphere should be able to answer these questions.

Our model may also apply to chondrule formation, although the application to this case is more speculative. The problem is that high relative velocities between colliding bodies is required to produce highly shocked melt plus vapor as in our model, and the ejected droplets would therefore be expected to encounter other bodies with similarly high velocities and be obliterated. This mechanism might work if chondrule formation took place while nebular gas concentration was high enough to slow the droplets by drag. The timing of events, however, may be rather delicate: condensation and accretion would have to have proceeded far enough to produce reasonably large planetesimals with high relative velocities to provide sources for the chondrules, but not so far that the nebular gas density was too low to slow down the ejected drops.

REFERENCES: [1] T. J. Ahrens, J. D. O'Keefe, *The Moon* 4, 214 (1972). [2] H. J. Melosh, in *Origin of the Earth* J.H. Jones & H.E. Newsom, Eds. (Oxford, New York, 1990) p. 69.[3] A. M. Vickery, *EOS* 71, 1429 (1990).[4] J. D. O'Keefe, T. J. Ahrens, Proc. Lunar Science Conference, 8th (1977)p. 3357.[5] A. Montanari, et al., *Geology* 11, 668 (1983).[6] W. Benz, et al., *Icarus* 81, 113 (1989). [7] S. L. Thompson, H. S. Lauson, Sandia National Laboratory, Improvements in the Chart D radiation-hydrodynamic CODE III: Revised analytic equations of state (1972). [8] H. J. Melosh, *Impact Cratering: A Geologic Process* (Oxford, 1989).[9] D. E. Grady, *J. Appl. Phys.* 53, 322 (1982). [10] H. J. Melosh, A. M. Vickery, *Nature*, submitted (1991). [11] C. Koeberl, *Ann. Rev. Earth Planet. Sci.* 14, 323 (1986).[12] J. Smit, G. Klaver, *Nature* 292, 47 (1981). [13] B. P. Glass, et al. *J. Geophys. Res.* 87 Suppl., A425 (1982). [14] B. P. Glass, et al., *J. Geophys. Res. Suppl.* 88, B319(1983). [15] D. R. Lowe, et al., *Science* 245, 959(1989). [16] W. A. Cassidy, et al., *J. Geophys. Res.* 74, 1008 (1969).

PRODUCTION OF IMPACT MELT IN CRATERS ON VENUS, EARTH, AND THE MOON, A. M. Vickery and H.J. Melosh, Lunar and Planetary Lab, The University of Arizona, Tucson, AZ 85721

Impact craters imaged by Magellan clearly show large amounts of flow-like ejecta whose morphology suggests that the flows comprise low-viscosity material (1). Phillips et al. (1) suggest that this material may be either turbidity flows of very fine-grained ejecta, flows of ejecta plus magma, or impact melt. We here consider the last of these hypotheses.

If these flows are composed of impact melt, there is much more melt relative to the crater volume than is observed on the moon. Basilevsky and Ivanov (2) used the approach of Onarato et al. (3) to estimate the amount of "excess" melt that might be produced in Venusian craters. In this model the amount of melt depends on the temperature on incorporated solid clasts. Because the clasts produced by impacts on Venus are assumed to be initially hotter than those produced by impacts on earth, their effectiveness in cooling the melt is less. Basilevsky and Ivanov found that Venusian craters should contain only 50% more impact melt than similar size craters on earth, which is not enough of an enhancement to account for the observed flows.

Other mechanisms for producing relatively more melt on Venus take into account the effects of ambient temperature and pressure as well as gravity. In general material shocked from some initial temperature and pressure will, upon release to ambient pressure, be at a higher temperature than originally because of the internal energy deposited in them by the shock wave. If the release temperature is high enough, the rocks will be melted. It is logical to assume that rocks whose pre-shock temperature and pressure are higher will require lower shock pressures in order to melt upon release. The shock wave generated by an impact initially propagates into the target material as a hemisphere, and the maximum shock pressure decreases away from the center of impact. Decreasing the shock pressure required for melting (P_m), then, increases the amount of material shocked to P_m and increases the amount of melt produced.

Gravity affects the relative amount of melt produced by changing the size of the crater produced. A given impactor size and impact velocity will produce a given amount of melt, but the crater formed will be smaller on a planet with higher gravity so that the amount of melt produced for a given crater size will be larger.

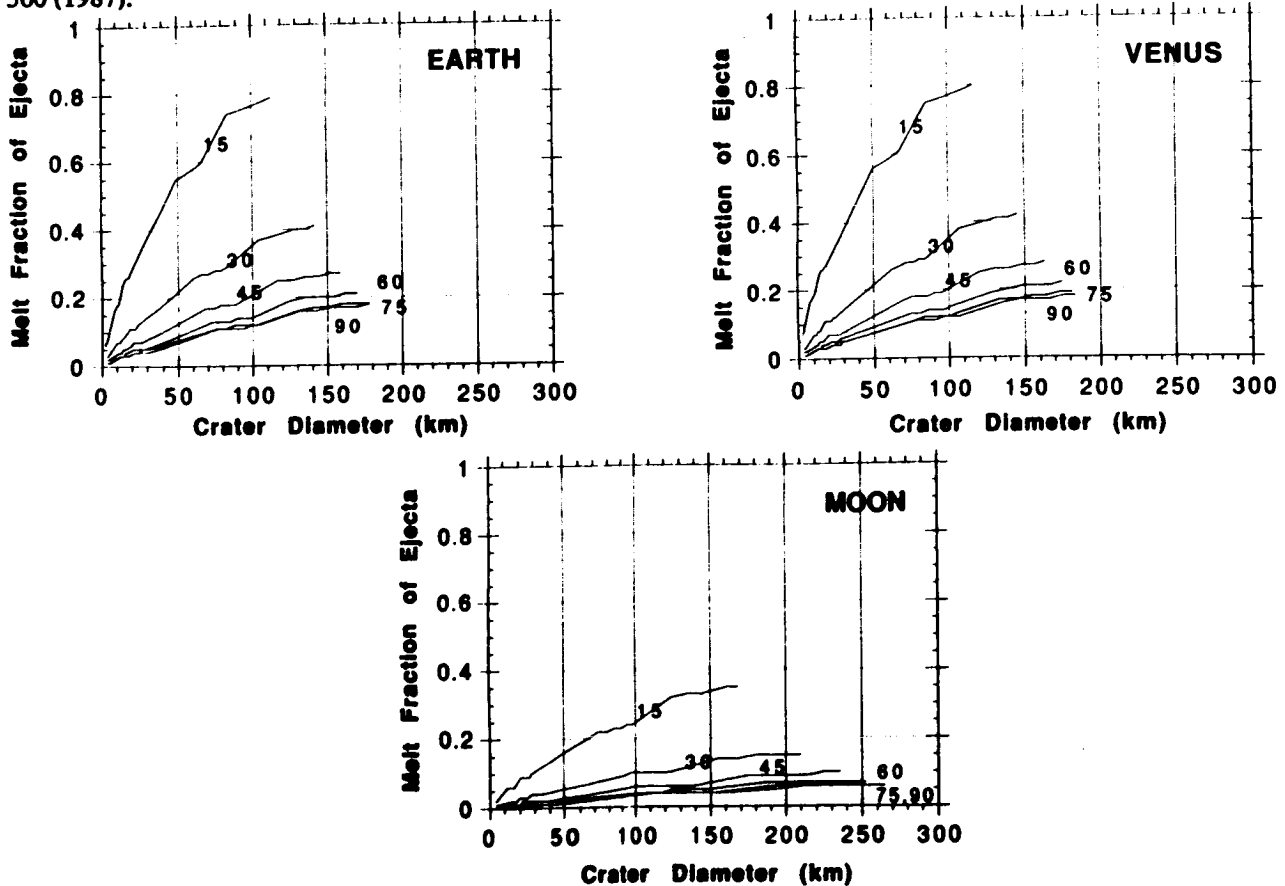
We used the ANEOS equation of state program (4) for dunite (5) to estimate the shock pressures required for melting, with initial conditions appropriate for Venus, Earth, and the moon. Assuming that ambient pressure and temperature on Earth and the moon are similar, we find that $P_m = 139$ GPa for earth and the moon and $P_m = 122$ GPa for Venus. We then developed a simple model, based on the Z-model for excavation flow and on crater scaling relations that allow us to estimate the ratio of melt ejecta to total ejecta as a function of crater size on the three bodies. If the difference in P_m is dominant in producing larger melt volumes, then the results for the moon and earth should be similar to each other and different from those for Venus, but if gravity plays the dominant role, then the results for earth and Venus should be similar to each other and different from those for the moon.

The impact of a projectile of radius a and velocity v_i impacting at an angle θ (measured from the horizontal) produces in the target a hemispherical core region in which the particle velocity is $v_{pc} = (1/2) v_i \sin\theta$. We estimate the radius of the core region, r_c , by assuming that the kinetic energy of the impact is initially equally partitioned between kinetic and internal energies of the core:

$r_c = a(2 / \sin^2 \theta)^{1/3}$. Momentum conservation requires that the particle velocity decline with increasing distance r as $v_p = v_{pc} (r_c/r)^2$, and the second Hugoniot relation gives the pressure as a function of v_p : $P = \rho_0 v_p (c + sv_p)$, where ρ_0 is the uncompressed density of the target material and c and s are material constants. Setting P equal to P_m , these two equations are solved to find r_m , the radius within which melting occurs. We next use the Z-model (6) to estimate the ratio of the amount of melt ejected to the total amount of ejecta. For $Z = 3$, appropriate for near-surface flow, we find the melt fraction, $F_m = 4 \{1 - 0.75(r_m/r_0)\} (r_m/r_0)^3$, where r_0 is the radius of the apparent transient crater. This radius is estimated from scaling relations (7,8) as $r_0 = 0.997(v_i^2 / g)^{0.22} a^{0.78} (\sin \theta)^{1/3}$.

The results of these calculations are presented in the accompanying figures, in which the melt fraction is plotted against crater size: the labels on the curves indicate impact angle in degrees. The similarity between the results for earth and Venus, and the contrast between these results and those for the moon, clearly indicate the dominant role of gravity in producing large amounts of melt for a given crater size. These results are consistent with the interpretation of the flow-like ejecta associated with Venusian craters as impact melt.

REFERENCES: 1.R. J. Phillips, et al., *Science*, submitted, (1991). 2. A. T. Basilevsky, B. A. Ivanov, *Geophys. Res. Lett.* 17, 175-178 (1990). 3. P. I. K. Onarato, D. R. Uhlmann, C. H. Simonds, *J. Geophys. Res.* 83, 2789-2798 (1978). 4.S. L.Thompson, H. S. Lauson, Sandia National Laboratory, Improvements in the Chart D radiation-hydrodynamic CODE III: Revised analytic equations of state (1972). 5.W. Benz, A. G. W. Cameron, H. J. Melosh, *Icarus* 81, 113-131 (1989). 6.D. E. Maxwell, in *Impact and Explosion Cratering* D. J. Roddy, R. O. Pepin, R. B. Merrill, Eds. (Pergamon, New York, 1977) pp. 1003-1008. 7.D. E. Gault, J. A. Wedekind, *Proc. Lunar Planet. Sci. Conf. 9th*, 3843-3875 (1978). 8.R. M. Schmidt, K. R. Housen, *Int. J. Impact Engng.* 5, 543-560 (1987).



IMPACTS AND ATMOSPHERIC EROSION ON THE EARLY EARTH; A. M. Vickery, Lunar and Planetary Laboratory, The University of Arizona, Tucson, AZ, 85715, U.S.A.

Until recently, models for the origin and evolution of the atmospheres of terrestrial planets ignored the effects of accretionary impacts. In the 1970's, however, it was suggested that heating and/or vaporization of accreting carbonaceous-chondrite-type planetesimals could result in the release of their volatile components (1,2). Modeling of this process (e.g., 3,4) strongly suggests that substantial atmospheres/hydrospheres could develop this way. During most of the accretionary process, impact velocities generally differed little from the escape velocity of the growing proto-planet because most of the collisions were between bodies in nearly matching orbits. Toward the end of accretion, however, collisions were rarer but much more energetic, involving large planetesimals and higher impact velocities (5). It has been postulated that such impacts result in a net loss of atmosphere from a planet, and that the cumulative effect impacts during the period of heavy bombardment might have dramatically depleted the original atmospheres (6,7).

Walker (8) showed that shock heating and compression of the atmosphere by the projectile during entry can eject at most a few times the mass of the air traversed, which is generally a negligible fraction of the total atmospheric mass. The solid ejecta are also unable to eject more than a few times the mass of the air traversed by the projectile (9). The vapor plume produced by a sufficiently energetic impact is, however, capable of ejecting the entire atmospheric mass lying above a plane tangent to the planet at the point of impact (10). Models developed to study atmospheric erosion by impacts on Mars and the interaction of the vapor plume produced by the KT impactor on earth (11,12) are here applied to the case of the evolution of earth's atmosphere.

The simplest model involves estimating the minimum impact velocity and impactor mass required to eject the atmospheric mass above the tangent plane (M_{tp}) and concatenating this information with estimates of the impact flux. A model for vapor plume expansion (13) gives the mean expansion velocity as $[2(\epsilon - \Delta H)]^{1/2}$, where ϵ is the initial internal energy of the vapor and ΔH is the vaporization energy. The internal energy of shocked material is $u^2/2$, where u is the particle velocity; for projectile and target of similar materials, the peak particle velocity is roughly half the impact velocity. By requiring that the mean expansion velocity exceed escape velocity, and using $\Delta H = 13$ MJ/kg for silicates, the minimum impact velocity for atmospheric blow-off on earth is ~ 25 km/sec. Simple momentum balance suggests that the minimum impactor mass for blow-off is $m^* = M_{tp}$. The evolution of atmospheric mass with time is then given by

$$\frac{dM_{atm}}{dt} = -N_{cum}(m^*, t) 4\pi R^2 M_p$$

where $N_{cum}(m, t)$ is the cumulative number of impactors with masses greater than or equal to m (per unit area and per unit time) and R is the radius of the target planet. Using the approximation that $M_{tp} = H/2R$, where H is the scale height of the atmosphere, allows this equation to be integrated to find $M/M_0 = P/P_0$, that is, the ratio of the atmospheric mass (or pressure) at any time to its current value. Using this equation, $P(-4.5 \text{ Gyr}) \cong 5 \times P_0$ for the earth (Figure 1). This contrasts sharply with the results of similar calculations for Mars, for which $P(-4.5 \text{ Gyr}) \cong 100 \times P_0$. For both planets, however, the atmospheric loss rate is greatest during heavy bombardment and has been negligible since the end of heavy bombardment.

These calculations implicitly assume that the atmosphere is distributed homogeneously with respect to zenith angle, but the atmosphere is in reality concentrated near the horizon. More detailed numerical work, which takes this inhomogeneity into account, suggests that $m^* = 5$ to $10 \times M_{tp}$. This makes atmospheric erosion by impacts less efficient. Other factors tend to make atmospheric blow-off more efficient than these

models indicate. First, the latent heat of vaporization will be added back to the internal energy of the vapor plume as the material begins to condense. Second, when the acceleration due to pressure gradients with the plume becomes comparable to the acceleration due to gravity, the plume will descend below the tangent plane and so a single impact may blow off more than Mtp. Third, these calculations ignore partial blow-off, that is, loss of less than Mtp; because partial loss may occur for smaller but more numerous impactors, the net effect may be significant. Fourth, the effect of obliquity of impact has been neglected. Experiments suggest that oblique impacts produce more vapor than normal impacts with the same impactor mass and speed (14). Furthermore, this vapor has a velocity component downrange, which means that it is directed toward the highest atmospheric mass concentration. Oblique impacts may thus be much more efficient at ejecting atmosphere than normal impacts.

REFERENCES:

- (1) Arrhenius et al. (1974) in: *The Sea*, vol 5 (E.D. Goldberg, Ed.), Wiley, p.839.
- (2) Benlow, A. and Meadows, A.J. (1977) *Astrophys. Space Sci.* **46**, 293.
- (3) Abe, Y. and Matsui, T. (1985) *Proc. Lunar Planet. Sci. Conf. 15th, Part 2, J. Geophys. Res.*, C545.
- (4) Lange, M. A. and Ahrens, T.J. (1982) *Icarus* **51**, 96.
- (5) Wetherill, G. W. (1985) *Science* **228**, 877.
- (6) Watkins, G. H. (1984) PhD Thesis, M.I.T.
- (7) Cameron, A. G. W. (1983) *Icarus* **56**, 195.
- (8) Walker, J.C.G. (1986) *Icarus* **68**, 87.
- (9) Melosh, H.J. and A. M. Vickery (1988) *EOS* **69**, 388.
- (10) Lin, S. C. (1966) *J. Geophys. Res.* **71**, 2427-2437.
- (11) Melosh, H. J. and A. M. Vickery (1989) *Nature* **338**, 487-489.
- (12) Vickery, A. M. and H. J. Melosh (1990) *Geol. Soc. Amer. Spec. Paper* **247**, in press.
- (13) Zel'dovich, Ya. B. and Razier, Yu. P. (1966) *Physics of Shock Waves and High-Temperature Hydrodynamic Phenomena*, Academic Press.
- (14) Schultz, P.H. and Crawford, D. (1987) *Lunar Planet. Sci. XVIII*, 888.

Characteristics of Ejecta and Alluvial Deposits at Meteor Crater, Arizona and Odessa Craters, Texas: Results from Ground Penetrating Radar; J.A. Grant and P.H. Schultz, Brown University, Providence, RI 02912.

Purpose: Previous ground penetrating radar (GPR) studies (1) around the 50,000 year old Meteor Crater revealed the potential for rapid, inexpensive, and non-destructive sub-surface investigations for deep reflectors (generally greater than 10 m). The present study summarizes new GPR results focusing on the shallow subsurface (1-2 m) around Meteor Crater and the main crater at Odessa and reveal: A) the thickness, distribution and nature of the contact between surrounding alluvial deposits and distal ejecta; and B) stratigraphic relationships between both the ejecta and alluvium derived from both pre and post crater drainages. These results support previous conclusions indicating limited vertical lowering (<1 m) of the distal ejecta at Meteor Crater (2,3) and allow initial assessment of the gradational state of the Odessa craters.

Approach: A SIR-3 GPR system manufactured by Geophysical Survey Systems, Inc., was used for all data collection. The present work differs significantly from previous GPR studies at Meteor Crater (1) in that both a bi-static 100 Mhz and 500 Mhz transducer was used, thereby allowing high-resolution probing of the uppermost few meters of the subsurface. Initial GPR deployment around the 1.2 km diameter Meteor Crater followed previously sampled transects crossing distal ejecta and distal diffuse drainage alluvial deposits (2,3). A metal plate was buried along several transects at variable depths to allow calculation of the dielectric constant and pulse travel time in the ejecta and alluvium. Calculated dielectric constants are 4.0-4.8 and ~7.3 and pulse travel times are 14.5 cm/ns and 11 cm/ns for the ejecta and alluvium, respectively. These values are slightly less than those derived for material beneath the crater floor (1). Subsequent transects crossed diffuse drainages west and south of the crater, portions of the distal continuous ejecta north and south of the crater, and low semi-concentric ejecta ridges 1.0R north and 0.5R south of the crater rim.

Results: Preliminary analysis of GPR data from transects through diffuse drainage deposits frequently revealed the presence of a very shallow, discontinuous reflector at depths of only ~30-45 cm. Based on stratigraphic information provided by pits excavated along the transects, this uppermost reflector probably marks the depth of discontinuous carbonate laminae in soils (Bk horizon) formed in most deposits. Variability in the depth of these characteristic soil horizons can be used to constrain local stability of the ejecta surface. The base of the alluvium in contact with the underlying ejecta was also detected as a distinct reflector in many locations despite the relatively high conductivity of these overlying calcic soil horizons. Deposit thicknesses derived from GPR data corroborate previous conclusions that where present, the alluvium forms only a 1-2 m thick veneer over the distal ejecta (4,1). In addition, GPR transects demonstrate that gradients along subsurface ejecta/alluvium interfaces are generally concordant with those on exposed ejecta surfaces emerging from beneath the deposits. Hence, there has been minimal vertical erosion of exposed ejecta during and following the emplacement of the adjacent alluvial deposits that were studied. Because many alluvial deposits appear to be latest Pleistocene in age (5,1), this statement supports our previous estimates of low erosion on the more distal ejecta (1,2). The relatively low variability, low relief nature of the buried alluvium/ejecta contact observed in the GPR transects approximates relief on the exposed ejecta and implies occurrence or little pre-deposit fluvial incision of the ejecta at least in the locations studied to date. Therefore, most of the investigated alluvial deposits occur as a depositional mantle filling topographic depressions on the ejecta created during primary ejecta emplacement. Identification of the nature of these deposits highlights the importance of depositional processes in reducing erosion of the distal ejecta.

Transects across exposed ejecta surfaces with the GPR did not reveal near-surface well-defined continuous reflectors. However, numerous local reflectors were observed at varying

depths that mark the location of buried ejecta blocks (>20–30 cm in diameter). Despite scattering and attenuation of the radar pulse by both these buried ejecta blocks and calcic soils, the bi-static 100 Mhz transducer revealed a strong, continuous reflector at depths close to those expected for the ejecta/country rock contact. Tracing the reflector beyond the edge of the continuous ejecta identified it as the contact between the upper Moqui and lower Waputki members of the Triassic Moenkopi Formation that lies beneath the ejecta (4). It is possible that similarities between the dielectric properties of the Moqui member of the Moenkopi Formation and the immediately overlying ejecta (perhaps dominated by ejected Moenkopi fragments; 4,5) precludes identification of the exact ejecta/country rock contact. Nevertheless, the Moqui/Waputki contact provides a widespread, approximate marker (generally with 1–3 m, but less in distal thin ejecta) that can be used to distinguish subtle variability (10's of cm) in primary emplacement morphology of the shallow, distal ejecta (6).

Transects crossing a low ridge north of the crater revealed a bedrock core rising to within 1 m of the surface. This conclusion is consistent with inferences drawn from previous maps of ejecta in the area (5,7) and indicates ejecta draping over pre-impact topography in the country rocks. However, a comparable bedrock core is not found within 1.5–2.0 m of the surface in transects across a segmented ridge south of the crater: either pre-crater topography is more deeply mantled by ejecta or the ridge reflects primary emplacement morphology.

The more advanced state of human modification and stage of calcic soil development around the 0.17 km diameter main crater at Odessa made GPR data collection more difficult than at Meteor Crater. A total of 28 radial and partially concentric transects around the main crater revealed that the dielectric constant of the ejecta (as determined by methods similar to those described at Meteor Crater) is ~12, whereas the radar pulse travel time is ~8–9 cm/ns. Differences between values noted at Meteor Crater may reflect the greater lithologic diversity at Odessa. These values were used to confirm ejecta thicknesses along radial trenches through the rim and near-rim ejecta (8). In addition, transects identified the extensive superposition of alluvial/eolian deposits on ejecta that are located much closer to the rim-crest than at Meteor Crater. Initial results demonstrate the potential for differentiation between artificial fill, alluvium, and ejecta and confirms the feasibility of future GPR studies to constrain the erosional history.

Summary: Preliminary GPR results from various transects at Meteor Crater and the Odessa Craters demonstrate the potential for high resolution, non-destructive evaluation of the shallow subsurface around impact craters. Transects across alluvial and distal ejecta deposits at Meteor Crater provide additional evidence supporting both the low estimates of vertical erosion and conclusions regarding the remarkably pristine preserved state. Studies at Odessa allow correlation between radar transects and stratigraphy exposed in trenches through the rim/near-rim ejecta and reveal patterns of alluvial/eolian deposition on the ejecta that are considerably different than those observed at Meteor Crater. Future GPR studies are planned to examine relationships between the timing of alluvial deposition and variations in the history of climate controlled erosion at both craters.

References: (1) Pilon, J., Grieve, R.A.F., Sharpton, V.L., Kennedy, J. and Coderre, J., 1989: p. 852–853, in *Lunar and Planet. Sci. XX* (abstracts), Lunar and Planetary Institute, Houston, Texas. (2) Grant, J.A. and Schultz, P.H., 1990: p. 433–434, in *Lunar and Planet. Sci. XXI* (abstracts), Lunar and Planetary Institute, Houston, Texas. (3) Grant, J. A., 1990: Ph.D. Dissertation: Geology, Brown University, Providence, Rhode Island, 401p. (4) Roddy, D.J., Boyce, J.M., Colton, G.W. and Dial, A.L., Jr., 1975: *Proc. Lunar and Planet. Sci. Conf.*, v. 6, p. 2621–2644. (5) Shoemaker, E.M. and Kieffer, S.E. 1974: Arizona State University Center for Meteorite Studies Publication 17, Tempe, AZ., 66p. (6) Schultz, P.H. and Grant, J.A., 1989, Styles of ejecta emplacement, Meteor Crater: p. 972–973, in *Lunar and Planet. Sci. XX* (abstracts), Lunar and Planetary Institute, Houston, Texas. (7) Shoemaker, E.M., 1960: PhD Dissertation, Geology, Princeton Univ., Princeton, N.J., 55p. (8) Evans, G.L., 1961: in *Proc. Geophys. Lab./Lawrence Rad. Lab. Cratering Symp.* (M.D. Nordyke, ed.), pt. 1, paper D, 11p., Livermore, Calif., Univ. Calif. Livermore Rad. Lab. Rept. UCRL-6438.

DEPTH/DIAMETER RELATIONSHIPS OF FRESH CRATERS WITHIN HESPERIA PLANUM, MARS.

P. J. Mouginis-Mark & J. N. Hayashi, Planetary Geosciences Division, Dept. Geology & Geophysics, SOEST, University of Hawaii, Honolulu, HI 96822.

INTRODUCTION

Meteorite impact craters represent important geological features for revealing the near-surface layers of a planetary surface. In the case of Mars, this characteristic has been proposed as a useful method to study spatial variations of such attributes as the distribution of sub-surface volatiles (1, 2) and heat flow (3). Using the Planetary Image Cartography System (PICS) software, we have completed a quantitative analysis of the geometry of fresh impact craters in the Hesperia Planum region of Mars (~23 - 38°S, 233 - 248°W), where a uniform target material and optimum viewing geometry make possible an analysis of target effects over a large geographic region. Because of the morphologic similarity to the lunar maria, it is likely that Hesperia Planum comprises a series of flood lavas that partially infilled topographic depressions within the Martian highlands (4). Measurements of partially buried crater rims suggest that the lava flows within Hesperia Planum are between 200 - 400 meters thick (5).

NEW DEPTH/DIAMETER DATA

Our measurements were made from Viking Orbiter images obtained during orbits 417S, 418S and 419S. These images provide an unusually constant range of illumination geometries (incidence angle = 63 - 80°) and spatial resolution (88 - 96 m/pixel) for a large geographic area, and to our knowledge represent the best data set that exists for the quantitative analysis of the ridged plains materials on Mars. Our sample contains 109 craters in the diameter range 1.97 - 15.44 km. Of these craters, 57 are morphologically very fresh, possessing complete rims, well preserved ejecta blankets that completely surround the parent crater, have radial striations upon the ejecta lobes or sharp distal ramparts, and have no superposed impact craters (cf. 6, 7).

Our depth/Diameter (d/D) data for the 57 pristine Hesperia Planum craters show significant scatter, but particularly for craters < 5 km dia. (Fig. 1a, 1b). We have divided the population of fresh craters into two categories, denoted as "shallow" and "deep" (the "deep" craters are ~50 - 100% deeper than the "shallow" fresh craters of the same diameter). Once the spatial distribution of these craters is investigated (Fig. 1c), differences in their distribution is evident. "Deep" craters are in general located in the northern part of Hesperia Planum that is investigated here, while "shallow" craters are more often found in the south. Clearly this relationship is non-exclusive, but the spatial pattern does appear to be a real phenomenon.

We have also investigated the possible existence of the equivalent "deep" and "shallow" craters for fresh craters larger than 6 km in diameter. From the d/D plot (Fig. 1b), it is less clear that two populations of large craters exist, so that we have separated craters that have the highest d/D ratios from those with lower ratios but the same diameter. When the spatial distribution of these two classes of large craters are compared (Fig. 1d), we see a less uniform trend. From Fig. 1d, we therefore infer that whatever property of Hesperia Planum is responsible for affecting craters smaller than 6 km diameter, this attribute does not affect larger craters.

DISCUSSION

Two mechanisms may explain this poleward shallowing of fresh craters: 1) spatial variations in the thickness of the lava flows that comprise the surface material of Hesperia Planum, and 2) latitudinal variations in the amount of volatiles in the near-surface (top 500 m?) of the target. The thickness of the Hesperia Planum lava flows is believed to vary from more than 400 m in the northwest of our study area to less than 200 m to the southeast (5), and the underlying materials are most likely to be heavily cratered terrain similar to the materials that outcrop around the perimeter of Hesperia Planum (4). In order for target properties to affect the geometry of the crater, we assume that the crater cavity must be excavated to the depth of the

interface between the lava flows and the underlying materials. The alternative method for modifying small crater geometry in Hesperia Planum is one that involves a spatially-variable concentration of volatiles in the top few hundred meters of the target at the time that the craters were formed. This idea is not new, indeed it was the preferred mechanism proposed by Cintala and Mouginis-Mark (8) to explain the variations in crater depth/diameter ratios. Fanale et al. (9) have modeled the situation where volatiles were driven towards the poles over Martian history, and the trends revealed for the small craters (Fig. 1c) would support this poleward migration model. Our current analysis of the Hesperia Planum craters may also show that for craters < 5 km in diameter, there is a gradual transition in the amount of volatiles present within the target. In particular, if a spatial variation in the amount of volatiles were the controlling factor in crater geometry, then we would expect to see a relationship between the crater's latitude and d/D .

A further test of the latitudinal variation in d/D ratio is to consider the geometry of other craters in Hesperia Planum that have well preserved rim crests but lack the continuous ejecta blankets that were a feature of the pristine craters. We have also measured the depth and diameter of 48 additional craters smaller than 6.0 km diameter that fall into this category, and have separated these craters into those that have high and low d/D ratios, using the same subdivisions that were applied to the pristine craters with ejecta blankets. When the spatial distribution of these craters without ejecta blankets is investigated, the same latitudinal variation can be seen as for the pristine craters: craters with large d/D values are typically equatorward of 30°S , while low d/D craters are found at all latitudes. From inspection of De Hon's (5) thickness map, the ridged plains at certain latitudes in this area are interpreted to vary from < 200 m in the east to > 400 m in the west. Indeed, it is apparent that all but two of the 24 craters with a large d/D ratio are equatorward of 30°S , but are formed in parts of Hesperia Planum that have estimated thicknesses between < 200 to > 400 m. Thus we feel that this east-west variation in plains thickness (which is probably the entire range of plains thicknesses within our study area) was not the primary physical characteristic of the target that caused some craters to be unusually deep or shallow. We therefore believe that the spatial variation in the amount of volatiles at shallow depth is the most reasonable explanation for the observed spatial distribution in crater geometries.

CONCLUSIONS

Our analysis of the d/D information has revealed that craters < 6.0 km dia. were most likely affected by a latitudinally variable layer of volatiles. Craters at higher latitudes are shallower than craters of the same diameter that are closer to the equator. This relationship appears to be true both for craters with well preserved ejecta blankets and for deeper craters that lack ejecta but have well preserved rims. While we are unable to quantify the change in the amount or depth of burial of the volatiles that we propose to have been responsible for the shallowing of these craters, our observations add to the current body of evidence that volatiles existed within the shallow Martian crust. Furthermore, these volatiles must have been present quite recently because they affected some of the freshest impact craters, which we infer to be quite young (<1 byrs?) due to the lack of erosion of their ejecta blankets and rim crests.

The Viking Orbiter data that we used are particularly well suited to this form of digital analysis, due to their uniform spatial resolution, large area of coverage of a single geologic unit, and the small range of illumination geometries; the use of the digital Viking Orbiter data for other areas of Mars may thus permit the qualitative inter-comparison of volatile concentrations based on the geometry of fresh meteorite craters. The depth of the largest crater with a high d/D ratio in any area may define the maximum thickness of the volatile-depleted layer during the time interval over which the craters formed. In addition, once the Mars Observer Laser Altimeter (MOLA) topographic data become available, MOLA measurements may also be useful for investigating the former distribution of volatiles on Mars.

This research was funded by NASA Planetary Geology Grant NAGW-437.

REFERENCES

- 1) Mouginis-Mark, P. (1979). *J. Geophys. Res.*, 84, 8011 - 8022.
- 2) Barlow, N. & T. Bradley (1990). *Icarus*, 87, 156 - 179.
- 3) Boyce, J. M. (1979). *Rpts. Planet. Geol. Prog.* 1978 - 1979, NASA TM-80339, 114 - 118.
- 4) Greeley, R. & J. Guest (1987). U.S. Geological Survey, Miscellaneous Map I-1802-B.
- 5) De Hon, R. A. (1985). *Rpt. Plan. Geol. Prog.*, 1984, NASA TM-87563, 242 - 244.
- 6) Pike, R. J. (1980). *Proc. Lunar Planet. Sci. Conf. 11th*, 2159 - 2189.
- 7) Mouginis-Mark, P. (1981). *Icarus*, 45, 60 - 76.
- 8) Cintala, M. & P. Mouginis-Mark (1980). *Geophys. Res. Ltrts.*, 7, 329 - 332.
- 9) Fanale, F. P., J. R. Salvail, A. P. Zent & S. E. Postawko (1986). *Icarus*, 67, 1 - 18.

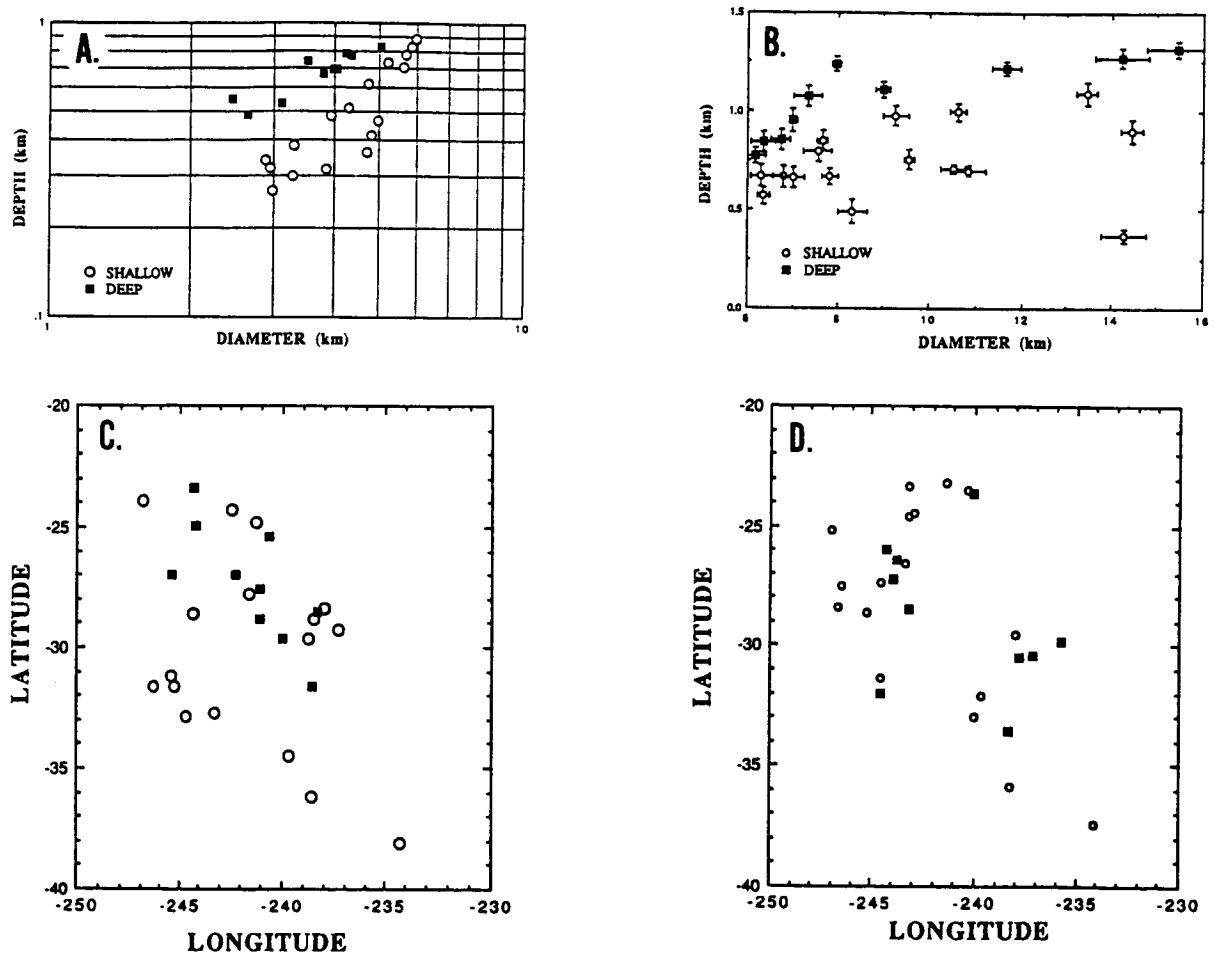


Fig. 1 A) d/D plot showing craters smaller than 6.0 km dia. Crater population has been subdivided into two classes of craters that appear to be "deep" or "shallow" for each diameter. B) d/D plot of pristine craters larger than 6.0 km in dia. Note that the scales used here are linear to expand the scatter of data points. Craters with the largest d/D ratio are called "deep" craters, while smaller d/D values are associated with "shallow" craters. C) Spatial distribution of the small fresh craters identified in Fig. 1a. Note that shallow craters are preferentially located poleward of 30°S , while "deep" craters are predominately equatorward of this latitude. D) Spatial distribution of deep and shallow fresh craters in the diameter range 6.0 - 15.44 km, as identified in Fig. 1b. Note that there does not appear to be any systematic pattern to the distribution of these two classes of crater, suggesting that the excavation depth exceeds the thickness of the near-surface volatile layer.

The Scaling of Secondary Craters. S. K. Croft, Lunar & Planetary Laboratory, University of Arizona, Tucson, AZ, 85721.

Secondary craters are common features around fresh planetary-scale primary impact craters throughout most of the Solar System. They derive from the ejection phase of crater formation, thus secondary scaling relations provide constraints on parameters affecting ejection processes. Secondary crater fields typically begin at the edge of the continuous ejecta blanket (CEB) and extend out several crater radii. Secondaries occur singly and in groups: clusters, radial chains and loops. Individual secondaries tend to have rounded rims and bilateral symmetry about an axis through the primary crater's center. Prominent secondary chains (e.g., Vallis Bouvard/Baade south of Orientale Basin on the Moon) can extend inward across the continuous ejecta blanket close to the rim. Such chains are more common on Mercury than on other planets.

A simple method for comparing secondary crater fields was employed by Allen (ref. 1): averaging the diameters and ranges from the center of the primary crater of the five largest craters in a secondary crater field. While not as much information is obtained about individual crater fields by this method as in more complete secondary field mappings (2,3,4), Allen's method facilitates rapid comparison of many secondary fields. Also, by quantifying a few specific aspects of the secondary crater field, Allen's method can be used to construct scaling relations for secondary craters, something which has not been done in the more detailed studies.

The diameters of the largest secondaries (D_s) around primaries on the Moon (1), Ganymede (5), Mercury, and Mars are shown as functions of the primary crater rim diameter (D_r) in fig. 1. The functional dependence of D_s on D_r is remarkably consistent on all four planets: $D_s \approx 0.07 D_r^{0.67}$. The mean ranges of the largest secondaries (R_s) on all four planets are also very similar and can be represented by: $R_s \approx 3 D_r^{0.86}$. (Complete numerical analyses are given in ref. 6). These empirical results may be quantitatively interpreted. The ejecta scaling theory of (7) indicates that the ballistic range of bits of ejecta scale with the diameter (D_p) of the gravity-scaled primary crater: $R_s \propto D_p^1$. Virtually all of the craters in the sample are complex, thus the empirical relation (8) between the gravity-scaled transient crater rim and the slump-enlarged final crater rim ($D_p \propto D_r^{0.85 \pm 0.05}$) can be applied, yielding: $R_s \propto D_r^{0.85 \pm 0.05}$, in agreement with the observed relation. Similarly, combining the crater-scaling relation of (8) with the ballistic equation and the secondary range relation yields: $D_s \propto D_p^B a_s^{1-B}$, where B is the radius-scaling exponent of (8), and D_s and a_s are, respectively, the secondary crater rim diameter and secondary impactor radius. Various assumptions can be made concerning the scaling of a_s to transform the above relation into a form comparable with observation. Adopting the spall model of (9), a model frequently invoked to account for secondary impactors, yields: $D_s \propto D_p^{1-(n-1)B}$, where n is the velocity exponent in the relation between ejection velocity and distance from point of impact. Inserting the probable values of n between 2 and 3, B = 0.17 (8), and complex rim diameter yields: $D_s \propto D_r^{0.56 \text{ to } 0.71}$. This is inconsistent with observation, indicating that the secondary impactors are not spalls. This result is consistent with the computational and experimental results of (10), who were also unable to confirm the spall model. Alternatively, assuming $a_s \propto a_p$, the primary impactor radius, yields: $D_s \propto D_p^{1+B}$, or $D_s \propto D_r^{0.99}$, again inconsistent with observation. An assumption that works is: $a_s \propto D_p$, which yields $D_s \propto D_p^1$, or $D_s \propto D_r^{0.85}$ for complex craters. Empirical ejecta scaling relations developed in (6) imply that the ejecta curtain fragments at a thickness that also scales with D_p to form the edge of the CEB. The correspondence in scaling and geometry between the CEB edge and secondary impactor radii suggests that both originate in the same fragmentation process in the cratering flow field.

Secondary crater fields are seldom seen on the smaller icy satellites. Secondary crater chains have been proposed for Arden on Miranda (11) and possibly for Odysseus on Tethys (6, prompted by the maps of 12), against which two objections have been raised: 1) fragments forming secondary craters move much too fast to be retained on any middle-sized icy satellite (13), and 2) large secondary craters cannot form from very slow moving (< 100 m/s) ejecta because of the low cratering efficiencies (ratio of crater volume to impactor volume) near unity; secondary mounds are the more likely outcome (14). The first objection is based on the assumption that the secondary impactors are the spalls of (9), an assumption indicated as incorrect by these results. But in either case, the computed impact velocities of impactors forming undisputed secondaries on the terrestrial planets are not absolute, relating, for example, to the primary impactor velocity, but scale with the primary crater diameter (as required by ejecta scaling theory (7)), reaching as low as 50 m/s in Allen's lunar data set (1). As long as gravity scaling applies, primary craters on smaller icy satellites should eject secondary-forming fragments at velocities low enough to be retained and form secondary craters. The validity of the second objection was tested by measuring the diameters and ranges of craters in prominent radial chains on the Moon, Mercury, and Ganymede, and the proposed chains on Miranda, and computing the cratering efficiencies (PI-V) using the scaling of (8). The resulting PI-V's are shown as functions of normalized range in Fig. 2. As may be seen, the cratering efficiencies of all large secondaries are near unity, but recognizable secondary craters are formed nonetheless. Thus the suggestion that secondary mounds would form for PI-V's near unity is not supported by

the data. The proposed Arden chains show the same absolute PI-V's and radial trends as the recognized secondary chains to which they were first compared (5). This result is consistent with the explicit cancellation of gravity out of ejecta scaling (7) and the secondary crater scaling relations derived above, which implies that, as long as gravity scaling applies, secondaries should form on arbitrarily small moons. Thus the Arden chains cannot be rejected as secondaries by scaling arguments. Similarly, secondary crater fields should be observed on smaller icy satellites. Where are they? A compilation given in (6) comparing secondary crater diameters predicted from the empirical relation in Fig 1 with resolutions in the best Voyager images of the smaller icy satellites indicates that, in most cases, the secondaries are at or below the limit of resolution. In those few cases where the predicted secondaries should be seen, they either are seen, or are found on surfaces too heavily cratered to confidently identify secondaries. Thus it is proposed that secondaries do occur on all icy satellites where gravity scaling applies, a proposal that will be tested by the Cassini spacecraft.

References. 1) Allen (1979) GRL 6:51. 2) Gault et al. (1975) JGR 80:2444. 3) Schultz & Singer (1980) PLPSC 11th, p. 2243. 4) Vickery (1986) Icarus 67:224. 5) Croft (1988) LPS XIX, p. 221. 6) Croft (1991), Icarus, submitted. 7) Housen et al (1983) JGR 88:2485. 8) Schmidt & Housen (1987) Int J Imp Eng 5:543. 9) Melosh (1984) Icarus 59:234. 10) Holsapple, K.A. & K.Y. Choe (1988) LPS XIX, p. 501-502. 11) Croft (1987) NASA TM 89810, p. 6. 12) Moore & Ahern (1983) PLPSC 13th, JGR 88(supp):A577. 13) Chapman & McKinnon (1986) Satellites, p. 492, U. of Ariz Press. 14) McKinnon & Chapman (1990) Uranus, in press, U of Ariz Press.

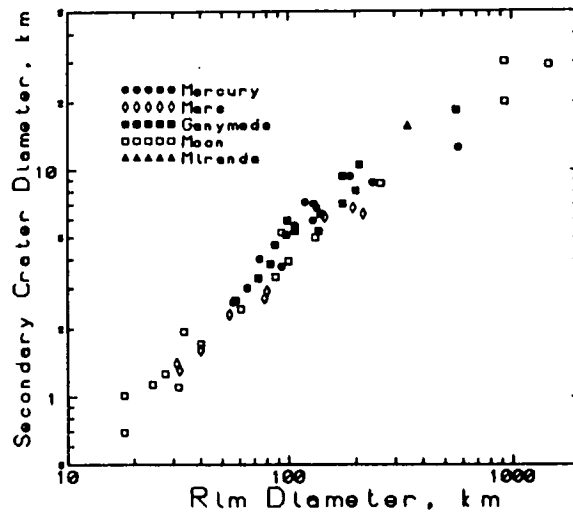


Figure 1. Mean Largest Secondary Crater Diameter vs. Primary Crater Rim Diameter.

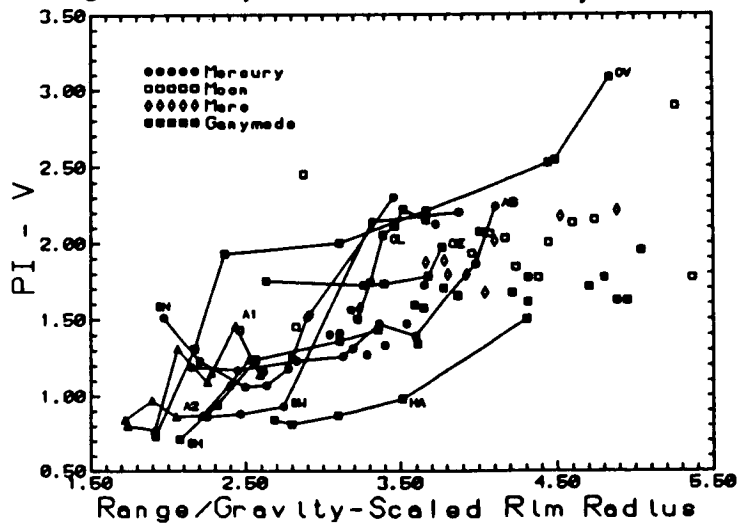


Figure 2. Cratering Efficiency (PI-V) vs. Normalized Range for Largest Secondaries in Fig. 1 and Selected Radial Crater Chains (connected symbols): OE, OL, and OV = Orientale (Moon); SH = Schrodinger (Moon); SW, SN = Strindberg (Mercury); AB = Ahmed Baba (Mercury); HA = Halius (Ganymede); A1, A2 = Arden (Miranda).

CHEMICAL FRACTIONATION OF SIDEROPHILE ELEMENTS IN IMPACTITES
FROM AUSTRALIAN METEORITE CRATERS

M. Attrep, Jr., C. J. Orth, and L. R. Quintana, Los Alamos National Laboratory, Los Alamos, NM 87545; C. S. Shoemaker and E. M. Shoemaker, U.S. Geological Survey, Flagstaff, AZ 86001; S. R. Taylor, The Australian National University, Canberra, ACT 2601, Australia.

The abundance pattern of siderophile elements in terrestrial and lunar impact melt rocks has been used extensively to infer the nature of the impacting projectiles [1-3]. An implicit assumption made in previous investigations is that the siderophile abundance ratios of the projectiles are approximately preserved during mixing of the projectile constituents with the impact melt. As this mixing occurs during flow of strongly shocked material at high temperature, however, there are grounds for suspecting that the underlying assumption is not always valid. In particular, fractionation of the melted and partially vaporized material of the projectile might be expected because of differences in volatility, solubility in silicate melts, and other characteristics of the constituent elements. Impactites from craters with associated meteorites offer special opportunities to test the assumptions on which projectile identifications are based and to study chemical fractionation that has occurred during the impact process.

Impactites have been found at 4 of the 15 known terrestrial meteorite crater localities: (1) Meteor Crater, Arizona, (2) the Wabar craters, Saudi Arabia, (3) the Henbury Craters, Northern Territory, Australia, and (4) Wolfe Creek Crater, Western Australia. At all four localities with impactites, the associated meteorites are irons. In the course of geologic investigations of Australian impact structures, the Shoemakers discovered rare impactites at Wolfe Creek Crater [4] and carried out a survey of the fairly abundant Henbury impactites. They provided samples of these impactites for the present investigation together with a representative suite of ten specimens of the target rocks at Wolfe Creek Crater. Splits of four samples previously analysed for major elements by S. R. Taylor were used to study the target rocks at the Henbury Craters.

Wasson has identified the meteorites at both Wolfe Creek Crater and Henbury Craters as type IIIAB irons [5]. We analysed a Wolfe Creek iron collected by S. R. Taylor and a Henbury iron collected by C. S. Shoemaker. Although both meteorites were partly oxidized, we were able to isolate fresh metal portions for analysis. Our measurements are consistent with those of Wasson [6].

Instrumental neutron activation analysis was used to determine abundances for about 40 major, minor and trace elements that included the siderophiles Co and Ni. Abundances for Au and the heavy platinum group elements (Os, Ir, Pt) were determined by radiochemical separations following neutron activation. Siderophile abundances and relative fractionation data are presented in Table 1; abundances shown for impactites are net abundances after subtraction of the average background abundances of the target rocks. For our independent classification of the two meteorites we also measured Ga, As, and W. For Wolfe Creek, we found Ga=20 ppm, As=9.6 ppm and W=1.5 ppm; for Henbury, Ga=19 ppm, As=3 ppm, and W=1.6 ppm. The Wolfe Creek meteorite is an Ir-poor type IIIAB (B) and Henbury is an Ir-rich type IIIAB (A).

The meteoritic component of the impactites analysed ranges from about 0.06% to 10%. Except for Au at Henbury, the siderophile abundances are much greater in the impactites than in the average target rocks. Therefore, estimation of the meteoritic component of most siderophiles in the impactites is fairly insensitive to the estimate of the background abundance in the target rocks. Large fractionation relative to Ni is observed for most noble metals in the impactites. Platinum group elements tend to be depleted relative to Ni by about an order of magnitude in Wolfe Creek impactites, and gold is depleted by two orders of magnitude. The pattern of fractionation at Henbury is rather similar to that at Wolfe Creek, even though the abundances of Pt group elements are drastically different in the two meteorites. At Henbury, where the meteorite is Pt rich, Pt is less strongly fractionated in the impactite. Cobalt is consistently enriched relative to Ni in both Wolfe Creek and Henbury impactites.

The strong fractionation observed in the impactites from the Australian craters suggests that caution should be exercised in deducing the nature of impacting projectiles from siderophile element patterns in impact melt rocks or in suevites. The amount of fractionation may depend on many factors, including the velocity of the projectile, the temperature history of both the projectile and target material, oxidation state of the target material, the size of the crater, and the degree to which melt rocks or fallout units are representative of the ejected material. Siderophile abundance patterns resembling those of CI chondrites observed at some large craters such as East Clearwater Lake [7] suggest that, in favorable cases, the fractionation may be small. On the other hand, the high frequency with which impactors have been identified as differentiated objects [8,9] suggests to us that projectiles may have been misidentified in a number of cases because of unrecognized fractionation effects [10].

References:

- [1] Hertogen, J., Janssen, M.-J., Takahasi, H., and Anders, E., 1977, Proc. Eighth Lunar Planet. Sci. Conf., Houston: New York, Pergamon Press, p. 17-48. [2] Palme, H., Janssens, M.-J., Takahasi, H., Anders, E., and Hertogen, J., 1978, Geochim. Cosmochim. Acta, v. 42, p. 313-323. [3] Palme, H., 1982, in Silver, L. T., and Schultz, P. H., eds., Geol. Soc. America Spec. Paper 190, p. 223-233. [4] Shoemaker, E. M., and Shoemaker, C. S., 1987, Geol. Soc. America Abs. with Programs, p. 842-843. [5] Wasson, J. T., 1974, Meteorites: Classification and Properties, Springer Verlag, 316 pp. [6] Wasson, J. T., 1985, Meteorites: Their Record of Early Solar System History, W. H. Freeman and Co., New York, 267 pp. [7] Palme, H., Gobel, E., and Grieve, R. A. F., 1979, in Proc. Tenth Lunar Planet. Sci. Conf., Houston: New York, Pergamon Press, p. 2465-2492. [8] Grieve, R. A. F., in Silver, L. T., and Schultz, P. H., eds., Geol. Soc. America Spec. Paper 190, p. 25-37. [9] Grieve, R. A. F., Sharpton, V. L., Goodacre, A. K., and Garvin, J. J., 1985, Earth Planet. Sci., Lett., v. 176, p. 1-9. [10] Shoemaker, E. M., and Wolfe, R. F., 1986, in Smoluchowski, R., Bahcall, J. N., and Matthews, M. S., eds., The Galaxy and the Solar System, Tucson, Univ. Arizona Press, p. 338-386.

Table 1. Siderophile element abundances and relative fractionations in meteorites, impactites and target rocks at Wolfe Creek Crater, Western Australia, and at Henbury Craters, Northern Territory.

Wolfe Creek Crater

Sample	Ni (ppm)	Co (ppm)	Os (ppb)	Ir (ppb)	Pt (ppb)	Au (ppb)
meteorite	86000	5100	6.8	24	1760	1220
impactite-A	3360*	-	<0.08*	0.134*	-	-
impactite-B	6920*	580*	-	0.120*	15.1*	1.17*
background (ave.)	2	1.5	<0.01	0.007	~0.13	0.12
(high)	6.9	4.5	<0.01	0.011	~0.13	0.12
(low)	0.9	0.4	-	0.005	-	-

Fractionation relative to Ni: Z (impactite/meteorite)
Ni (impactite/meteorite)

impactite-A	1	-	<0.3	0.14	-	-
impactite-B	1	1.42	-	0.062	0.11	0.012

Henbury Craters

meteorite	70600	5200	13200	15000	13500	400
impactite-A	161*	21.4*	5.25*	8.05*	20.6*	~0.03*
impactite-B	61*	12.8*	1.53*	2.64*	-	-
impactite-C	342*	38.9*	5.37*	13.9*	39.3*	~0.03*
background (ave.)	20	8.9	<0.02	0.017	~0.1	0.64
(high)	23	11.3	<0.02	0.027	~0.1	0.64
(low)	15	7.2	-	0.013	-	-

Fractionation relative to Ni

impactite-A	1	1.87	0.181	0.246	0.68	~0.04
impactite-B	1	2.83	0.133	0.202	-	-
impactite-C	1	1.52	0.084	0.190	0.60	~0.01

*Abundances shown for impactites are net abundances after subtraction of average backgrounds. For Os, Pt and Au, only one target rock background determination was performed for each impact site.

IGNEOUS INTRUSION MODELS FOR FLOOR FRACTURING IN LUNAR CRATERS. R.W. Wichman and P.H. Schultz, Dept. of Geological Sciences, Brown University, Providence, RI 02912.

INTRODUCTION: Lunar floor-fractured craters are primarily located near the maria (1,2,3) and frequently contain ponded mare units and dark mantling deposits (3,4,5). Fracturing is confined to the crater interior, often producing a moat-like feature near the floor edge, and crater depth is commonly reduced by uplift of the crater floor (3). Although viscous relaxation of crater topography can produce such uplift (6,7,8), the close association of modification with surface volcanism supports a model linking floor fracture to crater-centered igneous intrusions (3,4,5). A previous study (3) proposed several intrusion models on the basis of observed crater morphology and elevation data. In this study, we quantitatively explore the consequences of two intrusion models for the lunar interior. The first model is based on terrestrial laccoliths and describes a shallow intrusion beneath the crater. The second model is based on cone sheet complexes where surface deformation results from a deeper magma chamber. In this abstract, we describe both models, their fit to observed crater modifications and possible implications for local volcanism.

THE LACCOLITH MODEL: Laccoliths are nearly circular, tabular to domical intrusions that develop from an initial sill-like form by the uplift of overlying strata (9,10,11). Deformation is concentrated along the periphery of the intrusion in the form of either a monoclinial fold or an arcuate, near-vertical fault, depending on the ductility of the country rock (11,12). In certain cases, peripheral dikes extend upward and away from the laccolith edge (12). The nature of deformation changes with time, since failure around the intrusion modifies the interaction of the intrusion with the confining medium. For the initial sill, deformation is localized by stress concentrations at the edge of the intrusion and depends on P_d , the difference between total magma pressure and local lithostatic pressure (10). As the sill grows, the net upward load on the overburden increases in proportion to the floor area and eventually exceeds the rigid strength of the crust (9,11). If the overlying section flexes as a layered sequence of elastic plates, the extent of uplift is related to the size of the intrusion, the driving pressure, P_d , and the effective elastic thickness of the overburden, T_e (12). Later, after failure separates the uplifted block from its surroundings, this block is totally supported by the intrusion. The magma column in the laccolith balances the driving pressure in the feeder dike and intrusion thickness is directly related to P_d (12).

Deformation over a laccolith can account for many aspects of floor fracturing. The uplift of strata above a laccolith resembles the observed uplift of crater floors. Ring faulting near the edge of a laccolith can yield the observed moat structures and associated volcanic vents. Extension of peripheral concentric dikes from the intrusion could explain the degradation and concentric graben observed outside the crater rim in the most extreme cases of lunar floor fracture (3). The relation between driving pressure and lithostatic pressure, however, may confine most deformation to crater interiors: increased lithostatic pressure beneath a topographic rise reduces P_d and should diminish uplift of the crater rim. Finally, the range of modified crater forms on the Moon is consistent with the derived sequence of deformation. The least modified floor-fractured craters, showing little uplift and no moat features, may represent simple flexure with minor peripheral faulting, whereas the apparent magmatic equilibration of floor elevations in more modified craters (3) would result from late stage magmatic support of the roof block.

From the model, floor fracturing can provide information about the lunar interior. First, since elastic deformation does not thin the roof block, uplift provides an estimate for intrusion thickness. Consequently, if the uplifted floor diameter delineates the laccolith size, floor uplift reflects the magmatic driving pressure and the effective elastic thickness. Since T_e describes flexure of the floor plate as a single elastic layer, it represents the minimum possible depth to the intrusion. The uplifted section, however, probably does not deform as a single elastic layer and the true stratigraphic thickness for a layered sequence can be as much as $-6T_e$ (12), a maximum estimate for intrusion depth. Driving pressure represents the magmatic overpressure in an intrusion and is related to the magma column length beneath that intrusion (10). Since mare basalt magmas appear to be denser than the lunar crust, near-surface magmas on the Moon require a magma source at depth in the mantle (13); this mantle depth can be estimated from P_d if the crustal thickness and magma density are known.

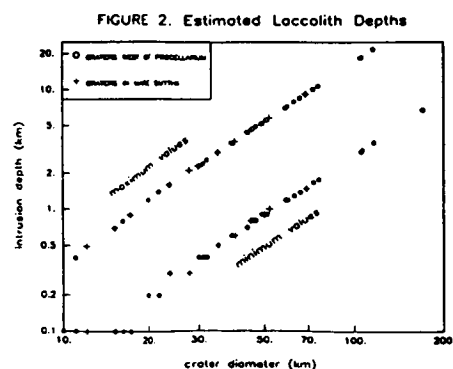
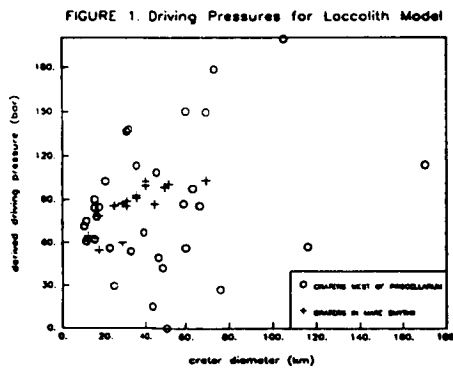
These relations have been applied to floor-fractured craters in Mare Smythii and west of Oceanus Procellarum (figure). The uniform driving pressures in Smythii are consistent with a common magma source of regional extent beneath the old impact basin. In contrast, the driving pressures west of Procellarum are widely scattered, with the lowest pressures corresponding to points adjacent to or isolated from clusters of floor-fractured craters. Since confined viscous flow causes a lateral pressure drop along a conduit (10), the distribution west of Procellarum could reflect the localization of subsurface magmas to a few areas revealed by extensive crater modification. The derived range of intrusion depths for both regions (figure) is consistent with both the emplacement depths of terrestrial laccoliths ($-3-4$ km, 14) and hydrostatic models of mare magma columns (magma depths less than $4-6$ km, 13). The larger crater diameters west of Procellarum, however, require slightly deeper intrusions since T_e is also a function of intrusion size. Hydrostatic magma columns rise higher if the mantle is shallow; hence, the regional differences in both intrusion depth and P_d may mirror

mantle topography. The uniformly shallow magmas in Smythii lie over a broad (~360 km dia), uniform mantle uplift at the center of the impact basin. West of Procellarum, however, the crust is thicker and no single basin dominates mantle topography. Instead, floor fracturing clusters near individual large craters (70-170 km dia) which may have perturbed the upper mantle.

Terrestrial laccoliths differ from the observed crater modifications in two ways. First, laccoliths on Earth rarely exceed 10 km in diameter, whereas the modeled diameters for floor fracturing range from ~10 km to over 60 km. This discrepancy, however, may reflect the broadly fractured nature of impact breccias and weaker confining pressures due to the lower lunar gravity. Second, coherent uplift of the crater floor as a whole contrasts with the uniform size of terrestrial laccoliths. Once terrestrial laccoliths have sufficient leverage to lift overburden, vertical growth occurs at the expense of lateral expansion (12). Since lunar rocks are colder and drier than terrestrial rocks, they should be less ductile; hence ring faulting should develop soon after uplift begins and also prevent further lateral growth. The observed floor uplift/crater rim diameter ratios, however, indicates that uplift on the Moon occurs only when intrusions approach the size of the crater floor. Nevertheless, such behavior might be expected if lateral expansion of a sill is unhindered beneath the crater floor but confining pressures under the crater rim, due to either the edge of brecciation or surface topography, force vertical rather than horizontal growth.

THE CONE SHEET MODEL: On Earth, cone sheet complexes are composed of inwardly-dipping, sub-parallel dikes exposed in a circular or elliptical plan typically 10-20 km in diameter (15,16). Individual sheets are only 3-15 m thick, but they usually form a belt 1-3 km wide around a central region with few intrusions (16). Anderson estimated the uplift across one such complex to be ~1100 m (16). While local stratigraphy controls laccolithic intrusions, cone sheets result from magma injected into axially symmetric fractures induced by dilation of a central magma chamber at depth (15,16,17). The depth and the small size of the magma chamber make the resulting fractures relatively insensitive to surface topography (15). Since cone sheet geometry is nearly invariant, the only real parameter that can be derived from this model is the depth of the source intrusion. If the edge of the floor plate marks the surface trace of the innermost cone sheets, then these sheets probably dip down to the source at between 45° and 70° (16).

The combined offsets across a swarm of cone sheets can produce the required floor uplifts for lunar floor-fractured craters. The concentration of deformation into an annulus surrounding a relatively coherent central block also resembles the concentration of fracture in moats around the crater floor plate, with cone sheets feeding the floor volcanism that preferentially occurs near the floor edge (3). The mean floor diameter west of Procellarum (~36 km) indicates magma chamber depths of ~18-50 km, while mean intrusion depths are ~10-21 km in Smythii. The maximum depths are on the order of the estimated crustal thicknesses (18) for both regions, whereas shallower intrusion depths (derived for the smallest craters) might reflect intrusions tapping major cone sheets centered on a deeper source intrusion beneath adjacent, larger craters.



Two difficulties, however, limit modeling floor fracture by cone sheet emplacement. First, strong radial components commonly associated with cone sheet formation (17,19) are typically absent from lunar patterns of floor fracture (3). Second, cone sheet deformation centered on a crater is difficult to envision. On Earth, impact fractures and slump faults do not reach depths comparable to the floor radius (20,21) and the depth of brecciation is similarly shallow (20). Since the derived source intrusion depths on the Moon exceed the floor block radius, there is no clear-cut structural control to center the cone sheet source beneath a crater. Although the derived depths may be consistent with a source at the base of the crust, only the largest crater-forming impacts could disturb the crust-mantle boundary and create a mantle uplift or trap for subsequent magma accumulation. Deep central intrusions, however, may not be necessary; rather, shallower intrusions may reactivate the slump faults, thereby producing cone sheet-like dikes beneath the crater rim. In particular, this might occur near laccolithic intrusions, since the peripheral dikes surrounding a laccolith should intercept these faults at depth.

REFERENCES: 1) Brennan, W.J. (1975) *Moon* 12, 449-461. 2) Whitford-Stark, J.L. (1974) *Nature* 248, 573-575. 3) Schultz, P.H. (1976) *Moon* 15, 241-273. 4) Young, R.A. (1972) *Apollo 16 Prelim. Sci. Rep.*, NASA SP-315, 29-89-29-90. 5) Bryan, W.B. et al (1975) *PLPSC* 6, 2563-2570. 6) Danes, Z.F. (1965) *Astronom. Stud. Ann. Prog. Rep. A (1964-1965)*, 81-100. 7) Scott, R.F. (1967) *Icarus* 7, 139-148. 8) Hall, J.L. et al (1981) *J. Geophys. Res.* 86, 9337-9552. 9) Gilbert, G.K. (1877) *Report on the Geology of the Henry Mountains*. 10) Johnson, A.M. and Pollard, D.P. (1973) *Tectonophy.* 18, 261-305. 11) Corry, C.E. (1988) *Geol. Soc. Amer. SP-220*. 12) Pollard, D.P. and Johnson, A.M. (1973) *Tectonophy.* 18, 261-309. 13) Solomon, S.C. (1975) *PLPSC* 6, 1021-1042. 14) Jackson, M.D. and Pollard, D.P. (1988) *Geol. Soc. Amer. Bull.* 100, 117-139. 15) Anderson, E.M. (1936) *Proc. Roy. Soc. Edin.* 56, 128-157. 16) Phillips, W.J. (1974) *Tectonophy.* 24, 69-84. 17) Koide, H. and Bhattacharji, S. (1975) *Econ. Geol.* 70, 781-799. 18) Brati, S.R. et al (1985) *J. Geophys. Res.* 90, 3049-3064. 19) Komaru, H. (1987) *J. Volcan. Geotherm. Res.* 31, 139-149. 20) Pohl, J. et al (1977) *Impact and Explosion Cratering*, pp. 343-404. 21) Scott, D and Hajnal, Z. (1988) *Meteoritics* 23, 239-246.

MAGNETIC EFFECTS OF LARGE-SCALE IMPACTS ON AIRLESS PLANETARY BODIES. L. L. Hood and Z. Huang, Lunar and Planetary Laboratory, University of Arizona, Tucson, Arizona 85721.

Background: The analysis of lunar orbital and sample data combined with laboratory measurements of impact-produced plasmas suggest that large-scale impacts on planetary surfaces may have had significant magnetic effects^{1,2}. These effects may potentially explain part or all of lunar crustal magnetization and, by extension, may be responsible for producing paleomagnetism on other airless silicate bodies in the solar system. We report here further theoretical studies of the magnetic field and remanent magnetization effects of basin-scale impacts on the Moon. The specific case of a Moon exposed to the solar wind plasma flow and its embedded magnetic field is treated. It is shown that maximum compressed field amplitudes occur antipodal to the impact point in agreement with the observed tendency for orbital magnetic anomalies to be concentrated antipodal to young large lunar basins³. Generalization of these results to include magnetic effects of impacts on other airless or nearly airless planetary bodies in the solar system (e.g., Mercury and outer planet satellites) is the subject of current work but is not specifically addressed here.

Model Calculations: To provide a basis for calculating magnetic field effects, numerical models of the vapor plume expansion following a basin-scale impact on a lunar-sized spherical body were constructed. An initial calculation was performed for a gabbroic anorthosite impactor and target using only an ideal gas equation of state; partial condensation of the vapor during the cloud expansion was therefore not accounted for. (Later work including the effects of partial condensation did not produce major alterations of the cloud evolution.) Initial conditions were set for a 15 km/s vertical impact using peak shock states and pressure thresholds for incipient and complete vaporization.⁵ The initial specific internal energy was 2.8×10^{11} erg/gm and the initial mass density was 6.43 gm/cm³. Approximately 41% of the material exposed to peak shock pressure was estimated to be vaporized. As a first approximation to the radial decay of shock pressure from the impact point, it was assumed that the peak pressure applies out to a distance of ~ 2 impactor radii beyond which the pressure falls to zero. Under these assumptions, a spherical impactor with radius 68 km produces a total vaporized mass of 2.77×10^{22} gm and a final basin diameter of about 912 km according to the Schmidt-Holsapple scaling law. Results showed that expansion of the vapor cloud periphery occurs at a velocity comparable to or somewhat larger than the impact velocity. For example, after 64 seconds, the cloud periphery has expanded approximately one-third of the way around the Moon. The mass density within the cloud falls off exponentially with radial distance while the specific internal energy is relatively constant but decreases monotonically with time. After approximately 410 seconds, the outer periphery of the cloud had begun to converge at the antipode of the impact point.

Magnetic Field Effects: Using the output of the vapor cloud calculations described above, the possible modes of magnetic field amplification and generation in basin-scale lunar impacts were investigated. Impact field generation mechanisms can be divided into two classes: (1) Spontaneous field generation within the impact plasma cloud due to thermal pressure gradients¹; and (2) field generation external to the cloud as the expanding ionized gas encounters ambient plasmas and fields.²

Transient electrical currents are generated in the plasma cloud itself by strong tem-

perature and density gradients combined with the basic difference in ion and electron mobilities. A scaling analysis of the governing equations yielded an estimate for the saturation magnetic field amplitude, $|B_s| \sim (ck/e)(\Delta T/VL)$, where c is the speed of light, k is Boltzmann's constant, e is the electron charge, $\Delta T/L$ is a typical cloud temperature gradient, and V is a representative gas expansion velocity. Although generated field amplitudes can be large for laboratory-scale events, $|B_s|$ decreases as L increases while ΔT and V remain relatively constant. In the basin-scale impact plasma cloud calculation described above, after 64 seconds the size of the cloud is comparable to the lunar diameter. Maximum temperatures near the impact point are $\sim 10^4$ K and decrease to much smaller values in a distance of ~ 1000 km. Typical expansion velocities are ~ 10 km s $^{-1}$. Substitution into the above expression yields $|B_s| \sim 10^{-6}$ G. Even at times of < 10 seconds after the impact, the estimated field amplitudes remain $< 10^{-4}$ G. It is therefore concluded that large-scale impacts on airless planetary surfaces are unlikely to produce significant large-scale magnetizing fields within the impact plasma cloud itself.

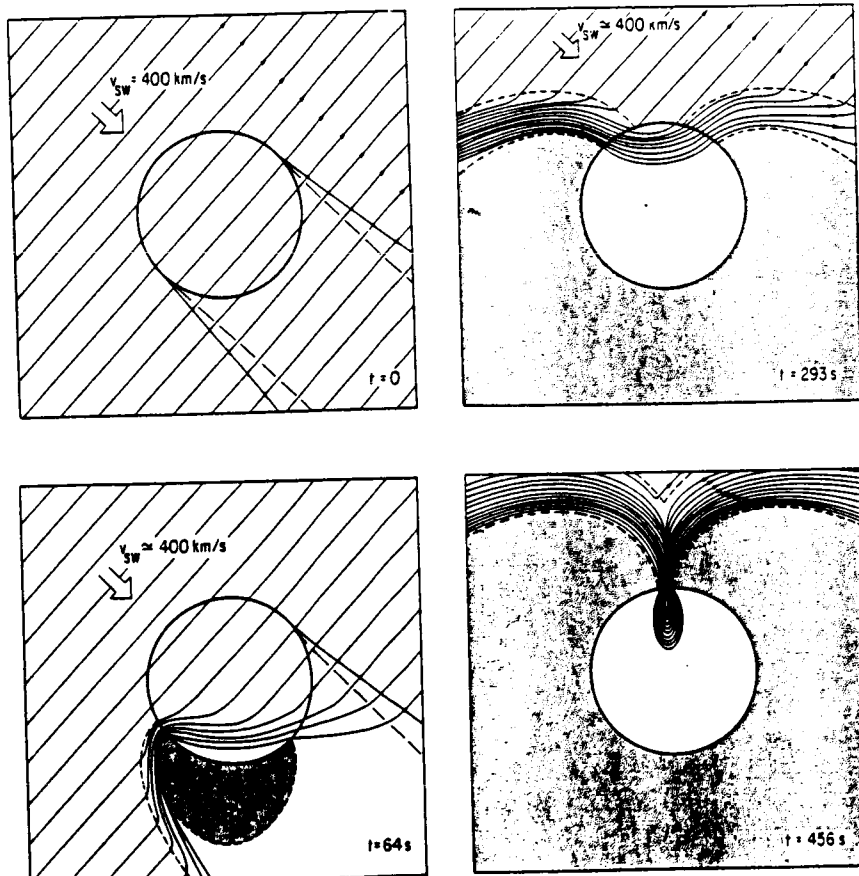
Thus far, we have undertaken one calculation of external field generation for a simplified but realistic ambient lunar plasma environment. The results are summarized in the Figure. The environment considered is the case in which the Moon is directly exposed to the outflowing solar wind plasma and its embedded magnetic field. Since the impact plasma cloud is partially ionized, the interaction of the solar wind with an expanding impact plasma cloud will initially resemble that between the solar wind and a planetary ionosphere. In particular, an MHD bow shock wave will develop ahead of the expanding cloud. Within the shocked layer, the field is amplified while outside the shock wave, the plasma and field environment is unperturbed. In order to determine the bow shock structure and shape, we have taken the approach of scaling the numerical gasdynamic results of Spreiter and Stahara⁴ for the Earth's bow shock with $M_s = 8$ and $\gamma = 5/3$, where γ is the usual ratio of specific heats. The outer dashed line in each plot of the Figure indicates the scaled location of the bow shock upstream of the impact plasma cloud at different times after the impact. In order to calculate the magnetic field change with time behind the bow shock wave, we have adopted a kinematic procedure in which the magnetic field exerts no influence on the solar wind flow past the impact plasma cloud. The incident magnetic field is assumed to be in the plane of the bow wave as shown in the Figure and to have an upstream magnitude of B_∞ . Induced fields in the lunar interior were neglected in this initial calculation. The resulting magnetic field lines are plotted in the Figure. As the bow shocks converge in the antipodal zone, the above procedure becomes invalid and the magnetic field amplitude is simply estimated from conservation of flux. No provision for the (likely) occurrence of plasma instabilities, reconnection of magnetic fields, etc. at the antipode has yet been made in these calculations. In any case, the results show a substantial magnetic field amplification at the basin antipode as the impact plasma converges approximately 400 seconds after the simulated impact.

Remanence Acquisition Mechanisms: The time scale for expansion of the impact plasma cloud to the antipode as deduced from the hydrocode calculations described above is of the order of 400 to 500 seconds for impact velocities of 15 to 20 km/s. This time scale has important implications for the mechanism responsible for remanence acquisition in the antipodal zone during the period of compressed field amplification. Since magnetization

must occur within a relatively short time interval, the main candidate mechanisms are: (1) Acquisition of shock or rapid thermal remanence resulting from compressive stresses generated by converging seismic waves at the antipode; and (2) acquisition of shock or rapid thermal remanence by impact of solid ejected secondaries from the basin forming event. In the case of mechanism (2), ballistic calculations on a spherical Moon for ejection angles of 30° to 60° yield antipodal arrival times of 28-50 minutes (1700-3000 seconds)⁵. In the case of mechanism (1), arrival times of seismic body waves with mantle velocities of ~ 8 km/s are about 8 minutes (480 seconds). Thus on the basis of time scale alone, convergence of seismic body waves appears to be the most likely candidate for effecting the magnetization of near-surface materials during the period of compressed magnetic field amplification by the impact plasma cloud.

Acknowledgment: Supported by NASA under grant NAGW-1881.

References: (1) Srnka, L. J., *PLSC 8th*, 795, 1977. (2) Hood, L. L. and A. Vickery, *J. Geophys. Res.*, 89, C211, 1984. (3) Lin, R. P., K. A. Anderson, and L. L. Hood, *Icarus*, 74, 529, 1988. (4) Spreiter, J. R. and S. S. Stahara, in *Collisionless Shocks in the Heliosphere: Reviews of Current Research*, pp. 85-108, AGU, Washington, 1985. (5) Schultz, P. and D. Gault, *Moon*, 12, 159-177, 1975.



THE SPATIAL DISTRIBUTION AND TIME EVOLUTION OF IMPACT-GENERATED MAGNETIC FIELDS. D. A. Crawford and P. H. Schultz, Dept. of Geological Sciences, Brown University, Providence, RI 02912.

The production of magnetic fields has been revealed by laboratory hypervelocity impacts in easily vaporized targets performed at the NASA Ames Vertical Gun Range[1,2]. As quantified by pressure measurements, high frame-rate photography and electrostatic probes, these impacts, tend to produce large quantities of slightly ionized vapor, which we refer to as impact-generated plasma[3-6]. Nonaligned electron density and temperature gradients within this plasma may lead to the production of the observed magnetic fields[7]. Past experiments were limited to measuring a single component of the impact-generated magnetic field at only a few locations about the developing impact crater and consequently gave little information about the field production mechanism. To understand this mechanism, we are extending our techniques to map the three components of the magnetic field both in space and time. By conducting many otherwise identical experiments with arrayed magnetic detectors we have produced a preliminary three-dimensional picture of impact-generated magnetic fields as they develop through time.

The magnetic detector array consists of fifteen overlapping search coils. Each coil, consisting of several hundred turns of 30 gauge copper magnet wire wound helically on an 8 cm plastic form, measures a single component of the magnetic field. The position of the search coils (x,y,z) is recorded with the origin at the point of impact, where +z measures the height (in cm) above the target surface, +y the distance uprange of the impact point and +x the distance away from the projectile line-of-flight in a right-handed sense. Fig. 1 is a time sequence of the magnetic field observed at $\tau = 1200, 1800$ and $2400 R_p/V_p$ ($-0.33, 0.50$ and 0.66 ms respectively) after the first contact of a 0.32 cm Fe projectile impacting a powdered dolomite target at a mean velocity of 5.75 km/s. The field observed within the target varies considerably with time but is predominantly horizontal. In the first time step (Fig. 1a), the field is nearly toroidal - consistent with near vertical electric currents in the plasma cloud. This suggests that the plasma is contained and redirected by the developing crater. The strong, homogeneous field in the second time step (Fig. 1b) is consistent with a large current system in the more extensive plasma cloud. In the final time step (Fig. 1c), the field is beginning to decay and the signals are consistent with local currents in the plasma that remains near the crater.

A relatively low signal-to-noise ratio results from two factors: 1) the impact-generated magnetic field far from the impact point is contaminated by interactions between the ambient field and the expanding plasma; the external (ambient) magnetic field has large gradients throughout the impact region making it difficult to entirely remove with cancellation techniques. Previously, this was not a problem as the impact-generated magnetic fields were observed in a limited area about the impact point. 2) the impact-generated magnetic field, though reproducible, varies enough from shot to shot to introduce a noise term when data sets are combined in this way. In future experiments, a passive magnetic shield should significantly reduce noise from the first factor while averaging many data sets should reduce noise from the second factor.

In a parallel set of experiments, the spatial extent and time evolution of impact-generated plasma is being derived with the use of electrostatic probes. Eventually, we want to determine the early-time projectile/target interaction that yields impact-generated plasma, to understand the production and remanence mechanisms of impact-generated magnetic fields and to find the scaling laws that will allow us to extend these observations to planetary scale.

IMPACT-GENERATED MAGNETIC FIELDS

D. A. Crawford and P. H. Schultz

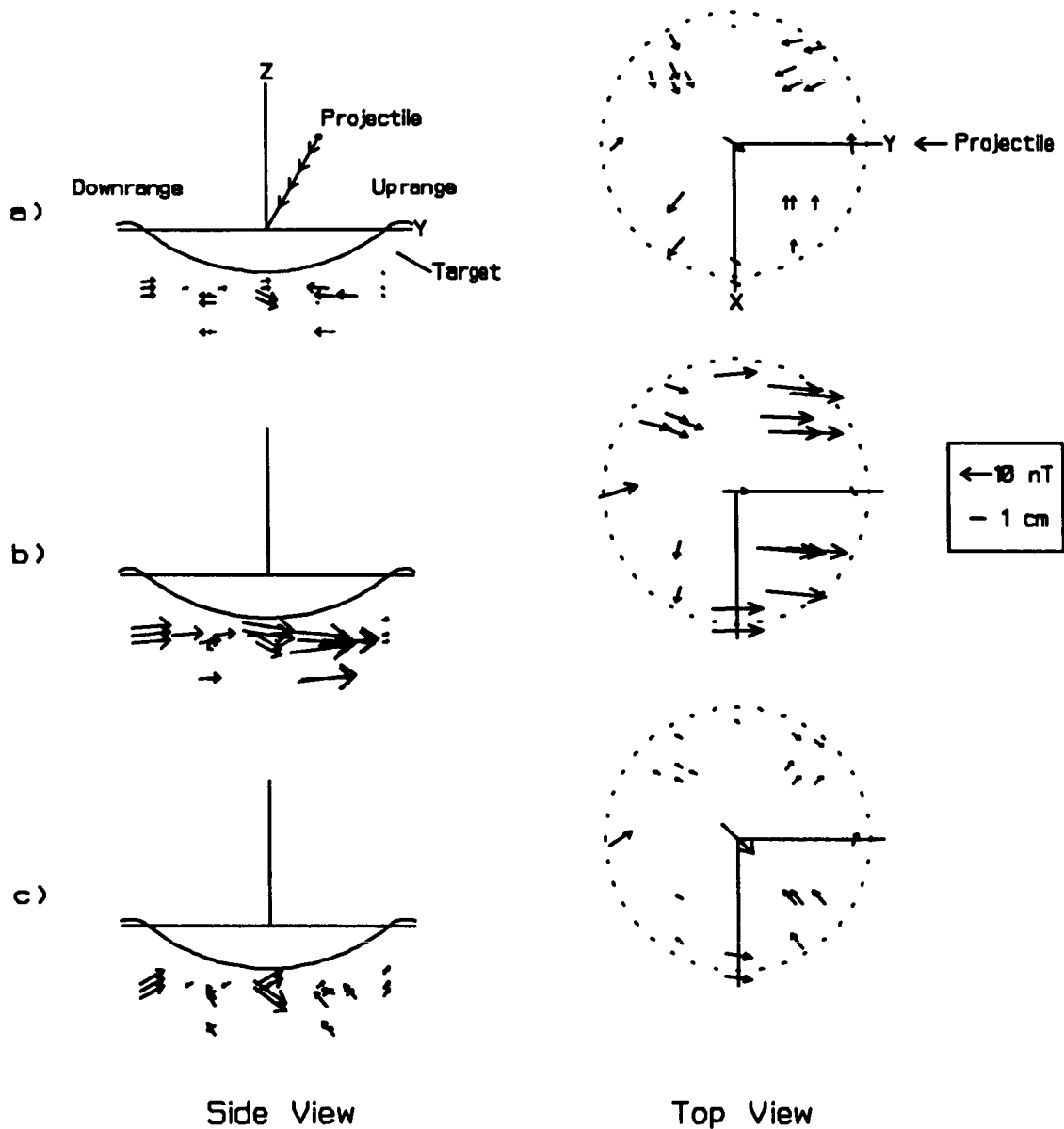


Fig. 1 Time sequence of the observed magnetic field at: a) $\tau = 1200 R_p/V_p$ (~ 0.33 ms), b) $\tau = 1800 R_p/V_p$ (~ 0.50 ms), and c) $\tau = 2400 R_p/V_p$ (~ 0.66 ms) after the first contact of a 0.32 cm Fe projectile impacting into a powdered dolomite target at a mean velocity of 5.75 km/s. This plot is a compilation of data from three nearly identical impacts at 5.52, 5.83 and 5.90 km/s. The projectile trajectory prior to impact was in the Y-Z plane, 60° from horizontal. First contact occurred at the origin. The final crater extent is shown in the Side View as the solid profile and in the Top View as the dashed circle.

[1] Crawford, D.A. and Schultz, P.H., *Nature* 336, 50-52 (1988). [2] Crawford, D.A. and Schultz, P.H., *Lunar Planet. Sci.* 20th, 197-198 (1989). [3] Crawford, D.A. and Schultz, P.H., *Lunar Planet. Sci.* 21st, 242-243 (1990). [4] Crawford, D.A. and Schultz, P.H., *J. Geophys. Res.*, (in revision). [5] Schultz, P.H., *Lunar Planet. Sci.* 19th, 1039-1040 (1988). [6] Schultz, P.H. and Gault, D.E., *Geo. Soc. Amer. Bull.* 247, (in press). [7] Srnka, L.J., *Proc. Lunar Sci. Conf.* 8th, 893-895 (1977).

GRAVITY SURVEY OF THE MT. TOONDINA IMPACT STRUCTURE, SOUTH AUSTRALIA: J. Plescia¹, E. M. Shoemaker², and C. Shoemaker², ¹Jet Propulsion Laboratory, California Institute of Technology, Pasadena, CA 91109; ² U. S. Geological Survey, Flagstaff, AZ 86001.

The Mt. Toondina impact structure [1] is located in northern South Australia, about 45 km south of the town of Oodnadatta at 27° 57'S, 135° 22'E.. Only the central uplift is exposed. It was first mapped by Freytag [2] who described beds of early Permian age that have been brought to the surface in the core of the uplift. Youles [3] suggested the structure was of impact origin; his suggestion was promptly rebutted by Wopfner [4] who thought the structure was related to the presence of evaporite beneath the Permian. Recent detailed mapping by Shoemaker et al. [5,6] has shown that the style of deformation of the exposed beds is consistent with an impact origin.

The outcrops at Mt. Toondina reveal a remarkable structural anomaly surrounded by a broad expanse of nearly flat-lying beds of the Bulldog Shale of Early Cretaceous age. Highly deformed beds of the Permian Mt. Toondina Formation, the Jurassic (?) Algebuckina Sandstone, and the Early Cretaceous Cadna-Owie Formation rise to the surface in the central uplift. On the basis of a seismic reflection profile through the center of the structure the top of the Permian rises about 350 m from the axis of a shallow structural depression that surrounds the uplift. The maximum structural relief near the center of the uplift is estimated to be between 400 and 500 m. The structure dies out at depth; the base of the structurally disturbed zone is near the base of the Permian section at about 1 km depth. Although numerous diapirs of late Precambrian evaporites occur in the region, no diapir is present beneath the Permian beds at Mt. Toondina.

A gravity survey was undertaken in 1989 to determine the diameter of the impact structure, define the form of the central uplift, and understand the local crustal structure. Data were collected along a two orthogonal lines trending N5°W and N85°E across the structure and extending about 4 km from the central uplift. The east- and a northeast-trending lines were run along seismic reflection profiles. In addition to the profiles, a significant number of measurements were made on and around the central uplift. The 1989 gravity data combined with 1963 gravity data (by J. McG Hall) provided by the South Australia Geological Survey and the seismic reflection data provides an excellent data base to interpret the subsurface structure of the Mt. Toondina feature.

Data from both surveys were reduced using a density of 1.9 g cm⁻³. Data from the 1988 survey were reduced using the USGS Bouguer Gravity Reduction Program which computes Free Air, Curvature, Latitude, and Bouguer Corrections. No terrain corrections were made to the data because of the lack of significant topography. Data for the 1963 survey were available only in the form of reduced Bouguer gravity.

The region around Mt. Toondina is marked by a significant gravity gradient resulting from regional structure. In the area of the impact, the regional gravity gradient is about 1.8 mGal/km, decreasing to the northwest. To isolate the anomalies associated with the feature itself, the regional trend of the data was removed by calculating a variable order polynomial surface and determining residuals. A third order polynomial was chosen as a good approximation of the regional data (accounting for about 97% of the total variation). The residual values were then gridded and contoured. Figure 1 illustrates the residual Bouguer gravity for a region within 2.5 km of the central uplift contoured from a 50x50 grid (100 m grid spacing) with a 0.1 mGal contour interval.

The regional gravity field is dominated by an approximately northwest-trending low displaying in excess of 1 mGal of relief. This linear low is the result of a northwest trending syncline in Precambrian rocks. This regional structure is well-defined by

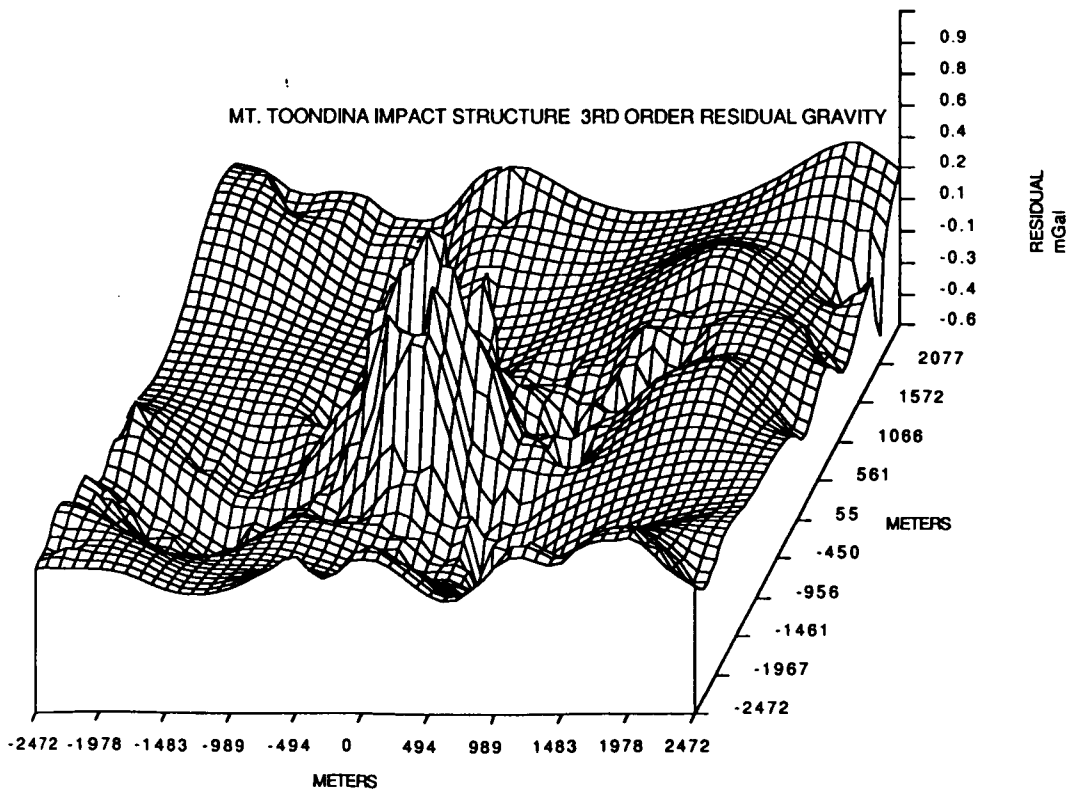
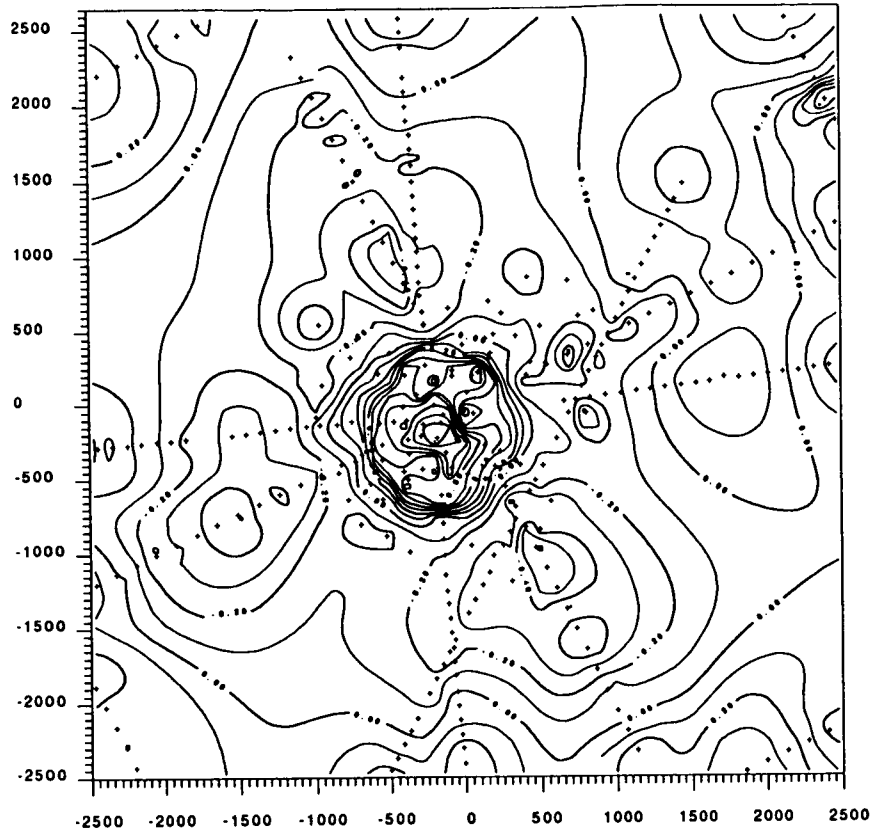
numerous seismic reflection lines crossing the area. Higher order polynomials remove this aspect of the field and define a central gravity high coincident with the central peak and an annular low surrounding the uplift.

The impact structure is dominated in the residual gravity by a prominent positive anomaly centered over the central uplift. The anomaly has about 1 mGal of positive relief relative to the surrounding areas and is about 1 km in diameter (an attribute noted by [1]). Around the high, residual gravity gradients of 2.5 mGal/km are observed. The central high is surrounded on all sides by a low beginning about 750 m from the central peak and extending out to a radius of about 1.5 km. This gravity data can be interpreted as: (1) the positive gravity anomaly at the center corresponds to the central uplift and resulting from relatively high density material having been drawn upward; and (2) surrounding the central uplift is an annular low resulting from thickening of the low density Bulldog Shale due to drawdown. The Bulldog shale has a relatively low density (about -0.15 g cm^{-3}). This annular thickening appears to have only about 50 m of relief. The east-west reflection line defines a disturbed zone about 3-4 km in diameter, with deformation extending to a depth of approximately 1 km. Together, the gravity and seismic data indicate an impact crater with a diameter of 3-4 km and a shallow structure.

References: [1] Shoemaker, E. M., and Shoemaker, C. S., 19??, Abstracts 19th Lunar Planet. Sci. Conf., 1079-1080. [2] Freytag, I. B., Trans. Roy. Soc. S. Aust., 89, 1965; Freytag, I. B., unpublished So. Aust. Dept. Mines Report, 1964. [3] Youles, I., Quat. Geol. Notes, Geol. Sur. So. Aust., No. 60, 10-12, 1976. [4] Wopfner, H., Quat. Geol. Notes, Geol. Sur. So. Aust., No. 62, 21-24, 1977. [5] Shoemaker, E.M., Shoemaker C. S., and Roddy, D. J., unpublished mapping, 1988. [6] Shoemaker, E.M., Shoemaker C. S., and Roddy, D. J., unpublished mapping, 1989.

Figure Caption: Upper panel shows the residual Bouguer gravity field over the Mt. Toondina impact structure. A 3rd order polynomial was fit to the data and removed to produce the residual contoured here. Contour interval is 0.1 mGal. Crosses indicate station locations. Lower panel shows the same 3rd order residual field in an oblique view from the southeast. The high associated with the central peak and the surrounding low are well illustrated by this perspective.

MT. TOONDINA 3RD ORDER RESIDUALS
50X50 GRID 0.1 MGAL CI



CHAPTER 7

ASTEROIDS AND COMETS

ASTEROID FLUX AND IMPACT CRATERING RATE ON VENUS. E.M. Shoemaker, R.F. Wolfe, and C.S. Shoemaker, U.S. Geological Survey, Flagstaff, AZ 86001.

By the end of 1990, 65 Venus-crossing asteroids had been recognized (Table 1); these represent 59% of the known Earth-crossing asteroids. Further studies, chiefly numerical integrations of orbit evolution, may reveal one or two more Venus crossers among the set of discovered asteroids. We define a Venus crosser as an asteroid whose orbit can intersect the orbit of Venus as a result of secular (long range) perturbations. Venus crossers revolving on orbits that currently overlap the orbit of Venus are here called Venapol asteroids, and those on orbits that don't overlap are called Venamor asteroids; we recognize 42 Venapols and 23 Venamors.

Collision probabilities with Venus for 60 of the known Venus crossers have been determined by the methods described in [1]. The mean collision probability with Venus is $6.2 \times 10^9 \text{ yr}^{-1}$, which is 1.45 times the mean collision probability of Earth-crossing asteroids with Earth [1]. Hence, the collision rate of asteroids on Venus is $0.59 \times 1.45 = 0.86$ times the collision rate on Earth. The collision rate per unit area on Venus is $0.86 \times 0.509 \times 10^8 \text{ km}^2 / 0.460 \times 10^8 \text{ km}^2 = 0.95$ times the rate per unit area on Earth.

The cratering efficiency (for sufficiently large asteroids) is somewhat higher on Venus than on Earth, owing partly to the higher rms impact speed of the asteroids and partly to the slightly lower surface gravity on Venus. If we neglect atmospheric retardation, the average cratering efficiency is 1.14 times higher on Venus than on Earth (as measured by relative crater diameters). This is equivalent to a correction to the cratering rate of $(1.14)^{2.27} = 1.34$ relative to the cratering rate on Earth. Hence, the nominal asteroid impact cratering rate on Venus is $0.95 \times 1.34 = 1.27$ times the asteroid cratering rate on Earth. Before accounting for losses, we add about 10% to the total asteroid cratering rate for the undiscovered Venus-crossing asteroids whose orbits lie entirely inside the orbit of Earth and remain undetected in the conventional search programs. Thus, the total (uncorrected) asteroid cratering rate on Venus is $1.1 \times 1.29 = 1.4$ times the rate on Earth.

Two corrections should be considered for asteroids impacting on Venus. First, extinct comets probably should be eliminated. The ratio of extinct comets among Earth-crossing asteroids is very uncertain. No known Earth crossers are D-type objects, but there is good presumptive evidence that a few dark asteroids (F-type and C-type) are extinct comets (e.g., Phaethon, the source of the Geminid meteors, and 1986 JK, which appears cometary from its radar properties). We estimate that about 10% of the Venus-crossing asteroids are extinct comets that won't survive atmospheric passage (unless they are very large--10 km diameter or greater). This reduces the cratering rate relative to Earth to about 1.27.

Secondly, a rough correction for atmospheric deceleration of projectiles can be made as follows. Nominally, a 20-km-diameter crater on Venus is produced by an S-type asteroid 1.71 km in diameter. At an average entry angle of 45° , this body sweeps out a mass of atmosphere equivalent to about $92 \text{ kg cm}^2 / \sin 45^\circ = 130 \text{ kg cm}^2$. The longitudinal mass at the stagnation point of a nominal S-type asteroid is $1.71 \times 10^5 \text{ cm} \times 2.4 \text{ gm cm}^3 = 410 \text{ kg cm}^2$. From conservation of momentum, the impact speed v_i will be $v_i = v_o \times 410 / (410 + 130) = 0.76 v_o$, and the cratering efficiency will be only $(0.76)^{2/3.4} = 0.85$ times the efficiency for the uncorrected velocity. The cratering rate will be reduced by the factor $(0.85)^{2.27} = 0.69$. About 40% of the craters are produced by S-type asteroids and the other 60% produced by C-type asteroids, which are larger but have lower density than S-type [1]. At the same kinetic energy, the longitudinal mass of C-types is the same as S-types and the correction for momentum transfer is the same. For crater production at 20-km diameter, the asteroid cratering rate on Venus is $0.69 \times 1.27 = 0.88$ times the rate on Earth. With increasing crater diameter, the relative rate increases; at 50-km crater diameter, the relative rate on Venus is $0.84 \times 1.27 = 1.06$ times the rate on Earth. For craters ≥ 20 km diameter, our best estimate of the asteroid impact cratering rate is $(3.7 \pm 2.0) \times 10^{15} \text{ km}^2 \text{ yr}^{-1}$ on Earth [1] and $(3.3 \pm 1.8) \times 10^{15} \text{ km}^2 \text{ yr}^{-1}$ on Venus.

All except a few of the largest impact craters on Venus probably have been produced by asteroids, as the atmosphere tends to shield the surface from impact of comets. Applying our estimate of the crater production rate, we find an average crater retention age at 20 km crater diameter of 260 + 310, - 90 million years for the Venusian surface imaged by the Venera spacecraft [2] and 240 + 290, - 85 million years for the portion of the surface imaged by the Magellan spacecraft [3].

References: [1] Shoemaker, E.M., Wolfe, R.F., and Shoemaker, C.S., 1990, in Sharpton, V.L., and Ward, P.D., eds., Geol. Soc. America Spec. Paper 247, p. 155-170. [2] Schaber, G.G., Shoemaker, E.M., and Kozak, R.C., 1987, Solar System Research, v. 21, p. 89-93. [3] Schaber, and 7 others, 1991, this volume. [4] Veeder and 5 others, 1989, Astron. Jour., v. 97, p. 1211-1219. [5] Williams, J.G., 1969, Ph.D. Thesis, Univ. Calif. at Los Angeles, 270 p. [6] Shoemaker, E.M., Williams, J.G., Helin, E.F., and Wolfe, R.F., 1979, in Gehrels, T., ed. Asteroids: Tucson, Univ. Ariz. Press, p. 253-282. [7] Opik, E.J., 1951, Proc. Roy. Irish Acad., v. 54A, p. 168-199.

TABLE 1. VENUS-CROSSING ASTEROIDS: MAGNITUDES, DIAMETERS CROSSING DEPTHS, AND COLLISION PARAMETERS

	H	Diam km	q AU	Depth AU	a AU	e	i deg	dr/dt AU 10 ⁴ yr	Tc 10 ⁴ yr	Ps 1 10 ⁴ yr	Po 1 10 ⁴ yr	vi km/s
VENAPOL ASTEROIDS												
3200 Phaethon	14.65	6.9	(0.14)	-----	1.271	(0.89)	(22)	-----	-----	-----	(2.2)	(41)
1566 Icarus	16.45	0.9	0.198	0.596	1.078	0.816	15.0	1.9	5.32	2.3	3.9	36.0
2212 Hephaistos	14.0	5	0.239	0.653	2.163	0.890	8.74	25	0.83	0.62	2.1	38.3
1990 UO	20.5	0.2	0.265	0.485	1.234	0.785	21.0	2.1	4.79	1.2	2.4	34.9
1989 VA	17.0	-1	(0.29)	-----	0.728	(0.60)	(29)	-----	-----	-----	(4.8)	(29)
3838 1986 WA	15.5	-3	0.381	0.302	1.505	0.747	24.7	1.9	4.11	0.77	1.6	32.6
1990 SM	16.5	-2	0.393	0.452	2.157	0.818	10.7	11	1.06	0.62	1.9	31.4
2100 Ra-Shalom	16.12	2.4	0.402	0.448	0.832	0.516	8.76	0.38	9.20	8.6	11	22.3
2340 Hathor	20.2	(0.2)	0.403	0.387	0.844	0.523	5.19	0.42	8.48	13	16	22.1
3753 1986 TO	15.0	-3	0.412	0.374	0.998	0.587	15.8	0.57	7.53	3.2	4.7	25.6
1974 MA	14.0	-5	(0.42)	-----	1.775	(0.76)	(38)	-----	-----	-----	(1.0)	(36)
1984 KB	16.4	1.4	0.429	0.485	2.221	0.807	3.27	14	0.76	1.7	4.2	29.2
5025 P-L	15.9	-2	(0.44)	-----	(4.2)	(0.90)	(6.2)	-----	-----	-----	(1.1)	(31)
1864 Daedalus	15.02	(3.1)	0.451	0.216	1.461	0.691	20.1	1.3	3.91	1.2	2.1	28.6
1954 XA	18.9	-0.5	0.471	0.368	0.777	0.394	4.41	0.21	10.9	23	23	17.8
3362 Khufu	18.15	0.7	0.479	0.302	0.990	0.516	7.76	0.44	7.36	7.2	9.3	21.4
2201 Oljato	15.56	1.4	0.511	0.382	2.174	0.765	1.38	7.4	0.89	3.8	6.0	25.4
2101 Adonis	18.2	-1	0.513	0.345	1.875	0.727	2.09	3.4	1.58	4.8	6.9	24.6
1865 Cerberus	16.91	1.0	0.522	0.226	1.080	0.517	14.4	0.40	6.81	4.0	5.1	22.0
1990 MU	15.0	-3	0.543	0.202	1.622	0.665	29.4	-----	-----	-----	-----	-----
4450 1987 SY	17.20	-1	0.555	0.247	1.442	0.615	1.97	0.94	3.35	11	11	21.1
1989 PB	17.2	-1	0.567	0.201	1.063	0.467	9.62	0.31	6.86	7.0	8.1	19.0
1979 XB	19.0	-0.5	0.586	0.286	2.264	0.741	12.0	3.27	0.99	1.2	2.0	23.4
4183 1959 LM	14.60	-4	0.594	0.152	1.981	0.700	10.2	-----	-----	-----	1.8	22.2
4341 1987 KF	15.70	-3	0.597	0.237	1.837	0.675	6.80	1.4	1.84	3.3	4.4	21.0
1983 TF2	17.5	-1	0.605	0.140	2.439	0.752	16.4	-----	-----	-----	0.60	24.1
4034 1986 PA	18.20	1	0.608	0.160	1.060	0.426	10.3	0.22	7.10	8.4	8.8	17.6
1981 Hidas	16.9	-1	(0.62)	-----	1.776	(0.65)	(40)	-----	-----	-----	(1.5)	(32)
1937 UB	17.0	-1	0.627	0.185	1.639	0.617	6.67	0.70	2.58	5.4	6.0	19.1
1990 BG	14.0	-5	0.634	0.126	1.486	0.573	32.2	0.11	4.81	6.2	2.4	27.5
1989 QF	17.0	-1	0.640	0.142	1.155	0.445	5.73	0.22	5.88	14	14	16.1
1989 UQ	19.0	-0.5	0.643	0.132	0.915	0.297	1.94	0.12	8.97	59	42	13.7
1862 Apollo	16.23	1.4	0.652	0.147	1.471	0.557	7.38	0.36	3.44	8.0	7.5	17.5
1987 OA	18.5	-1	0.658	0.140	1.490	0.558	13.5	0.26	3.50	6.2	4.7	18.8
1988 EG	18.0	-1	0.665	0.124	1.270	0.476	3.14	0.22	4.81	24	19	15.4
3554 Amun	15.94	2.0	0.672	0.074	0.974	0.310	22.7	-----	-----	-----	3.7	19.6
1990 VA	20.0	-0.3	0.679	0.090	0.984	0.310	14.2	0.07	8.56	16	13	15.8
1990 TG1	15.0	-3	0.681	0.286	2.486	0.726	8.63	1.4	0.55	4.8	3.5	18.5
4581 1989 FC	20.60	-0.2	0.681	0.095	1.023	0.334	4.79	0.10	7.16	35	30	13.5
3360 1981 VA	16.55	1.8	0.684	0.061	2.462	0.722	24.7	-----	-----	-----	1.7	24.3
1989 UR	18.0	-1	0.688	0.085	1.080	0.363	12.8	0.08	7.22	16	13	15.6
2063 Bacchus	17.6	-1	0.694	0.052	1.078	0.356	10.1	-----	-----	-----	13	14.7
VENAMOR ASTEROIDS												
1990 HA	17.0	-1	0.426	0.320	2.567	0.834	4.10	-----	-----	-----	1.5	30.1
1989 DA	18.0	-1	0.427	0.320	2.166	0.803	6.12	-----	-----	-----	1.6	29.4
4197 1982 TA	15.40	1.8	0.450	0.296	2.297	0.804	13.7	-----	-----	-----	0.88	29.5
3288 Seleucus	15.34	2.8	0.685	0.061	2.032	0.663	4.73	-----	-----	-----	0.68	17.0
1990 UA	19.5	-0.4	0.688	0.058	1.721	0.600	1.30	-----	-----	-----	8.1	15.9
1990 UQ	17.5	-1	0.691	0.054	1.571	0.560	4.52	-----	-----	-----	4.0	15.6
1990 UM	23.5	-0.05	0.692	0.054	1.709	0.595	3.00	-----	-----	-----	3.2	15.7
1988 VP4	15.5	-3	0.692	0.054	2.263	0.694	12.9	-----	-----	-----	0.77	18.9
1983 LC	19.0	-0.5	0.694	0.053	2.629	0.736	1.11	-----	-----	-----	1.2	17.0
1988 XB	17.5	-1	0.717	0.029	1.467	0.511	5.32	-----	-----	-----	4.0	14.1
1988 TA	21.0	-0.2	0.717	0.030	1.541	0.535	4.63	-----	-----	-----	3.5	14.2
1980 WF	18.5	0.6	0.721	0.026	2.231	0.677	5.07	-----	-----	-----	0.43	15.4
2329 Orthos	15.1	-3	0.726	0.019	2.404	0.698	20.1	-----	-----	-----	0.52	21.2
1978 CA	17.8	1.9	0.727	0.019	1.125	0.354	26.6	-----	-----	-----	0.45	21.5
2062 Aten	16.96	0.9	0.739	0.007	0.966	0.235	19.2	-----	-----	-----	0.71	16.8
6743 P-L	17.3	-1	0.740	0.007	1.681	0.560	8.89	-----	-----	-----	0.16	15.3
1950 DA	15.8	-2	0.742	0.003	1.683	0.559	13.4	-----	-----	-----	0.07	16.7
1983 VA	16.5	-2	(0.81)	-----	-----	-----	-----	-----	Chaotic orbit			-----
1973 NA	15.5	-3	(0.88)	-----	-----	-----	-----	-----	5:2 Commensurability			-----
1986 JK	19.0	-1	(0.90)	-----	-----	-----	-----	-----	3:1 Commensurability			-----
3752 Camillo	15.6	-2	(0.98)	-----	-----	-----	-----	-----	3:1 Commensurability			-----
2608 Seneca	17.57	0.9	(1.03)	-----	-----	-----	-----	-----	3:1 Commensurability			-----
1915 Quetzalcoatl	18.97	0.3	(1.08)	-----	-----	-----	-----	-----	3:1 Commensurability			-----

Note:

Within each class (Venapols and Venamors), asteroids are listed in order of increasing perihelion distance; estimated perihelion at the time of Venus crossing is used to order all asteroids with formally derived crossing depths. Other asteroids are listed in order of current perihelion distance.

H is absolute magnitude in the V band, as determined from observation by internationally adopted formulae.

The column headed Diam gives the estimated diameter in kilometers. Accurately determined diameters, based on infrared observations, have been taken chiefly from [4]. Diameters estimated from accurate magnitudes, where albedos have been assumed on the basis of spectrophotometric classification, are shown in parentheses. Approximate diameters, where magnitudes are based on photographic observations and spectrophotometric class is unknown, are preceded by symbol "-".

Perihelion distance, q, is at the time of Venus crossing, except for values in parentheses, which are osculating perihelion distances.

Depth is the crossing depth (the maximum overlap of the orbit of the asteroid with the orbit of Venus along the radius to the node) determined from the theory of Williams [5].

The orbital elements a (semimajor axis), e (eccentricity), and i (inclination with respect to the invariable plane) and the derivative of the radius to the node, dr/dt, are estimated representative values at the time of Venus crossing. Tc is the period of precession of the major axis with respect to the line of the nodes in the invariable plane. Ps is the probability of collision with Venus calculated from the equations of Shoemaker et al. [6], and Po is probability of collision with Venus calculated from the equations of Opik [7]. Uncertain values are shown in parentheses.

The column headed vi gives the impact speed in kilometers per second, corresponding to the orbital elements shown for the time of collision with Venus. Collision is assumed to occur at 0.723 AU for Venapols and at 0.746 AU for Venamors.

METEORITE SPECTROSCOPY AND CHARACTERIZATION OF ASTEROID SURFACE MATERIALS

Michael J. Gaffey, Geology Department, Rensselaer Polytechnic Institute, Troy, New York 12181

The asteroids and comets are the surviving primordial remnants of the early solar system. Because of their small size, they have limited potential for internally driven thermal evolution. Thus, these minor bodies are composed either of primitive materials that are essentially unaltered samples accreted from the solar nebula, or of such materials that were altered by transient heat sources during the very earliest epoch of solar system history, a period dominated by processes quite different than those seen in the present solar system.

The asteroids and meteorites provide our only direct record of the conditions and of the processes in the inner regions of the solar system during the formation epoch and during the initial period of solar system evolution. The asteroids provide significant constraints on conditions and processes as a function of heliocentric distance. The meteorites provide detailed constraints on the timing and sequence of conditions and processes in the solar nebula and early solar system. Asteroidal studies utilize the chronologies and models from the meteoritical investigations. Meteorite studies draw upon the observed distribution of materials within the asteroid belt to constrain the models of their origin and of nebular temperature and compositional gradients.

The mineralogical characterization of an asteroid's surface assemblage can provide significant insight into the history of that body. Such an assemblage is the product of the initial composition (chemistry, oxidation state, volatile inventory, etc.) and the conditions (temperature, pressure, gravitational field strength) under which the system was altered. Asteroids with mineral assemblages similar to specific meteorite types can reasonably be inferred to have undergone geochemical processes similar to those which produced the meteoritic assemblage.

In the present research program, the analysis of visible and near-infrared reflectance spectra is the primary means used to determine surface mineralogy and petrology of individual asteroids. These individual studies provide the data to investigate the broader relationships between the asteroids and meteorites (to establish a spatial context for the more detailed meteorite data) and between asteroids at different heliocentric distances (to establish the nature of nebular compositional gradients and the distribution of post-accretionary thermal events). It seems unlikely that any significant portion of the diverse asteroidal population will be visited by spacecraft within the professional lifetimes of most current investigators. Therefore, asteroid mineral characterizations from earth-based telescopic studies will remain our primary means of investigating the nature and history of most of these minor planets for the near future.

The purpose of this research program is to improve our understanding of the origin, evolution, and inter-relationships of the asteroids; of their relationships to the meteorites; and of the processes active and the conditions present in the early inner solar system. Empirical information from the study of asteroids and the meteorites is essential to the adequate development and testing of the theoretical models for the accretion of the terrestrial planets, and for their early post-accretionary evolution.

The recent results of two aspects of this research program are outlined in the following sections.

Asteroid Igneous Processes: Several asteroid classes (types M,A,E,V,R,S) appear to be composed primarily or exclusively of igneous assemblages formed by the melting and density-controlled separation of the metal and the various silicate phases^{1,2}. The observed mineral assemblages indicate that different bodies within this population experienced a wide range of histories³. Recent efforts have focused on the nature and selectivity of the asteroidal heating mechanisms and the igneous processes within the parent bodies of the present asteroids and meteorites⁴. The large variation within the diverse S-class has been investigated using available asteroid survey spectra. Figure 1 shows the distribution of two spectral parameters for igneous asteroids which were observed as a part of the 52-color asteroid survey⁵. The wide range in mafic mineral assemblages indicates a wide range in peak temperatures (from about 1000C to >1600C)^{3,4}.

The mineralogic variations seen among the igneous asteroids obviously represent a range of depths within their parent planetesimals (e.g. 16 Psyche [NiFe metal] from the core of its parent body, 4 Vesta [basaltic] from the crust, 446 Aeternitas [pure olivine] from the residual or cumulate mantle). An important additional source of the mineralogic variety among the igneous asteroids is the efficiency of phase segregation within the parent bodies. The large scale separation of solid and liquid phases within a parent body is a function of the density contrast between phases, the local gravitational force (body size and depth) and the degree of melting (peak temperature).

Rotational spectral variations are used to constrain the compositional gradients within individual asteroids to assess the efficiency of melt segregation which in turn constrains body size and peak temperature. Efficient melt segregation requires either a large body (a relatively strong gravitational field) or high temperatures (to produce large degrees of melt fraction and hence to lower the resistance to phase migration). For example, the silicate portion of the S-asteroid 113 Amalthea is composed of nearly pure olivine with only a minor (8±2 wgt %) calcic pyroxene and shows no significant variation in lithology with rotation⁴. Unless it is a fragment of a parent planetesimal much larger than most S-asteroids, the efficient segregation of such a homogeneous assemblage either as a cumulate or residuum requires complete melting or a very high degree of partial melting. Either option places the peak temperature within its parent body near or above the olivine solidus at about 1600C.

If the original assemblages in the parent planetesimals were chondritic, then relative displacement from the chondritic (OC) field (outlined on Figure 1) is a first-order measure of the degree of igneous differentiation. Relative distance from the OC-field is also a function of the efficiency of phase segregation and hence of body size (gravitational field) and peak temperature (melting fraction).

Spinel-Bearing Asteroids and the Nebular Compositional Gradient: Most cosmochemical models assume that nebular solids exhibited a significant compositional gradient as a function of heliocentric distance. Independent data on the original nebular material at various heliocentric distances

would provide important constraints on the temperature and pressure profiles in the solar nebula.

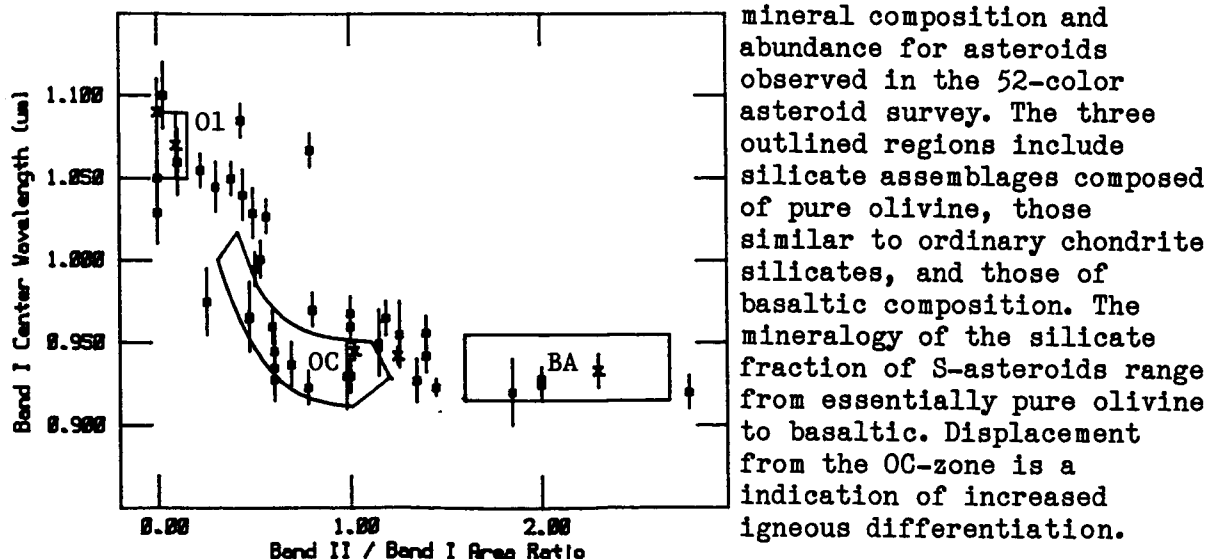
During the analysis of data from the 52-color asteroid survey, several anomalous spectra were identified⁶. The ECAS and 52-color data for S-type asteroids 387 Aquitania and 980 Anacostia both exhibit a broad spinel feature extending longwards from about 1.3-1.6 μ m⁷. These features were initially identified as the second pyroxene band centered near 2 μ m. However, these spectra do not show the expected 1 μ m feature which should be at least as strong as the 2 μ m feature in a pyroxene-dominated assemblage. Moreover the similar orbital elements of Aquitania and Anacostia suggest that they are fragments of a single parent body.

Spinel, a magnesium-aluminum oxide mineral, is a major constituent of the calcium-aluminum inclusions (CAI's) which are characteristic of CV meteorites such as Allende. These CAI's represent a suite of high temperature condensates and/or refractory residues formed by intense heating in some portions of the solar nebula. The presence of spinel features in an asteroidal spectrum provides a very strong indication of assemblages analogous to the CV3 and C03 meteorites. Since this assemblage must be nearly unaltered nebular material, it's presence requires that at this particular heliocentric distance when the parent planetesimal of these two asteroids accreted, the nebula contained a relatively high proportion of CAI-type grains mixed with a C3-type mineral assemblage.

ACKNOWLEDGMENT: This research was supported in whole or in part by NASA Grant NAGW-642.

REFERENCES: ¹Bell et al. (1989) in Asteroids II, U. Arizona Press, Tucson, pp. 921-945. ²Gaffey et al. (1989) ibid, pp. 98-127. ³Gaffey et al. (1990) LPSC XXI, 399-400. ⁴Gaffey (1991) LPSC XXII, 423-424. ⁵Bell et al. (1988) LPSC XIX, 57-58. ⁶Burbine et al. (1991) Meteoritics, submitted. ⁷Rajan and Gaffey (1984) LPSC XV, 284-285.

Figure 1: The distribution of two spectral parameters related to silicate mineral composition and abundance for asteroids observed in the 52-color asteroid survey. The three outlined regions include silicate assemblages composed of pure olivine, those similar to ordinary chondrite silicates, and those of basaltic composition. The mineralogy of the silicate fraction of S-asteroids range from essentially pure olivine to basaltic. Displacement from the OC-zone is a indication of increased igneous differentiation.



Will Galileo Resolve the S-Asteroid Controversy?

Jeffrey F. Bell (Dept. of Geology and Geophysics, Univ. of Hawaii, Honolulu HI 96822)

The longest running argument in asteroid science concerns the mineral composition and meteoritical association of the asteroids assigned to taxonomic type S. Over the past 20 years this controversy has occupied an immense number of abstracts, funding proposals, telescope time requests, progress reports, workshop proceedings, Arizona "Blue Book" chapters, NASA SPs, CPs, TMs, JPL internal documents, and occasionally even refereed journal articles. The approaching flyby of the S-type asteroid Gaspra by the Galileo spacecraft will drag an even larger section of the space science community into this turgid debate. This review is intended to introduce these unfortunate newcomers to the basics of the problem. Below are summarized the various proposed S asteroid surface compositions in roughly the order in which they appeared.

A) ORDINARY CHONDRITES: It was known long before asteroid spectroscopy began that ordinary chondrites (OCs) make up more than 75% of observed meteorite falls. Some (but not all) meteoriticists of the 1960s came to believe that these fall statistics must reflect the proportions of meteorite parent bodies in the asteroid belt. Thus when the first asteroid colors and albedos were obtained in the early 1970s there was a strong expectation that many asteroids would resemble OCs. Indeed, the spectral class "S" originally was intended to stand for "siliceous" as "M=metal" and "C=carbonaceous" (1). Thus the original 3 asteroid types neatly accounted for ordinary chondrites, irons, and carbonaceous chondrites. For a short time everyone was happy.

B) STONY-IRONS: Later, when spectra of ordinary chondrites were measured in the lab (2) it became apparent that they actually had little similarity to S asteroids other than having olivine and pyroxene absorption bands. The asteroids have a steep red continuum totally unlike that of the OCs, and the details of the silicate bands vary wildly, implying mineralogies usually far outside the OC range. To explain these facts it was suggested that most S-type surfaces are differentiated assemblages of metal, orthopyroxene, and olivine, similar to stony-iron meteorites such as pallasites, lodranites, and siderophyres. This material would be the product of melting in the deep interiors of the asteroid parent bodies, subsequently exposed by the collisional disruption. Advocates of this hypothesis have proposed various alternate source bodies for OCs. Probably the least objectionable of these is the Q-class asteroids, which conveniently are all tiny Earth-crossing asteroids with low-quality spectra. But current collisional models of the asteroids require that this population be constantly replenished from a reservoir in the main belt, where no Q-types have been found.

C) WEATHERED ORDINARY CHONDRITES: Upon discovery of the continuum slope problem, advocates of interpretation A) proposed that the red continuum of S asteroids is created by some "space weathering" process which alters the spectrum of the uppermost regolith. Usually they propose that this is associated with the metal component of chondrites, because it is obvious that pure-silicate asteroids of classes V, R, A, and E do not have any reddening. This proposal has inspired investigations of both synthetic metal-rich regoliths derived from OCs (3) and natural OC parent body regolith material preserved in some meteorite breccias (4). All these studies demonstrate that "weathered" OC material does not redden, but rather becomes spectrally flatter and in extreme cases approximates a C-type spectrum, never an S-type. In fact this similarity leads some to propose that the OCs actually come from C-type asteroids (5).

D) CARBONLESS CARBONACEOUS CHONDRITES: When the first near-IR spectra of S asteroids revealed that most had higher ol/pyx than any OC, it was proposed (6) that they represented unknown types of chondrites, specifically material with the silicate composition of carbonaceous chondrites but no carbon. But since no such meteorites have ever fallen on Earth, this hypothesis requires its advocates to abandon the very fall-statistics argument that had originally inspired the chondritic interpretation of S-types in the first place. Furthermore, the asteroid Flora which was cited in (6) as the most OC-like of the S-types was later shown to have large variations in silicate mineralogy between different regions of its surface, far outside the range of OCs (7). As a result, this theory is almost forgotten, except by die-hard supporters of interpretation A) above who mistakenly cite (6) as supporting them.

E) EVERYTHING: The mounting spectral evidence for wild variations in composition between different S asteroids and even across the surface of individual ones leads some workers (7) to wonder if both schools might be right. It is impossible to rule out some chondritic areas on the surfaces of S asteroids with the current data, if one allows the other areas to be made of extreme differentiated mineralogies (e.g. pure metal or pure olivine). Since we observe an entire "hemisphere" at once with Earth-based telescopes the chondritic areas could not be separated from the differentiated areas. Current ideas about asteroid differentiation lean toward such a complex pattern of heating. The fatal objection to this theory is that the actual OC breccias do not contain differentiated clasts, which would be sure to exist in the regolith of a "patchwork asteroid".

F) NOTHING: Alternatively one may take the wide variety of S spectra to indicate that there is really no such thing as a unified "S-type asteroid", but a variety of different objects with different origins and histories which we have not yet properly distinguished. For instance, the Eos asteroid family contains objects formally classified S in most systems, but with IR spectra that closely match those of CO or CV chondrites. A new class "K" was recently created to contain these objects (8). But this probably does not herald the beginning of the end for Class S. There does seem to be a hard core of well observed objects with classical S properties that will always remain even if some of the fainter objects which have only incomplete spectral data later turn out to be something else.

THE CURRENT POSITION: At present almost all scientists actively involved in research on asteroid composition appear to hold some version of interpretation B. In fact, no full journal article defending any other view has appeared for at least 10 years (the closest approximation being (9)). Yet some of them (especially C) continue to be defended vigorously in less formal situations. None can be rigorously excluded on the basis of current data, and very little new data is being collected due to funding and personnel shortages.

GASPRA: ROSETTA STONE OF THE ASTEROID BELT? Will the Galileo flyby of Gaspra end the Great Debate? Most attention has focused on spectral observations to be made by the NIMS IR spectrometer and SSI camera. But the spectral studies to be performed by these instruments will be essentially the same as those already being done from Earth. The whole debate outlined above has been between those who accept the fundamental usefulness of mineral spectroscopy, and those who reject it in favor of meteorite fall statistics. More spectral data is unlikely to convince the second group, who have been remarkably ingenious in proposing reasons why the hundreds of existing S-type asteroid spectra don't really mean what they obviously do. Alternatively, it is possible that some striking morphological evidence of a metal-rich composition will appear in the images of Gaspra. For instance, impact experiments in nickel-iron targets produce craters with rigid, "frozen" ejecta flaps, usually with many sharp prongs of metal visible. If similar structures were seen on Gaspra, they would strongly suggest that the bedrock was dominated by metal. Probably the least ambiguous datum would be an accurate density for Gaspra. Any density significantly above 3.8 would rule out a chondritic composition. The stony-iron model implies a density between 4.0 and 7.8. This determination is independent of any quibbles about spectral interpretation and would sense the entire body of the asteroid rather than a superficial layer. Obtaining accurate values for the mass and volume of Gaspra should be the highest priority during the flyby.

REFERENCES: (1) Chapman C. R., Morrison D., and Zellner B., *Icarus* 25, 104-130. (2) Chapman C. R. and Salisbury J. W., *Icarus* 19, 507-522; Gaffey M. J., *J. Geophys. Res.*, 81, 905-920. (3) Gaffey M. J., *Icarus* 66, 468-486. (4) Bell J. F. and Keil K., *Proc. LPSC 18th*, 573-580. (5) Britt D. *et al.*, *LPS XX*, p.111-112. (6) Feierberg M. *et al.*, *Astrophys J.* 257, 361-372. (7) Gaffey M. J., *Icarus* 60, 83-114. (8) Bell J. F., *Meteoritics* 23, 256-257; Tedesco *et al.*, *Astron. J.* 97, 580-606. (9) Wetherill G. W. and Chapman C. R., in *Meteorites and the Early Solar System*, Univ. of Arizona Press, 1988, p.35-67.

Cruikshank, D. P., D. J. Tholen, W. K. Hartmann, J. F. Bell, and R. H. Brown, Three basaltic asteroids and the source of the basaltic achondrite meteorites. *Icarus* **89**, 1-13 (1991).

Britt, D. T., D. J. Tholen, J. F. Bell, and C. Pieters. Classification of asteroid and meteorite spectra by principal components analysis. In *NASA TM-4210*, p. 118-119, July 1990.

Bell, J. F., K. Keil, and D. T. Britt. On the relationship between shocked ordinary chondrites and asteroids. In *NASA TM-4210*, p. 124-126, July 1990.

Britt, D. T., D. J. Tholen, J. F. Bell, and C. M. Pieters. Comparison of asteroid and meteorite spectra by principal component analysis. In *Lunar and Planet. Sci. XXI*, 131-132, March 1990.

Hawke, B. R., P. D. Spudis, P. G. Lucey, and J. F. Bell. The composition of the crust in the Orientale region of the Moon: A pre-Galileo view. In *Lunar and Planet. Sci. XXI*, 473-474, March 1990.

Gaffey, M. J., J. F. Bell, R. H. Brown, and T. Burbine. Mineralogical variations within the S-asteroid population. In *Lunar and Planet. Sci. XXI*, 399-400, March 1990.

Bell, J. F., "Igneous and metamorphic processing of asteroids: An observational perspective." *EOS Trans. Am. Geophys. Union*, **71**, p. 1432-1433.

Bell, J. F., and K. Keil, "Reflection spectra of shocked ordinary chondrites." *Bull. Am. Ast. Soc.* **22**, 1124 (October 1990).

Granahan, J. C., and J. F. Bell, "On the reality of some recently proposed asteroid families." *Bull. Am. Ast. Soc.* **22**, 1125 (October 1990).

Burbine, T. H., M. J. Gaffey, and J. F. Bell, "Principal component analysis of asteroid and meteorite spectra from 0.3 to 2.5 μ m." *Bull. Am. Ast. Soc.* **22**, 1124 (October 1990).

Veeder, G. J., J. Goguen, D. Matson, E. Tedesco, J. F. Bell, and J. C. Gradie, "The A-class asteroid 1951 Lick." *Bull. Am. Ast. Soc.* **22**, 1114 (October 1990).

Gaffey, M. J., J. F. Bell, R. H. Brown, T. Burbine, J. Piatek, K. L. Reed, "Evolutionary implications of compositional variations within the S-type and A-type asteroid populations." *Bull. Am. Ast. Soc.* **22**, 1114 (October 1990).

MAPPING THE STABILITY FIELD OF JUPITER TROJANS. H.F. Levison, U.S. Naval Observatory, Flagstaff, AZ 86002, E.M. Shoemaker and R.F. Wolfe, U.S. Geological Survey, Flagstaff, AZ 86001

Jupiter Trojans are a remnant of outer solar system planetesimals captured into stable or quasistable libration about the 1 : 1 resonance with the mean motion of Jupiter. The observed swarms of Trojans may provide insight into the original mass of condensed solids in the zone from which the Jovian planets accumulated, provided that the mechanisms of capture can be understood [1]. As a first step toward this understanding, we have undertaken to map the stability field of Trojans in the coordinates proper eccentricity, e_p , and libration amplitude, D . To accomplish this mapping, we integrated numerically the orbits of 110 particles with e_p in the range 0 to 0.8 and D in the range 0° to 140° . Orbits of the Sun, the four Jovian planets, and the massless particles were integrated as a full N-body system, in a barycentric frame using a fourth order symplectic scheme [2, 3]. Initial positions and velocities for the planets were taken from [4].

Our definitions of e_p and D for Trojans are an extension of those presented in [1]. We utilized the analytic work of Érdi [5] to obtain

$$e_p^2 = [e \cos \tilde{\omega} - e_j \cos (\tilde{\omega}_j \pm \tilde{\omega}_b)]^2 + [e \sin \tilde{\omega} - e_j \sin (\tilde{\omega}_j \pm \tilde{\omega}_a)]^2,$$

where e is the osculating eccentricity, $\tilde{\omega}$ is the longitude of perihelion,

$$\tilde{\omega}_a = \sin^{-1} \left(\frac{\sqrt{3}}{2} + \frac{73\sqrt{3}}{2^4 3^2} l^2 + \frac{6233\sqrt{3}}{2^8 3^4} l^4 \right), \quad \tilde{\omega}_b = \cos^{-1} \left(\frac{1}{2} + \frac{17}{2^4 3} l^2 + \frac{329}{2^8 3^3} l^4 \right),$$

and the subscript j refers to elements of Jupiter. The parameter $l \approx 8.58 \times 10^{-3} D$, a result not explicitly given by Érdi.

In our study of highly eccentric orbits we found that the longitude of the libration point is not fixed at $\pm 60^\circ$ from the mean longitude of Jupiter but is a function of e_p . This is illustrated by inserts in Fig. 1, that show the trajectories of three particles in the rotating frame. The trajectories illustrated correspond to small values of D ; $e_p = 0.03, 0.3,$ and 0.7 in frames A, B, and C respectively. Small circles in Fig. 1 represent measured values of the angle between the libration point and the mean longitude of Jupiter, ϕ_L , as a function of e_p ; the solid curve is a fourth order polynomial fit to the observations,

$$\phi_L = 1.047 + 1.56e_p + 0.901e_p^2 + 3.39e_p^3 - 3.71e_p^4.$$

We calculate D as follows: Let $x = |\sin((\phi - \phi_L + \pi/3)/2)|$, then

$$E_{eq} = -\frac{1}{6} \left(\frac{\partial \phi}{\partial t} \right)^2 - \frac{m\eta_j^2}{2x} [1 + 4x^3],$$

where $\frac{\partial \phi}{\partial t} = \eta - \eta_j$, ϕ is the difference in mean longitude between the Trojan and Jupiter, m is the mass of Jupiter in solar masses, and η is the mean motion of the object. Solutions for the minimum and maximum values of ϕ can be found [6] from $x_{min} = \sin(\alpha/3)/3A^{1/2}$ and $x_{max} = \sin(\alpha/3 + 120^\circ)/3A^{1/2}$, where $A = -m\eta_j^2/2E_{eq}$ and $\sin \alpha = (3A)^{3/2}$. The libration amplitude D is $\phi_{max} - \phi_{min}$.

We integrated the orbits for time intervals corresponding to 1500, 15000, and 150000 Jupiter orbital periods. Test particles were started with orbits in Jupiter's orbital plane. In a preliminary series of integrations carried out to 15000 orbital periods, where the initial inclination of the orbits was 10° , we found no significant difference in the limit of the stability field from that obtained with $i = 0$.

The distribution of orbits that are stable over the different intervals of time that we investigated is illustrated in Fig. 2, where the limits of stability for time intervals of 17 800, 178 000, and 1 780 000 years are contoured. Orbits with surprisingly high initial e_p are stable for nearly 2 million years, but no orbits with D exceeding about 110° are stable for more than 17 800 years. With increasing time the stability field shrinks in both e_p and D . The limit of the main field of observed Trojan asteroids shown in Fig. 2 may represent the approximate limit of stability for a time interval of 4.5 billion years.

One recently discovered Trojan, 1989 BQ, lies well outside the main Trojan field ($e_p = 0.22, D = 17^\circ$).

We suggest that the dynamical lifetime of 1989 BQ may be of order 10^8 years and that it has been captured late in solar system history. Capture may have occurred by diffusion, successively, from a free orbit to a horseshoe orbit to tadpole orbits of increasing stability. If one Trojan bright enough to be discovered by the usual methods of asteroid search has been captured late in solar system time, most of the known Trojans may have been captured by a similar process at an early time when the flux of Jupiter-crossing bodies was many orders of magnitude higher than at present [1].

References:

[1] Shoemaker, E.M., Shoemaker, C.S., and Wolfe, R.F., 1989, in Binsel, R.P., Gehrels, T., and Matthews, M.S., eds. *Asteroids II*, Univ. Ariz. Press, p. 487-523.
 [2] Gladman, B., and Duncan, M., 1990, *Astron. Jour.*, **100**, p. 1680-1693.
 [3] Gladman, B., Duncan, M., and Candy, J., 1990, Submitted to *Celest. Mech.*
 [4] Nobili, A.M., Milani, A., and Carpino, M., 1989, *Astron. Astrophys.*, **210**, p. 313-336.
 [5] Érdi, B., 1978, *Celest. Mech.*, **18**, p. 141-161.
 [6] Yoder, C.F., Colombo, G., Synnott, S.P., and Yoder, K.A., 1983, *Icarus*, **53**, p. 431-443.

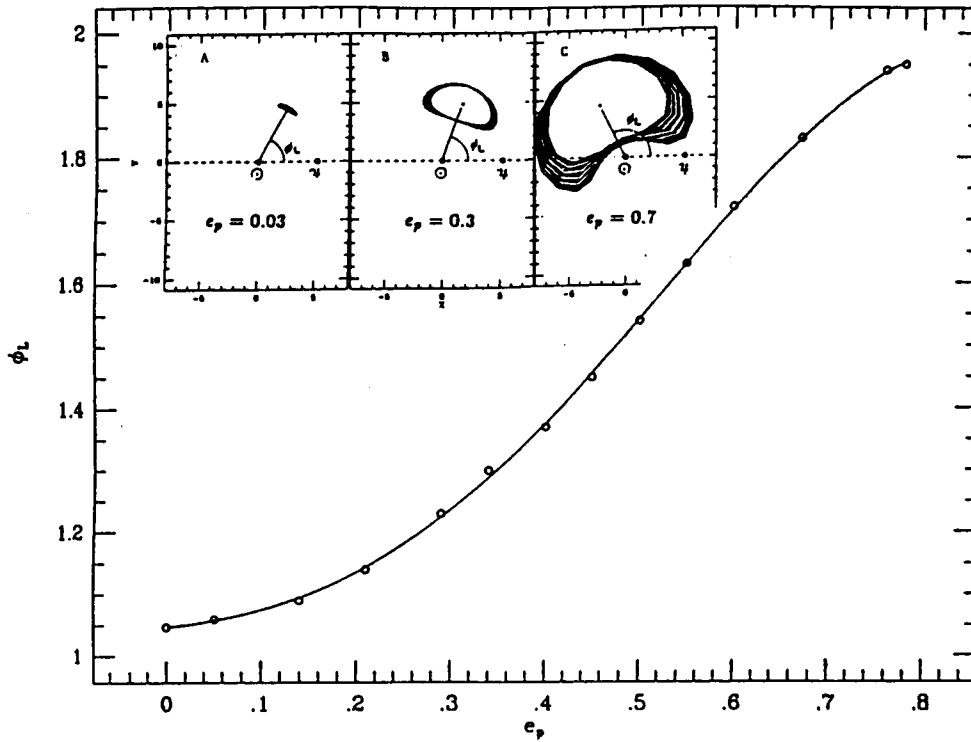


Figure 1: Position of libration point, ϕ_L , as a function of proper eccentricity, e_p .

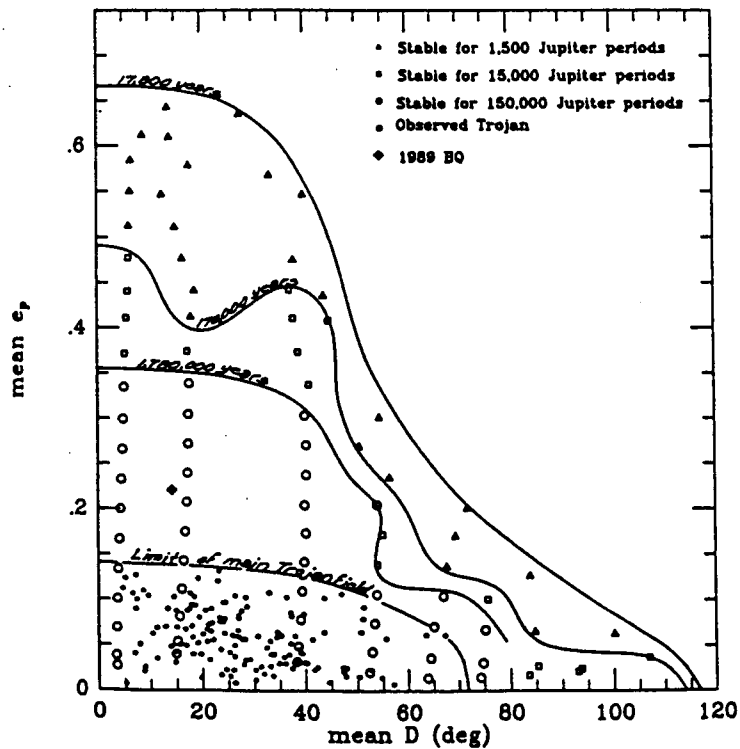


Figure 2: Map of stability of Jupiter Trojans in proper eccentricity (e_p) and libration amplitude (D) space.

UNDERSTANDING ASTEROID COLLISIONAL HISTORY THROUGH EXPERIMENTAL AND NUMERICAL STUDIES.

Donald R. Davis, E.V. Ryan, and S.J. Weidenschilling, Planetary Science Institute, Tucson AZ

It has long been known that the present size distribution of asteroids can collisionally evolve from many starting populations (Dohnanyi, 1969; Chapman and Davis, 1975; Davis *et al.* 1979). However, collisions affect other aspects of the asteroids (formation of dynamical families, exposure of M-type asteroids as the metallic cores of differentiated parent bodies, etc). Further understanding of asteroid collisional history came by identifying those initial populations that not only evolved to the present size distribution, but also produced the observed number of dynamical families and preserved the basaltic crust of Vesta (Davis *et al.*, 1985). Another major feature of the asteroids that has been significantly affected by collisions is the distribution of asteroid spin rates. We, in association with Italian colleagues, embarked on a project to develop a numerical code that would treat the collisional evolution of both the size and spin distributions simultaneously. Previous work on the collisional modification of asteroid spins dealt only with cratering impacts (Harris 1979; Dobrovolskis and Burns 1984). However, collisional disruption, rather than cratering, has been the dominant process acting on the asteroids over most of solar system history, but no one had developed a model for the spin rates of fragments or "rubble piles" formed by shattering collisions. Our initial application of this code to study the collisional evolution of asteroids could not produce the spindown observed in asteroids ~ 100 km in diameter (Davis *et al.*, 1989). Further work on the physics of asteroids that are shattered, but which partially reaccumulate due to gravity showed that such bodies can lose angular momentum due to what we termed the "splash" effect (Cellino *et al.* 1990), the analog to the "drain" effect of Dobrovolskis and Burns (1984) for cratering impacts; Figure 1 illustrates how asteroids 70-150 km in diameter can be spun down due to this effect.

In the past year we applied our numerical code with the "splash" effect incorporated to study the simultaneous evolution of asteroid sizes and spins; this work is described in a paper submitted to *Astronomy and Astrophysics* (Farinella *et al.*, 1991). We present results on the spin changes of asteroids due to various physical effects that are incorporated in our model. The goal in this paper was not to fit the observed spin distribution of asteroids (that will come next), but rather it is to understand the interplay between the evolution of sizes and spins over a wide and plausible range of model parameters. This work uses a single starting population for both the size distribution and the spin distribution of asteroids and calculates the changes in the spins over solar system history for different model parameters. We show that there is a strong coupling between the size and spin evolution, that the observed relative spindown of asteroids ~ 100 km diameter is likely to be the result of the angular momentum "splash" effect. An interesting problem arises in that this algorithm predicts a larger spinup of small asteroids than exists in the limited observational data now available. However, this "problem" arises only when the spinup rates of fragments derived from laboratory-scale impacts are used. Perhaps significantly lower spinup occurs when properly scaled to

asteroidal sized bodies, or perhaps there is a yet unrecognized process which despins small asteroids, such as the formation of binary objects.

Our collisional evolution studies to date have employed a particle-in-a-box algorithm to calculate collision rates and mean asteroid orbital elements to calculate impact speeds. However, collision rates and impact speed can vary significantly throughout the asteroid belt and these variations can produce different amounts of collisional evolution. We developed a computer program to study the variation of the collision rate and mean impact speed throughout the asteroid belt using the algorithm developed by Wetherill (1967) and the proper elements for the orbits of 682 asteroids larger than ~ 50 km diameter, a sample which is essentially complete (we assume that smaller asteroids have similar distributions of orbital elements). The Wetherill algorithm was selected over other more exact algorithms due to its ease of implementation and the fact that the differences are generally not significant for our study. We find that the mean collision speed for our sample asteroids is closer to 6 km/sec than the 5 km/sec usually quoted, and that it does not vary significantly across the asteroid zone (Fig. 2(a)). However, the mean collision rate does decrease by nearly a factor of 2 in going from the inner belt to the outer belt (Fig. 2(b)). A manuscript describing this work is currently in preparation.

We used this computer code to investigate the collisional lifetime of asteroid 951 Gaspra, the target of Galileo's October 1991 flyby. We found that the mean time between shattering collisions for a Gaspra-sized asteroid is probably $(1-2.5) \times 10^8$ years, using a basalt-like impact strength and the Housen and Holsapple (1990) scaling theory. However, if Gaspra, an S-type asteroid, has a stony-iron composition, then its strength could be considerably higher and its lifetime correspondingly lengthened. We also calculated the probability that Gaspra was a fragment from parent bodies of different sizes; Fig. 3 shows this distribution.

REFERENCES: Cellino *et al.* (1990) *Icarus* **87**, 391. Chapman and Davis (1975) *Science* **190**, 553. Davis *et al.* (1985) *Icarus* **62**, 30. Dobrovolskis and Burns (1984) *Icarus* **57**, 464. Dohnanyi (1969) *J. Geophys. Res.* **74**, 2531. Farinella *et al.* (1991) submitted to *Astronomy and Astrophysics*. Harris (1979) *Icarus* **40**, 145. Housen and Holsapple (1990) *Icarus* **84**, 226. Wetherill (1967) *J. Geophys. Res.* **72**, 2429.

Figure 1. Ratio of final to initial spin rates in a shattered collision plotted as a function of the preimpact target diameter D.

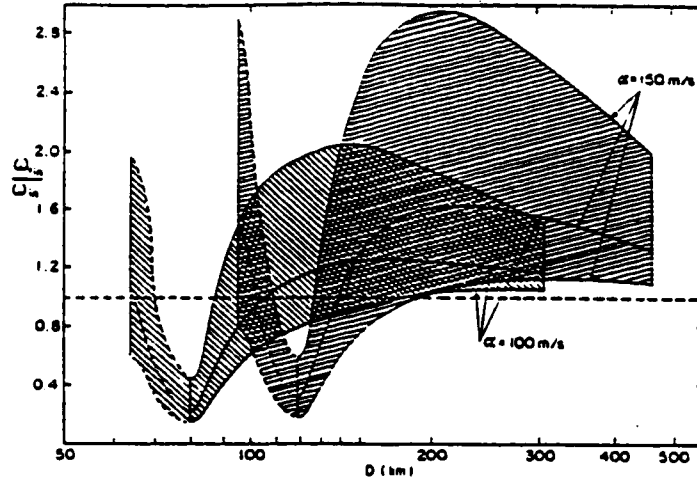


Figure 2(a). Variations of the running box mean impact speed with semimajor axis.

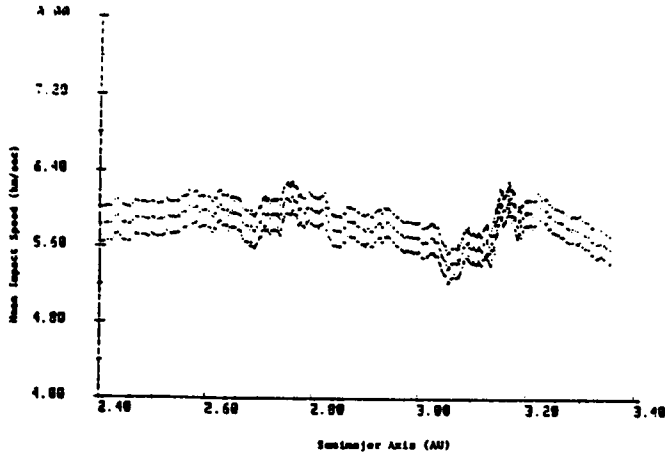


Figure 2(b). Variation of mean intrinsic collisional rate with semimajor axis.

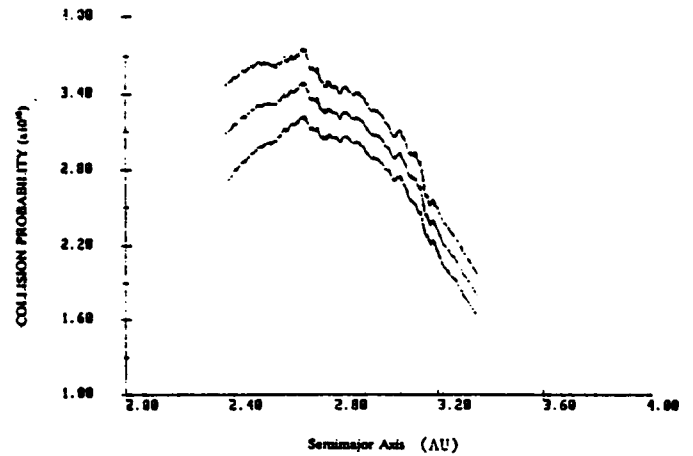
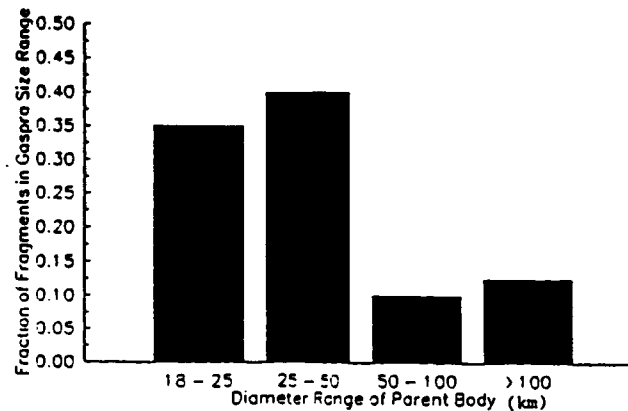


Figure 3. Distribution of parent body sizes for Gaspra-sized asteroids



BIBLIOGRAPHY

Asphaug, E., Melosh, H.J., and Ryan, E.V. (1991) A Numerical Laboratory for Fragmentation Studies: Some Insights Into Collisional Processes and Outcomes. In *Proceedings of the Conference on Lunar and Planetary Science 22*, p. 37-38. Houston, Tex.: Lunar and Planetary Institute.

Asphaug, E., Melosh, H.J., and Ryan, E.V. (1991) Impact Processes in the Solar System: New Understandings Through Numerical Modeling, press release at *The Lunar and Planetary Science Conference 22*. Houston, Tex.: Lunar and Planetary Institute.

Davis, D.R., and Chapman, C.R. (1991) On the Size Distribution of the S-type Asteroids. In *Proceedings of the Conference on Lunar and Planetary Science 22*, p. 283-284. Houston, Tex.: Lunar and Planetary Institute.

Farinella, P., Davis, D.R., Paolicchi, P., Cellino, A., and Zappalà, V. (1991) Asteroid Collisional Evolution: II. An Integrated Model for the Collisional Evolution of Asteroid Rotation Rates. Submitted to *Astronomy and Astrophysics*.

Farinella, P., and D.R. Davis (1991) The Collisional Lifetime of 951 Gaspra. In *Proceedings of the Conference on Lunar and Planetary Science 22*, p. 363-364. Houston, Tex.: Lunar and Planetary Institute.

Farinella, P., and Davis, D.R. (1991) Collision Rates and Collision Velocities in the Main Asteroid Belt. In preparation.

Housen, K.R., Schmidt, R.M., Holsapple, K.A., and Davis, D.R. (1991) Scaling of Fragmentation Experiments Conducted at Elevated Pressure. In *Proceedings of the Conference on Lunar and Planetary Science 22*, p. 593-594. Houston, Tex.: Lunar and Planetary Institute.

Ryan, E.V., Asphaug, E., and Melosh, H.J. (1991) Hydrocode Predictions of Collisional Outcomes: Effects of Target Size. In *Proceedings of the Conference on Lunar and Planetary Science 22*, p. 1155-1156. Houston, Tex.: Lunar and Planetary Institute.

Ryan, E.V., and Davis, D.R. (1991) Ejecta Mass-Velocity Distributions From Catastrophic Disruption Experiments. To be submitted to *Icarus*.

Ryan, E.V., and Davis, D.R. (1991) Laboratory Impact Experiments: Ejecta Velocity Distributions. In *Proceedings of the Conference on Lunar and Planetary Science 22*, p. 1153-1154. Houston, Tex.: Lunar and Planetary Institute.

Ryan, E.V., Hartmann, W.K., and Davis, D.R. (1991) Impact Experiments 3. Catastrophic Fragmentation of Aggregate Targets and Relation to Asteroids. Submitted to *Icarus*.

ASTEROID FAMILIES

James G. Williams, Jet Propulsion Laboratory, California Institute of Technology, Pasadena, CA.

More than 100 asteroid families are presented in Williams (1). In the illustrations the open symbols are the family members.

Several examples of cratering events are known including family numbers 150, 162, 169, and 189. These are recognizable as many small fragments adjacent to and to one side (in three dimensions) of the much larger cratered body (large open circle). 14 Irene is the parent of family number 150; it is also the source of family number 43 either by a second cratering event or the breakup of a large fragment from family 150. 20 Massalia is the source of family 162 which appears to result from two cratering events. 4 Vesta gave rise to family 169. Family 189 is one of several families originating from 8 Flora. The Galileo flyby candidate 951 Gaspra is a member of that family. The parent bodies and the measured fragments in families 150, 162, and 189 are Ss. No small fragment in the Vesta family has been classified.

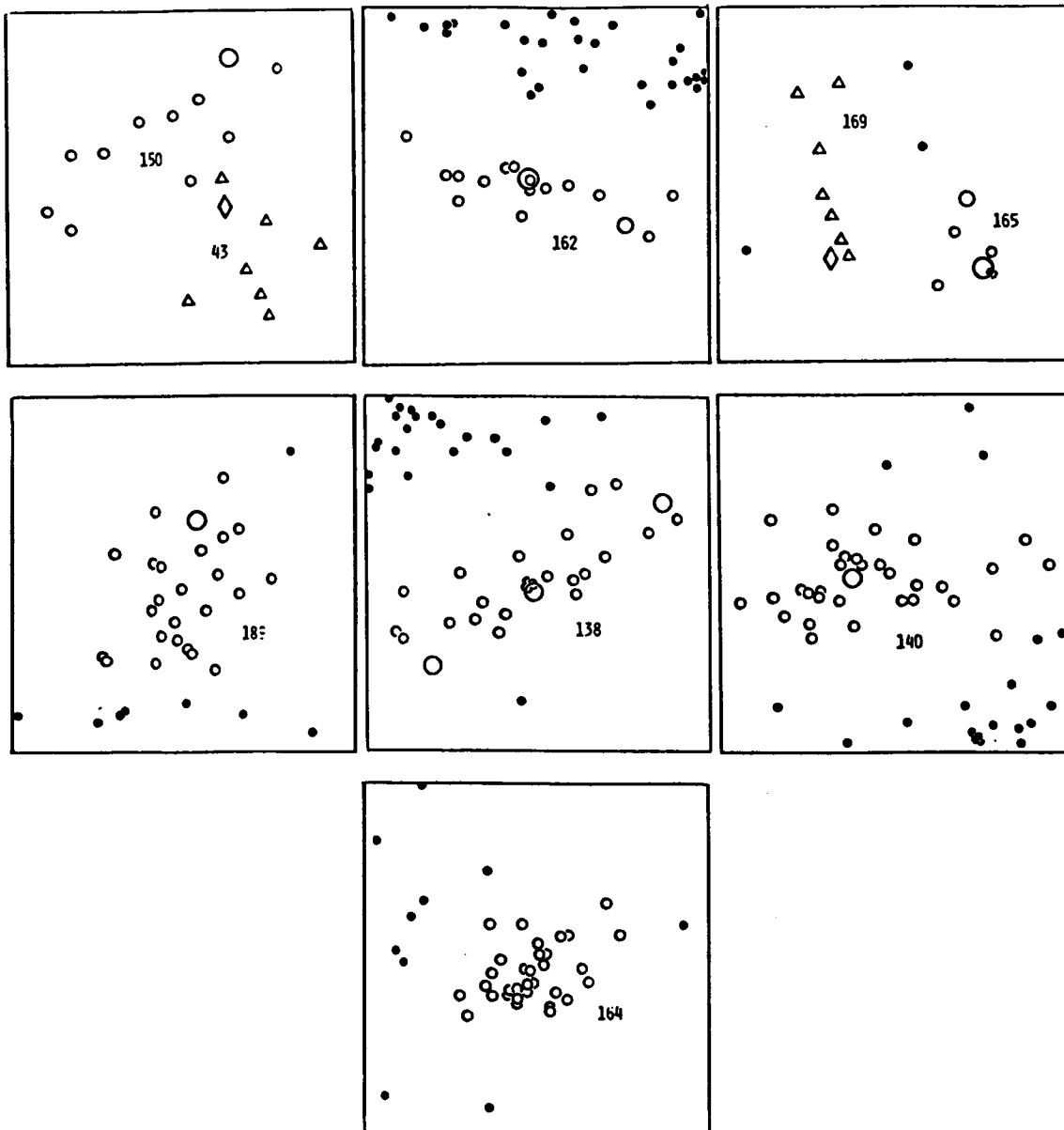
Family numbers 138 (Alexandra) and 140 (Eunomia) are adjacent in proper element space. In population they are an intermediate step between the long recognized families and the more frequent less populated families. The Alexandra family has been described in Williams (2). It is structurally complex. 93% of the volume is in three large bodies with diameters of 171, 155, and 127 km which are nearly aligned in three dimensions. About half of the family members, including one large object, lie in a thin disk (not recognizable in the projection of the figure). The fragmental size distribution (excluding the big three) starts at 67 km and is steeper than the belt average. The three large objects are Cs, but a disk member is a T. It may be that the parent body was already partitioned into three large blocks and the impact broke fragments from the area of impact and the block boundaries with the faces between blocks channeling the material into the disk.

The Eunomia family (number 140) contains the largest S asteroid (272 km diameter), two large Cs, and a fragmental branch which starts at 45 km diameter including three Ss, two Ms, and other objects with S/M-like albedos. The small Ss and Ms (<1% of the total volume of the family members) seem to be ejecta from cratering events on 15 Eunomia.

Family number 164 is the fifth most populous family in the belt. All members are faint and nothing is known of the physical properties.

References: (1,2) J. G. Williams, submitted to Icarus, 1991.

Proper e-sin i Projections of Selected Families



ORIGIN AND EVOLUTION OF THE ZODIACAL DUST CLOUD.

S. F. Dermott, D. Durda, R. S. Gomes, B. Gustafson, S. Jayaraman, Y-L Xu, Department of Astronomy, University of Florida, Gainesville, FL 32611 and P. D. Nicholson, Department of Astronomy, Cornell University, Ithaca, NY 14853.

In recent years, the astrophysical importance of the zodiacal cloud has become more apparent. It has been proved by Brownlee and others that some particles collected in the Earth's upper atmosphere are extraterrestrial in origin. At the same time, progress in laboratory techniques has made chemical and mineralogical analyses of particles less than $10\ \mu\text{m}$ possible. Thus, particles derived from the zodiacal cloud are now an important, and highly varied, source of extraterrestrial material. Unfortunately, the dominant source of these particles, whether asteroidal or cometary, is not known. It is hoped that the dust collectors (the Cosmic Dust Collection Facility) to be deployed on Space Station Freedom in the next decade will, for the first time, determine the orbits of captured particles and thus place direct constraints on their origins.

At present, the most useful source of information on the structure of the zodiacal cloud is the Infrared Astronomical Satellite (IRAS) observations in the 12, 25, 60, and $100\ \mu\text{m}$ wavebands. During its all-sky survey in 1983, IRAS discovered three prominent bands of warm emission circling the sky at geocentric ecliptic latitudes of -10 , 0 , and $+10$ degrees. We pointed out (Dermott et al., 1984): (a) that the latitudes of these bands appear to coincide with the known latitudes of the three most prominent Hirayama asteroid families, that is, the Eos, Themis, and Koronis families, and (b) that the expected *equilibrium* number density of particles in the 10 to $100\ \mu\text{m}$ size range associated with these families could be large enough to account for the IRAS observations.

We have now analysed a substantial fraction of the extensive IRAS data set. We have also developed a numerical model, the SIMUL model, that allows us to calculate the distribution of night-sky brightness that would be produced by any particular distribution of dust particle orbits. This model includes the effects of orbital perturbations by both the planets and solar radiation, it reproduces the exact viewing geometry of the IRAS telescope, and allows for the eccentricity of the Earth's orbit. The result is a model for the variation with ecliptic latitude of the brightness observed in a given waveband as the line of sight of the telescope sweeps through the modeled distribution of orbits at a constant elongation angle. We are now using SIMUL to model not just the solar system dust bands discovered by IRAS but the whole zodiacal cloud. This model is based on (a) the observed distribution of asteroidal orbits, (b) the calculated production rates of asteroidal dust, and (c) the calculated distributions of orbital elements of the dust particles after allowance for the secular perturbation of these orbits by the planets, light pressure, and Poynting-Robertson light drag.

Our main achievement this year has been the development of a new secular perturbation theory that describes the variations of the eccentricities, inclinations and semimajor axes of dust particle orbits and incorporates the effects of gravitational forces due to the planets and those due to solar radiation. In our previous work on the solar system dust bands (Dermott et al., 1984, 1985, 1986, 1988, 1989,), we described how the ecliptic latitudes of the peaks of the dustbands and the ecliptic latitude of the peak of the broad-scale zodiacal background should vary with the longitude of the Earth due to the forced inclinations imposed on the dust particle orbits by the planets. To calculate these forced orbital elements, we used the classical secular perturbation theory of Laplace and Lagrange. This theory is adequate for calculating variations in the orbital elements of the massive planets because the semimajor axes of these bodies are invariant. However, our calculations of the thermal properties of spherical silicate particles (Gustafson, 1991) have shown that particles in the 3 to 4 μm size range produce most of the thermal flux observed by IRAS in the 25 μm waveband. The orbits of particles as small as this decay due to Poynting-Robertson light drag on timescales of about 50,000 years and, thus, classical secular perturbation theory cannot be applied.

In our new theory (Gomes and Dermott, 1991), the classical concepts of forced and proper elements still hold good, but the magnitudes of the forced elements no longer depend on the semimajor axes of the dust particle orbits alone, they also depend on the drag rates of the particles and thus on their sizes and orbital histories. With this new theory, we have been able to:

1. Account for the observed inclination of the background zodiacal cloud.
2. Relate the distribution of orbital elements of asteroids in the Hirayama families to the observed shapes of the IRAS solar system dustbands.
3. Show that there is clear *observational* evidence in the IRAS data for the transport of dust particles from the asteroid belt to the Earth.

We now intend to determine the contribution of asteroidal collisions to the zodiacal cloud using the dust known to be associated with the Hirayama families as a calibrator. The ratio of the dust production rate associated with the prominent Hirayama families to that associated with the background asteroids will be modeled. By working with ratios, we will avoid the uncertainties inherent in specifying model dependent parameters (such as impact strength and energy partitioning) which strongly affect collisional outcomes. The observed ratio of the area of the dust associated with the families to that of the dust in the zodiacal background will be found by analysis of IRAS data. We will compare this ratio to the modeled ratio of family to background dust production rates and thus determine whether mutual asteroidal collisions alone are sufficient to supply the zodiacal background.

N92-10887

PHOTOMETRY OF THE COMET 2060 CHIRON

Bonnie J. Buratti, Robert L. Marcialis, R. Scott Dunbar
JPL/Caltech, Pasadena, CA 91109

Since its discovery by C. Kowal at Palomar Observatory in 1977, the comet 2060 Chiron has proven to be an interesting and enigmatic object. Situated between the orbits of Saturn and Uranus, it was originally classified as the most distant asteroid. It began to show cometary behavior in 1987 by increasing a full magnitude in brightness and developing a coma; there is evidence for similar, earlier outbursts (Bus et al., 1989; Hartmann et al., 1990; Luu and Jewitt, 1990; Meech and Belton, 1990). The diameter of Chiron is ~200 km - larger than other well-observed comets - and it has a geometric albedo and spectrum similar to primitive C-type (carbonaceous chondritic) asteroids. A rotational light curve with a period of 5.92 days has been observed, although its amplitude decreased significantly during the recent outburst. Chiron's chaotic, inward evolving orbit provides evidence that it formed in the Oort cloud. A thorough study of Chiron is important for two reasons: 1) it is a transition object defining the relationships between comets, asteroids, and meteorites; and 2) a full description of its changes in brightness - particularly on time scales of hours - will provide an empirical foundation for understanding the physical mechanisms (including outgassing, sublimation of volatiles, and even significant mass ejections) driving the evolution of comets.

In early 1989 Chiron began to show a decrease in brightness. Short term outbursts were observed (Luu and Jewitt, A. J., 1990, in press), and on 1990 January 19, we observed with the Palomar 60-inch a rapid decrease in the brightness of Chiron's coma in the V and R filters (Buratti and Dunbar, 1991, see Figure). We also detected a rotational lightcurve of the nucleus with an amplitude only 1/4 that observed in its quiescent state: this fact indicates the increased importance of the optically thin coma to the observed brightness. Clearly, Chiron appears to be undergoing short term fluctuations in its brightness, as well as a general decrease associated with the demise of its coma. The short term changes may indicate outgassing events, rapid sublimation, or the escape of dust which is possibly electrostatically charged. The fact that no color changes to a 1% level were observed during the night - a period corresponding to an increasing importance of the nucleus in the detected signal - implies that the coma is laden with dusty material from the nucleus.

During the 1991 apparition 157 CCD images in the R filter were obtained over a period of two nights. No bursts of the sort seen in 1990 were observed; however the overall brightness of Chiron was about 25% brighter than last year (Marcialis et al., 1991). The amplitude of the light curve was about 0.04

magnitudes, twice as large as that observed last year, but only half that of its quiescent state (Bus et al., 1989)

Our strategy over the next two years will be to obtain CCD images with temporal resolution of 5-10 minutes in the V and R filters. Our specific measurement goals and scientific objectives are to 1) derive an absolute magnitude to tie our observations in with the secular (~months or year) decrease in Chiron's brightness; 2) detect and characterize short term (~ hours) outbursts or decreases in brightness and understand their cause(s); and 3) measure the light curve of the nucleus to monitor the growth and decay of the comet's coma and to understand the dynamical properties of the nucleus (e.g., whether it's precessing).

Because other comets, including Halley and Schwassmann-Wachmann I, have exhibited anomalous outbursts and declines in brightness (although none of the events have been observed with such photometric accuracy or temporal resolution as the Palomar work), this study is important for understanding the present nature and evolution of comets as a class.

ACKNOWLEDGEMENT. Work done under contract to NASA/JPL.

REFERENCES

- Buratti, B., Dunbar, R.S. (1991). *Ap. J.* 366, p. L47.
 Bus, S.J., Bowell, E., Harris, A.W., Hewitt, A.V. 1989, *Icarus*, 77, p. 233.
 Hartmann, W.K., Tholen, D.J., Meech, K.J., Cruikshank, D.P. 1990, *Icarus*, 83, p. 1.
 Luu, J.X., Jewitt, D.C. 1990, *Astron. J.* 100, p. 913.
 Marcialis, R., Buratti, B. Bus, E., Noland, M. (1991). Photometry of 2060 Chiron in 1991. Abstract submitted to Asteroids, Comets, and Meteorites Conference III, Flagstaff, AZ, June 24-28 1991.
 Meech, K.J., Belton, M.J.S. 1990, *Astron. J.* 100, p. 1323.

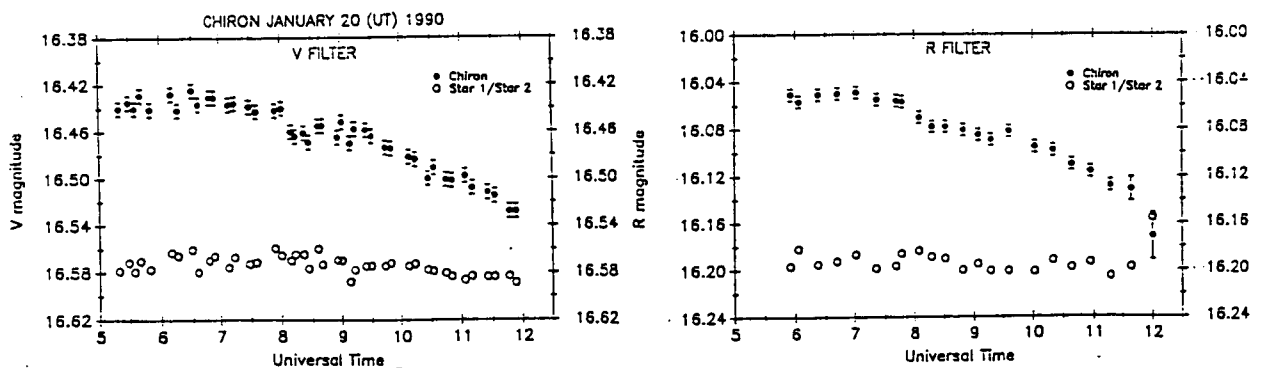


Figure. Palomar 60-inch observations of 2060 Chiron in the R and V filters. The ratio of two on-chip comparison stars used in our photometric reductions is also shown to demonstrate the certainty of the observations (Buratti and Dunbar, 1991)

A NEW ACTIVITY INDEX FOR COMETS

Fred L. Whipple, Smithsonian Astrophysical Observatory

The physical characteristics of comets have been measured in many ways including integrated or nuclear magnitudes and colors, coma and tail dimensions, polarizations and orientations, spectral characteristics of the various components and variations of all of these measured quantities. Few of these measures, however, provide classification criteria comparable to or correlated strongly with the criteria of orbital period and orientation. To achieve this goal, an activity index, AI, is derived from observational data to measure the magnitude increase of activity in comets when brightest near perihelion as compared to their inactive reflective brightnesses at great solar distances. Because the observational data are still instrumentally limited in the latter case and because many comets carry particulate clouds about them at great solar distances, the application of the activity index is still limited. A tentative application is made for the comets observed by Max Beyer (1969) over a period of nearly 40 years, providing a uniform magnitude system for the near-perihelion observations—a unique set of observations. The magnitudes at maximum distances were made mostly by Hamilton M. Jeffers, Elizabeth Roemer, and George van Biesbroek.

In all, determinations were made for 32 long-period (L-P) and for 14 short-period (S-P) comets. The total brightness increases for S-P comets range from $3^m.4$ to $9^m.0$ with the median at $6^m.0$ while for L-P comets the range is greater, from $3^m.3$ to $11^m.1$, and the median is $6^m.5$.

As expected, AI correlates strongly and inversely with perihelion distance, q . Two least squares solutions for the effect led to a correction term proportional to $1/q^{2.3}$. A small error still remained in which ΔAI increased slightly with the magnitude value at maximum distance. After both of these corrections were applied to ΔAI , the final values were used for comparisons among various classes of comets.

Among 19 L-P comets, of period, $P > 10^4$ yr, the value of ΔAI averaged $-0^m.27 \pm 0^m.25$ compared to $+0^m.39 \pm 0^m.26$ for 13 L-P comets in the group, $10^4 > P > 10^2$ yr. The difference is just a factor of two at the two σ (mean error) level suggesting greater activity among the shorter period group. Although this result must be taken as somewhat tentative, it fails to support any theory of aging among the L-P comets.

Ten highly retrograde comets of orbital inclination $i > 110^\circ$ show a mean ΔAI greater by $0^m.6$ than 22 of $i < 110^\circ$: The 7 comets in the period group, $10^4 > P > 10^3$ yr., appear to be the most active of all the L-P groups, ranged in decades of period.

Comparisons with the Dust/Gas, (D/G), ratios compiled by Donn (1977) show that 4 L-P comets with high D/G have mean $\Delta AI = +0^m.5$ compared to $-1^m.2$ for four with medium and low values of D/G.

As a concluding remark about the L-P comets, the range in ΔAI with $\sigma = \pm 1^m.06$ seems surprisingly small, suggesting, as do most of the comparisons above, that the comets are amazingly alike. Note that the range in absolute magnitude at maximum

distance is $7^m.2$ corresponding to a range of 28 times in diameter, if the albedos are assumed constant.

For the 14 S-P comets the values of ΔAI average smaller by $0^m.33 \pm 0^m.32$ than those of the 32 L-P comets. This means that S-P comets show almost as much activity variation with solar distance as do L-P comets, suggesting that there is little difference between the two groups.

In conclusion, the measures of the activity index suggest that short-period comets and long-period comets brighten in very much the same way. The same seems to be true of large comets and small comets. Hence, this evidence suggests a common nature and origin for L-P and S-P comets of all sizes and all ages. The interiors of comets of all kinds seem to be statistically similar throughout. Only the outer layers of "new" comets probably have been altered systematically.

This study was supported by NASA Grant NSG-7082. I am particularly grateful to Brian G. Marsden for a computer disc of his comet-orbit catalogue and for use of several of his programs.

Beyer, M. 1972, *Astr. Nach.*, 293, 241-257, for list of references.

Donn, B. 1977, *Comets, Asteroids, Meteorites*, ed. A.H. Delsemme, Univ. Toledo, 15-23.

THE ANGULAR MOMENTUM OF THE OORT CLOUD. Paul R. Weissman, Earth and Space Sciences Division, Jet Propulsion Laboratory, Pasadena, CA 91109

Marochnik et al. (1988) estimated that the angular momentum of the Oort cloud is between 5×10^{52} and 2×10^{53} $\text{g cm}^2 \text{sec}^{-1}$, two to three orders of magnitude greater than the total angular momentum of the planetary system. As a result, they argued that the comets could not have been ejected from the outer planets zone of the protosolar nebula, without having the planets spiral in towards the Sun. Thus, they claimed that the comets must have formed *in situ* at Oort cloud distances.

Several factors suggest that Marochnik's et al.'s estimate for the Oort cloud angular momentum is too high. First, a large fraction of the angular momentum in the present-day Oort cloud is the result of the action of external perturbers over the history of the solar system, and was not drawn from the protosolar nebula. Second, since orbital inclinations in the outer Oort cloud (and some fraction of the inner cloud) have been randomized by those external perturbers into a roughly spherical distribution, the net angular momentum in the cloud is actually fairly small. Finally, some of the parameters used by Marochnik et al. tended to overestimate the Oort cloud's population and mass.

New estimates of the Oort cloud angular momentum were derived using the most recent estimates (Weissman, 1990, 1991) for the cloud population and for the average mass of cometary nuclei. In addition, estimates of the original angular momentum of the comets at the time they were placed in the cloud were made, assuming ejection from the Uranus-Neptune zone and including corrections for the number of comets directly ejected to interstellar space and for the fraction of the Oort cloud population lost over the history of the solar system. Orbital distributions in the Oort cloud (both inner and outer) were based on the dynamical modeling of Duncan et al. (1987). It was shown that the total angular momentum of the current Oort cloud is between 6×10^{50} and 1.1×10^{51} $\text{g cm}^2 \text{sec}^{-1}$, and that the original angular momentum was about a factor of five less than that. This latter figure is between 2.6 and 4.9 times the current angular momentum of Uranus and Neptune combined. However, since the ejected cometesimals originated in roughly circular orbits around the Sun, the net angular momentum added to eject them to the Oort cloud is only about 29% of these figures, or 0.8 to 1.4 times the angular momentum of Uranus and Neptune.

These estimates are already well within the current bounds of theories of solar system origin, which estimate that the Uranus-Neptune zone originally contained a population of icy planetesimals ~ 10 times the mass of those two planets. However, when one recognizes that the growing protoplanets scattered planetesimals both inward and outward, it is easy to see that the net angular momentum lost by the protoplanets was fairly small. This was very effectively shown by Fernandez and Ip (1984) in their dynamical modeling of the growth of the outer planets from planetesimals.

Duncan, M., Quinn, T., and Tremaine, S., *Astron. J.* **94**, 1330-1338, 1987. Fernandez, J. A., and Ip, W.-H., *Icarus* **58**, 109-120, 1984. Marochnik, L. S., Mukhin, L. M., and Sagdeev, R. Z., *Science* **242**, 547-550, 1988. Weissman, P. R., *Nature* **344**, 825-830, 1990. Weissman, P. R., In *Conference on Global Catastrophes in Earth History*, eds. V. L. Sharpton and P. D. Ward, GSA Special Paper 247, in press.

WATER/ROCK INTERACTIONS IN EXPERIMENTALLY SIMULATED "DIRTY SNOWBALL" AND "DIRTY ICEBALL" COMETARY NUCLEI

James L. Gooding¹ and Judith H. Allton² ¹SN21/Planetary Science Branch, NASA/Johnson Space Center, Houston, TX 77058 USA. ²C23/Lockheed Engineering and Sciences Co., Houston, TX 77058 USA.

Introduction. In the "dirty snowball" model for cometary nuclei [1], comet-nucleus materials are regarded as mixtures of volatile ices and relatively non-volatile minerals or chemical compounds. Although results from the *Giotto* and *Vega* spacecraft flybys of comet P/Halley indicate a complex chemistry for both the ices and dust in the nucleus [2], carbonaceous chondrite meteorites are still regarded as useful analogs for the rocky component [3]. Previous considerations of the behavior of water in cometary nuclei have focussed on theoretical evaluations of the effects of phase transitions on heat balance [4] or the kinetics of ice retention [5]. Apparently, less attention has been paid to water/mineral interactions despite the wealth of information about the mineralogical dependence of water behavior in frozen soils [6]. To help elucidate the possible physical geochemistry of cometary nuclei, we report preliminary results of calorimetric experiments with two-component systems involving carbonaceous chondrites and water ice.

Based on collective knowledge of the physics of water ice [7,8], three general types of interactions can be expected between water and minerals at sub-freezing temperatures: (a) heterogeneous nucleation of ice by insoluble minerals; (b) adsorption of water vapor by hygroscopic phases; (c) freezing- and melting-point depression of liquid water sustained by soluble minerals. The relative and absolute magnitudes of all three effects are expected to vary with mineral composition.

Samples and Methods. Two series of experiments were performed in a differential scanning calorimeter (DSC) with homogenized powders (silt-sized and finer grains) of whole-rock meteorites and comparison samples [9]. In Series 1, approximately equal masses of mineral/rock powder and deionized water were blended into mud at room temperature (295-298 K) and crimp-sealed in an aluminum container; a physically separate droplet of deionized water, overhanging the mud, served as internal standard. Series 2 used the same procedure except that a dry mineral/rock sample was exposed only to water vapor from the overhanging droplet. Each sample container was placed in a Perkin-Elmer DSC-2C instrument and cooled at 10 K/min to ≤ 200 K, followed by re-heating at 10

K/min, under a continuous gas purge of 20 cm³ Ar/min. (Experiments down to 100 K verified absence of significant transitions below 200 K). DSC heat-flow data were acquired during multiple freeze/thaw cycles. Certified mercury ($\Delta H(\text{melt}) = 11.469$ J/g at 234.3 K; National Institute of Standards and Technology SRM-2225) was used for DSC primary calibration. Separate experiments were performed on the Allende (CV3), Murchison (CM2), Orgueil (CI), Holbrook (L6), and Pasamonte (eucrite) meteorites as well as on peridotite PCC-1 (U. S. Geological Survey), saponite (Clay Minerals Society SapCa-1), montmorillonite (CMS STx-1), and serpentine (Franciscan Formation, California).

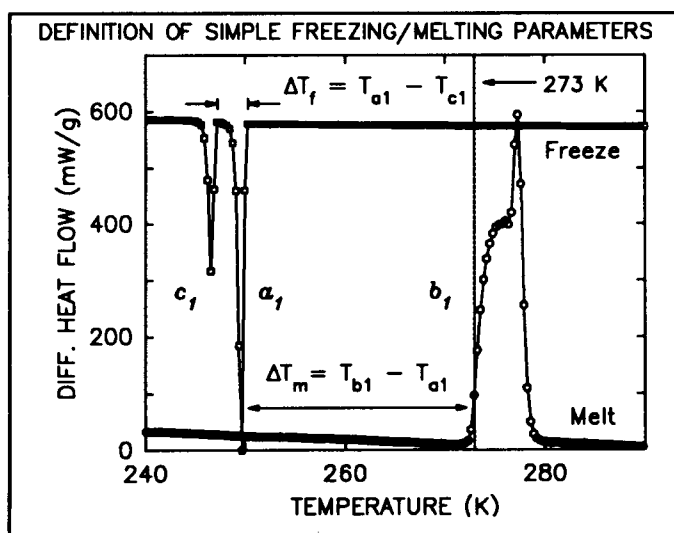


Figure 1. Simple parameters measured from DSC extrapolated-onset temperatures of freezing and melting peaks for water in sample (peaks a, b) and internal standard (peak c). The 273 K reference marker is not part of the parameterization.

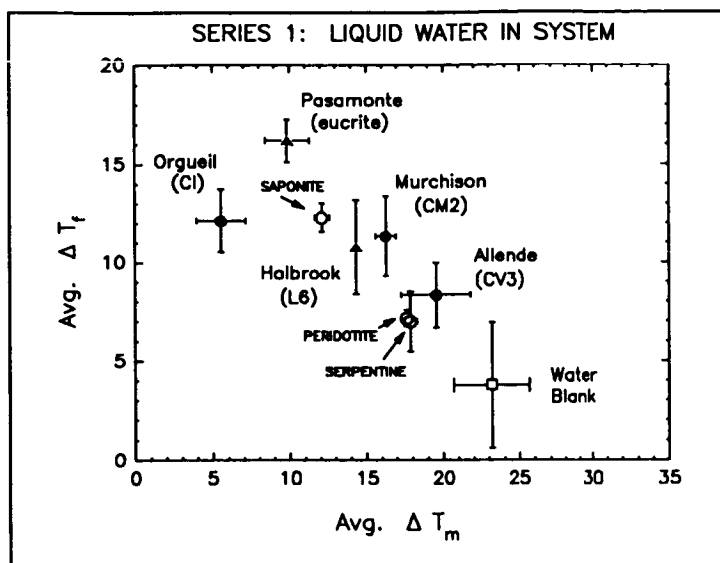


Figure 2. Summary of freezing/melting parameters measured for Series 1 ("dirty iceball") experiments. Points with error bars represent mean (\pm one standard deviation of the mean) results from replicate (3-4) analyses of individual samples. The overall negative trend of data points indicates control by heterogeneous nucleation of ice. Deviation of the Orgueil point from the trend reflects additional freezing- and melting-point depression by water-soluble salts.

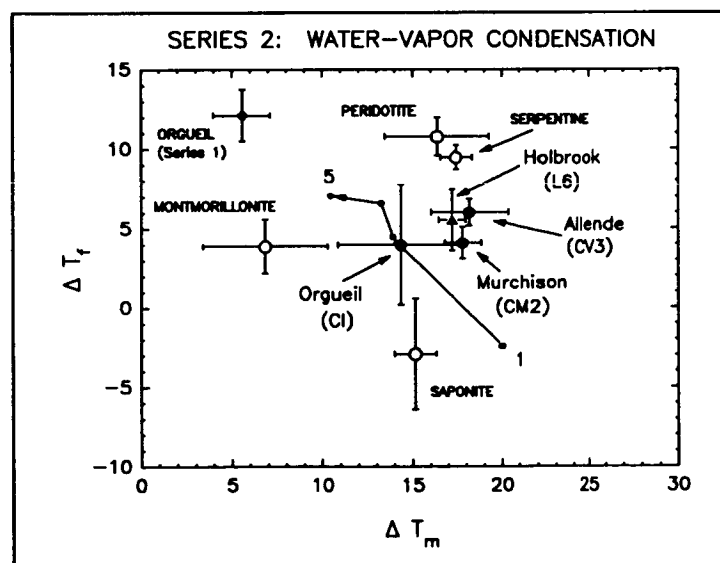


Figure 3. Summary of freezing/melting parameters measured for Series 2 ("dirty snowball") experiments. Points with error bars represent mean (\pm one standard deviation of the mean) results from replicate (3-4) analyses of individual samples. Numbered points (1-5) denote individual cycles for Orgueil. Absence of coherent trends (cf., Fig. 2) indicates different control of water/rock interaction relative to those involving liquid water. Here samples are distinguished mostly by their relative sorption of water vapor. Orgueil exhibits transition from "snowball" to "iceball" with repeated thermal cycling.

Although the DSC data contain substantial "fingerprint" (analog pattern) information for each sample [9], we wish to convey the systematics of water/rock interactions by reducing the measurements to simple parameters that describe the freezing and melting behavior of water. Accordingly, the parameters ΔT_m and ΔT_f are defined (Fig. 1) to quantitatively describe how mineralogy affects freezing and melting relative to a pure water internal standard. We emphasize that much additional diagnostic information could be derived by analyses of DSC peak shapes and enthalpic ratios; our use of ΔT_m and ΔT_f here serves only to conveniently summarize variations in water/rock systems under freezing conditions.

Results. SERIES 1. These experiments can be considered "dirty iceball" simulations in which water is uniformly distributed in a relatively dense mixture. Because freezing of water depends heavily on heterogeneous nucleation [7,8], and the aluminum container is a relatively poor nucleator, liquid water undercools substantially before freezing in the absence of minerals. The mineral/rock substrates were distinguished by their relative abilities to nucleate ice from undercooled water [9]. If heterogeneous nucleation was the only (or dominant) control of freezing, and melting-point depression by dissolved material was not important, a plot of ΔT_f vs. ΔT_m should comprise a negatively sloping data trend (i.e., ΔT_f and ΔT_m should be inversely correlated as defined in Fig. 1). Indeed, experimental results are consistent with dominance of heterogeneous nucleation (Fig. 2).

The trend among mineral and rock samples can be understood in terms of the major minerals in each material. As reviewed previously in another context [10], the relative ice-nucleation abilities of igneous silicates are expected to be olivine - plagioclase << pyroxene. Phyllosilicates are expected to exhibit a wide range of nucleation abilities; non-expandable clays (e.g., chlorites) are generally expected to be better nucleators than expandable clays (e.g., montmorillonite, saponite) [10]. The ice-nucleation effectiveness of montmorillonite-type clays, however, is expected to vary with degree of interlayer expansion which, in turn, will depend on degree of hydration and identities of interlayer cations [10]. As a kaolinite-type clay, serpentine is expected to be no more than a moderately good nucleator. Among our test samples, the poorest ice nucleators contain high abundances of olivine (e.g., peridotite, Allende) whereas the best ice nucleators are composed mostly of pyroxene (e.g., Pasamonte). The phyllosilicate-rich meteorites, Murchison and Orgueil, show intermediate ice-nucleation abilities that probably reflect a complex interplay of water with igneous silicates, clay minerals, and possibly organic matter. A second minor "melting" peak in frozen Orgueil, and a systematic decrease in the onset of melting in both Orgueil and Murchison [9], further suggest interactions of water with hygroscopic minerals. In fact, the deviation of Orgueil from the overall inverse trend in Fig. 2 can be understood as effects of freezing- and melting-point depressions created by dissolved salt minerals (e.g., epsomite).

SERIES 2. These experiments can be considered "dirty snowball" simulations in which water is progressively condensed within a porous substrate; in contrast with the "iceball" simulation, liquid water is less important and uniformity may be established only after significant elapsed time. Whereas freeze/thaw cycling of Series 1 samples revealed little, if any, systematic change with time, data for Series 2 samples showed pronounced changes with successive thermal cycles. Freezing and melting peaks controlled by the mineral/rock samples grow during successive freeze/thaw cycles, presumably as water vapor is progressively adsorbed and condensed on the initially dry samples. Characteristic signatures are well established after 3-5 cycles. Effects are seen in all three of the carbonaceous chondrites but are most pronounced for Orgueil, probably as a consequence of its abundant hygroscopic phyllosilicates and sulfates. For the complete suite of samples, absence of a coherent trend among the parameterized data (Fig. 3) indicates that, in contrast with Series 1, heterogeneous nucleation was not the dominant effect. The apparent formlessness of the simple $\Delta T_f/\Delta T_m$ parameterization belies the fact that better inter-sample discrimination is achieved by comparison of the full DSC curves [9]. For Orgueil, in particular, average values of the ΔT parameters fail to convey time-dependent changes. Successive "snowball" cycles for Orgueil gave parameterized results that showed a systematic trend toward "iceball" behavior (points 1-5 moving toward Series 1 point in Fig. 3).

Implications for In-Situ Cometary Analyzers. Besides identification of volatile ices (not addressed in this paper), DSC-type experiments could help diagnose the rocky component of a comet nucleus. In addition to conventional high-temperature DSC, in which minerals are identified by phase-transition or decrepitation reactions, low-temperature DSC could sense the freezing interactions of minerals with water. Based on our freezing/melting data, we would expect (at the minimum) that eucrites could be distinguished from ordinary and carbonaceous chondrites and that Orgueil-type chondrites could be distinguished from other chondrites. Additional experimental work would be necessary, however, to establish the possible effects of other volatile ices, minerals, and organic matter.

References: [1] Whipple F. L. (1978) *Moon and Planets*, 19, 305-315. [2] Kissel J. et al (1986) *Nature*, 321, 280-282. [3] McSween H. Y. Jr. and Weissman P. R. (1989) *Geochim. Cosmochim. Acta*, 53, 3263-3271. [4] Herman G. and Podolak M. (1985) *Icarus*, 61, 252-266. [5] Fanale F. P. and Salvail J. R. (1987) *Icarus*, 72, 535-554. [6] Anderson D. M. and Morgenstern N. R. (1973) In *Pernafrost: The North American Contribution to the Second International Conference*, National Academy of Sciences, Washington, DC, 257-288. [7] Hobbs P. V. (1974) *Ice Physics*, Clarendon, 837 pp. [8] Pruppacher H. R. and Klett J. D. (1978) *Microphysics of Clouds and Precipitation*, D. Reidel, 714 pp. [9] Gooding J. L. and Allton J. H. (1991) In *Lunar Planet. Sci. XXII*, Lunar and Planetary Institute, Houston, Texas, 459-460. [10] Gooding J. L. (1986) *Icarus*, 66, 56-74.

THERMAL MODELING OF COMET KOPFF: IMPLICATIONS FOR THE CRAF MISSION. Paul Weissman and Celia Clause, Earth and Space Sciences Division, Jet Propulsion Laboratory, Pasadena, CA 91109

A thermal model of periodic comet Kopff was developed to aid in planning for the Comet Rendezvous Asteroid Flyby mission (Neugebauer and Weissman, 1989). The model is based on the comet nucleus model of Weissman and Kieffer (1981, 1984), which estimates the surface temperature distribution and sublimation rates on a rotating icy sphere in heliocentric orbit. Assumed parameters for Comet Kopff are: nucleus radius = 4 km, surface albedo = 0.04, surface density = 0.5 g cm^{-3} , rotation period = 10 hours, and surface thermal inertia = $0.003 \text{ cal cm}^{-2} \text{ s}^{-1/2} \text{ K}^{-1}$. The model results are compared with the observed gas production rates from Kopff in 1983. It is found that approximately 15% of the sunlit nucleus surface is active, a relatively high fraction for a typical short-period comet. This suggests that the actual nucleus radius may be larger than the model value. The slope of the observed gas production curve with heliocentric distance is steeper than that predicted by the thermal model. This may indicate the existence of a more complex process than direct sublimation of surface ices, such as gas diffusion through a nonvolatile insulating crust.

If one assumes a nucleus obliquity near zero, then the resulting estimated sublimation rates pre- and post-perihelion are remarkably symmetric, suggesting that any observed asymmetries are the result of the distribution of active areas on the nucleus surface of Comet Kopff. On the other hand, if large obliquities are assumed, then pre- and post-perihelion gas production rates can vary accordingly. However, the greatest variation in gas production rate for high obliquities comes at large heliocentric distances, beyond 2.5 AU. Variations by orders of magnitude are possible. This is because the energy going into sublimation at large distances is comparable to the surface heat flow and radiation terms. Nearer to perihelion virtually all energy goes into sublimation and nucleus orientation becomes a less significant factor.

Estimates of subsurface temperatures on Kopff were of particular interest to the Penetrator experiment which would have delivered an instrumented package to the nucleus surface approximately one year after arrival at the comet, at a heliocentric distance of 4.0 AU (NASA recently de-selected the Penetrator from the CRAF payload). If one assumes a low obliquity for the nucleus, the thermal model results indicate that there will likely be a broad range of 20 to 30° in latitude near the nucleus rotation poles, which meets the Penetrator requirements of temperatures less than 120 K. For higher obliquities the problem becomes more complex, particularly if one must also deliver the Penetrator to a sunlit location. The diurnal thermal wave is not expected to penetrate more than 10 to 30 cm into the surface, assuming the modest thermal inertia used in the model. The estimated gas production rate at 4.0 AU is $\sim 10^{24} \text{ s}^{-1}$. These results are relevant to planning for the joint NASA/ESA Rosetta mission which will return a comet nucleus sample to the Earth for detailed analysis.

References: Neugebauer, M., and Weissman, P. R., EOS 70, 633, 1989; Weissman, P. R., and Kieffer, H. H., Icarus 47, 302, 1981; Weissman, P. R., and Kieffer, H. H., JGR 89, C358-C364, 1984.

THE INFLUENCE OF CO ICE ON THE ACTIVITY AND NEAR-SURFACE DIFFERENTIATION OF COMET NUCLEI

F.P. Fanale and J.R. Salvail (Planetary Geosciences Div., School of Ocean & Earth Sciences and Technology, Univ. of Hawaii, Honolulu, HI)

The role of unclathrated CO ice in the activity and near-surface differentiation of comet nuclei has been investigated. A computer program used in the authors' previous work (Fanale and Salvail, 1987, *Icarus* 72, 535-554) has been adapted to model a comet nucleus composed of a homogeneous mixture of H₂O ice, CO ice, and dust, in a Halley-type orbit. The difference in the volatility of CO and H₂O ices results in greatly different gas production rates, and recession of the CO ice surface occurs, forming a porous surface layer of H₂O ice and dust. Temperatures of H₂O and CO ice surfaces, fluxes of CO and H₂O gases, and depths of the CO ice are presented as functions of orbital position. Also considered are the pressures of subsurface CO as they relate to the stability of the overlying H₂O ices and dust mantle and the possibility of dust or H₂O ice grain emission. Possible pressures are in the range $3 \times 10^2 \text{ dyn cm}^{-2}$ to $1 \times 10^6 \text{ dyn cm}^{-2}$. These are insufficient to fragment annealed H₂O ice, yet capable of overcoming the lithostatic pressures of many meters of unannealed H₂O ice and emitting free surface grains in the 1- μm range. However, they are comparable to the inferred range of ice-poor mantle strength and may account for episodic regional changes in activity. It has been found that CO ice should always exist within 3 m from the surface, and that CO gas production exceeds H₂O gas production beyond 2.5 A.U. This has implications for planned *in situ* elemental analysis of nuclei. CO gas production from "new" comets can be as much as 3 orders of magnitude greater before perihelion. After perihelion there is little difference in CO production for "new" and periodic comets. The results have been found not to depend significantly on the permeability of the water ice mantle or the estimated variability of the mass fraction of CO.

CHAPTER 8

SOLAR SYSTEM DYNAMICS

Formation of the Protosolar Nebula

Werner M. Tscharnuter, Universität Heidelberg
Alan P. Boss, DTM, Carnegie Institution of Washington

In this review chapter for the *Protostars & Planets III* volume we discuss theoretical models of the collapse of a dense molecular cloud core to form the protosolar nebula that produced the sun and planets. The theoretical models use the equations of hydrodynamics, gravitation, and radiative transfer to follow the time evolution of a cloud collapsing under its own self-gravity. Both semi-analytical and fully numerical solutions (in two and three spatial dimensions) have been calculated by several workers. One challenge is to find a set of initial conditions that will lead to the formation of a suitable protosolar nebula. In principle, these initial conditions should be determined by observations of low-mass star-forming regions, but in practice substantial uncertainties remain because of the difficulty of determining key quantities such as the pre-collapse density profile, amount of angular momentum, and degree of magnetic field support. Hence a fair amount of modeling has been done to determine which initial conditions lead to single protostar formation and which to binary protostars, assuming magnetic fields can be neglected. Single protostars should result from the collapse of clouds that are initially very slowly rotating, close to thermal equilibrium, or strongly centrally condensed. Given one set of these initial conditions, the next challenge is to calculate the collapse as far as possible, ideally far enough to make contact with theoretical models of planetary formation. This second goal has not yet been fully achieved, largely because the resulting protosolar nebula must undergo significant dynamical evolution in order to transfer mass inward to form the sun, and to transfer angular momentum outward. The agent of this large-scale, angular momentum-mass differentiation is problematical, though several promising candidates have been identified: turbulent viscosity, gravitational torques, and magnetic fields. Detailed results are shown for two dimensional models, both with and without turbulent viscosity for redistributing angular momentum, and for three dimensional models investigating the strength of gravitational torques associated with nonaxisymmetry produced during the collapse phase. All of these models imply that the protosolar nebula may have been substantially hotter ($\sim 1500\text{K}$) in the inner few AU than has usually been assumed. As these models are further refined in the future, we will be able to improve our predictions of crucial quantities such as surface densities and midplane temperatures in the solar nebula, at a time when the sun has largely formed and the process of planetesimal accumulation is well underway.

FRAGMENTATION IN STELLAR COLLAPSE.

E. M. Myhill and W. M. Kaula, Department of Earth and Space Sciences, University of California, Los Angeles, CA.

A three dimensional, Cartesian code has been developed to model molecular cloud collapse and protostellar formation. The basic Eulerian scheme employs spatially second-order accurate, finite difference methods to advance the fluid variables in time. The hydrodynamic equations governing the collapse include the effects of self-gravity, rotation, and radiative transfer. Supplementary equations include Poisson's equation which relates the gravitational potential to the density distribution and a mean intensity equation derived with the Eddington approximation for radiative transfer. The gas pressures and internal energies are determined from equations of state derived for a molecular cloud composed of hydrogen, helium, and heavier elements¹. Rosseland mean opacity tables determined by Pollack et al.² are used to calculate the opacity values.

Initially the effects of opacity, heating, and radiative transfer were ignored, and an isothermal collapse code was developed. This type of scheme is appropriate for the early stages of molecular cloud collapse when the gas remains essentially transparent, and the dust grains radiate away any thermal energy generated by compression. The advective terms in the hydrodynamic equations are evaluated with the van Leer second-order, upwind difference scheme³, while second-order centered differencing is used to calculate the source terms. A second-order accurate scheme is an improvement over previous first-order methods as it results in considerably less numerical viscosity. Green's functions and Fourier transforms are used to solve Poisson's equations⁴.

After the isothermal collapse code had been rigorously tested, a nonisothermal version was developed by adding the energy equation to the basic set of hydrodynamic equations so that the effects of heating and radiative transfer would be included. The radiative flux term is evaluated with the Eddington approximation, and an alternating directions implicit method is used to solve the supplementary mean intensity equation. The Eddington approximation, which assumes that the ratio of the radiation pressure to the energy density is $1/3$, is a significant improvement over the more commonly used diffusion approximation which is strictly correct only at large optical depth. A regridding routine was also developed to improve the grid resolution in the later stages of collapse. The nonisothermal scheme was used to follow the gravitational collapse of molecular cloud cores. These calculations differed from previous computations in that the clouds began the collapse with centrally condensed density

distributions and varying amounts of differential rotation. Observations and studies of ambipolar diffusion indicate that cores are likely to have $1/r$ to $1/r^2$ density distributions^{4,5}. Two initial angular velocity profiles were investigated: (1) solid body rotation corresponding to an upper limit for magnetic braking during core formation and (2) differential rotation profiles appropriate for a minimum amount of magnetic braking. The other initial conditions (mass = 4 solar masses, initial temperature = 10K, initial radius = 1.5×10^{-17} cm) were based on radio observations of dense cores in Taurus-Aurigus⁷. All of the models began with similar thermal, rotational, and gravitational energies. Initially, the clouds had average density and angular velocity values of 5.6×10^{-19} g/cm³ and $4.0-5.0 \times 10^{-13}$ rad/s respectively.

ACKNOWLEDGEMENT: This research was supported by NASA under Grant NAGW-2085.

REFERENCES: ¹Boss, A. P. (1984). Astrophys. J., 277, 768-782. ²Pollack, J. B. et al (1985). Icarus, 64, 471-492. ³Van Leer, B. (1977). J. Comp. Phys., 23, 263-275. ⁴Hockney, R. W. (1970). Meth. Comp. Phys., 9, 135-211. ⁵Zhou, S. et al (1990) Astrophys. J., 363, 168. ⁶Lizano, S., & Shu, F. H. (1989). Astrophys. J., 342, 834. ⁷Myers, P. C. & Benson, P. J. (1983). Astrophys. J., 266, 309.

Spectral and Isophotal Appearance of 3D Protostellar Models

Alan P. Boss, DTM, Carnegie Institution of Washington
Harold W. Yorke, Universität Würzburg

Emergent spectra and isophotes were calculated for several different types of three dimensional (3D), low mass, protostellar models. The protostellar models include single and binary protostellar clouds, and protostellar nebulae with and without dominant central protostars. The spectra and isophotes are derived from 3D, frequency-dependent, ray tracing calculations using the temperature distribution obtained from either diffusion or Eddington approximation radiative transfer calculations.

The single protostar models are of direct interest for solar nebula formation. Model D is model A from Boss (1988, *Science*, 241, 565). This model depicts a protostar and surrounding nebula obtained by collapsing a very dense cloud with a mass of $0.102 M_{\odot}$ onto a point source of gravity with mass $1.000 M_{\odot}$ (note that the central protosun was not modeled in detail, and inclusion of its luminosity could significantly increase temperatures in the model.) At the time considered here, the model had evolved into a $0.061 M_{\odot}$ nebula surrounding a $1.041 M_{\odot}$ protosun. The nebula remained largely axisymmetric, with midplane temperatures reaching ≈ 1500 K within a few AU. This model represents a relatively low mass protoplanetary nebula surrounding a recently formed protostar.

Model E is model B from Boss (1988). This model consists of a protostellar nebula obtained by collapsing a very dense cloud with a mass of $1.025 M_{\odot}$ onto a point source of gravity with zero mass. This model forms a $\sim 0.8 M_{\odot}$ binary protostar that is extant at the time considered here, but should subsequently undergo orbital decay. The model is strongly nonaxisymmetric, with midplane temperatures varying from ≈ 1700 K to ≈ 200 K at a few AU from the center. This model represents a relatively high mass protoplanetary nebula that has not yet accumulated into a single protostar.

Model D produced a spectrum significantly different from a 10 K black body. The spectrum resembles that of a 35 K black body, reflecting the ability of some of the higher temperature emission to emerge from the hot (~ 1500 K) central region of the cloud. This is only possible because of the relatively small amount of mass in the envelope of model D. The total luminosity varies from 2.1×10^{32} erg s $^{-1}$ from pole-on to 1.7×10^{32} erg s $^{-1}$ for equator-on. This luminosity is the highest of all the models considered, reflecting the assumption of a pre-existing solar-type protostar with a deep gravitational potential well, leading to high infall velocities and consequently high temperatures, surrounded by a relatively low mass nebula.

The spectra for model E are similar to those of 10 K black bodies; in spite of having temperatures as high as 2200 K in the central regions, this inner region is effectively shielded by the overlying, massive, cool cloud envelope. The total luminosity for model E varies from 3.1×10^{29} erg s $^{-1}$ from pole-on to 3.6×10^{29} erg s $^{-1}$ for equator-on.

Based on calculating the spectral and isophotal appearance of five representative models of early protostellar evolution, the following conclusions may be drawn:

1) Isophotes tend to be considerably more rounded than the underlying density contours, and may flare out in directions that do not precisely follow density and temperature contours, increasing the difficulty of correctly identifying small scale structures such as binary protostars.

2) Early protostellar binaries may be most easily resolvable from lines of sight close to perpendicular to the binary midplane. For other lines of sight, the binary may appear to be single or simply to be a highly flattened disk. Thin nebula viewed edge-on may have intensity maxima above and below their midplanes that could be confused with binary protostars.

3) The spectral appearance of an early protostellar cloud without a well-developed central protostar is similar to that of a 10 K black body, even when substantial heating has occurred in the central regions.

4) High temperature regions surrounding well-developed protostars can be inferred from observations of objects with spectra similar to black bodies with temperatures significantly greater than 10 K, but the inferred temperatures (~ 35 K) may be far less than the typical temperatures in the nebula (~ 1500 K).

5) These protostellar phases are all too faint to have been detected by *IRAS*, but could be detected spectroscopically as essentially point sources by *SIRTF* and possibly *ISO*. The spatial resolution needed to differentiate between single and relatively close ($\sim 10 - 100$ AU) binary protostars appears to require the use of an interferometric millimeter-wave array.

AERODYNAMIC AND GASDYNAMIC EFFECTS IN COSMOGONY.

S. J. Weidenschilling, Planetary Science Institute

The solar system is the product of a primordial nebula that was composed mostly of gas, with only a small admixture of solid matter. The early evolution of solid bodies of various sizes in the disk was dominated by a variety of interactions with the gas, e.g., turbulent transport, differential settling, and orbital decay due to drag. These processes controlled relative velocities and hence collision rates and outcomes, over a range of particle sizes roughly from μm to km--some 9 orders of magnitude. Small grains, transported and mixed by turbulence, may have also influenced the gas. Since grains provided most of the opacity, their abundance and properties may have determined whether convection occurred in the disk. Earlier suggestions that turbulent viscosity might have caused major redistribution of mass and angular momentum in the solar nebula now seem unlikely, as recent analyses (Cabot et al., 1987) derive much lower convective velocities. However, even these can inhibit settling to the central plane and prevent formation of planetesimal by the "classical" mechanism of gravitational instability. A general feature of solar nebula models is a radial pressure gradient that causes non-keplerian rotation of the gaseous component. Even in the absence of global turbulence, formation of a relatively dense dust-rich layer would cause shear between it and the surrounding gas, producing localized turbulence sufficient to prevent gravitational instability. Thus planetesimals probably formed by collisional coagulation, with a range of initial sizes.

Weidenschilling has constructed an improved numerical code to model coagulation and settling of particles in a disk nebula containing "generic" turbulence with arbitrary velocities in the gas. The turbulence is assumed to have a Kolmogorov eddy spectrum. Relative velocities of particles, which lead to collisions and possible coagulation, are computed as due all significant causes in their appropriate regimes: thermal motion, shear and inertial effects in turbulent eddies, and systematic motions due to settling and non-keplerian rotation of the gas. Preliminary results have been obtained for a few different values of turbulent velocity (Weidenschilling and Cuzzi, 1991).

Recent work has produced significant improvements to this program. One significant problem was the disparity of timescales for turbulent mixing and coagulation. To accurately compute the former, the timestep must be shorter than the smallest spatial scale (layer thickness) divided by the turbulent velocity. However, the size distribution often varies due to coagulation on much longer timescales. To minimize the computational overhead associated with collisions between particles of all sizes, a dual timestep was introduced. Collisional changes in the size distribution are computed once in every N substeps, where the substep is controlled by the turbulent diffusion velocity, and N is determined by the rate of collisions. This algorithm has allowed simulations to be extended to longer times (up to 10^4 y) and later stages (largest bodies ~ 100 m diameter).

One significant finding that emerged from the later-stage calculations with turbulence was the realization that while growth of large bodies results in their decoupling from the turbulence, this decoupling does not allow them to settle into a thin layer. The particle layer remains thick because while the stirring due to turbulence decreases as the bodies grow larger, the damping of their velocities by gas drag decreases even more rapidly. In numerical simulations, when the mean particle size becomes large (tens of meters), the density of solids in the central plane of the disk begins to decrease. Thus, the suggestion of some theorists that particle growth would eventually allow a Safronov-Goldreich-Ward gravitational instability in a turbulent accretion disk is not correct. In fact, there are stringent limits (a few cm/sec) on turbulent velocities that would allow gravitational instability of a layer of particles, regardless of their size.

Additional improvements to the code include the provision to compute the evolution of the optical thickness of the nebula due to the particles, and variation with time as the size distribution and vertical distribution of the particles change. Opacities are taken from Pollack et al. (1985). Examples of results are shown in Figures 1 and 2.

Later stages of coagulation and settling lead to significant concentrations of particles in a layer near the central plane of the nebula. While the density of this particle layer is still much too low for gravitational instability, it may exceed the density of the gas. Under those conditions, collective effects become important; the particle layer drags the gas with it and produces shear between the dense layer and the surrounding gas (Weidenschilling 1980). The code has been modified to compute the rate of shearing, using the analytic model of Nakagawa et al. (1986). If the Reynolds number of the shear flow exceeds a critical value, then it generates turbulence of magnitude determined by a simple mixing-length model. This shear-generated turbulence can be significant in nebular models with little or no global turbulence. Its inclusion in the model allows simulations to be extended to later stages, with particle sizes approaching 100 m, at which point their mutual gravitational stirring will become important.

REFERENCES: Cabot et al. (1987) *Icarus*, **69**, 387. Nakagawa (1986) et al. *Icarus*, **67**, 375. Pollack et al. (1985) *Icarus* **64**, 471. Weidenschilling, S. (1980) *Icarus* **44**, 172. Weidenschilling, S. and Cuzzi, J. (1991) *Protostars and Planets III*, in press.

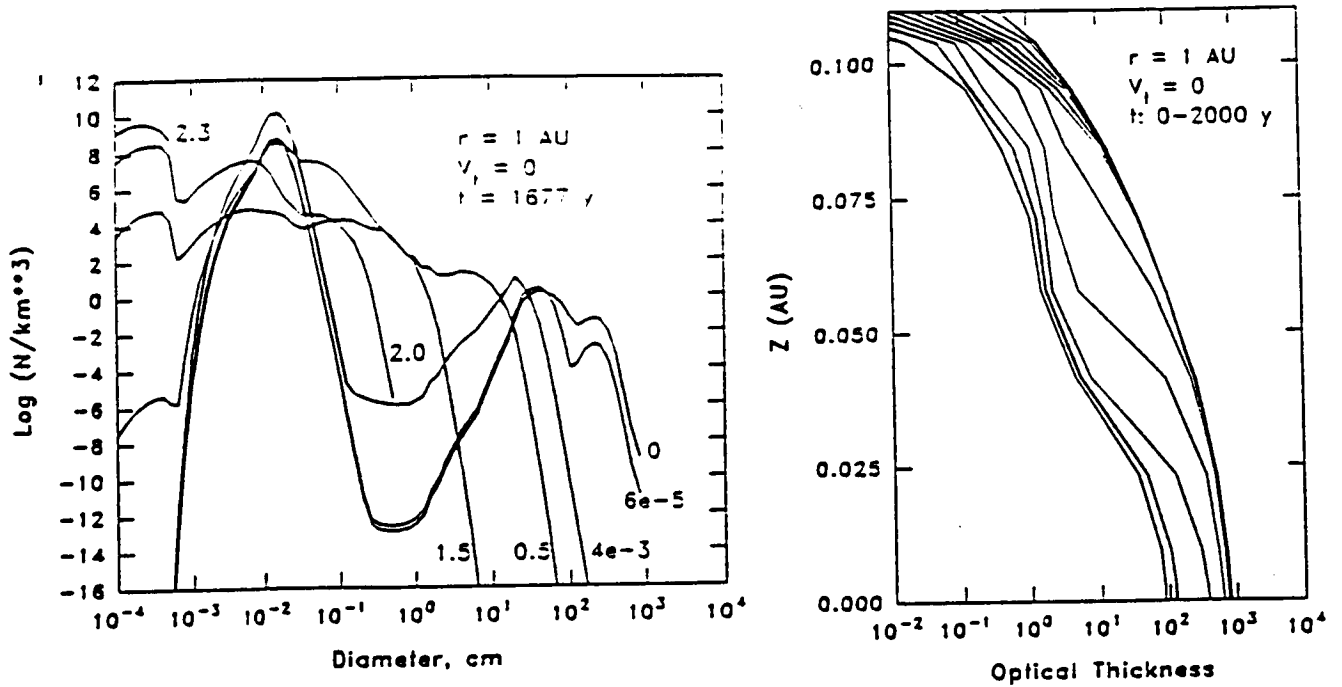


Figure 1. Particle evolution due to coagulation and settling in a nebular disk without turbulence. a) Size distribution at different levels (numbers refer to Z in units of scale height) at the time when solids/gas mass ratio equals unity at Z = 0. b) Cumulative optical thickness above each level (Z) vs. time; contour interval 200y.

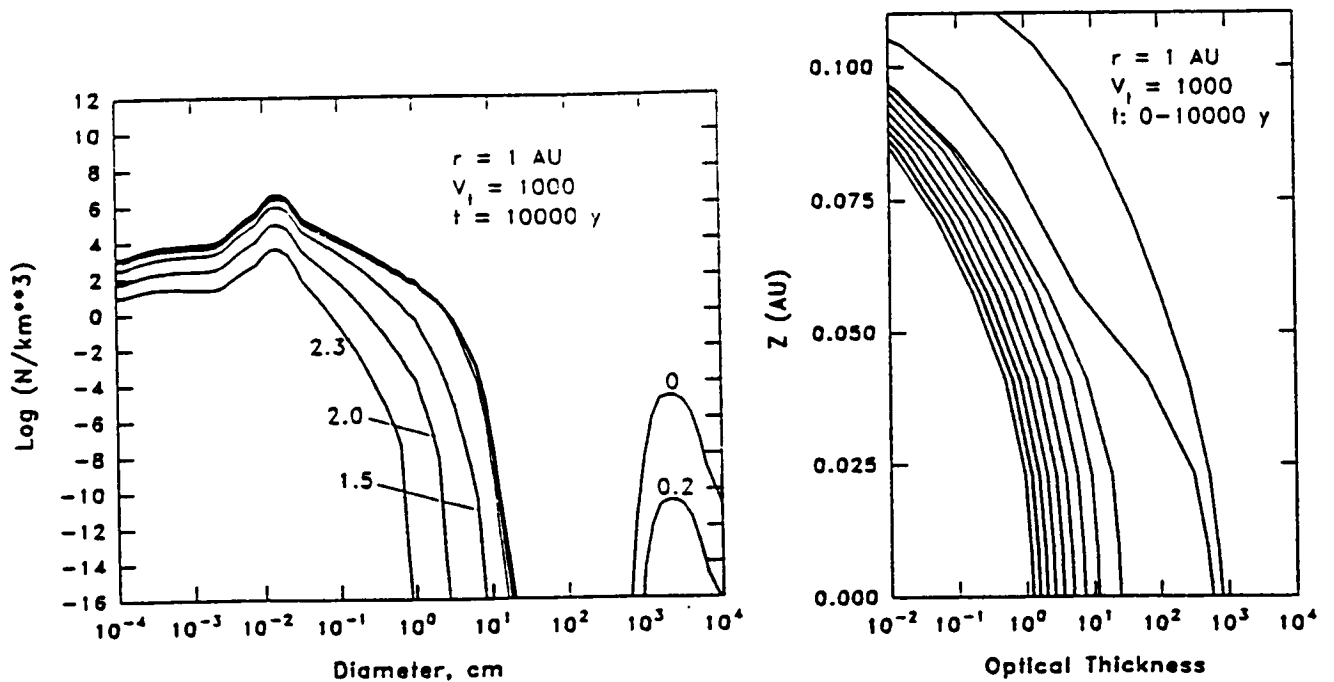


Figure 2. Same as Figure 1, but with turbulent velocity in the gas of 1000 cm/s. After 10000y, solids/gas ratio at Z = 0 has reached ≈ 0.4 .

Particle-gas dynamics in the protoplanetary nebula

Jeffrey N. Cuzzi (Ames Research Center)

Joelle M. Champney (A. T. M. inc.), Anthony R. Dobrovolskis (U. C. Santa Cruz)

In the past year we have made significant progress in improving our fundamental understanding of the physics of this problem, as detailed below. Furthermore, having brought our code to a state of fairly robust functionality, we devoted significant effort to optimizing it for running long cases. We optimized the code for vectorization to the extent that it now runs eight times faster than before (a typical case used to take a substantial fraction of a Cray 2 hour to run to convergence).

Physical improvements to the model

In starting to model very dense particle layers, when the particle mass density can exceed 100 times the local gas mass density, we realized that in such regions, the viscosity arising from interparticle collisions may become comparable to, or even exceed, the turbulent gas viscosity, and began to explore realistic implementations of particle viscosity ν_p . One simple parametrization of ν_p is the particle viscosity routinely used in planetary rings which are not overly optically thick (e.g. Goldreich and Tremaine 1978, Wisdom and Tremaine 1988):

$$\nu_p = \left(\frac{v_p^2}{2\Omega}\right) \frac{f}{1+f^2}, \tag{1}$$

where v_p is the average particle random velocity, Ω is the orbital frequency, and f is the vertically integrated particle area filling factor or optical depth. The trick is to estimate v_p . A simple ring-type assumption such as $v_p = \Omega\delta$, where δ is the particle layer thickness, is inappropriate in this case since *global* particle motions on the scales δ and Ω may be driven by turbulent eddies without *nearby* particles having much relative velocity at all if they are sufficiently well coupled to the local gas velocity.

We have come up with a simple model for ν_p based on the particle stopping time t_p , which determines the Schmidt number Sc . The model begins with the scaling relationships

$$\nu_p \sim \langle v \rangle \langle l \rangle \sim \langle \omega \rangle \langle l \rangle^2 \sim \langle v \rangle^2 / \langle \omega \rangle, \tag{2}$$

where $\langle v \rangle$, $\langle l \rangle$, and $\langle \omega \rangle$ are the characteristic relative velocity, length scale, and collision frequency of the particles respectively. There are two regimes of interest. If the collision time and length scales are not limited by the global scales of the system (layer thickness δ and orbital frequency Ω), then $\omega \sim n\pi r^2 v_{rel} \sim v_{rel}/l^*$, where l^* is the mean free path between collisions. From the work of Völk et al (1980), we identify v_{rel} as a fraction $\sqrt{t_p/t_g} \leq 1$ of the global average particle random velocity v_p when $t_p \leq t_g$, where t_p is the particle stopping time and t_g is the eddy turnover time. Naturally, v_{rel} can never exceed v_p , and we account for this in the limit $t_p \gg t_g$. We also note from our Schmidt number model (cf. also Völk et al 1980) that $(v_g/v_p)^2 = Sc = (1 + t_p/t_g)$, or $v_p \sim v_g Sc^{-1/2}$. Consequently, $\nu_p = l^* v_{rel} = l^* v_p \mathcal{F}(Sc)$, where

$$\mathcal{F}(Sc) = \frac{\sqrt{Sc-1}}{\sqrt{Sc}} \text{ if } t_p < t_g, \text{ and } \mathcal{F}(Sc) = \frac{1}{\sqrt{Sc}} \text{ if } t_p > t_g. \tag{3}$$

Note that this implies the particle viscosity goes to zero for very small t_p regardless of the particle density. This is because the particles are all trapped to the same local gas velocity and have no relative random velocity at all.

In another limit, if the scales of the system limit the collision frequency or mean free path (as in, for instance, optically thin planetary ring systems), $\nu_p \sim f \langle v \rangle \langle l \rangle$ or with the same assumptions as above, $\nu_p = f\nu_t/Sc$ where ν_t is the turbulent gas viscosity.

We have implemented viscous terms in our numerical code using these parametrizations of ν_p . For the cases we have been studying (30 - 100 cm radius particles, 1 and 10 AU, minimum mass solar nebula) the particle optical depth f is on the order of 0.1 and the Schmidt number is on the order of unity; consequently the particle viscosity is about 10% of the gas turbulent viscosity.

Numerical results

Using the newly vectorized code, we ran several models which included particle viscosity terms both at 1 AU and at 10 AU. The code is well behaved in both limits. The results differ from previous runs in that mean radial and azimuthal velocities in the particle layer are now more slowly varying with vertical distance from the midplane due to the increased coupling by particle viscosity.

Reynolds averaging of fluid equations

One aspect of our model that we wanted to put on firmer ground is our mixed use of Favre (mass) averaging for the momentum equations with Reynolds (time) averaging for the particle conservation equation. It is the Reynolds averaging that results in the diffusion term we use to model particle layer diffusion, whereas similar terms are suppressed in the Favre averaged equations. Feeling that this was rigorously inconsistent and perhaps even quantitatively important, we have devoted considerable effort to rewriting the momentum equations from the Reynolds-average standpoint. At this time we have obtained the new correlation terms but not as yet coded them up. They are all tractable and can be modeled in very much the same way as the gas eddy viscosity is always derived as a model of the Reynolds stresses, and heat transport and particle diffusion by convection are modeled with the gradient diffusion hypothesis (using the Prandtl and Schmidt numbers respectively). The terms are small, and we expect them to change our numerical results in minor but potentially very interesting ways.

Modeling of turbulence and viscosity

In our prior work, we have explored two independent parametrizations of the nebula turbulence, of differing complexity. In Champney and Cuzzi (1990), we pointed out the poorer than desirable agreement between the eddy viscosity as determined from the two-equation ($k - \epsilon$) model and that obtained with our current Prandtl model, which is characterized by only one parameter (the critical Reynolds number). Since the two-equation model is partly *ad hoc* and contains at least five constants, we have chosen so far to use the simpler Prandtl model. However, as we pointed out last year, not even the Prandtl model is without its uncertainties. The critical Reynolds number Re^* (Champney and Cuzzi 1990, equation 49) depends on the nature of the flow regime. Heretofore we have used a value of 500 for Re^* , but now believe that the true value of Re^* is about 100. Use of this number brings the two-equation and Prandtl models into agreement.

However, the Prandtl technique cannot model the damping of turbulence by the particle phase (Sproull 1961, Elghobashi and Abou-Arab 1973, Pourahmadi and Humphrey 1983); this may be very important not only in the shear layer, but also in earlier phases of the nebula

when particle settling and accretion occurs in the presence of widespread convective turbulence. Consequently we are delving more deeply into self-consistent turbulence models.

The two-equation models currently in use (*e.g.* Rodi 1984) postulate one equation for the generation, transport, and damping of the turbulent kinetic energy k , and a similar equation for the energy dissipation rate ϵ . We have verified that the k -equation (including its particle damping terms) is derivable in a straightforward way from the basic fluid equations, while as far as we can determine, the ϵ -equation is a relatively *ad hoc* creation designed to improve fits to data. In fact, prior to the current widespread use of $k - \epsilon$ models, use of only the k -equation was standard (Rodi 1984). We find that the dissipation rates ϵ calculated with our two-equation model are approximated by k/t_g , where the eddy turnover time t_g is simply the inverse of the orbital frequency. In the coming year, we plan to replace the ϵ -equation entirely by the simple scaling $\epsilon = k/t_g$ in the k -equation, simplifying the method to a one-equation model. This will expedite the study of turbulence in the shear layer, including particle damping.

References

- Champney, J. M., and J. N. Cuzzi (1990) A turbulent two-phase model for nebula flows; paper no. 90-0211, AIAA Aerospace Sciences Meeting, Reno, Nevada
- Elghobashi, K. E., and T. W. Abou-Arab (1973) A two-equation turbulence model for two-phase flows; *Phys. Fluids*, 26, 931-938
- Goldreich, P., and Tremaine, S. (1978), The Velocity Dispersion in Saturn's Rings, *Icarus*, 34, 227-239
- Pourahmadi, F. and J. A. C. Humphrey (1983) Modeling solid-fluid turbulent flows with application to predicting erosive wear; *Int. J. Physicochemical Hydrodynamics*, 4, 191 - 219
- Rodi, W. (1984) Turbulence models and their application in hydraulics; State of the art paper, International Association for Hydraulic research; Delft
- Sproull, W. T. (1961) Viscosity of dusty gases; *Nature*, 190, 976-978
- Völk, H., F. Jones, G. Morfill, and S. Röser (1980) Collisions between grains in a turbulent gas; *Astron. and Astrophys.* 85, 316-325
- Wisdom, J. and Tremaine, S. (1988), Local Simulations of Planetary Rings, *Astron. J.*, 95, 925.

BENDING WAVES AND ORBITAL INCLINATIONS.

Wm. R. Ward, Jet Propulsion Laboratory, California Institute of Technology, Pasadena, CA 91109, and San Juan Capistrano Research Institute, San Juan Capistrano, CA 92675.

Disc tides may play an important role in the formation of a planetary system. Modification of protoplanet semi-major axes and eccentricities through density waves was first suggested by Goldreich and Tremaine (1979, 1980) and calculations of linear and non-linear protoplanet-nebula interactions have been carried out by a number of researchers (e.g., Goldreich and Tremaine, 1979; Papaloizou and Lin, 1984; Lin, Papaloizou, and Savonije, 1990; and Ward, 1986, 1990). The possible significance of radial drift to the accretion process has been discussed by Hourigan and Ward (1984) and Ward (1986, 1989a), while the evolution of orbital eccentricities has been studied by Goldreich and Tremaine (1980, 1981) and Ward (1989b) for a perturber orbiting external to a ring and by Ward (1988) for a perturber embedded in the ring. Here we stress the possible importance of bending waves to the early evolution of protoplanet inclinations.

Resonant interactions between a disc and a perturber in an inclined orbit occur at locations of vertical resonance, which are analogues of Lindblad resonances and for which the disc disturbance takes the form of a spiral bending wave (e.g., Shu et al., 1983; Shu, 1984). The perturbing vertical acceleration can be Fourier decomposed into terms of the form $g_p = \text{Re}\{f_m \exp i(m\theta - \omega t)\}$. The strongest terms have frequencies $\omega_c = (m - \epsilon)\Omega_p$ and amplitudes

$$(1) \quad f_m = \epsilon \frac{GM_s}{2r_s^2} b_{3/2}^m(\gamma) \sin I e^{i\pi/2}$$

where r_s , Ω_s , and M_s are the semi-major axis, mean motion, and mass of the perturber, I is its inclination, and $b_{3/2}^m(\gamma)$ is a Laplace coefficient with argument $\gamma = r/r_s$. For each m there are two forcing terms given by $\epsilon = \pm 1$. Resonance occurs when the vertical oscillation frequency, Ω_z , equals the Doppler shifted forcing frequency, i.e., when

$$(2) \quad D = \Omega_z^2 - (m\Omega - \omega)^2 = 0$$

where Ω is the local disc orbital frequency. In a Keplerian disc about a primary, M_p ; $\Omega = \Omega_z = (GM_p/r^3)^{1/2}$, and resonances fall at $\gamma \approx 1 + 4\epsilon/3m$.

Borderies et al. (1984) determined the effects of the reaction torque from an m^{th} order resonance on the inclination of the perturber and found that it increased at a rate

$$(3) \quad \frac{dI}{dt} = \frac{\pi^2}{4} \left(\frac{M_s}{M_p}\right) \Omega \left(\frac{\Omega^2}{|D|}\right) \left(\frac{\sigma r^2}{M_p}\right) (b_{3/2}^m)^2 \sin I$$

where $D = r dD/dr$, and σ is the surface density of the disc. Both inner and outer resonances contribute to excitation. For a Keplerian disc, $|D| = 3|m + \epsilon|\Omega^2$. If $|1 - \gamma| \ll 1$, Laplace coefficients can be approximated by

modified Bessel functions, $b_{3/2}^m(\gamma) \approx (3m^2/2\pi)K_1(m|1-\gamma|)$. These are to be evaluated at resonance, i.e., $m|1-\gamma| = 4/3$. For $m \gg 1$, eqn (3) becomes, $(\text{csc } I)dI/dt = 0.0235(M_s/M_p)\Omega(\sigma r^2/M_p)m^3$. To find the total change in I, eqn (3) must be summed over all resonances.

As an application, consider a Jovian size protoplanet forming from a circumstellar disc. The protoplanet is assumed to have terminated its gas accretion phase by tidally truncating the disc as proposed by Lin and Papaloizou (1979). Truncation will abort radial drift and damp the eccentricity, provided corotation torques from the edges of the gap dominate Lindblad torques (e.g., Goldreich and Tremaine, 1980, 1981; Ward, 1989b). However, Borderies et al. (1984) point out that there are no analogous corotation torques in the vertical resonance problem and thus no analogous mechanism to halt inclination growth. Resonances are summed to $m_{\text{max}} = (4/3)(r/w)$, where w is the gap half-width. The resulting rate implies a characteristic inclination growth time, $\tau \sim \sin I/(dI/dt)$, of

$$(4) \quad \tau \sim \frac{27}{\Omega} \left(\frac{M_p}{M_s}\right) \left(\frac{M_p}{\sigma r^2}\right) \left(\frac{w}{r}\right)^4$$

The minimum size gap will be on the order of the scale height of the disc, $h \sim c/\Omega \sim .025r(aT_2)^{1/2}$, where a is in AU and T_2 is the disc temperature in 10^2 °K. Note that perturbation wavelengths, $\lambda \sim 2\pi r/m \geq h$, so that the thin disc model used to derive eqn (3) should be roughly applicable. Adopting a one solar mass primary, $M_p \sim 2 \times 10^{33}$ gm., a Jovian size protoplanet, $M_s/M_p \sim 10^{-3}$, at 5.2 A.U., and a nebula surface density and temperature of, 400 gm/cm², and 160 °K, respectively; eqn (4) reads, $\tau \sim 10^3 (w/h)^4$ years. The expected lifetime of the nebula is of order 10^7 years (Adams and Shu, 1986; Walter, 1986). A characteristic growth time this long would require a gap width of order 10 scale heights.

The critical protoplanetary mass necessary to open a gap against viscous diffusion depends on the turbulent viscosity, ν , of the disc, i.e., $M_c/M_p \sim (\nu/r^2\Omega)^{1/2}(c/r\Omega)^{3/2}$ (e.g., Hourigan and Ward, 1984; Papaloizou and Lin, 1984). The mass required to sustain the edge at a distance $w > h$, exceeds M_c by a factor $(w/h)^{3/2}$. Thus, a gap width $w \sim 10h$ could be maintained by a protoplanet ≥ 30 times that needed to truncate the disc. However, since disc truncation will inhibit further gas accretion, it is not obvious how to reconcile these requirements. Borderies et al. (1984) speculated that the sign of dI/dt may change when $I \geq w/a$, citing a similar behavior in the eccentricity case found by Goldreich and Tremaine (1981). Nevertheless, a minimum width gap would still permit inclination growth to $I \sim h/r \approx 4^\circ$ for both Jupiter and Saturn, which seems inconsistent with their small mutual inclination. Alternatively, eqn (4) could imply that much of the gas accretion phase of the giant planets was correlated with disc dispersal so that their co-existence was for an interval significantly shorter than the disc's lifetime.

We should point out that the excitation rate of eqn (3) was calculated for a thin, self-gravitating particle disc. By contrast, a minimum mass solar nebula is a pressure dominated disc with a finite thickness in hydrostatic equilibrium with the vertical component of the solar gravity. However, in the case of density waves, it is well known that the same angular momentum flux is carried by both gravity and pressure waves and that

the torque at a Lindblad resonance is independent of the restoring force responsible for the wave action. We suspect this is true for bending waves as well and that the torque strength will prove rather insensitive to the details of the wave process. The application discussed here underscores the importance of developing a more rigorous treatment of this problem.

REFERENCES

- Adams, F. C., and Shu, F. H. (1986). *Astrophys. J.*, 308, 836.
- Borderies, N. P., Goldreich, P., and Tremaine, S. (1984). *Astrophys. J.*, 284, 429.
- Goldreich, P. and Tremaine, S. (1979). *Astrophys. J.*, 233, 857.
- . (1980). *Astrophys. J.*, 241, 425.
- . (1981). *Astrophys. J.*, 243, 1062.
- Hourigan, K. and Ward, W. R. (1984). *Icarus*, 60, 29.
- Lin, D. N. C., and Papaloizou, J. (1979). *M.N.R.A.S.*, 186, 789.
- Lin, D. N. C., Papaloizou, J., and Savonije, G. (1990). *Astrophys. J.*, 364, 326.
- Papaloizou, J. and Lin, D. N. C. (1984). *Astrophys. J.*, 285, 818.
- Shu, F. H., Cuzzi, J. N., and Lissauer, J. J. (1983). *Icarus*, 53, 185.
- Shu, F. H. (1984). "Waves in planetary rings", in *Planetary Rings*, (Greenberg and Brahic, Eds.), University of Arizona Press, pp. 513-561.
- Walter, F. M. (1986). *Astrophys. J.*, 306, 573.
- Ward, W. R. (1986). *Icarus*, 67, 164.
- . (1988). *Icarus*, 73, 330.
- . (1989a). *Astrophys. J.*, 345, L99.
- . (1989b). *Astrophys. J.*, 326, 526.
- . (1990). in preparation.

ACCRETION AND EVOLUTION OF SOLAR SYSTEM BODIES.

S.J. Weidenschilling and D.R. Davis, Planetary Science Institute

We use a combination of analytical and numerical methods to study dynamical processes involved in the formation of planets and smaller bodies in the solar system. Our goal is to identify and understand critical processes and to link them in a numerical model of planetesimal accretion. We study effects of these processes by applying them in the context of the "standard" model of solar system formation (Wetherill, 1988), which involves accretion of the terrestrial planets and cores of the giant planets from small (\sim km sized) planetesimals. The principal focus of our research effort is the numerical simulation of accretion of a swarm of planetesimals into bodies of planetary size. Our computer code, based on the approach of Spaute *et al.*, (1985), uses a Monte Carlo method to determine collisional interactions within the swarm. These interactions are not determined simply by a relative velocity, but rather by explicit distributions of keplerian orbital elements. The planetesimal swarm is divided into a number of zones in semimajor axis, which are allowed to interact. The present version of our code has the capability of following detailed distributions of size, eccentricity, and inclination in each zone.

The statistical method allows simulations to begin with large numbers ($\geq 10^{12}$) of planetesimals. The spatial resolution of our model avoids the inherent limitations of the "particle-in-a-box" approach, particularly the fact that the "box" becomes inhomogeneous as accretion produces a small number of large protoplanetary bodies. Our method allows explicit inclusion of such phenomena as exchange of mass between zones, spreading of the swarm due to collisions, local depletion of the planetesimal population near the orbit of a large embryo ("dynamical isolation"), distant gravitational perturbations by bodies in non-crossing orbits, and secular decay of orbits due to gas drag. Our code also can follow the evolution of discrete bodies, i.e., a small number of bodies at the large end of the size distribution can be assigned individual values of orbital elements. Their subsequent evolution is followed separately as they interact with the continuum swarm and with each other. Early-stage modeling, using particle-in-box formalism (Greenberg *et al.*, 1978; Wetherill and Stewart 1989) has not been able to follow evolution of the swarm to produce bodies of planetary mass, due to breakdown of the assumptions of the models. Methods that follow the orbital evolution of individual bodies (Wetherill 1986) are limited to a few hundred bodies, and their initial conditions can be inferred only by extrapolation of the early-stage results. Our goal is to use the unique capabilities of our code to bridge the gap between the early and final stages of planet formation.

During the past year we have added new capabilities to our computer code and have begun to use it to model more complex and realistic situations, such as accretion of planetesimals in multiple zones spanning a broad range of semimajor axes. These simulations are being extended to later stages of planetary growth, using the "discrete bodies" algorithm. We have also continued testing and verification of our code in order to ensure its accuracy.

Wetherill and Stewart (1989) pointed out that there are two possible modes of planetary growth, with qualitatively different outcomes. One is "orderly" growth, in which many of the largest bodies maintain comparable sizes as they gain in mass. The other is "runaway" growth, in which a single large body forms at the large end of the size distribution. In the complex problem of planetary accretion, it is conceivable that growth in different stages might change from one mode to the other. Thus, a numerical code must be able to handle both types of growth. Recently, Wetherill (1990) demonstrated an analytic solution for a coagulation kernel proportional to the product of the masses, a situation that results in extreme runaway growth. A test of our code in this case demonstrates excellent agreement with the analytic solution (Fig. 1).

Agreement with analytic solutions is a necessary, but not sufficient, condition for correct computation of the more complex problem of planetary accretion. Our code, when applied to a single heliocentric distance zone, produced results in good agreement with the particle-in-a-box calculations of Wetherill and Stewart (1989). During the past year we have gone beyond these simulations in order to exploit the unique features of our code--its use of discrete bodies on individual orbits, and ability to model multiple zones over a range of heliocentric distances.

Discrete Bodies: The initially numerous ($\sim 10^{12}$) small planetesimals cannot be treated as individual bodies, but must be dealt with as having continuous distributions of size and orbital elements. However, accretion eventually produces some large bodies in numbers small enough to be treated individually. Indeed, they

must be treated separately, to the degree that their growth is a stochastic process involving discontinuous changes, e.g., due to mutual collisions of these large bodies. Once the planetesimal swarm has evolved to the point where there is a small number (typically < 10) of bodies in the largest size bin of a given radial zone, we assign each of these bodies orbital elements (a, e, i) chosen randomly within the limits of the continuum bin. Their later evolution--mass gain by accretion from the continuum, mutual collisions, and evolution of orbits due to gravitational stirring and impacts--is computed separately for each body. With this approach, we avoid problems due to small or fractional numbers of bodies in the largest size bins, and can determine whether the first-formed body will grow to dominate its zone, or perhaps whether two smaller ones will coalesce and form a new largest body.

Multiple Zones. Figures 2 and 3 show results of calculations of the simultaneous evolution of bodies in four heliocentric distance zones. Figure 2 tracks the mass of the largest body in each zone vs. time. Due to the higher surface density and shorter orbital periods in the innermost zone, runaway growth occurs there first, with the other zones following in order. After $\sim 10^5$ years, runaway growth slows down due to increasing relative velocities (eccentricities) of the smaller bodies by gravitational stirring. Figure 3 shows results for two such simulations using different seeds for the random number generator. The criterion for creating discrete bodies was such that ≤ 2 per zone were produced. The zones were broad enough, and their eccentricities low enough, that their orbits did not cross. However, the abundant smaller bodies in the swarm had higher eccentricities, and could interact with bodies in other zones. One result of this, seen in the second simulation (triangles), was that the largest body in the innermost zone "stole" enough mass from the next zone so that no discrete body formed there.

Figure 4 shows a simulation having 15 heliocentric distance zones from 0.9 to 1.1 AU. After 10^5 years of model time, stochastic effects have produced runaway growth and discrete bodies in most, but not all, zones.

REFERENCES: Greenberg (1978) *et al. Icarus* 35, 1. Ohtsuki *et al.* (1988) *Icarus* 75, 552. Spaute *et al.* (1985) *Icarus* 64, 139. Spaute *et al.* (1990) *Adv. Space Res.* 10, (3) 109. Stewart *et al.* (1988) *Icarus* 74, 542. Weidenschilling, S. J. (1989) *Icarus* 80, 179. Weidenschilling *et al.* (1985) *Icarus* 62, 16. Wetherill (1986) In *Origin of the Moon* pp. 519-550. Wetherill, G. W. (1988) In *Origins of Solar Systems Tech. Report* 88-04, pp. 81-83. Wetherill, G. W. (1990) *Icarus* 88, 336. Wetherill and Stewart (1989) *Icarus* 77, 330.

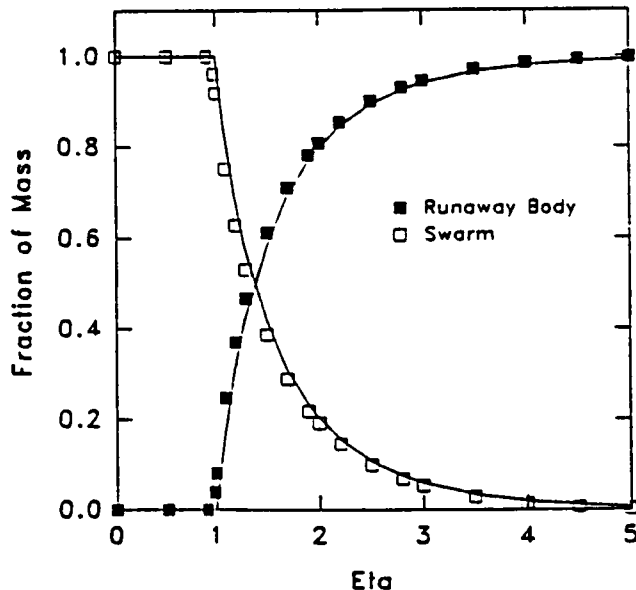


Figure 1. Results of numerical simulation of runaway growth of a large body. Solid lines are the analytic solution of Wetherill (1990a). Symbols are numerical solution for the runaway body that formed at $\eta = 0.97$.

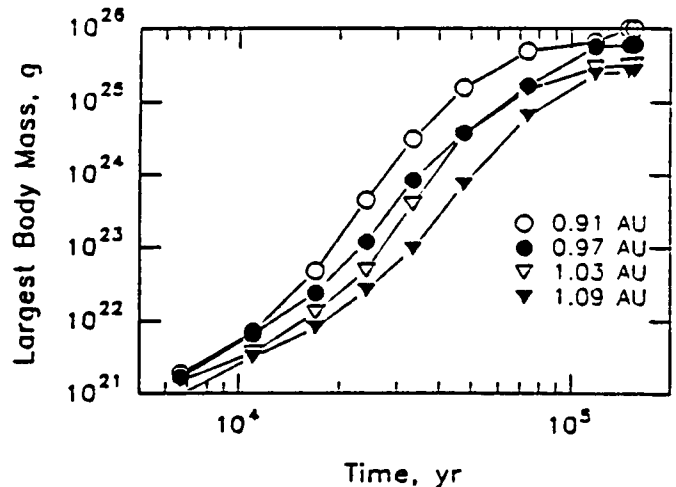


Figure 2. Growth of masses of largest bodies (continuum bins) in four heliocentric zones extending from 0.88 to 1.12 AU. Runaway growth occurs earlier at smaller heliocentric distances.

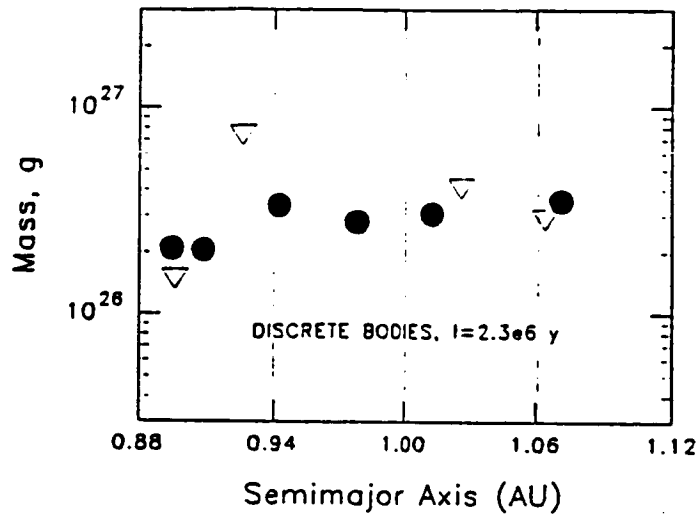


Figure 3. Outcomes of two simulations of accretion in four zones, with discrete bodies introduced at a threshold mass of 5×10^{25} g. Identical parameters were used, but with different sequences of random numbers.

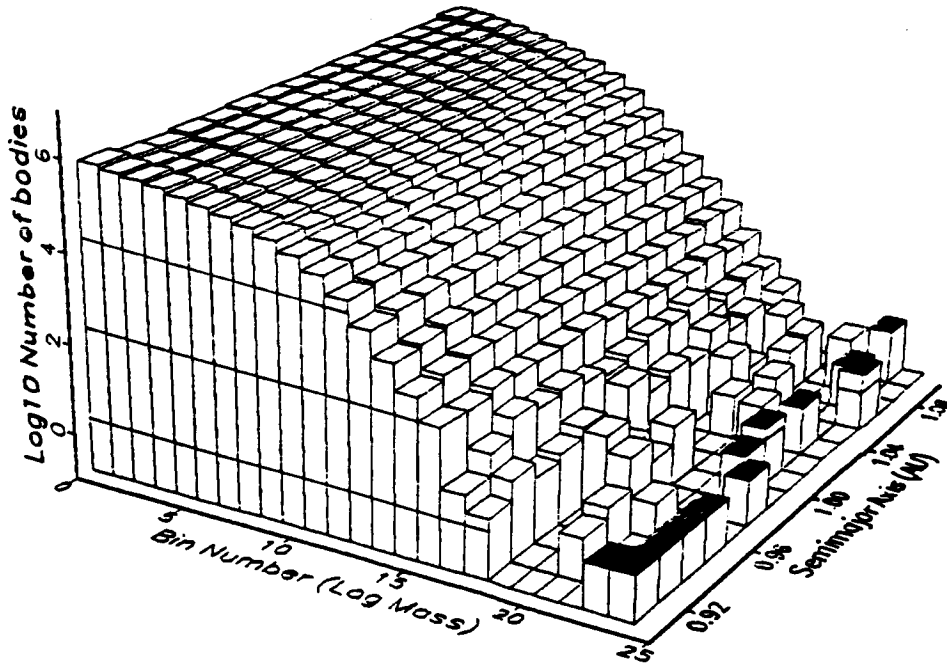


Figure 4. Size distribution of bodies in 15 heliocentric distance zones spanning a range 0.9-1.1 A.U. Initial surface density proportional to $r^{-3/2}$. Results are shown for a model time of 10^5 y. Columns with black tops represent discrete bodies.

Long-Term Evolution of a Planetesimal Swarm in the Vicinity of a Protoplanet

David M. Kary and Jack J. Lissauer, SUNY @ Stony Brook

Many models of planet formation involve scenarios in which one or a few large protoplanets interact with a swarm of much smaller planetesimals. In such scenarios, three-body perturbations by the protoplanet as well as mutual collisions and gravitational interactions between the swarm bodies are important in determining the velocity distribution of the swarm. We are developing a model to examine the effects of these processes on the evolution of a planetesimal swarm. The model consists of a combination of numerical integrations of the gravitational influence of one (or a few) massive protoplanets on swarm bodies together with a statistical treatment of the interactions between the planetesimals. Integrating the planetesimal orbits allows us to take into account effects that are difficult to model analytically or statistically, such as three-body collision cross-sections and resonant perturbations by the protoplanet, while using a statistical treatment for the particle-particle interactions allows us to use a large enough sample to obtain meaningful results.

Our model follows the interactions between planetesimals and protoplanets in a deterministic manner. Planetesimal orbits are numerically integrated using a predictor-corrector integrator on the three (or in some cases more) body problem. At intervals throughout the calculation, the orbital elements of the individual bodies will be used to develop a swarm density profile binned in both radius and height above the midplane. The associated velocity and size distributions will be recorded for each bin. Such a distribution can, in turn, be used to statistically compute the size and velocity evolution of individual planetesimals as they are affected by inelastic collisions and gravitational scattering with other swarm bodies. This will be accomplished using analytic and semi-analytic formulae analogous to those developed by Stewart and Wetherill (1988, *Icarus* 74, 542), but generalized to include the situation where eccentricities can be much larger than inclinations. In such a manner, we will be able to follow the growth of the protoplanet(s) and the evolution of the planetesimal swarm.

Thus far we have done simulations in which the planetesimals are only acted upon by the gravity of the star and the protoplanet. We have looked at both the low initial random velocity limit ($i_H = 0, e_H = 0$), and an intermediate initial velocity ($i_H = 1.0, e_H = 0.5$), where $i_H = \frac{ia}{R_H}$, $e_H = \frac{ea}{R_H}$, R_H is the protoplanet's Hill Sphere radius, and $e, i,$ and a are the particle's eccentricity, inclination, and semi-major axis, respectively. Our results are as follows:

- 1) The long-term collision probability varies slowly with protoplanet radius. Two different assumed protoplanet radii, $0.1R_H$ and $0.005R_H$ were tested. This factor of 20 change in the two-dimensional cross-section gave a change of less than a factor of 2 in the number of impacts in the longest low velocity run done so far (40 to 60 synodic periods). The intermediate velocity case gives a factor of 8 difference in the number

of impacts over the same period, but since this is a three-dimensional simulation the difference in cross-sections is 400.

2) Particles with semi-major axes within a few R_H of the protoplanet quickly impact the protoplanet or are perturbed into more distant orbits. If we define

$$b_H = |a_{\text{protoplanet}} - a_{\text{particle}}| / R_H,$$

then we find that most particles with $1.3 < b_H < 3.2$, including all of the material with $1.9 < b_H < 2.4$, collides with (passes $< 0.1R_H$ from) the protoplanet, while most of the bodies with larger b_H 's are perturbed outward. Particles with $b_H < 1.3$ are trapped in horseshoe orbits and don't approach the protoplanet.

3) In the far field ($b_H > 5$), the most striking features of the planetesimal distribution are the forced eccentricities near mean motion commensurabilities, particularly the $j/(j+1)$ resonances. These give localized bands of eccentricity up to an order of magnitude larger than the background value resulting from random perturbations by the protoplanet.

4) As indicated by the results of Greenzweig and Lissauer (1990, *Icarus* 87, 40), the inclination evolution does not keep pace with the eccentricity evolution. The intermediate velocity runs begin with $i = \frac{1}{2}e$; however, near field particles that are ejected to the far field have a much lower $i : e$ ratio.

This work is supported in part by NASA Planetary Geology and Geophysics grant NAGW-1107.

A REEXAMINATION OF EARLY NUMERICAL SIMULATIONS OF PLANETARY ACCRETION.

R.A. Kolvoord and R. Greenberg,
L.P.L., Univ. of Az., Tucson, Az., 85721.

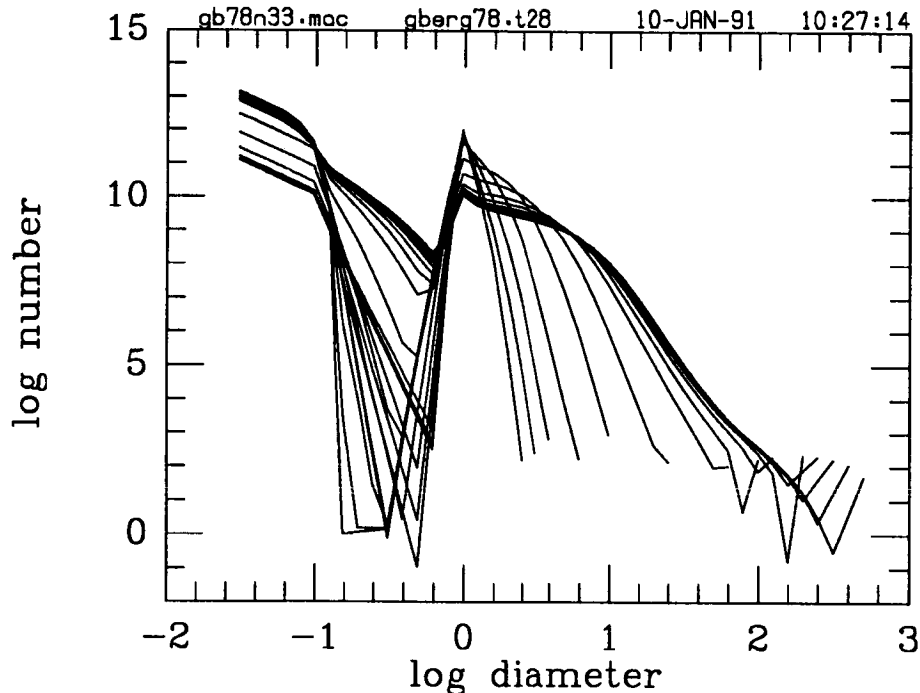
The intermediate stage of protoplanetary accretion, where sub-km sized bodies accrete in 500-1000 km diameter bodies, is critical in determining the character of subsequent evolution. Originally, Safronov (1972) posited that this accumulation occurred through "steady state" growth, where the largest bodies controlled (and stirred up) the random-velocity distribution of smaller particles. This model led to untenably long timescales for outer-planet formation. Greenberg et al. (1978) discovered that, at least through the formation of 500 km planetary embryos, the small particles dominate the population and control the velocity distribution, keeping velocities much smaller and setting up the possibility of "runaway accretion", where the largest body is able to accumulate quickly a much greater mass and separate itself from the continuum of the size distribution. This perspective has since been adopted by the majority of workers in the field. However, some controversy remains as to the exact methods used by Greenberg et al. (1978). I have reviewed that planet formation model in detail to address these criticisms and better explain the algorithms used in the study. In particular, the algorithms for mutual velocity stirring among planetesimals and mass shifting between adjacent diameter bins are rederived in detail. I have also examined the likelihood of artificial acceleration of the runaway growth phase of the intermediate stage of planetesimal formation.

A great deal of criticism has been leveled at the velocity stirring algorithm used by Greenberg et al. (cf. Wetherill 1990). In the 1978 paper, the velocity equations shown were approximations, given to demonstrate some of the salient features of velocity evolution; they were not the exact algorithms used in the numerical simulation. Upon reviewing the original algorithm and subsequent improvements (cf. Greenberg 1982 and Greenberg et al. 1984), I find that all relevant physical effects included in recent models by various authors were accounted for in the earlier work, including dynamical friction and the stirring due to random velocities to approximately the same accuracy as current models. A detailed exposition of this algorithm is beyond the scope of this abstract, but a more thorough examination is in preparation (Kolvoord and Greenberg 1991). While the exact form of the random velocity stirring algorithm was occasionally modified and experimentally improved (*e.g.*, between 1978 and 1982) from the original work of Greenberg et al. (1978) [Greenberg 1982 uses the improved form], dynamical friction (cited by Wetherill and Stewart (1989) as a key effect) was included from the outset, as part of accounting for rotation of the appropriate velocity vectors during gravitational encounters.

Much comment has also been made about the possibility of artificial acceleration of growth in the Greenberg et al. models (cf. Wetherill and Stewart 1989, Ohtsuki et al. 1990). It should be noted that this possibility was recognized by the authors

and discussed in Greenberg (1982). While some artificial acceleration is caused by the coarseness of the mass-binning algorithm, it is small (approximately a factor of 2), and given the other uncertainties in the problem it has a limited effect. The figure below shows a new simulation using the Greenberg model with a smaller bin size (each bin is separated by a factor of 2 in mass rather than in diameter) and nominal values for the various strength parameters. I find that it takes on the order of 50,000 years to form a 500 km body, in agreement with other findings in the current literature. The result of Greenberg et al. (1978) was of this same order of magnitude, i. e. reasonably accurate compared with various recent studies, and distinct from the Safronov paradigm which was current at that time.

In summary, our review and tests indicate that the model and conclusions of Greenberg et al. (1978), with the revisions as given in Greenberg (1982), are robust. The velocity stirring algorithms include all of the applicable physics and the artificial acceleration caused by too broad mass bins is a relatively minor effect.



A plot of the evolution of number versus size for a model initially populated by 1 km bodies. The parameters in the model are the same as those used in Greenberg, except for the bin size which is now a factor of 2 in mass.

References

- Greenberg, R. (1982). Planetesimals to planets. In **Formation of Planetary Systems** (A. Brahic, Ed.), pp. 515-569, Cepadues, Paris.
- Greenberg, R., J.F. Wacker, W.K. Hartmann, and C.R. Chapman (1978). Planetesimals to planets: Numerical simulation of planetesimal evolution. *Icarus* **35**, 1-26.

- Greenberg, R., S.J. Wiedenschilling, C.R. Chapman, and D.R. Davis (1984). From icy planetesimals to outer planets and comets. **Icarus** 57, 89-113.
- Kolvoord, R.A., and R. Greenberg (1991). In preparation for submittal to **Icarus**.
- Ohtsuki, K., Y. Nakagawa, and K. Nakazawa (1990). Artificial acceleration in accumulation due to coarse mass-coordinate divisions in numerical simulation. **Icarus** 83, 205-215.
- Safronov, V.S. (1969). *Evolution of the Protoplanetary Cloud and Formation of the Earth and the Planets*. Nauka, Moscow. NASA Tech. Trans. TTF-677, 1972.
- Wetherill, G.W. (1990). Formation of the terrestrial planets. **Ann. Rev. Earth and Planetary Science** 18, 205-256.
- Wetherill, G.W., and G.R. Stewart (1989). Accumulation of a swarm of small planetesimals. **Icarus** 77, 330-357.

Collision Probabilities in the Presence of Nebular Gas Drag

David. M. Kary and Jack. J. Lissauer, SUNY @ Stony Brook

The dynamics of the planetesimal swarm was likely to have been strongly affected by gas drag in the solar nebula. Significant amounts of gas were certainly present during the formation of Jupiter and Saturn, and may have been important in the formation of other planets (Nakagawa, Hayashi, and Nakazawa 1983, *Icarus* 59, 552). Work by Weidenschilling and Davis (1985, *Icarus* 62, 16) has shown that the combination of gas drag and perturbations due to mean motion resonances with a protoplanet is likely to have had important consequences for the evolution of planetesimal orbits. They pointed out that while gas drag tends to cause planetesimals to spiral in towards the Sun, resonant perturbations tend to force the planetesimals away from the protoplanet. For planetesimals starting outside the protoplanet orbit, these two forces oppose each other, and at some point there will be a balance between them. At these resonance locations the planetesimal eccentricities are strongly excited, which would lead to high velocity collisions that would grind down the planetesimals until they are much more strongly affected by the gas drag. This would cause a more rapid inward migration of the planetesimals and thereby make gas drag a more significant factor in planetary growth. This process would have been especially important in runaway accretion scenarios, in which large protoplanets would be expected to accrete much of their mass from significantly smaller planetesimals, often in the presence of nebular gas drag.

We are developing a model to determine what fraction of the planetesimals would have hit a protoplanet on their sunward journey as opposed to having a close approach and passing into an inferior orbit. The model involves direct numerical integration of restricted-three-body orbits using a predictor-corrector integrator. A simple gas drag law with a v^2 dependence has also been included in the equations of motion. Runs of 100 to 500 particles have already been performed, while some future runs may require several times this number in order to get good impact statistics. All planetesimals start in superior orbits with semi-major axes 5 to 10 R_H from the protoplanet, where R_H is the protoplanet's Hill Sphere radius. The orbit is followed until the planetesimal has passed into an inferior orbit at least 10 R_H from the protoplanet. This process typically requires 10^4 to 10^5 orbits.

The simulations performed thus far have used a protoplanet of mass $10^{-6}M_\odot$ and drag parameters corresponding to planetesimals with radii from 30m to 3km moving through a nebula with a density of $10^{-9}g/cm^3$. Planetesimals with the larger radii ($> 1km$) are found to be held in superior orbits by the perturbations from the planet at mean-motion resonances. The particles held at these resonances are excited to relatively high eccentricities. The smaller the planetesimals, the stronger the gas drag force and therefore the closer they get to the protoplanet. At small enough planetesimal radii, the gas drag force is strong enough to overcome mean-motion resonant perturbations, and all of the planetesimals pass the protoplanet. For 300m planetesimals, the probability of

impacting a protoplanet with the Earth's density and location is only $\frac{1}{3}$. The probability of hitting an icy core at the location of Jupiter is $\frac{1}{6}$, while at Neptune's location it is $\frac{1}{11}$. For still smaller planetesimals, the fraction of bodies impacting the planet decreases slowly, so that for $30m$ planetesimals the accretion probability is $\sim \frac{2}{3}$ that for $300m$ bodies.

In future work we will determine the dependence of the accretion probability on the mass of the protoplanet. The effects of a protoplanet in an eccentric orbit will also be investigated.

This work was supported in part by NASA Planetary Geology and Geophysics grant NAGW-1107.

Growth of Planets From Planetesimals

Jack J. Lissauer (SUNY Stony Brook) and Glen R. Stewart (U. Colorado, Boulder)

The formation of terrestrial planets and the cores of Jovian planets is reviewed in the framework of the planetesimal hypothesis, wherein planets are assumed to grow via the pairwise accumulation of small solid bodies. The rate of (proto)planetary growth is determined by the size and mass of the protoplanet, the surface density of planetesimals, and the distribution of planetesimal velocities relative to the protoplanet. Planetesimal velocities are modified by mutual gravitational interactions and collisions, which convert energy present in the ordered relative motions of orbiting particles (Keplerian shear) into random motions and tend to reduce the velocities of the largest bodies in the swarm relative to those of smaller bodies, as well as by gas drag, which damps eccentricities and inclinations. The evolution of the planetesimal size distribution is determined by the gravitationally enhanced collision cross-section, which favors collisions between planetesimals with smaller velocities. Deviations from the 2-body approximation for the collision cross-section are caused by the central star's tidal influence; this limits the growth rates of protoplanets. Runaway growth of the largest planetesimal in each accretion zone appears to be a likely outcome. The subsequent accumulation of the resulting protoplanets leads to a large degree of radial mixing in the terrestrial planet region, and giant impacts are probable. Gravitational perturbations by Jupiter probably were responsible for preventing runaway accretion in the asteroid belt, but detailed models of this process need to be developed. In particular, the method of removal of most of the condensed matter (expected in a nebula of slowly varying surface density) from the asteroid region and the resulting degree of radial mixing in the asteroid belt have yet to be adequately modeled. Accumulation of Jupiter's core before the dispersal of the solar nebula may require more condensable material at 5 AU than predicted by standard minimum mass solar nebula models.

This research was supported in part by NASA Planetary Geology and Geophysics grants NAGW-1107 and NAGW-769.

Tidal Disruption of Inviscid Protoplanets

A.P. Boss, DTM, Carnegie Institution of Washington
A.G.W. Cameron & W. Benz, Center for Astrophysics

Roche showed that equilibrium is impossible for a small fluid body synchronously orbiting a primary within a critical radius now termed the Roche limit. Roche's static criterion has been extended to bodies with tensile strength [1], and has been used to argue that even bodies on hyperbolic orbits would be tidally disrupted within the Roche limit [10,11]. Tidal disruption of orbitally unbound bodies is a potentially important process for planetary formation through collisional accumulation, because the area of the Roche limit is considerably larger than the physical cross section of a protoplanet. Tidal disruption of unbound bodies is also the basis for the disintegrative capture model of lunar origin [10,11]. Because there is only a limited amount of time for tidal forces to act on an unbound body, a dynamic rather than a static analysis is required to determine the outcome.

Several previous studies have been made of dynamical tidal disruption. Protoplanets with strong dissipation (e.g., solid or partially molten bodies) do not undergo tidal disruption, even for grazing encounters [8,9]. The case for inviscid (e.g., molten) bodies, however, has been in dispute, with one model implying disruption within a modified Roche limit [7] and another disclaiming the possibility of disruption [5]. Another model followed the orbits of a hypothetically disrupted body [11], but did not include the body's self-gravity.

Considerable insight into the dynamics of tidal disruption can be gained from a simple model based on comparing the velocity dispersion expected to be produced in a body by tidal forces with the escape velocity for segments of the body to be removed to infinity. While crude, this analysis does include the self-gravity of the body, which is the only agent capable of resisting tidal disruption in an inviscid body. We have considered three different models of disruption: (1) test particles leaving a sphere; (2) hemispherical breakup [6]; and (3) distortion of a cylinder of radius R_c and half-length R with $\epsilon = R_c/R$ being constant as $R \rightarrow \infty$. For each of these models, the criterion for tidal disruption is the same except for a factor c :

$$\left(1 - \frac{R}{r_P}\right)^{-1/2} - 1 > \left(\frac{M}{cM'}\right)^{1/2} \left(\frac{r_P}{R}\right)^{1/2},$$

where primes denote the primary, r_P is the perigee radius, R is the protoplanet's radius, M is the protoplanet mass, and c is 1 for (1), 8 for (2), and ϵ for (3). In the limit of a small protoplanet ($R \ll r_P$), the criterion for case (1) becomes $r_P < 0.63R'(\rho'/\rho)^{1/3}$, which shows that a small protoplanet cannot be tidally disrupted in this approximation for $\rho' \sim \rho$; $r_P < 0.63R'$ requires a collision. Roche's criterion has a similar form but with a factor of 2.5 instead of 0.63. The analytical criteria show that a massive protoplanet ($M/M' \rightarrow 1$) is tidally stable. For fixed protoplanet mass, as the perigee radius decreases, tidal disruption becomes possible if the protoplanet can disrupt before colliding with the primary. This can only occur for bodies less massive than $\sim 0.01 - 0.1M_\oplus$.

Because of the limitations of these analytical models, we have used a smoothed particle hydrodynamics (SPH) code to model the tidal disruption process. The code is basically the same as the one used to model giant impacts [2]; here we simply choose impact parameters large enough to avoid collisions. The primary and secondary both have iron cores and silicate mantles, and are initially isothermal at a molten temperature. Previous lunar formation calculations with the SPH code have shown that inviscid, Mars-sized bodies do not suffer tidal disruption by the Earth, even during glancing collisions, so we have restricted our models to lower mass protoplanets, specifically $0.01M_{\oplus}$. Two parameters have been varied, the distance (r_P) between the two centers of mass at closest approach, and the velocity at infinity (v_{∞}). Because of the boring nature of non-disruption models, our models have focused on parameters that do lead to tidal disruption.

Based on the analytical and numerical models, our conclusions may be summarized as follows. Protoplanets with masses greater than $\sim 0.1 M_{\oplus}$ do not suffer tidal disruption, even for grazing incidence, parabolic orbits. Smaller mass ($\sim 0.01M_{\oplus}$) inviscid protoplanets will be at least partially tidally disrupted if $r_P < 1.5R_{\oplus}$ for $v_{\infty} > 2 \text{ km s}^{-1}$. Up to half of the mass of a $0.01 M_{\oplus}$ protoplanet may impact the Earth if $v_{\infty} \leq 2 \text{ km s}^{-1}$ and $r_P < 2R_{\oplus}$. However, very little mass is captured in Earth orbit. Because typical protoplanets in the late phases of terrestrial planet accumulation are thought to have had $v_{\infty} \sim 10 \text{ km s}^{-1}$, tidal disruption was probably rare [5,8,9]. Tidal torques are efficient at producing rotational spin-up, rotational instability, and mass shedding [3]. Lunar formation through tidal disruption of a single protolunar body and capture of the debris into Earth orbit [10,11] appears impossible, and through multiple bodies very unlikely. Tidal disruption only occurs for relatively small bodies, and very little of their mass is injected into orbit. Orbital capture of a lunar mass would require many events, all favorably aligned, as well as having $v_{\infty} \sim 0$, both of which are unlikely [4]. Lunar formation following a giant impact appears to be preferable [2].

References:

- [1] Aggarwal, H. R., and V. R. Oberbeck (1974). *Astrophys. J.* 191, 577-588. [2] Benz, W., A. G. W. Cameron, and H. J. Melosh (1989). *Icarus* 81, 113-131. [3] Boss, A. P. (1986). *Icarus* 66, 330-340. [4] Boss, A. P., and S. J. Peale (1986). In *Origin of the Moon* (W. K. Hartmann, R. J. Phillips and G. J. Taylor, Eds.), pp. 59-101. Lunar & Planetary Institute, Houston. [5] Buck, W. R. (1982). *Lunar Planet. Sci. XIII*, 73-74. [6] Dobrovolskis, A. R. (1987). *Bull. Amer. Astron. Soc.* 19, 820-821. [7] Hayashi, C., K. Nakazawa, and Y. Nakagawa (1985). In *Protostars and Planets II* (D. C. Black and M. S. Matthews, Eds.), pp. 1100-1153. University of Arizona, Tucson. [8] Kaula, W. M., and A. E. Beachey (1986). In *Origin of the Moon* (W. K. Hartmann, R. J. Phillips, and G. J. Taylor, Eds.), pp. 567-576. Lunar & Planetary Institute, Houston. [9] Mizuno, H., and A. P. Boss (1985). *Icarus* 63, 109-133. [10] Smith, J. V. (1974). *Lunar Science V*, pp. 718-720. The Lunar Science Institute, Houston. [11] Wood, J. A., and H. E. Mitler (1974). *Lunar Science V*, pp. 851-853. The Lunar Science Institute, Houston.

A Geometrical Model for Shepherding

Jack J. Lissauer, SUNY Stony Brook

Shepherding is the process by which a satellite secularly exchanges angular momentum with a nearby particle or gaseous disk. The sense of the torque is such that the separation between the orbits of the particles and the shepherd increases secularly with time. The magnitude of the torque is proportional to the square of the mass of the satellite, and, as shown by Goldreich and Tremaine (1980) is the same for a wide variety of dissipative and dispersive mechanisms operative in the disk. However, as pointed out by Poisson in 1809, planetary-type perturbations cannot produce secular changes in orbital elements to second order in the perturbation parameters (e.g., the mass of the satellite); thus, some form of interaction among the disk particles is needed for shepherding to operate.

I have devised a new technique to analyze the physical nature of shepherding through study of the evolution of the vector eccentricity of the particles. This method appears to be especially useful for the study of shepherding in sparse particle disks. Thus, it may be very useful in calculating the torque on Neptune's rings and on protoplanets in the solar nebula. Moreover, the techniques are useful in estimating how long numerical simulations of resonant processes must be run in order to reach a quasi-steady state.

I plan to develop my model through a variety of analytic and numerical calculations. The first phase of these calculations will follow the buildup of forced eccentricities of particles near an isolated resonance. Several different eccentricity damping and eccentricity randomization formalisms will be studied in order to pin down the transition between a strongly interacting disk, in which the Goldreich and Tremaine (1980) torque formula applies, and non-interacting particles, which do not experience any secular torque.

This research was supported in part by NASA Planetary Geology and Geophysics grant NAGW-1107

*Dynamics of Low Velocity Collisions of Ice Particle, Coated with Frost.*F. Bridges[†], D. Lin^{*}, L. Boone[†], D. Darknell[†][†]Physics Dept., University of California at Santa Cruz, Santa Cruz, CA^{*}Astronomy and Astrophysics Dept., University of California at Santa Cruz

We have continued our investigations of low velocity collisions of ice particles for velocities in the range 10^{-3} cm/s $< v < 2$ cm/s. Our work this year focused on two efforts: 1) the sticking forces for ice particles coated with CO₂ frost, and 2) the completion of a 2-D pendulum system for glancing collisions. In addition, we revised our first paper on the sticking properties of water frost coated particles. This paper, published in 1991 has received considerable attention. The measured sticking forces for water frosts are of order 100 dynes. This is large enough to hold composite particles together in the tidal gravitational forces of Saturn, for clusters up to ~ 10 m in size. The fact that water frost provides a significant sticking force at low temperatures (100°K) provides a mechanism for the formation of larger particles via aggregation. We find that uncompacted frosts, for impact velocities in the range 0.2 mm/s - 0.8 mm/s give the largest sticking forces. Above a critical velocity (which varies with the frost layer) no sticking occurs and the frost becomes compacted after 8-10 collisions. At very low impact speeds, the particles will also stick but the force needed to separate them (i.e. the sticking force) is considerably smaller.

Our studies of sticking forces for CO₂ frost on the surfaces indicate very similar properties. The sticking forces are comparable, 2-20 dynes, and no sticking occurs for velocities greater than ~ 1 mm/sec. This property may be a general feature of frosts and not strongly dependent on the composite of the frost at temperatures low enough that sublimation and/or melting are not important. Future studies are planned to investigate this hypothesis.

The majority of our effort has been directed toward the 2-D pendulum. The pendulum and control electronics are built and we have balanced it in a room temperature set up. Both rotation axes have low loss, with Q's greater than 10 at a period of 15 sec have been achieved. Balancing for the vertical axis of rotation is more difficult than the horizontal axis, and we are now developing electronic sensors to simplify this process. We have also developed new computer software to control and monitor the position of the 2-D pendulum.

We are now in the process of testing the pendulum and the computer control system in a series of room temperature experiments. In Fig. 1 we plot the vertical and horizontal position of a rubber super-ball attached to the 2-D pendulum. For these tests, the ball bounced on a very rough surface (sandpaper on a solid platform) to simulate a condition with a very large

horizontal sliding friction force - a worst case situation. The pendulum handles the resulting sideways torque well, although the damping for vertical motion increased. At the collision indicated by the arrow, the change in the magnitude of the vertical velocity component is small (~ 0.9) but the horizontal component of velocity decreased by about a factor of 3. In collisions on smooth surfaces with little friction, the change in horizontal speed can be very small.

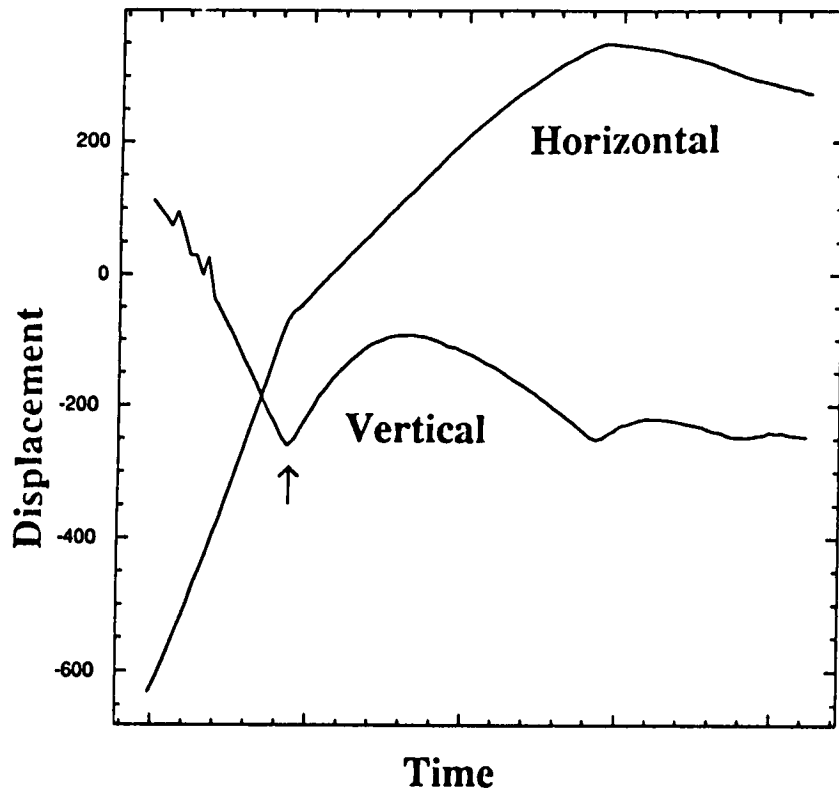


Fig. 1. The horizontal and vertical components of the displacement of the ball as a function of time. The arrow indicates the time of a collision.

Acknowledgement: This work was supported by NASA grant NAGW 590.

Planetary Ring Studies

Jeffrey N. Cuzzi (Ames Research Center),
 Anthony R. Dobrovolskis (U. C. Santa Cruz), Luke Dones (C. I. T. A.),
 Richard H. Durisen (Indiana), Linda Horn (J. P. L.), Mark R. Showalter (Stanford)

This research contains a large number of tasks, representing the efforts of the coinvestigators listed above. Limited space allows only the briefest highlights to be noted.

Characterization of the fine scale structure in Saturn's A and B rings

We have obtained the highest available resolution full scan of Saturn's B and inner A rings from about a dozen narrow angle camera images (Voyager 2 data, illuminated face, resolution about 3.5 km/pixel). This data was then analysed for its spatial frequency content using a Burg maximum entropy algorithm (Horn et al. 1990) and also using a standard FFT algorithm. We checked the ability of both the FFT and Burg algorithms to return detections of less than fully periodic simulated data in the presence of noise. The purposes of this check were to validate the Burg technique, and to assure ourselves that it was not producing spurious results.

The structure we are finding in the B and A rings does have characteristic scales which presumably contain clues as to its origin. The characteristic scale varies somewhat across the inner B ring but is all within the range of about 70-90 km. There is no significant spectral power on either shorter or longer scales, a conclusion which is validated by inspection of the images themselves. Beginning in the vicinity of the Janus 2:1 density wave at 96200 - 96500 km, the structural scale increases to 200 - 300 km, and this larger scale then dominates throughout the rest of the B ring. The central third or so of the B ring is practically devoid of structure on scales finer than about 200 km, but fine scale structure reappears in the outermost few thousand km of the B ring *superposed* on the 200 - 300 km scale structure.

Ballistic transport modeling and evolution of fine ring structure

We have improved our numerical scheme for computing the evolution of planetary rings due to ballistic transport (Durisen et al. 1989). We are now routinely able to compute evolutions over many tens of "gross erosion times" t_g , where $t_g = \sigma / \dot{\sigma}_{ej}$, with σ the ring surface mass density and $\dot{\sigma}_{ej}$ the rate of ejecta loss due to direct bombardment. Typically, $t_g \sim 1.5 \times 10^5 (10^5/Y)$ years where Y is the ejecta mass yield per unit mass projectile ($\sim 10^4 - 10^6$).

The detailed, strongly prograde *angular* ejecta distribution for nondisruptive impacts, computed by Cuzzi and Durisen (1990), has been incorporated. Along with this, two realistic ejecta *velocity* distributions $f(> v)$ are currently utilized in our code, where f is the ejecta fraction with ejection velocity magnitude $> v$ between 4 and 80 m/s. One has a "knee" at 10 m/s and another is a pure v^{-2} powerlaw. The code computes viscous spreading using various current models of viscosity which are normalized to an upper limit of 0.05 cm²/s for the C ring.

The inner edges of Saturn's A and B-rings have similar morphology but do not correspond to known external resonances or to resonances with oscillatory modes of Saturn, and are thus prime candidates for displaying effects of ballistic transport. Durisen et al. (1990,1991) demonstrate that, for a plausible range of f and Y , a steady-state edge about as sharp as observed can be produced in a few t_g and can thereafter be maintained *despite viscosity*. As long as Y is large enough for ballistic transport to dominate viscosity, we also find a "ramp" to be a robust feature in our inner edge simulations. We have used an analytic approximation show that a ramp near a high- τ edge is an inescapable consequence of ballistic transport for a power-law

f combined with a strongly prograde distribution of ejecta velocities. In fact, for a realistic $f \propto v^{-2}$, the ramp is precisely linear in $\tau(r)$, as is the case for the observed ramps.

Durisen et al. (1990,1991) also demonstrate how the typical ejecta velocities determine the typical length scales. For high Y and the power-law f , the edge is sharper and the undulatory structure has characteristic radial width of about 150 to 200 km (Horn and Cuzzi 1990).

Faint features in the rings of Saturn

By combining a variety of Voyager and Earth-based data, Showalter et al. (1991) have shown that the E Ring is composed of a very narrow distribution of particle sizes centered around 1 micron, which makes the E Ring unlike any other known planetary ring. This result rules out the possibility that the E Ring particles originate in collisional or disruptive processes, and therefore gives credibility to several prior theories that the particles originate in volcanic or geyser-like phenomena on Enceladus. These ideas are not implausible in light of the recent discovery of geyser-like plumes on Triton.

In a search for azimuthal periodicities in the F Ring images, Kolvoord et al. (1990) found the signature of Prometheus but not that of the more distant and less massive Pandora. In addition, potential signatures of several unidentified objects, possibly members of an F ring moonlet belt (Cuzzi and Burns 1988), were observed.

The Encke Moonlet Revealed

One of our research highlights in the last year was the visual detection of Saturn's eighteenth moon, now designated 1981S13. The body orbits within the Encke Gap of the A Ring. The presence of this moonlet was originally inferred indirectly in research supported under this RTOP. This year, Showalter used our solution for the moonlet's orbit to perform a computer search of the Voyager image collection which identified every frame whose field of view was expected to contain the moonlet. He has since located 1981S13 in 23 Voyager 2 images, and used its location to infer a precise orbit for the body (Showalter 1990, 1991).

Dynamics in ringmoon systems:

We are studying ringmoon belts with potential application to the F ring region, the Encke gap region, and the Uranian and Neptunian ringmoon systems in general. Our focus at present is on the steady state dynamics of a population of moonlets as perturbed by one or two nearby ringmoons. We had hoped to study the dynamical forcing aspects of this situation using a mapping approach (e.g. Duncan et al 1989). However, we noticed that the map-predicted onset of chaotic behavior was sensitive to the precision of the computer arithmetic and even the platform (Vax or Cray). We decided to check the map results with a Bulirsch-Stoer integration, which implied that the map often does predict chaos which is artificial.

We attempted to improve the mapping by introducing orbit curvature terms to correct for the less-than-fully-applicable Hill approximation which provided the basis for the map of Duncan et al (1989), and by trying to derive a symplectic or Hamiltonian-based mapping scheme which would be area preserving. So far, we have found no suitable way to treat this particular problem with confidence from a mapping standpoint. However, the Bulirsch-Stoer integration scheme is actually quite fast as well as thoroughly reliable, and we have decided to rely on it for the present.

Non-classical radiative transfer model

We have continued development of our "ray-tracing" light scattering code for modeling

realistic planetary rings (Dones et al. 1989). In the last year we have found a better way to treat multiple scattering. Both the old and new codes use a successive-orders-of-scattering approach. However, in the old version, each scattering event from a particle yielded only a single "daughter" ray, whose direction was selected in a rather complicated way. In the new code, each scattering except the final one to the observer results in several daughter rays, with directions uniformly distributed in solid angle in the outgoing hemisphere. The phase function of the particle is incorporated by assigning different weights to the rays.

Particle Properties from Stellar Occultation Data

Our derivation of the relationship between Voyager PPS photon counting statistics and Saturn ring particle sizes was published recently (Showalter and Nicholson 1990). The particle sizes derived in the C Ring and Cassini Division are generally compatible (within a factor of 1.5 - 2) with previous determinations using Voyager Radio Science data, but our technique provides a sense of particle size variation on radial scales much smaller than by any other means.

References

- Cuzzi, J. N. and J. A. Burns (1988) Charged Particle Depletion Surrounding Saturn's F Ring: Evidence for a Moonlet Belt; *Icarus*, 74, 284-324
- Cuzzi, J.N., and Durisen, R.H. (1990), Bombardment of Planetary Rings by Meteoroids: General Formulation and Effects of Oort Cloud Projectiles, *Icarus*, 84, 467 - 501
- Dones, L., Showalter, M., and Cuzzi, J. N. (1989). Simulations of Light Scattering in Planetary Rings. In "Dynamics of Astrophysical Discs"; Cambridge University Press.
- Duncan, M., T. Quinn, and S. Tremaine (1989) The long-term evolution of orbits in the solar system: a mapping approach; *Icarus*, 82, 402-418
- Durisen, R.H., Bode, P.W., Cederbloom, S.E., Murphy, B.W., and Cuzzi, J.N. (1990), Theoretical Models for the Structures at Saturn's A and B-Ring Inner Edges, *Bull. Am. Astron. Soc.*, 22, 1045 (abstract: poster paper).
- Durisen, R.H., N.L. Cramer, B.W. Murphy, J.N. Cuzzi, T.L. Millikin, and S.E. Cederbloom. (1989). Ballistic Transport in Planetary Ring Systems due to Particle Erosion Mechanisms. *Icarus*, 80, 136-166.
- Durisen, R.H., Bode, P.W., Cuzzi, J.N., Cederbloom, S.E., and Murphy, B.W. (1991), Ballistic Transport in Planetary Ring Systems due to Particle Erosion Mechanisms. II. Theoretical Models for Saturn's A and B-Ring Inner Edges, *Icarus*, in preparation.
- Horn, L.J., and Cuzzi, J.N. (1990), Spatial Scales in Saturn's B-Ring, *Bull. Am. Astron. Soc.*, 22, 1041
- Kolvoord, R. A., J. A. Burns, and M. R. Showalter 1990. Periodic features in Saturn's F Ring: Evidence for nearby moonlets. *Nature* 345, 695-697.
- Showalter, M. R. 1990. The visual detection of 1981S13, the Encke Gap moonlet. *Bull. Amer. Astron. Soc.* 22, 1040-1041.
- Showalter, M. R. 1991. The visual detection of 1981S13 and its role in the Encke Gap. Submitted to *Nature*.
- Showalter, M. R., J. N. Cuzzi, and S. M. Larson 1991. Structure and particle properties of Saturn's E Ring. Submitted to *Icarus*.
- Showalter, M. R., and P. D. Nicholson 1990. Saturn's rings through a microscope: Particle size constraints from the Voyager PPS scan. *Icarus* 87, 285-306.

RESEARCH PERFORMED IN 1990 UNDER NASA GRANT NAGW-310

Physical Processes in Planetary Rings

Joseph A. Burns, Principal Investigator

Perturbed Narrow Rings. Kolvoord *et al.* (*Nature* 345, 695-697) used a Fast-Fourier-Transform technique to show that the longitudinal brightness distribution of Saturn's F ring contains only a few distinct wavelengths rather than the continuum of values mentioned in the original 30-day *Science* reports. The wavelength corresponding to the gravitational signature of the inner shepherd Prometheus is found to be prominent in both Voyager 1 and 2 data; on the other hand, since Pandora is more distant and less massive than Prometheus, the outer shepherd's signature is not expected to be seen and is not. Several other wavelengths can be identified: one is nothing more than the spacing of two unusually bright clumps noticed in the Voyager 1 data while most other detected wavelengths seem to result from the beating between known signals. However, there is at least one other signal that appears real and that we ascribe to an as-yet undocumented nearby moonlet. From the signal's wavelength we are able to infer the perturber's separation in semimajor axis a . Given such a separation, the only way for the responsible perturber to have been missed in spacecraft images, while still imprinting its strong signal on the ring, is if the moonlet is on an elliptical orbit ($e \sim 10^{-3} - 10^{-2}$) that brushes against the ring. Voyager 2 data give similar, but less convincing, identifications. The presence of as-yet unseen moonlets on slightly elliptical and inclined rings in the environs of the F ring had been earlier suggested from magnetospheric data.

The consequences of a close satellite perturbing a narrow ring had been previously investigated numerically and analytically in 2-D by Showalter and Burns (1982). The 3-D version of this problem has now been pursued by Kolvoord and Burns (1991a, in preparation) who find, from the nature of out-of-plane motions in Saturn's F ring, that these displacements become noticeable only for certain configurations of the orbits of the perturbing satellite and the ring: closest approach between the ring and the satellite must occur near the time when the satellite reaches its maximum elevation above the ring plane. Since the satellite's argument of pericenter precesses at $2.7^\circ/\text{day}$ due to Saturn's oblate gravity field, the ability of Prometheus to produce significant out-of-plane motion will vary appreciably over relatively short timescales. The implication is that, if the braids develop by a mechanism like this, they will vary significantly with time and will not be present around the entire ring.

"Collisions" have been added by Kolvoord and Burns (*BAAS* 22, 1042; 1991b, in preparation) to their 2-D numerical simulation to ascertain the circumstances under which the ring's organization is disrupted. These "collisions" are modelled as random impulses to ring-particle velocities that are introduced in a Monte Carlo manner so as to be consistent with the impacts caused by a sea of background objects having orbital characteristics that are similar to those of the studied particles; energy loss can be included in an ad hoc fashion. As expected, such stirring of the system destroys the organized flow that is needed if the periodic signature of the shepherds is to be identified. Of course, in the specific case of the actual F ring, clumps and knots are seen even though, according to the high optical depths in the core of the ring, collisions must be common. This conundrum suggests that some key feature yet needs to be added to our model.

Dynamics of Circumplanetary Dust. Studies of the motion of circumplanetary dust under the action of radiation pressure and various electromagnetic processes have been emphasized during the past year. This emphasis is partly a result of a collaboration with M. Horanyi

during my sabbatical year and partly due to an attempt to prepare for publication various results originally obtained in the 1989 Ph.D. dissertation of L. E. Schaffer.

The dynamics of circumplanetary charged dust grains has not been widely explored even though it is recognized that tenuous dust disks are an important component of planetary rings. We have started a systematic explanation of the curious consequences of some of the perturbations that act on small particles. Lorentz resonances occur when orbital periodicities match the frequencies of electromagnetic forces. Orbital evolution through such Lorentz resonances has now been studied by Schaffer and Burns (1991b, submitted to *Icarus*), who find that large jumps in eccentricity and inclination are induced during resonance passage and that they persist after the particle leaves the region of the resonance. The electrical charging of a grain traveling through a magnetospheric plasma occurs stochastically but the resulting variability of the charge rarely limits the effectiveness of the Lorentz resonance (Schaffer and Burns 1991c, in preparation). Orbital evolution due to delayed, periodic charge oscillations have been studied numerically and qualitatively in the last few years. These models have now been analytically extended by Schaffer and Burns (1991d, submitted to *JGR*). Horanyi and Burns (1991, submitted to *JGR*) have followed the effects of the planetary shadow on the dynamics of charged grains orbiting through the shadow. An orbital resonance happens in this circumstance owing to the periodic oscillation in the photoelectric current as the latter shuts off on each passage through the shadow; hence energy can be transferred to the orbit. Nevertheless, because the orbit also precesses due to these same forces and therefore enters the shadow differently, no long-term evolution occurs.

A slightly different circumstance occurs for dust circling Mars, where no appreciable planetary magnetic field is present. Here the Lorentz force arises from passage through the solar wind's magnetic field (rather than the planet's field) that is being convected past the planet. Even though orbital resonances do not occur, Horanyi *et al.* (*Geophys. Res. Ltrs.* 17, 853-856) demonstrate that Lorentz forces can dramatically alter the nature of the trajectories, resulting in prolonged lifetimes for submicron-sized grains.

Electromagnetic processes may be very important on the micron-sized particles that are inferred to be the primary constituent of Saturn's E ring, the diffuse band that extends from 3 to 8 Saturnian radii and that peaks near the orbit of Enceladus at $4R_s$. Burns and Horanyi (*BAAS* 22, 1042; also IAU presentation) have shown that solar radiation pressure alone will rapidly cause particles injected at Enceladus to spread out widely ($3 \rightarrow 5 R_s$). If the particles are charged, the resulting distribution, which is asymmetric about the planet's orbital velocity vector, depends critically on the charge-to-mass ratio.

Hamilton *et al.* (*BAAS* 22, 1043-1044) have started to address the origin and fate of Neptunian dust, some of which is curiously located over the polar regions. Their preliminary results suggest that such highly inclined orbits can develop in at least two ways: the orbits of distant particles, which are weakly bound to the planet, are tilted up by radiation forces, or by passage through Lorentz resonances of Neptune's highly distorted B field.

CHAPTER 9

MARS GEOLOGIC MAPPING

PRELIMINARY GEOLOGIC MAPPING OF ARSIA MONS, MARS

James R. Zimbelman, Center for Earth and Planetary Studies,
National Air and Space Museum, Smithsonian Institution,
Washington, DC 20560

Geologic mapping of the Tharsis Montes at a scale of 1:500,000 was recently initiated as part of the Mars Geologic Mapping Program of NASA. Detailed mapping of the three large shield volcanoes and their surroundings will help to clarify the sequence of events which led to the formation of these features, as well as provide a basis for comparing the complex histories of the three related yet distinctive volcanic centers.

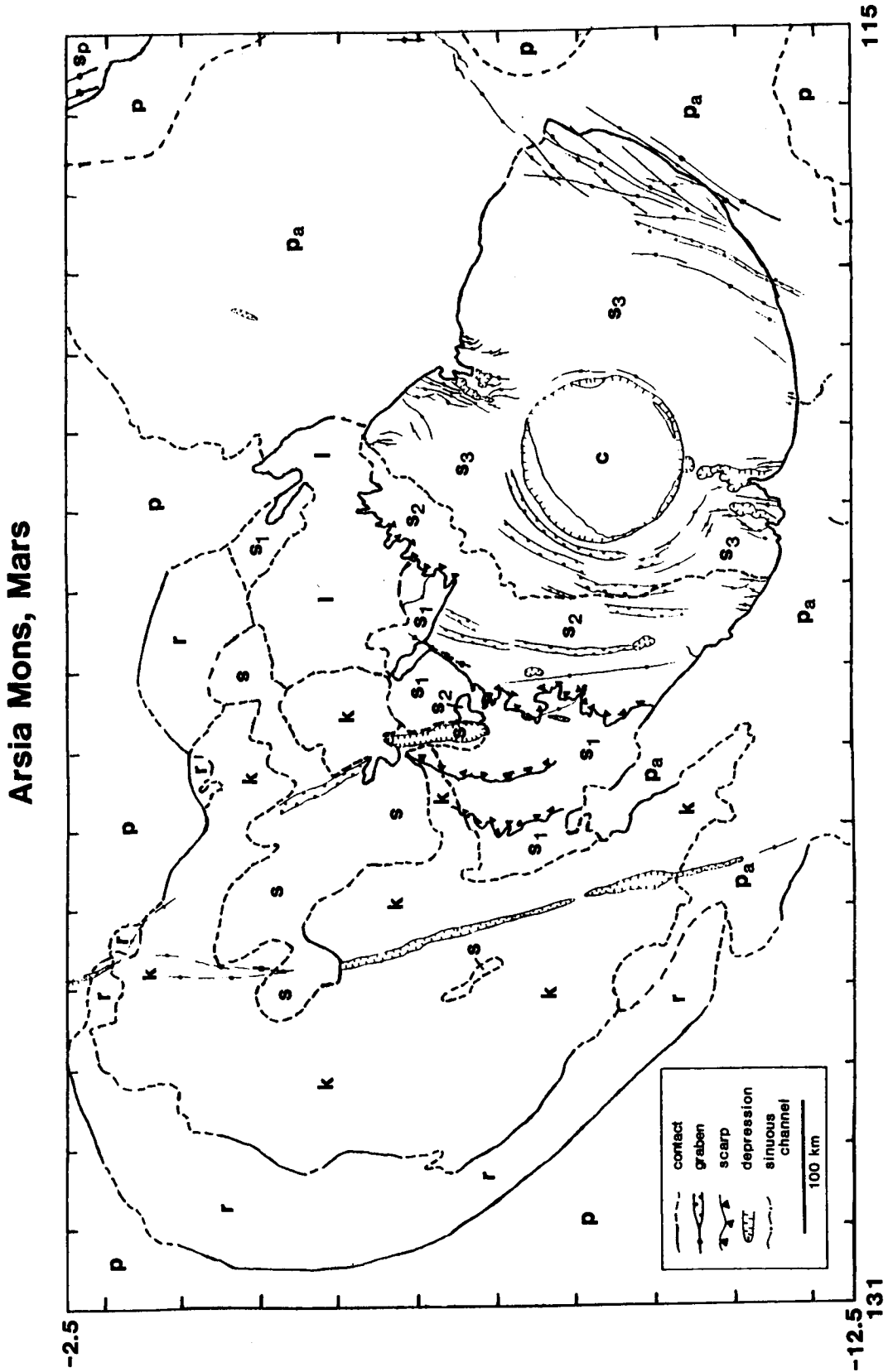
Preliminary mapping of Arsia Mons at a scale of 1:2M (see Fig. 1) was carried out in preparation for detailed mapping (1). The main shield construct of Arsia Mons is approximately 300 km in diameter along the axis of the Tharsis Montes (N40E azimuth), but the shield may be nearly twice as broad perpendicular to this trend. Lavas may have flowed around older portions of the volcano as they moved downslope, away from the Tharsis Montes axis. A 100-km-diameter caldera with a flooded floor (unit c) tops the volcano. The main construct (unit s₃) has numerous graben and aligned collapse pits that are generally circumferential to the caldera; the widest graben are near the summit on the western flank while the eastern flank has narrow graben that are at least 100 km from the caldera rim. "Parasitic calderas" embay the southern and north-northeastern flanks (2) and were the source for the latest plains emanating from Arsia Mons (unit p_a) and covering earlier Tharsis plains (unit p). The lower portions of the western flank, below an elevation of 15 km, are deeply eroded and undulatory (unit s₂), terminating along an irregular scarp which forms the contact with a smooth lower shield material (unit s₁).

The lobate aureole deposit northwest of the construct has at least four mappable textural units; knobby (unit k), lobate (unit l), ridged (unit r), and smooth (unit s) terrains. The lobate unit may consist of flow fronts, from lava flows and/or debris flows, emanating from the basal scarp for shield unit s₂. The ridged terrain has been interpreted to result from emplacement of a gravity-driven landslide (3) or as recessional moraines (4). The ridged terrain grades into knobby terrain, with lines of knobs leading directly into large adjacent ridges at some locations (-7°, 129°). The smooth unit is superposed on all other aureole units, as well as several large graben or depressions. Subtle lobate margins and lineations in the smooth unit suggest a possible pyroclastic origin, which could have emanated from large graben near the upslope edge of the aureole (located at -7°, 124° and -6°, 123°). An alternative interpretation is that the smooth unit formerly covered the entire aureole surface and is in the process of being eroded away, exposing the other aureole units below.

REFERENCES: 1) J.R. Zimbelman, LPS XXII, 1551-1552, 1991. 2) L.S. Crumpler and J.C. Aubele, Icarus 34, 496-511, 1978. 3) M.H. Carr et al., J. Geophys. Res. 82, 3985-4015, 1977. 4) B.K. Lucchitta, Icarus 45, 264-303, 1981. [Supported by NASA grant NAGW-1390]

GEOLOGIC MAPPING OF ARSIA MONS, MARS: J.R. Zimbelman

Figure 1. Simplified geologic map of Arsia Mons (see text).



PRELIMINARY GEOLOGIC MAPPING OF CENTRAL CHRYSE PLANITIA, MARS

Robert A. Craddock¹, L.S. Crumpler², and Jayne C. Aubele²;
¹Center for Earth and Planetary Studies, National Air and Space Museum,
 Smithsonian Institution, Washington, D.C. 20560; ²Department of
 Geological Sciences, Brown University, Providence, R.I. 02912

Because of the success of the Viking lander missions, central Chryse Planitia represents one of two areas on the martian surface where planetary geologic mapping is added by "ground-truth" observations. The broad-scale geology of Chryse Planitia [1] and the geology of the Viking 1 landing site [2] have been previously examined by other investigators. 1:500,000 scale mapping of central Chryse Planitia and the Viking 1 landing site (MTM's 20047 and 25047) has been undertaken to synthesize these results and to address the following questions: (1) What is the depositional and erosional history of the Chryse Planitia basin? (2) How representative are the Viking 1 surface materials of the Chryse Planitia region and of plains units in general? (3) What is the extent of channel materials versus ridged plains materials? (4) As a result of the Viking lander investigations, what are the initial, primary objectives future missions to the surface should address? The preliminary results of our investigation are presented below.

Figure 1 shows preliminary geologic unit boundaries. The oldest material is Hesperian in age, although degraded and/or buried craters may have formed on underlying Noachian materials. Ridged plains materials (Hr₁, Hr₂, and Hr₃) cover most of the surface within the map sheets and are characterized by numerous linear to sinuous wrinkle ridges (Xanthe Dorsa). The ridged plains units are defined on the basis of relative crater abundances, frequency of ridges, and degree of fluvial modification of the ridges. The ridges are morphologically similar to lunar mare-ridges and are interpreted to be the result of regional compressional strains in a competent, layered surface unit. Unlike lunar mare-ridges, the Xanthe Dorsa ridges trend north-south as opposed to being circumferential to the Chryse basin. This suggests basin subsidence was not the mechanism for Xanthe Dorsa formation as has been suggested for lunar ridges [3]. Despite the high resolution of the available images (<10 m/pixel), primary volcanic features such as flow fronts or vents have not been observed. This implies that such structures have been modified or buried, or that the ridged plains units are composed entirely of fluvial sediments. In the latter case, in order to agree with Viking lander x-ray fluorescence results [4], the highland source rocks would have to be basaltic in composition.

Unlike other plains units no degradational or channel features are visible within ridged plains, unit 3 (Hr₃), suggesting that this unit was formed from depositional processes and is probably not extensively incised or eroded. The depositional nature of ridged plains, unit 3 is further suggested by the occurrence of several partially buried craters (c₁) along its southern contact. Using rim height to diameter ratios for martian craters [5], the thickness of this unit is ~300 m. Despite these observations, at the surface no unequivocal depositional features have been identified [2].

Distinct flat-topped and isolated ridges (Hri) occur along the crest

of several of the more prominent mare-type ridges in the north-eastern half of the map area. These are interpreted to represent erosional remnants (i.e., inselbergs) of earlier ridges degraded and subsequently re-developed during continued regional deformation, or isolated highs representing buried structures (i.e, kipukas) such as large crater rims. The former suggests that ridge development is geologically long-lived [6] and span intervals of time great enough that several fluvial episodes occurred during the development of a single ridge. The latter interpretation suggests that ridge formation occurs where the ridged plains are thinnest, similar to mare wrinkle ridge development [3].

The incised channel unit (Hchi) occurs east of Kasei and Maja Valles and is superposed on the ridged plains. The location of individual channels appears to have been initiated at high-standing topographic features and to have often enveloped pre-existing topography. Characteristic striations distinguishing this unit occur in parallel and slightly arcuate groups that are interpreted to represent the direction of flow (Fig. 1; arrows) and corresponding erosional incision associated with large-scale fluvial outwash toward the topographic low of the Chryse basin.

Channeled plains materials, unit 1 (Hchp₁) consists of broad, planar surfaces associated with areas of extensive incised channels and are interpreted to be areas of little to no incision or may represent possible locations of deposition. Channeled plains materials, unit 2 (Hchp₂) contains small anastomosing and sinuous channels and occurs in two locations on the eastern edge of Maja Valles. These materials are interpreted to be late-stage depositional materials that were incised by smaller-scale, late-stage fluvial events, or by residual draining of internal volatiles during the waning stages of material emplacement.

Using block abundance models developed for Viking Infrared thermal mapper (IRTM) data [7], high-resolution ground tracks (<3-km spot size) over the southern portion of Chryse Planitia indicate that block abundances may be decreasing into the basin [8]. If the circum-Chryse outflow channels were formed by a catastrophic release of water [9], then materials released into the debouching area should be deposited in a typical Bouma sequence [10]. However, our observations support the proposal that at least the southern Chryse channels were formed by liquefaction. Coarse-grained materials released into the debouching area by this mechanism would be deposited closest to channel with finer-grained material being carried greater distances [11], as suggested by the remote sensing data.

Continued collaborative efforts between ourselves and investigators of adjacent map sheets will refine the unit contacts and interpretations. Further image analysis combined with remote sensing observations will allow the objectives of this study to be obtained.

Supported by NASA Grants NAGW-2187 (Smithsonian Institution) and NAGW-2171 (Brown University).

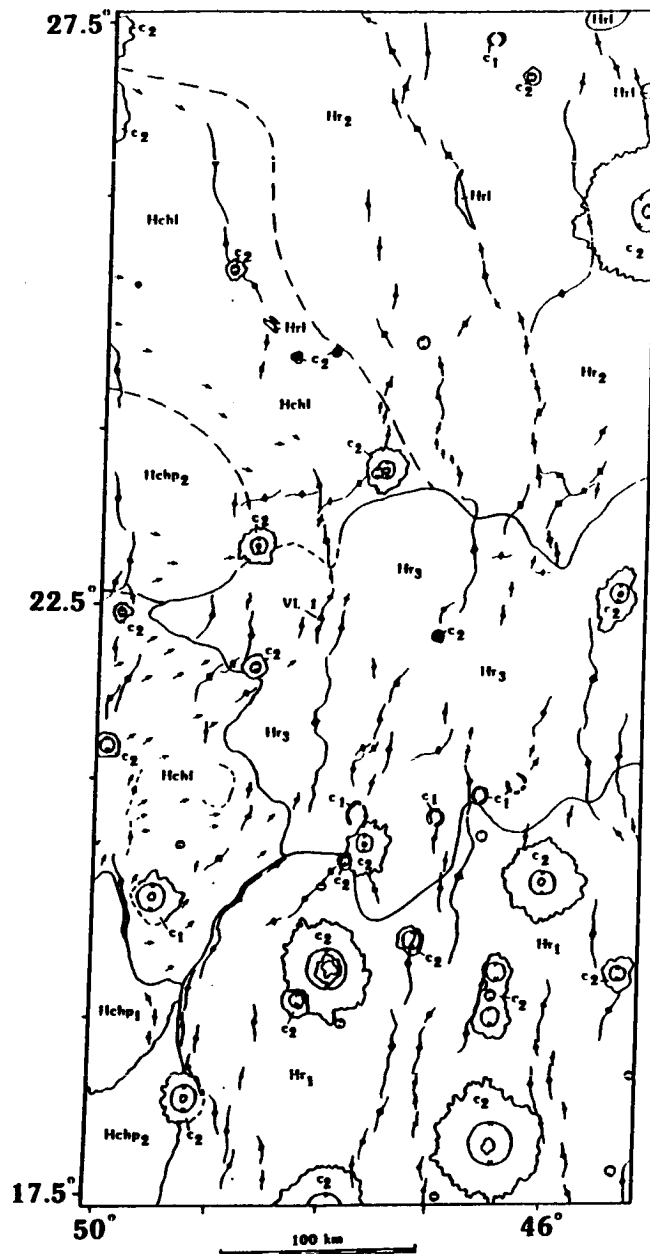


Figure 1. Preliminary geologic map of the central Chryse Planitia region and the Viking 1 landing site. Arrows show direction of flow as indicated by surface features. See text for explanation of units.

- References. [1] Greeley, R. *et al.*, *J. Geophys. Res.*, **82**, 4093-4109, 1977. [2] Binder, A.B. *et al.*, *J. Geophys. Res.*, **82**, 4439-4451, 1977. [3] Maxwell, T.A. *et al.*, *Geo. Soc. Am. Bull.*, **86**, 1273-1278, 1975. [4] Clark, B.C. *et al.*, *J. Geophys. Res.*, **82**, 4577-4594, 1977. [5] Pike R.J. and P.A. Davis, *Lunar, Planet. Sci.*, **XV**, 645-646, 1984. [6] Aubele, J.C., *LPI Tech. Rept.*, **89-06**, 13-15, 1989. [7] Christensen, P.R., *Icarus*, **68**, 217-238, 1986. [8] Craddock, R.A. *et al.*, *Lunar Planet. Sci.*, **XVIII**, 203-204, 1987. [9] Baker, V.R. and D.J. Milton, *Icarus*, **23**, 27-41, 1974. [10] Komar, P.D., *Icarus*, **42**, 317-329, 1980. [11] Nummedal, D. and D.B. Prior, *Icarus*, **45**, 77-86, 1981.

GEOLOGIC MAPPING OF NORTHERN LUNAE PLANUM, MARS

Robert A. Craddock and Ted A. Maxwell, Center for Earth and Planetary Studies, National Air and Space Museum, Smithsonian Institution, Washington, DC 20560

Lunae Planum is an elevated region east of the Tharsis rise and is approximately the size of the Tibetan Plateau of China ($>1,200,000 \text{ km}^2$). Ridged plains containing numerous Sacra Dorsa wrinkle ridges, cross-cutting Sacra Fossae grabens, and lobate scarps compose this martian plateau. Because the Sacra Dorsa are circumferential to the Tharsis rise, many investigators suspect that isostatic or loading stresses from the formation of Tharsis generated these features [1,2]. Over 3 km of relief associated with Kasei Valles separate Lunae Planum from Tharsis to the west [3]. The tilt of this Martian plateau may have also controlled fluvial sheet flows, which eventually created the eastern Lunae Planum outflow complex [i.e., Maja, Vedra, Maumee, and Bahram Valles; 4]. Geologic mapping of the northern Lunae Planum region was undertaken to better understand the emplacement history of the ridged plains, the structural history of deformation, and the periods of fluvial processes that have modified the region. These investigations are important for several reasons: the history of plains emplacement yields information valuable for understanding the evolution of Tharsis volcanism, interpretation of structural deformation has implications on the lithology of the martian crust, and determining the history and fate of martian volatiles is dependent upon knowing the periods of outflow activity.

Because of the occurrence of wrinkle ridges and lobate scarps in high resolution images, numerous investigators have interpreted the ridged plains as being the result of flood volcanism [e.g., 5,6]. Previously, however, no direct evidence has been presented to support this interpretation and the consideration that the ridged plains may be sedimentary in origin has been suggested [7,8]. Viking orbiter images (51A41-46) show numerous linear features 1- to 5-km-long, oriented roughly between 30° and 60° NE and NW, and frequently associated with low albedo materials. We interpret these features as volcanic fissures similar to those which occur in terrestrial flood basalt provinces. Major differences between these features and terrestrial fissures include the size (up to a factor or two larger) and the two sets of preferred orientation as opposed to one [9]. Commonly low albedo materials on Mars are aligned on the same side of topographic obstacles within a region and have thermophysical properties indicative of coarse-grained, windblown sediments [e.g., intracrater deposits; 10]. However, uniformly dark surfaces in the martian highlands have been interpreted as exposed lava flows [11]. The lack of preferred orientation, smooth edges, and close association with linear features suggests that some low albedo materials in northern Lunae Planum are exposed or partially buried lava flows also.

A number of flow fronts in the area investigated are superimposed on wrinkle ridge arches, indicating that plains emplacement and ridge formation were not events separated in time. Crater count statistics suggest that rather than being formed in a single event, the Lunae Planum surface is composed of multiple aged surfaces which vary in N(1) ages with longitude. Crater ages of eastern Lunae Planum are older than central

Lunae Planum, suggesting that later flows were not as extensive as initial flows that may have originated from the Tharsis region. These observations indicate that Lunae Planum may have experienced regional volcanism as part of Tharsis precursor volcanism, but with time this volcanism became local. Lunae Planum volcanism probably continued through the structural deformation associated with the formation of Tharsis--or at least until the end of the early Hesperian.

Because martian wrinkle ridges closely resemble lunar mare ridges and Columbia Basalt anticlines, they are commonly interpreted to represent structural features formed as a result of buckling followed by reverse or thrust faulting [7,8]. Interpretation of the mechanics necessary for creating the Sacra Dorsa wrinkle ridges has been undertaken by other investigators and involves modelling the ridged plains as linear elastic [8,12] or linear viscous material [8,13]. These models must be capable of not only explaining the periodic spacing of the wrinkle ridges, but the erosive nature of the ridged plains materials as well [i.e., Kasei Valles terraces, chaotic terrain, and wall erosion; 14]. If the ridged plains have the rheologic properties of an elastic material, they are relatively thick (>2.4 km; 8). Below 1 km, the ridged plains must have contained a volatile-rich zone, which cemented the material after deformation to explain Kasei Valles terracing. If the ridged plains have the rheologic properties of a viscous material, then the ridged plains should be relatively thin (>750 m; 8), and Kasei Valles terracing can be explained as the contact between ridged plains and underlying regolith.

Kasei Valles are nearly as long as the Mississippi River in the United States (>2,500 km). For over half of their distance, Kasei Valles flow N20°E before splitting into two main channels which flow N80°E into Chryse Planitia. The relief from the floors of Kasei Valles to the top of Lunae Planum is more than 3 km in some places [3,14]. The wrinkle ridges on Lunae Planum have not been affected by the erosional processes which formed these channels, and in some places ridges on the channel floors are continuous with ridges on the plateau. These observations suggest that Kasei Valles were following pre-existing topography, most likely the result of faulting. The upper, N80°E trending portion of Kasei Valles can be explained as a series of faults radial to the center of Tharsis as predicted by Tharsis isostatic stress models [1,2]. However, the fault controlling the southern, N20°E trending portion of Kasei Valles cannot be explained by any existing Tharsis stress models. We propose that the faults controlling the flow of Kasei Valles volatiles and some of the relief between the channels and Lunae Planum were the result of crustal adjustments following the formation of Tharsis and the evacuation of a large amount of mantle material (~110,000,000 km³). The uplift of Lunae Planum, if volatile-rich, may have also produced a large, regional hydrostatic head in local aquifers. Crustal adjustments, resulting faulting, and subsequent effects on volatile reservoirs may have initiated the formation of Kasei Valles and the eastern Lunae Planum outflow complex.

These results were presented at the Annual Geological Society of America Conference in Dallas, Texas, Oct. 29-Nov. 1, 1990 and the 22nd Lunar and Planetary Science Conference in Houston, Texas, March 18-22, 1991. Supported by NASA Grant NAGW-1780.

- References: [1] Banerdt, W.B. et al., J. Geophys. Res., 87, 9723-9733, 1982. [2] Sleep, N.H. and R.J. Phillips, J. Geophys. Res., 90, 4469-4489, 1985. [3] Downs, G.S. et al., J. Geophys. Res., 87, 9747-9754, 1982. [4] De Hon, R.A., Lunar Planet. Sci., XVIII, 227-228, 1987. [5] Greeley, R. et al., J. Geophys. Res., 82, 4093-4109, 1977. [6] Hartmann, W.K. et al., In Basaltic Volcanism on the Terrestrial Planets, Pergamon, New York, 1981. [7] Watters, T.R., J. Geophys. Res., 93, 10,236-10,254, 1988. [8] Watters, T.R., paper submitted to J. Geophys. Res., 1990. [9] Swanson, D.A. et al., Am. J. Sci., 275, 877-905, 1975. [10] Christensen, P.R., Icarus, 56, 496-518, 1983. [11] Wilhelms, D.E. and R.J. Baldwin, Proc. Lunar Planet. Sci., 19th, 355-365, 1989. [12] Plescia, J.B. and M.P. Golombek, Geo. Soc. Am. Bull., 97, 1289-1299, 1986. [13] Zuber, M.T. and L.L. Aist, J. Geophys. Res., 95, 14,215-14,230, 1990. [14] Robinson, M.S. and K.L. Tanaka, Geology, 18, 902-905, 1990.

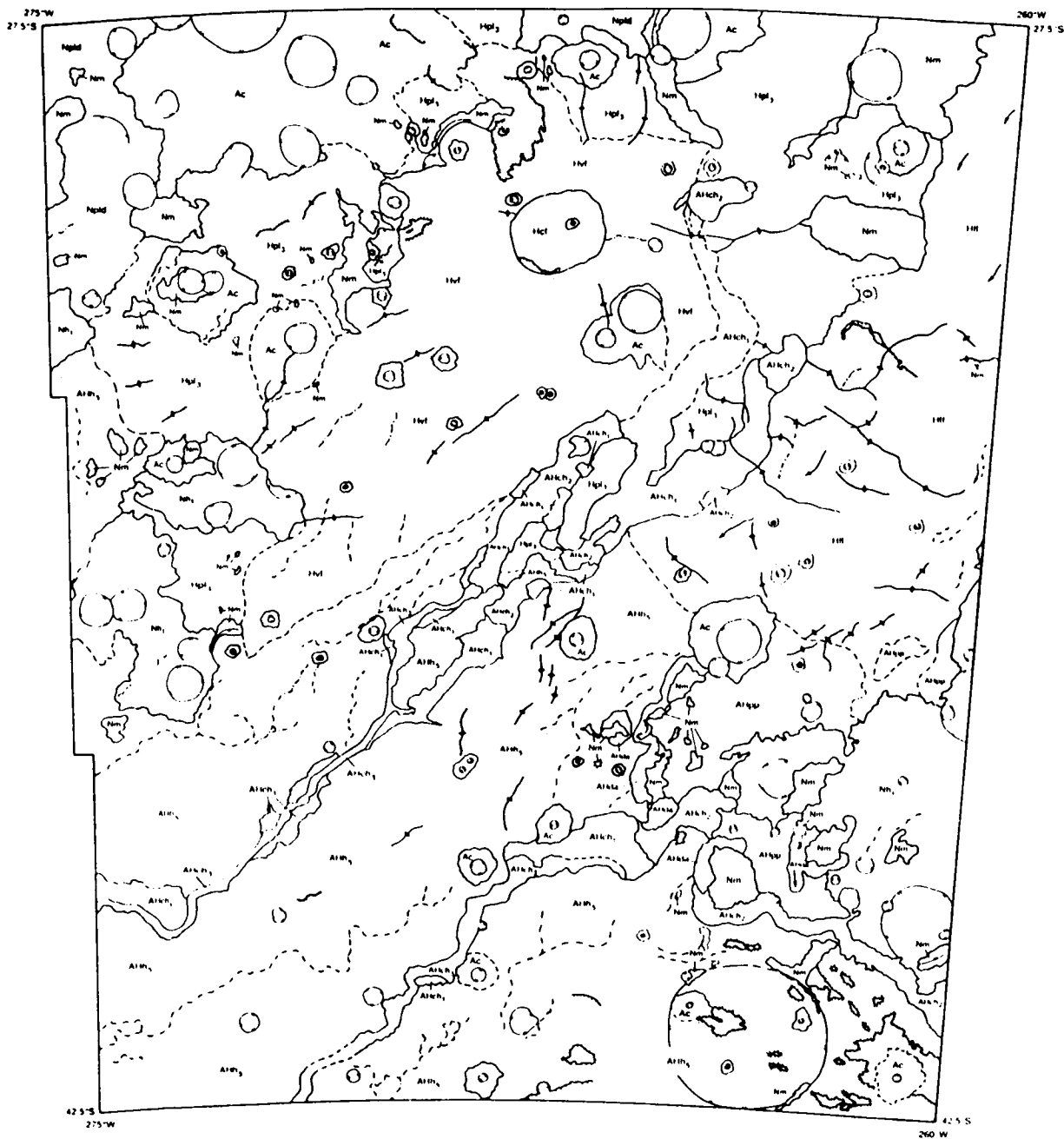
Mars Geologic Mapping: Dao, Harmakhis, and Reull Valles Region.

Katherine H. Price, Geology & Geography Department, DePauw University, Greencastle, Indiana.

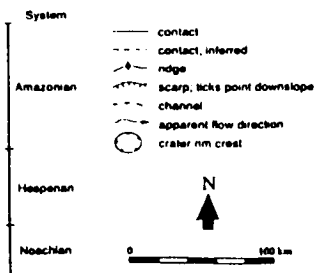
The east rim of Hellas basin is a complex geologic region affected by volcanic, tectonic, channeling, and resurfacing processes [1,2,3,4]. A regional geologic map of the area between 27.5-42.4°S and 260-275°W was compiled in order to establish general stratigraphic relationships between and among the geologic units exposed in the region (Figure 1) [5]. The southern one-third of the regional map, the area covered by three MGM 1:500,000 quadrangles -40272, -40267, and -40262, is to be mapped in more detail in this project.

Dao and Harmakhis Valles have lengths of about 500 km and trend approximately S45W. Outflow channel deposits have been subdivided into three facies which are interpreted to be (1) remnants of the plains in which the outflow channels formed (AHch₁), (2) channel floor materials which resulted from uniform removal of materials or uniform collapse (AHch₂), and (3) deposits suggesting fluvial modification (AHch₃). Cross-cutting relationships between these channel deposits and the channeled plains rim unit (AHh₅) indicate that channeling on the rim unit pre-and post-dates valles collapse. Details of the chronology of channeling events and of channeling relative to resurfacing events will emerge from geologic mapping at the 1:500,000 scale.

References: [1] Schultz, P.H. et al., 1982, *Lunar Planet. Sci. Conf. XIII*, 700-701. [2] Schultz, P.H., 1984, *Lunar Planet. Sci. Conf. XV*, 728-729. [3] Zurek, R.W., 1982, *Icarus*, 50, 288-310. [4] Greeley, R. and Guest, J.E., 1987, *U.S. Geol. Survey Misc. Inv. Series Map I-1802B*. [5] Crown, D.A. et al, 1990, *Lunar Planet. Sci. Conf. XXI*, 252-253.



Ac	Crater materials
Alch1	Debris apron materials
Alch2	Channel floor materials - sculpted
Alch3	Channel floor materials - smooth
Alch4	Channel floor materials - irregular
Alch5	Channelled plains rim unit
Alch6	Pried plains materials
Hcl	Calders filling materials
Hv	Volcanic flank materials
Hf	Flank flow materials
Hs	Smooth plateau materials
Hpd	Dissected plateau materials
Nm	Mountainous materials
Nh	Basin rim unit



CORRELATION CHART

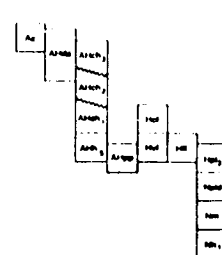


Figure 1. Geologic sketch map of the Hadriaca Patera region on the east rim of the Hellas basin.

Crown, D.A., Price, K.H., and Greeley, R., (1990) Evolution of the East Rim of the Hellas Basin, Mars. In *Proceedings of the Conference on Lunar and Planetary Science 21*, p.252-253. Houston, Tex.: Lunar and Planetary Institute.

EVOLUTION OF THE EAST RIM OF THE HELLAS BASIN, MARS

David A. Crown, Katherine H. Price*, and Ronald Greeley, Department of Geology, Arizona State University, Tempe, Arizona 85287; *Department of Geology & Geography, DePauw University, Greencastle, Indiana 46135

The Hellas basin, an ~2000 km impact structure with possible rings extending 4260 km in diameter [1], is a dominant feature in the ancient, southern cratered highlands of Mars. Impact basin control of volcanism and tectonism is evident on the Moon [2], and relationships between martian basins and surface processes have been identified [3-4]. The east rim of Hellas is a complex geologic region affected by volcanism, tectonism, and channeling. Remnants of an extensive mantling deposit and smooth deposits filling craters may be indicative of widespread aeolian activity, presumably related to the dust storms originating in the Hellas region [5]. A detailed study of the area between 27.5 - 42.4°S and 260 - 275°W has been initiated to analyze the processes forming surface materials and to decipher the evolution of this geologically important highland area (Figure 1). Major units include Hesperian volcanics associated with Hadriaca and Tyrrhena Paterae in the N and Hesperian and Amazonian channeled plains and outflow channels in the S. Remnants of Noachian mountains and plateaus are found throughout the region [6].

Hadriaca and Tyrrhena Paterae are low relief volcanoes thought to lie on inferred rings of Hellas [1]. The asymmetry exhibited by both volcanoes reflects the regional slope [7] caused by the topography of the basin. Materials associated with Hadriaca (Hvf) are interpreted to be ash deposits on the basis of their erosional characteristics, the low relief of the volcano, and the absence of primary lava flow features [8]. The distribution of units at both Hadriaca Patera and Tyrrhena Patera (located NE of the study area) are consistent with an origin by the emplacement of gravity-driven pyroclastic flows [8-11]. A large flank flow (Hff) containing lava flow lobes and leveed channels extends from Tyrrhena to the SW adjacent to Hadriaca Patera.

Dao and Harmakhis Valles have lengths >500 km and trend ~S45W. Outflow channel deposits have been subdivided into 3 facies: AHch₁, irregular materials forming channel floors, associated with channel walls, or forming dissected, low-lying regions connecting channel deposits; AHch₂, smooth, featureless deposits forming channel floors; and AHch₃, materials with linear to curvilinear features parallel to channel margins. AHch₁ materials are interpreted to be remnants of the plains in which the outflow channels formed and occur as sections of incompletely collapsed, dissected plains or as hummocky mounds and blocks on channel floors or slumped from channel walls. AHch₂ materials are smooth channel floors resulting from uniform removal of materials or uniform collapse. AHch₃ deposits indicate fluvial modification. These facies suggest that water flowed in part of the channels following dissection and collapse. Surrounding the channels in the S part of the mapped area is the channeled plains rim unit (AHh₅). Cross-cutting relationships N of Dao Vallis indicate that the channeling pre- and post-dates collapse.

Based upon photogeologic mapping the geologic history of the east rim of Hellas has been derived. Uplift of Noachian mountainous (Nm) and plateau (Npld, Nh₁) materials occurred in association with the Hellas impact event. The locations of mountains identify possible basin rings, which may have produced zones of weakness providing access to the surface for the magmas forming Hadriaca and Tyrrhena Paterae in Hesperian time. Erosion by runoff and/or sapping modified the plains and flanks of the volcanoes, followed by the formation of Dao and Harmakhis Valles. The presence of volatile-rich surface materials and possible fluvial or periglacial activity is suggested by the deflation and collapse of the

EVOLUTION OF HELLAS BASIN

Crown, D.A. et al.

channel deposits [12], the style of erosion of the channeled plains, and the debris aprons (AHda) and pitted materials (AHpp) observed in association with the older units. The origin and extent of the mantling deposit in the S and the role of aeolian processes are current topics of investigation. Crater counts will further constrain the temporal relationships observed.

References: [1] Peterson, J.E., 1978, *Proc. Lunar Planet. Sci. Conf.*, 9th, 3411-3432. [2] Solomon, S.C. and J.W. Head, 1980, *Rev. Geophys. Space Phys.*, 18, 107-141. [3] Schultz, P.H. et al., 1982, *Lunar Planet. Sci. Conf.*, XIII, 700-701. [4] Schultz, P.H., 1984, *Lunar Planet. Sci. Conf.*, XV, 728-729. [5] Zurek, R.W., 1982, *Icarus*, 50, 288-310. [6] Greeley, R. and J.E. Guest, 1987, *U.S. Geol. Survey Misc. Inv. Series Map I-1802B*. [7] U.S.G.S., 1987, *Topographic Map of Mars-Eastern Region, 1:15M*. [8] Crown, D.A. and R. Greeley, 1990, in *MEVTV Workshop on the Evolution of Magma Bodies on Mars*, L.P.I., in press. [9] Crown, D.A. and R. Greeley, 1988, *LPI Technical Report 89-04*, 29-31. [10] Crown, D.A. et al., 1988, *Lunar Planet. Sci. Conf.*, XIX, 229-230. [11] Greeley, R. and D.A. Crown, 1990, *J. Geophys. Res.*, in press. [12] Squyres, S.W. et al., 1987, *Icarus*, 70, 385-408.

EVOLUTION OF HELLAS BASIN

Crown, D.A. et al.

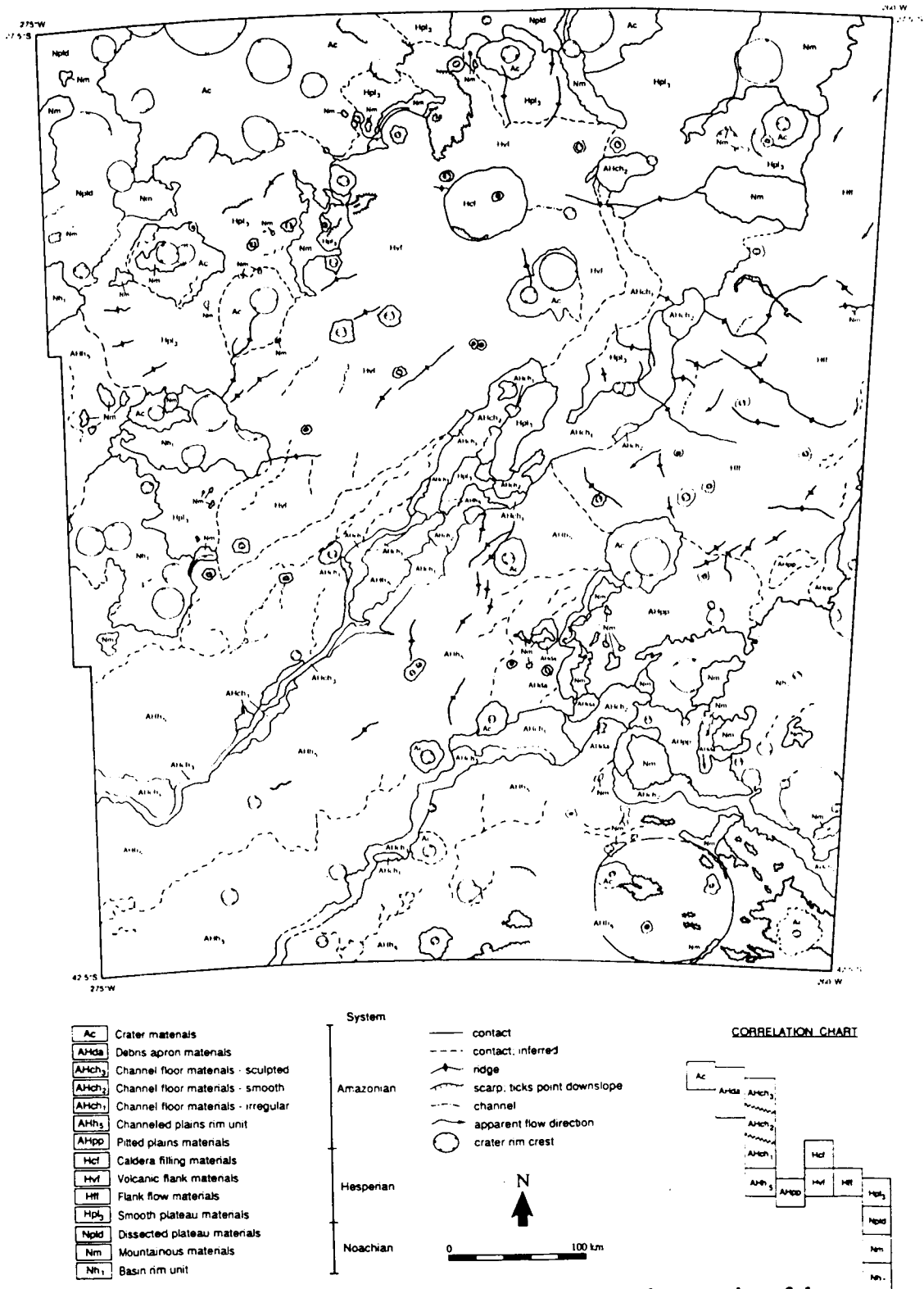


Figure 1. Geologic sketch map of the Hadriaca Patera region on the east rim of the Hellas basin.

GEOLOGIC MAPPING OF MTM QUADS 40292 AND 40297: IN THE UTOPIAN LOWLANDS NORTH OF THE NILOSRTIS MENSAE, MARS.

Steven H. Williams, Lunar and Planetary Institute, 3303 NASA Road 1, Houston, Texas 77598 and **James R. Zimbelman**, Center for Earth and Planetary Studies, National Air and Space Museum, Smithsonian Institution, Washington, DC 20560.

Introduction. Geologic mapping at 1:500,000 scale of the MTM quads 40292 and 40297 is being conducted under the auspices of the Mars Geologic Mapping Program. The study area is located in the southwestern portion of Utopia Planitia immediately north of the Nilosyrtis Mensae, between latitudes 37.5 and 42.5° and longitudes 290 and 300°. The goals of the mapping are to identify the major geologic features in the study area and to determine the sequence and scope of the geologic events that have modified the lowland side of the global dichotomy boundary in this region in order to at least partially constrain models of dichotomy boundary origin and evolution; this is a progress report.

Regional Geology. The study area has been mapped previously at a much larger scale by three previous investigations. The first (1,2) were the maps based on surface morphology based on Mariner 9 images. Viking images were used to derive a global view of martian geology (3) in which the study area was mapped to have Hesperian-age plains units to the north, Hesperian-age knobby material, and Amazonian-age cratered plains. Later mapping (4) grouped the older units of (3) together and identified the plains units in the map area as Amazonian-age smooth and etched plains. The plains units to the north of the study area are Hesperian in age and the plateau units south of the study area are Noachian in age and overlie older heavily cratered terrain (4).

The dichotomy boundary lies immediately south of the study area (Figure 1). It appears that the boundary predates the emplacement of the Hesperian-age plains for the following reasons. As one looks further to the south of the study area, there is a rather abrupt southern margin of the plains unit, then a region of valleys, many with lineated valley fill, where the elevation appears lower than the plains. Farther south is an irregular escarpment formed by Noachian-age plateau units of the highlands. It is very likely that the plateau units once extended farther north and that the plains were emplaced against them. Subsequent differential erosion has caused the retreat of the escarpment as much a hundred kilometers or more. If that is true, then the southern edge of the plains units marks the dichotomy boundary at the time of the emplacement of the plains.

Local Geology. The most obvious feature of the map area at first glance is the abundance of small knobs (Figure 2), termed the Colles Nili, or "Hills of the Nile Region" (after 5). Three possibilities of their origin have been recognized (2): a) they are bits of older terrain that protrude through younger terrain, b) they are erosional remnants of plateau materials with the edge of the plateau (highland side of the dichotomy boundary) now being farther south, or c) they are igneous intrusives exposed by differential erosion.

Another prominent local feature is the presence of a complex veneer of material that is prevalent throughout the study area (Figure 3). Its thickness varies widely from location to location, and the subunits of which it is composed appear to have little lateral continuity. In some locations, the knobs appear to be smoothly mantled by the veneer deposits, in others, the knobs clearly protrude through the plains units around them. The veneer is probably very young because there is not a single unequivocal example in the entire study area of an impact crater that was emplaced atop the veneer. Accurate mapping is rendered difficult by the presence of the veneer and the lack of medium to high-resolution photography for parts of the study area.

Most of the study area is covered by a plains unit. It is probably a flood basalt deposit because it contains a number of lunar mare-type wrinkle ridges. Its age is almost certainly Upper Hesperian, for the following reasons. Crater counting in the study area

gives an N(2) crater count of ~500 (corresponds to late Upper Hesperian (6)) and an N(1) crater count of ~1200 (corresponding to middle Lower Amazonian (6)). No doubt many of the 1 km craters were not counted because they were rendered unrecognizable by the younger veneer, hence, the N(2) age should be considered more reliable. The study area is too small and there are an insufficient number of larger craters to derive similar crater ages based on craters larger than 2 km. Another important factor in determining the age of the plains unit is that it contains a number of secondary clusters whose orientation suggest that they are from the Lyot impact over 1000 km to the northeast. If that is true, then the plains cannot be younger than Lyot, which was formed in early Amazonian time (6).

The veneer materials are of limited lateral continuity and vary in thickness throughout the study area. In a very few places, eroded remnants of channels mark their surface. It is likely that the veneer represents some sort of volatile-rich airfall-type deposit or deposits. It may be that the veneer represents many different, yet all recent, episodes of deposition and erosion. That would account for the varying thickness and poor lateral continuity of the deposits. Further evidence that the veneer is the result of multiple depositional and erosional events comes from the presence in the study area of many craters with concentric crater fill (Figure 4), which probably results from repeated deposition and erosion (7).

References.

1. Lucchitta, B.K., 1978, Geologic map of the Ismenius quadrangle of Mars, USGS Map I-1065.
2. Greeley, R., 1978, Geologic map of the Casius quadrangle of Mars, USGS Map I-1038.
3. Scott, D.H. and M.H. Carr, 1978, Geologic map of Mars, USGS Map I-1083.
4. Greeley, R. and J.E. Guest, 1987, Geologic map of the eastern equatorial region of Mars, USGS Map I-1802-B.
5. Blunck, J., 1977, *Mars and its Satellite: A Detailed Commentary on the Nomenclature*, Hicksville: Exposition Press, 200 p.
6. Tanaka, K.L., 1986, The stratigraphy of Mars, *Journal of Geophysical Research*, 91, B13, E139-E158.
7. Zimbelman, J.R., Clifford, S.M., and S.H. Williams, 1989, Concentric crater fill on Mars: An aeolian alternative to ice-rich mass wasting, Proceedings 19th Lunar and Planetary Science Conference, 397-407.

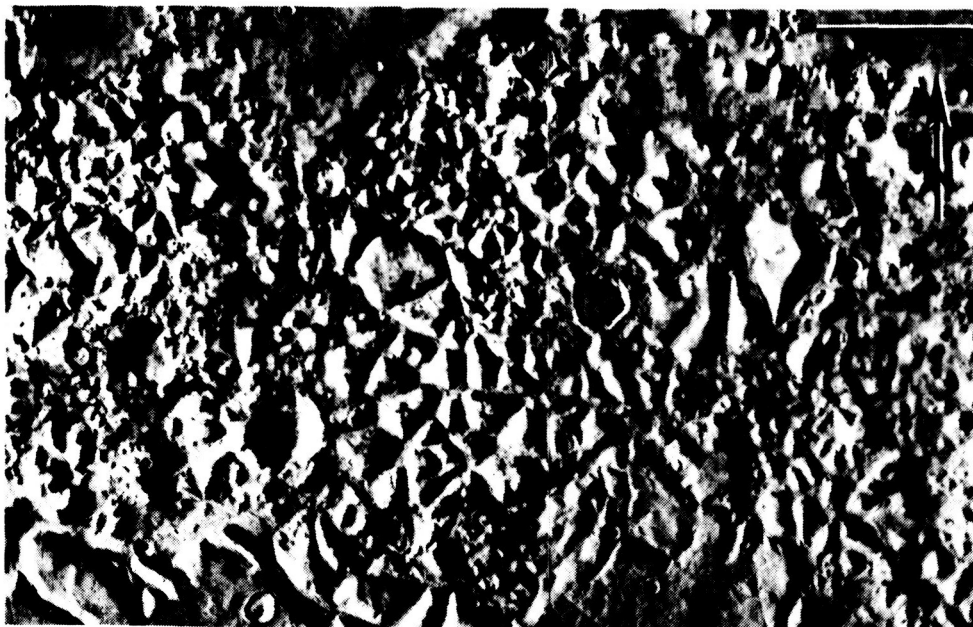


Figure 1. South of the map area, it appears that the Hesperian-age plains were emplaced against the dichotomy boundary, which has subsequently retreated by differential erosion. The edge of the plains is at the top of this image, the plateau highlands are at the bottom. The scale bar is 50 km long; these are portions of Viking frames 534A01 and 03, NGF version, orthographic projection.

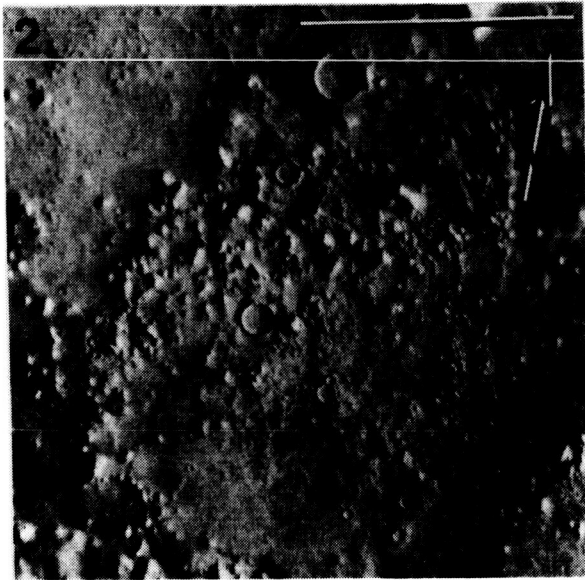


Figure 2. Knobby terrain is prevalent throughout the study area. The knobs appear to be remnants of ancient, heavily-cratered terrain that underlies both the Hesperian-age plains and the plateau units to the south. The scale bar is 100 km long; this is a portion of Viking frame 801A34, NGF version, orthographic projection.

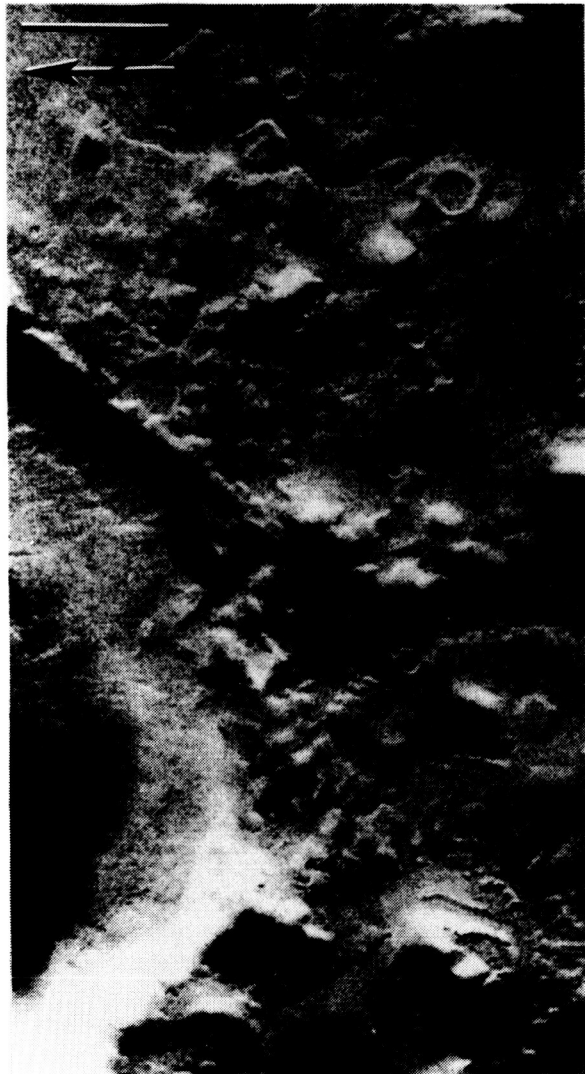


Figure 3. The veneer deposits are thickest just south of the crater Renaudot in quad 40297. Some small channel segments are visible in the veneer and several knobs appear to have eroded remnants of where the veneer once ramped up against them more completely than at present. The scale bar is 10 km long; this is a portion of Viking frame 234S74, NGF version, orthographic projection.

Figure 4. Craters with concentric crater fill may indicate repeated episodes of relatively recent deposition and erosion (7). The volume of the fill in the crater marked by an arrow is too great for the fill to have come entirely from the crater rim. The scale bar is 20 km long; this is a portion of Viking frame 11B44, SCR2 version, rectilinear projection.



STRATIGRAPHY OF THE PERRINE AND NUN SULCI QUADRANGLES (Jg-2 AND Jg-5), GANYMEDE.

George E. McGill, Department of Geology and Geography, University of Massachusetts, Amherst, MA, and Steven W. Squyres, Center for Radiophysics and Space Research, Cornell University, Ithaca, NY.

Dark and light terrain materials in the Perrine and Nun Sulci quadrangles are divided into 9 map units, 4 dark and 5 light. These are placed in time-stratigraphic sequence primarily by means of embayment and cross-cutting relationships. Dark terrain is generally more heavily cratered and thus older than light terrain but, at least in these quadrangles, crater densities are not reliable indicators of relative ages among the 4 dark material units.

Dark Materials: The 4 mapped material units within dark terrain are: cratered dark materials (dc), grooved dark materials (dg), transitional dark materials (di), and dark materials, undivided (d).

The most widespread dark terrain unit consists of cratered dark materials (dc). Although the average albedo is relatively low, these materials have a patchy, streaked, or mottled appearance in detail because the surface is actually a montage of high and low albedo areas at km to 10's of km scale. In places, this appearance seems due to the presence of grooves or fragments of crater rims that are too small to map, but generally it is not possible to identify the surface characteristics responsible. The surface texture is rough at a scale similar to the albedo variations or smaller. Craters and palimpsests of all sizes from the limits of resolution to the largest present in the mapped area are superposed on this unit. These span the full range of crater ages present. Individual large grooves are present in places, many of which cross-cut or coincide with contacts between light and dark terrains.

Grooved dark materials (dg) occur generally as small areas adjacent to larger areas of cratered dark materials, commonly along contacts between the latter and light materials. The average albedo is somewhat higher than for cratered dark materials, and in detail the surface has a linear or streaked appearance consistent with the groove topography. The only large area of grooved dark materials occurs in the northern third of the large, sub-circular portion of Perrine Regio on Jg-2. Here the crater density appears to be less than in the southern two-thirds of this region, which is underlain by cratered dark materials. However, this impression is based on a grand total of 20 mapped craters and crater fragments, three in the northern third, 17 in the southern two-thirds, and thus should be only provisionally accepted as evidence for a real age difference. In many places, grooves in dark materials are clearly continuous with grooves in adjacent light materials, hence the grooves represent a relatively young structural modification of the dark materials. Grooved dark materials may thus be simply cratered dark materials that have been structurally modified, and older craters would logically be less recognizable where they are cut by grooves. Consequently, the apparent difference in crater ages between cratered and grooved dark materials is possibly unrelated to the true formation ages of the materials. The large area of grooved terrain mapped in Perrine Regio is included in the group of "system III" furrowed dark-terrain polygons by Murchie and Head (1988). We believe that the materials of this area are more correctly mapped as grooved than as furrowed because the troughs are morphologically similar to grooves, and not similar to furrows, and because at least

some of them are continuous with typical grooves in the adjacent light terrain materials. However, the quality of the available images is so poor that it is not really possible to resolve this issue with any confidence.

Transitional dark materials (di) occur only in small patches adjacent to light materials. The distinguishing characteristic is an albedo intermediate between typical dark materials and typical light materials. Surface appearance may be similar to grooved dark materials or to dark materials, undivided. The intermediate albedo is presumably due to a smaller fraction of dark silicate(?) material near the surface than is the case for normal dark materials. The age relationships with cratered and grooved dark materials are unknown.

Dark materials, undivided (d) occur in small patches or in areas of very poor image resolution. Neither grooves nor craters can be resolved, and the surfaces generally appear to be smooth and of a uniform low albedo, an appearance most likely due to poor resolution in most instances. Undivided dark materials are inferred to be similar to either grooved or cratered dark materials.

Light Materials: The 5 mapped units within light terrain are: intermediate light materials (li), grooved light materials (lg), irregularly grooved light materials (lgi), smooth light materials (ls), and light materials, undivided. Intermediate light materials (li) are materials that are intermediate in albedo between other light materials (lg, lgi, ls, l) and the lightest dark material (di). Usage of this unit is restricted to a region in the northern portion of Jg-2. Texturally, this material appears similar to dark materials, but it is distinctly brighter than any of them. A possible explanation for the appearance of this unit is that the underlying material is in fact dark terrain that is blanketed by Ganymede's polar frost caps. These caps apparently are thin deposits of H₂O frost that cover the surface of Ganymede down to a latitude of 40°-50° in both hemispheres. They may be either the remnants of a formerly more extensive frost blanket that has been removed from lower latitudes by sublimation, or may be an accumulation of frost that has built up over time by transport from lower latitudes.

Grooved light materials (lg) are common, and are perhaps the most distinctive geologic unit on the satellite. Like irregularly grooved light and smooth light materials, they have a markedly lower crater density than is observed in dark terrains. Their distinguishing characteristic is the presence of very regular patterns of grooves transecting their surface. Grooves are curvilinear topographic depressions up to a few km wide, a few hundred m deep, and hundreds of km long. Grooves appear to be roughly U-shaped in cross-section, but unfortunately the resolution of the best images is insufficient to reveal the details of their geometry. Groove slopes are gentle; at Voyager resolution, typical slopes are less than 10° (Squyres, 1981). The grooves are arranged in subparallel or fan-shaped sets that intersect and crosscut one another with geometry that can be very complex. The grooves in some sets are packed closely together, producing roughly sinusoidal topographic profiles, while in others they are widely separated, with distinct smooth areas between them. Where these smooth units become extensive, they are mapped as a distinct unit, ls.

Irregularly grooved light materials (lgi) are similar to grooved light materials in having low crater density, high albedo, and a surface dominated by grooves. The distinction is that the grooves are not arranged in sets. Instead, they can have a variety of complex geometries. Individual grooves may be straight, arcuate, or sinusoidal, but the trends of adjacent grooves are not correlated as they are in grooves that are arranged in sets. Individual grooves may crosscut and truncate one another, and it is not uncommon for grooves to split and merge at acute angles, forming a crudely anastomosing pattern.

The simplest light terrain is composed of smooth light materials (ls). These materials are similar in albedo to most other light terrains, but are distinguished by being free of grooves at the best available image resolution. Except for impact craters, topography is very subdued. In particular, no volcanic flows or other features that might provide morphologic clues to the emplacement mechanism are seen. Albedo is commonly fairly uniform across individual regions of smooth light material. Some regions, however, have a mottled appearance suggesting local variations in silicate content. Smooth light materials are seen in a variety of geometric relationships with other light units. Some occur as irregularly-shaped groove-free patches in areas that are otherwise dominated by a complex pattern of grooves. They also occur as long curvilinear swaths with geometry similar to groove sets. Some of these have bounding grooves. Smooth swaths and regions commonly have very sharp boundaries, both with other light units and with dark units. In other cases, however, the boundaries are indistinct and transitional to dark materials or to other light materials.

Undivided light materials (l) are simply materials that appear to have an albedo similar to those of other light terrains, but that are observed at an image resolution, viewing geometry, or illumination geometry that prevents recognizing characteristics that would identify them as belonging to one of the other mapped light units. They are mapped primarily in the poorly-imaged central portion of Jg-2.

Crater and Basin Materials: Crater and palimpsest materials are divided into 4 morphologic classes from highly degraded (palimpsests) to very fresh (bright ray craters). This classification is inferred to correspond approximately to a relative age sequence. Caution is necessary, however, because of size-dependent effects on degradation by micrometeorite bombardment, favoring survival of large craters, and size-dependent effects on degradation by viscous relaxation, favoring survival of small craters. Nevertheless, if very large and very small craters and palimpsests are ignored, one can infer with reasonable confidence that morphologically degraded craters are older than fresh craters.

References Cited:

Murchie, S.L., and Head, J.W., 1988, Possible breakup of dark terrain on Ganymede by large-scale shear faulting: *Journal of Geophysical Research*, vol. 93, p. 8795-8824.

Squyres, S.W., 1981, The topography of Ganymede's grooved terrain: *Icarus*, vol. 46, p. 156-168.

ARE NOACHIAN-AGE RIDGED PLAINS (*Nplr*) ACTUALLY EARLY HESPERIAN IN AGE? H. V. Frey, C. E. Doudnikoff and A. M. Mongeon, Geodynamics Branch, Goddard Space Flight Center, Greenbelt MD 20771

Ridged Plains of Noachian Age?

The prominent ridged plains of Lunae Planum, Coprates, Hesperia Planum and elsewhere are generally considered to have erupted in the Early Hesperian (1,2) and are generally taken to define the base of that stratigraphic system (3). These plains are widespread, covering over 4×10^6 km² in western Mars alone (1) and are broad, planar surfaces with some flow lobes and parallel, linear to sinuous ridges similar to lunar mare ridges with a spacing of 30 to 70 km. The general interpretation is that the ridged plains (unit *Hr*) are due to relatively rapid eruptions of low viscosity lavas (1,2), and their occurrence at the base of the Hesperian represents a major volcanic episode in martian history (3).

In some areas these plains are gradational with another ridged plains unit, mapped as *Nplr*. The ridges of these apparently Noachian-age plains are generally further apart with rougher, more heavily cratered inter-ridge areas (1,2). *Nplr* terrains are widely distributed in both hemispheres of Mars but cover much less area than the more common *Hr* unit. The type area in Memnonia lies southwest of Tharsis in heavily cratered terrain (*Npl1*, *Npl2*). Other major occurrences are further south in Sirenum, between the Argyre and Hellas Basins in Noachis, in the southern portion of Cimmeria Terra and in the northeastern portion of Arabia (1,2). The Noachis and Cimmeria outcrops are distributed roughly concentrically about the Hellas impact basin at approximately 1 and 2 basin diameters, respectively.

The stratigraphic position of these apparently older ridged plains is Middle Noachian; in the current geologic maps the unit does not extend into the Upper Noachian and appears temporally unrelated to the more common Hesperian ridged plains (*Hr*) even though these two units are sometimes gradational. The assignment of stratigraphic position is based on superposition relationships and total crater counts; the high density of impact craters on *Nplr* would certainly suggest a Noachian age.

But total crater counts can be misleading: if multiple resurfacing or other crater depopulation events occur and successfully compete with crater production, a given terrain may have an apparently young total crater age even though very old surfaces remain partially exposed in the form of very large craters. Inefficient resurfacing events allow older surfaces to show through and give old crater retention ages based on total crater counts, which may not accurately reflect the age of the major terrain unit. In this paper we examine whether or not the *Nplr* units in Memnonia and Argyre truly represent ridged plains volcanism of Noachian age or are simply areas of younger (Early Hesperian age) volcanism which failed to bury older craters and therefore have a greater total crater age than really applies to the ridged plains portion of those terrains.

Resurfacing in Memnonia and Argyre

We used the Neukum and Hiller (4) technique to determine the number of preserved crater retention surfaces in the Memnonia and Argyre regions where Scott and Tanaka (1) show *Nplr* units to be common. The Memnonia outcrops are the type example of this unit, and we subdivided the study area in MC 16 into two broad units: cratered terrain *Npl* (mostly *Npl1* and *Npl2*) and the ridged plains *Nplr*. Our mapping is similar to but not identical with that previously done (1). We counted craters larger than 3 km in diameter and plotted cumulative frequency curves for each terrain unit, then broke these curves into separate branches where they departed from a standard production curve (4, 5). This departure is interpreted to be due to resurfacing, and breaking the curves into separate branches allows determination of the crater retention age of each post-depopulation "surface" independent of previous history (the survivors are subtracted and remaining craters compared independently to the crater production curve). Table 1 summarizes the results for cratered terrain (*Npl*) in Memnonia and for ridged plains (*Nplr*) in both Memnonia and Argyre, and compares these with similar results obtained by us for Tempe

Terra (6) and Lunae Planum (the type area for the Lunae Planum Age [LPA] ridged plains [*Hr*] resurfacing).

In Lunae Planum no craters larger than 50 km exist within the ridged plains; in Memnonia and Argyre there are craters as large as 117 and 100 km that survive in the *Nplr* unit. The population of old, large craters contributes to the total crater counts which suggest the *Nplr* unit is of Noachian age. We find the cumulative frequency curves for the ridged plains in Argyre/Memnonia can be broken into four branches which have remarkably similar crater retention ages $N(1)$: an oldest branch $\sim[121,000/115,000]$, a branch with $N(1) = [80,200/76,500]$, a "Lunae Planum Age" branch at $[28,100/22,100]$, and a still younger branch at $N(1) = [6700/6200]$. Note that the Argyre ages for *Nplr* are consistently slightly older. These ages compare with resurfacing ages for the cratered terrain *Npl* in Memnonia of $N(1) = [226,900]$, $[76,000]$, $[27,900]$, and $[6300]$. For all but the oldest (and most poorly determined) branch, the crater retention ages for the different branches are extremely similar from one area to the next.

The craters which determine the ridged plains resurfacing age (those superimposed on the ridges as opposed to showing through the plains) define the $N(1) = [25,000 \pm 3000]$ age branch for both Memnonia and Argyre. This age is nearly identical (with the precision this technique affords) with the oldest branch we find for Lunae Planum: $N(1) = [25,700]$, even though the craters which define this age branch (10-20 km in Argyre, 8-15 km in Memnonia) are significantly smaller than in Lunae Planum (25-50 km). This implies that the thickness of the *Nplr* ridged plains in Argyre and Memnonia is significantly less than we estimate (4,5) for Lunae Planum (350- 600 m). This reduced thickness is what allows the older craters to show through, preserving the older crater retention surfaces at $N(1) = [78,000 \pm 2000]$ and $[118,000 \pm 3000]$. These older preserved craters contribute to the high total crater counts that suggested the *Nplr* were of Noachian age.

We suggest that for these two areas at least the *Nplr* ridged plains are the same age as those (*Hr*) in Lunae Planum, Tempe and elsewhere: $N(1) = [25,000 \pm 3000]$. If this conclusion holds in general for the other outcrops of those units mapped as *Nplr*, it may imply that the eruption of ridged plains volcanism was more restricted in time than previously thought. This would have interesting implications for models of the thermal history of Mars, and would make the ridged plains even more important as a stratigraphic marker in martian history.

Table 1. Resurfacing Ages for Memnonia and Argyre

AREA	UNIT	CRATER RETENTION AGE $N(1)$			
Memnonia	<i>Npl</i>	226,858	75,980	27,866	6,343
Memnonia	<i>Nplr</i>	115,221	76,445	22,062	6,223
Argyre	<i>Nplr</i>	121,300	80,200	28,100	6,700
Lunae Planum	<i>Hr</i>	--	--	25,700	10,100
Tempe	<i>Hr</i>	--	--	22,100	6,500

References: (1) Scott, D. H. and K. L. Tanaka, Geol. Map Western Equatorial Region of Mars, USGS Map I-1802-A, 1986. (2) Greeley, R. and J. E. Guest, Geol. Map Eastern Equatorial Region of Mars, USGS Map I-1802-B, 1987. (3) Tanaka, K. L., Proceed. LPSC 17th, JGR 91, E139-E158, 1986. (4) Neukum, G. and K. Hiller, JGR 86, 3097-3121, 1981. (5) Frey, H., A. M. Semeniuk, J. A. Semeniuk and S. Tokarcik, Proceed. LPSC 18th, 679-699, 1988. (6) Frey, H. and T. D. Grant, submitted to JGR, 1989.

MARS GEOLOGIC MAPPING PROGRAM: REVIEW AND HIGHLIGHTS.

David H. Scott, U.S. Geological Survey, Flagstaff, Arizona 86001

The Mars Geologic Mapping Program (MGM) was introduced by NASA in 1987 as a new initiative in the Planetary Geology and Geophysics Program (PGG). The overall purpose of the program is to support research on topical science problems that address specific questions. Among the objectives of the project are (1) producing highly detailed geologic maps that will greatly increase our knowledge of the materials and processes that have contributed to the evolutionary history of Mars, (2) defining areas of special interest for possible future investigation by planned missions (Mars Observer, Mars Sample Return), and (3) maintaining the interest of the planetary community in the development of new concepts and the re-evaluation of Martian geology as new data in usable form become available. Two types of proposals may be submitted to the Mars Geologic Mapping Program: those involving the preparation of geologic maps on existing bases, or those requiring the preparation of 1:500,000-scale base maps. In both cases, the proposals must discuss the scientific rationale and the topical problems to be addressed by the geologic mapping. Completed maps will be published by the U.S. Geological Survey in the Miscellaneous Investigations Series.

At the close of FY90, 23 principal investigators (Fig. 1) were active in the Mars Geologic Mapping Program. They currently represent 9 universities, 2 NASA centers, 2 private institutions, the Lunar and Planetary Institute, the National Aeronautics and Space Museum, and the U.S. Geological Survey. During 1990, 9 new proposals and 10 renewal proposals were submitted to the MGM review panel for funding requests and 2 proposals submitted for base map constructions. Seventy-five MGM 1:500,000-scale quadrangles have been approved for geologic mapping; about 15 of these maps are in advanced stages of preparation. A meeting of MGM principal investigators was held at the USGS Center, Flagstaff, Arizona, during June 27-28, 1990. Scientific issues relevant to the program were discussed and specific mapping problems addressed. Presentations of mapping progress of some 20 quadrangles were made by PI's. Following the meeting, members of the MGM Steering Committee and Review Panel met on June 28-29 to evaluate new and renewal proposals to the program.

Some interesting highlights of the geologic mapping indicate that multiple flood episodes occurred at different times during the Hesperian Period in both Kasei and Maja Valles. Studies of small channels in the Memnonia, Mangala, and Tharsis regions show that fluvial events appear to have occurred during the Amazonian Period at equatorial latitudes. Flood waters from Mangala Valles may have seeped into surficial materials with the subsequent development of numerous sapping channels and debris flows; this suggests that the ancient highland terrain consists of relatively unconsolidated materials. Multiple layers have been observed for the first time in the ridged plains lava flows covering large areas of Lunae Planum; some wrinkle ridges in this area are associated with grabens and collapse pits, which suggests that the ridges originated as dikes. The distribution of volcanic units at Hadriaca and Tyrrhena Paterae indicates that the units may have been emplaced by gravity-driven pyroclastic flows. Unlike the north polar layered deposits, those in the south polar region show no angular unconformities or evidence of faulting and folding. Water ice in the south polar layered deposits may be protected from solar heating and sublimation by a weathering rind or lag deposit on the surface.

MARS GEOLOGIC MAPPING STATUS (1:500,000 scale) FY 90

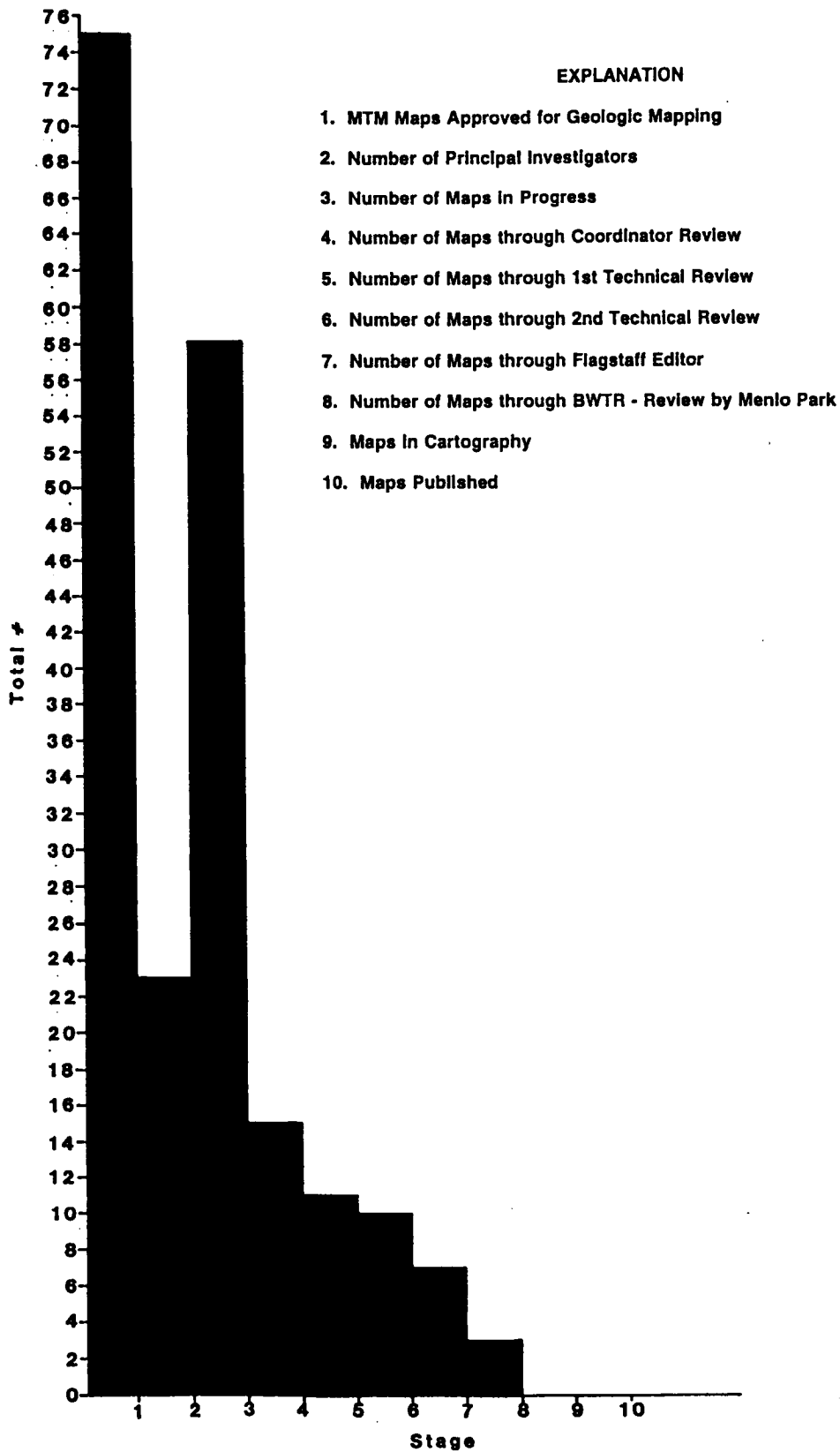


FIGURE 1

CHAPTER 10

**PLANETARY CARTOGRAPHY AND
PROGRAM SUPPORT**

VENUS MAPPING

R.M. Batson, H.F. Morgan, and Robert Sucharski, U.S. Geological Survey, Flagstaff, Arizona 86001

New semicontrolled image mosaics of Venus, based on Magellan data, are being compiled at 1:50,000,000, 1:10,000,000, 1:5,000,000 and 1:1,000,000 scales to support the Magellan Radar Investigator (RADIG) team. The mosaics are semicontrolled in the sense that data gaps have not been filled and significant cosmetic inconsistencies exist. Contours are based on preliminary radar altimetry data that is subject to revision and improvement. Final maps to support geologic mapping and other scientific investigations, to be compiled as the dataset becomes complete, will be sponsored by the Planetary Geology and Geophysics Program and/or the Venus Data Analysis Program. All maps, both semicontrolled and final, will be published as I-maps by the USGS. All of the mapping is based on existing knowledge of the spacecraft orbit; photogrammetric triangulation, a traditional basis for geodetic control on planets where framing cameras were used, is not feasible with the radar images of Venus, although an eventual shift of the coordinate system to a revised spin-axis location is anticipated. This is expected to be small enough that it will affect only large-scale maps.

Table 1 shows the Venus mapping plan. The first set of maps is being compiled on eight sheets (figure 1). They are radar image mosaics and will show preliminary nomenclature and topography. This eight-quadrangle format (8QF) was scaled at the pole to 1:10,000,000; the Mercator projections that join the Polar Stereographic projections are scaled to join at 56° lat (north and south), resulting in a scale of 1:10,000,000 at 52.305° N and S lat and 1:16,354,353 at the equator. Airbrushing on the 8QF sheets and on the 1:50,000,000-scale planetwide map (figure 2) will be done at the same time as the semicontrolled mapping. The airbrush maps will restore an impression of topographic relief that is lost in the radar image mosaics. Base maps for systematic geologic mapping will be made at 1:5,000,000 scale (figure 3); airbrushing will probably not be done at this scale. A 1:1,000,000-scale series of special high-resolution mosaics is being made of areas of high scientific interest. Preliminary versions are being compiled for the Magellan team, and it is anticipated that mapping at this scale will continue for many years, as has been the case with the Mars 1:500,000-scale geologic mapping program.

Table 1. Venus mapping plan.

SCALE	NUMBER OF SHEETS	DESCRIPTION	EXPECTED PUBL DATE
1:50M	1	Airbrush (preliminary), provisional nomenclature, contours from radar altimetry. Prepared under MGN project funding.	1992
1:50M	1	Airbrush map of Venus (final), IAU-approved nomenclature, contours from final altimetry version. Prepared under PGG funding.	1994
1:10M	8	Image mosaics (preliminary, nominal mission data only; gaps and tonal discrepancies will be present), provisional nomenclature, contours from radar altimetry. Prepared under MGN project funding.	1991, 1992
1:10M	8	Airbrush shaded relief and radar brightness markings, nomenclature (some may be provisional) contours from radar altimetry. Prepared under PGG funding.	1991 - 1993
1:5M	62	Image mosaics, with gaps filled with data from mapping cycles beyond those of the nominal mission; cosmetics and tone balancing appropriate to formal map series; contours primarily from radar altimetry, modified as feasible by other techniques; IAU approved nomenclature. Prepared under PGG funding.	1992 - 1995
1:1M	TBD	Areas selected on the basis of scientific interest; initial quads will be semicontrolled-- they may contain gaps, tonal inconsistencies, provisional nomenclature and contours derived from preliminary data. As the program continues, experimental and innovative cartographic image-processing methods will be	1991 - 2001

used, and final maps will display information appropriate to a formal map series. Initial quads prepared under MGN project; later quads under PGG funding.

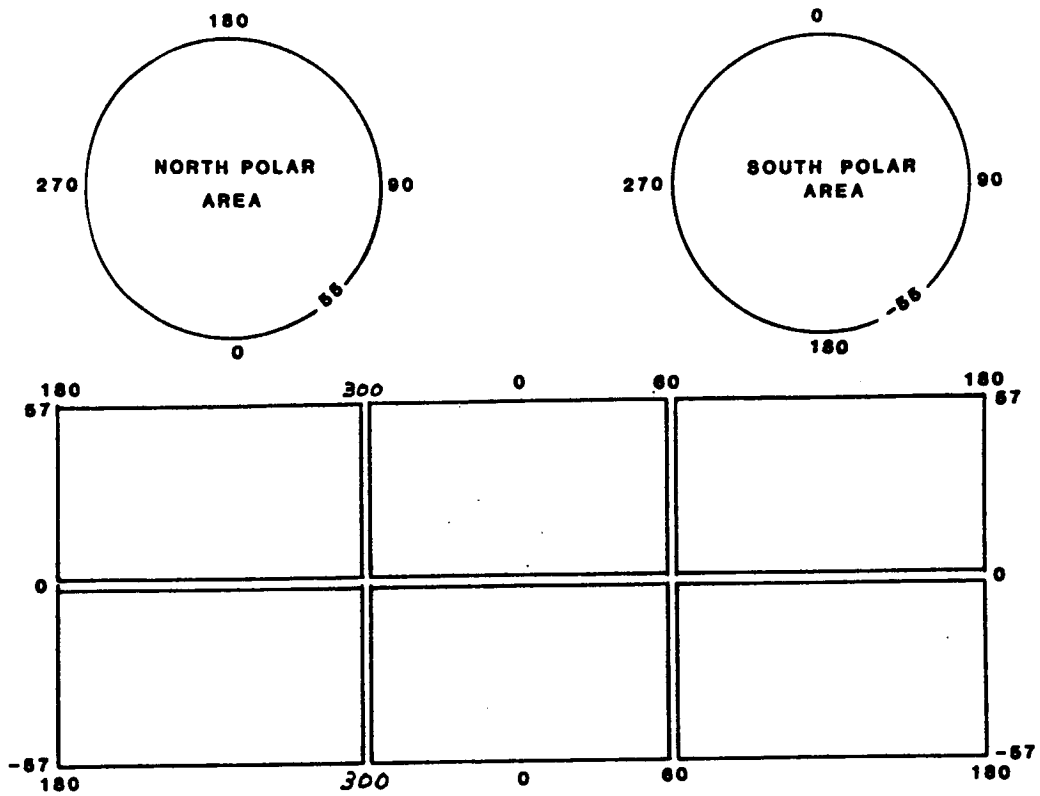


Figure 1. 1:10,000,000 mapping format

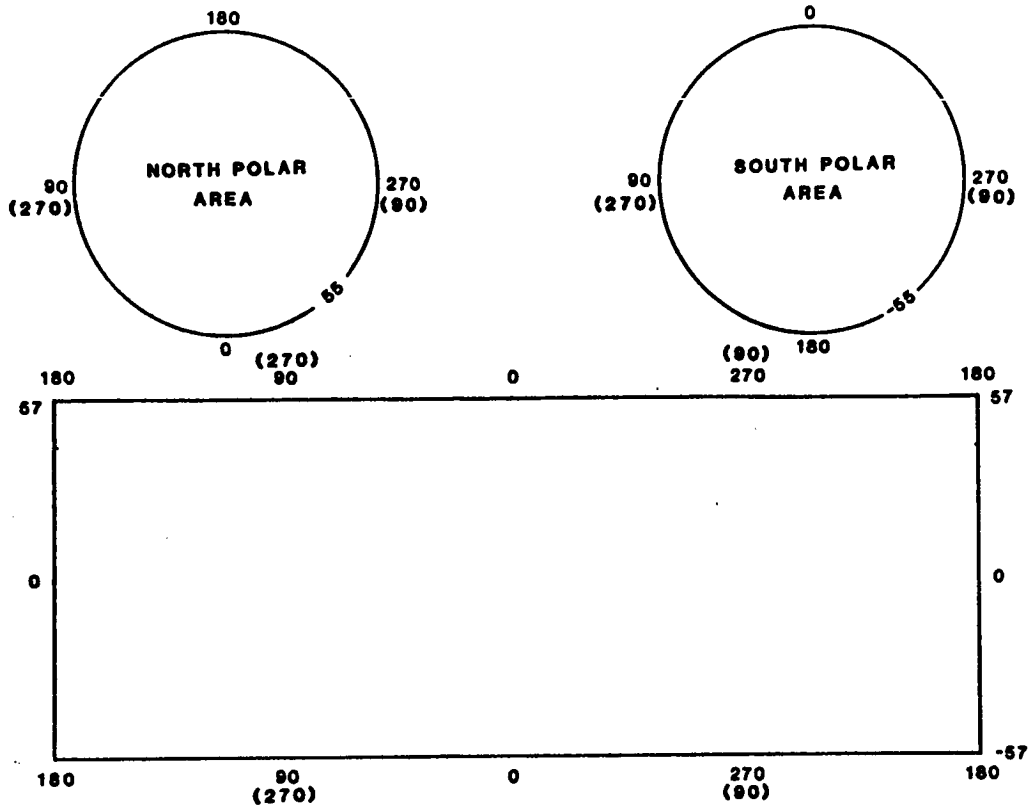


Figure 2. 1:50,000,000 planetwide format

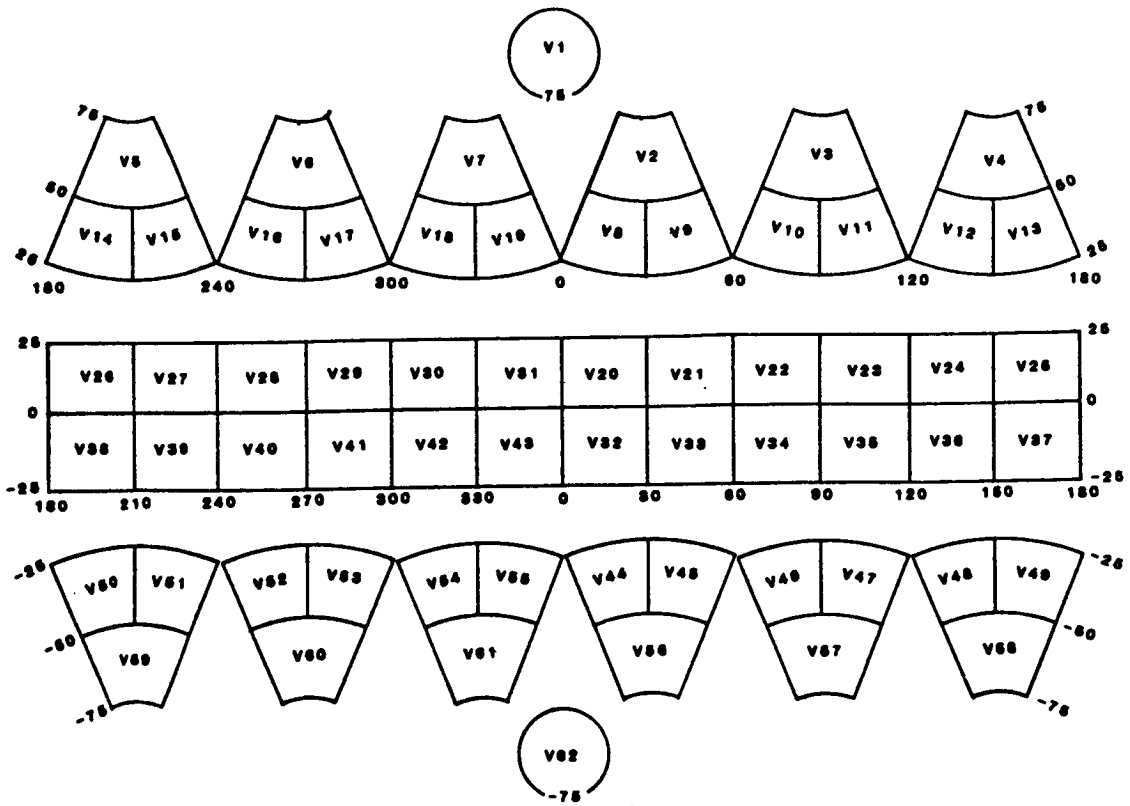


Figure 3. 1:5,000,000 mapping format

TRIANGULATION USING SYNTHETIC APERTURE RADAR IMAGES, Sherman S. C. Wu, and Annie E. Howington-Kraus, U.S. Geological Survey, Flagstaff, Arizona 86001

For the extraction of topographic information about Venus from stereoradar images obtained from the Magellan Mission, we have developed a Synthetic Aperture Radar (SAR) compilation system on analytical stereoplotters (Wu et al., 1986, 1987, 1988). The system software has been extensively tested by using stereoradar images from various spacecraft and airborne radar systems, including Seasat, SIR-B, ERIM XCL, and STAR-1. Stereomodeling from radar images has been proven feasible, and development is on a correct approach. During testing, the software was enhanced and modified to obtain more flexibility and better precision. Triangulation software for establishing control points by using SAR images has also been developed through a joint effort with the Defense Mapping Agency.

The SAR triangulation system comprises four main programs, TRIDATA, MODDATA, TRISAR and SHEAR. The first two programs are used to sort and update the data; the third program, the main one, performs iterative statistical adjustment; and the fourth program analyzes the results. Also, input are flight data and data from the global positioning system and inertial system (navigation information).

We have tested the SAR triangulation system with six strips of STAR-1 radar images on our VAX-750 computer. Each strip contains images of 10 minutes' flight time (equivalent to a ground distance of 73.5 km); the images cover a ground width of 22.5 km. All images were collected from the same side. With an input of 44 primary control points, 441 ground control points were produced. The adjustment process converged after eight iterations. With a 6-m/pixel resolution of the radar images, the triangulation adjustment has an average standard elevation error of 81 m.

Development of Magellan radargrammetry will be continued to convert both SAR compilation and triangulation systems into digital form.

References

- Wu, Sherman S. C., Schafer, Francis J., and Howington, Annie-Elpis, 1986, Radargrammetry for the Venus Radar Mapper Mission: Reports of Planetary Geology and Geophysics Program--1985, NASA Tech. Memo. 88383, 570-573.
- Wu, Sherman S. C., Schafer, Francis J., and Annie-Elpis Howington, 1987, A compilation system for Venus Radar Mission (Magellan): Reports of Planetary Geology and Geophysics Program--1986, NASA Tech. Memo 89810, 233-235.
- Wu, Sherman S. C., Schafer, Francis J., and Howington-Kraus,

NAMING THE NEWLY FOUND LANDFORMS ON VENUS; R.M. Batson and J.F. Russell,
U.S. Geological Survey, Flagstaff, Arizona 86001

The mapping of Venus is unique in the history of cartography; never has so much territory been discovered and mapped in so short a period of time. Therefore, in the interest of international scientific communication, there is a unique urgency to the development of a system of names for surface features on Venus. The process began with the naming of features seen on radar images taken from Earth (Goldstein, et al, 1978) and continued through mapping expeditions of the U.S. (Pettengill et al., 1980) and the U.S.S.R. (Basilevsky et al, 1990). However, the Magellan mission (Saunders et al., 1990) resolves features twenty-five times smaller than those mapped previously, and its radar data will cover an area nearly equivalent to that of the continents and the sea-floors of the Earth combined.

The International Astronomical Union (IAU) has been charged with the formal endorsement of names of features on the planets. Proposed names are collected, approved, and applied through the IAU Working Group for Planetary System Nomenclature (WGPSN) and its task groups, prior to final approval by the IAU General Assembly. Names approved by the WGPSN prior to IAU approval may be used on published maps and articles, provided that their provisional nature is stipulated.

Compilation of a regional network of names has been given the first priority; a more localized nomenclature will be developed as scientific studies become increasingly topical. To date, names have been proposed for more than 200 craters with diameters greater than 20 km; when the Magellan mission is complete, it is likely that about 900 such craters will have been discovered. We have proposed similar, but necessarily less explicit size criteria for other kinds of landforms. We also proposed that the topographic nature of features be unambiguous prior to naming, so that a ridge, for example, is not given a name appropriate for a valley before its true configuration is discovered.

A total of 382 names have been approved and applied to features on maps of Venus compiled from earlier explorations. A database containing 600 new names has been collected and proposed to the WGPSN for use on Venus. Upon approval, these will be applied to features suggested by map users. Experience with other planets indicates that names for 4000 or more features on Venus are likely to be required in the coming decade.

The IAU has established themes for the names to be used on each of the planets; names of historical and mythological women are used on Venus. Names of political entities and those identified with active religions are not acceptable, and a person must have been deceased for three years or more to be considered. Any interested person may propose a name for consideration by the IAU. Suggestions may be made to the authors of this paper or to the WGPSN directly. The suggestion must include a brief reference to the identity of the person, along with a brief written justification for the honor. A complete description of the naming process is given by Strobell and Masursky (1990).

REFERENCES

- Basilevsky, A.T., Batson, R.M., and Burba, G.A., 1990, Pre-Magellan mapping of northern Venus: Completion of a joint U.S./U.S.S.R. mapping project, in Abstracts of Papers Submitted to the Twenty-first Lunar and Planetary Science Conference, Houston, March 12-16, 1990, Lunar and Planetary Institute, Part 1, pp 50-51.
- Goldstein, R.M., Green, R.R., and Rumsey, H.C., 1978, Venus radar brightness and altitude images: *Icarus*, vol. 36, pp 334-352.
- Pettengill, Gordon H., Eliason, Eric, Ford, Peter G., Lorient, George B, Masursky, Harold, and McGill, George E., 1980, Pioneer Venus radar results: altimetry and surface properties: *Journal of Geophysical Research*, vol. 85, no. A13, pp 8261-8270.
- Saunders, R.S., Pettengill, G.H., Arvidson, R.E., Sjogren, W.L., Johnson, W.T.K., and Pieri, L., 1990, The Magellan Venus radar mapping mission: *Journal of Geophysical Research*, v. 95, no. B6, pp 8339-8355.
- Strobell, M.E., and Masursky, Harold, 1990, Nomenclature, in Greeley, Ronald, and Batson, R.M., eds., *Planetary mapping*: New York, Cambridge University Press, pp 96-140.

THE CONTROL NETWORK OF MERCURY: APRIL 1991

Merton E. Davies and Patricia G. Rogers
 RAND, Santa Monica CA 90406-2138

Features identified on Mariner 10 high-resolution images of Mercury, acquired during three flybys between 1974 and 1975, form the basis of Mercury's planetwide control network. Although images from all three flybys are used in the net, the large amount of contiguous coverage from the second flyby, a southern bright-side pass, make these images the strongest contributors to the control net.

Mercury is in synchronous rotation with a period of 58.6462 days and its spin axis is approximately normal to the equatorial plane. The 20° meridian is defined by the crater Hun Kal, located just south of the equator (Murray, et al., 1974; Davies and Batson, 1975).

The control network computations involve the photogrammetric determination of control point coordinates and an analytical triangulation solution. The current control network computations for Mercury are performed in the J2000 coordinate system according to the International Astronomical Union (IAU) convention. In recent years, updates to the control network have included improved trajectory solutions (Anderson, et al., 1987) and modification of the standard radii (2439 km) at several points based on Earth-based radar altimetry data (Harmon, et al., 1986).

The following represents the current status of the control network calculations:

Points	2406
Pictures	811
Observation Equations	26,240
Normal Equations	7,245
Overdetermination	3.62
Standard Error (μm)	21.46

Improvements have been made to existing control points and new control points have been added to the net to strengthen the overall network and improve the standard error of measurement.

References

- Anderson, J. D., G. Colombo, P. B. Esposito, E. L. Lau, and G. B. Trager, "The Mass, Gravity Field, and Ephemeris of Mercury," *Icarus*, **71**, 337-349, 1987.
- Harmon, J. K., D. B. Campbell, D. L. Bindschadler, J. W. Head, and I. I. Shapiro, "Radar Altimetry of Mercury: A Preliminary Analysis," *J. Geophys. Res.*, **91**, 385-401, 1986.
- Davies, M. E. and R. M. Batson, "Surface Coordinates and Cartography of Mercury," *J. Geophys. Res.*, **80**, 2417-2430, 1975.

Murray, J. B., M. J. S. Belton, G. E. Danielson, M. E. Davies, D.E. Gault, B. Hapke, B. O'Leary, R. G. Strom, V. Suomi, and N. Trask, "Mercury's Surface: Preliminary Description and Interpretation from Mariner 10 Pictures," *Science*, **185**, 169-179, 1974.

N92-10917.1

A UNIFIED LUNAR CONTROL NETWORK: APRIL 1991
Merton E. Davies, RAND, Santa Monica, CA 90406

This program has been designed to combine and transform various control networks of the Moon into a common center-of-mass coordinate system. The first phase, dealing with the near side, has been completed and published (Davies et al., 1987). This report contains coordinates of 1166 points on the near side of the Moon.

The location of the center-of-mass and the coordinate system on the Moon are defined by the locations of the laser ranging retroreflectors (Ferrari, et al., 1980). Coordinates of the retroreflectors are given in both principal axes and mean Earth/Polar axis systems. The IAU has recommended that mean Earth/Polar axis coordinates be used on the Moon (Davies et al., 1989). The difference in these coordinates systems is significant, more than 600 m in latitude and longitude. The coordinates of the Apollo 11, 14, and 15 retroreflectors and the Lunakhod 2 retroreflector are accurate to a few meters (Williams et al., 1987).

Very long base interferometry (VLBI) measurements of the Apollo 12, 14, 15, 16, and 17 ALSEP transmitters and laser observations of the Apollo 11, 14, and 15 were combined in a solution for the coordinates of the transmitters (King et al., 1976). The Apollo 15, 16, and 17 ALSEP stations have been identified on Apollo panoramic photography and their locations transferred to Apollo mapping frames. Transformation parameters involving translation, rotation and scale were derived to best fit the Apollo control network coordinates to the three ALSEP station coordinates (Davies et al., 1987). The coordinates of points in Apollo control network have been transformed into the coordinate system defined by the laser retroreflectors for the unified system.

Coordinates of points in the telescopic network of Meyer, 1980 have been transformed into the unified system using 130 points common to Meyer's network and the Apollo network (Davies et al., 1987). The Mariner 10 control network covering the north polar region has been added to the lunar network.

The most reliable control network for the far side is the Lunar Positional Reference System (1974), 1975. The estimated accuracy of the coordinates of the points varies between 1 km to 16 km. 159 points from this system that fell in the far side Apollo region have been remeasured on Apollo pictures and new coordinates computed that are consistent with the unified system. The amount of the differences in the coordinates have been computed. 60 points had a shift over 10 km; we suspect that identification errors account for many of these. 43 points had a shift between 6 km and 10 km, and 48 fall between 3 km and 6 km. Only 8 points had a shift of less than 3 km.

Because the coordinate system is directly tied to the laser ranging retroreflectors, their locations are very important. In most cases they are too small to be observed in photography. (See Figure 1.) For this reason, the coordinates of nearby craters to the Apollo 11 and 14 retroreflectors have been determined. Because these craters were related to the astronauts' surface exploration, they have been given names. Their coordinates are:

	<u>Crater Name</u>	<u>Latitude (°)</u>	<u>Longitude (°)</u>
Apollo 11	Double Crater	0.67373	23.47239
	Little West Crater	0.67435	23.47534
Apollo 14	South Doublet Crater	-3.64294	-17.48117
	North Doublet Crater	-3.64122	-17.48319
	North Triplet Crater	-3.64757	-17.46675
	Center Triplet Crater	-3.65022	-17.46669
	South Triplet Crater	-3.65478	-17.46678
	Weird Crater	-3.64334	-17.45945

References

Catalog of Lunar Positions Based on the Lunar Positional Reference System (1974), Defense Mapping Agency Aerospace Center, St. Louis AFS, MO 63118, April 1975.

Davies, M.E., Colvin, T.R., and Meyer, D.L. (1987) A Unified Lunar Control Network: The Near Side. *J. Geophys. Res.*, Vol. 92, No. B13, p. 14177-14184.

Davies, M. E., et al. (1989) Report of the IAU/IAG/COSPAR Working Group on Cartographic Coordinates and Rotational Elements of the Planets and Satellites: 1988. *Celestial Mechanics and Dynamical Astronomy*, Vol. 46: p. 187-204.

Ferrari, A.J., Sinclair, W.S., Sjogren, W.L., Williams, J.G., and Yoder, C.F. (1980) Geophysical Parameters of the Earth-Moon System. *J. Geophys. Res.*, Vol. 85, No. B7, p. 3939-3951.

King, R.W., Counselman, C.C., III, Shapiro, I.I. (1976) Lunar Dynamics and Selenodesy: Results from Analysis of VLBI and Laser Data. *J. Geophys. Res.*, Vol. 81, No. 35, p. 6251-6256.

Meyer, Donald L., Selenocentric Control System (1979). Defense Mapping Agency, DMA TR 80-001, April 1980.

Williams, J. G., Newhall, X.X., and Dickey, J.O. (1987) Lunar Science from Lunar Laser Ranging. In *Abstract, Eighteenth Lunar and Planetary Science Conference*.

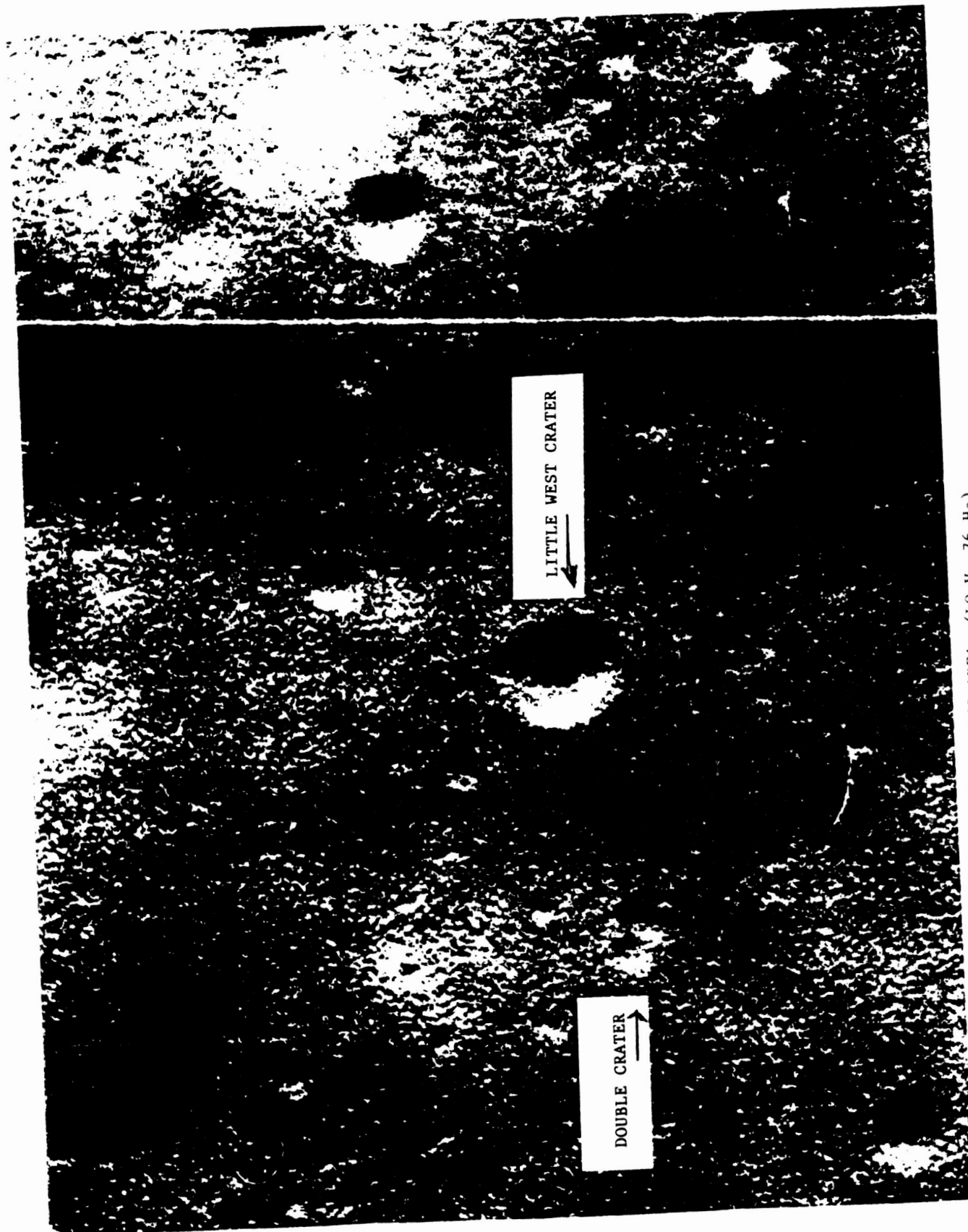


FIG. 1 THE APOLLO 11 LANDING AREA (LO V 76 H3)

THE CONTROL NETWORK OF MARS: APRIL 1991

Merton E. Davies and Patricia G. Rogers
 RAND, Santa Monica CA 90406-2138

The modern geodetic control network of Mars was first established based on Mariner 9 images with 1-2 km/pixel resolutions and covered almost the entire martian surface. The introduction of higher resolution (10-200 meter/pixel) Viking Orbiter images greatly improved the accuracy and density of points in the control network (Davies and Katayama, 1982).

Analysis of the Viking lander radio tracking data led to more accurate measurements of Mars' rotational period, spin axis direction, and the lander coordinates relative to the inertial reference frame (Mayo et al., 1977; Michael, 1979). The prime meridian on Mars has been defined by the Geodesy/Cartography Group of the Mariner 9 Television Team as the crater Airy-0, located about 5° south of the equator (de Vaucouleurs et al., 1873). The Viking 1 lander site was identified on a high resolution Viking frame (Morris and Jones, 1980).

The control point measurements form the basis of a least squares solution determined by analytical triangulation after the pixel measurements are corrected for geometric distortions and converted to millimeter coordinates in the camera focal plane.

Photogrammetric strips encircling Mars at the equator and at 60° north and south have been used to strengthen the overall net and improve the accuracy of the coordinates of points. In addition, photogrammetric strips along 0°, 90°, 180°, and 270° longitude from the equator to 60° north and south latitudes and a strip from 60° latitude, 90° longitude to the Viking 1 lander site have all significantly strengthened the control network. Most recently, photogrammetric strips have been added to the net along 30° north latitude between 0° and 180°, and along 30° between 180° and 360°.

The Viking 1 lander site and Airy-0 are linked through photogrammetric strips occurring along the 0° meridian from Airy-0 to 65° north, from that point through the Viking 1 lander site to the equator, and along the equator to 180° longitude. The Viking 1 lander site is thus a well calibrated area with coordinates of points accurate to approximately 200 meters relative to the J2000 inertial coordinate system. This will be a useful calibration region for upcoming missions.

The following represents the current status of the control network calculations:

Points	9380
Mariner 9 Images	1054
Viking Images	1468
Observation Equations	62,650
Normal Equations	26,326
Overdetermination	2.38
Standard Error (μm)	14.12

References

- Davies, M. E. and F. Y. Katayama, "The 1982 Control Network of Mars," *J. Geophys. Res.*, **88**, 7503-7504, 1983.
- de Vaucouleurs, G., M. E. Davies, and F. M. Sturms, Jr., "Mariner 9 Areographic Coordinate Systems," *J. Geophys. Res.*, **78**, 4395-4404, 1973.
- Mayo, A. P., W. T. Blackshear, R. H. Tolson, W. H. Michael, Jr., G. M. Kelly, J. P. Brenkle, and T. A. Komarek, "Lander locations, Mars Physical Ephemeris, and Solar System Parameters: Determination from Viking Lander Tracking Data," *J. Geophys. Res.*, **82**, 4297-4303, 1977.
- Michael, W. H., Jr., "Viking Lander Tracking Contributions to Mars Mapping," *The Moon and Planets*, **20**, 149-152, 1979.
- Morris, E. C. and K. L. Jones, "Viking I Lander on the Surface of Mars: Revised Location," *Icarus*, **44**, 217-222, 1980.

PUBLICATION OF TOPOGRAPHIC ATLAS AND CONTROL NETWORK OF MARS,
 Sherman S. C. Wu, Jennifer S. Billideau, and Beth A. Spare, U.S.
 Geological Survey, Flagstaff, Arizona 86001

To aid planetary studies and the planning of future Mars missions, we will submit by the end of fiscal year 1992 the Topographic Atlas and Control Network of Mars for publication as a NASA Special Publication. It will consist of reduced versions of 108 1:2 million-scale photomosaics that show contour lines from topographic maps at the same scale, as well as precisely located control points (Wu et al., 1990). The control points are from the planetwide network (Wu and Schafer, 1984), which is not only instrumental in the compilation of maps at various scales, but is also widely used in other research such as studies of Mars' gravity and atmosphere.

Figure 1, a combination of MC 8-NW and -SW, is an example of the photomosaics to be included in the atlas. Contour lines in the figure are at 1-km intervals. The final adjusted ground coordinates and elevations of the 77 control points shown are given in Table 1. The last column in the table lists the topographic datum (zero elevation) that can be used to compute the solid radius of the control point from the center of mass of Mars.

The atlas will also include information such as the adjusted C-matrices of each image, descriptions of the methods used and their accuracy, and guidelines for users.

References

- Wu, S. S. C., and Schafer, F. J., 1984, Mars control network, in Technical Papers of the 50th Annual Meeting of the American Society of Photogrammetry and Remote Sensing, Washington, D.C., March 11-16, v. 2, p. 456-463.
- Wu, S. S. C., Billideau, J. S., Howington-Kraus, A. E., and Spare, B. A., 1990, Publication of Mars control network: Report of Planetary Geology and Geophysics Program--1989, NASA Tech. Memo. 4210, p. 576-578.

Table 1: Control point information (picture numbers, ground coordinates, and topographic datum) for MC8W.

Figure 1: Distribution of control points on topographic map of MC8W.



Figure 1. Distribution of Control Points on the Contour Map of MC 8W
(MC 8-NW and -SW combined)

ORIGINAL PAGE IS
OF POOR QUALITY

Table 1. Control point information of MC 8-W (picture number, ground coordinates, and topographic datum).

ID	PICTURE NUMBERS						LON	LAT	ELEV (M)	DATUM (M)
3125	789A47	722A69	722A70				68 26 18.700	20 06 15.948	-1925.039	3391192.142
3126	722A69	646A65					170 04 25.731	16 10 16.956	-1977.958	3391881.884
3129	646A44	687A28					174 03 51.922	2 06 19.996	-74.815	3393191.589
10004	750A86	646A65					175 41 45.917	9 30 34.642	-1917.798	3392709.926
10010	687A45	646A65	750A84				179 25 53.641	10 04 28.046	-1015.414	3392636.380
10801	690A06	646A46	646A23				158 01 14.751	2 50 59.348	-955.360	3393515.645
10803	738A03	789A47	614A36	690A32	722A70	614A34	159 48 29.205	26 44 07.429	-3066.405	3389890.577
10806	690A35	646A24	789A47	614A36	690A32	722A70	159 43 18.461	20 44 19.975	-2912.572	3391266.406
10810	646A66	722A68	722A70	690A32	789A47		168 46 39.547	27 19 35.132	-1967.463	3389560.491
10813	690A35	738A03	614A36	690A32	789A47	722A70	160 29 35.155	21 37 34.166	-2215.069	3391058.160
10814	690A35	646A24	789A47	690A32	722A69	722A70	166 22 17.561	20 07 23.564	-1764.774	3391226.798
10815	690A35	646A24	722A69				164 03 20.179	15 55 26.720	-1925.866	3392042.670
10858	690A35	646A24					157 53 07.299	16 15 17.134	-1778.380	3392166.097
10859	614A36	690A32	646A24	722A70	789A47	738A03	161 27 09.736	24 01 04.333	-1548.579	3390501.245
10860	646A66	722A70	690A32	738A03	614A36	614A34	165 45 14.692	26 24 24.662	-2800.334	3389837.632
10861	690A35	722A70	690A32	722A69	646A24	789A47	164 14 56.454	19 25 13.819	-1412.662	3391411.311
10862	690A35	789A47	722A70	722A69	646A24	690A32	164 32 42.180	20 39 27.574	-2232.546	3391157.997
10864	646A66	722A70	789A47	722A69			169 23 47.970	22 05 22.016	-1612.144	3390767.173
10865	646A66	722A70	690A32	789A47	722A69		166 35 46.066	21 59 32.889	-903.116	3390835.977
10866	789A47	722A70	690A32	722A69	646A24		164 41 24.071	21 43 02.529	-1376.043	3390933.977
10867	738A03	646A24	690A32	722A70	722A69	789A47	162 52 43.003	23 28 40.973	-1346.599	3390589.354
10868	646A66	722A70	690A32	789A47	614A36	614A34	165 03 52.302	24 10 54.655	-1806.903	3390380.024
10870	690A35	646A24	722A69				162 46 34.138	12 47 55.961	-1908.758	3392542.208
10871	690A35	722A70	690A32	614A36	646A24	789A47	163 23 55.487	21 51 38.768	-1773.329	3390933.023
10872	646A66	722A70	789A47	646A24	722A69		169 41 06.463	19 48 03.624	-1708.513	3391231.917
10875	738A02	646A66	722A68	722A70	789A47		171 10 04.029	29 11 12.801	-1452.737	3389058.354
10877	687A28	750A85	646A44	646A23	646A46		165 06 39.454	45 58.133	-966.956	3393355.487
10881	646A66	722A70	722A68	789A47	722A68		173 05 51.451	27 23 00.774	-1264.036	3389497.346
10882	646A66	722A70	789A47	722A68			172 31 37.842	24 22 31.723	-1227.878	3390221.325
10885	722A68	646A66	789A45				179 08 44.524	29 24 25.205	-255.914	3388960.651
10886	722A68	646A66					178 53 11.124	26 02 51.618	-2575.684	3389796.454
10887	646A66	722A68					179 37 12.273	23 15 18.484	-1807.319	3390437.986
10888	646A65	722A67					179 50 18.721	17 34 24.587	-1923.690	3391568.201
10889	646A66	722A67	646A65	722A69			176 00 01.771	17 09 44.586	-2625.244	3391651.815
10890	690A35	738A03	614A36	690A32	722A70	646A24	162 06 34.566	21 22 14.431	-966.821	3391069.043
10892	690A35	646A24					157 47 06.371	14 24 18.148	-1698.919	3392464.750
10894	690A35	722A69	614A34				160 23 19.956	17 50 53.106	-1908.965	3391808.999
10895	690A35	646A24	722A69	646A23			159 54 17.769	13 51 00.719	-1336.716	3392478.502
10896	646A66	722A67	646A65	722A69			172 00 49.561	19 39 58.183	-1859.658	3391226.932
10897	722A67	646A65	646A66	722A69			172 47 41.343	20 48 46.680	-1450.515	3390221.278
11650	646A44	687A28	750A86				169 09 03.714	38 12.843	-613.311	3393277.508
20753	646A44	687A28	687A14	687A16	750A86		178 16 18.575	3 18 31.249	-539.569	3393130.163
20754	646A44	687A28	687A14	750A86	687A16		178 02 38.219	1 54 26.667	-378.379	3393173.165
20755	646A44	687A28	750A86				172 15 33.672	2 39 02.225	-221.482	3393195.313
20756	750A84	646A65	722A67				177 52 54.222	13 34 20.014	-1160.908	3392206.520
20757	646A65	750A84	722A67				175 44 58.090	13 18 16.414	-947.533	3392254.447
20760	646A66	646A65	722A68				178 25 15.051	20 38 15.833	-582.425	3390991.289
20761	646A66	722A67	646A65	722A68	722A69		176 54 08.745	20 44 10.095	-693.179	3390976.183
20762	722A67	646A65	646A66	722A69			174 39 52.601	19 58 01.649	-562.400	3391142.589
20768	722A67	646A65	722A69				169 56 29.411	13 53 49.008	-1268.726	3392235.647
20769	722A69	646A65					169 20 00.718	12 48 05.959	-853.501	3392397.768
20770	722A69	646A65					168 17 48.043	12 47 28.372	-818.590	3392417.454
20771	690A06	646A46	750A85	646A23			163 15 44.604	5 25 06.616	-447.370	3393244.894
20772	690A35	646A46	646A23	750A85	722A69		162 55 44.429	6 37 52.949	-436.539	3393175.090
20785	646A65	750A86					174 44 31.971	7 37 04.784	-851.756	3392890.724
20786	646A44	687A28	646A65	750A86	722A69		173 05 40.846	6 23 53.718	-203.277	3392998.940
20787	646A44	687A28	687A14	687A16	750A86	646A65	176 59 11.385	6 26 13.695	-463.267	3392966.151
20788	750A84	722A67	646A65	750A86			175 17 29.483	11 00 00.708	-1033.054	3392550.744
20789	646A65	750A86	722A69	722A67			172 14 52.850	9 50 24.617	-524.722	3392708.633
20790	646A65	722A67	722A69				173 04 49.529	16 10 56.271	-804.734	3391841.306
20791	646A44	646A23	646A65	722A69			169 11 02.587	9 25 52.190	-1680.163	3392795.658
20792	646A44	687A28	646A65	750A85	750A86	722A69	171 41 13.817	7 31 10.608	-314.154	3392931.311
20793	722A67	646A65	722A69				170 27 18.361	16 00 28.240	-763.811	3391903.027
20795	690A35	646A23	722A69				164 52 01.877	10 49 34.056	-1191.302	3392734.606
20796	646A44	687A28	646A23	722A69	750A85		168 18 41.569	6 48 08.537	-865.840	3393040.095
20798	722A67	646A65	722A69				170 10 11.645	11 52 26.909	-926.427	3392504.153
21471	722A68	646A66					176 39 57.270	27 08 12.761	-1259.761	3389537.125
21472	722A68	646A66					174 15 53.517	26 46 37.005	-1309.975	3389637.802
21473	646A66	722A68	789A65				178 29 02.088	27 53 13.084	-1432.233	3389347.073
23571	690A06	646A46	750A85	646A23			157 54 31.416	5 13 44.854	-1263.186	3393417.507
23758	646A23	750A85	722A69				165 42 41.243	8 37 13.963	-615.194	3392943.135
23759	687A28	646A46	646A23	750A85			166 24 18.801	5 12 43.265	-693.175	3393181.619
23760	646A23	646A46	750A85	722A69			164 28 46.970	5 59 32.538	-413.032	3393178.601
23761	687A28	646A23	646A46	750A85	722A69		166 58 19.816	7 01 00.170	-924.004	3393050.369
23762	646A65	722A69	646A23				167 34 25.735	8 31 28.122	-502.068	3392912.364
23763	687A28	750A85	646A44	646A23			167 53 05.632	4 45 29.352	-988.445	3393176.288
23764	687A28	646A46	646A23	646A44	750A85		165 47 42.675	3 24 11.348	-814.893	3393279.722

COLOR-CODED GLOBAL TOPOGRAPHIC MAPS OF MARS, Sherman S. C.
Wu, Annie E. Howington-Kraus, and Karyn Ablin, U.S.
Geological Survey, Flagstaff, Arizona 86001

A Digital Terrain Model (DTM) has been derived with both Mercator and Sinusoidal Equal-Area projections from the global topographic map of Mars at a scale of 1:15 million and a contour interval of 1 km [1]. Elevations on the map are referred to the Mars topographic datum that is defined by the gravity field at a 6.1-millibar pressure surface with respect to the center of mass of Mars [2]. The DTM has a resolution at the equator of $1/59.226^\circ$ (exactly 1 km) per pixel [3]. By using the DTM, we have generated color-coded global maps of Mars' topography in both the Mercator projection (Figure 1) and the Sinusoidal Equal Area projection (Figure 2). On both maps, colors indicate 1 km increments of height. From the equal-area dataset, the positive and negative elevation distributions are calculated to be 67% and 33%, respectively. The color-coded global topographic map in Mercator projection will be published as a USGS map.

References

- [1] U.S. Geological Survey, 1989, Misc. Inv. Ser. Map I-2030, 3 sheets.
- [2] Wu, S. S. C., 1981, Annales de Geophysique, Centre National de la Recherche Scientifique, Numero 1, Tome 37, p. 147-160.
- [3] Wu, S. S. C., and Howington-Kraus, A. E., 1987, LPS XVIII, p. 1108-1109.

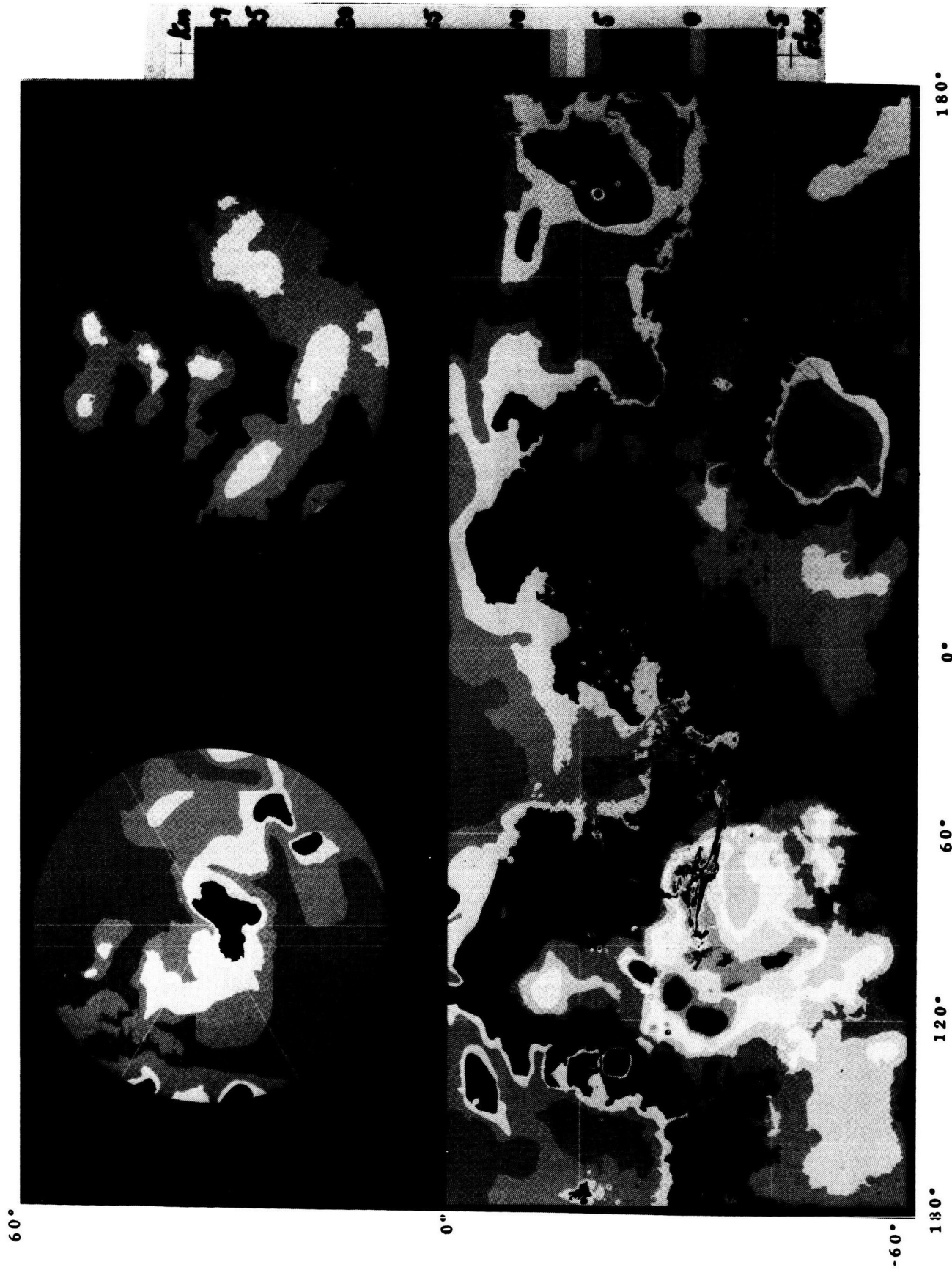


Figure 1: The global topographic map of Mars (Mercator projection)



Figure 2: The global topographic map of Mars (Sinusoidal Equal Area projection)

MARS ELEVATION DISTRIBUTION, Sherman S. C. Wu, Annie E. Howington-Kraus, and Karyn Ablin, U.S. Geological Survey, Flagstaff, AZ 86001

A Digital Terrain Model (DTM) of Mars has been derived with both Mercator and Sinusoidal Equal-Area Projections from the global topographic map of Mars (scale 1:15 million, contour interval 1 km [1]). Elevations on the map are referred to the Mars' topographic datum that is defined by the gravity field at a 6.1-millibar pressure surface with respect to the center of mass of Mars [2]. The DTM has a resolution at the equator of 1/59.226° (exactly 1 km) per pixel [3]. By using the DTM, the volumetric distribution of Mars topography above and below the datum has previously been calculated [4]. Three types of elevation distributions of Mars' topography have now been calculated from the same DTM: (1) the frequency distribution of elevations at the pixel resolution (Figure 1); (2) average elevations in increments of 6° in both longitude and latitude (Figure 2); and (3) average elevations in 36 separate blocks, each covering 30° of latitude and 60° of longitude (Table 1).

In Figure 1, the fractional areas having positive and negative elevation are shown to be 67% and 33%, respectively. Only 0.5% of elevations are above 9 km. In Table 1, the average elevations of each of the six longitudinal belts are listed on the bottom row, and the average elevations of each of the six latitudinal bands are listed in the last column. In elevation, the western hemisphere (0°-180°) averages about 0.993 km higher than the eastern (180°-360°). Also, the southern hemisphere averages about 3.191 km higher than the northern (due to a shifting of Mars' center of mass by approximately 3.4 km to the north of its center of figure). The mean elevation above the 6.1mb datum is 1,876 m.

Mars elevation distribution correlates with its volume distribution previously calculated [4].

References: [1] U.S. Geological Survey, 1989, Misc. Inv. Ser. Map I-2030, 3 sheets. [2] Wu, S. S. C., 1981, Annales de Geophysique, Centre National de la Recherche Scientifique, Numero 1, Tome 37, p. 147-160. [3] Wu, S. S. C., and Howington-Kraus, A. E., 1987, LPS XVIII, p. 1108-1109. [4] Wu, S. S. C., and Howington-Kraus, A. E., 1990, LPS XXI, p. 1355-1357.

Table 1. Elevation Distributions of Mars' Topography (in meters).

Longitude(\u03bd) Latitude	180°-120°	120°-60°	60°-0°	360°-300°	300°-240°	240°-180°	Average
N90°-60°	-1,940	-1,463	-2,313	-1,461	-1,258	-2,581	-1,836
N60°-30°	-1,030	2,343	-1,370	612	-899	-1,038	-230
N30°-0°	768	4,257	-445	1,569	399	-330	1,037
S0°-30°	3,803	6,980	1,519	3,336	3,045	2,232	3,264
S30°-60°	5,016	5,441	3,218	3,023	461	4,247	3,568
S60°-90°	4,232	3,832	3,698	3,252	3,591	4,470	3,846
Average	2,026	4,392	699	2,011	937	1,190	1,876

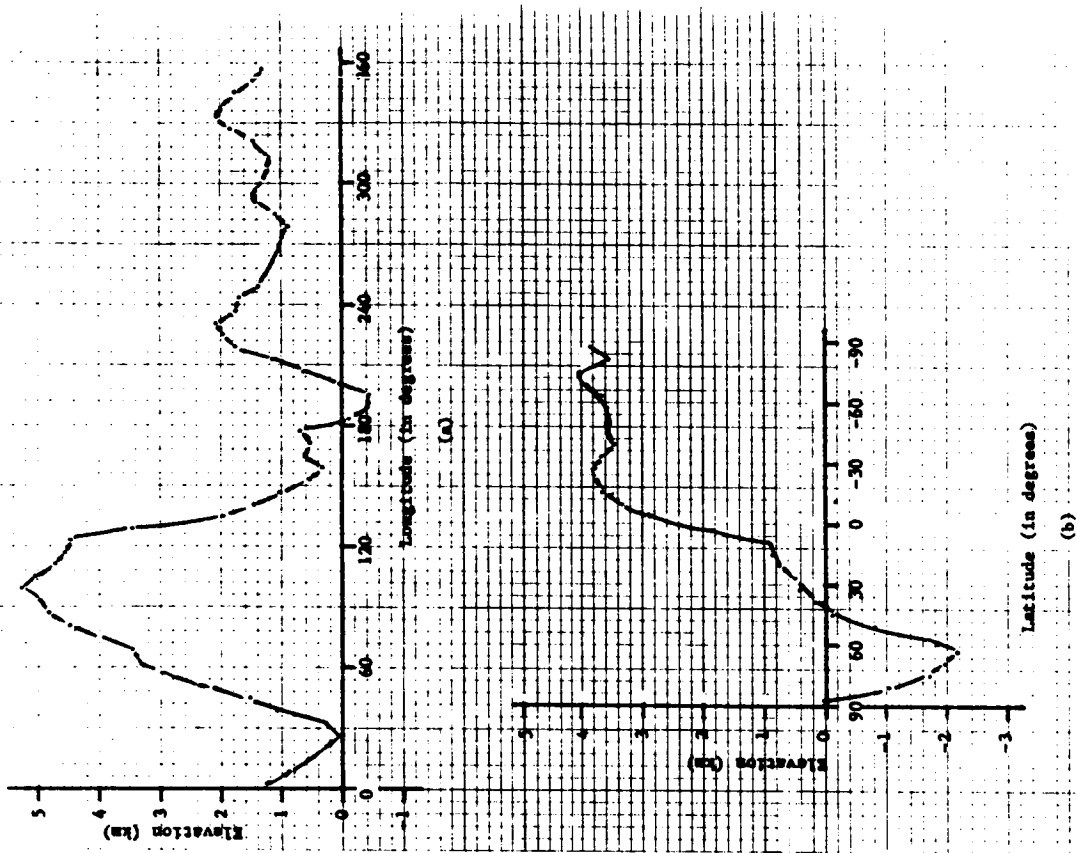


Figure 2. Elevation distribution of Mars' topography
 (a) based on longitude, (b) based on latitude

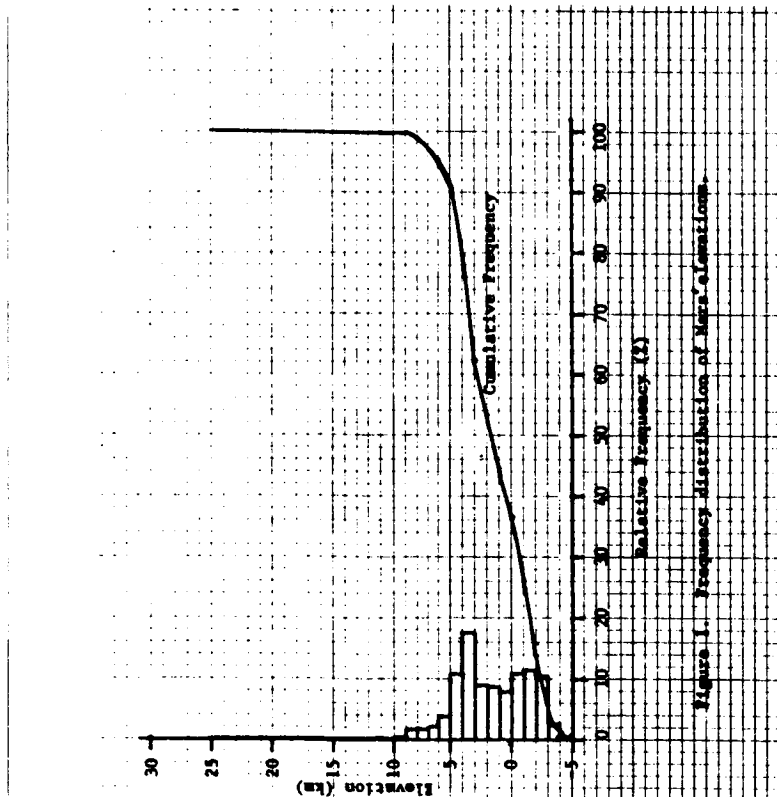


Figure 1. Frequency distribution of Mars' elevations

5194-21

27119

N92-10922

COMPLETION OF COMPILATION OF THE 1:2,000,000-SCALE
TOPOGRAPHIC MAP SERIES OF MARS, Sherman S. C. Wu, Raymond
Jordan, Patricia A. Garcia, and Karyn K. Ablin, U.S.
Geological Survey, Flagstaff, AZ 86001

P-1

Using special photogrammetric techniques (Wu et al., 1982), we have been systematically mapping Mars' topography at a scale of 1:2,000,000 from high-altitude Viking Orbiter images. Of the 140 maps in the series, 120 have previously been compiled on the AS-11AM analytical stereoplotters. In FY91, the remaining 20 maps will be compiled (most of these are between $\pm 30^\circ$ latitude and the poles). Elevations on the maps are related to the Mars topographic datum (Wu, 1981). The Mars planetwide control net (Wu and Schafer, 1984) is used for the control of compilation. The maps have a contour interval of 1 km and a vertical precision of ± 1 km, and thus they are more detailed than previous maps.

References

- Wu, S. S. C., 1981, A method of defining topographic datums of planetary bodies: *Annales de Geophysique*, AGEPA 7, Tome 37, fasc. 1, p. 141-160.
- Wu, S. S. C., and Schafer, F. J., 1984, Mars control network, in *Technical Papers of the 50th annual meeting of the American Society of Photogrammetry and Remote Sensing*, Washington, D.C., March 11-16, 1984, v. 2, p. 456-463.
- Wu, S. S. C., Elassal, A. A., Jordan, Raymond, and Schafer, F. J., 1982, Photogrammetric application of Viking orbital photography: *Planetary and Space Science*, v. 30, no. 1, p. 45-55.

5195-71 23

N92-109230 27/28

MARS HIGH-RESOLUTION MAPPING

R.M. Batson, P.K. Thomas, U.S. Geological Survey, Flagstaff, Arizona 86001

A series of photomosaics of high-resolution Viking Orbiter images of Mars is being prepared and published to support the Mars 1:500,000-scale geologic mapping program. More than 100 of these photomosaics were made manually, but for the last several years they have all been made digitally. The digital mosaics are published on the MTM (Mars Transverse Mercator) system, and they are also available to the appropriate principal investigators as digital files in the MDIM (mosaicked digital image model) format. We hope that they can eventually be published on CD-ROM disks. The mosaics contain Viking Orbiter images with the highest available resolution; in some areas as high as 10 m/pixel. This resolution where it exists, will support a 1:100,000 map scale. The full resolution of a mosaic is preserved in a digital file, but conventional lithographic publication of such large-scale inset maps will be done only if required by the geologic map author. When high-resolution images do not fill the neatlines of an MTM quadrangle, the medium-resolution (1/256°/pixel, or 231 m/pixel) MDIM is used.

The mosaics are tied by image-matching to the planetwide MDIM, in which random errors as large as 5 km (10 mm at 1:500,000 scale) are common; a few much larger, "worst-case" errors also occur. Because of the distribution of the errors, many large discrepancies appear along the cutlines between frames with very different resolutions. Furthermore, each block of quadrangles is compiled on its own local control system, and adjacent blocks, compiled later, are unlikely to match.

Selection of areas to be mapped is based on geologic mapping proposals reviewed and recommended by the Mars 1:500,000-scale geologic mapping review panel. There is no intention to map the entire planet at this scale.

519696
2712 N92-10924

A NEW EDITION OF THE MARS 1:5,000,000 MAP SERIES
R.M. Batson, A.S. McEwen, and S.S.C. Wu, U.S. Geological Survey,
Flagstaff, Arizona 86001

A new edition of the Mars 1:5,000,000-scale map series is in preparation. Two sheets will be made for each quadrangle. Sheet 1 will show shaded relief, contours, and nomenclature. Sheet 2 will be a full-color photomosaic prepared on the Mars digital image model (MDIM) base co-registered with the Mars low-resolution color database. The latter will have an abbreviated graticule (latitude/longitude ticks only) and no other line overprint.

The four major databases used to assemble this series are now virtually complete. These are (1) Viking-revised shaded relief maps at 1:5,000,000 scale, (2) contour maps at 1:2,000,000 scale (Wu et al., 1990), (3) the Mars digital image model (Batson and Edwards, 1990), and (4) a color image mosaic of Mars. Together, these databases form the most complete planetwide cartographic definition of Mars that can be compiled with existing data. The new edition will supersede the published Mars 1:5,000,000-scale maps, including the original shaded relief and topographic maps made primarily with Mariner 9 data and the Viking-revised shaded relief and controlled photomosaic series. Publication of the new series will begin in late 1991 or early 1992, and it should be complete within two years.

REFERENCES

- Batson, R.M., and Edwards, Kathleen, 1990, The Mars digital cartographic database (abs.), in Reports of the Planetary Geology and Geophysics Program--1989: National Aeronautics and Space Administration Technical Memorandum 4210, p. 567- 570.
- Wu, S.S.C., Ablin, K.F., Garcia, P.A., and Jordan, Raymond, 1990, Status of the 1:2,000,000-scale topographic map series of Mars (abs.), in Reports of the Planetary Geology and Geophysics Program--1989: National Aeronautics and Space Administration Technical Memorandum 4210, p. 72.

5/19791 25

27/22
N92-10925 p/1

PLANETARY ATLASES

R.M. Batson, J.L. Inge, and H.F. Morgan, U.S. Geological Survey, Flagstaff, Arizona 86001

Two kinds of planetary map atlases are in production. Atlases of the first kind, produced as NASA Special Publications, contain reduced-scale versions of maps in hard-bound books with dimensions of 11 X 14 inches. These new atlases are intended (1) to provide concise but comprehensive references to the geography of the planets needed by planetary scientists and others and (2) to allow inexpensive access to the planetary map dataset without requiring acquisition and examination of tens or hundreds of full-size map sheets. Two such atlases have been published (Batson et al., 1979, 1984) and a third is in press (Batson and Inge, eds.). We have begun work on an Atlas of the Satellites of the Outer Planets.

The second kind of atlas is a popular or semi-technical version designed for commercial publication and distribution. The first edition, titled "The Atlas of the Solar System," by Greeley and Batson, is nearly ready for publication. New funding and contracting constraints now make it unlikely that the atlas can be published in the format originally planned. We are currently exploring the possibility of publishing the maps (which have already been prepared) through the USGS, as a series of folios in the I-map series. The maps are global views of each solid-surface body of the Solar System. Each map shows airbrushed relief, albedo, and, where available, topography. A set of simplified geologic maps is also included. All of the maps are on equal-area projections. Scales are 1:40,000,000 for the Earth and Venus; 1:2,000,000 for the Saturnian satellites Mimas and Enceladus and the Uranian satellite Miranda; 1:100,000 for the Martian satellites, Phobos and Deimos; and 1:10,000,000 for all other bodies.

REFERENCES

Batson, R. M., Bridges, P. M., Inge, J. L., 1979, Atlas of Mars: The 1:5,000,000 Map Series: National Aeronautics and Space Administration Spec. Pub. 438, 146 p.

Batson, R.M., Lee, E.M., Mullins, K.F., Skiff, B.A., Bridges, P.M., Inge, J.L., Masursky, Harold, and Strobell, M.E., 1984, Voyager 1 and 2 atlas of six Saturnian satellites: National Aeronautics and Space Administration Spec. Pub. 474, 175 p.

Batson, R.M. and Inge, J.L., eds., (in press), Atlas of Mars: The Viking global survey: National Aeronautics and Space Administration Special Publication.

5198-91

57129 N92-10926.1

P-2

CD-ROM PUBLICATION OF THE MARS DIGITAL CARTOGRAPHIC DATA BASE
Batson, R.M., Eliason, E.M., Soderblom, L.A., Edwards, Kathleen,
and Wu, S.S.C., U.S. Geological Survey, Flagstaff, Arizona 86001

The recently completed Mars mosaicked digital image model (MDIM; Batson and Edwards, 1990) and the soon-to-be-completed Mars digital terrain model (DTM; Wu, et al., 1990) are being transcribed to optical disks to simplify distribution to planetary investigators. These models, completed in FY91, provide a cartographic base to which all existing Mars data can be registered.

The digital image map of Mars is a cartographic extension of a set of CD-ROM volumes containing individual Viking Orbiter images (USA NASA PDS VO 1001 through VO 1008) now being released. The data in these volumes are pristine in the sense that they were processed only to the extent required to view them as images. They contain the artifacts and the radiometric, geometric, and photometric characteristics of the raw data transmitted by the spacecraft. This new set of volumes, on the other hand, contains cartographic compilations made by processing the raw images to reduce radiometric and geometric distortions and to form geodetically controlled MDIMs. It also contains digitized versions of an airbrushed map of Mars as well as a listing of all feature names approved by the International Astronomical Union. In addition, special geodetic and photogrammetric processing has been performed to derive rasters of topographic data, or DTMs. The latter have a format similar to that of the MDIM, except that elevation values are used in the array instead of image brightness values.

The set consists of seven volumes:

- Volume 1. Vastitas Borealis Region of Mars (VO2001): MDIMs in 400 image files covering the north polar region of Mars as far south as lat 42.5° N.
- Volume 2. Xanthe Terra of Mars (VO2002): MDIMs in 512 image files covering lat 47.5° N. to lat 47.5° S., long 0° to 90° W.
- Volume 3. Amazonis Planitia Region of Mars (VO2003): MDIMs in 512 image files covering lat 47.5° N. to lat 47.5° S., long 90° W. to long 180° W.
- Volume 4. Elysium Planitia Region of Mars (VO2004): MDIMs in 512 image files covering lat 47.5° N. to lat 47.5° S., long 180° W. to long 270° W.
- Volume 5. Arabia Terra of Mars (VO2005): MDIMs in 512 image files covering lat 47.5° N. to lat 47.5° S., long 270° W. to long 0° W.
- Volume 6. Planum Australe Region of Mars (VO2006): MDIMs in 400 image files covering the south polar region as far north as lat 42.5° S.

Volume 7. Digital Topographic Map of Mars (VO2007): MDIMs of the entire planet at $1/64^\circ$, $1/16^\circ$, and $1/4^\circ$ /pixel, DTMs of the entire planet at $1/64^\circ$, $1/16^\circ$, and $1/4^\circ$ /pixel, and the digitized airbrush map of Mars at $1/16^\circ$ and $1/14^\circ$ /pixel.

Each of the first six volumes contains MDIMs of the areas specified at resolutions of $1/256^\circ$ (231 m)/pixel and at $1/64^\circ$ (943 m)/pixel. Each volume also contains MDIM coverage and a digitized airbrush map of the entire planet at $1/16^\circ$ (3.69 km)/pixel and at $1/4^\circ$ (16.76 km)/pixel.

The tiling layout of the $1/64^\circ$ /pixel digital models is the same on all 7 disks. Note that the $1/64^\circ$ /pixel MDIM, segments of which appear in Volumes 1 through 6, is duplicated in its entirety in Volume 7. All of the resolution compressions were done by averaging, not by subsampling. A gazetteer of feature names, referenced by latitude/longitude coordinates, is included as a text file in each of the seven volumes.

REFERENCES

- Batson, R.M., and Edwards, Kathleen, 1990, The Mars digital cartographic database (abs.), in Reports of the Planetary Geology and Geophysics Program--1989: National Aeronautics and Space Administration Technical Memorandum 4210, p. 567- 570.
- Wu, S.S.C., Howington-Kraus, Annie, and Ablin, Karyn, 1990, Quantitative analysis of Mars' topography (abs.), in Reports of the Planetary Geology Program--1989, NASA Technical Memorandum 4210, p. 573.

5199-21 N92-10927.3

27124

DIGITAL CARTOGRAPHY OF IO; A. McEwen, B. Duck, K. Edwards,
USGS, Flagstaff AZ.

P-1
We have produced a high-resolution (~1 km/pixel) controlled mosaic of the hemisphere of Io centered on longitude 310°. Digital cartographic techniques employed were those described by Batson [1] and Edwards [2]. Approximately 80 Voyager 1 clear- and blue-filter frames were utilized. This mosaic has been merged with low-resolution (~3.4 km/pixel) color mosaics in four colors to produce high-resolution color images [3]. We will compare this dataset to the geologic map of this region [4].

Passage of the Voyager spacecraft through the Io Plasma torus during acquisition of the highest resolution images exposed the vidicon detectors to ionized radiation, resulting in dark-current buildup on the vidicon. Because the vidicon is scanned from top to bottom, more charge accumulated toward the bottom of the frames, and the additive error increases from top to bottom as a ramp function. This ramp function was removed by using the model described in [5].

Photometric normalizations were applied using the Minnaert function [5]. An attempt to use Hapke's photometric function [6, 7, 8] revealed that this function does not adequately describe Io's limb darkening at emission angles greater than 80°. In contrast, the Minnaert function accurately describes the limb darkening up to emission angles of about 89°.

The improved set of discrete camera angles derived from this effort will be used in conjunction with the space telemetry pointing history file (the IPPS file), corrected on 4 or 12 second intervals, to derive a revised time history for the pointing of the Infrared Interferometric Spectrometer (IRIS). For IRIS observations acquired between camera shutterings, we can correct the IPPS file by linear interpolation, provided that the spacecraft motions were continuous. Image areas corresponding to the fields-of-view of IRIS spectra acquired between camera shutterings will be extracted from the mosaic to place the IRIS observations and hotspot models into geologic context.

REFERENCES: [1] R. Batson, 1987, Photogr. Eng. Remote Sensing 53, 1211; [2] K. Edwards, 1987, Photogr. Eng. Remote Sensing 53, 1219; [3] A. McEwen and L. Soderblom, 1984, LPSC XV, 529; [4] G. Schaber, D. Scott, and R. Greeley, 1989, USGS Misc. Inv. Map I-1980; [5] A. McEwen, 1988, Icarus 73, 385; [6] B. Hapke, 1984, Icarus 59, 41; [7] D. Simonelli and J. Veverka, 1986, Icarus 68, 503; [8] A. McEwen, T. Johnson, D. Matson, L. Soderblom, 1988, Icarus 75, 450.

DIGITAL SOLAR SYSTEM GEOLOGY

Batson, R.M., Kozak, R.C., and Isbell, N.K., U.S. Geological Survey, Flagstaff, Arizona 86001

All available synoptic maps of the solid-surface bodies of the Solar System have been digitized for presentation in the planned Atlas of the Solar System by Greeley and Batson. Since the last report (Batson et al., 1990), preliminary Uranian satellite maps have been replaced with improved versions, Galilean satellite geology has been simplified and digitized, structure has been added to many maps, and the maps have been converted to a standard format, with corresponding standard colors for the mapped units. Following these changes, the maps were re-reviewed by their authors and are now undergoing final editing before preparation for publication.

In some cases (for Mercury, Venus, and Mars), more detailed maps were digitized and then simplified for the Atlas. Other detailed maps are planned to be digitized in the coming year for the Moon and the Galilean satellites. For most of the remaining bodies such as the Uranian satellites, the current digitized versions contain virtually all the detail that can be mapped given the available data; those versions will be unchanged for the Atlas.

These digital geologic maps are archived at the digital scale of $1/16^\circ$ /pixel, in sinusoidal format. The availability of geology of the Solar System in a digital database will facilitate comparisons and integration with other data: digitized lunar geologic maps (Wilhelms, 1987) have already been used in a comparison with Galileo SSI observations of the Moon (McEwen et al., 1991).

REFERENCES

- Batson, R.M., Inge, J.L., and Morgan, H.F., 1990, Planetary atlases (abs.), in Reports of the Planetary Geology and Geophysics Program--1989: National Aeronautics and Space Administration Technical Memorandum 4210, p. 566.
- McEwen, A., Becker, T., Belton, M., and 27 others, 1991, Lunar multispectral mosaics from Galileo imaging, in Abstracts of papers submitted to the Twenty-Second Lunar and Planetary Science Conference, p. 871-872.
- Wilhelms, D.E., 1987, The geologic history of the Moon: U.S. Geological Survey Professional Paper 1348, 302 p.

N92-10929 :

A NEW CATALOG OF PLANETARY MAPS

R.M. Batson and J.L. Inge, U.S. Geological Survey, Flagstaff, Arizona 86001

A single, concise reference to all existing planetary maps, including lunar ones, is being prepared that will allow map users to identify and locate maps of their areas of interest. This will be the first such comprehensive listing of planetary maps. Although the USGS shows index maps on the collar of each map sheet, periodically publishes index maps of Mars, and provides informal listings of the USGS map database, no tabulation exists that identifies all planetary maps, including those published by DMA and other organizations. The catalog will consist of a booklet containing small-scale image maps with superposed quadrangle boundaries and map data tabulations. It should be ready for publication later this year, and it is planned to be updated and re-released in future years as needed.

IMAGE RETRIEVAL AND PROCESSING SYSTEM VERSION 2.0 DEVELOPMENT WORK

Susan Slavney and Edward A. Guinness, McDonnell Center for the Space Sciences, Department of Earth and Planetary Sciences, Washington University, St. Louis, Missouri 63130.

The Image Retrieval and Processing System (IRPS) is a software package developed at Washington University and used by the NASA Regional Planetary Image Facilities (RPIFs). IRPS combines data base management and image processing components to allow the user to examine catalogs of image data, locate the data of interest, and perform radiometric and geometric calibration of the data in preparation for analysis. Version 1.0 of IRPS was completed in August, 1989 and has been installed at several RPIFs. Other RPIFs use remote logins via NASA Science Internet to access IRPS at Washington University.

We have begun work on designing and populating a catalog of Magellan image products that will be part of IRPS Version 2.0, planned for release by the end of calendar year 1991. With this catalog, a user will be able to search by orbit and by location for Magellan Basic Image Data Records (BIDRs), Mosaicked Image Data Records (MIDRs), and Altimetry-Radiometry Composite Data Records (ARCDRs). The catalog will include the Magellan CD-ROM volume, directory and file name for each data product.

The image processing component of IRPS is based on the Planetary Image Cartography Software (PICS) developed by the USGS, Flagstaff, Arizona. To augment PICS capabilities, we have developed a set of image processing programs that are compatible with PICS-format images. This software includes general-purpose functions that PICS does not have, analysis and utility programs for specific data sets, and programs from other sources that have been modified to work with PICS images. Some of the software will be integrated into the Version 2.0 release of IRPS.

The table below lists the programs alphabetically with a brief functional description of each.

PICS-COMPATIBLE SOFTWARE DEVELOPED AT WASHINGTON UNIVERSITY

<u>Program</u>	<u>Description</u>
AZELINC	Compute the solar elevation and azimuth throughout a day
AVERSPEC	Average up to 5 Daedalus spectrometer files
BOXGEN	Generate a test image consisting of a set of boxes
BGRHUE	Transform color to hue, saturation, and brightness
CUT	Copy a section of an image to a new file
DESPIKE	Remove spikes in an image
DIF	Create a difference image
EXPAND	Increase the size of an image
FHIST	Histogram of 32-bit floating-point image
GEN	Generate a test pattern
HAPKE3	Solve the Hapke photometric function
HAPREF	Solve the Hapke photometric function
HISTOGRAM	Generate image histogram (byte image)

HUERGB	Transform hue, saturation and intensity to color
IHIST	Histogram of 16-bit signed integer image
IMUSE	List image disk space by user
INSERT	Insert an image into a mosaic
LABELTEST	Test image label processing routines
LASSCAN	Scan labels on an LAS tape
LASTAPE	Read images from tape in LAS format to disk in PICS format
LEAF	Combines a set of bands into one band-interleaved image
LINCMB	Perform a linear combination of images
LISTPIXEL	List pixel values in an image
LOADLUT	Load lookup table to Peritek display
LOGSTR	General logarithm stretch
LOWTRAN	Lowtran 7 - Atmospheric Transmittance and Radiance Model
LLXY	Compute line, sample from lat, lon for sinusoidal projection
MAPGRID	Create an image of a map projection grid
MF2	Function generator
MF2SPEC	A linear combination of up to 5 Daedalus spectrometer files
MGNCORR	Compute sigma zero and other things from Magellan data
MINMAX	Find minimum and maximum DN's in an image
MIXER	Create images of component proportions and sums of squares of residuals
MODCOL	Modify colors in an image by changing brightness
PACK	Pack records in a file
PASTE	Move a section of one image into another existing image
PHOTO	Photograph images using Matrix QCR film recorder
PICS2RASTER	Convert PICS image to unlabeled raster file
PICSCAN	Scan labels on a PICS tape
PRNCMP	Principal component analysis
PSCAN	Scan labels on a PICS tape
PWRSTR	General power-law stretch
QPOLREAD	Read quad-pol radar tape
QPOLSYN	Convert quad-pol data to PICS image
QPOLWRITE	Write quad-pol radar file to tape in original format
RASTER2PICS	Convert raster (unlabeled) image file to PICS image
RAV	Read VICAR-labeled AVIRIS tape
READMGN	Read Magellan MIDR framelets from CD-ROM
READSPEC	Read spectra files to produce a reflectance file
RGB	Color separates from single input
SAVELUT	Save lookup table from Peritek
SCANLAB	Scan labels of Viking Orbiter images on VSFEDR tapes
SHRINK	Decrease the size of an image
SOMTRAN	Transform a Landsat image from SOM to sinusoidal projection
STATS	Compute statistics within a window for a set of images
STR	Stretch the contrast of an image
TDEAD	Cratering model
TIMSCAL2	Calibrate TIMS data to ground radiance, ground temperature, or emittance
TLIB	Reusable tape library
TRELAX	Crater relaxation model
TSCAN	Scan any tape for number of files, records/file, and bytes/record
UNLEAF	Separate one band-interleaved image into individual bands

UNPACK	Unpack logical records in a file
VICAR2PICS	Convert VICAR image to PICS image
VICARTYPE	Type VICAR label embedded in an image
VL2PICS	Convert Viking Lander image to PICS image
VLNREAD	Read Viking Lander tape and update log file
VLREFL	Calibrate Viking Lander image
VOESCAN	Scan labels of Viking Orbiter images on VSFEDR tapes
XYLL	Compute lat, lon from line, sample for sinusoidal projection

CHAPTER 11

LATE ABSTRACTS

COMPOSITIONAL VARIABILITY OF THE MARTIAN SURFACE.

John B. Adams and Milton O. Smith, U. of Washington, Seattle, WA 98195

We analyzed spectral reflectance data from Viking Landers and Orbiters and from telescopic observations, with the objective of isolating compositional information about the Martian surface and assessing compositional variability. Two approaches were used to calibrate the data to reflectance to permit direct comparisons with laboratory reference spectra of well characterized materials (1-7). In Viking Lander multispectral images (six spectral bands) most of the spectral variation is caused by changes in lighting geometry within individual scenes, from scene to scene and over time. Lighting variations are both wavelength independent and wavelength dependent (1). By calibrating Lander image radiance values to reflectance using spectral mixture analysis (1) we assessed the possible range of compositions with reference to a collection of laboratory samples, also resampled to the Lander spectral bands. All spectra from the Lander images studied plot (in 6-space) within a planar triangle having at the apexes the respective spectra of tan basaltic palagonite, gray basalt and shade. Within this plane all Lander spectra fit as mixtures of these three endmembers; therefore, pure materials that occupy this space cannot be distinguished mixtures of these endmembers. Reference spectra that plot outside of the triangle are unable to account for the spectral variation observed in the images.

In earlier work (1) we concluded that the rocks at the Lander sites could be unweathered basalts or andesites, and that both oxidized and unweathered basaltic fines were present. Laboratory spectra of many basalts and andesites appear similar when sampled with the six Lander bands. The main difference between the two rock groups is that the basalts typically are darker than the andesites. Otherwise, both rock types are spectrally similar, having nearly equal reflectances at all wavelengths ("gray"). If andesitic rocks occur on Mars there also should be andesitic tephra, which, unaltered, has a substantially higher albedo than basaltic tephra. Accordingly, we searched Lander images for gray, moderate albedo rocks and for a light gray component of the fines. In addition, we postulated that aeolian abrasion might produce finely particulate crystalline basalt (unweathered) that would be expected to have a spectrum close to that of andesitic tephra.

Fig. 1 shows the endmember triangle on the plane defined by Lander bands 1 and 3, and illustrates that a small portion of the data encompasses andesites, andesitic tephra, and mixtures of basalt and crystalline basalt powder, giving the impression that these or spectrally similar materials are present in the Lander images and mix with the other spectral endmembers. However, when each spectrum is traced back to the image, the context reveals that this gray "component" always coincides with a specular lighting geometry. To compare image and laboratory spectra the lighting geometries of the measurements must be approximately the same. Bidirectional and total hemispherical laboratory measurements avoid specular reflections, because for most silicates they introduce a "gray" component that increases the overall lightness and reduces spectral contrast. Many Lander images, however, include local areas (especially on dust-free rocks) that have specular (or quasi-specular) reflection from surfaces that are oriented appropriately relative to the sun and the camera. These specular reflections, which occur at both pixel and sub-pixel scales, plot outside the basaltic spectral endmember plane, coincident with the spectra of andesitic materials and their mixtures with the basaltic materials. The specular reflections disappear when the same areas are imaged under different lighting conditions. Thus, there is no spectral evidence for an andesitic or other spectrally similar components at the Lander sites.

A Viking Orbiter image (3 bands) was analyzed of the Chryse Planitia - Kasei Valles - Lunae Planum region that includes the Lander 1 site. The calibrated spectra plot within the central part of the mixing triangle defined by the Lander data, indicating that these Orbiter pixels are consistent with mixtures of the Lander endmembers, and that the reference spectra (basaltic palagonite, basalt and shade) account for the spectral variation at a regional scale. The three broad Orbiter bands, although of limited use for identifying most materials, are sufficient to distinguish a light achromatic component. This component was not detected, therefore, we detected no areas of pure andesite or andesitic tephra, or mixtures of these materials with the modeled basaltic materials. The basaltic reference spectra also fit the spectral variation in 1969, 1973 and 1978 telescopic spectra.

The spectral detectability of andesite or of any other material on Mars depends on several factors, including the spectral contrast between the material and its background, the spectral and spatial resolution, and the signal-to-noise of the data. Although a few percent of andesitic materials cannot be ruled out, and other Orbiter

images and telescopic spectra remain to be analyzed, all of the spectral data examined so far fit the model of the Martian surface consisting primarily of basaltic rocks, unweathered basaltic fines, and chemically weathered basaltic fines.

REFERENCES. (1) Adams J. B., Smith M.O., and Johnson P. E. (1986) *J. Geophys. Res.* 91, 8098-8112. (2) Smith M. O., Adams J. B., and Johnson P. E. (1986) *Lunar and Planetary Science XVII*, 807-808. (3) Smith M. O., Adams J. B., Guinness E. A., and Arvidson P. E. (1987) *Lunar and Planetary Science XVIII*, 934-935. (4) Adams J. B., Smith M.O., Arvidson R. E., Dale-Bannister M. A., Guinness E. A., and Singer R. (1987) In *Mars Evolution of Volcanism, Tectonism and Volatiles*, LPI. (5) Smith M. O. and Adams J. B. (1988) *Lunar and Planetary Science XIX*. (6) Arvidson R. E., Guinness E. A., Dale-Banister M. A., Adams J. B., Smith M. O., Christensen P. R., and Singer R. B. (1989) *J. Geophys. Res.* 94, 1573-1587. (7) Smith M. O. and Adams J. B. (1989) *Lunar and Planetary Science XX*, 1024-1025.

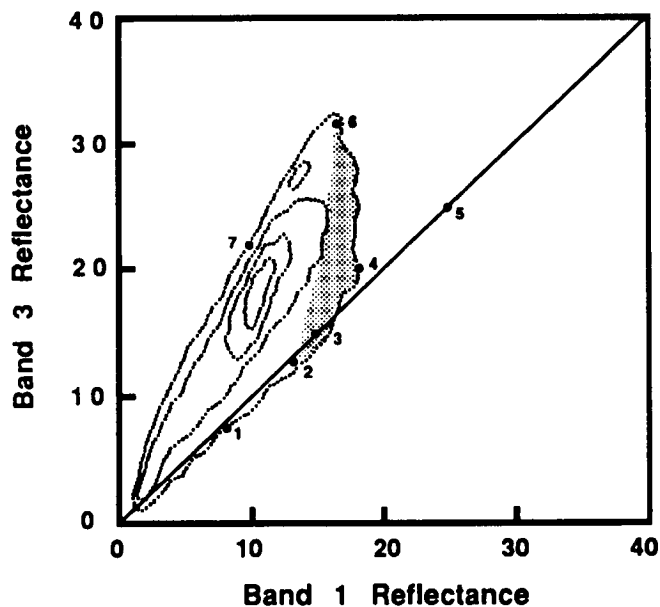


Figure 1. Histogram of six-band spectra from a Viking Lander image (VL1-28) displayed on the two-dimensional plane of bands 1 (blue) and 3 (red). Units are in percent reflectance. Contours show increasing number of pixels toward a maximum near blue = 10, red = 20. Laboratory reference spectra, resampled by the Lander bands, are plotted as filled circles. Basalt tephra (1), basaltic rocks (2), andesitic rocks (3), andesitic tephra (4), and basaltic rock powder (5) plot on or near the achromatic line (blue = red). The stippled region corresponds to specular reflections from a few (mostly rock) surfaces in the image. Basaltic rock (2), fine-grained weathered basaltic palagonite (6) and mixed grain-size basaltic palagonite (7) along with shade (blue = 0, red = 0) model the non-specular parts of the image.

Impact and Collisional Processes in the Solar System.

Thomas J. Ahrens^a, C. Gazis^a, R. Pepin^b, R. Becker^b, R. Cronin^c, J. Tyburczy^c, T. Tingle^d, T. Duffy^a, and L. Rowan^a, ^aCalifornia Institute of Technology, ^bUniversity of Minnesota, ^cArizona State University, ^dUniversity of California, Davis.

As impact cratered terranes have been successively recognized on the Moon, Mars, Mercury, and Venus, as well as on the satellites of Jupiter, Saturn, Uranus, and Neptune, and are inferred to have existed on the Hadean earth, it has become clear that impact processes are important to the understanding of the accretion and evolution of all solid planets. The noble gases (Ne, Ar, Kr, and Xe) in the normalized atmospheric inventories of the planets (Earth, Mars, and Venus), and the normalized gas content of meteorites are grossly similar, but demonstrate differences from each other which are not understood. In order to study shock devolatilization of the candidate carrier phases which are principally thought to be carbonaceous or hydrocarbons in planetesimals (Swindle, 1988), we conducted experiments on noble gas implantation in various carbons--carbon black, activated charcoal, graphite, and carbon glass. These were candidate starting materials for impact devolatilization experiments.

Initial experiments¹ were conducted on vitreous amorphous carbon samples which were synthesized under vapor-saturated conditions using argon as the pressurizing medium. Solubility of Ar in carbon data were obtained for temperatures of 500 to 800°C and pressures of 250 to 1500 bars. Up to 7 wt% Ar was dissolved in the carbon. Initial shock experiments showed that 28% of the total argon in amorphous carbon was released by driving 4 GPa shocks into the argon-rich carbon. We demonstrated that shock-induced argon loss is not simply caused by the impact-induced diminution of grain size. The present value of shock pressure required for partial impact devolatilization of Ar from carbon is below the range (5 to 30 GPa) at which H₂O is released from phyllosilicates, e.g. serpentine².

In collaboration with Professor R. Pepin and Dr. Richard Becker of the University of Minnesota, we have during the last year, conducted the first successful noble gas impact devolatilization experiment. We obtained an initial experimental result at ~6 GPa. Contrary to initial expectations, noble gases are in more retentative sites in Murchison than water! We found that while ~10% of the water was driven off in our initial experiment, only ~1% of the He was devolatilized.

Carbonaceous chondrites contain amino acids and hydrocarbons that were created early in the evolution of the solar system³. We have performed one amino acid and Surface Analysis by Laser Ionization (SALI) analyses of three samples of shocked Murchison meteorite. Peak shock pressures of ~19 to 36 GPa were achieved. Analyses for over 24 amino acids and simple amines were carried out both on hot-water extracted and acid hydrolyzed material. Several interesting and unanticipated results were evident. For a number of amino acids, including α -amino isobutyric acid (α -AIB) and isovaline, the extraterrestrial amino acids found in K-T sediments by Zhao and Bada (1989), the shocked material has a lower concentration that has the unshocked Murchison. However, for several amino acids (glycine, β -alanine), the post-shock content is greater than in unshocked Murchison. Several amines that may represent breakdown products of amino acids (for example, methyl amine, ethyl amine, and isopropylamine), are also present in greater abundance in shocked versus unshocked Murchison. For glutamic acid, alanine, and α -amino butyric acid, the post-shock content is approximately the same as in the unshocked material. Detailed interpretation of these preliminary results is currently in progress.

In order to tie shock recovery experiments to infall velocity and construct thermodynamic models for various porosity regoliths, knowledge of the Hugoniot and release isentrope equation of state is required. Serpentine is a key model of phyllosilicate material

which we assume was present in the planetesimals which accreted to form the planets and brought to them a large fraction of their H₂O inventory. Laboratory shock pressures can be related to planetesimal impact velocities by assuming uniform, homogeneous accretion. For impact between two bodies of the same material (“symmetric” impact), the impact velocity required to generate a given shock pressure is twice the particle velocity of the shocked state. Minimum impact velocities onto a planetary surface are equal to the body’s escape velocity. Thus, assuming constant density, the radius of the planet is a linear function of impact velocity:

$$r = V_p (8\pi G \bar{\rho} / 3)^{-1/2} = 2u_p (8\pi G \bar{\rho} / 3)^{-1/2} \quad (1)$$

The release adiabat data strongly suggest that a high pressure phase forms. If serpentine forms a high pressure hydrous phase, it appears possible to have a substantial H₂O reservoir within a terrestrial planetary mantle, as, for example, is speculated to be the case for the early Earth⁵. To further examine this issue, we have conducted a series of Hugoniot and release isentrope experiments for brucite, Mg(OH)₂⁶. For brucite, the effect of water on the equation of state is more clear-cut, as MgO by itself appears not to undergo any phase changes upon shock compression to at least 100 GPa.

It was Phillips *et al.*⁷ who showed there was a significant negative Bouguer gravity anomaly above a wide size range of impact craters on the Earth and Moon. Moreover, seismic refraction studies of terrestrial impact and explosion craters (e.g. Meteor crater, Oak explosion crater, Ries Crater) show that very marked seismic velocity deficits are incurred in an annular region around crater rims. Both the Bouguer gravity anomalies and P-wave (and presumed S wave) velocity deficits produced by cracks are not yet predicted by current physical or numerical models, because of the lack of an experimental basis for describing tensile wave induced cracking. However, it appears likely that with an understanding of the mechanisms of rock tensile failure via cracking, a constraint on the physical parameters of the impact event, e.g., energy and impact velocity, can be obtained from observed velocity deficits and Bouguer anomalies.

We recently completed a first study in which a series of shock loading experiments on a porous limestone and a non-porous gabbro in one and three dimensions were performed⁸. These demonstrated large (factors of ~2) decreases in compressional wave velocity within target blocks of rock within two crater radii. We have combined one-dimensional dynamic tensile (spall) study with a series of sample assemblies to test crack-induced failure models, and their time dependence, in a less complex geometry.

We have also conducted a series of recovery experiments in which shocked molten basalt at 1700°C is encapsulated in molybdenum containers and shock recovered from up to 6 GPa pressures. Post-shock temperatures are at least ~2000°C. The results (Fig. 1) are striking in that the basalt and Mo have strongly reacted in the ~1 sec or so (required for cooling) during and after the impact experiment which is conducted at low f_{O₂} in vacuum. By comparing apparent partitioning of elements between basalt and metal (Rowan and Ahrens 1991), it appears that the f_{O₂} is very low and controlled by the Mo-MoO₂ buffer. We envision these experiments represent a model of reaction which may occur upon planetary accretion upon infall of metallic planetesimals into a magma ocean.

REFERENCES: ¹Gazis and Ahrens (1991). *Earth Planet. Sci. Lett.*, in press. ²Tyburczy *et al.* (1991). *Earth Planet. Sci. Lett.*, **98**, 245-261. ³Cronin *et al.* (1988). In *Meteorites and the Early Solar System*, 819-857. ⁵Ahrens (1990). In *Origin of the Earth*, 211-227. ⁶Duffy *et al.* (1991). *J. Geophys. Res.*, in press. ⁷Phillips *et al.* (1978). *J. Geophys. Res.*, **83**,

5455-5464. ⁸Rubin and Ahrens (1991). *J. Geophys. Res.*, submitted.



Fig. 1: Back-scattered electron photograph of a cross-section of a recovered fragment taken on the scanning electron microscope. The bright white region is the molybdenum metal and the dark gray region is the basaltic glass. This fragment was shocked to 6 GPa and shows intimate intermixing and reaction between the molybdenum and the basalt.

Papers

1. Polanskey, C.A. and Ahrens, T.J., 1990, Impact spallation experiments: Fracture patterns and spall velocities, *Icarus*, 87, p. 140-155.
2. Svendsen, B. and Ahrens, T.J., 1990, Shock-induced temperatures of $\text{CaMgSi}_2\text{O}_6$, *J. Geophys. Res.*, 95, p. 6943-6953.
3. Tyburczy, J.A., Krishnamurthy, R.V., Epstein, S. and Ahrens, T.J., 1990, Impact-induced devolatilization and hydrogen isotopic fractionation of serpentine: Implications for planetary accretion, *Earth and Planet. Sci. Lett.*, 98, p. 245-260.
4. Tyburczy, J.A., Duffy, T.S., and Ahrens, T.J., 1990, Shock wave equation of state of serpentine to 140 GPa, *J. Geophys. Res.*, in press
5. Polanskey, C.A. and Ahrens, T.J., 1991, Craters in carbonate rocks: An electron paramagnetic resonance analysis of shock damage, to be submitted to *Geochimica et Cosmochimica Acta*.
6. Tan, H., and Ahrens, T.J., 1990, Shock-induced polymorphic transition in quartz, carbon, and boron nitride, *J. Appl. Phys.*, 67, 217-224.
7. Ahrens, T. J., 1990, Earth Accretion, *Origin of the Earth*, eds. J. Jones and H. Newsom, Oxford U. Press, p. 211-227.
8. Rubin, A. M. and Ahrens, T. J., 1991, Dynamic tensile-failure-induced velocity deficits in rock, *Geophys. Res. Lett.*, 18, p. 219-222.
9. Gazis, C. A., 1991, Solution and shock-induced exsolution of argon in vitreous carbon, *Earth Planet. Sci. Lett.*, in press.
10. Duffy, T. S., Ahrens, T. J., and Lange, M. A., 1990, The shock wave equation of state of brucite $\text{Mg}(\text{OH})_2$, submitted to *J. Geophys. Res.*.
11. Sekine, T., Rubin, A. M., and Ahrens, T. J., 1991, Shock wave equation of state of muscovite, submitted to *J. Geophys. Res.*.
12. Yanagisawa, M., Eluszkiewicz, J., and Ahrens, T. J., 1991, Angular momentum transfer in low velocity oblique impacts: Implications for asteroids, submitted to *Icarus*.
13. Rubin, A. M. and Ahrens, T. J., 1991, Impact-induced tensional failure in rock, to be submitted to *J. Geophys. Res.*.

Impact Cratering Calculations.

Thomas J. Ahrens, J.D. O'Keefe, C. Smither and T. Takata, Seismological Laboratory, California Institute of Technology, Pasadena, CA.

In the course of carrying out finite difference calculations¹, we discovered that for large craters, a previously unrecognized type of crater (diameter) growth occurred which we have called "lip wave propagation." This type of growth is illustrated in Figure 1 for an impact of a 1000 km (2a) silicate bolide at 12 km/sec (U) onto a silicate half-space at earth gravity (1 g). The von Misses crustal strength is 2.4 kbar. The motion at the crater lip associated with this wave type phenomenon is up, outward, and then down, similar to the particle motion of a surface wave. In Fig. 1, we see that the crater diameter has grown from $d/a \sim 25$ to $d/a \sim 4$ via lip propagation from $Ut/a=5.56$ to 17.0 during the time when rebound occurs.

We are starting to use a new code completely written at Caltech under this program to study partitioning of energy and momentum and cratering efficiency with self gravity for finite-sized objects rather than the planetary half-space problems discussed above. These are important and fundamental subjects which can be addressed with SPH codes. The Smoothed Particle Hydrodynamics (SPH) method of Gingold and Monaghan² has been used to model various problems in astrophysics and planetary physics.

Our initial work demonstrates that the energy budget for normal and oblique impacts are distinctly different than earlier calculations for silicate projectile impact on a silicate half space³. As illustrated in Fig. 2, energy budgets depend on impact geometry. We have not yet varied relative projectile size. For Fig. 2, the target radius was set at 1700 km; the impactor radius was 40% of the target radius. Both normal and oblique impacts were modeled for impact velocities of 10 and 20 km/sec. The fraction of the total energy in the kinetic energy of the impactor and target and the internal energy of the two bodies are plotted with respect to normalized time $\tau=Ut/a$, where U is the impact velocity, a is the impactor radius, and τ is the elapsed time after impact. Note that the amount of the total energy remaining in the kinetic energy of the impactor is much greater for the oblique case than in the normal impact case.

Motivated by the first striking radar images of Venus obtained by Magellan, we have been studying the effect of the atmosphere on impact cratering. In order to further quantify the processes of meteor break-up and trajectory scattering upon break-up, we have examined the reentry physics of meteors striking Venus' atmosphere versus that of the Earth. Because of the usual density gradient of an assumed adiabatic atmosphere, there is a strong tendency for the atmospheres, especially Venus, to "refract" incoming, obliquely incident projectiles toward a trajectory nearly normal to the planet. This "refraction" effect is a strong function of initial impact angle, the atmosphere scale height, as well as mass and velocity (Fig. 3). Because of the marked asymmetry of ejecta patterns on Venus, which are presumed to have been generated by atmospheric effects, the angular distribution of incoming projectiles needs to be understood. We are presently studying this effect.

REFERENCES: ¹O'Keefe and Ahrens (1977). *Proc. 8th Lunar Sci. Conf.*, 3357-3375.
²Gingold, R.A. and Monaghan, J.J. (1982). *J. Computational Physics* **46**, 429-453.
³Ahrens *et al.* (1989). *Origin and Evolution of Planetary and Satellite Atmospheres*, 328-385.

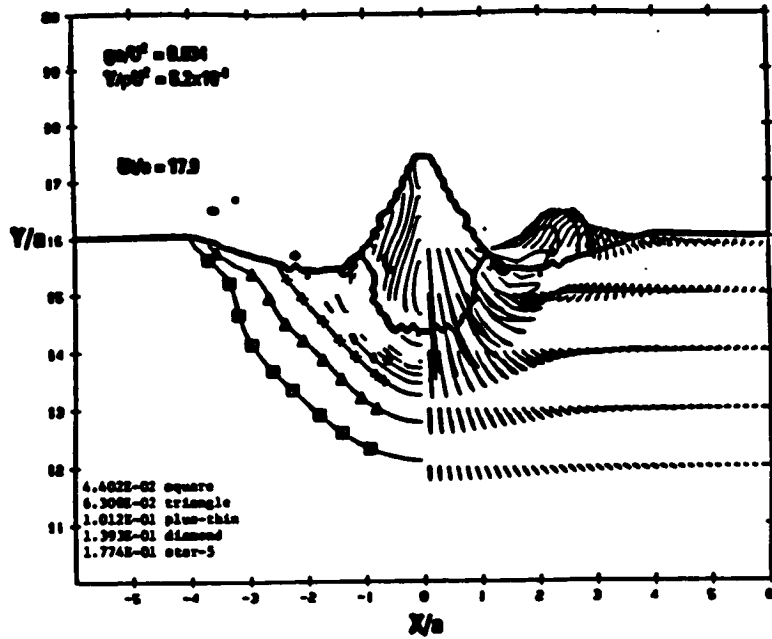


Fig. 1: Displacement history and internal energy induced by 1000 km, diameter, 12 km/sec 2.7 g/cm^3 silicate impact striking silicate planet with 2.4 kbar von Mises yield strength. Depth, D , and radius, d , are normalized by projectile radius, a . Nearly complete rebound has occurred at $Ut/a=17.9$ and shallow crater is still increasing its outer radius from its initial transient radius of $\sim 2.5 a$ to $\sim 4 a$. On left are contours of internal energy in ev/g , whereas on the right we show total displacement history for a series of markers in the initial spherical projectile and target.

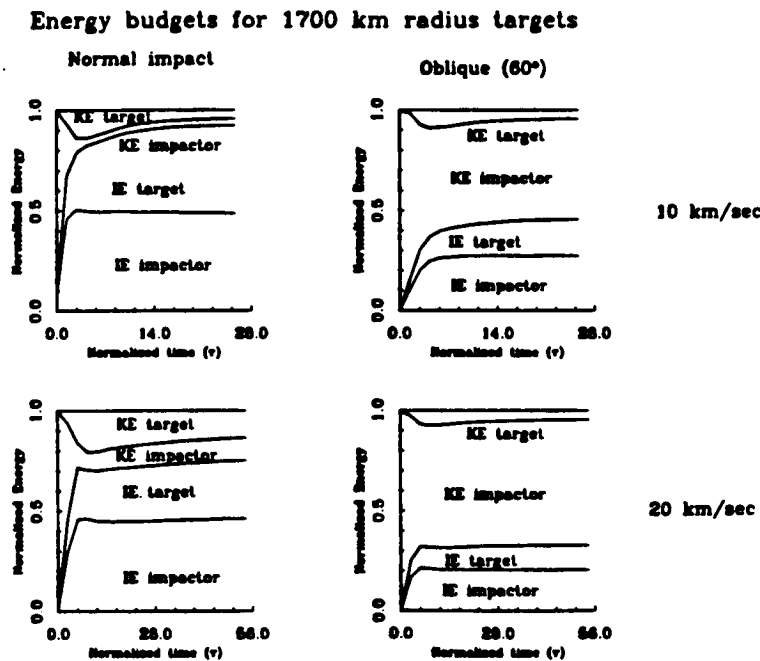


Fig.2: Partitioning between kinetic energy (KE) and internal energy (IE) budgets versus normal (left) and obliquely (right) at 10 (upper) and 20 (lower) km/sec by 680 km radius impactor.

Atmospheric Effect on the Trajectory of Meteor

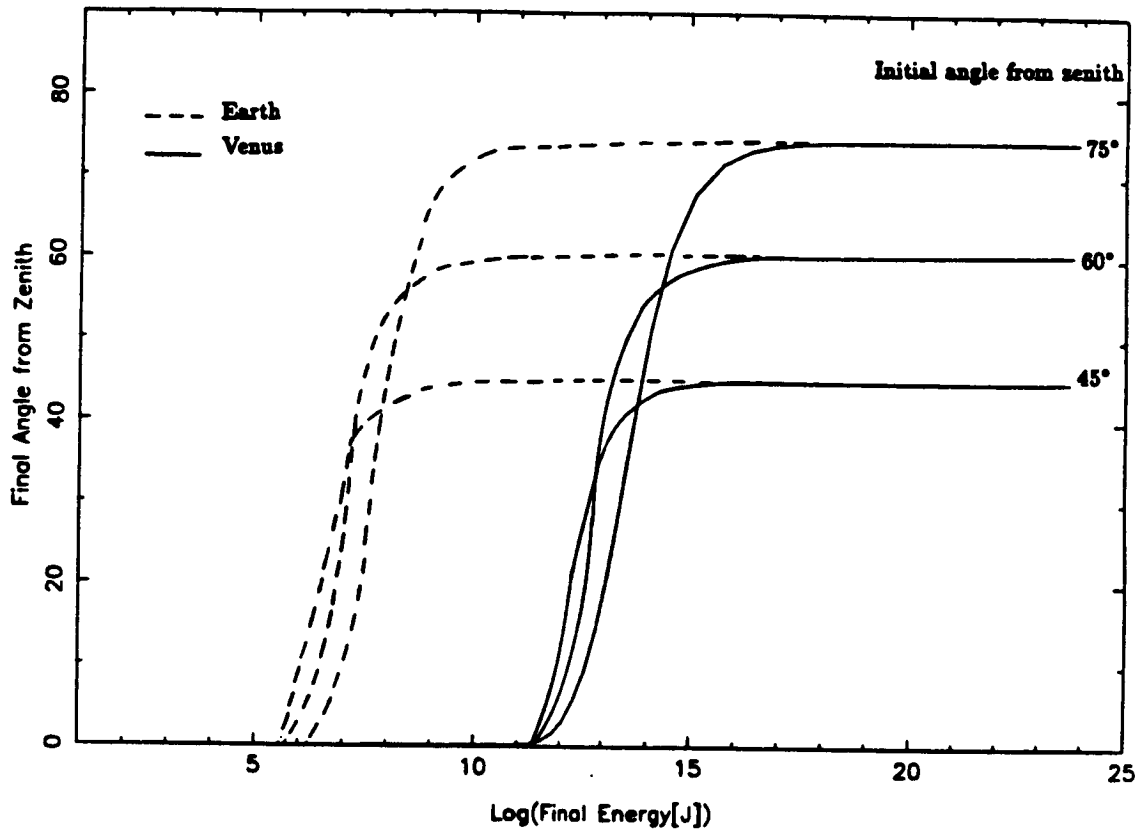


Fig. 3: Bolide-impact angle versus bolide energy for different orientations from the zenith for Earth and Venus atmospheres. Drag coefficient of 1.2, heat of vaporization and ionization of 30 MJ/kg and heat transfer coefficient 0.5 are assumed (Takata and Ahrens, unpublished).

MODELS OF PLANETARY RINGS.

L.W. Esposito, T.G. Brophy, G.R. Stewart (LASP, University of Colorado) and P.A. Yanamandra-Fisher (JPL)

The Voyager occultations provide several uniform and high quality data sets for Saturn, Uranus and Neptune. We intercompare these data and develop theoretical models for the particle sizes and the particle transport.

Ring Size Distribution. A bimodal size distribution model has been developed for Saturn's rings which allows an inversion of Voyager ring occultation data (PPS, UVS and RSS) and the determination of vertically integrated number densities at three reference particle radii for three regions: supracentimeter sized particles at a reference radius of 1 cm; subcentimeter sized particles at a reference radius of 4 μm ; and dust or micron-sized particles at a reference radius of 0.034 μm . The variations of these number densities permits quantification of the particle size distribution in Saturn's rings. We find that the size distribution is described by an inverse cube power law down to particle sizes of about 4 μm and for particles smaller than 4 μm or "dust," a gamma (Hansen-Hovenier) distribution is found to be adequate. We characterize the classical rings of Saturn (A, B, and C) by applying the model to 14 relatively large featureless regions (600-1000 km in width). Our results indicate that dust is nearly constant in all three main rings, about 6.87×10^{19} particles m^{-2} at a reference particle size of 0.034 μm for rings C and B and 7.54×10^{19} particles m^{-2} in ring A; and exhibits a slight anti-correlation with supracentimeter-sized particles. Inner regions of all three rings are dustier than the corresponding outer regions, which may be related to the observation that inner regions of the rings are relatively unperturbed compared to the outer regions where most of the resonances occur. Subcentimeter-sized particles increase outward in the rings, with a maximum in ring B, similar to the variation of supracentimeter-sized particles. The ratio of subcentimeter-sized particles to supracentimeter-sized particles appears to be constant for each ring, possibly an indication that smaller particles are produced by collisions of the particles, rather than mere release of dust regoliths from their surfaces.

Torques and Resonances. A kinetic equation has been solved numerically for a flattened planetary ring which is perturbed gravitationally by a near-by satellite. The Krook kinetic equation for planetary rings (see Brophy and Esposito (1989), or Shu and Stewart (1985)) is solved in two spatial dimensions, and in time, with interparticle collisions, and with satellite forcing, and without self-gravity. The phase-space fluid numerical method (Brophy et al. (1990)) is extended by two-dimensional systems by ignoring negligible high-order velocity moments. In simulations of satellite induced wakes, we verify the role of local shear reversal and angular momentum flux decrease as described by Borderies et al. (1983). A new result is that the amplitude of wakes is limited by purely kinematic effects, even in the absence of collisions.

The results of a simulation of an inner Lindblad resonance location, as the distribution approaches steady-state, are presented in detail. The surface mass density, pressure tensor components, and mean velocities are calculated during the simulation. The detailed mechanisms of local torque balance and forced eccentricity "damping" at resonance are illuminated. The angular momentum flux perturbations play the critical role of balancing the satellite torque on the surface mass density asymmetry. The eccentricities very close to resonance are limited by collisional

phase mixing. The resulting steady-state distribution feels a net radially integrated torque of essentially zero from the satellite, though the torque on radially confined regions can be large. We show that previous calculations of the torque (which asserted nonzero net torque) were based on impossible assumptions for the damping term which do not conserve momentum, and that our simulation results are consistent with the unaltered equations of motion. The considerations of energy conservation do not contradict the vanishing net angular momentum transfer since the particle velocity dispersions and eccentricities also adjust to new values in the resonance region.

Satellite Wakes. An explicit expression is derived for the phase-space density of a planetary ring perturbed by a nearby satellite. The derivation is facilitated by working in guiding center variables instead of local position and velocity variables and by neglecting collisions between ring particles. The usual equations for perturbed streamlines are recovered by taking first order moments of the phase-space density. The local surface density and the local mean velocity in a nonlinear satellite wake are obtained in the form of convergent infinite series. Unlike previous estimates based on streamline crowding, this surface density is positive definite because the finite velocity dispersion of ring particles streamlines of finite width. In other words, the phase-space density describes streamlines of finite width. The finite width of streamlines limits the maximum value of the local surface density that can result from streamline crowding. This result is consistent with numerical phase-space fluid simulations of perturbed rings reported by Brophy, Esposito, and Stewart (1991). The local mean velocity components in the satellite wake are found to deviate from the sinusoidal form of the streamline equations, and this deviation grows as the wake moves downstream from the shepherding satellite. These results suggest that collisional stresses between neighboring streamlines should depend on the second-order derivatives of the streamline parameters because the local mean velocity is itself a strong function of the first-order derivatives of the streamline parameters.

Dynamics and Structure of Planetary Rings

R. G. French, Astronomy Department, Wellesley College, Wellesley, MA

Our recent research efforts have been directed towards sharpening our view of the kinematical and dynamical properties of the Uranian rings, with the combination of Earth-based and Voyager observations, and in obtaining and interpreting new observations of the Saturn system from the remarkable stellar occultation of 3 July 1989. Some of the highlights of these studies are:

- *Detailed comparison of structure and dynamics of the Uranus rings* from joint analysis of high quality Earth-based data and the complete set of Voyager occultation measurements. A major task during this past year has been the completion of a comparative survey of the structure and dynamics of the Uranian rings, using all available high quality stellar occultation observations and the complete set of Voyager 2 ring occultation measurements. These have been published in a chapter (French *et al.*, 1990) of the University of Arizona's volume, *Uranus*. Much of the material in this chapter is new work supported by this grant. We have devoted considerable attention to a careful and self-consistent determination of ring widths and integrated optical depths (Tables V–VIII and Figures 7–10), and to quantifying the forced apsidal precession due to J₆, the small shepherd satellites, and the more distant classical Uranian satellites (Figure 6).
- *Comprehensive search for weak normal modes excited in the Uranian rings*, analogous to the $m=2$ and $m=0$ normal modes previously identified for the δ and γ rings. During the past year, we have searched for any low wavenumber ($m=0$ to 10) normal modes (both prograde and retrograde) that might significantly lower the post-fit radius residuals. Our goal is to detect additional excited normal modes, or to place quantitative limits on their amplitudes, for all nine of the classical narrow Uranian rings. Our complete survey has revealed *no additional normal modes for any of the rings*, for amplitudes larger than about 0.5 km. At the same time, there are provocative hints of smaller-amplitude modes for some of the rings. From our complete survey of all the rings and all normal modes from $m=0$ – 10, we have found *no definitive* evidence of excited normal modes in any rings (other than γ and δ) with an amplitude of 0.5 km or larger. At the same time, we have found provocative hints of possible normal modes in a number of rings:

Table I

Ring 6	$m=0$
Ring 5	$m=0$
Ring α	$m=2$ (prograde)
Ring η	$m=2$ (prograde)

Conclusive identification is hampered by undersampling at the higher wavenumber modes, and before we publish these results, we would like to include the additional data points to be obtained from two high-quality stellar occultations we have been awarded time to observe from the IRTF during June, 1991.

- *An on-going search for faint rings and ring arcs of Uranus*, using both Voyager images of the rings and Earth-based and spacecraft stellar occultation data. In collaboration with Mark Showalter of NASA/Ames, we have begun a study of the Uranian rings using the Voyager images. A new technique for finding and characterizing some of the faintest ring material is providing what amounts to a brand new look at this ring system. In the past, Showalter has pioneered the use of systematic pixel averaging to improve the signal-to-noise ratio of faint ring material in Voyager images. We are now exploring the logical extension of this technique, in which we use the same process to combine results from multiple images. Our best profile of the Uranian ring system generated in this manner represents a sum of 25 of the highest resolution Voyager images taken in backscattered light. Since each frame is a 15.36 second exposure, this is the equivalent of a profile generated from a single frame exposed for 384 seconds. Each 10 km radial bin in the profile contains an average of 10,000–20,000 pixels, making features visible that are no brighter than a few hundredths of a raw pixel DN, or "data number." The new profile reveals the faintest ring structures between the nine "blades of grass" that are the traditionally identified Uranian rings. The λ ring at 50,000 km is clearly visible, as are several more marginal features scattered among the major rings. One can also see a faint outward extension to ring 4, and perhaps an inward extension to ring η .
- *Comparison of upper stratospheric temperatures of Uranus* inferred from Voyager ultraviolet occultations with results of ground-based occultation observations. Earth-based stellar occultations by Uranus have been used to determine the temperature structure of the Uranian upper atmosphere near the 1 μ bar level. Traditional analysis methods, using inversion of the light curves and isothermal model fits to the data, have been in good accord, giving stratospheric temperatures of about 150K for most occultations, and in all cases below 200K. In contrast, Voyager UVS stellar and solar occultation observations have been interpreted as showing temperatures as high as 500–700K in the region just above the 1 μ bar level. These results seem inconsistent at first glance, and in order to connect the two adjacent sets of observations, Herbert *et al.* (1987, 1988) proposed that there is a very large temperature gradient (several hundred K per scale height) between the 3.3 and 0.5 μ bar levels. The energy budget of the upper stratosphere would clearly be strongly influenced by such large local temperature changes. We have now demonstrated that, in spite of the apparent incompatibility,

Herbert *et al.*'s thermal model for the Uranian stratosphere is indeed consistent with the Earth-based observations.

- *Observations of the 3 July 1989 Saturn occultation of 28 Sgr* at four visible wavelengths and at 2.1 μm , resulting in a complete ingress and egress scans of the ring system, atmospheric immersion and emersion light curves, and definitive observations of Saturn's central flash, including detection of multiple virtual stellar images around the limb of the planet. Much of our effort over the past year has been devoted to the reduction and analysis of the IR imaging data. The analysis is complicated by the presence of significant scattered sunlight from the rings at 2.1 μm , and we have developed sub-pixel image shifting and template subtraction algorithms to process the more than 40,000 individual images to obtain a high SNR light curve of the ingress and egress ring and atmosphere occultations. These observations also provided direct detection of multiple virtual stellar images along Saturn's limb during the 'central flash' portion of the occultation, when the star was behind the center of Saturn's disk as seen from the Earth. Although we are still in the process of obtaining our definitive normalized and calibrated light curve, we have used preliminary results to determine occultation timings of ring edges and sharp features, the projected diameter of the occulted star, astrometric fits to the Saturn system geometry, temperature profiles of Saturn's stratosphere, and models of Saturn's central flash, taking account of the effects of ring opacity. We have also developed color-correction algorithms to extract the occultation signal from the multi-channel visible wavelength observations.

References

- R. G. French, P. D. Nicholson, C. C. Porco, and E. A. Marouf (1990) "Dynamics and Structure of the Uranian Rings." A chapter in *Uranus*, U. of Arizona (Bergstralh and Miner, eds.)
- Herbert, F., B. R. Sandel, R. V. Yelle, J. B. Holberg, A. L. Broadfoot, D. E. Shemansky, S. K. Atreya, and P. N. Romani (1987). The upper atmosphere of Uranus: EUV occultations observed from Voyager 2. *J. Geophys. Res.* **92**, 15093-15109.
- Herbert, F. (1988). Heat sources in the thermosphere of Uranus. *B.A.A.S.* **20**, 822.

Accretion Rates of Protoplanets

Yuval Greenzweig and Jack J. Lissauer, Department of Physics, University of California at Santa Barbara, and Astronomy Program State University of New York at Stony Brook.

We calculate the rate at which planetesimals in a uniform surface density disk collide with, and are assumed to be accreted by, a massive protoplanet. The collision cross-section of a protoplanet is enhanced relative to its geometric cross-section due to its gravitational focusing of planetesimal trajectories. The gravitational enhancement factor of a protoplanet's cross section, F_g , increases as planetesimal random velocities (eccentricities and inclinations) decrease. For large random velocity planetesimals, encounters are sufficiently rapid ($\lesssim 5\%$ of an orbital period) that F_g is well approximated by the two-body "particle in a box" formula, which neglects the gravitational effect of the Sun. As planetesimal velocities decrease, F_g increases to approximately twice the two-body value, and then rises less rapidly than the two-body value, eventually dropping below it and asymptotically approaching a constant for sufficiently small random velocities. We present a scaling argument that generalizes our results to protoplanets of arbitrary mass, radius, and orbital semimajor axis. Gravitational scatterings by a protoplanet prevent random velocities of the planetesimals within its accretion zone from becoming too small. When gravitational stirring is included the maximum plausible value of the gravitational enhancement factor for rock protoplanets 1 AU from the Sun is $F_g \sim 1000$. If one protoplanet dominates gravitational scatterings in a given region of a protoplanetary disk, we find that planetesimal inclinations are excited much less rapidly than eccentricities, in contrast to the two-body approximation, in which energy is roughly equipartitioned between eccentric and inclined random motions. The resulting skewed velocity dispersion allows for a more rapid rate of protoplanet growth.

Acknowledgements: This research was supported by NASA under Grant NAGW 2061.

N 9 2 - 1 0 9 3 7 . 1

Accretion Rates of Protoplanets II: Gaussian Distribution of Planetesimal Velocities

Yuval Greenzweig and Jack J. Lissauer, Department of Physics, University of California at Santa Barbara and Astronomy Program, State University of New York at Stony Brook.

We calculate the growth rate of a protoplanet embedded in a uniform surface density disk of planetesimals having a triaxial Gaussian velocity distribution. The longitudes of the apsides and nodes of the planetesimals are uniformly distributed, and the protoplanet is on a circular orbit. The accretion rate in the two body approximation is enhanced by a factor of ~ 3 , compared to the case where all planetesimals have eccentricity and inclination equal to the root mean square (r.m.s.) values of those variable in the Gaussian distribution disk. Numerical three body integrations show comparable enhancements, except when the r.m.s. initial planetesimal eccentricities are extremely small. This enhancement in accretion rate should be incorporated by all models, analytical or numerical, which assume a single random velocity for all planetesimals, in lieu of a Gaussian distribution.

Acknowledgements: This research was supported by NASA under Grant NAGW 2061 at UCSB and Grant NAGW 1107 at SUNY.

MUD VOLCANOES ON MARS?

Paul D. Komar, College of Oceanography, Oregon State Univ., Corvallis

Mud volcanoes are common and widespread on Earth, but their possible presence on Mars has not been previously considered. The term "mud volcano" is applied to a variety of landforms having in common a formation by extrusion of mud from beneath the ground. Although mud is the principal solid material that issues from a mud volcano, there are many examples where clasts up to boulder size are found, sometimes thrown high into the air during an eruption.

Most spectacular are the Fuji-like mud volcanoes, showing a high degree of symmetry around the crater and steep (30 to 40°), concave-up slopes (Snead, 1964). The Chandragup mud volcano in Pakistan, Figure 1, has this classic form as it rises some 100 m above a level plane, with the base and crater diameters respectively being some 200 m and 30 m. This is one of a number of mud cones in Pakistan, impressive in their sizes and in the fact that they are well preserved due to the arid climate.

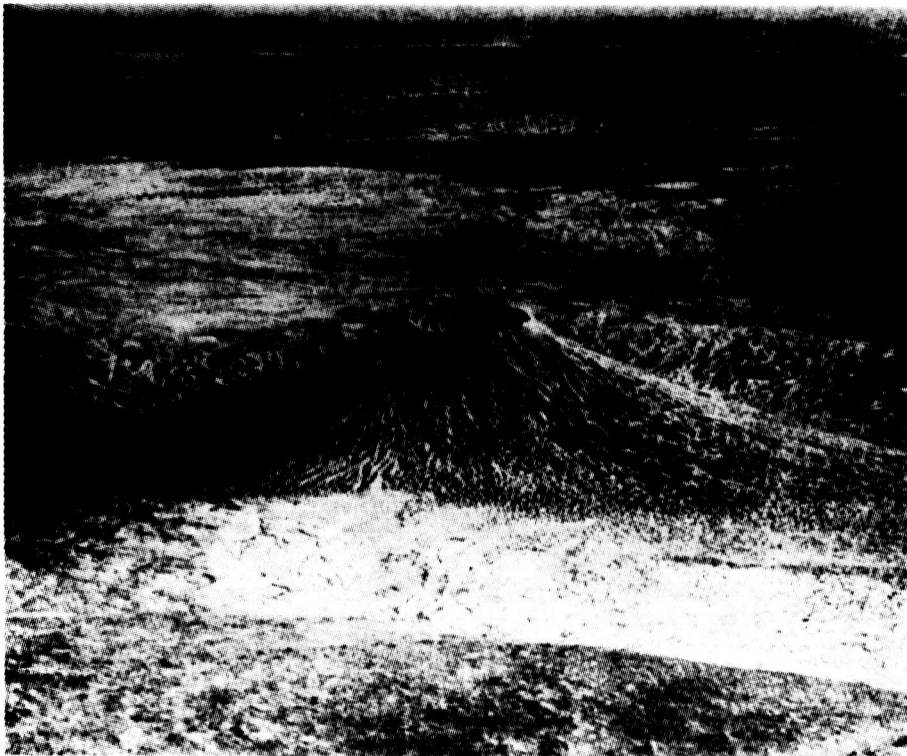


Figure 1: The Chandragup mud volcano in Pakistan.

When the Pakistan mud volcanoes are active, the craters become filled with black, watery mud (Snead, 1964). During a quiet eruption, the crater mud heaves up with the formation of large bubbles, and overflows the crater at a low point. The mud flows are composed mainly of clays and sand, but include large blocks of serpentinized ultrabasic rocks. As the mud flows slowly downslope, the side of the cone is built up and becomes a

barrier to later flows. Subsequent flows therefore cross other parts of the crater rim, and in this way a perfectly shaped cone is constructed. Explosive eruptions are rare in the Pakistan mud volcanoes. When they do occur, they are similar to the eruption of a geyser, "with rumbling noises and much agitation in the crater of the mud vent" (Snead, p. 556). In other locations the eruption of mud volcanoes has been observed to be highly explosive. Violent eruptions in New Zealand have been reported to throw mud and rocks about 100 m into the air (Ridd, 1970). Boulders weighing up to 60 pounds (27 kg) were found to have been thrown more than 100 m from one vent, and in another case a 2.5 m boulder was ejected. On Trinidad, the Devil's Woodyard mud volcano has had a history of explosive eruptions. Higgins and Saunders (1974) reported a "violent explosion heard for some miles...surface broken up and completely altered. Some of the adjacent trees had disappeared, others were thrown down." A 1909 eruption formed a crater 90 m in diameter and threw mud higher than the surrounding trees. A mud volcano on the island of Sakhalin north of Japan exploded in 1959, causing mud to cover an area of approximately 60,000 m² with a volume estimated at 150,000 to 200,000 m³ (Gorkun and Siryk, 1968).

Eruptions, particularly of the explosive type, are generally accompanied by emissions of large quantities of methane. In some cases the methane is in sufficient quantity that the eruption ignites naturally and burns for several days. Sokolov et al. (1969) describe eruptions in the Soviet Union with flames rising 100 to 200 m into the air.

Snead (1964) also has reported on mud ridges in Pakistan, in the same areas where the cones are found. Mud ridges appear to have no direct connection with central vents or with definite points of eruption, but instead occur as high, broad hills with steep sides. The largest are about 600 m high, and have lengths more than 30 km. The sides of the ridges are steeper than the cones, ranging from 40 to 70°. Some ridges appear to have originated from the wholesale upwelling of viscous mud along fault zones. Others formed by the coalescence of chains of cones; one such chain formed a ridge 400 m high and yielded an enormous quantity of mud from the closely grouped vents – a single mudflow was observed to extend for more than 3 km from its vent.

Another form of active mud volcanism creates an edifice consisting of hundreds of small individual craters. In reference to such features in Trinidad, Higgins and Saunders (1974) have adopted the name *tassik*; this is a native term which refers to a circular opening in the forest without vegetation cover due to the active formation of mud volcanoes. On one *tassik* Higgins and Saunders counted nearly 100 separate eruptive centers. The overall edifice can be large; a number of examples in Trinidad have diameters greater than 1 km, and two elliptical examples have dimensions 2.5 by 0.8 km and 2.2 by 1.0 km.

Comparable landforms are observed on the surface of Mars in Viking orbiter images. In particular, subkilometer cones having central craters, occurring randomly in groups and sometimes in chains, could be Martian analogs to terrestrial mud volcanoes. These generally have been interpreted as small cinder cones or as pseudocraters generated by lava flows coming in contact with water (Wood, 1979; Frey et al., 1979; Frey and Jarosewich, 1982). However, a volcanic-like cone may not be what it seems, and may not even establish the occurrence of igneous volcanic activity.

Reference

- Frey, H., and M. Jarosewich (1982) Subkilometer Martian volcanos: Properties and possible terrestrial analogs: *Journal of Geophysical Research*, v. 87, p. 9867-9870.

- Frey, H., B.L. Lowrey and S.A. Chase (1979) Pseudocraters on Mars: *Journal of Geophysical Research*, v. 84, p. 8075-8086.
- Gorkun, V.N., and I.M. Siryk (1968) Mud volcanoes of south Sakhalin (Pacific coast of USSR): *Internat. Geology Rev.*, 10/1, 4-12 (English translation).
- Higgins, G.E., and J.B. Saunders (1974) Mud volcanoes – their nature and origin: In *Contributions to the Geology and Paleobiology of the Caribbean and Adjacent Area*, Naturforsch. Ges. Basel, Verh., v. 84, no. 1 p. 101-152.
- Ridd, M.F. (1970) Mud volcanoes in New Zealand: *The Amer. Assoc. of Petroleum Geologists Bull.*, v. 54, p. 601-616.
- Snead, R.E. (1964) Active mud volcanoes of Baluchistan, West Pakistan: *Geogr. Rev.*, v.4, n. 4, p. 546-560.
- Sokolov, V.A., Z.A. Buniat-Zade, A.A. Geodekyan and F.G. Dadashev (1969) The origin of gases of mud volcanoes and the regularities of their powerful eruptions: In *Advances in Organic Geochemistry 1968*, Oxford, Pergamon Press, p. 473-484.
- Wood, C.A. (1979) Monogenetic volcanoes of the terrestrial planets: *Proc. Lunar Planet. Sci. Conf.*, 10th, p. 2815-2840.

N 9 2 - 1 0 9 3 9

GENERATION AND BEHAVIOR OF SOLAR SYSTEM MAGNETIC FIELDS.

Eugene H. Levy
Department of Planetary Sciences & Lunar and Planetary Laboratory
The University of Arizona
Tucson , Arizona 85721.

Many solar-system bodies possess intrinsically generated magnetic fields. The magnetic remanence carried by lunar rocks and chondritic meteorites contains a record of early solar-system magnetic fields. Both planetary and large-scale, solar-nebula fields may be recorded in this paleomagnetic record. In either case the evidence points to the early presence of magnetic fields perhaps as intense as or more intense than a Gauss. In the case of Moon or of meteorite parent bodies, the possible existence of a one Gauss surface field in a body of such dimensions challenges our understanding of the generation process. The possible existence of a general, nebula-scale magnetic field challenges us to discover its origin, its dynamical behavior, and its possibly startling influences on the evolution of the protoplanetary nebula and on physical processes that built the solar system.

The solar system is thought to have been born out of a dissipative disk nebula. Such disks seem to occur frequently as intermediate structures during the gravitational collapse and accumulation of cosmical matter. The usual picture of this dusty, gaseous protoplanetary disk suggests that it was a relatively quiet, well-behaved object. However, evidence found in meteorites suggests that this picture is likely to be oversimplified. The abundance of chondrules indicates that the protoplanetary nebula was the site of many short-lived, episodic events that were able to raise the temperatures of small pieces of silicate rock to the melting point for just a few minutes. The presence of high-temperature inclusions in meteorites, the thin, highly refractory rims found on these inclusions, and other manifestations also suggest that transient, very-high-temperature events, involving excursions far from the prevailing thermodynamic equilibria, were a common feature of the protoplanetary nebula. These phenomena, and others, challenge our basic understanding of the physical processes and the conditions out of which our planetary system was born. Experience with a variety of cosmical systems suggests that the mechanisms most commonly responsible for the transient and rapid release of energy involve the generation and explosive dissipation of magnetic field structures, although other phenomena may also be important. In this respect, it should be remembered that astronomical studies of star forming regions indicate that they are seats of intensely energetic phenomena, including high-speed, bipolar gaseous outflows associated with protostellar disks, Herbig-Haro objects, etc. There is probably no reason to believe that our solar system was a less interesting object during its birth.

This research covers a range of problems, aimed primarily at elucidating the character and consequences of magnetic-field generation in the solar system and at testing our ideas against the known properties of natural magnetic fields. Among the specific subjects currently under investigation are the magnetohydrodynamic character of the protosolar nebula, including the generation and behavior of magnetic fields, the electrical conductivity of dusty nebular gas, transient magnetodynamic and electrodynamic nebular phenomena, and the generation and dynamical behavior of planetary magnetic fields. During the past year, this project has focused on disk magnetic field generation and transient MHD heating events possibly associated with the protoplanetary nebula.

LARGE-SCALE NEBULAR MAGNETIC MODES. Although much remains to be learned about meteorite remanence, the magnetization of carbonaceous chondrites, as well as other meteorite types, suggests the presence of a nebula-scale magnetic field with an intensity that could have exceeded one Gauss during the formation of solar-system solids. Earlier we showed that such a field could be produced by hydromagnetic dynamo action under conditions thought likely to typify the disk-shaped protoplanetary nebula if a sufficient source of nonthermal ionization were present. During the past year, we developed an adiabatic approximation for calculating normal modes of MHD dynamos in thin disks. Among the advantages of such an adiabatic computational approach is its wide applicability, providing a way to obtain critical dynamo numbers and radial, as well as vertical, distributions of magnetic field in disk-dynamo normal modes for arbitrary distributions of the differential rotation, helical convection, electrical conductivity, etc. In the first investigation exploiting this technique, we focused on temporally stationary magnetic modes. However, this restriction is not dictated by the mathematical technique, and can be relaxed in the future, with the penalty of a heavier computational burden. We anticipate future efforts exploiting this technique to be directed toward understanding dynamical effects of the generated magnetic fields. In order to understand the general character of disk dynamo modes, we explored disks having effective dynamo numbers that remain constant, that decrease, and that increase as a function of increasing radius in a disk.

Disks with effective dynamo numbers that are independent of radius excite a large number of normal modes once the dynamo number exceeds some critical value. Although the stationary modes in such systems are global and encompass the entire disk, it is noteworthy that the magnetic field growth rate—even in disks with constant local dynamo number—vary strongly with position. This leads to a situation in which, even while the stationary modes have a global scale, dynamo modes that grow or decay appear to be highly localized. Although these mode characteristics were computed in the kinematical limit, the implications for dynamical behaviors of disks are likely to be profound. Even in the singular case—*viz.*, stationary modes in disks with dynamo numbers independent of radius—the magnetic field is not likely to behave as a single, globally extended state, evolving with a well defined time scale. Instead, as the disk fluid and magnetic field attempt to find an equilibrium, the system is better described as a set of many quasilocalized states each evolving on a different time scale. We suspect that in such a system, a quietly evolving near-equilibrium is unlikely to be achieved. It seems more likely that such systems will be characterized by highly variable and episodic dynamical behaviors.

Dynamo modes in disks having local dynamo numbers that vary with radius should display this kind of behavior even more strongly. In such disks even the stationary modes are highly localized. The nonstationary modes—with amplitudes growing or decaying—also have growth rates that vary strongly with radial position in the disk. Again, even within the regions capable of generating magnetic fields, these modes are best described as a set of quasilocalized magnetic states, each evolving with its own time scale. For disks with local dynamo number decreasing as a function of radius, we found that normal modes are localized, as expected, in the innermost part of a disk. Similarly, for disks having an effective dynamo number that increases with increasing radius, we found that normal modes are localized in the outermost parts of a disk.

Although there remain many uncertainties about the characteristics of protoplanetary disks, the results of these idealized model calculations suggest that dynamo-generated magnetic field can occur at distances of several astronomical units from the central star; this thus supports the idea

Although there remain many uncertainties about the characteristics of protoplanetary disks, the results of these idealized model calculations suggest that dynamo-generated magnetic field can occur at distances of several astronomical units from the central star; this thus supports the idea that meteorites, which formed at several astronomical units from the protosun, could be carrying a record of ancient nebular magnetic fields. To proceed further in this work, it will be necessary to compute more realistic models of nebulae, something which will be taken up in future years.

NEBULAR DISK FLARES & METEORITE DISEQUILIBRIUM PHENOMENA. We have investigated the possible occurrence magnetic reconnection flares in the nebula's corona. In recent work we found that such flares occurring in a tenuous corona of the protoplanetary disk could produce transient energy fluxes capable of melting preexisting dust accumulations and thereby make meteoritic chondrules. For this work, we assumed the existence of the magnetic field that seems to be implied by meteorite remanence. The magnetic field is wound, by the Keplerian differential rotation, to an intensity at which magnetic buoyancy causes flux tubes to rise through the steep gas density gradient toward the faces of the disk. As flux tubes emerge through the disk faces, they find themselves in a region where fluid stresses are insufficient to prevent the field structure from evolving toward a vacuum (or, at least, a force-free) configuration. However, since the field's topological evolution is hindered by the high conductivity, singular regions can be expected to develop and become the sites of explosive rearrangement of the magnetic field line topology. Indeed, this seems to be the process that gives rise to many solar flares and has similarities to mechanisms responsible for planetary magnetospheric outbursts. The flares discussed here release large amounts of energy in relatively brief times, of the order of 10^{33} – 10^{36} ergs in minutes to hours. During the next phase of this research we plan to investigate the externally observable manifestations of such flares and compare these with outbursts observed in association with protostars.

PLANETARY GEOMORPHOLOGY RESEARCH: FY 1990-1991

M. C. Malin, Department of Geology, Arizona State University, Tempe, AZ 85287-1404

Progress in research supported by NAGW-1 included completion of the dissertation of Jeffrey Moore (volatile ice sublimation in simulated martian polar environment), continuation of research of Robert Sullivan (hillslope processes on Mars), and completion of a global synthesis of venusian tectonics (M. Malin with R. Phillips and R. Grimm of Southern Methodist University). Work also continued on completing papers summarizing nearly a decade of field studies of eolian processes in cold volcanic deserts (M. Malin) and on a new model for interpretation of martian sediment distribution using Viking observations (M. Malin with P. Christensen, ASU).

Moore's dissertation research examined the effects of non-volatile mantling materials on the sublimation rate of water ice under simulated martian conditions. Using the Mars Environment Simulator chamber described in previous progress reports, Moore examined the effects of single layers of either "dust" (silt ~10 microns in diameter) or "sand" (modal size ~125 microns) on the rate of sublimation of water ice granules at 3 mb 95% CO₂ and 5% Earth atmosphere (i.e., 4% N₂, 0.6% O₂, 0.25% Ar, etc.). In order to observe effects within the timescale available for experiments, temperatures were elevated with respect to martian conditions, and results then scaled to Mars. Moore was also able to examine the effect on sublimation of atmospheric vapor transport using as a circulation pump. The principal variable examined was mantle thickness, which was increased from 1 mm to 5 cm in roughly logarithmic increments.

Three major conclusions can be drawn from the first set of experiments performed. First, the rate of mantle-free ice sublimation was nearly an order of magnitude smaller than that predicted by Ingersoll's 1970 model, which has served as the basis for most subsequent treatments. More recent models (but not yet published, e.g., that by Haberle and Clow) appear more in concert with the experimental results. Second, atmospheric transport of even a small amount of latent heat and water vapor can play an important role in ice sublimation when ice is exposed or mantled by thin layers of sand. Differences between the effects of dust and sand mantles on "wind-induced" sublimation were observed and are interpreted to arise from the control of diffusion rate by pore size and partial pressure. Third, variations in sublimation rates resulting both from mantle thickness and from mantle particle size were investigated--in general, mantles greater in thickness than 5 cm, of either grain-size material, effectively insulated the underlying ice from sublimation. This result can be used to understand the role non-volatile mantles play in the evolution of the martian polar deposits.

The work of Sullivan will be reported at a later date by Sullivan and Jonathan Fink, who is now Sullivan's research and thesis advisor.

In an attempt to balance the "plate"-oriented view of venusian tectonics espoused by J. Head and co-workers over the past five years, R. Phillips, R. Grimm, and M. Malin prepared a synthesis of the SMU/ASU research for publication in *Science* (3 May 1991 issue). This "pre-Magellan" work outlines a vertical tectonics model wherein venusian hot spots create plateaus of uplifted and underplated crust that evolve into *tesserae* with time. Deformation is distributed both laterally and vertically (as opposed to occurring in specific, narrow zones). The model provides an integrated view of venusian structure and geophysics.

A synthesis of results of a 4-year study of eolian processes in the cold volcanic desert of central Iceland was completed for publication. By judicious choice of study sites, information on a

broad range of topics pertaining to eolian abrasion by basaltic materials was gathered. Material properties as a function of height vary dramatically, both in composition and caliber, depending on wind speed and surface configuration. Only the simplest surface (one composed entirely of well-sorted eolian sand) appears to be successfully represented by present analytical and numerical models. Sand transport as a function of time is highly episodic. Flux measurements suggest that periods of sand transport were relatively short and separated by long periods of little or no transport. Abrasion appears to have occurred during periods of wind speeds demonstrably higher than those necessary to initiate and sustain motion. Together, these observations suggest that eolian processes may be relatively catastrophic, reflecting brief, intense winds. For rocks protruding above the surface by only a few centimeters, abrasion is very low because particle impact speeds are small. Some evidence suggests it increases rapidly to a maximum, and then decreases with increasing height. However, this pattern appears sensitive to many factors, and the stochastic nature of air flow and particle motion greatly affect what happens at a given location. Combined with effects associated with the physical properties of the target rock material itself, including variations in the properties on the scale of individual sand grains, it is unlikely that a simple model of rock abrasion with height can be applied to more than an arbitrarily small and hence unrepresentative number of cases. The implications for Mars of these and other observations were also considered. They can, for example, be used to support the conclusion that infrequent winds of sufficient magnitude to cause major abrasion is the primary cause of the apparent lack of abrasion of martian rocks as seen in the Viking Orbiter images.

Finally, a model for the interpreting the clastic sediment distribution on Mars has been developed with P. Christensen. This model is based on three major assumptions: 1) surface albedo is proportional to the fraction of the surface covered by a thin deposit of high albedo dust, 2) thermal inertia, in particular the "fine-component" inertia (average minus rock contribution), reflects the effective "mean" particle size of wind-transportable fine particles, and 3) "rock fraction" is directly related to the thickness of the mantle of fine particles as they fill-in and cover non-wind-transportable materials. The model is used to investigate sediment transport and depositional patterns in both regional and global context. It is found, for example, that the global mean thickness of transportable fines, averaged over 1 degree square areas (3600 km²) is about 35 cm, and that the thickest deposit on that scale is less than a meter thick. It is thus possible, using this model, to reconcile thermophysical interpretations of major martian surface features (e.g., the low inertia of the Tharsis volcanos) with photogeological analyses.

Owing to funding limitations in FY 1990, no funds were available after October 1990 to support research other than for student stipends. FY 1991 funds have not been received as of this date (22 May 1991), and owing to the change in location of the Principal Investigator, the prognosis for funding in the near future is poor. Future work in Planetary Geomorphology, contingent upon receiving funding, and following recommendations of the LGPRP, will focus on examining the thermophysical properties of deposits of non-volatile particulates using the Mars Environmental Simulator Chamber to which most of the funding derived from NAGW-1 has been devoted the past three years. The results of this study will be used to develop observational strategies and predictive tests for remote sensing observations of Mars using the Mars Observer Thermal Emission Spectrometer, on which the proposer is Co-Investigator.

N 9 2 - 1 0 9 4 1

ASTEROID SURFACE PROCESSES: EXPERIMENTAL STUDIES OF THE SOLAR WIND ON REFLECTANCE AND OPTICAL PROPERTIES OF ASTEROIDS.

Lucy-Ann McFadden, California Space Institute-0216
University of California, San Diego, La Jolla, CA 92093-0216

The effect of the solar wind on the optical properties of meteorites is being studied to determine whether the solar wind can alter the properties of ordinary chondrite parent bodies resulting in the spectral properties of S-type asteroids. We are analyzing the existing database of optical properties of asteroids to determine the effect of solar wind in altering asteroid surface properties. Justifications include: Previous models of the effects of solar wind on asteroids have not included sputtering, previous studies of solar wind bombardment on lunar materials can be built upon and expanded, problems of laboratory simulation of the solar wind are currently better known than in the past and can be overcome. New analytical techniques are available to determine the physical and chemical changes due to solar wind, increasing the potential to understand the processes producing the observed optical properties. The structure of the solar wind in the asteroid belt is different than that used in simulations at the Moon. The asteroid database has not been systematically examined since the 1970's. Analysis of asteroids near the 3:1 Kirkwood gap measured in the near-infrared between 0.8-2.5 mm has proceeded to the point of manuscript preparation (Figure 1). We have reviewed literature on the nature of the solar wind and theories and experiments relating to solar wind alteration of the lunar surface. A topical reference index using Hypercard on a Macintosh Computer was created by an undergraduate working for the summer of 1990. We investigated sample set-up methods using the ion-bombardment equipment in Robert Johnson and John Boring's laboratory at the University of Virginia and planned our measurement protocol. The first chemical analyses on our samples have begun. Within the next year we will apply a sputtering model to asteroids, and measure the optical properties of forsterite olivine and three ordinary chondrite meteorites (an H, L, LL), bombard them with 1-3 KeV protons simulating the solar wind at doses simulating both ambient solar wind over time, and high velocity, high density streams. We will measure the neutral and ion mass spectrum above the sample using a Scanning Electron Microprobe at the surface of the sample before and after bombardment to document the physical-chemical changes independently of the optical properties. Measurements of the optical properties of the bombarded samples will be made. We will compare the results with existing asteroid optical

properties to evaluate the validity of the current working assumption used to interpret optical properties of asteroids: that asteroids are represented by unaltered, powdered meteoritic material. This research represents the beginning of a collaboration bringing together expertise from the areas of asteroid geology and geophysics, atomic physics, and analytical chemistry.

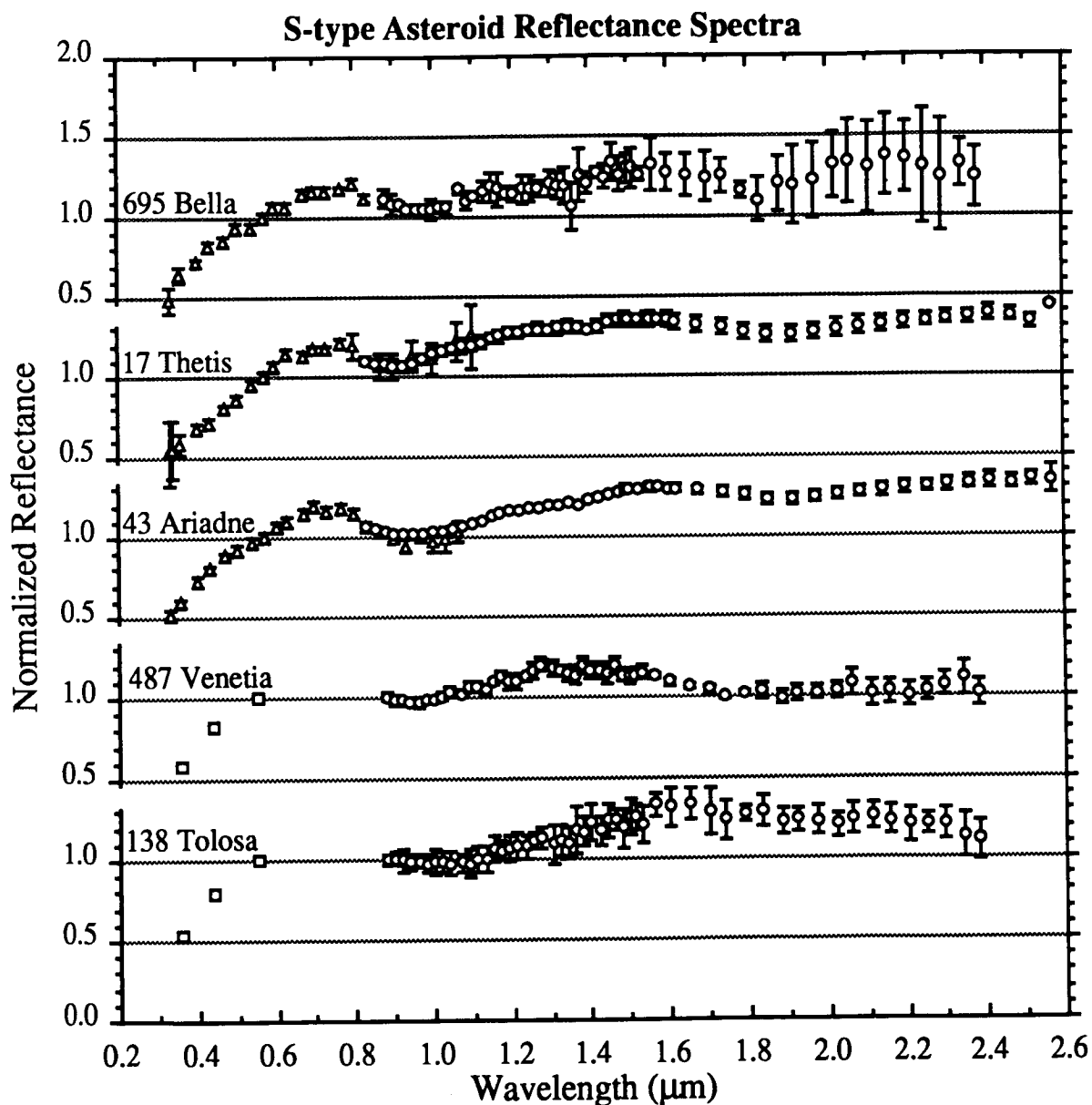


Figure 1: Near-IR reflectance spectra of S-type Asteroids. Laboratory studies will enable us to explain the differences in IR reflectance values.

Are the Equatorial Highlands on Venus Formed by Mantle Plume Diapirs?

Peter Olson

Department of Earth and Planetary Sciences, Johns Hopkins University, Baltimore, Md. 21218

Several origins have been proposed for the Equatorial Highlands on Venus, including (i) *spreading centers*, analogous to mid-ocean ridges on Earth (Head and Crumpler, 1987), and (ii) *plume-related uplift*, analogous to hotspots on Earth (Phillips and Malin, 1984; Stofan and Saunders, 1990). Recently, the spreading center hypothesis has been shown to be incompatible with the measured geoid and topography variations over the Highlands (Kiefer, 1990). It is also difficult to reconcile the range of geoid anomalies over the Highlands with a steady-state plume model. There is a large variation in admittance values (geoid/topography ratios) among Highland regions (see table 1). This variation suggests different uplifted regions represent distinct stages in a time-dependent process. Herrick and Phillips (1990) have proposed that the Highland regions listed in table 1 are formed by large mantle diapirs. According to this model, topography and geoid height decrease with increasing age of the highland, as the diapir spreads out beneath the lithosphere. A similar dynamical process has been proposed for continental flood basalt and ocean plateau volcanism on Earth (Richards et al, 1989). On Earth, rapid uplift and massive volcanism are hypothesized to accompany formation of a new hotspot, when a large mantle plume diapir rises toward the lithosphere and undergoes decompression partial melting.

In order to determine if the diapir model is compatible with the sequence of tectonic and volcanic events recorded in the surface geology of the Highlands, a series of finite difference calculations have been made of the ascent and partial melting of a spherical thermal diapir in an incompressible, infinite Prandtl number, isoviscous fluid. The upper surface of the fluid is a rigid lid, representing the crust. The initial conditions include a conductive thermal boundary layer at the upper surface, representing the thermal lithosphere, and a buoyant spherical diapir with initial temperature T_D , located near the base of the fluid. The diapir is released at the beginning of the calculation, and allowed to rise. The diapir shown in Figure 1 began with an excess temperature $\Delta T = T_D - T_\infty = 400\text{K}$. Appropriate thermodynamic and transport parameters were chosen for the mantle of Venus. Partial melting is calculated using a simplified pressure-dependent melting law. The dynamical behavior of the melt phase is represented as a bimodal process. Where the porosity ϕ is below a critical value, ϕ_c , percolation

is ignored, and melt is advected along with the unmelted matrix. Where $\phi \geq \phi_c$, the excess melt is assumed to be infinitely mobile, and is added immediately to the overlying crust.

Figure 1 shows the main stages in the evolution of the diapir, and the corresponding stages in surface volcanism and tectonics. Figure 1a illustrates the first stage, as the diapir approaches the lithosphere from below. During this stage, broad-scale, dynamically supported uplift and the first phase of volcanism occur. Most of the new crustal material is derived from partial melting *ahead* of the diapir. The peak geoid anomaly is approximately 100 m, and the admittance is large. In the second stage (Figures 1b-c) the diapir spreads out at the base of the lithosphere. The main phase of volcanism occurs at this stage, with melt derived from the diapir at 100-150 km depth. The dynamically supported topography subsides, the component of topography due to crustal thickening develops, and the peak geoid anomaly drops to about 25 m. In the final stage (Figure 1d), melt production has ceased, and a ring-shaped instability develops in the thermal boundary layer around the collapsed diapir. Topography at this stage consists of a low plateau surrounded by a broad, depressed plain, and a central highland region elevated by thick crust. The ring instability generates extensional stress in the central highlands, and compressional stress along plateau margin.

The time scale for evolution is quite short: the dynamic topography subsides in about 10 Myr, and volcanism is essentially finished within 15 Myr. These timescales are consistent with the rapid extrusion of flood basalts and ocean plateau on Earth. They also place an important constraint on models of Highland formation on Venus. According to the mantle diapir model, Beta Regio represents stage 1, while Thetis and Ovda and the Artemis Plateau in Aphrodite Terra represent stages 2 and 3. If this interpretation is correct, then Beta, Thetis and Ovda must all be rather young, probably 50 Ma or less. Preliminary age estimates derived from crater statistics indicates substantially older ages for the uplifted areas in Aphrodite Terra (Phillips et al, 1991).

References .

- Head, J.W. and L.S. Crumpler, *Science* 238, 1380-1385, 1987.
- Herrick, R.R. and R.J. Phillips, *Geophys. Res. Lett.* 17, 1373-1376, 1990.
- Kiefer, W.S., *Geophys. Res. Lett.* 17, 1373-1376, 1990.
- Phillips, R.J. et al, *XXII Lunar Planet. Sci. Conf.*, 1991.
- Phillips, R.J. and M.C. Malin, *Ann. Rev. Earth Planet. Sci.* 12, 411-413, 1984.
- Stofan, E.R. and R.S. Saunders, *Geophys. Res. Lett.* 17, 1377-1380, 1990.
- Richards, M.A., R.A. Duncan and V.E. Courtillot, *Science* 246, 103-107, 1989.

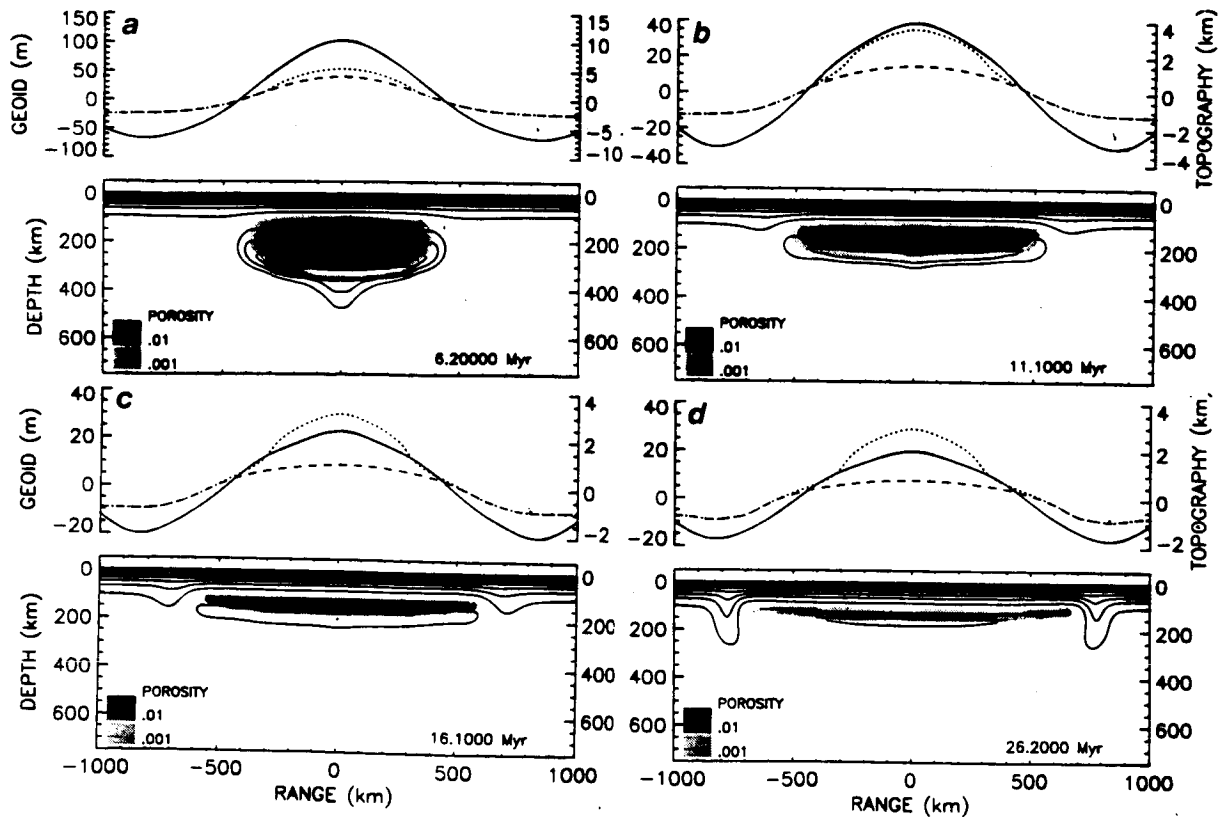
Table 1: Equatorial Highlands

Dome	Diameter (km)	Elevation (km)	Geoid (m)
Beta Regio	2800	4.5	90
Thetis Regio	3000	4	70
Ovda Regio	3400	4.8	35
Artemis Plateau	2500	1.5	<20

Table 2: Diapir tectonics

Stage	Time (Myr)	Tectonic Style	Volcanic Style
1	0-5	Rapid Uplift + Extension	Rift Volcanism
2	5-20	Rapid Subsidence	Flood Volcanism
3	>20	Slow Subsidence + Marginal Compression	none

Figure 1: A numerical calculation of the evolution of a rising thermal diapir. Upper panels: Profiles of geoid height (solid) topography (dotted) and dynamical topography (dashed). Lower panels: Contours of the temperature field. Shaded regions show partial melt concentration.



THERMAL AND ALBEDO MAPPING OF THE NORTH AND SOUTH POLAR REGIONS OF MARS; D. A. Paige and K. D. Keegan, Dept. of Earth and Space Sciences, UCLA, Los Angeles, CA 90024.

Here we present the first maps of the thermal properties of the north and south polar region of Mars. The thermal properties of the midlatitude regions from -60° to $+60^\circ$ latitude have been mapped in previous studies¹. The maps presented here complete the mapping of the entire planet.

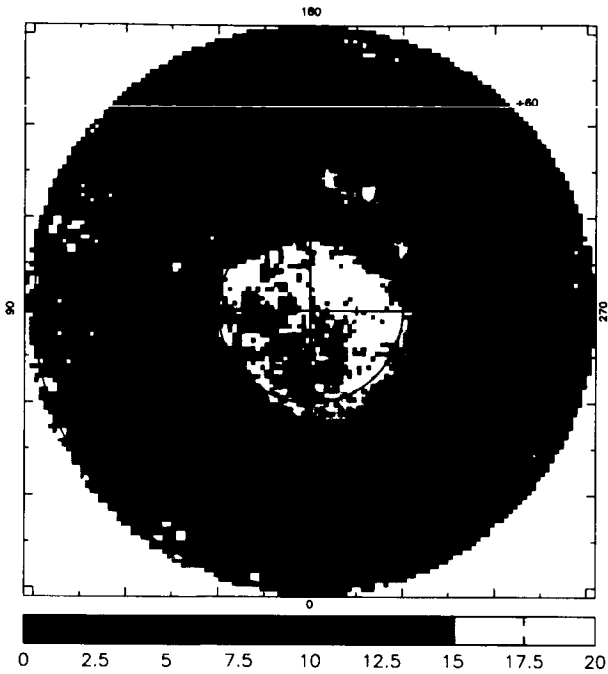
The maps for the north polar region were derived from Viking Infrared Thermal Mapper (IRTM) observations obtained between June 10, 1978 to Sept. 30, 1978 ($L_s = 98.39$ to 121.25 , Julian Date = 2443670 to 2443720). This period corresponded to the early summer season in the north, when the north residual water ice cap was exposed, and polar surface temperatures were near their maximum. The maps in the south were derived from observations obtained between Aug. 24, 1977 to Sept. 23, 1977 ($L_s = 321.58$ to 338.07 , Julian Date = 2443380 to 2443410). This period corresponded to the late summer season in the south, when the seasonal polar cap had retreated to close to its residual configuration, and the second global dust storm of 1977 had largely subsided. Best fit thermal inertias were determined by comparing the available IRTM 20μ channel brightness within a given region to surface temperatures computed by a diurnal and seasonal thermal model. The model assumed no atmospheric contributions to the surface heat balance. Standard deviations of the model fits were typically less than 3K. Figures 1ab and 2ab show the resulting maps of apparent thermal inertia and average IRTM measured solar channel lambert albedo for the north and south polar regions from the poles to $\pm 60^\circ$ latitude.

Thus far, the major results of this work can be summarized as follows:

- Surface Water Ice: High albedo, high thermal inertia water ice deposits are widespread within the north residual cap, and in outlying deposits at latitudes as low as $+74^\circ$. The diurnal thermal inertias derived here are consistent with seasonal thermal inertias derived from measurements of the polar heat balance², which implies that these deposits are dense and coherent from the surface to great depths. No surface water ice appears to be present in the southern hemisphere.
- Polar Dune Material: In the north, regions containing low albedo polar dune material can not be distinguished from the surrounding polar planes units solely on the basis of thermal inertia. Regions covered by dunes generally have intermediate thermal inertias, which is consistent with transportation by the martian atmosphere under current climatic conditions. The inertias of the polar dune materials are distinctly lower than the low albedo material that extends northward from the Acidalia region at 45° longitude. Large regions of exposed sand and rock are not present in the south polar region.
- Dust Deposits: The south polar region appears to be the site of a major new low thermal inertia region. The apparent inertias near the south pole are similar to those in the Tharsis and Arabia regions in the northern hemisphere, and are consistent with the presence of a dust layer that extends a depth of at least one diurnal thermal skin depth. The unique location of this deposit may provide clues to the processes responsible for the formation of the northern hemisphere low thermal inertia regions and the layered deposits at both poles. In sharp contrast to the south, there are no extensive regions of contiguous exposed low thermal inertia materials in the north polar region. If the north polar region is presently a major sink for material raised during global dust storms, then this material must be incorporated into the residual water ice deposits.

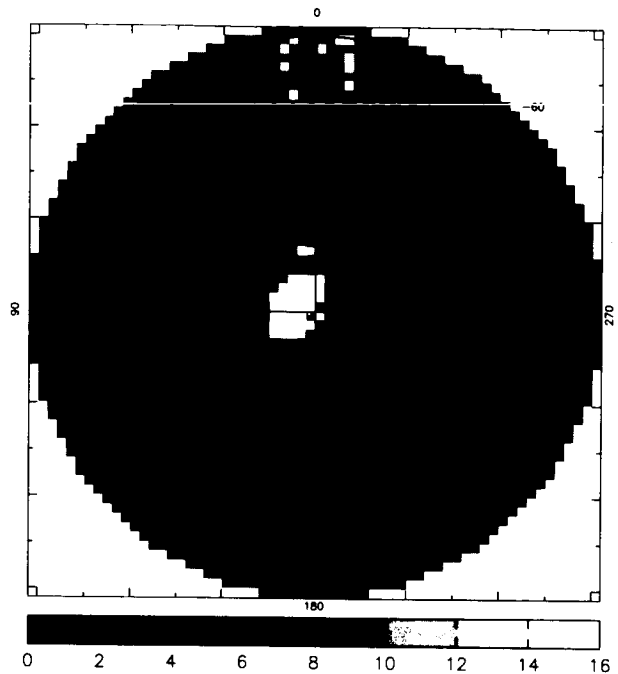
1. Palluconi, F. D. and H. H. Kieffer, *Icarus* **45**, 415 (1981).
2. Paige, D. A. and A. P. Ingersoll, *Science* **228**, 1160 (1985).

MARS NORTH POLE DERIVED THERMAL INERTIA



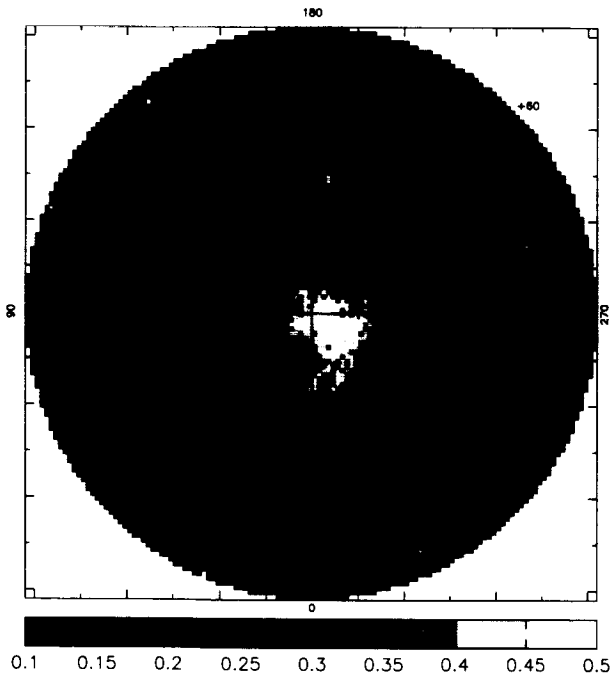
1

MARS SOUTH POLE DERIVED THERMAL INERTIA



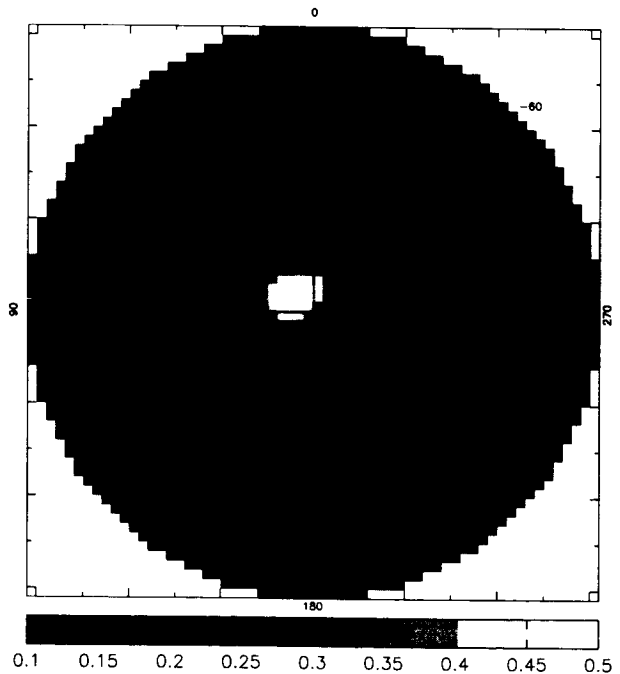
2

MARS NORTH POLE IRTM LAMBERT ALBEDO



A

MARS SOUTH POLE IRTM LAMBERT ALBEDO



A

Figures 1-2. Thermal inertia and albedo maps of the north (left) and south (right) polar regions of Mars from Viking IRTM observations. The upper figures show derived thermal inertia in units of $\times 10^{-3} \text{ cal cm}^{-2} \text{ sec}^{-1/2}$. The lower figures show measured IRTM Lambert albedo. (data points with values outside the limits of the gray scales below each image were mapped to the highest or lowest gray scale values.)

THE WIDTH OF FAULT ZONES IN A BRITTLE-VISCOUS LITHOSPHERE: STRIKE-SLIP FAULTS; E.M. Parmentier, Department of Geological Sciences, Brown University, Providence, RI 02912

A fault zone in an ideal brittle material overlying a very weak substrate could, in principal, consist of a single slip surface. Real fault zones have a finite width consisting of a number of nearly parallel slip surfaces on which deformation is distributed. This study explores the hypothesis that the finite width of fault zones reflects stresses due to quasistatic flow in the ductile substrate of a brittle surface layer. Because of the simplicity of theory and observations, strike-slip faults are examined first, but the analysis can be extended to normal and thrust faulting.

Other factors have been suggested to explain the finite width of strike-slip fault zones. For example the fault zone may be a zone of preexisting faults whose width was determined by some unspecified process. In a more analytical approach, thin viscous sheet models, based on a vertically averaged deformation and rheology of the lithosphere, have been used to calculate the width of fault zones (1). The only length scale in such a model is the along-strike length of the fault; and the width of a fault must be proportional to its length. There is no evidence that the width of fault zones is proportional to their length. The width of well studied terrestrial oceanic transform faults appears to be relatively independent of their length (2), but depends on their slip rate.

Consider a strike-slip fault zone in a lithosphere consisting of a brittle layer overlying a viscous layer in which the viscosity η varies with depth. For a strike-slip fault that is long compared to either its width or the lithosphere thickness, d , the horizontal velocity u along the fault is the only nonzero velocity component. This leads to the boundary value problem defined in Figure 1. Outside a fault zone of width w , the velocity at the top of the viscous layer is defined by the strike-slip motion of the lithosphere across the fault zone with relative velocity U . Within the fault zone the shear stress on vertical planes in the brittle layer averaged over its thickness h , is $\mu\rho gh/2$ where μ is coefficient of sliding friction (3). Since the product of this average stress and h is independent of x , the viscous shear stress, $\tau = \eta \partial u / \partial z$, on the bottom of the brittle layer (top of the viscous layer) must vanish. Shear stress on the bottom of the lithosphere vanishes if the mantle beneath it is very weak. Solutions for $u(x,z)$ are obtained using finite difference approximations. For a prescribed fault width, the stress within the brittle fault zone is obtained by integrating τ along the bottom of the rigid brittle layer assuming that the stress in the brittle layer far from the fault zone is small compared to the frictional sliding stress.

For a fault width $w=d$, the calculated velocity distributions are shown in Figure 2 for two cases: a uniform viscosity ductile lithosphere and one containing a low viscosity layer representing a weak, ductile lower crust. In this case the viscosity in the low viscosity layer is 0.1η , and the layer thickness is $0.2d$. In these two cases the horizontal velocity distribution across the fault zone is shown in Figure 3. For a prescribed fault zone w/d , the resulting stress within the fault zone corresponds to a particular value of the parameter $\eta U / \mu \rho g h^2$, given in Figure 4 for a range of w/d . For $\mu=0.6$ (3), $\rho=3 \times 10^3 \text{ kg/m}^3$, $g=10 \text{ m/sec}^2$, $u=1 \text{ cm/yr}$, $h=15 \text{ km}$, and $\eta=10^{22} \text{ Pa-s}$, $\eta U / \mu \rho g h^2 \cong 0.7$. For the range of parameters considered thus far (see Figure 4), this choice of physical parameters predicts a fault zone width comparable to the thickness of the viscous lithosphere. Note that the predicted fault zone width is proportional to d , increases with decreasing h , and increases with increasing η and U .

Because they are simpler than continental faults, oceanic transforms are an obvious first application of this model. The width of transform faults along the Mid-Atlantic Ridge range from 1-5 km (2) and show a clear dependence on slip (spreading) rate, becoming progressively wider as the spreading rate increases southward. On the fast spreading East Pacific Rise, transform fault zones, which have been frequently described as multiple transforms, have a width sometimes exceeding 20 km. After confirming that the model explains characteristics of terrestrial fault zones, it will be applied to interpret the structure of fault zones on Venus and the Icy satellites.

References: (1) England, P.C., et al., J.G.R. 90, 3551-3557, 1985. (2) Searle, R.C., J. Geol.Soc. Lond. 143, 743-756, 1986. (3) Brace, W.F., and D.L. Kohlstedt, J.G.R. 85, 6248-6252, 1980.

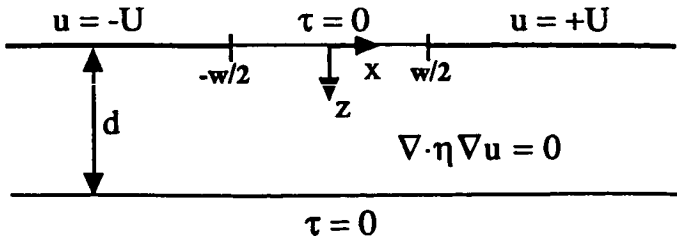


Figure 1. Boundary value problem for quasistatic flow in the ductile (viscous) layer of the lithosphere. Velocities within the layer are governed by the equilibrium equation. See text for discussion of boundary conditions.

Figure 2. Velocity distributions in the ductile layer of the lithosphere due to strike-slip motion across a fault zone (vertical lines) in the brittle surface layer (shaded). Two solutions are shown, one on each side of the diagram. Both velocity distributions are antisymmetric about $x=0$. The viscosity in the low viscosity layer is $.1\eta$ and the bottom of this layer is shown by the dashed line. With a low viscosity zone present, shearing motions are concentrated in this layer and the lithosphere deformation is distributed horizontally over a larger region.

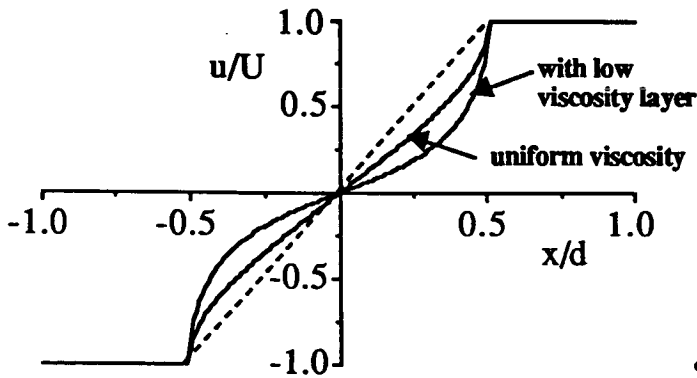
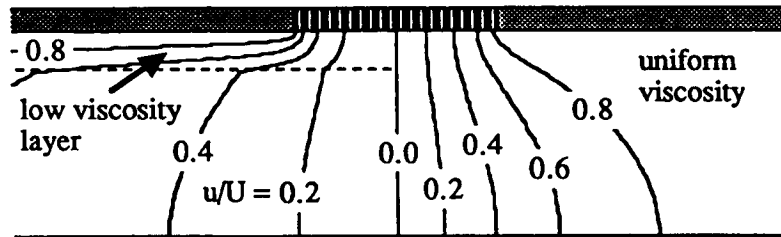
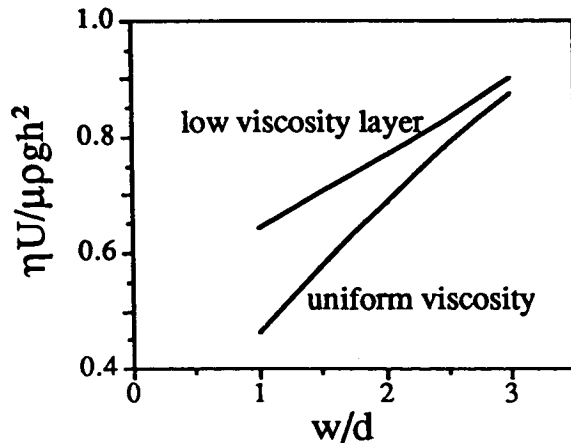


Figure 3. Velocity distributions within the fault zone for uniform viscosity and with a low viscosity layer. The shear strain rate in the fault zone is not uniform, but has a distribution consistent with a vanishing viscous shear stress on the bottom of the deforming brittle layer.

Figure 4. Relationship of fault zone width and a dimension-less parameter that controls the magnitude of stresses.



The ring arcs of Neptune

S. J. Peale, Department of Physics, University of California at Santa Barbara.

After the corotation resonance with an exterior satellite proved inapplicable to the Neptune ring arc confinement, a search for other mechanisms settled on the possible influence of Neptune's magnetic field. The areas of greater optical depth around the ring are much dustier than the low optical depth regions. These particles reside in a plasma and must therefore carry some charge. Fig. 1 shows the components of Neptune's magnetic field on the equator at the radius of the ring arcs as a function of Neptunian longitude. The components are those of the offset tilted dipole model of Ness *et al.*, (1989). Although the dipole model is probably not a good approximation so close to the planet, the magnitude of the field given in Fig.4 is probably not too far wrong. The possible importance of the magnetic field on the smallest particles in the ring is indicated by the ratio of the magnetic force to the central gravitational attraction with the field strength $B = 0.01$ gauss at the ring distance.

$$\epsilon = \frac{qa(n - \Omega)Ba^2}{GMmc} = 2.2 \times 10^{-4}|V|,$$

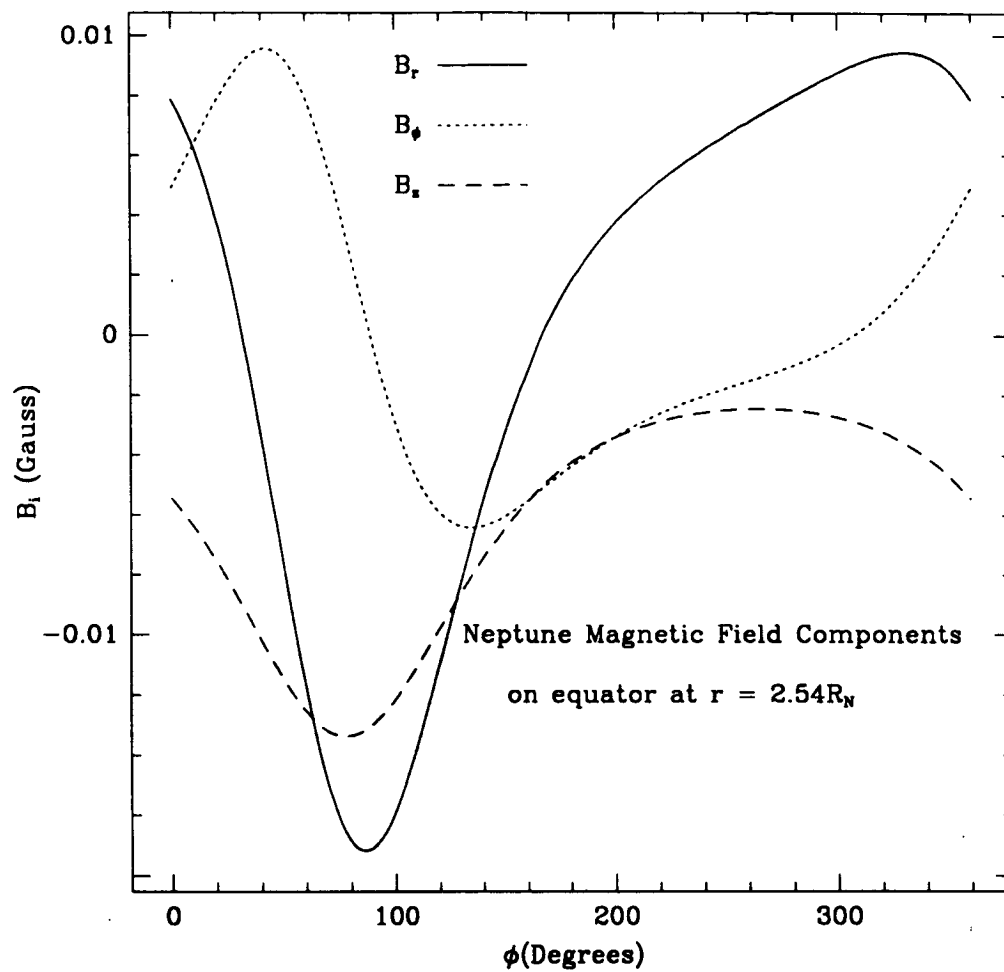
where q is the charge, a the radial distance from the planet center, n the orbital angular velocity, Ω the rotational angular velocity of Neptune, G the gravitational constant, M and m the masses of Neptune and the particle respectively, c the velocity of light and V the particle electrostatic potential in volts due to the charge q , where V may exceed 10 Volts. The numerical value on the right hand side assumes m is that for a 0.5 micron particle of density 1 g/cm^3 .

A preferred position in the orbit for magnetically perturbed particles seems to require a commensurability between the rotation of the planet and the motion of the particle in the orbit. The period of rotation is assumed to be that of the radio bursts at 16.11 hours. However, without a model for the radio emission, one cannot be absolutely sure. Jupiter's decametric radiation depends on Io's orbital position as well as the rotation, so a synodic periodicity might be appropriate. But the latter radiation is highly directed, whereas Neptune's was seen all along the spacecraft trajectory on the 16.11 hour schedule, *i.e.*, with no shifts in phase relative to a fixed longitude on the planet. The ring orbital period is 10.536 hours which is not commensurate with the rotation period. If the 16.11 hours is interpreted as a synodic period between the rotation and a satellite motion, the closest rotation periods to 16 hours are 15.9 hours if the satellite is 1989N4 and 18.2 hours if the satellite is Triton. The former is near, but not at, a 3:2 resonance with the ring particle motion. The problem deserves some more thought before a possible herding of small particles by the magnetic field is abandoned.

Acknowledgement: This research was supported by NASA under Grant NAGW 2061.

Reference: Ness, N. F., M. H. Acuña, L. F. Burlaga, J. E. P. Connerney, R. P. Lepping, and F. M. Neubauer (1989) Magnetic Fields at Neptune, *Science* 246, 1473-1478.

Fig. 1



The Titan-Hyperion Orbital Resonance

S. J. Peale, Department of Physics, University of California at Santa Barbara.

Considerable effort was spent investigating the applicability of a Hamiltonian averaged over high frequency terms, where long period and secular terms up to second order in eccentricity were kept. The planar, elliptic, restricted three body problem applied to Titan-Hyperion, when the Kepler terms are also expanded to second order in small quantities and several canonical transformations are carried out, gives the Hamiltonian

$$\begin{aligned}
 H = & (j\dot{\lambda}_1 - (j+1)\dot{\lambda}_2 + \dot{\varpi}_2) \left(\Theta_1 - \frac{x_2^2 + y_2^2}{2} \right) + (\dot{\varpi}_1 - \dot{\varpi}_2)\Theta_1 \\
 & - \frac{3\mu_1^2}{2L_{2j}^4} (j+1)^2 \left(\Theta_1 - \frac{x_2^2 + y_2^2}{2} \right)^2 - \frac{\mu\mu_1}{L_{2j}^{5/2}} C_{01} e_1 (x_2 \cos \theta_1 - y_2 \sin \theta_1) \\
 & - \frac{\mu\mu_1}{L_{2j}^2} C_{j+1} e_1 \cos \theta_1 - \frac{\mu\mu_1}{L_{2j}^{5/2}} C_j x_2 - \frac{\mu\mu_1}{L_{2j}^2} C_{2(j+1)} e_1^2 \cos 2\theta_1 \\
 & - \frac{\mu\mu_1}{L_{2j}^3} C_{2j} (x_2^2 - y_2^2) - \frac{\mu\mu_1}{L_{2j}^{5/2}} C_{2j+1} e_1 (x_2 \cos \theta_1 + y_2 \sin \theta_1),
 \end{aligned}$$

where subscripts 1 and 2 refer to Titan and Hyperion respectively and $j = 3$ for the 4/3 orbital resonance. Here $x_2 = (2\Theta_2)^{1/2} \cos \theta_2$, $y_2 = (2\Theta_2)^{1/2} \sin \theta_2$, $\Theta_2 = L_2 e^2 / 2$, $\theta_2 = j\lambda_1 - (j+1)\lambda_2 + \varpi_2$, $L_2 = \sqrt{\mu_1 a_2}$, $L_{2j} = L_2$ evaluated at the exact resonance, $\Theta_1 = \{L_{2j} - L_2[1 - (j+1)e_2^2/2]\} / (j+1)$, $\theta_1 = j\lambda_1 - (j+1)\lambda_2 + \varpi_1$, the C 's are constants involving the Laplace coefficients and their derivatives, $\mu = M / (M + m)$, $\mu_1 = m / (M + m)$, M is Saturn's mass, m is Titan's mass and a_i , e_i , ϖ_i , λ_i are semimajor axes, eccentricities, longitudes of periapse and mean longitudes respectively.

In these variables the Hamiltonian is analytic at the origin of x_2, y_2 , is mapable and demonstrates all of the characteristics of the motion inside and just outside the resonance. It works wonderfully for small eccentricities and it was hoped that one could apply it to the Titan-Hyperion system as Titan approached the resonance. However, the motion could not be followed to eccentricities approaching that of the current Hyperion orbit (0.1). Also, since Titan's mass is so large and its own orbital eccentricity is also large (0.029), Hyperion's eccentricity oscillates to large values very early in the resonance history. To check the applicability of the Hamiltonian, I programmed the exact equations for the system in the planar, elliptic, restricted three body approximation, and compared the integrations with the results derived from the above Hamiltonian. For conditions where the Hamiltonian showed a bifurcation of the stable point of libration, so that the Hyperion would not librate about the usual conjunctions at its orbital apoapse, the exact equations revealed perfectly normal libration still centered at the apse. The periods of libration differed by more than a factor of 2. It was thus clear that any results obtained from the above Hamiltonian for this particular system would have a very limited range of applicability. Hence, the approach will now be to use the new map developed by Jack Wisdom (1991, Submitted to *Icarus*) to follow the evolution for arbitrary eccentricities while avoiding the constraints and inappropriateness of various expansions.

Acknowledgement: This research was supported by NASA under Grant NAGW 2061.

Rotational Properties of Planetary Satellites

S. J. Peale, Department of Physics, University of California at Santa Barbara.

Properties of satellite rotation that are observable in principle, include the rotation period, the orientation of the spin axis relative to the orbit plane, precession of the spin axis due to gravitational torques, non principal axis rotation or wobble, and deviations from uniform principal axis rotation or libration. Considerable order is observed in current satellite rotation states, and it is of interest to ascertain how this order came about and why some satellites do not conform to the dominant norm. There is a strong coupling between the spin and orbital motions that is primarily responsible for maintaining the ordered rotation states in most cases, but this coupling is equally responsible for destroying any chance of orderly rotation for Saturn's satellite Hyperion. Understanding the processes which constrain current rotation states as well as those of an evolutionary nature which could have brought the individual satellites to their observed rotation and orbit states allows us to sometimes infer interior properties of some satellite or even of its primary planet, although attempts to deduce primordial rotation states are usually frustrated. We shall summarize the observed rotational properties of the planetary satellites, outline our understanding of the processes maintaining and those leading to the observed states and indicate some of the inferences that can be drawn about intrinsic properties of the bodies themselves.

Acknowledgements: This research was supported by NASA under Grant NAGW 2061.

OPTICAL PROPERTIES OF GRAINS IN MOLECULAR CLOUDS AND ACCRETION DISKS; J. Pollack¹, D. Hollenbach¹, D. Simonelli¹, S. Beckwith², T. Roush^{1,3}, and W. Fong⁴

¹ Space Science Division, NASA Ames Research Center, Moffett Field, CA 94035, ² Astronomy Department, Cornell University, Ithaca, NY 14853, ³ San Francisco State University, Department of Geosciences, San Francisco, CA 94132, ⁴ Synernet Corporation, Fremont, CA.

We define a baseline model of the composition and abundances of grains and gases in molecular cloud cores and accretion disks around young stars by employing a wide range of astronomical data and theory, the composition of primitive bodies in the solar system, and solar elemental abundances. In the coldest portions of these objects, we propose that the major grain species include amorphous olivine ($[\text{Fe,Mg}]_2\text{SiO}_4$), amorphous orthopyroxene ($[\text{Fe,Mg}]\text{SiO}_3$), volatile and refractory organics, water ice, troilite (FeS), and metallic iron. Using a combination of laboratory measurements of optical constants and asymptotic theory, we derive values of the real and imaginary indices of refraction of these grain species over a wavelength range that runs from the vacuum UV to the radio domain. We also provide auxiliary information for these grain species, such as their vaporization temperatures bulk densities, and their fractional abundances by mass.

The above information on grain properties in molecular cloud cores and accretion disks is used to estimate the Rosseland mean opacity of the grains in both environments and the IR and microwave opacity of grains in accretion disks. We find that organics make the largest contribution to the Rosseland mean extinction coefficient at temperatures below their vaporization temperatures ($\simeq 575$ K in molecular cloud cores and 375 K in accretion disks), and that silicates and metallic iron jointly determine the Rosseland mean opacity at higher temperatures.

At mid infrared wavelengths, the computed monochromatic opacities are in approximate accord with the spectral characteristics of "astronomical silicates". At low temperatures (< 500 K), the position, strength, width, and contrast of the 10 and 20 μm silicate vibrational fundamentals can be significantly affected by the opacities of organics and water ice.

The spectral index β of the grain opacity at long wavelengths shows marked variation. In particular, we estimate that it has a value between about 2 and 2.5 between 100 and 650 μm and a value between about 0 and 1 between 650 μm and 2.7 mm, in rough agreement with spectral flux measurements of the ISM and disks around young stars. In the latter spectral region, grain opacity is dominated by troilite and silicates. We also find that the grain absorption coefficient lies within a factor of 3 of $6.5 \times 10^{-3} \text{ cm}^2/\text{g}$ (of gas and dust) at 1 mm. This value will help to constrain the masses of these disks.

STUDIES IN PLANETARY RINGS

Carolyn C. Porco, Lunar and Planetary Laboratory, University of Arizona, Tucson
AZ 85721

Research supported during 1990 by the Planetary Geology and Geophysics program under the grant entitled 'Studies in Planetary Rings' was, in part, devoted to examining Voyager imaging data for the purpose of understanding the kinematics and dynamics of the Neptune ring arcs (1). I have found that a radial distortion of amplitude 30 km is traveling through the arcs with a wavenumber, orientation, and pattern speed expected for Lindblad resonance perturbation by the nearby satellite 1989N4 (Figs. 1 and 2.) Two new and smaller arcs within the outer Neptunian ring have also been discovered. The longitudinal spacing of all arcs, which now appear to be 5 in number, is roughly that expected for corotational arc shepherding by 1989N4 providing that not all the corotation sites in the arc region are filled. The semimajor axis of the arcs' orbit inferred from their observed mean motion (2) and the latest Neptune gravitational parameters (3) is, within uncertainties, identical to the location of the 42:43 corotation-inclination resonance of 1989N4, an observation which supports the notion of corotational arc-shepherding (4). This hypothesis also explains the 15 km radial width of the arcs as being due to a spread in forced orbital eccentricities, NOT a spread in orbital semimajor axis. 'Clumps' within the arcs have been observed at a greater frequency than previously reported (5). These features may be the manifestation of big bodies within the arcs providing a source of ring dust (5), or they may be a kinematical effect associated with the crossing of eccentric orbits at quadrature. The inclusion of groundbased observations of the arcs taken up to 5 years ago will lengthen the baseline over which arc dynamics may be studied and should lead to a refinement in the position of the Neptune spin and invariable plane poles. (This research was supported in part by NASA grant NAGW-960.)

REFERENCES. 1. Porco, C.C. (1990). *Science*, submitted; 2. Nicholson, P. D., et al. (1990). *Icarus*, 87, 1; 3. Jacobson, R., et al. (1990). AIAA/AAS Astrodynamics Conference, Paper 90-2881, Portland OR; 4. Goldreich, P., Tremaine, S., and Borderies, N. (1986). *Astron. J.*, 92, 490; 5. Smith, B. A., et al. (1989). *Science*, 246, 1422.

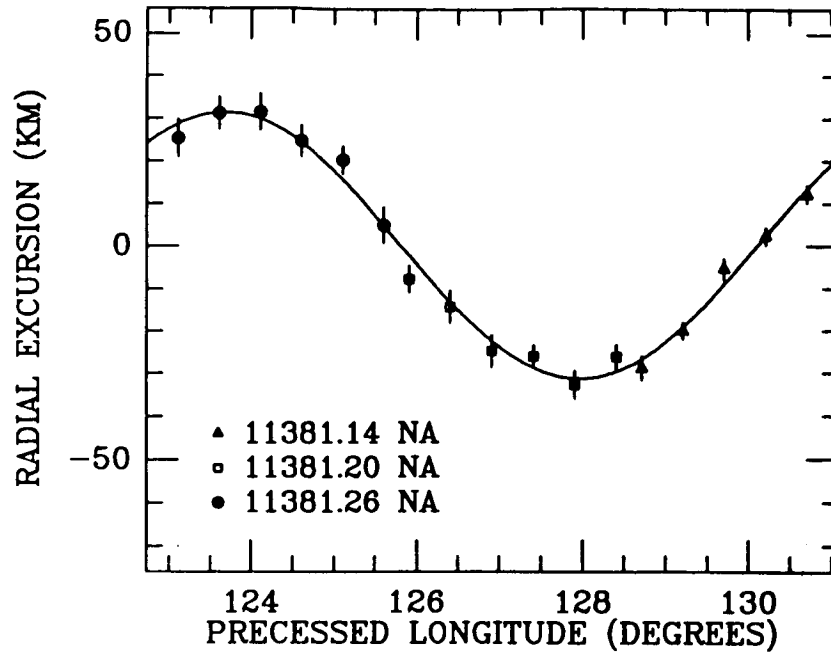


Figure 1. The measurements of longitude and radial excursion made on the trailing arc as imaged in three narrow angle Voyager frames taken 7.2 hours before Voyager closest approach to Neptune. All data points have been precessed back to a common epoch using a pattern speed equal to the 1989N4's mean motion, 839.6598 deg/day. The solid line indicates a portion of the 42-lobed pattern which best fits the data.

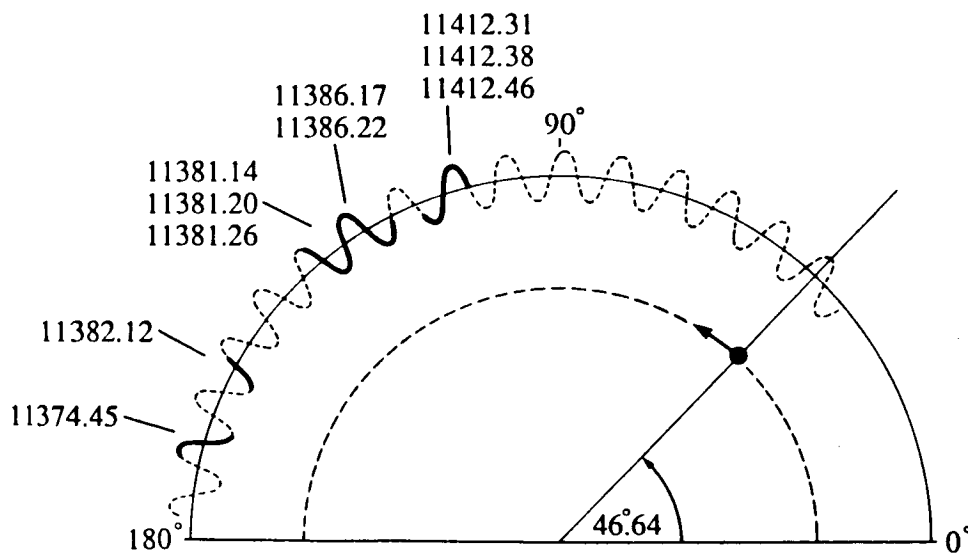


Figure 2. The orientation of the 42-lobed pattern and the position of 1989N4 on 18 August, 1989, 12:00 Ephemeris Time. Voyager observations of this pattern as it was imaged passing through the arcs at the times of the high resolution retargetted frames (indicated by FDS number) are shown as solid lines.

DERIVATION OF MID-INFRARED (5-25 μ m) OPTICAL CONSTANTS OF SOME SILICATES AND PALAGONITE

T.L. Roush^{1,2}, J.B. Pollack², and J.B. Orenberg¹, ¹San Francisco State University, ²NASA Ames Research Center

Recent reports concerning the mid-infrared reflectance properties of silicates [1,2,3] coupled with recent observations of the Earth [4] and other planets [5,6,7,8,9,10] in the mid-infrared and the planned Thermal Emission Spectrometer scheduled as an instrument to be included on the Mars Observer all illustrate the increasing interest in the optical properties of materials in the mid-infrared and their direct application to remote sensing observations of other planetary surfaces. As the laboratory and observational data increase they will ultimately be modeled to aid in the understanding of the composition mineralogy, and distribution of the surface and atmospheric constituents on these bodies.

In order to facilitate such quantitative analyses, knowledge regarding the optical constants (real (n) and imaginary (k) indices of refraction) of a wide variety of pertinent materials is required. Examples of the application of such quantitative analyses to the interpretation of martian surface and atmospheric constituents, based on the optical constants of minerals, are presented in [8,11,12].

Optical constants can be readily derived from polished surfaces of cohesive materials using standard geological thin sectioning and polishing techniques. The mid-infrared optical constants of only a few specific silicate minerals are available in the literature [12,13,14,15]. Additionally, optical constants have been determined for a number of specific rock types including silicates [14,16] and limestone [17]. Recently optical constants for palagonite, typically a poorly characterized mineralogical assemblage resulting from the alteration of basaltic glass, were presented for a limited wavelength range [18].

This study was initially conceived in order to aid in the interpretation of martian surface and atmospheric aerosol mineralogy. As a result, the minerals included are biased toward samples which represent hydrated and hydroxylated silicates. These include: 1) the Al and Mg end members of the 1:1 layer lattice silicates, kaolinite and serpentine, respectively; 2) an Al-bearing 2:1 layer lattice silicate, pyrophyllite; 3) the Mg and Al smectite clays saponite and montmorillonite, respectively; and 4) a palagonite, typically a poorly characterized alteration product of basaltic glass. Due to their physical particle size clays and other materials, such as palagonite, can not be prepared using typical preparation techniques. Yet in some cases, such as for Mars, these are the materials of perhaps the greatest interest. In order to obtain a suitable sample of these less cohesive materials for the laboratory measurements a KBr pellet die was used and a pellet of the pure sample was prepared. The powders were previously separated by dry sieving and roughly 200 mg of the finest grain size fraction ($\leq 38\mu$ m) placed in the KBr die. The die was placed in a hydraulic press and the pressure increased to a maximum of roughly 0.5 to 7 Kbars on the 12mm die, depending upon the sample, and held at that pressure for five minutes. For all clays and the palagonite this produced a pellet with highly reflective surfaces at visible wavelengths.

Silicate & Palagonite Mid-IR Optical Constants: Roush, T.L. *et al.*

The reflectivities of all samples were determined by placing them at the focus of a near-normal reflectance attachment located in a Fourier transform spectrometer. The data from each sample was ratioed to the data obtained from a first surface aluminum mirror which was conservatively assumed to have a reflectance of 0.96 at all wavelengths. Data were collected from 4000 to 400 cm^{-1} (2.5-25 μm) with a constant spectral resolution of 4 cm^{-1} however, due to an increase in multiple scattering optical constants were derived only in the 2000-400 cm^{-1} (5.0-25 μm) region.

To derive the optical constants of a material as a function of wavelength we used the commonly employed technique of dispersion analysis [13,14,15,16,17,19] which describes n and k as the contributions due to a sum of classical oscillators and relates them via Fresnel's equations for non-normal incidence, to the measured near-normal reflectivity. Non-linear least squares techniques was used to minimize the differences between the observed and calculated reflectivities. In our analyses we varied both the total number of oscillators and the high frequency dielectric constant (ϵ_{∞}) to most accurately describe the measured reflectances. The final values determined represent averages of several model fits to each data set using the same number of oscillators but varying ϵ_{∞} . In all cases we required oscillator central wavelengths to fall within the range of our observations, and the oscillator strengths and widths to be non-negative. The kaolinite and serpentine data were fit with 15 and 10 oscillators, respectively, while the pyrophyllite data required 17 oscillators. The saponite data needed 8 oscillators and the montmorillonite data 15 oscillators. The palagonite data were described by 7 oscillators. For those minerals which contain abundant water, the smectites and palagonite, we were able to include an oscillator for the $\approx 6.25\mu\text{m}$ H-O-H bending mode.

Overall we found our results were extremely consistent with values previously determined for similar materials [12,15,18] but some discrepancies remain. These discrepancies may be due to differences in analysis techniques, in one study [12] only qualitative assessment of a best fit criteria was used, in another [18] transmission measurements were used along with the assumption that the real index of refraction was constant, and in another study [15] additional measurements at longer wavelengths were included. The discrepancies may also arise from differences in sample composition between the various studies.

References: [1]Salisbury *et al.*, *USGS Open-File Report 87-263*, 1987; [2]Salisbury & Walter, *JGR*, **94**, 9192, 1989; [3]Walter & Salisbury, *JGR*, **94**, 9203, 1989; [4]Bartholomew *et al.*, *J. Remote Sens.*, **10**, 529, 1989; [5]Potter & Morgan, *Proc. 12th Lunar Planet. Sci.*, 703, 1981; [6]Tyler *et al.*, *GRL*, **15**, 808, 1988; [7]Roush *et al.*, *Lunar Planet. Sci. Conf. XX*, 928, 1989; [8]Pollack *et al.*, *JGR*, **95**, 14,595, 1990; [9]Lucey *et al.*, *Bull. Am. Astron. Soc.*, **21**, 970, 1989; [10]Roush *et al.*, *submitted to Lunar Planet. Sci. XXII*, 1991; [11]Aronson & Emslie *JGR*, **80**, 4925, 1975; [12]Toon *et al.*, *Icarus*, **30**, 663, 1977; [13]Spitzer & Kleinman, *Phys. Rev.*, **121**, 1324, 1961; [14]Aronson & Strong, *Appl. Opt.*, **14**, 2914, 1975; [15]Mooney & Knacke, *Icarus*, **64**, 493, 1985; [16]Pollack *et al.*, *Icarus*, **19**, 372, 1973; [17]Querry *et al.*, *Appl. Opt.*, **17**, 353, 1978; [18]Crisp & Bartholomew, *Lunar Planet. Sci. XX*, 201, 1989; [19]Toon *et al.*, *JGR*, **81**, 5733, 1976;

THERMAL INFRARED OBSERVATIONS OF MARS (7.5-12.8 μ m) DURING THE 1990 OPPOSITION; T. Roush^{1,2,3}, F. Witteborn^{1,3}, P. Lucey^{1,4}, A. Graps^{1,5}, and J. Pollack³

¹Visiting Astronomer at the Infrared Telescope Facility which is operated by the Univ. Hawaii under contract from NASA, ²San Francisco State Univ., ³NASA Ames Research Center, ⁴Univ. Hawaii, ⁵Sterling Software

Thirteen spectra of Mars, in the 7.5 to 12.8 μ m wavelength region, were obtained on 7 December 1990 from the Infrared Telescope Facility (IRTF) atop Mauna Kea, Hawaii. Throughout the night the humidity was $6 \pm 3\%$. For these observations a grating with an ultimate resolving power of 120 (shortest wavelengths) to 250 (longest wavelengths) was used and wavelengths were calibrated for each grating setting by comparison with the absorption spectrum of polystyrene measured prior to each set of observations. By sampling at the Nyquist limit at the shortest wavelengths, an effective resolving power of about 120 over the entire wavelength range was achieved. A total of four grating settings were required to cover the entire wavelength region. The wavelength of each was: 1) 7.50-9.53 μ m; 2) 7.615-9.64 μ m; 3) 9.50-11.35 μ m; and 4) 11.23-12.83 μ m. A typical observing sequence consisted of: 1) positioning the grating in one of the intervals; 2) calibrating the wavelength positions; and 3) obtaining spectra for a number of spots on Mars. Several observations of the nearby stellar standard star α Tauri were also acquired throughout the night. Each Mars spectrum represents an average of 4 to 6 measurements of the individual Mars spots. As a result of this observing sequence, the viewing geometry for a given location or spot on Mars does not change, but the actual location of the spot on Mars' surface varies somewhat between the different grating settings (see Figure 1).

A 1.6 arc second aperture was used and when convolved with the nominal seeing (≈ 1.5 arc seconds) results in an effective aperture size of 2.2 arc seconds. Because 1) the effective size of the aperture was small relative to Mars (≈ 18 arc seconds) and 2) the center of the spots were separated by 2.5 arc seconds the spectra were able to sample variations in both martian surface albedo and air mass. Ten of the spectra sampled along the central meridian of Mars during two different times during the night (e.g. Figure 1). Early in the evening these spectra sampled from 200-220W and 45N-70S. Late in the evening these spectra sampled from 260-280W and roughly the same latitudinal range. Also, late in the evening two additional spectra sampled along the photometric equator, providing spectra of relatively high martian air mass with both relatively high and low ground temperatures. One additional spectrum was obtained by tracking the classical low albedo feature, Syrtis Major as it rotated across the disk.

Initial analysis of these data is underway and comparisons with similar observations obtained from the Kuiper Airborne Observatory during the 1988 [1] and 1990 [2] oppositions are planned. Several ratio spectra are shown in Figure 2 where the spectrum of each spot on Mars is divided by the spectrum of the center spot. These ratios exhibit differences which are due to both atmospheric and surface variations.

References: [1]Pollack *et al.*, JGR, 95, 14,595 [2]Pollack *et al.*, pers. comm. 1991.

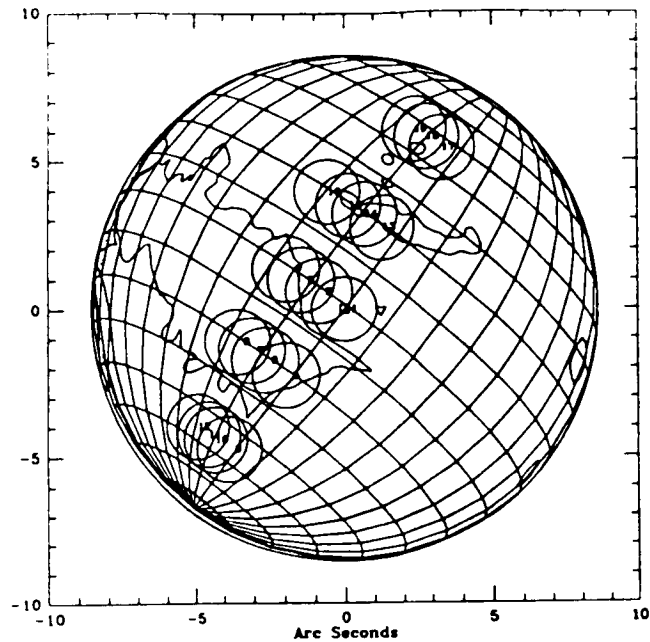


Figure 1. Location of spots where spectral data were obtained during the early observing session. The outline of several topographic and albedo features of Mars are included for orientation, North is to the upper right and the morning limb is to the left. Each circle represents the region of the surface for which spectra were collected. Circle number 1 at the center of the disk represents the area sampled by the shortest wavelength grating setting and by the time the data was collected for the next grating setting the region indicated by circle number 2 had rotated to the position of circle 1. Sub-Earth point (\square), Lat.=10.96S, Long.=200.06W. Sub-solar point (∇) Lat.=6.23S, Long.=193.23W.

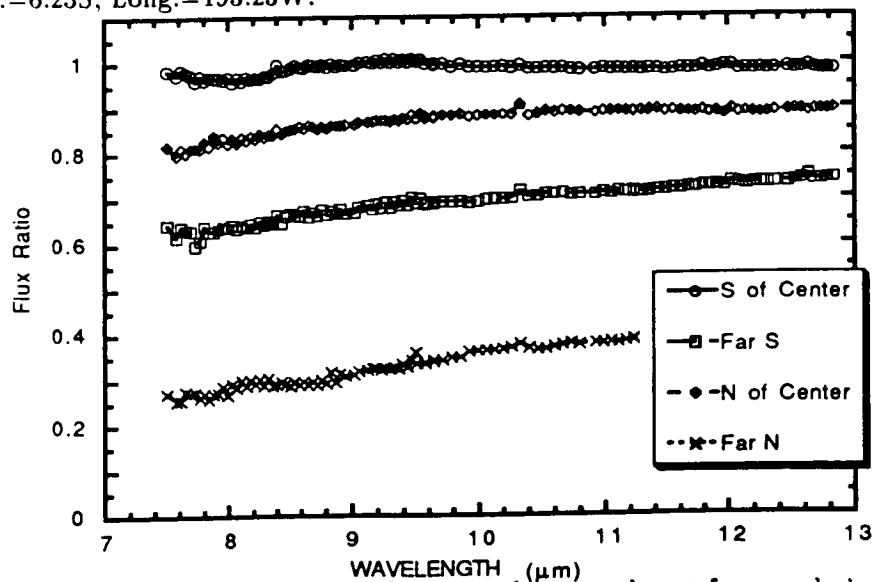


Figure 2. Spectra of the various spots relative to the central spot from early in the evening on 7 December 1990. Spectra from each grating setting are scaled to each other in the region of overlap.

PLANETARY ORIGIN, EVOLUTION AND STRUCTURE

David J. Stevenson, Division of Geological and Planetary Sciences, Caltech, Pasadena, CA 91125.

Here are three areas of recent and ongoing research under this general title:

Giant Planet Heatflows

Conventional wisdom¹ attributes the heatflow of the giant planets to the gradual loss of primordial heat, except in the case of Saturn where helium separation is evidently occurring.² There are two problems with this picture: (1) The observed helium abundance of Saturn's atmosphere is so low³ that Jupiter must also be differentiating helium since its internal entropy cannot be much higher than Saturn; (2) The heatflow of *Neptune* (not to mention *Uranus*) is too high to be consistent with adiabatic cooling from an initial hot state.

I believe that I have a self-consistent solution to these difficulties. In the case of Jupiter and Saturn; my cooling models yield the correct present-day heatflows and present-day atmospheric helium abundances for both planets, but only if both planets have an innermost region (~30% of the mass) that does not participate in the cooling. In the case of Jupiter, this cannot be a core of ice and rock (since it is too large) but must be a region of stable stratification, presumably created by the partial mixing and imperfect settling that occurs during the accretion of large ice and rock planetesimals early in Jupiter's history. The stably stratified region must have a substantial molecular weight gradient, yet is thermally superadiabatic. In effect, this model denies the validity of the simple, adiabatic cooling for Jupiter even though that model yields the correct heatflow. The implication of stable stratification is consistent with ideas of planetary accretion.⁴ The Jupiter model will be testable by the Galileo probe.

In the case of *Uranus* and *Neptune*, stable stratification is even more important and is predicted to be larger for *Uranus* than for *Neptune*. This is compatible with but not readily tested by interior models based solely on the gravity field.⁵ The necessary presence of large, stably stratified zones in these planets is probably essential to an understanding of their unusual magnetic fields.

Despinning Protogiant Planets

There are two views of giant planet accretion. In the best quantified view,⁶ protoJupiter or protoSaturn fills much of its Hill sphere and then cools and contracts, leaving behind a disk of material from which the satellite system forms. An alternative view envisages an accretion disk even as gas accumulation continues; this is analogous to the standard picture of solar system formation⁷ and arises if the dust opacity is low because of aggregation into "large" bodies (centimeters is large enough). In either case, there is certain to be a late phase in which the protogiant planet is surrounded by a disk of material with which it interacts through "viscous" torques, inflow, and outflow. In these circumstances, it is not possible for the protoplanet to exhibit a surface rotation rate very different than rotational break-up.^{8,9} For reasonable moments of inertia, this implies an angular momentum substantially larger (typically by a factor of two) than currently observed for Jupiter and Saturn. This is a fundamental problem in the spin of giant planets.

Graduate student Toshiko Takata and I have been modeling the possible despinning of these protoplanets by hydromagnetic torques. Our model has some similarity with stellar despinning models.^{10,11} The main idea of the model is exhibited in Figure 1, which shows that angular momentum is transferred from the protoplanet to the disk at all radii beyond corotation because of the coupling of planetary dipole field lines to the disk fluid and the resulting current and Lorentz force thereby created. We find that bombardment of high energy particles created by *Jupiter* and flowing along fieldlines is a potentially adequate source of ionization and conductivity. Figure 2 shows despin times (time to reach the current angular momentum) as a function of protoplanet surface magnetic field and for two choices of protoplanet radius and two choices of magnetic diffusivity. Our most optimistic diffusivity model yields $\lambda = 10^{14}$ cm²/s, but the solid lines ($\lambda = 10^{15}$ cm²/s) are probably more realistic. The dashed lines are a pessimistic case. All these models assume a disk of the kind believed appropriate for spawning the Galilean satellites.¹² This model is uncomfortably marginal but seems capable in principal of explaining the spin states of *Jupiter* and *Saturn*, provided both planets had large primordial fields.

How Titan Hides its Ocean

Until recent, the favored picture for *Titan's* surface was a roughly kilometer-thick ethane/methane ocean,¹³ presumably global in extent with at most a few outcroppings of "dry" land. The depth of the ocean is well constrained (to within a factor of two) by *observed* atmospheric properties (presence of methane, escape of hydrogen) and the constraints on subaerial topography are obtained indirectly from tidal considerations.¹⁴

The only observational approach currently available for directly establishing the character of the surface is radar.¹⁵ They observe a radar albedo of ~ 0.35 , clearly incompatible with a global hydrocarbon ocean. I have been pursuing a different picture for *Titan's* surface, partially motivated by ideas that Jon Lunine and I considered many years ago,¹⁶ but primarily motivated by the perspective that methane on *Titan* should more properly be considered as a magmatic fluid. In this picture, methane is stored subsurface in "magma chambers" fed from deep-seated (perhaps very ancient) sources of methane, most probably due to the high pressure breakdown of methane clathrate, as previously suggested.¹⁷ I show that magma chambers of methane tend to sink because of the temperature and pressure-dependent solubility of water in methane; this can balance the tendency to rise because of buoyancy. A natural "perching level" for these chambers is predicted, typically ten or so kilometers beneath *Titan's* surface for kilometer-sized diapirs. From this level, a labyrinth of cracks and caverns could connect to the surface, providing a continuous source of methane for the atmosphere. Only a few square meters of opening between deep storage and the atmosphere is needed to maintain chemical and vapor pressure equilibria between these reservoirs. The model is compatible with tidal dissipation provided the subsurface hydrocarbon liquid is *not* globally interconnected by large aperture ("rapid transit") tunnels. The model is most plausible for methane supplied from below but may even work for methane supplied from above (and seeping downward).

Acknowledgement

This work was supported by NASA under grant NAGW-185.

References

- (1.) Hubbard (1980). *Rev. Geophys. Space Phys.* **18**, 1. (2.) Hubbard and Stevenson (1984). In *Saturn*, Univ. Arizona Press, p. 47. (3.) Gautier and Owen (1989). In *Origin and Evolution of Planetary and Satellite Atmospheres*, Univ. Arizona Press, p. 487. (4.) Stevenson (1985). *Icarus* **62**, 4. (5.) Podolak, Hubbard, and Stevenson (1991). *Uranus*, Univ. Arizona Press, in press. (6.) Pollack and Bodenheimer (1989). In *Origin and Evolution of Planetary and Satellite Atmospheres*, Univ. Arizona Press, p. 564. (7.) Cameron (1988). *Ann. Rev. Astron. Astrophys.* **26**, 441. (8.) Paczynski (1991). *Ap. J.* **370**, 597. (9.) Popham and Narayan (1991). *Ap. J.* **370**, 604. (10.) Ghosh and Lamb (1979). *Ap. J.* **232**, 259. (11.) Königl (1991). *Ap. J.* **370**, L39. (12.) Lunine and Stevenson (1982). *Icarus* **52**, 14. (13.) Lunine, Stevenson, and Yung (1983). *Science* **222**, 1229. (14.) Sagan and Dermott (1982). *Nature* **300**, 731. (15.) Muhleman *et al.* (1990). *Science*, **248**, 975. (16.) Lunine and Stevenson (1985). In *Proc. NATO Conf. Ices in the Solar System*, p. 741. (17.) Lunine and Stevenson (1987). *Icarus* **70**, 61.

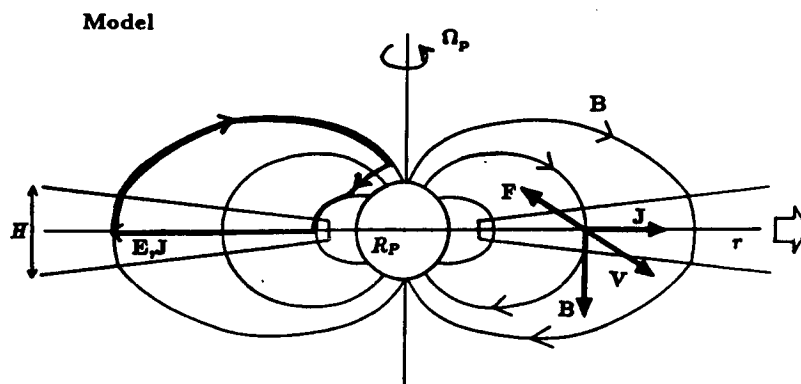


Figure 1. Model for a hydromagnetically coupled disk and protogiant planet.

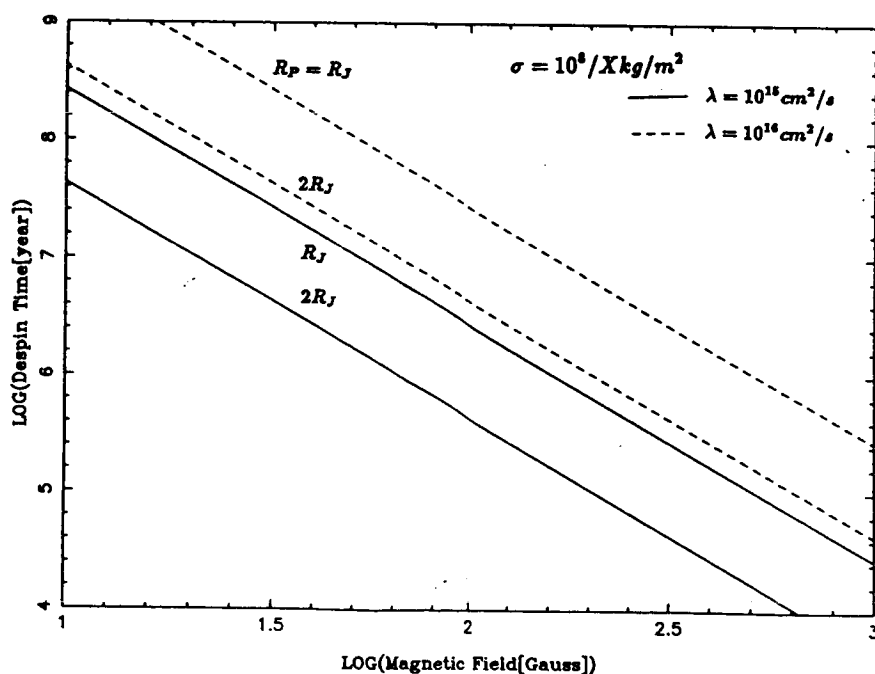


Figure 2. Despin time (time to reduce spin angular momentum of the giant planet to its current value) as a function of planetary surface magnetic field.

Tidal Evolution of Planetary Satellites

William C. Tittlemore, Lunar and Planetary Laboratory,
University of Arizona, Tucson, AZ 85721

Early in the history of the Solar System, Europa and Ganymede may have evolved through a 3:1 mean-motion commensurability (Tittlemore 1990b), which would have been encountered prior to the establishment of the current Laplace resonance involving Io, Europa and Ganymede. If Europa and Ganymede passed through the 3:1 mean-motion commensurability, the orbital eccentricities of both satellites may have increased to large values during a phase of chaotic behavior, after which the satellites would have escaped from the resonance. In spite of the relatively large J_2 of Jupiter, Europa and Ganymede are sufficiently massive and distant from the planet that resonances at the 3:1 mean-motion commensurability interact strongly, leading to chaotic behavior via the same kinds of dynamical mechanisms present at resonances among the Uranian satellites (see Tittlemore and Wisdom 1988, 1989, 1990; Tittlemore 1990a).

As a result of the large eccentricity increases possible during the evolution of Europa and Ganymede through the 3:1 mean-motion commensurability, tidal heating may have melted water ice in the mantles of both satellites, and stresses on the lithospheres of both satellites due to tidal deformation may have been sufficient to cause extensive fracturing, making resurfacing possible. This may account for the post-heavy bombardment geological activity on both Europa and Ganymede. In addition, the effects of resonance passage on Ganymede may provide an explanation of the Ganymede-Callisto dichotomy – that is, Ganymede has had a much more active geological history than Callisto, despite the fact that the two have similar bulk properties – by providing Ganymede with an intense source of internal heat and lithospheric stress not present in Callisto.

This model is consistent with a number of suggested mechanisms for the resurfacing of Ganymede. For example, if both Ganymede and Callisto were deeply differentiated during accretion, they both may have undergone a convective instability during freezing of the ice mantle proposed by Kirk and Stevenson (1987). If this instability occurred during heavy bombardment, the evidence would have been obliterated by impact craters. If tidal heating later on led to the remelting of Ganymede's ice mantle after the cessation of heavy bombardment, a second episode of diapirism may have occurred on Ganymede only as the mantle refroze.

Alternatively, if Ganymede and Callisto were only partly differentiated during accretion, both may have possessed an "accretional trigger" (Mueller and McKinnon 1988). Tidal heating may have been sufficient in Ganymede to "pull the trigger" and initiate runaway differentiation (*e.g.* Friedson and Stevenson 1983), while Callisto remained only partly differentiated. During runaway differentiation, further melting of the ice and global expansion of Ganymede (*e.g.* Squyres 1980) would have occurred, and as pointed out by Mueller and McKinnon (1988), after runaway differentiation Ganymede may have been susceptible to the

convective instability of Kirk and Stevenson (1987) as the mantle froze again.

Either way, the combination of melting and fracturing due to tidal effects and the resurfacing mechanisms described above may explain the timing and duration of the late resurfacing of Ganymede, which in turn provides an explanation of the Ganymede-Callisto dichotomy.

Acknowledgements:

This research was supported in part by the NASA Planetary Geology and Geophysics Program under Grant NAGW-1720.

References:

- Friedson A. J. and Stevenson, D. J. (1983). *Icarus* **56**, 1-14.
Kirk R. L. and Stevenson, D. J. (1987). *Icarus* **69**, 91-134.
Mueller S. and McKinnon, W. B. (1988). *Icarus*, **76**, 437-464.
Squyres, S. W. (1980). *Geophys. Res. Lett.* **7**, 593-596.
Tittlemore, W. C. (1990a). *Icarus* **87** 110-139.
Tittlemore, W. C. (1990b). *Science* **250**, 263-267.
Tittlemore, W. C. and Wisdom, J. (1988). *Icarus* **74**, 172-230.
Tittlemore, W. C. and Wisdom, J. (1989). *Icarus* **78**, 63-89.
Tittlemore, W. C. and Wisdom, J. (1990). *Icarus* **85**, 394-443.

WRINKLE RIDGE - UPLAND SCARP TRANSITIONS: IMPLICATIONS FOR THE MECHANICAL PROPERTIES OF THE DEFORMED MATERIALS.

Thomas R. Watters and Michael J. Tuttle, Center for Earth and Planetary Studies, National Air and Space Museum, Smithsonian Institution, Washington, D.C. 20560, and Debra Simpson, Department of Geology and Astronomy, West Chester University, West Chester, Pennsylvania, 19383

Wrinkle ridge - upland scarp transitions are structures that occur at the contact between smooth plains material and highlands or uplands materials on the Moon and Mars. In the smooth plains material the structures have a morphology typical of wrinkle ridges, interpreted to be the result of a combination of folding and thrust faulting [see 1, 2]. Where the structures extend into the uplands, a distinct change in the morphology occurs. The generally asymmetric cross sectional geometry characteristic of wrinkle ridges becomes that of a one-sided, often lobate scarp. The scarp is indistinguishable from other highland/upland scarps, interpreted to be the result of reverse or thrust faulting.

On the Moon wrinkle ridge - scarp transitions occur at the margins of mare basins and extend into adjacent highlands. Examples are found in the Taurus-Littrow area of Mare Serenitatis (Lee Lincoln scarp), in western Serenitatis (West Serenitatis scarp), in the area of Montes Rhipaeus and near Fra Mauro [3, 4, 5]. On Mars two examples of wrinkle ridge - scarp transitions have been found. The smooth plains (presumably volcanic in origin) of a roughly 80 km basin, in the area just northeast of Herschel basin, have been deformed into a first-order ridge [see 1]. Deformation can be trace along the trend of the ridge outside the basin into the adjacent uplands. In the uplands the morphology of the structure is clearly that of a scarp. Another wrinkle ridge - scarp transition has been found in southwestern Lunae Planum at the contact between the ridged plains material and a elevated and highly degraded unit (Fig. 1). Within the unit the morphology of the structure is that of a sharp, linear scarp. Detailed mapping of the region, as part of the Mars Geologic Mapping Program, indicates that this unit is Noachian upland material.

Although these structures are rare, they provide important insight into the mechanical properties of the deformed materials. Wrinkle ridges on the Moon and analogous structures on the Columbia Plateau [1] occur in flood basalt sequences that are emplaced as a series of extensive planar sheets or layers. Based on photogeologic evidence, ridged plains units on Mars are also interpreted to be volcanic in origin, possible akin to flood basalts. Evidence of layering in ridged plains material has also been recently discovered [6]. Individual or groups of flows in a flood basalt sequence are commonly separated by interbeds. Evidence of interbeds has been found in mare basalts [7], the Grand Ronde basalts of the Columbia River Basalt Group [8] and have been suggested to exist in ridged plains sequences on Mars [9].

A layered material may be mechanically anisotropic under conditions of deformation and the anisotropy may control the geometry of the structure. Where deformation occurs at the free surface, a layered sequence of rocks would be expected to exhibit brittle behavior and

folding will occur by slip between layers or flexural slip [10]. Of course this will occur only if the shear stress on the surfaces of the layers exceeds the frictional resistance to slip between the layers. Slip would preferentially, but not exclusively, occur between layers separated by mechanically weak interbeds. It is plausible then that the presence of layering and interbeds in the mare basalts, the CRBG and martian ridged plains have influenced, if not controlled, the style of deformation. This is being explored using finite element modeling where variable slip conditions between layers can be assigned. The lunar highlands and martian uplands, in contrast, probably lack any dominant fabric such as layering and would be expected to be mechanically isotropic. Under conditions at the free surface, a mechanically isotropic material would be expected to fail in shear resulting in reverse or thrust faulting. Wrinkle ridge - scarp transitions and the contrast between the dominant style of compressional deformation in smooth plains volcanic sequences (i.e., wrinkle ridges) and uplands (i.e., scarps) on the Moon and Mars can thus be explained by a contrast in the mechanical properties of the materials.

These results were presented at the 22nd Lunar and Planetary Science Conference in Houston, Texas, March 18-22, 1991. This research was supported by NASA grant NAGW-940 and NAGW-1172.

References:

- [1] Watters, T.R., *JGR* 93, 10,236-10,254, 1988.
- [2] Plescia, J.B. and M.P. Golombek, *GSA Bull.*, 97, 1289-1299, 1986.
- [3] Lucchitta, B.K., *Proc. LSC VII*, 2761-2782, 1976.
- [4] Howard, K.A. and W.R. Muehlberger, *NASA Spec. Publ.*, SP-330, 31-12--31-21, 1973.
- [5] Watters, T.R., Tuttle, M.J. and J. Chadwick, *LPSC*, XIX, 1247-1248, 1988.
- [6] Scott, D.H., Work in progress in Kasei Valles, MTM 25052, 25057, 1991.
- [7] Peeples, W.J., R.W. Sill, T.W. May, S.H. Ward, R.J. Phillips, R.L. Jordan, E.A. Abott, and T.J. Killpack, *JGR*, 83, 3459-3468, 1978.
- [8] Reidel, S.P., T.L. Tolan, P.R. Hooper, M.H. Beeson, K.R. Fecht, R.D. Bentley, and J.L. Anderson, *Geol. Soc. Am. Sp. Paper* 239, 21-53, 1989.
- [9] Watters, T.R., *JGR*, in press, 1991.
- [10] Donath, F.A. and R.B. Parker, *GSA Bull.*, 75, 45-62, 1964.

ORIGINAL PAGE
BLACK AND WHITE PHOTOGRAPH



Fig. 1. Wrinkle ridge-scarp transition located in southwest Lunae Planum.

WRINKLE RIDGES IN THE FLOOR MATERIAL OF
KASEI VALLES, MARS: NATURE AND ORIGIN

Thomas R. Watters and Robert A. Craddock, Center for Earth and Planetary Studies, National Air and Space Museum, Smithsonian Institution, Washington, D.C. 20560

Wrinkle ridges on Mars occur almost exclusively in smooth plains material referred to as ridged plains. One of the largest contiguous units of ridged plains occurs on Lunae Planum on the eastern flank of the Tharsis rise (Fig. 1). The eastern, western and northern margins of the ridged plains of Lunae Planum suffered extensive erosion in early Amazonian channel-forming events. The most dramatic example of erosion of the ridged plains is in Kasei Valles. Robinson and Tanaka [1,2] describe two stratigraphic units exposed in Kasei Valles. The surface of the upper unit is the surface of the ridged plains material, most of which has not been affected by erosion [3]. The surface of the lower unit is estimated to be 1,000 m below the surface of the ridged plains [1].

Some landforms on the lower surface are recognizable as wrinkle ridges, but they are rare and generally heavily degraded (Fig. 2). The degraded ridges are dimensionally equivalent to first-order ridges [4] and their orientations are consistent with those on Lunae Planum. This suggests that they are erosional remnants of preexisting ridges formed in the same tectonic episode that produced the Tharsis circumferential wrinkle ridge system [5]. If this is the case, the existing topographic relief of the ridges in the lower unit represents some fraction of the total structural relief and suggests that the entire ridged plains to depth has deformed or buckled [4].

In addition to the degraded ridges, more pristine appearing ridges have been identified (Fig. 3). These ridges are rare and are smaller-scale features relative to the degraded ridges, in the size range of second-order ridges [see 2]. The pristine wrinkle ridges, in contrast to the degraded ones, appear to be the result of post-erosion deformation. The limited number and extent of these structures suggests that they are the result of local compressional stresses, confined to the lower unit or floor of Kasei Valles. One explanation for the origin of the compressional stresses is that they are the result of the removal of the overlying material. If the materials behave elastically and are laterally confined so that uniaxial strain can be assumed (the horizontal components of strain are zero), then the horizontal stresses can be determined from elastic theory. Given that the state of stress in the materials prior to erosion is lithostatic, erosion reduces the horizontal stress by

$$[\nu/(1-\nu)]\rho g\Delta h$$

where Δh is the thickness of the section removed and ν is Poisson's ratio. The horizontal stress is thus given by

$$[(1-2\nu)/(1-\nu)]\rho g\Delta h$$

[6,7]. The horizontal stress as a function of Δh , assuming a mean density of the overburden is equal to that of basalt ($2,900 \text{ kg m}^{-3}$), is shown in Fig. 4. If as much as 1,000 m of material was removed by erosion,

the horizontal stress in the lower unit would be on the order of 7.3 to 14.5 MPa, perhaps sufficient to generate small scale wrinkle ridges. Residual tectonic stresses may have been a component of the total compression that resulted in ridge formation. This would explain the agreement between the orientation of the wrinkle ridges in the floor materials with those in the ridged plains material of Lunae Planum. Thermal as well as mechanical effects may influence the horizontal stress after erosion [see 5]; however, because the thermal gradient on Mars is estimated to be low, this effect is considered to be negligible.

These results were presented at the 22nd Lunar and Planetary Science Conference in Houston, Texas, March 18-22, 1991. Supported by NASA Grants NAGW-940, NAGW-1172, and NAGW-1780.

Figure 1. Photomosaic of northeastern Lunae Planum and a portion of Kasei Valles from 20° to 30° Lat. and 67.5° to 55° Long. Insets show location of Figs. 2 and 3. Map is from the U.S. Geological Survey, Miscellaneous Investigations Series Map I-1305 (MC-10NE), 1980.

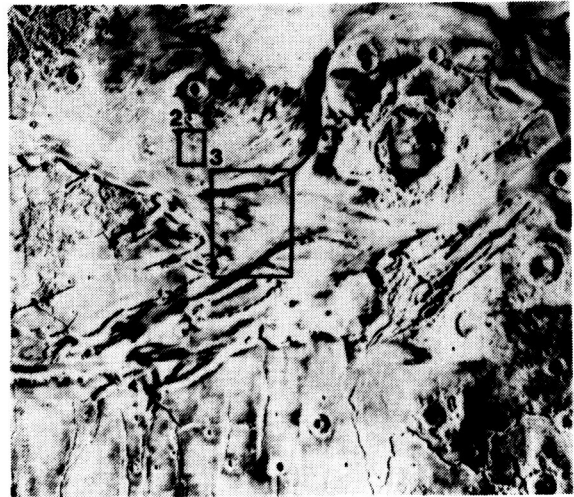


Figure 2. Heavily degraded first-order ridge on the floor of Kasei Valles. Viking orbiter photographs 226A07, 226A09, 226A11, 520A29, 665A40, 665A42, and 665A44. Resolutions range from 35 to 195 m/pixel.

ORIGINAL PAGE
BLACK AND WHITE PHOTOGRAPH

Figure 3. Pristine, small ridge which deform channel materials. Such ridges may be the result of overburden removal after channel formation. Viking orbiter photographs 665A35-38 with resolutions of 35 m/pixel.



ORIGINAL PAGE
BLACK AND WHITE PHOTOGRAPH

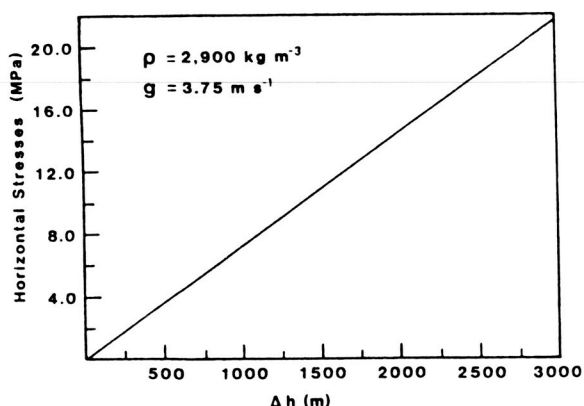


Figure 4. Diagram showing horizontal stress as a function of the amount of overburden removed (Δh). As much as 3 km of material may have been removed in areas of Kasei Valles [2].

References:

- [1] Robinson, M.S. and K.L. Tanaka, *MEVTV Workshop on Surface Units on Mars, LPI 88-05*, 106-108, 1988.
- [2] Robinson, M.S. and K.L. Tanaka, *Geology*, 18, 902-905, 1990.
- [3] Craddock, R.A. and T.A. Maxwell, *Lunar Planet. Sci.*, XXII, v. 1, 247-248, 1991.
- [4] Watters, T.R., *JGR*, 93, 10, 236-10, 254, 1988.
- [5] Watters, T.R. and T.A. Maxwell, *JGR*, 91, 8113-8125, 1986.
- [6] McGarr, A. and N.C. Gay, *Ann. Rev. Earth & Planet. Sci.*, 6, 405-436, 1978.
- [7] Turcotte, D.L. and G. Schubert, *Applications of Continuum Physics to Geological Problems*, John Wiley & Sons, New York, 1982, 450p.

**PROPERTIES OF DUST AND CLOUDS IN THE MARS ATMOSPHERE:
ANALYSIS OF VIKING IRTM EMISSION PHASE FUNCTION SEQUENCES;**
R.T. Clancy and S.W. Lee, Laboratory for Atmospheric and Space Physics, University of Colorado, Boulder, CO 80309

An analysis of emission-phase-function (EPF) observations from the Viking Orbiter infrared thermal mapper (IRTM) yields a wide variety of results regarding dust and cloud scattering in the Mars atmosphere and atmospheric-corrected albedos for the surface of Mars. Several hundred of these EPF sequences were returned during the Viking Orbiter missions, in which the visual brightness (solar band $\lambda = 0.3 - 3.0 \mu\text{m}$, $0.3 - 3.0 \mu\text{m}$ band width) of the surface/atmosphere over a given region was viewed over a substantial range of phase angles as the spacecraft passed overhead. These observations include polar latitudes, the Viking Lander sites, and other regions of specific interest such as Olympus Mons and the Hellas basin. They also span a considerable range of solar longitude (L_s), including periods before, during, and after the global dust storms of 1977, and periods of polar hood formation at mid-latitudes and spring clouds at northern polar latitudes.

A multiple scattering radiative transfer model incorporating a bidirectional phase function for the surface and atmospheric scattering by dust and clouds is used to derive surface albedos and dust and ice optical properties and optical depths for these various conditions on Mars. The specific photometric function of the surface of Mars is not well constrained by the EPF observations, although a resolved phase coefficient of $\sim 0.01 \text{ mag/deg}$ is indicated by low-phase-angle, low-dust-loading sequences for both bright and dark regions on Mars. The dust and cloud optical depths are well constrained by the increased scattering present at high phase angles ($> 70^\circ$) within the EPF data. Furthermore, the single scattering albedos ($\tilde{\omega}_0$) and phase functions of dust and cloud particles are also well defined for EPF sequences in which the dust optical depths are large ($\tau > 0.5$) and/or the range of observed phase angles is large ($> 80^\circ$).

It is possible to fit all of the analyzed EPF sequences corresponding to dust scattering with $\tilde{\omega}_0 = 0.92$, compared to the value of 0.86 derived by Pollack et al. (1979) from Viking Lander observations. The derived dust scattering phase function agrees very well with the results of Pollack et al., although the resulting single scattering asymmetry parameter is 0.55 for both measurements rather than the value of 0.79 reported by Pollack et al. The observed dust phase function and the observed ratios of infrared and visible dust opacities suggest that dust particle sizes may be 5-10 times smaller than previous analyses have indicated. Observed dust optical depths range from 2 - 3 at the peak of the global dust storms to 0.2 after the second dust storm of 1977; a dust opacity of 0.8 is determined for the south polar region during the second global dust storm of 1977. Three dust opacity determinations coinciding with Viking Lander measurements provide consistency with the Viking Lander dust opacity measurements. The surface elevation dependence of dust loading over Olympus Mons is derived from an EPF sequence during the first global dust storm of 1977. EPF sequences corresponding to cloud scattering indicate $g = 0.66$ for mid-latitude fall clouds and $g = 0.55$ for north polar spring clouds, with $\tilde{\omega}_0 = 1.0$. Cloud opacities range from 0.2 - 0.7, with a typical value of 0.5 for both the fall mid-latitude and polar spring clouds. The global range of surface albedos resulting from this EPF analysis are $\sim 10\%$ darker for bright regions and $\sim 25\%$ darker for dark regions on Mars than are currently provided by studies that do not explicitly account for the effects of atmospheric scattering.

This research was supported under NASA Planetary Geology grant NAGW-1378.

REFERENCES: Pollack, J. B., D. S. Colburn, F. M. Flasar, R. Kahn, C. E. Carston, and D. Pidek (1979). Properties and effects of dust particles suspended in the martian atmosphere. *J. Geophys. Res.*, 84, 2929-2945.

FACTORS CONTROLLING THE STRUCTURES OF MAGMA CHAMBERS IN BASALTIC VOLCANOES.
 L. Wilson^{1,2} & J.W. Head². ¹ Environmental Sci. Div., Institute of Environmental & Biological Sciences, Lancaster Univ., Lancaster LA1 4YQ, U.K. ² Geological Sciences Dept., Brown Univ., Providence RI 02912, U.S.A.

Magma chamber depths The depth to the center of a magma chamber is most probably determined by the density structure of the lithosphere. A chamber forms where the density of melts ascending from partial melting zones at depth is equal to the density of the surrounding crustal rocks: the melts are trapped at a neutral buoyancy level [1, 2]. The density of ascending melts decreases slowly as they rise at first due to decompression; eventually, at depths shallow enough that gas exsolution begins, a much more rapid decrease occurs. The density of the country rocks increases with depth due to the compaction of vesicles and pore spaces, filling of vesicles and pore spaces by hydrothermal alteration products, and ultimately by mineral phase changes.

For a given surface rock density, the depth to reach a given compaction state is probably pressure dependant, and so scales as g^{-1} : magma chamber centers would be ~ 2.65 times deeper on Mars than Earth (i.e. ~ 10 to 15 km), and about 15% shallower on Venus than Earth, if this were the only factor. If the surface rock density is less on Mars than Earth (lower atmospheric surface pressure leading to greater rock vesicularity in volcanic areas), the depths to chamber centers would be even deeper on Mars (by a factor closer to 1 than 2). If surface rock densities are higher on Venus than Earth (the high surface pressure essentially eliminating vesicularity [3]), the depths to chamber centers could be much shallower on Venus than Earth.

Presumably hydrothermal alteration is absent on Venus; however, the chemical consequences of migration of carbon dioxide-rich fluids needs to be assessed. The temperature and water availability controls on hydrothermal alteration processes on Mars are also not easy to assess, but are more likely to be depth-dependent than pressure-dependent, thus acting in opposition to the pressure-related reduced compaction trend.

Vertical extents of magma chambers It is commonly assumed that magma chambers grow until the stress on the roof, floor and side-wall boundaries exceeds the strength (compressive or tensile, as appropriate) of the wall rocks. Attempts to grow further lead to dike propagation events which reduce the stresses below the critical values for rock failure. If a magma chamber center lies at a depth D below the surface in country rocks of density ρ_{cu} , the local pressure is $P_L = \rho_{cu} g D$, where g is the gravity. If the pressure at the magma chamber center is P_C , then the excess pressure acting across the side-wall is $P_0 = P_C - P_L$. At a vertical height h above the chamber center the pressure inside the chamber is $P_{iu} = P_C - \rho_m g h$ and outside the chamber is $P_{eu} = P_L - \rho_{cu} g h$, where ρ_m is the magma density. The stress across the wall is then $(P_{iu} - P_{eu}) = (P_C - P_L) - g h (\rho_m - \rho_{cu}) = P_0 - g h (\rho_m - \rho_{cu})$. Typically $(\rho_m - \rho_{cu}) \sim 300 \text{ kg/m}^3$.

Table 1 shows values of $(P_{iu} - P_{eu})$ for P_0 in the range 1 to 9 MPa and a series of values of h ; equivalent values of h for the Earth, Mars and Venus are given. On the assumption that the tensile strength of the country rocks is 4 MPa and the compressive strength is 7 MPa, the Table indicates by (T) and (C) the combinations of P_0 and h which lead to tensile or compressive failure of the walls. The tensile failure conditions near $h = 0$ lead to lateral dike intrusion events. Compressive failure at large values of h leads to cracks in the roof and possibly slight subsidence of roof blocks. Any magma intruded into these cracks freezes and re-seals the roof; any massive

subsidence of blocks extending all the way to the surface represents a caldera collapse event, but also leads to loading of the magma in the chamber by the weight of the overlying blocks. The consequent increase in $P_0 = P_C - P_L$ then causes lateral, rather than vertical, dike propagation. These arguments suggest that vertical magma chamber extents will be ~ 2-65 times greater on Mars than Earth (the ratio of the gravities).

Failure of the magma chamber roof in compression does not lead to upward magma migration since $\rho_m > \rho_{cu}$; summit eruptions are most likely triggered by magma vesiculation in the upper part of the chamber where ambient pressures are lowest. Table 2 shows the consequences of introducing a "foam" layer Δh thick which contains 50% by volume gas at the top of a magma chamber. It is clearly possible to produce tensile failure of the roof as long as a sufficiently thick layer of foam can be generated.

Lateral extents of magma chambers The later growth of magma chambers is accomplished by lateral dike injection into the country rocks. The patterns of growth and cooling of such dikes are controlled in a complex way by a combination of the current value of P_0 , the regional stress gradients, and the previous history of activity of the chamber [1, 4, 5]. Much further work is required in this area, but ultimately the lateral extent of a chamber must represent a balance between two episodic (and probably stochastic) processes: recharge from the mantle and discharge to form intrusions or eruptions to the surface.

References: [1] Rubin, A.M. & Pollard, D.D. (1987) Ch. 53, U.S.G.S. Prof. Paper 1350. [2] Walker, G.P.L. (1988) Ch. 41, U.S.G.S. Prof. Paper 1350. [3] Head, J.W. & Wilson, L. (1986) J.G.R. 91, 9407-66. [4] Parfitt, E.A. & Wilson, L. LPSC XIX, 903-4. [5] Parfitt, E.A., this vol.

Table 1. Values of the interior excess pressure ($P_{iu} - P_{eu}$) in a magma chamber as a function of the height, h , above the center line and the center-line excess pressure P_0 . Failure conditions are indicated by the letters T (tensile) and C (compressive).

$h(\text{Earth})$	$h(\text{Venus})$	$h(\text{Mars})$	$P_0 = 1$	3	5	7	9 MPa
0	0	0	1.00	3.00	5.00T	7.00T	9.00T
1000	1114	2649	-1.94	0.06	2.06	4.06T	6.06T
2000	2227	5297	-4.88	-2.88	-0.88	1.12	3.12
3000	3341	7946	-7.82C	-5.82	-3.82	-1.82	0.18
4000	4455	10595	-10.76C	-8.76C	-6.76	-4.76	-2.76

Table 2. Values of the interior excess pressure in a magma chamber as a function of the height, h , above the center line and the thickness, Δh , of a foam layer at the top of the chamber, for a center-line excess pressure of $P_0 = 5$ MPa. To use the table, read down the column for $\Delta h = 0$ as far as the height proposed and then replace the entry for that height with the entry on the same line in the column for the value of Δh proposed.

$h(\text{Earth})$	$h(\text{Venus})$	$h(\text{Mars})$	$\Delta h = 0$	100	300	500	700	900 m
0	0	0	5.00:T	6.27:T	8.82:T	11.37:T	13.92:T	16.47:T
1000	1114	2649	2.06	3.33	5.88:T	8.43:T	10.98:T	13.53:T
2000	2227	5297	-0.88	0.39	2.94	5.49:T	8.04:T	10.59:T
3000	3341	7946	-3.82	-2.55	0.00	2.55	5.10:T	7.65:T
4000	4455	10595	-6.76	-5.49	-2.94	-0.39	2.16	4.71

STUDIES OF VOLATILES AND ORGANIC MATERIALS IN EARLY TERRESTRIAL AND PRESENT-DAY OUTER SOLAR SYSTEM ENVIRONMENTS

Carl Sagan, W. Reid Thompson, Christopher F. Chyba, and B. N. Khare, Laboratory for Planetary Studies, Cornell University, Ithaca, NY 14853

This report constitutes a review and partial summary of individual projects within several areas of research generally involving the origin, distribution, chemistry, and spectral/dielectric properties of volatiles and organic materials in outer solar system and early terrestrial environments. Other collaborators play a prominent role in some of these studies, as indicated in the references for specific topics.

Impact delivery of volatiles and organic compounds to the early terrestrial planets.

Cometary delivery of organic molecules to the early Earth. Here (Chyba *et al.* 1990) we assess with a state-of-the-art smooth particle hydrodynamic code the survivability of the organic carbon complement of asteroids and comets during the latter part of the heavy bombardment, 4.5 Gyr to 3.8 Gyr ago. Our characterizations of the impactor flux and size distribution show that most of the mass is contributed by large impactors whose organic complement cannot survive the impact process in a 1-bar atmosphere. However, we show that objects ≤ 100 m in radius aerobraked through the ~ 10 -bar CO_2 atmosphere proposed for this period can contribute organic material at a rate $\sim 10^6$ – 10^7 kg yr^{-1} that exponentially decreases with a half-life of $\sim 10^8$ yr. Total amounts delivered could then be comparable to the contemporary oceanic (3×10^{12} kg) and total (6×10^{14} kg) terrestrial biomasses. (Fig. 1, 2.)

Exogenous sources of prebiotic organic molecules on the early Earth. In this work (Chyba and Sagan, 1991) we investigate (in addition to the delivery by direct impacts considered above) the contribution of interplanetary dust particles, airbursts, and organic synthesis driven by atmospheric and impact shock waves. We find that the inclusion of additional direct (non-shock) sources increases the delivery rate to $\sim 10^8$ kg yr^{-1} , comparable to *in situ* production rates (from lightning, coronal discharge, aurorae, etc.) for CO_2 atmospheres with high H_2 abundance. Of potentially much greater importance is the additional energy source provided by the shock waves associated with impacts, which can induce organic synthesis at rates $\sim 10^{12}$ kg yr^{-1} . At this rate a contemporary biomass is produced every 10^3 yr; even in CO_2 -dominated atmospheres the shock-driven rate is comparable to the highest rates possible from other *in situ* sources even from highly reducing atmospheres. Impact processes, directly and indirectly, likely were very important for the geochemical carbon cycle and surface organic inventory through the period leading up to the first known biological activity. (Fig. 3.)

Constraints on terrestrial volatile accretion during the heavy bombardment. Further pursuing associated questions arising from earlier work on impact delivery of volatiles (especially H_2O) to the early terrestrial planets, we investigate (Chyba 1991) the consistency between the elemental composition of Earth's upper mantle and lunar highland material, compared to the contribution we compute from heavy bombardment impacts. The delivery of large amounts of volatiles — in particular, oceanic volumes of H_2O — is consistent with known geochemical constraints. While we point out a critical need for more laboratory measurements of the H_2O content of chondritic material, we show that a nominal model of the impactor flux and composition results in the delivery of sufficient H_2O to account for the present mantle+crust inventory, while contributing quantities of C, N, S, and Cl not exceeding those estimated for the mantle+crust. The abundances of highly siderophilic "noble metals" in Earth's upper mantle are also consistent with the expected flux of late heavy bombardment meteoritic material.

Extraterrestrial amino acids and terrestrial life. In a note (Chyba 1990), we comment on recent work explaining the distribution of extraterrestrial amino acids in sediments near the K-T boundary in terms of accretion of comet-derived interplanetary dust particles associated with a main impact event, and on other work reporting a predominance of L-amino acids in the Murchison meteorite. The additional possibility of shock-production of amino acids *in situ* is raised, and is relevant to the concentration of the paper (Chyba and Sagan 1991) summarized above.

Optical constants measurements.

Optical constants of solid methane. Here (Khare *et al.* 1990) we present results for CH_4 in the VIS-NIR, including measurements of those absorption bands in solid crystalline CH_4 with complex part $k > 10^{-6}$ in the wavelength range 1.10–2.65 μm . Since CH_4 is known to be present on the surfaces of Triton and Pluto and C_2H_6 is a major photochemical product, these materials are probably both major

contributors to the still incompletely-understood reflection spectra of Triton and Pluto. (Similar results for C_2H_6 are soon to be published.)

Spectral classification, chemical processes, and distribution of materials.

Color and chemistry on Triton. Using quantitative multiband spacecraft imaging data, one can identify spectrally distinct units of material, and relate these units to the coupled chemical and volatile transport processes controlling the spectral evolution and deposition of the material. In this work (Thompson and Sagan 1990) we find that Triton's surface can be characterized by 6 major spectral units: (1) lightly colored southern hemisphere cap (SHC) material; (2) a bluish thick frost unit beyond the permanent SHC margin; (3) a thin frost unit incompletely covering the equatorial material; (4) a more strongly colored equatorial unit; (5) extremely bright spectrally neutral units; and (6) units showing anomalous UV or red absorption. We also show that sedimenting photochemical organic dust composed of C_2H_4 and C_2H_2 can be rapidly converted to colored products (over a few Triton seasons), while direct surface modification by magnetospheric electrons and cosmic rays requires much longer times. The chemical evidence would then suggest that more strongly colored units are older, while lightly colored units represent seasonal lag deposits and bright units are younger than a few Triton seasons, an interpretation consistent with the major morphological features of Triton's surface.

Triton's streaks as windblown dust. The encounter of the Voyager 2 spacecraft with Neptune's satellite Triton revealed many "dark" (about 10–20% darker than the adjacent frost) surface streaks in Triton's southern hemisphere, resembling the streaks that are due to windblown dust on Mars. It seems therefore that dust transport by winds in Triton's tenuous atmosphere is required, the main question being the mechanism for raising dust from the surface or sub-surface. The two obvious candidates are geyser-like eruptions and direct lofting by surface winds. We have demonstrated (Sagan and Chyba 1990) that, despite Triton's tenuous ($16 \pm 3 \mu\text{bar}$) atmosphere, low-cohesion grains with diameters of $\lesssim 5 \mu\text{m}$, may be carried into suspension by aeolian surface shear stress, given expected geostrophic wind speeds of $\sim 10 \text{ms}^{-1}$. (The wind velocities needed to lift grains as cohesive as those found on Earth, however, are implausibly high.) For erupting plumes, we show that dust-settling timescales and expected wind velocities yield streak length scales in good agreement with those observed. Both candidate mechanisms therefore seem to be consistent with present observations of Triton.

Radar properties of ice, hydrocarbons, and organic heteropolymers.

Titan and other icy satellites: Dielectric properties of constituent materials and implications for radar sounding. Here (Thompson and Squyres 1990) we assess the state of experimental measurements on the dielectric properties of materials relevant to radar sounding of icy satellites, and especially Titan, in expectation of further ground-based work and of planning for the Cassini spacecraft's radar system. Using straightforward dielectric theory appropriate to each type of material, we present and/or fit available measurements for H_2O ice, polyacetylene, tholins, and hydrocarbon liquids without and with polar solutes. Transmission of any surface lakes or oceans on Titan varies from optically thin to optically thick over centimeter to decimeter wavelength ranges. Using a proposed sounding mode for a Cassini radar system, only surface reflections will result at 2.2 cm wavelength, while the sub-liquid layers can be sounded at 13.6 cm. Further, both the ocean-sediment and organic sediment- H_2O ice boundaries could be detected. (Fig. 4.)

References.

- Chyba C.F. (1990) Extraterrestrial amino acids and terrestrial life. *Nature* 348, 113–114 (1990).
Chyba C.F. (1991) Constraints on terrestrial volatile accretion during the heavy bombardment. *Icarus*, in press.
Chyba C.F., Sagan C. (1991) Exogenous sources of prebiotic organic molecules on the early Earth. Submitted to *Nature*.
Chyba C.F., Thomas P.J., Brookshaw L., Sagan C. (1990) Cometary delivery of organic molecules to the early Earth. *Science* 249, 366–373.
Khare B.N., Thompson W.R., Sagan C., Arakawa E.T., Bruel C., Judish J.P., Khanna R.K., Pollack J.B. (1990) Optical constants of solid methane. In *Proceedings of the First International Conference on Laboratory Research for Planetary Atmospheres*, NASA CP-3077, pp. 327–339.
Thompson W.R., Sagan C. (1990) Color and chemistry on Triton. *Science* 250, 415–418.
Thompson W.R., Squyres S.W. (1990) Titan and other icy satellites: Dielectric properties of constituent materials and implications for radar sounding. *Icarus* 86, 336–354.
Sagan C., Chyba C.F. (1990) Windblown dust on Triton. *Nature* 346, 546–548.

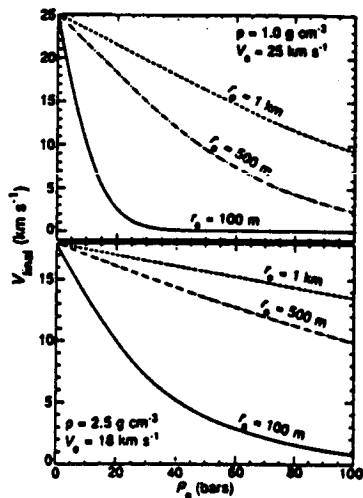


Fig. 1. Impact velocities as a function of surface atmospheric pressure for generic cometary and chondritic impactors at an incidence angle of 0° with radii of 100, 500, or 1000 m. In this illustrative model, the atmosphere is equivalent to the contemporary terrestrial one, with a surface pressure increased to P_0 .

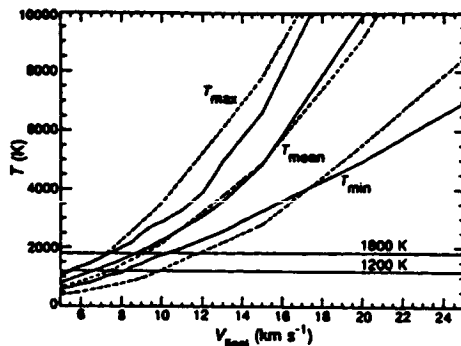


Fig. 2. Maximum, minimum, and mean temperatures for a comet impacting an ocean 3 km deep. The results here are independent of comet radius, provided the ocean is at least several cometary radii deep. The dotted lines denote temperatures obtained from the Tillotson EOS with an assumed constant specific heat capacity for ice. The solid lines represent temperatures from Sesame EOS. The temperatures 1800 and 1200 K are the temperatures for which HCN and simple organics (such as short-chain aliphatics, benzene, and H_2CO), respectively, survive shock heating for time scales comparable with those of impact. For impact velocities $\leq 10 \text{ km s}^{-1}$, a significant fraction of the organic inventory survives impact.

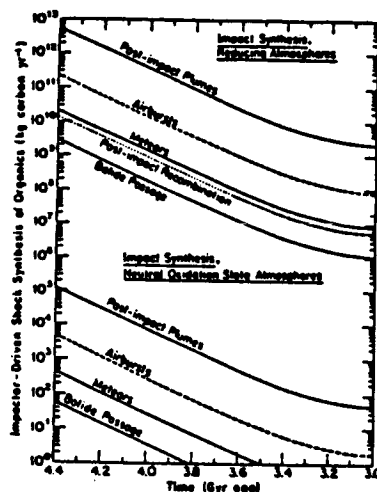
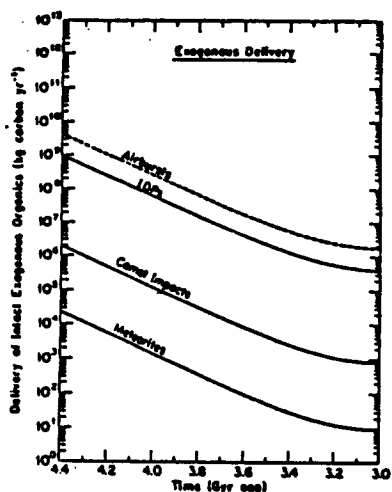


Fig. 3. Exogenous organic carbon provided to Earth as a function of time, from (a) sources delivering intact extraterrestrial organic molecules, and (b) impactor-driven shock synthesis of organics in the terrestrial atmosphere or post-impact vapor plume. Curves are labeled according to source. In (b), the upper curves are for $CH_4 + (NH_3/N_2) + H_2O$ reducing atmospheres, and the lower curves are for $CO_2 + N_2 + H_2O$ neutral oxidation state atmospheres. Solid lines represent the more secure estimates. Dashed lines indicate upper bounds, and the dotted line denotes an estimate that, while uncertain, is largely independent of the oxidation state of the atmosphere.

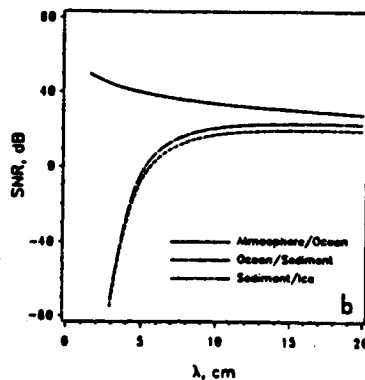
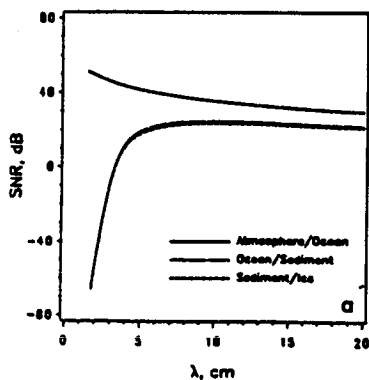


Fig. 4. Calculated signal to noise ratio (SNR) vs wavelength for radar sounding using a possible Cassini mission radar system in a 1000-km flyby of Titan. (a) low- CH_4 ($X_{CH_4} = 0.058$); (b) high- CH_4 ($X_{CH_4} = 0.81$). (See Table V.) Curves show the SNR for reflections from the upper surface of the ocean, the ocean/solid organics interface, and the solid organics/ice interface (see text for model details). Operating wavelengths for this proposed Cassini radar system are 2.2 and 13.6 cm; the longer wavelength could possibly sound the ocean floor, provided the (poorly understood) absorption of polar solutes is sufficiently low.

PRELIMINARY 1:500,000-SCALE GEOLOGIC MAPPING OF CLARITAS FOSSAE, MARS

James R. Underwood, Jr., Department of Geology, Kansas State University, Manhattan, KS 66502-3102

The Claritas Fossae system is a complex, linear fracture zone that extends from its northern intersection with Noctis Labyrinthus 1800 km south-southeast to its southern intersection with Thaumasia Fossae. The width of the fracture zone varies from 150 km in the north to 550 km in the south; topographic relief, based on radar data from Earth, is 1.0-1.5 km (Roth and others, 1980). Claritas Fossae and its co-incident ridge or rise have been interpreted to be a horst with more than 8 km of vertical uplift; the greatest such uplift on Mars (Masursky and others, 1978).

Interest in the Claritas Fossae system derives from:

1. The relationship between Claritas Fossae and other major tectonic systems with which it is associated, Noctis Labyrinthus and Thaumasia Fossae.
2. The role played by Claritas Fossae in the geologic evolution of the greater Tharsis Montes and Valles Marineris regions.
3. The possibility of the occurrence there of small volcanic centers in, or marginal to, the Claritas Fossae system.
4. The likely possibility of identifying there suitable sites for Mars landing(s), sample collection(s), and rover traverses.

Viking orbital images of sufficiently high resolution exist to provide the basis only for two 1:500,000-scale photomosaic base maps of Claritas Fossae. They extend en echelon east and west, i.e. the southeast corner of the northern and western quadrangle (MTM-30102) is coincident with the northwest corner of the eastern and southern quadrangle (MTM-25107). Preliminary geologic maps of the two quadrangles have been prepared.

Materials in the quadrangles are Noachian and Hesperian age (Scott and Tanaka, 1986), and the quadrangles are characterized by the widespread occurrence of fractured and cratered plateau material, the oldest material in the map areas. Younger smooth plains material covers the floors of craters of varied size and is widespread along the western margin of the western quadrangle. Intermediate in age are plains material, cratered plains material, fractured plains material and cratered plateau material.

Craters mostly are flat-floored and range up to 50 km in diameter. Three relative ages of crater materials have been mapped.

The structural grain is dominated by north-south fractures, and most of those occur in the fractured and cratered plateau material. Both quadrangles have a few east-west fractures; the relative ages of the two dominant fracture sets are not everywhere the same.

The apparent surface smoothness and the diversity of materials over much of the area of the two quadrangles would provide appealing sites for landing, sample collection, and traversing were it not for the problem of air-breaking at the relatively high altitude, 7-9 km above the Mars datum, of the Claritas Fossae system.

REFERENCES:

Masursky, H., A. L. Dial, and M. E. Strobell, 1978, Geologic map of Phoenicis Lacus quadrangle of Mars, U. S. Geol. Survey Misc. Invest. Ser., Map I-896.

Roth, L. E., G. S. Downs, R. S. Saunders, and G. Schubert, 1980, Radar altimetry of South Tharsis, Mars, *Icarus*, 42. 287-316.

Scott, D. H. and K. L. Tanaka, 1986, Geologic map of the western equatorial region of Mars, Scale 1:15,000,000, U. S. Geol. Surv. Misc. Invest. Ser., Map I-1802-A.

AUTHOR INDEX

- Albin, K., 503, 506
 Albin, K. K., 508
 Alexander, M. J., 229
 Allton, J. H., 412
 Arvidson, R. E., 296, 298, 301, 304, 306
 Asphaug, E., 350, 354
 Attrep, M., Jr., 375
 Aubele, J. C., 459
 Austin, R. T., 310
- Baker, V. R., 109
 Baker, V., 111
 Balsler, R. A., 80
 Banerdt, W. B., 46, 54, 82
 Batson, R. M., 483, 490, 509, 510, 511, 512, 515, 516
 Becker, T., 218
 Bell, J. F., 220, 223, 394
 Belton, M., 215, 218
 Benz, W., 444
 Bertolini, L. M., 80
 Besancon, J. R., 253
 Bibring, J-P, 234, 249
 Billideau, J. S., 499
 Bindschadler, D. L., 37
 Bishop, J. L., 240
 Blewett, D., 220, 223, 323
 Blumberg, D., 198
 Bolef, L., 215
 Bonne, U. A., 280
 Boone, L., 447
 Boss, A. P., 419, 422, 444
 Bridges, F., 447
 Bridges, N., 172
 Britt, D. T., 249, 265, 267
 Brown, R. H., 15, 20, 22, 251
 Buratti, B. J., 288, 407
 Burns, J. A., 452
 Burns, R. G., 207, 253, 256, 259
- Calvin, W. M., 244, 251, 294
 Cameron, A. G. W., 444
 Campbell, B., 223
 Campbell, D. B., 308
 Carr, M. H., 187, 215, 218
 Champney, J. M., 427
 Chang, S., 240
 Chapman, C., 215, 218
 Chapman, M. G., 75, 138
 Choe, K. Y., 352
 Clark, R. N., 251, 294
- Clause, C., 415
 Clow, G. D., 199, 201
 Coombs, C. R., 179, 181, 183, 223
 Coyne, L. M., 240
 Craddock, R. A., 143, 459, 462
 Crawford, D. A., 382, 383
 Crisp, J., 165
 Croft, S. K., 95, 98, 101, 373
 Crown, D. A., 65, 167, 468
 Crumpler, L. S., 459
 Cuzzi, J. N., 427, 449
- D'Aria, D. M., 262
 Dale-Bannister, M. A., 306
 Darknell, D., 447
 Davies, M. E., 215, 492, 494, 497
 Davis, P. A., 73, 170
 Davis, D. R., 399, 433
 De Hon, R. A., 140
 Deering, D. W., 304
 Dermott, S. F., 405
 Dobrovolskis, A., 195, 198
 Dobrovolskis, A. R., 427, 449
 Dohm, J. M., 63, 131
 Dominique, D., 291
 Dones, L., 449
 Doose, L., 215
 Doudnikoff, C. E., 477
 Duck, B., 514
 Durda, D., 405
 Durham, W. B., 17
 Durisen, R. H., 449
- Edwards, J. O., 240
 Edwards, K., 512, 514
 Eliason, E. M., 512
 England, A. W., 310
 Erard, S., 234, 249
 Eshleman, V. R., 320
 Evans, D., 296
- Fanale, F. P., 20, 149, 203, 206, 215,
 218, 314, 416
 Farr, T., 296
 Farrand, W. H., 238
 Fink, J., 172
 Fischer, E. M., 218, 236
 Fisher, D. S., 256
 Frank, S. L., 35
 Franklin, B. J., 51

- Frey, H. V., 49, 50, 57, 477
 Fricke, S. K., 85
- Gaddis, L., 195, 198, 215, 218, 296, 313
 Gaffey, M. J., 391
 Ganasan, J. P., 27
 Garcia, P. A., 508
 Gault, D. E., 342
 Geissler, P. E., 191
 Goguen, J. D., 276
 Golombek, M. P., 51, 54, 73, 82
 Gomes, R. S., 405
 Gooding, J. L. 412
 Grant, J. A., 152, 154, 156, 368
 Greeley, R., 59, 61, 65, 93, 104, 163, 167, 194, 195, 198, 215, 218, 296, 313, 468
 Greenberg, R., 215, 218, 438
 Griffiths, R., 172
 Grimm, R. E., 13, 39, 44
 Guinness, E. A., 298, 517
 Guinness, E. E., 306
 Gulick, V. C., 109
 Gurrola, E. M., 320
 Gustafson, B., 405
- Haberle, R. M., 199, 201
 Hager, B. H., 7
 Haines, E. L., 242
 Hansen, G. B., 246
 Hapke, B., 291, 323, 325
 Harding, D. J., 298
 Hartmann, W. K., 347
 Hawke, B. R., 179, 181, 183, 220, 223
 Hayashi, J. N., 370
 Head, J. W., 215, 218, 234, 249
 Heiken, G., 183
 Helfenstein, P., 218, 280, 285
 Henderson, B. G., 229
 Herrick, R. R., 336
 Hiroi, T., 274
 Hoffman, H., 215, 218
 Hogenboom, D. L., 27
 Holmes, N. C., 29
 Holsapple, K. A., 352
 Hood, L. L., 379
 Horn, L., 449
 Horton, K., 220
 Howard, A. D., 114, 117, 120
- Howington-Kraus, A. E., 489, 503, 506
 Huang, Z., 379
 Hudson, R. S., 326
- Inge, J. L., 511, 516
 Irons, J. R., 298
 Isbell, N. K., 75, 515
 Iversen, J., 198
 Iversen, J. D., 195
- Jakosky, B. M., 229
 Janes, D. M., 37
 Jarosewich, E., 262
 Jauman, R., 215, 218
 Jayaraman, S., 405
 Jeanloz, R., 3
 Johnson, N., 123, 125, 127
 Johnson, R. E., 292
 Johnson, T. V., 215, 218, 288
 Jordan, R., 508
 Jurgens, R. F., 315
- Kahle, A. B., 301
 Kale, V. S., 109
 Kargel, J. S., 25, 27, 109, 123, 125, 127, 129
 Kary, D. M., 436, 441
 Kaula, W. M., 420
 Keller, J. M., 160
 Kieffer, S. W., 32
 King, T. V. V., 244, 251, 294
 Kirby, S. H., 17
 Kirk, R. L., 22
 Klaasen, K., 215, 218
 Knight, C., 123, 125
 Kolvoord, R. A., 215, 438
 Komatsu, G., 109, 133
 Kozak, R. C., 515
- Lancaster, N., 195, 198, 296, 313
 Langevin, Y., 234, 249
 Lebofsky, L. A., 271
 Lee, P., 285
 Leovy, C. B., 246
 Lerch, F. J., 85
 Levison, H. F., 397
 Lewis, J. S., 27
 Lin, D., 447
 Lissauer, J. J., 436, 441, 443, 446
 Lockwood, W., 291

- Lucchitta, B. K., 75, 80
 Lucey, P. G., 220, 223
 Lunine, J. I., 210
- Marcialis, R. L., 407
 Marshall, J. R., 194
 Martin, T. Z., 231
 Matson, D. L., 20
 Maxwell, T. A., 143, 462
 McCarthy, D., 285
 McCollom, T. M., 229
 McEwen, A. S., 87, 215, 218, 510, 514
 McGill, G. E., 35, 90, 474
 McKay, D. S., 183
 Melosh, H. J., 350, 354, 355, 357, 359,
 360, 362, 364
 Metzger, A. E., 242
 Mitchell, A. C., 29
 Mongeon, A. M., 477
 Moore, H. J., 158, 160, 170, 315
 Morgan, H. F., 483, 511
 Moroz, L. V., 269
 Mosher, J. A., 288
 Mouginis-Mark, P. J., 174, 370
 Mueller, S., 44
 Murchie, S. L., 215, 218, 249
 Mustard, J. F., 234, 249
 Myhill, E. M., 420
- Namiki, N., 10
 Nash, D. B., 227-228
 Nellis, W. J., 29
 Nerem, R. S., 85
 NeuRum, G., 215, 218
 Nicholson, P. D., 405
- Oberst, J., 215, 218
 O'Brien, T. C., 315
 Orth, C. J., 375
 Ostro, S. J., 326
- Paisley, E. C. I., 313
 Pappalardo, R., 93, 104
 Patel, G. B., 85
 Peterson, C. A., 220, 223
 Petroy, S. B., 296, 301
 Phillips, R. J., 13, 39, 44, 334, 336
 Pieters, C. M., 177, 215, 218, 226, 234,
 236, 240, 249, 265, 267, 269, 274,
 279
- Pilcher, C., 215, 218
 Plaut, J. J., 296
 Plescia, J., 73, 384
 Plescia, J. B., 67, 77
 Plutchak, J., 215, 218
 Porter, T. K., 65, 167
 Postawko, S. E., 203
 Pratt, S. F., 218, 236, 253
 Price, K. H., 465, 468
- Quintana, L. R., 375
- Randall, C. E., 229
 Rasmussen, K. R., 195, 198
 Rice, J. W., Jr., 131
 Robinson, M. S., 174, 215, 218
 Rogers, P. G., 492, 497
 Roth, L. E., 314
 Rotto, S. L., 146
 Russell, J. F., 490
 Ryan, E. V., 350, 354, 399
- Salisbury, J. W., 262
 Salvail, J. R., 20, 149, 416
 Saunders, R. S., 195, 198
 Schaber, G. G., 329, 332
 Schmidt, R. M., 344
 Schneid, B., 163
 Schneid, B. D., 61
 Schubert, G., 37
 Schultz, P. H., 152, 154, 156, 338, 340,
 342, 368, 377, 382, 383
 Schultz, R. A., 49, 50, 57, 70
 Scott, D. H., 63, 131, 407, 479
 Sharpton, V. L., 37
 Shepard, M. K., 296, 304
 Sherman, D. M., 251
 Shkuratov, Y. G., 279
 Shoemaker, C. S., 375, 384, 389
 Shoemaker, E. M., 375, 384, 389, 397
 Showalter, M. R., 449
 Simons, M., 7
 Simpson, R. A., 317
 Singer, R. B., 191, 238
 Slade, M. A., 315
 Slavney, S., 517
 Slavney, S. H., 306
 Smith, D. E., 85

Smrekar, S. E., 41
 Soderblom, L. A., 512
 Solomon, S. C., 7, 10, 35, 41
 Spare, B. A., 499
 Spencer, J. R., 206
 Spudis, P., 220, 223
 Squyres, S. W., 35, 37, 90, 474
 Stacy, N. J. S., 308
 Stankevich, D. G., 279
 Stein, T. C., 306
 Stewart, G. R., 443
 Stofan, E. R., 37
 Stolovy, S. 280
 Straub, D. W., 207
 Strom, R. G., 109, 123, 125, 127, 129,
 131
 Sucharski, R., 483
 Sullivan, R., 215, 218
 Sunshine, J., 215, 218
 Swayze, G. A., 251

 Tanaka, K. L., 54, 70, 73, 82, 135, 138,
 146
 Taylor, G. J., 220, 223
 Taylor, S. R., 375
 Thomas, P. C., 150
 Thomas, P. K., 509
 Thompson, D., 291
 Thompson, T. W., 315
 Tonks, W. B., 355
 Tralli, D., 82
 Tscharnuter, W. M., 419
 Turcotte, D. L., 5
 Tyler, G. L., 317

 Verbiscer, A., 283
 Veverka, J., 215, 218, 280, 283, 285
 Vickery, A. M., 359, 361, 362, 364, 366

 Wall, S., 195, 198
 Ward, W. R., 430
 Warren, S. G., 246
 Weidenschilling, S. J., 399, 424, 433
 Weissman, P. R., 411, 415
 Whipple, F. L., 409
 White, B., 198
 White, B. R., 195
 Wichman, R. W., 377
 Williams, D. A., 59
 Williams, J. G., 403

 Williams, S. H., 471
 Wolfe, R. F., 389, 397
 Wu, S. S. C. 489, 499, 503, 506, 508, 510,
 512

 Xu, Y-L, 405

 Yorke, H. W., 422

 Zent, A. P., 314
 Zimbelman, J. R., 457, 471
 Zisk, S. H., 174
 Zuber, M. T., 85



Report Documentation Page

1. Report No. NASA TM-4300		2. Government Accession No.		3. Recipient's Catalog No.	
4. Title and Subtitle Reports of Planetary Geology and Geophysics Program - 1990				5. Report Date June 1991	
				6. Performing Organization Code SL	
7. Author(s)				8. Performing Organization Report No.	
				10. Work Unit No.	
9. Performing Organization Name and Address NASA Office of Space Science and Applications Solar System Exploration Division Planetary Geosciences Program				11. Contract or Grant No.	
				13. Type of Report and Period Covered Technical Memorandum	
12. Sponsoring Agency Name and Address National Aeronautics and Space Administration Washington, DC 20546				14. Sponsoring Agency Code	
				15. Supplementary Notes	
16. Abstract <p>This is a compilation of abstracts of reports from Principal Investigators of NASA's Planetary Geology and Geophysics Program, Office of Space Science and Applications. The purpose is to document in summary form research work conducted in this program during 1990. Each report reflects significant accomplishments within the area of the author's funded grant or contract.</p>					
17. Key Words (Suggested by Author(s)) planetary geology planetary geophysics solar system evolution planetary geologic processes formation and evolution of planets				18. Distribution Statement Unclassified - Unlimited Subject Category 91	
19. Security Classif. (of this report) Unclassified		20. Security Classif. (of this page) Unclassified		21. No. of pages 612	22. Price A99